

Texte des articles
dans des revues internationales à comité de lecture

Benoît PIER

Laboratoire de mécanique des fluides et d'acoustique
CNRS, École centrale de Lyon, Université Claude-Bernard Lyon 1, INSA Lyon
36 avenue Guy-de-Collongue
69134 Écully

9 avril 2024

- [A1] B. Pier & P. Huerre,
Fully nonlinear global modes in spatially developing media,
Physica D **97**, 206–222 (1996).
doi:10.1016/0167-2789(96)00152-2
<https://hal.archives-ouvertes.fr/hal-00120026>
- [A2] B. Pier, P. Huerre, J.-M. Chomaz & A. Couairon,
Steep nonlinear global modes in spatially developing media,
Physics of Fluids **10**, 2433–2435 (1998).
doi:10.1063/1.869784
<https://hal.archives-ouvertes.fr/hal-00119908>
- [A3] A. Kudrolli, B. Pier & J.P. Gollub,
Superlattice patterns in surface waves,
Physica D **123**, 99–111 (1998).
doi:10.1016/S0167-2789(98)00115-8
<https://hal.archives-ouvertes.fr/hal-00120028>
- [A4] B. Pier, P. Huerre & J.-M. Chomaz,
Bifurcation to fully nonlinear synchronized structures in slowly varying media,
Physica D **148**, 49–96 (2001).
doi:10.1016/S0167-2789(00)00146-9
<https://hal.archives-ouvertes.fr/hal-00119920>
- [A5] B. Pier & P. Huerre,
Nonlinear self-sustained structures and fronts in spatially developing wake flows,
Journal of Fluid Mechanics **435**, 145–174 (2001).
doi:10.1017/S0022112001003652
<https://hal.archives-ouvertes.fr/hal-00119721>
- [A6] B. Pier & P. Huerre,
Nonlinear synchronization in open flows,
Journal of Fluids and Structures **15**, 471–480 (2001).
doi:10.1006/jfls.2000.0349
<https://hal.archives-ouvertes.fr/hal-00119923>
- [A7] B. Pier,
On the frequency selection of finite-amplitude vortex shedding in the cylinder wake,
Journal of Fluid Mechanics **458**, 407–417 (2002).
doi:10.1017/S0022112002008054
<https://hal.archives-ouvertes.fr/hal-00120025>
- [A8] B. Pier,
Open-loop control of absolutely unstable domains,
Proceedings of the Royal Society of London A **459**, 1105–1115 (2003).
doi:10.1098/rspa.2002.1086
<https://hal.archives-ouvertes.fr/hal-00120027>

- [A9] B. Pier,
Finite amplitude crossflow vortices, secondary instability and transition in the rotating-disk boundary layer,
Journal of Fluid Mechanics **487**, 315–343 (2003).
doi:10.1017/S0022112003004981
<https://hal.archives-ouvertes.fr/hal-00120026>
- [A10] B. Pier,
Primary crossflow vortices, secondary absolute instabilities and their control in the rotating-disk boundary layer,
Journal of Engineering Mathematics **57**, 237–251 (2007).
doi:10.1007/s10665-006-9095-5
<https://hal.archives-ouvertes.fr/hal-00197478>
- [A11] B. Pier,
Local and global instabilities in the wake of a sphere,
Journal of Fluid Mechanics **603**, 39–61 (2008).
doi:10.1017/S0022112008000736
<https://hal.archives-ouvertes.fr/hal-00206267>
- [A12] B. Pier,
Signalling problem in absolutely unstable systems,
Theoretical and Computational Fluid Dynamics **25**, 7–17 (2011).
doi:10.1007/s00162-009-0166-x
<https://hal.archives-ouvertes.fr/hal-00426387>
- [A13] M. E. Siddiqui, V. Mukund, J. Scott & B. Pier,
Experimental characterization of transition region in rotating-disk boundary layer,
Physics of Fluids **25**, 034102 (10 pages) (2013).
doi:10.1063/1.4798435
<https://hal.archives-ouvertes.fr/hal-00806379>
- [A14] B. Pier,
Periodic and quasiperiodic vortex shedding in the wake of a rotating sphere,
Journal of Fluids and Structures **41**, 43–50 (2013).
doi:10.1016/j.jfluidstructs.2012.09.002
<https://hal.archives-ouvertes.fr/hal-00733514>
- [A15] C. Leclercq, B. Pier & J. Scott,
Temporal stability of eccentric Taylor–Couette–Poiseuille flow,
Journal of Fluid Mechanics **733**, 68–99 (2013).
doi:10.1017/jfm.2013.437
<https://hal.archives-ouvertes.fr/hal-00865631>
- [A16] B. Pier,
Transition near the edge of a rotating disk,
Journal of Fluid Mechanics **737**, R1 (9 pages) (2013).
doi:10.1017/jfm.2013.578
<https://hal.archives-ouvertes.fr/hal-00907846>

- [A17] C. Leclercq, B. Pier & J. Scott,
Absolute instabilities in eccentric Taylor–Couette–Poiseuille flow,
Journal of Fluid Mechanics **741**, 543–566 (2014).
doi:10.1017/jfm.2013.646
<https://hal.archives-ouvertes.fr/hal-00948589>
- [A18] S. S. Gopalakrishnan, B. Pier & A. Biesheuvel,
Global stability analysis of flow through a fusiform aneurysm : steady flows,
Journal of Fluid Mechanics **752**, 90–106 (2014).
doi:10.1017/jfm.2014.292
<https://hal.archives-ouvertes.fr/hal-01084523>
- [A19] S. S. Gopalakrishnan, B. Pier & A. Biesheuvel,
Dynamics of pulsatile flow through modal abdominal aortic aneurysms,
Journal of Fluid Mechanics **758**, 150–179 (2014).
doi:10.1017/jfm.2014.535
<https://hal.archives-ouvertes.fr/hal-01084537>
- [A20] B. Pier & N. Peake,
Global modes with multiple saddle points,
European Journal of Mechanics B-Fluids **49**, 335–344 (2015).
doi:10.1016/j.euromechflu.2014.03.006
<https://hal.archives-ouvertes.fr/hal-01084705>
- [A21] M. P. Juniper & B. Pier,
The structural sensitivity of open shear flows calculated with a local stability analysis,
European Journal of Mechanics B-Fluids **49**, 426–437 (2015).
doi:10.1016/j.euromechflu.2014.05.011
<https://hal.archives-ouvertes.fr/hal-01084708>
- [A22] S. Derebail Muralidhar, B. Pier, J. F. Scott & R. Govindarajan,
Flow around a rotating, semi-infinite cylinder in an axial stream,
Proceedings of the Royal Society A **752**, 20150850 (17 pages) (2016).
doi:10.1098/rspa.2015.0850
<https://hal.archives-ouvertes.fr/hal-01330462>
- [A23] S. Derebail Muralidhar, B. Pier & J. F. Scott,
Instability of flow around a rotating, semi-infinite cylinder,
Physical Review Fluids **1**, 053602 (15 pages) (2016).
doi:10.1103/PhysRevFluids.1.053602
<https://hal.archives-ouvertes.fr/hal-01368877>
- [A24] B. Pier & P. J. Schmid,
Linear and nonlinear dynamics of pulsatile channel flow,
Journal of Fluid Mechanics **815**, 435–480 (2017).
doi:10.1017/jfm.2017.58
<https://hal.archives-ouvertes.fr/hal-01385093>
- [A25] S. Jose, V. Kuzhimpampil, B. Pier & R. Govindarajan,
Algebraic disturbances and their consequences in rotating channel flow transition,
Physical Review Fluids **2**, 083901 (25 pages) (2017).
doi:10.1103/PhysRevFluids.2.083901
<https://hal.archives-ouvertes.fr/hal-01578604>

- [A26] B. Pier & R. Govindarajan,
Nonlinear travelling waves in rotating Hagen–Poiseuille flow,
Fluid Dynamics Research **50**, 031402 (14 pages) (2018).
doi:10.1088/1873-7005/aaaa9f
<https://hal.archives-ouvertes.fr/hal-01693277>
- [A27] B. Pier & P. J. Schmid,
Optimal energy growth in pulsatile channel and pipe flows,
Journal of Fluid Mechanics **926**, A11 (34 pages) (2021).
doi:10.1017/jfm.2021.702
<https://hal.archives-ouvertes.fr/hal-03084366>
- [A28] S. Lebbal, F. Alizard & B. Pier,
Revisiting the linear instabilities of plane channel flow between compliant walls,
Physical Review Fluids **7**, 023903 (32 pages) (2022).
doi:10.1103/PhysRevFluids.7.023903
<https://hal.archives-ouvertes.fr/hal-03337441>
- [A29] N. Poumaëre, F. Raynal & B. Pier,
Residence time distributions for in-line chaotic mixers,
Physical Review E **106**, 015107 (13 pages) (2022).
doi:10.1103/PhysRevE.106.015107
<https://hal.archives-ouvertes.fr/hal-03727867>
- [A30] S. Lebbal, F. Alizard & B. Pier,
Linear instabilities of pulsatile plane channel flow between compliant walls,
Journal of Fluid Mechanics **948**, A15 (32 pages) (2022).
doi:10.1017/jfm.2022.658
<https://hal.archives-ouvertes.fr/hal-03559481>
- [A31] F. Alizard, B. Pier & S. Lebbal,
Transient energy growth in channel flow with compliant walls,
Physical Review Fluids **9**, 043905 (26 pages) (2024).
doi:10.1103/PhysRevFluids.9.043905
<https://hal.archives-ouvertes.fr/hal-04512520>

[A1]

Fully nonlinear global modes in spatially developing media

B. Pier & P. Huerre

Physica D **97**, 206–222 (1996)

doi:10.1016/0167-2789(96)00152-2

<https://hal.archives-ouvertes.fr/hal-00120026>



ELSEVIER

Physica D 97 (1996) 206–222

PHYSICA D

Fully nonlinear global modes in spatially developing media

Benoît Pier, Patrick Huerre *

Laboratoire d'Hydrodynamique (LadHyX), École Polytechnique, F-91128 Palaiseau Cedex, France

Abstract

Global modes on a doubly infinite one-dimensional domain $-\infty < x < +\infty$ are studied in the context of the complex Ginzburg–Landau equation with slowly spatially varying coefficients, i.e., coefficients depending only on a slow streamwise coordinate $X = \epsilon x$, where ϵ is a small parameter. A fully nonlinear frequency selection criterion is derived for global mode solutions under the assumption of weak inhomogeneity of the medium. The global mode is found to be governed by the fully nonlinear equations in a region of finite size, and by the linearized equations in the vicinity of $X = \pm\infty$. Asymptotic matching techniques are used to relate the WKBJ approximations in the linear and nonlinear regions through appropriate transition layers. The *real* global frequency is determined by requiring that spatial branches issuing from $X = -\infty$ and $X = +\infty$ be continuously connected at a saddle point of the local nonlinear dispersion relation $\omega = \Omega^{nl}(k, R^2, X)$ between the frequency ω , the wave number k and amplitude R at a given station X . The results constitute a fully nonlinear generalization of the linear frequency selection criteria previously obtained by Chomaz et al. (1991), Monkewitz et al. (1993), and Le Dizès et al. (1996).

1. Introduction

Our present understanding of hydrodynamic instabilities relies, to a great extent, on the scientific achievements of Fritz Busse and his colleagues. For instance, an intimate knowledge of the Busse balloon [3] has indeed become prerequisite reading to any serious student of Rayleigh–Bénard convection in a fluid layer heated from below, one of the most widely studied closed flow systems. This is just one example of Fritz Busse's fundamental and lasting contributions to hydrodynamics. Fritz has devoted a relatively small portion of his boundless energy to the study of open shear flows, which may explain why our comprehension of instabilities in open flows may have not reached the same fully mature stage. This contribution, which is dedicated to Fritz Busse in celebration of his 60th birthday, illustrates one possible approach which could be successful in spatially developing open flows exhibiting a global resonance.

Spatially developing flows may, under certain conditions, develop self-sustained oscillations. Fluctuations saturate at a finite amplitude in the locally unstable regions of the flow and become tuned at an overall frequency. The intrinsic frequency and the associated spatial distribution of fluctuations define a *global mode*. Relatively little is known regarding the nonlinear evolution stage of such objects. Chomaz [4] and Couairon and Chomaz [7] have

* Corresponding author.

recently introduced generalized definitions of absolute, convective and global instability applicable to the fully nonlinear case and demonstrated that linear absolute instability is not always synonymous with global instability. Furthermore, these authors have brought to light the close relationship existing between the dynamical systems point of view and the more classical description in terms of a dispersion relation. The goal of the present study is the derivation of a *fully nonlinear* global mode selection criterion in the context of the one-dimensional complex Ginzburg–Landau equation with slowly varying coefficients.

The main stability concepts pertaining to spatially developing open flows have been reviewed by Huerre and Monkewitz [11]. Recent developments have been discussed in Le Dizès et al. [16]. It is here sufficient to recall that specific classes of spatially developing open flows such as bluff-body wakes [9,13,18,24], low density jets [19,23] and counterflow mixing layers [25] may sustain in specific parameter ranges synchronized periodic oscillations over an extended region of the flow. In other words, such systems undergo a Hopf bifurcation as some control parameter is continuously varied. Global mode concepts have precisely been introduced to account for this peculiar behavior of open flows.

In most basic flows of interest, the velocity profile is nonuniform in the streamwise direction, and in order to distinguish between local and global properties it is essential to assume that streamwise variations are slow over a typical instability wavelength. Under this hypothesis, local stability properties are obtained within the parallel flow approximation by freezing the slow streamwise coordinate X . At the local level of description, linear stability properties of normal modes $e^{i(kx-\omega t)}$ are then characterized by a local dispersion relation $D(k, \omega, X) = 0$ between complex wave number k and frequency ω . The goal of a global analysis is to construct in a self-consistent manner a global spatial distribution made up of saturated instability waves governed by the local properties of the flow. The global frequency ω_g is then considered as an eigenvalue to be determined by requiring that perturbations decay at $X = \pm\infty$. The resulting global mode is viewed as a theoretical analog of the self-sustained oscillatory structures that are observed experimentally.

The analysis by Chomaz et al. [6] of the linearized Ginzburg–Landau equation with slowly varying coefficients has demonstrated that a region of absolute instability is a necessary condition for linearly unstable global modes to exist. The dominant complex global frequency ω_g is obtained, at leading order in the WKBJ approximation, for a saddle point of the local linear dispersion relation $\omega = \Omega^\ell(k_s, X_s)$, i.e.,

$$\omega_g \sim \omega_s = \Omega^\ell(k_s, X_s), \quad (1)$$

where the complex pair (k_s, X_s) satisfies

$$\frac{\partial \Omega^\ell}{\partial k}(k_s, X_s) = \frac{\partial \Omega^\ell}{\partial X}(k_s, X_s) = 0. \quad (2)$$

The same linear frequency selection criterion has been derived by Monkewitz et al. [20] in the framework of the Navier–Stokes equations linearized around an arbitrary weakly nonparallel basic flow. More recently, the frequency selection criterion pertaining to the Ginzburg–Landau equation over a doubly infinite domain has been examined anew by resorting to a comparison equation method [16]. It has been shown that global modes are either of type 1, with two simple turning points in the complex X -plane, or type 2, with a double turning point as defined in (2). The validity of the selection criterion (2) has further been confirmed by the exact Green function calculations of Hunt and Crighton [12].

The extension of these concepts to the nonlinear régime has until recently appeared somewhat problematic. It seems, at first sight, natural to perform a weakly nonlinear analysis in the vicinity of the global mode onset. Such an approach is straightforward for nonparallel effects of *order unity*, as shown by Chomaz et al. [5] in the case of the Ginzburg–Landau equation with a linearly or quadratically varying control parameter. Paradoxically, the introduction of a weakly nonparallel assumption in addition to the weakly nonlinear one leads to unexpected

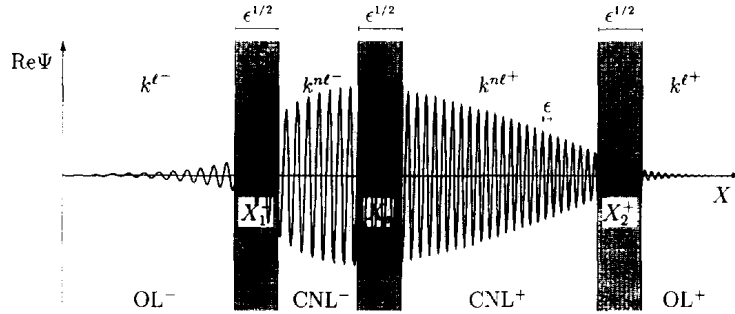


Fig. 1. Fully nonlinear global mode spatial structure: OL^\pm , outer semi-infinite linear regions close to $X = \pm\infty$; $TL^{1,2}$, transition layers of thickness $O(\epsilon^{1/2})$ connecting linear and nonlinear regions; CNL^\pm , central nonlinear regions of size $O(1)$; SP, saddle point region of thickness $O(\epsilon^{1/2})$.

difficulties [16]: in the limit of zero nonparallelism, the Landau constant does not converge to a well-defined limit of *constant* sign. In other words, the Landau equation formalism which purportedly describes a Hopf bifurcation near onset does not apply unless drastic conditions are met. In order to circumvent these difficulties, we choose in the present study to jump to the fully nonlinear régime while keeping the weakly nonparallel assumption. Thus we implement a nonlinear WKBJ approximation scheme which remains valid for amplitudes of order unity, as encountered in the phase dynamics of patterns [8,15,17,21] or in the description of slowly varying fully nonlinear wavetrains [2,10].

The main objective of the paper is the generalization of the linear frequency selection criterion (1), (2) to fully nonlinear global modes provided that the local nonlinear dispersion relation of the weakly inhomogenous flow is given. We should emphasize that, in contrast to the linear criterion, the present formulation will only involve purely real values of the wave number, frequency and local streamwise variable. In the present study there is no need to extend analytically the dispersion relation in the complex k -plane and X -plane, a feature which considerably simplifies the analysis.

The inhomogeneities of the medium are characterized by a small parameter

$$\epsilon \sim \lambda/L \ll 1, \quad (3)$$

where L is a typical evolution length scale of the basic flow and λ a typical wavelength of the instability. Under the assumption $\epsilon \ll 1$, global mode solutions depend on two different length scales: a fast space variable x related to the rapid spatial oscillations of the carrier wave and a slow variable $X = \epsilon x$ describing the slow spatial evolution of the “basic flow”. Fluctuations $\Psi(x, t)$ around a given basic state are governed by a partial differential equation, the coefficients of which depend on the slow variable X . The local properties of the flow are then recovered by freezing X . This separation of scales calls for an analysis in terms of nonlinear WKBJ approximations: the slowly evolving local characteristics may be exploited to construct global mode solutions composed of slowly varying nonlinear wavetrains.

In the course of the study, we are led to distinguish different regions characterizing the global mode spatial structure, as sketched in Fig. 1. In central nonlinear regions of finite size (CNL^\pm) the wave has finite amplitude and satisfies the fully nonlinear governing equation of the problem. These central nonlinear regions are surrounded by two semi-infinite outer linear regions (OL^\pm) where the global mode satisfies the linearized equation and is exponentially decaying towards infinity, as required by the boundary conditions. Transition layers ($TL^{1,2}$) of size $\epsilon^{1/2}$ (measured in units of X) allow a smooth crossover from the central nonlinear regions (CNL^\pm) into the outer linear regions (OL^\pm). As shown later, the existence of a nonlinear global mode requires two wave number branches to meet in the core of the nonlinear regions, at a saddle point of the local nonlinear dispersion relation. An additional

internal layer (SP) of size $\epsilon^{1/2}$ around this saddle point needs to be introduced in order to generate the nonlinear frequency selection criterion at arbitrary order. The selection mechanism is therefore entirely determined by the saddle point structure. Thus this inner transition layer (SP) is surrounded by nonlinear regions of finite extent (CNL^\pm) which in turn are connected through transition layers ($TL^{1,2}$) to the outer linear regions (OL^\pm) extending towards infinity.

The organization of the present paper reflects the global mode structure. The global mode problem is stated in Section 2 and the linear WKBJ approximations pertaining to the outer regions (OL^\pm) are recalled in Section 3. Corresponding nonlinear WKBJ solutions relevant to the central nonlinear regions (CNL^\pm) are derived in Section 4. In Section 5 the leading order nonlinear frequency selection criterion is obtained in the following form: *a global mode can only be constructed if two wave number branches meet at a saddle point in the bulk of the nonlinear regions.* The structure of the transition layers connecting linear and nonlinear regions is analyzed in Section 6. In closing we summarize the main conclusions and address some future developments.

2. Nonlinear eigenvalue problem

Throughout the study, complex scalar fluctuations $\Psi(x, t)$ around a given basic state are assumed to be governed by a nonlinear equation of the form

$$i\frac{\partial\Psi}{\partial t} = \Omega^{nl}\left(-i\frac{\partial}{\partial x}, |\Psi|^2, X\right)\Psi, \quad (4)$$

where $X = \epsilon x$ is a slow space variable which describes the inhomogeneities of the medium and ϵ is the WKBJ parameter introduced in (3). The operator Ω^{nl} is the physical space counterpart of the local nonlinear dispersion relation $\omega = \Omega^{nl}(k, R^2, X)$ to be defined later.

A nonlinear global mode is then defined as a time-periodic solution of Eq. (4) of *real* frequency ω , satisfying vanishing boundary conditions at infinity. Thus it can be written as

$$\Psi(x, t) = \psi(x, \omega)e^{-i\omega t},$$

where the global frequency ω and the amplitude ψ are governed by the differential equation

$$\left[\omega - \Omega^{nl}\left(-i\frac{\partial}{\partial x}, |\psi|^2, X\right)\right]\psi = 0 \quad (5)$$

with the boundary conditions

$$\lim_{x \rightarrow \pm\infty} \psi(x, \omega) = 0. \quad (6)$$

In the particular case of the complex Ginzburg–Landau equation [11],

$$i\frac{\partial\Psi}{\partial t} = (\omega_0(X) + \frac{1}{2}\omega_{kk}(X)k_0^2(X))\Psi + i\omega_{kk}(X)k_0(X)\frac{\partial\Psi}{\partial x} - \frac{1}{2}\omega_{kk}(X)\frac{\partial^2\Psi}{\partial x^2} + \gamma(X)|\Psi|^2\Psi, \quad (7)$$

the nonlinear dispersion operator Ω^{nl} may be separated into linear and nonlinear parts as

$$\Omega^{nl}\left(-i\frac{\partial}{\partial x}, |\Psi|^2, X\right) \equiv \Omega^\ell\left(-i\frac{\partial}{\partial x}, X\right) + \gamma(X)|\Psi|^2,$$

where the linear dispersion operator Ω^ℓ reads

$$\Omega^\ell\left(-i\frac{\partial}{\partial x}, X\right) \equiv \omega_0(X) + \frac{1}{2}\omega_{kk}(X)k_0^2(X) + i\omega_{kk}(X)k_0(X)\frac{\partial}{\partial x} - \frac{1}{2}\omega_{kk}(X)\frac{\partial^2}{\partial x^2}. \quad (8)$$

The complex functions $\omega_0(X)$, $\omega_{kk}(X)$, $k_0(X)$, and $\gamma(X)$ which solely depend on the slow space variable X account for the weak inhomogeneities of the medium and their meaning is discussed in Section 3.

The goal of the present study is to solve the nonlinear eigenvalue problem (5),(6) where the global mode amplitude ψ is $O(1)$ in an interval of finite extent. We construct such global mode solutions in the régime $\epsilon \ll 1$ and determine how the global frequencies ω_g depend on the characteristics of the “basic flow”, as specified by the nonlinear dispersion relation.

Since global modes must decay at infinity, they are governed by the linearized equation for sufficiently large X . The solutions of the associated linear equation are therefore required in outer linear regions (OL^\pm), as reviewed in Section 3.

3. Outer linear WKBJ regions OL^\pm

In the present section we examine the structure of the outer linear regions (OL^\pm) in Fig. 1 and recall the main features of the solutions of the linearized equation

$$i\frac{\partial\Psi}{\partial t} = \Omega^\ell \left(-i\frac{\partial}{\partial x}, X \right) \Psi \quad (9)$$

for an arbitrary frequency ω of order unity, as studied by Chomaz et al. [6] and Le Dizès et al. [16].

Upon substituting $\partial/\partial x \rightarrow ik$ and $\partial/\partial t \rightarrow -i\omega$ in (8) and (9) one obtains the associated local linear dispersion relation of the Ginzburg–Landau model in the form

$$\omega = \Omega^\ell(k, X) \equiv \omega_0(X) + \frac{1}{2}\omega_{kk}(X)(k - k_0(X))^2. \quad (10)$$

In order to enforce causality we assume throughout that sufficiently large wave numbers are damped, i.e., $\omega_{kk,i}(X) \equiv \text{Im}[\omega_{kk}(X)] < 0$ for all X . According to (10) the frequency ω is a simple quadratic function of the complex wave number k . Thus there exist for each value of the frequency two linear spatial branches given by

$$k_i^{\ell\pm}(X, \omega) \equiv k_0(X) \pm \sqrt{2\frac{\omega - \omega_0(X)}{\omega_{kk}(X)}}. \quad (11)$$

Under the assumption $\omega_{kk,i}(X) < 0$ for all X , the square root branch in (11) can always be chosen such that $k_i^{\ell+}(X) > 0$ and $k_i^{\ell-}(X) < 0$ for large enough ω . The introduction of the functions $k_0(X)$ and $\omega_0(X)$ may now be justified: at each station X , k_0 and ω_0 denote the complex absolute wave number and frequency defined by $(\partial\Omega^\ell/\partial k)(k_0, X) = 0$, $\omega_0 = \Omega^\ell(k_0, X)$, as extensively discussed in [11]. In other words, $\omega_0(X)$ is a branch point of the function $k^\ell(X, \omega)$ in the complex ω -plane, as clearly displayed in (11).

Under the slowly varying medium hypothesis ($\epsilon \ll 1$) a solution of Eq. (9) with frequency ω can be obtained in terms of WKBJ approximations [1]. The spatial behavior of the solution is described by a rapidly varying phase, corresponding to the local wave number, and a slowly varying envelope which, for a given value of the frequency ω , read

$$\psi^\ell(X, \omega) = A^\ell(X, \omega) \exp \frac{i}{\epsilon} \int_s^X k^\ell(s, \omega) ds, \quad (12)$$

where $k^\ell(X, \omega)$ is one of the spatial branches (11).

In classical WKBJ fashion, the envelope¹ $A^\ell(X)$ is expanded in powers of ϵ

$$A^\ell(X) \sim A_0^\ell(X) + \epsilon A_1^\ell(X) + \epsilon^2 A_2^\ell(X) + \dots, \quad (13)$$

and the spatial derivative operator is decomposed into

$$\partial_x = ik^\ell(X) + \epsilon \partial_X. \quad (14)$$

Upon substituting (12)–(14) into the governing equation (9), one obtains

$$\omega(A_0^\ell + \epsilon A_1^\ell + \dots) = \Omega^\ell(k^\ell(X) - i\epsilon \partial_X, X)(A_0^\ell + \epsilon A_1^\ell + \dots). \quad (15)$$

Note that differentiation with respect to the fast variable, i.e., multiplication by $ik^\ell(X)$, does not commute with the slow derivative operator ∂_X [14]. Thus $\Omega^\ell(k^\ell(X) - i\epsilon \partial_X)$ admits the expansion

$$\begin{aligned} \Omega^\ell(k^\ell(X) - i\epsilon \partial_X) &= \Omega^\ell - i\epsilon \frac{1}{2}(\Omega_k^\ell \partial_X + \partial_X \Omega_k^\ell) + O(\epsilon^2) \\ &= \Omega^\ell - i\epsilon(\Omega_k^\ell \partial_X + \frac{1}{2}\Omega_{kk}^\ell k_X^\ell(X)) + O(\epsilon^2). \end{aligned} \quad (16)$$

On the r.h.s. of these equations, Ω^ℓ and its derivatives with respect to k are evaluated at $k^\ell(X)$. In Eq. (15) the slow derivative operator ∂_X only applies to the wave function, hence to $k^\ell(X)$, but *not* to the second argument X of $\Omega^\ell(k, X)$.

At lowest order, Eq. (15) reduces to the dispersion relation (10), which yields the local wave number $k^\ell(X)$ in terms of ω , as given by (11).

At order ϵ , we obtain

$$[\omega - \Omega^\ell(k^\ell(X), X)]A_1^\ell = -i\Omega_k^\ell(X) \frac{dA_0^\ell}{dX} - \frac{i}{2}\Omega_{kk}^\ell(X)k_X^\ell(X)A_0^\ell$$

with the notations

$$\Omega_k^\ell(X) = \frac{\partial \Omega^\ell}{\partial k}(k^\ell(X), X) \quad \text{and} \quad \Omega_{kk}^\ell(X) = \frac{\partial^2 \Omega^\ell}{\partial k^2}(k^\ell(X), X).$$

By invoking the local dispersion relation (10), one obtains the obvious solvability condition for A_0^ℓ :

$$\frac{dA_0^\ell}{dX} = -\frac{1}{2}k_X^\ell(X) \frac{\Omega_{kk}^\ell(X)}{\Omega_k^\ell(X)} A_0^\ell(X).$$

Thus, at first order, the solution of the linearized equation reads

$$\psi^\ell(X) \sim A_0^\ell(X_1) \exp\left(-\frac{1}{2} \int_{X_1}^X k_X^\ell(s) \frac{\Omega_{kk}^\ell(s)}{\Omega_k^\ell(s)} ds\right) \exp\left(\frac{i}{\epsilon} \int_{X_1}^X k^\ell(s) ds\right), \quad (17)$$

where X_1 is some arbitrarily specified reference point.

The linear Ginzburg–Landau equation admits two spatial branches $k^{\ell\pm}(X)$ given by (11); thus Eq. (17) yields two WKBJ approximations $\psi^{\ell\pm}(X)$ for two linearly independent solutions of Eq. (9). Let us assume that $k_i^{\ell+}(X) > 0$ and $k_i^{\ell-}(X) < 0$ for sufficiently large $|X|$ (for a discussion of the relationship between this assumption and causality see [16]). Under this assumption the WKBJ approximation $\psi^{\ell-}(X)$ is subdominant when $X \rightarrow -\infty$, i.e., exponentially

¹ For simplicity we no longer explicitly mention the frequency dependence.

small with respect to $\psi^{\ell+}(X)$; similarly the solution $\psi^{\ell+}(X)$ becomes subdominant for $X \rightarrow +\infty$. Boundary conditions (6) require the choice of $\psi^{\ell\pm}(X)$ for $X \rightarrow \pm\infty$. A global mode solution is thus solely composed of the branch $k^{\ell-}$ for $X \rightarrow -\infty$ and of the branch $k^{\ell+}$ for $X \rightarrow +\infty$. In the following sections a nonlinear solution is derived which allows a smooth crossover from one linear branch to the other as X varies from $-\infty$ to $+\infty$.

4. Central nonlinear WKBJ regions CNL^\pm

In this section a *fully nonlinear* solution of Eq. (4) is constructed in the central regions (CNL^\pm) of Fig. 1 by means of the nonlinear dispersion relation, for an arbitrary frequency of order unity.

Let us first consider in the same notations as Eq. (4) the *homogenous* nonlinear equation with *constant* coefficients

$$i\frac{\partial\Psi}{\partial t} = \Omega^{n\ell} \left(-i\frac{\partial}{\partial x}, |\Psi|^2 \right) \Psi.$$

This equation admits nonlinear travelling wave Stokes solutions of the form

$$\Psi(x, t) = R e^{i(kx - \omega t)}, \quad (18)$$

where the amplitude R , wave number k , and frequency ω are *real* parameters bound by the *nonlinear* dispersion relation

$$\omega = \Omega^{n\ell}(k, R^2). \quad (19)$$

This complex equation completely defines the family of solutions (18). It is also convenient to introduce a *reduced nonlinear dispersion relation* as follows.

Taking the imaginary part of complex equation (19) shows that the amplitude R^2 is slaved to the wave number k and is implicitly given by

$$0 = \Omega_i^{n\ell}(k, R^2).$$

Replacing the amplitude R^2 as a function of k in the real part of (19),

$$\omega = \Omega_r^{n\ell}(k, R^2),$$

yields the reduced nonlinear dispersion relation in the form

$$\omega = \Omega^{\text{NL}}(k) \equiv \Omega_r^{n\ell}(k, R^2(k)).$$

This reduced form clearly demonstrates that Stokes travelling waves (18) indeed constitute a one-parameter family of finite amplitude solutions, of real parameter k .

In the context of the complex Ginzburg–Landau model (7), the *complete* nonlinear dispersion relation reads

$$\omega = \Omega^{n\ell}(k, R^2) \equiv \omega_0 + \frac{1}{2}\omega_{kk}(k - k_0)^2 + \gamma R^2 = \Omega^\ell(k) + \gamma R^2, \quad (20)$$

and the reduced dispersion relation may explicitly be determined by following the procedure outlined above. Extracting R^2 from the imaginary part of (20), one finds

$$R^2 = \frac{\text{Im}[\Omega^\ell(k)]}{\text{Im}[\gamma^*]}, \quad (21)$$

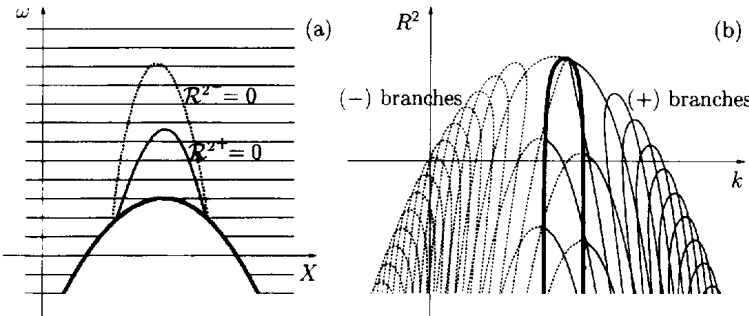


Fig. 2. Nonlinear spatial branches in the $X-\omega$ and $k-R^2$ planes. In (a) the horizontal lines $\omega = \text{const.}$ indicate in the $X-\omega$ plane the allowable domain, delineated by the bold critical curve, where the nonlinear dispersion relation (23) admits real solutions in the $k-R^2$ plane sketched in (b). Each of the lines $\omega = \text{const.}$ is mapped into two spatial branches $(k^{n\ell^\pm}(X), R^{2\pm}(X))$ in the $k-R^2$ plane: the $(+)$ branches are represented by solid curves, the $(-)$ branches by dotted curves. For frequencies such that the line $\omega = \text{const.}$ intersects the boundary of the allowable domain (bold curve in (a)), the two branches in the $k-R^2$ plane meet at the corresponding image critical curve (bold curve in (b)). The subregions of the allowable domain corresponding to $R^2 > 0$ are delimited in (a) by the curves $\mathcal{R}^{2+}(X, \omega) = 0$ (solid) and $\mathcal{R}^{2-}(X, \omega) = 0$ (dotted).

where a * superscript denotes the complex conjugate, and by substitution into the real part of (20), one readily obtains the reduced nonlinear dispersion relation

$$\omega = \Omega^{\text{NL}}(k) = \frac{\text{Im}[\gamma^* \Omega^\ell(k)]}{\text{Im}[\gamma^*]}. \quad (22)$$

Since (22) is quadratic in k , to each frequency ω are associated, under suitable conditions, two nonlinear spatial branches $k^{n\ell^\pm}(\omega)$, and, via (21), two amplitudes $R^{2\pm}(\omega)$. Thus the complete nonlinear dispersion relation (20) is seen to possess two pairs of solutions

$$(k, R^2) = (k^{n\ell^\pm}(\omega), R^{2\pm}(\omega)).$$

Such pairs of solutions only exist if (20) can be solved for *real* k and *real non-negative* R^2 . For given coefficients in (20) these conditions correspond to a range of allowable frequencies.

In a *weakly inhomogeneous* medium where the coefficients of the nonlinear equation are now functions of the slow space variable X (Eqs. (4) and (7)), a *local* nonlinear dispersion relation may still be derived of the form

$$\omega = \Omega^{n\ell}(k, R^2, X) \equiv \omega_0(X) + \frac{1}{2}\omega_{kk}(X)(k - k_0(X))^2 + \gamma(X)R^2 = \Omega^\ell(k, X) + \gamma(X)R^2, \quad (23)$$

and the corresponding local reduced nonlinear dispersion relation may be formally expressed as

$$\omega = \Omega^{\text{NL}}(k, X) \equiv \frac{\text{Im}[\gamma^*(X)\Omega^\ell(k, X)]}{\text{Im}[\gamma^*(X)]}. \quad (24)$$

Local wave number and amplitude are obtained in the same way as in the homogenous case; they are real functions of the frequency and the slow space variable:

$$(k, R^2) = (k^{n\ell^\pm}(X, \omega), R^{2\pm}(X, \omega)), \quad (25)$$

solutions of (23) and (24).

Let us now examine the properties of the double-valued mapping between the $X-\omega$ and $k-R^2$ planes defined by solution pairs (25). The $X-\omega$ plane separates into an allowable region where two *real* solution pairs (25) satisfy the local nonlinear dispersion relation (23) and a region where no such real solutions are obtained (Fig. 2(a)). For given X , real wave number solutions of the quadratic equation (24) are found to exist when $\omega \rightarrow +\infty(-\infty)$ if $\omega_{kk,r} - \omega_{kk,i}\gamma_r/\gamma_i > 0(< 0)$. Let us assume that $\omega_{kk,r}(X) - \omega_{kk,i}(X)\gamma_r(X)/\gamma_i(X) > 0$ for all X . As ω decreases

for a given X , the two pairs merge at a critical value of ω when the discriminant of the quadratic equation (24) vanishes. The set of such points in the X - ω plane defines the critical line (bold curve of Fig. 2(a)), i.e., the boundary of the allowable domain indicated by the hatched region of Fig. 2(a). Below this critical line the nonlinear dispersion relations (23) or (24) admit no real solutions. Each point (X, ω) of the allowable domain then maps into two points in the k - R^2 plane (Fig. 2(b)) through the mapping functions (25). A solution of real uniform frequency is in fact represented in the X - ω plane by a straight horizontal line $\omega = \text{const}$. As X varies for a given ω , solutions of eq.(25) move along two distinct branches $(k^{n\ell+}(X), R^{2+}(X))$ and $(k^{n\ell-}(X), R^{2-}(X))$ in the k - R^2 plane, as indicated by the continuous and dashed curves in Fig. 2(b). If the line $\omega = \text{const}$. is high enough and does not meet the critical line delimiting the allowable domain in the X - ω plane, the two corresponding branches in the k - R^2 plane do not intersect; if by contrast the horizontal line $\omega = \text{const}$. is not entirely contained in the allowable hatched domain, spatial branches in the k - R^2 plane are not defined for the portion of the line situated outside the allowable domain. In fact, upon hitting the critical line in the X - ω plane, (+) and (−) branches in the k - R^2 plane meet along the image of the critical line (bold curve of Fig. 2(b)) and cease to exist.

Note also that each branch of (25) has physical meaning only if $R^2 \geq 0$. Thus the subregions of the allowable domain, where meaningful nonlinear solutions are obtained, are further restricted to $R^{2\pm}(X, \omega) \geq 0$. These regions are located within the curves labelled $R^{2+} = 0$ and $R^{2-} = 0$ in Fig. 2(a). If one assumes $\gamma_1(X) < 0$ uniformly in X (locally supercritical behavior), the condition $R^{2\pm}(X, \omega) \geq 0$ corresponds to linearly unstable wave numbers $k^{n\ell\pm}(X, \omega)$, as seen by inspection of (21). Elsewhere in the X - ω plane, $R^{2\pm}(X, \omega) < 0$, nonlinear solutions pertaining to (+) or (−) branches do not exist and only linear solutions are allowed.

As in the outer linear regions, the spatial distribution is taken to be a rapidly oscillating wave modulated by a slowly varying envelope

$$\psi^{n\ell}(X) = A^{n\ell}(X) \exp \frac{i}{\epsilon} \int_s^X k^{n\ell}(s) ds. \quad (26)$$

Upon expanding the envelope in powers of ϵ

$$A^{n\ell}(X) \sim A_0^{n\ell}(X) + \epsilon A_1^{n\ell}(X) + \epsilon^2 A_2^{n\ell}(X) + \dots,$$

interpreting the spatial derivatives as

$$\partial_x = ik^{n\ell}(X) + \epsilon \partial_X,$$

and substituting these expansions into Eq. (4), one readily obtains the nonlinear counterpart of (15), i.e.,

$$\omega(A_0^{n\ell} + \epsilon A_1^{n\ell} + \dots) = \Omega^{n\ell}(k^{n\ell}(X) - i\epsilon \partial_X, |A_0^{n\ell} + \epsilon A_1^{n\ell} + \dots|^2, X)(A_0^{n\ell} + \epsilon A_1^{n\ell} + \dots). \quad (27)$$

At lowest order, we recover the local nonlinear dispersion relation (23), i.e.,

$$\omega = \Omega^{n\ell}(k^{n\ell}(X), |A_0^{n\ell}(X)|^2, X), \quad (28)$$

which determines the local wave number $k^{n\ell}(X)$ and the leading order amplitude $|A_0^{n\ell}(X)|^2 = R^2(X)$ as functions of the slow space variable X for a given frequency ω . Note that the phase $\theta_0(X)$ of $A_0^{n\ell}(X)$ is as yet undetermined.

After expanding the operator $\Omega^{n\ell}$ in powers of ϵ in the same fashion as in (16), the ϵ terms of (27) yield

$$(\omega - \Omega^{n\ell})A_1^{n\ell} = -i\Omega_k^{n\ell} \frac{dA_0^{n\ell}}{dX} - \frac{i}{2}\Omega_{kk}^{n\ell}k_X^{n\ell}A_0^{n\ell} + \Omega_{R^2}^{n\ell}(A_0^{n\ell*}A_1^{n\ell} + A_1^{n\ell*}A_0^{n\ell})A_0^{n\ell},$$

where $\Omega^{n\ell}$ and its partial derivatives are evaluated at $(k^{n\ell}(X), R^2(X), X)$. In the following, $\Omega^{n\ell}(X)$ stands for $\Omega^{n\ell}(k^{n\ell}(X), R^2(X), X)$.

Upon exploiting the identity $\omega = \Omega^{n\ell}(X)$, the fact that $dA_0^{n\ell}/dX = (i d\theta_0/dX + \mathcal{R}_X^2/2\mathcal{R}^2)A_0^{n\ell}$, and the real nature of $A_0^{n\ell*}A_1^{n\ell} + A_1^{n\ell*}A_0^{n\ell}$, we readily obtain a solvability condition for $\theta_0(X)$ of the form

$$\frac{d\theta_0}{dX} = \frac{1}{2} \frac{\text{Re}[\Omega_{R^2}^{n\ell}(X)^*\Omega_k^{n\ell}(X)]}{\text{Im}[\Omega_{R^2}^{n\ell}(X)^*\Omega_k^{n\ell}(X)]} \frac{\mathcal{R}_X^2(X)}{\mathcal{R}^2(X)} - \frac{1}{2} \frac{\text{Re}[\Omega_{R^2}^{n\ell}(X)^*\Omega_{kk}^{n\ell}(X)]}{\text{Im}[\Omega_{R^2}^{n\ell}(X)^*\Omega_k^{n\ell}(X)]} k_X^{n\ell}(X). \quad (29)$$

Eqs. (26), (28) and (29) entirely specify the nonlinear solution at leading order.

5. Saddle point region SP: Leading-order nonlinear frequency selection criterion

In this section the global frequency ω_g is obtained at lowest order by matching the nonlinear spatial branches $k^{n\ell+}(X)$ and $k^{n\ell-}(X)$.

Solving the linear dispersion relation (10) yields the local complex wave numbers $k^{\ell\pm}(X, \omega)$ as functions of the frequency at any location. By contrast the nonlinear dispersion relation (23) admits solution pairs $(k^{n\ell\pm}(X, \omega), \mathcal{R}^{2\pm}(X, \omega))$ only in the allowable region of the $X-\omega$ plane. Moreover only nonlinear solutions with $\mathcal{R}^{2\pm}(X, \omega) > 0$ have physical meaning.

The relationship between linear and nonlinear spatial branches as a function of frequency is illustrated in Fig. 3. In the $X-\omega$ plane a solution of uniform frequency is represented by the line $\omega = \text{const}$. This line is mapped, in the complex k -plane, into two linear spatial branches $k^{\ell\pm}(X)$ defined in (11).

Let us recall that, for large enough frequencies $\omega = \omega_a$ (see $X-\omega$ plane of Fig. 3), the linear branches do not cross the k_r -axis in the complex k -plane as long as $\omega_{kk,i}(X) < 0$ for all X (Fig. 3(a1)), and that $k^{\ell\pm}(X)$ denotes the linear branch located in the $k_i > 0$ and $k_i < 0$ half-planes, respectively. Corresponding variations of $k_r^{\ell\pm}$ with X are displayed on Fig. 3(a2).

When the frequency is decreased to $\omega = \omega_b$ (see $X-\omega$ plane of Fig. 3), the linear branches move about in the complex k -plane. The branch $k^{\ell\pm}(X)$ crosses the k_r -axis (Fig. 3(b1)) whenever the frequency is such that the line $\omega = \omega_b$ intersects, in the $X-\omega$ plane, the region $\mathcal{R}^{2\pm}(X, \omega) > 0$. Indeed a local solution of the nonlinear dispersion relation with $R^2 = 0$ is precisely a solution of the linear dispersion relation, and this linear solution happens to have a *real* wave number.

Thus at locations where $R^2 = 0$, linear and nonlinear branches meet. Let us denote by $k^{n\ell\pm}(X, \omega)$ the nonlinear branches that match to the corresponding linear branches $k^{\ell\pm}(X, \omega)$. In the specific case of Fig. 3(b), the line $\omega = \omega_b$ is partly contained within the region $\mathcal{R}^{2-} > 0$ of the $X-\omega$ plane and, as a result, the nonlinear branch $k^{n\ell-}$ is seen to take over from $k_r^{\ell-}$ in a finite X -subinterval.

For frequencies such that the line $\omega = \omega_c$ in the $X-\omega$ plane intersects both regions $\mathcal{R}^{2\pm}(X, \omega) > 0$, both linear branches cross the k_r -axis (Fig. 3(c1)) and are connected to the corresponding nonlinear branches (Fig. 3(c2)). Let $X_1^\pm(\omega)$ and $X_2^\pm(\omega)$ be the locations where $\mathcal{R}^{2\pm}(X, \omega) = 0$, whereby $k^{\ell\pm}(X_{1,2}^\pm) = k^{n\ell\pm}(X_{1,2}^\pm)$. A nonlinear solution with local wave number $k^{n\ell\pm}(X, \omega)$ then exists in the range $X_1^\pm < X < X_2^\pm$. The locations $X_{1,2}^\pm$ depend on the frequency, and in Section 6 we show that, for any frequency, the linear and nonlinear solutions can be matched at all orders in ϵ through transition layers centered around $X_{1,2}^\pm(\omega)$. Recall that boundary conditions (6) require keeping only the linear branch $k^{\ell\pm}(X)$ in the regions $X \rightarrow \pm\infty$, respectively. At the locations X_1^- and X_2^+ where the linear branches $k^{\ell-}$ and $k^{\ell+}$ cross the k_r -axis they change over to the corresponding nonlinear branches $k^{n\ell-}$ and $k^{n\ell+}$. Thus the nonlinear region is delimited by X_1^- (where $k^{\ell-} = k^{n\ell-}$) and X_2^+ (where $k^{n\ell+} = k^{\ell+}$), and a continuous global mode solution must necessarily connect both these nonlinear branches.

A smooth crossover between the nonlinear branches $k^{n\ell-}$ and $k^{n\ell+}$ (Fig. 3(s2)) can only be achieved for frequencies such that the line $\omega = \text{const}$. meets the critical curve limiting the allowable domain in the $X-\omega$ plane.

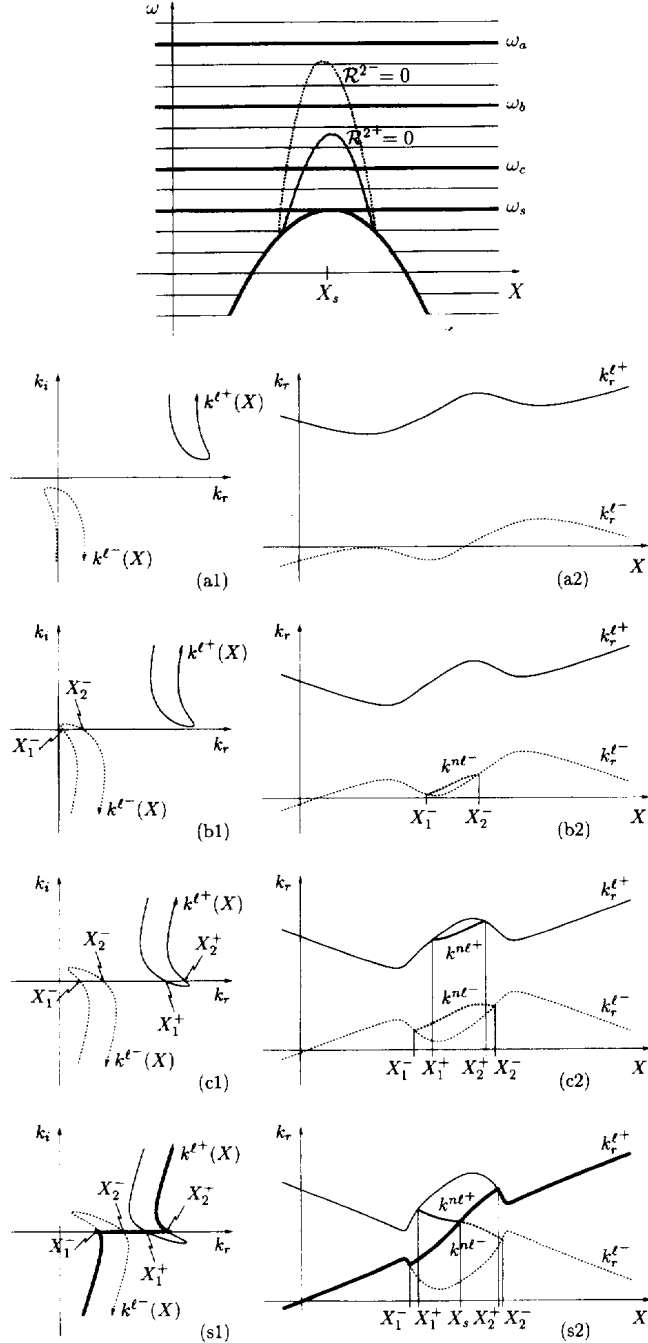


Fig. 3. Relationship between linear and nonlinear spatial branches for different values of the frequency. For a large frequency ω_a , the line $\omega = \omega_a$ does not intersect the regions $\mathcal{R}^{2\pm}(X, \omega) \geq 0$ in the $X-\omega$ plane, the linear branches $k^{\ell\pm}(X)$ do not cross the k_r -axis in the complex k -plane (a1), and nonlinear branches do not exist; the real parts $k_r^{\ell\pm}(X)$ are represented in (a2). For ω_b such that the line $\omega = \omega_b$ intersects the region $\mathcal{R}^{2-}(X, \omega) \geq 0$ in the $X-\omega$ plane, the branch $k^{\ell-}(X)$ crosses the k_r -axis for $X = X_1^-$ and $X = X_2^-$ in (b1); as a result, the nonlinear $k^{n\ell-}(X)$ exists for $X_1^- < X < X_2^-$ and is connected to $k^{\ell-}(X)$ in (b2). The line $\omega = \omega_c$ intersects both regions $\mathcal{R}^{2\pm}(X, \omega)$, thus both linear branches cross the k_r -axis in (c1); both nonlinear branches exist in the ranges $X_1^\pm < X < X_2^\pm$, respectively (c2). When the frequency equals ω_s such that the line $\omega = \omega_s$ is tangent to the boundary of the allowable domain at X_s in the $X-\omega$ plane, the nonlinear branches meet at X_s in (s2), and the crossover between branches is possible; the global spatial branch selected by the global mode is indicated in bold in (s1,2).

Furthermore, the line $\omega = \text{const.}$ has to be entirely contained within the allowable domain. Thus, *the leading order global frequency ω_s is obtained by requiring that the line $\omega = \omega_s$ be tangent to the allowable domain in the $X-\omega$ plane at a point X_s .* Since, to each point in the allowable domain of the $X-\omega$ plane, correspond two pairs $(k^{n\ell+}, R^{2+})$ and $(k^{n\ell-}, R^{2-})$, the allowable domain may be considered as the superposition of two sheets, respectively, labelled (+) and (−) which necessarily join along the critical curve where $(k^{n\ell+}, R^{2+}) = (k^{n\ell-}, R^{2-})$. A plane $\omega = \text{const.}$ cuts the surface made up of the two sheets along two lines, one on each sheet, which correspond to the (+) and (−) spatial branches, respectively. Passing from one sheet to the other on such a line is possible only for $\omega = \omega_s$. The additional condition that the line $\omega = \omega_s$ be entirely contained in the allowable domain guarantees that the surface made up of the two sheets exhibits a saddle point when cut by the plane $\omega = \omega_s$. Thus, *at leading order, the global frequency ω_g is given by a saddle point of the nonlinear dispersion relation.* Moreover nonlinear global modes only exist if the saddle point is located in a region where the wave number $k_s \equiv k^{n\ell+}(X_s, \omega_s) = k^{n\ell-}(X_s, \omega_s)$ is linearly unstable, i.e., $R_s^2 \equiv R^{2+}(X_s, \omega_s) = R^{2-}(X_s, \omega_s) > 0$.

An explicit condition for the existence of a saddle point may be derived from the local reduced nonlinear dispersion relation (24)

$$\omega = \Omega^{\text{NL}}(k, X).$$

This relation defines a surface in (ω, k, X) space which bears the same features as the complete nonlinear dispersion relation (23). For a given frequency ω , the spatial branches $k^{n\ell\pm}(X, \omega)$ are obtained as the intersection of this surface and the plane $\omega = \text{const.}$ The condition that the branches $k^{n\ell\pm}(X)$ be connected, requires that the global frequency be given by a saddle point of the surface $\omega = \Omega^{\text{NL}}(k, X)$. Thus, the global frequency ω_g is obtained, at leading order in the WKBJ approximation, for a saddle point of the reduced nonlinear dispersion relation, i.e.,

$$\omega_g \sim \omega_s = \Omega^{\text{NL}}(k_s, X_s), \quad (30)$$

where the pair (k_s, X_s) satisfies

$$\frac{\partial \Omega^{\text{NL}}}{\partial k}(k_s, X_s) = \frac{\partial \Omega^{\text{NL}}}{\partial X}(k_s, X_s) = 0. \quad (31)$$

The additional condition²

$$(\Omega_{kX,s}^{\text{NL}})^2 - \Omega_{kk,s}^{\text{NL}} \Omega_{XX,s}^{\text{NL}} > 0 \quad (32)$$

guarantees that (ω_s, k_s, X_s) is actually a saddle point and not a local extremum.

Criterion (30), (31) may also be expressed in terms of the complete dispersion relation (23)

$$\omega = \Omega^{n\ell}(k, R^2, X).$$

Bearing in mind that

$$\Omega^{\text{NL}}(k, X) = \Omega_r^{n\ell}(k, R^2(k, X), X),$$

where $R^2(k, X)$ is implicitly defined by

$$\Omega_i^{n\ell}(k, R^2(k, X), X) = 0,$$

one may relate the derivatives of Ω^{NL} to those of $\Omega^{n\ell}$. After elementary calculations, one finds that criterion (31) takes the alternate form

$$\text{Im}[(\Omega_{R^2,s}^{n\ell})^* \Omega_{k,s}^{n\ell}] = \text{Im}[(\Omega_{R^2,s}^{n\ell})^* \Omega_{X,s}^{n\ell}] = 0,$$

² Throughout, subscript (s) denotes evaluation at the saddle point (k_s, R_s^2, X_s) .

i.e., the derivatives of the complex function $\Omega^{n\ell}$ with respect to each of its arguments have the same phase. Thus the leading order global frequency ω_s and the associated quantities (k_s, R_s^2, X_s) are equivalently determined by

$$\omega_s = \Omega^{n\ell}(k_s, R_s^2, X_s) \quad \text{and} \quad \operatorname{Arg} \Omega_{k,s}^{n\ell} = \operatorname{Arg} \Omega_{R^2,s}^{n\ell} = \operatorname{Arg} \Omega_{X,s}^{n\ell}.$$

Additional condition (32) may also be expressed in terms of $\Omega^{n\ell}$ after cumbersome but straightforward calculations.

The essential result of this section is summarized by the saddle point conditions (30) and (31) applicable to the reduced nonlinear dispersion relation $\omega = \Omega^{\text{NL}}(k, X)$: to leading order, the *nonlinear* global frequency ω_s satisfies a criterion that is formally identical to its *linear* counterpart (1) and (2). However it should be emphasized that the linear criterion involves *complex* values of the wave number, frequency and spatial coordinate, whereas the nonlinear criterion only involves purely real values for these quantities.

It is possible to compute higher order corrections to the global frequency ω_g by a detailed analysis of the saddle point region (SP). As in the case of linear global modes with a double turning point [6,11,16,20], it is found that its characteristic thickness is $O(\epsilon^{1/2})$. Matching between the SP layer and the surrounding CNL^\pm regions leads to an expansion of the form

$$\omega_g \sim \omega_s + \epsilon \omega_{1,n},$$

where the $O(\epsilon)$ frequency correction term $\omega_{1,n}$ is parametrized by a nonnegative integer n . Detailed calculations of this quantified set of fully nonlinear global modes are postponed to a future publication.

6. Spatial structure of transition layers $\text{TL}^{1,2}$

At the locations X_1^- and X_2^+ where the amplitude of nonlinear WKBJ approximations vanishes, nonlinearities become weak, and, in the semi-infinite regions (OL^\pm) extending towards $X = \pm\infty$, the solution is described by linear WKBJ approximations. The structure of the transition layer connecting the finite amplitude nonlinear solution in (CNL^\pm) to exponentially decaying linear solutions in (OL^\pm) is analyzed in this section.

It is essential to bear in mind that this transition layer plays no role in the global frequency selection mechanism which solely depends on the local nonlinear dispersion relation at the saddle point X_s , in the core of the nonlinear region. The locations of the transition layers indeed depend on the frequency ω_g but the linear and nonlinear solutions can be matched for any frequency. For this reason matching is carried out for an arbitrary fixed real frequency ω .

With the definitions of Section 5, the linear branch $k^{\ell^-}(X)$ meets the nonlinear branch $k^{n\ell^-}(X)$ at $X = X_1^-$. Let $k_1 \equiv k^{\ell^-}(X_1^-) = k^{n\ell^-}(X_1^-)$ be the local real wave number at ³ X_1 . For $X < X_1$ the global mode is approximated by the linear WKBJ ψ^ℓ approximation (17) and for $X > X_1$ by the nonlinear WKBJ $\psi^{n\ell}$ approximation (26). None of these expressions are uniformly valid in a full neighborhood of X_1 . An inner solution must then be constructed in an inner layer TL^1 around X_1 to allow a smooth transition between both outer WKBJ approximations.

The form of the inner solution is obtained from the behavior of the outer solutions as $X \rightarrow X_1$. Near X_1 the nonlinear solution (26) expands into

$$\psi^{n\ell}(X) \sim (X - X_1)^{1/2} \sqrt{\mathcal{R}_{X,1}^2} e^{i\theta_0(X_1)} e^{ik_1 x} \exp\left(\frac{i}{2\epsilon} k_{X,1}^{n\ell}(X - X_1)^2\right) \quad (33)$$

³ For simplicity we drop from now on the superscript $(-)$.

with⁴

$$\mathcal{R}_{X,1}^2 = -\frac{\text{Im}[(\Omega_{k,1}^{n\ell})^* \Omega_{X,1}^{n\ell}]}{\text{Im}[(\Omega_{k,1}^{n\ell})^* \Omega_{R^2,1}^{n\ell}]} \quad \text{and} \quad k_{X,1}^{n\ell} = -\frac{\text{Im}[(\Omega_{R^2,1}^{n\ell})^* \Omega_{X,1}^{n\ell}]}{\text{Im}[(\Omega_{R^2,1}^{n\ell})^* \Omega_{k,1}^{n\ell}]}, \quad (34)$$

while the linear solution displays the following asymptotic behavior:

$$\psi^\ell(X) \sim A_0^\ell(X_1) e^{ik_1 x} \exp\left(\frac{i}{2\epsilon} k_{X,1}^\ell (X - X_1)^2\right) \quad (35)$$

with

$$k_{X,1}^\ell = -\Omega_{X,1}^\ell / \Omega_{k,1}^\ell.$$

The expansion of the outer solutions (33) and (35) shows that the inner solution proceeds in the form

$$\tilde{\psi}(\tilde{X}) \sim \epsilon^{1/4} (\tilde{A}_0(\tilde{X}) + \epsilon^{1/2} \tilde{A}_{1/2}(\tilde{X}) + \dots) e^{ik_1 x}, \quad (36)$$

where $\tilde{X} = (X - X_1)/\epsilon^{1/2}$ is the inner local space variable in the TL¹ layer.

From the governing equation for the inner solution $\tilde{\psi}$ in the transition layer

$$\begin{aligned} \omega(\tilde{A}_0 + \epsilon^{1/2} \tilde{A}_{1/2} + \dots) &= \Omega^{n\ell}(k_1 - i\epsilon^{1/2} \partial_{\tilde{X}}, \epsilon^{1/2} |\tilde{A}_0 + \epsilon^{1/2} \tilde{A}_{1/2} + \dots|^2, X_1 + \epsilon^{1/2} \tilde{X}) \\ &\times (\tilde{A}_0 + \epsilon^{1/2} \tilde{A}_{1/2} + \dots), \end{aligned} \quad (37)$$

we recover at lowest order

$$\omega = \Omega^{n\ell}(k_1, 0, X_1) = \Omega^\ell(k_1, X_1). \quad (38)$$

At order $\epsilon^{1/2}$ Eq. (37) reduces to

$$(\omega - \Omega_1^\ell) \tilde{A}_{1/2} = -i\Omega_{k,1}^{n\ell} \frac{d\tilde{A}_0}{d\tilde{X}} + \Omega_{R^2,1}^{n\ell} |\tilde{A}_0|^2 \tilde{A}_0 + \Omega_{X,1}^{n\ell} \tilde{X} \tilde{A}_0.$$

Bearing in mind (38), this leads to a solvability condition for \tilde{A}_0

$$i\Omega_{k,1}^{n\ell} \frac{d\tilde{A}_0}{d\tilde{X}} = (\Omega_{X,1}^{n\ell} \tilde{X} + \Omega_{R^2,1}^{n\ell} |\tilde{A}_0|^2) \tilde{A}_0. \quad (39)$$

This equation is of the form

$$\frac{d\tilde{A}_0}{d\tilde{X}} = ((a_r + ia_i)\tilde{X} + (b_r + ib_i)|\tilde{A}_0|^2) \tilde{A}_0, \quad (40)$$

and admits the solution

$$\tilde{A}_0(\tilde{X}) = \frac{\tilde{A}_0(0) \exp[\frac{1}{2}(a_r + ia_i)\tilde{X}^2 - \frac{1}{2}i(b_i/b_r) \ln(1 - 2b_r|\tilde{A}_0(0)|^2 \int_0^{\tilde{X}} e^{a_r u^2} du)]}{\sqrt{1 - 2b_r|\tilde{A}_0(0)|^2 \int_0^{\tilde{X}} e^{a_r u^2} du}}. \quad (41)$$

⁴ Subscript (1) always denotes evaluation at $k = k_1$, $R_1^2 = 0$, $X = X_1$. Note that $\Omega_1^{n\ell} = \Omega_1^\ell$ because $\mathcal{R}^2(X_1) = 0$.

The inner solution $\tilde{\psi}$ in the TL¹ layer has to be matched for $\tilde{X} \rightarrow \pm\infty$ with the outer solutions $\psi^{n\ell}$ and ψ^ℓ in the CNL[−] and OL[−] regions, respectively. The square root behavior of $\psi^{n\ell}$ in (33) requires that $\tilde{A}_0(\tilde{X}) = O(\tilde{X}^{1/2})$ as $\tilde{X} \rightarrow +\infty$. This implies that

$$2b_r |\tilde{A}_0(0)|^2 \int_0^\infty e^{a_r u^2} du = 1 \quad \text{or} \quad |\tilde{A}_0(0)|^2 = \frac{1}{4b_r} \sqrt{\frac{\pi}{-a_r}}.$$

With this value for $|\tilde{A}_0(0)|$ the inner solution (41) admits for $\tilde{X} \rightarrow +\infty$ the asymptotic expansion

$$\tilde{A}_0(\tilde{X}) \sim \sqrt{-\frac{a_r}{b_r} \tilde{X}} \exp \frac{i}{2} \left[\left(a_i - \frac{b_i}{b_r} a_r \right) \tilde{X}^2 + \frac{b_i}{b_r} (\ln \tilde{X} + \text{const.}) \right]. \quad (42)$$

Comparison of the coefficients in (39) and (40), and use of (34) leads to

$$-\frac{a_r}{b_r} = \mathcal{R}_{X,1}^2 \quad \text{and} \quad a_i - \frac{b_i}{b_r} a_r = k_{X,1}^{n\ell}.$$

Thus the choice of

$$\tilde{A}_0(0) = \left(\frac{\pi}{-a_r} \right)^{1/4} \frac{e^{i\theta_0(X_1)}}{(4b_r)^{1/2}}$$

completely matches, at leading order, the inner solution $\tilde{\psi}$ given by (36) and (42) with the outer nonlinear solution $\psi^{n\ell}$ in the limit (33).

For this value of $\tilde{A}_0(0)$ the asymptotic behavior of the inner solution (41) as $\tilde{X} \rightarrow -\infty$ is

$$\tilde{A}_0(\tilde{X}) \sim \frac{\tilde{A}_0(0)}{\sqrt{2}} 2^{-ib_i/2b_r} \exp(\frac{1}{2}(a_r + ia_i)\tilde{X}^2).$$

As $a_r + ia_i = ik_{X,1}^\ell$, the inner solution $\tilde{\psi}$ matches the outer linear WKBJ approximation ψ^ℓ given by (35) as long as

$$A_0^\ell(X_1) = \epsilon^{1/4} \frac{\tilde{A}_0(0)}{\sqrt{2}} 2^{-ib_i/2b_r}.$$

This completes the proof that, for a given frequency, the linear and nonlinear WKBJ approximations can be matched at leading order through a transition layer of width $\epsilon^{1/2}$ (in terms of X). A similar analysis holds for the transition layer at X_2^+ .

7. Conclusions and discussion

A fully nonlinear frequency selection criterion has been derived for global modes on a doubly infinite interval, governed by the complex Ginzburg–Landau equation with spatially varying coefficients.

Let $\omega = \Omega^{\text{NL}}(k, X)$ denote the local reduced nonlinear dispersion relation obtained by eliminating the amplitude R^2 from the complete local nonlinear dispersion relation $\omega = \Omega^{n\ell}(k, R^2, X)$ pertaining to finite amplitude travelling waves. The global frequency ω_g on the doubly infinite interval is then, at leading order, a *real saddle point* ω_s of Ω^{NL} associated with the *real* wave number k_s and station X_s such that

$$\omega_g \sim \omega_s = \Omega^{\text{NL}}(k_s, X_s) \quad \text{and} \quad \frac{\partial \Omega^{\text{NL}}}{\partial k}(k_s, X_s) = \frac{\partial \Omega^{\text{NL}}}{\partial X}(k_s, X_s) = 0. \quad (43)$$

This saddle point condition is selected so as to ensure a smooth crossover between the two nonlinear spatial branches $k^{n\ell^-}$ and $k^{n\ell^+}$ present on either side of X_s .

The nonlinear global mode spatial structure is illustrated in Fig. 1. A spatially evolving complex k^ℓ^- branch issuing from $X = -\infty$ and governed by the local linear dispersion relation $\omega = \Omega^\ell(k, X)$ in the OL^- region experiences a transition to the fully nonlinear régime within a layer TL^1 of thickness $O(\epsilon^{1/2})$ centered around a point X_1^- of local neutral stability. In a “downstream” CNL^- region of finite extent, the wave is fully nonlinear and its real wave number $k^{n\ell^-}$ and amplitude \mathcal{R}^{2^-} are governed by the local nonlinear dispersion relation $\omega = \Omega^{n\ell}(k, R^2, X)$. As the wave enters the SP layer centered around X_s , it is smoothly converted into a $k^{n\ell^+}$ spatial branch since condition (43) is satisfied. The CNL^+ region mirrors, for the $k^{n\ell^+}$ wave, the CNL^- region for the $k^{n\ell^-}$ wave. A second transition layer TL^2 centered around the locally neutral station X_2^+ allows a return to a linear k^ℓ^+ spatial wave in the OL^+ region, and a final exponential decay at $X = +\infty$.

These results should be compared with the corresponding double turning point *linear* frequency selection criterion derived in [6,16,20]. For infinitesimal waves governed by a local linear dispersion relation $\omega = \Omega^\ell(k, X)$ between *complex* wave number k and frequency ω , the complex global frequency ω_g is given by the saddle point condition (1), (2), where the frequency ω_s , wave number k_s , and spatial coordinate X_s are all *complex*. The linear global mode spatial structure is thus made up of complex k^ℓ^- and k^ℓ^+ spatially evolving waves governed by the local linear dispersion relation $\omega = \Omega^\ell(k, X)$ in corresponding OL^- and OL^+ regions near $X = \mp\infty$. The saddle point condition (2) ensures a smooth crossover from the k^ℓ^- to the k^ℓ^+ branch in an inner region SP of thickness $O(\epsilon^{1/2})$ centered around the *complex* saddle point X_s . In the linear case, the $TL^{1,2}$ and CNL^\pm regions are naturally absent, but an inner SP layer structure is necessary in both linear and nonlinear studies. Indeed, both frequency selection criteria are formally identical. Paradoxically the nonlinear criterion involves only real variables and therefore appears simpler to implement, without any of the complexities associated with analytic continuation in the complex X -plane.

According to [6,16], a necessary condition for the existence of a growing *linear* global mode is that the basic state be linearly absolutely unstable in a region of finite extent. According to the present study, a necessary condition for the existence of a self-sustained *nonlinear* global mode appears to be that the basic state only contain a linearly unstable region of finite extent corresponding to $\mathcal{R}^{2^\pm} > 0$. Fully nonlinear global modes of the type shown here may in principle occur even if the medium is only convectively unstable.

The latter result is entirely consistent with the studies of Chomaz [4] and Couairon and Chomaz [7]. In these recent investigations, nonlinear global modes on the semi-infinite interval $0 < X < \infty$ and governed by the real Ginzburg–Landau equation with constant coefficients and both cubic and quintic nonlinearities have been examined from the dynamical systems point of view. In the supercritical case (stabilizing nonlinear terms), it is found that nonlinear global modes may exist even if the basic state is only linearly convectively unstable. Thus, there is clearly more and more evidence that the relation between local *linear* stability properties and global modes becomes somewhat tenuous as the fully nonlinear régime is approached.

The recent numerical simulations of wakes in shallow layers performed by Schär and Smith [22] underscore the importance of nonlinearities in the frequency selection process. When nonlinearities were turned off, the wake was found to oscillate at a Strouhal frequency $\omega \sim 0.17$, to be compared with $\omega_s = 0.19$ resulting from the linear frequency selection criterion (1), (2). Upon retaining nonlinear terms, the “observed” wake frequency increased substantially to $\omega \sim 0.27$. The criterion proposed in the present study could possibly account for this discrepancy.

Acknowledgements

We wish to thank Stéphane Le Dizès for many stimulating discussions and his careful reading of the manuscript. We are particularly indebted to the gentle people of LadHyX for providing and maintaining a friendly research

atmosphere. LadHyX is jointly supported by the École polytechnique and by the Engineering Science Directorate of the French National Center for Scientific Research (CNRS UMR-156).

References

- [1] C.M. Bender and S.A. Orszag, Advanced Mathematical Methods for Scientists and Engineers (McGraw-Hill, New York, 1978).
- [2] A.J. Bernoff, Slowly varying fully nonlinear wavetrains in the Ginzburg–Landau equation, *Physica D* 30 (1988) 363.
- [3] F.H. Busse, Transition to turbulence in Rayleigh–Bénard convection, in: *Hydrodynamic Instabilities and the Transition to Turbulence*, eds., H.L. Swinney and J.P. Gollub (Springer, New York, 1985) p. 97.
- [4] J.-M. Chomaz, Absolute and convective instabilities in nonlinear systems, *Phys. Rev. Lett.* 69 (1992) 1931.
- [5] J.-M. Chomaz, P. Huerre and L.G. Redekopp, The effect of nonlinearity and forcing on global modes, in: *New Trends in Nonlinear Dynamics and Pattern-Forming Phenomena*, eds. P. Coullet and P. Huerre (Plenum Press, New York, 1990) p. 259.
- [6] J.-M. Chomaz, P. Huerre and L.G. Redekopp, A frequency selection criterion in spatially developing flows, *Stud. Appl. Math.* 84 (1991) 119.
- [7] A. Couairon and J.-M. Chomaz, Absolute and convective instabilities, front velocities and global modes in nonlinear systems, in preparation.
- [8] M.C. Cross and A.C. Newell, Convection patterns in large aspect ratio systems, *Physica D* 10 (1984) 299.
- [9] K. Hannemann and H. Oertel Jr., Numerical simulation of the absolutely and convectively unstable wake, *J. Fluid Mech.* 199 (1989) 55.
- [10] L.N. Howard and N. Kopell, Slowly varying waves and shock structures in reaction-diffusion equations, *Stud. Appl. Math.* 56 (1977) 95.
- [11] P. Huerre and P.A. Monkewitz, Local and global instabilities in spatially developing flows, *Ann. Rev. Fluid Mech.* 22 (1990) 473.
- [12] R.E. Hunt and D.G. Crighton, Instability of flows in spatially developing media, *Proc. Roy. Soc. London A* 435 (1991) 109.
- [13] G.E. Karniadakis and G.S. Triantafyllou, Frequency selection and asymptotic states in laminar wakes, *J. Fluid Mech.* 199 (1989) 441.
- [14] J. Kevorkian and J.D. Cole, *Perturbation Methods in Applied Mathematics* (Springer, New York, 1981).
- [15] Y. Kuramoto, Phase dynamics of weakly unstable periodic structures, *Prog. Theor. Phys.* 71 (1984) 1182.
- [16] S. Le Dizès, P. Huerre, J.-M. Chomaz and P.A. Monkewitz, Linear global modes in spatially-developing media, *Phil. Trans. Roy. Soc. London A* 354 (1996) 169.
- [17] P. Manneville, *Structures Dissipatives, Chaos et Turbulence* (Aléa Saclay, 1991).
- [18] C. Mathis, M. Provansal and L. Boyer, The Bénard-von Karman instability: an experimental study near the threshold, *J. Phys. Paris Lett.* 45 (1984) 483.
- [19] P.A. Monkewitz, D.W. Bechert, B. Lehmann and B. Barsikow, Self-excited oscillations and mixing in heated round jets, *J. Fluid Mech.* 213 (1990) 611.
- [20] P.A. Monkewitz, P. Huerre and J.M. Chomaz, Global linear stability analysis of weakly non-parallel shear flows, *J. Fluid Mech.* 251 (1993) 1.
- [21] Y. Pomeau and P. Manneville, Stability and fluctuations of a spatially periodic convective flow, *J. Phys. Lett.* 40 (1979) L-609.
- [22] C. Schär and R.B. Smith, Shallow-water flow past isolated topography. Part II. Transition to vortex shedding, *J. Atmos. Sci.* 50 (1993) 1401.
- [23] K.R. Sreenivasan, S. Raghu and D. Kyle, Absolute instability in variable density round jets, *Exp. Fluids* 7 (1989) 309.
- [24] P.J. Strykowski and K.R. Sreenivasan, On the formation and suppression of vortex ‘shedding’ at low Reynolds numbers, *J. Fluid Mech.* 218 (1990) 71.
- [25] P.J. Strykowski and D.L. Niccum, The stability of countercurrent mixing layers in circular jets, *J. Fluid Mech.* 227 (1991) 309.

[A2]

Steep nonlinear global modes in spatially developing media

B. Pier, P. Huerre, J.-M. Chomaz & A. Couairon

Physics of Fluids **10**, 2433–2435 (1998)

doi:10.1063/1.869784

<https://hal.archives-ouvertes.fr/hal-00119908>

LETTERS

The purpose of this Letters section is to provide rapid dissemination of important new results in the fields regularly covered by Physics of Fluids. Results of extended research should not be presented as a series of letters in place of comprehensive articles. Letters cannot exceed three printed pages in length, including space allowed for title, figures, tables, references and an abstract limited to about 100 words. There is a three-month time limit, from date of receipt to acceptance, for processing Letter manuscripts. Authors must also submit a brief statement justifying rapid publication in the Letters section.

Steep nonlinear global modes in spatially developing media

Benoît Pier,^{a)} Patrick Huerre, Jean-Marc Chomaz, and Arnaud Couairon
*Laboratoire d'Hydrodynamique (LadHyX), CNRS UMR 7646, École polytechnique,
F-91128 Palaiseau cedex, France*

(Received 16 April 1998; accepted 15 June 1998)

A new frequency selection criterion valid in the fully nonlinear regime is presented for extended oscillating states in spatially developing media. The spatial structure and frequency of these modes are dominated by the existence of a sharp front connecting linear to nonlinear regions. A new type of fully nonlinear time harmonic solutions called *steep global modes* is identified in the context of the supercritical complex Ginzburg–Landau equation with slowly spatially varying coefficients. A similar formulation is likely to be applicable to fully nonlinear synchronized global oscillations in spatially developing free shear flows. © 1998 American Institute of Physics.

[S1070-6631(98)00410-3]

Spatially developing free shear flows such as mixing layers,¹ wakes,^{2,3} and jets⁴ typically give rise to intrinsic self-sustained oscillations when they exhibit a sufficiently large region of absolute instability.⁵ Fluctuations saturate at a finite amplitude in the locally unstable regions of the flow and become tuned at an overall frequency. The intrinsic frequency and the associated spatial distribution of fluctuations define a *global mode* living on the underlying unstable basic flow. In the present letter we show the existence of fully nonlinear global modes with a sharp stationary front separating linear and nonlinear regions. The complex Ginzburg–Landau (CGL) equation is chosen as a model of open flows since families of linear and nonlinear wave solutions are readily determined analytically. As summarized below, the study of CGL models has been found to lead to linear frequency selection criteria⁶ that remain applicable for the Navier–Stokes equations.⁷ The same approach is adopted here in the fully nonlinear context.

In the *linear* approximation, global frequency selection in *doubly infinite domains* is dictated by saddle point conditions^{6,7} imposed on the local linear dispersion relation. Such a criterion predicts remarkably well the vortex shedding frequency behind blunt edged plates.⁸ *Nonlinear* extensions of these concepts have only recently been developed, mainly in the context of various one-dimensional evolution models in *semi-infinite*^{9,10} or *finite*¹¹ *domains*. The results compare satisfactorily with numerical simulations and experiments for Taylor–Couette flow¹² and Rayleigh–Bénard convection with throughflow.^{13,10} Surprisingly, fully nonlinear *soft global modes* of the CGL equation varying smoothly over a doubly infinite domain have been shown,¹⁴ by application of Wentzel–Kramers–Brillouin–Jeffreys (WKB) theory, to satisfy a nonlinear saddle point criterion which is

formally analogous to its linear counterpart. Here we show the existence of a second class of nonlinear spatially extended states in doubly infinite domains: *steep global modes* with a sharp front.

We assume that the fluctuating complex scalar field $\psi(x, t)$ is governed by the supercritical CGL equation written as

$$i\frac{\partial\psi}{\partial t} = \left(\omega_0(X) + \frac{1}{2}\omega_{kk}(X)k_0(X)^2 \right)\psi + i\omega_{kk}(X)k_0(X)\frac{\partial\psi}{\partial x} - \frac{1}{2}\omega_{kk}(X)\frac{\partial^2\psi}{\partial x^2} + \gamma(X)|\psi|^2\psi, \quad (1)$$

where the complex functions $\omega_0(X)$, $\omega_{kk}(X)$, $k_0(X)$, and $\gamma(X)$ solely depend on the slow space variable $X=\epsilon x$, $\epsilon \ll 1$, to account for the weak inhomogeneity of the medium. The choice of these functions and their meaning will become clear when we discuss the resulting linear and nonlinear dispersion relations.

In regions where the amplitude of ψ is small, its behavior is governed by the linearized counterpart of (1). Under the assumption of weak inhomogeneity, linear solutions are approximated at leading order by waves of the form $\exp((i/\epsilon)\int^x k(u)du - i\omega t)$. The corresponding *local linear dispersion relation* reads

$$\omega = \Omega^l(k, X) \equiv \omega_0(X) + \frac{1}{2}\omega_{kk}(X)(k - k_0(X))^2, \quad (2)$$

with associated complex local linear spatial branches

$$k^{l\pm}(X; \omega) \equiv k_0(X) \pm \sqrt{2\frac{\omega - \omega_0(X)}{\omega_{kk}(X)}}. \quad (3)$$

As defined in Ref. 5, the complex absolute frequency ω_0 necessarily coincides with the branch point of (3): at $\omega=\omega_0$ both wave number branches are equal to the local absolute wave number k_0 . The following basic flow structure is assumed: a central absolutely unstable (AU) region of finite extent characterized by $\omega_{0,i}(X)\equiv\text{Im } \omega_0(X)>0$, surrounded by convectively unstable (CU) regions with $\omega_{0,i}(X)<0$, which in turn become stable far downstream ($X\rightarrow+\infty$) and upstream ($X\rightarrow-\infty$). In order to enforce causality, sufficiently large wave numbers are assumed to be damped, i.e., $\omega_{kk,i}(X)<0$ for all X . We assume a basic flow advection towards increasing X which is readily shown to correspond to $k_{0,i}<0$. The + and - superscripts are unambiguously assigned to the spatial branches exponentially decaying towards $X=+\infty$ and $X=-\infty$, respectively.

In unstable regions the CGL equation admits local nonlinear traveling wave solutions of the form $\psi=R(X)\exp((i/\epsilon)\int^X k(u)du-i\omega t)$, with *real* wave number k , *real* frequency ω and *real* amplitude R governed by the *local nonlinear dispersion relation*

$$\omega=\omega_0(X)+\frac{1}{2}\omega_{kk}(X)(k-k_0(X))^2+\gamma(X)R^2. \quad (4)$$

This complex equation with three real unknowns can easily be cast in the form

$$\omega=\Omega^{nl}(k,X) \quad (5a)$$

and

$$R^2=\mathcal{R}_2(k,X), \quad (5b)$$

where the functions Ω^{nl} and \mathcal{R}_2 are quadratic polynomials in k with X -dependent *real* coefficients. The real nonlinear wave number branches $k^{nl\pm}(X;\omega)$ are derived from (5a); the allowed wave numbers are those for which $\mathcal{R}_2(k,X)>0$. We only consider CGL coefficients for which the finite amplitude traveling waves are stable.

Global mode solutions over the entire flow are obtained by asymptotically matching together local traveling wave solutions of the same frequency. By definition, a global mode is necessarily made up of the decaying k^{l-} branch for $X\rightarrow-\infty$ and the decaying k^{l+} branch for $X\rightarrow+\infty$. The frequency selection gives rise to a nonlinear eigenvalue problem: the matching of finite amplitude oscillations in a central region to exponentially decaying tails in both upstream and downstream directions can only be achieved for a specific frequency.

This problem has been solved for purely *linear global modes* in Ref. 6. In the fully nonlinear regime, *soft global modes* with an overall slowly varying spatial envelope have been identified and described in Ref. 14; their real global frequency ω_s is obtained at a saddle point (k_s, X_s) of the nonlinear dispersion relation $\Omega^{nl}(k,X)$. The objective of this letter is to report the existence of a second type of fully nonlinear solutions: in situations where *soft* modes fail to exist, they are replaced by a *steep* mode with a sharp front.

The spatial structure of a steep global mode of frequency ω_f is given in Fig. 1(a). Such a solution is characterized by a sharp front at the upstream boundary X_f of the AU region indicated in gray. Associated linear $k^{l\pm}$ and nonlinear $k^{nl\pm}$ wave number branches at the frequency ω_f vary along the

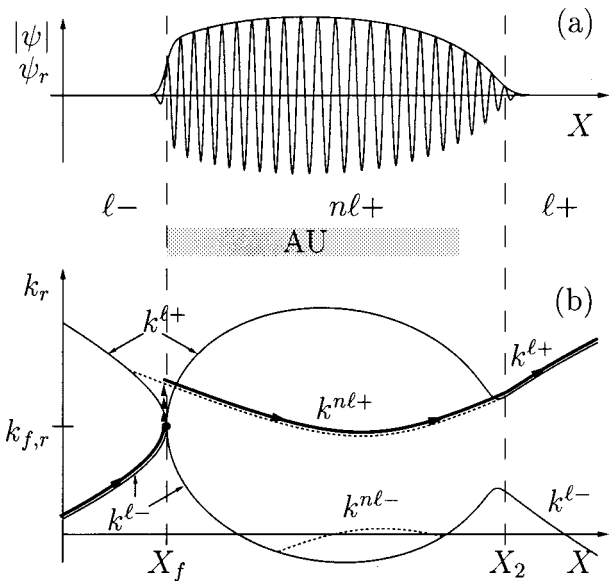


FIG. 1. (a) Envelope $|\psi|$ and real part ψ_r of steep global mode with sharp front at upstream boundary X_f of AU region (in gray). (b) Corresponding linear and nonlinear spatial branches in the $X-k_r$ plane. Local wave number making up solution in (a) follows path indicated by a thick line. The wave number jump at the front is indicated by repeated arrows.

streamwise direction X , as shown by solid and dashed lines in the $X-k_r$ plane of Fig. 1(b). The local wave number making up the actual solution follows the path indicated by a thick line in Fig. 1(b). Except for the jump at the front [repeated arrows in Fig. 1(b)] local wave number and amplitude vary slowly. The nonlinear solution prevails in the region $X_f < X < X_2$ which extends beyond the AU region.

The steep global frequency ω_f and the front location X_f are then solely determined by applying the following criterion to the local *linear* dispersion relation:

$$\omega_f=\Omega^l(k_f, X_f), \quad (6)$$

where the pair (k_f, X_f) satisfies

$$\frac{\partial \Omega^l}{\partial k}(k_f, X_f)=0 \quad \text{and} \quad \Omega_i^l(k_f, X_f)=0. \quad (7)$$

In terms of $\omega_0(X)$ these conditions read

$$\omega_f=\omega_0(X_f) \quad \text{and} \quad \omega_{0,i}(X_f)=0. \quad (8)$$

The above equations are reminiscent of the Dee–Langer selection criterion¹⁵ for a propagating front connecting an unstable state $\psi=0$ to a fully nonlinear wave pattern in a homogeneous medium undergoing a supercritical bifurcation. According to this criterion, a stationary front exists in homogeneous media only when the control parameters are chosen to be exactly at the CU/AU transition. In the present inhomogeneous, i.e., spatially varying context, the CU/AU transition precisely occurs at the single location X_f . The front at this station has the overall frequency ω_f and the complex wave number at the decaying front edge coincides [Fig. 1(b)] with the local absolute wave number $k_f=k_0(X_f)=k^{l\pm}(X_f, \omega_f)$.

By definition of the absolute wave number, the linear $k^{l\pm}$ branches meet at k_f for $\omega=\omega_f$ and $X=X_f$. In a neighborhood of X_f , the upstream k^{l-} branch decays towards X

$=-\infty$ when $X < X_f$, whereas the downstream spatially amplified k^{l+} branch is replaced by the nonlinear k^{nl+} branch when $X > X_f$. The front at X_f exactly connects the linear k^{l-} branch in the CU region $X < X_f$ with the nonlinear k^{nl+} branch prevailing in the AU region $X > X_f$. Further downstream the nonlinear k^{nl+} branch eventually returns to the linear k^{l+} via a neutral stability station X_2 where the nonlinear amplitude vanishes, exactly as for soft global modes.¹⁴

A front located at the upstream boundary of the AU region is a stable configuration due to the following argument. Consider a small displacement from the front equilibrium position at X_f towards $X > X_f$. The front now experiences a slightly AU medium and hence¹⁵ propagates slowly towards its decaying edge, i.e., upstream. When the front is displaced to $X < X_f$, it penetrates into a CU region and is thus pushed downstream. In any case the front is seen to return to its equilibrium position. The complete asymptotic representation of steep global modes is obtained by linear and nonlinear WKBJ matching techniques as in Ref. 14.

According to the present theory the CGL equation with spatially varying coefficients has been shown to admit two types of time harmonic solutions. Soft global modes are characterized by a nonlinear saddle point condition,¹⁴ whereas steep global modes display a stationary front (6) and (7) at the upstream boundary of the AU domain. The nature of the selected global mode is determined by formally computing the respective characteristic frequencies ω_s and ω_f : in a future publication we will show that the mode of largest frequency is selected and that no other global mode type occurs. The validity of these theoretical criteria is confirmed by spatio-temporal numerical simulations of (1). Furthermore, according to the results of Ref. 16, one expects the nature of the bifurcation to a fully nonlinear global mode to be extremely sensitive to ϵ .

In both instances, frequency selection takes place at the downstream position where a $-$ branch is linked to a $+$ branch: k^{nl-} and k^{nl+} at X_s for a soft global mode, k^{l-} and k^{nl+} at X_f for a steep global mode. These stations effectively act as frequency generators for the entire flow. Such locations may be interpreted as local oscillators inducing the upstream $-$ branch and the downstream $+$ branch, regardless whether these branches are linear or nonlinear. It is noteworthy that the present steep frequency selection criterion (6) and (7) demonstrates, in the CGL context, the validity of the initial resonance principle postulated by Monkewitz and Nguyen¹⁷ to account for self-excited resonances in bluff body wakes.

An essential difference between steep and soft global

modes is that steep global modes only involve one nonlinear spatial branch k^{nl+} . The sharp front allows an immediate crossover from the linear $-$ to the nonlinear $+$ branch. Generalization of the present theory to real flows is in progress: In the context of free shear flows governed by the Navier-Stokes equations, the local k^{nl+} is represented by fully nonlinear saturated solutions on a streamwise periodic domain as obtained in direct numerical simulations for a given parallel basic flow. To our knowledge local k^{nl-} branches for free shear flows have never been identified. It therefore seems likely that fully nonlinear global modes in wakes, jets or shear-layers may be described as steep rather than soft global modes.

^{a)}Electronic mail: benoit@ladhyx.polytechnique.fr

¹P. Huerre and P. Monkewitz, "Absolute and convective instabilities in free shear layers," *J. Fluid Mech.* **159**, 151 (1985).

²W. Koch, "Local instability characteristics and frequency determination on self-excited wake flows," *J. Sound Vib.* **99**, 53 (1985).

³P. A. Monkewitz, "The absolute and convective nature of instability in two-dimensional wakes at low Reynolds numbers," *Phys. Fluids* **31**, 999 (1988).

⁴P. A. Monkewitz and K. D. Sohn, "Absolute instability in hot jets," *AIAA J.* **26**, 911 (1988).

⁵A. Bers, in *Handbook of Plasma Physics*, edited by M. N. Rosenbluth and R. Z. Sagdeev (North-Holland, Amsterdam, 1983).

⁶J.-M. Chomaz, P. Huerre, and L. G. Redekopp, "A frequency selection criterion in spatially developing flows," *Stud. Appl. Math.* **84**, 119 (1991).

⁷P. A. Monkewitz, P. Huerre, and J.-M. Chomaz, "Global linear stability analysis of weakly non-parallel shear flows," *J. Fluid Mech.* **251**, 1 (1993).

⁸D. A. Hammond and L. G. Redekopp, "Global dynamics and aerodynamics flow vectoring of wakes," *J. Fluid Mech.* **338**, 231 (1997).

⁹J.-M. Chomaz, "Absolute and convective instabilities in nonlinear systems," *Phys. Rev. Lett.* **69**, 1931 (1992).

¹⁰A. Couairon and J.-M. Chomaz, "Absolute and convective instabilities, front velocities and global modes in nonlinear systems," *Physica D* **108**, 236 (1997).

¹¹N. Meunier, M. R. E. Proctor, D. D. Sokoloff, A. M. Soward, and S. M. Tobias, "Asymptotic properties of a nonlinear $\alpha\omega$ -dynamo wave: period, amplitude and latitude dependence," *Geophys. Astrophys. Fluid Dyn.* **86**, 249 (1997).

¹²P. Büchel, M. Lücke, D. Roth, and R. Schmitz, "Pattern selection in the absolutely unstable regime as a nonlinear eigenvalue problem: Taylor vortices in axial flow," *Phys. Rev. E* **53**, 4764 (1996).

¹³H. W. Müller, M. Lücke, and M. Kamps, "Transversal convection patterns in horizontal shear flow," *Phys. Rev. A* **45**, 3714 (1992).

¹⁴B. Pier and P. Huerre, "Fully nonlinear global modes in spatially developing media," *Physica D* **97**, 206 (1996).

¹⁵G. Dee and J. S. Langer, "Propagating pattern selection," *Phys. Rev. Lett.* **50**, 383 (1985).

¹⁶S. Le Dizès, P. Huerre, J.-M. Chomaz, and P. A. Monkewitz, *Proceedings of the IUTAM Symposium on Bluff-Body Wakes, Dynamics and Instabilities*, edited by H. Eckelmann et al. (Springer, Berlin, 1993), p. 147.

¹⁷P. A. Monkewitz and L. N. Nguyen, "Absolute instability in the near-wake of two-dimensional bluff bodies," *J. Fluids Struct.* **1**, 165 (1987).

[A3]

Superlattice patterns in surface waves

A. Kudrolli, B. Pier & J.P. Gollub

Physica D **123**, 99–111 (1998)

doi:10.1016/S0167-2789(98)00115-8

<https://hal.archives-ouvertes.fr/hal-00120028>

Superlattice patterns in surface waves

A. Kudrolli^{a,1}, B. Pier^a, J.P. Gollub^{a,b,*}

^a Department of Physics, Haverford College, Haverford, PA 19041, USA

^b Physics Department, University of Pennsylvania, Philadelphia, PA 19104, USA

Abstract

We report novel superlattice wave patterns at the interface of a fluid layer driven vertically. These patterns are described most naturally in terms of two interacting hexagonal sublattices. Two frequency forcing at very large aspect ratio is utilized in this work. A superlattice pattern (“superlattice-I”) consisting of two hexagonal lattices oriented at a relative angle of 22° is obtained with a 6 : 7 ratio of forcing frequencies. Several theoretical approaches that may be useful in understanding this pattern have been proposed. In another example, the waves are fully described by two superimposed hexagonal lattices with a wavelength ratio of $\sqrt{3}$, oriented at a relative angle 30° . The time dependence of this “superlattice-II” wave pattern is unusual. The instantaneous patterns reveal a time-periodic stripe modulation that breaks the sixfold symmetry at any instant, but the stripes are absent in the time average. The instantaneous patterns are not simply amplitude modulations of the primary standing wave. A transition from the superlattice-II state to a 12-fold quasi-crystalline pattern is observed by changing the relative phase of the two forcing frequencies. Phase diagrams of the observed patterns (including superlattices, quasicrystalline patterns, ordinary hexagons, and squares) are obtained as a function of the amplitudes and relative phases of the driving accelerations.

Copyright © 1998 Elsevier Science B.V.

Keywords: Patterns; Surface waves; Superlattice; Hexagons; Symmetries

1. Introduction

Surface waves produced by the Faraday instability are known to give rise to many different patterns (including stripes, squares, hexagons, and even quasi-crystalline patterns) as a function of driving frequency and amplitude, viscosity, and the driving waveform [1–4]. However, regular space-filling patterns formed as a result of nonlinearity are even more diverse than the wide range reviewed by Cross and

Hohenberg [5]. For example, in recent optical experiments in a Kerr-like medium, phase locking of several wave vectors results in novel patterns with several unequal wave vectors [6]. In this paper we report novel regular patterns observed in experiments on surface waves generated by two frequency forcing that extend earlier systematic work limited to single-frequency forcing [3]. *We will refer to these new patterns as superlattices because these are composed of two discrete but interacting sublattices.* Their occurrence extends the striking variety of symmetric states than can occur in nonlinear surface waves.

In our earlier study hexagonal wave patterns were observed for low driving frequencies, for which the

* Corresponding author. Tel.: (610) 896 1196; fax: (610) 896 4904; e-mail: jgollub@haverford.edu.

¹ Permanent address: Department of Physics, Clark University, 950 main Street, Worcester, MA 01610, USA. E-mail: akudrolli@clarku.edu.

gravitational restoring force was comparable to the capillary force. For high frequencies, i.e. in the capillary limit, square patterns were observed for low kinematic viscosity ($\nu < 50 \text{ cm}^2 \text{ s}^{-1}$), and textured stripes for higher viscosity. Recent theoretical work by Chen and Viñals [7] has explained these observations using quasi-potential equations derived from the underlying hydrodynamic equations.

Good agreement of measured onset accelerations for two frequency forcing have been found with predictions of linear stability analysis of the full hydrodynamic equations [8]. Edwards and Fauve [4] observed 12-fold quasi-crystalline patterns using two frequency forcing with ratio 4 : 5. They argued that an even frequency perturbed by an odd frequency breaks the subharmonic symmetry (invariance with respect to translation in time by one driving period) and therefore allows quadratic terms (which would otherwise be excluded) to appear in the amplitude equations. Stabilization of patterns such as hexagons can then occur by quadratic interaction as in non-Boussinesq convection. These 12-fold quasi-crystalline patterns may be described as two hexagonal lattices that are oriented at 30°. A clear mechanism for their formation is not available, although recent work on a generalized Swift–Hohenberg model equation has shown 12-fold quasi-patterns [9].

In other work by Müller using 1 : 2 forcing, triangular and hexagonal lattices were observed; the type of lattice could be selected by using a third perturbing frequency [10], but no superlattices were reported. These experimental observations were reproduced theoretically by Zhang and Viñals [11] using an extension of their quasi-potential equations to the case of two frequencies.

In the present work we report and discuss several new patterns formed with even–odd forcing. We study two frequency ratios (6 : 7 and 4 : 5), to explore the formation of patterns with novel symmetries. In both cases, there is a prominent region of hexagons in parameter space. By making relatively small adjustments in the relative amplitude or phase of the forcing components, we find several distinct patterns that are described most naturally as being composed of multiple hexagonal sublattices. In these patterns, the spatial

power spectrum contains peaks at smaller wave numbers than those observed at the onset of surface waves (for either driving frequency). These superlattice patterns arise from an instability of the base hexagonal lattice that is formed at onset. Superlattice structures are of course common in condensed matter physics, but to our knowledge the term has not previously been applied to patterns in nonlinear systems.

2. Experimental setup and forcing function

The apparatus is essentially as described in [8]. The experimental setup consists of a 32 cm diameter circular aluminum container filled with silicone oil to a height of 3 mm. This material gives stable behavior over many weeks, and is available over a wide range of kinematic viscosity, though the present work is limited mainly to $\nu = 20\text{--}50 \text{ cm}^2 \text{ s}^{-1}$ because of the large number of other parameters that need to be varied. The fluid depth is generally greater than the viscous penetration depth at the typical fluid oscillation frequency. The container is rigidly attached to a Vibration Test Systems electromagnetic shaker that is capable of applying peak forces of 2200 N.

The forcing waveform that controls the acceleration of the container is described by

$$a(t) = a[\cos(\chi) \cos(n\omega t) + \sin(\chi) \cos(m\omega t + \phi)], \quad (1)$$

where, $\omega = 2\pi f$, n and m are integers, $1/f$ is the overall period T of the driving, and χ is used to control the relative amplitudes. By measuring the actual acceleration and using feedback, the acceleration is forced to follow Eq. (1) to within about 1%. We generally choose n to be even and m to be odd so that nonlinear interactions can occur at quadratic order, as explained in Section 1. We thoroughly explore two cases: $(m, n) = (6, 7)$ and $(4, 5)$, and we systematically vary a , ϕ , χ for each case. For some purposes it is useful to define $a_n = a \cos(\chi)$ and $a_m = a \sin(\chi)$.

Lighting is provided by a circular array of lights, and the reflected light from the fluid surface is imaged. Roughly speaking, nodes appear dark because light

is deflected away from the camera, while antinodes appear bright. The intensity is a (nonlinear) function of the surface slope, reaching a maximum at an angle (4.2°) that is often small compared to the slopes typically present in the patterns. We typically average over 1–2 wave periods; this causes the apparent wavelength to be half the actual wavelength, since there are two nodes (or antinodes) per period. Though the images are not quantitative measures of the surface height function or slope, they are useful for determining the symmetries of the patterns. In some cases, instantaneous images are used to determine the variation of the waves with time within one wave period.

The patterns formed at the surface are imaged using a 512×512 pixel Dalsa variable scan CCD camera controlled by the same computer that generates the driving waveform of the shaker. The camera exposure times may be varied with a minimum exposure time of about 10^{-3} s. The phase of the image acquisition with respect to the forcing function is adjustable by means of a programmable liquid crystal shutter. Pattern analysis is implemented using Khoros image processing software.

3. Experimental results

3.1. Parameter space for $6\omega : 7\omega$ forcing

First we discuss the patterns obtained using $n = 6$ and $m = 7$, i.e. a $6:7$ frequency ratio. We find that in the capillary limit (where the capillary force dominates over gravitation) the patterns do not depend strongly on the frequency f . Therefore, detailed studies of the patterns observed as a function of a , χ , and ϕ in Eq. (1) were conducted at $f = 16.44$ Hz. The phase diagram of the patterns obtained as a function of the relative strength of acceleration is shown in Fig. 1(a) for $f = 16.44$ Hz, and $\phi = 20^\circ$. The data shown in the phase diagram were obtained by observing the pattern after incrementing the acceleration a in steps 0.1 g, and χ and ϕ in steps of 5° .

A square lattice is observed when the accelerations a_6 and a_7 are substantially unequal. This

observation is consistent with previous studies using single frequency forcing at the same viscosity [3]. The square patterns corresponding to the even frequency are harmonic since the phase of the fluid motion has the same sign after a drive period T . On the other hand, the square patterns corresponding to the odd frequency are subharmonic, i.e. they change sign after one drive period and will have the same sign only after two periods. (However, the subharmonic pattern does recur at a shorter time interval $2T/7$. The use of the term subharmonic refers to the phase of the pattern after one drive period T .)

More complex patterns are obtained when both components are comparable. In this situation, hexagons are formed at onset, as shown in Fig. 1. This transition is subcritical, since hysteresis is observed at onset. Because of the observation of hysteresis and the role played by the odd frequency 7ω , these hexagons are thought to arise from quadratic interactions in the amplitude equations [4]. They arise from a fundamentally different mechanism than those observed with single frequency forcing, where the interactions are at cubic order in the amplitude equations and triad resonances (which occur at low frequencies) are important [3,12]. As the variable χ (which specifies the relative strength of the two frequencies) is increased near onset, the wavelength changes suddenly from the one corresponding to the even forcing term to that corresponding to the odd term at a particular value $\chi_0 \equiv 61.5^\circ$ that is independent of ϕ . This point in the parameter space may be regarded as a “bi-critical point”.

Time-dependent patterns are also visible in the phase diagrams. These include: transverse amplitude modulations (TAM), which have been predicted in a simpler form [13] and observed [14] previously; and spatiotemporal chaos (STC) similar to that which develops from square patterns for single frequency forcing [3].

The main features of the phase diagram are relatively independent of ϕ . This is shown in the phase diagram near the bi-critical point for fixed χ as shown in Fig. 1(b). However, the secondary instability leading to disorder does depend significantly on ϕ .

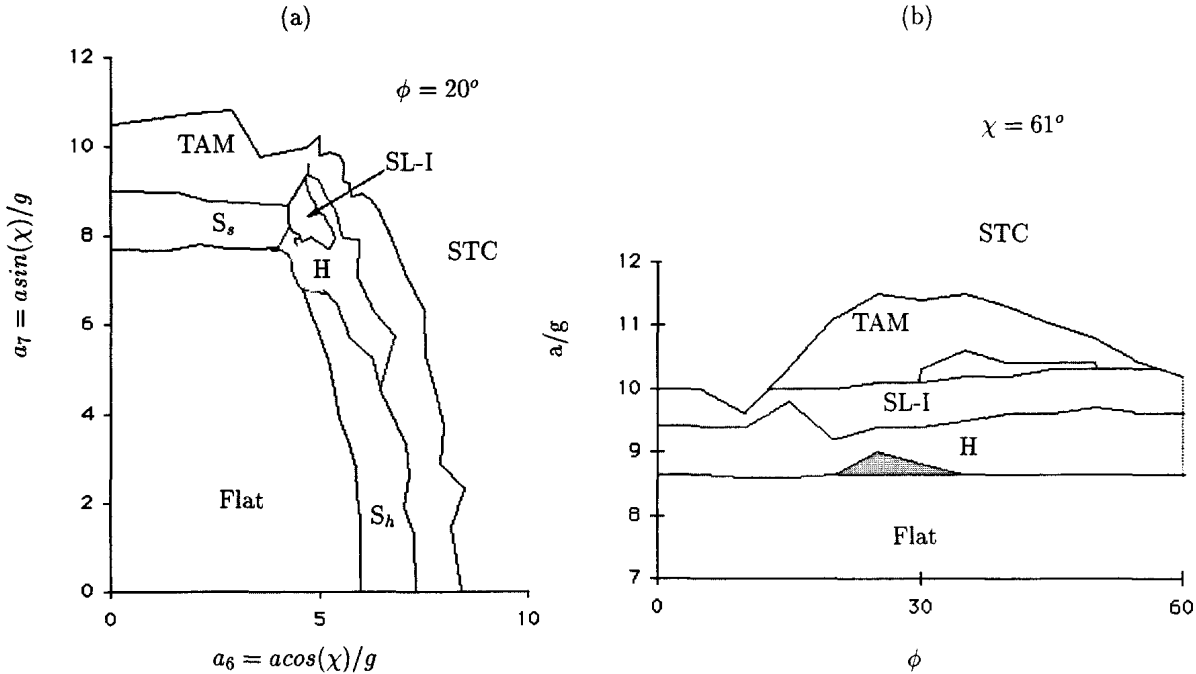


Fig. 1. Phase diagrams of patterns obtained for a forcing frequency ratio of 6:7 (see Eq. (1)). (a) The axes represent the forcing amplitudes a_6 and a_7 at the two frequencies $6f$ and $7f$, and the phase angle ϕ is held fixed at 16° ($\nu = 20 \text{ cm}^2 \text{ s}^{-1}$, 16.4 Hz). (b) Phase variation of the patterns for fixed $\chi = 61^\circ$. H = hexagons; S_s = subharmonic squares; S_h = harmonic squares; SL-I = Superlattice-I state; TAM = transverse amplitude modulations; STC = spatiotemporal chaos. In shaded regions competition occurs.

3.2. Superlattice-I patterns and their spectra

An additional instability occurs as the acceleration is increased in the vicinity of the bi-critical point (see Fig. 1(a)). We refer to the resulting pattern, shown in Fig. 2, as a *superlattice-I (SL-I) pattern* (to distinguish it from another case that we describe later in this section). This pattern shows a triangular (three-fold) lattice at large scales, with each lattice point being composed of discrete clusters of three small cells. Each of the small cells is approximately the same size as the hexagons in the “nearby” hexagonal state. We use stroboscopic illumination to determine that this pattern is harmonic with the drive period T ; the image shown in Fig. 2 has been obtained with an exposure time equal to the drive period.

We compare the two-dimensional power spectrum of the SL-I state with that of the hexagonal pattern in Fig. 3. The SL-I spectrum has the sixfold symmetry of a hexagonal lattice, but the minimum lattice vector (corresponding to the *inner* set of six peaks) is

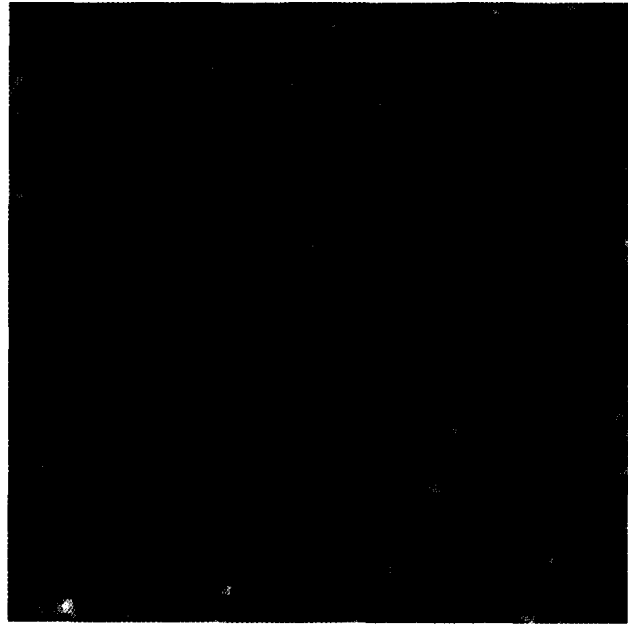


Fig. 2. Example of the superlattice-I pattern obtained for two-frequency forcing with ratio 6:7 ($f = 16.44 \text{ Hz}$, $\phi = 20^\circ$, $\chi = 61^\circ$).

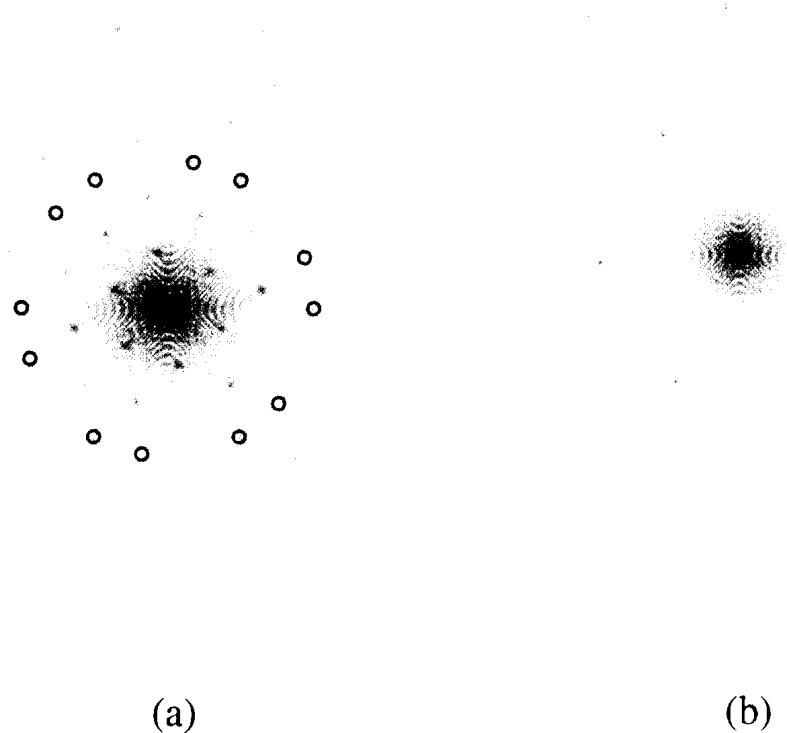


Fig. 3. Two-dimensional power spectrum of the superlattice-I state (a) and hexagonal state (b). The two sets of circles in black highlight the peaks corresponding to the two hexagonal lattices of the same wave number as the onset hexagons shown in (b).

quite different in magnitude from the wave number k_0 that is forced directly and corresponds to the onset hexagons, shown in Fig. 3(b). Instead, k_0 corresponds to the *fourth* circle in Fig. 3(a) that is concentric with the origin; these peaks have been highlighted artificially and are *further* from the origin by a factor $\sqrt{7}$. Furthermore, the 12 peaks on this circle are *not* equally spaced. They may be described as two sets of six peaks forming two hexagons oriented at an angle $2 \sin^{-1}(1/2\sqrt{7}) \approx 22^\circ$ to each other. (This situation is quite different from the 12 peaks of the quasi-crystalline pattern discussed in Section 3.3. In that case, there are also 12 dominant peaks, but they are equally spaced on a circle centered at the origin.)

We note that the onset wave number k_0 corresponds (via the dispersion relation) to the 6ω forcing. We propose that the SL-I pattern results from resonances involving quadratic interactions between the highlighted peaks on the fourth circle with wave

number k_0 ; such interactions are allowed for harmonic patterns produced by even–odd forcing, and they are capable of generating all of the other peaks in the power spectrum. The six peaks located on the slightly larger *fifth* circle have a wave number that approximately corresponds to the 7ω term. This frequency matching may also be important in generating the SL-I pattern [9], but we are unable to assess its importance.

3.2.1. Phenomenological description of the SL-I state

As we have indicated, a description of this SL-I state can be given in terms of two interacting hexagonal lattices; we give it more explicitly here. Each hexagonal lattice may be specified by an instantaneous surface height function given (to within a constant of proportionality) by

$$F_{\text{hex}}(x, y) = \sum_{i=1}^3 \cos(\mathbf{k}_i \cdot \mathbf{r} + \beta_i) \quad (2)$$

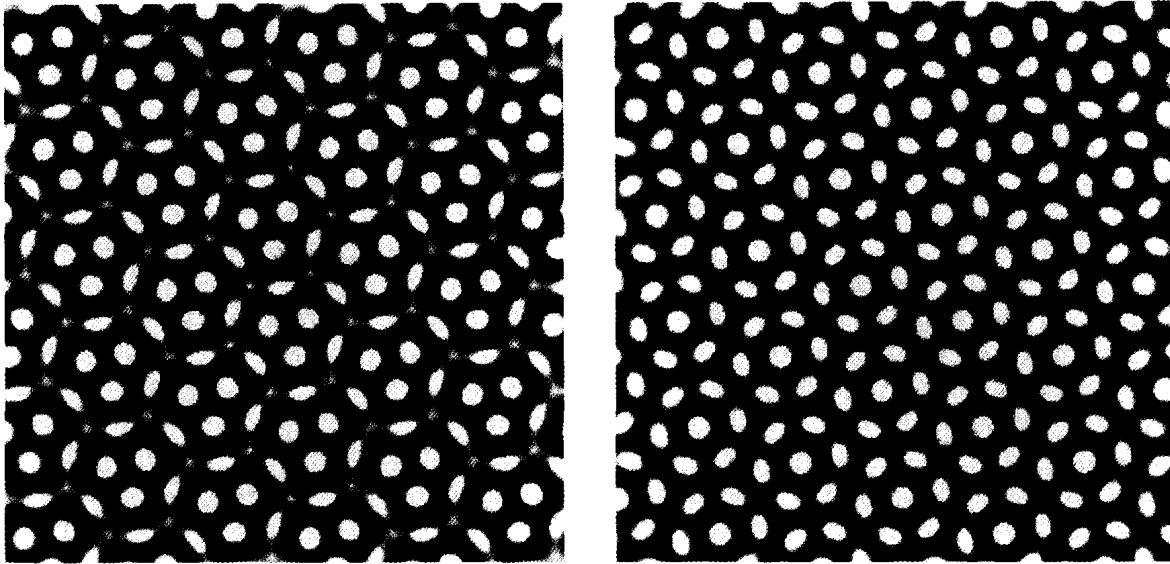


Fig. 4. Patterns formed by superposing two hexagonal lattices at an angle $\theta = 2 \sin^{-1}(1/2\sqrt{7}) \approx 22^\circ$. The total phases defined below Eq. (2) are the same for both lattices. (a) A point of sixfold symmetry of the first lattice coincides with a point of triangular symmetry of the second lattice; this gives a pattern that closely matches the experimental SL-I pattern with overall triangular symmetry. (b) A point of sixfold symmetry of one lattice corresponds to a similar point of the other lattice.

with

$$\begin{aligned} \mathbf{k}_1 &= (1, 0), & \mathbf{k}_2 &= (-1/2, \sqrt{3}/2), \\ \mathbf{k}_3 &= (-1/2, -\sqrt{3}/2), & \mathbf{r} &= (x, y). \end{aligned}$$

We denote the arguments of the cosine functions by ψ_i ; the total phase $\Phi \equiv \sum \psi_i = \sum \beta_i$ can take on only two possible values: 0 (corresponding to the centers of the hexagons having positive or upward displacement) and π (corresponding to hexagons with centers down at the given instant). Hexagonal patterns have points of sixfold symmetry where $\psi_i = 0$ (for all i), and points of triangular symmetry for which $\psi_i = +2\pi/3$ (for all i) or $\psi_i = -2\pi/3$ (for all i).

If a second lattice, rotated by an angle $\theta = 2 \cdot \sin^{-1}(1/2\sqrt{7}) \approx 22^\circ$, is also present, then the combined pattern is *periodic* because of the commensurability or resonance condition $2\mathbf{k}'_1 - \mathbf{k}'_3 = \mathbf{k}_1 - 2\mathbf{k}_3$. However, it is still necessary to specify the total phases and the relative positions of the centers of the hexagons of the two lattices. We choose the total phases of the two lattices to be the same, i.e. $\Phi = \Phi' = 0$ (If they are unequal, the constructed pattern does not resemble the experimental pattern.) The texture also depends on

the displacement of the second lattice with respect to the first one. It turns out that the pattern we observe is obtained if a point of sixfold symmetry of the first lattice (where all the $\psi_i = 0$) coincides with a point of three-fold symmetry of the second lattice (where all the $\psi_i = \pm 2\pi/3$). This pattern is shown in Fig. 4(a). Another interesting pattern is obtained by superimposing *either* points of hexagonal symmetry $\psi_i = 0$, or points of triangular symmetry of different type, i.e. $\psi_i = 2\pi/3$ with $\psi_i = \pm 2\pi/3$. This pattern is shown in Fig. 4(b); symmetry considerations have been used to argue for its stability [15], but we do not observe it. Finally, if points on the two lattices with no rotational symmetry are superimposed, then stripe patterns are generally obtained.

From these considerations, we learn that to form the observed SL-1 pattern from two hexagonal lattices, it is essential *not only* that the wave vectors of the two lattices be locked at the correct angle in Fourier space, but *also* that a phase-locking condition be satisfied in real space: the positions of the two patterns must have the relationship described in the preceding paragraph. Note that the constructed pattern of Fig. 4(a) closely resembles the experimental one even though it does

not contain the smaller wave vectors that are present in the power spectrum of the experimental image. These smaller wave vectors are probably a mixture of (a) nonlinear interactions arising from three-wave resonances between the various Fourier components and (b) imaging nonlinearity. There is no easy way to determine the relative importance of these two contributions.

3.2.2. Transition to the SL-I state

The inner ring of peaks in Fig. 3(a) is present in the SL-I state but not in the hexagon state. Therefore, we use the strength of these peaks to follow the transition qualitatively as the acceleration is varied, while remaining cognizant of the fact that imaging nonlinearity can contribute significantly to their strength. We define a *superlattice amplitude* S_I by first integrating the power spectrum azimuthally and then integrating over $\Delta k = 0.3 \text{ cm}^{-1}$ centered at the peak corresponding to the first ring of peaks. The variation of S_I with driving acceleration a is shown in Fig. 5. The contribution from the background noise has been subtracted. The transition appears to be continuous, and could be a transcritical bifurcation. Visually the domains of the SL-I state spread with increasing acceleration until they gradually cover the entire container. However, it is possible that the transition is actually discontinuous, and that the discontinuity is masked by a slightly inhomogeneous driving acceleration (variation $\pm 1.5\%$).

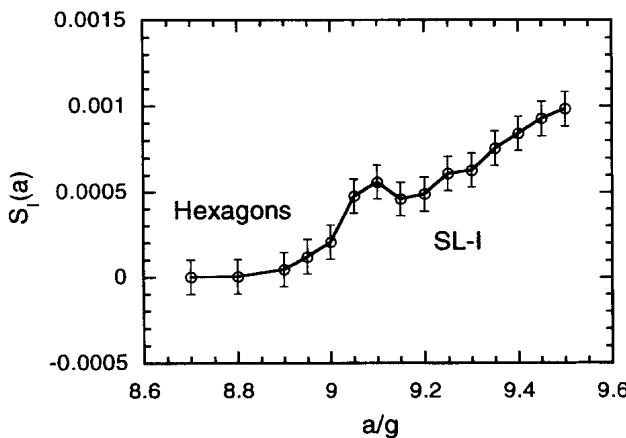


Fig. 5. The superlattice amplitude $S_I(a)$ (see text) as a function of acceleration shows a continuous transition from hexagons to the SL-I state ($f = 16.44 \text{ Hz}$, $\phi = 20^\circ$, $\chi = 61^\circ$).

3.2.3. Defects

The superlattice-I patterns generally show weak time dependence due to the presence of defects in the patterns. The most prominent of these are phase defects that cause the “triangular” structure in the SL-I pattern to vary locally in orientation. A typical defect-free region is of the same size as that shown in Fig. 2. Small domains of ordinary hexagons are also present with accompanying grain boundaries. We found that the number of defects does not decrease appreciably with time.

3.2.4. Other superpositions

Edwards and Fauve [4] have reported quasi-crystalline patterns with 6:7 forcing frequency ratio. We did not observe them with 6:7 forcing, but our viscosity was significantly lower ($20 \text{ cm}^2 \text{ s}^{-1}$ versus $100 \text{ cm}^2 \text{ s}^{-1}$ in their case). Given the large number of parameters that affect the superlattice patterns, it was impractical to explore the variation with viscosity in the present work. Earlier work in our laboratory using single frequency forcing showed that the pattern symmetry depends on the viscosity [3].

3.3. Parameter space for $4\omega : 5\omega$ forcing

Next we discuss the patterns observed with a 4:5 forcing frequency ratio. The phase diagram of the patterns obtained as a function of the two forcing amplitudes is shown in Fig. 6(a) for $f = 22 \text{ Hz}$, and $\phi = 16^\circ$. As for the 6:7 frequency ratio, the frequency again is high enough that the waves are in the capillary limit. The patterns do not depend strongly on f . The overall structure of the phase diagram is similar to that observed for the 6:7 frequency ratio: square lattices when one component is much larger than the other, and hexagons and superlattices when both components are comparable. The bi-critical point is also at a similar location in the phase space: $\chi_0 \equiv 61.5^\circ$ and is independent of ϕ . As in the 6:7 frequency ratio case, the main features of the phase diagram do not change qualitatively with ϕ except near χ_0 .

Quasi-crystalline patterns are observed as the acceleration is increased beyond onset, for χ slightly less than χ_0 . An example of such a 12-fold

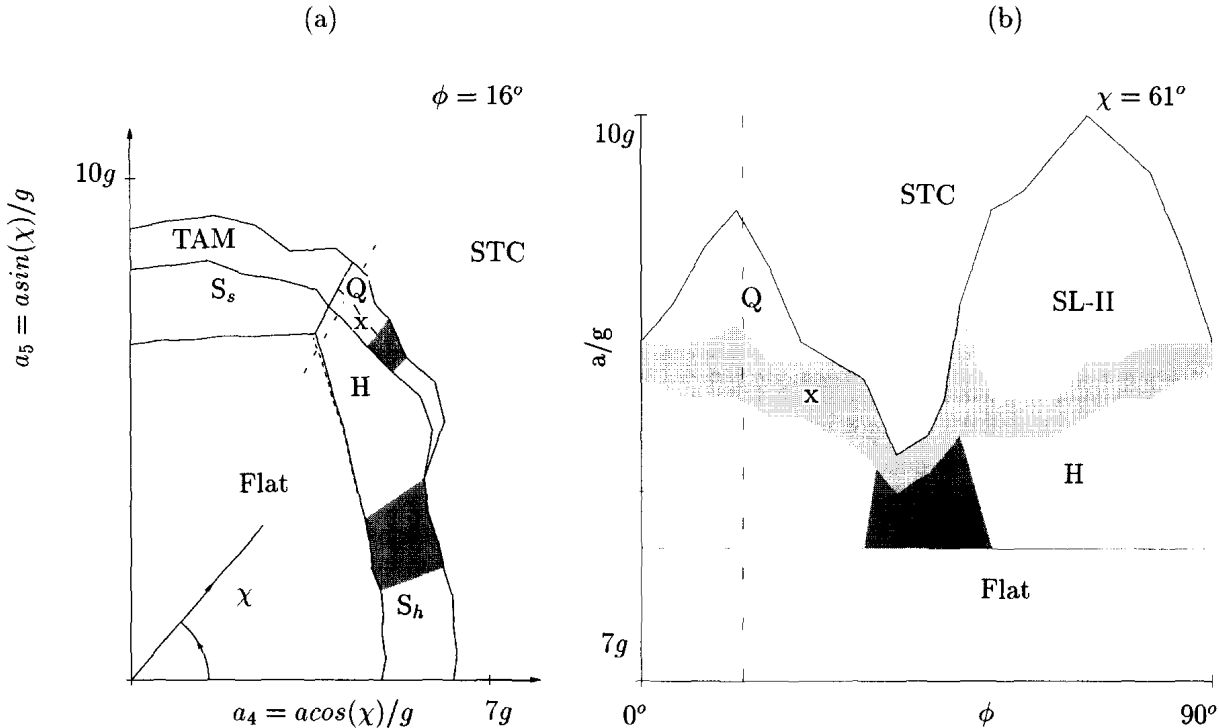


Fig. 6. Phase diagrams of patterns obtained for a forcing frequency ratio of 4:5 with $f = 22$ Hz. The axes are the same as in Fig. 1. SL-II = superlattice-II state (see text); S_s = subharmonic squares; S_h = harmonic squares; H = hexagons; Q = quasi-crystalline patterns; x = competition between quasi-patterns and hexagons; TAM = transverse amplitude modulations; STC = spatiotemporal chaos; dark shading = no stable pattern near onset; light shading = competition between neighboring states.

quasi-crystalline pattern is shown in Fig. 7. The field of view is approximately $20\text{ cm} \times 20\text{ cm}$. Competition between hexagons and quasi-crystalline patterns, which makes them time-dependent, is observed for parameters between those of the pure states. An example of this competition is shown in Fig. 8. We believe that this competition is inherent and not due to an inhomogeneous driving force because the domains exchange position in time.

We studied the transition from hexagons to quasi-crystalline patterns using a spectral *quasi-crystalline amplitude* $S_Q(a)$ that is similar to that used for the SL-I state; it denotes the amplitude of the inner ring of peaks in the corresponding spectrum; they arise due to nonlinear interactions between the main spectral components (but are also affected by imaging nonlinearity) and is shown in Fig. 9. The onset of hexagonal-quasi-crystal competition appears to be abrupt; this regime leads smoothly to the pure quasi-crystalline state around $a/g = 8.9$.



Fig. 7. Example of a quasi-crystalline pattern obtained at $\phi = 16^\circ$ ($f = 22$ Hz, 4:5 frequency ratio). This pattern has 12-fold orientational symmetry but no translational order.

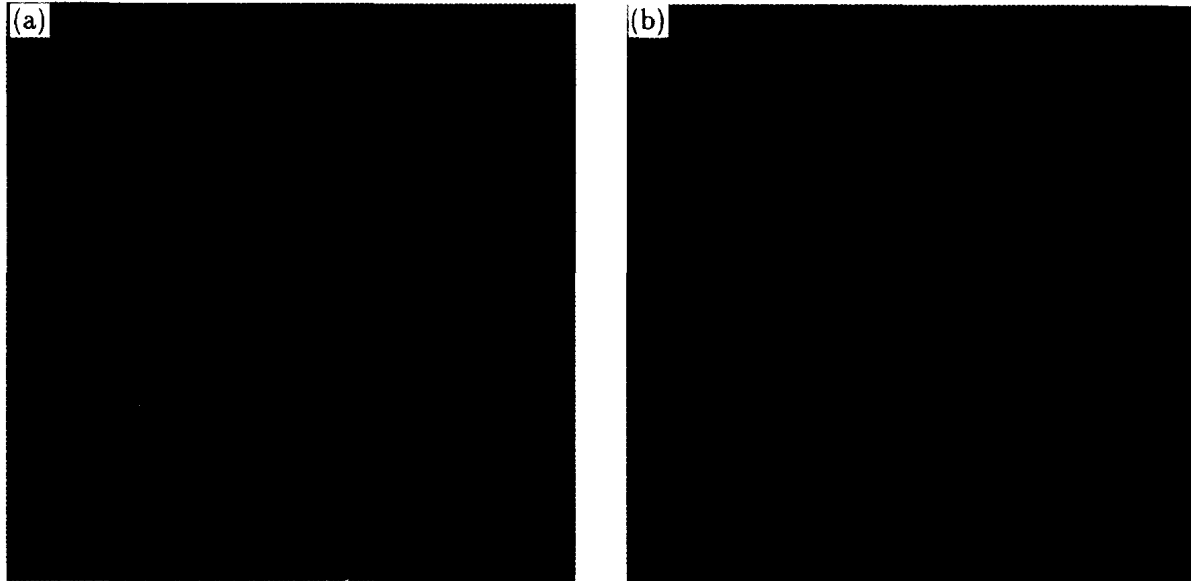


Fig. 8. Quasi-crystalline patterns and hexagons compete on a slow timescale in the region between the pure states indicated by the symbol x in the phase diagram of Fig 6(a). (a,b) are separated in time by 1600 drive periods.

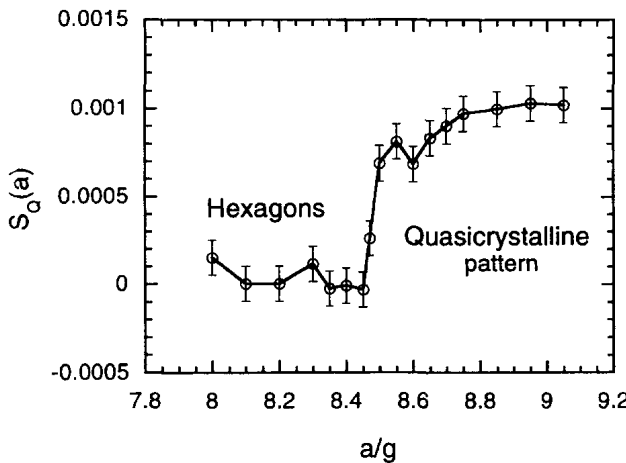


Fig. 9. The quasi-crystal spectral amplitude S_Q (a) as a function of acceleration shows a discontinuous jump at the onset of the region of quasi-crystal-hexagon competition ($f = 22$ Hz, $\phi = 16^\circ$, $\chi = 61^\circ$).

3.4. Superlattice-II state

When ϕ is increased with $\chi \approx 61^\circ$ (slightly less than χ_0), the quasi-crystalline patterns are replaced by a superlattice structure that is quite different from the superlattice-I state discussed in Section 3.2. This superlattice-II pattern, whose stable region is shown in

Fig. 6(b), is subharmonic with respect to f and shows a distinctive periodic time dependence. It was first reported by Pier in his undergraduate thesis [16]. An image obtained by averaging over two drive cycles is shown in Fig. 10 at two different scales. This pattern is composed of hexagonal cells, but there is also a larger wavelength hexagonal lattice superimposed upon it. The cells in the large lattice have higher amplitude and hence appear darker (since more light is scattered away from the camera). The higher amplitude of these cells was checked with a strobe light using side illumination; it is clearly real, and not a lighting artifact.

Additional information about this pattern may be obtained by examining the two-dimensional power spectrum, which is shown in Fig. 11. The peaks corresponding to the hexagonal patterns formed at onset are indicated by the outer ring of six circles. The corresponding wave number k_0 is that obtained by using the dispersion relation with 2ω as the wave frequency (the subharmonic of the 4ω forcing). In addition to these peaks and their harmonics, a set of six peaks occurs at smaller k . The wave number of this inner ring is smaller than k_0 by a factor $\sqrt{3}$.

The experimental spectrum suggests a description of the superlattice-II state in terms of two hexagonal

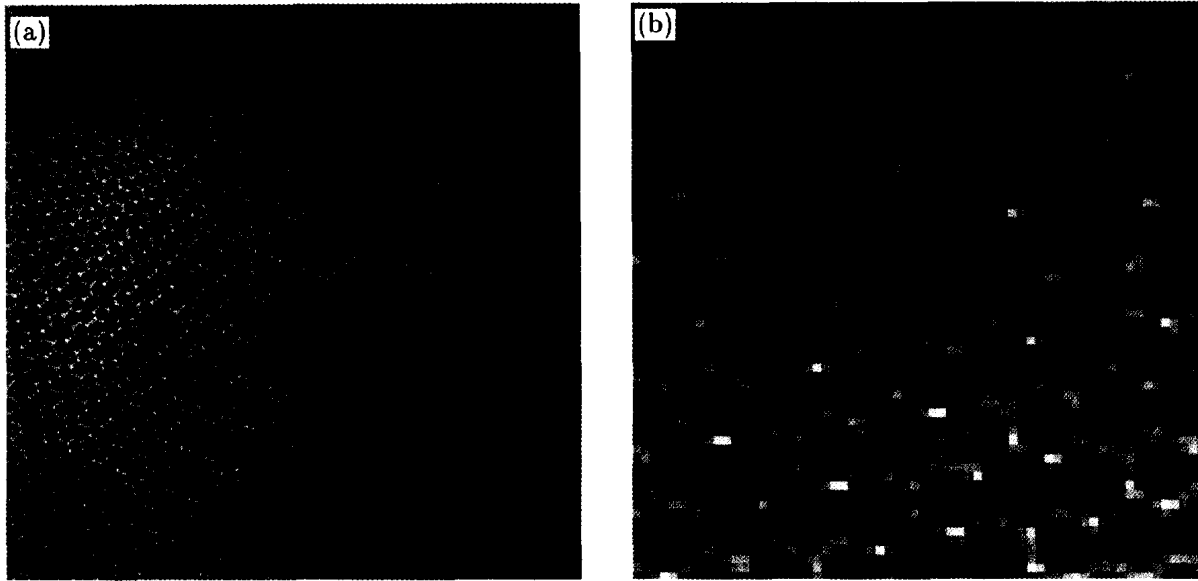


Fig. 10. (a) Superlattice-II state obtained with 4:5 forcing frequency ratio by changing ϕ to 60° . The wave periodicity is $2T$; this pattern was obtained by averaging the image over two drive periods ($f = 22$ Hz). (b) Pattern after magnification by a factor of 4. The scale is within a few percent of that used in Fig. 2.

lattices oriented at 30° to each other, and with wave numbers having a ratio equal to $\sqrt{3}$. (Using the inner peaks alone could reproduce all of the observed spectral peaks by quadratic interactions, but only at the cost of not including the directly forced modes in the description.) A simulated pattern obtained in this way is shown in Fig. 12. Each of the two component lattices has been chosen to place points of hexagonal symmetry at the origin so that $\psi_i = 0$ (for all i) in the notation defined below Eq. (2). The result is qualitatively similar to the experimental pattern of Fig. 10(a). In this description, we have ignored any direct forcing at the wave number corresponding to 5ω , though it may be significant.

The SL-II state displays additional complexity that is not shown by the SL-I state. An instantaneous image (exposure over $1/20$ th of the drive period) reveals this complexity: the sixfold symmetry is broken, and the observed pattern depends on the instant at which the image is obtained. Examples of instantaneous images obtained at four different phases (with respect to 4ω) separated by $T/20$ are shown in Fig. 13. A stripe modulation is visible that is not present in the average images. Power spectra of these images indicate

that the wave number of this modulation is half that of the onset hexagons. The stripes are not a simple amplitude modulation of the primary standing wave, since in that case they would survive in the averaged picture as do the subharmonic stripes observed with single frequency forcing [3]. The stripe modulation is always present; time averaging yields the hexagonal superlattice-II patterns shown in Fig. 10.

The phase diagram as a function of ϕ is shown in Fig. 6(b). The onset acceleration for this pattern does not change appreciably with ϕ . A disordered region occurs for parameters between the quasi-crystalline SL-II states.

4. Discussion

We have reported novel superlattice patterns that occur when Faraday waves are driven at two frequencies. They are closely related to the hexagonal state that occurs near onset. The superlattice-I state, shown in Fig. 2, is harmonic with respect to the total drive frequency ω . It can be described in terms of two superimposed hexagonal lattices whose wave numbers are both equal to that of the onset hexagonal state,

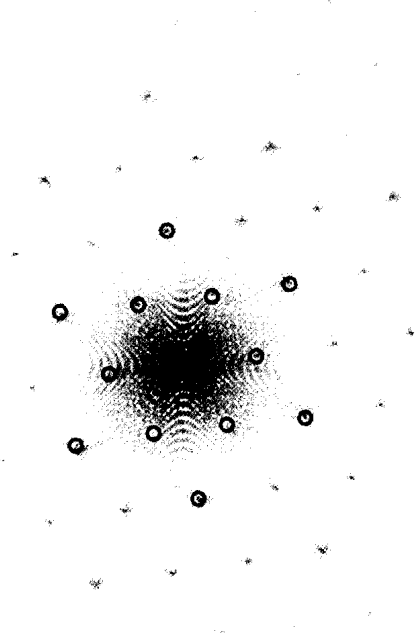


Fig. 11. Two-dimensional power spectrum corresponding to Fig. 10. The outer ring of six peaks (marked by circles) are those of the hexagonal pattern formed near onset. The inner ring of highlighted peaks are associated with the transformation of the hexagonal state into the superlattice state. Their wave number is a factor $\sqrt{3}$ smaller than that of the onset hexagons.

but whose wave vectors are oriented at an angle of $2 \sin^{-1}(1/2\sqrt{7}) \approx 22^\circ$ (Fig. 3). (While other representations are possible, we believe that it is important to include at least one of the wave vectors that are directly forced.) The discussion of Section 3.2 shows that the two lattices are phase-locked together in real space so that a point of sixfold symmetry of the first lattice coincides with a point of triangular symmetry of the second lattice. The new SL-I state differs from the other regular patterns, and from the quasi-crystalline patterns which also have 12 primary spectral peaks, in that the overall orientational symmetry (threefold) is less than the number of primary spectral components.

This SL-I pattern seems to be one of the generic possibilities that can be expected on the basis of symmetry considerations, as explained by Silber

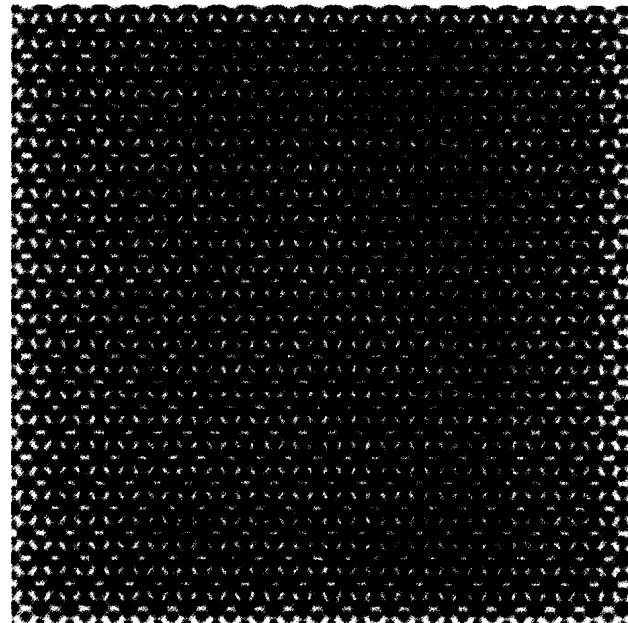


Fig. 12. Simulated SL-II superlattice pattern generated by adding two hexagonal lattices with a wave number ratio $\sqrt{3}$; the orientations of the lattices differ by 30° .

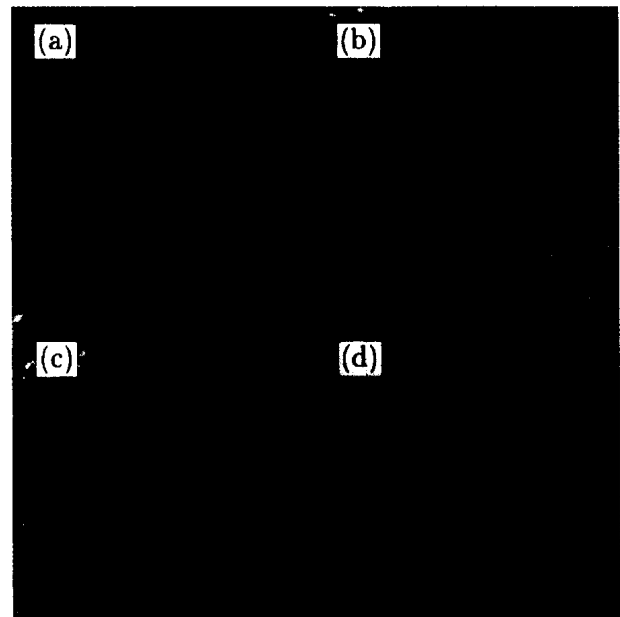


Fig. 13. The sixfold symmetry of the SL-II averaged pattern is broken by the presence of a temporal modulation. Instantaneous images obtained with exposure times of $1/20$ th of the drive period T show a stripe modulation during the drive cycle. Starting times are as follows: (a) $t = 6T/20$, (b) $t = 7T/20$, (c) $t = 8T/20$, and (d) $t = 9T/20$.

and Proctor [17]. These authors show that a low-dimensional model with degenerate bifurcations can be constructed to reproduce the observed transition sequence. The transition shown by their model is hysteretic, whereas the experimental transition appears to be continuous. However, in studying the SL-I state and the transition connecting it to the hexagonal state, we are limited by imaging nonlinearity and a slightly inhomogeneous driving acceleration. An alternate approach to understanding patterns resulting from forcing at two frequencies, such as the SL-I pattern, has been proposed by Lifshitz and Petrich [9]. It is based on a Swift–Hohenberg model with two preferred length scales and both quadratic and cubic nonlinear terms in the wave amplitude. The quadratic term includes the effect of triad interactions between standing waves. In this model, the selected patterns do more than satisfy symmetry considerations; they lead to a lower value of a certain Lyapunov functional. We are unable to test this model, but it is not inconsistent with what we observe.

Using a $4\omega : 5\omega$ frequency ratio, we find and characterize a second superlattice state, which we call superlattice-II (Fig. 10). Its time average can be represented primarily as a combination of two hexagonal lattices differing in wave number by a factor $\sqrt{3}$. This state shows a remarkable time-dependent stripe modulation (Fig. 13) that breaks the hexagonal symmetry at an instant, yet leaves this symmetry unbroken on average. There is at present no theory applicable to this state.

The various hexagonal, quasi-crystalline, and superlattice states show additional complexity due to the presence of defects and competition between patterns that are adjacent in parameter space. Competition between hexagonal and quasi-crystalline patterns was illustrated in Fig. 8. Using spectral methods, we find that the onset of this competition is abrupt. In the regime of hexagons near onset, hepta–penta defects may be formed by sudden increase of driving acceleration. These generally anneal out over a very long time scale and a defect free pattern is usually obtained.

A “clean” hexagonal pattern is best obtained by slowly increasing the acceleration near the wave onset. In this respect the hexagonal patterns obtained using

two frequency forcing differ from those obtained for single frequency forcing, where defects, including π -phase defects are more common (see [3]). No phase defects were observed for two frequency forcing over the range of parameters we investigated. The ease with which defects are eliminated may be related to the fact that the transition from the flat state is subcritical, i.e., there is a small amount of hysteresis, typically about 0.1 g in the driving amplitude a . This hysteresis was first discussed by Edwards and Fauve [4]. This situation is different from that of single frequency forcing, where the coupling, giving rise to hexagons, is at third order in the amplitudes, and both gravity and capillarity are significant.

Defects are also observed in the superlattice-I state. These defects cause the *orientations* of the triangular structures shown in Fig. 2 to vary from place to place. (This variation can be seen when larger areas are examined.) In fact we were unable to obtain a single superlattice-I pattern in which the whole pattern had the same orientation. These defects move slowly, and therefore the patterns are weakly time-dependent. On the other hand the superlattice-II patterns show few defects when the acceleration is increased slowly. Defects that do appear in the superlattice-II state can probably be attributed to the slightly inhomogeneous driving acceleration.

It seems likely that other patterns with distinct symmetries can also be created using two-frequency forcing; because of the large number of parameters that can be varied, we have not explored all of the possibilities. We believe that the patterns discussed in this paper can be used to explore the role of nonlinearity in stabilizing structures with different symmetries that are composed of interacting waves.

Acknowledgements

We appreciate helpful discussions with M. Abraham, R. Lifshitz, and Mary Silber. W.S. Edwards designed the apparatus, taught us about two-frequency forcing, and was involved in the early stages of this

investigation. B. Boyes provided technical support. This work was supported in part by the National Science Foundation under Grants DMR-9319973 and DMR-9704301.

References

- [1] B. Christiansen, P. Alstrom, M.T. Levinsen, Ordered capillary-wave states: quasicrystals, hexagons, and radial waves, *Phys. Rev. Lett.* 68 (1992) 2157.
- [2] K. Kumar, K.M.S. Bajaj, Competing patterns in the Faraday experiment, *Phys. Rev. E* 52 (1995) R4606.
- [3] A. Kudrolli, J.P. Gollub, Patterns and spatiotemporal chaos in parametrically forced surface waves: a systematic survey at large aspect ratio, *Physica D* 97 (1996) 133.
- [4] W.S. Edwards, S. Fauve, Patterns and quasipatterns in the Faraday experiment, *J. Fluid Mech.* 278 (1994) 123.
- [5] M.C. Cross, P.C. Hohenberg, Pattern formation outside of equilibrium, *Rev. Mod. Phys.* 65 (1993) 851.
- [6] E. Pampaloni, S. Residori, S. Soria, F.T. Arecchi, Phase locking in nonlinear optical patterns, *Phys. Rev. Lett.* 78 (1997) 1042.
- [7] P. Chen, J. Viñals, Pattern selection in Faraday waves, *Phys. Rev. Lett.* 79 (1997) 2670.
- [8] T. Besson, W.S. Edwards, L.S. Tuckerman, Two-frequency parametric excitation of surface waves, *Phys. Rev. E* 54 (1996) 507.
- [9] R. Lifshitz, D. Petrich, Theoretical model for Faraday waves with multi-frequency forcing, *Phys. Rev. Lett.* 79 (1997) 1261.
- [10] H.M. Müller, Periodic triangular patterns in the Faraday experiment, *Phys. Rev. Lett.* 71 (1993) 3287.
- [11] W. Zhang, J. Viñals, Pattern formation in weakly damped parametric surface waves driven by two frequency components, *J. Fluid Mech.* 341 (1997) 225.
- [12] W. Zhang, Pattern formation in weakly damped parametric surface waves, Ph.D. Thesis, Florida State University, 1994.
- [13] S.T. Milner, Square patterns and secondary instabilities in driven capillary waves, *J. Fluid Mech.* 225 (1991) 81.
- [14] L. Daudet, V. Ego, S. Manneville, J. Bechhoefer, Secondary instabilities of surface waves on viscous fluids in the Faraday instability, *Europhys. Lett.* 32 (1995) 313.
- [15] B. Dionne, M. Silber, A.C. Skeldon, Stability results for steady, spatially periodic planforms, *Nonlinearity* 10 (1997) 321.
- [16] B. Pier, Patterns, quasipatterns, and defects in a Faraday experiment, Undergraduate Thesis, Haverford College and Ecole Normale Supérieure, 1994.
- [17] M. Silber, M.R.E. Proctor, Nonlinear competition between small and large hexagonal patterns, to be published.

[A4]

Bifurcation to fully nonlinear synchronized structures in slowly varying media

B. Pier, P. Huerre & J.-M. Chomaz

Physica D **148**, 49–96 (2001)

doi:10.1016/S0167-2789(00)00146-9

<https://hal.archives-ouvertes.fr/hal-00119920>



ELSEVIER

PHYSICA D

Physica D 148 (2001) 49–96

www.elsevier.com/locate/physd

Bifurcation to fully nonlinear synchronized structures in slowly varying media

Benoît Pier*, Patrick Huerre, Jean-Marc Chomaz

Laboratoire d'Hydrodynamique (LadHyX), CNRS-École polytechnique, F-91128 Palaiseau Cedex, France

Received 9 December 1999; received in revised form 5 July 2000; accepted 17 July 2000

Communicated by S. Fauve

Abstract

The selection of fully nonlinear extended oscillating states is analyzed in the context of one-dimensional nonlinear evolution equations with slowly spatially varying coefficients on a doubly infinite domain. Two types of synchronized structures referred to as *steep* and *soft* global modes are shown to exist. Steep global modes are characterized by the presence of a sharp stationary front at a marginally absolutely unstable station and their frequency is determined by the corresponding linear absolute frequency, as in Dee–Langer propagating fronts. Soft global modes exhibit slowly varying amplitude and wave number over the entire domain and their frequency is determined by the application of a saddle point condition to the local nonlinear dispersion relation. The two selection criteria are compared and shown to be mutually exclusive. The onset of global instability first gives rise to a steep global mode via a saddle-node bifurcation as soon as local linear absolute instability is reached somewhere in the medium. As a result, such self-sustained structures may be observed while the medium is still globally stable in a strictly linear approximation. Soft global modes only occur further above global onset and for sufficiently weak advection. The entire bifurcation scenario and state diagram are described in terms of three characteristic control parameters. The complete spatial structure of nonlinear global modes is analytically obtained in the framework of WKBJ approximations. © 2001 Elsevier Science B.V. All rights reserved.

PACS: 47.20.Ft; 47.20.Ky; 47.54.+r; 03.40.Kf

Keywords: Hydrodynamic stability; Frequency selection; Nonlinear global modes

1. Introduction

It is now well established that spatially developing open shear flows may be divided into two classes: some flows are very sensitive to inflow conditions and essentially behave as *noise amplifiers*, others display intrinsic dynamics and may be interpreted as *global oscillators* [20–22]. The present paper is concerned with the latter class of systems and examines in detail the synchronized self-sustained structures which they can support. In previous studies, we have demonstrated the existence of nonlinear *soft global modes* [33] and *steep global modes* [34]. The objective of the present investigation is to analyze the bifurcation scenarios which lead from the basic state to either of these

* Corresponding author. Present address: Department of Applied Mathematics and Theoretical Physics, University of Cambridge, Silver Street, Cambridge CB3 9EW, UK.

fully nonlinear structures as the global control parameters are varied. The analysis is carried out in the context of one-dimensional evolution models with spatially varying coefficients in order to account for the streamwise development of the basic state.

A variety of physical systems give rise to intrinsic self-sustained oscillations: mixing layers with strong enough counterflow [46], low-density jets [29,44], cylinder wakes [27,38,45], wakes behind blunt-edged plates [18,19], thin aerofoil wakes [49], Taylor–Couette flow between concentric spheres [43], Taylor–Couette flow between circular cylinders with throughflow [5], Rayleigh–Bénard convection with throughflow [31], baroclinically unstable atmospheric flows [17,37], sunspot cycles [1,28], etc. Many of these flows display a spatially varying basic state, and hence a spatial dependence of the local instability characteristics. The goal of a global analysis is to obtain in a self-consistent manner a spatially extended structure made up of wave trains governed by the local properties of the medium and tuned at an overall global frequency ω_g . The unknown global frequency ω_g is to be derived from a nonlinear eigenvalue problem consisting of the evolution equation and associated boundary conditions. The associated eigenfunction yields the spatial structure of the corresponding self-sustained oscillations. The resolution of the eigenvalue problem is typically undertaken under the hypothesis of slow spatial variations whereby the underlying basic state evolves slowly over a typical instability length scale. In this framework, the main objective of the global mode analysis is to derive *global* frequency selection criteria from the *local* dispersion relation prevailing at each streamwise station.

Linear global mode analyses are now fairly complete. Chomaz et al. [7] demonstrated that the complex global frequency is determined by a saddle point (equivalently a double turning point) condition applied to the local linear dispersion relation for the linear complex Ginzburg–Landau equation with spatially varying coefficients. This criterion had previously been discovered and implemented by Soward and Jones [43] to describe oscillating states in Taylor–Couette flow between concentric spheres. According to Monkewitz et al. [30], the same criterion also holds for the Navier–Stokes equations linearized about an arbitrary slowly varying basic flow. More recently, Le Dizès et al. [25] reexamined the case of the spatially varying linear complex Ginzburg–Landau equation and demonstrated the existence of another family of linear global modes with two simple turning points. The causal nature of these linear global modes has been established for the same model by Hunt and Crighton [23]: the exact linear impulse response does converge, for large time, to the most unstable linear global mode. The validity of the linear saddle point criterion has been fully confirmed in the direct numerical simulations of the Kármán vortex street behind a blunt-edged plate by Hammond and Redekopp [19].

Paradoxically, the weakly nonlinear extension of these concepts is fraught with difficulties, as emphasized by Chomaz et al. [6] and Le Dizès et al. [24]: the Landau constant pertaining to the Hopf bifurcation near global mode onset does not display a well-defined sign as the WKBJ spatial inhomogeneity parameter is decreased. Furthermore, the weakly nonlinear formulation is only valid in an exponentially small vicinity of threshold.

To obviate such weakly nonlinear studies, it appears natural to resort to a fully nonlinear approach where fluctuations are of order unity. Such a line of thought has been consistently pursued since the early 1990s in the framework of nonlinear Ginzburg–Landau type models. The classical absolute/convective instability concepts introduced in a linear context by Bers [3] and Briggs [4] have been generalized to the fully nonlinear regime by Chomaz [8]. The absolute/convective nature of the nonlinear dynamics is then directly related to the propagation direction of the front separating the basic state from the bifurcated state [16,39–41]. The properties of fully nonlinear global modes on a semi-infinite domain governed by Ginzburg–Landau type equations with constant coefficients have been thoroughly studied by Couairon and Chomaz [10,12,13]. In this case, a nonlinear global mode is obtained when an upstream travelling front is halted in its motion by the upstream boundary point. This event occurs whenever the medium is nonlinearly absolutely unstable in the sense of Chomaz [8]. The reader is referred to Chomaz and Couairon [9] and Tobias et al. [47] for a corresponding analysis of the finite interval problem.

Corresponding fully nonlinear analyses have been performed for the complex Ginzburg–Landau equation with *spatially varying coefficients in infinite media*. Two varieties of nonlinear global modes have been identified. Soft global modes, obtained by Pier and Huerre [33], obey a saddle point frequency selection criterion applied to the local nonlinear dispersion relation. This criterion is formally analogous to its linear counterpart. The associated spatial eigenfunction structure displays smoothly varying amplitude and wave number over the entire domain. By contrast, according to the preliminary results reported by Pier et al. [34], steep global modes are governed by a marginal linear instability criterion: the steep global frequency is imposed by the real absolute frequency [3] prevailing at the transition station between local linear convective and absolute instability. This criterion is akin to the linear front velocity selection principle put forward by Dee and Langer [16]: for a wide class of systems, the speed of the front separating the basic state from the bifurcated state is such that in the co-moving frame the medium is marginally linearly absolutely unstable. The steep global spatial structure displays a stationary sharp front at the transition station with a sudden jump in wave number. In all other regions, the amplitude and wave number are slowly varying. Similar steep self-sustained structures have been numerically identified and analytically determined in amplitude evolution models pertaining to solar and stellar magnetic activity cycles by Bassom et al. [1] and Meunier et al. [28]. The properties of nonlinear global modes governed by the real Ginzburg–Landau equation in a semi-infinite domain with combined distributed spatial inhomogeneity have been obtained by Couairon [11] and Couairon and Chomaz [14]. Predicted scaling laws for the amplitude and position of the maximum very favorably compare with experimental and numerical observations of bluff-body wakes.

The purpose of the present study is two-fold: first, we wish to map out the domains of existence of soft or steep global modes in an appropriate control parameter space and to characterize the associated bifurcations. Secondly, we present the detailed asymptotic structure of the various layers and regions which make up their spatial distribution.

Consider a system governed by a one-dimensional nonlinear partial differential equation that is first-order in time of the form

$$\frac{\partial \psi}{\partial t} = \mathcal{F}(\partial_x; X)[\psi], \quad (1)$$

where x and t represent space and time coordinates, respectively, and X a slow space variable to be defined shortly. The basic state is assumed to be $\psi = 0$, and the function $\psi(x, t)$ represents the fluctuations riding on the basic state. In regions of finite amplitude, ψ is governed by the full nonlinear operator \mathcal{F} . In small amplitude regions, ψ is a perturbation governed by Eq. (1) linearized around the basic state, i.e.,

$$\frac{\partial \psi}{\partial t} = \mathcal{L}(\partial_x; X)[\psi]. \quad (2)$$

A crucial assumption of the present investigation is the slow spatial development of the medium as exemplified by the introduction of the slow spatial variable X in the operators \mathcal{F} and \mathcal{L} . The weak non-uniformity hypothesis is fulfilled if the ratio $\epsilon = \lambda/L$ between the typical instability length scale λ and the inhomogeneity length scale L is small. As a result of this scale separation, the weak variations of the medium instability properties may be described through the slow variable

$$X = \epsilon x \quad \text{with } \epsilon \ll 1. \quad (3)$$

If the slow space variable X is frozen, system (1) becomes a PDE in x and t with constant coefficients which captures the local properties prevailing at that station X . In order to construct a global mode it is necessary to “piece together” local wave trains at different X by explicitly accounting for the weak coupling between local and global properties via relation (3).

The outline of this paper is as follows. The essential concepts necessary to carry out this study are introduced in Sections 2 and 3. Local instability properties where X is frozen are summarized in Section 2. Emphasis is

given to the relationship between causality and the spatial response to a localized harmonic forcing (Section 2.3). In this framework, stationary fronts are shown to naturally arise as the limiting spatial response of the system in the absence of forcing when the medium is marginally absolutely unstable (Section 2.4). Variations of the local instability properties over the entire X -domain are analyzed in Section 3. More specifically, the distribution over X of linear spatial branches (Section 3.2) and nonlinear spatial branches (Section 3.3) is investigated as the global frequency is varied.

Section 4 is concerned with the determination of the leading-order approximation to the global frequency and spatial distribution of fully nonlinear synchronized states governed by (1). It contains the essential results concerning the structure of steep global modes (Section 4.2), the nature of their bifurcation from the basic state (Sections 4.3–4.5), the structure of soft global modes (Section 4.6), and finally the respective domains of existence of steep and soft global modes (Sections 4.7 and 4.8) in control parameter space.

Section 5 is devoted to the complete higher-order asymptotic analysis of the various regions and layers which make up the spatial structure of global modes (cf. Fig. 15). Higher-order corrections to the global frequencies are then obtained. The results are derived in the general context of system (1) by following a methodology analogous to that previously used by Bassom et al. [1] and Pier and Huerre [33].

All the results in principle apply to any nonlinear system governed by an equation of the form (1). However, in order to obtain explicit results and to validate them by direct numerical simulations, we repeatedly use as an illustrative example the complex Ginzburg–Landau (CGL) equation

$$i\frac{\partial\psi}{\partial t} = \left(\omega_0(X) + \frac{1}{2}\omega_{kk}(X)k_0(X)^2\right)\psi + i\omega_{kk}(X)k_0(X)\frac{\partial\psi}{\partial x} - \frac{1}{2}\omega_{kk}(X)\frac{\partial^2\psi}{\partial x^2} + \gamma(X)|\psi|^2\psi \quad (4)$$

for a complex function $\psi(x, t)$. For convenience, the CGL equation is written here as derived from the Taylor expansion of the dispersion relation around $k_0(X)$ in the same manner as [20]. The precise meaning of all the quantities appearing in (4) is discussed in detail in Section 2. The complex X -dependent coefficients $\omega_0(X)$ and $k_0(X)$ denote the usual local absolute frequency and wave number, respectively, while $\omega_{kk}(X)$ is the second derivative of the linear dispersion relation with respect to the wave number k . The complex Landau “constant” $\gamma(X)$ is chosen so that nonlinearities are stabilizing everywhere (supercritical bifurcation), i.e., $\gamma_1(X) \equiv \text{Im } \gamma(X) < 0$ for all X . In the entire paper, the field $\psi(x, t)$ is assumed to be advected in the positive x -direction everywhere to mimic the dynamics of open flows. As demonstrated in Section 4.8, this assumption is equivalent to $k_{0,i}(X) < 0$ for all X . Thus, the increasing and decreasing x -directions will be referred to as “downstream” and “upstream”, respectively. The Ginzburg–Landau model (4) has been shown to successfully describe a large range of pattern formation phenomena [15,26,32]. Here this idealized representation of spatially developing flows is invoked as a specific example. Similar conclusions may be shown to hold for real flows governed by the Navier–Stokes equations [35,36].

2. Local instability properties

Under the assumption that the governing equation only depends on space through the slow variable X , local characteristics of the medium are recovered by freezing X in (1) and studying the corresponding strictly uniform medium. In the sequel, “local” always refers to properties of spatially uniform systems obtained by extending the medium at a specific downstream station X towards $x = \pm\infty$. At this local level of analysis, X and x are then considered to be independent: the fast component x is involved in spatial differentiation whereas X plays the part of an independent control parameter. The rigorous asymptotic analysis re-establishing the link between x and X via (3) in terms of WKBJ approximations [2] is postponed to Section 5.

In this section, the properties of infinite spatially uniform media governed by an equation of the form

$$\frac{\partial \psi}{\partial t} = \mathcal{F}(\partial_x)[\psi] \quad (5)$$

are reviewed. The results are applicable to any nonlinear operator $\mathcal{F}(\partial_x) = \mathcal{F}(\partial_x; X_0)$ derived from (1) for some fixed location $X = X_0$. Explicit forms are obtained for the uniform CGL equation

$$i \frac{\partial \psi}{\partial t} = \left(\omega_0 + \frac{1}{2} \omega_{kk} k_0^2 \right) \psi + i \omega_{kk} k_0 \frac{\partial \psi}{\partial x} - \frac{1}{2} \omega_{kk} \frac{\partial^2 \psi}{\partial x^2} + \gamma |\psi|^2 \psi. \quad (6)$$

The linear properties dictating the dynamics of small amplitude perturbations are routinely obtained. The main assumption used throughout the study is that (5) admits a continuous family of nonlinear travelling waves. This is guaranteed as long as the nonlinearities are supercritically stabilizing, as demonstrated below.

Small amplitude perturbations are governed by the counterpart of (5) linearized around $\psi = 0$,

$$\frac{\partial \psi}{\partial t} = \mathcal{L}(\partial_x)[\psi]. \quad (7)$$

Any perturbation is a superposition of elementary waves $e^{i(kx-\omega t)}$ where the complex wave number k and frequency ω satisfy the linear dispersion relation

$$\omega = \Omega^l(k) \equiv i\mathcal{L}(ik). \quad (8)$$

For Eq. (6), it takes the simple form

$$\omega = \omega_0 + \frac{1}{2} \omega_{kk} (k - k_0)^2, \quad (9)$$

where it is assumed that $\omega_{kk,i} \equiv \text{Im } \omega_{kk} < 0$ in order to enforce causality (see Section 2.3).

Dispersion relation (8) governs all linear properties of the system. Three situations are of particular interest: the temporal evolution problem, the impulse response, and the spatial response problem.

2.1. Temporal evolution and nonlinear dispersion relation

A spatially harmonic perturbation $\psi(x, t = 0) = A e^{ikx} + \text{c.c.}$ of real wave number k and small amplitude $A \ll 1$ initially evolves according to the linear dispersion relation (8). Its linear temporal growth rate is $\Omega_i^l(k) \equiv \text{Im } \Omega^l(k)$. Two typical variations of Ω_r^l and Ω_i^l with k are sketched by solid lines in Fig. 1. Whenever $\Omega_i^l(k) > 0$, the wave is temporally amplified and eventually governed by the full nonlinear equation (5). Assume that stabilizing nonlinearities lead to a fully nonlinear travelling wave of the form

$$\psi(x, t) = \Psi(kx - \omega t; k), \quad (10)$$

where ω is a real frequency and the function $\Psi(\theta; k)$ is 2π periodic in θ . This one-parameter family of nonlinear solutions parameterized by k is characterized by the nonlinear dispersion relation

$$\omega = \Omega^{nl}(k), \quad (11)$$

represented by the dashed curves in Fig. 1a and c. The travelling waves (10) and dispersion relation (11) are the nonlinear counterparts of the linear normal modes $e^{i(kx-\omega t)}$ and dispersion relation (8). Since the medium is assumed to be supercritical, nonlinear solutions $\Psi(\theta; k)$ only exist in the unstable wave number range defined by $\Omega_i^l(k) > 0$.

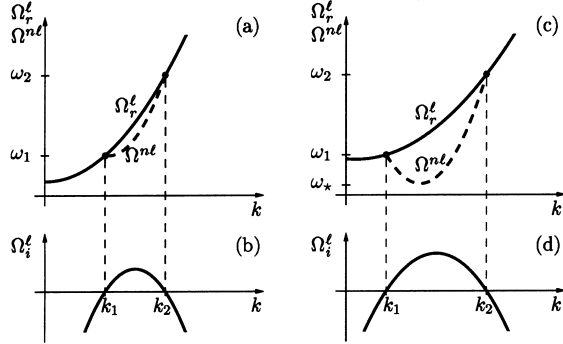


Fig. 1. Linear and nonlinear temporal branches of the CGL equation. (b), (d) Temporal growth rate $\Omega_i^l(k)$ as a function of the real wave number. Unstable wave numbers lie in the range $k_1 < k < k_2$. (a), (c) The nonlinear temporal branch $\Omega^{nl}(k)$ (dashed curves) is defined in the unstable wave number range and is connected to the $\Omega_r^l(k)$ curve (solid lines) at the neutrally stable boundaries where $\omega_1 = \Omega^l(k_1) = \Omega^{nl}(k_1)$ and $\omega_2 = \Omega^l(k_2) = \Omega^{nl}(k_2)$. The nonlinear branch may be (a) monotonous or (c) exhibit an extremum, at ω_* .

As the boundaries of this range are approached, the linear growth rate vanishes as well as the nonlinear saturation amplitude of $\Psi(\theta; k)$. In the neutrally stable limit, the nonlinear frequency equals the linear real frequency,

$$\Omega^{nl}(k) = \Omega^l(k) \quad \text{when } \Omega_i^l(k) = 0 \quad (12)$$

(see Fig. 1). In weakly unstable media, the unstable wave number range is small and in general the nonlinear frequency is a monotonous function of the wave number (Fig. 1a). Further above threshold, the unstable wave number range increases and the nonlinear temporal branch $\Omega^{nl}(k)$ may exhibit an extremum ω_* (Fig. 1c). As a result, one value of ω may be associated to two distinct wave numbers as further discussed in Section 2.3.

In general, the functions Ψ as well as Ω^{nl} cannot be calculated analytically. They are obtained by performing a numerical simulation in a spatially periodic interval of wavelength $2\pi/k$ [35,36]. In the particular case of the CGL equation (6), nonlinear solutions are explicitly obtained as finite amplitude harmonic waves,

$$\psi(x, t) = R(k) \exp\{i[kx - \Omega^{nl}(k)t]\},$$

with

$$\Omega^{nl}(k) = \frac{\text{Im}(\gamma^* \Omega^l(k))}{\text{Im} \gamma^*}, \quad R^2(k) = \frac{\text{Im}(\Omega^l(k))}{\text{Im} \gamma^*},$$

where the superscript \star denotes the complex conjugate. Recall that the condition of stabilizing nonlinearities implies $\gamma_i < 0$.

2.2. Impulse response and absolute instability

Unstable systems may be further characterized by studying their response to an impulsive localized perturbation [3,4,20–22]: in an unstable medium, at least one growing wave packet develops from the impulse location. If the growing wave packet moves away from its source and eventually leaves the medium unperturbed, the instability is said to be *convective*. If, by contrast, the instability grows in place and invades the system both upstream and downstream, the instability is said to be *absolute*. The convective or absolute nature of the instability depends on the absolute frequency ω_0 associated with the absolute wave number k_0 defined by a zero group velocity condition as

$$\omega_0 = \Omega^l(k_0), \quad \frac{d\Omega^l}{dk}(k_0) = 0. \quad (13)$$

The medium is absolutely unstable (AU) if $\omega_{0,i} > 0$, convectively unstable (CU) if $\omega_{0,i} < 0$. The form (6) in which the CGL equation has been cast explicitly puts forward its dependence on ω_0 and k_0 .

2.3. Spatial response and causality

Consider the response of the medium to a localized time-harmonic excitation. The response to a forcing of real frequency ω_f and amplitude A_f , switched on at $t = 0$, is governed by the signaling problem

$$\frac{\partial \psi}{\partial t} = \mathcal{F}(\partial_x)[\psi] + A_f \delta(x) H(t) e^{-i\omega_f t} + \text{c.c.} \quad (14)$$

with H denoting the Heaviside unit step function and δ the Dirac delta function.

For small amplitude forcing ($A_f \ll 1$), the response in the neighborhood of the forcing location is governed by the linear spatial problem with \mathcal{F} replaced by \mathcal{L} in (14). Switching on the forcing at $t = 0$ produces a transient wave packet together with the steady-state response at the forcing frequency. Whenever the medium is stable or convectively unstable, transients decay or move away out of the system, and the longtime response is established at the forcing frequency. When the medium is absolutely unstable, switch-on transients overwhelm the response at the forcing frequency and the signaling problem (14) is ill-posed [3,4]. Hence, we only consider the spatial problem (14) for at most CU systems. The steady-state linear response is made up of normal modes $e^{i(kx - \omega_f t)}$ satisfying $\omega_f = \Omega^1(k)$. For a given ω_f , this linear dispersion relation in general admits several solutions $k_m^1(\omega_f)$ indexed by m , the number of which very much depends on the particular form of $\Omega^1(k)$.

Causality requires that $\psi = 0$ for all $t < 0$. Using a residue calculation in the complex ω -plane to solve (14) with \mathcal{F} replaced by \mathcal{L} , and assuming that temporal growth rates are bounded ($\max\{\Omega_i^1(k), k \text{ real}\}$ finite), it is readily shown [3,4,20] that the spatial branches k_m^1 either pertain to the downstream ($x > 0$) or to the upstream ($x < 0$) response to forcing. The downstream (upstream) branches are denoted by k_m^{1+} (k_m^{1-}). For a given real forcing frequency the distribution of the spatial branches $k_m^1(\omega)$ into + or – branches is derived, according to classical arguments [3,4], from an examination of the complete linear dispersion relation $\Omega^1(k)$ in the entire complex k -plane. In the sequel, spatial branches are said to be causal + or causal – branches according to whether they prevail downstream ($x > 0$) or upstream ($x < 0$) of the forcing location. Hence, causality always refers to the spatial response to a localized harmonic forcing.

For simplicity assume that $\Omega^1(k)$ exhibits a single second-order branch point ω_0 with only two spatial branches k^{1+} and k^{1-} , as in the case of the CGL dispersion relation (9) where

$$k^{1\pm}(\omega) = k_0 \pm \sqrt{2 \frac{\omega - \omega_0}{\omega_{kk}}}. \quad (15)$$

The spatial growth rate of the response depends on $k_i^1 \equiv \text{Im } k^1$. The downstream response decays for frequencies such that $k_i^{1+}(\omega) > 0$; upstream decay occurs when $k_i^{1-}(\omega) < 0$. This is always the case for stable media (Fig. 2a). Whenever a linear spatial $k^{1+}(\omega)$ branch is amplified, nonlinear terms have to be taken into account at some distance from the source, however small the forcing amplitude. When the response reaches finite amplitude, nonlinear saturation prevents further amplification and leads to a nonlinear travelling wave at the excitation frequency for some real wave number k^{nl} (Fig. 2b). Since the nonlinear wave train is asymptotically reached far downstream of the source, it is denoted as $k^{nl+}(\omega)$. This nonlinear wave train would also be obtained in a temporal evolution problem at the same wave number. Thus, the forcing frequency ω_f and the nonlinear response wave number k^{nl+} again satisfy the nonlinear dispersion relation (11). Hence, nonlinear spatial branches $k^{nl\pm}(\omega)$ may formally be obtained by solving (11) for a given frequency. Following the convention of the “front community” [42], the superscripts + and – in this formal definition are assigned according to the sign of the “nonlinear group velocity” $d\Omega^{nl}/dk$. In

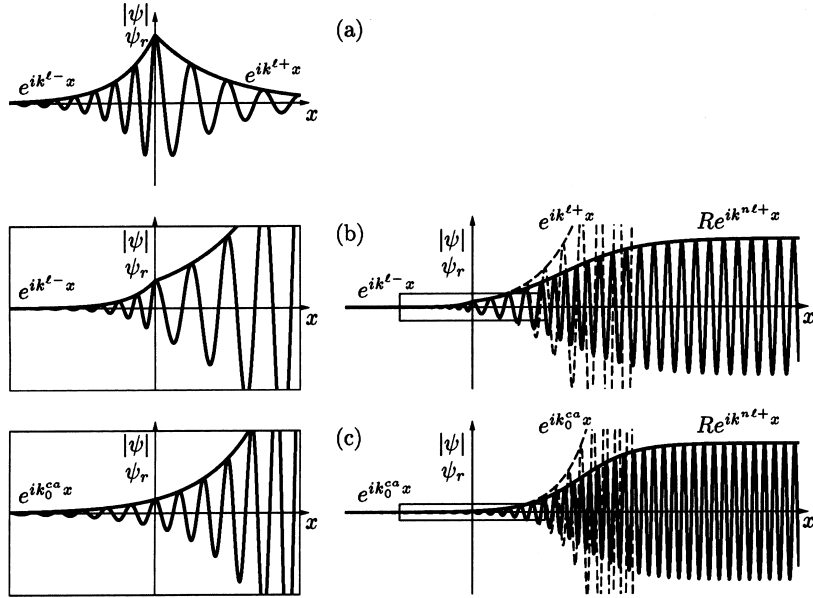


Fig. 2. Response to time harmonic forcing applied at $x = 0$. (a) Upstream and downstream decaying response in a stable or CU medium. (b) Linearly amplified downstream response and nonlinearly saturated solution in a CU medium. (c) Stationary front in a marginally absolutely unstable medium. Note that slope discontinuity at the forcing location has vanished. Dashed lines indicate exponentially growing branches in the linear approximation.

the situation of Fig. 1a, only $k^{\text{nl}+}(\omega)$ exists for $\omega_1 < \omega < \omega_2$, whereas both nonlinear spatial branches appear for the situation in Fig. 1c: $k^{\text{nl}+}(\omega)$ for $\omega_* < \omega < \omega_2$ and $k^{\text{nl}-}(\omega)$ for $\omega_* < \omega < \omega_1$. These definitions of $k^{\text{nl}+}(\omega)$ and $k^{\text{nl}-}(\omega)$ branches apply to CU as well as AU systems. We stress, however, that only those branches accessible via a spatial response problem in a CU medium have causal meaning. In particular, due to the choice of a basic advection towards $x = +\infty$, only the downstream response may be spatially amplified, and the $k^{\text{nl}-}(\omega)$ branch is never accessible via a forcing problem.

2.4. Stationary fronts as spatial response without forcing

Many studies [16,39–42] have been devoted to the derivation of selection criteria for propagating fronts connecting an unstable $\psi = 0$ state to a fully nonlinear saturated state in a uniform medium. In situations where the front velocity is linearly selected [16,40], the front moves towards its decaying edge in AU media, towards its finite-amplitude edge in CU media. A stationary front is then precisely obtained when the medium is exactly at the CU/AU transition. The same stationary front solution may be recovered in the context of the spatial response to time-harmonic forcing as discussed below.

Consider the signaling problem (14) in a uniform medium

$$\frac{\partial \psi}{\partial t} = \mathcal{F}(\partial_x; X)[\psi] + A_f \delta(x) H(t) e^{-i\omega_f t} + \text{c.c.}, \quad (16)$$

where the frozen slow scale X has been explicitly introduced as an external control parameter. Let us examine how the response to a localized forcing of frequency ω_f varies with the parameter X which controls the instability properties of the medium. Assume that the medium is stable or CU for $X < X^{\text{ca}}$ and marginally AU at $X = X^{\text{ca}}$, i.e., $\omega_{0,i}(X) < 0$ for $X < X^{\text{ca}}$ and $\omega_0^{\text{ca}} \equiv \omega_0(X^{\text{ca}})$ real. Let $k_0^{\text{ca}} \equiv k_0(X^{\text{ca}})$ denote the complex absolute wave

number at the CU/AU transition. Since basic advection is assumed to be in the positive x -direction, $k_{0,i}^{ca} < 0$, as shown in Section 4.8.

Let us use as an illustrative example the CGL equation (4) with forcing as in (16). Upon making use of the associated linear dispersion relation Ω^l given by (9) and invoking continuity of the solution at $x = 0$, the exact longtime linear response is obtained as

$$\psi(x, t) = \frac{2A_f}{\omega_{kk}(X)} \frac{\exp\{i[k^{l+}(X, \omega_f)x - \omega_f t]\}}{k^{l+}(X, \omega_f) - k^{l-}(X, \omega_f)} + \text{c.c.} \quad (17)$$

The $e^{ik^{l+}x}$ and $e^{ik^{l-}x}$ branches naturally pertain to the regions $x > 0$ and $x < 0$, respectively. In order to obtain a normalized response such that $\max|\psi(0, t)| = \alpha$, the forcing amplitude is adjusted to the level

$$A_f(X, \omega_f) = \frac{1}{4}\alpha\omega_{kk}(X)[k^{l+}(X, \omega_f) - k^{l-}(X, \omega_f)]. \quad (18)$$

If $\alpha \ll 1$, the linear response is guaranteed to remain valid in a neighborhood of $x = 0$ even though the response may reach a finite amplitude further downstream.

If the medium is stable for large $X < 0$, both upstream and downstream parts of the response decay, i.e., $k_i^{l+}(X, \omega_f) > 0$ and $k_i^{l-}(X, \omega_f) < 0$ for large $X < 0$ (cf. Fig. 2a). As the control parameter X and forcing frequency ω_f are varied continuously to approach the limit X^{ca}, ω_0^{ca} , the downstream response k^{l+} is eventually amplified, whereas the upstream branch k^{l-} still decays (Fig. 2b). Indeed, by definition of ω_0^{ca} (see also (15)) both spatial branches meet at $X = X^{ca}$ and $\omega_f = \omega_0^{ca}$, i.e.,

$$k^{l+}(X^{ca}, \omega_0^{ca}) = k^{l-}(X^{ca}, \omega_0^{ca}) = k_0^{ca}.$$

Since $k_{0,i}^{ca} < 0$, it is therefore guaranteed that $k_i^{l+}(X, \omega_f)$ changes sign and becomes negative as (X, ω_f) approach (X^{ca}, ω_0^{ca}) , while $k_i^{l-}(X, \omega_f)$ does not. In such a regime, the downstream growing response $\alpha \exp[i k^{l+}(X, \omega_f)x]$ reaches a finite amplitude at $x \sim \ln \alpha/k_i^{l+} > 0$. At this station, the linearly growing wave $k^{l+}(X, \omega_f)$ gives way to its nonlinear counterpart $k^{nl+}(X, \omega_f)$.

In the stable or convectively unstable regime ($X < X^{ca}$), both the spatial growth rate and wave number are discontinuous at $x = 0$, i.e., $k^{l+} \neq k^{l-}$. The forcing location is then a singular point of the total response (Fig. 2a and b). When $(X, \omega_f) \rightarrow (X^{ca}, \omega_0^{ca})$, the medium approaches absolute instability and both branches $k^{l+}(X, \omega_f)$ and $k^{l-}(X, \omega_f)$ tend towards k_0^{ca} . Thus, in this process, the slope discontinuity in the response at $x = 0$ smoothes out. Moreover, according to (18), the forcing amplitude $A_f(X, \omega_f)$ required to maintain the normalization condition $\max|\psi(0, t)| = \alpha$ vanishes. Thus, in the marginally AU regime $X = X^{ca}$, a smooth stationary front of frequency $\omega_f = \omega_0^{ca}$ prevails without any forcing (Fig. 2c). This front directly connects the upstream linear k^{l-} branch to the downstream nonlinear k^{nl+} branch. As mentioned in Section 2.3, the + and – notations have causal meaning only in CU systems. The previous argument indicates that, in a marginally AU system, the two branches on both sides of a front are still determined by causal considerations through a continuation procedure from the CU side. From the above discussion, a stationary front in a spatially uniform system is obtained for zero amplitude forcing whenever the medium becomes marginally AU and the forcing frequency equals the corresponding real absolute frequency ω_0^{ca} . This strategy may be implemented numerically to obtain front-like structures not only in the context of one-dimensional evolution equations (16) but also in more complex systems, e.g., wake flows governed by the Navier–Stokes equations [35,36].

3. Spatial variations of local instability properties

The previous results derived for spatially uniform media also yield the local linear and nonlinear instability characteristics of weakly nonuniform media, provided that the control parameter X now be interpreted as the slow

streamwise coordinate. The respective dispersion relations at each station X read

$$\omega = \Omega^l(k, X), \quad \omega \text{ and } k \text{ complex}, \quad (19)$$

$$\omega = \Omega^{nl}(k, X), \quad \omega \text{ and } k \text{ real}. \quad (20)$$

The local linear dispersion relation pertains to any complex wave number whereas the local nonlinear dispersion relation is defined only for real wave numbers associated with a positive temporal growth rate $\Omega_i^l(k, X) > 0$. In strictly uniform media, linear normal modes are sought in the form $\psi = A \exp\{i[k^l(\omega)x - \omega t]\} + \text{c.c.}$ In weakly nonuniform media, such modes are replaced by

$$\psi = A(X) \exp\left(\frac{i}{\epsilon} \int^X k^l(u, \omega) du - i\omega t\right) + \text{c.c.} \quad (21)$$

As demonstrated in the classical WKBJ procedure carried out in Section 5, the local linear wave number $k^l(X, \omega)$ necessarily satisfies the local linear dispersion relation (19). In strictly uniform media, nonlinear travelling waves are sought in the form $\Psi[k^{nl}(\omega)x - \omega t; k^{nl}(\omega)]$ (10). In weakly nonuniform media, such travelling waves are replaced by slowly modulated wave packets of the form

$$\psi \sim \Psi\left(\frac{1}{\epsilon} \int^X k^{nl}(u, \omega) du - \omega t + \Theta(X); k^{nl}(X, \omega), X\right), \quad (22)$$

where the local nonlinear wave number $k^{nl}(X, \omega)$ satisfies the nonlinear local dispersion relation (20). The slowly varying functions $A(X)$ and $\Theta(X)$ appearing in (21) and (22), respectively, are obtained in the complete asymptotic analysis (Section 5).

The objective of this section is then to study the changing topology of linear complex k^l and nonlinear real k^{nl} spatial branches as the global real frequency is varied. The globally synchronized structures obtained in Sections 4 and 5 crucially depend on these spatial branches.

3.1. Instability domains

Let us first introduce the regions of local convective or absolute instability in physical X -space and determine the domain of existence of nonlinear wave trains in (X, k) -space. The local absolute frequency $\omega_0(X)$ and wave number $k_0(X)$ are derived from the local linear dispersion relation (19) as in (13). The local convective or absolute nature of the medium is determined by the sign of $\omega_{0,i}(X)$. In a typical situation of interest, absolute instability occurs in a central finite domain. For definiteness, consider $\omega_0(X)$ to be of the parabolic form sketched in the complex ω -plane in Fig. 3a: $\omega_{0,i}(X)$ is an increasing-decreasing function of X with a single maximum $\omega_{0,i}^{\max}$ reached at $X = X^{\max}$.

Whenever $\omega_{0,i}^{\max} > 0$, there exists a finite AU domain, $X^{ca} < X < X^{ac}$, defined as the region where $\omega_{0,i}(X) > 0$. Its boundaries X^{ca} and X^{ac} are the stations where the local absolute frequency is real, $\omega_0^{ca} \equiv \omega_0(X^{ca})$ and $\omega_0^{ac} \equiv \omega_0(X^{ac})$, respectively.

The domain of local instability, characterized by unstable real wave numbers, $\Omega_i^l(k, X) > 0$, defines the *nonlinear balloon* in the (X, k) -plane (Fig. 3b). In the X -direction, the balloon extends beyond the AU domain to the stations of linear neutral stability, denoted X^{sc} and X^{cs} . At each unstable location, the nonlinear balloon extends in the k -direction over the local unstable wave number range. Note that, due to causality, large wave numbers are always temporally decaying; thus, the nonlinear balloon is necessarily bounded in the k -direction.

A typical system, therefore, displays the following structure: a central AU domain $X^{ca} < X < X^{ac}$ of finite extent, surrounded by two CU regions $X^{sc} < X < X^{ca}$ and $X^{ac} < X < X^{cs}$, which in turn are embedded in

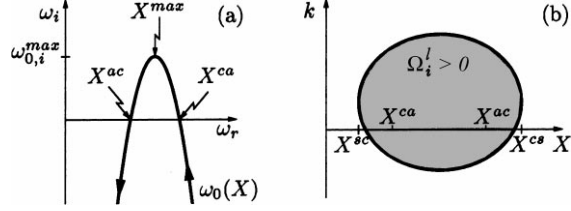


Fig. 3. (a) Locus of the local absolute frequency $\omega_0(X)$ in the complex frequency plane for $-\infty < X < +\infty$. The AU interval $X^{ca} < X < X^{ac}$ is associated with $\omega_{0,i}(X) > 0$. (b) Nonlinear balloon of the CGL equation in the (X, k) -plane defined by $\Omega_i^l(k, X) > 0$ and bounded by the curve of neutral stability $\Omega_i^l(k, X) = 0$. In the X -direction the balloon spans the domain of local linear instability $X^{sc} < X < X^{cs}$ and extends beyond the AU interval.

two semi-infinite stable regions extending to $X = \pm\infty$. As mentioned in Section 4.1, one may relax the stability requirement at $X = \pm\infty$ and the medium may remain CU to $X = \pm\infty$.

3.2. Linear spatial branches

The loci of linear spatial branches $k^l(X, \omega)$ as functions of X is now qualitatively discussed in the complex k -plane for different values of the complex frequency ω . Such an analysis will illustrate the relationship between the behavior of linear spatial branches and the local CU/AU properties of the medium. Linear spatial branches $k^l(X, \omega)$ are obtained by solving the local linear dispersion relation (19) for a given frequency ω . In the case of the CGL equation (4) they read

$$k^{l\pm}(X, \omega) = k_0(X) \pm \sqrt{2 \frac{\omega - \omega_0(X)}{\omega_{kk}(X)}}. \quad (23)$$

In Section 2.3, the choice of the + and – branches was shown to be dictated by causality for real frequencies in stable or CU media. The fate of spatial branches in the AU range $X^{ca} < X < X^{ac}$ is now examined for different frequencies in the complex ω -plane, as illustrated for the CGL equation in Fig. 4.

As a result of causality [3,4], the spatial branches $k^{l\pm}(X, \omega)$ do not cross the k_r -axis in the complex k -plane for large enough $\omega_i > 0$. For such frequencies far above the absolute frequency curve $\{\omega_0(X)\}$ (cf. Fig. 4a), the k^{l+} (k^{l-}) branch is globally defined as the one located in the upper (lower) half k -plane for all real X . The $k^{l\pm}(X, \omega)$ branches continuously deform as ω is varied. They may cross the k_r -axis for finite values of X (Fig. 4b–d), but remain in the same half k -plane for $X \rightarrow \pm\infty$. As ω is kept above the curve $\{\omega_0(X)\}$ (denoted by $\omega > \{\omega_0(X)\}$), no branch switching may occur (Fig. 4b–d) as readily seen by inspection of Eq. (23). This property yields definitions of the $k^{l\pm}$ branches that remain uniformly valid in X , for all complex frequencies $\omega > \{\omega_0(X)\}$, even though the medium may be locally AU.

When $\omega \in \{\omega_0(X)\}$, say $\omega = \omega_0(X_0)$, the two $k^{l\pm}$ branches pinch at $k_0(X_0)$ for $X = X_0$ (Fig. 4e illustrates the case of particular interest where $X_0 = X^{ca}$). For frequencies $\omega < \{\omega_0(X)\}$ below the absolute frequency curve, the continuous k^l curves connect the upper and lower half k -planes as X is varied from $-\infty$ to $+\infty$ (Fig. 4f). Global $k^{l\pm}$ branches can no longer be defined, but the + and – superscripts may still be assigned according to causality in the distinct $X < X^{ca}$ and $X > X^{ac}$ regions represented by thick lines in Fig. 4. For $\omega < \{\omega_0(X)\}$ (Fig. 4f), the k^{l-} branch for $X < X^{ca}$ is connected to the k^{l+} branch in the region $X > X^{ac}$, across the AU domain (part of the curve being represented by a thin line).

These considerations apply in particular to real ω . For frequencies outside the $\omega_0^{ca} - \omega_0^{ac}$ interval, i.e., $\omega > \{\omega_0(X)\}$, the k^{l+} and k^{l-} branches are globally defined, although causality considerations do not apply in the central AU

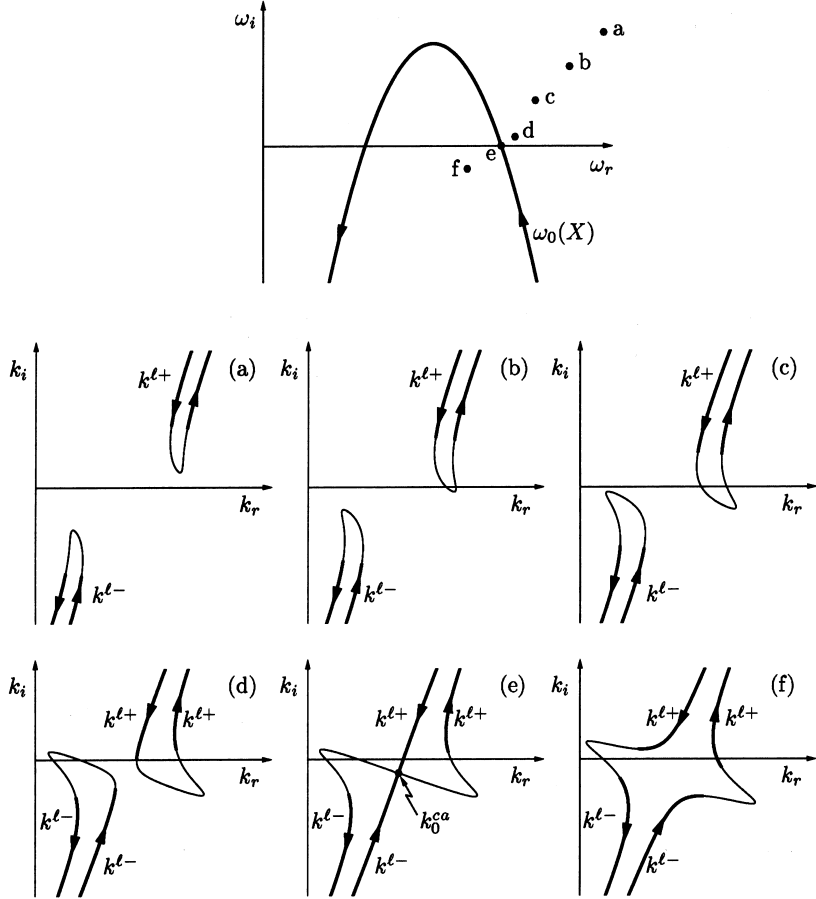


Fig. 4. (a–f) Loci of linear spatial branches $k^l(X, \omega)$ of CGL equation in the complex k -plane for frequencies ω indicated in the complex frequency plane on top sketch. Arrows on the curves indicate direction of increasing X . Thick lines pertain to the stable or CU regions $X < X^{ca}$ and $X > X^{ac}$, thin lines to the central AU region $X^{ca} < X < X^{ac}$. (a–d) For frequencies $\omega > \{\omega_0(X)\}$, the spatial branches $k^{l\pm}(X)$ remain distinct and are located in the same half k -plane for $X \rightarrow \pm\infty$, but they may cross the k_r -axis for finite values of X . As the frequency approaches the $\omega_0(X)$ curve, the spatial branches move closer to each other. (e) For a frequency located on the $\omega_0(X)$ curve, here $\omega = \omega_0(X^{ca})$, pinching occurs at the corresponding absolute wave number, here at $k = k_0^{ca}$, when $X = X^{ca}$. (f) When $\omega \prec \{\omega_0(X)\}$, the continuous curves connect the upper and lower half k -planes as $X \rightarrow \pm\infty$. Definition as $k^{l\pm}$ branches still holds in the distinct CU domains $X < X^{ca}$ and $X > X^{ac}$, but not in the central AU region.

domain. For frequencies in the $\omega_0^{ca} - \omega_0^{ac}$ interval, i.e., $\omega \prec \{\omega_0(X)\}$, the k^{l+} and k^{l-} branches turn one into the other across the AU domain.

3.3. Nonlinear spatial branches

The goal of this section is to describe synthetically the qualitative properties of the nonlinear spatial branches $k^{nl}(X, \omega)$ as functions of X for different values of the real frequency ω . Finite amplitude waves are governed by the nonlinear dispersion relation (20). Fig. 5 illustrates its properties in the case of the CGL equation, by projecting the surface defined as $\omega = \Omega^{nl}(k, X)$ in the (X, k, ω) -space onto the (X, k) -plane. Nonlinear spatial branches $k^{nl}(X, \omega)$ for a given real frequency ω are obtained as the level contours $\Omega^{nl}(k, X) = C^{st}$ indicated by long dashed lines.

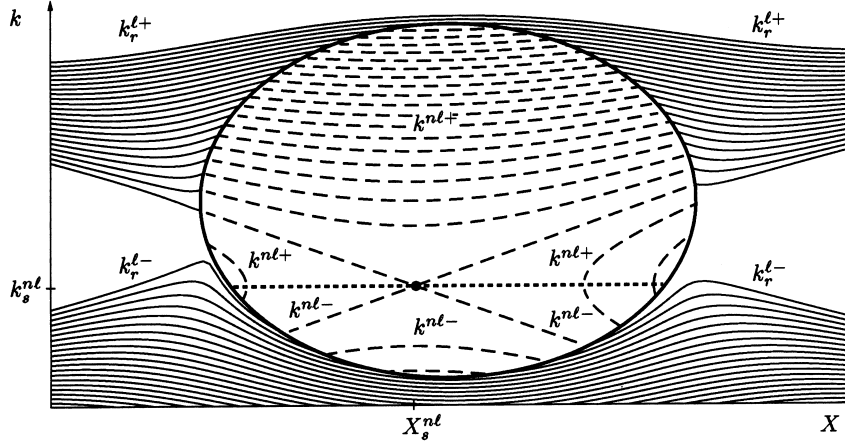


Fig. 5. Projection of the CGL nonlinear dispersion relation surface $\omega = \Omega^{\text{nl}}(k, X)$ on the (X, k) -plane. Nonlinear spatial branches $k^{\text{nl}\pm}(X, \omega)$ and $k^{\text{nl}\mp}(X, \omega)$ represented by constant frequency level curves (dashed lines) live within the nonlinear balloon bounded by the neutral stability boundary (thick solid line). Nonlinear spatial branches display a saddle structure and, by convention, $k^{\text{nl}+}$ and $k^{\text{nl}-}$ refer to the upper and lower regions on either side of the steepest descent curve (thick dotted line) emerging from the saddle point $X_s^{\text{nl}}, k_s^{\text{nl}}$ (solid dot) corresponding to the frequency ω_s^{nl} . The real parts $k_r^{l\pm}$ of the linear spatial branches (thin solid lines) are also shown outside the nonlinear balloon for the same frequencies as the nonlinear branches. Note their continuous connection at the neutral stability boundary.

Nonlinear wave trains only exist inside the nonlinear balloon of the (X, k) -plane, defined by $\Omega_i^1(k, X) > 0$ (see Fig. 3b). Its neutrally stable boundary characterized by $\Omega_i^1(k, X) = 0$ is represented by the thick closed curve in Fig. 5. Since the nonlinear dispersion relation $\omega = \Omega^{\text{nl}}(k, X)$ is always a single-valued function of k , the mapping in the (X, k) -plane is one-to-one and all the nonlinear solutions are contained inside the neutral stability boundary. By contrast, $k^{\text{nl}}(X, \omega)$ is not ensured to be a single-valued function of ω . We have deliberately chosen a configuration displaying this double-valuedness, which is made manifest here by the saddle point structure in the dashed contour levels $\Omega^{\text{nl}}(k, X) = C^{\text{st}}$. Following the definition adopted in Section 2.3, the nonlinear spatial branches are labeled $k^{\text{nl}+}$ and $k^{\text{nl}-}$ according to the sign of the “nonlinear group velocity” $\partial \Omega^{\text{nl}} / \partial k$. Accordingly, the $k^{\text{nl}+}$ and $k^{\text{nl}-}$ domains of Fig. 5 are precisely connected via the steepest descent curve (short dashed line) emerging from the saddle point (solid dot).

In order to emphasize the relationship between linear and nonlinear branches, the linear spatial branches $k^{l\pm}(X, \omega)$ have also been displayed by thin solid lines in Fig. 5 through their real part $k_r^{l\pm}(X, \omega)$ at the same frequencies. Note that linear branches continuously connect to nonlinear branches at the neutral stability boundary. This property is not surprising: at the neutral stability boundary in the (X, k) -plane, the linear branch $k^l(X, \omega)$ is purely real and equals its nonlinear counterpart $k^{\text{nl}}(X, \omega)$.

As discussed in Section 3.2 (Fig. 4), the linear spatial branches are globally defined as k^{l+} or k^{l-} for $\omega > \{\omega_0(X)\}$. While lowering the frequency, starting from large positive values, the k^{l+} and/or k^{l-} branch may cross the k_r -axis in the complex k -plane (Fig. 4b–d). As this linear wave number branch moves into the opposite half k -plane, it becomes spatially amplified and gives birth to a nonlinear branch. This corresponds in the (X, k) -plane to the emergence of a k^{nl} branch connected at the boundary of the nonlinear balloon to a k_r^l branch (Fig. 5).

By further lowering the frequency, switching between the nonlinear branches may take place, as implied by the saddle structure of the dashed curves in Fig. 5. When the frequency decreases, pinching between $k^{\text{nl}-}$ and $k^{\text{nl}+}$ will take place for $\omega = \omega_s^{\text{nl}}$ at the saddle point $(X_s^{\text{nl}}, k_s^{\text{nl}})$ of the nonlinear dispersion relation (20) in the (X, k) -plane. Below this saddle point frequency, the nonlinear spatial branches move into the left- and right-hand sectors bounded by the saddle point asymptotes. For a given frequency in this range, nonlinear spatial branches are indeed generated

at the boundary of the nonlinear balloon but they fail to exist in the heart of the nonlinear region surrounding the saddle point. This behavior is provoked by the merging of k^{nl+} and k^{nl-} on the steepest descent line (thick dotted line of Fig. 5) and their subsequent disappearance. The implications of such a nonlinear saddle point structure on global mode selection are profound, as discussed in Section 4.6.

4. Globally synchronized structures

Having investigated local instability properties of the spatially developing medium, we now turn to the study of globally synchronized solutions of system (1) and associated bifurcations. Such global modes are defined as stationary time-periodic solutions satisfying

$$\psi \left(x, t + \frac{2\pi}{\omega_g} \right) = \psi(x, t),$$

where ω_g is the global real frequency. Selection criteria for self-sustained global oscillations are derived below and the leading-order approximations of their global frequency and spatial structure are obtained. The properties of the medium which dictate the selected global mode type are identified and the ensuing bifurcations are analyzed as global control parameters are varied.

4.1. Boundary conditions and nonlinear eigenvalue problem

To completely determine the global mode problem, proper boundary conditions in connection with Eq. (1) have to be specified. Global modes are defined as intrinsic oscillations which are due to the dynamics of the central region and not to perturbations invading the system from $X = \pm\infty$. Consequently, the boundary conditions must be causal: the solution close to the boundaries is necessarily dictated by the intrinsic oscillations occurring in the central region. Thus, far downstream near $X = +\infty$ the solution is necessarily made up of a + branch caused by the dynamics governing the central region upstream of it. Similarly, the solution necessarily involves a – branch towards $X = -\infty$. Such boundary conditions at $X = \pm\infty$ will be referred to as causal.

When the medium is assumed to be stable in the far downstream and upstream regions, causal boundary conditions are equivalent with decaying ones. Indeed, in the stable regions no nonlinear solutions exist. Causality then requires a linear k^{l+} (k^{l-}) branch towards $X = +\infty(-\infty)$. Due to stability, $k_i^{l+} > 0$ and $k_i^{l-} < 0$, thus the solution necessarily decays towards $X = \pm\infty$.

However, the medium may remain CU up to $X = \pm\infty$. In such instances, decaying boundary conditions are not necessarily fulfilled. However, causality still holds: if the solution remains fully nonlinear down to $X = +\infty$, it is there necessarily made up of the k^{nl+} branch only. Thus, proper boundary conditions for the global mode problem do not necessarily require exponential decay, provided they satisfy causality.

Since a global mode is a solution over the entire X -axis, it necessarily connects a – branch at $X = -\infty$ to a + branch at $X = +\infty$. This crossover from – to + branches may only be achieved for specific frequencies. The search for global modes is thus a nonlinear eigenvalue problem for the global frequency ω_g . The manner in which this crossover takes place in the central region gives rise to different types of global modes as described below.

4.2. Steep global modes

According to Pier et al. [34], the spatial structure of steep global modes is characterized by the presence of a sharp front at the upstream boundary X^{ca} of the AU region. The sketch in Fig. 6a represents the envelope $|\psi|$ and

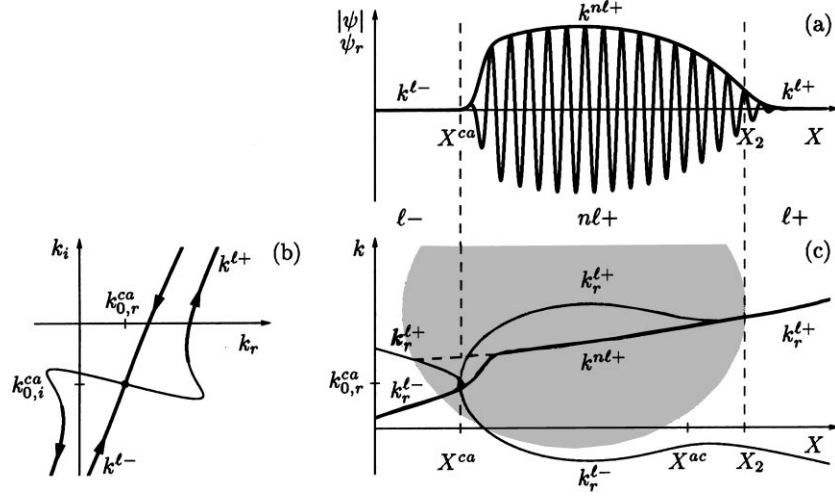


Fig. 6. Structure of steep global mode obtained by direct numerical simulation of CGL equation. (a) Envelope $|\psi|$ and real part ψ_r as functions of downstream distance X . The sharp front located at the upstream boundary X^{ca} of AU region initiates the fully nonlinear development extending down to the neutral station X_2 . (b) Analytically computed linear spatial branches $k^{l\pm}(X)$ of steep global frequency ω_0^{ca} in the complex k -plane. Pinching occurs for the absolute wave number k_0^{ca} at $X = X^{ca}$. Thick lines pertain to the stable or CU regions $X < X^{ca}$ and $X > X^{ac}$, thin lines to the central AU region $X^{ca} < X < X^{ac}$. (c) Corresponding linear $k_r^{l\pm}$ (solid) and nonlinear k_r^{nl+} (dashed) spatial branches in the (X, k) -plane. Local wave number of simulation in (a) follows path indicated by thick line. Three domains are identified: the $k^{\ell-}$ branch prevails in the upstream linear $\ell-$ region $X < X^{ca}$; the front at X^{ca} is associated with a jump in wave number, and in its wake the $k^{\ell+}$ branch develops in the fully nonlinear $n\ell+$ domain $X^{ca} < X < X_2$ extending towards the boundary of the nonlinear balloon (shaded); the $k^{\ell+}$ branch continuously takes over in the linear $\ell+$ region downstream of the neutral station X_2 .

real part ψ_r of a steep global mode obtained by direct numerical simulation of the CGL equation (4). The length of the computational domain is $L = 102$. Linear and parabolic variations are, respectively, used for $\omega_{0,r}(X)$ and $\omega_{0,i}(X)$, as in Fig. 3a, so that $\omega_0^{ca} = 0.4$, $\omega_0^{ac} = 0$, $\omega_{0,i}^{\max} = 0.5$ and $X^{ca} = \frac{3}{16}L$, $X^{ac} = \frac{11}{16}L$. Other coefficients take the constant values $k_0 = 0.5 - 0.8i$, $\omega_{kk} = 1 - i$ and $\gamma = 0.1 - i$.

The front at the location X^{ca} of marginal absolute instability [$\omega_{0,i}(X^{ca}) = 0$] is precisely of the type obtained in Section 2.4: it oscillates at the real absolute frequency $\omega_g = 0.42 \sim \omega_0^{ca} = 0.40$ and allows a crossover between the upstream $k^{\ell-}$ and the downstream k^{nl+} branches. Indeed, in Fig. 6c the numerically obtained local wave number $\text{Re}((-i/\psi)\partial\psi/\partial x)$ represented by a thick line follows the corresponding analytically determined $k_r^{l\pm}(X, \omega_0^{ca})$ (thin solid curves) and $k^{nl+}(X, \omega_0^{ca})$ (thin dashed curve). The exponential decay of the upstream tail of the front is determined by the imaginary part of the corresponding absolute wave number $k_0^{ca} \equiv k_0(X^{ca})$. The upstream $k^{\ell-}(X, \omega_g)$ branch extending towards $X = -\infty$ is precisely generated at the pinch point $X = X^{ca}$ in the complex k -plane (Fig. 6b). As depicted in the (X, k) -plane of Fig. 6c, nonlinear travelling waves following the k^{nl+} branch prevail in the region $X^{ca} < X < X_2$ extending down to the location X_2 where the k^{nl+} branch meets the boundary of the nonlinear balloon in the (X, k) -plane. At the neutrally stable station X_2 the amplitude of the nonlinear travelling wave vanishes and the linear branch $k^{\ell+}(X, \omega_g)$ continuously takes over in the downstream linear region $X > X_2$.

The following frequency selection criterion then holds: the steep global frequency ω_g is given by the real absolute frequency ω_0^{ca} prevailing at the front location X^{ca} separating the CU and AU regions. In other words,

$$\omega_g = \omega_0(X^{ca}), \quad \omega_{0,i}(X^{ca}) = 0. \quad (24)$$

The front at X^{ca} effectively acts as a wave maker for the entire flow. It may be interpreted as a local oscillator inducing the linear upstream – branch and the nonlinear downstream + branch.

4.3. Saddle-node bifurcation to steep global modes

It should be noted that the steep global mode criterion (24) is also fulfilled by the absolute frequency ω_0^{ac} prevailing at the downstream boundary X^{ac} of the AU region. Thus, whenever $\omega_{0,i}^{\max} > 0$, two steep global modes exist: one of frequency ω_0^{ca} with a front at the upstream boundary X^{ca} of the AU region and one of frequency ω_0^{ac} with a front at its downstream boundary X^{ac} (see Fig. 3a). When $\omega_{0,i}^{\max} < 0$, no AU region is present and no steep global mode exists. Thus, $\omega_{0,i}^{\max}$ constitutes the global control parameter governing the existence of steep global modes. When $\omega_{0,i}^{\max}$ is varied, transition to steep global modes occurs via a saddle-node bifurcation at $\omega_{0,i}^{\max} = 0$ as demonstrated below.

The spatial structure of a solution with a front at X^{ca} has been detailed in the previous section. The structure of a solution with a front at X^{ac} is similar. Indeed, both linear $k^{1\pm}(X, \omega_0^{\text{ac}})$ branches equal $k_0^{\text{ac}} \equiv k_0(X^{\text{ac}})$ at $X = X^{\text{ac}}$. Due to the assumption $k_{0,i} < 0$, the k^{1-} branch is again exponentially damped while the k^{1+} branch is amplified. As a result, nonlinear travelling waves $k^{\text{n}l+}$ are only present downstream of the front ($X > X^{\text{ac}}$) and linear damped waves k^{1-} upstream of the front ($X < X^{\text{ac}}$). Thus, the nonlinear part of such a global mode extends in the downstream CU region, whereas the central AU domain is covered by an exponentially decaying upstream tail.

Let us now show that an upstream front is a stable configuration whereas a downstream front is unstable. Consider a small displacement of the upstream front from its equilibrium location X^{ca} towards $X > X^{\text{ca}}$. The front now experiences a slightly AU medium, hence, according to Dee and Langer [16], the nonlinear part grows and the front propagates towards its decaying edge, i.e., upstream. When this front is displaced towards $X < X^{\text{ca}}$, it penetrates into a CU region and is thus pushed downstream. In any case the front is seen to return to its equilibrium position X^{ca} . Thus, the corresponding steep global mode is an attractor onto which direct numerical simulation converges.

On the contrary, a downstream front displaced from its equilibrium position X^{ac} towards the AU region $X < X^{\text{ac}}$ continues to propagate upstream and completely invades the AU domain. When the front is displaced towards the CU region $X > X^{\text{ac}}$, it is swept away downstream towards $X = +\infty$. A downstream front is therefore unstable.

Thus when $\omega_{0,i}^{\max} > 0$, a pair of steep global modes exists: the mode with a front at the upstream (resp. downstream) boundary of the AU region is stable (resp. unstable). In the limit $\omega_{0,i}^{\max} \downarrow 0$, the AU domain shrinks and the front locations move in closer to each other, $X^{\text{ca}} \uparrow X^{\max}$ and $X^{\text{ac}} \downarrow X^{\max}$. When $\omega_{0,i}^{\max} = 0$ both front frequencies ω_0^{ca} and ω_0^{ac} equal $\omega_0(X^{\max})$, and both steep global modes coincide. When $\omega_{0,i}^{\max} < 0$, the domain is nowhere AU and no steep global mode exists.

This behavior is typical of a saddle-node bifurcation: while decreasing the bifurcation parameter $\omega_{0,i}^{\max}$, a stable and an unstable solution meet and disappear at the critical value $\omega_{0,i}^{\max} = 0$. Note that in general the steep global mode remains fully nonlinear for all $\omega_{0,i}^{\max} > 0$. Indeed, for $0 < \omega_{0,i}^{\max} \ll 1$ the extent of the convectively unstable domain remains $\mathcal{O}(1)$ (in terms of X) and so does the nonlinear region where the global mode lives.

4.4. Linear global modes

The linear global instability of the unperturbed $\psi = 0$ state has been studied by Chomaz et al. [7] and Le Dizès et al. [25]. The instability properties were derived from an analytic continuation of the local absolute frequency $\omega_0(X)$ in the complex X -plane, as summarized below.

Linear global modes are assumed to be of the form $\psi(x, t) = \phi(X) e^{-i\omega_g t}$ of complex global frequency ω_g . The spatial function ϕ is defined over the complex X -plane and the local complex wave number then satisfies the linear dispersion relation (19) with complex X . A linear global mode is entirely made up of linear spatial branches $k^{1\pm}$. Due to causal boundary conditions, the k^{1-} branch prevailing near $X = -\infty$ must necessarily connect to the k^{1+} branch near $X = +\infty$. This can be achieved at a saddle point X_s^1 of the absolute frequency in the complex

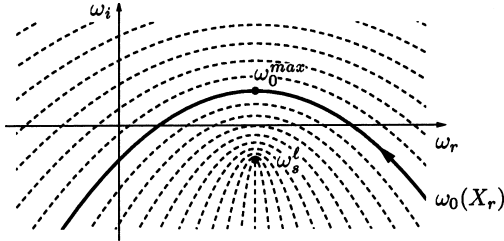


Fig. 7. Curves $\omega_0(X_r + iX_i)$ in the complex frequency plane for different values of X_i when X_r varies along the entire real axis. Bold curve pertains to $X_i = 0$. The linear saddle point frequency ω_s^1 is obtained at a cusp of this set of curves and is seen to lie below ω_0^{\max} , towards the center of curvature of the $\omega_0(X_r)$ curve.

X -plane.¹ The frequency of the linear global mode is then equal to the saddle point frequency ω_s^1 , defined by

$$\omega_s^1 = \omega_0(X_s^1), \quad \frac{d\omega_0}{dX}(X_s^1) = 0, \quad (25)$$

or equivalently by

$$\omega_s^1 = \Omega^1(k_s^1, X_s^1), \quad \frac{\partial \Omega^1}{\partial k}(k_s^1, X_s^1) = \frac{\partial \Omega^1}{\partial X}(k_s^1, X_s^1) = 0. \quad (26)$$

Linear global instability is determined by the sign of $\omega_{s,i}^1 \equiv \text{Im } \omega_s^1$, when $\omega_{s,i}^1 < 0$ (resp. $\omega_{s,i}^1 > 0$) the state $\psi = 0$ is linearly stable (resp. unstable).

4.5. Hysteresis

The existence of nonlinear steep global modes is determined by the sign of $\omega_{0,i}^{\max}$, while the linear global instability of the unperturbed state $\psi = 0$ is dictated by the sign of $\omega_{s,i}^1$. It is now shown qualitatively that always $\omega_{0,i}^{\max} \geq \omega_{s,i}^1$, and in general $\omega_{0,i}^{\max} > \omega_{s,i}^1$. Thus, steep global modes may exist in globally linearly stable media (situations where $\omega_{s,i}^1 < 0 < \omega_{0,i}^{\max}$), and the saddle-node bifurcation implies hysteretic behavior as $\omega_{0,i}^{\max}$ is varied.

The relative position of $\omega_{0,i}^{\max}$ and $\omega_{s,i}^1$ is most conveniently illustrated in the complex frequency plane as sketched in Fig. 7. The solid curve represents $\omega_0(X)$ for real X . The AU region corresponds to the X -interval over which $\omega_0(X)$ lies in the $\omega_i > 0$ half-plane. The maximum $\omega_{0,i}^{\max}$ is reached at $X = X^{\max}$. Thus, steep global modes exist whenever the curve $\omega_0(X)$ crosses the real ω -axis. The complex frequency ω_s^1 is obtained at a saddle point of the analytically continued function $\omega_0(X)$. For most situations of physical interest, $\omega_{0,i}(X)$ is an increasing-decreasing function on the real X -axis, while $\omega_{0,r}(X)$ is simply a smooth function. The dashed curves of Fig. 7 represent the loci of $\omega_0(X_r + iX_i)$ for different values of X_i when X_r varies along the entire real axis. The saddle point frequency ω_s^1 is obtained at a cusp of this set of curves and lies below the $\omega_0(X_r)$ curve, towards its center of curvature. Thus, it follows clearly that $\omega_{0,i}^{\max} > \omega_{s,i}^1$ and one recovers the well-known result that global linear instability requires an AU region of finite extent [7,25].

In the neighborhood of ω_0^{\max} , the absolute frequency $\omega_0(X)$ may be approximated by the Taylor expansion

$$\omega_0(X) \sim \omega_0^{\max} + \omega_{0X}(X - X^{\max}) + \frac{1}{2}\omega_{0XX}(X - X^{\max})^2 \quad (27)$$

¹ Only linear global modes with a double turning point are considered here. The reader is referred to Le Dizès et al. [25] for a detailed analysis of linear global modes with two simple turning points.

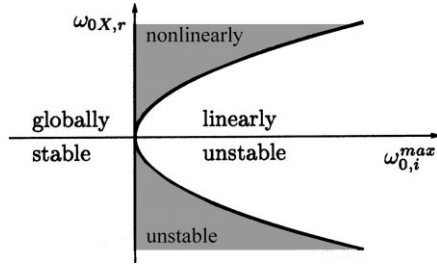


Fig. 8. Global linear and nonlinear stability in the $(\omega_{0,i}^{\max}, \omega_{0X,r})$ -plane. Global stability is governed by the sign of $\omega_{0,i}^{\max}$. When $\omega_{0,i}^{\max} > 0$, the medium is globally nonlinearly unstable although linearly stable in the gray region.

with $\omega_{0X,i} = 0$ and $\omega_{0XX,i} < 0$. The linear saddle point, solution of (25), is then explicitly given by

$$X_s^1 = X^{\max} - \frac{\omega_{0X,r}}{\omega_{0XX}}, \quad \omega_s^1 = \omega_0^{\max} - \frac{1}{2} \frac{(\omega_{0X,r})^2}{|\omega_{0XX}|^2}, \quad (28)$$

thus

$$\text{Im } \omega_s^1 = \omega_{0,i}^{\max} + \frac{1}{2} \frac{(\omega_{0X,r})^2}{|\omega_{0XX}|^2} \omega_{0XX,i}.$$

Only if $d\omega_{0,r}(X^{\max})/dX = 0$, does the saddle point X_s^1 coincide with X^{\max} on the real X -axis and, under such a condition, $\omega_s^1 = \omega_0(X^{\max})$. The difference between $\omega_{0,i}^{\max}$ and $\omega_{s,i}^1$ is seen to depend on the magnitude of $\omega_{0X,r} \equiv d\omega_{0,r}(X^{\max})/dX$ and to scale as $(\omega_{0X,r})^2$. The influence of the two parameters $\omega_{0,i}^{\max}$ and $\omega_{0X,r}$ on global linear and nonlinear instability is illustrated in Fig. 8.

The following scenario holds as the global control parameter $\omega_{0,i}^{\max}$ is varied at a fixed $\omega_{0X,r}$ setting. When $\omega_{0,i}^{\max} < 0$ (left-hand half-plane of Fig. 8), the unperturbed state is stable, no nonlinear global mode exists. When $\omega_{0,i}^{\max} > 0$ while $\omega_{s,i}^1 < 0$ (shaded region of Fig. 8), a pair of steep global modes exist, one of which is stable, the other unstable. However, the unperturbed state is still linearly globally stable,² but nonlinearly unstable. Only for $\omega_{0,i}^{\max}$ large enough such that $\omega_{s,i}^1 > 0$ (clear region inside parabola of Fig. 8), does the basic state become linearly unstable. Whereas the global saddle-node bifurcation is controlled by $\omega_{0,i}^{\max}$, the extent of the hysteresis range in $\omega_{0,i}^{\max}$ is governed by a second control parameter, namely $\omega_{0X,r}$.

4.6. Soft global modes

The existence of soft global modes has been analyzed in an earlier study [33]. Their structure is now briefly summarized, as well as their relationship to steep global modes. The sketch in Fig. 9a represents the envelope $|\psi|$ and real part ψ_r of a soft global mode obtained by direct numerical simulation of the CGL equation (4). The length of the computational domain is $L = 102$. Linear and parabolic variations are, respectively, used for $\omega_{0,r}(X)$ and $\omega_{0,i}(X)$ so that $\omega_0^{\text{ca}} = 0.5$, $\omega_0^{\text{ac}} = 0.6$, $\omega_{0,i}^{\max} = 0.5$ and $X^{\text{ca}} = \frac{1}{5}L$, $X^{\text{ac}} = \frac{4}{5}L$. Other coefficients take the constant values $k_0 = 1.0 - 0.1i$, $\omega_{kk} = 1 - 0.5i$ and $\gamma = 0.2 - i$.

In contrast to steep modes, no front is present and soft modes display an overall smoothly varying envelope and wave number (thick curve in Fig. 9c). The connection between the upstream – branch and the downstream + branch occurs here in the core of the nonlinear region, at a saddle point of the nonlinear dispersion relation (20).

² The unperturbed state is, however, locally unstable.

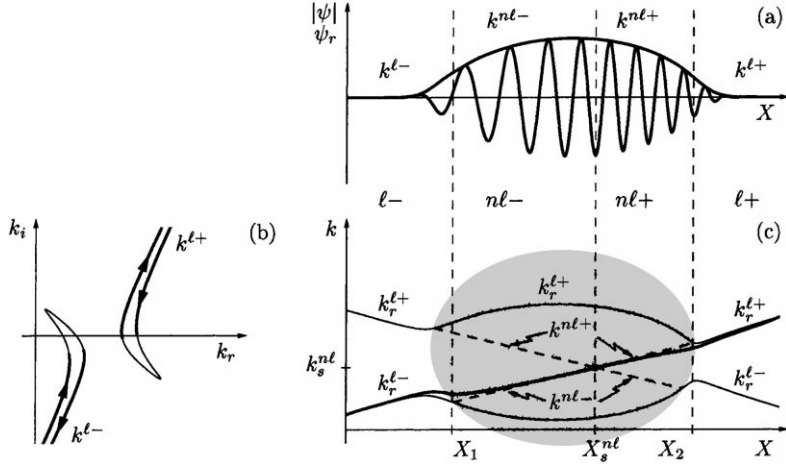


Fig. 9. Structure of soft global mode obtained by direct numerical simulation of CGL equation. (a) Overall smoothly varying envelope $|\psi|$ and real part ψ_r as functions of downstream distance X . (b) Analytically computed linear spatial branches $k^{\pm}(X)$ of nonlinear saddle point frequency ω_s^{nl} in the complex k -plane. Both linear branches cross the k_r -axis and give birth to their nonlinear counterparts at the respective neutral stations. Thick lines pertain to the stable or CU regions $X < X^{\text{ca}}$ and $X > X^{\text{ac}}$, thin lines to the central AU region $X^{\text{ca}} < X < X^{\text{ac}}$. (c) Corresponding linear k^{\pm} (thin solid) and nonlinear $k^{\text{nl}\pm}$ (thin dashed) spatial branches in the (X, k) -plane. Pinching of nonlinear branches occurs for k_s^{nl} at $X = X_s^{\text{nl}}$ in the core of the nonlinear region. Local wave number of simulation in (a) follows path indicated by thick line. Four domains are identified: the central nonlinear $\text{nl}-$ and $\text{nl}+$ regions prevail upstream and downstream of X_s^{nl} where the nonlinear spatial branches $k^{\text{nl}-}$ and $k^{\text{nl}+}$ meet; at the upstream X_1 and downstream X_2 boundaries of the nonlinear balloon (shaded) the nonlinear spatial branches are continuously connected to their respective linear counterparts k^{\pm} prevailing in the semi-infinite linear regions $\text{l}-$ and $\text{l}+$, respectively.

As already discussed in Section 3.3, the nonlinear branches $k^{\text{nl}\pm}(X, \omega)$, formally defined as the level contours $\Omega^{\text{nl}}(k, X) = C^{\text{st}}$, may display a saddle point $(X_s^{\text{nl}}, k_s^{\text{nl}})$ in the (X, k) -plane (solid dot in Fig. 5). More precisely, pinching of the nonlinear branches, defined by the condition

$$k^{\text{nl}+}(X_s^{\text{nl}}, \omega_s^{\text{nl}}) = k^{\text{nl}-}(X_s^{\text{nl}}, \omega_s^{\text{nl}}) = k_s^{\text{nl}},$$

then occurs at the real station X_s^{nl} for the real saddle point frequency ω_s^{nl} of Ω^{nl} such that

$$\omega_s^{\text{nl}} = \Omega^{\text{nl}}(k_s^{\text{nl}}, X_s^{\text{nl}}), \quad \frac{\partial \Omega^{\text{nl}}}{\partial k}(k_s^{\text{nl}}, X_s^{\text{nl}}) = \frac{\partial \Omega^{\text{nl}}}{\partial X}(k_s^{\text{nl}}, X_s^{\text{nl}}) = 0 \quad (29)$$

with the saddle condition

$$\left(\frac{\partial^2 \Omega^{\text{nl}}}{\partial k \partial X}(k_s^{\text{nl}}, X_s^{\text{nl}}) \right)^2 - \frac{\partial^2 \Omega^{\text{nl}}}{\partial k^2}(k_s^{\text{nl}}, X_s^{\text{nl}}) \frac{\partial^2 \Omega^{\text{nl}}}{\partial X^2}(k_s^{\text{nl}}, X_s^{\text{nl}}) > 0. \quad (30)$$

Note the formal analogy of this nonlinear saddle point criterion (29) with its linear counterpart (26) which involves in general complex values of k_s^{l} and X_s^{l} . The upstream $k^{\text{nl}-}(X, \omega_s^{\text{nl}})$ branch and downstream $k^{\text{nl}+}(X, \omega_s^{\text{nl}})$ branch are precisely initiated at the nonlinear saddle point X_s^{nl} , as depicted in Fig. 9c. These nonlinear travelling waves prevail in the range $X_1 < X < X_2$, where X_1 and X_2 denote the neutrally stable stations of frequency ω_s^{nl} at the boundary of the nonlinear balloon in the (X, k) -plane. At X_1 and X_2 , the amplitudes of the nonlinear travelling waves $k^{\text{nl}-}$ and $k^{\text{nl}+}$, respectively, vanish and give way to their linear counterparts $k^{\text{l}-}$ and $k^{\text{l}+}$, respectively.

For the CGL equation (4) with $\omega_0(X)$ of the form (27), all other coefficients being kept uniform in X , the nonlinear saddle point location is explicitly obtained as

$$X_s^{\text{nl}} = X^{\text{max}} + \frac{\gamma_i \omega_{0X,r}}{\text{Im}(\gamma^* \omega_{0XX})}, \quad (31)$$

$$k_s^{\text{nl}} = k_{0,r} + \frac{\text{Re}(\gamma^* \omega_{kk})}{\text{Im}(\gamma^* \omega_{kk})} k_{0,i}, \quad (32)$$

and the soft global mode frequency reads

$$\omega_s^{\text{nl}} = \omega_{0,r}^{\text{max}} - \frac{\gamma_i}{\gamma_i} \omega_{0,i}^{\text{max}} + \frac{\gamma_i (\omega_{0X,r})^2}{2 \text{Im}(\gamma^* \omega_{0XX})} + \frac{|\gamma^* \omega_{kk}|^2}{2 \gamma_i \text{Im}(\gamma^* \omega_{kk})} k_{0,i}^2. \quad (33)$$

The numerically obtained global frequency $\omega_g = 0.64$ of Fig. 9 very favorably compares with the analytical prediction (33) of $\omega_s^{\text{nl}} = 0.65$.

Condition (30) requires that $(\text{Im} \gamma^* \omega_{kk})(\text{Im} \gamma^* \omega_{0XX}) < 0$. It was shown in [33] that in situations where

$$\text{Im}(\gamma^* \omega_{kk}) > 0, \quad (34)$$

the nonlinear branches $k^{\text{nl}\pm}$ exist in the neighborhood of X_s^{nl} for frequencies such that $\omega > \omega_s^{\text{nl}}$. When $\omega \downarrow \omega_s^{\text{nl}}$, the branches pinch at k_s^{nl} for $X = X_s^{\text{nl}}$, and for $\omega < \omega_s^{\text{nl}}$, they fail to be defined around X_s^{nl} . In the following it is always assumed that the possible frequencies for the nonlinear spatial branches lie in the range $\omega > \omega_s^{\text{nl}}$. The opposite situation is exactly analogous and applies when $\text{Im}(\gamma^* \omega_{kk}) < 0$.

4.7. Transition between soft and steep global modes

The selection mechanisms governing steep and soft global modes are now compared. The steep criterion (24) only involves the boundary of the AU domain on the physical X -axis, regardless of the characteristics of the regions $X \neq X^{\text{ca}}$. Nevertheless, a steep global mode only exists if the nonlinear $k^{\text{nl}+}(X, \omega_0^{\text{ca}})$ branch can be followed from X^{ca} down to the boundary of the nonlinear balloon and if there it can be continuously connected to the linear branch $k^{l+}(X, \omega_0^{\text{ca}})$. In contrast, the soft criterion (29) involves a saddle point of the nonlinear dispersion relation. Again, a soft global mode only exists if the nonlinear spatial branches issuing from this nonlinear pinch point may effectively be continued via corresponding linear $k^{l\pm}$ branches in the respective downstream and upstream linear domains.

Selection of either steep or soft global modes depends not only on the local criteria (24) and (29), but also on the necessity to enforce the boundary conditions. The key argument in the following derivation is based on a careful monitoring of the linear wave number branches in the complex k -plane and of their nonlinear counterparts in the (X, k) -plane as the global frequency is varied. As always, the CGL equation is used to illustrate the different scenarios. The connection between linear and nonlinear spatial branches is shown to crucially depend on the relative magnitude of the characteristic frequencies ω_s^{nl} and ω_0^{ca} . In all instances, only one global mode, steep or soft, is capable of continuously converting k^{l-} at $X = -\infty$ to k^{l+} at $X = +\infty$, as X is varied. The two main scenarios of interest are illustrated in Figs. 10 and 11, respectively, as discussed below.

Since nonlinear global modes necessarily involve real frequencies, let us focus on frequencies on the real ω -axis. As shown in Section 3.2, for large positive or negative ω the linear spatial branches do not cross the k_r -axis in the complex k -plane. Since nonlinear spatial branches are assumed to exist for $\omega > \omega_s^{\text{nl}}$, we start with large positive values of the frequency.

As ω is decreased, the $k^{l\pm}(X, \omega)$ branches move in closer to each other and one or both cross the k_r -axis for finite values of X . A change in sign of k_r^l signifies that the corresponding branch is spatially growing: downstream spatial

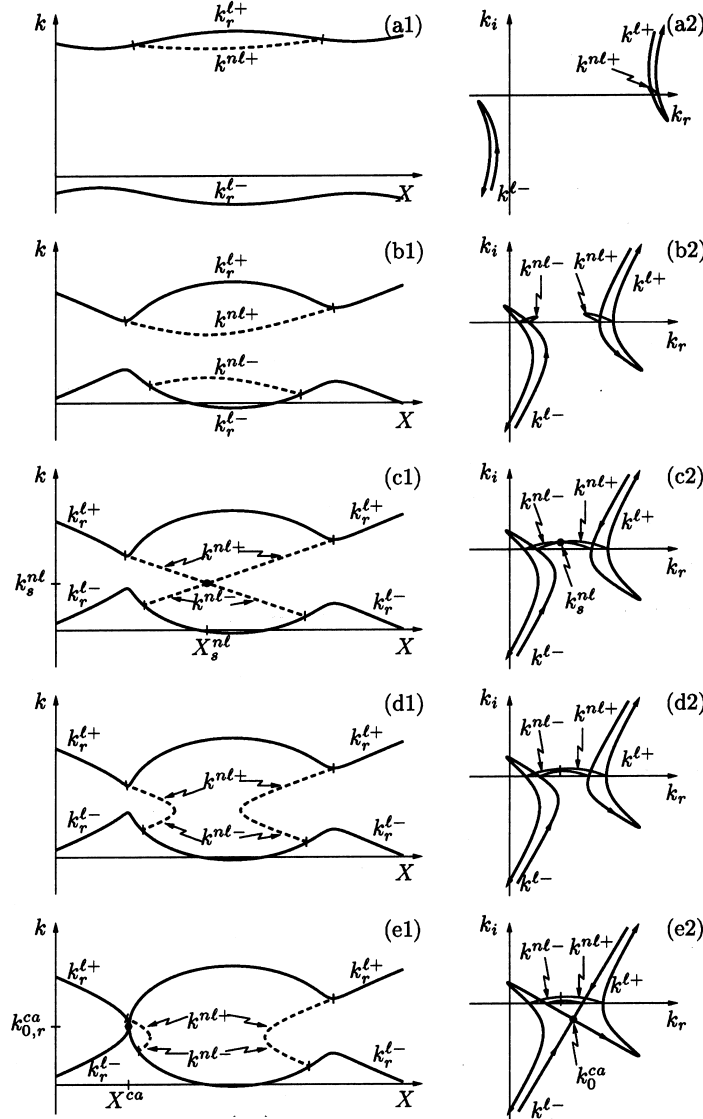


Fig. 10. Evolution of CGL spatial branches with decreasing real frequency in a situation where the soft global mode is selected. The left sequence illustrates the evolution of the real part of linear branches $k_r^{l\pm}(X, \omega)$ (solid lines) and of nonlinear branches $k_r^{nl\pm}(X, \omega)$ (dashed lines) in the (X, k) -plane. Connecting points between linear and nonlinear branches are indicated with tick marks. In the right sequence, corresponding complex linear $k^{l\pm}(X, \omega)$ branches are sketched in the complex (k_r, k_i) -plane; superimposed on the same graphs are the curves $(k^{nl\pm}, R^2)$ of the nonlinear spatial branches. (a), (b) For frequencies $\omega > \omega_s^{nl}$ linear $k^{l\pm}$ spatial branches successively cross the k_r -axis in the complex k -plane and give birth to the nonlinear $k^{nl\pm}$ branches between the corresponding neutral stations. (c) For the nonlinear saddle point frequency ω_s^{nl} , nonlinear spatial branches pinch at k_s^{nl} when $X = X_s^{nl}$. This pinch point joining k^{nl-} and k^{nl+} branches gives rise to a soft global mode connecting the k^{l-} branch near $X = -\infty$ to the k^{l+} branch prevailing near $X = +\infty$. (d), (e) For frequencies $\omega < \omega_s^{nl}$, the nonlinear spatial branches fail to exist in the neighborhood of X_s^{nl} , but linear $k^{l\pm}$ branches are still defined. (e) When $\omega = \omega_0^{ca}$, the linear branches in turn pinch at $k = k_0^{ca}$ at the upstream boundary X^{ca} of AU region. However, this pinch point is not associated with a steep global mode since the k^{nl+} branch prevailing for $X > X^{ca}$ is not connected to the k^{l+} branch extending to $X = +\infty$.

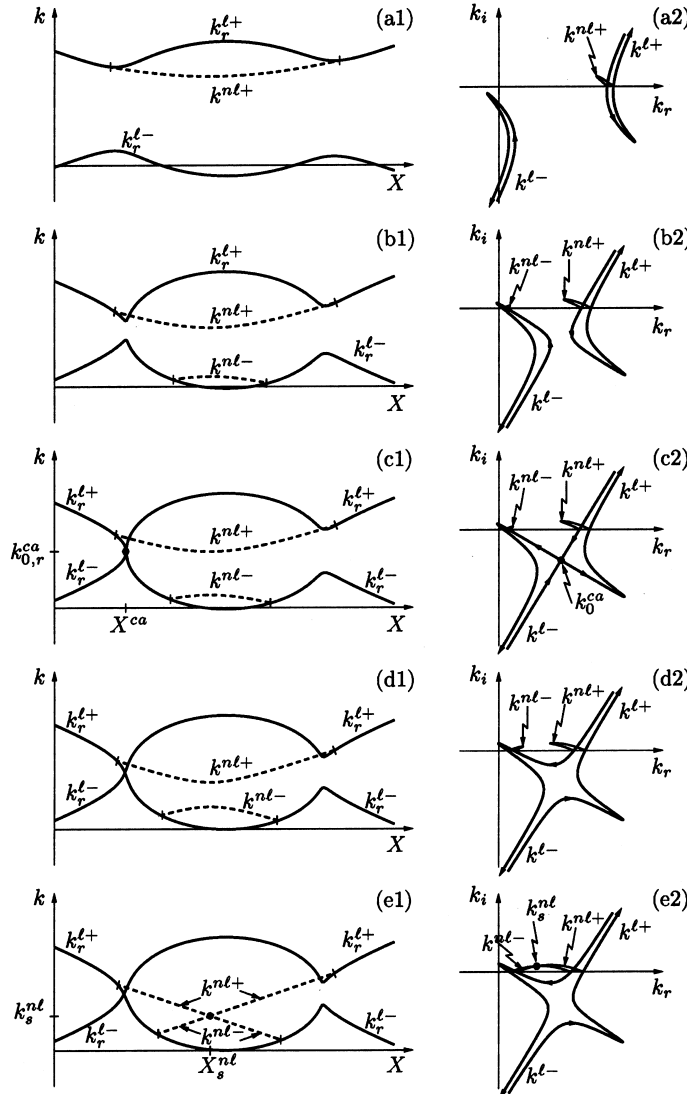


Fig. 11. Evolution of CGL spatial branches with decreasing real frequency in a situation where the steep global mode is selected. The left sequence illustrates the evolution of the real part of linear branches $k_r^{l\pm}(X, \omega)$ (solid lines) and of nonlinear branches $k_r^{nl\pm}(X, \omega)$ (dashed lines) in the (X, k) -plane. Connecting points between linear and nonlinear branches are indicated with tick marks. In the right sequence, corresponding complex linear $k^{l\pm}(X, \omega)$ branches are sketched in the complex (k_r, k_i) -plane; superimposed on the same graphs are the curves $(k^{nl\pm}, R^2)$ of the nonlinear spatial branches. (a), (b) For frequencies $\omega > \omega_0^{ca}$ linear spatial branches remain separated, nonlinear branches exist between the corresponding neutral stations. (c) For the front frequency ω_0^{ca} , linear spatial branches pinch at $k_{0,r}^{ca}$ when $X = X^{ca}$. A sharp front at X^{ca} associated with a wave number jump from k^{l-} to k^{nl+} then gives rise to a global mode connecting the k^{l-} branch near $X = -\infty$ to the k^{l+} branch prevailing near $X = +\infty$. (d), (e) For frequencies $\omega < \omega_0^{ca}$, branch switching between k^{l+} and k^{l-} occurs. (e) When $\omega = \omega_s^{nl}$, the nonlinear branches meet at the nonlinear saddle point location X_s^{nl} . However, this saddle point is not associated with a global mode since no continuous connection to the k^{l-} branch prevailing near $X = -\infty$ exists.

growth for $k_i^{l+} < 0$ and upstream spatial growth for $k_i^{l-} > 0$. As already mentioned (Section 2.3) a spatially growing branch $k^{l\pm}$ gives way to its nonlinear counterpart $k^{nl\pm}$ as a neutrally stable station is crossed in the (X, k) -plane.

Nonlinear k^{nl} branches are by construction always real-valued. However, to illustrate their relationship with the linear k^l branches they are also represented in the complex k -planes of Figs. 10 and 11. For clarity their missing

imaginary part is replaced by the square of the amplitude of the corresponding nonlinear solution. This avoids the collapse of the k^{nl} branches onto the k_r -axis, and brings to the fore the continuity between linear and nonlinear branches at the neutral stations where k_i^1 as well as the nonlinear amplitude vanish.

In the following discussion representations in the (X, k_r) - and the (k_r, k_i) -planes are always shown in parallel. Although the + and – superscripts may not be derived from causality considerations in the AU domain, linear as well as nonlinear + and – branches may be defined without ambiguity as long as the linear and nonlinear branches remain distinct (cf. Sections 3.2 and 3.3).

The branch switching scenario as ω decreases depends on the relative values of the characteristic frequencies ω_s^{nl} and ω_0^{ca} . The frequency ω_0^{ac} which corresponds to an unstable steep global mode with a front at the downstream boundary of the AU domain does not play an essential part. For clarity assume that $\omega_0^{\text{ca}} > \omega_0^{\text{ac}}$ and $\omega_s^{\text{nl}} > \omega_0^{\text{ac}}$. If these assumptions are not satisfied, the same selection mechanisms as discussed below prevail, although the detailed topology of spatial branches may be different. Two possibilities now arise: $\omega_s^{\text{nl}} > \omega_0^{\text{ca}}$ or $\omega_s^{\text{nl}} < \omega_0^{\text{ca}}$.

The scenario for $\omega_s^{\text{nl}} > \omega_0^{\text{ca}}$ is illustrated in the sequence of Fig. 10. As ω is decreased, the two linear spatial branches successively cross the k_r -axis while remaining separated as depicted in Fig. 10a and b. Each crossing gives birth to a corresponding nonlinear branch connected to its linear counterpart at the neutrally stable locations where k^1 is real. Both linear and nonlinear + and – branches are well identified and separated. When $\omega \downarrow \omega_s^{\text{nl}}$, the nonlinear branches gradually approach each other. For $\omega = \omega_s^{\text{nl}}$ (Fig. 10c), the $k^{\text{nl}+}$ branch meets the $k^{\text{nl}-}$ branch at k_s^{nl} for $X = X_s^{\text{nl}}$ as determined by (29). This is the soft global mode configuration, where the nonlinear saddle point at X_s^{nl} connects the nonlinear $k^{\text{nl}-}(X, \omega_s^{\text{nl}})$ in the region $X < X_s^{\text{nl}}$ to the nonlinear $k^{\text{nl}+}(X, \omega_s^{\text{nl}})$ in the region $X > X_s^{\text{nl}}$. Further outward, the nonlinear $k^{\text{nl}\pm}$ branches give way to their respective linear counterparts $k^{1\pm}$ at the locations of their respective neutral growth. When decreasing the global frequency to values $\omega < \omega_s^{\text{nl}}$, the nonlinear branches fail to exist in the neighborhood of X_s^{nl} (Fig. 10d). As ω reaches ω_0^{ca} (Fig. 10e), linear spatial branches do pinch at $X = X^{\text{ca}}$, but the nonlinear spatial branch $k^{\text{nl}+}$ prevailing around X^{ca} cannot be continued far downstream towards the k^{1+} branch extending down to $X = +\infty$; there is no global mode of frequency ω_0^{ca} .

The scenario for $\omega_0^{\text{ca}} > \omega_s^{\text{nl}}$ is sketched in the sequence of Fig. 11. As ω decreases, the first characteristic frequency encountered is now ω_0^{ca} . When $\omega \downarrow \omega_0^{\text{ca}}$ (Fig. 11a–c), the linear branches approach and pinch at k_0^{ca} for $X = X^{\text{ca}}$ determined by (29). Since $k_{0,i}^{\text{ca}} < 0$, the relevant branches in a neighborhood of X^{ca} are k^{1-} and $k^{\text{nl}+}$. A front of frequency ω_0^{ca} at X^{ca} allows a discontinuous jump in wave number from $k^{1-}(X^{\text{ca}}, \omega_0^{\text{ca}}) = k_0^{\text{ca}}$ to $k^{\text{nl}+}(X^{\text{ca}}, \omega_0^{\text{ca}})$. This front performs the connection between – and + branches necessary to obtain a steep global mode: further downstream, the amplitude of the nonlinear $k^{\text{nl}+}$ branch vanishes at a neutrally stable station and there the linear k^{1+} branch takes over to $X = +\infty$. Note that the $k^{1+}(X, \omega_0^{\text{ca}})$ branch necessarily crosses the k_r -axis; the $k^{1-}(X, \omega_0^{\text{ca}})$ branch however may or may not cross. For $\omega = \omega_0^{\text{ca}}$, the nonlinear branches, if they both exist, do not meet. Decreasing further ω towards ω_s^{nl} (Fig. 11d and e), the nonlinear branches in turn approach and pinch for $\omega = \omega_s^{\text{nl}}$. However, since $\omega_s^{\text{nl}} < \omega_0^{\text{ca}}$, the linear $k^{1\pm}$ branches have undergone branch switching for $\omega = \omega_0^{\text{ca}}$. As can be seen in Fig. 11e, the nonlinear branches issuing at k_s^{nl} , X_s^{nl} cannot be continued towards the k^{1-} branch near $X = -\infty$. In this situation, due to global considerations, no soft mode exists, although the local criterion (29) may be satisfied.

This completes the discussion of the global mode selection mechanism: the type of selected global mode depends on the relative values of the linear pinchpoint frequency ω_0^{ca} and nonlinear pinchpoint frequency ω_s^{nl} . If

$$\omega_s^{\text{nl}} < \omega_0^{\text{ca}},$$

linear spatial branches meet first as the overall frequency is lowered: the steep criterion (24) yields a global solution on the entire X -axis with a sharp front located at X^{ca} . However, if

$$\omega_0^{\text{ca}} < \omega_s^{\text{nl}},$$

the nonlinear saddle point is encountered first and a soft global mode with overall smoothly varying envelope and wave number prevails. There exists also situations where the nonlinear dispersion relation displays no saddle point in the nonlinear balloon. Then a steep mode is necessarily obtained. The preceding close inspection of spatial linear and nonlinear branches guarantees that the selection criteria for steep and soft global modes are mutually exclusive, and that all situations are accounted for.

According to this discussion, when a global control parameter is continuously varied, the transition mechanism between soft and steep global modes is the following. Starting with a system where a soft mode is selected, i.e., where $\omega_s^{nl} > \omega_0^{ca}$, two possibilities arise if the control parameter is changed:

- The saddle point frequency ω_s^{nl} may equal the front frequency ω_0^{ca} for a critical value of the control parameter. Beyond this value, $\omega_s^{nl} < \omega_0^{ca}$, and a steep mode prevails. The transition to a steep mode of the same frequency takes place when $\omega_s^{nl} = \omega_0^{ca}$.
- The nonlinear saddle point may reach the boundary of the nonlinear balloon and disappear while still $\omega_s^{nl} > \omega_0^{ca}$. Then, transition to a steep mode again occurs, but in this situation the global frequency is discontinuous at transition.

This will be fully justified in Section 4.9, where we map out the domains of existence of soft and steep global modes in an appropriate control parameter space. To identify the relevant control parameters, a discussion of the role of the absolute wave number is first required.

4.8. Role of the absolute wave number

The local instability properties are seen to be essentially controlled by the streamwise evolution of the absolute frequency $\omega_0(X)$ and wave number $k_0(X)$ which in principle can be varied independently. The criterion for steep global modes (24) only depends on the local absolute frequency $\omega_0(X)$ regardless of the local absolute wave number $k_0(X)$. The soft global mode criterion (29), however, depends on $k_0(X)$ through the complete nonlinear dispersion relation. In this section, the role of the absolute wave number is discussed by varying $k_0(X)$ in the CGL equation, all other coefficients remaining fixed.

From expressions (23) for the linear spatial $k^{l\pm}$ branches it is readily seen that a change in $k_0(X)$ by some constant value, say κ , results in a displacement of the $k^{l\pm}$ curves in the complex k -plane. Under this process, the linear pinchpoint properties are not affected. Nonlinear characteristics, however, are closely related to the crossing of the k_r -axis by the $k^{l\pm}$ branches; it follows that changes in $k_{0,i}$ strongly influence the nonlinear properties of the medium, unlike changes of $k_{0,r}$. This calls for two distinct physical interpretations of $k_{0,r}$ and $k_{0,i}$, respectively.

Consider the uniform CGL equation (6) with k_0 replaced by $k_0 - \kappa_r$. Then, under the change of unknown function

$$\psi(x, t) = \phi(x, t) e^{ik_r x},$$

the original CGL equation (6) is recovered for ϕ . This shows that the only effect of a change in $k_{0,r}$ is a change in wavelength; linear spatial growth or decay rates, frequencies as well as nonlinear amplitudes remain the same. A variation of $k_{0,r}$ results in a change of carrier wave but does not alter the linear or the nonlinear stability properties of the system. In the spatially dependent CGL equation (4), the following change of unknown function

$$\psi(x, t) = \phi(x, t) \exp\left(\frac{i}{\epsilon} \int^X \kappa_r(u) du\right)$$

results in modifying the local absolute wave number to $k_0(X) - \kappa_r(X)$. Any slowly modulated carrier wave defined by the real function $\kappa_r(X)$ may thus be used to transform the real part of the absolute local wave number. Under such a transformation, the global mode selection criteria as well as the characteristic frequencies remain unaltered: the function $k_{0,r}(X)$ may then be chosen arbitrarily since it does not affect the local and global dynamics.

In order to bring to the fore the role of $k_{0,i}(X)$, it is convenient, in the remainder of this section, to select $k_{0,r}(X)$ so that the function $\omega_{kk}(X)k_0(X)$ appearing in front of the advection term $\partial\psi/\partial x$ in (4) is real [12]. Under such a condition,

$$k_{0,r}(X) = -\frac{\omega_{kk,r}(X)}{\omega_{kk,i}(X)}k_{0,i}(X),$$

and the CGL equation reads

$$\frac{\partial\psi}{\partial t} + \frac{|\omega_{kk}|^2}{\omega_{kk,i}}k_{0,i}\frac{\partial\psi}{\partial x} = -i\left(\omega_0 + \frac{1}{2}\omega_{kk}k_0^2\right)\psi + \frac{i}{2}\omega_{kk}\frac{\partial^2\psi}{\partial x^2} - i\gamma|\psi|^2\psi. \quad (35)$$

The form (35) clearly indicates that the real factor

$$U(X) = \frac{|\omega_{kk}(X)|^2}{\omega_{kk,i}(X)}k_{0,i}(X)$$

may be interpreted as an advection velocity. Since causality requires that $\omega_{kk,i} < 0$, a negative (positive) $k_{0,i}$ is readily seen to correspond to advection towards $X = +\infty$ ($X = -\infty$). Thus, the sign of $k_{0,i}$ controls the advection direction whereas its magnitude is directly related to the advection velocity. As stated in Section 1, it is assumed that $U(X) > 0$, i.e., $k_{0,i}(X) < 0$ in the entire domain. The basic advection is then directed towards $X = +\infty$.

In order to further discuss the role of $k_{0,i}$ in the selection of global modes, consider, for simplicity, that $k_{0,i}$ is constant over the entire domain. A change in $k_{0,i}$ is seen to be associated with a displacement of the $k^{l\pm}$ curves along the k_i -axis in the complex k -plane. Its effect on the nonlinear balloon and nonlinear spatial branches in the (X, k) -plane is outlined in Fig. 12. Since the function $\omega_0(X)$ is kept fixed, a change of $k_{0,i}$ leaves the extent of the AU

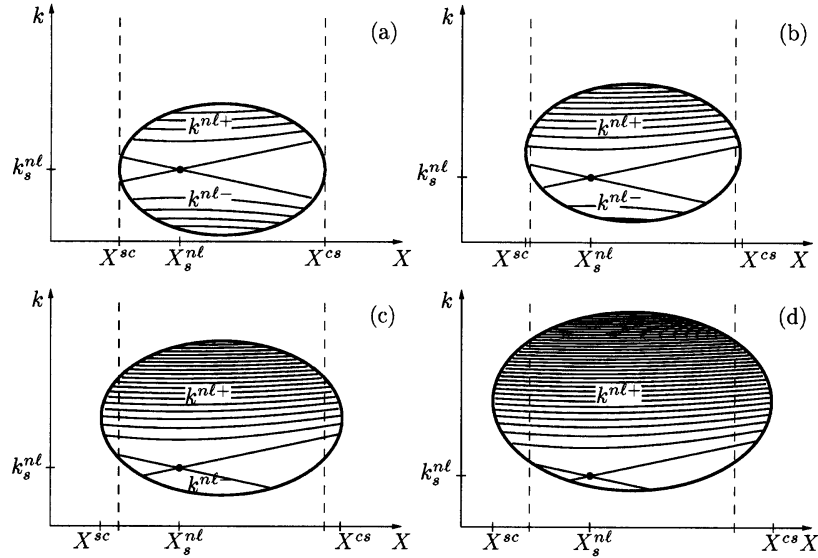


Fig. 12. Evolution of CGL nonlinear balloon and spatial $k^{nl\pm}$ branches in the (X, k) -plane as the advection towards $X = +\infty$ is increased. Vertical dashed lines indicate AU domain extending over $X^{ca} < X < X^{ac}$. (a) Without mean advection ($k_{0,i} = 0$), spatial branches display symmetry with respect to the nonlinear saddle point wave number k_s^{nl} and the nonlinear domain exactly spans the AU region, $X^{sc} = X^{ca}$ and $X^{ac} = X^{cs}$. (b)–(d) With increasing downstream advection $k_{0,i} < 0$, the nonlinear balloon inflates and extends beyond the AU region, $X^{sc} < X^{ca}$ and $X^{ac} < X^{cs}$. During this process the fraction of the nonlinear balloon covered by the downstream k^{nl+} branches increases with respect to the k^{nl-} branches. Simultaneously, the nonlinear saddle point (X_s^{nl}, k_s^{nl}) is seen to descend to eventually leave the nonlinear balloon.

range $X^{ca} < X < X^{ac}$ unaltered, as indicated by vertical dashed lines $X = X^{ca}$ and $X = X^{ac}$ in Fig. 12. Without mean advection, $k_{0,i} = 0$ (Fig. 12a), the nonlinear balloon exactly spans the AU region. In this situation, local linear instability coincides with local absolute instability: $X^{sc} = X^{ca}$ and $X^{ac} = X^{cs}$. Nonlinear spatial branches cover the nonlinear balloon symmetrically with respect to $k = k_s^{nl}$. Fig. 12b–d is obtained for increasing negative values of $k_{0,i}$, i.e., increasing advection towards $X = +\infty$. Increasing $|k_{0,i}|$ then shifts the $k^{l\pm}$ branches (23) towards negative k_i in the complex k -plane, thereby enhancing the instability of the downstream k^{l+} branches and reducing the instability of the upstream k^{l-} branches. Under such circumstances, the onset of linear instability no longer coincides with transition to absolute instability: the nonlinear balloon inflates and extends beyond the AU range into the CU regions $X^{sc} < X < X^{ca}$ and $X^{ac} < X < X^{cs}$. The basic flow advection breaks the k^{nl+}/k^{nl-} symmetry, and the part of the nonlinear balloon spanned by the k^{nl+} branches increases to the detriment of the k^{nl-} branches. During this process, the nonlinear saddle point moves towards the lower neutral stability boundary and eventually leaves the nonlinear balloon. The advection velocity, measured by $k_{0,i}$, thus strongly affects the existence of the nonlinear saddle point and hence the existence of smooth global modes.

In the remainder of this section, we temporarily allow advection in the positive or negative direction so that $k_{0,i}$ may change sign. It has been shown in Section 4.2 that among the two stationary fronts at X^{ca} and X^{ac} , only the one located at the upstream boundary of the AU region is stable. Since flow direction is directly related to the sign of $k_{0,i}$, the stable steep global mode frequency is ω_0^{ca} for $k_{0,i} < 0$ and ω_0^{ac} for $k_{0,i} > 0$. These are indeed the fronts at the stations of local marginal absolute instability with their nonlinear wave train covering the AU domain and their exponentially decaying tail extending into the CU region (see also Fig. 13). The soft global mode frequency ω_s^{nl} has been obtained in (33), and, in contrast to the steep global mode frequencies ω_0^{ca} and ω_0^{ac} , it is seen to depend on $k_{0,i}$.

In the previous section, it has been demonstrated that the global mode of largest frequency is selected; thus, the transition scenario between steep and soft global modes as a function of $k_{0,i}$ is derived from the relative values of ω_0^{ca} , ω_0^{ac} and $\omega_s^{nl}(k_{0,i})$, as displayed in Fig. 13. According to (33), the soft frequency ω_s^{nl} is largest for $k_{0,i} = 0$, all other coefficients being kept fixed. Thus, soft modes prevail when advection is small enough, $\omega_s^{nl} > \omega_0^{ca}$ and $\omega_s^{nl} > \omega_0^{ac}$. With increasing downstream advection ($k_{0,i} < 0$), the nonlinear saddle point frequency ω_s^{nl} decreases. When $\omega_s^{nl} < \omega_0^{ca}$, the soft mode is replaced by a steep mode with a sharp front at X^{ca} (left-hand side of Fig. 13). Similarly, if $k_{0,i}$ increases from 0 ($k_{0,i} > 0$), which corresponds to advection towards $X = -\infty$, the nonlinear

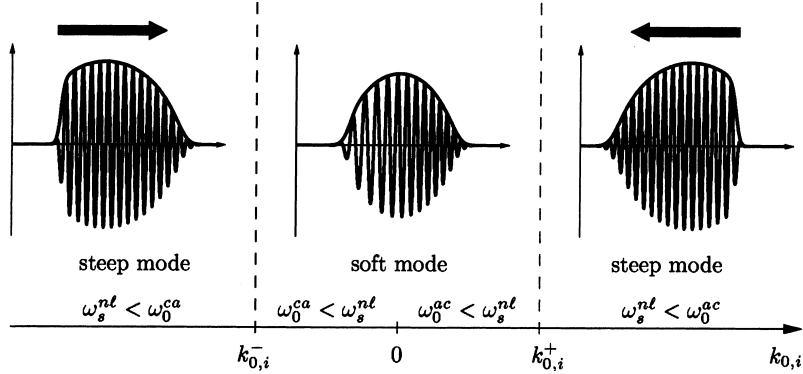


Fig. 13. Transition between steep and soft global modes as a function of $k_{0,i}$ in CGL equation. Black arrows indicate advection direction. For small advection velocities ($k_{0,i}$ small), the saddle point frequency ω_s^{nl} is larger than the front frequencies ω_0^{ca} and ω_0^{ac} , and thus a soft global mode is selected. With increasing advection towards $X = +\infty$ ($k_{0,i} < 0$), the saddle point frequency ω_s^{nl} decreases, and, when $k_{0,i} < k_{0,-}$, the soft mode is replaced by a steep global mode with a front at the left boundary of the AU region. Similarly, with increasing advection towards $X = -\infty$ ($k_{0,i} > 0$), the saddle point frequency ω_s^{nl} again decreases, and at $k_{0,i} = k_{0,+}$ transition takes place to a steep global mode with a front at the right boundary of the AU region.

saddle point frequency ω_s^{nl} again decreases. When $\omega_s^{\text{nl}} < \omega_0^{\text{ac}}$, the soft mode is now replaced by a steep mode with a front at $X = X^{\text{ac}}$ (right-hand side of Fig. 13). Since $k_{0,i} > 0$, the front at X^{ac} is now the stable one: upstream and downstream directions have been interchanged. In any case, the front location corresponds to the upstream boundary of the AU region. The critical transition values $k_{0,i}^- < 0$ and $k_{0,i}^+ > 0$ between soft and steep global modes are defined by $\omega_0^{\text{ca}} = \omega_s^{\text{nl}}$ and $\omega_0^{\text{ac}} = \omega_s^{\text{nl}}$, respectively.

4.9. Domains of existence in control parameter space

Now that the roles of $\omega_{0,i}^{\text{max}}$, $\omega_{0X,r}$ and $k_{0,i}$ have been separately discussed, the domains of existence of steep and soft global modes may be obtained in the three-dimensional space of these control parameters (Fig. 14). Consider the CGL equation (4) with $\omega_0(X)$ of the form (27), all other coefficients being assumed uniform in X for simplicity. The front frequencies ω_0^{ca} and ω_0^{ac} then read

$$\omega_0^{\text{ca}}, \omega_0^{\text{ac}} = \omega_{0,r}^{\text{max}} - \frac{\omega_{0XX,r} \omega_{0,i}^{\text{max}}}{\omega_{0XX,i}} \mp \omega_{0X,r} \sqrt{\frac{2\omega_{0,i}^{\text{max}}}{-\omega_{0XX,i}}}. \quad (36)$$

They exist whenever $\omega_{0,i}^{\text{max}} > 0$ and their values are seen to be effectively independent of $k_{0,i}$.

The selected global mode type depends on the relative values of the front frequencies (36) and the nonlinear saddle point frequency ω_s^{nl} (33). However, note that the nonlinear saddle point formally defined by (31) and (32) only exists if $(k_s^{\text{nl}}, X_s^{\text{nl}})$ lies in the nonlinear balloon, i.e., if

$$\Omega_i^1(k_s^{\text{nl}}, X_s^{\text{nl}}) > 0. \quad (37)$$

For the CGL equation under study, one readily obtains

$$\Omega_i^1(k_s^{\text{nl}}, X_s^{\text{nl}}) = \omega_{0,i}^{\text{max}} + \frac{1}{2} \omega_{0XX,i} \left(\frac{\gamma}{\text{Im } \gamma^* \omega_{0XX}} \right)^2 (\omega_{0X,r})^2 + \frac{|\omega_{kk}|^2 \text{Im } \gamma^2 \omega_{kk}^* (k_{0,i})^2}{2(\text{Im } \gamma^* \omega_{kk})^2}. \quad (38)$$

Whenever $\Omega_i^1(k_s^{\text{nl}}, X_s^{\text{nl}}) < 0$, the nonlinear saddle point does not exist, and only a steep global mode is obtained. In the control parameter space of Fig. 14, the domain where condition (37) is satisfied is located above the surface labeled $\Omega_i^1(k_s^{\text{nl}}, X_s^{\text{nl}}) = 0$. According to (38), this surface is a paraboloid entirely contained in the half-space $\omega_{0,i}^{\text{max}} \geq 0$ and tangent to the plane $\omega_{0,i}^{\text{max}} = 0$ at $\omega_{0X,r} = k_{0,i} = 0$. Below this surface no soft mode may exist and only steep modes are obtained. Above this surface, the soft global frequency ω_s^{nl} must be compared to ω_0^{ca} and ω_0^{ac} . We only consider situations with advection towards $X = +\infty$, i.e., the half-space $k_{0,i} < 0$, so that only ω_0^{ca} comes into consideration for steep modes. Within the region where a nonlinear saddle point exists, transition between soft and steep modes occurs when $\omega_s^{\text{nl}} = \omega_0^{\text{ca}}$. This transition surface is derived from (33) and (36) and is sketched in Fig. 14. It is seen to meet the surface $\Omega_i^1(k_s^{\text{nl}}, X_s^{\text{nl}}) = 0$ along a curve in the plane $k_{0,i} = 0$. As may be inferred from these critical surfaces, the parameter space is divided into four regions (Fig. 14):

- (a) Below the global threshold, $\omega_{0,i}^{\text{max}} < 0$, no front and no saddle point exists, the unperturbed state $\psi = 0$ remains stable.
- (b) When $\omega_{0,i}^{\text{max}} > 0$ and $\Omega_i^1(k_s^{\text{nl}}, X_s^{\text{nl}}) < 0$, no saddle point exists and a steep global mode prevails.
- (c) When $\Omega_i^1(k_s^{\text{nl}}, X_s^{\text{nl}}) > 0$ and $\omega_s^{\text{nl}} < \omega_0^{\text{ca}}$, a saddle point exists but the steep mode is selected.
- (d) When $\Omega_i^1(k_s^{\text{nl}}, X_s^{\text{nl}}) > 0$ and $\omega_s^{\text{nl}} > \omega_0^{\text{ca}}$, the soft mode is selected.

Thus, at global mode onset $\omega_{0,i}^{\text{max}} = 0$, transition occurs always via a steep global mode except for the triply degenerate case $\omega_{0,i}^{\text{max}} = k_{0,i} = \omega_{0X,r} = 0$. With increasing $\omega_{0,i}^{\text{max}}$, transition from a steep to a soft mode occurs for finite values of $\omega_{0,i}^{\text{max}}$ either as soon as the nonlinear saddle point comes into existence (on the surface $\Omega_i^1(k_s^{\text{nl}}, X_s^{\text{nl}}) = 0$) or when its frequency reaches the steep frequency (on the surface $\omega_s^{\text{nl}} = \omega_0^{\text{ca}}$).

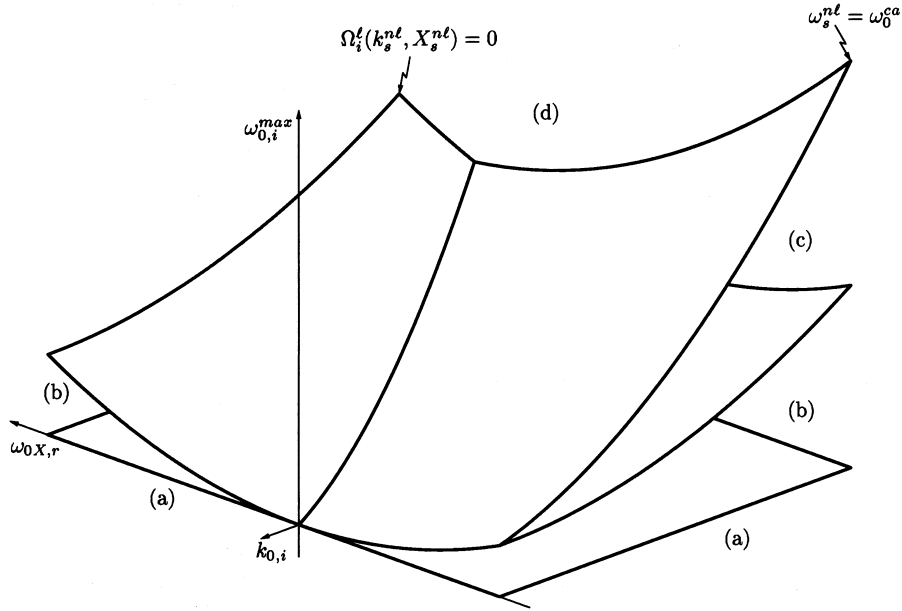


Fig. 14. Domains of existence of steep and soft global modes in the three-dimensional control parameter space $(\omega_{0X,r}, k_{0,i}, \omega_{0,i}^{max})$ of CGL equation. A nonlinear saddle point exists above the surface $\Omega_i^l(k_s^{nl}, X_s^{nl}) = 0$. The associated frequency ω_s^{nl} is larger than the front frequency ω_0^{ca} above the surface labeled $\omega_s^{nl} = \omega_0^{ca}$. Hence soft global modes prevail in region (d). In region (c), steep modes are selected according to $\omega_s^{nl} < \omega_0^{ca}$. In region (b), no nonlinear saddle point exists and only steep modes are obtained. In region (a), below global threshold $\omega_{0,i}^{max} < 0$, the unperturbed state is stable.

4.10. Summary of transition mechanisms

The main global mode selection mechanisms have been shown to be governed by three distinct control parameters. The global bifurcation parameter is the maximum absolute growth rate over the entire medium $\omega_{0,i}^{max}$. Nonlinear global modes exist whenever a region of absolute instability is present ($\omega_{0,i}^{max} > 0$). The transition to a steep global mode occurs discontinuously at $\omega_{0,i}^{max} = 0$ through a saddle-node bifurcation. In the absence of absolute instability ($\omega_{0,i}^{max} < 0$), no self-sustained global modes exist and the basic state is globally stable.

The basic state remains globally linearly stable up to a finite positive value of $\omega_{0,i}^{max}$. The hysteresis width in $\omega_{0,i}^{max}$ is governed by $\omega_{0X,r}$ and scales as $(\omega_{0X,r})^2$. The advection parameter $k_{0,i}$ strongly influences transition from steep to soft nonlinear global modes. Soft modes exist for small values of $k_{0,i}$, whereas for increasing upstream or downstream advection, steep modes prevail. The main global mode properties may be inferred from the three above-mentioned control parameters.

5. Asymptotic spatial structure of global modes

The preceding results have been derived under the assumption that the global mode is, at each station close to the local wave train at the global frequency. This local wave train is governed by the local linear dispersion relation (19) in regions where the amplitude is small, whereas it follows the local nonlinear dispersion relation (20) in finite amplitude domains. These considerations, which only involve the local characteristics of the medium, yield the leading-order WKBJ approximation to the spatial structure. Within this framework, the selection criteria for steep

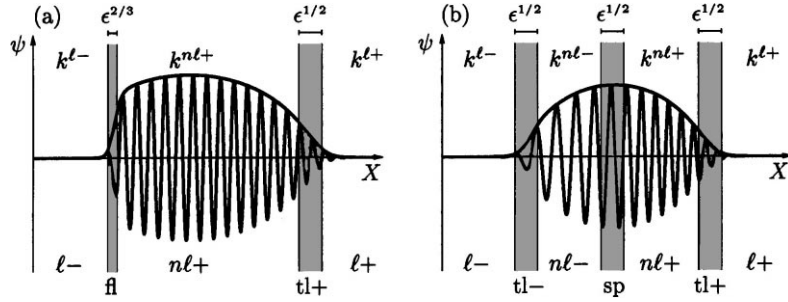


Fig. 15. Spatial structure of (a) steep and (b) soft global modes. ($l\pm$) outer semi-infinite linear regions near $X = \pm\infty$ with respective linear spatial $k^{l\pm}$ branch; ($nl\pm$) central nonlinear regions of size $\mathcal{O}(1)$ with respective nonlinear spatial $k^{nl\pm}$ branch; ($tl\pm$) weakly nonlinear transition layers of width $\mathcal{O}(\epsilon^{1/2})$ connecting linear and nonlinear branches of same superscript; (fl) front layer of size $\mathcal{O}(\epsilon^{2/3})$ connecting the k^{l-} and k^{nl+} branches and selecting the steep global mode; (sp) saddle point layer of size $\mathcal{O}(\epsilon^{1/2})$ connecting the $k^{nl\pm}$ branches and selecting the soft global mode.

and soft global modes have been identified and the leading-order steep (24) and soft (29) frequencies have been derived.

The objective of this section is to incorporate the previous results into a consistent WKBJ approximation scheme [2] in order to obtain higher-order correction terms, and to establish that the global mode structures outlined in the preceding sections may effectively be constructed by matching together extended wave packets prevailing in different regions.

The organization of the following sections is motivated by the spatial structure of both steep and soft global modes illustrated in Fig. 15. As already discussed, global modes display nonlinear regions of finite amplitude as well as linear regions of infinitesimal amplitude. In the outer semi-infinite linear regions ($l\pm$) extending towards $X = \pm\infty$ (Section 5.1) the respective complex linear spatial branch $k^{l\pm}$ prevails. The central nonlinear regions ($nl\pm$) are of finite extent, i.e., order unity measured in terms of X , and they are dominated by the respective nonlinear spatial branch $k^{nl\pm}$ as discussed in Section 5.2. These extended regions are connected via three types of narrow *transition layers*:

- The *front layer* (fl) of size $\mathcal{O}(\epsilon^{2/3})$ located at the upstream boundary of the steep global mode nonlinear region connects k^{l-} and k^{nl+} branches (Section 5.3).
- The *nonlinear saddle point layer* (sp) of size $\mathcal{O}(\epsilon^{1/2})$ allows crossover between the $k^{nl\pm}$ branches within the nonlinear soft global mode region (Section 5.4).
- *Weakly nonlinear transition layers* ($tl\pm$) of size $\mathcal{O}(\epsilon^{1/2})$ at the downstream end of the steep global mode nonlinear region and at both ends of the soft global mode nonlinear region connect the fully developed nonlinear branches with their linear counterparts (Section 5.5).

Each of these regions is analyzed in turn to obtain a uniformly valid asymptotic approximation over the entire range $-\infty < X < +\infty$. Close inspection of the front layer and the nonlinear saddle point layer yields higher-order corrections of the steep (72) and soft (88) global frequencies, respectively. Since the width of the narrow layers is $\mathcal{O}(\epsilon^{1/2})$ or $\mathcal{O}(\epsilon^{2/3})$ measured in units of X , their characteristic scale is intermediate between the inhomogeneity length scale $\mathcal{O}(1)$ and the instability length scale $\mathcal{O}(\epsilon)$. Thus, although the medium may be considered uniform in the transition layers, they still display many wavelengths, typically $\mathcal{O}(\epsilon^{-1/2})$ or $\mathcal{O}(\epsilon^{-1/3})$.

In the preceding sections, the bifurcation study was largely based on the CGL equation (4) and a complete understanding of the global selection mechanisms was achieved in this context. In this section, the WKBJ approximation scheme is presented in the more general framework of PDE (1).

5.1. Linear WKBJ instability waves

In the semi-infinite linear regions extending towards $X = \pm\infty$ ($1\pm$ in Fig. 15a and b), the global mode amplitude exponentially decays on the fast x -scale. These regions are thus governed by the linear equation (2). Under the slowly varying medium hypothesis (3) a solution of (2) with global frequency ω_g may be obtained in terms of WKBJ approximations [2]. The spatial structure is described by a rapidly varying complex phase, accounting for the local wavelength and spatial decay rate, and a slowly varying envelope. For a given value of the frequency ω_g , the solution reads

$$\psi(x, t) = A^1(X) \exp\left(\frac{i}{\epsilon} \int^X k^1(u) du - i\omega_g t\right) + \text{c.c.}, \quad (39)$$

where $k^1(X)$ is one of the linear spatial branches associated with the frequency ω_g . The functions $A^1(X)$ and $k^1(X)$ implicitly depend on ω_g ; for simplicity their frequency dependence is omitted.

In classical WKBJ fashion, the slowly varying envelope $A^1(X)$ is expanded in powers of ϵ as

$$A^1(X) \sim A_0^1(X) + \epsilon A_1^1(X) + \epsilon^2 A_2^1(X) + \dots \quad (40)$$

Thus, spatial differentiation takes the form

$$\frac{\partial \psi}{\partial x} = [(ik^1(X) + \epsilon \partial_X) A^1(X)] \exp\left(\frac{i}{\epsilon} \int^X k^1(u) du - i\omega_g t\right) + \text{c.c.} \quad (41)$$

Upon substituting (39)–(41) into the governing equation (2) and bearing in mind that $\Omega^1(-i\partial_x) = i\mathcal{L}(\partial_x)$, see (8), one obtains

$$\omega_g(A_0^1 + \epsilon A_1^1 + \dots) = \Omega^1(k^1(X) - i\epsilon \partial_X, X)(A_0^1 + \epsilon A_1^1 + \dots). \quad (42)$$

Note that differentiation with respect to the fast variable, i.e., multiplication by $ik^1(X)$, does not commute with the slow derivative operator ∂_X . The linear operator appearing in (42) admits the expansion

$$\Omega^1(k^1(X) - i\epsilon \partial_X, X) = \Omega^1(X) - i\epsilon(\Omega_k^1(X)\partial_X + \frac{1}{2}k_X^1(X)\Omega_{kk}^1(X)) + \mathcal{O}(\epsilon^2) \quad (43)$$

with the notations

$$\Omega^1(X) \equiv \Omega^1(k^1(X), X), \quad \Omega_k^1(X) \equiv \frac{\partial \Omega^1}{\partial k}(k^1(X), X), \quad \text{etc.}$$

At lowest-order, Eq. (42) reduces to the linear dispersion relation (19), i.e.,

$$\omega_g = \Omega^1(k^1(X), X), \quad (44)$$

which yields the local wave number $k^1(X)$ for a given frequency ω_g .

The order ϵ terms read

$$[\omega_g - \Omega^1(k^1(X), X)]A_1^1(X) = -i\Omega_k^1(X) \frac{dA_0^1}{dX} - \frac{i}{2}\Omega_{kk}^1(X)k_X^1(X)A_0^1(X).$$

By invoking (44), one obtains the obvious solvability condition for $A_0^1(X)$, namely

$$\frac{dA_0^1}{dX} = -\frac{1}{2}k_X^1(X) \frac{\Omega_{kk}^1(X)}{\Omega_k^1(X)} A_0^1(X). \quad (45)$$

Thus, the first-order asymptotic approximation to the solution of the linearized equation reads

$$\psi \sim A_0^1(X_1) \exp \left(-\frac{1}{2} \int_{X_1}^X k_X^1(u) \frac{\Omega_{kk}^1(u)}{\Omega_k^1(u)} du \right) \exp \left(\frac{i}{\epsilon} \int_{X_1}^X k^1(u) du - i\omega_g t \right) + \text{c.c.}, \quad (46)$$

where X_1 is some arbitrarily specified reference point. In each of the semi-infinite linear regions the respective causal k^1 branch has to be chosen: k^{1-} for $X \rightarrow -\infty$ and k^{1+} for $X \rightarrow +\infty$.

In the linear region, the nonlinear terms of (1) are seen to be exponentially smaller than the linear ones. Their exact expressions are therefore irrelevant to this work and will not be computed here.

5.2. Nonlinear WKB wave trains

In the central nonlinear regions ($\text{nl}\pm$ in Fig. 15a and b), the solution of (1) is obtained in terms of local nonlinear wave trains (10). An asymptotic approximation scheme for nonlinear wave trains is derived in this section, which is formally analogous to linear WKB theory.

The fast oscillations of the propagating wave and its slowly varying local wave number and amplitude suggest the following change of variables:

$$\psi(x, t) = \psi(\theta; X),$$

where the real phase function $\theta(x, t)$ is 2π periodic and accounts for propagation on the fast space and time scales, whereas $X = \epsilon x$ allows for slow spatial modulation. Local frequency and wave number are defined as

$$\omega = -\partial_t \theta, \quad k = \partial_x \theta.$$

For a synchronized global solution, the frequency $\omega = \omega_g$ is constant, whereas the local wave number $k = k^{\text{nl}}(X)$ depends on the slow space variable.

Upon expanding the derivative operators according to

$$\partial_x = k^{\text{nl}}(X)\partial_\theta + \epsilon\partial_X, \quad \partial_t = -\omega_g\partial_\theta,$$

the governing equation (1) is recast in the form

$$\omega_g \partial_\theta \psi + \mathcal{F}(k^{\text{nl}}(X)\partial_\theta + \epsilon\partial_X; X)[\psi] = 0. \quad (47)$$

Again note that differentiation of $\psi(\theta; X)$ with respect to the fast variable does not commute with ∂_X since $k^{\text{nl}}(X)$ depends on X . Next ψ is expanded according to

$$\psi \sim \psi_0 + \epsilon\psi_1 + \epsilon^2\psi_2 + \dots,$$

and substituted into (47).

The lowest-order in ϵ yields the local equation

$$\omega \partial_\theta \psi + \mathcal{F}(k \partial_\theta; X)[\psi] = 0, \quad (48)$$

where X acts as an external parameter. When X is considered frozen, the family of local nonlinear wave trains $\Psi(\theta; k, X)$ is recovered. This equation admits solutions only if $\omega = \Omega^{\text{nl}}(k, X)$. In other words, for a global frequency ω_g , the nonlinear spatial branch $k^{\text{nl}}(X)$ is derived from the local nonlinear dispersion relation (20) as

$$\omega_g = \Omega^{\text{nl}}(k^{\text{nl}}(X), X), \quad (49)$$

and the leading-order solution ψ_0 then reads

$$\psi_0 = \Psi(\theta; k^{\text{nl}}(X), X). \quad (50)$$

The function Ψ is 2π periodic in the phase variable θ which accounts for the fast propagation through

$$\theta = \frac{1}{\epsilon} \int_0^X k^{\text{nl}}(u) du - \omega_g t + \theta_0(X). \quad (51)$$

The so far undetermined slowly drifting phase function $\theta_0(X)$ obeys a solvability condition to be obtained at next order.

The $\mathcal{O}(\epsilon)$ terms in (47) require some care. For clarity of presentation, assume that spatial differentiation only occurs in the linear operator,

$$\mathcal{F}(\partial_x; X)[\psi] = \mathcal{L}(\partial_x; X)[\psi] + \mathcal{N}(X)[\psi].$$

The linear terms are expanded as

$$\begin{aligned} & \mathcal{L}(k^{\text{nl}}(X)\partial_\theta + \epsilon\partial_X; X)[\psi_0(\theta; X) + \epsilon\psi_1(\theta; X) + \dots] \\ & + \sim \mathcal{L}(X)[\psi_0]\epsilon \left(\mathcal{L}(X)[\psi_1] + \mathcal{L}'(X)[\partial_X\psi_0] + \frac{1}{2} \frac{dk^{\text{nl}}}{dX} \mathcal{L}''(X)[\partial_\theta\psi_0] \right) + \mathcal{O}(\epsilon^2), \end{aligned}$$

where the notation $\mathcal{L}(X)$ is shorthand for $\mathcal{L}(k^{\text{nl}}(X)\partial_\theta; X)$ and the primes denote differentiation of $\mathcal{L}(\partial_x; X)$ with respect to its first argument. The nonlinear terms are expanded as

$$\mathcal{N}(X)[\psi_0 + \epsilon\psi_1 + \dots] = \mathcal{N}(X)[\psi_0] + \epsilon \frac{\partial \mathcal{N}(X)[\psi_0]}{\partial \psi} \psi_1 + \mathcal{O}(\epsilon^2).$$

Thus (47) yields at $\mathcal{O}(\epsilon)$,

$$L[\psi_1] = -\mathcal{L}'(X)[\partial_X\psi_0] - \frac{1}{2} \frac{dk^{\text{nl}}}{dX} \mathcal{L}''(X)[\partial_\theta\psi_0], \quad (52)$$

where the linear differential operator L on the left-hand side is defined as

$$L \equiv \omega_g \partial_\theta + \mathcal{L}(X) + \frac{\partial \mathcal{N}(X)[\psi_0]}{\partial \psi}. \quad (53)$$

Thus, ψ_1 satisfies a linear differential equation with respect to θ with X -dependent coefficients. The operator L is singular since one may readily verify that

$$L[\Psi_\theta] = 0 \quad \text{with } \Psi_\theta \equiv \partial_\theta \Psi(\theta; k^{\text{nl}}(X), X).$$

Thus (52) admits solutions for ψ_1 only if its right-hand side satisfies a solvability condition.

Let us introduce an inner product for 2π periodic functions of θ defined by

$$\langle \phi, \psi \rangle = \frac{1}{2\pi} \int_0^{2\pi} \phi(\theta) \psi(\theta) d\theta. \quad (54)$$

The adjoint operator L^\dagger of L is then obtained via successive integration by parts through the relation $\langle \phi, L\psi \rangle = \langle L^\dagger \phi, \psi \rangle$, and it reads

$$L^\dagger = -\omega_g \partial_\theta + \mathcal{L}(-k^{\text{nl}}(X)\partial_\theta; X) + \frac{\partial \mathcal{N}(X)[\psi_0]}{\partial \psi}. \quad (55)$$

Let Ψ_θ^\dagger be the adjoint eigenfunction of Ψ_θ . Taking the inner product of (52) with Ψ_θ^\dagger and substituting

$$\partial_X \psi_0 = \frac{d\theta_0}{dX} \Psi_\theta + \frac{dk^{\text{nl}}}{dX} \Psi_k + \Psi_X,$$

yields the following solvability condition for $\theta_0(X)$,

$$\frac{d\theta_0}{dX} \langle \Psi_\theta^\dagger, \mathcal{L}' \Psi_\theta \rangle + \frac{1}{2} \frac{dk^{\text{nl}}}{dX} \langle \Psi_\theta^\dagger, 2\mathcal{L}' \Psi_k + \mathcal{L}'' \Psi_\theta \rangle + \langle \Psi_\theta^\dagger, \mathcal{L}' \Psi_X \rangle = 0. \quad (56)$$

This entirely specifies the leading-order approximation to the global nonlinear solution

$$\psi(x, t) \sim \Psi \left(\frac{1}{\epsilon} \int^X k^{\text{nl}}(u) du - \omega_g t + \theta_0(X); k^{\text{nl}}(X), X \right), \quad (57)$$

where the parametric dependence of $k^{\text{nl}}(X)$ on the global frequency ω_g is entirely determined by (49).

5.3. Front layer

According to Section 4.2, the front of steep global modes is located at the station of local marginal absolute instability X^{ca} and it is associated with a wave number jump from the k^{1-} to the $k^{\text{nl}+}$ branch. On the slow scale X , the front discontinuously connects the linear solution (46) of wave number k^{1-} prevailing in the upstream domain $X < X^{\text{ca}}$ to the nonlinear solution (57) of wave number $k^{\text{nl}+}$ on the downstream side of the front $X > X^{\text{ca}}$. In this section, the linear solution is shown to match to the nonlinear solution through a narrow front layer (fl) as depicted in Fig. 15a. The formulation essentially follows the same approach as in the asymptotic description of the front boundary layer arising in nonlinear dynamo waves developed by Bassom et al. [1] and is based on linear turning point theory [48].

The envelope of the outer linear solution is governed by the amplitude equation (45) which is singular at a turning point X_0 of the dispersion relation (44) defined by

$$\omega_0(X_0) = \omega_g. \quad (58)$$

For $\omega_g = \omega_0^{\text{ca}}$, the turning point is at $X_0 = X^{\text{ca}}$. However, it is to be anticipated that the global frequency does not exactly equal ω_0^{ca} . As outlined below, it is convenient to implement a matching procedure in the turning point region for an arbitrary complex global frequency ω_g . Thus, consider the linear governing equation (2) for complex X . The results of Section 5.1 pertaining to linear instability waves remain valid in the complex X -plane, provided that $\Omega^1(k, X)$ and hence $\omega_0(X)$ are analytically continued for complex values of X . Then (58) associates to a frequency ω_g the turning point $X_0(\omega_g)$ in the complex X -plane.

Expansion of the dispersion relation (44) in the neighborhood of the turning point X_0 yields

$$0 = \frac{1}{2} \Omega_{kk,0}^1 (k^1(X) - k_0)^2 + \Omega_{X,0}^1 (X - X_0) + \text{h.o.t.}, \quad (59)$$

where k_0 is the associated absolute wave number $k_0 \equiv k_0(X_0)$ and the subscript 0 denotes evaluation at (k_0, X_0) . By definition of the turning point, $\Omega_{k,0}^1 = 0$, and under the assumption that the turning point is simple, $\Omega_{X,0}^1 \neq 0$. Thus

$$k^1(X) \sim k_0 \pm \sqrt{\frac{-2\Omega_{X,0}^1}{\Omega_{kk,0}^1}} (X - X_0)^{1/2}.$$

The linear amplitude equation (45) then reduces to

$$\frac{dA_0}{dX} \sim -\frac{A_0(X)}{4(X - X_0)}.$$

Hence $A_0(X) \sim C^{\text{st}}(X - X_0)^{-1/4}$ as $X \rightarrow X_0$, and the complete behavior of the outer linear solution (46) as $X \rightarrow X_0$ reads

$$\psi \sim C^{\text{st}}(X - X_0)^{-1/4} \exp \left[\frac{2i}{3\epsilon} \sqrt{\frac{-2\Omega_{X,0}^1}{\Omega_{kk,0}^1}} (X - X_0)^3 \right] e^{i(k_0 x - \omega_g t)} + \text{c.c.} \quad (60)$$

Here it is assumed that the square root branch cut is chosen so that the wave number k^{1-} prevailing in the domain $X \rightarrow -\infty$ is recovered.

It is seen that in the neighborhood of the turning point X_0 , the amplitude A_0 becomes singular. Balance of dominant terms, as shown below, yields an inner turning point region of size $\mathcal{O}(\epsilon^{2/3})$. Thus, define an inner variable \tilde{X} by

$$X = X_0 + \epsilon^{2/3} \tilde{X}, \quad (61)$$

and expand ψ as

$$\psi = \tilde{A}(\tilde{X}) e^{i(k_0 x - \omega_g t)} + \text{c.c.} \quad (62)$$

with

$$\tilde{A}(\tilde{X}) = \tilde{C}^{\text{st}}[\tilde{A}_0(\tilde{X}) + \epsilon^{2/3} \tilde{A}_{2/3}(\tilde{X}) + \dots], \quad (63)$$

where $\tilde{A}_0(\tilde{X})$ is $\mathcal{O}(\epsilon^0)$. Spatial differentiation now becomes $\partial_x = ik_0 + \epsilon^{1/3} \partial_{\tilde{X}}$. In this inner transition layer, the leading-order wave number is constant and equal to k_0 , thus $\partial_{\tilde{X}}$ and ik_0 now commute. The governing equation (2) then yields

$$\omega_g \tilde{A}(\tilde{X}) = \Omega^1(k_0 - i\epsilon^{1/3} \partial_{\tilde{X}}, X_0 + \epsilon^{2/3} \tilde{X}) \tilde{A}(\tilde{X}) \sim [\Omega^1(k_0, X_0) + \epsilon^{2/3} (\tilde{X} \Omega_{X,0}^1 - \frac{1}{2} \Omega_{kk,0}^1 \partial_{\tilde{X}} \tilde{X})] \tilde{A}(\tilde{X}),$$

where $\omega_g = \Omega^1(k_0, X_0)$. The scaling $X - X_0 \sim \epsilon^{2/3} \tilde{X}$ and $x \sim \epsilon^{-1/3} \tilde{X}$ guarantees the balance of dominant terms at order $\mathcal{O}(\epsilon^{2/3})$ in the previous equation and leads to the following Airy equation for the leading-order amplitude:

$$\frac{1}{2} \Omega_{kk,0}^1 \frac{d^2 \tilde{A}_0}{d \tilde{X}^2} = \tilde{X} \Omega_{X,0}^1 \tilde{A}_0(\tilde{X}). \quad (64)$$

Thus, $\tilde{A}_0(\tilde{X})$ is a linear superposition of the Airy functions $Ai(-\lambda \tilde{X})$ and $Bi(-\lambda \tilde{X})$ with

$$\lambda^3 = -\frac{2\Omega_{X,0}^1}{\Omega_{kk,0}^1}.$$

Upon choosing for λ the solution with $|\text{Arg } \lambda| < \pi/3$, the Bi component exponentially grows whereas the Ai component decays according to

$$Ai(-\lambda \tilde{X}) \sim \frac{1}{2\sqrt{\pi}} (-\lambda \tilde{X})^{-1/4} \exp \left[\frac{2i}{3} \sqrt{\frac{-2\Omega_{X,0}^1}{\Omega_{kk,0}^1}} \tilde{X}^3 \right], \quad (65)$$

as $\tilde{X} \rightarrow -\infty$ [2]. Expressing the outer solution (60) in terms of the inner variable \tilde{X} , shows that it matches with the inner solution (62) provided that

$$\tilde{A}(\tilde{X}) = \tilde{C}^{\text{st}}[Ai(-\lambda\tilde{X}) + \mathcal{O}(\epsilon^{2/3})] \quad (66)$$

with $C^{\text{st}} = \epsilon^{1/6}((- \lambda)^{-1/4}/2\sqrt{\pi})\tilde{C}^{\text{st}}$.

Thus, for any frequency ω_g , linear instability waves are governed by the Airy equation (64) in a region of size $\mathcal{O}(\epsilon^{2/3})$ located at the turning point of the linear local dispersion relation. The location of the turning point in the complex X -plane depends on ω_g . For frequencies $\omega_g = \omega_0^{\text{ca}} + \delta\omega$, close to the marginal absolute frequency, the turning point is located at

$$X_0 \sim X^{\text{ca}} + \frac{\delta\omega}{\omega_{0,X}(X^{\text{ca}})}.$$

For $\mathcal{O}(\epsilon^{2/3})$ frequency corrections, $\delta\omega = \epsilon^{2/3}\omega_{2/3}$, the inner Airy region in the complex X -plane contains in its neighborhood the point X^{ca} on the real X -axis.

Before analyzing in more detail the properties of the Airy solutions on the \tilde{X} -scale, let us turn to the front structure. As discussed in Section 5.3, a uniform medium at the transition between convective and absolute instability admits stationary front solutions oscillating at its real absolute frequency. Thus, the original nonlinear governing equation (1) rewritten at $X = X^{\text{ca}}$ as

$$\omega_0^{\text{ca}} \frac{\partial\psi}{\partial\theta} + \mathcal{F}(\partial_x; X^{\text{ca}})[\psi] = 0, \quad (67)$$

admits the front solution $\Psi_f(x, \theta)$, which is 2π periodic in the phase function $\theta = \omega_0^{\text{ca}}t$. Towards $x = +\infty$, this solution approaches a fully nonlinear wave train of the form (50). Thus,

$$\Psi_f(x, \omega_0^{\text{ca}}t) \sim \Psi[k^{\text{nl+}}(X^{\text{ca}}, \omega_0^{\text{ca}})x - \omega_0^{\text{ca}}t; k^{\text{nl+}}(X^{\text{ca}}, \omega_0^{\text{ca}}), X^{\text{ca}}] \quad \text{as } x \rightarrow +\infty.$$

Towards $x = -\infty$, the exponential decay rate is dictated by the absolute wave number $k_0^{\text{ca}} = k_0(X^{\text{ca}})$ and the front solution reads

$$\Psi_f(x, \omega_0^{\text{ca}}t) \sim (c_0^{\text{st}} + c_1^{\text{st}}x) e^{i(k_0^{\text{ca}}x - \omega_0^{\text{ca}}t)} + \text{c.c.}, \quad (68)$$

where the secular term is due to the double root $k^{1+} = k^{1-} = k_0^{\text{ca}}$ of the linear dispersion relation. In the uniform medium, the front has no preferred location. A translation of Δx only changes the phase by $k^{\text{nl+}}(\omega_0^{\text{ca}})\Delta x$ in the asymptotic behavior towards the nonlinear side $x = +\infty$ and leads to an additional factor $e^{ik_0^{\text{ca}}\Delta x}$ in the upstream exponentially decaying tail.

The exponentially decaying tail (68) has to be matched with (62) in the Airy region. Due to the secular term in (68), matching with (62) is only possible at the zeroes of the Airy function. The Airy function Ai appearing in (66) admits real negative zeros a_i . Thus, the zeros of \tilde{A}_0 are located at $\tilde{X}_i = -a_i/\lambda$. In terms of the outer variable X these occur at

$$X_i \equiv X_0(\omega_g) + \epsilon^{2/3}\tilde{X}_i = X^{\text{ca}} + \epsilon^{2/3} \left(\frac{\omega_{2/3}}{\omega_{0,X}} - \frac{a_i}{\lambda} \right) + \mathcal{O}(\epsilon^{4/3}). \quad (69)$$

Whereas the linear WKBJ approximations as well as the turning point region may be investigated in the complex X -plane, the front involves a nonlinear wave train and is thus necessarily restricted to the real X -axis. Requiring that the i th zero (69) of the Airy function is on the real X -axis yields the frequency correction term

$$\omega_{2/3} = a_i \frac{|\omega_{0,X}|^2}{|\lambda|^2} \frac{\text{Im } \lambda}{\text{Im } \omega_{0,X}}$$

for a zero located at

$$X_i \sim X^{ca} + \epsilon^{2/3} \frac{a_i}{|\lambda|^2} \frac{\text{Im}(\omega_{0,X}^* \lambda)}{\text{Im} \omega_{0,X}}.$$

Since X^{ca} is the transition location from convective to absolute instability, $\text{Im} \omega_{0,X}$ is positive. Under the slightly more restrictive assumption that $\pi/3 < \text{Arg} \omega_{0,X} < 2\pi/3$, we are guaranteed that $\text{Im}(\omega_{0,X}^* \lambda) < 0$. In most situations of physical interest, variations of $\omega_{0,r}$ are small compared to those of $\omega_{0,i}$ and thus the condition on $\text{Arg} \omega_{0,X}$ is readily fulfilled.

So far the matching conditions yield a countable set of frequencies

$$\omega_g \sim \omega_0^{ca} + \epsilon^{2/3} a_i \Omega_{2/3} \quad \text{with } \Omega_{2/3} = \frac{|\omega_{0,X}|^2}{|\lambda|^2} \frac{\text{Im} \lambda}{\text{Im} \omega_{0,X}}, \quad (70)$$

each being associated with the i th zero $a_i < 0$ of the Airy function. The corresponding fronts are located at

$$X \sim X^{ca} - \epsilon^{2/3} a_i X_{2/3} \quad \text{with } X_{2/3} = \frac{-\text{Im}(\omega_{0,X}^* \lambda)}{|\lambda|^2 \text{Im} \omega_{0,X}} > 0. \quad (71)$$

Since $X_{2/3} > 0$, higher-order global modes display a front located further downstream in the AU domain. These situations are likely to be unstable since the exponentially decaying tail of the front partly penetrates into the AU domain. Such a higher-order front prevailing in a slightly AU medium tends to move upstream, until it reaches the most upstream possible station associated with a_0 . Thus we argue, although we have not proven the result, that the only stable global mode solution is obtained for the first zero indexed by a_0 . Up to $\mathcal{O}(\epsilon^{2/3})$, the global frequency and the front location therefore, respectively, read

$$\omega_g \sim \omega_0^{ca} + \epsilon^{2/3} a_0 \Omega_{2/3}, \quad X \sim X^{ca} - \epsilon^{2/3} a_0 X_{2/3} \quad (72)$$

with

$$a_0 = -2.3381 \dots$$

This completes the investigation of the detailed structure of the front region.

5.4. Fully nonlinear saddle point layer

The nonlinear saddle point is defined as the location X_s^{nl} where the two nonlinear wave number branches meet. The saddle point frequency ω_s^{nl} is given by the criterion (29). In the nonlinear regions surrounding the saddle location X_s^{nl} the asymptotic approximation of the global solution is of the form (57) and the slowly drifting phase function $\theta_0(X)$ is governed by the solvability condition (56).

At the saddle point, the first-order differential equation (56) for θ_0 becomes singular since $\langle \Psi_\theta^\dagger, \mathcal{L}' \Psi_\theta \rangle = 0$ at X_s^{nl} (cf. Eq. (90)). Thus, the nonlinear WKBJ approximation worked out in Section 5.2 is no longer valid in the neighborhood of X_s^{nl} , because θ_0 varies there on a spatial scale which is faster than X . In this section, a nonlinear saddle point layer at X_s^{nl} is introduced, (sp) in Fig. 15b, and a second-order differential equation for the phase θ_0 is derived after rescaling the spatial variable in the neighborhood of X_s^{nl} . This inner solution in the saddle point region allows a smooth crossover between the WKBJ wave trains in both nonlinear regions.

Let us introduce an inner local space variable \tilde{X} in the saddle point region defined as

$$X = X_s^{nl} + \epsilon^{1/2} \tilde{X},$$

and expand ψ according to

$$\psi \sim \tilde{\psi}_0 + \epsilon^{1/2} \tilde{\psi}_{1/2} + \epsilon \tilde{\psi}_1 + \dots . \quad (73)$$

The subsequent analysis yields the higher-order corrections to the global frequency as

$$\omega_g \sim \omega_s^{\text{nl}} + \epsilon^{1/2} \omega_{1/2} + \epsilon \omega_1 + \dots . \quad (74)$$

Replacing the spatial derivative ∂_x in the inner region by $k_s^{\text{nl}} \partial_\theta + \epsilon^{1/2} \partial_{\tilde{X}}$, the linear operator expands as³

$$\begin{aligned} \mathcal{L}(k_s^{\text{nl}} \partial_\theta + \epsilon^{1/2} \partial_{\tilde{X}}, X_s^{\text{nl}} + \epsilon^{1/2} \tilde{X}) &= \mathcal{L}_s + \epsilon^{1/2} (\mathcal{L}'_s \partial_{\tilde{X}} + \tilde{X} \mathcal{L}_{X,s}) \\ &\quad + \frac{1}{2} \epsilon (\mathcal{L}''_s \partial_{\tilde{X}} \tilde{X} + 2 \tilde{X} \mathcal{L}'_{X,s} \partial_{\tilde{X}} + \tilde{X}^2 \mathcal{L}_{XX,s}) + \mathcal{O}(\epsilon^{3/2}). \end{aligned} \quad (75)$$

Substituting the expansions (73)–(75) into the governing equation (1), one recovers at leading order

$$\omega_s^{\text{nl}} \partial_\theta \tilde{\psi}_0 + \mathcal{L}(k_s^{\text{nl}} \partial_\theta, X_s^{\text{nl}}) \tilde{\psi}_0 + \mathcal{N}(X_s^{\text{nl}})[\tilde{\psi}_0] = 0.$$

Thus,

$$\tilde{\psi}_0 = \Psi_s \equiv \Psi(\theta + \tilde{\theta}_0(\tilde{X}); k_s^{\text{nl}}, X_s^{\text{nl}}), \quad (76)$$

where the fast phase function in the inner saddle point layer reads $\theta = k_s^{\text{nl}} x - \omega_s^{\text{nl}} t$ and the slow phase $\tilde{\theta}_0(\tilde{X})$ is a so far an undetermined function varying on the intermediate length scale \tilde{X} .

The nonlinear term is expanded as

$$\begin{aligned} \mathcal{N}(X_s^{\text{nl}} + \epsilon^{1/2} \tilde{X})[\Psi_s + \epsilon^{1/2} \tilde{\psi}_{1/2} + \epsilon \tilde{\psi}_1 + \mathcal{O}(\epsilon^{3/2})] &= \mathcal{N}_s + \epsilon^{1/2} (\tilde{X} \mathcal{N}_{X,s} + \mathcal{N}_{\psi,s} \tilde{\psi}_{1/2}) \\ &\quad + \epsilon (\frac{1}{2} \tilde{X}^2 \mathcal{N}_{XX,s} + \tilde{X} \mathcal{N}_{X\psi,s} \tilde{\psi}_{1/2} + \frac{1}{2} \mathcal{N}_{\psi\psi,s} \tilde{\psi}_{1/2}^2 + \mathcal{N}_{\psi,s} \tilde{\psi}_1) + \mathcal{O}(\epsilon^{3/2}), \end{aligned} \quad (77)$$

where

$$\mathcal{N}_s \equiv \mathcal{N}(X_s^{\text{nl}})[\Psi_s], \quad \mathcal{N}_{\psi,s} \equiv \partial_\psi \mathcal{N}(X_s^{\text{nl}})[\Psi_s], \quad \mathcal{N}_{X,s} \equiv \partial_X \mathcal{N}(X_s^{\text{nl}})[\Psi_s], \quad \text{etc.}$$

The order $\epsilon^{1/2}$ problem reads

$$L_s \tilde{\psi}_{1/2} + \omega_{1/2} \Psi_{\theta,s} + \frac{d\tilde{\theta}_0}{d\tilde{X}} \mathcal{L}'_s \Psi_{\theta,s} + \tilde{X} (\mathcal{L}_{X,s} \Psi_s + \mathcal{N}_{X,s}) = 0, \quad (78)$$

where

$$L_s \equiv \omega_s^{\text{nl}} \partial_\theta + \mathcal{L}_s + \mathcal{N}_{\psi,s}.$$

Let $\Psi_{\theta,s}^\dagger$ be the adjoint eigenfunction of $\Psi_{\theta,s}$. Eq. (78) admits solutions for $\tilde{\psi}_{1/2}$ if the following solvability condition is met:

$$\omega_{1/2} \langle \Psi_{\theta,s}^\dagger, \Psi_{\theta,s} \rangle + \frac{d\tilde{\theta}_0}{d\tilde{X}} \langle \Psi_{\theta,s}^\dagger, \mathcal{L}'_s \Psi_{\theta,s} \rangle + \tilde{X} \langle \Psi_{\theta,s}^\dagger, \mathcal{L}_{X,s} \Psi_s + \mathcal{N}_{X,s} \rangle = 0.$$

In Section 5.4.1 below, the last two terms of this equation are shown to vanish (90) and (91). Thus, the solvability condition requires that

$$\omega_{1/2} = 0.$$

There is no correction to the global frequency at order $\epsilon^{1/2}$ and no equation for $\tilde{\theta}_0$ is obtained at this order.

³ Subscript “s” always denotes evaluation at $\partial_x = k_s^{\text{nl}} \partial_\theta$, $X = X_s^{\text{nl}}$, $k = k_s^{\text{nl}}$.

With $\omega_{1/2} = 0$ and using (92) and (93), the general solution of the linear inhomogeneous equation (78) is obtained as

$$\tilde{\psi}_{1/2} = \tilde{X}\Psi_{X,s} + \frac{d\tilde{\theta}_0}{d\tilde{X}}\Psi_{k,s} + \tilde{A}(\tilde{X})\Psi_{\theta,s}, \quad (79)$$

where $\tilde{A}(\tilde{X})$ is an arbitrary real amplitude function.

At order ϵ , the following inhomogeneous equation for $\tilde{\psi}_1$ is obtained

$$\begin{aligned} L_s \tilde{\psi}_1 &+ \frac{1}{2} \frac{d^2 \tilde{\theta}_0}{d\tilde{X}^2} (2\mathcal{L}'_s \Psi_{k,s} + \mathcal{L}''_s \Psi_{\theta,s}) + \frac{1}{2} \left(\frac{d\tilde{\theta}_0}{d\tilde{X}} \right)^2 (2\mathcal{L}'_s \Psi_{\theta,k,s} + \mathcal{L}''_s \Psi_{\theta\theta,s} + \mathcal{N}_{\psi\psi,s}(\Psi_{k,s})^2) \\ &+ \tilde{X} \frac{d\tilde{\theta}_0}{d\tilde{X}} ((\mathcal{L}_{X,s} + \mathcal{N}_{X\psi,s})\Psi_{k,s} + \mathcal{L}'_{X,s}\Psi_{\theta,s} + \mathcal{L}'_s\Psi_{\theta,X,s} + \mathcal{N}_{\psi\psi,s}\Psi_{k,s}\Psi_{X,s}) \\ &+ \frac{1}{2} \tilde{X}^2 (2(\mathcal{L}_{X,s} + \mathcal{N}_{X\psi,s})\Psi_{X,s} + \mathcal{L}_{XX,s}\Psi_s + \mathcal{N}_{XX,s} + \mathcal{N}_{\psi\psi,s}(\Psi_{X,s})^2) \\ &+ \frac{d\tilde{\theta}_0}{d\tilde{X}} \tilde{A}(\tilde{X})(\mathcal{L}'_s \Psi_{\theta\theta,s} + \mathcal{N}_{\psi\psi,s}\Psi_{\theta,s}\Psi_{k,s}) + \tilde{X} \tilde{A}(\tilde{X})((\mathcal{L}_{X,s} + \mathcal{N}_{\psi X,s})\Psi_{\theta,s} + \mathcal{N}_{\psi\psi,s}\Psi_{\theta,s}\Psi_{X,s}) \\ &+ \frac{d\tilde{A}}{d\tilde{X}} \mathcal{L}'_s \Psi_{\theta,s} + \frac{1}{2} \tilde{A}(\tilde{X})^2 \mathcal{N}_{\psi\psi,s}(\Psi_{\theta,s})^2 + \mathcal{L}'_s \Psi_{X,s} + \omega_1 \Psi_{\theta,s} = 0. \end{aligned} \quad (80)$$

This equation admits solutions for $\tilde{\psi}_1$ if the inner product of the forcing terms (everything except $L_s \tilde{\psi}_1$) with $\Psi_{\theta,s}^\dagger$ vanishes. The different inner products are computed in Section 5.4.1. From (94)–(96), it follows that all the terms involving the function $\tilde{A}(\tilde{X})$ vanish: this function remains undetermined at this order. Using (97)–(99), the solvability condition for $\tilde{\theta}_0$ reads

$$A \frac{d^2 \tilde{\theta}_0}{d\tilde{X}^2} = B \left(\frac{d\tilde{\theta}_0}{d\tilde{X}} \right)^2 + 2C\tilde{X} \frac{d\tilde{\theta}_0}{d\tilde{X}} + D\tilde{X}^2 - E - 2\omega_1, \quad (81)$$

where

$$A = \frac{\langle \Psi_{\theta,s}^\dagger, 2\mathcal{L}'_s \Psi_{k,s} + \mathcal{L}''_s \Psi_{\theta,s} \rangle}{\langle \Psi_{\theta,s}^\dagger, \Psi_{\theta,s} \rangle}, \quad B = \Omega_{kk,s}^{\text{nl}}, \quad C = \Omega_{kX,s}^{\text{nl}}, \quad D = \Omega_{XX,s}^{\text{nl}}, \quad E = \frac{\langle \Psi_{\theta,s}^\dagger, \mathcal{L}'_s \Psi_{X,s} \rangle}{\langle \Psi_{\theta,s}^\dagger, \Psi_{\theta,s} \rangle}.$$

Let

$$\Theta(\tilde{X}) = \exp \left[-\frac{B}{A} \tilde{\theta}(\alpha \tilde{X}) - \frac{C\alpha^2}{2A} \tilde{X}^2 \right] \quad (82)$$

with

$$\alpha^4 = \frac{A^2}{4(C^2 - BD)}. \quad (83)$$

Note that $C^2 - BD > 0$ since $(k_s^{\text{nl}}, X_s^{\text{nl}})$ is a saddle point of $\Omega^{\text{nl}}(k, X)$. Rewriting the solvability condition (81) in terms of Θ yields the parabolic cylinder equation [2]

$$\frac{d^2 \Theta}{d\tilde{X}^2} = \left(\frac{1}{4} \tilde{X}^2 - v - \frac{1}{2} \right) \Theta, \quad (84)$$

where

$$\nu + \frac{1}{2} = \frac{1}{2} \frac{AC - B(E + 2\omega_1)}{\sqrt{A^2(C^2 - BD)}}.$$

This solution in the inner saddle point layer needs to be matched with the wave trains (57) in the outer nonlinear regions. In terms of the inner variable \tilde{X} , the phase of the outer nonlinear solutions (57) expands as

$$\frac{1}{\epsilon} \int_{X_s^{\text{nl}}}^{X_s^{\text{nl}} + \epsilon^{1/2}\tilde{X}} k^{\text{nl}}(u) du - \omega_g t + \theta_0(X) = (k_s^{\text{nl}}x - \omega_s^{\text{nl}}t) + \frac{1}{2}k_{X,s}^{\text{nl}}\tilde{X}^2 + \mathcal{O}(\epsilon^{1/2}). \quad (85)$$

Matching to the phase $k_s^{\text{nl}}x - \omega_s^{\text{nl}}t + \tilde{\theta}_0(\tilde{X})$ of the inner solution (76) when $\tilde{X} \rightarrow \pm\infty$ requires that

$$\tilde{\theta}_0(\tilde{X}) \sim \frac{1}{2}k_{X,s}^{\text{nl}}\tilde{X}^2 \quad \text{when } \tilde{X} \rightarrow \pm\infty. \quad (86)$$

At the saddle point, the derivative of the wave number reads

$$k_{X,s}^{\text{nl}} = \frac{-\Omega_{kX,s}^{\text{nl}} + \sqrt{(\Omega_{kX,s}^{\text{nl}})^2 - \Omega_{kk,s}^{\text{nl}}\Omega_{XX,s}^{\text{nl}}}}{\Omega_{kk,s}^{\text{nl}}} = \frac{-C + \sqrt{C^2 - BD}}{B}. \quad (87)$$

Using (86) with (87) in (82) shows that the function $\Theta(\tilde{X})$ behaves asymptotically as

$$\ln \Theta(\tilde{X}) \sim -\frac{1}{4}\tilde{X}^2,$$

when $\tilde{X} \rightarrow \pm\infty$. The only solution of (84) satisfying this asymptotic behavior and taking only non-negative values is obtained for $\nu = 0$ and simply reads

$$\Theta(\tilde{X}) = \exp(-\frac{1}{4}\tilde{X}^2).$$

Thus, the asymptotic expansion (86) is exact for all \tilde{X} . Then the soft global mode frequency reads to $\mathcal{O}(\epsilon)$

$$\omega_g \sim \omega_s^{\text{nl}} + \epsilon\omega_1 \quad (88)$$

with

$$\omega_1 = \frac{1}{2B}(AC - BE - \sqrt{A^2(C^2 - BD)}).$$

5.4.1. Computation of inner products

The values of the inner products used in the previous analysis are obtained from

$$\Omega^{\text{nl}}(k, X)\partial_\theta\Psi + \mathcal{L}(k\partial_\theta, X)\Psi + \mathcal{N}(X)[\Psi] = 0. \quad (89)$$

Differentiating (89) separately with respect to θ , k and X , taking the inner product of the three results with Ψ_θ^\dagger , and exploiting the fact that the derivatives Ω_k^{nl} and Ω_X^{nl} vanish at the saddle point $(k_s^{\text{nl}}, X_s^{\text{nl}})$, yields

$$\langle \Psi_{\theta,s}^\dagger, \mathcal{L}'_s \Psi_{\theta,s} \rangle = 0, \quad (90)$$

$$\langle \Psi_{\theta,s}^\dagger, \mathcal{L}_{X,s} \Psi_s + \mathcal{N}_{X,s} \rangle = 0. \quad (91)$$

$$L_s \Psi_{k,s} = -\mathcal{L}'_s \Psi_{\theta,s}, \quad (92)$$

$$L_s \Psi_{X,s} = -\mathcal{L}_{X,s} \Psi_{\theta,s} - \mathcal{N}_{X,s}. \quad (93)$$

From these identities, the particular solution (79) to Eq. (78) follows.

The order ϵ problem in the saddle point region specified by (80) requires to compute inner products by double differentiation. Differentiating (89) separately with respect to $\theta\theta$, θk and θX , and taking the inner product of the three results with Ψ_θ^\dagger at the saddle point, one obtains

$$\langle \Psi_{\theta,s}^\dagger, \mathcal{N}_{\psi\psi,s}(\Psi_{\theta,s})^2 \rangle = 0, \quad (94)$$

$$\langle \Psi_{\theta,s}^\dagger, \mathcal{L}'_s \Psi_{\theta\theta,s} + \mathcal{N}_{\psi\psi,s} \Psi_{\theta,s} \Psi_{k,s} \rangle = 0, \quad (95)$$

$$\langle \Psi_{\theta,s}^\dagger, (\mathcal{L}_{X,s} + \mathcal{N}_{X\psi,s}) \Psi_{\theta,s} + \mathcal{N}_{\psi\psi,s} \Psi_{\theta,s} \Psi_{X,s} \rangle = 0. \quad (96)$$

Differentiating (89) separately with respect to kk , kX and XX similarly yields at the saddle point

$$\langle \Psi_{\theta,s}^\dagger, 2\mathcal{L}'_s \Psi_{\theta k,s} + \mathcal{L}''_s \Psi_{\theta\theta,s} + \mathcal{N}_{\psi\psi,s}(\Psi_{k,s})^2 \rangle = -\Omega_{kk,s}^{\text{nl}} \langle \Psi_{\theta,s}^\dagger, \Psi_{\theta,s} \rangle, \quad (97)$$

$$\langle \Psi_{\theta,s}^\dagger, (\mathcal{L}_{X,s} + \mathcal{N}_{X\psi,s}) \Psi_{k,s} + \mathcal{L}'_{X,s} \Psi_{\theta,s} + \mathcal{L}'_s \Psi_{\theta X,s} + \mathcal{N}_{\psi\psi,s} \Psi_{k,s} \Psi_{X,s} \rangle = -\Omega_{kX,s}^{\text{nl}} \langle \Psi_{\theta,s}^\dagger, \Psi_{\theta,s} \rangle, \quad (98)$$

$$\langle \Psi_{\theta,s}^\dagger, 2(\mathcal{L}_{X,s} + \mathcal{N}_{X\psi,s}) \Psi_{X,s} + \mathcal{L}_{XX,s} \Psi_s + \mathcal{N}_{XX,s} + \mathcal{N}_{\psi\psi,s}(\Psi_{X,s})^2 \rangle = -\Omega_{XX,s}^{\text{nl}} \langle \Psi_{\theta,s}^\dagger, \Psi_{\theta,s} \rangle. \quad (99)$$

Results (94)–(99) are invoked to cast the phase evolution equation in its final form (81).

5.5. Weakly nonlinear transition layers

Frequency corrections for steep and soft global modes have been derived by performing a detailed asymptotic analysis of the corresponding narrow transition layers where their respective frequency selection mechanism takes place: the front layer for steep modes and the nonlinear saddle point layer for soft modes. The only type of layer that remains to be investigated in order to obtain uniformly valid asymptotic approximations for global modes is the weakly nonlinear transition layer. This layer applies to the downstream end of the steep mode nonlinear region (tl+ in Fig. 15a) and to both ends of the soft mode nonlinear region (tl± in Fig. 15b). It should be emphasized that these layers are slaved to the dynamics imposed by the front or the nonlinear saddle point frequency.

A smooth transition between nonlinear and linear solutions occurs at the boundary of the nonlinear balloon (Figs. 3 and 5) in the (X, k) -plane. Consider a global solution of frequency ω_g . Its local linear and nonlinear wave number branches $k^l(X, \omega_g)$ and $k^{\text{nl}}(X, \omega_g)$ are derived, respectively, from the curves $\Omega^l(k, X) = \omega_g$ and $\Omega^{\text{nl}}(k, X) = \omega_g$. A $k^{\text{nl}}(X, \omega_g)$ branch is connected at the border of the nonlinear balloon to the corresponding linear $k^l(X, \omega_g)$ branch at the particular station $X = X_t(\omega_g)$ for $k = k_t(\omega_g)$ where the pair (k_t, X_t) is defined by

$$\omega_g = \Omega^l(k_t, X_t) = \Omega^{\text{nl}}(k_t, X_t). \quad (100)$$

As demonstrated in Sections 4.2 and 4.6, a continuous transition between linear and nonlinear wave number branches occurs at the downstream boundary of the nonlinear region of a steep global mode and at both downstream and upstream boundaries of the nonlinear region of a soft global mode. At a downstream boundary, the $k^{\text{nl}+}$ branch prevailing in the region $X < X_t$ is continuously connected to the k^{l+} branch for $X > X_t$. At an upstream boundary, transition from k^{l-} for $X < X_t$ to $k^{\text{nl}-}$ for $X > X_t$ occurs.

When $X \rightarrow X_t$ from within the nonlinear region, the amplitude of the nonlinear wave train decays, nonlinearities weaken, higher harmonics become slaved to the fundamental, and eventually a linear instability wave takes over. In the present section, we show how the connection between linear and nonlinear solutions is achieved across a narrow transition layer located at X_t .

Let us focus on an upstream transition layer ($\text{tl}-$), i.e., the solution is fully nonlinear for $X > X_t$ and decays exponentially for $X < X_t$. The same analysis applies in the downstream transition layer ($\text{tl}+$). The asymptotic behavior of the nonlinear wave trains $\Psi(\theta; k, X)$ is first derived as (k, X) approaches the neutral stability boundary of the nonlinear balloon (Section 5.5.1). This result is then used along the particular path $(k^{\text{nl}}(X), X)$ to derive expansions for the modulus (Section 5.5.2) and phase (Section 5.5.3) of the global mode as $X \downarrow X_t$. This outer expansion is shown in Section 5.5.4 to match with the inner solution prevailing in the transition layer. Finally, the inner solution is matched in Section 5.5.5 to the outer linear WKBJ approximation prevailing in the region $X < X_t$.

5.5.1. Weakly nonlinear behavior

In the nonlinear balloon of the (X, k) -plane characterized by $\Omega_i^1(k, X) > 0$, the governing equation (1) admits local solutions of the form (50). Let us first study the behavior of the periodic functions $\Psi(\theta; k, X)$ in the (k, X) -plane as (k, X) approaches the boundary of the nonlinear balloon, i.e., $\Omega_i^1(k, X) \downarrow 0$.

The nonlinear operator $\mathcal{F}[\psi]$ in (1) is expanded in powers of ψ so as to read

$$\frac{\partial \psi}{\partial t} = \mathcal{L}(\partial_x, X)[\psi] + \sum_{r=2}^{\infty} \mathcal{N}_r(\partial_x, X)[\psi], \quad (101)$$

where the operators \mathcal{N}_r are of r th order in ψ . In all generality, each \mathcal{N}_r depends on ∂_x , but to simplify the subsequent computations, it is assumed that the \mathcal{N}_r 's do not involve spatial derivation, i.e.,

$$\mathcal{N}_r(\partial_x, X)[\psi] = N_r(X)\psi^r. \quad (102)$$

The results would remain valid for any nonlinear operator with spatial derivatives, but the notation and results become unwieldy in more general cases. The method is easily extended to specific examples.

The 2π periodic function Ψ is expanded as the Fourier series

$$\Psi(\theta; k, X) = \sum_n \Psi^{(n)}(k, X) e^{in\theta}, \quad (103)$$

where $\Psi^{(-n)} = (\Psi^{(n)})^*$. Due to the invariance of the governing equation under the transformation $\theta \rightarrow \theta + C^{\text{st}}$, $\Psi^{(1)}(k, X)$ may be chosen to be real for each (k, X) .

Substituting (102) and (103) into (101) yields the equations for the harmonic components of Ψ ,

$$\Delta^{(n)}(k, X)\Psi^{(n)}(k, X) = i \sum_{r=2}^{\infty} N_r(X) \sum_{n_1+\dots+n_r=n} \Psi^{(n_1)}(k, X) \dots \Psi^{(n_r)}(k, X) \quad (104)$$

with the definition

$$\Delta^{(n)}(k, X) = n\Omega^{\text{nl}}(k, X) - \Omega^1(nk, X).$$

When $\Omega_i^1(k, X) \downarrow 0$, the term $\Delta^{(1)}(k, X)$ vanishes, whereas the $\Delta^{(n)}(k, X)$ remain finite for $|n| \neq 1$. Thus, in this limit, the components with $|n| \neq 1$ are slaved to the fundamental $n = \pm 1$ and scale as

$$\Psi^{(n)}(k, X) = \begin{cases} \mathcal{O}[(\Psi^{(1)}(k, X))^{|n|}] & \text{if } n \neq 0, \\ \mathcal{O}[(\Psi^{(1)}(k, X))^2] & \text{if } n = 0, \end{cases} \quad (105)$$

when $\Omega_i^1(k, X) \downarrow 0$. The dominant terms of (104) for $n = 2$ read

$$\Delta^{(2)}(k, X)\Psi^{(2)}(k, X) = iN_2(X)[\Psi^{(1)}(k, X)]^2 + \mathcal{O}[(\Psi^{(1)})^4], \quad (106)$$

and for $n = 0$,

$$\Delta^{(0)}(k, X)\Psi^{(0)}(k, X) = 2iN_2(X)\Psi^{(1)}(k, X)\Psi^{(-1)}(k, X) + \mathcal{O}[(\Psi^{(1)})^4]. \quad (107)$$

For $n = 1$, Eq. (104) yields

$$\begin{aligned} \Delta^{(1)}(k, X)\Psi^{(1)}(k, X) &= 2iN_2(X)[\Psi^{(2)}(k, X)\Psi^{(-1)}(k, X) + \Psi^{(1)}(k, X)\Psi^{(0)}(k, X)] \\ &\quad + 3iN_3(X)|\Psi^{(1)}(k, X)|^2\Psi^{(1)}(k, X) + \mathcal{O}[(\Psi^{(1)})^5]. \end{aligned} \quad (108)$$

Substituting (106) and (107) into (108) yields the leading-order expression for $\Psi^{(1)}$

$$|\Psi^{(1)}(k, X)|^2 \sim \frac{\Delta^{(1)}(k, X)}{3iN_3(X) - 2N_2(X)^2((1/\Delta^{(2)}(k, X)) + (2/\Delta^{(0)}(k, X)))}. \quad (109)$$

Thus,

$$|\Psi^{(1)}(k, X)|^2 = \mathcal{O}[\Delta^{(1)}(k, X)],$$

and

$$\Psi^{(1)}(k, X) = \mathcal{O}[\sqrt{\Omega_i^1(k, X)}]. \quad (110)$$

5.5.2. Asymptotic amplitude decay of outer nonlinear wave trains

The preceding results, valid for any (k, X) when $\Omega_i^1(k, X) \downarrow 0$ are now used to derive the asymptotic behavior of the nonlinear wave train (57) of specific frequency ω_g as $X \downarrow X_t$. Let us expand the nonlinear solution (57) into harmonic components as follows:

$$\Psi(\theta; k^{nl}(X), X) = \sum_n (\psi_0^{(n)}(X) + \epsilon\psi_1^{(n)}(X) + \dots) \exp \left\{ in \left(\frac{1}{\epsilon} \int^X k^{nl}(u) du - \omega_g t \right) \right\}. \quad (111)$$

Then, according to (103),

$$\psi_0^{(n)}(X) = \Psi^{(n)}(k^{nl}(X), X) e^{in\theta_0(X)}.$$

From (105) and (110) with $\Omega_i^1(k^{nl}(X), X) = \mathcal{O}(X - X_t)$, it follows that, for each $n \neq 0$,

$$\psi_0^{(n)}(X) = \mathcal{O}[(X - X_t)^{|n|/2}] \quad \text{as } X \downarrow X_t. \quad (112)$$

The asymptotic behavior of $\psi_0^{(1)}(X)$ for $X \downarrow X_t$ is derived from (109) as

$$\psi_0^{(1)}(X) \sim \Psi_0^{(1)} e^{i\theta_0(X)} (X - X_t)^{1/2} \quad (113)$$

with

$$|\hat{\Psi}_0^{(1)}|^2 = \frac{\Delta_{X,t}^{(1)}}{3iN_{3,t} - 2(N_{2,t})^2(1/\Delta_t^{(2)} + 2/\Delta_t^{(0)})}, \quad (114)$$

where subscript t means evaluation at $X = X_t$ and $k = k_t = k^{nl}(X_t)$, and

$$\Delta_{X,t}^{(1)} = \frac{d}{dX} \Delta^{(1)}(k^{nl}(X), X) \Big|_{X=X_t}.$$

In the same fashion one obtains for the second harmonic

$$\hat{\psi}_0^{(2)}(X) \sim \hat{\Psi}_0^{(2)} e^{i2\theta_0(X)}(X - X_t) \quad (115)$$

with, according to (106),

$$\hat{\Psi}_0^{(2)} = \frac{N_{2,t}}{\Delta_t^{(2)}} (\Psi_0^{(1)})^2. \quad (116)$$

In the bulk of the nonlinear region the harmonic spectrum is fully developed but towards the neutral stability boundary the higher-order harmonics become slaved to the fundamental. Since the higher-order harmonics decay faster than $\Psi^{(1)}$ as the neutral stability boundary is approached, the nonlinear solution is approximated by a purely sinusoidal wave of vanishing amplitude. Matching to a linear solution in the region $X < X_t$ therefore becomes possible.

5.5.3. Diverging slow phase of outer nonlinear wave trains

So far only the behavior of the amplitude as $X \downarrow X_t$ has been obtained. In this section the asymptotic behavior of the slow phase $\theta_0(X)$ near the neutral stability boundary of the nonlinear region is computed.

Let us write the phase solvability condition (56) as

$$0 = \frac{d\theta_0}{dX} \langle \Psi_\theta^\dagger, \mathcal{L}' \Psi_\theta \rangle + \frac{1}{2} \frac{dk^{nl}}{dX} \langle \Psi_\theta^\dagger, \mathcal{L}'' \Psi_\theta \rangle + \left\langle \Psi_\theta^\dagger, \mathcal{L}' \left(\frac{dk^{nl}}{dX} \Psi_k + \Psi_X \right) \right\rangle. \quad (117)$$

According to (103) the nonlinear solution Ψ admits the expansion

$$\Psi(\theta + \theta_0(X); k^{nl}(X), X) = \sum_n \Psi^{(n)}(k^{nl}(X), X) e^{in\theta_0(X)} e^{in\theta}.$$

Tedious but straightforward calculations [35] based on this Fourier expansion lead to the asymptotic behavior of the various inner products appearing in (117). One ultimately finds that

$$\begin{aligned} \langle \Psi_\theta^\dagger, \mathcal{L}' \Psi_\theta \rangle &= (X - X_t)[\mathcal{L}'(ik_t; X_t) + \text{c.c.}]|\hat{\Psi}_0^{(1)}|^2 + \mathcal{O}[(X - X_t)^2], \\ \langle \Psi_\theta^\dagger, \mathcal{L}'' \Psi_\theta \rangle &= (X - X_t)[\mathcal{L}''(ik_t; X_t) + \text{c.c.}]|\hat{\Psi}_0^{(1)}|^2 + \mathcal{O}[(X - X_t)^2], \\ \langle \Psi_\theta^\dagger, \mathcal{L}'(k_X^{nl}\Psi_k + \Psi_X) \rangle &= \frac{1}{2}[i\mathcal{L}'(ik_t; X_t) + \text{c.c.}]|\hat{\Psi}_0^{(1)}|^2 + \mathcal{O}[X - X_t]. \end{aligned}$$

Upon substituting these results into (117), the governing equation for the slow phase at the boundary of the nonlinear region becomes

$$\frac{d\theta_0}{dX} = -\frac{1}{2} \frac{1}{X - X_t} \frac{\text{Im } \mathcal{L}'(ik_t; X_t)}{\text{Re } \mathcal{L}'(ik_t; X_t)} + \mathcal{O}[(X - X_t)^0].$$

Hence, θ_0 diverges logarithmically as

$$\theta_0(X) = -\frac{1}{2} \frac{\text{Im } \mathcal{L}'(ik_t; X_t)}{\text{Re } \mathcal{L}'(ik_t; X_t)} \ln(X - X_t) + C^{\text{st}} + \mathcal{O}[X - X_t], \quad (118)$$

when $X \downarrow X_t$.

5.5.4. Inner transition layer solution

The asymptotic matching of a finite amplitude nonlinear wave train to an exponentially decaying linear solution takes place via a narrow inner transition layer at X_t between the nonlinear and linear regions.

Define an inner variable \tilde{X} in the neighborhood of X_t by $X = X_t + \epsilon^{1/2}\tilde{X}$. The outer solution obtained in the previous section is rewritten in terms of this inner variable. The fast phase θ reads

$$\theta \equiv \frac{1}{\epsilon} \int_{X_t}^{X_t + \epsilon^{1/2}\tilde{X}} k^{\text{nl}}(u) du - \omega_g t = (k_t x - \omega_g t) + \frac{1}{2} k_{X,t}^{\text{nl}} \tilde{X}^2 + \mathcal{O}(\epsilon^{1/2}), \quad (119)$$

whereas the slow phase θ_0 of Eq. (118) is expanded as

$$\theta_0 \sim -\frac{1}{2} \frac{\text{Im } \mathcal{L}'(ik_t; X_t)}{\text{Re } \mathcal{L}'(ik_t; X_t)} \ln \tilde{X} + C^{\text{st}}. \quad (120)$$

Thus, as $X \downarrow X_t$, keeping only the leading-order terms in the harmonics $|n| \leq 2$ of the outer solution given by (111) yields the following expansion:

$$\psi \sim \epsilon^{1/4} \tilde{X}^{1/2} [\hat{\Psi}_0^{(1)} e^{i(\theta+\theta_0)} + \text{c.c.}] + \epsilon^{1/2} \tilde{X} \left(\frac{iN_{2,t}}{\Delta_t^{(2)}} [(\hat{\Psi}_0^{(1)})^2 e^{2i(\theta+\theta_0)} + \text{c.c.}] + \frac{iN_{2,t}}{\Delta_t^{(0)}} 2|\hat{\Psi}_0^{(1)}|^2 \right) + \mathcal{O}(\epsilon^{3/4}). \quad (121)$$

This behavior of the outer solution in terms of the inner variable \tilde{X} suggests to expand the harmonic components of the inner solution as

$$\psi \sim \sum_n \epsilon^{n/4} (\tilde{\psi}_0^{(n)}(x, \tilde{X}) + \epsilon^{1/2} \tilde{\psi}_{1/2}^{(n)}(x, \tilde{X}) + \dots) e^{-in\omega_g t} \quad (122)$$

with $\tilde{\psi}_0^{(0)} = 0$ since $\psi^{(0)} = \mathcal{O}(|\psi^{(1)}|^2)$. Each component of the inner expansion has to be matched for $\tilde{X} \rightarrow +\infty$ with the corresponding component of the outer expansion in the nonlinear region. Due to the presence of slow and fast spatial scales \tilde{X} and x , the spatial derivative in the governing equation (1) now reads $\partial_x + \epsilon^{1/2} \partial_{\tilde{X}}$.

For $n = 1$, the leading-order problem reads

$$\omega_g \tilde{\psi}_0^{(1)} = i\mathcal{L}(\partial_x; X_t)[\tilde{\psi}_0^{(1)}].$$

Hence

$$\tilde{\psi}_0^{(1)} = \tilde{A}_0^{(1)}(\tilde{X}) e^{ik_t x}, \quad (123)$$

where $\tilde{A}_0^{(1)}(\tilde{X})$ is a slowly varying amplitude. For $n = 2$, the leading-order problem reads

$$2\omega_g \tilde{\psi}_0^{(2)} - i\mathcal{L}(\partial_x; X_t)[\tilde{\psi}_0^{(2)}] = iN_{2,t} \tilde{\psi}_0^{(1)} \tilde{\psi}_0^{(1)}, \quad (124)$$

which yields the solution

$$\tilde{\psi}_0^{(2)} = \frac{iN_{2,t}}{\Delta_t^{(2)}} [\tilde{A}_0^{(1)}(\tilde{X})]^2 e^{2ik_t x}. \quad (125)$$

For $n = 0$, the order $\epsilon^{1/2}$ problem

$$0 = \mathcal{L}(\partial_x; X_t)[\tilde{\psi}_{1/2}^{(0)}] + 2N_{2,t} |\tilde{\psi}_0^{(1)}|^2$$

yields

$$\tilde{\psi}_{1/2}^{(0)} = \frac{2iN_{2,t}}{\Delta_t^{(0)}} |\tilde{A}_0^{(1)}(\tilde{X})|^2. \quad (126)$$

For $n = 1$, the order $\epsilon^{1/2}$ terms read

$$0 = i\omega_g \tilde{\psi}_{1/2}^{(1)} + \mathcal{L}(\partial_x; X_t)[\tilde{\psi}_{1/2}^{(1)}] + [\mathcal{L}'(\partial_x; X_t)\partial_{\tilde{X}} + \tilde{X}\mathcal{L}_X(\partial_x; X_t)]\tilde{\psi}_0^{(1)} \\ + 3N_{3,t}|\tilde{\psi}_0^{(1)}|^2\tilde{\psi}_0^{(1)} + 2N_{2,t}[\tilde{\psi}_0^{(2)}\tilde{\psi}_0^{(-1)} + \tilde{\psi}_{1/2}^{(0)}\tilde{\psi}_0^{(1)}]. \quad (127)$$

This inhomogeneous differential equation in x admits solutions for $\tilde{\psi}_{1/2}^{(1)}$ only if the resonant part in e^{ik_tx} of the forcing terms vanishes. Upon using (123), (125) and (126) in (127), this leads to the solvability condition

$$0 = \mathcal{L}'(ik_t; X_t)\frac{d\tilde{A}_0^{(1)}}{d\tilde{X}} + \mathcal{L}_X(ik_t; X_t)\tilde{X}\tilde{A}_0^{(1)}(\tilde{X}) + \left(3N_{3,t} + 2i(N_{2,t})^2\left(\frac{1}{\Delta_t^{(2)}} + \frac{2}{\Delta_t^{(0)}}\right)\right)|\tilde{A}_0^{(1)}(\tilde{X})|^2\tilde{A}_0^{(1)}(\tilde{X}). \quad (128)$$

This amplitude equation for $\tilde{A}_0^{(1)}(\tilde{X})$ is of the form

$$\frac{d\tilde{A}_0^{(1)}}{d\tilde{X}} + ((a_r + ia_i)\tilde{X} + (b_r + ib_i)|\tilde{A}_0^{(1)}(\tilde{X})|^2)\tilde{A}_0^{(1)}(\tilde{X}) = 0, \quad (129)$$

and its solutions are

$$\frac{\tilde{A}_0^{(1)}(\tilde{X})}{\tilde{A}_0^{(1)}(0)} = \frac{\exp[-\frac{1}{2}(a_r + ia_i)\tilde{X}^2 - \frac{1}{2}i(b_r/b_r)\ln(1 + 2b_r|\tilde{A}_0^{(1)}(0)|^2\int_0^{\tilde{X}}e^{-a_ru^2}du)]}{\sqrt{1 + 2b_r|\tilde{A}_0^{(1)}(0)|^2\int_0^{\tilde{X}}e^{-a_ru^2}du}}, \quad (130)$$

where $\tilde{A}_0^{(1)}(0)$ is the integration constant. Matching of the inner solution $\tilde{\psi}_0^{(1)}$ to the outer nonlinear solution $\psi_0^{(1)}$ of (113) requires that $|\tilde{A}_0^{(1)}(\tilde{X})| \sim \sqrt{\tilde{X}}$ as $\tilde{X} \rightarrow +\infty$. This implies that

$$1 + 2b_r|\tilde{A}_0^{(1)}(0)|^2\int_0^{+\infty}e^{-a_ru^2}du = 0, \quad |\tilde{A}_0^{(1)}(0)|^2 = \frac{-1}{b_r}\sqrt{\frac{a_r}{\pi}}.$$

With this value for $|\tilde{A}_0^{(1)}(0)|$ the inner solution (130) admits for $\tilde{X} \rightarrow +\infty$ the asymptotic expansion

$$\tilde{A}_0^{(1)}(\tilde{X}) \sim \sqrt{-\frac{a_r}{b_r}\tilde{X}} \exp\frac{i}{2}\left[\left(\frac{b_i}{b_r}a_r - a_i\right)\tilde{X}^2 + \frac{b_i}{b_r}\ln\tilde{X} + C^{\text{st}}\right]. \quad (131)$$

Comparison of (128) and (129) yields

$$a_r + ia_i = \frac{\mathcal{L}_X(ik_t; X_t)}{\mathcal{L}'(ik_t; X_t)} = -ik_{X,t}^1, \quad b_r + ib_i = |\hat{\psi}_0^{(1)}|^{-2}\frac{\Delta_{X,t}^{(1)}}{i\mathcal{L}'(ik_t; X_t)} = -|\hat{\psi}_0^{(1)}|^{-2}\left(ik_{X,t}^{\text{nl}} + \frac{\mathcal{L}_X(ik_t; X_t)}{\mathcal{L}'(ik_t; X_t)}\right)$$

with $|\hat{\psi}_0^{(1)}|^2$ obtained in (114). Thus,

$$-\frac{a_r}{b_r} = |\hat{\psi}_0^{(1)}|^2, \quad \frac{b_i}{b_r}a_r - a_i = k_{X,t}^{\text{nl}}, \quad -\frac{b_i}{b_r} = \frac{\text{Im } \mathcal{L}'(ik_t, X_t)}{\text{Re } \mathcal{L}'(ik_t, X_t)}.$$

This completes the proof that the fundamental component of the outer nonlinear solution given by Eq. (121) completely matches the fundamental component of the inner weakly nonlinear solution $\epsilon^{1/4}\tilde{A}_0^{(1)}(\tilde{X})e^{i(k_tx - \omega_g t)}$, where $\tilde{A}_0^{(1)}(\tilde{X})$ is given by (130).

5.5.5. Matching to the outer linear solution

As $X \uparrow X_t$, the outer linear WKBJ approximation (39) reads, at leading order,

$$\psi \sim A_0^1(X_t) e^{i(k_t x - \omega_g t)} \exp\left(\frac{i}{2} k_{X,t}^1 \tilde{X}^2\right) + \text{c.c.}, \quad (132)$$

when expressed in terms of the inner variable \tilde{X} . Using (130), the asymptotic behavior of the inner solution as $\tilde{X} \rightarrow -\infty$ yields

$$\psi \sim \epsilon^{1/4} \frac{\tilde{A}_0^{(1)}(0)}{\sqrt{2}} e^{i(k_t x - \omega_g t)} \exp\left(-\frac{a_r + ia_i}{2} \tilde{X}^2 - \frac{i}{2} \frac{b_i}{b_r} \ln 2\right) + \text{c.c.} \quad (133)$$

Since $a_r + ia_i = -ik_{X,t}^1$, both expansions (132) and (133) asymptotically match provided that

$$A_0^1(X_t) = \epsilon^{1/4} \frac{\tilde{A}_0^{(1)}(0)}{\sqrt{2}} e^{-ib_i(\ln 2)/2b_r}.$$

Thus, at leading order, the weakly nonlinear inner expansion (133) exactly matches the outer linear WKBJ approximation (39). In the inner transition layer the slaved higher-order harmonics scale as $\epsilon^{|n|/4}$ and automatically match their slaved counterparts in the outer linear region.

6. Conclusions

It has been demonstrated that a wide class of one-dimensional nonlinear evolution equations with spatially varying coefficients may support two types of fully nonlinear self-sustained global modes in a doubly infinite domain. Steep global modes are triggered by the presence of a sharp stationary front located at the upstream transition point between local convective and absolute instability. This front acts as a source and imposes its real absolute frequency to the entire medium. Soft global modes are due to the presence of a saddle point of the local nonlinear dispersion relation which again acts as a source and imposes its frequency to the entire medium, as given by saddle point conditions.

A necessary condition for the occurrence of either of these modes is the existence of a region of local absolute instability. Recall that linearly unstable global modes given by a complex saddle point of the local linear dispersion relation [7,25,30] also require a range of local absolute instability. But, this range must in general be of finite extent whereas nonlinear global modes exist, however small the AU domain. The relationship between linear global instability and the existence of fully nonlinear global modes is non-trivial: in the generic case, nonlinear global instability does not coincide with linear global instability. The nature of the various global bifurcation scenarios constitute the major result of the present investigation. Steep global modes occur right at local absolute instability onset below the linear global instability threshold, via a saddle-node bifurcation, while the medium is still linearly globally stable.

Soft global modes generically do not appear at local absolute instability onset but only for a sufficiently large domain of local absolute instability. Furthermore, they are more likely to be observed in systems with weak advection. It is essential to note that steep and soft global modes are mutually exclusive, as dictated by the relative magnitude of their respective frequencies. The existence and selection of either kind of global modes has been confirmed by direct numerical simulations of the CGL equation with varying coefficients for small but finite values of ϵ . As a word of caution, it should be stated that soft global modes are likely to be more fragile than their steep counterparts. They may become unstable whenever the region of local absolute instability protrudes beyond the central nonlinear regions, in the tails of the extended wave packet. This lack of robustness is all the more acute as the WKBJ limit $\epsilon = 0$ is approached.

In several physical systems [1,37] linear and nonlinear global instabilities have been found to occur at the same value of the global control parameter. This peculiar feature takes place in situations where the entire spatial dependence is accounted for in a single real spatially varying parameter, say $R(X)$, which displays an extremum at a real position X^{\max} such that $dR(X^{\max})/dX = 0$. Under these circumstances, the local linear dispersion relation is necessarily of the form $\Omega^1(k, X) = \Omega_*^1[k, R(X)]$ and the local absolute frequency is readily obtained as $\omega_0(X) = \omega_{0*}[R(X)]$. The real station X^{\max} is then simultaneously associated with a maximum of $\omega_{0,i}(X)$ and with a saddle point X_s^1 of $\omega_0(X)$.

The analytical structure underlying the spatial distribution of steep and soft global modes has been systematically derived in the WKBJ approximation $\epsilon \ll 1$. It has been shown that for a wide class of one-dimensional evolution equations the various inner layers and outer regions may be matched together to arrive at a consistent description valid over the entire spatial domain. In particular, higher-order frequency corrections have been obtained.

It should be emphasized that the different transition scenarios depend on the precise form of the linear and nonlinear dispersion relations. Due to the number of parameters required to specify the spatial variations of the medium, only situations of physical significance have been presented and a comprehensive survey of all possible configurations has not been attempted.

This study has been undertaken in order to understand the nature of synchronized structures in real slowly varying open shear flows. In the latter framework, the local linear dispersion relation is obtained from the Rayleigh or the Orr–Sommerfeld equation, whereas the local nonlinear dispersion relation requires the computation of finite amplitude structures in a streamwise periodic interval. In this context, steep global modes may be constructed as reported elsewhere [35,36].

Acknowledgements

The authors have benefited from many enlightening and fruitful discussions with Arnaud Couairon.

References

- [1] A.P. Bassom, K.M. Kuzanyan, A.M. Soward, A nonlinear dynamo wave riding on a spatially varying background, Proc. R. Soc. London A 455 (1999) 1443–1481.
- [2] C.M. Bender, S.A. Orszag, Advanced Mathematical Methods for Scientists and Engineers, McGraw-Hill, New York, 1978.
- [3] A. Bers, Space–time evolution of plasma instabilities — absolute and convective, in: M.N. Rosenbluth, R.Z. Sagdeev (Eds.), Handbook of Plasma Physics, North–Holland, Amsterdam, 1983, pp. 451–517.
- [4] R.J. Briggs, Electron-stream Interaction with Plasmas, MIT Press, Cambridge, MA, 1964.
- [5] P. Büchel, M. Lücke, D. Roth, R. Schmitz, Pattern selection in the absolutely unstable regime as a nonlinear eigenvalue problem: Taylor vortices in axial flow, Phys. Rev. E 53 (1996) 4764–4777.
- [6] J.-M. Chomaz, P. Huerre, L.G. Redekopp, The effect of nonlinearity and forcing on global modes, in: P. Coullet, P. Huerre (Eds.), New Trends in Nonlinear Dynamics and Pattern Forming Phenomena, Plenum Press, New York, 1990, pp. 259–274.
- [7] J.-M. Chomaz, P. Huerre, L.G. Redekopp, A frequency selection criterion in spatially developing flows, Stud. Appl. Math. 84 (1991) 119–144.
- [8] J.-M. Chomaz, Absolute and convective instabilities in nonlinear systems, Phys. Rev. Lett. 69 (1992) 1931–1934.
- [9] J.-M. Chomaz, A. Couairon, Against the wind, Phys. Fluids 11 (1999) 2977–2983.
- [10] A. Couairon, J.-M. Chomaz, Global instability in fully nonlinear systems, Phys. Rev. Lett. 77 (1996) 4015–4018.
- [11] A. Couairon, Modes globaux fortement nonlinéaires dans les écoulements ouverts, Ph.D. Thesis, École Polytechnique, 1997.
- [12] A. Couairon, J.-M. Chomaz, Absolute and convective instabilities, front velocities and global modes in nonlinear systems, Physica D 108 (1997) 236–276.
- [13] A. Couairon, J.-M. Chomaz, Pattern selection in the presence of cross flow, Phys. Rev. Lett. 79 (1997) 2666–2669.
- [14] A. Couairon, J.-M. Chomaz, Fully nonlinear global modes in slowly varying flows, Phys. Fluids 11 (1999) 3688–3703.
- [15] M.C. Cross, P.C. Hohenberg, Pattern formation outside of equilibrium, Rev. Mod. Phys. 65 (1993) 851–1112.
- [16] G.T. Dee, J.S. Langer, Propagating pattern selection, Phys. Rev. Lett. 50 (1983) 383–386.

- [17] T.M. DelSole, B.F. Farrell, Nonlinear equilibrium of localized instabilities on a baroclinic jet, *J. Atmos. Sci.* 51 (1994) 2270–2284.
- [18] K. Hannemann, H. Oertel Jr., Numerical simulation of the absolutely and convectively unstable wake, *J. Fluid Mech.* 199 (1989) 55–88.
- [19] D.A. Hammond, L.G. Redekopp, Global dynamics of symmetric and asymmetric wakes, *J. Fluid Mech.* 331 (1997) 231–260.
- [20] P. Huerre, P.A. Monkewitz, Local and global instabilities in spatially developing flows, *Ann. Rev. Fluid Mech.* 22 (1990) 473–537.
- [21] P. Huerre, M. Rossi, Hydrodynamic instabilities in open flows, in: C. Godrèche, P. Manneville (Eds.), *Hydrodynamics and Nonlinear Instabilities*, Cambridge University Press, Cambridge, 1998, pp. 81–294.
- [22] P. Huerre, Open shear flow instabilities, in: G.K. Batchelor, H.K. Moffatt, M.G. Worster (Eds.), *Developments in Fluid Mechanics: A Collection for the Millennium*, Cambridge University Press, Cambridge, 2000.
- [23] R.E. Hunt, D.G. Crighton, Instability of flows in spatially developing media, *Proc. R. Soc. London A* 435 (1991) 109–128.
- [24] S. Le Dizès, P. Huerre, J.-M. Chomaz, P.A. Monkewitz, Nonlinear stability analysis of slowly diverging flows: limitations of the weakly nonlinear approach, in: H. Eckelmann, J.M.R. Graham, P. Huerre, P.A. Monkewitz (Eds.), *Proceedings of the IUTAM Symposium on Bluff Body Wakes, Dynamics and Instabilities*, Springer, Berlin, 1993, pp. 147–152.
- [25] S. Le Dizès, P. Huerre, J.-M. Chomaz, P.A. Monkewitz, Linear global modes in spatially developing media, *Phil. Trans. R. Soc. London A* 354 (1996) 169–212.
- [26] P. Manneville, *Structures Dissipatives, Chaos et Turbulence*, Aléa, Saclay, 1991.
- [27] C. Mathis, M. Provansal, L. Boyer, The Bénard–von Karman instability: an experimental study near the threshold, *J. Phys. Paris Lett.* 45 (1984) L83–L491.
- [28] N. Meunier, M.R.E. Proctor, D.D. Sokoloff, A.M. Soward, S.M. Tobias, Asymptotic properties of a nonlinear $\alpha\omega$ -dynamo wave: period, amplitude and latitude dependence, *Geophys. Astrophys. Fluid Dyn.* 86 (1997) 249–285.
- [29] P.A. Monkewitz, D.W. Bechert, B. Barsikowr, B. Lehmann, Self-excited oscillations and mixing in heated round jets, *J. Fluid Mech.* 213 (1990) 611–639.
- [30] P.A. Monkewitz, P. Huerre, J.M. Chomaz, Global linear stability analysis of weakly non-parallel shear flows, *J. Fluid Mech.* 251 (1993) 1–20.
- [31] H.W. Müller, M. Lücke, M. Kamps, Transversal convection patterns in horizontal shear flow, *Phys. Rev. A* 45 (1992) 3714–3726.
- [32] A.C. Newell, T. Passot, J. Lega, Order parameter equations for patterns, *Ann. Rev. Fluid Mech.* 25 (1993) 399–453.
- [33] B. Pier, P. Huerre, Fully nonlinear global modes in spatially developing media, *Physica D* 97 (1996) 206–222.
- [34] B. Pier, P. Huerre, J.-M. Chomaz, A. Couairon, Steep nonlinear global modes in spatially developing media, *Phys. Fluids* 10 (1998) 2433–2435.
- [35] B. Pier, Comportement non linéaire synchronisé dans les écoulements cisaillés, Ph.D. Thesis, École Polytechnique, 91128 Palaiseau, France, 1999.
- [36] B. Pier, P. Huerre, Nonlinear self-sustained structures and fronts in spatially developing wake flows, *J. Fluid Mech.*, submitted for publication.
- [37] R.T. Pierrehumbert, Local and global baroclinic instability of zonally varying flow, *J. Atmos. Sci.* 41 (1984) 2141–2162.
- [38] M. Provansal, C. Mathis, L. Boyer, Bénard–von Kármán instability: transient and forced regimes, *J. Fluid Mech.* 182 (1987) 1–22.
- [39] W. van Saarloos, Dynamical velocity selection: marginal stability, *Phys. Rev. Lett.* 58 (1987) 2571–2574.
- [40] W. van Saarloos, Front propagation into unstable states: marginal stability as a dynamical mechanism for velocity selection, *Phys. Rev. A* 37 (1988) 211–229.
- [41] W. van Saarloos, Front propagation into unstable states. II. Linear versus nonlinear marginal stability and rate of convergence, *Phys. Rev. A* 39 (1989) 6367–6390.
- [42] W. van Saarloos, P.C. Hohenberg, Fronts, pulses, sources and sinks in generalized complex Ginzburg–Landau equations, *Physica D* 56 (1992) 303–367.
- [43] A.M. Soward, C.A. Jones, The linear stability of the flow in the narrow gap between two concentric rotating spheres, *Q. J. Mech. Appl. Math.* 36 (1983) 19–42.
- [44] K.R. Sreenivasan, S. Raghu, D. Kyle, Absolute instability in variable density round jets, *Exp. Fluids* 7 (1989) 309–317.
- [45] K.R. Sreenivasan, P.J. Strykowski, D.J. Olinger, On the Hopf bifurcation and the Landau–Stuart constants associated with vortex “shedding” behind circular cylinders, unpublished, 1990.
- [46] P.J. Strykowski, D.L. Niccum, The stability of countercurrent mixing layers in circular jets, *J. Fluid Mech.* 227 (1991) 309–343.
- [47] S. Tobias, M.R.E. Proctor, E. Knobloch, Convective and absolute instabilities of fluid flows in finite geometry, *Physica D* 113 (1998) 43–72.
- [48] W. Wasow, *Linear Turning Point Theory*, Springer, New York, 1985.
- [49] B.M. Woodley, N. Peake, Global linear stability analysis of thin aerofoil wakes, *J. Fluid. Mech.* 339 (1997) 239–260.

[A5]

Nonlinear self-sustained structures and fronts in spatially developing wake flows

B. Pier & P. Huerre

Journal of Fluid Mechanics **435**, 145–174 (2001)

doi :10.1017/S0022112001003652

<https://hal.archives-ouvertes.fr/hal-00119721>

Nonlinear self-sustained structures and fronts in spatially developing wake flows

By BENOÎT PIER[†] AND PATRICK HUERRE

Laboratoire d'Hydrodynamique (LadHyX), CNRS – École polytechnique,
F-91128 Palaiseau cedex, France

(Received 29 February 2000 and in revised form 25 September 2000)

A family of slowly spatially developing wakes with variable pressure gradient is numerically demonstrated to sustain a synchronized finite-amplitude vortex street tuned at a well-defined frequency. This oscillating state is shown to be described by a steep global mode exhibiting a sharp Dee–Langer-type front at the streamwise station of marginal absolute instability. The front acts as a wavemaker which sends out nonlinear travelling waves in the downstream direction, the global frequency being imposed by the real absolute frequency prevailing at the front station. The nonlinear travelling waves are determined to be governed by the local nonlinear dispersion relation resulting from a temporal evolution problem on a local wake profile considered as parallel. Although the vortex street is fully nonlinear, its frequency is dictated by a purely linear marginal absolute instability criterion applied to the local linear dispersion relation.

1. Introduction

The qualitative behaviour of spatially developing free shear flows such as wakes, jets and mixing layers may be reasonably well understood within the framework of *linear* instability theory. In this context, one may distinguish between *amplifiers*, the dynamics of which are sensitive to inflow perturbations, and *oscillators*, which sustain intrinsic global modes tuned at a well-defined frequency. Co-flow mixing layers, constant-density jets, and wakes below the onset of Kármán vortex shedding belong to the former class, while mixing layers with a sufficiently strong countercurrent (Strykowski & Niccum 1991), wakes in the Kármán vortex shedding régime (Provansal, Mathis & Boyer 1987; Triantafyllou, Triantafyllou & Chryssostomidis 1986), and inhomogenous jets (Monkewitz *et al.* 1990) belong to the latter class. The amplifier or oscillator behaviour is intimately related to the convective or absolute nature of the linear instability (Huerre & Rossi 1998). Note however that absolute instability may also induce a rapid transition to turbulence as strikingly demonstrated by Lingwood (1995, 1996) for rotating disk boundary layers.

One of the central problems regarding the dynamics of flow oscillators is concerned with the prediction of the overall frequency and associated spatial structure, hereafter referred to as the *global mode*. For real flows, governed by the Navier–Stokes equations, this question has until now been studied solely in the framework of linear theory (Monkewitz, Huerre & Chomaz 1993). The objective of the present analysis is to address the same issue in the *fully nonlinear* régime.

[†] Present address: Department of Applied Mathematics and Theoretical Physics, University of Cambridge, Silver Street, Cambridge CB3 9EW, UK.

Koch (1985) appears to be the first to have related the onset of global oscillations in wakes to the existence of an absolutely unstable region immediately downstream of the obstacle. Further progress in our understanding of frequency selection mechanisms has typically proceeded in two distinct steps. The theoretical formulation is first established for relatively simple one-dimensional evolution models such as the celebrated complex Ginzburg–Landau (CGL) equation (Cross & Hohenberg 1993). It is then adapted and generalized to real flows governed by the Navier–Stokes equations. This line of thought has been fully implemented in the linear approximation. Linear global modes pertaining to the CGL equation with varying coefficients on an infinite interval have been analysed by Chomaz, Huerre & Redekopp (1991), and Le Dizès *et al.* (1996). The formulation essentially relies on the assumption of slow spatial variations characterized by the slow space variable $X = \epsilon x$, where $\epsilon \ll 1$ is a small non-uniformity parameter. A complex local absolute frequency $\omega_0(X)$ may then be defined in classical fashion (Briggs 1964, Bers 1983, Huerre & Monkewitz 1990) by imposing a zero group velocity condition on the local linear dispersion relation. Under these conditions, the complex global frequency ω_s of self-sustained linear structures is given by the saddle point criterion

$$\omega_s = \omega_0(X_s) \quad \text{with} \quad \frac{d\omega_0}{dX}(X_s) = 0, \quad (1.1)$$

where it is understood that $\omega_0(X)$ has been analytically continued in the complex X -plane. Whenever $\omega_{s,i} \equiv \text{Im } \omega_s > 0$, the medium is globally unstable. Global instability then requires a finite region of local absolute instability where $\omega_{0,i}(X) > 0$ for real X , as demonstrated by Chomaz *et al.* (1991) and Le Dizès *et al.* (1996). The same criterion (1.1) was previously derived by Soward & Jones (1983) for oscillating states in Taylor–Couette flow between concentric spheres. As shown by Monkewitz *et al.* (1993) it also holds for the two-dimensional Navier–Stokes equations linearized about an arbitrary slowly streamwise developing shear flow. It should be emphasized that other frequency selection criteria have been proposed. In spatially developing flows of semi-infinite streamwise extent, say $x > 0$, the global frequency is given by the absolute frequency $\omega_0(0)$ at the upstream boundary (Monkewitz *et al.* 1993; Woodley & Peake 1997; Taylor & Peake 1999). The initial resonance principle conjectured by Monkewitz & Nguyen (1987) is of particular interest in the present context: according to these authors, in spatially developing flows with an absolutely unstable region, the first streamwise station of non-negative absolute growth rate imposes its absolute frequency on the global oscillations.

The theoretical prediction (1.1) has been tested in direct numerical simulations. Schär & Smith (1993) have numerically investigated the flow behind a vertical cylinder in the shallow-water wave régime. At a critical value of the Froude number, the wake is observed to undergo a transition to large-scale Kármán vortex shedding. When all nonlinear terms in the numerical code are turned off, the wake beats at a global frequency $\omega_g \sim 0.17 + 0.045i$. Application of criterion (1.1) leads to the prediction $\omega_g \sim 0.19 + 0.040i$, which compares very favourably with the computed value. However, when all nonlinearities are restored, the observed global frequency becomes $\omega_g \sim 0.27$, which is noticeably different from the predicted linear value. Such a comparison clearly calls for a fully nonlinear formulation of the global mode problem. A similar comparative study has recently been undertaken by Hammond & Redekopp (1997) in the case of the wake behind a blunt-edged plate. At a Reynolds number 25% above global onset, the numerically determined non-dimensional global frequency is found to be $\omega_g/2\pi \sim 0.1000$, whereas the saddle-point criterion (1.1)

yields $\omega_{s,r}/2\pi \equiv Re \omega_s/2\pi \sim 0.1006$. In view of the linear nature of the criterion, such a close agreement is somewhat surprising. It is worth noting, however, that the complex absolute frequency $\omega_0(X)$ has been computed on the mean velocity profile in the presence of finite-amplitude oscillations and not on the undisturbed basic flow, as in the case of Schär & Smith (1993). Nonlinear effects are thereby partially accounted for through the Reynolds stresses which produce the mean flow.

The next step in the theoretical analysis of spatially developing flows would naturally involve a weakly nonlinear formulation in the vicinity of global mode onset. As emphasized by Le Dizès *et al.* (1993), this approach is fraught with difficulties. For slowly spatially developing flows the Landau constant governing the nature of the bifurcation has neither a well-defined limit nor a constant sign as ϵ goes to zero. As a result, the bifurcation keeps switching between subcritical and supercritical. In order to circumvent these technical difficulties, it seems appropriate to directly proceed to a fully nonlinear approach.

Most nonlinear studies have so far been restricted to amplitude evolution equations in one space dimension. Linear absolute/convective instability concepts have been generalized to finite-amplitude disturbances by Chomaz (1992): the propagation direction of fronts separating the basic state from the bifurcated state, as originally defined by Dee & Langer (1983), Saarloos (1988, 1989) and Saarloos & Hohenberg (1992), is found to essentially determine the absolute/convective nature of the instability in the nonlinear régime. Fully nonlinear global modes on a semi-infinite domain ($x > 0$) governed by Ginzburg–Landau-type model equations with constant coefficients have been thoroughly analysed by Couairon & Chomaz (1996, 1997a,b). Whenever the medium is nonlinearly absolutely unstable, an upstream travelling front is pinned at the upstream boundary point and a nonlinear global mode is sustained. The corresponding analysis of the finite interval problem has been addressed by Tobias, Proctor & Knobloch (1998) and Chomaz & Couairon (1999). Couairon & Chomaz (1999) have further investigated the existence of nonlinear global modes of the real Ginzburg–Landau equation with varying coefficients on the semi-infinite domain $x > 0$. In this case, spatial inhomogeneities due to both a boundary point and varying bulk properties are combined. Although this model constitutes only a crude approximation of real flows, predicted scaling laws for the global mode amplitude and the position of its maximum agree surprisingly well with experimental and numerical results pertaining to the wake structure behind bluff bodies.

Fully nonlinear global modes on an infinite interval, have also been investigated for the CGL equation with varying coefficients in order to mimic the streamwise non-uniformity of spatially developing shear flows. Two distinct varieties of nonlinear objects are then possible. *Soft global modes* obtained by Pier & Huerre (1996) satisfy a saddle-point frequency selection criterion applied to the local nonlinear dispersion relation governing finite-amplitude states. The corresponding extended spatial structure displays smoothly varying amplitude and wavenumber everywhere. By contrast, *steep global modes*, as described by Pier *et al.* (1998), obey a marginal stability criterion: the steep global frequency coincides with the real absolute frequency at the transition station between linear convective and absolute instability. More specifically, the steep global mode is triggered at the upstream boundary X^{ca} of the absolutely unstable domain and is tuned at the associated real absolute frequency

$$\omega_0^{ca} = \omega_0(X^{ca}) \quad \text{where} \quad \omega_{0,i}(X^{ca}) = 0. \quad (1.2)$$

This condition is merely the linear frequency criterion put forward by Dee & Langer (1983), according to which the front velocity is such that, in the co-moving frame, the

medium is marginally absolutely unstable. The associated spatial structure consists of a stationary sharp front located at the transition station and separating an upstream decaying tail from a finite-amplitude downstream wavetrain. The front acts as a wave maker and imposes its frequency on the entire flow. In contrast with soft global modes, the wavenumber exhibits a sharp jump across the front. Similar nonlinear states with sharp Dee–Langer-type fronts were previously identified in amplitude evolution models of solar and stellar magnetic activity cycles by Meunier *et al.* (1997). The reader is referred to Soward (2001) for a review of related WKBJ asymptotic studies in the astrophysical context.

The transition scenarii towards fully nonlinear global modes have been analysed by Pier (1999) and Pier, Huerre & Chomaz (2001) for the CGL evolution model in an infinite domain. The results of interest to the present investigation are as follows. The onset of steep global modes takes place via a saddle node bifurcation as soon as a point of local linear absolute instability appears within the medium. Since linear global modes in general become unstable only for a finite region of local linear absolute instability, the transition to a steep mode occurs while the medium is still globally linearly stable. Paradoxically, the onset of local linear absolute instability is seen to provide an accurate criterion for the bifurcation to fully nonlinear steep global modes while it is only a necessary condition for linear global instability. Local linear absolute instability in a sense prevails over global linear instability and dictates the nature of the observed finite-amplitude state.

The objective of the present study is to demonstrate that nonlinear self-sustained structures in real shear flows may be described in terms of steep global modes triggered by a stationary front located at the streamwise station of marginal absolute instability. Strong supporting evidence for this line of thought has recently been given by Delbende & Chomaz (1998) in a direct numerical simulation of the nonlinear impulse response in a parallel wake. The nonlinear wavepacket is observed to be confined between the same leading and trailing edges as its linear counterpart. The sharp fronts delineating the saturated wavepacket then travel according to the linear Dee & Langer (1983) velocity selection criterion.

In order to strictly enforce the weak streamwise non-uniformity condition underlying all the above notions, the basic flow must be carefully chosen. Bluff body wakes present a recirculation bubble near the obstacle which violates this assumption. To bypass this difficulty, we consider a ‘synthetic’ wake with no solid obstacle(!) and no reverse flow region, which still displays the essential features of wake flows, namely a region of local absolute instability. The basic *ansatz* is the same as in the numerical simulations of wakes ‘without obstacles’ performed by Triantafyllou & Karniadakis (1990): vortex streets are produced by a wavemaker within the wake flow itself and the obstacle is only necessary in real laboratory experiments to generate the basic flow!

The outline of the study is as follows. The general formulation is presented in §2 together with the spatially developing basic wake flow derived as a solution of the Prandtl boundary layer equations. The ensuing local properties of linear instability waves are described in §3 in terms of a local linear dispersion relation at each downstream station. Corresponding local properties of fully nonlinear travelling waves are presented in §4 as solutions of a local nonlinear dispersion relation. These linear and nonlinear waves constitute the elementary building blocks of the globally synchronized structures in the upstream and downstream regions of the wake. Attention is then given in §5 to the missing link, namely the front structure supported by the wake profile at the marginally absolutely unstable station. Following the

procedure proposed by Pier (1999) and Pier *et al.* (2001), the front is obtained as the limit state of the spatial response to time-harmonic forcing in a parallel wake, when the convective/absolute transition is reached. The self-sustained structures supported by the spatially developing basic flow are documented in §6, as computed by direct numerical simulation of the Navier–Stokes equations. Finally, §7 is concerned with the interpretation of these results in terms of the constitutive elements identified in the previous sections.

2. General formulation and basic flow

Two-dimensional incompressible flows are conveniently studied in terms of the streamfunction $\Psi(x, y, t)$ governed by the vorticity equation

$$\left(\frac{\partial}{\partial t} + \frac{\partial \Psi}{\partial y} \frac{\partial}{\partial x} - \frac{\partial \Psi}{\partial x} \frac{\partial}{\partial y} \right) \Delta \Psi = \frac{1}{Re} \Delta^2 \Psi. \quad (2.1)$$

From the start non-dimensional variables based on the characteristic length and velocity scales ℓ^* and U^* have been introduced (see below (2.5)). The Reynolds number is then defined as $Re = \ell^* U^*/v$, where v is the kinematic viscosity. If x and y denote the streamwise and cross-stream coordinates, the corresponding x and y velocity components are obtained as $\partial \Psi / \partial y$ and $-\partial \Psi / \partial x$, and the vorticity as $-\Delta \Psi$.

The basic flow is steady and assumed to slowly develop in the streamwise direction. This is the case at large Reynolds numbers, where viscous spreading takes place on a slow streamwise scale. The order of magnitude of the weak streamwise non-uniformity is then effectively defined as

$$\epsilon = \frac{1}{Re} \ll 1, \quad (2.2)$$

which is the only small parameter of the present investigation. Under this quasi-parallel flow approximation, the basic flow streamfunction Ψ_b only depends on y and the slow streamwise coordinate

$$X = \epsilon x,$$

and it is expanded as

$$\Psi_b(y; X) \sim \Psi_0(y; X) + \epsilon \Psi_1(y; X) + \epsilon^2 \Psi_2(y; X) + \dots . \quad (2.3)$$

The leading-order basic flow approximation Ψ_0 is then readily shown to obey the Prandtl boundary layer equation

$$\left(\frac{\partial \Psi_0}{\partial y} \frac{\partial}{\partial X} - \frac{\partial \Psi_0}{\partial X} \frac{\partial}{\partial y} \right) \frac{\partial \Psi_0}{\partial y} = -\frac{dP}{dX} + \frac{\partial^3 \Psi_0}{\partial y^3}, \quad (2.4)$$

where the given streamwise pressure gradient dP/dX is the integration ‘constant’ arising in the integration of the leading-order vorticity equation. Corresponding basic velocity components are then $U_0(y; X) = \partial \Psi_0 / \partial y$ and $\epsilon V_1(y; X) = -\epsilon \partial \Psi_0 / \partial X$.

The basic flow is affected by viscous diffusion and by the externally applied pressure field $P(X)$ which allows its streamwise evolution to be precisely controlled. The parabolic boundary layer equation (2.4) is numerically integrated from $X = 0$, with the sech^2 inlet velocity profile

$$U_0(y; 0) = 1 - \frac{\Delta U}{\cosh^2(y \sinh^{-1} 1)}. \quad (2.5)$$

Such a non-dimensional representation holds when the previously introduced velocity

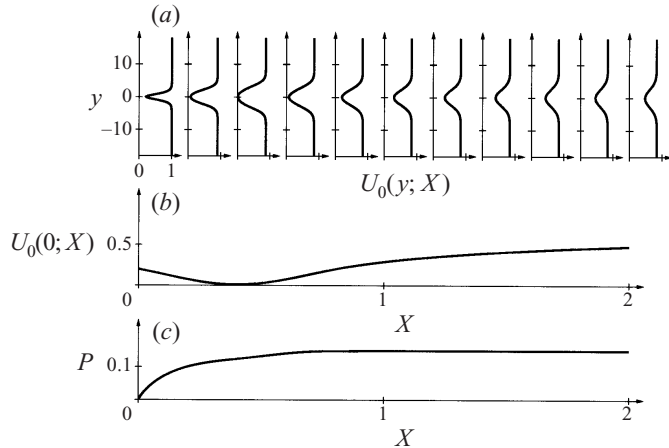


FIGURE 1. Streamwise development of the basic flow. (a) Velocity profiles $U_0(y; X)$ at different streamwise X locations. (b) Evolution of centreline velocity $U_0(0; X)$. The smallest value $U_0(0; X) = 0.01$ is reached at $X = 0.4$. (c) Basic pressure field $P(X)$.

scale U^* is specified to be the streamwise basic flow inlet velocity at $y = \pm\infty$. The length scale ℓ^* is chosen to be the half-width of the wake so that, in non-dimensional variables, $U_0(1; 0) = \frac{1}{2}[U(\infty; 0) + U(0; 0)]$. The non-dimensional parameter ΔU measures the depth of the wake at the inlet and, in the present paper, we choose $\Delta U = 0.8$.

In the upstream part of the flow, an adverse pressure gradient is carefully tailored in order to generate a central region of absolute instability, while avoiding reverse flow. The characteristics of the resulting basic flow are displayed in figure 1. For the adverse pressure gradient sketched in figure 1(c), the centreline velocity (figure 1b) decreases from $1 - \Delta U = 0.2$ at the inlet to reach a minimum 0.01 at the streamwise station $X = 0.4$. The relatively strong adverse pressure gradient close to the inlet slows down the basic flow while increasing the wake depth and rounding off the dip of the profile (figure 1a). Further downstream a uniform pressure is reached and thus the flow evolves solely under the action of viscosity: the wake depth decreases and slow diffusive spreading takes place.

Note that the Reynolds number in the boundary layer equation (2.4) has been scaled out and incorporated in the slow streamwise variable $X = \epsilon x$. As a result, the above basic flow applies to all large Reynolds numbers: changes in Re are simply handled by a dilatation of the streamwise coordinate according to $x/X = Re$, the velocity profile shapes remaining unaltered.

The total streamfunction is then decomposed into steady basic and unsteady perturbation contributions according to

$$\Psi(x, y, t) = \Psi_b(y; X) + \psi(x, y, t). \quad (2.6)$$

Substitution of (2.6) with (2.3) into the governing equation (2.1), yields

$$\begin{aligned} & \Delta\psi_t + \Psi_{0,y}\Delta\psi_x - \Psi_{0,yy}\psi_x + (\psi_y\partial_x - \psi_x\partial_y)\Delta\psi \\ & + \epsilon[\Psi_{1,y}\Delta\psi_x - \Psi_{0,X}\Delta\psi_y - \Psi_{1,yyy}\psi_x + \Psi_{0,Xyy}\psi_y - \Delta^2\psi] = \mathcal{O}(\epsilon^2), \end{aligned} \quad (2.7)$$

where the subscripts t, x, y and X denote differentiation with respect to these variables.

The slow streamwise variations of the basic flow call for an analysis of the perturbation field in terms of both linear and nonlinear WKBJ approximations (Bender & Orszag 1978). The properties of local linear and nonlinear wavetrain solutions sustained by the basic flow are derived in the following two sections.

3. Local linear instability waves

Following e.g. Crighton & Gaster (1976) and Monkewitz *et al.* (1993), in the linear approximation ψ is sought in the form of a slowly varying wavetrain of frequency ω :

$$\psi(x, y, t) = \psi_*(y; X) \exp\left(\frac{i}{\epsilon} \int^X k(u) du - i\omega t\right) + \text{c.c.}, \quad (3.1)$$

where $k(X)$ denotes the local complex wavenumber and

$$\psi_*(y; X) \sim \psi_0(y; X) + \epsilon \psi_1(y; X) + \dots \quad (3.2)$$

accounts for the local cross-stream structure. Substitution of expressions (3.1), (3.2) into the linearized version of (2.7) shows that the leading-order approximation ψ_0 is governed by the local Rayleigh equation

$$(k U_0(y; X) - \omega) \left(\frac{\partial^2 \psi_0}{\partial y^2} - k^2 \psi_0 \right) - k U_{0,yy}(y; X) \psi_0 = 0. \quad (3.3)$$

Linear eigenmodes $\Psi^\ell(y; k, X)$ that are solutions of (3.3) and exponentially decaying at $y = \pm\infty$ are obtained when the complex frequency ω and complex wavenumber k are bound by the *local linear dispersion relation*

$$\omega = \Omega^\ell(k, X), \quad (3.4)$$

at each station X . For a given wavenumber and a given wake velocity profile there exists a set of eigenfunctions to the Rayleigh equation. We only consider the *sinuous mode* (ψ even) since it is the most amplified (Drazin & Reid 1981). In what follows, the functions Ψ^ℓ and Ω^ℓ always refer to this particular eigenfunction and eigenvalue respectively. For definiteness, the linear Ψ^ℓ eigenfunctions are normalized by $\Psi^\ell(0; k, X) = 1$.

The Rayleigh equation (3.3) has been solved via a Chebyshev spectral method (Canuto *et al.* 1988). The Chebyshev collocation points $-1 \leq \xi_i = -\cos[\pi/(n_y+1)] \leq +1$ for $i = 0, \dots, n_y + 1$ are mapped onto $-\infty \leq y_i \leq +\infty$ through the transformation

$$\frac{\sqrt{2}}{l_y} y = \frac{\xi}{1 - \xi^2}. \quad (3.5)$$

The parameter l_y dictates the distribution of collocation points on the y -axis: half are located in the interval $-l_y < y < l_y$ and are approximately equispaced; the remaining points extend towards $y = \pm\infty$ and their density decreases algebraically. For a given k , the differential Rayleigh equation is thus recast into a linear eigenvalue problem: the frequency ω and cross-stream distribution Ψ^ℓ are obtained as eigenvalues and eigenfunctions respectively. As many eigenfunctions as collocation points are obtained. The relevant sinuous eigenfrequency is then identified by inspection of its eigenfunction. The complete linear dispersion relation $\Omega^\ell(k, X)$ is generated by continuation in k and X . Note that, since the eigenfunctions Ψ^ℓ exponentially decay towards $y = \pm\infty$ as $e^{-|k_y y|}$, the transformation (3.5) is appropriate for this problem. In general $n_y = 50$ collocation points with $l_y = 5$ are found to be sufficient to accurately

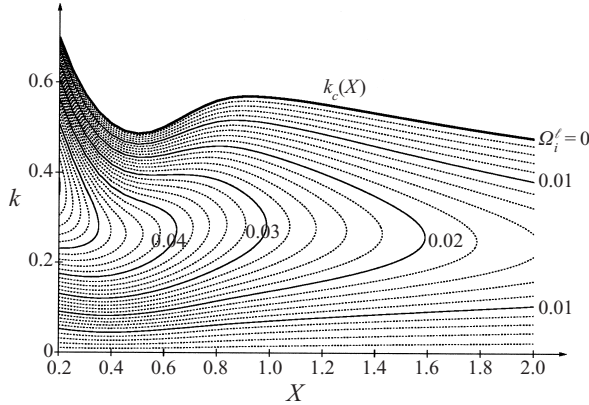


FIGURE 2. Isocontours of sinuous mode temporal growth rates Ω_i^ℓ in the (X, k) -plane in the interval $0.2 < X < 2.0$ of figure 1. Solid contours are separated by $\delta\Omega_i^\ell = 0.01$, dashed contours by $\delta\Omega_i^\ell = 0.002$. Larger growth rates occur in the upstream region whereas instability weakens further downstream. The unstable domain is bounded by the neutral curve $k_c(X)$ (thick line).

resolve the eigenfunction and precisely obtain the frequency; however for small values of k_r a larger n_y is necessary. As a validation, the mode shape is required not to vary when doubling the number of collocation points.

The dispersion relation (3.4) yields the local wavenumber $k^\ell(X, \omega)$ as a function of the global frequency. Thus at leading order in the WKBJ expansion

$$\psi(x, y, t) \sim A_0(X) \Psi^\ell(y; k^\ell(X, \omega), X) \exp\left(\frac{i}{\epsilon} \int^X k^\ell(u, \omega) du - i\omega t\right) + \text{c.c.}, \quad (3.6)$$

where the slowly varying complex amplitude function $A_0(X)$ could be determined at next order by a secular condition.

Local linear instability is characterized by the temporal growth of real wavenumbers. Figure 2 illustrates the streamwise evolution of sinuous temporal growth rates $\Omega_i^\ell(k, X) \equiv \text{Im } \Omega^\ell(k, X)$ in the (X, k) -plane for the basic flow of figure 1. All wake profiles exhibit long-wavelength instability and the wake flow remains linearly unstable far downstream. However, the maximum temporal growth rate $\text{Max}\{\Omega_i^\ell(k, X), k \text{ real}\}$ decreases with X . The unstable domain in the (X, k) -plane is defined by the condition $\Omega_i^\ell(k, X) > 0$. Its boundary yields the neutral curve $k_c(X)$ (thick line in figure 2) associated through (3.4) with a real frequency. Linear growth of unstable waves is limited by nonlinear saturation effects: the corresponding nonlinear wavetrains are then obtained as discussed in the next section.

The local complex absolute frequency $\omega_0(X)$ and absolute wavenumber $k_0(X)$ are defined via dispersion relation (3.4) as

$$\omega_0(X) = \Omega^\ell(k_0(X), X) \quad \text{with} \quad \frac{\partial \Omega^\ell}{\partial k}(k_0(X), X) = 0. \quad (3.7)$$

The locus of $\omega_0(X)$ pertaining to the basic wake flow is represented in the complex ω -plane in figure 3(a) and the corresponding streamwise variation of absolute growth rate $\omega_{0,i}(X)$ is sketched in figure 3(b). According to these sketches, the properties of the flow under consideration present the following desirable features. The upstream region extending from the inlet at $X = 0$ to $X^{ca} = 0.24$ is convectively unstable (CU). The adverse pressure gradient prevailing in this domain induces an increase of $\omega_{0,i}$

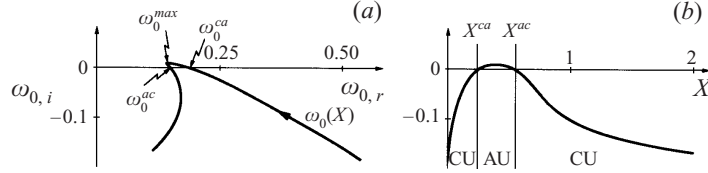


FIGURE 3. (a) Locus of local absolute frequency $\omega_0(X)$ in the complex frequency plane.
(b) Local absolute growth rates $\omega_{0,i}(X)$ as a function of streamwise station.

which leads to absolute instability at X^{ca} . Beyond this station of marginal absolute instability, the flow displays a central absolutely unstable (AU) region extending over the interval $X^{ca} < X < X^{ac}$, with $X^{ac} = 0.55$. In the absence of further adverse pressure gradient, the flow then returns to convective instability far downstream $X > X^{ac}$.

According to Pier *et al.* (1998), the boundaries of the AU region are of particular interest. These specific locations are defined by real absolute frequencies, $\omega_0^{ca} \equiv \omega_0(X^{ca}) = 0.190$ and $\omega_0^{ac} \equiv \omega_0(X^{ac}) = 0.150$ respectively. Note that $\omega_0^{ca} > \omega_0^{ac}$, a feature which has been observed for all wake flows of the present study. Although not essential to the observation of steep global modes, this inequality was taken as a working assumption in Pier *et al.* (2001). The largest absolute growth rate occurs at $X^{max} = 0.38$ where $\omega_0^{max} \equiv \omega_0(X^{max}) = 0.144 + 0.010i$.

Following Chomaz *et al.* (1991) and Monkewitz *et al.* (1993), we may analyse the linear global instability of the present flow by applying the saddle point criterion (1.1). The analytic continuation of $\omega_0(X)$ in the complex X -plane yields a saddle point at $X_s = 0.43 + 0.03i$, associated with a linear global mode of frequency $\omega_s = 0.143 + 0.008i$. Since $\omega_{s,i} > 0$, the wake flow is linearly globally unstable.

4. Local fully nonlinear travelling waves

In regions where perturbations reach finite amplitude levels, the flow is governed by the complete nonlinear equation (2.7). The experiments of Provansal *et al.* (1987) as well as the numerical simulations of Hammond & Redekopp (1997) reveal that nonlinear structures in wakes are propagating in the streamwise direction: they are locally periodic and their (x, t) -dependence occurs solely via a phase function with only slow streamwise deformations. Guided by these observations and following the WKBJ formalism, we seek nonlinear slowly varying wavetrains to equation (2.7) of the form

$$\psi(x, y, t) = \psi_*(\theta, y; X) \quad \text{with} \quad \theta = \frac{1}{\epsilon} \int^X k(u) du - \omega t, \quad (4.1)$$

where ψ_* is a 2π -periodic function of θ , and $k(X)$ is the real local wavenumber. Following the nonlinear WKBJ approximation scheme of Pier & Huerre (1996) and Pier *et al.* (2001), the nonlinear wavetrain is again expanded as

$$\psi_*(\theta, y; X) \sim \psi_0(\theta, y; X) + \epsilon \psi_1(\theta, y; X) + \dots . \quad (4.2)$$

At leading order, one obtains

$$\begin{aligned} (k U_0(y; X) - \omega) \frac{\partial}{\partial \theta} \left(\frac{\partial^2 \psi_0}{\partial y^2} + k^2 \frac{\partial^2 \psi_0}{\partial \theta^2} \right) - k U_{0,yy}(y; X) \frac{\partial \psi_0}{\partial \theta} \\ + k \left(\frac{\partial \psi_0}{\partial y} \frac{\partial}{\partial \theta} - \frac{\partial \psi_0}{\partial \theta} \frac{\partial}{\partial y} \right) \left(\frac{\partial^2 \psi_0}{\partial y^2} + k^2 \frac{\partial^2 \psi_0}{\partial \theta^2} \right) = 0. \end{aligned} \quad (4.3)$$

As shown below, this partial differential equation in θ and y admits periodic solutions $\Psi^{n\ell}(\theta, y; k, X)$ when the real frequency ω and the real wavenumber k are related by the local nonlinear dispersion relation

$$\omega = \Omega^{n\ell}(k, X), \quad (4.4)$$

at each station X . The dispersion relation (4.4) yields the local nonlinear wavenumber $k^{n\ell}(X, \omega)$ as a function of the global frequency. Thus at leading order in the nonlinear WKBJ expansion

$$\psi(x, y, t) \sim \Psi^{n\ell} \left(\frac{1}{\epsilon} \int^X k^{n\ell}(u, \omega) du - \omega t + \theta_0(X), y; k^{n\ell}(X, \omega), X \right), \quad (4.5)$$

where the slowly varying phase function $\theta_0(X)$ could be determined at next order by a solvability condition.

Due to the separation of scales, the phase function θ governs the fast oscillations on a typical instability length scale, whereas X accounts for the slow development of the basic velocity profile and is not involved in spatial differentiation. Hence local properties at a given streamwise station X are recovered by freezing the X -dependence of the velocity profile and studying the corresponding strictly parallel flow. Thus the term ‘local’ always refers to properties of strictly parallel flows obtained by extending towards $x = \pm\infty$ the velocity profile prevailing at a specific downstream station X .

The local nonlinear travelling waves $\Psi^{n\ell}(\theta, y; k, X)$ are now shown to arise naturally from a purely temporal analysis of the strictly parallel flow $U_0(y; X)$ obtained by freezing X . To this extent, the slow coordinate X is regarded as an external control parameter, frozen at a constant value although x varies on the entire real axis. The initial value problem of interest is the study of the development of a spatially periodic perturbation of given real wavenumber k . The initial evolution of such a small-amplitude perturbation is dictated by the linear temporal growth rate $\Omega_i'(k, X)$. Whenever $\Omega_i' > 0$, its amplitude exponentially grows until nonlinearity sets in. Stabilizing nonlinearities lead to saturation at finite amplitude and, at large time, a fully nonlinear solution is obtained with streamwise periodicity imposed by the initial wavenumber k . In the absence of secondary instabilities, a propagating nonlinear wave solution is reached, and its frequency yields the nonlinear dispersion relation (4.4). The same thought experiment may be carried out at each streamwise station X . It should be emphasized that, without viscous dissipation, the above procedure does not single out a unique attracting wavetrain solution onto which the system converges for large time. In order to circumvent this difficulty, we have chosen to regard the pertinent finite-amplitude states as long-time saturated solutions of the full viscous vorticity equation

$$\left(\frac{\partial}{\partial t} + U_0(y) \frac{\partial}{\partial x} \right) \Delta \psi_0 - U_{0,yy}(y) \frac{\partial \psi_0}{\partial x} + \left(\frac{\partial \psi_0}{\partial y} \frac{\partial}{\partial x} - \frac{\partial \psi_0}{\partial x} \frac{\partial}{\partial y} \right) \Delta \psi_0 = \frac{1}{Re} \Delta^2 \psi_0, \quad (4.6)$$

for the perturbation stream function ψ_0 . In the above expression, the basic flow is strictly parallel and its parametric dependence on X has been omitted. Note that the viscous term $\Delta^2 \psi_0 / Re$ would only appear at higher order if the WKBJ asymptotic scheme were strictly applied. The use of a large but finite Re is brought in to select a unique periodic nonlinear wavetrain. The precise value of Re will later be proven unimportant.

One should also note that such a solution can only be preserved at large time if the basic wake shear is maintained steady and parallel. In the calculation, this is achieved by separating basic and perturbation fields. In effect, as in the direct

numerical simulations of shear flows, e.g. Ehrenstein & Koch (1995), it is implicitly assumed that a body force is present to counteract viscous diffusion of the basic flow. Note that the extra terms introduced in the equations for the basic flow and perturbations are higher-order corrections: they are introduced for computational convenience, and in the limit $\epsilon = 1/Re \rightarrow 0$ the original equation is recovered.

The temporal evolution of an initial spatially periodic perturbation $\psi_0(x, y, t)$ of real wavenumber k is treated by solving (4.6) on a streamwise periodic interval of given wavelength $2\pi/k$. The temporal linear sinuous eigenmode of real wavenumber k is chosen as initial perturbation, and, in the linear régime, it evolves according to $\Omega'(k, X)$. Whenever $\Omega'_i(k, X) > 0$, it is amplified, and nonlinear terms come into play to promote higher harmonics as well as a non-fluctuating mean flow correction. The long-time finite-amplitude state is precisely the nonlinear travelling wave $\psi_0(x, y, t) = \Psi^{n'}(kx - \omega t, y)$ solution of frequency ω of the nonlinear dispersion relation (4.4) for the basic flow at the station X under consideration. In order to complete the specification of the temporal evolution problem, we assume that the flow rate is unaltered by the presence of the finite-amplitude perturbations.

An example of a nonlinear travelling wave state of wavenumber $k = 0.30$ is illustrated in figure 4 for the basic velocity field (thick line in figure 4a) at $X = 1.0$. This wavenumber is linearly amplified according to $\Omega' = 0.183 + 0.029i$. Beyond a transient régime, a periodic state is reached, at the numerically determined nonlinear frequency $\Omega^{n'}(k, X) = 0.205$. In figure 4(a), the basic velocity profile $U_0(y)$ (thick line) is compared with the nonlinear mean flow correction $u_{(0)}(y)$ (thin line) and the total mean flow $U_0 + u_{(0)}$ (dashed line). The non-fluctuating component of the perturbation field is seen to essentially reduce the depth of the wake and to increase its width. Contour levels of the perturbation vorticity field $-\Delta\psi_0$ are displayed in figure 4(b). The periodic spatial structure is seen to consist of a double row of counter-rotating vortices as one would expect in a Kármán vortex street. The main vortex street is surrounded by two vortex rows of smaller amplitude and opposite sign. The whole nonlinear structure propagates in the downstream direction at the celerity $\Omega^{n'}/k = 0.68$, slower than the far-field basic velocity $U_0(\pm\infty) = 0.84$. Since the basic flow is maintained, such a periodic state persists at large time and the nonlinear frequency is well defined. Note however that the mean flow correction $u_{(0)}(y)$ (thin line in figure 4a) is observed to slowly diffuse in the y -direction over a slow viscous time scale.

Such nonlinear states naturally only exist in the unstable domain of the (X, k) -plane, defined by a positive linear growth rate (figure 2). Isocontours of $\Omega^{n'}$ in this region are represented in figure 5(a) and they should be compared to the corresponding isocontours of Ω'_r displayed in figure 5(b). At the neutral stability boundary (thick curves in figure 5), the linear temporal growth rate vanishes and the finite-amplitude wavetrains smoothly turn into the linear neutral eigenmodes. As a result, on the neutral curve

$$\Omega^{n'}(k, X) = \Omega'_r(k, X) \quad \text{and} \quad \Omega'_i(k, X) = 0.$$

Note that linear and nonlinear frequencies identically vanish for $k = 0$.

A careful comparison of figures 5(a) and 5(b) reveals that the nonlinear frequencies are always larger than the linear ones. Thus nonlinear interactions tend to increase the celerity ω/k of the wavetrains. It should be emphasized that the nonlinear iso-frequency curves in the (X, k) -plane displayed in figure 5(a) precisely coincide with the nonlinear spatial branches $k^{n'}(X, \omega)$ at the corresponding frequency, as introduced in the nonlinear wavetrain (4.5).

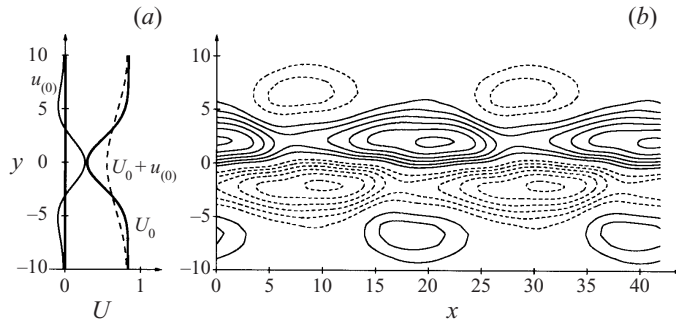


FIGURE 4. Local nonlinear travelling wave of wavenumber $k = 0.30$ at the downstream station $X = 1.0$ with $Re = 100$ at time $t = 6000$. (a) Basic velocity profile $U_0(y)$ (thick line), meanflow correction $u_{(0)}(y)$ (thin line) and total mean flow $U_0(y) + u_{(0)}(y)$ (dashed line). (b) Isolines of the perturbation vorticity field over two wavelengths. Positive isolines 0.025, 0.050, ..., 0.150 and negative isolines -0.025, -0.050, ..., -0.150 are represented by solid and dashed curves respectively.

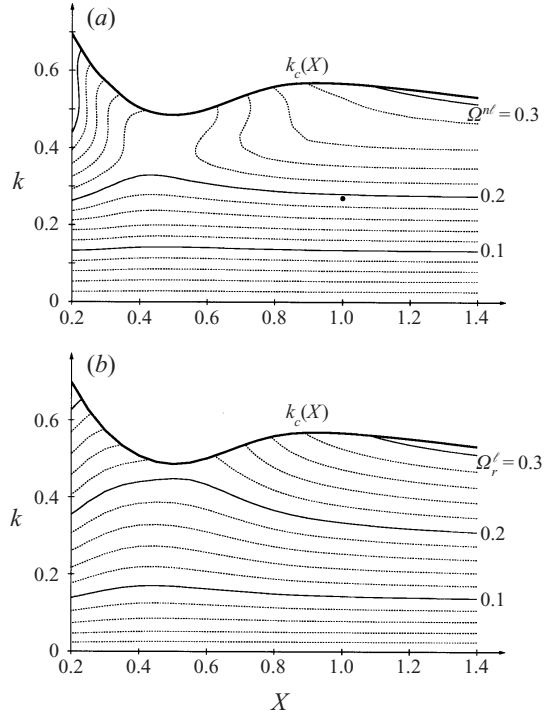


FIGURE 5. Isofrequency contours in the linearly unstable domain of the (X, k) -plane. Solid contours are separated by $\delta\Omega = 0.1$, dashed contours by $\delta\Omega = 0.02$. (a) Isocontours of $\Omega^{n'}$. (b) Isocontours of $\Omega_r^{n'}$.

The numerical technique used to solve (4.6) is based on the spectral method of Ehrenstein & Koch (1989) suitably adapted to wake flows. The streamfunction is decomposed into harmonic components as

$$\psi_0(x, y, t) = \sum_{-\infty < n < \infty} \phi_{(n)}(y, t) e^{inx}, \quad (4.7)$$

with $\phi_{(-n)}(y, t) = \phi_{(n)}^*(y, t)$, where \star denotes the complex conjugate. Substitution of (4.7) into the governing equation (4.6) and identification of corresponding exponentials leads to the modal equations

$$\left[\partial_t D_n + ink[U_0(y)D_n - U_{0,yy}(y)] - \frac{1}{Re} D_n^2 \right] \phi_{(n)} + ik \sum_{-\infty < m < \infty} N_{n-m,m} = 0, \quad (4.8)$$

where $D_n = \partial_{yy} - (nk)^2$ and

$$N_{n,m} = m(\partial_y \phi_{(n)})(D_m \phi_{(m)}) - n\phi_{(n)}(D_m \partial_y \phi_{(m)}). \quad (4.9)$$

Assuming that the nonlinear perturbation does not change the pressure gradient at $y = \pm\infty$ and leaves the flow rate unaltered, equation (4.8) may be integrated twice for $n = 0$ to obtain the mean flow distortion equation

$$\frac{\partial \phi_{(0)}}{\partial t} - \frac{1}{Re} \frac{\partial^2 \phi_{(0)}}{\partial y^2} = 2k \operatorname{Im} \sum_{m>0} m \phi_{(m)}^* \frac{\partial \phi_{(m)}}{\partial y}. \quad (4.10)$$

The unknown functions $\phi_{(n)}(y, t)$ all vanish at $y = \pm\infty$, and the mean flow correction reads $u_{(0)} = \partial \phi_{(0)} / \partial y$.

The set of modal equations (4.8), (4.10) is truncated at a finite number of harmonics $|n| \leq n_h$ and again a Chebyshev collocation method with n_y collocation points is implemented in the y -direction together with the mapping (3.5). Thus the governing equation (4.6) has been recast as a system of $n_y(2n_h + 1)$ real algebraic ordinary differential equations of the first order in time. These are solved via a fourth-order Runge–Kutta scheme of time step δt . In the particular example of figure 4 at $Re = 100$ and $t = 6000$, $n_h = 5$, $n_y = 71$, $l_y = 5$ and $\delta t = 0.05$. It has been checked that higher resolutions leave the results unchanged.

The temporal evolution of the wavenumber spectrum is illustrated in figure 6. The kinetic energy $E_n(t)$ of each harmonic is sketched as a function of time on both logarithmic and linear scales. If $u_{(n)} = \partial_y \psi_{(n)} e^{inkx} + \text{c.c.}$ and $v_{(n)} = -ink \psi_{(n)} e^{inkx} + \text{c.c.}$ denote the velocity field associated with the n th harmonic ($n > 0$), its energy is defined as

$$E_n(t) = \int_{-\infty}^{+\infty} \int_0^{2\pi/k} \frac{1}{2} (u_n^2 + v_n^2) dx dy.$$

During the linear growth phase ($t < 800$, figure 6a), all harmonics are exponentially amplified. The measured slope of the fundamental E_1 (thick line) in the semi-log plot is 0.0255, and precisely coincides with its theoretical value given by $2\Omega_i^f / \ln 10$. Higher harmonics $E_n(t)$ ($n > 1$, dashed lines) are naturally slaved to the fundamental and grow as $[E_1(t)]^n$ whereas the mean flow correction $E_0(t)$ (thin solid line) scales as $[E_1(t)]^2$.

Beyond the nonlinear transient régime ($800 < t < 2000$), the system relaxes towards a quasi-stationary travelling wave state. The duration of the transients depends on the dissipation time scale as dictated by the magnitude of the selected Reynolds number. The choice $Re = 100$ appears to be a good compromise between reasonably long transients and inviscid-like dynamics. Although the motion is fully nonlinear, only a few harmonic components partake in the dynamics. Even for the most unstable wavenumber, only three harmonics are necessary to accurately capture the saturated wave state.

The final nonlinear propagating wave and its frequency hardly depend on the particular value of the Reynolds number, as illustrated in figure 7. For $Re > 50$, the frequency changes by less than 0.0025. It is only for $Re < 20$ that drastic changes

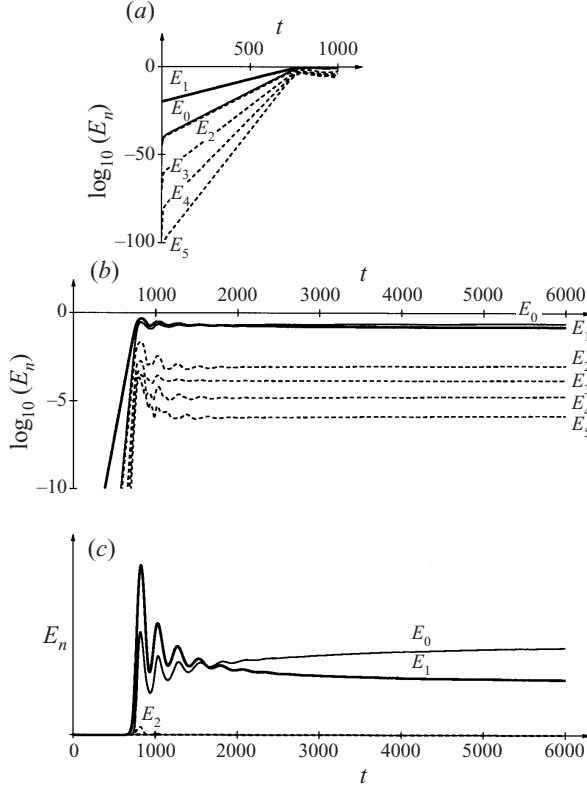


FIGURE 6. Temporal evolution of the energy contained in each harmonic component (nonlinear travelling wave of figure 4) for $0 < t < 6000$. (a) Semi-log plot of the initial linear growth phase ($t < 800$). The fundamental E_1 (thick solid line) grows according to $\exp 2\Omega^\ell t$, higher harmonics E_n ($n > 1$, dashed lines) are slaved as the n th power of E_1 , the mean flow correction E_0 as E_1^2 . (b,c) Semi-log and linear plots of the long time evolution display a nonlinear transient régime ($800 < t < 2000$) with damped oscillations towards a quasi-stationary state. Note that the harmonics ($n > 2$) reach much lower saturation levels.

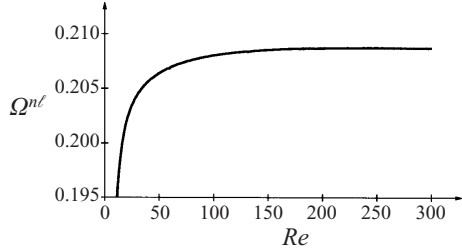


FIGURE 7. Variation of the nonlinear frequency Ω^{n*} associated with $k = 0.30$ and $X = 1.0$ as a function of the Reynolds number Re . Note the magnified vertical scale.

in the frequency occur! This insensitivity to Reynolds number fully justifies the approach adopted in the present study. The addition of the viscous term in (4.6) does not significantly affect the properties of the nonlinear wavetrain. In the present calculation, the value $Re = 100$ has been deemed sufficient.

5. Nonlinear spatial response and fronts in parallel wakes

At each downstream location we have now at our disposal a complete family of linear as well as nonlinear local wavetrains which constitute the elementary building blocks of a globally synchronized flow. Whereas the upstream region extending to the inlet is expected to sustain small perturbation levels, correctly handled within a linear approximation, the downstream wake should be made up of fully nonlinear travelling wavetrains. In the framework of one-dimensional evolution models, it has been demonstrated (Pier 1999) that, for steep global modes, a stationary front constitutes the missing link converting the upstream linear waves into the downstream nonlinear waves at a station of marginal local absolute instability. In this section it is shown that an analogous front structure exists in wake flows. According to Dee & Langer (1983) and van Saarloos (1987, 1988), a propagating front moves towards its decaying edge if the basic state is AU, towards its finite-amplitude edge if the basic state is CU, and a stationary front is obtained when the medium is exactly at the CU/AU transition.

Here a slightly different point of view is adopted: instead of studying front propagation, we focus on the spatial response of a CU profile to a localized time-harmonic forcing and argue that the stationary front is recovered at the CU/AU transition. This approach is motivated by the difficulty in directly computing the propagation of a front connecting a fully nonlinear wavetrain to an unperturbed wake profile: in the co-moving frame the flow is marginally AU and thus very sensitive to various uncontrolled perturbations. In contrast, the signalling problem in a CU flow is not affected since the response to noise is swept away, and the stationary régime is easily identified.

Consider again a strictly parallel wake profile at a given streamwise station X . The forced perturbation vorticity and streamfunction fields ϖ and ψ are then governed by

$$\left(\frac{\partial}{\partial t} + U_0(y) \frac{\partial}{\partial x} \right) \varpi + U_{0,yy}(y) \frac{\partial \psi}{\partial x} + \left(\frac{\partial \psi}{\partial y} \frac{\partial}{\partial x} - \frac{\partial \psi}{\partial x} \frac{\partial}{\partial y} \right) \varpi = \frac{\Delta \varpi}{Re} + S(x, y, t), \quad (5.1a)$$

$$\Delta \psi = -\varpi, \quad (5.1b)$$

where the temporally harmonic forcing function is taken to be of the form

$$S(x, y, t) = H(t) A_f \exp \left(-\frac{x^2 + (y - y_f)^2}{\ell_f^2} \right) \cos \omega_f t, \quad (5.2)$$

with $H(t)$ denoting the Heaviside unit step function, and ω_f and A_f the forcing frequency and amplitude. The forcing is applied in a region of size ℓ_f centred at $(0, y_f)$. Switching on the forcing at $t = 0$ produces a transient wavepacket together with the steady-state response at the forcing frequency. Whenever the basic flow is CU, transients move away from the source and a steady-state signal is left at the forcing frequency. When the medium is AU, switch-on transients overwhelm the response at the forcing frequency and the signalling problem is ill-posed. Hence only the spatial problem for CU velocity profiles is considered in the following discussion.

The linear signalling problem in shear flows has been investigated by Huerre & Monkewitz (1985). Here, the linear dispersion relation (3.4) gives rise to two linear spatial branches $k^{\ell\pm}(X, \omega)$ and $k^{\ell\mp}(X, \omega)$. The response streamfunction then reads

$$\psi(x, y, t) \propto A_f \frac{\Psi'(y; k^{\ell\pm}(X, \omega_f), X)}{(\partial \Omega' / \partial k)(k^{\ell\pm}(X, \omega_f), X)} \exp i [k^{\ell\pm}(X, \omega_f)x - \omega_f t] + \text{c.c.}, \quad (5.3)$$

where labels (+) and (-) pertain to the downstream ($x > 0$) and upstream ($x < 0$)

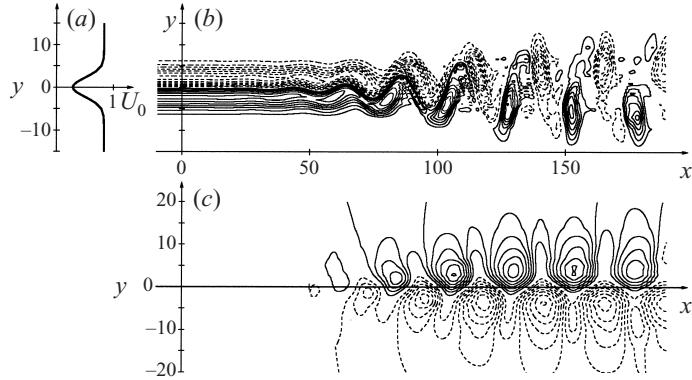


FIGURE 8. Spatial response of a CU parallel wake to harmonic forcing of frequency $\omega_f = 0.19$, amplitude $A_f = 10^{-3}$ and width $\ell_f = 1$ applied at the origin and given by (5.2). $Re = 100$. (a) Basic velocity profile at $X = 1$. (b) Total vorticity levels at $t = 500$. Positive contours $0.02, 0.04, \dots, 0.14$ and negative contours $-0.02, -0.04, \dots, -0.14$ are represented by solid and dashed lines respectively. (c) Corresponding perturbation streamlines. Solid (dashed) isocontours pertain to the levels $0.2, 0.4, \dots, 1.4$ ($-0.2, -0.4, \dots, -1.4$). Close to the forcing location the downstream response grows exponentially to reach a finite amplitude around $x = 70$. Further downstream, a nonlinear travelling wave is generated. The entire streamwise extent $-10 < x < 190$ of the computational domain is shown.

response respectively. Note again that for convenience the viscous dissipation term $\Delta\varpi/Re$ has been added to (5.1a). Thus the linear dispersion relation Ω^ℓ and corresponding eigenfunctions Ψ^ℓ are derived from the Orr–Sommerfeld equation rather than the Rayleigh equation (3.3), the streamwise decay or growth rates being dictated by $k_i^{\ell\pm} \equiv \text{Im } k^{\ell\pm}$. An extensive survey of all the CU velocity profiles encountered in the present study reveals that the linear $k^{\ell-}(X, \omega)$ branches always remain in the $k_i < 0$ half-plane and thus never give rise to upstream amplification. Only downstream spatial branches $k^{\ell+}$ grow in a certain frequency range.

Whenever a linear spatial branch is amplified, nonlinear terms have to be taken into account at some distance from the source, however small the forcing amplitude. As the response reaches finite amplitude, nonlinear saturation prevents further amplification and leads to a nonlinear travelling wave at the excitation frequency for some real wavenumber $k^{n\ell}$. Since this nonlinear propagating wavetrain is reached downstream of the source, it is denoted as $k^{n\ell+}(X, \omega)$. The forcing frequency ω_f and the nonlinear response wavenumber $k^{n\ell+}$ satisfy the nonlinear dispersion relation (4.4). For a more complete discussion of the relationship between linear and nonlinear spatial branches, see Pier (1999) and Pier *et al.* (2001).

Figure 8 illustrates the spatial response of the parallel CU wake velocity profile (a) prevailing at $X = 1$, at a Reynolds number $Re = 100$. Forcing is applied at the origin $y_f = 0$ with a frequency $\omega_f = 0.19$, amplitude $A_f = 10^{-3}$ and $\ell_f = 1$. Total isovorticity contours and perturbation streamlines are displayed in (b) and (c) respectively. Close to the forcing location, the downstream response grows exponentially to reach a finite amplitude around $x \sim 70$. The measured nonlinear saturation wavenumber is $k^{n\ell+}(X, \omega_f) = 0.27$. The solid dot at $(k, X) = (0.27, 1)$ in figure 5(a) lies close to the contour level $\Omega^{n\ell} = \omega_f = 0.19$, which confirms that $k^{n\ell+} = 0.27$ is indeed a solution of the nonlinear dispersion relation (4.4).

The signalling problem (5.1) is numerically integrated via a finite difference scheme

with n_x mesh points of size δx in the x -direction and n_y Chebyshev collocation points in the y -direction. According to the Poisson equation (5.1b), the perturbation streamfunction ψ is generated by the vorticity field ϖ which is confined within the shear region. Thus, in general, ψ decays algebraically far away from the vortical region. As a result, the algebraic transformation (3.5) is still well adapted to this problem. The perturbation vorticity and streamfunction are both assumed to vanish at the upstream boundary and at infinity in the cross-stream direction. The non-reflecting boundary conditions introduced by Jin & Braza (1993)

$$\frac{\partial \varpi}{\partial t} = - \left(U_0 + \frac{\partial \psi}{\partial y} \right) \frac{\partial \varpi}{\partial x} + \frac{1}{Re} \frac{\partial^2 \varpi}{\partial y^2}, \quad (5.4a)$$

$$\frac{\partial}{\partial t} \frac{\partial \psi}{\partial x} = - \left(U_0 + \frac{\partial \psi}{\partial y} \right) \frac{\partial^2 \psi}{\partial x^2} + \frac{1}{Re} \frac{\partial^2}{\partial y^2} \frac{\partial \psi}{\partial x}, \quad (5.4b)$$

are implemented at the outlet. The Poisson equation (5.1b) is solved by a generalized Thomas algorithm with given boundary values of ψ at the inlet and ψ_x at the outlet. Integration in time is performed with a second-order Runge–Kutta scheme of time step δt .

The parameters chosen in the computation of figure 8 are $n_x = 400$, $\delta x = 0.5$, $n_y = 31$, $l_y = 5$, $\delta t = 0.05$. The entire streamwise extent of the computational domain $-10 < x < 190$ is displayed to demonstrate that the outflow boundary is truly non-reflecting.

In order to analyse the spatio-temporal structure of the nonlinear response, harmonic components have been computed over one period in the stationary régime according to the Fourier expansion

$$\psi(x, y, t) = \sum_{-\infty < n < +\infty} \phi_{(n)}(x, y) e^{-in\omega_f t}. \quad (5.5)$$

Figure 9(a) displays a snapshot of the fundamental streamwise velocity $u_{(1)}(x, y) = \partial_y \phi_{(1)}(x, y) + \text{c.c.}$ It is seen that at the onset of nonlinearity, the fluctuation amplitude is higher than in the periodic nonlinear wavetrain reached further downstream. The associated envelope $|v_{(1)}|(x, y) = 2|\partial_x \phi_{(1)}(x, y)|$ plotted in figure 9(b) effectively represents the amplitude of the fundamental cross-stream velocity fluctuations. The non-fluctuating component of the streamfunction at $n = 0$ is associated with the nonlinear mean flow correction induced by Reynolds stresses. Figure 9(c) shows the isocontours of the mean streamwise perturbation velocity $u_{(0)}(x, y) = \partial_y \phi_{(0)}(x, y)$. In the finite-amplitude region, the mean flow distortion is seen to fill up the dip of the wake, thereby effectively reducing the shear experienced by the nonlinear travelling waves.

The Fourier expansion (5.5) allows the streamwise evolution of the kinetic energy $E_n(x)$ contained in each harmonic component to be monitored, defined as

$$E_n(x) = \int_{-\infty}^{+\infty} (|\partial_y \phi_{(n)}|^2 + |\partial_x \phi_{(n)}|^2) dy \quad (n > 0), \quad (5.6a)$$

$$E_0(x) = \int_{-\infty}^{+\infty} \frac{1}{2} ((\partial_y \phi_{(0)})^2 + (\partial_x \phi_{(0)})^2) dy. \quad (5.6b)$$

Semi-log plots of the streamwise evolution of $E_n(x)$ are given in figure 10. In the linear region, the fundamental component (thick line) grows exponentially according to $\exp(-k_i^{f+} x)$ until a finite amplitude level is reached. The mean slope over the

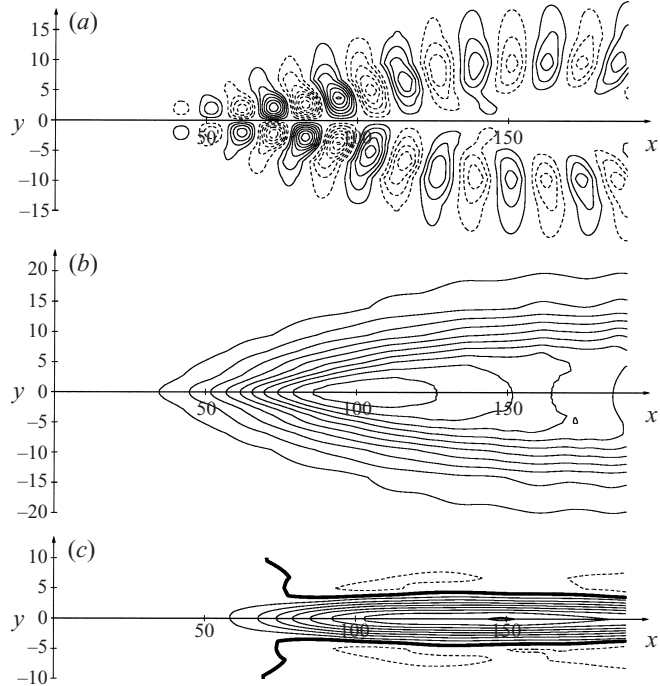


FIGURE 9. Same parallel wake spatial response as in figure 8. (a) Snapshot of fundamental streamwise velocity $u_{(1)}(x,y)$. Solid (dashed) lines pertain to $0.02, 0.04, \dots, 0.14$ ($-0.02, -0.04, \dots, -0.14$) contour levels. (b) Contour levels of envelope of cross-stream velocity $|v_{(1)}|(x,y)$ ($0.02, 0.04, \dots, 0.20$). (c) Isolines of nonlinear mean streamwise velocity correction $u_{(0)}(x,y)$. Thick line separates regions of positive ($0.05, 0.10, \dots, 0.40$ solid lines) and negative (-0.05 dashed line) levels.

interval $20 < x < 60$ is 0.054, close to its theoretical linear value $-2k_i^{\ell+}/\ln 10 = 0.055$ as predicted by the spatial branch $k^{\ell+} = 0.316 - 0.064i$ computed from the Orr-Sommerfeld equation. Although the numerical results are not as clean as in the temporal evolution problem of figure 6, higher harmonics are nonetheless slaved to the fundamental according to $E_n(x) \sim [E_1(x)]^n$. Note however that the variations of the mean-flow correction energy $E_0(x)$ are algebraic rather than exponential. Presumably, the vortical structures produced in the nonlinear domain generate a global mean pressure field which does not simply scale as $[E_1(x)]^2$ with the local linear spatial instability properties. This feature is absent in the temporal evolution case where the waves are strictly streamwise periodic.

With the exception of the mean flow correction, there is no feedback of the fully nonlinear downstream wavetrain on the upstream linear region. A proof of this assertion is obtained by measuring the nonlinear saturation location as a function of the forcing amplitude. The saturation station $x_{n\ell}$ may be precisely defined from the envelope of the fundamental cross-stream velocity component (see figure 9b) along the centreline $y = 0$ as the location where $|v_{(1)}|(x, 0)$ reaches a preset value. The resulting variation of $x_{n\ell}$ with $-\log A_f$ displayed in figure 11 is clearly linear with a measured slope of 35.5, which favourably compares with the theoretical value $-\ln 10/k_i^{\ell+} = 36.0$ predicted by linear theory. The nonlinear saturation station is thus solely controlled by the linear growth phase: it depends only on the forcing amplitude A_f and linear spatial growth rate $-k_i^{\ell+}$.

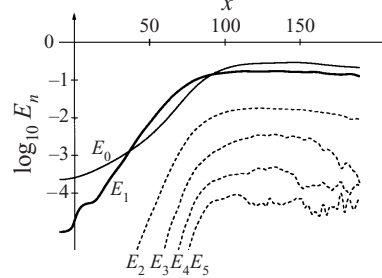


FIGURE 10. Same parallel wake spatial response as in figure 8. Semi-log plots of the streamwise evolution of the energy $E_n(x)$ pertaining to each harmonic component.

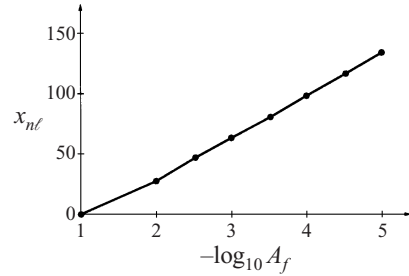


FIGURE 11. Evolution of nonlinear saturation station x_{nl} with forcing amplitude A_f in parallel wake. All other parameter settings same as in figure 8.

The signalling problem (5.1) may be solved for any forcing frequency ω_f and any station X associated with a given CU wake velocity profile. As the AU threshold at X^{ca} is approached, the receptivity of the flow to forcing at the corresponding real absolute frequency ω_0^{ca} increases (Pier *et al.* 2001). At the marginal AU station X^{ca} , upstream and downstream spatial branches pinch, i.e. $k^+(X^{ca}, \omega_0^{ca}) = k^-(X^{ca}, \omega_0^{ca}) = k_0(X^{ca}) \equiv k_0^{ca}$ and by definition $\Omega_k'(k_0^{ca}, X^{ca}) = 0$. Thus, according to (5.3), the spatial response diverges. In other words, the forcing amplitude required to maintain a fixed location of nonlinear saturation x_{nl} vanishes as $(X, \omega_f) \rightarrow (X^{ca}, \omega_0^{ca})$. In this limit, a front structure is obtained connecting a downstream fully nonlinear wavetrain to an upstream decaying tail without any forcing. This is precisely the stationary Dee–Langer front residing in the marginally AU medium.

A numerical implementation of this strategy is illustrated in figure 12(a,b). The forcing frequency is kept constant at $\omega_f = 0.19 \simeq \omega_0^{ca}$ and the signalling problem is solved at $X = 0.20$ and $X = 0.22$, all other parameters being kept at the same settings. The resulting perturbation field is seen to only weakly depend on X as the limit $X^{ca} = 0.24$ is approached. The spatial response distribution arising from a forced problem on the CU side of X^{ca} in effect provides a good approximation of the self-sustained front structure prevailing at X^{ca} in the absence of forcing. The fact that resonance takes place at X^{ca} is not associated with any drastic change in the perturbation field. It is only manifested by pinching of k^+ and k^- branches in the complex k -plane.

It is naturally impractical to perform a numerical simulation at the actual CU/AU transition since in this limit the forcing problem becomes ill-defined. However, one may attempt to verify that the spatial response would reach such a self-sustained front-

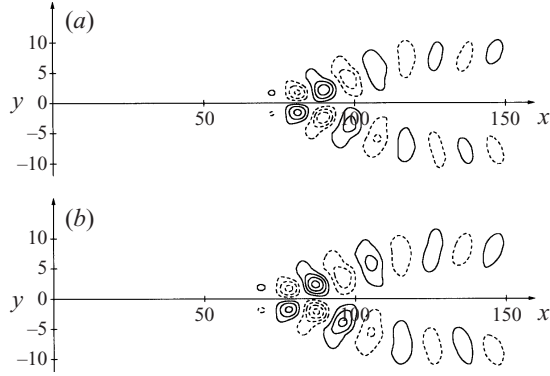


FIGURE 12. Parallel wake spatial response to forcing at frequency $\omega_0^{ca} = 0.19$ as CU/AU transition station $X^{ca} = 0.24$ is approached: isocontours of fundamental streamwise velocity at (a) $X = 0.20$ (b) $X = 0.22$ (0.05, 0.10, 0.15, 0.20 solid lines, -0.05, -0.10, -0.15, -0.20 dashed lines).

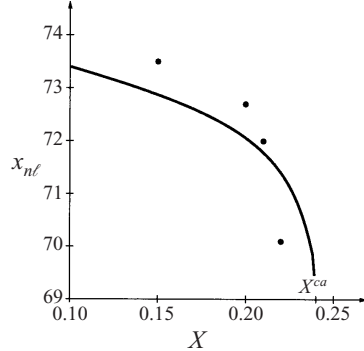


FIGURE 13. Evolution of spatial response nonlinear saturation station $x_{n\ell}$ as the marginal AU wake profile at X^{ca} is approached. Comparison of numerical measurements (dots) and theoretical prediction derived from the linear dispersion relation (solid line).

like structure by tracking the nonlinear saturation station $x_{n\ell}$ as $(X, \omega_f) \rightarrow (X^{ca}, \omega_0^{ca})$. Accordingly, the station $x_{n\ell}$ is measured for different wake velocity profiles pertaining to $X < X^{ca} = 0.24$, for $\omega_f = \omega_0^{ca} = 0.19$ while keeping the forcing amplitude A_f at a fixed constant value. Results are displayed in figure 13 together with the theoretically predicted curve

$$x_{n\ell} = \frac{\ln |\Omega_k'(k^{\ell+}(X, \omega_0^{ca}), X)|}{-k_i^{\ell+}(X, \omega_0^{ca})} + \text{const.}, \quad (5.7)$$

arising from the forced response (5.3). It is straightforward to demonstrate via a Taylor expansion of $\Omega_k'(k^{\ell+}(X, \omega_0^{ca}), X)$ in the neighbourhood of X^{ca} that $|\Omega_k'| \propto |X - X^{ca}|^{1/2}$. Thus, according to (5.7), the nonlinear saturation station $x_{n\ell}$ scales as

$$x_{n\ell} \sim \frac{1}{2} \ln |X - X^{ca}| + \text{const.} \quad \text{when } X \uparrow X^{ca}.$$

The constant appearing in the theoretical prediction (5.7) depends on the forcing amplitude A_f and would in principle be determined by calculating the multiplicative constant in (5.3). We are solely concerned here with the functional form of $x_{n\ell}$ versus X and the constant has been adjusted to achieve a reasonable fit with the numerical

data points. Due to the slow logarithmic divergence and the insufficient accuracy of the measured x_{nl} values, the theoretical curve only poorly fits the numerical data. This somewhat mixed result is not too surprising: the perturbation field is exponentially growing along the stream, and in order to check the validity of the scaling law (5.7), one must extract from the numerics the prefactor multiplying the exponential term. This process is numerically risky since a small error in the evaluation of the growth rate drastically contaminates the evaluation of the prefactor. It is well known that asymptotic limits are often hard to reach numerically!

6. Self-sustained global structures in a spatially developing wake

This part of the study is devoted to the detailed presentation of globally synchronized self-sustained structures, as obtained by direct numerical simulation of the spatially developing wake flow defined in § 2. Their interpretation in terms of the previously identified elements is postponed to the next section.

Numerical simulations are performed in the vorticity/streamfunction formulation

$$\left(\frac{\partial}{\partial t} + U_0(x, y) \frac{\partial}{\partial x} \right) \varpi + U_{0,yy}(x, y) \frac{\partial \psi}{\partial x} + \left(\frac{\partial \psi}{\partial y} \frac{\partial}{\partial x} - \frac{\partial \psi}{\partial x} \frac{\partial}{\partial y} \right) \varpi = \frac{1}{Re} \Delta \varpi, \quad (6.1a)$$

$$\Delta \psi = -\varpi, \quad (6.1b)$$

governing the dynamics of the perturbation fields. Note that the spatial variation of the basic flow is here expressed in terms of $x = XRe$. The following results pertain to a simulation at $Re = 100$ over the domain $0 < x < 200$ ($0 < X < 2$). The numerical scheme exactly follows the method implemented for the signalling problem in § 5 with the parallel basic flow being replaced by the spatially developing wake. Harmonic forcing is suppressed and perturbations are triggered by a small-amplitude initial impulse close to the inlet. The precise localization of the impulse is unimportant and it has been checked that the same final state is obtained for a variety of initial conditions. In the initial stage, the impulse wavepacket grows and spreads in space to perturb the entire domain. Perturbations at each streamwise station slowly synchronize and eventually lead to a global structure tuned at an overall frequency. The following results were obtained at $t = 5000$, with the parameters $n_x = 200$, $\delta x = 1.0$, $n_y = 61$, $l_y = 6$, $\delta t = 0.05$.

Isolines of basic and total vorticity are shown in figure 14(a, b), and of basic and total streamwise velocity in figure 14(c, d). Comparison of basic and total fields shows that the region close to the inlet is governed by small-amplitude dynamics, whereas a nonlinear wavetrain develops further downstream. In figure 14(b) the two vorticity layers of opposite sign are seen to be unstable and to give rise to periodic vortices which completely mask the underlying basic wake flow. The Kármán-like vortex street is more vividly illustrated by the streaklines in figure 14(e). Note that in sketches (a–d) the cross-stream scale has been magnified for clarity, while x - and y -coordinates are on the same scale in (e).

Snapshots of the perturbation vorticity, u - and v -velocity contours and streamlines are displayed in figure 15(a–d). The interpretation of the global mode in terms of an extended nonlinear wavepacket is illustrated by the centreline cross-stream velocity $v(x, 0, t)$ shown in figure 16.

Vorticity time series have been recorded at different locations within the flow in order to ascertain the synchronized behaviour of the global structure. The examination of the associated frequency spectra (figure 17) indicates that all stations are tuned to

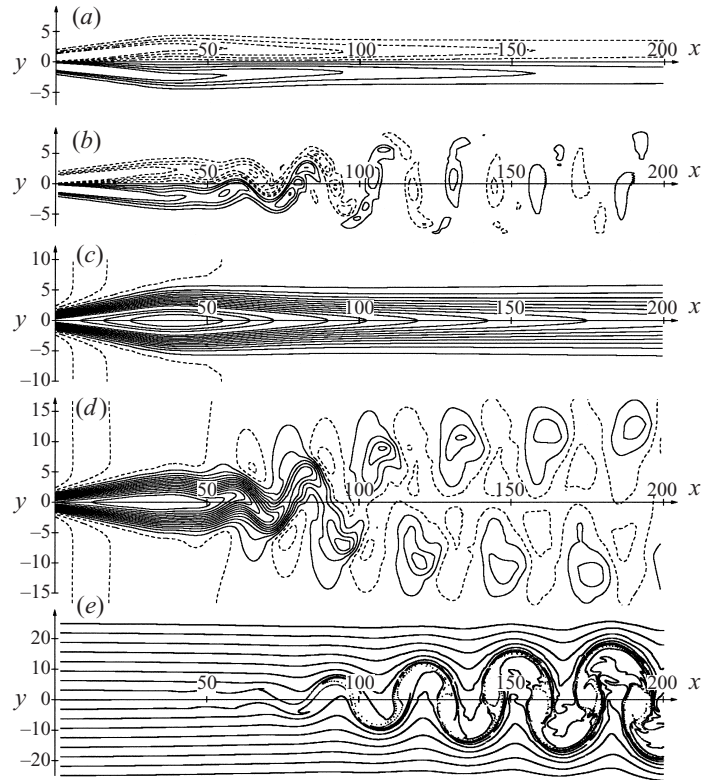


FIGURE 14. Self-sustained global structure at $Re = 100$ and $t = 5000$ in spatially developing wake flow defined in figure 1. (a, b) Basic and total vorticity contours. Solid lines pertain to positive levels (0.05, 0.10, 0.15, 0.20), dashed lines to negative levels (-0.05, -0.10, -0.15, -0.20). (c, d) Basic and total streamwise velocity. Dashed lines represent the levels 0.95, 0.90, 0.85 above the outlet free-stream velocity, solid lines pertain to the levels 0.80, 0.75, ..., 0.10. (e) Corresponding streaklines.

the same global fundamental frequency $\omega_g = 0.186 \pm 0.002$ and its harmonics. At the station $(x, y) = (54, 0)$ (figure 17a) the fluctuations are seen to be almost sinusoidal. Further downstream on the centreline at $(x, y) = (150, 0)$ (figure 17c) higher odd harmonics are excited. Sketch (b) at $(x, y) = (114, 5.6)$ shows that off the centerline all harmonics are represented. Following the analysis of Dušek, Le Gal & Fraunié (1994) and Dušek (1996), the spatial distribution of different harmonics may be computed as displayed in figure 18. These graphs clearly demonstrate the wavetrain nature of the global mode in the downstream region. The nonlinear structures sustained by the basic wake flow give rise to a finite mean-flow distortion as shown in figure 19. Reynolds stresses are seen to induce a mean-flow modification in the form of a pair of counter-rotating large-scale vortices (figure 19a). The associated streamwise velocity contours displayed in figure 19(b) reveal that the velocity defect of the basic wake profiles has been reduced by nonlinearities. The corresponding overall entrainment pattern is displayed in figure 19(c). Most of the dominant dynamics are captured by the fundamental and mean-flow components: superposition of the u -velocity contours pertaining respectively to the fundamental (figure 18a) and mean-flow distortion (figure 19b) yields a pattern which is indeed close to the total perturbation u -velocity

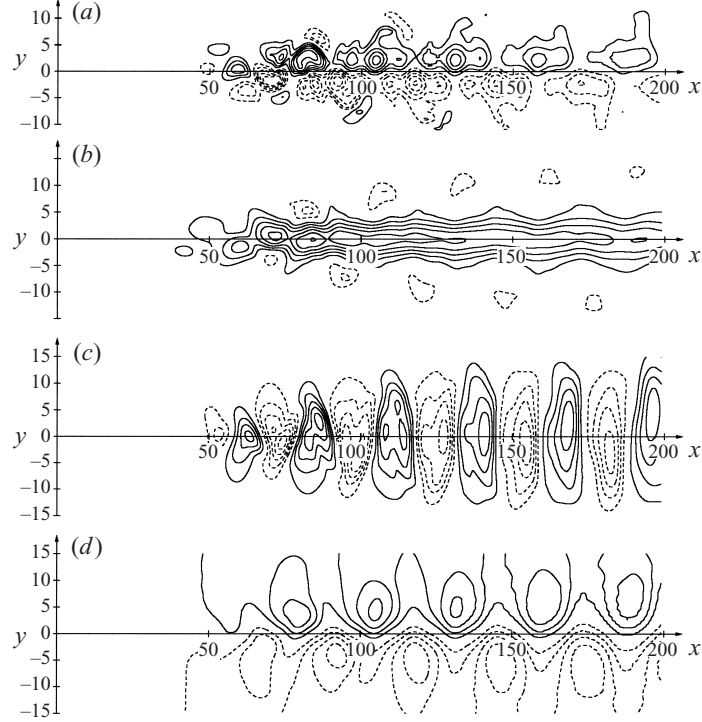


FIGURE 15. Global mode structure: instantaneous perturbation fields. Same conditions as in figure 14. (a) Isovorticity contours ($0.05, 0.10, \dots, 0.25$ solid lines, $-0.05, -0.10, \dots, -0.25$ dashed lines). (b) Streamwise velocity contours ($0.1, 0.2, \dots, 0.6$ solid lines, $-0.1, -0.2$ dashed lines). (c) Cross-stream velocity contours ($0.05, 0.10, \dots, 0.25$ solid lines, $-0.05, -0.10, \dots, -0.25$ dashed lines). (d) Streamlines ($0.5, 1.0, 1.5, 2.0$ solid, $-0.5, -1.0, -1.5, -2.0$ dashed).

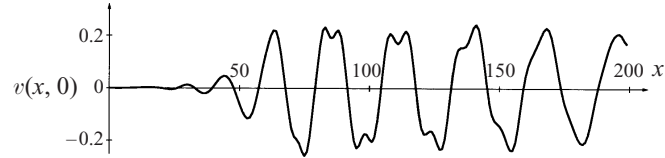


FIGURE 16. Global mode structure: instantaneous centreline cross-stream velocity $v(x, 0, t)$. Same conditions as in figure 14.

contours (figure 15b). In the same line of thought as in § 5, one may display the streamwise evolution of the energy $E_n(x)$ contained in each harmonic (see equations (5.6)) as shown in figure 20. Higher harmonics ($n > 1$) are seen to reach very low amplitude levels even in the nonlinear region. This observation is also corroborated by the power spectra of figure 17.

It may be concluded that the spatio-temporal development of the vortex street is essentially determined by three components: the imposed unstable basic flow, the fundamental wavetrain of frequency ω_g which it sustains and the ensuing mean-flow distortion produced by Reynolds stresses.

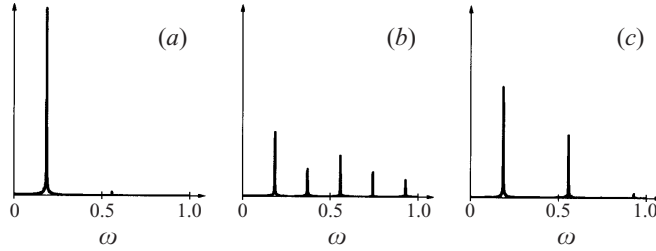


FIGURE 17. Global mode power spectrum of vorticity time series at stations (a) $x = 54$, $y = 0$, (b) $x = 114$, $y = 5.6$, (c) $x = 150$, $y = 0$, based on signal recorded over $5000 < t < 10000$. Same conditions as in figure 14.

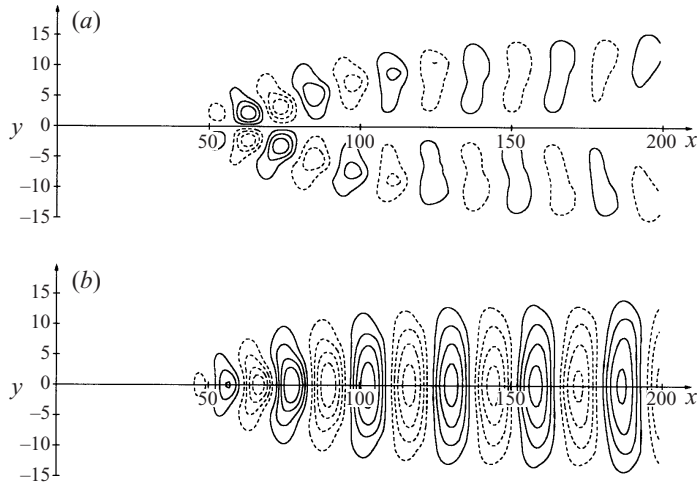


FIGURE 18. Global mode structure: fundamental velocity components. (a) Streamwise velocity contours (0.05, 0.10, 0.15 solid lines, $-0.05, -0.10, -0.15$ dashed lines). (b) Cross-stream velocity contours (0.05, 0.10, 0.15, 0.20 solid lines, $-0.05, -0.10, -0.15, -0.20$ dashed lines). Same conditions as figure 14.

7. Interpretation of the vortex street as a steep global mode

The objective of this section is to demonstrate that the vortex street observed in the direct numerical simulations of spatially developing wakes in § 6 is indeed a steep global mode as defined by Pier *et al.* (1998). In other words, its frequency obeys the marginal stability criterion (1.2) and its spatio-temporal structure is controlled by a front which generates nonlinear travellings wavetrains further downstream.

The application of the steep frequency selection criterion (1.2) to the local absolute frequency $\omega_0(X)$ calculated in § 3 and displayed in figure 3 yields

$$X^{ca} = 0.24 \quad \text{and} \quad \omega_0^{ca} = \omega_0(X^{ca}) = 0.190, \quad (7.1)$$

to be compared with the observed global vortex street frequency $\omega_g = 0.186$. The prediction (7.1), which is only a leading-order approximation in $\epsilon = 1/Re = 0.01$, is seen to be in excellent agreement with the value obtained by direct numerical simulation. The observed frequency should also be compared with the complex linear global frequency $\omega_s = 0.143 + 0.008i$ obtained from the linear saddle-point

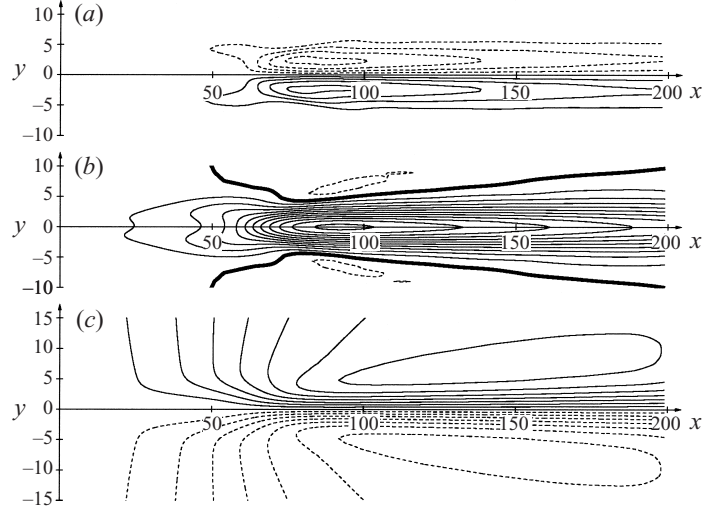


FIGURE 19. Global mode structure: finite-amplitude mean flow correction. (a) Isovorticity contours (0.04, 0.08, 0.12, 0.16 solid lines, -0.04, -0.08, -0.12, -0.16 dashed lines). (b) Streamwise velocity contours. Thick line separates regions of positive (0.05, 0.10, ..., 0.55 solid lines) and negative (-0.05 dashed line) levels. (c) Streamlines (0.2, 0.4, ..., 1.4 solid lines, -0.2, -0.4, ..., -1.4 dashed lines). Same conditions as in figure 14.

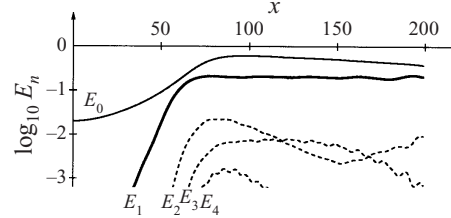


FIGURE 20. Semi-log plot of global mode spatial energy distribution of different harmonics $E_n(x)$. Same conditions as in figure 14.

criterion (1.1). The complex ω_s only applies to uniformly linear global mode structures, and does not capture the nonlinear dynamics governing the present vortex street.

The global mode spatial distribution is compared with the associated front structure and local nonlinear travelling wavetrains in figure 21. Contour levels of the fundamental streamwise velocity pertaining to the vortex street (figure 21a, already displayed in figure 18a) are compared with the same field for the quasi-front of frequency $\omega_0^{ca} = 0.19$ at $X = 0.22$ (figure 21b, already displayed in figure 12b). The pattern in figure 12(b) has been suitably shifted in the streamwise direction and in time so as to adjust amplitude and phase to those of figure 21(a). Although this X -station is below the absolute transition point $X^{ca} = 0.24$, the structure of the fundamental is seen to be approximately reproduced by the front.

The same vortex street contour levels (figure 21a) are compared with those for a fully nonlinear travelling wave at $X = 1.40$ obtained via temporal numerical simulation (figure 21c). More specifically, the local wavenumber $k^{n\ell+} = 0.27$ prevailing at $X = 1.40$ and $\omega_0^{ca} = 0.19$ is determined from the local nonlinear dispersion relation

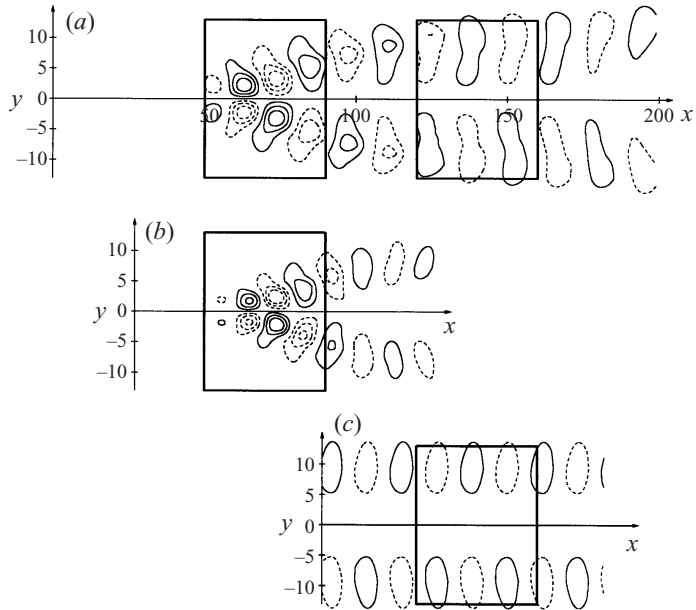


FIGURE 21. Interpretation of global mode structure (a) in terms of a front (b) and fully nonlinear travelling waves (c). Isolevels of fundamental streamwise velocity component are shown (0.05, 0.10, 0.15 solid lines, -0.05, -0.10, -0.15 dashed lines).

plotted in figure 5(a), and a streamwise periodic temporal simulation is performed as detailed in §4. Here again, the downstream region of the global mode is seen to be approximately represented by nonlinear wavetrains which travel according to the local nonlinear dispersion relation at each streamwise station.

Note however that the characteristic wavelengths of the quasi-front in (b) and nonlinear travelling wave in (c) appear to be somewhat smaller to those of the corresponding global mode structure in (a). This feature may be related to the frequency difference between the two cases: $\omega_0^{ca} = 0.190$ in (b, c) and $\omega_g = 0.186$ in (a). The wavemaker triggering the vortex street is located at the marginally AU station $x^{ca} = ReX^{ca} = 24$; however, full nonlinearity is only attained about a wavelength downstream of this location. Thus the region where the global mode structure reaches finite amplitude is actually pushed to the downstream side of the AU region $24 < x < 55$. This result is not all that surprising: the front characterizing the streamwise transition between linear waves and a fully nonlinear wavetrain is known to typically extend over one wavelength (see e.g. van Saarloos 1987).

8. Conclusion

This study has demonstrated that the steep global modes previously identified and analysed in one-dimensional CGL evolution equations also arise in spatially developing shear flows exhibiting a region of absolute instability. The self-sustained structures have been shown to be controlled by a front located at the upstream edge of the AU region which acts as a wavemaker to generate nonlinear travelling waves in its wake. Provided that the streamwise variations of the underlying basic flow are sufficiently slow (WKBJ approximation), such wavetrains are governed at each

station by the associated local nonlinear dispersion relation obtained from a purely temporal evolution problem on the local shear flow profile considered as parallel. Fast streamwise variations are confined to the front layer where the full Navier–Stokes equations have to be resolved for the wave field on the fast x -scale.

It should again be noted that the stationary fronts identified in the present shear flow framework are of the same nature as the propagating fronts studied in the context of pattern formation: the criterion (1.2) is merely an application of the marginal instability criterion of Dee & Langer (1983) and van Saarloos (1987, 1988). The present findings are also consistent with the nature of the nonlinear impulse response in parallel wakes studied by Delbende & Chomaz (1998). Furthermore, the conjecture put forward by Monkewitz & Nguyen (1987) has been fully confirmed: the first streamwise station X^{ca} of non-negative absolute growth rate indeed supports a front which imposes its frequency ω_0^{ca} on the entire flow.

The present approach constitutes a significant departure from the landmark nonlinear hydrodynamic instability analyses of spatially evolving shear flows developed by Goldstein & Leib (1988) and Goldstein & Hultgren (1988). These investigations require the simultaneous enforcing of the assumptions of overall small wave amplitude and slow streamwise variations. As a result, finite-amplitude effects arise only within nonlinear critical layers of small cross-stream extent. An asymptotically consistent description of the streamwise development of perturbations of given frequency may then be obtained for convectively unstable shear flows. In the present study, the small-amplitude assumption has been totally relaxed and only the slow streamwise variation hypothesis has been retained. The fully nonlinear evolution of perturbations of order unity may then be captured either for the forced problem in CU flows or for self-sustained structures in flows with an AU region. Nonlinearities then extend over the entire shear region in the cross-stream direction. Whereas critical layer studies succeed in achieving a quasi-analytic formulation of the forced dynamics, the present approach relies on local numerical simulations to identify the various constitutive elements of the dominant WKBJ approximation. It is surmised that the same fully nonlinear theory is applicable to a wide variety of spatially evolving shear flows whether they are in a self-sustained mode or subjected to forcing.

A systematic asymptotic approximation scheme of the kind presented in Pier *et al.* (2001) has not been attempted here. Furthermore, the Reynolds number has been kept relatively small at $Re = 100$. Larger values of Re increase the streamwise extent of the computational domain and computing time. Moreover, exploratory simulations indicate that secondary instabilities occur for the present basic flow beyond $Re \sim 200$. However, computation of the local nonlinear wavetrains on a streamwise periodic interval is not affected by secondary instabilities. We therefore presume that a synchronized finite-amplitude vortex shedding régime exists analytically for all large Re but is unstable in the spatially developing simulation beyond $Re \sim 200$. It is thus impractical to push Re up to larger values in order to move closer to the WKBJ limit $\epsilon = 1/Re = 0$.

It should be emphasized that the steep frequency selection criterion (1.2) which has been demonstrated here to apply to real flows is purely based on the local linear dispersion relation, although it pertains to fully nonlinear synchronized structures. The saddle-point criterion (1.1) is also linear but it is solely applicable to strictly linear global modes. And indeed, the numerically obtained $\omega_g = 0.186$ is much closer to $\omega_0^{ca} = 0.190$ of criterion (1.2) than to $\omega_s = 0.143 + 0.008i$ of criterion (1.1), which in any case is incompatible with the saturated nonlinear wavetrains observed downstream of the front at X^{ca} . Furthermore, as demonstrated by Pier (1999), steep

global modes are triggered as soon as local linear absolute instability appears, while linear global modes become unstable only when the linear AU region is of sufficiently large extent (Chomaz *et al.* 1991). To confirm this argument, the same simulation has been carried out with a spatially developing wake obtained for a pressure gradient designed to yield a minimum centerline velocity of 0.047 instead of 0.010 as in figure 1. The saddle-point frequency is then $\omega_s = 0.155 - 0.001i$, which corresponds to a decaying linear global mode. Nevertheless, there is still a small locally absolutely unstable region $0.34 < X < 0.44$ with $\omega_{0,i}^{max} = 0.001$. In this case, a steep global mode is observed in the direct numerical simulation, whereas no self-sustained structure survives if nonlinear terms are turned off. This result is entirely consistent with the transition scenario outlined in Pier *et al.* (2001).

It is somewhat paradoxical that the intricate complex X -plane analyses developed over the years to uncover the selection properties of linear global modes are masked in practice by the onset of local absolute instability which immediately prevails and imposes its frequency and the overall structure of the synchronized oscillations.

As a final note of caution, it should be stressed that the present analysis cannot be obviously extended to bluff-body wakes where the AU region lies immediately behind the obstacle. In spite of the fact that the synthetic wake considered here is purely co-flowing, it can nonetheless sustain a synchronized vortex street which qualitatively displays the same features.

The authors are grateful to Jean-Marc Chomaz and Arnaud Couairon for enlightening discussions. The expert advice and suggestions of Carlo Cossu played an essential rôle in the design and validation of the numerical scheme.

REFERENCES

- BENDER, C. M. & ORSZAG, S. A. 1978 *Advanced Mathematical Methods for Scientists and Engineers*. McGraw-Hill.
- BERS, A. 1983 Space-time evolution of plasma instabilities – absolute and convective. In *Handbook of Plasma Physics* (ed. M. Rosenbluth & R. Sagdeev), pp. 451–517. North-Holland.
- BRIGGS, R. 1964 *Electron-Stream Interaction with Plasmas*. MIT Press.
- CANUTO, C., HUSSAINI, M. J., QUARTERONI, A. & ZANG, T. A. 1988 *Spectral Methods in Fluid Dynamics*. Springer.
- CHOMAZ, J.-M. 1992 Absolute and convective instabilities in nonlinear systems. *Phys. Rev. Lett.* **69**, 1931–1934.
- CHOMAZ, J.-M. & COUAIRON, A. 1999 Against the wind. *Phys. Fluids* **11**, 2977–2983.
- CHOMAZ, J.-M., HUERRE, P. & REDEKOPP, L. 1991 A frequency selection criterion in spatially developing flows. *Stud. Appl. Maths* **84**, 119–144.
- COUAIRON, A. & CHOMAZ, J.-M. 1996 Global instabilities in fully nonlinear systems. *Phys. Rev. Lett.* **77**, 4015–4018.
- COUAIRON, A. & CHOMAZ, J.-M. 1997a Absolute and convective instabilities, front velocities and global modes in nonlinear systems. *Physica D* **108**, 236–276.
- COUAIRON, A. & CHOMAZ, J.-M. 1997b Pattern selection in the presence of a cross flow. *Phys. Rev. Lett.* **79**, 2666–2669.
- COUAIRON, A. & CHOMAZ, J.-M. 1999 Fully nonlinear global modes in slowly varying flows. *Phys. Fluids* **11**, 3688–3703.
- CRIGHTON, D. & GASTER, M. 1976 Stability of slowly diverging jet flow. *J. Fluid Mech.* **77**, 397–413.
- CROSS, M. & HOHENBERG, P. 1993 Pattern formation outside of equilibrium. *Rev. Mod. Phys.* **65**, 851–1112.
- DEE, G. & LANGER, J. 1983 Propagating pattern selection. *Phys. Rev. Lett.* **50**, 383–386.
- DELBENDE, I. & CHOMAZ, J.-M. 1998 Nonlinear convective/absolute instabilities in parallel two-dimensional wakes. *Phys. Fluids* **10**, 2724–2736.

- DRAZIN, P. G. & REID, W. H. 1981 *Hydrodynamic Stability*. Cambridge University Press.
- DUŠEK, J. 1996 Spatial structure of the Bénard von Kármán instability. *Eur. J. Mech. B/Fluids* **15**, 619–650.
- DUŠEK, J., LE GAL, P. & FRAUNIÉ, P. 1994 A numerical and theoretical study of the first Hopf bifurcation in a cylinder wake. *J. Fluid Mech.* **264**, 59–80.
- EHRENSTEIN, U. & KOCH, W. 1989 Nonlinear bifurcation study of plane Poiseuille flow. *DLR Forschungsbericht* 89–42. Institut für theoretische Strömungsmechanik, Göttingen.
- EHRENSTEIN, U. & KOCH, W. 1995 Homoclinic bifurcation in Blasius boundary-layer flow. *Phys. Fluids* **7**, 1282–1291.
- GOLDSTEIN, M. & HULTGREN, L. 1988 Nonlinear spatial evolution of an externally excited instability wave in a free shear layer. *J. Fluid Mech.* **197**, 295–330.
- GOLDSTEIN, M. & LEIB, S. 1988 Nonlinear roll-up of externally excited free shear layers. *J. Fluid Mech.* **191**, 481–515.
- HAMMOND, D. & REDEKOPP, L. 1997 Global dynamics of symmetric and asymmetric wakes. *J. Fluid Mech.* **331**, 231–260.
- HUERRE, P. & MONKEWITZ, P. 1985 Absolute and convective instabilities in free shear layers. *J. Fluid Mech.* **159**, 151–168.
- HUERRE, P. & MONKEWITZ, P. 1990 Local and global instabilities in spatially developing flows. *Ann. Rev. Fluid Mech.* **22**, 473–537.
- HUERRE, P. & ROSSI, M. 1998 Hydrodynamic instabilities in open flows. In *Hydrodynamics and Nonlinear Instabilities* (ed. C. Godrèche & P. Manneville), pp. 81–294. Cambridge University Press.
- JIN, G. & BRAZA, M. 1993 A nonreflecting outlet boundary condition for incompressible unsteady Navier–Stokes calculations. *J. Comput. Phys.* **107**, 239–253.
- KOCH, W. 1985 Local instability characteristics and frequency determination on self-excited wake flows. *J. Sound Vib.* **99**, 53–83.
- LE DIZÈS, S., HUERRE, P., CHOMAZ, J. & MONKEWITZ, P. 1993 Nonlinear stability analysis of slowly-diverging flows: limitations of the weakly nonlinear approach. In *Proc. IUTAM Symp. on Bluff-Body Wakes, Dynamics and Instabilities* (ed. H. Eckelmann, J. Graham, P. Huerre & P. Monkevitz), pp. 147–152. Springer.
- LE DIZÈS, S., HUERRE, P., CHOMAZ, J.-M. & MONKEWITZ, P. 1996 Linear global modes in spatially developing media. *Phil. Trans. R. Soc. Lond. A* **354**, 169–212.
- LINGWOOD, R. J. 1995 Absolute instability of the boundary layer on a rotating disk. *J. Fluid Mech.* **299**, 17–33.
- LINGWOOD, R. J. 1996 An experimental study of absolute instability of the rotating-disk boundary-layer flow. *J. Fluid Mech.* **314**, 373–405.
- MEUNIER, M., PROCTOR, M., SOKOLOFF, D., SOWARD, A. & TOBIAS, S. 1997 Asymptotic properties of a nonlinear $\omega\omega$ -dynamo wave: period, amplitude and latitude dependence. *Geophys. Astrophys. Fluid Dyn.* **86**, 249–285.
- MONKEWITZ, P., BECHERT, D., BARSIKOW, B. & LEHMANN, B. 1990 Self-excited oscillations and mixing in a heated round jet. *J. Fluid Mech.* **213**, 611–639.
- MONKEWITZ, P., HUERRE, P. & CHOMAZ, J. 1993 Global linear stability analysis of weakly non-parallel shear flows. *J. Fluid Mech.* **251**, 1–20.
- MONKEWITZ, P. & NGUYEN, L. 1987 Absolute instability in the near-wake of two-dimensional bluff bodies. *J. Fluid Struct.* **1**, 165–184.
- PIER, B. 1999 Comportement non linéaire synchronisé dans les écoulements cisailés. PhD thesis, École polytechnique, 91128 Palaiseau, France.
- PIER, B. & HUERRE, P. 1996 Fully nonlinear global modes in spatially developing media. *Physica D* **97**, 206–222.
- PIER, B., HUERRE, P. & CHOMAZ, J.-M. 2001 Bifurcation to fully nonlinear synchronized structures in slowly varying media. *Physica D* **148**, 49–96.
- PIER, B., HUERRE, P., CHOMAZ, J.-M. & COUAIRON, A. 1998 Steep nonlinear global modes in spatially developing media. *Phys. Fluids* **10**, 2433–2435.
- PROVANSAL, M., MATHIS, C. & BOYER, L. 1987 Bénard–von Kármán instability: transient and forced regimes. *J. Fluid Mech.* **182**, 1–22.
- SAARLOOS, W. VAN 1987 Dynamical velocity selection: marginal stability. *Phys. Rev. Lett.* **58**, 2571–2574.

- SAARLOOS, W. VAN 1988 Front propagation into unstable states: marginal stability as a dynamical mechanism for velocity selection. *Phys. Rev. A* **37**, 211–229.
- SAARLOOS, W. VAN 1989 Front propagation into unstable states. ii. linear versus nonlinear marginal stability and rate of convergence. *Phys. Rev. A* **39**, 6367–6390.
- SAARLOOS, W. VAN & HOHENBERG, P. 1992 Fronts, pulses, sources and sinks in generalized complex Ginzburg–Landau equations. *Physica D* **56**, 303–367.
- SCHÄR, C. & SMITH, R. 1993 Shallow-water flow past isolated topography. Part ii: Transition to vortex shedding. *J. Atmos. Sci.* **50**, 1404–1412.
- SOWARD, A. 2001 Thin aspect ratio $\alpha\omega$ -dynamo in galactic discs and stellar shells. In *Advances in Nonlinear Dynamos* (ed. M. Núñez & A. Mas), *The Fluid Mechanics of Astrophysics and Geophysics*. To appear.
- SOWARD, A. & JONES, C. 1983 The linear stability of the flow in the narrow gap between two concentric rotating spheres. *Q. J. Mech. Appl. Math.* **36**, 19–42.
- STRYKOWSKI, P. & NICCUM, D. 1991 The stability of counter-current mixing layers in circular jets. *J. Fluid Mech.* **227**, 309–343.
- TAYLOR, M. & PEAKE, N. 1999 A note on the absolute instability of wakes. *Eur. J. Mech. B/Fluids* **18**, 573–579.
- TOBIAS, S., PROCTOR, M. & KNOBLOCH, E. 1998 Convective and absolute instabilities of fluid flows in finite geometry. *Physica D* **113**, 43–72.
- TRIANTAFYLLOU, G. & KARNIADAKIS, G. 1990 Computational reducibility of unsteady viscous flows. *Phys. Fluids A* **2**, 653–656.
- TRIANTAFYLLOU, G., TRIANTAFYLLOU, M. & CHRYSOSTOMIDIS, C. 1986 On the formation of vortex streets behind stationary cylinders. *J. Fluid. Mech.* **170**, 461–477.
- WOODLEY, B. & PEAKE, N. 1997 Global linear stability analysis of thin aerofoil wakes. *J. Fluid. Mech.* **339**, 239–260.

[A6]

Nonlinear synchronization in open flows

B. Pier & P. Huerre

Journal of Fluids and Structures **15**, 471–480 (2001)

doi:10.1006/jfls.2000.0349

<https://hal.archives-ouvertes.fr/hal-00119923>

NONLINEAR SYNCHRONIZATION IN OPEN FLOWS

B. PIER* AND P. HUERRE

*Laboratoire d'Hydrodynamique (LadHyX), CNRS – École Polytechnique
F-91128 Palaiseau Cedex, France*

(Received 14 September 2000, and in final form 7 November 2000)

The selection criteria governing finite-amplitude synchronized oscillating states are discussed for model systems and real wake flows in a domain of infinite streamwise extent. Two types of nonlinear global modes are possible: *hat* modes with overall smoothly varying amplitude and *elephant* modes with a sharp front. The vortex street in wake flows is of elephant type, as observed in direct numerical simulations of a real spatially developing wake. Furthermore, the elephant frequency selection criterion is in excellent agreement with the numerically determined vortex shedding frequency.

© 2001 Academic Press

1. INTRODUCTION

A VARIETY OF OPEN FLOWS may sustain globally synchronized oscillations. Wakes behind bluff-bodies are well known [for a review see Williamson (1996)] to undergo a transition to a periodic vortex shedding régime at moderate Reynolds numbers. Experimentally and numerically, the features of a globally synchronized vortex street are now well documented [e.g., Provansal *et al.* (1987), Hammond & Redekopp (1997)]. However, the selected frequency of the global structure has not been theoretically predicted in the framework of hydrodynamic stability theory. The aim of the present paper is to discuss recent progress made in the identification of resonance mechanisms which are responsible for global synchronization in spatially developing flows. We restrict here our attention to one-dimensional complex Ginzburg–Landau (CGL) equations with spatially varying coefficients in an infinite domain and to two-dimensional spatially developing wake flows governed by the Navier–Stokes (NS) equations. The paper is mainly based on the recent dissertation of Pier (1999) and the corresponding publications by Pier & Huerre (1996), Pier *et al.* (1998), Pier *et al.* (2001) and Pier & Huerre (2001). For a general background on the hydrodynamic stability theory of spatially developing flows, the reader is referred to the review articles and tutorial presentations of Huerre & Monkewitz (1990), Huerre & Rossi (1998) and Huerre (2000). A brief summary of relevant issues is given below.

The existence of self-sustained oscillations in shear flows is closely related to the transition from *convective* to *absolute instability* (Briggs 1964; Bers 1983). In convectively unstable (CU) systems, the basic flow carries growing perturbations away in the downstream direction, and the system eventually returns to its unperturbed state. Hence, if a flow changes from local stability to convective instability, only its transient response to perturbations is affected. In a locally stable configuration all perturbations are damped, whereas in a CU basic flow they grow in the downstream direction. In the latter configuration, perturbations eventually leave the domain of interest: in the long term, the flow is globally

*Present address: Department of Applied Mathematics and Theoretical Physics, University of Cambridge, Silver Street, Cambridge CB3 9EW, UK. E-mail: b.pier@damtp.cam.ac.uk

stable and it may only be kept out of equilibrium if perturbations are continuously entering the inflow boundary. Thus, CU flows may be interpreted as *amplifiers* since perturbations entering the inlet grow along the stream until they leave the system at the outlet.

In contrast, transition from convective to absolute instability drastically changes the dynamical behaviour. In absolutely unstable (AU) systems, instabilities grow *in situ* and survive for all times. A self-sustained nontrivial state may therefore be observed without external input. Thus, as far as the long term asymptotic behaviour is concerned, transition from local stability to convective instability proves irrelevant, whereas transition from convective to absolute instability plays a crucial rôle.

The above-mentioned instability properties are defined for infinite and spatially homogenous systems. Since real flows develop in the streamwise direction, stable, CU and AU domains may coexist as the local properties vary along the stream. Under the assumption that the streamwise variations be small on a typical instability length scale, the previous definitions still apply locally at each streamwise station. In wake flows at moderate Reynolds numbers, which are of particular interest to readers of this Special Issue, the transient régime leads to a stationary time-periodic state; the flow globally behaves as an *oscillator*. Characteristics such as spatial structure and global frequency become intrinsic to the flow: They are selected in the bulk and largely independent of inflow conditions.

The following questions then arise. (i) Under which conditions does global instability occur? Does global instability coincide with the onset of local absolute instability or is an AU domain of finite extent required? (ii) In the case of globally synchronized oscillations, how is the global frequency determined? Which part of the flow acts as a wave maker? (iii) How is the global behaviour affected by nonlinearities? Are finite-amplitude oscillations governed by linear or nonlinear selection criteria? What is the importance of the mean flow correction generated by nonlinear interactions?

In the following, these issues are preferentially addressed in the context of streamwise developing flows in an *infinite domain*, whether in the form of CGL model equations or real wakes. In the latter instance, we solely consider wakes produced by a velocity deficit introduced at some streamwise station and boldly set aside the wake producing body. This assumption is in marked contrast with the recent investigations by Couairon & Chomaz (1997, 1999a, b) of nonlinear global modes governed by one-dimensional CGL model equations in *semi-infinite domains*. In this case, global mode onset takes place whenever a front succeeds in propagating upstream against the advecting flow, thereby getting pinned at the upstream boundary point. This precisely takes place when transition from convective to absolute instability occurs at the upstream boundary. Furthermore, Couairon & Chomaz (1999b) have derived scaling laws for the global mode characteristic length scale and its streamwise shape near onset which are in excellent agreement with experimental and numerical studies of vortex shedding behind bluff bodies by Goujon-Durand *et al.* (1994) and Zielinska & Wesfreid (1995). Such a scenario is also supported by the direct numerical simulations of the nonlinear impulse response in parallel wakes conducted by Delbende & Chomaz (1998): although the impulse response is of finite amplitude, its upstream edge is governed by linear dynamics.

2. SCALE SEPARATION

The theoretical formulation underlying all global mode analyses, whether linear or nonlinear, essentially relies on the assumption of *slow streamwise variations* of instability properties. This hypothesis is required if one is to establish a specific relationship between global behaviour and local properties.

At an intuitive level of understanding, in open systems the mean flow introduces a preferred streamwise direction along which the entire dynamics develops. Let x denote the streamwise distance, increasing from the inlet to the outlet. The coordinate x appears both as a *variable* in streamwise derivative operators related to the instability properties and as a *parameter* to account for the streamwise evolution of the basic flow. If λ denotes a typical instability length scale and L the streamwise evolution length scale of the basic flow, weak inhomogeneity is characterized by the small parameter

$$\varepsilon \equiv \frac{\lambda}{L} \ll 1. \quad (1)$$

Under assumption (1), the parametric streamwise dependence of the dynamics only occurs through the slow coordinate $X = \varepsilon x$. At leading order, the slow parameter X may be considered independent of the fast variable x . Local instability characteristics are then retrieved by freezing X in the governing equations and studying the equivalent homogenous system in the infinite domain $-\infty < x < +\infty$. Hence the fast evolving local dynamics is slaved to the slow evolution of the basic flow. This technique is fully justified by resorting to the method of multiple scales (Crighton & Gaster 1976; Bender & Orszag 1978).

3. MODEL FLOWS AND REAL FLOWS

The global behaviour of spatially developing flows has typically been studied in the context of the one-dimensional CGL model or the complete two-dimensional Navier–Stokes (NS) equations.

The spatially inhomogenous Ginzburg–Landau evolution equation for a complex field $\psi(x, t)$ may conveniently be written as

$$\begin{aligned} i \frac{\partial \psi}{\partial t} &= \left(\omega_0(X) + \frac{1}{2} \omega_{kk}(X) k_0(X)^2 \right) \psi + i \omega_{kk}(X) k_0(X) \frac{\partial \psi}{\partial x} \\ &\quad - \frac{1}{2} \omega_{kk}(X) \frac{\partial^2 \psi}{\partial x^2} + \gamma(X) |\psi|^2 \psi, \end{aligned} \quad (2)$$

where ω_0 and k_0 denote the absolute frequency and wavenumber, respectively, ω_{kk} the second derivative of the frequency with respect to wavenumber. The choice $\gamma_i \equiv \text{Im } \gamma < 0$ ensures that nonlinearities are stabilizing everywhere. All complex coefficients of equation (2) depend on $X = \varepsilon x$ to enforce assumption (1) of weak spatial inhomogeneity.

For two-dimensional incompressible flows, the total streamfunction $\Psi(x, y, t)$ is governed by the nondimensional vorticity equation

$$\left(\frac{\partial}{\partial t} + \frac{\partial \Psi}{\partial y} \frac{\partial}{\partial x} - \frac{\partial \Psi}{\partial x} \frac{\partial}{\partial y} \right) \Delta \Psi = \frac{1}{\text{Re}} \Delta^2 \Psi, \quad (3)$$

where y denotes the cross-stream coordinate and Re the Reynolds number. Real flows fulfill the assumption of slow streamwise development in high Reynolds number situations, and the inhomogeneity parameter then reads

$$\varepsilon = \frac{1}{\text{Re}}. \quad (4)$$

When $\varepsilon \ll 1$, the leading-order time-independent basic flow resulting from (3) obeys the Prandtl boundary-layer equation

$$\left(\frac{\partial \Psi}{\partial y} \frac{\partial}{\partial X} - \frac{\partial \Psi}{\partial X} \frac{\partial}{\partial y} \right) \frac{\partial \Psi}{\partial y} = - \frac{dP}{dX} + \frac{\partial^3 \Psi}{\partial y^3}, \quad (5)$$

where the streamwise pressure gradient dP/dX arises as an integration constant. Basic streamwise and cross-stream velocity components are then obtained as $U(y; X) = \partial \Psi / \partial y$ and $V(y; X) = -\varepsilon \partial \Psi / \partial X$, respectively. Decomposition of the total streamfunction into basic field and finite-amplitude perturbations according to $\Psi(x, y, t) = \int_0^y U(\eta; X) d\eta + \psi(x, y, t)$ yields the governing vorticity equation for $\psi(x, y, t)$ as

$$\left(\frac{\partial}{\partial t} + U(y; X) \frac{\partial}{\partial x} \right) \Delta \psi - \frac{\partial^2 U}{\partial y^2}(y; X) \frac{\partial \psi}{\partial x} + \left(\frac{\partial \psi}{\partial y} \frac{\partial}{\partial x} - \frac{\partial \psi}{\partial x} \frac{\partial}{\partial y} \right) \Delta \psi = \frac{1}{Re} \Delta^2 \psi. \quad (6)$$

Although real flows are two dimensional, there is only one slow streamwise coordinate X that accounts for the evolution of local instability properties as described by a local dispersion relation. The study of two-dimensional flows is more complex since cross-stream eigenfunctions have to be computed; however, the analysis of CGL or NS global modes proceeds in exactly the same manner since all the fast evolving features are slaved to X .

Note that in the CGL model (2) any variations of the complex coefficients with X may be considered. In the hydrodynamic context (6) however, the basic flow $U(y; X)$ governed by (5) is uniquely determined by the inlet velocity profile, say $U(y; X = 0)$, and the streamwise pressure distribution $P(X)$ for $X > 0$. In a self-consistent formulation, the velocity profiles $U(y; X)$ appearing as coefficients in (6) cannot be arbitrarily specified. In the present analysis, a coflowing wake profile is chosen for $U(y; X = 0)$ and the pressure field $P(X)$ is then carefully tailored so that the essential features of experimental wake flows are reproduced. In this procedure, a “synthetic wake” is thereby generated without requiring the presence of a solid obstacle [cf. Figure 2(a)]!

4. LINEAR RESONANCE CRITERION

In a strictly linear framework, theoretically consistent results have first been derived by Chomaz *et al.* (1991) for the linear version of model (2) and by Monkewitz *et al.* (1993) for the linear version of the vorticity equation (6). The essential physical property is the complex local absolute frequency $\omega_0(X)$ defined in classical fashion (Briggs 1964; Bers 1983) by imposing a zero group velocity condition on the *local linear dispersion relation*

$$\omega = \Omega^l(k, X). \quad (7)$$

The form of the CGL model (2) already displays its dependence on $\omega_0(X)$, whereas for real flows the dispersion relation (7) is derived by solving the Orr-Sommerfeld equation applied to the velocity profiles $U(y; X)$ prevailing at each station X .

The criterion for linear global instability is then based on the variations of $\omega_0(X)$ and states that the complex frequency ω_s^l of a self-sustained linear global mode is given by the saddle-point condition

$$\frac{d\omega_0}{dX}(X_s^l) = 0 \quad \text{and} \quad \omega_s^l = \omega_0(X_s^l), \quad (8)$$

where it is understood that $\omega_0(X)$ has been analytically continued in the complex X -plane. In general, the saddle point X_s^l does not occur on the real axis, and linear global instability characterized by $\text{Im } \omega_s^l > 0$ requires an AU region of *finite extent* in the slow variable X . Thus, in the linear framework, absolute instability is a prerequisite for global instability. However, it is not a sufficient condition: Linear global modes are observed to decay in time for AU domains of finite but small extent in X , which may correspond to very large AU domains in terms of x .

The typical shape of a linear CGL global mode is sketched in Figure 1(a). Note that, in general, maximum amplitude occurs downstream of $\text{Re } X_s^l$.

5. NONLINEAR RESONANCE CRITERIA

A weakly nonlinear approach (Le Dizès *et al.* 1993) conducted close to the onset of global instability specified by $\text{Im } \omega_s^l = 0$ has proven that the bifurcation analysis is ill-behaved and suggested that only a fully nonlinear theory is appropriate. In the nonlinear framework, two types of finite-amplitude oscillating states have been identified for the inhomogenous CGL equation in infinite media: *soft* or *hat* (Pier & Huerre 1996) and *steep* or *elephant* (Pier *et al.* 1998) *nonlinear global modes* [cf. Figure 1(b, c)]. Their selection criteria are obtained from the local linear and nonlinear dispersion relations, as summarized below.

The *local nonlinear dispersion relation* is defined via a temporal evolution problem in the following way. Consider a homogenous medium obtained by freezing X at a prescribed value. An unstable spatially periodic perturbation of *real* wavenumber k grows according to $\Omega_i^l(k, X) > 0$ until its amplitude reaches a finite level. Due to stabilizing nonlinearities, a fully nonlinear wavetrain is generated with spatial periodicity imposed by the initial wavenumber. Its frequency, measured for each k , then yields the nonlinear dispersion relation

$$\omega = \Omega^{nl}(k, X). \quad (9)$$

Whereas the local linear dispersion relation (7) yields a *complex* frequency for any *complex* wavenumber, the nonlinear dispersion relation (9) is defined only for *real* wavenumbers k associated with a positive growth rate $\Omega_i^l(k, X) > 0$ and it necessarily yields *real* frequencies. For the CGL model (2), nonlinear wave-trains are finite-amplitude harmonic waves of the form $\text{Re}^{i(kx - \omega t)}$ and (9) reads $\omega = \text{Im}(\gamma^*(X) \Omega^l(k, X)) / \text{Im} \gamma^*(X)$. Computation of (9) for real flows, however, requires a numerical integration as discussed by Pier & Huerre (2000).

Hat global modes [Figure 1(b); Pier & Huerre 1996] have an overall smoothly varying amplitude, and their real frequency ω_s^{nl} is selected at a saddle-point X_s^{nl} of the nonlinear dispersion relation according to

$$\frac{\partial \Omega^{nl}}{\partial X}(X_s^{nl}, k_s^{nl}) = \frac{\partial \Omega^{nl}}{\partial k}(X_s^{nl}, k_s^{nl}) = 0 \quad \text{and} \quad \omega_s^{nl} = \Omega^{nl}(k_s^{nl}, X_s^{nl}). \quad (10)$$

Elephant global modes [Figure 1(c); Pier *et al.* 1998] are characterized by a sharp front governed by the Dee & Langer (1983) marginal stability criterion and located at the upstream transition station X^{ca} between CU and AU regions. The entire structure is tuned to the front frequency given by the corresponding real absolute frequency

$$\omega_0^{ca} = \omega_0(X^{ca}) \quad \text{with} \quad \text{Im } \omega_0(X^{ca}) = 0. \quad (11)$$

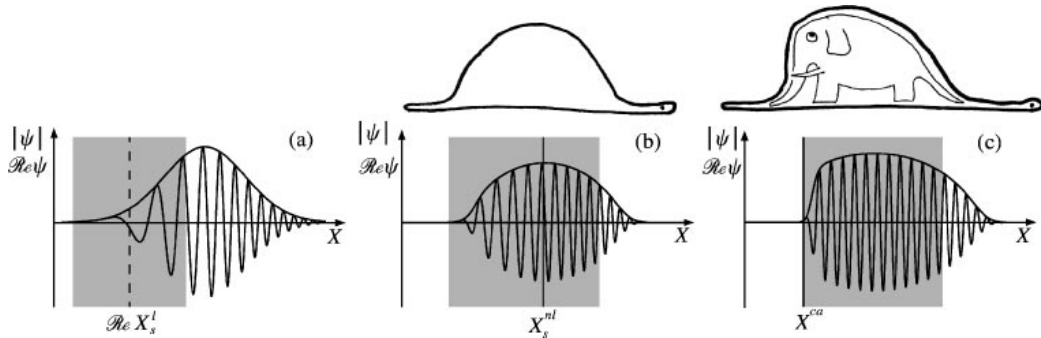


Figure 1. Shapes of CGL global modes. Shaded regions indicate extent of AU domain. (a) Linear global mode. (b) Nonlinear soft global mode or hat mode. (c) Nonlinear steep global mode or elephant mode. The names ‘‘hat’’ and ‘‘elephant’’ have been chosen in reference to Saint-Exup  ry (1946).

The detailed analysis of the transition scenarii between the unperturbed state and either type of nonlinear global mode reveals (Pier 1999, Pier *et al.* 2001) that the two nonlinear resonance criteria (10, 11) are mutually exclusive and that the appropriate global bifurcation parameter is the maximum absolute growth rate over the entire medium $\omega_{0,i}^{\max} \equiv \max \omega_{0,i}(X)$. Nonlinear global modes exist whenever an AU region is present ($\omega_{0,i}^{\max} > 0$). At transition ($\omega_{0,i}^{\max} = 0$) an elephant mode is always selected. Hat modes exist further above threshold and are more readily obtained in systems where the basic advection velocity is weak. Absolute instability is therefore a *necessary and sufficient* condition for the existence of self-sustained *nonlinear* structures. This is in contrast with the results of Section 4: Local absolute instability is only a necessary condition for the existence of amplified *linear* global modes.

6. FINITE-AMPLITUDE VORTEX STREET AS AN ELEPHANT MODE

The generalization of the above nonlinear theory to real flows governed by the Navier-Stokes equations has been conducted by Pier (1999) and Pier & Huerre (2001).

In order to obtain unambiguous results that can be compared with the theory, the basic flow has to strictly comply with the condition of weak streamwise nonuniformity. Bluff body wakes display a recirculation bubble near the obstacle which violates this assumption. The ‘‘synthetic wakes’’ governed by the Prandtl boundary-layer equation (5) all avoid this difficulty. In the example represented in Figure 2(a) for $Re = 100$, the pressure gradient has been selected to be mildly adverse in order to produce a central AU region (displayed in gray), which is an essential feature of real wakes.

Direct numerical simulations of the temporal evolution of this basic flow [see Pier & Huerre (2001) for details] leads to a finite-amplitude vortex shedding r  gime [Figure 2(b)] tuned at a well-defined global frequency $\omega_g = 0.186 \pm 0.002$. This vortex street is made up of wave-trains which slowly deform while travelling downstream: such structures are locally periodic and their (x, t) -dependence solely occurs via a phase function with only slow streamwise variations. Hence the multiple-scale formalism (Bender & Orszag 1978) applies and the global structure may be analysed in terms of local linear and nonlinear waves.

In the upstream domain ($x < 25$), the basic flow is seen to remain unperturbed: small-amplitude wave-trains prevail in this linear region. Further downstream, nonlinear travelling waves develop and completely mask the underlying basic wake flow. In order to

establish that the nonlinear globally synchronized state [Figure 2(b)] follows the elephant resonance criterion (11), its numerically determined features are now compared with predictions based on the local linear and nonlinear instability analyses of the basic flow [Figure 2(a)].

The computation of the local linear dispersion relation (7) via the Orr–Sommerfeld equation reveals an AU domain extending over the streamwise interval $24 < x < 55$ (gray regions in Figure 2). The real absolute frequency prevailing at its upstream boundary $x^{ca} = 24$ reads $\omega_0^{ca} = 0.190$. The nonlinear resonance criterion (11) therefore accurately predicts the vortex shedding frequency, unlike the linear criterion (8) which yields $\omega_s^l = 0.143 + 0.008i$.

The local nonlinear dispersion relation (9) is illustrated in Figure 2(c) by isofrequency contours in the linearly unstable domain of the (X, k) -plane. These contours precisely define the nonlinear spatial branches $k^n(X, \omega)$ obtained by solving the nonlinear dispersion relation (9) at a given frequency. A global mode synchronized at the frequency ω_0^{ca} is expected to follow the spatial branch $k^n(X, \omega_0^{ca})$ represented by a thick dashed curve. The local wave number of the numerically computed spatially developing vortex street [Figure 2(b)] is represented by a thick solid curve in the same sketch and it is seen to closely follow the path predicted by the elephant global mode structure.

The finite-amplitude vortex street is thus described by a nonlinear elephant global mode. This theory not only accurately predicts the vortex shedding frequency but also the spatial structure of the downstream developing vortex street.

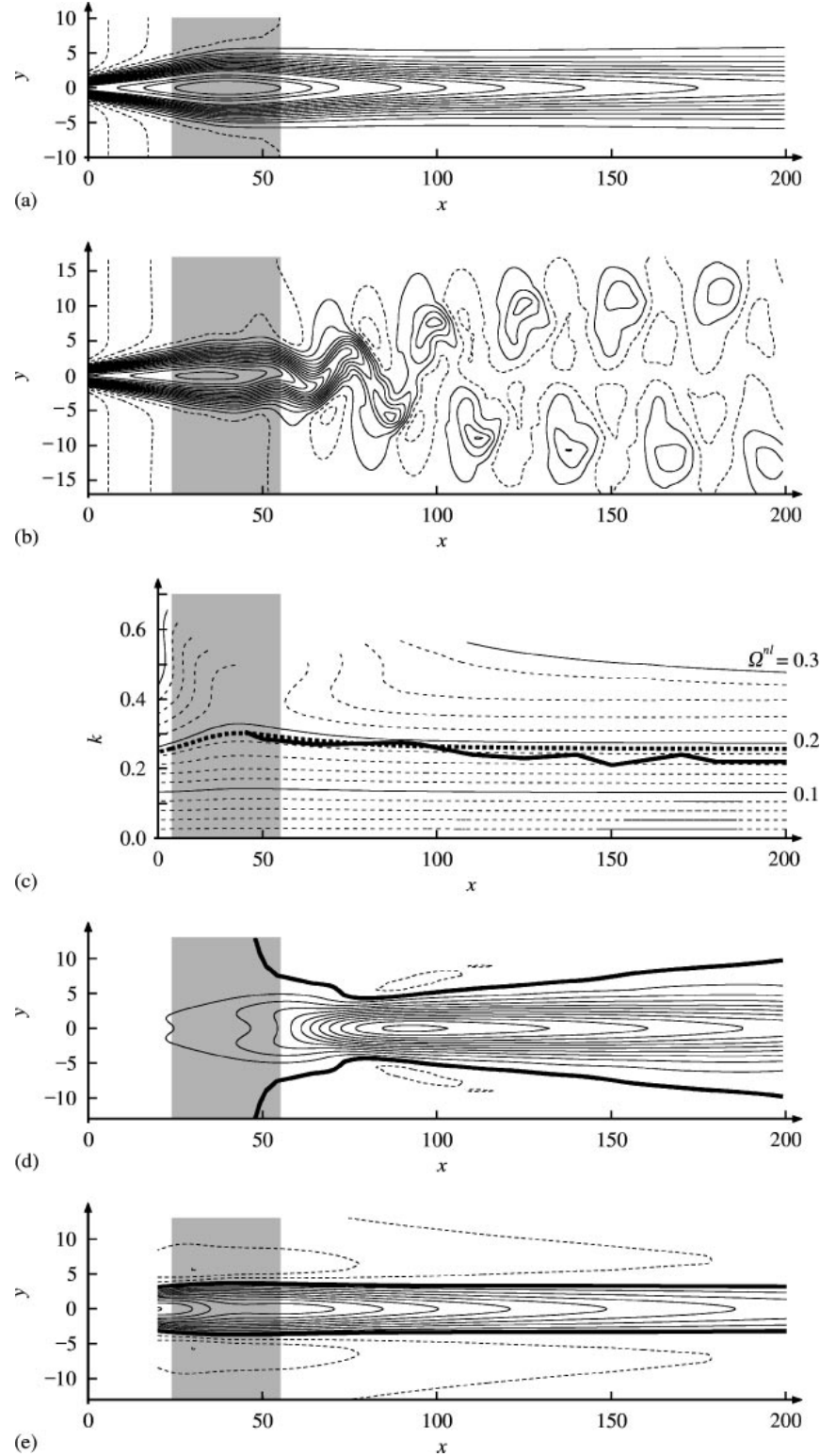
The *mean-flow correction*, which is absent in CGL models, is specific to real shear flows. Indeed, nonlinear quadratic interactions in the NS equations generate a time-independent mean-flow component as well as higher harmonics. In the fully developed vortex shedding régime, the total mean flow then results from the superposition of the basic flow [Figure 2(a)] and the mean-flow correction [Figure 2(d)]. According to Figure 2(d), the mean-flow correction tends to fill up the velocity deficit in the wake. It is instructive to compare the results of direct numerical simulations with those emerging from a temporal evolution problem pertaining to a parallel wake frozen at a prescribed X station and perturbed with a spatially periodic wave of wavenumber $k^n(X, \omega_0^{ca})$. Via this procedure, a finite-amplitude wave-train is obtained for large time, the frequency of which is precisely ω_0^{ca} . Local mean-flow corrections are thereby computed for each station X , which may be pieced together to generate a spatially evolving mean correction field as displayed in Figure 2(e). The agreement between direct numerical simulation [Figure 2(d)] and local predictions [Figure 2(e)] is less satisfactory than for the unsteady part of the flow field [Figure 2(c)]. Whereas in the limit of vanishing inhomogeneity, the local analysis predicts a mean-flow correction of almost constant cross-stream width, the width of the mean flow in the direct numerical simulation is seen to increase with downstream distance. The mean-flow correction field is generated in the central shear region by nonlinear interactions and slowly diffuses on a viscous scale into the outer cross-stream direction. This diffusion process takes place in time [Figure 2(e)] or along the stream [Figure 2(d)], and there is no obvious relationship between these two situations.

7. CONCLUSIONS

We are now in a position to answer the questions listed in the introductory section.

1. In a strictly linear approximation global instability in general requires an AU region of finite extent, whereas *nonlinear global instability takes place as soon as local absolute instability arises at some point in the flow*. When nonlinearities are present, the linear

resonance criterion (8) becomes irrelevant. It is the existence of a transition point from convective to absolute instability which is crucial in the establishment of a self-sustained nonlinear state.



Note that the *real* cylinder wake becomes absolutely unstable at $\text{Re} \sim 25$, whereas onset of vortex shedding occurs only for $\text{Re} \sim 46$. This discrepancy is presumably due to a violation of the assumption of slow spatial development in the neighborhood of the obstacle.

2. The complex frequency of a linear global mode [Figure 1(a)] is obtained at a saddle point X_s^l of $\omega_0(X)$ analytically continued in the complex X -plane see (8). Due to this continuation procedure, no frequency generating location may be identified in physical space; note however, that the region of maximum absolute growth rate plays an essential part. In contrast, the global frequency of nonlinear global modes [Figure 1(b, c)] is selected at a specific location: either the saddle point X_s^{nl} of the nonlinear dispersion relation (10) or the upstream boundary X^{ca} of the AU region (11). These nonlinear resonance criteria are purely local in the sense that only the properties of the system at these stations are involved. In the case of wake flows, the vortex street is triggered by a front structure at X^{ca} which acts as a source and imposes its frequency to the entire flow.

3. The selection mechanisms pertaining to hat and elephant nonlinear global modes are markedly distinct. The hat frequency selection criterion (10) involves a saddle point of the nonlinear dispersion relation (9) in the bulk of the finite-amplitude region [Figure 1(b)]. Elephant modes [Figure 1(c)] are selected by a front located at the upstream boundary of the AU domain; finite amplitude wave-trains develop downstream of this location. Since the elephant frequency selection criterion (11) only involves the linear dispersion relation, this variety of *nonlinear global* mode is surprisingly governed by a *local linear* criterion.

Finite-amplitude vortex shedding in wakes generates a mean-flow correction comparable in magnitude to the basic flow. Nonlinearities thus completely modify the underlying basic flow which becomes unobservable unless one artificially kills the perturbations by imposing for example a symmetry condition.

The comparison between the results of direct numerical simulations and locally computed nonlinear wave-trains has demonstrated the validity of a *linear* and *nonlinear* analyses based on a scale separation assumption. The theory has led to the identification of two varieties of global modes: elephants and hats. The vortex street has been shown to be of elephant type with a front located at the convective-absolute instability transition point imposing its frequency to the entire flow. There remains to determine a real flow that sustains a global mode of hat type. Rayleigh-Bénard convection in the presence of a horizontally varying temperature difference or Taylor-Couette flow between rotating coaxial cylinders with a varying gap may be good candidates for such a situation since there is no basic advection.

REFERENCES

- BENDER, C. M. & ORSZAG, S. A. 1978 *Advanced Mathematical Methods for Scientists and Engineers*. New York: McGraw-Hill.

Figure 2. Intrinsic synchronization of spatially developing wake flow at $\text{Re} = 100$. Shaded regions indicate extent of AU domain. (a) Streamwise velocity isolines of unperturbed basic wake flow. (b) Snapshot of total streamwise velocity isolines in periodic vortex shedding régime. (a, b) Dashed lines represent the levels 0.95, 0.90, 0.85 above the outlet free-stream velocity; solid lines pertain to the levels 0.80, ..., 0.10. (c) Isofrequency contours of the nonlinear dispersion relation $\Omega''(k, X)$ in the linearly unstable domain of the (X, k) -plane. Thin solid contours are separated by $\delta\Omega = 0.1$, thin dashed contours by $\delta\Omega = 0.02$. Predicted nonlinear spatial branch $k''(X, \omega_0^{ca})$ of global frequency $\omega_0^{ca} = 0.19$ is represented by thick dashed curve. Observed local wave number in (b) follows path indicated by thick solid line. (d) Mean streamwise velocity correction of vortex street sketched in (b). (e) Mean streamwise velocity correction of local nonlinear wave-trains of wavenumber $k''(X, \omega_0^{ca})$. (d, e) Thick line separates regions of positive (0.05, 0.10, ... solid lines) and negative (-0.05, -0.10, ... dashed line) levels.

- BERS, A. 1983 Space-time evolution of plasma instabilities — absolute and convective. In *Handbook of Plasma Physics* (eds M. N. Rosenbluth & R. Z. Sagdeev), pp. 451–517, Amsterdam: North-Holland.
- BRIGGS, R. J. 1964 *Electron-Stream Interaction with Plasmas*. Cambridge, MA: MIT Press.
- CHOMAZ, J.-M., HUERRE, P. & REDEKOPP, L. G. 1991 A frequency selection criterion in spatially developing flows. *Studies in Applied Mathematics* **84**, 119–144.
- COUAIRON, A. & CHOMAZ, J.-M. 1997 Absolute and convective instabilities, front velocities and global modes in nonlinear systems. *Physica D* **108**, 236–276.
- COUAIRON, A. & CHOMAZ, J.-M. 1999a Primary and secondary nonlinear global instability. *Physica D* **132**, 428–456.
- COUAIRON, A. & CHOMAZ, J.-M. 1999b Fully nonlinear global modes in slowly varying flows. *Physics of Fluids* **11**, 3688–3703.
- CRIGHTON, D. & GASTER, M. 1976 Stability of slowly diverging jet flow. *Journal of Fluid Mechanics* **77**, 397–413.
- DEE, G. & LANGER, J. S. 1983 Propagating pattern selection. *Physical Review Letters* **50**, 383–386.
- DELBENDE, I. & CHOMAZ, J.-M. 1998 Nonlinear convective/absolute instabilities in parallel two-dimensional wakes. *Physics of Fluids* **10**, 2724–2736.
- GOUJON-DURAND, S., JENFFER, P. & WESFREID, J. E. 1994 Downstream evolution of the Bénard–von Kármán instability. *Physical Review E* **50**, 308–313.
- HAMMOND, D. & REDEKOPP, L. 1997 Global dynamics of symmetric and asymmetric wakes. *Journal of Fluid Mechanics* **331**, 231–260.
- HUERRE, P. 2000 Open shear flow instabilities. *Perspectives in Fluid Dynamics* (eds G. K. Batchelor, H. K. Moffatt & M. G. Worster), Cambridge: Cambridge University Press.
- HUERRE, P. & MONKEWITZ, P. A. 1990 Local and global instabilities in spatially developing flows. *Annual Review of Fluid Mechanics* **22**, 473–537.
- HUERRE, P. & ROSSI, M. 1998 Hydrodynamic instabilities in open flows. In *Hydrodynamics and Nonlinear Instabilities* (eds C. Godrèche & P. Manneville), pp. 81–294, Cambridge: Cambridge University Press.
- LE DIZÈS, S., HUERRE, P., CHOMAZ, J.-M. & MONKEWITZ, P. A. 1993 Nonlinear stability analysis of slowly-diverging flows: limitations of the weakly nonlinear approach. In *Bluff-Body Wakes, Dynamics and Instabilities* (eds H. Eckelmann, J. M. R. Graham, P. Huerre & P. A. Monkewitz), pp. 147–152, Berlin: Springer.
- MONKEWITZ, P. A., HUERRE, P. & CHOMAZ, J.-M. 1993 Global linear stability analysis of weakly non-parallel shear flows. *Journal of Fluid Mechanics* **251**, 1–20.
- PIER, B. 1999 Comportement non linéaire synchronisé dans les écoulements cisaillés. Ph.D. Dissertation, École polytechnique, Palaiseau, France.
- PIER, B. & HUERRE, P. 1996 Fully nonlinear global modes in spatially developing media. *Physica D* **97**, 206–222.
- PIER, B. & HUERRE, P. 2000 Nonlinear self-sustained structures and fronts in wake flows. *Journal of Fluid Mechanics* (in press).
- PIER, B., HUERRE, P. & CHOMAZ, J.-M. 2001 Bifurcation to fully nonlinear synchronized structures in slowly varying media. *Physica D* **148**, 49–96.
- PIER, B., HUERRE, P., CHOMAZ, J.-M. & COUAIRON, A. 1998 Steep nonlinear global modes in spatially developing media. *Physics of Fluids* **10**, 2433–2435.
- PROVANSAL, M., MATHIS, C. & BOYER, L. 1987 Bénard–von Kármán instability: transient and forced regimes. *Journal of Fluid Mechanics* **182**, 1–22.
- SAINT-EXUPÉRY, A. DE 1946 *Le Petit Prince*. Paris: Gallimard.
- WILLIAMSON, C. H. K. 1996 Vortex dynamics in the cylinder wake. *Annual Review of Fluid Mechanics* **28**, 477–539.
- ZIELINSKA, B. J. A. & WESFREID, J. E. 1995 On the spatial structure of global modes in wake flow. *Physics of Fluids* **7**, 1418–1424.

[A7]

On the frequency selection of finite-amplitude vortex shedding in the cylinder wake

B. Pier

Journal of Fluid Mechanics **458**, 407–417 (2002)

doi:10.1017/S0022112002008054

<https://hal.archives-ouvertes.fr/hal-00120025>

On the frequency selection of finite-amplitude vortex shedding in the cylinder wake

By BENOÎT PIER

Department of Applied Mathematics and Theoretical Physics, University of Cambridge,
Silver Street, Cambridge CB3 9EW, UK

(Received 15 November 2001 and in revised form 26 January 2002)

In this paper it is shown that the two-dimensional time-periodic vortex shedding régime observed in the cylinder wake at moderate Reynolds numbers may be interpreted as a nonlinear global structure and its naturally selected frequency obtained in the framework of hydrodynamic stability theory. The frequency selection criterion is based on the local absolute frequency curve derived from the unperturbed basic flow fields under the assumption of slow streamwise variations. Although the latter assumption is only approximately fulfilled in the vicinity of the obstacle, the theoretically predicted frequency is in good agreement with direct numerical simulations for Reynolds numbers $Re > 100$.

1. Introduction

Strouhal (1878) appears to be the first to have studied the periodic features produced by the movement of a cylindrical body in air. Ever since, experimental frequency measurements have been refined and the relationship between Strouhal vortex shedding frequency and Reynolds number is now well established, e.g. Provansal, Mathis & Boyer (1987), Williamson (1988), Norberg (1994), Leweke & Provansal (1995); for a review see Williamson (1996). On the theoretical side, understanding of the spatiotemporal dynamics of oscillatory flows has proceeded by successively considering linear model equations (Chomaz, Huerre & Redekopp 1991; Le, Dizès *et al.* 1996), the linearized version of the Navier–Stokes equations (Monkewitz, Huerre & Chomaz 1993), and nonlinear model equations on semi-infinite (Couairon & Chomaz 1996, 1997a,b, 1999a,b) and infinite (Pier & Huerre 1996; Pier *et al.* 1998; Pier, Huerre & Chomaz 2001) domains. In the framework of the fully nonlinear Navier–Stokes equations, the frequency selection criterion has been obtained (Pier & Huerre 2001a) for a particular ‘synthetic’ wake: a wake with no solid obstacle and no reverse flow region. The objective of the present analysis is to demonstrate that the same criterion holds for natural wake flows around solid obstacles.

In the context of spatially developing flows giving rise to self-sustained oscillations, an essential feature is the complex local absolute frequency $\omega_0(X)$ (Briggs 1964; Bers 1983; Huerre & Monkewitz 1990) which depends on the streamwise X -coordinate. In absolutely unstable (AU) regions, characterized by $\omega_{0,i}(X) \equiv \text{Im } \omega_0(X) > 0$, perturbations are not swept away by advection and grow *in situ* thus leading to non-trivial dynamics without external input. In the past, growing evidence has been gathered to support the existence of a relationship between the global wake frequency and the

$\omega_0(X)$ curve derived from measured or model wake profiles, e.g. Betchov & Criminale (1966), Koch (1985), Triantafyllou, Triantafyllou & Chryssostomidis (1986), Monkewitz & Nguyen (1987), Monkewitz (1988), Hannemann & Oertel (1989), Karniadakis & Triantafyllou (1989); for a review see Huerre & Monkewitz (1990) and Huerre & Rossi (1998). Different resonance principles have been conjectured: Koch (1985) proposed a feedback mechanism associated with the real absolute frequency $\omega_0^{ac} \equiv \omega_0(X^{ac})$ prevailing at the downstream boundary X^{ac} of the AU region. Monkewitz & Nguyen (1987) considered an initial resonance principle where the real global frequency $\omega_0^{ca} \equiv \omega_0(X^{ca})$ is provided by the upstream transition station X^{ca} from convective to absolute instability.

According to the first theoretically consistent criterion established in a strictly linear setting by Chomaz *et al.* (1991), Monkewitz *et al.* (1993) and Le Dizès *et al.* (1996), the complex global frequency ω_s^ℓ is given by a saddle-point condition

$$\omega_s^\ell = \omega_0(X_s^\ell) \quad \text{with} \quad \frac{d\omega_0}{dX}(X_s^\ell) = 0, \quad (1.1)$$

based on the analytic continuation of $\omega_0(X)$ in the complex X -plane. This linear criterion was shown by Hammond & Redekopp (1997) to yield a strikingly accurate frequency prediction for the fully developed vortex street in the wake of a blunt-edged plate. Note, however, that $\omega_0(X)$ in that study is based on the time-averaged mean flow instead of the unperturbed basic flow, thus implicitly taking into account nonlinear effects. The performance of criterion (1.1) based on mean flows will be discussed in the final section.

In the framework of fully nonlinear amplitude evolution equations and by investigating semi-infinite domains, Couairon & Chomaz (1997a,b, 1999a,b) have derived scaling laws that are in excellent agreement with experimental and numerical results pertaining to the spatial structure of bluff-body wakes close to threshold. In infinite systems, self-sustained time-periodic finite-amplitude structures have been found as soft ('hat') modes (Pier & Huerre 1996) or steep ('elephant'†) modes (Pier *et al.* 1998), and the respective frequency selection criteria have been established. The analysis of the relevant transition scenarios (Pier *et al.* 2001) has shown that the unperturbed basic state always first bifurcates to an elephant structure. Moreover, hat modes may only exist in situations of weak mean flow advection, so that they are ruled out in wake flows. Nonlinear elephant modes are characterized by a stationary front located at the upstream transition station X^{ca} from local convective to absolute instability. This front acts as a source generating a downstream-propagating nonlinear wavetrain and effectively tuning the entire system to its frequency. The stationary front obeys the Dee & Langer (1983) marginal stability criterion, hence the frequency of elephant modes equals the real absolute frequency prevailing at the front location and is given by

$$\omega_0^{ca} = \omega_0(X^{ca}) \quad \text{with} \quad \omega_{0,i}(X^{ca}) = 0 \quad \text{and} \quad \frac{d\omega_{0,i}}{dX}(X^{ca}) > 0. \quad (1.2)$$

Downstream of the front, a fully nonlinear wavetrain prevails that is governed by the local nonlinear dispersion relation and follows the nonlinear wavenumber branch of frequency ω_0^{ca} . It should be noted that this criterion governing a fully nonlinear global structure only involves the purely linear local absolute frequency, and that it fully confirms the conjecture of Monkewitz & Nguyen (1987).

All theoretical analyses rely on slow streamwise variations to establish the relationship between global behaviour and local characteristics. In this context, the linear (1.1)

† The choice of the terms 'hat' and 'elephant' is motivated by Pier & Huerre (2001b).

and nonlinear (1.2) criteria yield a leading-order approximation of the respective global frequency, and corrections of higher order in the inhomogeneity parameter are obtained by further asymptotic analyses (Monkewitz *et al.* 1993; Pier *et al.* 2001). In order to solve the global mode problem in the context of the fully nonlinear Navier–Stokes equations, a ‘synthetic’ wake (Pier & Huerre 2001a) was designed that fulfils the quasi-parallel flow assumption. In this configuration, local linear and nonlinear dispersion relations derived from the basic flow velocity profiles predict the existence of a nonlinear elephant mode, the global frequency and spatial structure of which are in excellent agreement with the synchronized finite-amplitude vortex street obtained by direct numerical simulations.

Whereas the synthetic wake was tailored to obey the assumption of slow streamwise variations required by theory, bluff body wakes are strongly non-parallel near the obstacle surface. Nevertheless, the present study has been undertaken, bearing in mind that perturbation analyses often yield reasonable predictions for finite values of the ‘small’ parameter. The results then validate *a posteriori* the method and assess the utility of asymptotic analyses of quasi-parallel flows in situations of practical interest.

2. Governing equations and solution method

The following study is carried out for two-dimensional incompressible flows governed by the Navier–Stokes equations. The Reynolds number is defined as $Re = UD/v$, where U represents the free-stream velocity, D the obstacle diameter and v the kinematic viscosity. Using non-dimensional variables based on D and U , the governing momentum and continuity equations are then given by

$$\frac{\partial u}{\partial t} + u \frac{\partial u}{\partial x} + v \frac{\partial u}{\partial y} = -\frac{\partial p}{\partial x} + \frac{1}{Re} \Delta u + f_u, \quad (2.1a)$$

$$\frac{\partial v}{\partial t} + u \frac{\partial v}{\partial x} + v \frac{\partial v}{\partial y} = -\frac{\partial p}{\partial y} + \frac{1}{Re} \Delta v + f_v, \quad (2.1b)$$

$$\frac{\partial u}{\partial x} + \frac{\partial v}{\partial y} = 0, \quad (2.1c)$$

where x and y denote streamwise and cross-stream coordinates, u and v the corresponding components of the velocity and p the pressure field.

For fast numerical integration, the above equations are discretized on a Cartesian grid, and the presence of the obstacle is enforced by a penalization method similar to that used by Angot, Bruneau & Fabrie (1999): inside the domain covered by the cylinder ($x^2 + y^2 \leq 1/4$), a ‘body force’ is applied with components

$$f_u = -u/\tau \quad \text{and} \quad f_v = -v/\tau, \quad (2.2)$$

where τ is a relaxation parameter. A value of $\tau = 0.01$ was found sufficient to drive the components of the total velocity field to negligible values, and results are not affected when further decreasing τ . Thus, the entire domain is filled with fluid and there is no need for body-fitted coordinates or for boundary conditions on the obstacle surface.

Spatial discretization combines finite differences with $n_x = n_u + n_o + n_d$ points in the x -direction and n_y Chebyshev collocation points in the y -direction. The streamwise mesh is constructed with n_o equispaced grid points separated by δ_x in the obstacle region and n_u (n_d) elements in the upstream (downstream) regions uniformly stretched according to a stretching factor of κ_u (κ_d). The Chebyshev collocation points $-1 \leq$

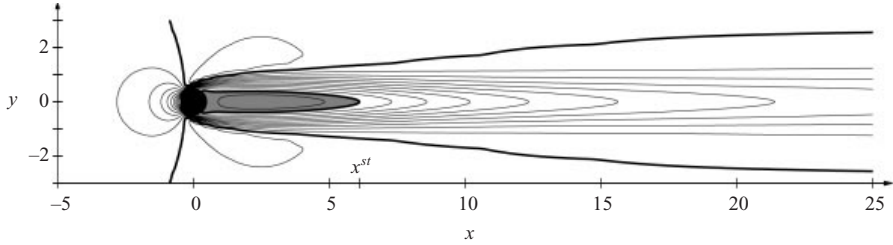


FIGURE 1. Streamwise velocity field of the basic flow around the cylinder at $Re = 100$. Isolines pertain to the levels $-0.1, 0.0, \dots, 1.1$ ($0, 1$ thick lines). A reverse flow region ($u < 0$, shown in grey) prevails between the obstacle and the stagnation point at x^{st} .

$\xi_i = -\cos[i\pi/(n_y + 1)] \leq +1$ for $i = 0, \dots, n_y + 1$ are mapped onto the entire cross-stream axis $-\infty \leq y_i \leq +\infty$ through the algebraic transformation $y\sqrt{2}/\ell_y = \xi/(1-\xi^2)$, where the parameter ℓ_y governs the distribution of collocation points on the y -axis. Assuming that $u - U, v$ and p vanish at $y = \pm\infty$, the computation may be restricted to the interior collocation points associated with $1 \leq i \leq n_y$. At the inlet the free-stream velocity is imposed, and at the outlet non-reflecting boundary conditions (Jin & Braza 1993) are implemented. The grid used in the present computations is defined by $n_y = 55$, $\ell_y = 1$ and $n_u = 60$, $n_o = 140$, $n_d = 300$, $\delta_x = 0.01$, $\kappa_u = 1.10$, $\kappa_d = 1.02$; the total streamwise extent of the domain is then $-35 < x < 195$.

Time-integration of system (2.1) is performed via a fractional-step method of second-order accuracy in time. At the intermediate time-step, the two components of the velocity field are obtained by solving Helmholtz-type problems. A Poisson problem then yields a correction to the pressure required to enforce divergence-free velocity fields. A Crank–Nicholson scheme is used for the viscous terms; the advection terms are obtained at the intermediate time-step by extrapolation based on the two previous time-steps.

Using a Cartesian grid, the second-order y -derivative operator may be diagonalized so that the two-dimensional Helmholtz (Poisson) problems transform into a series of decoupled one-dimensional problems† that are efficiently solved by making use of a generalized Thomas algorithm. Thus the required computational time only increases linearly with the total number of grid points. Most of the results have been obtained on a laptop computer; a typical run takes on the order of one hour.

3. Basic flow and local absolute frequency

This part of the study investigates the unperturbed basic wake flow and the corresponding local absolute frequency curve, upon which the frequency selection criteria are based. By definition, the basic flow is a steady solution of the Navier–Stokes equations (2.1). This flow is unstable for Reynolds numbers beyond critical and then impossible to observe experimentally. Following Fornberg (1985), however, the steady solution is obtained when imposing a stabilizing symmetry condition on the $y = 0$ axis and considering only the domain $y \geq 0$. Figure 1 shows the basic streamwise velocity field around the circular cylinder at $Re = 100$. The near wake displays a reverse flow region ($u < 0$, shown in grey) extending from the obstacle

† The author is indebted to Uwe Ehrenstein for bringing this method to his attention.

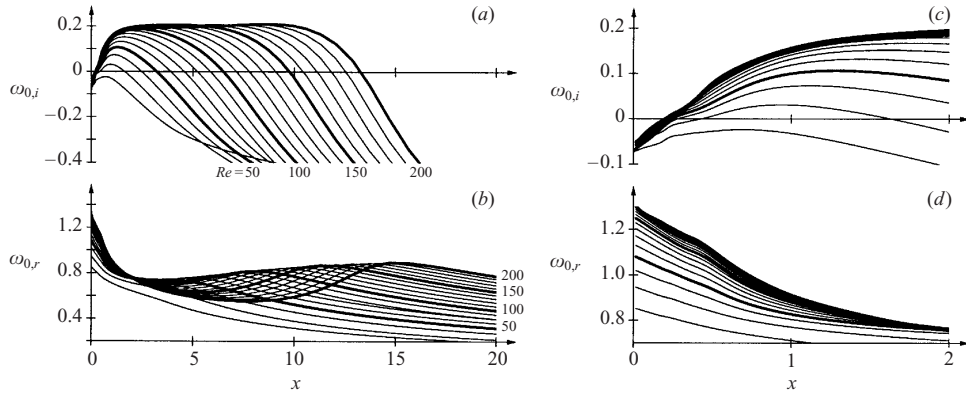


FIGURE 2. Imaginary (a, c) and real (b, d) parts of local absolute frequency for basic wake flows obtained with $Re = 20, 30, \dots, 200$ (thick curves pertain to $Re = 50, 100, 150, 200$).

down to the stagnation point x^{st} . The variation with Reynolds number of the reverse flow extent is discussed below (see figure 3).

In a previous investigation (Pier & Huerre 2001a) resorting to the academic configuration of a ‘synthetic’ wake with no solid boundaries, no reverse flow and no stagnation point, the existence of a small inhomogeneity parameter $\epsilon \ll 1$ made possible a rigorous asymptotic analysis based on the separation of fast x and slow $X \equiv ex$ streamwise scales. In an attempt to prove the applicability of these results in situations of practical interest where $\epsilon = O(1)$, we boldly ignore that the present flow is non-parallel in the near-wake region and do not use the slow X -coordinate in the rest of the paper. Local characteristics are then derived at a given streamwise station by freezing the x -coordinate and studying the equivalent parallel shear flow of velocity profile $U_0(y) = u(x, y)$. Linear instability waves are governed by the Orr–Sommerfeld equation (Drazin & Reid 1981) which yields the local linear dispersion relation $\omega = \Omega'(k, x)$ between the complex frequency ω and complex wavenumber k at the streamwise station x under consideration. These linear eigenvalue problems in the cross-stream coordinate are solved via a Chebyshev spectral method based on the previously introduced collocation points. The complex local absolute frequency $\omega_0(x)$ is then derived in classical fashion by applying a zero group velocity condition on the local linear dispersion relation (Briggs 1964; Bers 1983). Figure 2 illustrates the streamwise evolution of the absolute growth rate $\omega_{0,i}$ and real absolute frequency $\omega_{0,r}$ for different values of the Reynolds number in the range $20 \leq Re \leq 200$. Local absolute instability ($\omega_{0,i} > 0$) prevails downstream of the obstacle when $Re > Re_a \approx 25$, in agreement with the findings of Monkewitz (1988). The magnified graphs (figure 2c, d) show that the near wake is insensitive to changes in Re when $Re > 100$. It should also be noted that the local absolute growth rate rapidly decays with decreasing x in the boundary layers along the cylinder ($-0.5 < x < 0.5$) and reaches very large negative values for $x < -0.5$ (not shown on graph).

The evolution with Reynolds number of the AU and reverse flow regions is shown in figure 3. Absolute instability prevails in the interval $x^{ca} < x < x^{ac}$ (both shades of grey), the extent of which is seen to increase approximately linearly with Re . Note that the maximum absolute growth rate remains almost constant for $Re > 100$ (see figure 2a). A comparison of the stagnation point location x^{st} (thick solid curve

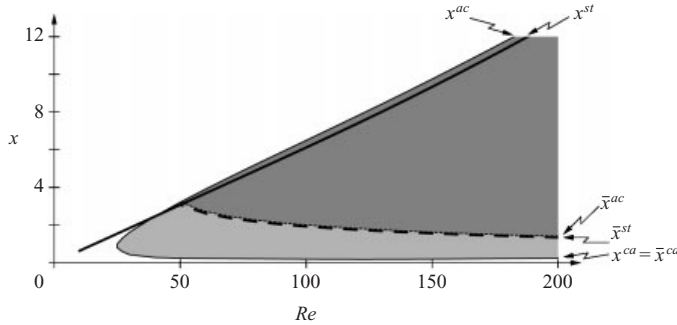


FIGURE 3. Reynolds number dependence of local absolute instability and reverse flow region for the basic flow (AU region extends over both shaded areas $x^{ca} < x < x^{ac}$ and the stagnation point location x^{st} follows the thick solid curve) and the mean flow (AU region covers light grey area $\bar{x}^{ca} < x < \bar{x}^{ac}$ and stagnation point \bar{x}^{st} follows the thick dashed curve).

in figure 3) and the marginally absolutely unstable station x^{ac} shows that the AU domain closely follows the reverse flow region, slightly extending beyond it. The remaining elements of figure 3 pertain to the time-averaged mean flows and are discussed below.

4. Periodic vortex shedding

Above a critical value of Reynolds number, finite-amplitude periodic vortex streets develop in the wake of the cylinder when the entire cross-stream domain $-\infty \leqslant y \leqslant +\infty$ is considered. Direct numerical simulations of system (2.1) are performed using the method outlined in § 2. Simulations are started with the basic flow fields and the instability is triggered by a small-amplitude initial impulse. After a transient growth, nonlinearities rapidly lead to saturation of a fully developed downstream-propagating periodic vortex street. Figure 4 shows a snapshot of the velocity fields at $Re = 100$ in the central region of the computational domain. Time series are recorded at different locations and corresponding frequency spectra computed (figure 5) to ascertain the synchronized behaviour of the flow. Inspection of these spectra demonstrates that the entire vortex street is tuned to a global fundamental frequency and its harmonics. Figure 6 shows that the numerically obtained frequencies (open squares) are in good agreement with the experimental relationship (solid curve) between Strouhal number $St = \omega/2\pi$ and Reynolds number (Williamson 1988). Moreover, the critical Reynolds number Re_c for onset of periodic vortex shedding has been localized in the range $49.0 < Re_c < 49.5$ which nearly corresponds to the experimental threshold of 47 measured by Provansal *et al.* (1987). Bearing in mind that the cylindrical obstacle is discretized on a Cartesian grid, these agreements are deemed sufficient validation of the code for the present purpose; more accurate numerical results have been obtained e.g. by Barkley & Henderson (1996).

The nonlinear vortex street is associated with Reynolds stresses leading to a finite mean flow correction. The main effect of this mean flow distortion is a shortening of the recirculation bubble, as indicated by the stagnation point location \bar{x}^{st} of the time-averaged flows (thick dashed curve in figure 3). It should be noted that the average flow is a result of the nonlinear vortex street and does not obey the Navier–Stokes equations. For comparison, however, the local linear stability analysis of the previous section may be repeated for the time-averaged flows. This reveals that

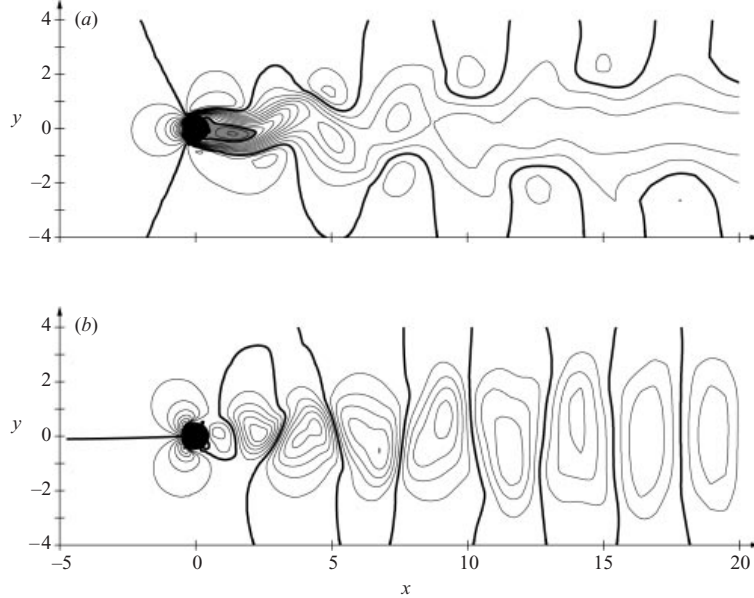


FIGURE 4. Snapshot of (a) streamwise and (b) cross-stream velocity fields in the periodic nonlinear vortex shedding régime at $Re = 100$. (a) Contour levels $u = -0.2, -0.1, \dots, 1.2$ (0, 1 thick lines). (b) Contour levels $v = -0.6, -0.5, \dots, 0.6$ (0 thick line).

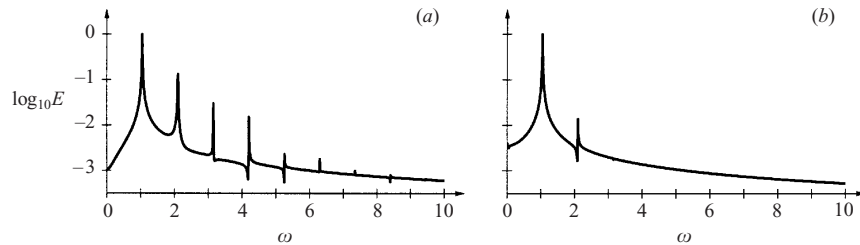


FIGURE 5. Harmonic spectra of velocity time series in the vortex shedding régime at $Re = 100$. (a) v -component at $x = 2.2, y = 0.7$. (b) u -component at $x = 0.2, y = 2.1$.

the reduction of the reverse flow region is associated with a similar reduction of the absolutely unstable domain ($\bar{x}^{ca} < x < \bar{x}^{ac}$, lightly shaded region in figure 3). There is, however, no feedback of the nonlinear downstream vortices in the upstream region; in particular the neighbourhood of the upstream boundary $x^{ca} = \bar{x}^{ca}$ of the AU region is not affected by mean flow corrections.

5. Discussion of frequency selection criterion

The objective of this last section is to show that the vortex shedding régime may be interpreted in terms of a nonlinear elephant mode, i.e. that its global frequency is dictated by criterion (1.2). The frequency of nonlinear elephant global modes is imposed by a sharp front located at the transition station x^{ca} from local convective to absolute instability. The global frequency of the system then equals the real absolute

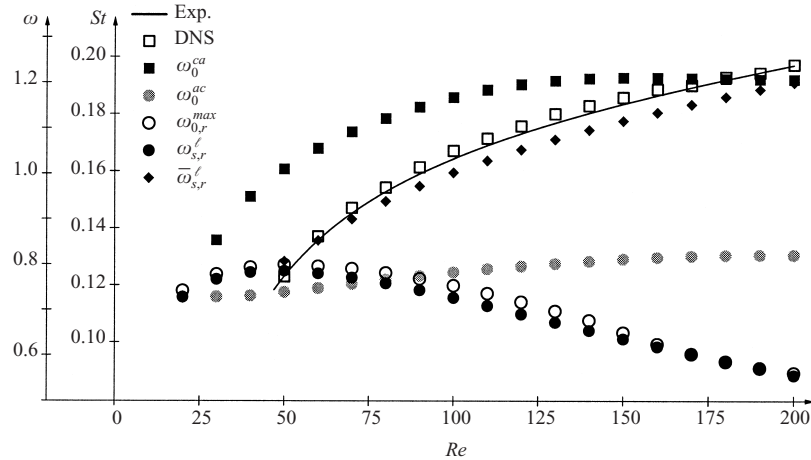


FIGURE 6. Reynolds number dependence of cylinder wake characteristic frequencies. Vortex shedding frequencies of the present simulations (open squares) closely follow the experimental Strouhal number curve from Williamson (1988) (solid line). Theoretical elephant frequencies ω_0^{ca} (filled squares) approximately predict the actual vortex shedding frequencies for $Re > 100$. The other characteristic frequencies ω_0^{ac} (grey circles), $\omega_{0,r}^{max}$ (open circles) and $\omega_{s,r}'$ (filled circles) are unable to account for the fully developed vortex street beyond onset at $Re \simeq 49$. Note the good performance of $\bar{\omega}_{s,r}'$ based on the mean flow (diamonds).

frequency ω_0^{ca} prevailing at x^{ca} . For the wake flows under consideration, transition from convective to absolute instability occurs in the boundary layer along the cylinder near its trailing edge, as demonstrated by figure 2(c). Monitoring the corresponding frequency ω_0^{ca} as the Reynolds number is varied (filled squares in figure 6) shows that this frequency plateaus at $\omega_0^{ca} \simeq 1.2$ for $Re > 100$. Comparison of these theoretical predictions with the results obtained by the present simulations (open squares) or by experiment (solid line) shows that the discrepancy is less than 10% over the entire range $100 < Re < 200$. Thus the theory is fairly successful in predicting the actual vortex shedding frequency, considering that criterion (1.2) is a leading-order approximation derived under the condition of slow streamwise evolution of the entire flow. The agreement improves at higher Reynolds numbers since then the assumption of weakly diverging flows is more closely fulfilled. Note also that perfect agreement occurs at $Re = 180$, beyond which the two-dimensional vortex street undergoes a transition to three-dimensionality (Barkley & Henderson 1996; Williamson 1996). For $Re < 100$, finite non-parallel effects result in a poorer frequency prediction. This strong non-parallelism may also account for the discrepancy between onset of absolute instability at $Re = Re_a \simeq 25$ and onset of global instability at $Re = Re_c \simeq 47$. Indeed, in the range $Re_a < Re < Re_c$ the extent of the AU region is much less than the typical vortex street wavelength and thus unable to sustain a stationary front.

The mechanism leading to the synchronized vortex street at moderate Reynolds numbers may be interpreted in the following way. The initial impulse triggers a wavepacket of growing amplitude and its envelope advances against the basic flow in the absolutely unstable region. Perturbations thus penetrate into the boundary layer near the cylinder trailing edge. Further upstream, at the station x^{ca} of neutral

absolute instability, a balance between upstream perturbation growth and downstream advection is reached, and perturbations pile up at that location. Nonlinearities lead to saturation of the fluctuating amplitude, a front is formed at x^{ca} and a fully nonlinear wavetrain obtained in the region $x > x^{ca}$. Its frequency is dictated by the front and is ω_0^{ca} . The domain $x < x^{ca}$ is covered by the front tail and the fluctuation amplitude exponentially decays towards the inlet. At the marginal x^{ca} station, weakly nonlinear fluctuations prevail (as illustrated in figure 5(b) for $Re = 100$ when $x^{ca} = 0.2$). It should be emphasized that perturbations evolve in the infinite $-\infty < x < +\infty$ system and no boundary condition is imposed at the obstacle trailing edge $x = 0.5$. This is in contrast with the investigations of semi-infinite domains with upstream boundary condition by Couairon & Chomaz (1997a,b, 1999a,b). In the latter configuration, analysis of one-dimensional model equations close to global instability yields scaling laws that account for experimental observations remarkably well. The present study does not rely on the assumption of near criticality, but rather on reasonably parallel flows as obtained for $Re > 100$.

To fully appreciate the quality of criterion (1.2) in predicting the vortex shedding frequency, it should be compared with the other basic flow characteristic frequencies (round symbols on figure 6). The filled grey circles represent the real absolute frequency ω_0^{ac} prevailing at the downstream boundary x^{ac} of the AU region. Although the location x^{ac} continuously moves downstream with increasing Reynolds number (see figure 3a), the frequency ω_0^{ac} is seen to remain approximately constant at 0.8. Another characteristic frequency is derived from the location x^{max} where the absolute frequency $\omega_0^{max} \equiv \omega_0(x^{max})$ with maximum absolute growth rate occurs. Its real part $\omega_{0,r}^{max}$ is plotted by open circles in figure 6. The filled circles in figure 6 represent $\omega_s^\ell \equiv Re \omega_s^\ell$ of criterion (1.1) governing spatially extended and globally synchronized structures when the governing equations are linearized with respect to the basic flow. The frequencies ω_s^ℓ , obtained by analytic continuation of the $\omega_0(x)$ curves in the complex x -plane, are found to approximately follow ω_0^{max} since the complex saddle point x_s^ℓ is located near the position x^{max} of maximum absolute growth rate. Both $\omega_{0,r}^{max}$ and ω_s^ℓ display even lower values than ω_0^{ac} for $Re > 100$ and none of these frequencies can account for the actual global frequency. This is not a surprise since they are not derived from a nonlinear theory. In contrast, as already established by Hammond & Redekopp (1997) in a similar configuration, the linear criterion (1.1) applied on the mean flows obtained by averaging in time the fully nonlinear régime yields frequencies $\bar{\omega}_{s,r}^\ell$ (diamonds in figure 6) which very closely follow the actually observed frequencies. Unfortunately, since these frequencies are based on the fully developed vortex street, this excellent agreement does not help identifying the mechanism that is responsible for the vortex shedding.

To conclude, it has been shown that the vortex shedding frequency governing bluff body wakes can be understood and predicted by local instability analyses of the basic flow considered to be weakly diverging. Despite non-parallel effects in the vicinity of the obstacle, reasonable agreement is obtained for $Re > 100$. It should also be emphasized that the aim of the present method is to reveal the underlying frequency selection mechanism and not to accurately estimate the global frequency: the frequency predictions require almost the same numerical effort as the complete simulations!

Present and past fruitful collaborations with Nigel Peake and Patrick Huerre, suggestions and advice from Uwe Ehrenstein, John Hinch, Paul Metcalfe and Laurette Tuckerman are gratefully acknowledged.

REFERENCES

- ANGOT, P., BRUNEAU, C.-H. & FABRIE, P. 1999 A penalization method to take into account obstacles in incompressible viscous flows. *Numer. Maths.* **81**, 497–520.
- BARKLEY, D. & HENDERSON, R. 1996 Three-dimensional Floquet stability analysis of the wake of a circular cylinder. *J. Fluid Mech.* **322**, 215–241.
- BERS, A. 1983 Space-time evolution of plasma instabilities—absolute and convective. In *Handbook of Plasma Physics* (ed. M. Rosenbluth & R. Sagdeev), pp. 451–517. North-Holland.
- BETCHOV, R. & CRIMINALE, W. 1966 Spatial instability of the inviscid jet and wake. *Phys. Fluids* **9**, 359–362.
- BRIGGS, R. 1964 *Electron-Stream Interaction with Plasmas*. M.I.T. Press.
- CHOMAZ, J.-M., HUERRE, P. & REDEKOPP, L. 1991 A frequency selection criterion in spatially developing flows. *Stud. Appl. Maths* **84**, 119–144.
- COUAIRON, A. & CHOMAZ, J.-M. 1996 Global instabilities in fully nonlinear systems. *Phys. Rev. Lett.* **77**, 4015–4018.
- COUAIRON, A. & CHOMAZ, J.-M. 1997a Absolute and convective instabilities, front velocities and global modes in nonlinear systems. *Physica D* **108**, 236–276.
- COUAIRON, A. & CHOMAZ, J.-M. 1997b Pattern selection in the presence of a cross flow. *Phys. Rev. Lett.* **79**, 2666–2669.
- COUAIRON, A. & CHOMAZ, J.-M. 1999a Fully nonlinear global modes in slowly varying flows. *Phys. Fluids* **11**, 3688–3703.
- COUAIRON, A. & CHOMAZ, J.-M. 1999b Primary and secondary nonlinear global instability. *Physica D* **132**, 428–456.
- DEE, G. & LANGER, J. 1983 Propagating pattern selection. *Phys. Rev. Lett.* **50**, 383–386.
- DRAZIN, P. & REID, W. 1981 *Hydrodynamic Stability*. Cambridge University Press.
- FORNBERG, B. 1985 Steady viscous flow past a circular cylinder up to Reynolds number 600. *J. Comput. Phys.* **61**, 297–320.
- HAMMOND, D. & REDEKOPP, L. 1997 Global dynamics of symmetric and asymmetric wakes. *J. Fluid Mech.* **331**, 231–260.
- HANNEMANN, K. & OERTEL JR, H. 1989 Numerical simulation of the absolutely and convectively unstable wake. *J. Fluid Mech.* **199**, 55–88.
- HUERRE, P. & MONKEWITZ, P. 1990 Local and global instabilities in spatially developing flows. *Annu. Rev. Fluid Mech.* **22**, 473–537.
- HUERRE, P. & ROSSI, M. 1998 Hydrodynamic Instabilities in open flows. In *Hydrodynamics and Nonlinear Instabilities* (ed. C. Godrèche & P. Manneville), pp. 81–294. Cambridge University Press.
- JIN, G. & BRAZA, M. 1993 A nonreflecting outlet boundary condition for incompressible unsteady Navier–Stokes calculations. *J. Comput. Phys.* **107**, 239–253.
- KARNIADAKIS, G. & TRIANTAFYLLOU, G. 1989 Frequency selection and asymptotic states in laminar wakes. *J. Fluid Mech.* **199**, 441–469.
- KOCH, W. 1985 Local instability characteristics and frequency determination on self-excited wake flows. *J. Sound Vib.* **99**, 53–83.
- LE DIZÈS, S., HUERRE, P., CHOMAZ, J.-M. & MONKEWITZ, P. 1996 Linear global modes in spatially developing media. *Phil. Trans. R. Soc. Lond. A* **354**, 169–212.
- LEWEKE, T. & PROVANSAL, M. 1995 The flow behind rings: bluff body wakes without end effects. *J. Fluid Mech.* **288**, 265–310.
- MONKEWITZ, P. 1988 The absolute and convective nature of instability in two-dimensional wakes at low Reynolds numbers. *Phys. Fluids* **31**, 999–1006.
- MONKEWITZ, P., HUERRE, P. & CHOMAZ, J.-M. 1993 Global linear stability analysis of weakly non-parallel shear flows. *J. Fluid Mech.* **251**, 1–20.
- MONKEWITZ, P. & NGUYEN, L. 1987 Absolute instability in the near-wake of two-dimensional bluff bodies. *J. Fluid Struct.* **1**, 165–184.
- NORBERG, C. 1994 An experimental investigation of the flow around a circular cylinder: influence of aspect ratio. *J. Fluid Mech.* **258**, 287–316.
- PIER, B. & HUERRE, P. 1996 Fully nonlinear global modes in spatially developing media. *Physica D* **97**, 206–222.

- PIER, B. & HUERRE, P. 2001a Nonlinear self-sustained structures and fronts in spatially developing wake flows. *J. Fluid Mech.* **435**, 145–174.
- PIER, B. & HUERRE, P. 2001b Nonlinear synchronization in open flows. *J. Fluids Struct.* **15**, 471–480.
- PIER, B., HUERRE, P. & CHOMAZ, J.-M. 2001 Bifurcation to fully nonlinear synchronized structures in slowly varying media. *Physica D* **148**, 49–96.
- PIER, B., HUERRE, P., CHOMAZ, J.-M. & COUAIRON, A. 1998 Steep nonlinear global modes in spatially developing media. *Phys. Fluids* **10**, 2433–2435.
- PROVANSAL, M., MATHIS, C. & BOYER, L. 1987 Bénard–von Kármán instability: transient and forced regimes. *J. Fluid Mech.* **182**, 1–22.
- STROUHAL, V. 1878 Über eine besondere Art der Tonerregung. *Ann. d. Phys. u. Chem. N. F. (Leipzig)* **5**(10), 216–251.
- TRIANTAFYLLOU, G., TRIANTAFYLLOU, M. & CHRYSOSTOMIDIS, C. 1986 On the formation of vortex streets behind stationary cylinders. *J. Fluid Mech.* **170**, 461–477.
- WILLIAMSON, C. 1988 Defining a universal and continuous Strouhal-Reynolds number relationship for the laminar vortex shedding of a circular cylinder. *Phys. Fluids* **31**, 2742–2744.
- WILLIAMSON, C. 1996 Vortex dynamics in the cylinder wake. *Annu. Rev. Fluid Mech.* **28**, 477–539.

[A8]

Open-loop control of absolutely unstable domains

B. Pier

Proceedings of the Royal Society of London A **459**, 1105–1115 (2003)

doi:10.1098/rspa.2002.1086

<https://hal.archives-ouvertes.fr/hal-00120027>

Open-loop control of absolutely unstable domains

BY BENOÎT PIER†

*Department of Applied Mathematics and Theoretical Physics,
University of Cambridge, Silver Street, Cambridge CB3 9EW, UK*

Received 1 May 2002; accepted 16 October 2002; published online 14 February 2003

Spatially varying systems with a central absolutely unstable region are known to give rise to self-sustained finite-amplitude globally synchronized structures. The present investigation shows how such an intrinsic behaviour may be controlled by small-amplitude forcing applied upstream of the fully developed oscillations. This technique allows the tuning of the entire system to any frequency in a wide range, expending only an exponentially small power.

Keywords: absolute instability; self-sustained oscillations; control

1. Introduction

Self-sustained finite-amplitude oscillations are produced in a great variety of situations, ranging from fluid flows (Huerre 2000), chemical reactions (Kapral & Showalter 1995) and biological processes (Winfree 1987) to solar activity cycles (Meunier *et al.* 1997). Such an intrinsic behaviour is often unwanted, e.g. it induces structural damage in flows around obstacles or affects performance of turbocompressors. Understanding the mechanism responsible for these oscillations may then suggest methods of suppressing or controlling them. In many situations, e.g. three-dimensional boundary layers (Reed & Saric 1989), the naturally occurring nonlinear waves are prone to secondary instabilities, which in turn lead to a turbulent regime. Hence, a controlled modification of the primary nonlinear state is desirable if one wants to delay (or possibly to enhance) the onset of turbulence. Although very efficient, optimal or robust control theory (Bewley & Liu 1998) is difficult to implement, since it relies on heavy numerical computations and on a precise knowledge of the system state. Our objective is to devise a control strategy applicable to a broad class of systems that takes advantage of the global instability mechanism and requires only extremely weak localized action.

In the context of spatially varying systems, the existence of intrinsic oscillations (Huerre & Monkewitz 1990; Pier *et al.* 2001) is closely related to the transition from convective to absolute instability, as determined by the complex *local absolute frequency* $\omega_0(X)$ (Briggs 1964; Bers 1983). In stable or convectively unstable (CU) regions, characterized by $\omega_{0,i}(X) \equiv \text{Im } \omega_0(X) < 0$, perturbations either decay or are swept away by advection. Convectively unstable systems thus display no intrinsic

† Present address: Laboratoire de mécanique des fluides et d'acoustique, École centrale, 36 avenue Guy-de-Collongue, 69130 Écully, France.

behaviour and essentially behave as amplifiers of external noise: without continuous external input, the medium returns to its unperturbed state. By contrast, in absolutely unstable (AU) regions where $\omega_{0,i}(X) > 0$, perturbations grow *in situ* and hence may lead to non trivial dynamics without external forcing. It has been shown that the onset of global nonlinear oscillations in infinite systems occurs as soon as local absolute instability is reached somewhere in the medium (Pier *et al.* 2001). Other varieties of nonlinear global modes have been obtained in semi-infinite systems (Couairon & Chomaz 1996, 1997a, b, 1999), which are not discussed here.

The sensitivity of CU open flows to external perturbations has been well established, e.g. for free shear layers (Ho & Huerre 1984), the Taylor–Couette flow with through flow (Babcock *et al.* 1991) or the wake behind a cylinder (Le Gal & Croquette 2000). In the AU regime, similar systems generally display robust natural oscillations that are believed to be insensitive to low noise levels (Huerre 2000). However, a variety of unstable systems, e.g. side-branching dendrites (Bouissou *et al.* 1990), are known to exhibit a strong receptivity to periodic rather than random perturbations. Similarly, by revisiting spatially developing media displaying a central AU domain embedded in two semi-infinite at most CU regions, the present investigation shows that small-amplitude *harmonic* forcing can completely modify the natural nonlinear behaviour. It should be emphasized that the aim is not to suppress the fluctuations but to tune them to an externally imposed frequency and thereby also to modify the local wavelengths and amplitudes.

2. Problem formulation

The present study is based on a general one-dimensional model equation that accounts for the dynamics of a variety of physical systems and is tractable by analytical methods. The model (2.1) has on many occasions proven to be a convenient test ground to recognize and study generic features that have later been identified in a variety of situations. The same strategy is adopted here. We assume that the system under consideration is described by a complex scalar field $\psi(x, t)$ in an infinite one-dimensional spatially inhomogeneous domain and is governed by

$$\begin{aligned} \frac{\partial\psi}{\partial t} = & -i(\omega_0(X) + \frac{1}{2}\omega_{kk}(X)k_0(X)^2)\psi + \omega_{kk}(X)k_0(X)\frac{\partial\psi}{\partial x} \\ & + \frac{1}{2}i\omega_{kk}(X)\frac{\partial^2\psi}{\partial x^2} - i\gamma(X)|\psi|^2\psi + S(x, t), \end{aligned} \quad (2.1)$$

where the complex functions $\omega_0(X)$, $k_0(X)$, $\omega_{kk}(X)$ and $\gamma(X)$ account for the local properties of the medium and only depend on a slow space variable $X = \epsilon x$. The weak inhomogeneity parameter $\epsilon \ll 1$ is defined as the ratio of the typical instability length-scale to the non-uniformity length-scale of the medium. The source function $S(x, t)$ represents an externally applied forcing, to be used below.

In the subsequent discussion, constant use is made of the *local* linear and nonlinear properties of system (2.1), which are presented now. Local characteristics are derived from (2.1) by freezing X and studying the corresponding spatially homogeneous medium. Linear properties pertain to the dynamics of small-amplitude normal modes of the form $e^{i(kx-\omega t)}$, where the complex frequency ω and complex wavenumber k satisfy the linear dispersion relation

$$\omega = \Omega^1(k, X) \equiv \omega_0(X) + \frac{1}{2}\omega_{kk}(X)(k - k_0(X))^2. \quad (2.2)$$

The particular form in which the coefficients of (2.1) have been cast brings to the fore the local complex absolute frequency $\omega_0(X)$ associated with the local complex absolute wavenumber $k_0(X)$ determined by a zero group velocity condition as (Briggs 1964; Bers 1983)

$$\omega_0(X) = \Omega^l(k_0(X), X) \quad \text{with} \quad \frac{\partial \Omega^l}{\partial k}(k_0(X), X) = 0.$$

In a typical situation of interest, the local absolute growth rate $\omega_{0,i}(X)$ displays a single maximum $\omega_{0,i}^{\max}$ and the medium is stable for large $|X|$. The system under consideration then exhibits an AU domain whenever $\omega_{0,i}^{\max} > 0$.

The model equation (2.1) also admits finite-amplitude travelling waves $R e^{i(kx - \omega t)}$, where the real amplitude R , real frequency ω and real wavenumber k satisfy the nonlinear dispersion relations

$$\omega = \Omega^{nl}(k, X) \equiv \frac{\text{Im}[\gamma(X)^* \Omega^l(k, X)]}{-\gamma_i(X)}, \quad (2.3)$$

$$R^2 = \mathcal{R}(k, X)^2 \equiv \frac{\Omega_i^l(k, X)}{-\gamma_i(X)}, \quad (2.4)$$

with superscript $*$ denoting complex conjugate. Note that the condition of stabilizing nonlinearities requires that $\gamma_i(X) < 0$. At a given value of X , nonlinear wavetrains thus exist ($R^2 > 0$) for the range of real wavenumbers k associated with a positive temporal growth rate $\Omega_i^l(k, X) > 0$, and the nonlinear amplitude R vanishes for marginal wavenumbers associated with $\Omega_i^l(k, X) = 0$.

3. Signalling problem

Of particular importance to the present work is the spatial response to localized time-harmonic forcing switched on at $t = 0$. This problem is governed by equation (2.1) with the source term

$$S(x, t) = A_f \delta(x - x_f) H(t) e^{-i\omega_f t}, \quad (3.1)$$

where A_f , $X_f \equiv \epsilon x_f$ and ω_f represent the forcing amplitude, location and (real) frequency, respectively, δ denotes the Dirac delta function† and H the Heaviside unit step function.

Consider the spatial response of system (2.1) in a situation where no AU region is present, i.e. $\omega_{0,i}^{\max} < 0$. Then no self-sustained oscillations are produced and the resulting field $\psi_f(x, t)$ is purely due to the external forcing (figure 1). Under the slowly varying medium hypothesis ($\epsilon \ll 1$), the long-time response of constant frequency ω_f is obtained in terms of Werner–Kramers–Brillouin (WKB) asymptotic approximations (Bender & Orszag 1978) of the form

$$\psi_f = A(X; \omega_f) \exp\left(\frac{i}{\epsilon} \int_{X_f}^X k(u; \omega_f) du - i\omega_f t\right). \quad (3.2)$$

† The representation $\delta(x) = (1/(\sqrt{\pi}\sigma)) \exp(-x^2/\sigma^2)$ with $\sigma = 1/4$ is used in the numerical implementation below.

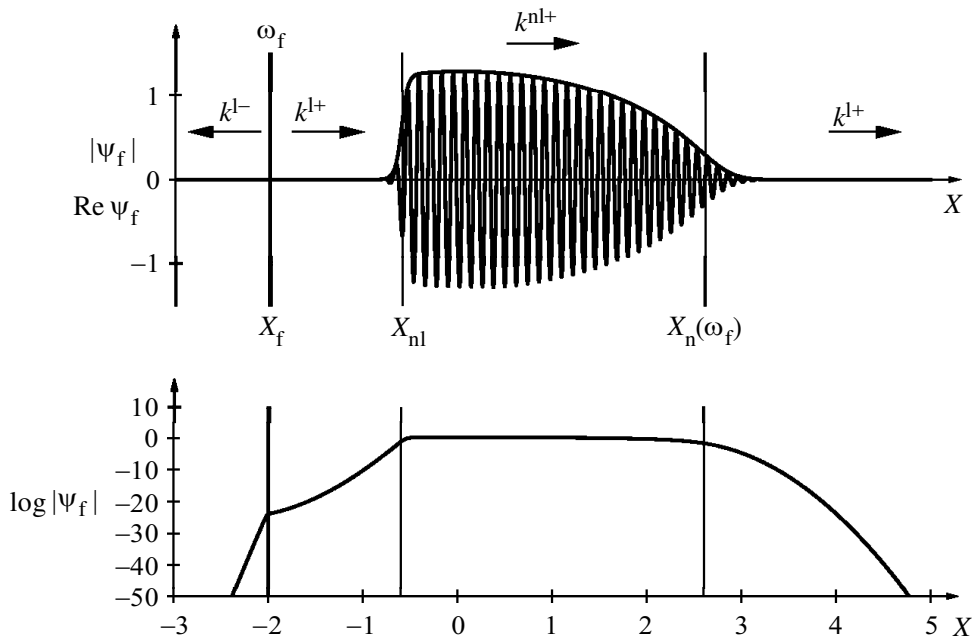


Figure 1. Envelope $|\psi_f|$ and real part $\text{Re } \psi_f$ of spatial response of governing equation to time-harmonic forcing of frequency $\omega_f = 1$ and amplitude $A_f = 10^{-10}$ applied at $X_f = -2$. Numerical simulation performed with $\omega_0 = 0.4 - 0.2(1 + X^2)i$, $k_0 = 1 - 1.5i$, $\omega_{kk} = 1 - 0.5i$, $\gamma = 0.2 - i$ and $\epsilon = 1/25$. Decaying upstream response follows $k^{l-}(X; \omega_f)$ branch. Downstream response exponentially grows according to $k^{l+}(X; \omega_f)$ to reach finite amplitude at $X_{nl} = -0.6$, where the nonlinear $k^{nl+}(X; \omega_f)$ branch takes over. Further downstream, beyond the neutral station $X_n(\omega_f) = 2.6$, the decaying $k^{l+}(X; \omega_f)$ prevails.

In this expression, the local wavenumber branch $k(X; \omega_f)$ accounts for the fast spatial variations, whereas the amplitude function $A(X; \omega_f)$ only depends on slow space and is obtained in classical WKB fashion as a series expansion

$$A(X; \omega_f) \sim A_0(X; \omega_f) + \epsilon A_1(X; \omega_f) + \epsilon^2 A_2(X; \omega_f) + \dots \quad (3.3)$$

For reasons that become clear below, we only consider exponentially small forcing amplitudes $A_f = e^{\alpha/\epsilon}$ with $\alpha < 0$. In the vicinity of the forcing location X_f , the spatial response is then governed by linear dynamics, and the resulting complex local wavenumber branch is obtained by solving (2.2) for $\omega = \omega_f$ as

$$k^{l\pm}(X; \omega_f) = k_0(X) \pm \sqrt{2 \frac{\omega_f - \omega_0(X)}{\omega_{kk}(X)}}. \quad (3.4)$$

Causality considerations (Briggs 1964; Bers 1983) allow the unambiguous definition of the square-root branches in (3.4) such that the k^{l+} (k^{l-}) spatial branch pertains to the downstream $X > X_f$ (upstream $X < X_f$) side of the forcing location. Upon substituting (3.4) with (3.2) into the governing equation (2.1), a solvability condition governing the leading-order amplitude is derived as

$$\frac{dA_0}{dX} = -\frac{1}{2} \frac{dk^{l\pm}/dX}{k^{l\pm}(X; \omega_f) - k_0(X)} A_0(X; \omega_f). \quad (3.5)$$

Invoking continuity of the response at $X = X_f$, the exact long-time linear response is then obtained to leading order as

$$A_0(X; \omega_f) = A_f C_f \exp\left(\int_{X_f}^X -\frac{1}{2} \frac{dk^{l\pm}/du}{k^{l\pm}(u; \omega_f) - k_0(u)} du\right), \quad (3.6)$$

with

$$A_f = \exp \frac{\alpha}{\epsilon} \quad \text{and} \quad C_f = \frac{2}{\omega_{kk}(X_f)[k^{l+}(X_f; \omega_f) - k^{l-}(X_f; \omega_f)]}. \quad (3.7)$$

The modulus $|\psi_f|$ of the forced response (3.2) in the linear regions is then derived to leading order as

$$\log |\psi_f| \sim \frac{1}{\epsilon} \left(\alpha - \int_{X_f}^X k_i^{l\pm}(u; \omega_f) du \right). \quad (3.8)$$

In stable or at most CU regions, the upstream spatial response decays for all frequencies, $k_i^{l-}(X; \omega) < 0$. The linear approximation then applies to the entire region $-\infty < X < X_f$ upstream of the forcing location. For forcing applied at a CU location, there exists a range of frequencies associated with downstream growth, i.e. such that $k_i^{l+}(X_f; \omega_f) < 0$. The downstream spatial response then exponentially grows to reach finite amplitude levels. Nonlinear saturation prevents further growth and leads to a nonlinear wavetrain at the forcing frequency. The nonlinear saturation station X_{nl} where the modulus $|\psi_f|$ takes $\mathcal{O}(1)$ values depends on the forcing amplitude and is determined by (3.8) as

$$\int_{X_f}^{X_{nl}} k_i^{l+}(u; \omega_f) du = \alpha. \quad (3.9)$$

Thus, the downstream linear $k^{l+}(X; \omega_f)$ spatial branch prevails in the interval $X_f < X < X_{nl}$, which is of finite extent in terms of the slow variable X only for an exponentially weak forcing amplitude $A_f = e^{-|\alpha|/\epsilon}$ with $|\alpha| = \mathcal{O}(\epsilon^0)$.

Downstream of X_{nl} , the spatial response is made up of a finite-amplitude saturated wavetrain of frequency ω_f governed by the local nonlinear dispersion relations (2.3), (2.4). The local wavenumber in (3.2) then follows the real spatial branch $k^{nl+}(X; \omega_f)$ obtained by solving (2.3) for the prescribed forcing frequency $\omega = \omega_f$. In the nonlinear regime, the modulus of the leading-order amplitude (3.3) is determined by (2.4) as

$$|A_0(X; \omega_f)| = \mathcal{R}(k^{nl+}(X; \omega_f), X), \quad (3.10)$$

whereas its phase is governed by a solvability condition at higher order. A detailed discussion of the relationship between nonlinear spatial response and causality as well as a full derivation of nonlinear WKB approximations can be found in Pier *et al.* (2001).

The nonlinear wavetrain of local wavenumber $k^{nl+}(X; \omega_f)$ prevails in the interval $X_{nl} < X < X_n(\omega_f)$ beyond which the spatial response exponentially decays. The transition station $X_n(\omega_f)$ from a nonlinear to a linear regime is characterized by the neutral stability condition $\Omega_i^l(k^{nl+}(X_n; \omega_f), X_n) = 0$. The amplitude of the nonlinear travelling wave vanishes there, and the complex branch $k^{l+}(X; \omega_f)$ continuously takes over in the downstream linear region $X > X_n(\omega_f)$. It should be noted that for a given forcing frequency the onset station of nonlinearities X_{nl} also depends on the forcing amplitude whereas the neutral station X_n does not.

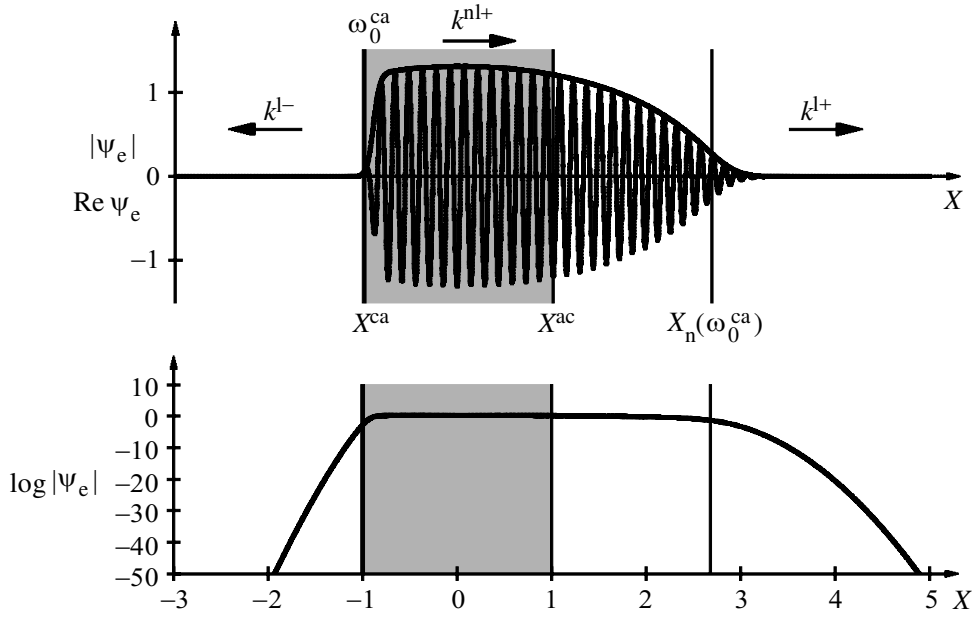


Figure 2. Envelope $|\psi_e|$ and real part $\text{Re } \psi_e$ of the self-sustained structure illustrated by the numerical simulation of unforced governing equation with $\omega_0 = 0.4 + 0.3(1 - X^2)i$, $k_0 = 1 - 1.5i$, $\omega_{kk} = 1 - 0.5i$, $\gamma = 0.2 - i$ and $\epsilon = 1/25$. Central AU domain $X^{\text{ca}} = -1 < X < X^{\text{ac}} = 1$ is shaded. The front of frequency $\omega_0^{\text{ca}} = 0.4$ at X^{ca} generates the upstream linear $k^{l-}(X; \omega_0^{\text{ca}})$ branch and the downstream nonlinear $k^{\text{n}l+}(X; \omega_0^{\text{ca}})$ branch. Further downstream, beyond the neutral station $X_n(\omega_0^{\text{ca}}) = 2.8$, the exponentially decaying $k^{l+}(X; \omega_0^{\text{ca}})$ prevails.

4. Self-sustained oscillations

Before applying the above results to control media displaying a central AU region, their self-sustained behaviour is summarized. Consider a situation where $\omega_{0,i}^{\max} > 0$, associated with an AU interval $X^{\text{ca}} < X < X^{\text{ac}}$. Then a fully nonlinear temporally periodic state is reached without external input (Pier *et al.* 2001). At $\omega_{0,i}^{\max} = 0$, onset of a self-sustained state occurs via a saddle-node bifurcation; for moderate values of $\omega_{0,i}^{\max} > 0$ an ‘elephant’ or ‘steep’ nonlinear structure (Pier & Huerre 2001) is selected (figure 2), characterized by a sharp (Dee & Langer 1983) front at the upstream boundary X^{ca} of the AU domain. This front of real frequency $\omega_0^{\text{ca}} \equiv \omega_0(X^{\text{ca}})$ acts as a wavemaker, hence tuning the entire system to a single frequency. The entire field $\psi_e(x, t)$ may then be interpreted as the spatial response to this front. Indeed, in the upstream linear region $X < X^{\text{ca}}$, the complex field $\psi_e(x, t)$ follows the complex spatial $k^{l-}(X; \omega_0^{\text{ca}})$ branch and its modulus exponentially decays according to

$$\log |\psi_e| \sim -\frac{1}{\epsilon} \int_{X^{\text{ca}}}^X k_i^{l-}(u; \omega_0^{\text{ca}}) du. \quad (4.1)$$

The region $X^{\text{ca}} < X < X_n(\omega_0^{\text{ca}})$ is made up of finite-amplitude waves following the nonlinear $k^{\text{n}l+}(X; \omega_0^{\text{ca}})$ branch. Beyond the neutrally stable station $X_n(\omega_0^{\text{ca}})$, the decaying linear $k^{l+}(X; \omega_0^{\text{ca}})$ branch prevails. Further above onset of a nonlinear self-sustained state, i.e. for larger values of $\omega_{0,i}^{\max}$, ‘steep’ modes may give way to ‘soft’ modes (Pier *et al.* 2001; Pier & Huerre 2001); their control is not discussed here.

We emphasize the important fact that the fully nonlinear self-sustained structure is determined by a purely linear criterion, based only on the local absolute frequency curve $\omega_0(X)$. The front is of ‘pulled’ (Ebert & van Saarloos 2000) type and its

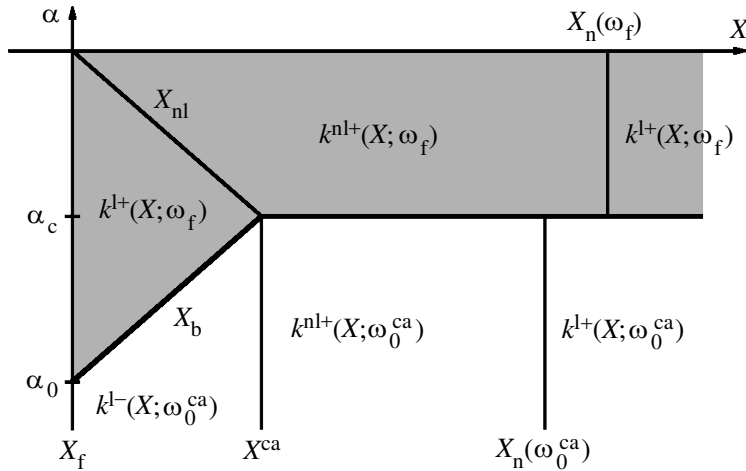


Figure 3. Map of regions tuned to forcing frequency ω_f (shaded) or to intrinsic frequency ω_0^{ca} as a function of the forcing amplitude $A_f = e^{\alpha/\epsilon}$ while forcing frequency ω_f and location X_f are kept constant. Below the control threshold $\alpha < \alpha_c$, the forcing frequency ω_f prevails in the region $X_f < X < X_b$, whereas the self-sustained structure of frequency ω_0^{ca} survives in $X > X_b$. For $\alpha > \alpha_c$, the forced response supersedes the intrinsic oscillations in the *entire* system. At each α , the dominant component of the total field ψ follows the spatial linear or nonlinear branches indicated in the corresponding regions.

dynamics is determined by the decaying tail: the front envelope is stationary in time if the front location is precisely at the CU–AU transition station X^{ca} . Note also that the region $X > X^{ca}$ downstream of the AU domain is slaved to the wavemaker prevailing at X^{ca} and does not play an active part in the dynamics. The result that self-sustained nonlinear oscillations are triggered by a stationary front at X^{ca} suggests that this intrinsic behaviour may be modified by perturbing the front.

5. Control

Consider now applying to the intrinsic nonlinear structure a forcing of frequency ω_f and small amplitude $A_f = e^{\alpha/\epsilon}$ localized at X_f in the CU region, $X_f < X^{ca}$. For small forcing amplitudes, both the spatial response of frequency ω_f and the self-sustained mode of frequency ω_0^{ca} are governed by linear dynamics in the neighbourhood of X_f . The resulting field in the linear region is then obtained as a superposition $\psi = \psi_f + \psi_e$ of the forced response of frequency ω_f and the natural oscillations of frequency ω_0^{ca} . At a given location, the dominant component in the total field depends on the relative modulus of ψ_f (3.8) and ψ_e (4.1).

In the interval $X_f < X < X^{ca}$, the local spatial growth rates of ψ_f and ψ_e are respectively given by $-k_i^{l+}(X; \omega_f)$ and $-k_i^{l-}(X; \omega_0^{ca})$. From (3.4) and causality it is seen that always $k_i^{l+}(X; \omega) > k_i^{l-}(X; \omega)$; hence the result

$$k_i^{l+}(X; \omega_f) > k_i^{l-}(X; \omega_0^{ca}) \quad (5.1)$$

holds for forcing frequencies ω_f sufficiently close to the natural frequency ω_0^{ca} . A comprehensive survey of all possible configurations of equation (2.1) has not been attempted, but inequality (5.1) was found to hold for all forcing frequencies associated with downstream growth. The result (5.1) means that from the forcing location X_f towards the front location X^{ca} the modulus of the natural oscillations $|\psi_e|$ grows

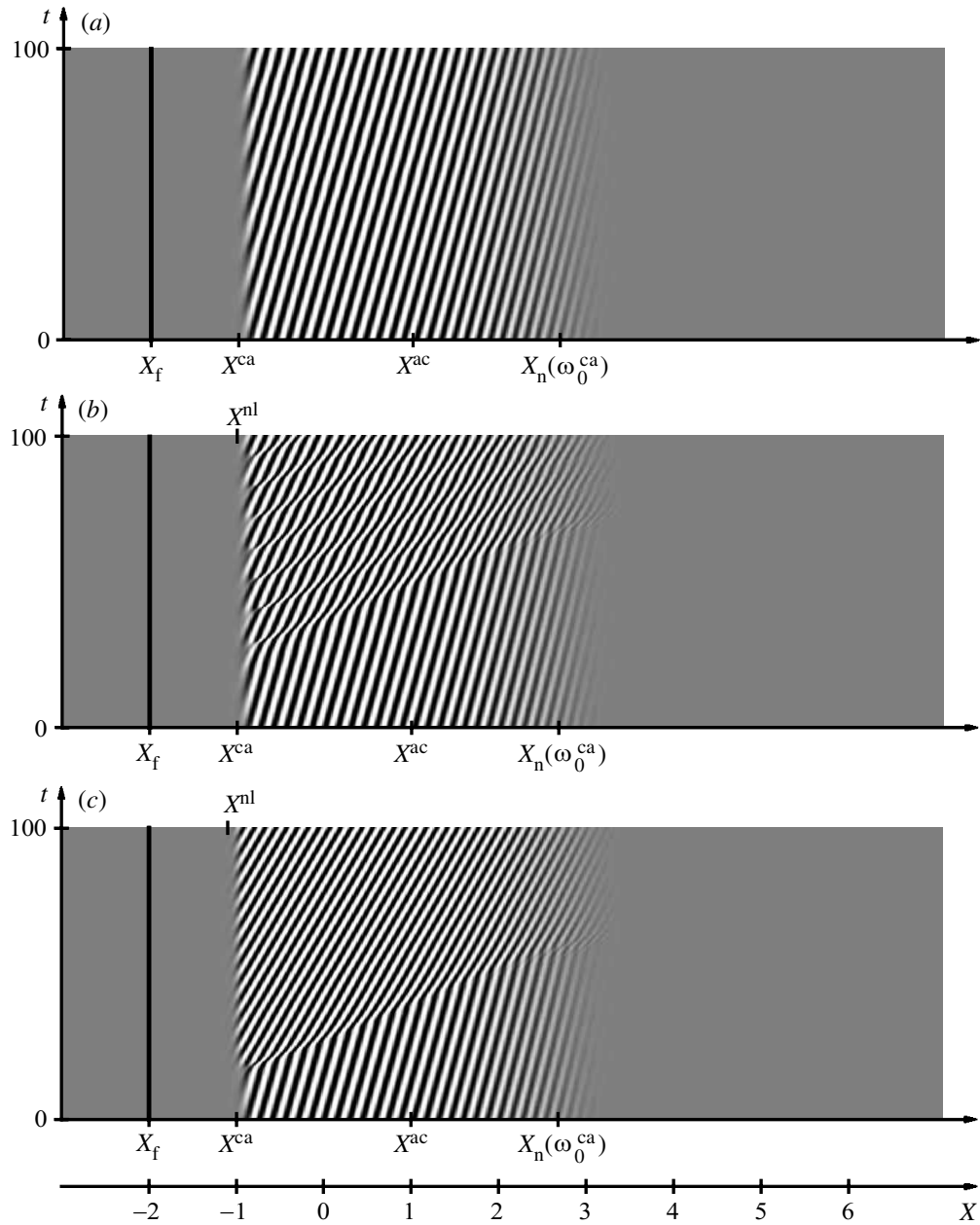


Figure 4. Control of self-sustained structure by localized harmonic forcing. Spatio-temporal greylevel representation of $\text{Re}\psi(x, t)$. Parameter settings are as in figure 2, and for $t < 0$ the system is in a state of natural oscillations tuned to $\omega_0^{\text{ca}} = 0.4$ with a front at $X^{\text{ca}} = -1$. Forcing of frequency $\omega_f = 1$ is applied at $X_f = -2$ and switched on at $t = 0$ with different amplitudes A_f . (a) With $A_f = 10^{-12}$, external forcing is unable to perturb nonlinear self-sustained structure. (b) With $A_f = 10^{-11}$, spatial response reaches finite amplitude precisely at the front location $X_{\text{nl}} = X^{\text{ca}}$ and continuous competition between both frequencies takes place. (c) With $A_f = 10^{-10}$, spatial response achieves nonlinear regime at $X_{\text{nl}} = -1.1$ upstream of X^{ca} and rapidly replaces the natural oscillations.

faster than the forced response $|\psi_f|$. The regions dominated by either the forcing frequency ω_f or the natural frequency ω_0^{ca} may then be monitored for different values of the forcing amplitude $e^{\alpha/\epsilon}$ while keeping the forcing location and frequency at prescribed values (figure 3).

For extremely weak forcing $\alpha < \alpha_0$ with

$$\alpha_0 \equiv \int_{X_f}^{X^{ca}} k_i^{1-}(u; \omega_0^{ca}) du < 0, \quad (5.2)$$

the forced response is dominated by the intrinsic oscillations at the very forcing location. Due to the different spatial growth rates (5.1), the self-sustained mode of frequency ω_0^{ca} then prevails over the forced response in the entire system.

For higher forcing amplitudes $\alpha > \alpha_0$, the response ψ_f dominates ψ_e at the forcing location X_f . However, since $|\psi_e|$ grows faster than $|\psi_f|$ with increasing X , the forcing frequency ω_f only prevails in the interval $X_f < X < X_b$ extending towards the location X_b , where both components display a similar modulus and beyond which ψ_e prevails. The boundary X_b between the regions tuned to the forcing frequency ω_f or to the natural frequency ω_0^{ca} is thus determined as

$$\int_{X_f}^{X_b} k_i^{1+}(u; \omega_f) du - \int_{X_b}^{X^{ca}} k_i^{1-}(u; \omega_0^{ca}) du = \alpha. \quad (5.3)$$

With increasing forcing level, the region dominated by ω_f grows in size and the boundary X_b eventually reaches the front location X^{ca} . This occurs at the critical forcing amplitude, α_c , given by

$$\alpha_c \equiv \int_{X_f}^{X^{ca}} k_i^{1+}(u; \omega_f) du. \quad (5.4)$$

For forcing levels in the range $\alpha_0 < \alpha < \alpha_c$, the response of frequency ω_f does not achieve $\mathcal{O}(1)$ amplitudes at the front location X^{ca} and is thus unable to perturb the nonlinear self-sustained waves of frequency ω_0^{ca} prevailing for $X > X^{ca}$ (figure 4a). For $\alpha = \alpha_c$, however, the forced response reaches finite amplitude precisely at X^{ca} and competes with the stationary front of the intrinsic nonlinear structure. Numerical simulations performed in this situation (figure 4b) reveal that the forced response is then able to continually perturb the natural oscillations and the system does not converge to an equilibrium state tuned at a single frequency.

For slightly stronger forcing, $\alpha > \alpha_c$, the response at frequency ω_f reaches nonlinear saturation upstream of the front, i.e. $X_{nl} < X^{ca}$. In this regime (figure 4c), *the intrinsic oscillations at ω_0^{ca} are completely suppressed and replaced by the forced response in the entire domain*. For still higher forcing amplitudes, the system remains tuned at ω_f , and its spatial structure does not evolve except that the nonlinear saturation station X_{nl} moves upstream towards X_f (cf. figure 3).

This behaviour may be interpreted as the result of two competing sources of different frequencies at different locations: the self-sustained ω_0^{ca} -front at X^{ca} responsible for the natural nonlinear structure and the external ω_f -forcing at X_f . In the absence of external forcing, the front at X^{ca} acts as a cornerstone upon which the global structure is based; this front dictates its frequency to the entire system and generates the downstream developing nonlinear wavetrain covering the AU region. When forcing is applied at X_f , the intrinsic wavemaker at X^{ca} survives only if the upstream decaying front tail experiences an unperturbed medium. As soon as the front is overwhelmed by a finite-amplitude wave, the source of the ‘steep’ mode is suppressed and so is the entire self-sustained structure. The underlying AU region then plays no role

in the dynamics, since it is effectively masked by an externally imposed nonlinear wavetrain. Thus, the oscillator-type behaviour of AU domains appears to be robust with respect to external forcing *only* if the strength of the forcing does not exceed an exponentially small level.

Effective control of the central AU domain requires that the forcing location and frequency are chosen so as to produce a downstream growing response, i.e. $k_i^{1+}(X_f; \omega_f) < 0$. This condition of downstream growth is fulfilled for a range of frequencies ω_f when forcing is applied at a position X_f in the CU domain. Moreover, tuning to a single frequency can only be achieved when this forcing frequency produces nonlinear waves that are stable with respect to secondary perturbations. The precise range of possible control frequencies depends on the particular parameter settings of (2.1). In typical configurations, control of the system at twice or half the natural frequency is readily obtained.

In summary, an externally imposed nonlinear wave at the transition station from local convective to absolute instability entirely suppresses the intrinsic behaviour. Self-sustained oscillations may thus be controlled and tuned to a prescribed frequency, chosen such as to avoid damaging resonances or to improve performance of the system under consideration. Due to exponential growth of the forced response in the CU region, only an exponentially small forcing amplitude, and hence controller power, is required to achieve this result.

Enlightening and fruitful collaboration with Nigel Peake is gratefully acknowledged.

References

- Babcock, K. L., Ahlers, G. & Cannel, D. S. 1991 Noise-sustained structure in Taylor–Couette flow with through flow. *Phys. Rev. Lett.* **67**, 3388–3391.
- Bender, C. M. & Orszag, S. A. 1978 *Advanced mathematical methods for scientists and engineers*. New York: McGraw-Hill.
- Bers, A. 1983 Space-time evolution of plasma instabilities: absolute and convective. In *Handbook of plasma physics* (ed. M. N. Rosenbluth & R. Z. Sagdeev), pp. 451–517. Amsterdam: North-Holland.
- Bewley, T. R. & Liu, S. 1998 Optimal and robust control and estimation of linear paths to transition. *J. Fluid Mech.* **365**, 305–349.
- Bouissou, P., Chiffaudel, A., Perrin, B. & Tabeling, P. 1990 Dendritic side-branching forced by an external flow. *Europhys. Lett.* **13**, 89–94.
- Briggs, R. J. 1964 *Electron-stream interaction with plasmas*. Cambridge, MA: MIT Press.
- Couairon, A. & Chomaz, J.-M. 1996 Global instabilities in fully nonlinear systems. *Phys. Rev. Lett.* **77**, 4015–4018.
- Couairon, A. & Chomaz, J.-M. 1997a Absolute and convective instabilities, front velocities and global modes in nonlinear systems. *Physica D* **108**, 236–276.
- Couairon, A. & Chomaz, J.-M. 1997b Pattern selection in the presence of a cross flow. *Phys. Rev. Lett.* **79**, 2666–2669.
- Couairon, A. & Chomaz, J.-M. 1999 Fully nonlinear global modes in slowly varying flows. *Phys. Fluids* **11**, 3688–3703.
- Dee, G. & Langer, J. S. 1983 Propagating pattern selection. *Phys. Rev. Lett.* **50**, 383–386.
- Ebert, U. & van Saarloos, W. 2000 Front propagation into unstable states: universal algebraic convergence towards uniformly translating pulled fronts. *Physica D* **146**, 1–99.
- Ho, C.-M. & Huerre, P. 1984 Perturbed free shear layers. *A. Rev. Fluid Mech.* **16**, 365–424.

- Huerre, P. 2000 Open shear flow instabilities. In *Perspectives in fluid dynamics* (ed. G. K. Batchelor, H. K. Moffatt & M. G. Worster), pp. 159–229. Cambridge University Press.
- Huerre, P. & Monkewitz, P. A. 1990 Local and global instabilities in spatially developing flows. *A. Rev. Fluid Mech.* **22**, 473–537.
- Kapral, R. & Showalter, K. (eds) 1995 *Chemical waves and patterns*. Dordrecht: Kluwer.
- Le Gal, P. & Croquette, V. 2000 Visualization of the space-time impulse response of the sub-critical wake of a cylinder *Phys. Rev. E* **62**, 4424–4426.
- Meunier, N., Proctor, M. R. E., Sokoloff, D. D., Soward, A. M. & Tobias, S. M. 1997 Asymptotic properties of a nonlinear $\alpha\omega$ -dynamo wave: period, amplitude and latitude dependence. *Geophys. Astrophys. Fluid Dynam.* **86**, 249–285.
- Pier, B. & Huerre, P. 2001 Nonlinear synchronization in open flows. *J. Fluids Struct.* **15**, 471–480.
- Pier, B., Huerre, P. & Chomaz, J.-M. 2001 Bifurcation to fully nonlinear synchronized structures in slowly varying media. *Physica D* **148**, 49–96.
- Reed, H. L. & Saric, W. S. 1989 Stability of three-dimensional boundary layers. *A. Rev. Fluid Mech.* **21**, 235–284.
- Winfrey, A. T. 1987 *When time breaks down*. Princeton, NJ: Princeton University Press.

[A9]

**Finite amplitude crossflow vortices, secondary instability and transition
in the rotating-disk boundary layer**

B. Pier

Journal of Fluid Mechanics **487**, 315–343 (2003)

doi :10.1017/S0022112003004981

<https://hal.archives-ouvertes.fr/hal-00120026>

Finite-amplitude crossflow vortices, secondary instability and transition in the rotating-disk boundary layer

By BENOÎT PIER†

Department of Applied Mathematics and Theoretical Physics, University of Cambridge,
Centre for Mathematical Sciences, Wilberforce Road, Cambridge, CB3 OWA, UK

(Received 6 December 2002 and in revised form 17 March 2003)

In the three-dimensional boundary layer produced by a rotating disk, the experimentally well-documented sharp transition from laminar to turbulent flow is shown to coincide with secondary absolute instability of the naturally selected primary nonlinear crossflow vortices. Fully saturated primary finite-amplitude waves and the associated nonlinear dispersion relation are first numerically computed using a local parallel flow approximation. Exploiting the slow radial development of the basic flow, the naturally selected primary self-sustained flow structure is then derived by asymptotic analysis. In this state, outward-spiralling nonlinear vortices are initiated at the critical radius where primary absolute instability first occurs. A subsequent secondary stability analysis reveals that as soon as the primary nonlinear waves come into existence they are absolutely unstable with respect to secondary perturbations. Secondary disturbances growing in time at fixed radial locations continuously perturb the primary vortices, thus triggering the direct route to turbulence prevailing in this configuration.

1. Introduction

The flow due to an infinite disk rotating in otherwise still fluid has served as the archetypal configuration for the study of three-dimensional boundary layers ever since von Kármán (1921) obtained the basic flow as an exact similarity solution of the Navier–Stokes equations. Interest in this flow has been renewed by Lingwood's (1995) discovery that it exhibits a transition from local linear convective to absolute instability at a radius R^{ca} which closely corresponds to the location of experimentally observed turbulence onset (Theodorsen & Regier 1944; Gregory, Stuart & Walker 1955; Chin & Litt 1972; Fedorov, *et al.* 1976; Kobayashi, Kohama & Takamadate 1980; Malik, Wilkinson & Orszag 1981; Lingwood 1996). The present investigation, inspired by Lingwood's (1995) result, addresses the fully nonlinear régime. The objective is to analyse the naturally selected finite-amplitude state and its secondary stability properties in order to elucidate the process responsible for the sudden transition to turbulence.

The Kármán boundary layer is a rather crude and academic representation of a centrifugal pump, a turbomachinery rotor or even of a computer hard disk. However,

† Present address: Laboratoire de mécanique des fluides et d'acoustique, École centrale, 36 avenue Guy-de-Collongue, 69130 Écully, France.

despite its simplicity, it displays most of the features observed in situations of higher complexity or with more elaborate geometries, e.g. with the fluid at infinity in rigid-body rotation at the same or a different rate (Batchelor 1951; Zandbergen & Dijkstra 1987), the flow between a stationary and a rotating disk enclosed by a cylinder (Jarre, Le Gal & Chauve 1996a; Gauthier, Gondret & Rabaud 1999; Schouwiler, Le Gal & Chauve 2001), and the flow in a rotor–stator annular cavity with radial throughflow (Serre, Crespo del Arco & Bontoux 2001a; Serre *et al.* 2001b). The rotating-disk problem is also closely related to the flow over a backward swept wing (Gregory *et al.* 1955; Cebeci & Stewartson 1980; Bippes, Müller & Wagner 1991; Cebeci *et al.* 1991; Lin & Reed 1993; Malik, Li & Chang 1996, Koch 1996), and it is often claimed that their behaviour is governed by analogous principles. All these types of boundary layers display similar three-dimensional velocity profiles, are subject to inviscid crossflow instabilities and undergo transition to turbulent flow, cf. Reed & Saric (1989). Despite intensive work and recent advances, cf. Schmid & Henningson (2000) and Saric, Reed & White (2003), no full understanding of the turbulent breakdown process has yet been achieved. Identification of the mechanism(s) responsible for transition would improve the prediction methods and lead to new and efficient control strategies, of considerable practical importance e.g. to the aeronautics industry.

However the analogy between a rotating disk and a swept wing is not complete. First, the rotating disk displays self-similar velocity profiles, so that only the study of a single flow instance is required, while the swept-wing boundary layer depends on several control parameters such as sweep angle and chordwise pressure gradient. But the essential difference resides in the azimuthal periodicity of the disk, while the wing lacks any periodic coordinate. Thus perturbations may be naturally recycled in the disk flow, and this property greatly affects its long-time behaviour.

Consider the response to a brief and localized perturbation applied in a region where the boundary layer is unstable, e.g. blowing through a small hole in the disk/wing surface. With time, a wavepacket develops that propagates along the surface while it grows in amplitude and size. The interplay of propagation and growth dictates the long-time behaviour. If the wavepacket is blown away by the basic flow faster than it expands, the flow is said to be *convectively unstable* and, without continuous external input, eventually returns to its unperturbed state. If, by contrast, growth of the wavepacket dominates over advection, the medium is said to be *absolutely unstable* and perturbations grow *in situ* without further external forcing (Briggs 1964; Bers 1983; Huerre & Monkewitz 1990).

In the three-dimensional boundary layer produced by a swept wing, wavepackets may be advected along chordwise and spanwise directions: a genuine absolute instability thus requires the disturbances to maintain themselves in both directions. Investigations of the long-time behaviour of the impulse response in the swept-wing problem (Lingwood 1997b; Ryzhov & Terent'ev 1998; Taylor & Peake 1998) have revealed the possibility of a chordwise absolute instability, but no instance of spanwise absolute instability has so far been found, i.e. perturbations grow in time at a fixed chordwise location while they continue to be advected in the spanwise direction so as to eventually be shed from the wing tip. These results suggest that the persistent fluctuations over aircraft wings are triggered by continuous external disturbances such as roughness elements on the surface or atmospheric turbulence.

The rotating-disk boundary layer contrasts with the above scenario. Due to the exact periodicity in the azimuthal coordinate, a mere radial absolute instability (as theoretically established by Lingwood 1995) is a sufficient condition for disturbance

growth at a fixed location. Indeed, a wavepacket triggered by an initial impulse and amplifying at a constant radial position may, in the early stage of its development, be carried around in the azimuthal direction but, in the long term, it will grow and eventually cover the full circumferential extent of the disk. While many experimental studies (Gregory *et al.* 1955; Kohama 1984; Wilkinson & Malik 1985) have focused on perturbations that are fixed with respect to the disk, and thus certainly generated by roughness elements, the study of the impulse response by Lingwood (1996) has experimentally validated the above scenario of self-sustained disturbances triggered by an initial perturbation and surviving without further external input.

The close relationship between global self-sustained oscillations and local absolute instability has been clarified over the past decade by successively considering one-dimensional model equations and the two-dimensional Navier–Stokes equations, first in a linear approximation and then in a fully nonlinear framework: linear model equations (Chomaz, Huerre & Redekopp 1991; Le Dizès *et al.* 1996), linear Navier–Stokes equations (Monkewitz, Huerre & Chomaz 1993), nonlinear model equations (Couairon & Chomaz 1996, 1997a,b, 1999a,b; Pier & Huerre 1996; Pier *et al.* 1998; Pier, Huerre & Chomaz 2001), nonlinear Navier–Stokes equations (Pier & Huerre 2001a; Pier 2002b), for a review see Huerre (2000). In the strictly linear framework, these investigations have shown that absolute instability is only a necessary condition for global instability and, in general, an absolutely unstable region of finite extent is a prerequisite. By contrast, the fully nonlinear governing equations admit self-sustained finite-amplitude solutions as soon as a point of local absolute instability appears and in some extreme cases even without absolute instability at all (Couairon & Chomaz 1997a). In the context of the rotating-disk flow, recent numerical (Davies & Carpenter 2003) and theoretical (Peake & Garrett 2003) investigations have shown that this configuration does not exhibit global instability in the linear approximation, even though absolute instability prevails in the semi-infinite region beyond a critical radius. These results suggest that only a nonlinear approach can possibly account for the self-sustained behaviour of the rotating-disk flow.

In situations where finite-amplitude waves develop, either as a naturally selected global mode or by continuous external forcing, the question arises of whether this primary nonlinear state is stable with respect to secondary disturbances. The techniques to carry out local secondary stability analyses are now well-established (Herbert 1988): the most common is to derive a Floquet system of linear differential equations with periodic coefficients after linearization of the governing equations about the primary nonlinear waves. Such an analysis requires first computation of the saturated primary periodic solution, e.g. in terms of a Fourier series, and then use of this as the new basic flow, which usually results in a large Floquet eigensystem. In view of this numerical task, when applied to three-dimensional boundary layers, most early secondary stability analyses (Reed 1987; Fischer & Dallmann 1991; Balachandar, Streett & Malik 1992) used the ‘shape assumption’ by which the nonlinear equilibrium solution is replaced by the linear eigenfunction scaled to a finite amplitude. It is only the recently available computing power that has made possible fully consistent secondary stability analyses (Malik, Li & Chang 1994; Höglberg & Henningson 1998; Malik *et al.* 1999; Janke & Balakumar 2000; Koch *et al.* 2000; Koch 2002).

Whether or not the primary saturated wavetrain survives in the long-term is determined by the convective or absolute nature of the secondary instability: only absolutely unstable secondary perturbations are able to resist basic flow advection, to grow at fixed spatial locations and to permanently destroy the underlying primary nonlinear wave. The mathematical foundation of secondary absolute instability

analysis has been firmly laid by Brevdo & Bridges (1996), but so far only a few periodic flows have been found to be absolutely unstable (Brancher & Chomaz 1997; Chomaz, Couairon & Julien 1999).

Huerre (1988) appears to be the first to have shown that secondary absolute instability may occur prior to onset of primary absolute instability. This is particularly relevant in the context of self-sustained oscillations, as demonstrated by Couairon & Chomaz (1999b) in a study of the Ginzburg–Landau equation: a primary nonlinear global mode exists whenever primary absolute instability occurs; this global mode is dynamically unstable whenever secondary absolute instability prevails for the selected primary nonlinear wavetrain. In familiar scenarios, primary and secondary absolute instability thresholds are crossed successively when a control parameter is increased. A stable global mode is then observed over a finite parameter range. Recent findings by Le Gal *et al.* (2003) seem to indicate that this scenario applies to the Batchelor flow between a rotating and a stationary disk. However, the order of thresholds may be reversed, and then the primary nonlinear global mode is unstable as soon as it comes into existence. In this latter situation, which is shown in the present paper to apply to the Kármán boundary layer over a single rotating disk, the global instability at the primary threshold leads in a single step to a disordered state.

As discussed above, the boundary layer over a swept wing does not display primary absolute instability and thus does not give rise to self-sustained fluctuations. Nonetheless, transition in that flow could be due to secondary absolute instability of the primary waves produced by roughness elements. In recent studies, Koch *et al.* (2000) and Koch (2002) have computed saturated zero-frequency crossflow vortices and investigated their secondary stability properties ‘in order to examine whether a change from convective to absolute instability is possible in crossflow vortices’. However, despite the remarkable techniques deployed by these authors, no secondary absolute instability has been found and the mechanism of laminar–turbulent breakdown remains to be elucidated in that configuration.

In the rotating-disk flow, azimuthal periodicity appears to facilitate the occurrence of absolute instability thus motivating the present study, a brief account of which has been previously given in Pier (2002a). The investigation was carried out in the same spirit as the work by Koch *et al.* (2000) and Koch (2002), and the outline is as follows. The self-similar laminar basic flow is presented in § 2 and the governing equations of the problem are given in § 3. For the sake of completeness the primary local linear stability characteristics are briefly reviewed in § 4 although these results are already well-established (Cebeci & Stewartson 1980; Malik *et al.* 1981; Malik 1986; Bassom & Gajjar 1988; Balakumar & Malik *et al.* 1990; Bassom & Hall 1991; Cebeci *et al.* 1991; Faller 1991; Lin & Reed 1993; Malik *et al.* 1994; Lingwood 1995). The core of the study is then aimed at characterizing and understanding the fully nonlinear régime. Local properties of fully nonlinear waves are computed in § 5 as solutions of a local nonlinear dispersion relation. Following the results of Pier *et al.* (2001), the naturally selected spatially extended global solution is derived in § 6 by asymptotic matching of these linear and nonlinear wavetrains. Finally, the stability of this self-sustained structure with respect to secondary perturbations is investigated in § 7 and the existence of a secondary absolute instability is established.

2. Laminar basic flow

The rotating-disk configuration calls for a formulation using cylindrical coordinates. Throughout this investigation an inertial frame of reference is used with r , θ and z

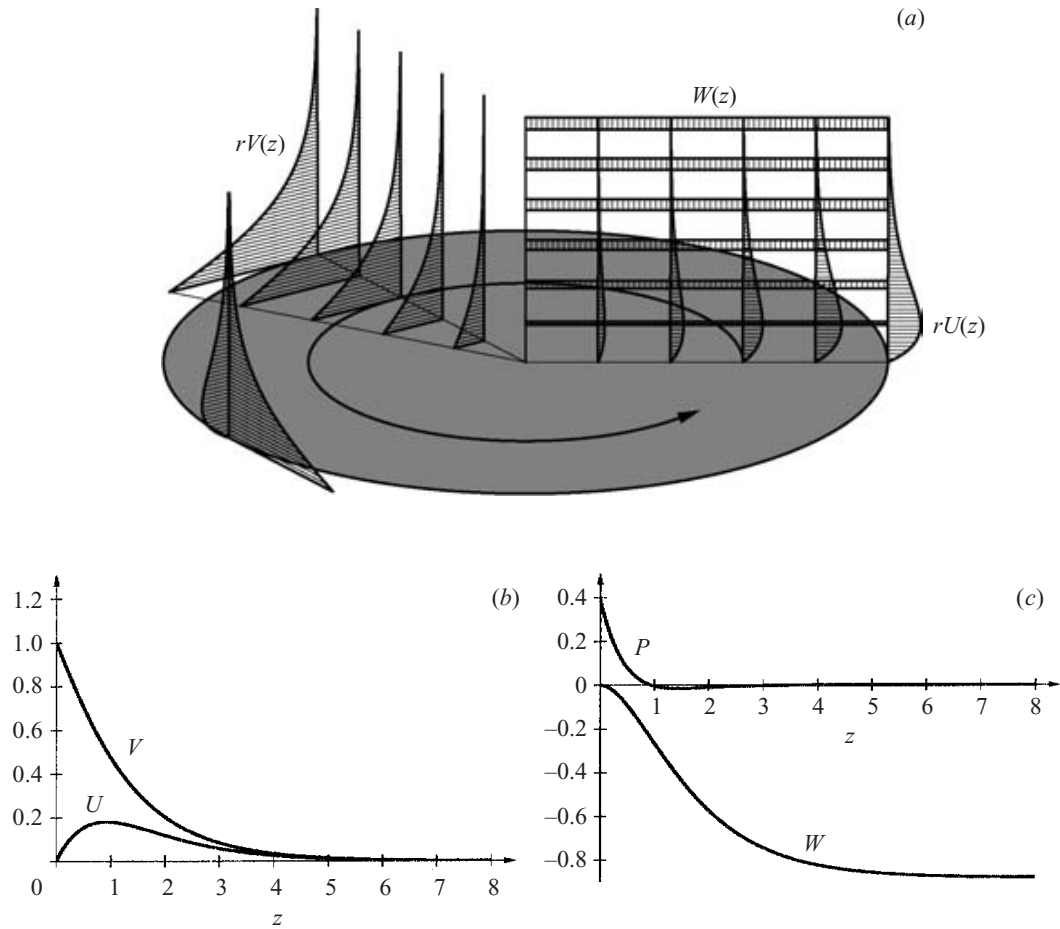


FIGURE 1. Basic flow over a rotating disk. (a) Radial $rU(z)$ and azimuthal $rV(z)$ velocity profiles linearly increase with radial distance while the axial flow $W(z)$ towards the disk surface does not depend on radius. (b, c) Similarity profiles of radial U , azimuthal V and axial W velocity components and pressure P .

denoting radial, azimuthal and axial coordinates respectively. The fluid in the domain $z > 0$ is brought into motion by the disk rotating at constant angular frequency about the axis $r = 0$ normal to the disk surface (figure 1a). The fluid near the disk acquires, by viscous stresses, an azimuthal velocity $rV(z)$ which linearly increases with radial distance. This circular motion results in centrifugal forces pulling the fluid outwards. The radial outflow $rU(z)$ induces, by continuity, a weak axial flow component $W(z)$ towards the disk. This axial flow reaches a constant value far from the disk surface and counteracts diffusion of vorticity away from the disk, thus maintaining a constant boundary layer thickness in the entire system (Batchelor 1967).

The infinite-disk problem lacks a characteristic length scale and thus allows the use of non-dimensional variables based on disk rotation rate, kinematic viscosity and fluid density, so that the flow does not depend on any control parameter. The time-independent axisymmetric basic flow is then given by von Kármán's (1921) exact similarity solution to the Navier–Stokes equations in cylindrical coordinates as

$$\mathbf{U}(r, z) \equiv \begin{pmatrix} rU(z) \\ rV(z) \\ W(z) \end{pmatrix} \quad \text{and} \quad P(z), \quad (2.1)$$

where rU , rV and W are the non-dimensional radial, azimuthal and axial velocity components respectively and P is the pressure. Figure 1(b, c) displays the self-similar components $U(z)$, $V(z)$ and $W(z)$ that are governed by the set of ordinary differential equations

$$U'' = U^2 - V^2 + U'W, \quad (2.2a)$$

$$V'' = 2UV + V'W, \quad (2.2b)$$

$$W' = -2U, \quad (2.2c)$$

with the boundary conditions

$$U(0) = 0, \quad V(0) = 1, \quad W(0) = 0 \quad \text{and} \quad U(\infty) = 0, \quad V(\infty) = 0. \quad (2.3)$$

With a reference pressure at $z = +\infty$, the associated local pressure is obtained as

$$P(z) = W'(z) + (W(\infty)^2 - W(z)^2)/2. \quad (2.4)$$

3. Mathematical formulation

After separating the total instantaneous flow fields into basic and perturbation quantities according to

$$\left. \begin{aligned} &U(r, z) + \mathbf{u}(r, \theta, z, t), \\ &P(z) + p(r, \theta, z, t), \end{aligned} \right\} \quad (3.1)$$

the momentum and continuity equations for the perturbation may be written as

$$\frac{\partial \mathbf{u}}{\partial t} + (\mathbf{u} \cdot \nabla) \mathbf{u} + \mathcal{L} \mathbf{u} = -\nabla p + \Delta \mathbf{u}, \quad (3.2a)$$

$$\nabla \cdot \mathbf{u} = 0, \quad (3.2b)$$

with the boundary conditions

$$\begin{aligned} \mathbf{u} &= 0, \quad \partial_z p = \partial_{zz} w \quad \text{at} \quad z = 0, \\ \mathbf{u} &= 0, \quad p = 0 \quad \text{at} \quad z = +\infty, \end{aligned}$$

and the notation

$$\begin{aligned} \mathbf{u} &\equiv \begin{pmatrix} u \\ v \\ w \end{pmatrix}, \quad \nabla p \equiv \begin{pmatrix} \partial_r p \\ (\partial_\theta p)/r \\ \partial_z p \end{pmatrix}, \\ (\mathbf{u} \cdot \nabla) \mathbf{u} &\equiv \left(u \frac{\partial}{\partial r} + \frac{1}{r} v \frac{\partial}{\partial \theta} + w \frac{\partial}{\partial z} \right) \mathbf{u} + \frac{1}{r} \begin{pmatrix} -v^2 \\ uv \\ 0 \end{pmatrix}, \\ \mathcal{L} \mathbf{u} &\equiv \left(rU \frac{\partial}{\partial r} + V \frac{\partial}{\partial \theta} + W \frac{\partial}{\partial z} \right) \mathbf{u} + \begin{pmatrix} rU'w \\ rV'w \\ W'w \end{pmatrix} + \begin{pmatrix} Uu - 2Vv \\ Uv + 2Vu \\ 0 \end{pmatrix}, \\ \Delta \mathbf{u} &\equiv \left(\frac{\partial^2}{\partial r^2} + \frac{1}{r^2} \frac{\partial^2}{\partial \theta^2} + \frac{\partial^2}{\partial z^2} \right) \mathbf{u} + \frac{1}{r} \frac{\partial \mathbf{u}}{\partial r} + \frac{1}{r^2} \begin{pmatrix} -u - 2\partial_\theta v \\ -v + 2\partial_\theta u \\ 0 \end{pmatrix}, \\ \nabla \cdot \mathbf{u} &\equiv \frac{\partial u}{\partial r} + \frac{1}{r} u + \frac{1}{r} \frac{\partial v}{\partial \theta} + \frac{\partial w}{\partial z}. \end{aligned}$$

The boundary layer thickness is constant in the entire system, of order unity in non-dimensional coordinates, while the non-axial velocity components linearly increase with radius. Hence when investigating features far from the disk axis and near a given radial location $R \gg 1$, the assumption of slow radial development is appropriate. Local properties for $r \simeq R$ are then derived by freezing the variable r which appears in the coefficients of the governing equations above and studying the corresponding three-dimensional flow

$$\mathbf{U}(z; R) \equiv \begin{pmatrix} RU(z) \\ RV(z) \\ W(z) \end{pmatrix}. \quad (3.3)$$

This is the parallel-flow assumption: equations (3.2) with the variable r replaced by the prescribed value of R are homogenous in both θ and r and will be referred to as the *local governing equations*. Local linear and nonlinear characteristics are derived from these equations; the link between local properties and global behaviour will be re-established in §6. Under the parallel-flow assumption, the value of R appears as a control parameter rather than a variable in the equations. It determines the magnitude of the basic flow velocity components (3.3) and thus plays the role of an effective local Reynolds number.

4. Primary linear instability properties

Under the parallel-flow assumption both r and θ are homogenous directions; infinitesimally small velocity and pressure disturbances prevailing at a given location R may thus be written in normal-mode form as

$$\begin{aligned} \mathbf{u}(r, \theta, z, t) &= \mathbf{u}^l(z; \alpha, \beta; R) \exp i(\alpha r + \beta \theta - \omega t), \\ p(r, \theta, z, t) &= p^l(z; \alpha, \beta; R) \exp i(\alpha r + \beta \theta - \omega t), \end{aligned} \quad (4.1)$$

where α is a complex radial wavenumber, β an integer azimuthal mode number, ω a complex angular frequency and \mathbf{u}^l , p^l the associated complex velocity and pressure components. After substitution of (4.1) into the linearized version of the local governing equations (3.2), dropping the $(\mathbf{u} \cdot \nabla) \mathbf{u}$ term and replacing r by R in the coefficients, an eigenvalue problem in the axial direction yields the local linear dispersion relation

$$\omega = \Omega^l(\alpha, \beta; R) \quad (4.2)$$

together with the eigenfunctions $\mathbf{u}^l(z; \alpha, \beta; R)$ and $p^l(z; \alpha, \beta; R)$.

4.1. Numerical solution procedure

The differential eigenproblem in the axial coordinate z is solved via a Chebyshev collocation method (Canuto, Hussaini & Quarteroni 1988). The collocation points $-1 \leq \xi_i \equiv -\cos(i\pi/N_z) \leq 1$ for $0 \leq i \leq N_z$ are mapped onto the semi-infinite domain $0 \leq z \leq +\infty$ through the transformations

$$z = a_* \frac{1 + \xi'}{1 - \xi'} \quad \text{and} \quad \xi' = b_* \xi + (1 - b_*)(\xi^3 + c_*(1 - \xi^2)). \quad (4.3)$$

The parameters $a_* > 0$, $0 < b_* \leq 1$ and $0 \leq c_* \leq 1$ determine the distribution of the collocation points on the z -axis: with $c_* = 0$, half of the points are located in the interval $0 \leq z \leq a_*$, while the remaining points are stretched towards $z = +\infty$ with an algebraically decreasing density; the parameters b_* and c_* allow refined

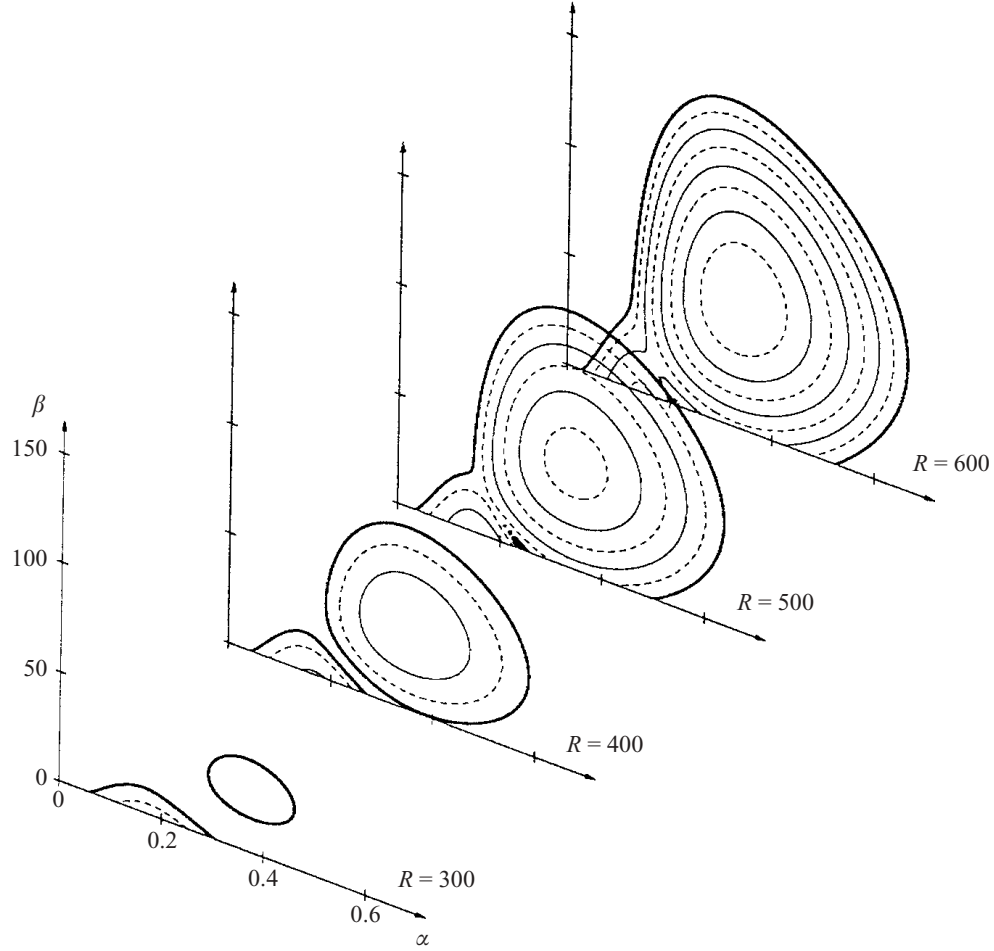


FIGURE 2. Local primary linear dispersion relation. Isocontours of the temporal growth rate Ω_i^l in (α, β) -planes for $R = 300, \dots, 600$. $\Omega_i^l = 0$ thick curves, $\Omega_i^l = 1, 2, 3$ thin solid curves, $\Omega_i^l = 0.5, 1.5, 2.5, 3.5$ thin dashed curves.

control of the distribution, smaller values of b_* resulting in a better resolution of the region corresponding to $\xi = 0$. A similar mapping has been used by Balachandar *et al.* (1992).

The numerical discretization yields a large number of spurious eigenvalues and eigenfunctions. The physically relevant solutions are identified by inspection of the eigenfunctions, which are required not to vary with increasing resolution. Extensive resolution tests have revealed that remapping the collocation points via (4.3) with $a_* = 2$, $b_* = 0.6$ and $c_* = 0.5$ is the most appropriate choice for the various numerical procedures implemented in the present investigation. Unless otherwise stated, these parameters are used throughout the rest of the paper. In general $N_z = 40$ collocation points are found to very accurately resolve the eigenfunctions. Due to the spectral accuracy of this method, a lower resolution of $N_z = 30$ still yields quite reliable results and has been used in situations where $N_z = 40$ would require prohibitively long computational time. Various resolution tests are reported in the Appendix.

4.2. Linear dispersion relation

Temporal growth rates of the local linear dispersion relation are given in figure 2. Two types of modes are identified: the region of main interest is centred around finite values of β and corresponds to an inviscid instability, also known as branch 1, caused

by inflection points in the basic velocity profiles. The maximum growth rate increases with Reynolds number R and the first inviscid instability occurs for $R \simeq 284$ at $\alpha \simeq 0.37$ and $\beta = 27$. The unstable modes prevailing at small values of β , also known as branch 2, are due to viscosity and persist at low R . These latter modes are not relevant to the present investigation and will not be discussed further.

4.3. Local absolute frequency

In the context of self-sustained fluctuations, a crucial feature is the complex absolute frequency ω_0 defined as the frequency observed at a fixed spatial location in the long-time linear response to an initial localized impulse. For a radially localized impulse with a given azimuthal mode number β , the local absolute frequency ω_0 and associated absolute wavenumber α_0 are derived from the linear dispersion relation (4.2) by applying the Briggs (1964) and Bers (1983) pinch-point criterion which is associated with a vanishing radial group velocity condition:

$$\omega_0(\beta; R) = \Omega^l(\alpha_0, \beta; R) \quad \text{with} \quad \frac{\partial \Omega^l}{\partial \alpha}(\alpha_0, \beta; R) = 0. \quad (4.4)$$

Isolines of absolute frequency $\omega_{0,r}$ and growth rate $\omega_{0,i}$ in the (R, β) -plane are given in figure 3. As already discovered by Lingwood (1995) (see also Lingwood 1997a, p. 424 for the corrected values) transition from local convective to absolute instability first occurs at $R^{ca} \simeq 507.4$ for $\beta = 68$ (marked by solid dots) with a marginal real absolute frequency of $\omega_0^{ca} \simeq 50.5$ and $\alpha_0^{ca} \simeq 0.227 - 0.122i$ (see also § A.1).

Computation of the neutral curve $\omega_{0,i} = 0$ (thick line in figure 3b) shows that each mode number $\beta \geq 51$ is associated with an absolutely unstable region. The radial extent of the absolutely unstable interval remains finite for all β ; absolute instability has been shown by Peake & Garrett (2003) to prevail for $3.8 < R/\beta < 38.6$ in the limit $\beta \rightarrow \infty$.

5. Primary saturated crossflow vortices

Whenever infinitesimally small perturbations are amplified according to the above linear stability results, they eventually reach finite-amplitude levels and are then governed by the complete nonlinear equations. Several experimental studies, e.g. by Kohama (1984), Jarre, Le Gal & Chauve (1996b), reveal a pattern of outward-spiralling crossflow vortices before transition to a turbulent régime occurs. These finite-amplitude spiral vortices are periodic in space and time and can be sought as nonlinearly saturated wavetrains evolving in the three-dimensional boundary layer.

Local nonlinearly saturated waves arise naturally from a purely temporal analysis. The initial-value problem of interest is the temporal development of a radially and azimuthally periodic small-amplitude perturbation of the form (4.1), characterized by real values α , evolving in the three-dimensional flow (3.3) pertaining to a prescribed radial station R . The initial evolution is dictated by the linear temporal growth rate $\Omega_i^l(\alpha, \beta; R)$. Whenever $\Omega_i^l(\alpha, \beta; R) > 0$, exponential temporal growth takes place until nonlinear effects come into play. The quadratic nonlinear terms of the Navier–Stokes equations then promote higher spatial harmonics of the form $\exp[in(\alpha r + \beta \theta)]$ as well as a mean flow correction. These nonlinearities are stabilizing and lead to saturation at finite amplitude. In the absence of secondary instabilities, a fully nonlinear travelling wave is then reached in the long-time limit with spatial periodicity imposed by the prescribed values of α and β . The final perturbation velocity and pressure fields

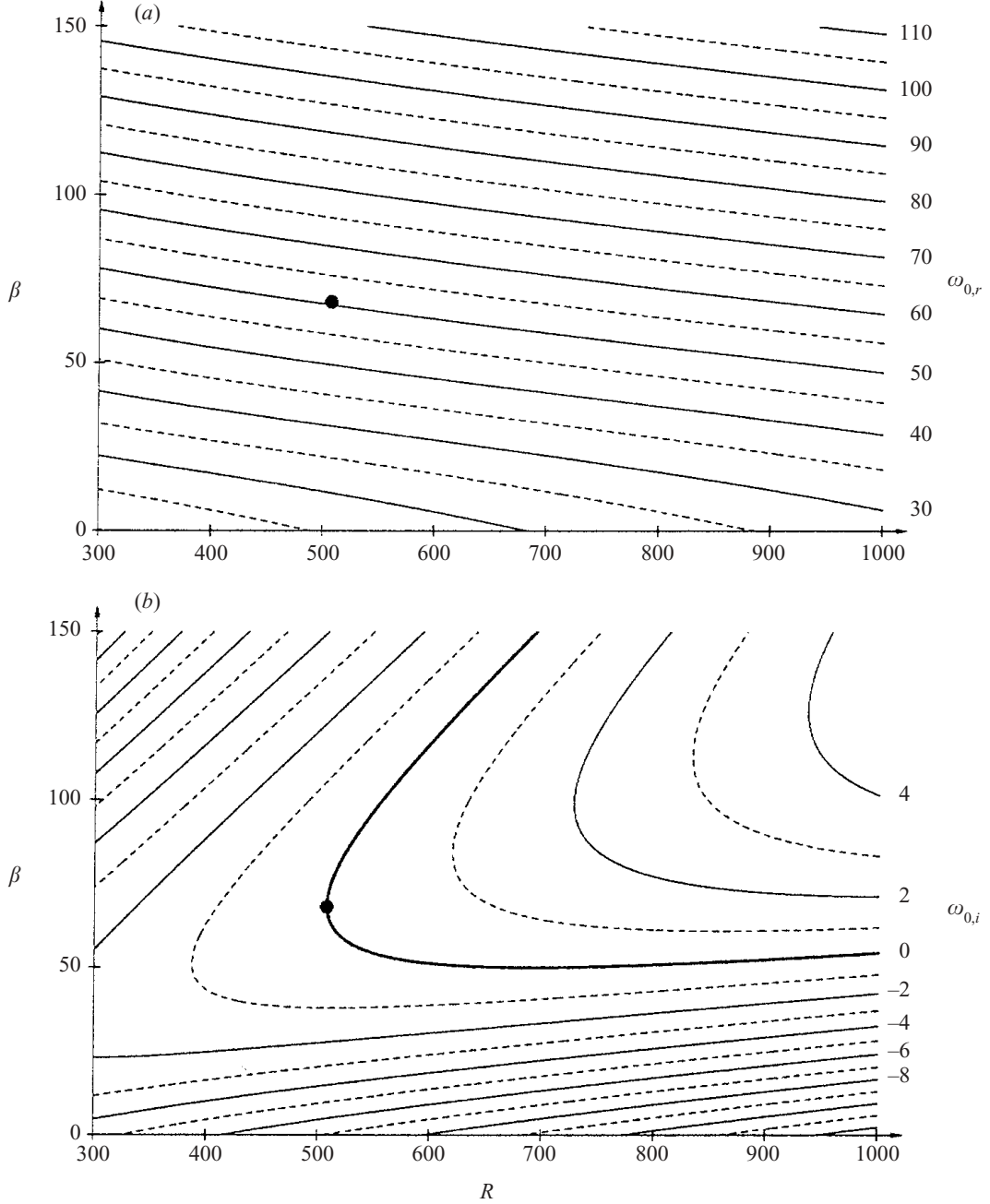


FIGURE 3. Primary local absolute frequency. Isolines of (a) $\omega_{0,r}$ and (b) $\omega_{0,i}$ in (R, β) -plane. The solid dot marks the onset of absolute instability at $R^{ca} \approx 507$ and $\beta = 68$ with $\omega_0^{ca} \approx 50.5$.

associated with the travelling saturated crossflow vortices are thus of the form

$$\left. \begin{aligned} \mathbf{u}(r, \theta, z, t) &= \mathbf{u}^{nl}(z, \alpha r + \beta \theta - \omega t; \alpha, \beta; R), \\ p(r, \theta, z, t) &= p^{nl}(z, \alpha r + \beta \theta - \omega t; \alpha, \beta; R), \end{aligned} \right\} \quad (5.1)$$

where the functions \mathbf{u}^{nl} and p^{nl} are 2π -periodic in their second variable $\phi \equiv \alpha r + \beta \theta - \omega t$. The real frequency ω of the saturated waves is determined by the local nonlinear dispersion relation

$$\omega = \Omega^{nl}(\alpha, \beta; R), \quad (5.2)$$

while the wave amplitude is conveniently measured by the mean fluctuating energy defined below in (5.5). In the present section the existence of these finite-amplitude travelling waves is studied. Their stability with respect to secondary perturbations is investigated in § 7.

Note that instead of using radial wavenumber α and azimuthal mode number β , it is sometimes appropriate to specify the crossflow vortices by the wave angle ε and wave vector modulus a . These equivalent representations are related by

$$\left. \begin{aligned} \tan \varepsilon &= \beta/R\alpha, & \alpha &= a \cos \varepsilon, \\ a^2 &= \alpha^2 + (\beta/R)^2, & \beta/R &= a \sin \varepsilon. \end{aligned} \right\} \quad (5.3)$$

5.1. Numerical solution procedures

The temporal evolution of a spatially periodic perturbation of real radial wavenumber α and azimuthal mode number β is treated by resorting to the spatial Fourier series

$$\left. \begin{aligned} \mathbf{u}(r, \theta, z, t) &= \sum_n \begin{pmatrix} u_n(z, t) \\ v_n(z, t) \\ w_n(z, t) \end{pmatrix} \exp in(\alpha r + \beta \theta), \\ p(r, \theta, z, t) &= \sum_n p_n(z, t) \exp in(\alpha r + \beta \theta). \end{aligned} \right\} \quad (5.4)$$

Substitution of expansions (5.4) into the local governing equations (3.2) yields an infinite set of coupled differential equations of first order in time. These are truncated at a finite number of harmonics $|n| \leq N_h$ and the Chebyshev collocation method (4.3) is again used in the axial direction.

Time-integration of the resulting system is performed via a fractional-step method of second-order accuracy in time. At the intermediate time step, the three components of the velocity field are obtained by solving Helmholtz-type problems. A Poisson problem then yields a correction to the pressure required to enforce divergence-free velocity fields. A Crank–Nicholson scheme is used for the viscous terms, the advection terms are obtained at the intermediate time step by extrapolation based on the two previous time steps.

When initializing the temporal integration with the linear eigenmode at small amplitude in a configuration where $\Omega_i^l(\alpha, \beta; R) > 0$, the system evolves from an initial exponential growth phase, via a transient régime, to reach a time-periodic state corresponding to fully saturated crossflow vortices travelling without deformation. Measuring the frequency of this wave then yields the nonlinear dispersion relation (5.2), while the fluctuating energy is derived from the Fourier components as

$$E(\alpha, \beta; R) = \int_0^\infty dz \sum_{n>0} (|u_n(z)|^2 + |v_n(z)|^2 + |w_n(z)|^2). \quad (5.5)$$

This time-marching technique fails to converge towards a periodic solution when the primary finite-amplitude vortices are affected by secondary instabilities. In order to capture all primary nonlinear states, whether or not they are unstable with respect to secondary instabilities, a Newton–Raphson search procedure has been implemented that directly solves for the saturated time-periodic waves. In this formulation, the

periodic solution is expanded as

$$\left. \begin{aligned} \mathbf{u}^{nl}(z, \alpha r + \beta \theta - \omega t) &= \sum_n \begin{pmatrix} u_n(z) \\ v_n(z) \\ w_n(z) \end{pmatrix} \exp i n(\alpha r + \beta \theta - \omega t), \\ p^{nl}(z, \alpha r + \beta \theta - \omega t) &= \sum_n p_n(z) \exp i n(\alpha r + \beta \theta - \omega t), \end{aligned} \right\} \quad (5.6)$$

and substituted into the local governing equations. Truncating at a finite number of harmonics and implementing the collocation method in the z -direction then results in a large system of nonlinear algebraic equations relating all components of the wave fields and the real parameters α , β , ω and R . To fix the phase of the solution, the normalization condition $\text{Im } p_1(0) = 0$ is used. A good initial guess for Newton–Raphson iteration is available from the above time-marching procedure using parameter settings that are stable with respect to secondary perturbations. In practice, the lengthy time-marching technique is only used once; the complete set of nonlinear waves is thereafter obtained by the much faster iteration procedure, continuously varying the parameters.

In general, β and R are kept at fixed values, and the nonlinear dispersion relation (5.2) is then obtained by following temporal branches, i.e. continuously varying α and solving for the wave fields and frequency ω . A further difficulty arises due to the existence of critical values of α where the Jacobian used in the Newton–Raphson iteration procedure becomes singular. These singularities are associated with turning points and the fact that (5.2) is not single-valued in a small region of the parameter space. In order to follow solution branches past these turning points, the usual continuation in α must be replaced by an arclength continuation (Keller 1977). For the present purpose it is convenient to consider both α and ω as unknowns and to complement the governing system by a parameterizing equation

$$\Pi(\alpha, \omega; s) = 0, \quad (5.7)$$

where s denotes an arclength coordinate in the (α, ω) -plane. Following of the entire solution branch is then achieved using a simplified version of the pseudo-arclength parameterization of Keller (1977),

$$\Pi \equiv (1 - \mu)[\alpha(s) - \alpha(s_0)] \frac{d\alpha}{ds}(s_0) + \mu[\omega(s) - \omega(s_0)] \frac{d\omega}{ds}(s_0) - (s - s_0), \quad (5.8)$$

where s_0 denotes the arclength coordinate at the previously computed point and the constant $0 \leq \mu \leq 1$ controls the relative importance given to variations in α or ω . Note that the limiting values $\mu = 0$ and $\mu = 1$ yield the nonlinear temporal and spatial branches, respectively parameterized by α and ω .

5.2. Nonlinear wave near onset of primary absolute instability

As shown below in § 6, the transition location $R^{ca} = 507.4$ from convective to absolute instability is of particular importance for the self-sustained behaviour of the rotating-disk flow. Figure 4 illustrates the structure of the nonlinear saturated waves prevailing near onset of absolute instability, at $R = 510$ and $\beta = 68$. The waves shown are 2π -periodic in the phase variable $\phi \equiv \alpha r + \beta \theta - \omega t$ and propagate according to a frequency of $\omega = 50.5$ and a radial wavenumber of $\alpha = 0.35$ (see also § A.2). A systematic study of the nonlinear dispersion relation (5.2) is postponed to the next subsection.

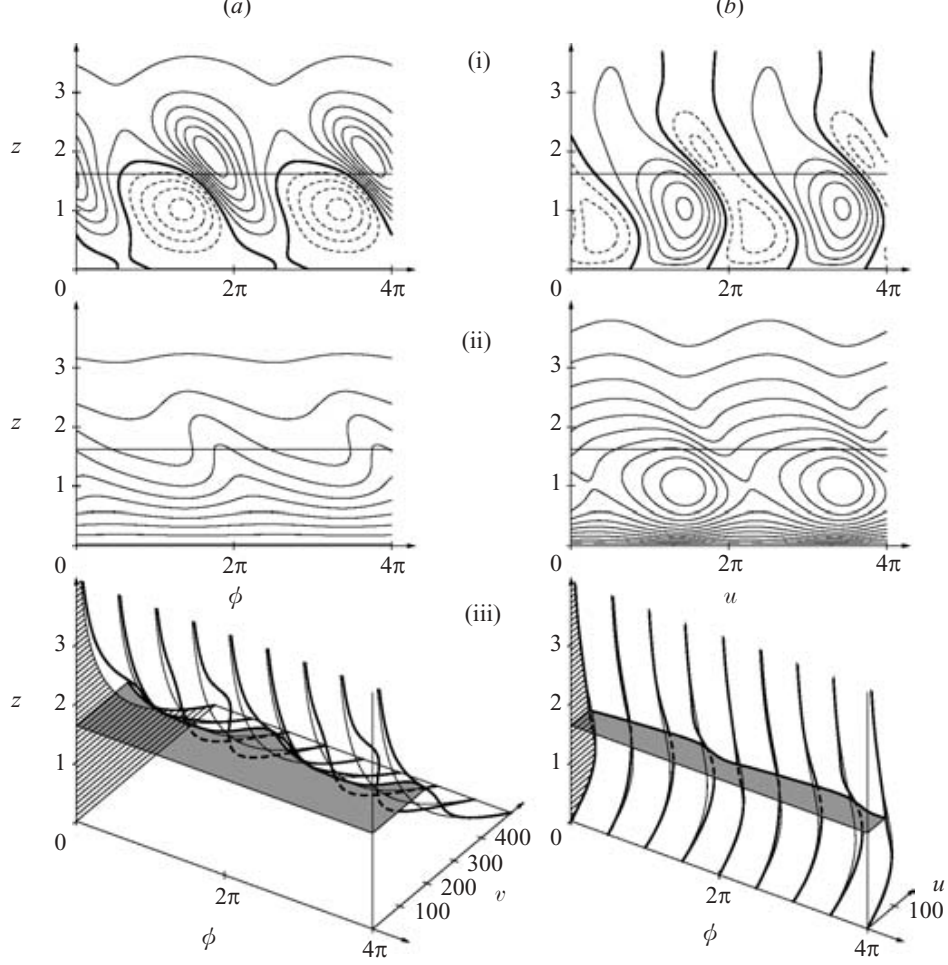


FIGURE 4. Structure of nonlinear saturated wave at $R = 510$, $\beta = 68$, $\alpha = 0.35$ and $\omega = 50.5$. (a) Azimuthal and (b) radial velocity components. (i) Isolines of perturbation velocity fields over two wavelengths (azimuthal levels $-40, \dots, -10$ dashed, 0 thick, $10, \dots, 60$ thin; radial levels $-10, -5$ dashed, 0 thick, $5, \dots, 25$ thin). (ii) Isolines of total velocity fields (azimuthal levels $50, 100, \dots, 500$; radial levels $10, 20, \dots, 110$). (iii) Comparison of basic (thin lines) and total (thick lines) velocity profiles.

Figure 4(i)(a,b) displays snapshots of the perturbation azimuthal v - and radial u -velocity contours over two wavelengths in the (z, ϕ) -plane. The corresponding total components $RV(z) + v(z, \phi)$ and $RU(z) + u(z, \phi)$ are shown in figure 4(ii)(a,b). Figure 4(iii)(a,b) compares the total velocity profiles at four different phases $\phi = 0, \pi/2, \pi$ and $3\pi/2$ (thick lines) with the basic flow (thin lines). Also shown are cuts of the total velocity fields at $z = 1.6$ (grey regions). These profiles display several inflection points in both velocity components, most clearly at $\phi = 3\pi/2$. It is thus very likely that these saturated crossflow vortices will be unstable with respect to secondary perturbations, as shown in § 7.

5.3. Nonlinear dispersion relation and fluctuating energy

The fluctuating energy and nonlinear frequency of waves corresponding to the critical azimuthal wavenumber $\beta = 68$ are given in figure 5. The energy E , as defined by (5.5), of the nonlinear solution branches is shown in (a) together with isolines of the positive linear growth rates Ω_i^l . As can be seen, the nonlinear amplitude vanishes on

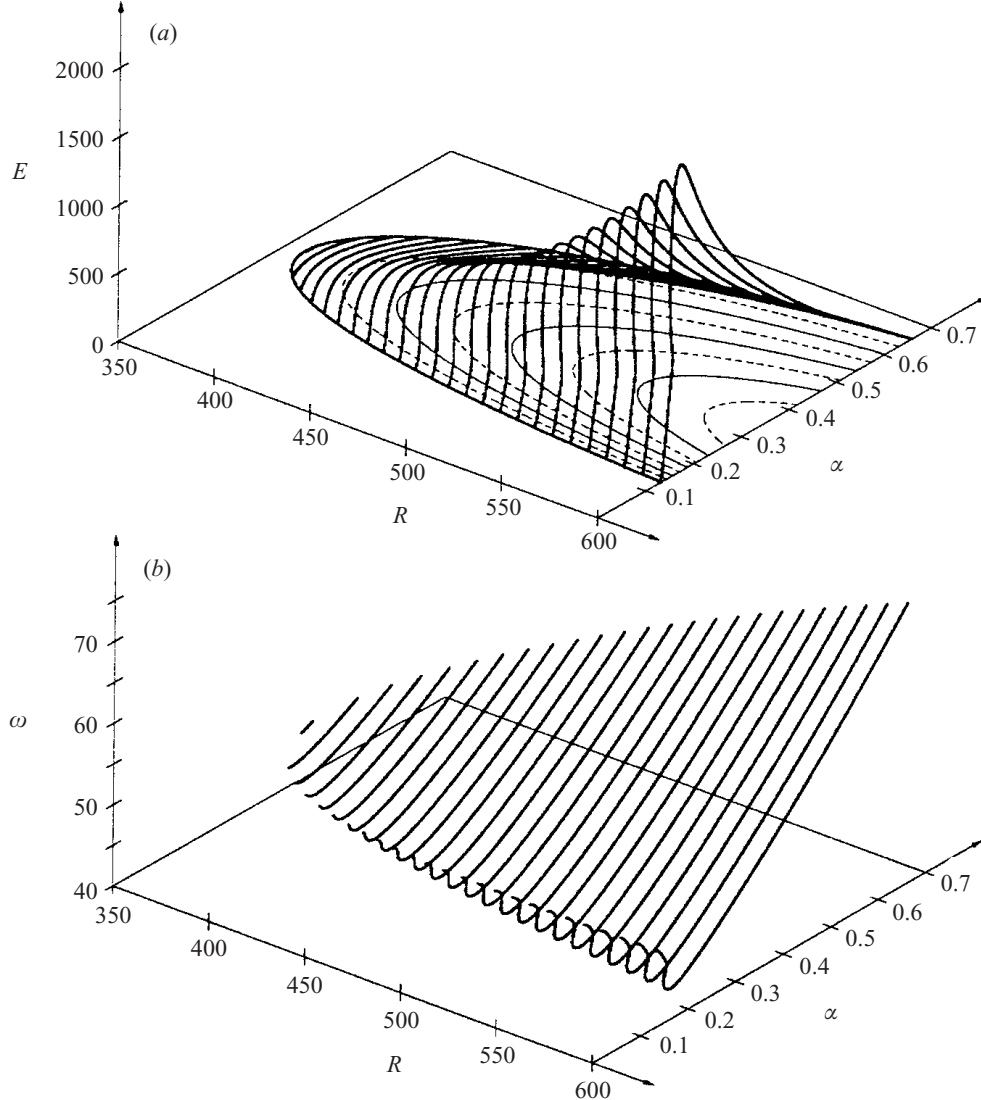


FIGURE 5. Local nonlinear waves in the (R, α) -plane for a fixed $\beta = 68$. (a) Fluctuating energy curves and (b) nonlinear frequency. Also shown in (a) are isolines of linear temporal growth rate (levels 0 thick, 1, 2, 3 thin solid, 0.5, 1.5, 2.5, 3.5 thin dashed).

the neutral curve where $\Omega_i^l = 0$ while nonlinear waves with largest amplitude occur near the lower end of the α -wavenumber range and do not coincide with the highest linear growth rates. The frequency curves corresponding to the nonlinear dispersion relation (5.2) are given in figure 5(b). It is towards the lower marginal curve, where the energy sharply drops, that turning points in the dispersion relation occur. These turning points are related to the proximity in parameter space of viscous instability modes; however, since they are not essential in the present investigation no further details will be given here. A similar feature has been found by Koch *et al.* (2000) in the swept-plate boundary layer (see their figure 6).

Saturated waves have been systematically computed for radial locations up to $R = 600$. The structure of the nonlinear dispersion relation $\Omega^{nl}(\alpha, \beta; R)$ is illustrated in figure 6 by cuts of the three-dimensional parameter space along planes of constant azimuthal mode number.

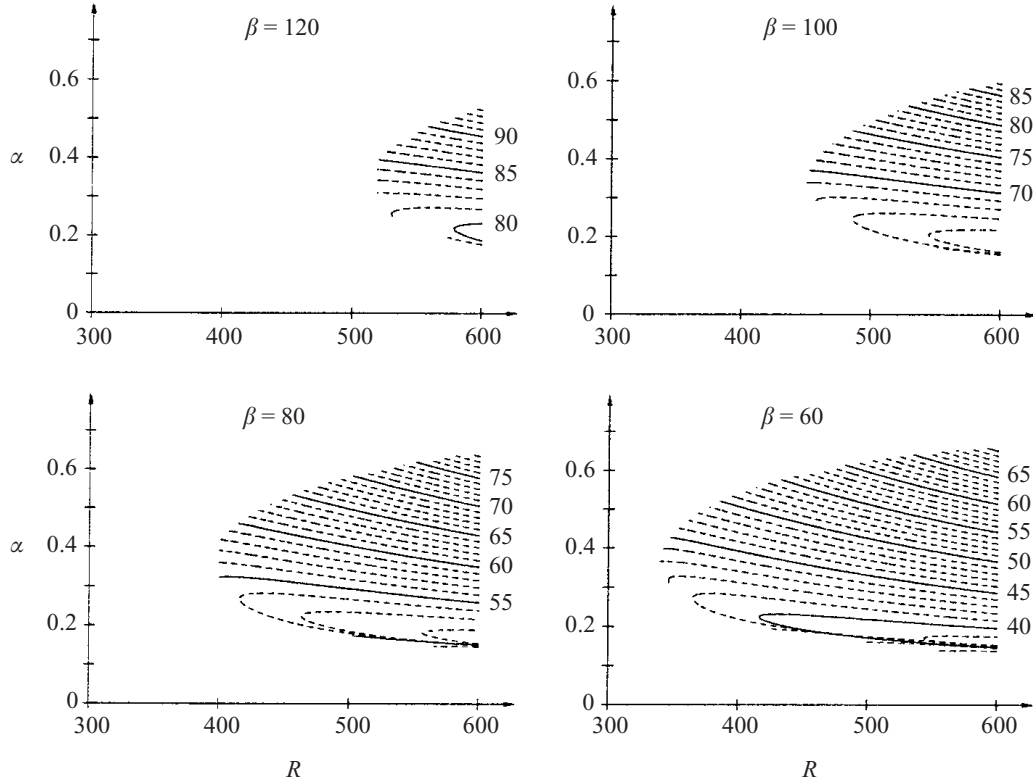


FIGURE 6. Nonlinear dispersion relation $\Omega^{nl}(\alpha, \beta; R)$. Isofrequency lines in the (R, α) -plane for $\beta = 120, 100, 80$ and 60 .

6. Self-sustained spatially extended structure

Having obtained the local linear and nonlinear waves in the boundary layer at each radial location in the previous sections, a global solution developing over an extended radial interval may be sought in the form of wavetrains that are slowly modulated in the radial direction. This approach is set on firm theoretical ground using WKBJ asymptotic techniques (Bender & Orszag 1978). Such a line of thought has previously been fully implemented for one-dimensional model equations and the two-dimensional Navier–Stokes equations. The generalization of this formalism to the present three-dimensional case is obtained with no more than algebraic difficulty. Only an outline of the method will be given here.

In the rotating-disk flow, the region of particular interest is the neighbourhood of $R^{ca} \simeq 507.4$ where onset of absolute instability first occurs. This characteristic radius is large compared to the boundary layer thickness, hence fulfilling the assumption of weak radial development, or equivalently of large Reynolds number since the radius acts as an effective local Reynolds number. It is thus legitimate to use

$$\epsilon \equiv \frac{1}{R^{ca}} \ll 1 \quad (6.1)$$

as small parameter in the asymptotic formulation and to introduce the slow radial coordinate

$$\bar{R} = \epsilon r. \quad (6.2)$$

In this multiple-scales approach, the fast r -scale accounts for the oscillatory behaviour of the spatially extended wavetrain, while its envelope and local structure are slowly modulated on the \bar{R} -scale so as to adjust to the variations of the underlying basic

flow. This suggests the following change of variables:

$$\left. \begin{aligned} \mathbf{u}(r, \theta, z, t) &= \mathbf{u}(z, \phi; \bar{R}), \\ p(r, \theta, z, t) &= p(z, \phi; \bar{R}), \end{aligned} \right\} \quad (6.3)$$

with 2π -periodicity in the fast phase function $\phi(r, \theta, t)$ whereas the \bar{R} -dependence accounts for the slow radial evolution. Local radial wavenumber, azimuthal mode number and frequency are respectively defined as

$$\alpha = \frac{\partial \phi}{\partial r}, \quad \beta = \frac{\partial \phi}{\partial \theta}, \quad \omega = -\frac{\partial \phi}{\partial t}. \quad (6.4)$$

For a global solution displaying no singularities, both the frequency and azimuthal mode number remain constant in the entire system. Indeed, any spatial variation of either of these two quantities necessarily introduces dislocations. A smooth global solution (6.3) is thus made up of waves that all have same global frequency ω_g and azimuthal mode number β_g . The fast phase is then of the form

$$\phi = \left(\frac{1}{R^{ca}} \int^{\bar{R}} \alpha(\bar{\rho}) d\bar{\rho} \right) + \beta_g \theta - \omega_g t, \quad (6.5)$$

where $\alpha(\bar{R})$ is an as yet undetermined slowly varying local radial wavenumber. Next the wave fields and the derivative operators are expanded in powers of ϵ as

$$\left. \begin{aligned} \mathbf{u}(z, \phi; \bar{R}) &= \mathbf{u}_0 + \epsilon \mathbf{u}_1 + \epsilon^2 \mathbf{u}_2 + \dots, \\ p(z, \phi; \bar{R}) &= p_0 + \epsilon p_1 + \epsilon^2 p_2 + \dots, \end{aligned} \right\} \quad (6.6)$$

and

$$\frac{\partial}{\partial r} = \alpha(\bar{R}) \frac{\partial}{\partial \phi} + \epsilon \frac{\partial}{\partial \bar{R}}, \quad \frac{\partial}{\partial \theta} = \beta_g \frac{\partial}{\partial \phi}, \quad \frac{\partial}{\partial t} = -\omega_g \frac{\partial}{\partial \phi}, \quad (6.7)$$

and substituted into the governing equations (3.2). At leading order in the expansion parameter ϵ , the derivative $\partial/\partial \bar{R}$ may be neglected and the slow coordinate \bar{R} acts solely as an external control parameter. For each value of \bar{R} , the global solution (6.3) then obeys, to leading order, the local governing equations and follows, among all possible waves, the one that matches the overall frequency ω_g and mode number β_g . Note that in the previous sections, local properties have been derived with the local Reynolds number R as control parameter. When carrying out the present asymptotic analysis, however, it is more appropriate to rescale this parameter as $\bar{R} = \epsilon R$ and to consider that the local properties depend on \bar{R} instead.

Two different situations arise depending on the magnitude of the global solution (6.3): in small-amplitude regions the global structure is described by the linearized equations while the fully nonlinear equations prevail in regions of finite amplitude.

Small-amplitude regions are governed by the local linear equations and the corresponding dispersion relation (4.2). The radial wavenumber $\alpha(\bar{R})$ in the rapidly varying phase (6.5) is then complex, accounting for both the wavelength and decay rate in the radial direction, and obtained by solving the linear dispersion relation (4.2) with prescribed β_g and ω_g . When solving (4.2) for the wavenumber α , two complex spatial branches $\alpha'^{\pm}(\bar{R}; \omega_g, \beta_g)$ are obtained. The separation of the spatial branches into + and - branches is determined, according to classical arguments (Briggs 1964; Bers 1983), by whether they correspond to a downstream or upstream spatial response to localized harmonic forcing. As discussed below, in the present configuration the

relevant spatial branch in the central linear region is always the α^{l-} branch. The global solution (6.3), (6.5) then locally follows the wave indexed by $\alpha^{l-}(\bar{R})$, β_g and \bar{R} within the family (4.1) of linear eigenfunctions.

In contrast, the finite-amplitude régime is governed by the local nonlinear equations and the corresponding dispersion relation (5.2). Solving (5.2) with prescribed β_g and ω_g then yields the corresponding real wavenumber branch $\alpha^{nl}(\bar{R})$. These nonlinear spatial branches correspond to the isofrequency lines represented in figure 6. This figure also shows that a single nonlinear spatial branch is generally obtained; it is only for lower frequencies than those of interest here that two α^{nl} -branches coexist. In nonlinear regions, the global solution then locally follows the wavetrains associated with $\alpha^{nl}(\bar{R})$, β_g and \bar{R} within the family (5.1) of saturated crossflow vortices.

It remains to determine which global frequency ω_g and mode number β_g are naturally selected in the rotating-disk flow.

As demonstrated in earlier investigations (Pier *et al.* (2001)), spatially developing systems display a nonlinear self-sustained state whenever a region of absolute instability is present. These finite-amplitude solutions (also called ‘elephant’ global modes (Pier & Huerre 2001*b*)) are characterized by a stationary front located at the upstream transition from local convective to absolute instability. The selection mechanism is the following: in the absolutely unstable region amplified perturbations develop and their envelope advances upstream against the basic flow. At the location of neutral absolute instability a balance between upstream perturbation growth and downstream advection is reached and perturbations pile up at that location. Nonlinearities lead to saturation of the fluctuating amplitude and a stationary front is formed. This front generates a downstream-propagating fully nonlinear wavetrain and an upstream exponentially decaying tail. It thus connects linear and nonlinear regions, acts as a source and effectively tunes the entire system to its frequency. The stationary front obeys the Dee & Langer (1983) marginal stability criterion, hence the global frequency of these modes equals the real absolute frequency prevailing at the front location.

In the present configuration, the transition radius from convective to absolute instability depends on the azimuthal mode number β (see the neutral curve in figure 3*b*). Each $\beta \geq 51$ is associated with an absolutely unstable region and thus gives rise, in principle, to a self-sustained global structure displaying a front at the corresponding marginal radius. However, it is for $\beta = 68$ that absolute instability first occurs, at $R^{ca} \simeq 507.4$, and hence that perturbations are able to propagate inwards closest to the disk centre. Global modes with $\beta \neq 68$ would reach finite amplitude levels further outwards and are thus dominated by the solution with $\beta = 68$.

Assuming for now that there are no secondary instabilities, the expected self-sustained behaviour is thus a time-harmonic solution with frequency $\omega_g = \omega_0^{ca} \simeq 50.5$ and azimuthal mode number $\beta_g = 68$. Onset of nonlinearity coincides with onset of absolute instability and is triggered by a front at R^{ca} . The spatial structure is the following (figure 7): nonlinear outward-spiralling vortices of frequency ω_g and mode number β_g are initiated at R^{ca} and prevail in the outer region. They are governed by the local nonlinear dispersion relation (5.2) and follow the associated real spatial wavenumber branch α^{nl} (figure 7*b*). The inner region $r < R^{ca}$ is covered by the front tail. Since this tail is caused by the front at R^{ca} , it decays exponentially towards the disk centre according to the complex radial wavenumber α^{l-} derived from the local linear dispersion relation (4.2). Note that the front at R^{ca} is associated with a jump in wavenumber from the complex α^{l-} to the real α^{nl} . However, the fundamental assumption of slowly varying radial change is not violated: this jump merely reflects

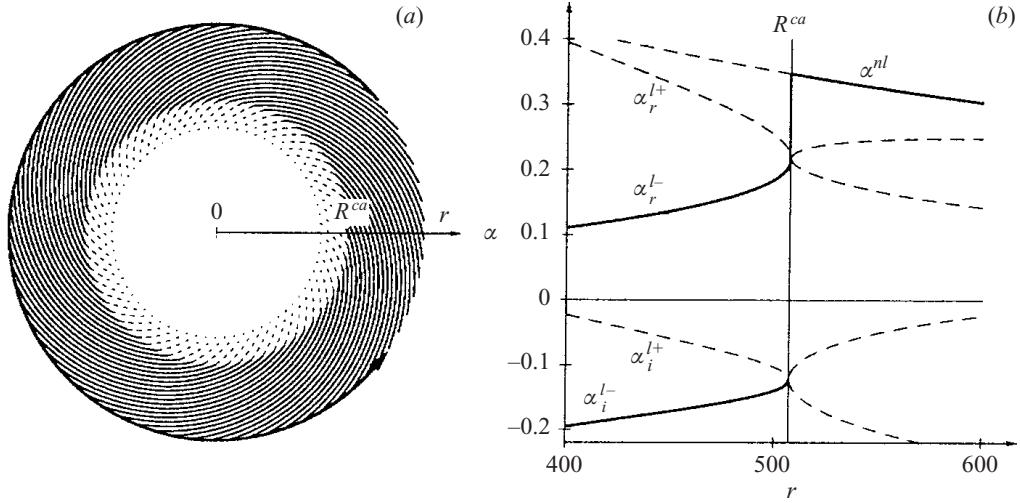


FIGURE 7. Spatial structure of self-sustained nonlinear global solution of frequency $\omega_0^{ca} \simeq 50.5$ and azimuthal modenumber $\beta = 68$. (a) Sketch of outward-spiralling nonlinear vortices triggered at $R^{ca} \simeq 507.4$; exponentially decaying tail covers the inner region. (b) Corresponding numerically computed spatial branches obtained by solving the linear (two complex branches $\alpha^{l\pm}$) and the nonlinear (real branch α^{nl}) dispersion relation. Pinching of the linear branches occurs for the absolute wavenumber $\alpha_0 = 0.227 - 0.122i$ at R^{ca} . Radial wavenumber of the global solution follows the path indicated by the thick line: the linear α^{l-} branch prevails in the central region; the front at R^{ca} is associated with a jump in wavenumber; the nonlinear α^{nl} branch prevails in the outer region.

the existence of an inner layer (of size $\mathcal{O}(\epsilon^{2/3})$ see Pier *et al.* 2001) in the complete asymptotic analysis.

The WKBJ procedure outlined above guarantees the existence of a global time-harmonic solution but does not tell us whether or not it is stable with respect to secondary perturbations. The experimental observation of a rapid transition to turbulence near R^{ca} suggests that it is not. The aim of the remainder of this paper is to understand this transition and therefore analyses in detail the secondary stability of the saturated waves that make up the global solution near R^{ca} .

7. Secondary stability analysis

When investigating the stability of primary saturated vortices of wavenumbers α and β and frequency ω at a radial station R with respect to secondary perturbations, the total flow fields are decomposed as

$$\left. \begin{aligned} U(z; R) + \mathbf{u}^{nl}(z, \alpha r + \beta \theta - \omega t; \alpha, \beta; R) + \hat{\mathbf{u}}(r, \theta, z, t), \\ P(z) + p^{nl}(z, \alpha r + \beta \theta - \omega t; \alpha, \beta; R) + \hat{p}(r, \theta, z, t), \end{aligned} \right\} \quad (7.1)$$

where $\mathbf{U} + \mathbf{u}^{nl}$, $P + p^{nl}$ represent the new basic flow solution which is perturbed by $\hat{\mathbf{u}}$, \hat{p} .

Linear secondary stability of the primary periodic crossflow vortices is governed by Floquet theory (Herbert 1988) and infinitesimally small secondary velocity and pressure disturbances can be written in normal-mode form as

$$\left. \begin{aligned} \hat{\mathbf{u}}(r, \theta, z, t) = \hat{\mathbf{u}}^l(z, \alpha r + \beta \theta - \omega t; \hat{\alpha}, \hat{\beta}; \alpha, \beta; R) \exp i(\hat{\alpha}r + \hat{\beta}\theta - \hat{\omega}t), \\ \hat{p}(r, \theta, z, t) = \hat{p}^l(z, \alpha r + \beta \theta - \omega t; \hat{\alpha}, \hat{\beta}; \alpha, \beta; R) \exp i(\hat{\alpha}r + \hat{\beta}\theta - \hat{\omega}t), \end{aligned} \right\} \quad (7.2)$$

where $\hat{\alpha}$ is the secondary complex radial wavenumber, $\hat{\beta}$ is the secondary integer azimuthal mode number and $\hat{\omega}$ is the corresponding complex frequency; the eigenfunctions $\hat{\mathbf{u}}^l$ and \hat{p}^l have the same periodicity as the primary wave, i.e. are 2π -periodic in the real phase variable $\phi \equiv \alpha r + \beta \theta - \omega t$. Two-dimensional eigenproblems in the variables z and ϕ are then obtained after substitution of (7.1) with (7.2) into the local governing equations and linearization about the new basic flow. For each primary nonlinear wave characterized by the real parameters α , β and R and for each choice of $\hat{\alpha}$ and $\hat{\beta}$, the solution of the corresponding eigenproblem yields the secondary complex frequency

$$\hat{\omega} = \hat{\Omega}^l(\hat{\alpha}, \hat{\beta}; \alpha, \beta; R) \quad (7.3)$$

together with the associated eigenfunctions $\hat{\mathbf{u}}^l$ and \hat{p}^l . Note that the eigenproblem admits many modes, but in general only the most unstable are physically relevant.

7.1. Numerical solution procedure

The linear local governing equations for the small-amplitude secondary perturbations (7.2) are formally similar to the linearized version of (3.2)

$$\frac{\partial \hat{\mathbf{u}}}{\partial t} + \hat{\mathcal{L}} \hat{\mathbf{u}} = -\nabla \hat{p} + \Delta \hat{\mathbf{u}}, \quad (7.4a)$$

$$\nabla \cdot \hat{\mathbf{u}} = 0, \quad (7.4b)$$

except that advection occurs by the primary vortices (5.1) as well as by the laminar base flow (3.3) so that now

$$\begin{aligned} \hat{\mathcal{L}} \hat{\mathbf{u}} \equiv & \left((RU + u^{nl}) \frac{\partial}{\partial r} + \left(V + \frac{1}{R} v^{nl} \right) \frac{\partial}{\partial \theta} + (W + w^{nl}) \frac{\partial}{\partial z} \right) \hat{\mathbf{u}} \\ & + \begin{pmatrix} rU'\hat{w} \\ rV'\hat{w} \\ W'\hat{w} \end{pmatrix} + \left(\hat{u} \frac{\partial}{\partial r} + \frac{1}{R} \hat{v} \frac{\partial}{\partial \theta} + \hat{w} \frac{\partial}{\partial z} \right) \mathbf{u}^{nl} \\ & + \begin{pmatrix} U\hat{u} - 2V\hat{v} \\ U\hat{v} + 2V\hat{u} \\ 0 \end{pmatrix} + \frac{1}{R} \begin{pmatrix} -2v^{nl}\hat{v} \\ u^{nl}\hat{v} + v^{nl}\hat{u} \\ 0 \end{pmatrix}. \end{aligned}$$

Upon substituting the previously obtained Fourier expansion (5.6) for the primary solution and expanding the secondary eigenfunctions (7.2) in a similar fashion as

$$\left. \begin{aligned} \hat{\mathbf{u}}^l(z, \alpha r + \beta \theta - \omega t) &= \sum_n \begin{pmatrix} \hat{u}_n(z) \\ \hat{v}_n(z) \\ \hat{w}_n(z) \end{pmatrix} \exp in(\alpha r + \beta \theta - \omega t), \\ \hat{p}^l(z, \alpha r + \beta \theta - \omega t) &= \sum_n \hat{p}_n(z) \exp in(\alpha r + \beta \theta - \omega t), \end{aligned} \right\} \quad (7.5)$$

the local governing equations (7.4) transform into an eigenproblem where the infinite set of eigenfunctions \hat{u}_n , \hat{v}_n and \hat{w}_n are linearly coupled via the harmonics u_n , v_n and w_n of the primary wave (5.6). After truncating primary and secondary Fourier expansions at $|n| \leq N_h$ and $|n| \leq \hat{N}_h$ respectively and using the Chebyshev collocation method in the z -direction, a large algebraic eigensystem is obtained, the solution of which yields the secondary dispersion relation (7.3) and the associated eigenfunctions. As for the primary linear stability analysis, the physically relevant modes are identified by monitoring the structure of the eigenfunctions while varying the resolution.

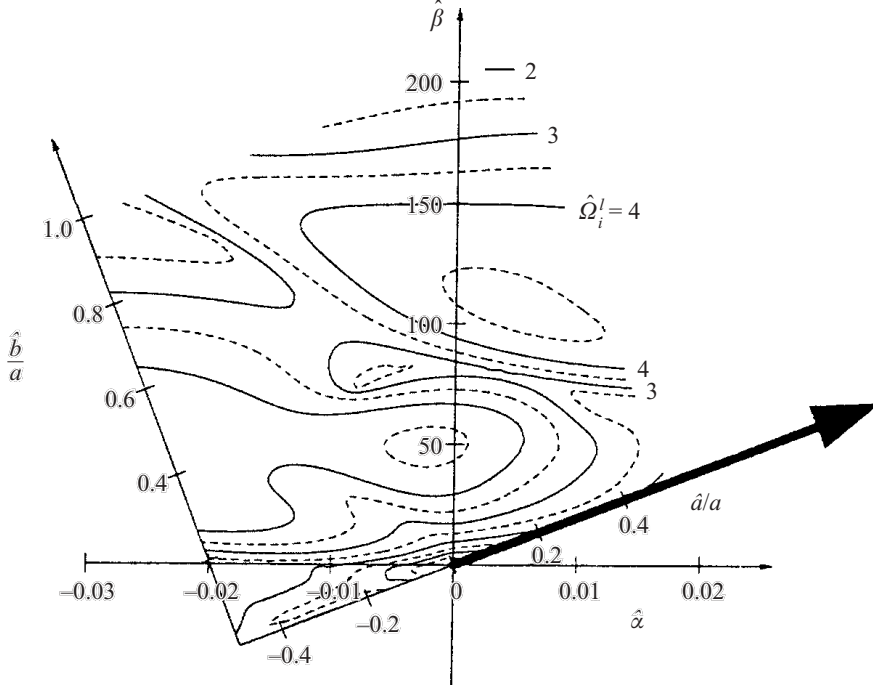


FIGURE 8. Secondary temporal growth rate $\hat{\Omega}_i^l$ of saturated crossflow vortices prevailing for $R = 510$, $\beta = 68$, $\alpha = 0.35$ and $\omega = 50.5$ (levels 1, 2, 3, 4 solid; 0.5, 1.5, 2.5, 3.5, 4.5 dashed). Isoline pattern is invariant under translation of the primary wavevector, indicated by the thick arrow.

7.2. Secondary temporal analysis

In a temporal analysis, the radial wavenumber $\hat{\alpha}$ of the secondary perturbation is prescribed and real, while the frequency $\hat{\omega}$ as obtained from dispersion relation (7.3) is complex.

Figure 8 shows the secondary temporal growth rate $\hat{\Omega}_i^l$ in the real $(\hat{\alpha}, \hat{\beta})$ -plane for the saturated crossflow vortices prevailing near onset of primary absolute instability and analysed in § 5.2. Such results are usually presented by resorting to wave-oriented coordinates, i.e. expressing $\hat{\alpha}$ and $\hat{\beta}$ in terms of the wave angle ε (5.3) of the primary nonlinear vortices as

$$\left. \begin{aligned} \hat{\alpha} &= \hat{a} \cos \varepsilon - \hat{b} \sin \varepsilon, \\ \hat{\beta}/R &= \hat{a} \sin \varepsilon + \hat{b} \cos \varepsilon, \end{aligned} \right\} \quad (7.6)$$

and prescribing \hat{a} and \hat{b} instead of $\hat{\alpha}$ and $\hat{\beta}$. With $a = \sqrt{\alpha^2 + (\beta/R)^2}$ denoting the primary wavevector modulus, the ratio \hat{a}/a is the detuning of the primary wavenumber, and \hat{b} is the secondary wavenumber in the direction of the primary vortex axis. By periodicity of the primary waves it is sufficient to consider the range $-a/2 \leq \hat{a} \leq a/2$. Here the parameters of the primary wave are $R = 510$, $\beta = 68$, $\alpha = 0.35$ and $\omega = 50.5$ which correspond to $\varepsilon = 0.368$ and $a = 0.371$, and figure 8 shows the highest temporal growth rate of all unstable modes.

From these results it is found that the crossflow vortices under consideration are unstable to secondary perturbations for any \hat{a} at small and order-unity values of \hat{b} . It is only at much higher values of \hat{b} that secondary perturbations are found to decay, since the maximum growth rate decreases with \hat{b} .

7.3. Secondary absolute instability and transition

Whether or not the primary finite-amplitude waves are permanently affected by secondary disturbances depends on the absolute or convective nature of the secondary instability. Indeed, for convectively unstable secondary instabilities, an external impulse may only trigger a transient perturbation that is eventually carried away radially outwards. Without external noise and for a perfectly smooth rotating disk, transition can only occur because of secondary absolute instability of the naturally selected primary crossflow vortices.

In contrast to the previous purely temporal analysis, the use of vortex-oriented coordinates is not appropriate for a full spatio-temporal analysis where the radial wavenumber $\hat{\alpha}$ needs to be considered complex while the mode number $\hat{\beta}$ remains integer.

Following Brevdo & Bridges (1996), the secondary absolute frequency $\hat{\omega}_0$ and absolute radial wavenumber $\hat{\alpha}_0$ for periodic wave solutions are obtained by a ‘pinching condition’ in the complex $\hat{\alpha}$ -plane which is formally analogous to that of Briggs (1964) and Bers (1983) established for spatially homogenous systems. This criterion is equivalent to a condition of vanishing radial group velocity,

$$\hat{\omega}_0(\hat{\beta}; \alpha, \beta; R) = \hat{\Omega}^l(\hat{\alpha}_0, \hat{\beta}; \alpha, \beta; R) \quad \text{where} \quad \frac{\partial \hat{\Omega}^l}{\partial \hat{\alpha}}(\hat{\alpha}_0, \hat{\beta}; \alpha, \beta; R) = 0, \quad (7.7)$$

with the additional requirement that the two spatial $\hat{\alpha}$ -branches colliding at the branch-point singularity $\hat{\alpha}_0$ originate from distinct half $\hat{\alpha}$ -planes for sufficiently large and positive values of $\hat{\omega}_i$.

Pinch points are readily identified by the ‘cusp map’ method (Kupfer, Bers & Ram 1987), i.e. by monitoring how the dispersion relation (7.3) maps the complex $\hat{\alpha}$ -plane onto the complex $\hat{\omega}$ -plane. This process is illustrated in figure 9 for the primary nonlinear wave obtained with $R = 510$, $\alpha = 0.35$, $\beta = 68$ and $\omega = 50.5$; the secondary azimuthal mode number is fixed at $\hat{\beta} = 20$. To start with, dispersion relation (7.3) is computed on a coarse rectangular grid in the complex wavenumber plane (part of which is shown by solid dots in figure 9a) to yield an outline of the mapping in the frequency plane (figure 9b) and the approximate location of a potential pinch point. Zooming in and recomputing the dispersion relation for a refined rectangular grid in the wavenumber plane reveals the characteristic cusp in the frequency plane (magnified portion of figure 9b). The corresponding values of the absolute frequency and wavenumber

$$\hat{\omega}_0 = 8.52 + 1.16i \quad \text{and} \quad \hat{\alpha}_0 = -0.0012 - 0.0369i \quad (7.8)$$

are then found by solving $\partial \hat{\Omega}^l / \partial \hat{\alpha} = 0$ (see also §A.3). In order to ascertain that this singularity of $\hat{\Omega}^l$ corresponds to a genuine pinch point, the two spatial branches $\hat{\alpha}^+(\hat{\omega})$ and $\hat{\alpha}^-(\hat{\omega})$ are computed for $\hat{\omega} = \hat{\omega}_{0,r} + \hat{\omega}_i$ with $\hat{\omega}_i \downarrow \hat{\omega}_{0,i}$ (thick curve in figure 9b). The curves labelled $\hat{\alpha}^+$ and $\hat{\alpha}^-$ in figure 9(a) demonstrate that indeed they originate from opposite half-planes.

After a first pinch point has been found, a continuation technique associated with an iterative procedure searching for zeros of $\partial \hat{\Omega}^l / \partial \hat{\alpha}$ yields the absolute frequency $\hat{\omega}_0$ and associated wavenumber $\hat{\alpha}_0$ for nearby values of $\hat{\beta}$ or of R , α and β . This iterative search requires only the computation of the mapping $\hat{\alpha} \mapsto \hat{\omega}$, which is numerically much faster (but still slow!) since the governing equations are of first order in time. Occasional spot checks using the (computationally more intensive) mapping $\hat{\omega} \mapsto \hat{\alpha}$

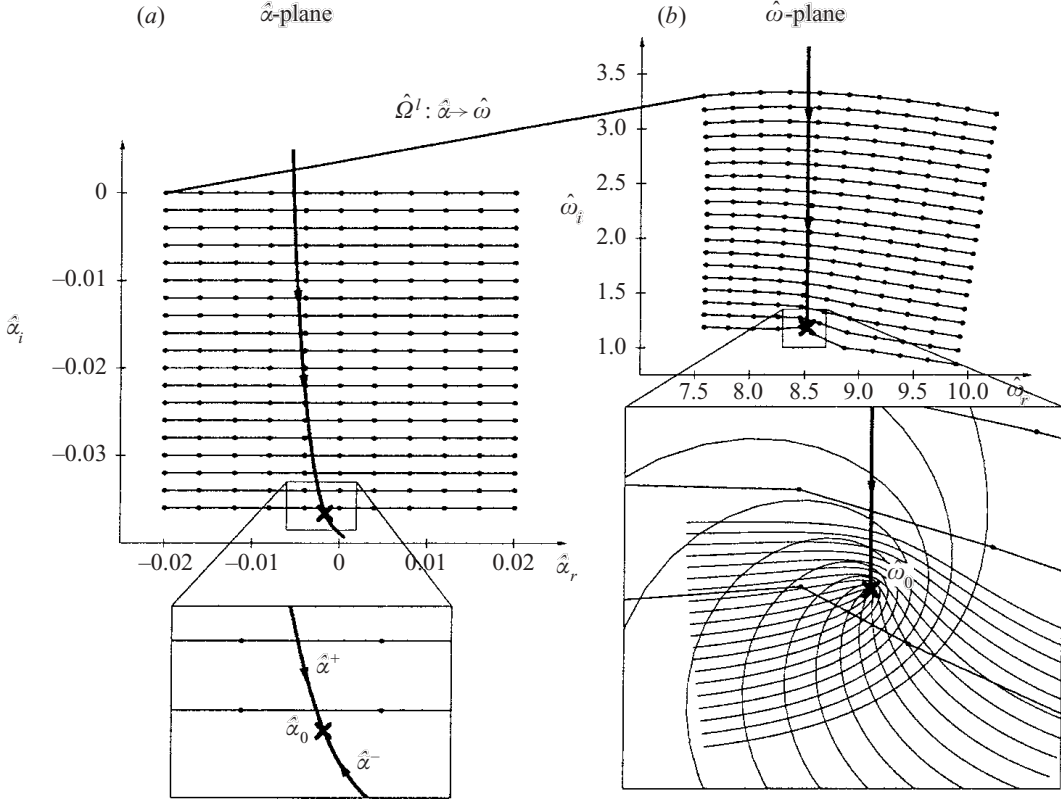


FIGURE 9. Mapping of the complex $\hat{\alpha}$ -plane (a) onto the complex $\hat{\omega}$ -plane (b) under the secondary dispersion relation $\hat{\Omega}^l$ and identification of pinch point (\times). Same primary wave as in figure 4, fixed secondary azimuthal wavenumber $\hat{\beta} = 20$. Magnified portion of (b) shows cusp structure at $\hat{\omega}_0$. Vertical frequency path (thick line in b) is associated with two spatial branches $\hat{\alpha}^+$ and $\hat{\alpha}^-$ indicated by thick lines in (a). The two branches collide at absolute wavenumber $\hat{\alpha}_0$ and originate from opposite half-planes for large values of $\hat{\omega}_i$.

are performed to ensure that the values of $\hat{\alpha}_0$ and $\hat{\omega}_0$ thus obtained are still associated with genuine pinch points.

The above analysis and result (7.8) are based on the nonlinear waves that are part of the self-sustained global solution and prevail for $R = 510$. As depicted in figure 9, the location of $\hat{\omega}_0$ in the upper complex frequency plane then reveals that the *saturated crossflow vortices that are naturally selected near R^{ca} are absolutely unstable with respect to secondary perturbations*. This strong secondary absolute instability explains why the naturally selected spiral vortices (sketched in figure 7) are not observed experimentally: as soon as the primary nonlinear vortices are generated near R^{ca} , secondary perturbations develop *in situ* and are amplified by a factor of $\exp(2\pi\hat{\omega}_{0,i}) \simeq 1500$ per disk rotation, and transition to turbulence immediately occurs.

The structure of the secondary eigenfunction associated with the pinch point of figure 9 is illustrated in figure 10 by its azimuthal velocity field $\hat{v}^l(z, \phi)$. Isocontours of (a) the velocity modulus $|\hat{v}^l|$ and (b) its real part \hat{v}_r^l are shown over two wavelengths, superimposed on v^{nl} -levels of the primary nonlinear wave, from figure 4(ii)(a). The largest amplitude of the eigenfunction is seen to occur for $\phi \simeq 3\pi/2$ and precisely correlates with the region where the primary wave displays strongly sheared velocity profiles, cf. figure 4(iii).

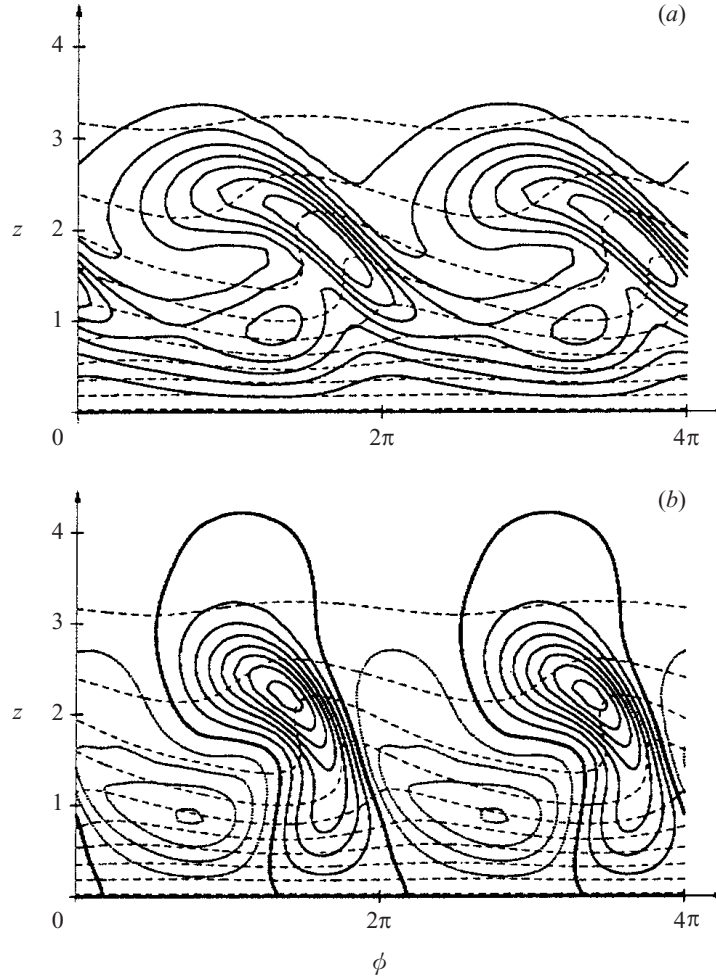


FIGURE 10. Structure of secondary eigenfunction associated with the pinch point of figure 9. Equispaced isolines of (a) modulus and (b) real part of azimuthal velocity component $\hat{v}^l(z, \phi)$ superimposed on azimuthal isolines of primary nonlinear wave (thin dashed curves, cf. figure 4ii(a)). Negative (zero) levels are shown by dotted (thick) curves.

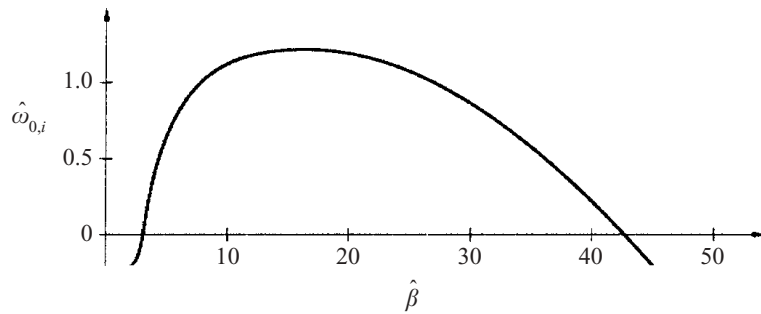


FIGURE 11. Secondary absolute growth rate $\hat{\omega}_{0,i}(\hat{\beta})$ pertaining to primary crossflow vortices near onset of nonlinearity $\alpha = 0.35$, $\beta = 68$, $\omega = 50.5$ and $R = 510$.

Figure 11 displays the variation of secondary absolute growth rate $\hat{\omega}_{0,i}$ with mode number $\hat{\beta}$, computed for the same primary saturated vortices, and shows that secondary absolute instability prevails for a wide range of azimuthal mode numbers.

8. Conclusion

This study has demonstrated that the behaviour of the three-dimensional boundary layer produced by a rotating disk can be analysed in terms of an ‘elephant’ global mode: the self-sustained finite-amplitude fluctuations are produced at the inner boundary R^{ca} of the absolutely unstable domain. This boundary for onset of absolute instability acts as a source and generates outward-spiralling saturated primary crossflow vortices. Due to the slow radial development of the boundary layer, these wavetrains are governed locally by the associated nonlinear dispersion relation derived numerically from the local boundary layer velocity profiles considered as parallel. A secondary stability analysis has revealed that the primary saturated waves initiated at R^{ca} are already absolutely unstable with respect to secondary perturbations. The naturally selected structure is thus dynamically unstable and gives way to a disordered state. (Note that, strictly speaking, these results only pave the way towards transition: in order to fully document the route to turbulence one would need to establish that secondary instabilities themselves do not saturate.) In consequence, the rotating-disk flow follows the scenario first outlined by Huerre (1988), using model equations rather than based on the Navier–Stokes equations, that secondary absolute instability may occur prior to primary absolute instability.

It should be emphasized that, in the present configuration, transition to a turbulent flow is triggered by secondary absolute instability while the transition location itself is controlled by primary absolute instability. Indeed, primary nonlinear waves are a prerequisite for the development of secondary instability leading to transition. Since the secondary disturbances feed on the primary vortices, the turbulent régime cannot propagate inwards of R^{ca} and the central region remains unperturbed. As a result, the transition location from basic to turbulent flow precisely coincides with the onset of primary absolute instability. Thus the primary instability remains essential, even though the primary spiral waves are obliterated.

In the present findings, transition occurs via a primary state of azimuthal mode number $\beta = 68$, while the spiral structures that have been observed experimentally generally display fewer spiral arms, in the range 25–50. There is no inconsistency, however, since experimental measurements of β have only been done for crossflow vortices that are steady with respect to the disk: these steady structures are presumably produced by roughness elements on the disk surface, depend on the experimental conditions and differ in frequency and wavenumber from the naturally selected ones. Also, using a smooth disk, Lingwood (1996) has not observed any periodic vortices, only a sharp transition from the unperturbed boundary layer to turbulence. Hence it seems that the observation of primary vortices requires external forcing whereas transition is an intrinsic feature of the boundary layer. A further confirmation of this assertion is the wide scatter in the number of observed spiral arms, whereas transition always occurs at a well-defined location.

The present results emphasize the essential difference between rotating-disk and swept-wing boundary layers. The rotating-disk problem is primarily one-dimensional: its dynamics is organized in the radial direction while the azimuthal and wall-normal coordinates appear as eigendirections. In contrast, the swept-wing problem is genuinely two-dimensional which makes its investigation much harder both analytically and numerically. Azimuthal periodicity of the disk enables the intrinsic route to turbulence via primary and secondary absolute instabilities. The swept-wing flow undergoes primary and secondary convective instabilities which ‘initiate but do not instantly cause breakdown to turbulence’ (Koch 2002).

$N_z = 30$	R^{ca}	ω_0^{ca}	α_0^{ca}	$N_z = 40$	R^{ca}	ω_0^{ca}	α_0^{ca}
$a_* = 1$	502.645	50.3471	$0.21686 - 0.11819i$	$a_* = 1$	508.475	50.5285	$0.21719 - 0.12281i$
	507.537	50.5043	$0.21757 - 0.12208i$		507.504	50.4952	$0.21679 - 0.12188i$
	507.284	50.4885	$0.21676 - 0.12166i$		507.369	50.4926	$0.21694 - 0.12177i$
	507.561	50.4974	$0.21694 - 0.12184i$		507.402	50.4933	$0.21691 - 0.12180i$
	507.216	50.4876	$0.21712 - 0.12190i$		507.403	50.4934	$0.21692 - 0.12180i$
	506.895	50.4822	$0.21655 - 0.12202i$		507.386	50.4929	$0.21692 - 0.12180i$
$N_z = 50$	R^{ca}	ω_0^{ca}	α_0^{ca}	$N_z = 60$	R^{ca}	ω_0^{ca}	α_0^{ca}
$a_* = 1$	507.088	50.4836	$0.21688 - 0.12148i$	$a_* = 1$	507.500	50.4961	$0.21690 - 0.12191i$
	507.368	50.4925	$0.21693 - 0.12177i$		507.403	50.4934	$0.21692 - 0.12181i$
	507.401	50.4934	$0.21692 - 0.12180i$		507.398	50.4932	$0.21692 - 0.12180i$
	507.396	50.4932	$0.21692 - 0.12180i$		507.397	50.4932	$0.21692 - 0.12180i$
	507.397	50.4932	$0.21692 - 0.12180i$		507.397	50.4932	$0.21692 - 0.12180i$
	507.397	50.4932	$0.21692 - 0.12180i$		507.397	50.4932	$0.21692 - 0.12180i$

TABLE 1. Onset location R^{ca} of primary absolute instability at $\beta = 68$ and corresponding absolute frequency ω_0^{ca} and wavenumber α_0^{ca} . Values computed with $N_z = 30, 40, 50$ and 60 collocation points using transformation (4.3) with a_* as given, $b_* = 0.6$ and $c_* = 0.5$.

$N_z = 30$	α	E_1	E_2	E_3	E_4	E_5	$N_z = 40$	α	E_1	E_2	E_3	E_4	E_5
$N_h = 1$	0.33660	625.49					$N_h = 1$	0.33660	625.60				
	0.34450	628.03	41.09					0.34450	628.09	41.12			
	0.34607	622.24	37.63	3.88				0.34607	622.07	37.55	3.87		
	0.34620	621.11	37.20	3.48	0.39			0.34616	621.10	37.13	3.45	0.38	
	0.34620	620.97	37.13	3.45	0.35	0.04		0.34616	621.03	37.09	3.43	0.35	0.04
$N_z = 50$	α	E_1	E_2	E_3	E_4	E_5	$N_z = 60$	α	E_1	E_2	E_3	E_4	E_5
$N_h = 1$	0.33660	625.66					$N_h = 1$	0.33660	625.70				
	0.34450	628.14	41.13					0.34450	628.16	41.14			
	0.34607	622.11	37.56	3.87				0.34607	622.14	37.56	3.87		
	0.34616	621.15	37.14	3.46	0.38			0.34616	621.17	37.14	3.46	0.38	
	0.34616	621.08	37.10	3.43	0.35	0.04		0.34616	621.11	37.10	3.44	0.35	0.04

TABLE 2. Nonlinear wave at $R = 510$ and $\beta = 68$ with prescribed frequency $\omega = 50.5$. Values of radial wavenumber α and harmonic energy content computed with $N_z = 30, 40, 50, 60$ and $N_h = 1, \dots, 5$.

Suggestions and advice from Nigel Peake and Werner Koch are gratefully acknowledged. Special thanks go to Julian Scott for a careful reading of the manuscript and to Paul Metcalfe for so efficiently setting up the Linux boxes which made possible the numerical computations of the present paper.

Appendix. Resolution tests

A.1. Onset of primary absolute instability

Transition from primary linear convective to absolute instability first occurs for $\beta = 68$. Table 1 shows how the marginal location R^{ca} , the real marginal absolute frequency ω_0^{ca} and the corresponding absolute wavenumber α_0^{ca} depend on the number and distribution of axial collocation points.

$N_z = 30$	$\hat{N}_h = 1$	2	3	4	5
$N_h = 1$	8.8017 + 1.2062i	8.7483 + 1.1959i	8.7549 + 1.2132i	8.7556 + 1.2127i	8.7556 + 1.2127i
	2	8.6422 + 1.0452i	8.5613 + 1.1728i	8.5409 + 1.2081i	8.5435 + 1.2110i
	3	8.5978 + 1.0262i	8.5197 + 1.1485i	8.5282 + 1.1858i	8.5266 + 1.1904i
	4	8.5931 + 1.0260i	8.5162 + 1.1470i	8.5254 + 1.1827i	8.5286 + 1.1882i
	5	8.5929 + 1.0263i	8.5163 + 1.1471i	8.5256 + 1.1827i	8.5289 + 1.1881i
$N_z = 40$	$\hat{N}_h = 1$	2	3	4	5
$N_h = 1$	8.7915 + 1.1754i	8.7389 + 1.1699i	8.7457 + 1.1866i	8.7463 + 1.1862i	8.7463 + 1.1862i
	2	8.6296 + 1.0153i	8.5492 + 1.1446i	8.5297 + 1.1792i	8.5324 + 1.1819i
	3	8.5859 + 0.9973i	8.5085 + 1.1208i	8.5182 + 1.1564i	8.5170 + 1.1609i
	4	8.5825 + 0.9975i	8.5062 + 1.1197i	8.5162 + 1.1539i	8.5200 + 1.1592i
	5	8.5825 + 0.9978i	8.5063 + 1.1198i	8.5165 + 1.1539i	8.5202 + 1.1592i

TABLE 3. Secondary absolute frequency $\hat{\omega}_0(\hat{\beta} = 20)$ pertaining to primary crossflow vortices near onset of nonlinearity $\omega = 50.5$, $\beta = 68$ and $R = 510$.

A.2. Nonlinear wave near onset of primary absolute instability

Nonlinear waves prevailing at $R = 510$ with $\beta = 68$ and a prescribed frequency of $\omega = 50.5$ have been computed for a range of resolutions. Table 2 shows how the corresponding radial wavenumber α and the distribution of the energy content by harmonics depends on the number of collocation points and of harmonics used in the computation.

A.3. Secondary absolute frequencies

Table 3 shows how the secondary absolute frequency $\hat{\omega}_0$ for $\hat{\beta} = 20$ depends on the number of primary N_h and secondary \hat{N}_h Fourier modes taken into account. The primary nonlinear wave at $R = 510$, $\beta = 68$ and $\omega = 50.5$ is computed with $N_z = 30$ or 40 collocation points remapped according to (4.3) using $a_* = 2$, $b_* = 0.6$ and $c_* = 0.5$.

REFERENCES

- BALACHANDAR, S., STREETT, C. L. & MALIK, M. R. 1992 Secondary instability in rotating-disk flow. *J. Fluid Mech.* **242**, 323–347.
- BALAKUMAR, P. & MALIK, M. R. 1990 Traveling disturbances in rotating-disk flow. *Theor. Comput. Fluid Dyn.* **2**, 125–137.
- BASSOM, A. P. & GAJJAR, J. S. B. 1988 Non-stationary cross-flow vortices in three-dimensional boundary-layer flows. *Proc. R. Soc. Lond. A* **417**, 179–212.
- BASSOM, A. P. & HALL, P. 1991 Concerning the interaction of non-stationary crossflow vortices in a three-dimensional boundary layer. *Q. J. Mech. Appl. Maths* **44**, 147–172.
- BATCHELOR, G. K. 1951 Note on a class of solutions for the Navier–Stokes equations representing steady rotationally-symmetric flow. *Q. J. Mech. Appl. Maths* **4**, 29–41.
- BATCHELOR, G. K. 1967 *An Introduction to Fluid Dynamics*. Cambridge: Cambridge University Press.
- BENDER, C. M. & ORSZAG, S. A. 1978 *Advanced Mathematical Methods for Scientists and Engineers*. McGraw-Hill.
- BERS, A. 1983 Space-time evolution of plasma instabilities—absolute and convective. In *Handbook of Plasma Physics* (ed. M. Rosenbluth & R. Sagdeev), pp. 451–517. North-Holland.
- BIPPES, H., MÜLLER, B. & WAGNER, M. 1991 Measurements and stability calculations of the disturbance growth in an unstable three-dimensional boundary layer. *Phys. Fluids A* **3**, 2371–2377.
- BRANCHER, P. & CHOMAZ, J.-M. 1997 Absolute and convective secondary instabilities in spatially periodic shear flows. *Phys. Rev. Lett.* **78**, 658–661.

- BREVDO, L. & BRIDGES, T. J. 1996 Absolute and convective instabilities of spatially periodic flows. *Phil. Trans. R. Soc. Lond. A* **354**, 1027–1064.
- BRIGGS, R. J. 1964 *Electron-stream Interaction with Plasmas*. MIT Press.
- CANUTO, C., HUSSAINI, M. J. & QUARTERONI, A. 1988 *Spectral Methods in Fluid Dynamics*. Springer.
- CEBEKI, T., CHEN, H. H., ARNAL, D. & HUANG, T. T. 1991 Three-dimensional linear stability approach to transition on wings and bodies of revolution at incidence. *AIAA J.* **29**, 2077–2085.
- CEBEKI, T. & STEWARTSON, K. 1980 On stability and transition in three-dimensional flows. *AIAA J.* **18**, 398–405.
- CHIN, D.-T. & LITT, M. 1972 An electrochemical study of flow instability on a rotating disk. *J. Fluid Mech.* **54**, 613–625.
- CHOMAZ, J.-M., COUAIRON, A. & JULIEN, S. 1999 Absolute and convective nature of the Eckhaus and zigzag instability with throughflow. *Phys. Fluids* **11**, 3369–3373.
- CHOMAZ, J.-M., HUERRE, P. & REDEKOPP, L. G. 1991 A frequency selection criterion in spatially developing flows. *Stud. Appl. Maths* **84**, 119–144.
- COUAIRON, A. & CHOMAZ, J.-M. 1996 Global instabilities in fully nonlinear systems. *Phys. Rev. Lett.* **77**, 4015–4018.
- COUAIRON, A. & CHOMAZ, J.-M. 1997a Absolute and convective instabilities, front velocities and global modes in nonlinear systems. *Physica D* **108**, 236–276.
- COUAIRON, A. & CHOMAZ, J.-M. 1997b Pattern selection in the presence of a cross flow. *Phys. Rev. Lett.* **79**, 2666–2669.
- COUAIRON, A. & CHOMAZ, J.-M. 1999a Fully nonlinear global modes in slowly varying flows. *Phys. Fluids* **11**, 3688–3703.
- COUAIRON, A. & CHOMAZ, J.-M. 1999b Primary and secondary nonlinear global instability. *Physica D* **132**, 428–456.
- DAVIES, C. & CARPENTER, P. W. 2003 Global behaviour corresponding to the absolute instability of the rotating-disk boundary layer. *J. Fluid Mech.* **486**, 287–329.
- DEE, G. & LANGER, J. S. 1983 Propagating pattern selection. *Phys. Rev. Lett.* **50**, 383–386.
- FALLER, A. 1991 Instability and transition of disturbed flow over a rotating disk. *J. Fluid Mech.* **230**, 245–269.
- FEDOROV, B. I., PLAVNIK, G. Z., PROKHOROV, I. V. & ZHUKHOVITSKH, L. G. 1976 Transitional flow conditions on a rotating disk. *J. Engng Phys.* **31**, 1448–1453.
- FISCHER, T. M. & DALLMANN, U. 1991 Primary and secondary stability analysis of three-dimensional boundary-layer flow. *Phys. Fluids A* **3**, 2378–2391.
- GAUTHIER, G., GONDRET, P. & RABAUD, M. 1999 Axisymmetric propagating vortices in the flow between a stationary and a rotating disk enclosed by a cylinder. *J. Fluid Mech.* **386**, 105–126.
- GREGORY, N., STUART, J. T. & WALKER, W. S. 1995 On the stability of three-dimensional boundary layers with application to the flow due to a rotating disk. *Phil. Trans. R. Soc. Lond. A* **248**, 155–199.
- HERBERT, T. 1988 Secondary instability of boundary layers. *Annu. Rev. Fluid Mech.* **20**, 487–526.
- HÖGBERG, M. & HENNINGSON, D. 1998 Secondary instability of cross-flow vortices in Falkner–Skan Cooke boundary layers. *J. Fluid Mech.* **368**, 339–357.
- HUERRE, P. 1988 On the absolute/convective nature of primary and secondary instabilities. In *Propagation in Systems far from Equilibrium* (ed. J. E. Wesfreid, H. R. Brand, P. Manneville, G. Albinet & N. Boccara), pp. 340–353. Springer.
- HUERRE, P. 2000 Open shear flow instabilities. In *Perspectives in Fluid Dynamics* (ed. G. K. Batchelor, H. K. Moffatt & M. G. Worster), pp. 159–229. Cambridge University Press.
- HUERRE, P. & MONKEWITZ, P. A. 1990 Local and global instabilities in spatially developing flows. *Annu. Rev. Fluid Mech.* **22**, 473–537.
- JANKE, E. & BALAKUMAR, P. 2000 On the secondary instability of three-dimensional boundary layers. *Theor. Comput. Fluid Dyn.* **14**, 167–194.
- JARRE, S., LE GAL, P. & CHAUVE, M. P. 1996a Experimental study of rotating disk instability, I. Natural flow. *Phys. Fluids* **8**, 496–508.
- JARRE, S., LE GAL, P. & CHAUVE, M. P. 1996b Experimental study of rotating disk flow instability, II. Forced flow. *Phys. Fluids* **8**, 2985–2994.
- VON KÁRMÁN, T. 1921 Über laminare und turbulente Reibung. *Z. Angew. Math. Mech.* **1**, 232–252.
- KELLER, H. B. 1977 Numerical solution of bifurcation and nonlinear eigenvalue problems. In *Applications of Bifurcation Theory* (ed. P. Rabinowitz), pp. 359–384. Academic.

- KOBAYASHI, R., KOHAMA, Y. & TAKAMADATE, C. 1980 Spiral vortices in boundary layer transition regime on a rotating disk. *Acta Mechanica* **35**, 71–82.
- KOCH, W. 1996 Nonlinear crossflow saturation in three-dimensional boundary layers. In *IUTAM Symp. on Nonlinear Instability and Transition in Three-Dimensional Boundary Layers* (ed. P. W. Duck & P. Hall), pp. 299–308. Kluwer.
- KOCH, W. 2002 On the spatio-temporal stability of primary and secondary crossflow vortices in a three-dimensional boundary layer. *J. Fluid Mech.* **456**, 85–111.
- KOCH, W., BERTOLOTTI, F., STOLTE, A. & HEIN, S. 2000 Nonlinear equilibrium solutions in a three-dimensional boundary layer and their secondary instability. *J. Fluid Mech.* **406**, 131–174.
- KOHAMA, Y. 1984 Study on boundary layer transition of a rotating disk. *Acta Mechanica* **50**, 193–199.
- KUPFER, K., BERS, A. & RAM, A. K. 1987 The cusp map in the complex-frequency plane for absolute instabilities. *Phys. Fluids* **30**, 3075–3082.
- LE DIZÈS, S., HUERRE, P., CHOMAZ, J.-M. & MONKEWITZ, P. A. 1996 Linear global modes in spatially developing media. *Phil. Trans. R. Soc. Lond. A* **354**, 169–212.
- LE GAL, P., RAVOUX, J. F., FLORIANI, E. & DUDOK DE WIT, T. 2003 Recovering coefficients of the complex Ginzburg–Landau equation from experimental spatio-temporal data: two examples from hydrodynamics. *Physica D* **174**, 114–133.
- LIN, R. S. & REED, H. L. 1993 Effect of curvature on stationary cross-flow instability of a three-dimensional boundary layer. *AIAA J.* **31**, 1611–1617.
- LINGWOOD, R. J. 1995 Absolute instability of the boundary layer on a rotating disk. *J. Fluid Mech.* **299**, 17–33.
- LINGWOOD, R. J. 1996 An experimental study of absolute instability of the rotating-disk boundary-layer flow. *J. Fluid Mech.* **314**, 373–405.
- LINGWOOD, R. J. 1997a Absolute instability of the Ekman layer and related rotating flows. *J. Fluid Mech.* **331**, 405–428.
- LINGWOOD, R. J. 1997b On the impulse response for swept boundary-layer flows. *J. Fluid Mech.* **344**, 317–334.
- MALIK, M. R. 1986 The neutral curve for stationary disturbances in rotating-disk flow. *J. Fluid Mech.* **164**, 275–287.
- MALIK, M. R., LI, F. & CHANG, C.-L. 1994 Crossflow disturbances in three-dimensional boundary layers: nonlinear development, wave interaction and secondary instability. *J. Fluid Mech.* **268**, 1–36.
- MALIK, M. R., LI, F. & CHANG, C.-L. 1996 Nonlinear crossflow disturbances and secondary instabilities in swept-wing boundary layers. In *IUTAM Symp. on Nonlinear Instability and Transition in Three-Dimensional Boundary Layers* (ed. P. W. Duck & P. Hall), pp. 299–308. Kluwer.
- MALIK, M. R., LI, F., CHOUDHARI, M. M. & CHANG, C.-L. 1999 Secondary instability of crossflow vortices and swept-wing boundary-layer transition. *J. Fluid Mech.* **399**, 85–115.
- MALIK, M. R., WILKINSON, S. P. & ORSZAG, S. A. 1981 Instability and transition in rotating disk flow. *AIAA J.* **19**, 1131–1138.
- MONKEWITZ, P. A., HUERRE, P. & CHOMAZ, J.-M. 1993 Global linear stability analysis of weakly non-parallel shear flows. *J. Fluid Mech.* **251**, 1–20.
- PEAKE, N. & GARRETT, S. J. 2002 On the global linear stability of the boundary layer on rotating bodies. *J. Fluid Mech.* (submitted).
- PIER, B. 2002a Fully nonlinear waves and transition in the boundary layer over a rotating disk. In *Advances in Turbulence IX, Proc. 9th European Turbulence Conf.* (ed. I. Castro & P. Hancock), pp. 13–16. Barcelona: CIMNE.
- PIER, B. 2002b On the frequency selection of finite-amplitude vortex shedding in the cylinder wake. *J. Fluid Mech.* **458**, 407–417.
- PIER, B. & HUERRE, P. 1996 Fully nonlinear global modes in spatially developing media. *Physica D* **97**, 206–222.
- PIER, B. & HUERRE, P. 2001a Nonlinear self-sustained structures and fronts in spatially developing wake flows. *J. Fluid Mech.* **435**, 145–174.
- PIER, B. & HUERRE, P. 2001b Nonlinear synchronization in open flows. *J. Fluid Struct.* **15**, 471–480.
- PIER, B., HUERRE, P. & CHOMAZ, J.-M. 2001 Bifurcation to fully nonlinear synchronized structures in slowly varying media. *Physica D* **148**, 49–96.

- PIER, B., HUERRE, P., CHOMAZ, J.-M. & COUAIRON, A. 1998 Steep nonlinear global modes in spatially developing media. *Phys. Fluids* **10**, 2433–2435.
- REED, H. L. 1987 Wave interactions in swept-wing flows. *Phys. Fluids* **30**, 3419–3426.
- REED, H. L. & SARIC, W. S. 1989 Stability of three-dimensional boundary layers. *Annu. Rev. Fluid Mech.* **21**, 235–284.
- RYZHOV, O. S. & TERENT'EV, E. D. 1998 Streamwise absolute instability of a three-dimensional boundary layer at high Reynolds number. *J. Fluid Mech.* **373**, 111–153.
- SARIC, W. S., REED, H. L. & WHITE, E. B. 2003 Stability and transition of three-dimensional boundary layers. *Annu. Rev. Fluid Mech.* **35**, 413–440.
- SCHMID, P. J. & HENNINGSON, D. S. 2000 *Stability and Transition in Shear Flows*. Springer.
- SCHOUVEILER, L., LE GAL, P. & CHAUVE, M. P. 2001 Instabilities of the flow between a rotating and a stationary disk. *J. Fluid Mech.* **443**, 329–350.
- SERRE, E., CRESPO DEL ARCO, E. & BONTOUX, P. 2001a Annular and spiral patterns in flows between rotating and stationary disks. *J. Fluid Mech.* **434**, 65–100.
- SERRE, E., HUGUES, S., CRESPO DEL ARCO, E., RANDRIAMAMPIANINA, A. & BONTOUX, P. 2001b Axisymmetric and three-dimensional instabilities in an Ekman boundary layer flow. *Intl. J. Heat Fluid Flow* **22**, 82–93.
- TAYLOR, M. J. & PEAKE, N. 1998 The long-time behaviour of incompressible swept-wing boundary layers subject to impulsive forcing. *J. Fluid Mech.* **355**, 359–381.
- THEODORSEN, T. & REGIER, A. 1944 Experiments on drag of revolving disks, cylinders, and streamline rods at high speeds. *Tech. Rep.* 793. NACA.
- WILKINSON, S. P. & MALIK, M. R. 1985 Stability experiments in the flow over a rotating disk. *AIAA J.* **23**, 588–595.
- ZANDBERGEN, P. J. & DIJKSTRA, D. 1987 Von Kármán swirling flows. *Annu. Rev. Fluid Mech.* **19**, 465–491.

[A10]

**Primary crossflow vortices, secondary absolute instabilities and their control
in the rotating-disk boundary layer**

B. Pier

Journal of Engineering Mathematics **57**, 237–251 (2007)

doi:10.1007/s10665-006-9095-5
<https://hal.archives-ouvertes.fr/hal-00197478>

Primary crossflow vortices, secondary absolute instabilities and their control in the rotating-disk boundary layer

Benoît Pier

Received: 9 May 2006 / Accepted: 14 September 2006 / Published online: 11 January 2007
© Springer Science+Business Media B.V. 2006

Abstract The three-dimensional boundary layer produced by a disk rotating in otherwise still fluid is analytically investigated and its stability properties are systematically established. Using a local parallel flow approximation, finite-amplitude primary travelling vortices governed by a nonlinear dispersion relation are obtained. A secondary stability analysis yields the secondary linear dispersion relation and the secondary absolute growth rate, which determines the long-term stability of the primary nonlinear vortex-trains. By using these local characteristics, spatially developing global patterns of crossflow vortices are derived by employing asymptotic techniques. This approach accounts for both the self-sustained behaviour, exhibiting a sharp transition from laminar to turbulent flow, and the spatial response to external harmonic forcing, for which onset of nonlinearity and transition both depend on the forcing parameters. Based on these results, an open-loop control method is described in detail. Its aim is not to suppress the primary fluctuations but rather to enhance them and to tune them to externally imposed frequency and modenumber, and thereby to delay onset of secondary absolute instability and transition. It is shown that transition can be delayed by more than 100 boundary-layer units.

Keywords Absolute instabilities · Boundary layers · Control · Rotating disk

1 Introduction

The von Kármán [1] boundary layer on an infinite disk rotating in otherwise still fluid is certainly a rather crude and academic representation of centrifugal pumps, fans, turbomachinery elements, or backwards-swept aircraft wings. However, despite its simplicity, it displays most of the features observed in situations of higher complexity or with more elaborate geometries. All these types of boundary layers display similar three-dimensional velocity profiles, are subject to inviscid crossflow instabilities and rapidly undergo transition to turbulent flow [2–4]. Thus, ever since the pioneering work of Kármán [1] and Gregory et al. [5],

B. Pier (✉)
Laboratoire de mécanique des fluides et d'acoustique,
École centrale de Lyon—CNRS—Université Claude-Bernard Lyon I—INSA,
36 avenue Guy-de-Collongue,
69134 Écully cedex, France
e-mail: benoit.pier@ec-lyon.fr

the rotating disk flow has served as the archetypal three-dimensional boundary layer, and its study has lead to many results of considerable practical importance, e.g., to the aeronautics industry.

In the rotating-disk flow, the magnitude of the local boundary-layer velocity profiles increases linearly with radial distance. As a result, the nature of the local stability features successively displays the three well-known régimes from the disk axis outwards: stability, convective instability, absolute instability (for theoretical definitions see [6, 7]). Lingwood's theoretical local linear stability analyses [8] have revealed that absolute instability first occurs at a critical radius closely corresponding to the experimentally observed transition from laminar to turbulent flow. Her findings suggested that the onset of absolute instability is the driving mechanism responsible for the self-sustained time-dependent flow. Indeed, in stable or convectively unstable systems, perturbations either decay or are carried away by basic advection so that, at given position, the flow returns to its unperturbed state in the long term. It is only when the instability is absolute that an initial disturbance may grow in time at fixed spatial position and thus lead to a permanently perturbed flow. While this scenario for the behaviour of the rotating-disk flow seems to be confirmed by most experimental studies (including Lingwood's [9]), it does not, however, take into account two major effects: spatial inhomogeneity and nonlinearity.

Global stability analyses of spatially inhomogenous systems governed by strictly linear dynamics are by now fairly complete. For the linear complex Ginzburg–Landau equation with spatially varying coefficients, Chomaz et al. [10] demonstrated that the complex frequency of a linear global mode is determined by a saddle point condition applied to the local linear dispersion relation. According to Monkewitz et al. [11], the same criterion also holds for the Navier–Stokes equations linearized about an arbitrary slowly varying basic flow. In this linear setting, local absolute instability is a necessary but not sufficient condition for global instability: in general, the existence of unstable global modes requires a finite range of local absolute instability. The question whether or not the local absolute instability in the rotating-disk boundary layer is strong enough to lead to unstable linear global modes has recently been addressed via direct numerical simulations [12] (see also [13] in this volume). These simulations have shown that the local absolute instability of this flow *does not* produce a linear amplified global mode and is only associated with a transient temporal growth; a result, also in agreement with analytical developments ([14] and N. Peake, Private communication). These findings seem to be further supported by recent experimental work [15], carefully designed to remain within the linear régime.

Thus, it appears that the self-sustained transition experimentally observed in the rotating-disk flow cannot be explained within linear hydrodynamic-stability theory applied to spatially developing flows: a fully nonlinear approach is thus required. The study of finite-amplitude states covering spatially inhomogenous systems [16–22] has shown that there exists a variety of nonlinear global modes. The main result [21] of interest here is that now local absolute instability is a necessary *and* sufficient condition: nonlinear global modes exist, however small the absolutely unstable domain. In this context, nonlinear global modes may exist in globally linearly stable media and their onset occurs via a saddle-node bifurcation [21].

Thus, Lingwood's scenario can be restored by taking into account both spatial inhomogeneity and nonlinearity: the rotating-disk boundary layer is locally absolutely unstable [8], globally linearly stable [12] and globally nonlinearly unstable [28].

The discrepancy between the global linear and nonlinear dynamics is, among others, due to the important radial outflow and the large convectively unstable region upstream of the absolutely unstable region. Thus, even small external perturbations may undergo a strong transient amplification and trigger nonlinear dynamics. When external perturbations are switched off, such an externally forced perturbed state would decay in the long term according to linear theory, but can survive forever due to nonlinear interactions if finite amplitudes are reached. Most experimental studies [5, 24–26] have focused on perturbations that are fixed with respect to the disk, generated by roughness elements and permanently applied. Two already mentioned studies [9, 15] specifically address the impulse response and the related issue of self-sustained disturbances. In these two experiments, a short air pulse is applied, either through a hole in the disk surface once every disk rotation [9] or from above the boundary layer at independent timings [15]. So far the

competition between self-sustained and externally forced dynamics has not been investigated in terms of complete hydrodynamic linear and nonlinear stability analyses.

The present investigation outlines a new control method where a carefully designed periodic forcing is continuously applied in the convectively unstable region so as to modify the self-sustained nonlinear dynamics and to delay onset of transition.

This contribution first reviews and extends recent results from [23, 27–29], and then applies them to control the flow and delay transition beyond a radius at which the unforced flow would have become transitional. By systematically computing primary (Sect. 3) and secondary (Sect. 4) stability characteristics, and using asymptotic developments (Sect. 5), the naturally selected flow dynamics is explained (Sect. 6) and the spatial response to localized harmonic forcing established (Sect. 7). Based on these results, a new open-loop control method to delay transition is described (Sect. 8).

2 Basic flow structure

The infinite-disk problem lacks a characteristic length scale and thus allows the use of nondimensional variables based on disk rotation rate, fluid viscosity and density, so that the flow does not depend on any control parameter. Throughout this paper an inertial frame of reference is used with r , θ and z denoting radial, azimuthal and axial coordinates, respectively. The time-independent axisymmetric basic flow is then given by von Kármán's [1] exact similarity solution to the Navier–Stokes equations as

$$\mathbf{U}(r, z) \equiv \begin{pmatrix} rU(z) \\ rV(z) \\ W(z) \end{pmatrix} \quad \text{and} \quad P(z), \quad (1)$$

where rU , rV and W are the non-dimensional radial, azimuthal and axial velocity components, and P is the pressure.

The boundary-layer thickness is constant, of order unity in non-dimensional coordinates. As a result, when features far from the disk axis and near a given radial location $R \gg 1$ are investigated, the assumption of slow radial development is appropriate and local properties at given $r = R$ are derived by freezing the radial dependence of the basic flow (1) and studying the corresponding homogenous three-dimensional flow $\mathbf{U}(z; R) \equiv (RU(z), RV(z), W(z))$. The value of R then appears as a control parameter rather than a coordinate and plays the rôle of an effective local Reynolds number.

3 Local linear and nonlinear travelling vortices

In subsequent developments, the total instantaneous flow field prevailing at a given location R is separated into basic and perturbation quantities according to

$$\begin{cases} \mathbf{U}(z; R) + \mathbf{u}(r, \theta, z, t), \\ P(z) + p(r, \theta, z, t). \end{cases} \quad (2)$$

Local linear instability properties are then derived by assuming infinitesimally small velocity and pressure disturbances, written in normal-mode form as

$$\begin{cases} \mathbf{u}(r, \theta, z, t) = \mathbf{u}^l(z; \alpha, \beta; R) \exp i(\alpha r + \beta \theta - \omega t), \\ p(r, \theta, z, t) = p^l(z; \alpha, \beta; R) \exp i(\alpha r + \beta \theta - \omega t), \end{cases} \quad (3)$$

where α is a complex radial wavenumber, β an integer azimuthal modenumber, ω a complex angular frequency and \mathbf{u}^l , p^l the associated complex velocity and pressure components. Substitution of (3) in the linearized version of the local governing equations yields an eigenvalue problem in the z -direction. From it, the local linear dispersion relation

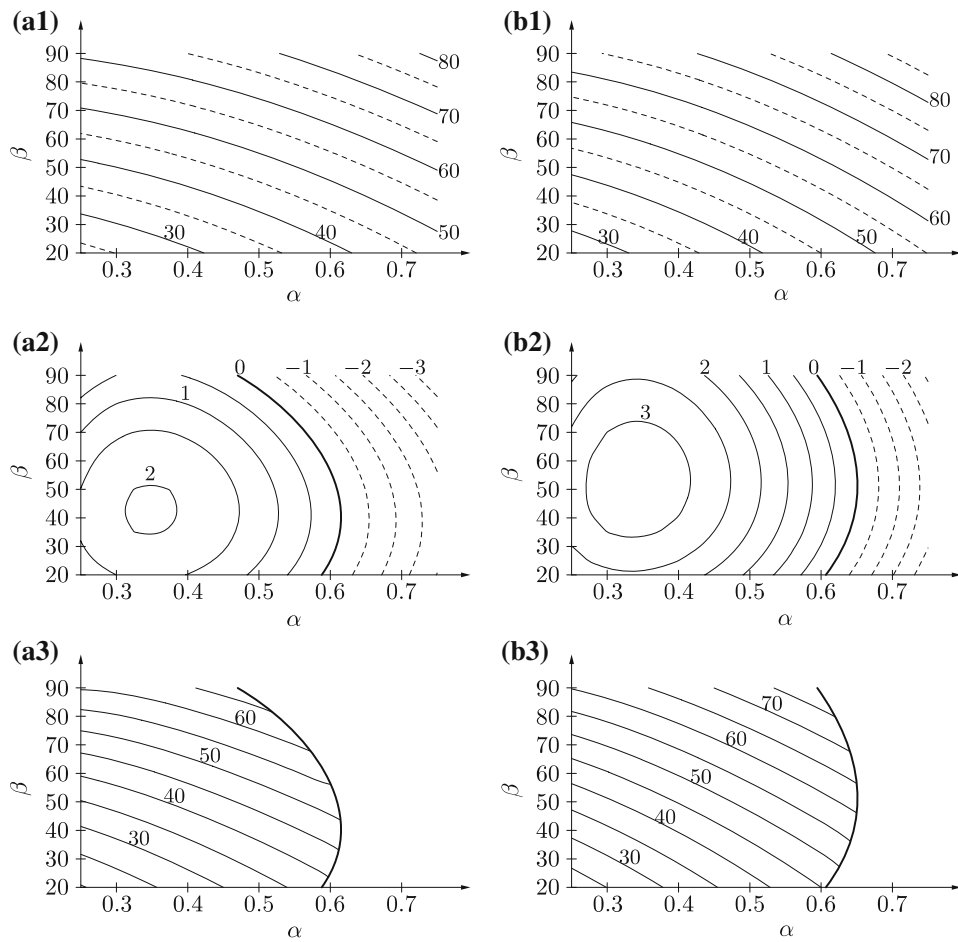


Fig. 1 Local linear and nonlinear dispersion relations in (α, β) -plane for **(a)** $R = 450$ and **(b)** $R = 550$. (a1, b1) Isocontours of linear real frequency Ω_r^l . (a2, b2) Isocontours of linear temporal growth rate Ω_i^l . (a3, b3) Isocontours of nonlinear frequency Ω^{nl} , in subregion of (α, β) -plane where saturated wave solutions exist

$$\omega = \Omega^l(\alpha, \beta; R), \quad (4)$$

together with the eigenfunctions $\mathbf{u}^l(z; \alpha, \beta; R)$ and $p^l(z; \alpha, \beta; R)$ are routinely derived. Complex values of Ω^l computed in the (α, β) -plane for $R = 450$ and $R = 550$ are shown in Fig. 1(a1,a2,b1,b2).

In the context of open flows [6,7], a crucial feature is the complex absolute frequency ω_0 and the associated absolute wavenumber α_0 , defined by a vanishing group velocity condition [30,31] as

$$\omega_0(\beta; R) = \Omega^l(\alpha_0, \beta; R) \quad \text{with} \quad \frac{\partial \Omega^l}{\partial \alpha}(\alpha_0, \beta; R) = 0. \quad (5)$$

The linear instability properties of the rotating-disk boundary layer are well known [8,32]. Local growth rates increase with radial distance away from the disk axis: the central region $R < R^{sc} \simeq 285$ is linearly stable, convective instability prevails for $R^{sc} < R < R^{ca} \simeq 507$, and absolute instability in the outer region $R > R^{ca}$. Transition from the convectively unstable (cu) to the absolutely unstable (au) domains occurs at R^{ca} for an azimuthal modenumber of β^{ca} and with a marginal real absolute frequency of ω_0^{ca} , where

$$\omega_0^{ca} \simeq 50.5, \quad \beta^{ca} = 68, \quad R^{ca} \simeq 507. \quad (6)$$

In regions of linear instability, the three-dimensional boundary layer admits nonlinearly saturated travelling crossflow vortices, governed by the complete nonlinear equations. The finite-amplitude perturbation velocity and pressure fields of these nonlinear wave solutions are of the form

$$\begin{cases} \mathbf{u}(r, \theta, z, t) = \mathbf{u}^{\text{nl}}(z, \alpha r + \beta \theta - \omega t; \alpha, \beta; R), \\ p(r, \theta, z, t) = p^{\text{nl}}(z, \alpha r + \beta \theta - \omega t; \alpha, \beta; R), \end{cases} \quad (7)$$

where the functions \mathbf{u}^{nl} and p^{nl} are 2π -periodic in their second variable $\phi \equiv \alpha r + \beta \theta - \omega t$ with α and ω now real quantities. After expanding \mathbf{u}^{nl} and p^{nl} as Fourier series in ϕ and substituting them in the local nonlinear governing equations, these finite-amplitude spiral waves are numerically obtained by a Newton–Raphson search procedure [23]. The real frequency ω of the saturated waves is then determined by the local nonlinear dispersion relation

$$\omega = \Omega^{\text{nl}}(\alpha, \beta; R). \quad (8)$$

Values of Ω^{nl} , computed in the domain of the (α, β) -plane where non-linear travelling vortices exist and delimited by $\Omega_i^l = 0$, are shown in Fig. 1 (a3) and (b3) for $R = 450$ and $R = 550$, respectively.

4 Secondary stability analyses

In order to investigate the stability of the above primary finite-amplitude crossflow vortices (7) with respect to secondary perturbations, a secondary stability analysis needs to be carried out. For nonlinear travelling waves of wavenumber α , modenumber β and frequency ω at a radial station R , the total flow fields are then decomposed as

$$\begin{cases} \mathbf{U}(z; R) + \mathbf{u}^{\text{nl}}(z, \alpha r + \beta \theta - \omega t; \alpha, \beta; R) + \hat{\mathbf{u}}(r, \theta, z, t), \\ P(z) + p^{\text{nl}}(z, \alpha r + \beta \theta - \omega t; \alpha, \beta; R) + \hat{p}(r, \theta, z, t), \end{cases} \quad (9)$$

where $\mathbf{U} + \mathbf{u}^{\text{nl}}$, $P + p^{\text{nl}}$ represent the new basic flow solution which is perturbed by $\hat{\mathbf{u}}, \hat{p}$. Assuming infinitesimally small secondary velocity and pressure disturbances and using Floquet theory [33], the perturbation quantities are written in normal-mode form as

$$\begin{cases} \hat{\mathbf{u}}(r, \theta, z, t) = \hat{\mathbf{u}}^l(z, \alpha r + \beta \theta - \omega t; \hat{\alpha}, \hat{\beta}; \alpha, \beta; R) \exp i(\hat{\alpha}r + \hat{\beta}\theta - \hat{\omega}t), \\ \hat{p}(r, \theta, z, t) = \hat{p}^l(z, \alpha r + \beta \theta - \omega t; \hat{\alpha}, \hat{\beta}; \alpha, \beta; R) \exp i(\hat{\alpha}r + \hat{\beta}\theta - \hat{\omega}t), \end{cases} \quad (10)$$

where $\hat{\alpha}$ is the secondary complex radial wavenumber, $\hat{\beta}$ is the secondary integer azimuthal modenumber and $\hat{\omega}$ is the associated complex secondary frequency. The eigenfunctions $\hat{\mathbf{u}}^l$ and \hat{p}^l have the same periodicity as the primary wave, i.e., are 2π -periodic in the real phase variable $\phi \equiv \alpha r + \beta \theta - \omega t$, so that a Fourier series in ϕ is again appropriate. Two-dimensional eigenproblems in the variables z and ϕ are then obtained after substitution of (9) with (10) into the local governing equations and linearization about the new basic flow (see [23] for numerical details). For each primary nonlinear wave characterized by the real parameters α, β and R and for each combination of $\hat{\alpha}$ and $\hat{\beta}$, the solution of the corresponding eigenproblem yields the secondary linear dispersion relation

$$\hat{\omega} = \hat{\Omega}^l(\hat{\alpha}, \hat{\beta}; \alpha, \beta; R) \quad (11)$$

together with the associated eigenfunctions $\hat{\mathbf{u}}^l$ and \hat{p}^l .

Whether or not the primary finite-amplitude waves are permanently affected by a secondary disturbance depends on the absolute or convective nature of the secondary instability. Indeed, in the case of secondary convective instability an external impulse only triggers a transient perturbation that is eventually carried away radially outwards, while, for secondary absolute instability, perturbations are exponentially amplified at fixed radial position.

Following Brevdo and Bridges [34], the secondary absolute frequency $\hat{\omega}_0$ and absolute radial wavenumber $\hat{\alpha}_0$ for periodic wave solutions are obtained by a saddle point condition in the complex $\hat{\alpha}$ -plane

$$\hat{\omega}_0(\hat{\beta}; \alpha, \beta; R) = \hat{\Omega}^l(\hat{\alpha}_0, \hat{\beta}; \alpha, \beta; R) \quad \text{where} \quad \frac{\partial \hat{\Omega}^l}{\partial \hat{\alpha}}(\hat{\alpha}_0, \hat{\beta}; \alpha, \beta; R) = 0, \quad (12)$$

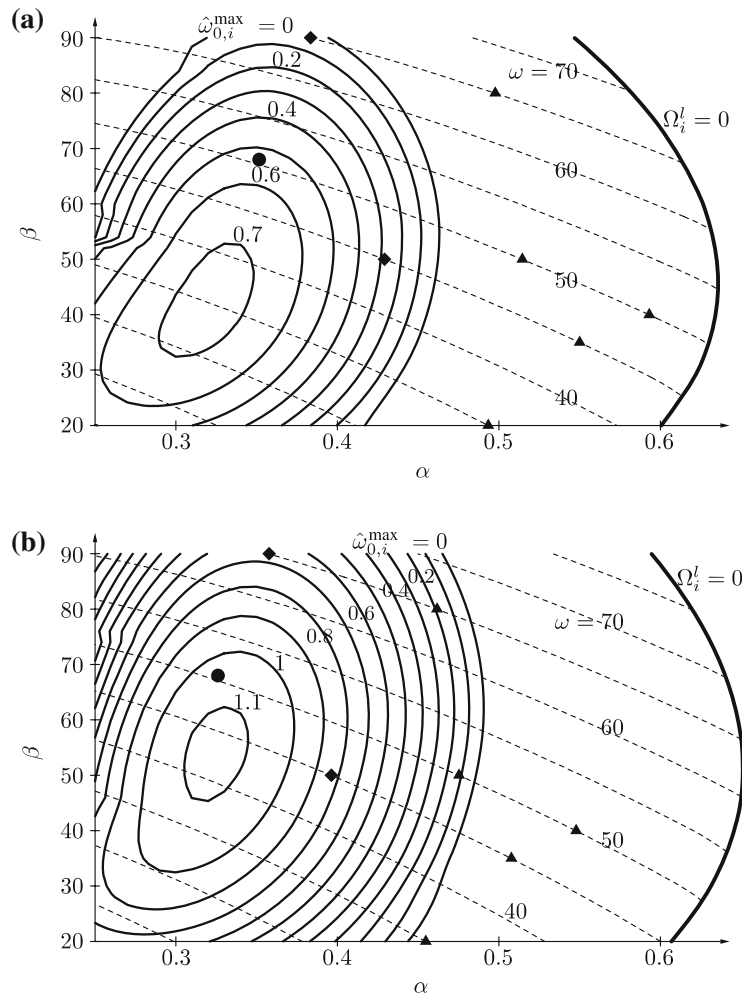


Fig. 2 Isolines (thin solid curves) of nonnegative maximum secondary absolute growth rate $\hat{\omega}_{0,i}^{\max}(\alpha, \beta; R)$ for (a) $R = 500$ and (b) $R = 550$. Nonlinear vortex trains exist to the left of the marginal curve $\Omega_i^l(\alpha, \beta; R) = 0$ (thick solid line) with frequencies corresponding to the dashed isolines. Symbols refer to crossflow vortices at $(\omega, \beta) = (\omega_0^{\text{ca}}, \beta^{\text{ca}})$ (thick dot), $(\omega, \beta) = (65, 90)$, $(45, 50)$ (diamonds), and $(\omega, \beta) = (65, 80), (50, 50), (50, 40), (45, 35), (35, 20)$ (triangles)

which is formally analogous to the criterion of Briggs [30] and Bers [31] established for spatially homogeneous systems.

The stability of a system of periodic nonlinear crossflow vortices corresponding to given values α, β and R depends on the maximum secondary absolute growth rate

$$\hat{\omega}_{0,i}^{\max}(\alpha, \beta; R) \equiv \max_{\hat{\beta}} \operatorname{Im} \hat{\omega}_0(\hat{\beta}; \alpha, \beta; R). \quad (13)$$

Thus, it is the sign of this quantity which determines whether the primary spiral vortices are stable ($\hat{\omega}_{0,i}^{\max} < 0$) or not ($\hat{\omega}_{0,i}^{\max} > 0$) in the long term with respect to secondary perturbations.

Figure 2 shows isocontours (thin solid curves) of $\hat{\omega}_{0,i}^{\max} \geq 0$ computed in the (α, β) -plane for $R = 500$ and $R = 550$. Nonlinear crossflow vortices exist in the region delimited by the (thick solid) marginal curve $\Omega_i^l(\alpha, \beta; R) = 0$, and their nonlinear frequencies $\omega = \Omega_i^{\text{nl}}(\alpha, \beta; R)$ are indicated by dashed isolines. The symbols in these plots correspond to crossflow vortices at particular values of β and ω and will be used in Sect. 8.

5 Spatially developing pattern of crossflow vortices

The analyses described in the previous sections entirely characterize the *local* properties of the rotating-disk boundary layer: primary linear stability, primary nonlinear saturated waves, secondary stability of these finite-amplitude periodic vortices. Based on these results, we are now in a position to derive a *global* structure of spiral vortices developing over an extended radial domain and to express them in the form of wavetrains that are slowly modulated in the radial direction. This approach is set on a firm theoretical basis by using WKBJ asymptotic techniques [35, Chap. 10].

In the rotating-disk flow, the region of particular interest is the neighbourhood of $R^{\text{ca}} \simeq 507$ where onset of primary absolute instability first occurs. This characteristic radius is large compared to the boundary layer thickness, hence fulfilling the assumption of slow radial development. It is thus legitimate to use

$$\epsilon \equiv \frac{1}{R^{\text{ca}}} \ll 1 \quad (14)$$

as a small parameter in the asymptotic formulation and to introduce the slow radial coordinate

$$\bar{R} = \epsilon r. \quad (15)$$

In this multiple-scales approach, the fast r -scale accounts for the oscillatory behaviour of the spatially extended wavetrain, while its amplitude and local structure are slowly modulated on the \bar{R} -scale so as to adjust to the radial evolution of the underlying basic flow. In classical WKBJ fashion, the flow fields are expanded in powers of ϵ and written as

$$\begin{cases} \mathbf{u}(r, \theta, z, t) = \mathbf{u}(z, \phi; \bar{R}) = \mathbf{u}_0 + \epsilon \mathbf{u}_1 + \epsilon^2 \mathbf{u}_2 + \dots, \\ p(r, \theta, z, t) = p(z, \phi; \bar{R}) = p_0 + \epsilon p_1 + \epsilon^2 p_2 + \dots, \end{cases} \quad (16)$$

with 2π -periodicity in the fast phase function $\phi(r, \theta, t)$ whereas the \bar{R} -dependence accounts for the slow radial development. For regular spatially developing global solutions, the local frequency $\omega = -\partial_t \phi$ and local azimuthal modenumber $\beta = \partial_\theta \phi$ necessarily remain constant in the entire system, while the local radial wavenumber $\alpha(\bar{R}) = \partial_r \phi$ varies slowly with radial distance, leading to a fast phase function of the form

$$\phi = \left(\frac{1}{\epsilon} \int^{\bar{R}} \alpha(\bar{\rho}) d\bar{\rho} \right) + \beta\theta - \omega t. \quad (17)$$

After substitution of the global solution (16) with (17) into the Navier–Stokes equations, the local governing equations are recovered at leading order in the expansion parameter ϵ . At the local level, \bar{R} solely acts as an external control parameter, and for each value of \bar{R} the leading-order solution, among all possible waves, is the one that matches the overall frequency ω and modenumber β , as derived from the relevant dispersion relation. Note that in the previous sections, local properties were derived with the local Reynolds number R as control parameter. When carrying out the present asymptotic analysis, however, it is more appropriate to rescale this parameter as $\bar{R} = \epsilon R$ and to consider the local properties as functions of the slow \bar{R} instead.

Two different situations arise depending on the magnitude of the perturbation fields: in small-amplitude regions the wave pattern is described by the linearized equations while the fully nonlinear equations are needed in regions of finite amplitude vortex-trains.

Small-amplitude regions are governed by the *linear* dispersion relation (4). The radial wavenumber $\alpha(\bar{R})$ in the rapidly varying phase (17) is then complex, accounting for both wavelength and growth rate in the radial direction. When solving (4) for the wavenumber α with prescribed β and ω , two complex spatial branches $\alpha^{l\pm}(\bar{R}; \omega, \beta)$ are obtained. The separation of these into + and – branches is dictated according to classical causality arguments [30, 31] and determined whether they correspond to a downstream or upstream spatial response to localized harmonic forcing. The leading-order WKBJ solution (16, 17) corresponding to a branch $\alpha^l(\bar{R}; \omega, \beta)$ takes the form

$$\mathbf{u} \sim A_0(\bar{R}) \mathbf{u}^l \left(z; \alpha^l(\bar{R}; \omega, \beta), \beta; \bar{R} \right) \exp i \left(\frac{1}{\epsilon} \int^{\bar{R}} \alpha^l(\bar{\rho}; \omega, \beta) d\bar{\rho} + \beta\theta - \omega t \right), \quad (18)$$

where \mathbf{u}^l is one of the family (3) of linear eigenfunctions and $A_0(\bar{R})$ is a slowly varying amplitude determined by a solvability condition at order ϵ .

In contrast, the finite-amplitude régime is governed by the local *nonlinear* equations and the associated dispersion relation (8). Solving (8) with prescribed β and ω yields the corresponding real wavenumber branch $\alpha^{nl}(\bar{R}; \omega, \beta)$. In nonlinear regions, the global solution associated with $\alpha^{nl}(\bar{R}; \omega, \beta)$ within the family (7) of saturated crossflow vortices has the form

$$\mathbf{u} \sim \mathbf{u}^{nl} \left(z, \frac{1}{\epsilon} \int^{\bar{R}} \alpha^{nl}(\bar{\rho}; \omega, \beta) d\bar{\rho} + \beta\theta - \omega t + \Phi_0(\bar{R}); \alpha^{nl}(\bar{R}; \omega, \beta), \beta; \bar{R} \right), \quad (19)$$

where the slowly varying phase function $\Phi_0(\bar{R})$ obeys a solvability condition obtained at order ϵ .

The stability of the spatially developing finite-amplitude vortices (19) with respect to secondary perturbations is determined by the secondary local dispersion relation (11) and in particular by the maximum secondary absolute growth rate (13) along the relevant nonlinear wavenumber branch

$$\hat{\omega}_{0,i}^{\max}(\bar{R}; \omega, \beta) = \hat{\omega}_{0,i}^{\max} \left(\alpha^{nl}(\bar{R}; \omega, \beta), \beta; \bar{R} \right). \quad (20)$$

In regions where $\hat{\omega}_{0,i}^{\max}(\bar{R}; \omega, \beta) > 0$, secondary perturbations develop on top of the nonlinear WKBJ solution (19), grow at fixed radial positions and trigger transition. In contrast, while $\hat{\omega}_{0,i}^{\max}(\bar{R}; \omega, \beta) < 0$, secondary perturbations are at most convectively unstable and do not permanently affect the underlying primary wavetrain of frequency ω and modenumber β .

6 Self-sustained behaviour

As demonstrated in earlier investigations [21], spatially developing systems display a nonlinear self-sustained state whenever a region of absolute instability is present. This intrinsic state is the only non-trivial behaviour that would be observed in the absence of any external perturbations: a perfectly smooth disk and no residual perturbations in the surrounding fluid.

The naturally selected finite-amplitude solutions (so-called ‘elephant’ global modes [36]) are characterized by a stationary front located at the transition radius from local convective to absolute instability. The selection mechanism is the following: in the AU region, amplified perturbations develop and their envelope advances inwards against the radial flow. At the station of neutral absolute instability a balance between upstream perturbation growth and downstream advection is reached and perturbations pile up at that location. Nonlinearities lead to saturation of the perturbation amplitude and a stationary front is formed. This front generates a downstream propagating fully nonlinear wavetrain and an upstream exponentially decaying tail. It thus connects linear and nonlinear regions, acts as a source and effectively tunes the entire system to its own frequency. The stationary front obeys a marginal stability criterion [37], hence the global frequency of these modes equals the real absolute frequency prevailing at the front location.

In the rotating-disk flow, the absolute growth rate $\omega_{0,i}(\beta; R)$ depends on both azimuthal modenumber and radial position, and it is for $\beta^{ca} = 68$ that absolute instability first occurs: at $R^{ca} \simeq 507$ with a marginal frequency $\omega_0^{ca} \simeq 50.5$ (6). Hence the expected self-sustained behaviour (see sketch in Fig. 3a) is characterized by a front at R^{ca} of frequency ω_0^{ca} and azimuthal modenumber β^{ca} [23]. The naturally selected flow fields can then be interpreted as the spatial response to this source, which generates the inwards exponentially decaying linear wavetrain and the outwards spiralling finite-amplitude crossflow vortices. In terms of WKBJ expansions, the inner region $R < R^{ca}$ is described by linear waves of the form (18), decaying towards the disk centre and following the complex $\alpha^{l-}(R; \omega_0^{ca}, \beta^{ca})$ radial wavenumber branch. In the outer

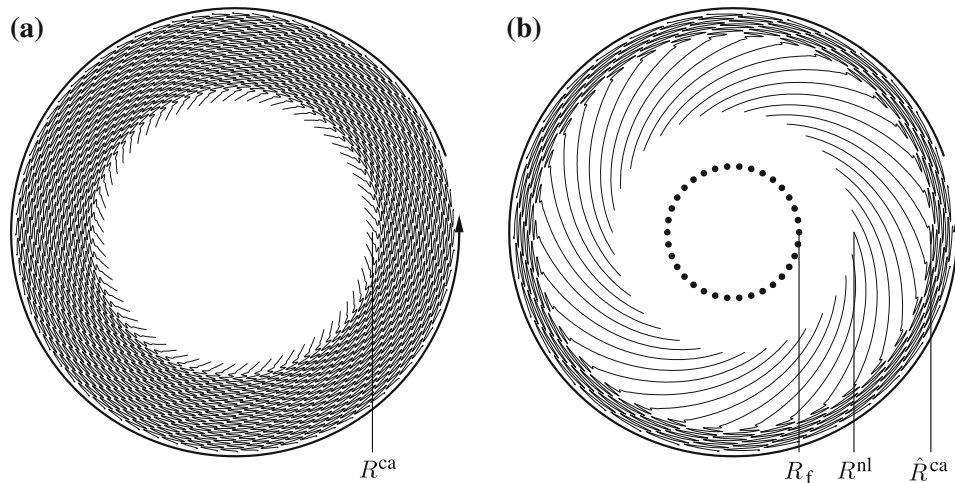


Fig. 3 (a) Self-sustained flow structure. Finite-amplitude spiral vortices are triggered at R^{ca} , by onset of primary absolute instability, and immediately give way to turbulence, caused by secondary absolute instability. (b) Externally forced flow structure. Localised harmonic forcing applied at R_f produces a radially amplified response. Finite-amplitude crossflow vortices develop beyond saturation radius R^{nl} and break down by secondary absolute instability beyond \hat{R}^{ca}

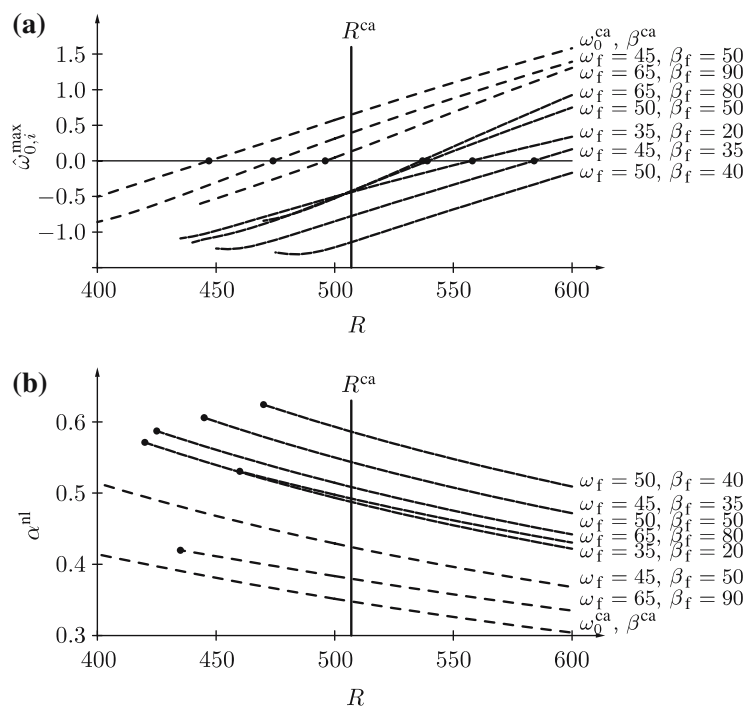


Fig. 4 (a) Maximum secondary absolute growth rate $\hat{\omega}_{0,i}^{\max}(R; \omega_f, \beta_f)$ and (b) nonlinear spatial branches $\alpha^{nl}(R; \omega_f, \beta_f)$ for different values of ω_f and β_f . The zero-crossings of $\hat{\omega}_{0,i}^{\max}$ in (a) define the corresponding $\hat{R}^{ca}(\omega_f, \beta_f)$ and are marked by dots. The α^{nl} branches in (b) terminate at low R when the marginal $R^m(\omega_f, \beta_f)$ is reached. Solid lines in (a) and (b) correspond to forcing parameters which delay onset of secondary absolute instability to beyond R^{ca}

region $R > R^{\text{ca}}$, a nonlinear wavetrain of the form (19) prevails and follows the nonlinear wavenumber branch $\alpha^{\text{nl}}(R; \omega_0^{\text{ca}}, \beta^{\text{ca}})$. Computation of $\hat{\omega}_{0,i}^{\max}(R; \omega_0^{\text{ca}}, \beta^{\text{ca}})$, the maximum secondary absolute growth rate (20) along this naturally selected nonlinear wavenumber branch (see also Fig. 4), reveals that the primary saturated waves initiated by the front at R^{ca} are already absolutely unstable with respect to secondary perturbations [23].

In view of these results, the intrinsic behaviour of the rotating-disk boundary layer (Fig. 3a) may be explained in the following way. The self-sustained finite-amplitude fluctuations are produced at the inner boundary R^{ca} of the absolutely unstable domain. This frontier for onset of primary absolute instability acts as a source and generates outwards spiralling saturated crossflow vortices, governed locally by the associated nonlinear dispersion relation. Due to secondary absolute instability, this naturally selected primary structure is dynamically unstable and immediately gives way to a disordred state.

7 Externally forced behaviour

The rotating-disk boundary layer is convectively unstable over the radial interval $R^{\text{sc}} \simeq 284 < R < R^{\text{ca}} \simeq 507$ and can thus also act as an amplifier of external perturbations, such as roughness elements on the disk surface or fluctuations in the external flow. In order to characterize the response of the boundary layer to external perturbations, this section addresses the *signalling problem*: the spatial response to radially localized harmonic forcing applied in the at most CU domain (see sketch in Fig. 3b).

Consider a radially localized forcing at R_f with frequency ω_f , azimuthal modenumber β_f and small amplitude A_f . In the vicinity of the forcing location, the magnitude of the response is of the same order as the forcing amplitude and thus governed by linear dynamics, provided that $A_f \ll 1$. Near R_f the spatial response then follows a linear WKBJ expansion of the form (18) where the complex local radial wavenumber branches $\alpha_i^{l\pm}(R; \omega_f, \beta_f)$ are obtained by solving (4) with $\omega = \omega_f$ and $\beta = \beta_f$: the α_i^{l+} -branch pertains to the outwards $R > R_f$ side of the forcing and the α_i^{l-} -branch to the inwards $R < R_f$ side.

In stable or CU regions, the upstream spatial response decays for all frequencies and modenumbers, thus $\alpha_i^{l-}(R; \omega_f, \beta_f) < 0$ for all $R < R_f$. The linear WKBJ approximation (18) which is exponentially decaying towards the disk axis with local wavenumber $\alpha_i^{l-}(R; \omega_f, \beta_f)$ then applies to the entire region upstream of the forcing location.

For forcing applied at R_f in the CU domain, there exists however a range of frequencies and modenumbers yielding downstream growth, i.e., with $\alpha_i^{l+}(R_f; \omega_f, \beta_f) < 0$. At leading order, the order of magnitude, ψ_{ext} , of the externally forced linear spatial response (18) for $R > R_f$ is

$$\psi_{\text{ext}} \sim A_f \exp \int_{R_f}^R -\alpha_i^{l+}(\rho; \omega_f, \beta_f) d\rho \quad (21)$$

and hence grows exponentially radially outwards. The nonlinear saturation station R^{nl} where the spatial response takes $\mathcal{O}(1)$ values is determined by the condition

$$\int_{R_f}^{R^{\text{nl}}} -\alpha_i^{l+}(\rho; \omega_f, \beta_f) d\rho = -\log A_f. \quad (22)$$

At R^{nl} , nonlinear saturation prevents further growth and leads to a nonlinear wavetrain, again with frequency and modenumber determined by the forcing. Beyond R^{nl} , the spatial response thus consists of a finite-amplitude saturated wavetrain of the form (19), uniquely determined by the forcing parameters ω_f and β_f , and whose local radial wavenumber follows the nonlinear branch $\alpha^{\text{nl}}(R; \omega_f, \beta_f)$.

The long-term stability of these primary nonlinear spiral vortices is dictated by $\hat{\omega}_{0,i}^{\max}(R; \omega_f, \beta_f)$, the maximum secondary absolute growth rate (20) following along the nonlinear wavenumber branch $\alpha^{\text{nl}}(R; \omega_f, \beta_f)$ (see Fig. 4). Denote by $\hat{R}^{\text{ca}}(\omega_f, \beta_f)$ the radius corresponding to transition from secondary convective to

absolute instability, i.e., defined by

$$\hat{\omega}_{0,i}^{\max}(R; \omega_f, \beta_f) = 0 \quad \text{for } R = \hat{R}^{\text{ca}}(\omega_f, \beta_f). \quad (23)$$

For $R < \hat{R}^{\text{ca}}(\omega_f, \beta_f)$, a secondary perturbation is at most convectively unstable ($\hat{\omega}_{0,i}^{\max}(R; \omega_f, \beta_f) < 0$) and thus does not succeed in permanently affecting the primary crossflow vortices. For $R > \hat{R}^{\text{ca}}(\omega_f, \beta_f)$, however, the AU finite-amplitude crossflow vortices ($\hat{\omega}_{0,i}^{\max}(R; \omega_f, \beta_f) > 0$) give way to a disordered state.

It should be noted that, for given ω_f and β_f , the saturation location R^{nl} depends on both forcing amplitude A_f and radius R_f , whereas the nonlinear wavetrain (19) prevailing beyond R^{nl} does not. Thus, the radius $\hat{R}^{\text{ca}}(\omega_f, \beta_f)$ for onset of secondary absolute instability is uniquely determined by the forcing parameters ω_f and β_f , while that, R^{nl} , for primary nonlinearity further depends on the parameters A_f and R_f .

The character of the forced spatial response depends on the relative positions of \hat{R}^{ca} and R^{nl} . In situations where $R^{\text{nl}} < \hat{R}^{\text{ca}}$ (sketched in Fig. 3b), the linear spatial response (18) grows from R_f to R^{nl} , followed by nonlinear periodic crossflow vortices (19) in the domain $R^{\text{nl}} < R < \hat{R}^{\text{ca}}$. Secondary absolute instability occurs at \hat{R}^{ca} , leading to a disordered state in $R > \hat{R}^{\text{ca}}$. An increase/decrease of the forcing amplitude A_f results in earlier/later onset of nonlinearity (R^{nl}) but does not modify the secondary stability properties nor transition at $\hat{R}^{\text{ca}}(\omega_f, \beta_f)$.

With very low forcing amplitudes, onset of nonlinearity may be delayed beyond \hat{R}^{ca} , i.e., $R^{\text{nl}} > \hat{R}^{\text{ca}}$. Near R^{nl} , nonlinear saturation then leads to a wavetrain which is already AU with respect to secondary perturbations ($\hat{\omega}_{0,i}^{\max}(R^{\text{nl}}; \omega_f, \beta_f) > 0$). Thus the nonlinear periodic régime (19) is bypassed and a disordered state covers the entire region beyond R^{nl} . Since the transition radius then directly depends on R^{nl} , an increase/decrease of the forcing amplitude A_f then brings about earlier/later transition. Due to the exponential growth of the response, a situation where $R^{\text{nl}} > \hat{R}^{\text{ca}}$ generally occurs, however, only for extremely small forcing amplitudes.

8 Open-loop control

The above results show that the rotating-disk boundary layer displays all the features required for successful implementation of the open-loop control method previously developed for a one-dimensional model problem [28]. In this strategy, localized periodic forcing is applied in the cu region so as to replace the naturally selected nonlinear global structure by the spatial response to external forcing. The aim is not to suppress the primary vortices but to tune them to an externally imposed frequency and modenumber and thereby delay onset of secondary absolute instability and transition.

Assuming that the boundary layer displays the self-sustained behaviour described in Sect. 6, the AU domain $R > R^{\text{ca}} \simeq 507$ is covered by finite-amplitude fluctuations initiated at R^{ca} , while a linear WKBJ approximation (18) of frequency ω_0^{ca} and modenumber β^{ca} describes the inner range $R < R^{\text{ca}}$. The resulting linear wavetrain decays exponentially towards the disk centre and, to leading order, the order of magnitude, ψ_{int} , of its amplitude varies with radial distance R as

$$\log \psi_{\text{int}} \sim \int_R^{R^{\text{ca}}} \alpha_i^{l-}(\rho; \omega_0^{\text{ca}}, \beta^{\text{ca}}) d\rho. \quad (24)$$

Suppose that a radially localised external forcing of frequency ω_f and modenumber β_f is applied to the above flow structure at R_f in the cu region, i.e., $R^{\text{sc}} < R_f < R^{\text{ca}}$. For small forcing amplitude A_f , the order of magnitude (21) of the linear spatial response for $R > R_f$ is given by

$$\log \psi_{\text{ext}} \sim a_f - \int_{R_f}^R \alpha_i^{l+}(\rho; \omega_f, \beta_f) d\rho, \quad (25)$$

where $a_f = \log A_f$. In the neighbourhood of R_f , both the spatial response and the self-sustained global mode are governed by linear dynamics and the resulting flow is a superposition of both fields. This linear

régime prevails through the region extending from R_f outwards until either ψ_{ext} or ψ_{int} reaches finite levels. Nonlinearity of the self-sustained field appears at R^{ca} , whereas the forced response achieves $\mathcal{O}(1)$ amplitude at the saturation radius R^{nl} , defined by (22) and which depends on the forcing parameters. The nature of the nonlinear dynamics taking over from the linear régime thus crucially depends on the relative positions of R^{ca} and R^{nl} .

For given ω_f , β_f and R_f , there exists a critical forcing amplitude $A_c \equiv e^{a_c}$, defined by

$$a_c = \int_{R_f}^{R^{\text{ca}}} \alpha_i^{l+}(\rho; \omega_f, \beta_f) d\rho, \quad (26)$$

for which the nonlinear saturation radius R^{nl} of the externally forced response coincides with the onset radius R^{ca} of intrinsic nonlinearities. For stronger forcing levels $A_f > A_c$ (resp. weaker levels $A_f < A_c$), the saturation radius moves upstream $R^{\text{nl}} < R^{\text{ca}}$ (resp. downstream $R^{\text{nl}} > R^{\text{ca}}$).

The open-loop control strategy [28] to be applied here for the rotating-disk boundary layer is based on the following results. For weak forcing levels $A_f < A_c$, the spatial response does not achieve $\mathcal{O}(1)$ amplitudes at radius R^{ca} and is thus unable to perturb the nonlinear self-sustained state selected by the front at R^{ca} and triggering finite-amplitude fluctuations for $R > R^{\text{ca}}$. However, for higher forcing levels $A_f > A_c$, the spatial response reaches nonlinear saturation upstream of the front, i.e., $R^{\text{nl}} < R^{\text{ca}}$, and *the naturally selected behaviour is then suppressed and replaced by the forced spatial response throughout the flow*.

This behaviour may be interpreted as the result of two competing sources of different periodicities at different locations: the self-sustained $(\omega_0^{\text{ca}}, \beta^{\text{ca}})$ -front at R^{ca} (responsible for the intrinsic nonlinear structure) and the external (ω_f, β_f) -forcing at R_f . In the absence of external forcing, the front at R^{ca} acts as a keystone upon which the global structure is based. When forcing is applied at R_f , the intrinsic wavemaker at R^{ca} survives only if its upstream decaying tail experiences an unperturbed medium. As soon as the front is overwhelmed by incoming finite-amplitude perturbations, the source of the global mode is suppressed and hence so is the entire self-sustained structure. The underlying (primary) AU region then plays no rôle in the dynamics, since it is effectively masked by an externally imposed nonlinear wavetrain.

Without external input, the boundary layer displays transition to turbulence near $R^{\text{ca}} \simeq 507$ (Fig. 3a). With open-loop control by external forcing of periodicity ω_f and β_f , transition occurs instead near $\hat{R}^{\text{ca}}(\omega_f, \beta_f)$, where the externally forced nonlinear crossflow vortices become AU with respect to secondary perturbations (Fig. 3b). The goal of delaying transition can then be achieved if the two conditions

$$R^{\text{nl}} < R^{\text{ca}} \quad \text{and} \quad \hat{R}^{\text{ca}} > R^{\text{ca}} \quad (27)$$

are both fulfilled. Identification of efficient control parameters thus requires a systematic investigation of primary and secondary instability characteristics.

The condition $R^{\text{nl}} < R^{\text{ca}}$ is necessary for control of the primary wavetrain to be effective: the forced spatial response needs to reach nonlinear levels and to saturate upstream of R^{ca} in order to supersede the self-selected dynamics. The second condition, $\hat{R}^{\text{ca}} > R^{\text{ca}}$, then guarantees that onset of secondary absolute instability, and thus of transition, is postponed to beyond R^{ca} . Thus the forcing parameters ω_f and β_f must be chosen so that, near R^{ca} , the resulting nonlinear crossflow vortices have negative secondary absolute growth rate.

Suitable control parameters may be derived from Fig. 2(a) which shows the (α, β) -plane for $R = 500$, slightly upstream of R^{ca} . Saturated travelling waves exist to the left of the marginal boundary $\Omega_i^l(\alpha, \beta) = 0$ (thick solid curve) and their nonlinear frequencies $\Omega^{\text{nl}}(\alpha, \beta)$ are indicated by dashed curves. Among these nonlinear waves, those associated with secondary absolute instability ($\hat{\omega}_{0,i}^{\max} \geq 0$, indicated by thin solid isocontours) must be avoided. As a result, the two control conditions (27) may be met for frequencies ω_f and modenumbers β_f associated with nonlinear vortices located between the curves $\Omega_i^l = 0$ and $\hat{\omega}_{0,i}^{\max} = 0$. In Fig. 2(a), selected forcing parameters are indicated by symbols: transition can be delayed for $(\omega_f, \beta_f) = (65, 80), (50, 50), (50, 40), (45, 35)$ or $(35, 20)$ (triangles), but not for $(\omega_f, \beta_f) = (65, 90), (45, 50)$ (diamonds), nor of course for the self-sustained $(\omega_0^{\text{ca}}, \beta^{\text{ca}})$ (thick dot).

With external forcing, the new transition radius $\hat{R}^{\text{ca}}(\omega_f, \beta_f)$ is determined by the zero crossing of the maximum secondary absolute growth rate $\hat{\omega}_{0,i}^{\max}(R; \omega_f, \beta_f)$. Figure 4(a) shows the radial evolution of $\hat{\omega}_{0,i}^{\max}$ for different values of ω_f and β_f ; the associated nonlinear wavenumber branches $\alpha^{\text{nl}}(R; \omega_f, \beta_f)$ are given in Fig. 4(b). The values of $\hat{\omega}_{0,i}^{\max}$ for $R = 500$ and $R = 550$, corresponding to the forcing parameters used in Fig. 4, are shown by symbols in Fig. 2(a) and (b) respectively.

It is seen that the naturally selected vortices, for ω_0^{ca} and β^{ca} (corresponding to the solid dot in Fig. 2), are among the most unstable primary nonlinear waves. The associated $\hat{\omega}_{0,i}^{\max}$ and α^{nl} curves are given in Fig. 4 for $400 < R < 600$, but note that the values for $R < R^{\text{ca}}$ are irrelevant to the self-sustained global mode, since it has finite amplitude only for $R > R^{\text{ca}}$.

When the intrinsic dynamics at $(\omega_0^{\text{ca}}, \beta^{\text{ca}})$ is replaced by nonlinear waves with $(\omega_f, \beta_f) = (65, 90)$ or $(45, 50)$ (diamonds in Fig. 2), secondary instability is reduced and the $\hat{\omega}_{0,i}^{\max}$ curves in Fig. 4(a) are lowered. For these forcing parameters, however, the radius R^{ca} remains within the secondarily AU region $\hat{\omega}_{0,i}^{\max} > 0$. In consequence, rather than reducing the size of the turbulent domain, external harmonic forcing actually promotes earlier transition because the secondary perturbations propagate inwards below R^{ca} down to the corresponding marginal radius $\hat{R}^{\text{ca}}(\omega_f, \beta_f) < R^{\text{ca}}$ (indicated by small dots in Fig. 4a).

External forcing of nonlinear waves between the marginal $\Omega_i^l = 0$ and $\hat{\omega}_{0,i}^{\max} = 0$ curves in Fig. 2(a) sufficiently weakens secondary instability that the critical radius \hat{R}^{ca} for onset of secondary absolute growth is located beyond R^{ca} , fulfilling the second condition (27). Values corresponding to $(\omega_f, \beta_f) = (65, 80)$, $(50, 50)$, $(50, 40)$, $(45, 35)$ and $(35, 20)$ are indicated by triangles in Fig. 2, and the corresponding $\hat{\omega}_{0,i}^{\max}$ and α^{nl} branches are represented by solid lines in Fig. 4. With $\omega_f = 50$ and $\beta_f = 40$ (lowest curve in Fig. 4a), onset of secondary absolute instability is postponed to beyond $\hat{R}^{\text{ca}} > 600$. Hence it is possible to delay the turbulent régime by approximately 100 boundary layer units from R^{ca} to \hat{R}^{ca} .

Due to the condition $R^{\text{nl}} < R^{\text{ca}}$, it seems unlikely that forcing parameters exist that would delay transition much further. Indeed, the nonlinear solution branches are governed by the local nonlinear dispersion relation (8) and terminate at low R when the marginal radius associated with ω_f and β_f , denoted as $R^m(\omega_f, \beta_f)$ and indicated by dots in Fig. 4(b), is reached. Thus for given ω_f and β_f , saturation of the spatial response may only occur for $R^{\text{nl}} > R^m(\omega_f, \beta_f)$, and the range of possible control parameters is therefore limited by the condition

$$R^m(\omega_f, \beta_f) < R^{\text{ca}}. \quad (28)$$

As can be seen from Fig. 4, settings of ω_f and β_f that yield high values of $\hat{R}^{\text{ca}}(\omega_f, \beta_f)$ also push $R^m(\omega_f, \beta_f)$ outwards.

The spatial response at ω_f and β_f is radially exponentially amplified over the interval $R^m(\omega_f, \beta_f) < R < R^{\text{ca}}$, and the largest amplification is obtained when forcing is applied at $R_f = R^m(\omega_f, \beta_f)$. Due to the exponential growth of the forced response, only small forcing amplitudes (26) are generally necessary to reach a nonlinear state at $R^{\text{nl}} < R^{\text{ca}}$. However, when R^m is too close to R^{ca} , the radial amplification of the spatial response is only moderate and more substantial forcing amplitudes are required.

As a result, the values of $\omega_f = 50$ and $\beta_f = 40$ are deemed to be very close to the optimal forcing parameters for delaying transition by the present open-loop control method.

9 Discussion

For the three-dimensional boundary layer produced by a rotating disk, the scenario leading from the unperturbed boundary layer to the turbulent state takes place in two steps and involves both primary and secondary instabilities: primary nonlinear waves are the prerequisite for a possible development of secondary absolute instability leading to transition. Since the secondary disturbances feed on the primary vortices, the turbulent régime prevailing at large radial distances may propagate inwards until either the

nonlinear waves cease to exist ($R = R^{\text{nl}}$) or until their secondary absolute growth rate changes sign ($R = \hat{R}^{\text{ca}}$).

The intrinsic dynamics, observed without external perturbations, display a sudden transition from basic to turbulent states, where primary and secondary instabilities simultaneously take place. At the radius $R^{\text{ca}} \simeq 507$ of transition from primary linear convective to absolute instability, a stationary front of frequency $\omega_0^{\text{ca}} \simeq 50.5$ and azimuthal modenumber $\beta^{\text{ca}} = 68$ generates outward spiralling nonlinear crossflow vortices. These finite-amplitude waves are already AU with respect to secondary perturbations. Hence a disordered state covers the whole region $R > R^{\text{ca}}$, while the unperturbed boundary layer prevails for $R < R^{\text{ca}}$. In this situation, the transition location is dictated by onset of primary nonlinear waves, which in turn corresponds to onset of primary absolute instability ($R^{\text{nl}} = R^{\text{ca}}$).

When harmonic forcing is applied at R_f in the CU region with frequency ω_f and modenumber β_f in the unstable range, the linear response exponentially grows with radial distance and reaches finite-amplitude at radius $R^{\text{nl}} > R_f$. The associated nonlinear vortices display secondary absolute instability for $R > \hat{R}^{\text{ca}}$. When forcing parameters are chosen so that $R^{\text{nl}} < \hat{R}^{\text{ca}}$, the spatial response displays three successive régimes downstream of R_f : linear growth over $R_f < R < R^{\text{nl}}$, nonlinear crossflow vortices over $R^{\text{nl}} < R < \hat{R}^{\text{ca}}$ and a turbulent state for $R > \hat{R}^{\text{ca}}$. In this situation, transition is due to onset of secondary absolute instability at \hat{R}^{ca} , and this radius is uniquely determined by ω_f and β_f .

The aim of the open-loop control strategy is to delay onset of secondary AU perturbations, and thus transition, from R^{ca} to larger radii by a controlled modification of the primary nonlinear state. This technique consists in replacing the naturally selected flow state by the spatial response to carefully chosen harmonic forcing. Transition is effectively postponed for control parameters such that $R^{\text{nl}} < R^{\text{ca}} < \hat{R}^{\text{ca}}$: by enhancing primary instability, onset of secondary instability may be delayed. Thus, the natural dynamics, where primary and secondary instabilities occur simultaneously at R^{ca} , is replaced by an externally forced flow structure whose primary nonlinearities appear earlier (at $R^{\text{nl}} < R^{\text{ca}}$) but whose secondary perturbations develop only later (at $\hat{R}^{\text{ca}} > R^{\text{ca}}$). In other words, the linear (ω_f, β_f) -waves must be sufficiently unstable to reach nonlinear saturation before R^{ca} and at the same time not too unstable so that the resulting finite-amplitude waves display secondary absolute instability only after R^{ca} . Best control (large \hat{R}^{ca}) is thus obtained by applying weakly unstable forcing: transition may be delayed by approximately 100 boundary layer units beyond R^{ca} when using $\omega_f = 50$ and $\beta_f = 40$. However, optimizing for large \hat{R}^{ca} requires a very precise tuning of the forcing parameters and is expected to be difficult to implement experimentally.

References

1. von Kármán T (1921) Über laminare und turbulente Reibung. Z Angew Math Mech 1:232–252
2. Reed HL, Saric WS (1989) Stability of three-dimensional boundary layers. Ann Rev Fluid Mech 21:235–284
3. Saric WS, Reed HL, White EB (2003) Stability and transition of three-dimensional boundary layers. Annu Rev Fluid Mech 35:413–440
4. Schmid PJ, Henningson DS (2001) Stability and transition in shear flows, Applied Mathematical Sciences. Springer, New York
5. Gregory N, Stuart JT, Walker WS (1955) On the stability of three-dimensional boundary layers with application to the flow due to a rotating disk. Phil Trans R Soc Lond, A 248:155–199
6. Huerre P (2000) Open shear flow instabilities. In: Batchelor GK, Moffatt HK, Worster MG (eds) Perspectives in fluid dynamics. Cambridge University Press, Cambridge, pp 159–229
7. Huerre P, Monkewitz PA (1990) Local and global instabilities in spatially developing flows. Ann Rev Fluid Mech 22:473–537
8. Lingwood RJ (1995) Absolute instability of the boundary layer on a rotating disk. J Fluid Mech 299:17–33
9. Lingwood RJ (1996) An experimental study of absolute instability of the rotating-disk boundary-layer flow. J Fluid Mech 314:373–405
10. Chomaz J-M, Huerre P, Redekopp LG (1991) A frequency selection criterion in spatially developing flows. Stud Appl Math 84:119–144
11. Monkewitz PA, Huerre P, Chomaz J-M (1993) Global linear stability analysis of weakly non-parallel shear flows. J Fluid Mech 251:1–20

12. Davies C, Carpenter PW (2003) Global behaviour corresponding to the absolute instability of the rotating-disk boundary layer. *J Fluid Mech* 486:287–329
13. Davies C, Thomas C, Carpenter PW (2007) Global stability of the rotating-disc boundary layer. *J Eng Math*, doi: 10.1007/s10665-006-9112-8 (this issue)
14. Garrett SJ (2002) The stability and transition of the boundary layer on rotating bodies. Ph.D. thesis, University of Cambridge, Cambridge.
15. Othman H, Corke T (2006) Experimental investigation of absolute instability of a rotating-disk boundary layer. *J Fluid Mech* 565: 63–94
16. Couairon A, Chomaz J-M (1996) Global instabilities in fully nonlinear systems. *Phys Rev Lett* 77:4015–4018
17. Couairon A, Chomaz J-M (1997) Absolute and convective instabilities, front velocities and global modes in nonlinear systems. *Physica D* 108:236–276
18. Couairon A, Chomaz J-M (1999) Fully nonlinear global modes in slowly varying flows. *Phys Fluids* 11:3688–3703
19. Pier B, Huerre P (1996) Fully nonlinear global modes in spatially developing media. *Physica D* 97:206–222
20. Pier B, Huerre P (2001) Nonlinear self-sustained structures and fronts in spatially developing wake flows. *J Fluid Mech* 435:145–174
21. Pier B, Huerre P, Chomaz J-M (2001) Bifurcation to fully nonlinear synchronized structures in slowly varying media. *Physica D* 148:49–96
22. Pier B, Huerre P, Chomaz J-M, Couairon A (1998) Steep nonlinear global modes in spatially developing media. *Phys Fluids* 10:2433–2435
23. Pier B (2003) Finite-amplitude crossflow vortices, secondary instability and transition in the rotating-disk boundary layer. *J Fluid Mech* 487:315–343
24. Wilkinson SP, Malik MR (1985) Stability experiments in the flow over a rotating disk. *AIAA J.* 23:588–595
25. Jarre S, Le Gal P, Chauve MP (1996) Experimental study of rotating disk flow instability. II. Forced flow. *Phys Fluids* 8:2985–2994
26. Kohama Y (1984) Study on boundary layer transition of a rotating disk. *Acta Mechanica* 50:193–199
27. Pier B (2002) Fully nonlinear waves and transition in the boundary layer over a rotating disk. In: Castro IP, Hancock PE (eds) *Advances in Turbulence IX*, Proceedings of the 9th European turbulence conference. Barcelona, pp 13–16
28. Pier B (2003) Open-loop control of absolutely unstable domains. *Proc R Soc Lond, A* 459:1105–1115
29. Pier B (2004) Open-loop control and delay of transition in the rotating-disk boundary layer. In: Andersson HI, Krogstad P-A (eds) *Advances in Turbulence X*, Proceedings of the 10th European turbulence conference. Barcelona, pp 775–778
30. Briggs RJ (1964) Electron-stream interaction with plasmas. M.I.T. Press, Cambridge, Mass
31. Bers A (1983) Space-time evolution of plasma instabilities—absolute and convective. In: Rosenbluth M, Sagdeev R (eds) *Handbook of plasma physics*. North-Holland, Amsterdam pp 451–517
32. Lingwood RJ (1997) Absolute instability of the Ekman layer and related rotating flows. *J Fluid Mech* 331:405–428
33. Herbert T (1988) Secondary instability of boundary layers. *Ann Rev Fluid Mech* 20:487–526
34. Brevdo L, Bridges TJ (1996) Absolute and convective instabilities of spatially periodic flows. *Phil Trans R Soc Lond, A* 354:1027–1064
35. Bender CM, Orszag SA (1978) Advanced mathematical methods for scientists and engineers. McGraw-Hill, New York
36. Pier B, Huerre P (2001) Nonlinear synchronization in open flows. *J Fluids Struct* 15:471–480
37. Dee G, Langer JS (1983) Propagating pattern selection. *Phys Rev Lett* 50:383–386

[A11]

Local and global instabilities in the wake of a sphere

B. Pier

Journal of Fluid Mechanics **603**, 39–61 (2008)

doi:10.1017/S0022112008000736

<https://hal.archives-ouvertes.fr/hal-00206267>

Local and global instabilities in the wake of a sphere

BENOÎT PIER

Laboratoire de mécanique des fluides et d'acoustique,
École centrale de Lyon, CNRS, Université Claude-Bernard Lyon 1, INSA Lyon,
36 avenue Guy-de-Collongue, 69134 Écully cedex, France

(Received 27 July 2007 and in revised form 16 January 2008)

The global dynamics of open shear flows is closely related to the nature of their local instability characteristics, either convective or absolute. The present investigation revisits the wake of a sphere, obtains its global behaviour by direct numerical simulations and derives its local stability features, computed for the underlying basic flow under a quasi-parallel flow assumption. It is shown that both the axisymmetric and the planar symmetric basic flows exhibit domains of local absolute instability in the near-wake region. The largest absolute growth rates occur for instabilities developing on the non-axisymmetric basic wake and conserving its planar symmetry.

1. Introduction

The global dynamics of shear flows is known to closely depend on the local instability characteristics, either convective or absolute (Huerre 2000). Convectively unstable systems are sensitive to inflow perturbations and they behave as amplifiers of external noise. In contrast, absolutely unstable systems display non-trivial dynamics without external input, often leading to self-sustained oscillations. Thus, onset of absolute instability is generally associated with drastic changes in the naturally selected global flow features. With this in mind, the present investigation has been undertaken to work out the detailed instability properties prevailing in the wake of a sphere. By analysing the wake structure and its local stability characteristics, it is attempted to establish a link between the naturally selected *global* flow and the dynamics prevailing *locally*. A similar line of thought has already been successfully implemented for the two-dimensional wake of a cylinder (Pier 2002). This approach is here generalized to the fully three-dimensional flow around a solid sphere.

At moderate Reynolds numbers, the global dynamics of the wake flow around a sphere is now fairly well established, both experimentally and numerically (Roos & Willmarth 1971; Nakamura 1976; Sakamoto & Haniu 1995; Johnson & Patel 1999; Mittal 1999; Ghidersa & Dućek 2000; Tomboulides & Orszag 2000; Schouveiler & Provansal 2002; Bouchet, Mebarek & Dućek 2006). The steady axisymmetric wake is stable for $Re < Re_1 \simeq 212$ and a steady non-axisymmetric flow is observed for $Re_1 < Re < Re_2 \simeq 272$. This non-axisymmetric wake displays a symmetry plane and is characterized by two vortex threads aligned with the outer flow. At Re_2 , a Hopf bifurcation leads to periodic vortex shedding. The resulting time-harmonic regime conserves the planar symmetry and the associated Strouhal frequency is in the range

$0.12 < St < 0.18$. At even larger Reynolds numbers, the planar symmetry is lost (Mittal 1999) and further bifurcations lead to a more complex behaviour.

Monkewitz (1988b) investigated the linear stability of an analytic two-parameter family of model axisymmetric, locally parallel and incompressible wake profiles. In that study, the first helical mode was found to display the largest growth rates and to be the only one to become absolutely unstable for velocity profiles approximating those found in the near wake.

Natarajan & Acrivos (1993) computed the axisymmetric basic flow past a sphere and examined its global linear instability to three-dimensional modal perturbations. The first instability was found at $Re \simeq 210$, associated with a vanishing frequency (regular bifurcation). At $Re \simeq 277.5$, a second mode was found to become unstable via a Hopf bifurcation. While these authors only investigated the stability of the axisymmetric wake, this second critical Reynolds number is remarkably close to $Re_2 \simeq 272$, corresponding to the transition from a steady non-axisymmetric wake to periodic vortex shedding.

More recently, the role of local absolute instability in self-sustained oscillations developing in three-dimensional axisymmetric flows has been analysed by Sevilla & Martínez-Bazán (2004) for the wake of a bullet-shaped body, by Gallaire *et al.* (2006) for spiral vortex breakdown, and by Lesshafft *et al.* (2006) and Nichols, Schmid & Riley (2007) for variable-density round jets. These studies have all confirmed the importance of local absolute instability in triggering large-scale global oscillations of these spatially developing flows.

The present investigation has been undertaken in the same spirit and revisits the wake of a sphere in order to establish its complete local absolute instability characteristics. Unlike the above studies, however, not only axisymmetric but also planar symmetric basic wake flows are considered here. Indeed, at Re_2 , onset of vortex shedding occurs via a bifurcation from a planar symmetric basic flow, which therefore requires stability analyses of these non-axisymmetric velocity profiles.

The paper is organized as follows. The governing equations and numerical solution methods for the flow around a sphere are presented in §2. The results obtained by direct numerical simulations are given in §3. This section serves two purposes: first, to validate the numerical code by accurately reproducing the different known flow regimes; second, to obtain the exact time-independent solutions of the Navier–Stokes equations that are used as basic flows for the subsequent stability analyses. In §4, the local linear stability analyses are carried out for both the axisymmetric and the non-axisymmetric basic flows. Here the local dispersion relations are derived, absolute frequencies are computed and the existence of absolutely unstable domains is established.

2. Governing equations and numerical solution methods

The following study is carried out for incompressible flows governed by the Navier–Stokes equations. The Reynolds number is defined as $Re = U_\infty D/\nu$, where U_∞ represents the free-stream velocity, D the sphere diameter and ν the kinematic viscosity.

Throughout this investigation, cylindrical coordinates are used with r , θ and z (u , v and w) denoting radial, azimuthal and axial coordinates (velocities) respectively. The z -axis is aligned with the free-stream velocity and has its origin at the center of the sphere. For future use, a Cartesian (x, y, z) -frame is also introduced where the x - and y -axes coincide with the directions defined by $\theta = 0$ and $\theta = \pi/2$ respectively.

Using non-dimensional variables based on U_∞ , D and ν , and denoting the total velocity and pressure fields by $\mathbf{u}(r, \theta, z, t)$ and $p(r, \theta, z, t)$ respectively, the governing momentum and continuity equations may be written as

$$\partial_r \mathbf{u} + (\mathbf{u} \cdot \nabla) \mathbf{u} + \nabla p = \frac{1}{Re} \Delta \mathbf{u} + \mathbf{f}, \quad (2.1a)$$

$$\nabla \cdot \mathbf{u} = 0, \quad (2.1b)$$

where the different terms are defined in cylindrical coordinates as

$$\begin{aligned} \mathbf{u} &\equiv \begin{pmatrix} u \\ v \\ w \end{pmatrix}, \quad \nabla p \equiv \begin{pmatrix} \partial_r p \\ (\partial_\theta p)/r \\ \partial_z p \end{pmatrix}, \\ (\mathbf{u} \cdot \nabla) \mathbf{u} &\equiv \left(u \frac{\partial}{\partial r} + \frac{1}{r} v \frac{\partial}{\partial \theta} + w \frac{\partial}{\partial z} \right) \mathbf{u} + \frac{1}{r} \begin{pmatrix} -v^2 \\ uv \\ 0 \end{pmatrix}, \\ \Delta \mathbf{u} &\equiv \left(\frac{\partial^2}{\partial r^2} + \frac{1}{r^2} \frac{\partial^2}{\partial \theta^2} + \frac{\partial^2}{\partial z^2} \right) \mathbf{u} + \frac{1}{r} \frac{\partial \mathbf{u}}{\partial r} + \frac{1}{r^2} \begin{pmatrix} -u - 2\partial_\theta v \\ -v + 2\partial_\theta u \\ 0 \end{pmatrix}, \\ \nabla \cdot \mathbf{u} &\equiv \frac{\partial u}{\partial r} + \frac{1}{r} u + \frac{1}{r} \frac{\partial v}{\partial \theta} + \frac{\partial w}{\partial z}, \end{aligned}$$

and $\mathbf{f}(r, \theta, z, t)$ is an externally applied volume force to be specified below. The boundary conditions are vanishing velocity fields on the sphere surface and free-stream conditions in the far field:

$$\mathbf{u} = 0 \quad \text{for} \quad r^2 + z^2 = 1/4, \quad (2.2a)$$

$$u = v = w = p = 0 \quad \text{for} \quad r \rightarrow \infty \quad \text{or} \quad z \rightarrow \pm\infty. \quad (2.2b)$$

2.1. Immersed boundary method

For the purpose of fast numerical integration, the above equations are discretized on a Cartesian grid in the (r, z) -plane, and the spherical obstacle is treated by an *immersed boundary* method (for a review of this technique see Mittal & Iaccarino (2005)). Thus the entire space is assumed to be filled with fluid, and a body force \mathbf{f}_b is applied inside the region covered by the sphere ($r^2 + z^2 \leq 1/4$) so that the fluid is brought to rest there and condition (2.2a) is satisfied. In the present investigation, several implementations for the force \mathbf{f}_b have been tested to drive the components of the velocity fields to negligible values. Best results have been obtained when the effect of the sphere is modelled via a visco-elastic restoring force

$$\mathbf{f}_b = - \left(\frac{1}{\tau_v} \mathbf{u} + \frac{1}{\tau_e^2} \int_0^t \mathbf{u}(\tau) d\tau \right) \phi \left(\sqrt{r^2 + z^2} \right), \quad (2.3)$$

with $\tau_v = 0.01$ and $\tau_e = 1$; the shape function is defined as

$$\phi(\rho) \equiv \frac{1}{2} \left(1 + \tanh \frac{0.5 - \rho}{\delta} \right)$$

with $\delta = 0.001$.

By implementing this method, there is no need for body-fitted coordinates or explicit boundary conditions on the obstacle surface, thus enabling fast computations

on a Cartesian (r, z) -grid. Another advantage is that the hydrodynamic drag and lift forces acting on the sphere (see §3.4) are directly obtained by spatial integration of the volume force \mathbf{f}_b and there is no need to evaluate components of the stress tensor near the surface.

2.2. Spatial discretization

All flow quantities are expanded as Fourier modes in the azimuthal direction (indexed by the integer β)

$$\mathbf{u}(r, \theta, z, t) = \sum_{\beta} \mathbf{u}_{\beta}(r, z, t) e^{i\beta\theta} \quad \text{and} \quad p(r, \theta, z, t) = \sum_{\beta} p_{\beta}(r, z, t) e^{i\beta\theta}, \quad (2.4)$$

their complex components satisfying the conditions $u_{-\beta} = u_{\beta}^*$, $v_{-\beta} = v_{\beta}^*$, $w_{-\beta} = w_{\beta}^*$ and $p_{-\beta} = p_{\beta}^*$, where \star denotes complex conjugation. However, when considering flow fields which exhibit a symmetry plane containing the z -axis, the numerical effort may be reduced: if the flow is symmetric about the (x, z) -plane, i.e. about the $(\theta = 0)$ -plane, it is invariant under the planar symmetry operator Π mathematically defined as

$$\Pi : \begin{pmatrix} u(r, \theta, z, t) \\ v(r, \theta, z, t) \\ w(r, \theta, z, t) \\ p(r, \theta, z, t) \end{pmatrix} \mapsto \begin{pmatrix} u(r, -\theta, z, t) \\ -v(r, -\theta, z, t) \\ w(r, -\theta, z, t) \\ p(r, -\theta, z, t) \end{pmatrix}, \quad (2.5)$$

and the components u_{β} , w_{β} and p_{β} are then real while v_{β} is purely imaginary (and $v_0 = 0$). In the numerical implementation, the expansions (2.4) are truncated at a finite number of harmonics $|\beta| \leq N_h$. For the moderate Reynolds numbers of interest here, it has been found that only a small number of modes ($N_h = 3$ or 4) are required to accurately capture all the flow features, a fact already noticed by Ghidelsa & Duček (2000). Note that analyses of the axisymmetric wake features are simply carried out by setting $N_h = 0$.

The discretization of the (r, z) -plane on a Cartesian grid combines finite differences in the z -direction with Chebyshev collocation points in the r -direction (Canuto, Hussaini & Quarteroni 1988; Boyd 2001).

An axial mesh of $n_z = n_u + n_o + n_d$ points is constructed with n_o equispaced grid points separated by δ_z and clustered around $z = 0$, and n_u (n_d) elements in the upstream (downstream) regions uniformly stretched according to a stretching factor of κ_u (κ_d). All the results shown in this paper have been obtained with $n_u = 142$, $n_o = 101$, $n_d = 335$, $\delta_z = 0.01$, $\kappa_u = \kappa_d = 1.02$. The total streamwise extent of the domain is then $-8.5 < z < 387$.

The radial discretization of the r -axis on n_r collocation points is obtained by mapping the Chebyshev points $-1 \leq \xi_i \equiv -\cos[i\pi/(n_r+1)] \leq +1$ for $i = 0, \dots, n_r+1$ onto the entire radial axis $-\infty \leq r_i \leq +\infty$ through the algebraic transformation $r\sqrt{2}/\ell_r = \xi/(1 - \xi^2)$. The parameter ℓ_r governs the distribution of collocation points over the r -axis: half of the points are located in the interval $-\ell_r < r < \ell_r$. Using the vanishing boundary conditions (2.2b) at $r = \pm\infty$, the computation may be restricted to the interior collocation points associated with $1 \leq i \leq n_r$. Moreover, taking advantage of radial parity properties of the Fourier components (2.4), only positive r -values need to be taken into account: the components $u_{\beta+1}$, $v_{\beta+1}$, w_{β} and p_{β} are symmetric (antisymmetric) in r for β even (odd). The use of the appropriate (anti)symmetric operators when computing radial derivatives then also resolves the apparent singularity at $r = 0$, due to the formulation of the governing equations in

polar coordinates (Boyd 2001). Throughout, $\ell_r = 1$ has been used. Different resolution tests have shown that reasonable but approximate results are obtained with $n_r = 80$, and that a high accuracy is achieved for $n_r \geq 160$.

2.3. Time-marching algorithm

The integration in time of the incompressible Navier–Stokes equations (2.1) is carried out by a second-order-accurate predictor–corrector fractional-step method (Goda 1979; Raspo *et al.* 2002). At the intermediate time-step, the velocity components are obtained by solving Helmholtz-type problems. A Poisson problem then yields a correction to the pressure required to enforce divergence-free velocity fields. A Crank–Nicholson scheme is used for the viscous terms; the advection terms are obtained at the intermediate time-step by extrapolation based on the previous time-steps.

3. Global flow behaviour and basic velocity fields

The present section considers the global wake dynamics for moderate Reynolds numbers, $Re \leq 350$, and compares its features with those obtained by previous experiments or simulations. The direct numerical simulations carried out here serve two purposes. (1) Validate the numerical code by accurately reproducing the different known flow regimes: steady axisymmetric flow for $Re < Re_1$, steady non-axisymmetric flow for $Re_1 < Re < Re_2$ and unsteady flow for $Re > Re_2$. (2) Obtain the time-independent solutions of the Navier–Stokes equations that are used as basic flows for the stability analyses of the next section. These basic flow fields must be computed at all relevant Reynolds numbers, including those for which they are globally unstable: $Re > Re_1$ for the axisymmetric and $Re > Re_2$ for the non-axisymmetric basic flows. These globally unstable non-axisymmetric basic wakes have been computed for the first time here, by the frequency damping method of Åkervik *et al.* (2006).

3.1. Steady axisymmetric flow

A steady axisymmetric solution

$$\begin{aligned} \mathbf{u} &= \mathbf{u}^A(r, z; Re), \\ p &= p^A(r, z; Re), \end{aligned} \quad (3.1)$$

of the Navier–Stokes equations (2.1) exists at all Reynolds numbers and can easily be computed via direct numerical simulations. By truncating the Fourier expansions (2.4) at $|\beta| \leq N_h = 0$, the system converges in time towards the steady state (3.1), even for $Re > Re_1$ when this basic state is globally unstable to non-axisymmetric perturbations (see §3.2).

The structure of the basic axisymmetric wake fields at $Re = 100, 200$ and 300 is illustrated in figure 1 where isolines of the pressure field p and the azimuthal vorticity $\omega_\theta \equiv \partial_z u - \partial_r w$ are shown. These fields are in excellent agreement with those obtained for $Re < Re_1$ by Johnson & Patel (1999, figures 6 and 7) using a discretization based on spherical coordinates, a spatial grid fitted to the sphere surface and explicitly implementing surface boundary conditions. Thus the ability of the present immersed boundary technique to capture the flow fields with great accuracy is demonstrated.

3.2. Global instabilities

At $Re_1 \simeq 212$, a regular bifurcation occurs (Ghidersa & Duček 2000) and the axisymmetric flow becomes globally unstable with respect to non-axisymmetric perturbations. Thus, for $Re > Re_1$, the wake flow naturally evolves towards a new

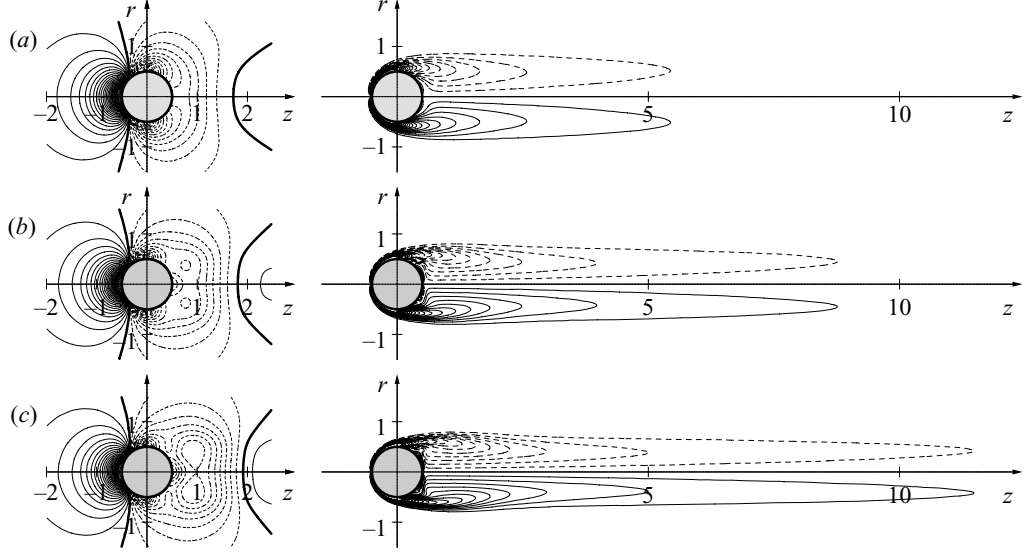


FIGURE 1. Flow structure of steady axisymmetric wake. Isolines of pressure p (left) and azimuthal vorticity ω_θ (right) at (a) $Re = 100$, (b) $Re = 200$ and (c) $Re = 300$. Solid (dashed) contours correspond to positive (negative) values. Pressure contours are spaced by 0.04 and vorticity contours by 0.5.

steady non-axisymmetric state exhibiting a symmetry plane containing the z -axis. This steady planar symmetric flow in turn becomes globally unstable at $Re_2 \simeq 272$, where a Hopf bifurcation leads to periodic vortex shedding.

The breaking of axisymmetry is associated with the appearance of higher azimuthal Fourier modes. Figure 2 shows the temporal evolution of energy contained in the first azimuthal ($\beta = 1$) Fourier component; in these simulations the axisymmetric basic flow solution (3.1) is non-axisymmetrically perturbed at $t = 0$. From figure 2(a) it is derived that global instability of the axisymmetric state occurs for $210 < Re_1 < 220$, while onset of periodic vortex shedding is seen in figure 2(b) to occur for $270 < Re_2 < 280$. The steady planar symmetric wake obtained with $Re = 250$ can be seen in figure 4(a) below, and a snapshot of the vortex shedding regime prevailing at $Re = 300$ is shown in figure 3. The vortex shedding frequency measured for $Re > Re_2$ weakly increases with Reynolds number and equals $\omega = 0.85$ at $Re = 300$, which corresponds to a Strouhal number of $St = \omega/2\pi = 0.135$. These results are in good agreement with the usually assumed critical Reynolds numbers of $Re_1 = 212$ and $Re_2 = 272$, as well as the expected Strouhal number (Johnson & Patel 1999; Ghidelsa & Dućek 2000). Since the purpose of the present investigation is not the precise determination of these thresholds, these results are deemed sufficient validation of the code and no further numerical refinement has been pursued.

3.3. Steady planar symmetric flow

For $Re > Re_1$, there exists a steady non-axisymmetric but *planar symmetric* solution

$$\begin{aligned} \mathbf{u}(r, \theta, z, t) &\equiv \mathbf{u}^P(r, \theta, z; Re), \\ p(r, \theta, z, t) &\equiv p^P(r, \theta, z; Re), \end{aligned} \quad (3.2)$$

of the Navier–Stokes equations (2.1). Below, the coordinates are always chosen so that the symmetry plane coincides with the (x, z) -plane defined by $\theta = 0$. This steady planar symmetric wake flow is globally stable up to Re_2 . A direct numerical simulation

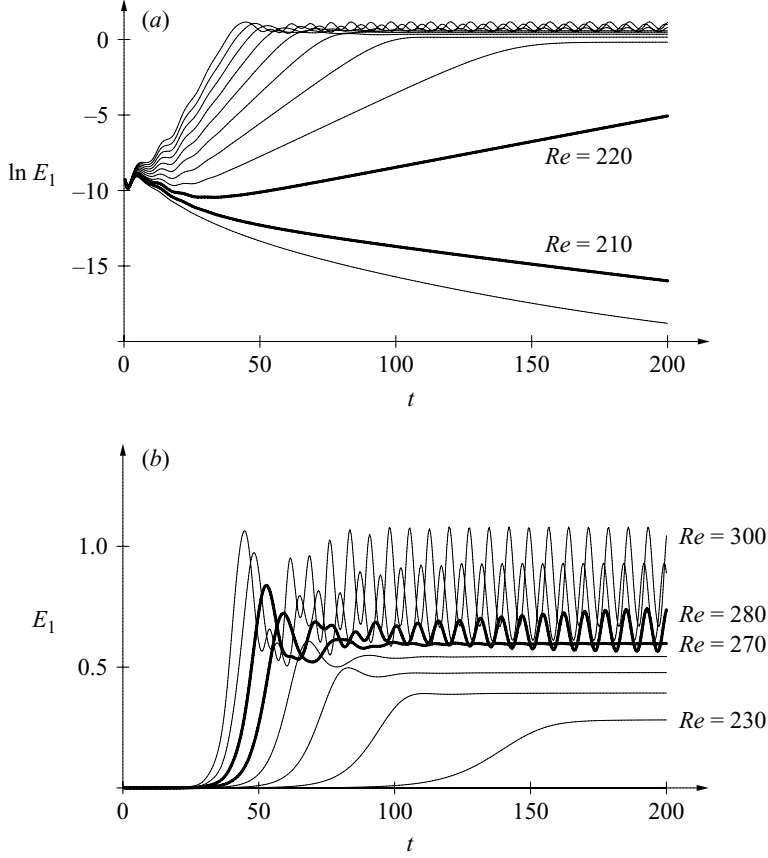


FIGURE 2. Temporal evolution of energy E_1 (arbitrary units) contained in the first azimuthal Fourier mode for $Re = 200, 210, \dots, 300$.

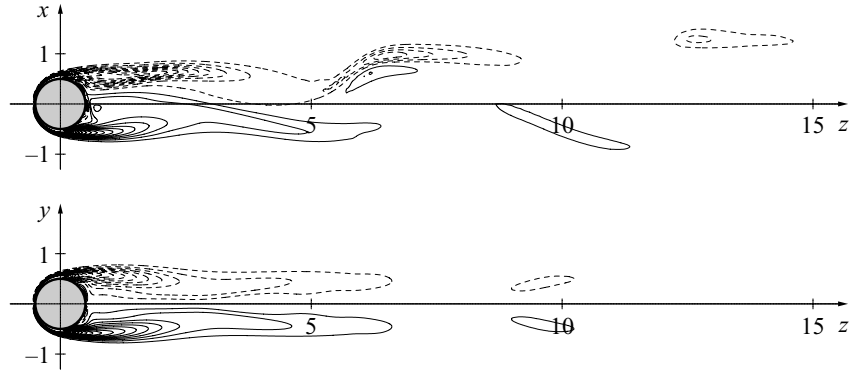


FIGURE 3. Snapshot of periodic vortex shedding regime at $Re = 300$. Isolines of azimuthal vorticity ω_θ in the (x, z) -plane (symmetry plane $\theta = 0$) and (y, z) -plane ($\theta = \pi/2$). Solid (dashed) contours correspond to positive (negative) values, spaced by 0.5.

(with $N_h > 0$) thus evolves in time towards the steady planar symmetric wake for $Re_1 < Re < Re_2$ and towards a time-dependent regime for $Re > Re_2$. It should be noted that the onset of periodic vortex shedding does not break the planar symmetry of the underlying unstable basic flow: the time-dependent flow fields (see figure 3) conserve the (x, z) -symmetry plane. Thus there is no way to obtain the steady unstable flow solution (3.2) for $Re > Re_2$ by imposing an additional symmetry condition in the direct numerical simulations.

In order to compute the planar symmetric basic flow for $Re > Re_2$, a Newton–Raphson search procedure could be numerically implemented that solves for steady solutions of the full system. However, owing to the size of the system of non-linearly coupled equations, this procedure turned out to be extremely time and memory consuming (even when resorting to approximate iterative methods) and poorly converging.

A much more efficient way to compute the unstable basic flow was to implement the selective frequency damping method of Åkervik *et al.* (2006). In a nutshell, this *frequency damping* method enables the computation of steady solutions by adding to the right-hand side of (2.1a) a linear forcing term f_d driving the system towards a target solution

$$f_d(r, \theta, z, t) = -\frac{1}{\tau_d}(\mathbf{u}(r, \theta, z, t) - \bar{\mathbf{u}}(r, \theta, z, t)), \quad (3.3)$$

where τ_d can be understood as a characteristic damping time. The target solution $\bar{\mathbf{u}}$ must be chosen so that it converges towards the unknown steady solution, and this can be achieved by low-pass filtering (with cutoff frequency $1/\tau_f$) the already computed velocity fields

$$\bar{\mathbf{u}}(r, \theta, z, t) = \int_0^t \frac{1}{\tau_f} \exp\left(-\frac{t-t'}{\tau_f}\right) \mathbf{u}(r, \theta, z, t') dt', \quad (3.4)$$

or equivalently

$$\partial_t \bar{\mathbf{u}} = \frac{1}{\tau_f}(\mathbf{u} - \bar{\mathbf{u}}). \quad (3.5)$$

Time-marching of the target solution governed by (3.5) can be done simultaneously with the simulation of the Navier–Stokes equations (2.1) with $\mathbf{f} = \mathbf{f}_b + \mathbf{f}_d$ and only requires minimal modifications to the original code. As this coupled system converges towards a steady state, the additional damping term (3.3) vanishes and the resulting time-independent flow fields are exact steady solutions of the original Navier–Stokes equations. In the present investigation, a good compromise between stability of the scheme and fast convergence towards a steady solution was obtained with $\tau_d = 1$ and $\tau_f = 10$.

The structure of the steady planar symmetric wake at $Re = 200, 250$ and 300 is shown in figure 4.

3.4. Drag, lift and reverse flow

As a final check, and to conclude this section on the global flow behaviour, the drag and lift forces acting on the sphere as well as the reverse-flow regions in the different wake regimes have also been computed.

As mentioned in §2.1, the hydrodynamic forces are here simply obtained by spatial integration of the volume forces (2.3) required by the immersed boundary method. Since these volume forces are designed to maintain the fluid at rest in the domain covered by the sphere, they exactly oppose the hydrodynamic forces due to the surrounding flow. The drag force is the component acting in the z -direction. Since the symmetry plane of the wakes is chosen to lie at $\theta = 0$, defined as the (x, z) -plane, the lift force is obtained by projection onto the x -axis, while the lateral force along the y -axis vanishes. Drag and lift coefficients C_D and C_L are shown in figure 5. The thick solid lines correspond to the steady axisymmetric wakes; the thick dashed lines represent the hydrodynamic forces computed for the steady planar symmetric fields.

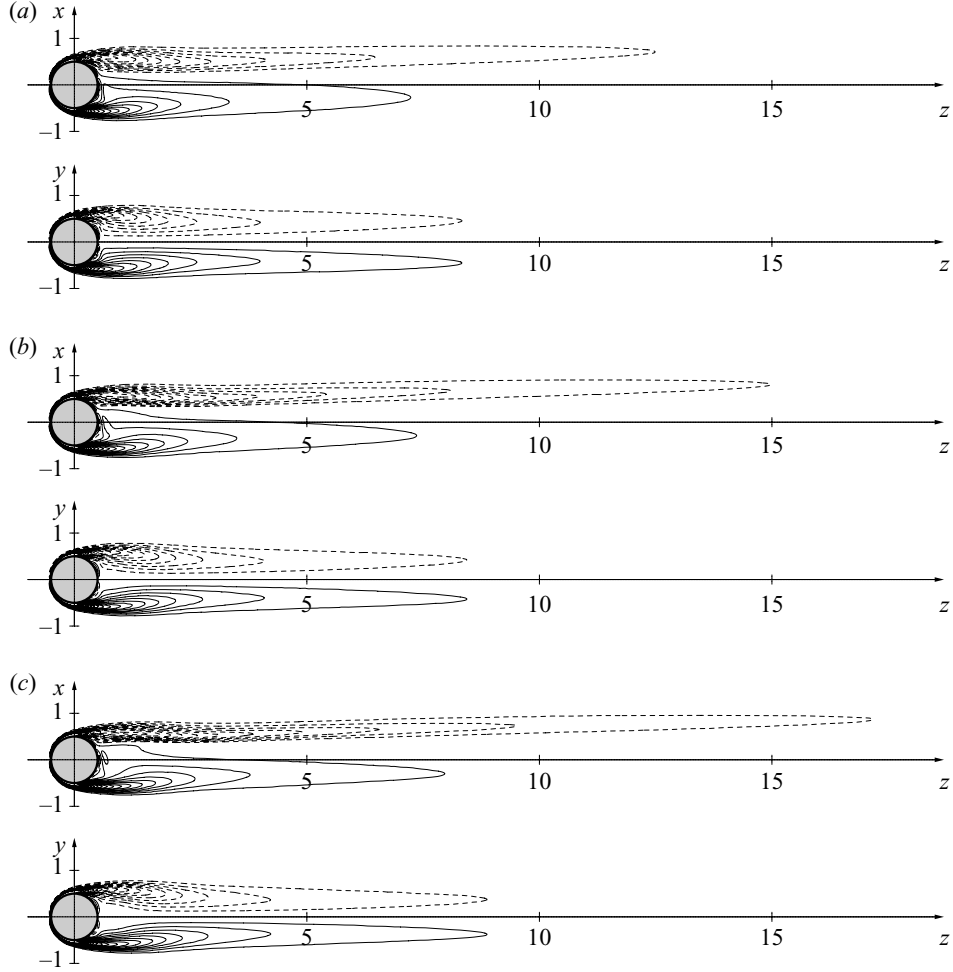


FIGURE 4. Flow structure of a steady planar symmetric wake. Isolines of azimuthal vorticity ω_θ in (x, z) -plane (symmetry plane $\theta = 0$) and (y, z) -plane ($\theta = \pi/2$) at (a) $Re = 250$, (b) $Re = 300$ and (c) $Re = 350$. Solid (dashed) contours correspond to positive (negative) values, spaced by 0.5.

Beyond Re_2 , the wake naturally evolves towards a time-dependent state, and the thin lines illustrate the maximum and minimum values in this periodic regime.

Since absolute instability is often associated with the existence of reverse flow, the evolution with Reynolds number of the recirculation region is plotted in figure 6. For axisymmetric basic wakes, the reverse-flow region terminates at a stagnation point located at Z_*^A (solid curve) on the z -axis (note that the recirculation length is given by $Z_*^A - 0.5$). For the steady planar symmetric wakes, two quantities have been computed: the downstream boundary of the reverse flow region Z_*^P (dashed curve), defined as the zero-crossing of $\min_{r,\theta} w^P(r, \theta, z; Re)$, and the location Z_{**}^P (dotted curve) where the z -axis crosses the reverse flow region, i.e. the zero-crossing of $w^P(r = 0, \theta, z; Re)$. At $Re = Re_1$, the breaking of axisymmetry causes a lateral shift of the reverse-flow region, which entails a drop in Z_{**}^P . However, reverse flow prevails off the z -axis beyond Z_{**}^P down to Z_*^P , which is seen to increase almost linearly with Re .

The results shown in figures 5 and 6 are in excellent agreement with the data recently obtained by Bouchet *et al.* (2006) using a different method; note however that these authors did not compute the globally unstable planar symmetric base flow for $Re > Re_2$.

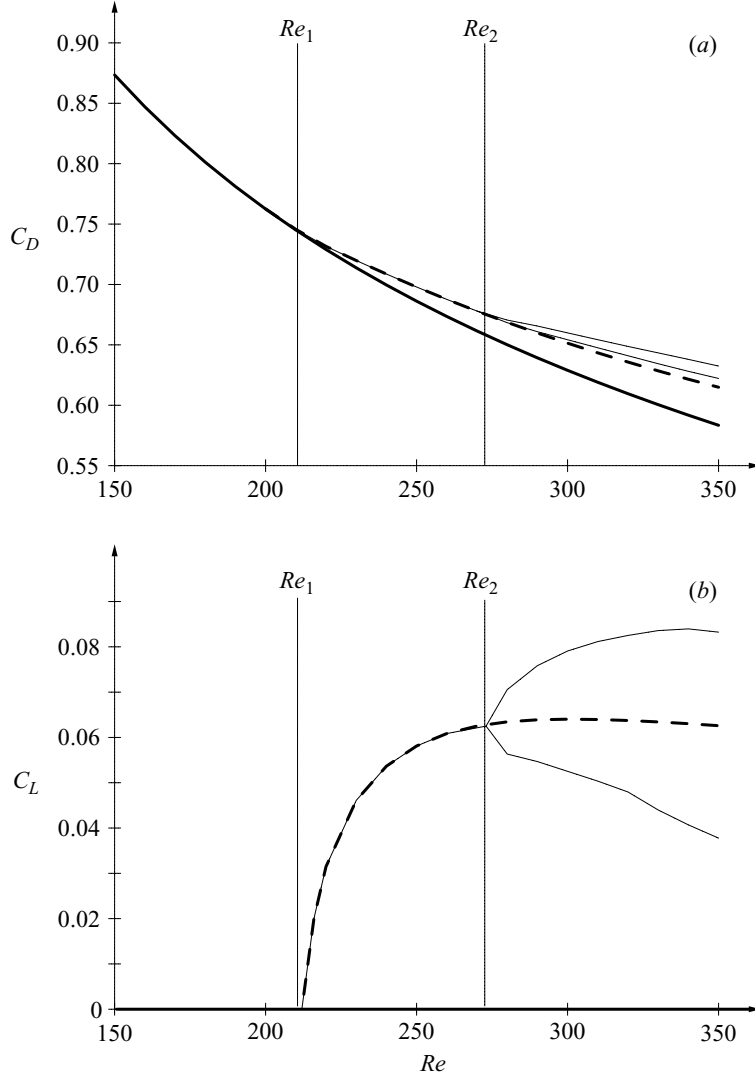


FIGURE 5. (a) Drag and (b) lift coefficients as a function of the Reynolds number for the different flow regimes: axisymmetric wake (thick solid), steady planar symmetric wake (thick dashed), unsteady planar symmetric wake (two thin lines corresponding to minimum and maximum values).

4. Local linear stability analyses

The next two subsections of this study investigate the local stability properties of the previously obtained basic wake flows: both the axisymmetric $\mathbf{u}^A(r, z; Re)$ (3.1) and the planar symmetric $\mathbf{u}^P(r, \theta, z; Re)$ (3.2) steady solutions of the Navier–Stokes equations. Local properties of these flows, valid at a given axial position z , are derived from the velocity profiles prevailing at that station. Such an approach can be justified by a rigorous asymptotic analysis based on the assumption of a slow axial development of the basic flow. The flow around a spherical obstacle is clearly non-parallel in the near-wake region; however, following the successful treatment of the cylinder wake (Pier 2002), we again ignore the non-parallelism of the present flow and study its local stability features. Local properties are then derived by freezing the z -coordinate, at say $z = Z$, and studying the equivalent axially parallel shear flows of either axisymmetric or planar symmetric velocity profiles

$$\mathbf{U}^A(r; Z, Re) \equiv \mathbf{u}^A(r, Z; Re) \quad \text{or} \quad \mathbf{U}^P(r, \theta; Z, Re) \equiv \mathbf{u}^P(r, \theta, Z; Re), \quad (4.1)$$

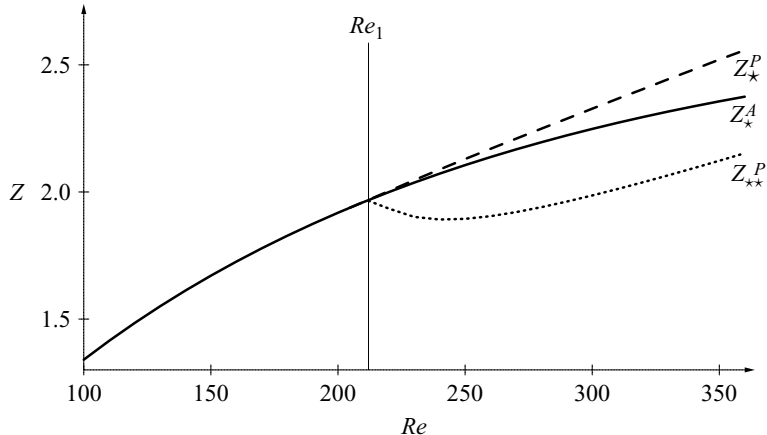


FIGURE 6. Reynolds-number dependence of reverse-flow region. For axisymmetric basic wakes, the recirculation region terminates at Z_*^A (solid curve). For planar symmetric basic wakes, it extends down to Z_*^P (dashed) and crosses the z -axis at Z_{**}^P (dotted).

where Z now acts as a parameter rather than a coordinate.

4.1. Local stability of axisymmetric basic wake

When studying the local stability properties of the axisymmetric basic wake under the parallel flow assumption, both z and θ are homogenous directions, and the total flow fields may then be separated into basic and perturbation quantities according to

$$\begin{aligned} \mathbf{u}(r, \theta, z, t) &= \mathbf{U}^A(r; Z, Re) + \mathbf{u}'(r; \alpha, \beta; Z, Re) \exp i(\alpha z + \beta \theta - \omega t), \\ p(r, \theta, z, t) &= P^A(r; Z, Re) + p'(r; \alpha, \beta; Z, Re) \exp i(\alpha z + \beta \theta - \omega t). \end{aligned} \quad (4.2)$$

Here the infinitesimally small velocity and pressure disturbances have been written in normal-mode form, where α is a complex axial wavenumber, β an integer azimuthal mode number, ω a complex angular frequency and \mathbf{u}' , p' the associated complex velocity and pressure components. After substitution of (4.2) into the Navier–Stokes equations, the linearization in the perturbation quantities yields an eigenvalue problem in the radial direction. By using a Chebyshev spectral method based on the same radial collocation points for which the base flow has been computed, the full ω -spectrum is obtained for each setting of the wavenumbers α and β and of the parameters Z and Re . In figure 7, the ω -spectra are shown corresponding to $\alpha = 2$ and $|\beta| \leq 4$ for the velocity profiles obtained in the axisymmetric wake at $Z = 1$ with $Re = 300$ (illustrated in figure 1c). The full spectra are made up of many modes, among which only a few are physically relevant. Note that the numerical method approximates a continuous spectrum at $\omega_r = \alpha$, associated with modes oscillating in the free stream. For each β the most unstable (or least stable) mode is indicated by a bold dot in figure 7. Identification of these modes yields the local linear dispersion relation

$$\omega = \Omega^A(\alpha, \beta; Z, Re). \quad (4.3)$$

For axisymmetric base flows, the eigenfunctions $\mathbf{u}'(r; \alpha, \beta)$ and $\mathbf{u}'(r; \alpha, -\beta)$ are associated with the same frequency, i.e. $\Omega^A(\alpha, \beta) = \Omega^A(\alpha, -\beta)$, and transform into each other under the symmetry operator Π (2.5), with respect to the ($\theta = 0$)-plane. A planar symmetric eigenmode is thus obtained as the combination $\mathbf{u} = \mathbf{u}'(r; \alpha, \beta)e^{i\beta\theta} + \mathbf{u}'(r; \alpha, -\beta)e^{-i\beta\theta}$, which satisfies $\Pi\mathbf{u} = \mathbf{u}$, whereas the combination $\mathbf{u} = \mathbf{u}'(r; \alpha, \beta)e^{i\beta\theta} - \mathbf{u}'(r; \alpha, -\beta)e^{-i\beta\theta}$ satisfies $\Pi\mathbf{u} = -\mathbf{u}$ and thus represents an eigenmode that is antisymmetric with respect to the ($\theta = 0$)-plane. For comparison

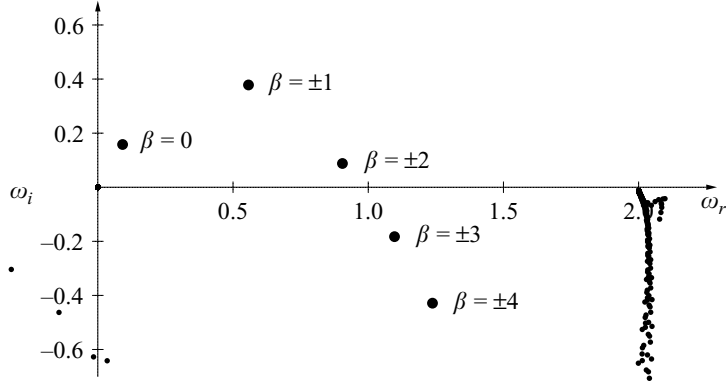


FIGURE 7. Superposition of temporal ω -spectra corresponding to $\alpha = 2$ and $\beta = 0, 1, 2, 3, 4$ for axisymmetric wake flow at $Z = 1$ with $Re = 300$.

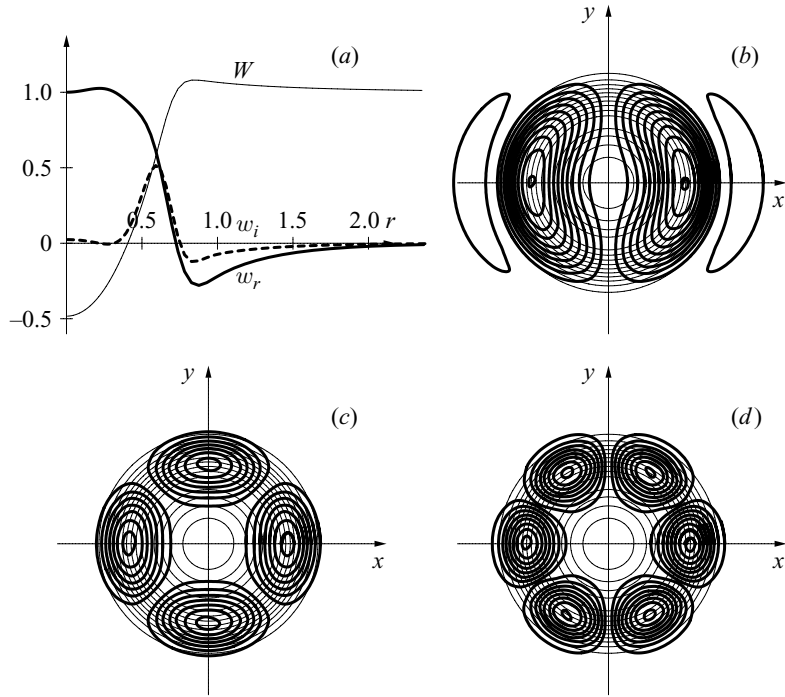


FIGURE 8. Structure of eigenfunctions obtained for axisymmetric wake flow at $Z = 1$, $Re = 300$ with $\alpha = 2$ and (a) $\beta = 0$, (b) $\beta = 1$, (c) $\beta = 2$, (d) $\beta = 3$. The axial velocity component $w(r, \theta)$ of the normalized modes (thick curves) is shown together with the axial basic flow component $W(r)$ (thin curves). (a) Radial profile of real w_r (thick solid) and imaginary w_i (thick dashed) parts of the axisymmetric mode corresponding to $\alpha = 2$ and $\beta = 0$. (b-d) Modulus $|w|$ (thick equispaced isolines) of planar symmetric modes corresponding to $\alpha = 2$ and $\beta = 1$ (b), $\beta = 2$ (c) and $\beta = 3$ (d). In (b-d), the basic wake profile W is indicated by thin equispaced isolines.

with eigenmodes pertaining to non-axisymmetric wakes (figure 13), the structure of the symmetric eigenmodes is illustrated in figure 8.

In the context of open shear flows, a crucial feature is the complex absolute frequency defined as the frequency observed at a fixed spatial location in the long-time linear response to an initial impulse. For an axially localized impulse with given azimuthal mode number β , the local absolute frequency ω_0^A and associated absolute axial wavenumber α_0^A are derived from the linear dispersion relation (4.3) by applying

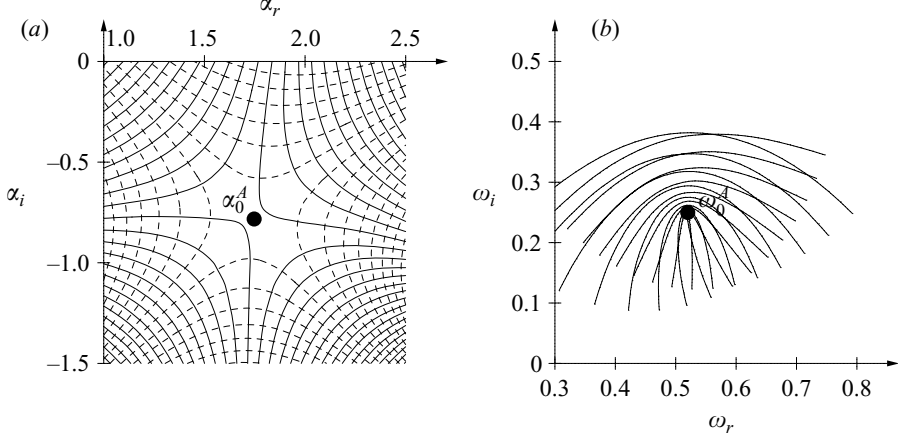


FIGURE 9. Identification of absolute frequency ω_0 and wavenumber α_0 for $\beta = 1$, $Z = 1$ in an axisymmetric wake at $Re = 300$, by monitoring how the dispersion relation maps the complex α -plane onto the complex ω -plane. (a) Isocontours of ω_r (solid) and ω_i (dashed) in the α -plane display a saddle point at $\alpha_0^A \approx 1.75 - 0.78i$ marked by a solid dot. (b) The temporal curves $\Omega^A(\alpha)$ computed for lines of constant α_i display a cusp at $\omega_0^A \approx 0.52 + 0.25i$ in the ω -plane.

the Briggs (1964) and Bers (1983) pinch-point criterion, equivalent to the vanishing group velocity condition

$$\omega_0^A(\beta; Z, Re) = \Omega^A(\alpha_0^A, \beta; Z, Re) \quad \text{and} \quad \frac{\partial \Omega^A}{\partial \alpha}(\alpha_0^A, \beta; Z, Re) = 0 \quad (4.4)$$

with the additional requirement that the two spatial α -branches that coalesce at the branch-point singularity α_0^A originate from distinct half- α -planes for sufficiently large and positive values of ω_i . Pinch points are readily identified by computing the dispersion relation (4.3) on a rectangular grid in the α -plane and monitoring how it maps the complex α -plane onto the complex ω -plane. Plotting the associated temporal branches in the ω -plane and ω_r - and ω_i -isolines in the α -plane reveals respectively the characteristic cusp near ω_0^A and saddle point near α_0^A . Once a pinch point has thus been approximately located, the exact values of ω_0^A and α_0^A are found by iteratively solving (4.4) with this initial guess. This method is illustrated in figure 9 for $\beta = 1$, $Z = 1$ and $Re = 300$, which yields $\omega_0^A = 0.52 + 0.25i$ and $\alpha_0^A = 1.75 - 0.78i$. The structure of the absolute eigenmodes obtained for azimuthal mode numbers $\beta = 0, 1$ and 2 at $Z = 1$ in an axisymmetric wake with $Re = 300$ is given in figure 10.

The streamwise evolutions of the local absolute growth rate $\omega_{0,i}$ and real absolute frequency $\omega_{0,r}$ are illustrated in figure 11 for $\beta = 0, 1, 2, 3$ and axisymmetric basic wakes in the range $100 \leq Re \leq 350$.

From these plots it is found that the near wake displays absolutely unstable regions when $Re > Re_a \approx 130$ and that the strongest instability always occurs for $|\beta| = 1$. Axisymmetric ($\beta = 0$) perturbations are weakly absolutely unstable for $Re > 170$ while higher azimuthal modes ($|\beta| \geq 2$) never reach absolute instability at these Reynolds numbers. The discrepancy between onset of local absolute instability at $Re_a \approx 130$ and of global vortex shedding at $Re_2 \approx 272$ will be addressed in the concluding section.

4.2. Local stability of planar symmetric basic wake

When investigating the local stability features of a planar symmetric basic flow, the local velocity profiles depend on both radial and azimuthal directions, and z is the

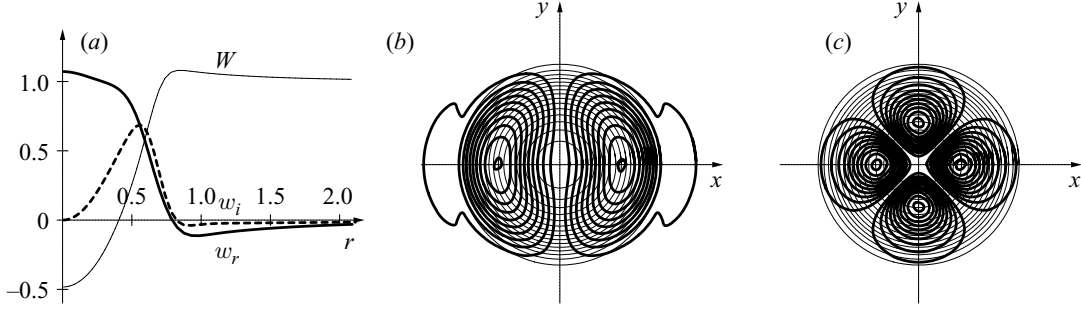


FIGURE 10. Structure of absolute eigenfunctions for axisymmetric wake flows at $Z = 1$ and $Re = 300$. The axial velocity component $w(r, \theta)$ of the modes (thick curves) is shown together with the axial basic flow component $W(r)$ (thin curves). (a) Axisymmetric mode $\beta = 0$, radial profile of real w_r (thick solid) and imaginary w_i (thick dashed) parts. (b,c) Non-axisymmetric modes $\beta = 1$ and $\beta = 2$ respectively, equispaced (thick solid) isolines of modulus $|w|$.

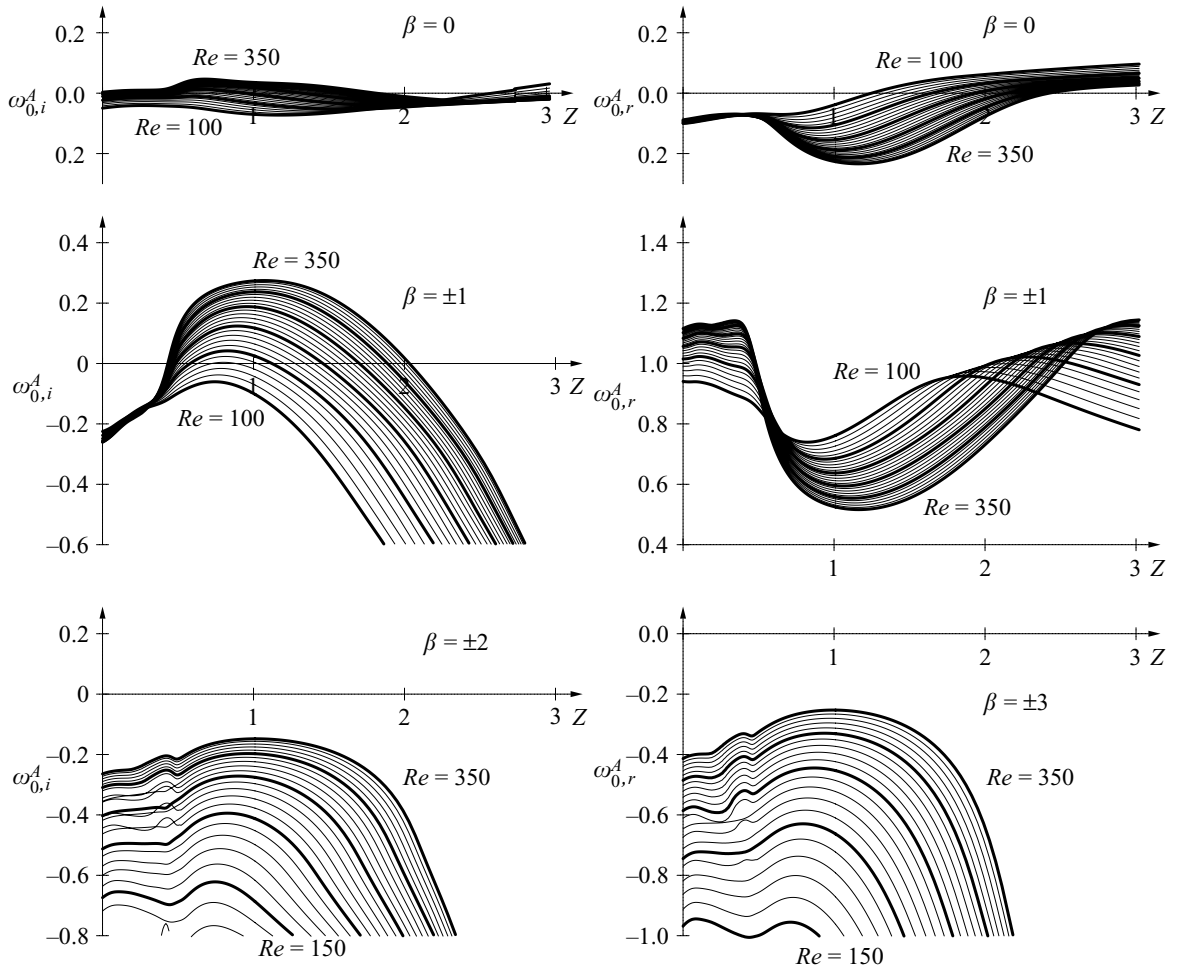


FIGURE 11. Local absolute growth rates $\omega_{0,i}^A$ and frequencies $\omega_{0,r}^A$ for $|\beta| \leq 3$ in axisymmetric basic wake flows at $Re = 100, 110, \dots, 350$.

only spatial homogenous coordinate. The total flow fields are then separated into basic and perturbation quantities as

$$\begin{aligned} \mathbf{u}(r, \theta, z, t) &= \mathbf{U}^P(r, \theta; Z, Re) + \mathbf{u}^l(r, \theta; \alpha; Z, Re) \exp i(\alpha z - \omega t), \\ p(r, \theta, z, t) &= P^P(r, \theta; Z, Re) + p^l(r, \theta; \alpha; Z, Re) \exp i(\alpha z - \omega t), \end{aligned} \quad \{ \quad (4.5)$$

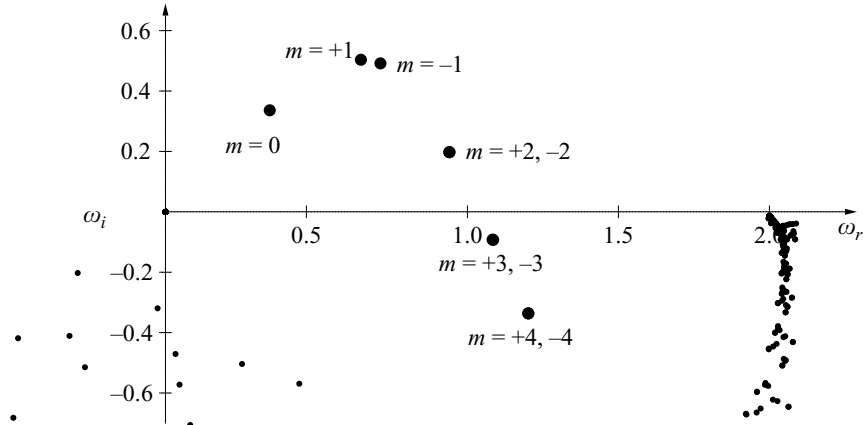


FIGURE 12. Frequency eigenvalues obtained with $\alpha = 2$ for non-axisymmetric wake flow at $Z = 1$ with $Re = 300$.

where α is again a complex axial wavenumber, ω a complex angular frequency and the eigenmodes \mathbf{u}^l and p^l are now functions of both r and θ and are governed by the local Navier–Stokes equations linearized about the local planar symmetric wake flow.

For a given Reynolds number above onset of non-axisymmetry ($Re > Re_1$), computation of the planar symmetric steady wake following the method outlined in §3.3 provides the basic flow fields required in (4.5). For these basic flow quantities, the values of their azimuthal Fourier components are known on a set of radial collocation points. Thus the same Fourier–Chebyshev expansion is used for the two-dimensional eigenfunctions \mathbf{u}^l and p^l in (4.5), and the associated eigenproblems are then obtained as a large system of linear equations where the different azimuthal harmonics of the eigenfunctions are linearly coupled via the harmonics of the basic flow. The solution of these eigensystems then yields the full ω -spectrum for each setting of the wavenumber α and the parameters Re and Z . Since the basic flow is symmetric about the plane $\theta = 0$, i.e. invariant under the symmetry operator Π (2.5), the associated eigenfunctions are either symmetric ($\Pi\mathbf{u} = \mathbf{u}$) or antisymmetric ($\Pi\mathbf{u} = -\mathbf{u}$), and the numerical resolution of the eigenproblems can be speeded up by taking advantage of these symmetry properties. By analogy with two-dimensional jets or wakes, the present symmetric (resp. antisymmetric) modes are also termed varicose (resp. sinuous). Figure 12 shows the frequency spectrum corresponding to $\alpha = 2$, computed with the planar symmetric basic wake profile at $Z = 1$ for $Re = 300$ (illustrated in figure 4b). By comparison of this spectrum with the corresponding spectra obtained at similar parameter settings for the axisymmetric wake flow (see figure 7), the physically relevant eigenvalues in figure 12 are labelled as $m = 0, \pm 1, \pm 2, \dots$ where the values $m \geq 0$ denote symmetric or varicose modes while the values $m < 0$ denote antisymmetric or sinuous modes. Identification of these modes then yields the local linear dispersion relation governing the planar symmetric wake flows

$$\omega = \Omega^P(\alpha, m; Z, Re). \quad (4.6)$$

Comparison of figures 7 and 12 reveals that the non-axisymmetric basic flow displays larger growth rates ω_i than the axisymmetric case. Unlike the situation prevailing for axisymmetric velocity profiles where the modes $\pm\beta$ are degenerate, here the non-axisymmetric components of the basic flow lift the degeneracy of the $\pm m$ modes, i.e. $\Omega^P(\alpha, m) \neq \Omega^P(\alpha, -m)$ for $m \neq 0$. However, the influence of the non-axisymmetric components is relatively weak: only the modes $m = \pm 1$

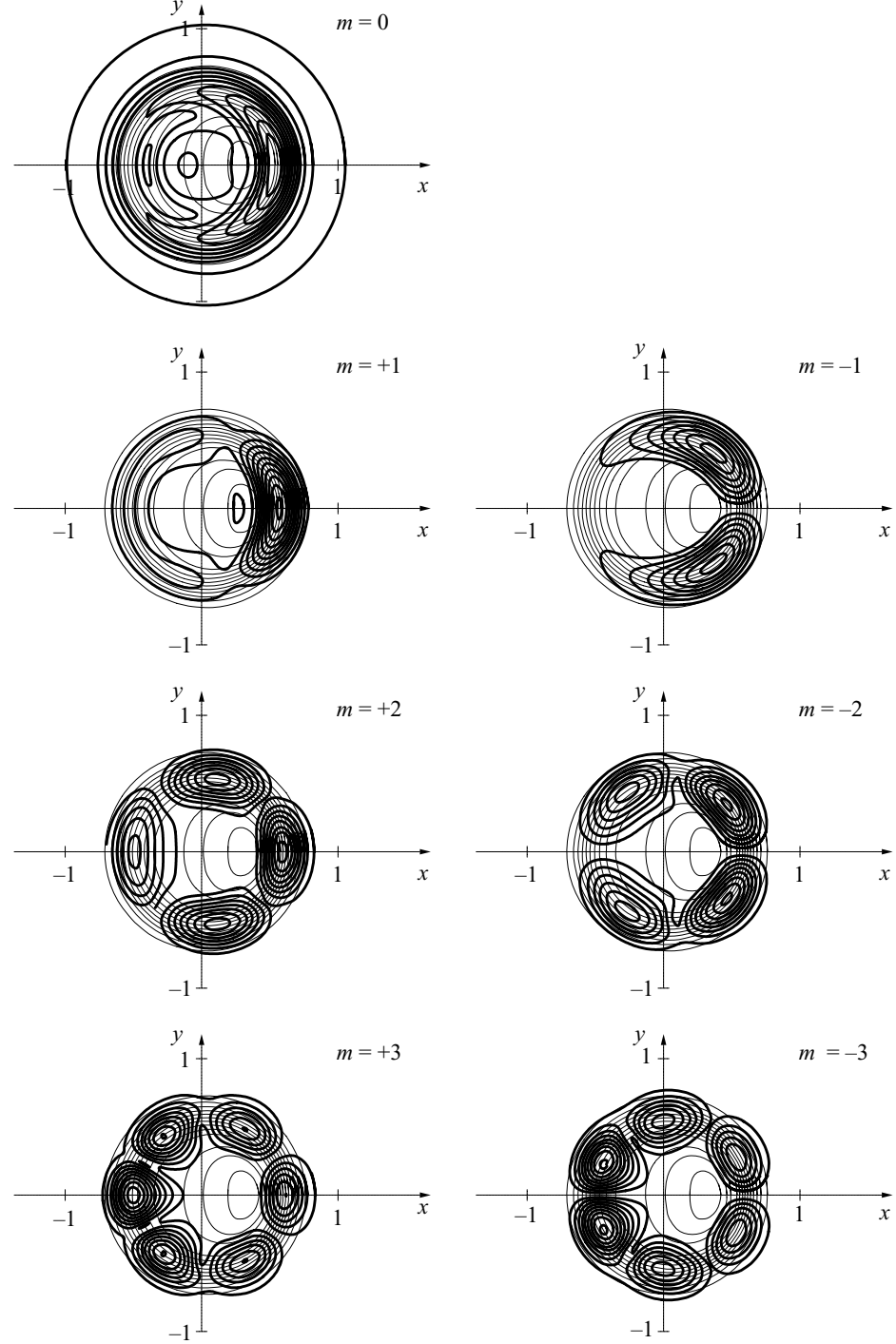


FIGURE 13. Structure of eigenfunctions obtained for planar symmetric wake flow at $Z = 1$ and $Re = 300$, with $\alpha = 2$ and $m = 0, \pm 1, \pm 2, \pm 3$. The modulus of the axial velocity component $|w(r, \theta)|$ of the modes (thick equispaced isolines) is shown together with the axial basic flow component $W(r, \theta)$ (thin equispaced isolines).

are clearly distinguished in the frequency plane of figure 12. The spatial structure of the associated eigenfunctions is illustrated in figure 13 by isolines of $|w|$, the modulus of their complex-valued axial velocity component. Again, only the modes $m = \pm 1$ are clearly differentiated while the higher modes closely resemble their axisymmetric counterparts (see figure 8). Note that plots of $|w|$ are all

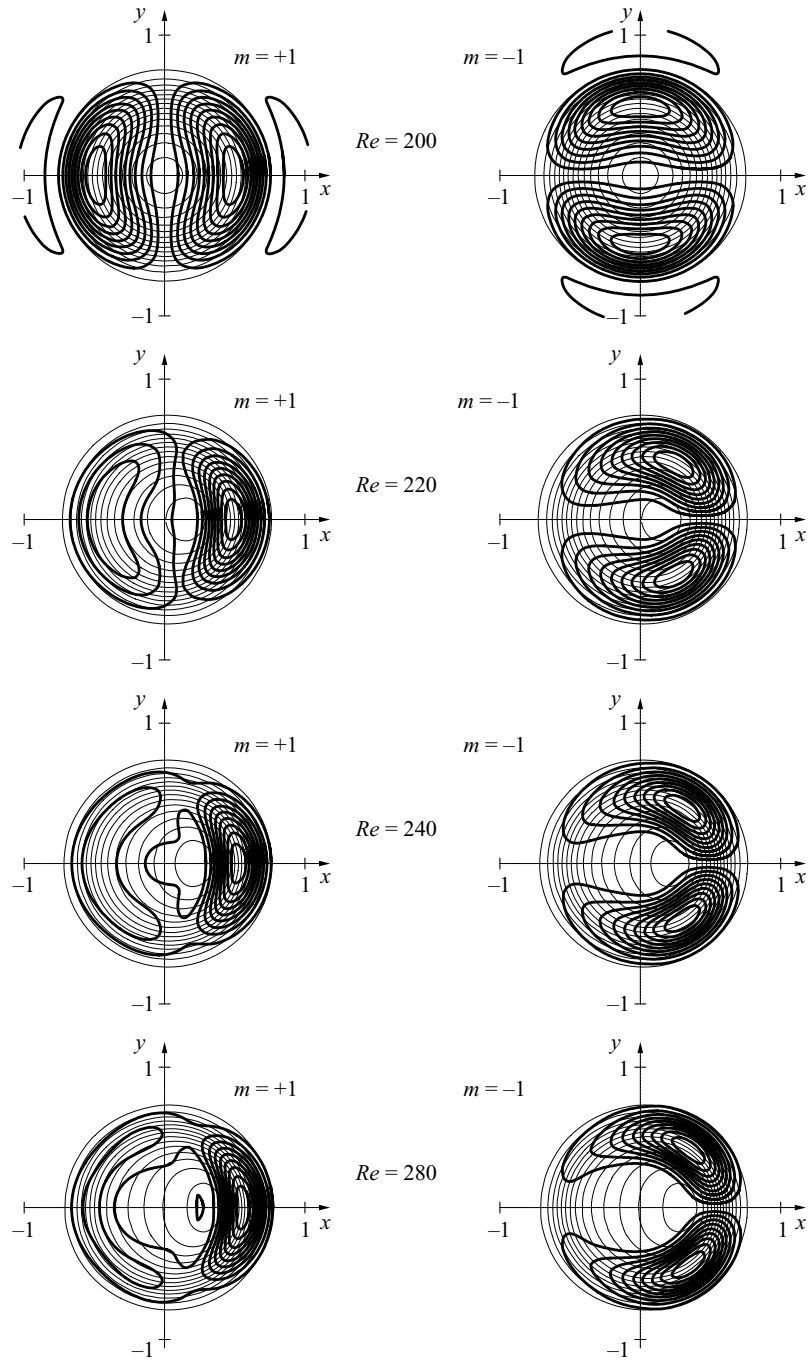


FIGURE 14. Evolution with Reynolds number of planar symmetric $m = +1$ and antisymmetric $m = -1$ eigenfunctions obtained for the basic wake at $Z = 1$, $\alpha = 2$ and $Re = 200, 220, 240, 280$. While the modes are degenerate for the axisymmetric wake prevailing at $Re = 200$, they evolve separately for $Re > Re_1 \simeq 212$ with increasing departure from axisymmetry. The modulus of the axial velocity component $|w(r, \theta)|$ of the modes (thick equispaced isolines) is shown together with the axial basic flow component $W(r, \theta)$ (thin equispaced isolines).

symmetric with respect to the x -axis: in this representation antisymmetric eigenmodes are characterized by the vanishing of the w component on the x -axis, while planar-symmetric eigenmodes display non-vanishing values of $|w|$ over the x -axis. It should be noted also that the unstable eigenfunctions ($|m| \leq 2$) are shifted towards

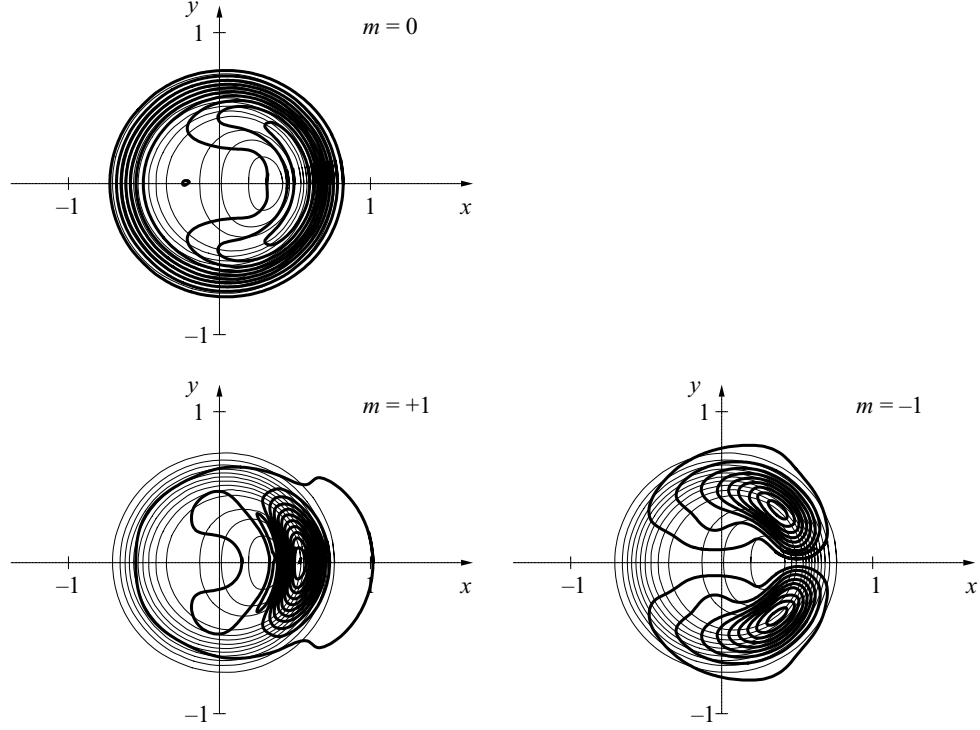


FIGURE 15. Structure of absolute eigenfunctions for planar symmetric wake flow at $Z = 1$ and $Re = 300$, with $m = 0$, $m = +1$ and $m = -1$. The modulus of the axial velocity component $|w(r, \theta)|$ of the modes (thick equispaced isolines) is shown together with the axial basic flow component $W(r, \theta)$ (thin equispaced isolines).

the regions where the basic wake displays the largest shear, i.e. the neighbourhood of $(x, y) = (0.5, 0)$ in these plots.

To further illustrate how the non-axisymmetric modes emerge from their axisymmetric equivalents with increasing Reynolds number, figure 14 plots both planar symmetric $m = +1$ and antisymmetric $m = -1$ eigenmodes obtained with $\alpha = 2$ and $Z = 1$ for $Re = 200, 220, 240$ and 280 . For $Re = 200$, below onset of non-axisymmetry, both modes are identical up to a rotation around the z -axis. For $Re > Re_1 \simeq 212$, with increasing departure from axisymmetry, the discrepancy between the $m = +1$ and $m = -1$ modes is seen to increase as they concentrate towards the region of largest shear in the basic flow.

The analysis of absolute instability properties for non-axisymmetric wakes is carried out in a similar fashion as for the axisymmetric case in the previous section; its numerical implementation, however, is more demanding on computational resources. Application of the Briggs (1964) and Bers (1983) pinch-point criterion with dispersion relation (4.6) yields, for each mode m , the local absolute frequency ω_0^P and associated absolute axial wavenumber α_0^P by solving

$$\omega_0^P(m; Z, Re) = \Omega^P(\alpha_0^P, m; Z, Re) \quad \text{with} \quad \frac{\partial \Omega^P}{\partial \alpha}(\alpha_0^P, m; Z, Re) = 0. \quad (4.7)$$

The structure of the absolute eigenfunctions obtained for the modes $m = 0, +1$ and -1 for the non-axisymmetric basic wake at $Z = 1$ and $Re = 300$ is illustrated in figure 15. These modes are associated respectively with the absolute frequencies $\omega_0^P(m = 0) \simeq -0.15 + 0.03i$, $\omega_0^P(m = +1) \simeq 0.76 + 0.41i$ and $\omega_0^P(m = -1) \simeq 0.78 + 0.27i$. Comparison with the corresponding absolute modes pertaining to

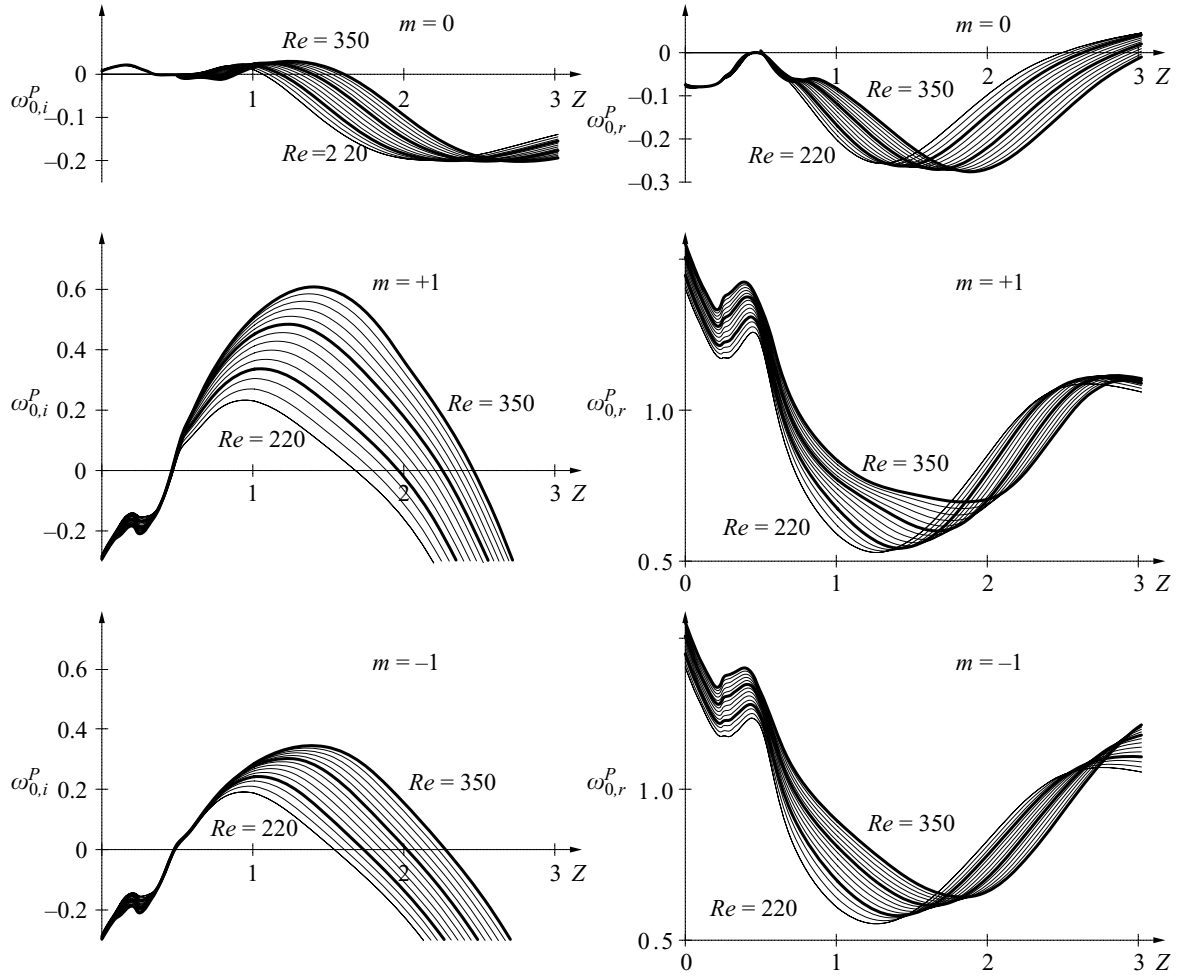


FIGURE 16. Local absolute growth rates $\omega_{0,i}^P$ and frequencies $\omega_{0,r}^P$ for planar symmetric basic wake flows at $Re = 220, 230, \dots, 350$ and $m = 0, +1$ and -1 .

axisymmetric wakes (illustrated in figure 10) reveals again that the non-axisymmetric eigenfunctions are concentrated in the regions where the planar symmetric wake displays larger axial shear.

The streamwise evolution of local absolute growth rate $\omega_{0,i}^P$ and real absolute frequency $\omega_{0,r}^P$ are illustrated in figure 16 for $m = 0, +1, -1$ and non-axisymmetric basic wakes in the range $220 \leq Re \leq 350$.

These results reveal that local absolute instability ($\omega_{0,i}^P > 0$) prevails in the near wake for all Reynolds numbers $Re > Re_1$, for which a planar symmetric wake exists. For Re close to Re_1 , the non-axisymmetric components of the basic flow are relatively small, and the symmetric $m = +1$ and antisymmetric $m = -1$ modes display very similar features. With increasing Reynolds number, however, the non-axisymmetric basic wake components strengthen and the $m = +1$ and $m = -1$ modes evolve separately. It is the symmetric $m = +1$ mode that displays the largest absolute instability, while the growth rate of the antisymmetric $m = -1$ increases more weakly with Reynolds number. At $Re = 350$, the maximum absolute growth rate of the $m = +1$ mode is in excess of 0.6, about twice the maximum value reached by the $m = -1$ mode for the same Reynolds number. For the axisymmetric configuration, the $m = 0$ modes are at most weakly absolutely unstable while the higher modes ($|m| \geq 2$, not shown) do not reach absolute instability.

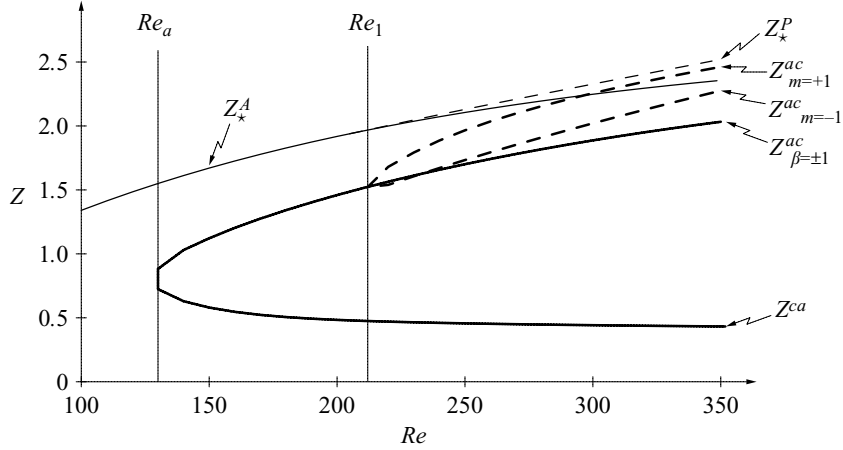


FIGURE 17. Reynolds-number dependence of absolutely unstable (thick curves) and reverse-flow (thin curves from figure 6) regions. For $Re > Re_a$, absolute instability prevails over the interval $Z^{ca} < Z < Z^{ac}$, and the different downstream marginal locations correspond to axisymmetric ($Z_{\beta=\pm 1}^{ac}$) and planar symmetric ($Z_{m=+1}^{ac}$ and $Z_{m=-1}^{ac}$) basic wakes.

5. Discussion

Local absolute instability analyses, based on both the axisymmetric and the planar symmetric basic wake flows, have demonstrated the existence of absolutely unstable regions in the near wake. The strength and the spatial extent of the absolute instabilities increase with Reynolds number. The axisymmetric basic wakes display absolute instability for $Re > Re_a \simeq 130$; planar symmetric basic wakes exist for $Re > Re_1 \simeq 212$ and are always absolutely unstable.

For axisymmetric sphere wakes, the largest absolute growth rates are reached for the $\beta = \pm 1$ modes, i.e. the first azimuthal harmonic. This corresponds to the general result (Monkewitz 1988b) that the first helical modes are the most unstable in axisymmetric wake profiles. For planar symmetric basic wakes, the non-axisymmetric basic flow components are found to enhance the instability, and the strongest absolute growth rates are found for the varicose $m = +1$ eigenmodes, which conserve the planar symmetry of the underlying basic flow.

The relationship between absolutely unstable and reverse-flow regions is illustrated in figure 17. For $Re > Re_a$, transition from convective to absolute instability occurs at Z^{ca} in the very near wake, and the flow returns to convective instability further downstream at Z^{ac} . For axisymmetric wakes, the absolutely unstable region terminates at $Z_{\beta=\pm 1}^{ac}$ where $\omega_{0,i}^A(\beta = \pm 1; Z, Re)$ changes sign. For planar symmetric wakes, the domains where the $m = +1$ ($m = -1$) modes display absolute instability are delimited by $Z_{m=+1}^{ac}$ ($Z_{m=-1}^{ac}$) defined as zero-crossings of $\omega_{0,i}^P(m = +1; Z, Re)$ (respectively of $\omega_{0,i}^P(m = -1; Z, Re)$). As already noted, the varicose $m = +1$ modes developing in the planar symmetric basic wakes display the strongest absolute instabilities: $Z_{m=+1}^{ac} > Z_{m=-1}^{ac} > Z_{\beta=\pm 1}^{ac}$. Comparison of the marginal Z^{ac} -curves with the stagnation Z_* -curves (from figure 6) shows that reverse flow prevails beyond the absolutely unstable region, both for the axisymmetric and the planar symmetric wakes: $Z_*^A > Z_{\beta=\pm 1}^{ac}$ and $Z_*^P > Z_{m=+1}^{ac}$. For planar symmetric wakes, however, the curves $Z_{m=+1}^{ac}$ and Z_*^P display the same asymptotic trend, which suggests that absolutely unstable and reverse-flow regions exactly overlap in the limit of large Reynolds numbers.

These results confirm the presence of a ‘wave-maker’ in the near wake of the sphere: the absolutely unstable region sustains fluctuations that develop *in situ* and

feed waves into the downstream convectively unstable domain. Moreover, since the dominant instability is a varicose ($m = +1$) mode, this is in agreement with the observed planar symmetry, rather than antisymmetry, of vortex shedding.

In the context of slowly spatially developing flows, theoretical investigations have shown that the onset of self-sustained nonlinear oscillations coincides with the appearance of local absolute instability (Pier, Huerre & Chomaz 2001; Chomaz 2005). According to this theory, vortex shedding in the sphere wake should occur as soon as $Re > Re_a \simeq 130$ and not only for $Re > Re_2 \simeq 272$. However, these theoretical analyses rely on the assumption of asymptotically slow streamwise variation, which is clearly not the case in the near wake of a sphere. This strong non-parallelism is thought to be responsible for the discrepancy between onset of absolute instability and onset of global instability. A similar discrepancy prevails for the two-dimensional wake of a circular cylinder, where absolute instability starts at $Re \simeq 25$, while the onset of vortex shedding is at $Re \simeq 47$ (Monkewitz 1988a; Provansal, Mathis & Boyer 1987; Pier 2002).

Concerning the Strouhal number, the frequency of a self-sustained time-periodic finite-amplitude vortex shedding regime is expected to be governed by the criterion of ‘steep’ or ‘elephant’ nonlinear global modes (Pier *et al.* 1998; Pier & Huerre 2001). According to this theory, the global frequency equals the real absolute frequency prevailing at the transition location from convective to absolute instability. From the plots of figures 11 and 16, it is seen that transition from convective to absolute instability occurs near the rear boundary of the sphere, for $Z \simeq 0.5$. In this very near-wake region, the associated real absolute frequencies are in the range $0.7 < \omega < 1.3$, which corresponds to $0.11 < St < 0.21$. More specifically, the frequencies prevailing at the convective/absolute transition cover the range $0.7 < \omega_{0,r}^A < 1.0$ for axisymmetric wakes ($130 \leq Re \leq 350$) and the range $1.2 < \omega_{0,r}^P < 1.3$ for planar symmetric wakes ($220 \leq Re \leq 350$). It would thus appear that the instability properties of the axisymmetric base flows yield frequency predictions closer to the actually observed shedding frequencies ($\omega = 0.85$ at $Re = 300$), while the non-axisymmetric base flows somewhat overestimate the shedding frequencies. However, these quantitative differences are thought to be inconclusive since the theoretical frequency selection criterion is based on the assumption of weakly non-uniform systems, while the local absolute frequency displays an important drop in the region $0.5 < Z < 1$. In view of these strong non-parallel effects in the vicinity of the sphere, the qualitative agreement found with the actually observed frequencies is deemed very reasonable. Note also that for the two-dimensional cylinder wake the global frequencies were similarly found to be systematically below those derived from the local absolute frequencies (Pier 2002). Also for the cylinder wake, Barkley (2006) has recently shown that a linear stability analysis of the mean flow yields better frequency predictions than a nonlinear frequency selection criterion applied to the basic flow. For the three-dimensional wake of a sphere, the relevance of this result and comparisons with different frequency selection criteria (reviewed in Chomaz 2005) are currently being investigated and will be reported in a future publication.

To conclude, it should be emphasized that the motivation of the present study was to completely work out the local absolute instability features of real sphere wakes in order to address the link between these local properties and the fundamental mechanisms dictating the global flow dynamics. While this link is not adequately verified, due, among other factors, to non-parallel effects, the existence of an absolutely unstable pocket has been clearly established.

The author is indebted to Arie Biesheuvel for triggering interest in the dynamics of the wake of spherical particles and to Jérôme Hœpffner for bringing the frequency damping method to his attention. Stimulating discussions with Marie Rastello and Jean-Louis Marié are gratefully acknowledged.

REFERENCES

- ÅKERVIK, E., BRANDT, L., HENNIGSON, D. S., HŒPFFNER, J., MAXEN, O. & SCHLATTER, P. 2006 Steady solutions of the Navier–Stokes equations by selective frequency damping. *Phys. Fluids* **18**, 068102.
- BARKLEY, D. 2006 Linear analysis of the cylinder wake mean flow. *Europhys. Lett.* **75**, 750–756.
- BERS, A. 1983 Space-time evolution of plasma instabilities—absolute and convective. In *Handbook of plasma physics* (ed. M. Rosenbluth & R. Sagdeev), pp. 451–517. North-Holland.
- BOUCHET, G., MEBAREK, M. & DUŠEK, J. 2006 Hydrodynamic forces acting on a rigid fixed sphere in early transitional regimes. *Eur. J. Mech. B/Fluids* **25**, 321–336.
- BOYD, J. P. 2001 *Chebyshev and Fourier Spectral Methods*. Dover.
- BRIGGS, R. J. 1964 *Electron-Stream Interaction with Plasmas*. MIT Press.
- CANUTO, C., HUSSAINI, M. J. & QUARTERONI, A. 1988 *Spectral Methods in Fluid Dynamics*. Springer.
- CHOMAZ, J.-M. 2005 Global instabilities in spatially developing flows: non-normality and nonlinearity. *Annu. Rev. Fluid Mech.* **37**, 357–392.
- GALLAIRE, F., RUITH, M., MEIBURG, E., CHOMAZ, J.-M. & HUERRE, P. 2006 Spiral vortex breakdown as a global mode. *J. Fluid Mech.* **549**, 71–80.
- GHIDERSA, B. & DUČEK, J. 2000 Breaking of axisymmetry and onset of unsteadiness in the wake of a sphere. *J. Fluid Mech.* **423**, 33–69.
- GODA, K. 1979 A multistep technique with implicit difference schemes for calculating two- or three-dimensional cavity flows. *J. Comut. Phys.* **30**, 76–95.
- HUERRE, P. 2000 Open shear flow instabilities. In *Perspectives in Fluid Dynamics* (ed. G. K. Batchelor, H. K. Moffatt & M. G. Worster), pp. 159–229. Cambridge: University Press.
- JOHNSON, T. A. & PATEL, V. C. 1999 Flow past a sphere up to a Reynolds number of 300. *J. Fluid Mech.* **378**, 19–70.
- LESSHAFT, L., HUERRE, P., SAGAUT, P. & TERRACOL, M. 2006 Nonlinear global modes in hot jets. *J. Fluid Mech.* **554**, 393–409.
- MITTAL, R. 1999 Planar symmetry in the unsteady wake of a sphere. *AIAA J.* **37**, 388–390.
- MITTAL, R. & IACCARINO, G. 2005 Immersed boundary methods. *Annu. Rev. Fluid Mech.* **37**, 239–261.
- MONKEWITZ, P. A. 1988a The absolute and convective nature of instability in two-dimensional wakes at low Reynolds numbers. *Phys. Fluids* **31**, 999–1006.
- MONKEWITZ, P. A. 1988b A note on vortex shedding from axisymmetric bluff bodies. *J. Fluid Mech.* **192**, 561–575.
- NAKAMURA, I. 1976 Steady wake behind a sphere. *Phys. Fluids* **19**, 5–8.
- NATARAJAN, R. & ACRIVOS, A. 1993 The instability of the steady flow past spheres and disks. *J. Fluid Mech.* **254**, 323–344.
- NICHOLS, J. W., SCHMID, P. J. & RILEY, J. J. 2007 Self-sustained oscillations in variable-density round jets. *J. Fluid Mech.* **582**, 341–376.
- PIER, B. 2002 On the frequency selection of finite-amplitude vortex shedding in the cylinder wake. *J. Fluid Mech.* **458**, 407–417.
- PIER, B. & HUERRE, P. 2001 Nonlinear synchronization in open flows. *J. Fluid Struct.* **15**, 471–480.
- PIER, B., HUERRE, P. & CHOMAZ, J.-M. 2001 Bifurcation to fully nonlinear synchronized structures in slowly varying media. *Physica D* **148**, 49–96.
- PIER, B., HUERRE, P., CHOMAZ, J.-M. & COUAIRO, A. 1998 Steep nonlinear global modes in spatially developing media. *Phys. Fluids* **10**, 2433–2435.
- PROVANSAL, M., MATHIS, C. & BOYER, L. 1987 Bénard–von Kármán instability: transient and forced regimes. *J. Fluid Mech.* **182**, 1–22.
- RASPO, I., HUGUES, S., SERRE, E., RANDRIAMAMPIANINA, A. & BONTOUX, P. 2002 A spectral projection method for the simulation of complex three-dimensional rotating flows. *Computers Fluids* **31**, 745–767.

- Roos, F. W. & WILLMARTH, W. W. 1971 Some experimental results on sphere and disk drag. *AIAA J.* **9**, 285–291.
- SAKAMOTO, H. & HANIU, H. 1995 The formation mechanism and shedding frequency of vortices from a sphere in uniform shear flow. *J. Fluid Mech.* **287**, 151–171.
- SCHOUVEILER, L. & PROVANSAL, M. 2002 Self-sustained oscillations in the wake of a sphere. *Phys. Fluids* **14**, 3846–3854.
- SEVILLA, A. & MARTÍNEZ-BAZÁN, C. 2004 Vortex shedding in high Reynolds number axisymmetric bluff-body wakes: local linear instability and global bleed control. *Phys. Fluids* **16**, 3460–3469.
- TOMBOULIDES, A. G. & ORSZAG, S. A. 2000 Numerical investigation of transitional and weak turbulent flow past a sphere. *J. Fluid Mech.* **416**, 45–73.

[A12]

Signalling problem in absolutely unstable systems

B. Pier

Theoretical and Computational Fluid Dynamics **25**, 7–17 (2011)

doi :10.1007/s00162-009-0166-x
<https://hal.archives-ouvertes.fr/hal-00426387>

Benoît Pier

Signalling problem in absolutely unstable systems

Received: 11 May 2009 / Accepted: 1 September 2009 / Published online: 22 October 2009
© Springer-Verlag 2009

Abstract The dynamics of unstable systems crucially depends on the nature of the instability, either convective or absolute. The signalling problem, which is the study of the spatial response to a localized time-harmonic forcing, is generally believed to be relevant only for stable or convectively unstable systems and to be ill-posed for absolutely unstable systems, where the self-sustained perturbations grow faster than the forced harmonic response. The present investigation shows that the signalling problem may still be well posed for media displaying absolutely unstable regions. Considering weakly spatially inhomogenous systems, conditions are derived for the validity of the signalling problem. The complete spatial response to harmonic forcing is first analytically derived in terms of asymptotic approximations and then confirmed by direct numerical simulations.

Keywords Absolute instabilities · Causality · Signalling problem · WKBJ

PACS 47.10.A-, 47.15.Fe, 47.20.-k, 47.11.St, 47.20.Ib, 47.35.-i

1 Introduction

In spatially homogenous systems, linear stability characteristics are derived from the dispersion relation $\omega = \Omega(k)$ between the frequencies ω and the wave numbers k of normal modes of the form $e^{i(kx - \omega t)}$, with x and t denoting streamwise distance and time, respectively. These stability properties can be understood by resorting to different methods: temporal, spatial or spatio-temporal [8, 10, 18].

In a *temporal* approach, a spatially harmonic perturbation of real wave number k is considered. This wave-like initial perturbation evolves in time with a complex frequency ω . Its spatial structure, determined by the wave number k , remains unchanged while its amplitude grows or decays with time. Growth or decay is determined by the sign of the temporal growth rate¹ ω_i , while propagation takes place with a phase speed ω_r/k . This analysis based on real wave numbers and complex frequencies is known as the temporal problem.

In a *spatial* approach, localized harmonic forcing is applied with real frequency ω , say at $x = 0$. The spatial response to this forcing yields waves with complex wave numbers k . The wavelength of the spatial response is determined by k_r while the spatial growth or decay depends on k_i : for $x \rightarrow +\infty$, the spatial response grows when $k_i < 0$ and decays when $k_i > 0$; the reverse holds for $x \rightarrow -\infty$. The analysis based on real frequencies and complex wave numbers is known as the spatial, or signalling, problem.

¹ Throughout this paper, subscripts r and i denote real and imaginary parts of complex values.

Communicated by T. Colonius

B. Pier ()

Laboratoire de mécanique des fluides et d'acoustique, École centrale de Lyon—CNRS—Université Claude-Bernard Lyon 1—INSA Lyon, 36 avenue Guy-de-Collongue, 69134 Écully cedex, France
E-mail: benoit.pier@ec-lyon.fr

The full *spatio-temporal* stability properties may be investigated by applying an impulsive localized perturbation: the analysis of the resulting wave packet yields the complete dispersion relation between complex wave numbers k and complex frequencies ω . While the impulsively started wave packet decays in stable media, a growing response develops from the impulse location in unstable systems. If the growing wave packet propagates away from its source and eventually leaves the medium unperturbed, the instability is said to be *convective*. If, by contrast, the instability grows in place and invades the system both upstream and downstream, the instability is said to be *absolute*. Convectively unstable (CU) systems do not display intrinsic dynamics and essentially behave as amplifiers: external perturbations are amplified while propagating through the system, and without continuous external input the medium returns to its unperturbed state. By contrast, absolutely unstable (AU) systems display non-trivial dynamics without external forcing: perturbations expand in both upstream and downstream directions so as to cover the entire domain and continue to grow exponentially at every point.

These stability concepts remain valid *locally* for spatially inhomogenous systems, provided the characteristic inhomogeneity length scale is large compared to a typical instability length scale. However, the connection between local stability characteristics and the long-term global dynamics of spatially developing systems is far from obvious. In a linear framework, it has been shown [4, 5, 11] that the presence of local absolute instability is a necessary but not sufficient condition for global instability: in general an AU region of finite extent is required for a spatially developing medium to become globally unstable. Thus there exists a wide range of parameter settings for which a medium does not support any self-sustained fluctuations despite the presence of a region of local absolute instability. In such a situation, the linear signalling problem is legitimate and this is precisely the class of systems addressed in the present paper.

Globally stable but locally absolutely unstable systems are encountered in a variety of configurations of practical interest, among which wakes and boundary layers: the cylinder wake flow for Reynolds numbers in the range $25 < Re < 49$ [12], a class of “synthetic” wake flows [16, 17], the wake of a sphere [15], the three-dimensional boundary layer produced by a rotating disk [7].

The paper is organized as follows: After formulating the problem in terms of the widely used partial differential complex Ginzburg–Landau equation (Sect. 2), its local (Sect. 3) and global (Sect. 4) stability properties are recalled. In Sect. 5, the correspondence between the complex space and frequency planes and the structure of the wave number branches are analysed. The complete analytic solution to the signalling problem is obtained in Sect. 6 in terms of asymptotic approximations and discussed in Sect. 7. These results are confirmed by direct numerical simulations in Sect. 8.

2 Problem formulation

Partial differential model equations account for the dynamics of a variety of physical systems [6] and are often tractable by analytical methods. The linearized complex Ginzburg–Landau model (1) has on many occasions proven to be a convenient testground to recognize and study generic features that have later been identified in a variety of situations. The same strategy is adopted here.

The system under consideration is assumed to be described by a complex scalar field $\psi(x, t)$ in an infinite one-dimensional spatially inhomogenous domain and it is governed by

$$\frac{\partial \psi}{\partial t} = -i \left(\omega_0(X) + \frac{1}{2} \omega_{kk}(X) k_0(X)^2 \right) \psi + \omega_{kk}(X) k_0(X) \frac{\partial \psi}{\partial x} + \frac{i}{2} \omega_{kk}(X) \frac{\partial^2 \psi}{\partial x^2} + S(x, t), \quad (1)$$

where the complex functions $\omega_0(X)$, $k_0(X)$ and $\omega_{kk}(X)$ account for the local properties of the medium and only depend on a slow space variable $X = \epsilon x$. The coefficients of (1) have been cast in this form for reasons that will become clear in the next section. The weak inhomogeneity parameter $\epsilon \ll 1$ is defined as the ratio of the typical instability length scale to the inhomogeneity length scale of the medium. The source function $S(x, t)$ represents an externally applied forcing to be specified below. While Eq. 1 applies to the real x -axis, the functions $\omega_0(X)$, $k_0(X)$ and $\omega_{kk}(X)$ are assumed to be analytic and their continuation in the complex X -plane will be used in the following sections.

3 Local stability properties

In the subsequent discussion, constant use is made of the *local* properties of system (1). Local characteristics are derived from (1) by freezing X to some arbitrary (possibly complex) value and studying the corresponding spatially homogenous system

$$\frac{\partial \psi}{\partial t} = -i \left(\omega_0 + \frac{1}{2} \omega_{kk} k_0^2 \right) \psi + \omega_{kk} k_0 \frac{\partial \psi}{\partial x} + \frac{i}{2} \omega_{kk} \frac{\partial^2 \psi}{\partial x^2} + S(x, t), \quad (2)$$

where the dependence of the coefficients on the parameter X has been omitted. Normal modes of the form $e^{i(kx - \omega t)}$, with complex frequency ω and complex wave number k , are then governed by the local dispersion relation

$$\omega = \Omega(k) \equiv \omega_0 + \frac{1}{2} \omega_{kk} (k - k_0)^2. \quad (3)$$

To satisfy causality, temporal growth rates must be bounded which requires that $\text{Im } \omega_{kk} < 0$. The particular form in which the coefficients of (1) and (2) have been cast brings to the fore the local complex absolute frequency ω_0 associated with the local complex absolute wave number k_0 determined by the zero group velocity condition [2,3]

$$\omega_0 = \Omega(k_0) \quad \text{with} \quad \frac{\partial \Omega}{\partial k}(k_0) = 0.$$

For impulsive forcing of the form $S(x, t) = \delta(x)\delta(t)$, where δ denotes the Dirac delta function, the absolute frequency ω_0 characterizes the temporal evolution of the resulting wave packet observed at a fixed station: when $\text{Im } \omega_0 < 0$, the system is stable or convectively unstable and the wave packet either decays or grows while being swept away by advection; when $\text{Im } \omega_0 > 0$, the system is absolutely unstable and the impulse response exponentially grows at each point in space.

Now consider a spatially localized but temporally harmonic forcing of (possibly complex) frequency ω_f , switched on at $t = 0$, i.e., $S(x, t) = \delta(x)H(t)e^{-i\omega_f t}$ where H denotes the Heaviside unit step function. The spatial response to this harmonic forcing consists in traveling waves of frequency ω_f and their wave numbers are derived from (3) as

$$k^\pm(\omega_f) = k_0 \pm \sqrt{2 \frac{\omega_f - \omega_0}{\omega_{kk}}}. \quad (4)$$

Upon choosing the square-root branch cut in (4) along the positive real axis and with the square-root symbol denoting the root with positive imaginary part, the k^+ and k^- branches pertain to the domains $x > 0$ and $x < 0$ on either side of the forcing. However, turning on the forcing at $t = 0$ also produces a transient wave packet that grows according to the absolute growth rate $\text{Im } \omega_0$ at any fixed spatial location. Hence, two different situations arise depending on the relative values of $\text{Im } \omega_f$ and $\text{Im } \omega_0$:

- When $\text{Im } (\omega_f - \omega_0) > 0$ the switch-on wave packet is overwhelmed for large time by the spatial response tuned to the forcing frequency ω_f , and the signalling problem is well-posed.
- When $\text{Im } (\omega_f - \omega_0) < 0$, the switch-on wave packet overwhelms the spatial response at ω_f and the harmonic forcing does not succeed in tuning the medium to the externally applied frequency. The signalling problem is then ill-posed.

4 Global stability properties

In spatially inhomogeneous systems governed by (1), the above discussion yields stability characteristics prevailing locally at each X . However the associated global behaviour cannot be immediately derived and must be analysed carefully [5,11].

In a typical situation of interest, the local absolute growth rate $\text{Im } \omega_0(X)$ displays a single maximum over the real X -axis and the medium is stable for $X \rightarrow \pm\infty$. In the same spirit as Huerre and Monkewitz [9] and in order to keep computational difficulties to a minimum, it is assumed that

$$\omega_0(X) = \omega_s + \frac{1}{2} \omega_{XXs} (X - X_s)^2, \quad (5)$$

where ω_s , ω_{XXs} and X_s are complex parameters with $\text{Im } \omega_{XXs} < 0$. By resorting to asymptotic expansions, it has been shown [5,11] that the impulse response of the spatially developing system is then dominated for large time by a global mode of frequency ω_s . Hence, whenever $\text{Im } \omega_s < 0$ the system does not display self-sustained solutions: any perturbation eventually decays even though large amplification may be observed in

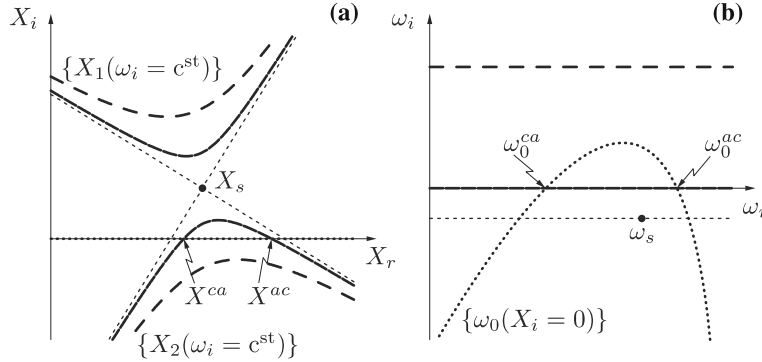


Fig. 1 Correspondence by the analytic mapping $\omega_0(X)$ between **a** complex X -plane and **b** complex ω -plane. Associated curves are rendered by the same symbols. The real X -axis is mapped onto the dotted curve $\{\omega_0(X_i = 0)\}$, and the real frequencies ω_0^{ca} , ω_0^{ac} correspond to the boundaries X^{ca} , X^{ac} of the AU interval. Horizontal lines in **(b)** are associated in **(a)** with the corresponding isolines $\{X_{1,2}(\omega_i = c^{st})\}$ of constant absolute growth rate

the transient régime. Systems with $\text{Im } \omega_s < 0$ are thus globally stable whether or not they exhibit an interval of local absolute instability.

The paper is concerned with globally stable but locally absolutely unstable systems. In this situation all transient behaviour displays eventual decay, and it is legitimate to study the long-term spatial response to an externally applied time-harmonic forcing.

5 Structure of complex X -plane and spatial branches

When media are considered that are both globally stable and locally absolutely unstable, the local absolute frequency is of the form (5) with $\text{Im } \omega_s < 0$ and positive absolute growth rate ($\omega_{0,i}(X) > 0$) occurs over some finite interval $X^{ca} < X < X^{ac}$. Note that this is possible only if the saddle point X_s of $\omega_0(X)$ is not located on the real X -axis. Let $\omega_0^{ca} \equiv \omega_0(X^{ca})$ and $\omega_0^{ac} \equiv \omega_0(X^{ac})$ denote the real marginal absolute frequencies at the boundaries of the AU interval.

The function $\omega_0(X)$ defines an analytic mapping between the complex X -plane and the complex ω -plane as shown in Fig. 1. The real X -axis is mapped onto the locus denoted as $\{\omega_0(X_i = 0)\}$ (dotted parabolic curve in Fig. 1b) crossing the real frequency axis twice at ω_0^{ca} and ω_0^{ac} , corresponding to the marginally absolutely unstable positions X^{ca} and X^{ac} . Note that Fig. 1 illustrates a configuration where $\omega_0^{ca} < \omega_0^{ac}$ and $\text{Im } X_s > 0$; situations with $\omega_0^{ac} < \omega_0^{ca}$ and/or $\text{Im } X_s < 0$ yield similar pictures and results.

In the complex X -plane (Fig. 1a), isolines of constant absolute growth rate $\text{Im } \omega_0(X)$ are obtained as pre-images by ω_0^{-1} of horizontal lines in the ω -plane. When such a line $\{\omega_i = c^{st}\}$ is located above the $\{\omega_0(X_i = 0)\}$ curve in the ω -plane (thick dashed line in Fig. 1b), the two corresponding isolines in the X -plane (thick dashed curves in Fig. 1a) do not cross the real axis and may be labelled $\{X_{1,2}(\omega_i = c^{st})\}$, where the subscripts 1 or 2 correspond to curves confined to the upper or lower half X -planes, respectively. When the line $\{\omega_i = c^{st}\}$ is lowered onto the real ω -axis, the associated X_1 and X_2 curves move towards each other. Since the real ω -axis is crossed by the $\{\omega_0(X_i = 0)\}$ -curve at ω_0^{ca} and ω_0^{ac} , one of the associated isolines (indicated by solid curves in Fig. 1a) necessarily crosses the real X -axis at X^{ca} and X^{ac} . In Fig. 1a, it is the lower $\{X_2(\omega_i = 0)\}$ -isoline that crosses the X -axis while the associated $\{X_1(\omega_i = 0)\}$ -isoline lies entirely within the upper half-plane. Note that the (thin-dashed) curves $\{X_{1,2}(\omega_i = \text{Im } \omega_s)\}$ pinch at the saddle point X_s for the line $\{\omega_i = \text{Im } \omega_s\}$, which is however located in the lower frequency half-plane and will not be considered here.

When solving the dispersion relation (3) with coefficients depending on X for a given frequency ω_f , the two spatial branches are obtained as

$$k^\pm(X, \omega_f) = k_0(X) \pm \sqrt{2 \frac{\omega_f - \omega_0(X)}{\omega_{kk}(X)}}. \quad (6)$$

In the complex X -plane, these expressions display two branch points at $X_{1,2}(\omega_f)$, where $\omega_0(X) = \omega_f$, and branch cuts must be introduced. Upon choosing the branch cut for the square-root function in (6) along positive real values of its argument, the causality condition $\text{Im } \omega_{kk}(X) < 0$ guarantees that the branch cuts for

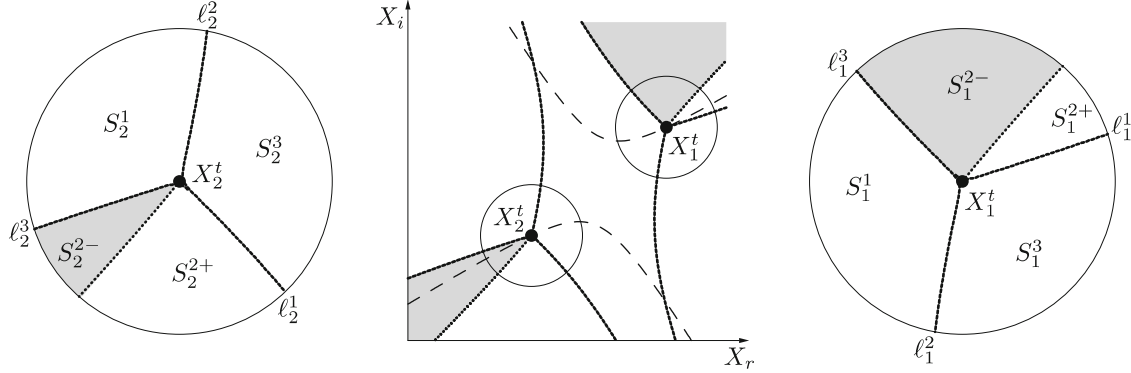


Fig. 2 Turning points and Stokes lines in the complex X -plane. The two turning points $X_{1,2}^t$ are located on their respective $\{X_{1,2}(\omega_i = 0)\}$ -isocontours (dashed lines). Each turning point is associated with a branch cut (dotted curves) and gives rise to a network of three Stokes lines (solid curves)

k^\pm lie within the regions where $\text{Im}[\omega_f - \omega_0(X)] < 0$ and thus do not intersect the region located between the $\{X_{1,2}(\omega_i = \text{Im } \omega_f)\}$ -curves where $\text{Im}[\omega_f - \omega_0(X)] > 0$. Hence the branch cut starting at $X_1(\omega_f)$ is located above the $\{X_1(\omega_i = \text{Im } \omega_f)\}$ -curve and the branch cut starting at $X_2(\omega_f)$ is located below the $\{X_2(\omega_i = \text{Im } \omega_f)\}$ -curve (see also Fig. 2). As indicated in Sect. 3, the spatial branches (6) may be unambiguously interpreted as downstream k^+ or upstream k^- branches when $\text{Im}[\omega_f - \omega_0(X)] > 0$, which corresponds to the domain of the X -plane located between the X_1 and X_2 curves. The above choice of branch cuts thus extends the definition of the $k^\pm(X, \omega_f)$ wave number branches to the entire complex X -plane for any frequency ω_f with $\text{Im } \omega_f > \text{Im } \omega_s$ (region above thin-dashed line in Fig. 1b). When considering *real* forcing frequencies ω_f in (6), the choice of k^+ and k^- branches corresponds to the downstream and upstream branches derived by traditional causality considerations in the stable or convectively unstable domain of the complex X -plane, characterized by $\text{Im } \omega_0(X) < 0$ and located between the solid $\{X_{1,2}(\omega_i = 0)\}$ -curves of Fig. 1.

6 Signalling problem in spatially developing medium

For the signalling problem, the system is driven at some position on the real axis, say X_f , with a real frequency, say ω_f , and the spatial response to this localized time-harmonic forcing is considered. Since the medium is assumed to be globally stable, any switch-on transients will eventually decay and it is legitimate to seek a long-term response of the form $\psi(x, t) = \phi(x)e^{-i\omega_f t}$, globally tuned to the forcing frequency.

Under the slowly-varying medium hypothesis characterized by $\epsilon \ll 1$, time-periodic solutions may be obtained in terms of WKBJ approximations [1] where the spatial structure is described by a rapidly varying complex phase, accounting for the local wavelength and spatial growth/decay rate, and a slowly varying envelope. For a given global frequency ω_f , a WKBJ approximation is of the form

$$\psi(x, t) = A(X) \exp \left[\frac{i}{\epsilon} \int_{X_f}^X k(u, \omega_f) du - i\omega_f t \right] \quad (7)$$

where the envelope $A(X)$ is expanded in powers of ϵ as $A \sim A_0 + \epsilon A_1 + \dots$ and governed by amplitude equations that can be computed recursively up to any order. In (7), the local wave number $k(X, \omega_f)$ satisfies the local dispersion relation and follows one of the two spatial branches (6). Hence, in different domains of the complex X -plane, the solution may be approximated by different WKBJ expansions of the form (7) pertaining to different spatial wave number branches.

The above WKBJ expansions are singular [1] at each of the two turning points $X^t = X_{1,2}(\omega_f)$ of the dispersion relation, where $k^+(X^t, \omega_f) = k^-(X^t, \omega_f)$. These turning points are located on their respective $\{X_{1,2}(\omega_i = 0)\}$ -contours, see Fig. 2. From a turning point, three Stokes lines emerge, defined by $\text{Im} \int_{X^t}^X [k^+(u, \omega_f) - k^-(u, \omega_f)] du = 0$, and partition the complex plane into three different sectors. Along these Stokes lines both WKBJ approximations remain of the same order of magnitude, while inside the sectors one approximation is exponentially large with respect to the other.

Consider first the turning point $X_1^t \equiv X_1(\omega_f)$, located on the upper $\{X_1(\omega_i = 0)\}$ -contour in the complex X -plane (upper dashed curve in Fig. 2), and the two associated linearly independent WKBJ approximations

$$\Psi_1^\pm = A^\pm(X) \exp \left[\frac{i}{\epsilon} \int_{X_1^t}^X k^\pm(u, \omega_f) du - i\omega_f t \right]. \quad (8)$$

Three Stokes lines and one branch cut emanate from X_1^t . The branch cut (dotted line), along which k^+ and k^- branches get exchanged, is located above the $\{X_1(\omega_i = 0)\}$ -curve and extends from X_1^t towards infinity in the upper complex X -plane. The three Stokes lines ℓ_1^1 , ℓ_1^2 and ℓ_1^3 divide the complex plane into three sectors S_1^1 , S_1^2 and S_1^3 , and sector S_1^2 is further divided into S_1^{2-} and S_1^{2+} by the branch cut, see zoom to right of Fig. 2. Along these Stokes lines both approximations Ψ_1^\pm are of the same magnitude, and the dominant (resp. subdominant) solution becomes subdominant (resp. dominant) whenever a Stokes line is crossed.

Since the region near $X = +\infty$ is at most convectively unstable, the spatial response to the external forcing there necessarily features the k^+ wave number branch and is thus made up of the subdominant Ψ_1^+ approximation. Hence the dominant approximation Ψ_1^- is not present in the sector S_1^3 , defined as the sector containing the region near $X = +\infty$, and the solution of the signalling problem in S_1^3 and along its bordering Stokes lines ℓ_1^1 and ℓ_1^2 is of the form $\psi \sim C_1^+ \Psi_1^+$, solely made up of the subdominant Ψ_1^+ approximation with, say, coefficient C_1^+ . When continuing the solution from S_1^3 into S_1^1 across ℓ_1^1 , approximation Ψ_1^+ becomes dominant. Inside sector S_1^1 , any subdominant contribution of the form $C_1^- \Psi_1^-$ may be present. On the next Stokes line ℓ_1^3 , both approximations are again of the same order, and the solution is then approximated by

$$\psi \sim C_1^- \Psi_1^- + C_1^+ \Psi_1^+ \quad \text{along } \ell_1^3. \quad (9)$$

Similarly, when continuing the solution from S_1^3 into S_1^{2+} across ℓ_1^1 , approximation Ψ_1^+ becomes dominant and a solution of the form $C_1^\mp \Psi_1^\mp + C_1^\pm \Psi_1^\pm$ must be considered inside sector S_1^{2+} . When crossing the branch cut, the approximations Ψ_1^+ and Ψ_1^- get exchanged so that the same WKBJ superposition reads $C_1^+ \Psi_1^- + C_1^\mp \Psi_1^\pm$ in S_1^{2-} , with Ψ_1^- now the dominant term. On the Stokes line ℓ_1^3 , both approximations are again of the same order, and the solution is then approximated by

$$\psi \sim C_1^+ \Psi_1^- + C_1^\mp \Psi_1^\pm \quad \text{along } \ell_1^3. \quad (10)$$

Finally, comparing both expansions (9) and (10) shows that all coefficients C_1^\mp , C_1^- and C_1^+ are identical to, say, C_1 . In the different regions around turning point X_1^t , the following approximations to the signalling problem are then obtained

$$\psi \sim \begin{cases} C_1 \Psi_1^+ & \text{in } S_1^{2+}, S_1^3, S_1^1 \text{ and along } \ell_1^1, \ell_1^2, \\ C_1 (\Psi_1^+ + \Psi_1^-) & \text{along } \ell_1^3, \\ C_1 \Psi_1^- & \text{in } S_1^{2-}. \end{cases} \quad (11)$$

Note that nothing special happens across the branch cut, except relabeling of the superscripts of k^\pm and Ψ_1^\pm . Hence a result similar to the above holds even in situations where the orientation of the Stokes lines is such that the branch cut is not confined between ℓ_1^1 and ℓ_1^3 (see example in Fig. 3a).

Thus it is only across the Stokes line ℓ_1^3 , defined as the Stokes line opposite the sector containing the region near $X = +\infty$ (see also Fig. 3 for further examples), that a change in the dominant WKBJ approximation occurs: a crossover between k^+ and k^- as dominant wave number branches takes place across ℓ_1^3 while everywhere else the dominant local wave number continuously depends on X .

Consider now the turning point $X_2^t \equiv X_2(\omega_f)$, located on the lower $\{X_2(\omega_i = 0)\}$ -contour (lower dashed curve in Fig. 2). The same reasoning as above holds for the expansion of the spatial response in terms of the two associated WKBJ approximations

$$\Psi_2^\pm = A^\pm(X) \exp \left[\frac{i}{\epsilon} \int_{X_2^t}^X k^\pm(u, \omega_f) du - i\omega_f t \right]. \quad (12)$$

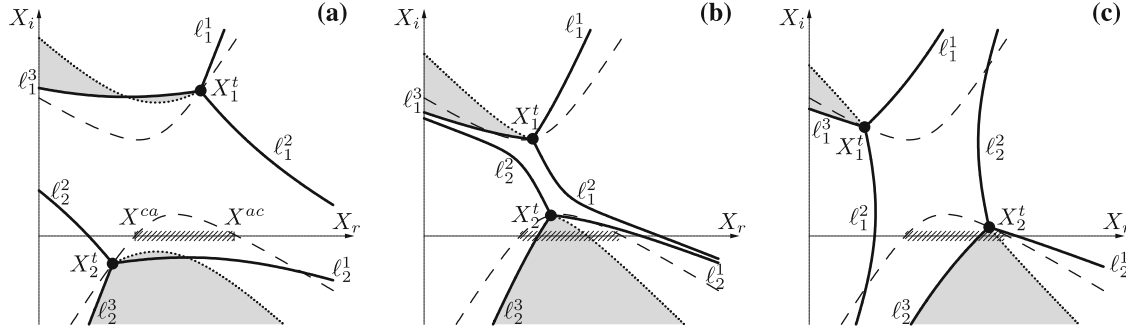


Fig. 3 Spatial structure of the signalling problem in the complex X -plane for different forcing frequencies ω_f . The two turning points $X_{1,2}^t$ (thick dots) are located on their respective $\{X_{1,2}(\omega_i = 0)\}$ -isolines (dashed curves) and give rise to a network of Stokes lines (solid curves) and branch cuts (dotted lines). The spatial response is dominated by the k^- wave number branch in the shaded regions and by the k^+ branch everywhere else. The AU interval of the real X -axis is hatched. **a** With ω_f outside the range $\omega_0^{ca} - \omega_0^{ac}$, the turning points $X_{1,2}^t$ are located in opposite half X -planes and the k^+ wave number dominates over the entire real X -axis. **b,c** With ω_f within the range $\omega_0^{ca} - \omega_0^{ac}$, the turning points $X_{1,2}^t$ are located in same half X -planes, and the spatial response displays a jump in the dominant wave number on the real axis at the intersection with the ℓ_2^3 Stokes line

The associated branch cut (dotted curve) is now located below the $\{X_2(\omega_i = 0)\}$ -curve. With Stokes lines and sectors around X_2^t labeled as in Fig. 2 (left zoom), the solution to the signalling problem is then approximated by

$$\psi \sim \begin{cases} C_2 \Psi_2^+ & \text{in } S_2^{2+}, S_2^3, S_2^1 \text{ and along } \ell_2^1, \ell_2^2, \\ C_2(\Psi_2^+ + \Psi_2^-) & \text{along } \ell_2^3, \\ C_2 \Psi_2^- & \text{in } S_2^{2-}, \end{cases} \quad (13)$$

and crossover between the dominant k^+ and k^- wave number branches takes place across the Stokes line ℓ_2^3 , located opposite the sector containing the region near $X = +\infty$. In the complex X -plane, the solution is thus dominated by the k^+ branch everywhere except in the two sectors issuing from the turning points X_1^t and X_2^t , respectively, and delimited by the Stokes lines ℓ_1^3 or ℓ_2^3 and the corresponding branch cuts; these regions are indicated in grey in Fig. 2. Note that, although the approximations (12) are formally identical to (8), the spatial branches in (12) are integrated from X_2^t and the dominant/subdominant character depends on the behaviour for X radiating away from this turning point.

The relationship between the constants C_1 and C_2 is readily derived by comparing the WKBJ expansions (11) and (13) in regions where they overlap, for example for $X \rightarrow +\infty$. From

$$\psi \sim C_1 A^+(X) \exp \left[\frac{i}{\epsilon} \int_{X_1^t}^X k^+(u, \omega_f) du - i\omega_f t \right]$$

and $\psi \sim C_2 A^+(X) \exp \left[\frac{i}{\epsilon} \int_{X_2^t}^X k^+(u, \omega_f) du - i\omega_f t \right]$

it follows that

$$C_2 = C_1 \exp \left[\frac{i}{\epsilon} \int_{X_1^t}^{X_2^t} k^+(u, \omega_f) du - i\omega_f t \right]. \quad (14)$$

The above results (11, 13, 14) entirely specify the asymptotic WKBJ approximation to the unique solution of frequency ω_f satisfying a causal boundary condition, i.e., made up of the k^+ branch near $X = +\infty$. The spatial response of system (1) to harmonic forcing of frequency ω_f thus follows this solution over the real X -axis on the right side of the forcing location, for $X_f < X < +\infty$. When the external forcing is applied with

$\mathcal{O}(1)$ amplitude, the response is also $\mathcal{O}(1)$ near X_f which yields the magnitude of the remaining unknown constant as $C_1 \sim \exp \frac{i}{\epsilon} \int_{X_f}^{X'_1} k^+(u, \omega_f) du$. Note however that in this linear setting the precise value of C_1 , and thus the exact spatial location of the forcing, does not influence the spatial structure of the response to the right side of the forcing.

The spatial response pertaining to the domain $-\infty < X < X_f$ on the left side of the forcing is similarly derived from the unique solution of frequency ω_f made up of the subdominant k^- branch for $X \rightarrow -\infty$. The corresponding details are straightforward and will not be presented here. In a typical situation of interest, forcing is applied upstream of the AU domain, i.e., $X_f < X^{ca}$, so that all relevant features concerning the structure of the spatial response over the AU interval are derived from the solution valid over $X_f < X < +\infty$.

7 Discussion

The previous analysis yields the spatial response to harmonic forcing over the entire X -axis, including the AU interval $X^{ca} < X < X^{ac}$.

For harmonic forcing of real frequency ω_f applied at some station X_f upstream of the AU domain, local causality considerations suggest that the spatial response follows the $k^+(X, \omega_f)$ wave number branch over the stable or CU interval $X_f < X < X^{ca}$, between the forcing location and onset of absolute instability. Similarly, in the at most convectively unstable downstream domain extending from $X = X^{ac}$ to $X \rightarrow +\infty$, the solution is obtained as the downstream response to some upstream located cause and is there also expected to follow the $k^+(X, \omega_f)$ wave number branch.

However, local considerations fail to predict the structure of the spatial response in the AU interval $X^{ca} < X < X^{ac}$ since the k^\pm wave number branches (6) are there only formal solutions of the local dispersion relation and cannot be interpreted in terms of upstream or downstream spatial branches.

Based on the developments of the previous section, it will now be shown that in the AU region $X^{ca} < X < X^{ac}$ the structure of the spatial response and the dominant wave number essentially depend on the positions of the turning points $X'_{1,2} \equiv X_{1,2}(\omega_f)$ relative to the real X -axis and thus on the relative values of ω_f , ω_0^{ca} and ω_0^{ac} .

Indeed, a forcing frequency ω_f outside the range $\omega_0^{ca} - \omega_0^{ac}$ lies above the $\{\omega_0(X_i = 0)\}$ curve in the complex ω -plane (dotted parabolic curve of Fig. 1b). The associated turning points are then located on either side of the real X -axis: X'_1 in the upper half-plane and X'_2 on parts of the $\{X_2(\omega_i = 0)\}$ -isoline in the lower half-plane, as illustrated in Fig. 3a. In this situation, the branch cuts emanating from $X'_{1,2}$ and, respectively, extending into the far upper and lower half X -planes do not cross the real X -axis. As a result, the spatial branches $k^\pm(X, \omega_f)$ continuously depend on X over the entire real axis, and the $k^+(X, \omega_f)$ branches prevailing on either side of the AU interval (hatched in Fig. 3) are continuously connected over the real X -axis. Note that the branch cut starting at X'_2 , while remaining below the $\{X_2(\omega_i = 0)\}$ -isoline, could cross the real axis twice before heading toward the far lower X -plane; however, the conclusions are not affected as long as an even number of crossings occurs since the branch cut could then be modified so as to avoid the X -axis. At the same time, the Stokes lines ℓ_1^3 and ℓ_2^3 over which an exchange of the dominant WKBJ approximations occurs do not cross the real X -axis either. The regions in the complex X -plane where the spatial response is dominated by the k^- branch (shaded regions in Fig. 3a) then do not overlap the real X -axis. Hence the spatial response to harmonic forcing is approximated by the WKBJ approximation featuring the k^+ wave number branch over the entire domain $X_f < X < +\infty$ including the AU interval $X^{ca} < X < X^{ac}$.

By contrast, for a forcing frequency ω_f within the range $\omega_0^{ca} - \omega_0^{ac}$, i.e., below the $\{\omega_0(X_i = 0)\}$ -curve in the complex ω -plane, both turning points are located on the same side of the real X -axis: turning point X'_2 has moved to the part of the $\{X_2(\omega_i = 0)\}$ -isoline located in the upper complex half-plane, as illustrated in Fig. 3b, c. Thus the branch cut emanating from X'_2 crosses the real X -axis and the spatial $k^\pm(X, \omega_f)$ branches display a discontinuity across the branch cut. The $k^+(X, \omega_f)$ branches prevailing on either side of the AU interval are no longer continuously connected over the real X -axis. It follows that the local wave number of the spatial response to harmonic forcing applied at X_f must display a jump somewhere in the AU interval $X^{ca} < X < X^{ac}$ if the k^+ branches prevailing for both $X_f < X < X^{ca}$ and $X^{ac} < X < +\infty$ are to be reconciled. In this situation indeed, the real X -axis is also crossed by the ℓ_2^3 Stokes line and, as shown in the previous section, an exchange in the dominant WKBJ solution approximating the spatial response precisely takes place across this Stokes line. Hence the region where the spatial response is dominated by the k^- branch (shaded regions in Fig. 3b, c) overlaps the real X -axis, and along the AU interval both the branch cut and the ℓ_2^3 Stokes line are encountered.

As a result, the spatial response to harmonic forcing is then obtained in terms of both WKBJ approximations and the jump of the dominant local wave number occurs at the intersection of the ℓ_2^3 Stokes line with the real X -axis.

8 Confirmation by direct numerical simulation

The structure of the spatial response derived by analytic methods in the previous sections has been confirmed by direct numerical simulations of system (1). The results presented in Fig. 4 have been obtained with a spatially varying local absolute frequency (5) defined by $\omega_s = 2 - 0.5i$, $X_s = 2 + i$ and $\omega_{Xs} = -1 - 2i$ and $\epsilon = 0.1$, while the parameters $k_0 = 1 - i$ and $\omega_{kk} = 1 - 0.5i$ were kept at constant values. These parameter settings correspond to an AU interval characterized by $X^{ca} \simeq 1.6$, $\omega_0^{ca} \simeq 3.2$ and $X^{ac} = 3.3$, $\omega_0^{ac} \simeq -1.1$. Harmonic forcing is applied upstream at $X_f = 1$ with frequencies $\omega_f = 5$ (left sequence of Fig. 4) and $\omega_f = 2$ (right sequence). The thick curves in Fig. 4 illustrate the different characteristics of the numerically computed spatial response: envelope $|\psi|$ and real part ψ_r (first row), envelope on a logarithmic scale (second row), real part k_r (third row) and imaginary part k_i (fourth row) of local wave number. The thin curves in the wave number plots represent the wave number branches $k^\pm(X, \omega_f)$ analytically computed via (6) with the corresponding ω_f .

The forcing frequency $\omega_f = 5$ lies outside the range $\omega_0^{ca} - \omega_0^{ac}$, so that the associated turning points $X_1^t \simeq 2.7 + 2.5i$ and $X_2^t \simeq 1.3 - 0.5i$ are located on either side of the real X -axis, which is thus free from any branch cuts. Figure 3a has been computed with exactly these parameter values. The critical Stokes lines ℓ_1^3 and ℓ_2^3 do not cross the real axis and the spatial response for $X > X_f$ is thus predicted to be entirely made up of the k^+ wave number branch. Inspection of the numerical results given in Fig. 4a1–a4 reveals that this is indeed the case. From Fig. 4a1, a2 it is seen that the spatial response grows from X_f through the entire AU interval to reach maximum amplitude beyond X^{ac} , before eventual decay further downstream. The local wave number in the spatial response, numerically computed as $-i\partial_x \psi / \psi$ and corresponding to the thick curves in Fig. 4a3, a4, very closely follows the analytically computed wave number branches (thin curves). The salient feature is that the spatial response follows the k^+ branch in the entire domain to the right of the forcing location X_f , including the AU interval $X^{ca} < X < X^{ac}$ (delimited by dashed vertical lines).

The forcing frequency $\omega_f = 2$ lies within the range $\omega_0^{ca} - \omega_0^{ac}$, so that the associated turning points $X_1^t \simeq 1.8 + 1.7i$ and $X_2^t \simeq 2.2 + 0.3i$ are both located in the upper complex half plane, as illustrated in Fig. 3b obtained with these parameter values. Now the Stokes line ℓ_2^3 crosses the real axis for $X_2^3 \simeq 1.9$ where a jump in the dominant wave number of the spatial response is predicted. This phenomenon is indeed observed in Fig. 4b3, b4. The spatial response is seen to be dominated by the k^+ branch from the forcing location X_f to the Stokes line at X_2^3 , beyond which the k^- branch dominates. This exchange in dominant WKBJ approximations at X_2^3 materializes by a cross-over of the numerically computed local wave number in Fig. 4b3, b4 and by a kink of the envelope in Fig. 4b2. The spatial response then follows the k^- branch from X_2^3 to the branch cut at $X_\star \simeq 3.0$ (vertical dotted line), beyond which the k^- branch is seemlessly relabelled as k^+ . As anticipated from the previous section, the spatial response displays the k^+ wave number branch in the two at most CU domains $X_f < X < X^{ca}$ and $X^{ac} < X < +\infty$. However, with ω_f in the range $\omega_0^{ca} - \omega_0^{ac}$ these branches are not continuously connected through the central AU interval. Hence the solution is there made up of both branches and cross-over of the dominant wave number occurs at the intersection with the Stokes line.

9 Conclusion

The signalling problem in spatially developing systems is fairly well understood for media that are at most convectively unstable, and it is generally believed to be ill-posed for absolutely unstable systems. The present investigation has shown that this problem remains well-posed for a certain class of absolutely unstable systems: whenever the system is globally stable (i.e., all global modes decay with time) all transient behaviour is eventually damped and a spatial response tuned at the forcing frequency establishes for large time. By resorting to asymptotic WKBJ expansions, the spatial structure of the time-harmonic response has been obtained in the entire domain, including the AU interval. In the AU interval, the dominant local wave number of the spatial response has been shown to depend on the positions in the complex X -plane of the turning points associated with the forcing frequency. The positions of these turning points depend on the relative values of the forcing frequency ω_f and the (real) marginal absolute frequencies ω_0^{ca} and ω_0^{ac} prevailing at the end points of the AU

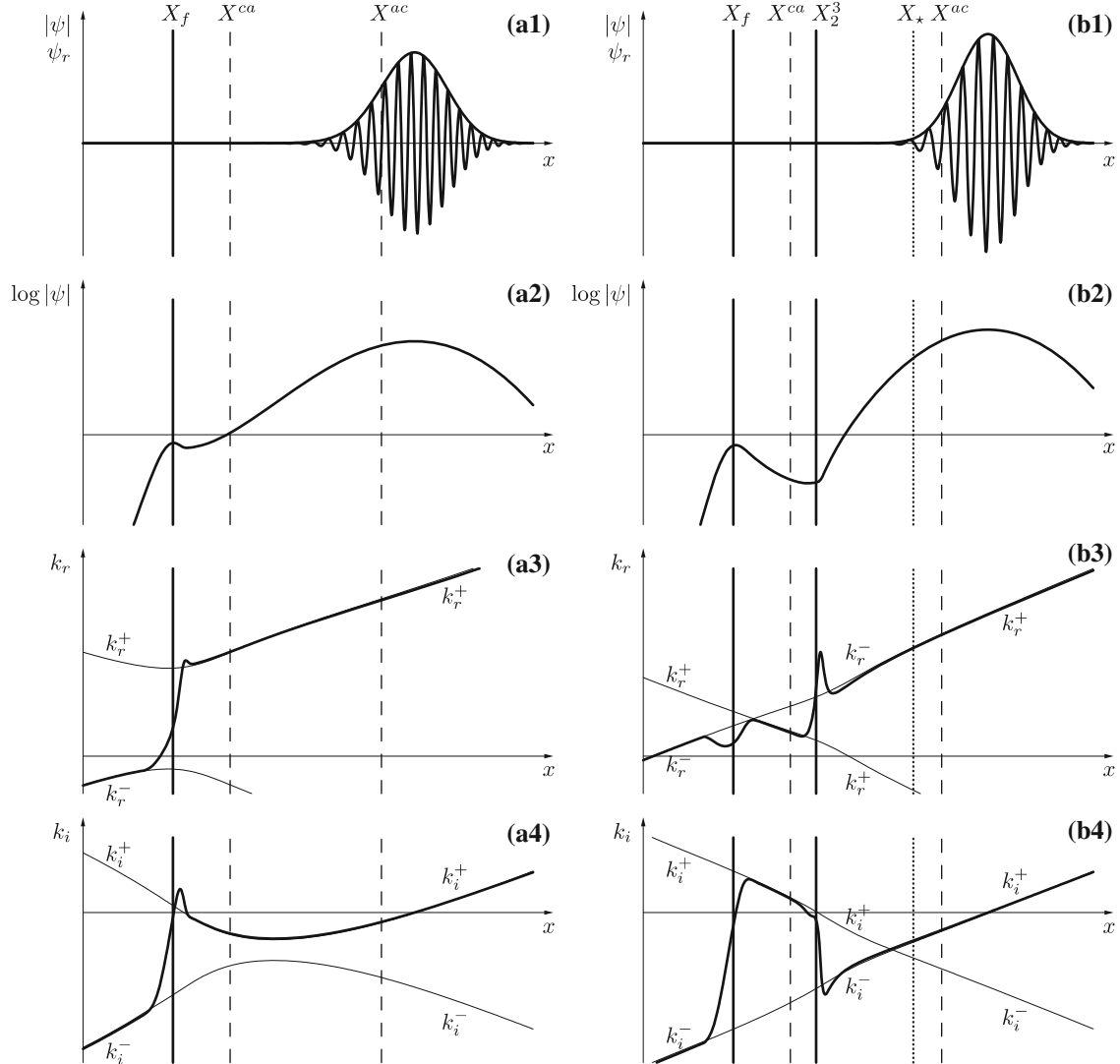


Fig. 4 Envelope $|\psi|$, real part ψ_r , local wave numbers k_r and k_i of spatial response to harmonic forcing obtained by direct numerical simulation. Forcing is applied at X_f , upstream of the absolutely unstable interval $X^{ca} < X < X^{ac}$. **a** With ω_f outside the range $\omega_0^{ca} - \omega_0^{ac}$, the spatial response follows the k^+ wave number branch for $X_f < X < +\infty$, including the AU interval. **b** For ω_f within the range $\omega_0^{ca} - \omega_0^{ac}$, the real X -axis intersects the Stokes line ℓ_2^3 at X_2^3 , where a jump in the dominant wave number is observed. Beyond the branch cut at X_* , the k^- wave number branch prevailing for $X_2^3 < X < X_*$ becomes k^+ and extends to $X = +\infty$

interval. The detailed analysis in the complex X -plane of the Stokes lines and branch cuts has revealed that two distinct situations arise:

- For forcing frequencies ω_f outside the range $\omega_0^{ca} - \omega_0^{ac}$, the local wave number observed in the spatial response continuously depends on streamwise distance and follows the k^+ -branch everywhere downstream of the forcing location.
- For forcing frequencies within the range $\omega_0^{ca} - \omega_0^{ac}$, the spatial response displays a jump in the dominant local wave number branch at the location within the AU domain where the real X -axis is crossed by a Stokes line.

The above results have been analytically derived in a general setting and confirmed by numerical integration of the Ginzburg–Landau model equation. Work currently in progress concerns application of the present findings to the spatial response in the rotating-disk three-dimensional boundary-layer and its implications for an open-loop control strategy [13, 14], based on localized harmonic forcing.

References

1. Bender, C.M., Orszag, S.A.: Advanced Mathematical Methods for Scientists and Engineers. McGraw-Hill, New York (1978)
2. Bers, A.: Space-time evolution of plasma instabilities—absolute and convective. In: Rosenbluth, M., Sagdeev, R. (eds.) Handbook of Plasma Physics, pp. 451–517. North-Holland, Amsterdam (1983)
3. Briggs, R.J.: Electron-Stream Interaction with Plasmas. M.I.T. Press, Cambridge, MA (1964)
4. Chomaz, J.M., Huerre, P., Redekopp, L.G.: Bifurcations to local and global modes in spatially developing flows. *Phys. Rev. Lett.* **60**, 25–28 (1988)
5. Chomaz, J.M., Huerre, P., Redekopp, L.G.: A frequency selection criterion in spatially developing flows. *Stud. Appl. Math.* **84**, 119–144 (1991)
6. Cross, M.C., Hohenberg, P.C.: Pattern formation outside of equilibrium. *Rev. Mod. Phys.* **65**, 851–1112 (1993)
7. Davies, C., Carpenter, P.W.: Global behaviour corresponding to the absolute instability of the rotating-disk boundary layer. *J. Fluid Mech.* **486**, 287–329 (2003)
8. Huerre, P.: Open shear flow instabilities. In: Batchelor, G.K., Moffatt, H.K., Worster, M.G. (eds.) Perspectives in Fluid Dynamics, pp. 159–229. Cambridge University Press, Cambridge (2000)
9. Huerre, P., Monkewitz, P.A.: Local and global instabilities in spatially developing flows. *Ann. Rev. Fluid Mech.* **22**, 473–537 (1990)
10. Huerre, P., Rossi, M.: Hydrodynamic instabilities in open flows. In: Godrèche, C., Manneville, P. (eds.) Hydrodynamics and Nonlinear Instabilities, pp. 81–294. Cambridge University Press, Cambridge (1998)
11. Le Dizès, S., Huerre, P., Chomaz, J.M., Monkewitz, P.A.: Linear global modes in spatially developing media. *Philos. Trans. R. Soc. Lond. A* **354**, 169–212 (1996)
12. Monkewitz, P.A.: The absolute and convective nature of instability in two-dimensional wakes at low Reynolds numbers. *Phys. Fluids* **31**, 999–1006 (1988)
13. Pier, B.: Open-loop control of absolutely unstable domains. *Proc. R. Soc. Lond. A* **459**, 1105–1115 (2003)
14. Pier, B.: Primary crossflow vortices, secondary absolute instabilities and their control in the rotating-disk boundary layer. *J. Eng. Math.* **57**, 237–251 (2007)
15. Pier, B.: Local and global instabilities in the wake of a sphere. *J. Fluid Mech.* **603**, 39–61 (2008)
16. Pier, B., Huerre, P.: Nonlinear self-sustained structures and fronts in spatially developing wake flows. *J. Fluid Mech.* **435**, 145–174 (2001)
17. Pier, B., Huerre, P.: Nonlinear synchronization in open flows. *J. Fluids Struct.* **15**, 471–480 (2001)
18. Schmid, P.J., Henningson, D.S.: Stability and Transition in Shear Flows. Applied Mathematical Sciences. Springer, New York (2001)

[A13]

Experimental characterization of transition region in rotating-disk boundary layer

M. E. Siddiqui, V. Mukund, J. Scott & B. Pier

Physics of Fluids **25**, 034102 (10 pages) (2013)

doi:10.1063/1.4798435

<https://hal.archives-ouvertes.fr/hal-00806379>

Experimental characterization of transition region in rotating-disk boundary layer

M. E. Siddiqui,^{1,2} V. Mukund,^{1,3} J. Scott,¹ and B. Pier^{1,a)}

¹*Laboratoire de mécanique des fluides et d'acoustique, École centrale de Lyon, CNRS, Université Claude-Bernard Lyon 1, INSA, 36 avenue Guy-de-Collongue, 69134 Écully cedex, France*

²*Ghulam Ishaq Khan Institute of Engineering Sciences and Technology, Topi, Swabi, Pakistan*

³*Max Planck Institute for Dynamics and Self-Organization, 37077 Göttingen, Germany*

(Received 12 October 2012; accepted 6 March 2013; published online 29 March 2013)

The three-dimensional boundary layer due to a disk rotating in otherwise still fluid is well known for its sudden transition from a laminar to a turbulent regime, the location of which closely coincides with the onset of local absolute instability. The present experimental investigation focuses on the region around transition and analyses in detail the features that lead from the unperturbed boundary layer to a fully turbulent flow. Mean velocity profiles and high-resolution spectra are obtained by constant-temperature hot-wire anemometry. By carefully analysing these measurements, regions in the flow are identified that correspond to linear, weakly nonlinear, or turbulent dynamics. The frequency that dominates the flow prior to transition is explained in terms of spatial growth rates, derived from the exact linear dispersion relation. In the weakly nonlinear region, up to six clearly identifiable harmonic peaks are found. High-resolution spectra reveal the existence of discrete frequency components that are deemed to correspond to fluctuations stationary with respect to the disk surface. These discrete components are only found in the weakly nonlinear region. By systematically acquiring low- and high-resolution spectra over a range of narrowly spaced radial and axial positions, it is shown that while the transition from laminar to turbulent regimes occurs sharply at some distance from the disk surface, a complex weakly nonlinear region of considerable radial extent continues to prevail close to the disk surface. © 2013 American Institute of Physics. [<http://dx.doi.org/10.1063/1.4798435>]

I. INTRODUCTION

Three-dimensional boundary layers are characterized by a rapid variation of all three velocity components in the neighbourhood of a solid surface. This happens whenever a body is rotating with respect to the surrounding fluid or if a flow impacts an obstacle obliquely. Practical configurations include the flow around compressor blades, aircraft wings, ship hulls, or wind turbines. All these configurations are prone to strong instabilities that rapidly lead to turbulence. The objective of the present investigation is to carry out detailed measurements of the dynamics of such a flow in order to shed new light on the mechanisms governing the complex transition scenario that leads from a laminar to a turbulent state.

Within the class of three-dimensional boundary layers, the flow with the simplest geometry is probably that due to a large disk rotating in otherwise still fluid: von Kármán¹ obtained the basic flow as an exact similarity solution of the Navier–Stokes equations. This basic-flow solution, illustrated

^{a)}Electronic mail: benoit.pier@ec-lyon.fr

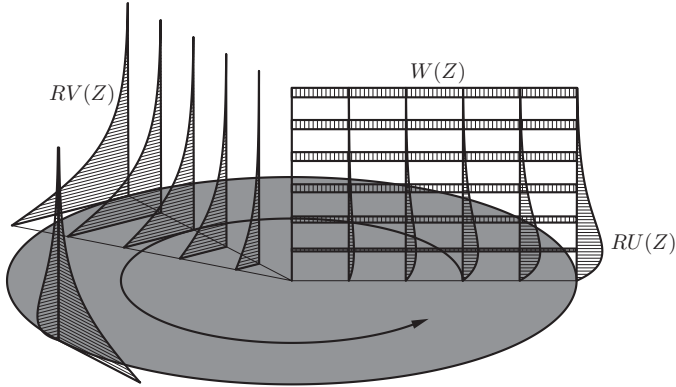


FIG. 1. Basic flow over rotating disk.

in Figure 1, displays a constant boundary layer thickness proportional to

$$\delta = \sqrt{\frac{\nu}{\Omega}}, \quad (1)$$

where ν is the kinematic viscosity and Ω the disk rotation rate. Note that the azimuthal velocity drops to about 1% of the disk velocity at a distance 5δ from the disk surface. Throughout this study, the axial coordinate Z and radial coordinate R are non-dimensionalized by δ . The radial, azimuthal, and axial basic flow velocity components, non-dimensionalized by $\Omega\delta$, are

$$U_r = RU(Z) \quad \text{and} \quad U_\theta = RV(Z) \quad \text{and} \quad U_z = W(Z), \quad (2)$$

where $U(Z)$, $V(Z)$, and $W(Z)$ are the von Kármán similarity profiles.

When unstable, this boundary layer develops cross-flow vortices, as observed experimentally by Gregory *et al.*² Transition from laminar to turbulent regimes occurs at a non-dimensional radius in the range 500–550.^{2–7} Lingwood⁸ has found that this boundary layer undergoes transition from convective to absolute instability at a critical radius $R^{ca} = 507$ that closely corresponds to the position of experimentally observed transition to turbulence. However, it has been shown by Davies and Carpenter⁹ that, within a strictly linear framework, this flow is globally stable despite the presence of an extended region of local absolute instability. Subsequently, a fully nonlinear analysis¹⁰ led to a consistent theory able to account for the onset of self-sustained finite-amplitude fluctuations beyond R^{ca} . While all the previous theoretical analyses assume a rotating disk of infinite extent, Healey¹¹ has recently been able to take into account the effect of the outer edge of the disk, study its influence on the global instability, and provide a possible explanation for the scatter in transition locations reported by different experimental studies.

Despite numerous investigations, it appears that the precise mechanism leading from laminar to turbulent states is not yet fully understood. The present experimental investigation has been undertaken to precisely map out the near transition region by determining how mean-flow deviations from the von Kármán solution and the spectral content of the fluctuations vary with radial and axial positions, with special attention to the near-disk region. A similar aim, but with a different approach, has been independently pursued by Imayama *et al.*¹² The present paper is based on Ref. 13 and a preliminary account of our findings was given in Ref. 14.

The structure of the manuscript is the following. The experimental arrangement is described in Sec. II. Then we describe our experimental observations of mean velocity profiles (Sec. III A), low-resolution spectra (Sec. III B 1), and high-resolution spectra (Sec. III B 2). These results are discussed in detail in Sec. IV.

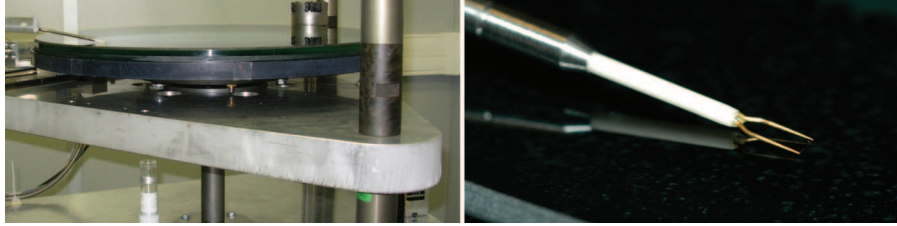


FIG. 2. Experimental setup. (Left) 50 cm diameter glass disk that may be rotated up to 1500 rpm. (Right) Hot-wire probe positioned parallel to the disk surface and aligned in the radial direction, positioned by a high-precision two-axes mechanism.

II. EXPERIMENTAL ARRANGEMENT

The rotating-disk facility designed for the present investigation (Figure 2) consists of a glass disk of 500 mm in diameter that is rotated at constant angular velocity Ω , up to 1500 rpm. Details of the experimental arrangement are given in Ref. 13. The disk surface was measured by a linear variable differential transducer (LVDT) and its position adjusted so as to achieve best alignment with a plane normal to the rotation axis. The disk roughness, characterized by the arithmetic average of absolute surface values, was measured as $1.6 \mu\text{m}$. A high-precision two-axes traversing mechanism was used for positioning of a hot-wire probe, with radial and axial precisions of $20 \mu\text{m}$ and $2 \mu\text{m}$, respectively.

For the local velocity measurements, constant-temperature hot-wire anemometry is used, being particularly suitable for the measurement of flows with very fast fluctuations at a fixed point in space. A single Dantec hot wire of type 55P01 is used, consisting of a $5 \mu\text{m}$ diameter and 3 mm wide platinum-plated tungsten wire with a 1.25 mm flow sensitive length at its center. The hot wire is positioned parallel to the disk surface and aligned in the radial direction so as to measure the azimuthal flow component. The traversing mechanism and velocity measurements are controlled and recorded by a dedicated computer.

The hot wire must be calibrated using known flow velocities. Rather than using a separate wind tunnel, which would require frequent removal of the probe from its support, we always calibrated the hot-wire probe against the laminar boundary-layer profile, given by the von Kármán solution. Knowing the disk rotation rate, the distance of the hot wire from the disk surface and from the disk axis, the boundary-layer velocity at the hot-wire position can be calculated. The hot wire is then calibrated by measuring the mean output voltage from the anemometer for a range of flow speeds. In this calibration process, the disk rotation rate and position of the probe are chosen to remain well within the laminar region. A fourth-order polynomial was used to fit the velocity-voltage data pairs, and this polynomial subsequently used to convert measured instantaneous voltages to flow velocities. Keeping in mind that the hot-wire anemometry has a sensitive temperature dependence, this calibration was repeated before each measurement. Data acquisition is performed by moving the hot wire in the radial and axial directions for a constant disk speed. This process is then repeated for different values of the disk speed, and, after non-dimensionalization, the data acquired at different rotation rates collapse to the same values. See Ref. 13 for details of the experimental procedure.

III. RESULTS

A. Mean velocity profiles

The main focus of this paper is the spectral analysis of velocity time-series. However, the measured mean velocity profiles are briefly presented first for completeness and validation of the setup.

Mean azimuthal velocity components are shown in Figure 3 over the range $350 \leq R \leq 600$. In these plots, velocities are normalized by the velocity of the disk surface at the corresponding radial position.

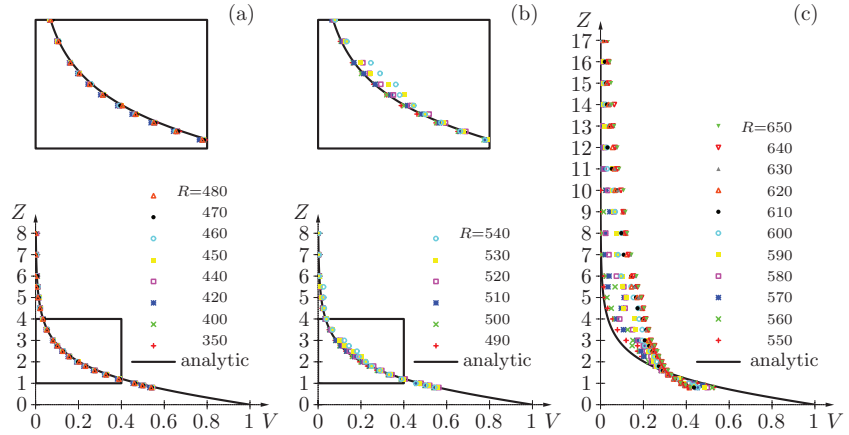


FIG. 3. Azimuthal mean-flow velocity profiles for non-dimensional radii in the range $350 \leq R \leq 650$, along with the analytical profile (solid line); insets show magnified view of region from $Z = 1$ to $Z = 4$. (a) Measured profiles closely follow the analytical curve for $R \leq 480$. (b) Small deviations of the measured profile from the analytical curve are observed for $2 \leq Z \leq 3$ and $490 \leq R \leq 540$. (c) For $R \geq 550$, strong mean-flow corrections, extending beyond $Z = 15$ by $R = 650$, characterize a transitional and fully turbulent boundary layer.

At low values of R , the measured profiles very closely follow the von Kármán similarity profile, see Figure 3(a).

For $490 \leq R \leq 540$, small but significant differences between the measured profiles and the analytical profile are observed. Figure 3(b) shows that these mean flow corrections are confined to a narrow region of the boundary layer ($2 \leq Z \leq 3$) and their amplitude is less than 5% of the maximum velocity in this range. In the convectively unstable range, $284 < R < 507$, they can be interpreted as reflecting the radial growth of instabilities (cross-flow vortex modes) in the boundary layer. The confinement in Z is consistent with the structure of the unstable-mode eigenfunctions, as computed, e.g., in Ref. 10.

For $R \geq 550$, stronger mean-flow distortions are observed, which progressively extend beyond $Z = 15$, see Figure 3(c). Such boundary-layer thickening is the characteristic of the development of turbulent boundary layers. This behaviour of the mean-flow profiles corresponds exactly to what has been obtained in previous studies^{6,7} and is thus deemed a sufficient validation of the present experimental setup.

B. Spectral analysis

Frequency contents of disturbances in the boundary-layer are investigated by calculating Fourier power spectra from azimuthal-velocity time series at different non-dimensional radii R and disk normal positions Z .

For most of the previously published experimental results, power spectra have a low frequency resolution, of the order of $\Delta\omega = 1$, non-dimensionalized by the disk rotation rate. In order to obtain high-resolution spectra, the velocity signals were recorded over long time intervals, typically a few thousand revolutions of the disk.

In post-processing, the power spectra are obtained by Fourier analyses of these signals. The procedure is the following. The signal is split into n series covering m disk revolutions each. Each of the n series is Fourier analysed and the squared moduli of the complex Fourier amplitudes are then averaged over the n spectra. By varying m , spectra of different frequency resolutions are obtained. Typical “low-resolution” spectra are obtained with $m = 1$, while spectra obtained with $m = 100$ or $m = 1000$ are referred to as high-resolution spectra, with resolution $\Delta\omega = 0.01$ or 0.001 , respectively. Thus, spectra with different resolutions can be obtained from the same data, shedding new light on the frequency content of the fluctuations developing in the rotating-disk boundary layer.

1. Low-resolution spectra

Low-resolution power spectra are shown in Figure 4. At low values of R , these mainly consist of uniform background noise. Starting at $R = 450$, a peak with a maximum near $\omega = 30$ emerges. This is an indication of the development of growing cross-flow modes with a characteristic frequency around 30, but these modes as yet cause no significant distortion of the mean flow: as shown in Sec. III A, for $R \leq 480$, the measured mean-flow profiles closely follow the von Kármán solution.

At higher R , power spectra show the progressive growth and development of the disturbance. A second-harmonic peak appears for $R = 490$ (Figure 4(b)), indicating effects of nonlinear interactions. At even larger values of R , higher harmonics of the fundamental peak arise near $\omega = 60, 90, 120, 150$, and 180. Note that the harmonics first appear at different values of R depending on the distance Z from the disk surface. This will be further discussed in Sec. IV.

At and above $R = 520$, Figures 4(e)–4(h) show the progressive increase of a broadband spectral component, followed by the disappearance of the modal peaks. This corresponds to transition to turbulence. By $R = 600$ (Figure 4(h)), there are no longer any clear peaks associated with the modes and the flow is fully turbulent throughout the boundary layer.

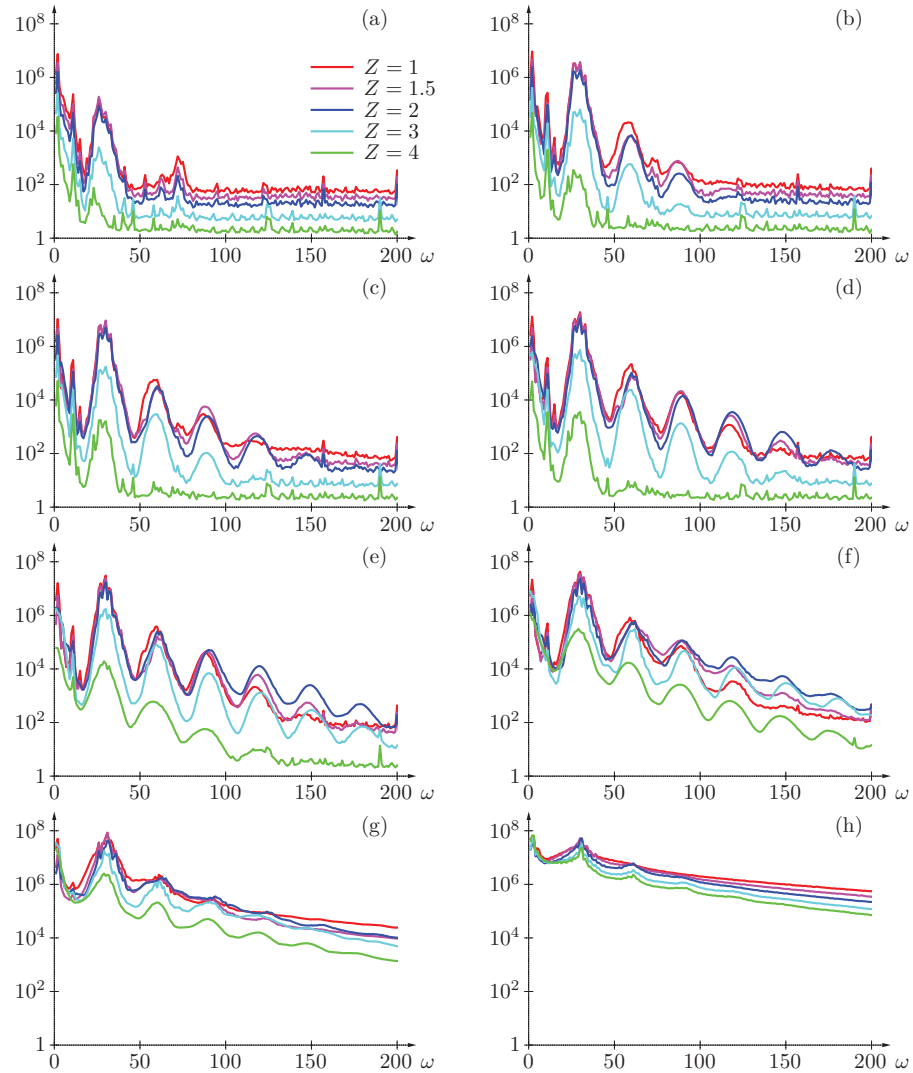


FIG. 4. Low-resolution spectra for (a) $R = 450$, (b) $R = 490$, (c) $R = 500$, (d) $R = 510$, (e) $R = 520$, (f) $R = 530$, (g) $R = 550$, and (h) $R = 600$. Spectral amplitudes are plotted on a logarithmic scale for disk normal positions $Z = 1, 1.5, 2, 3$, and 4.

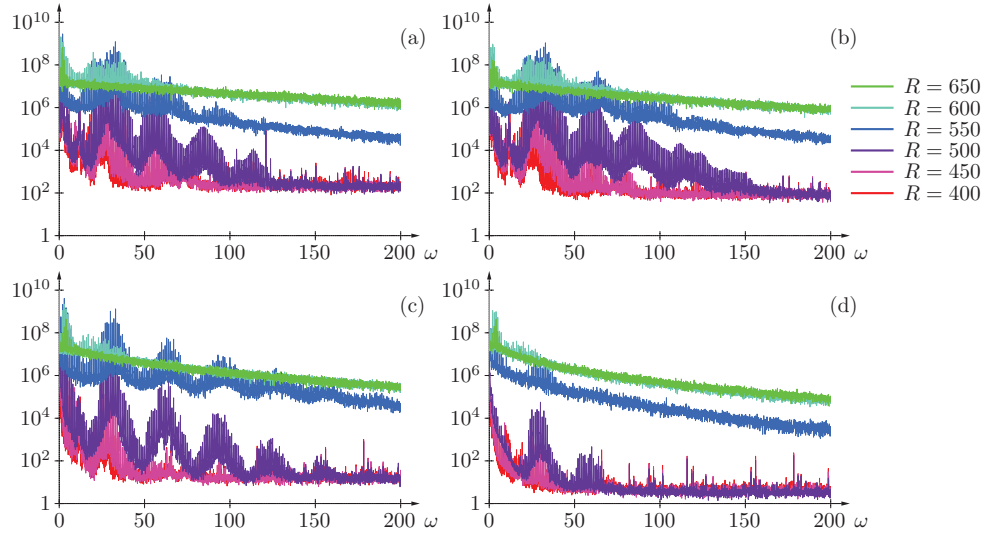


FIG. 5. High-resolution spectra corresponding to $R = 400, 450, \dots, 650$ and (a) $Z = 0.8$, (b) $Z = 1.5$, (c) $Z = 3.0$, and (d) $Z = 6.0$.

From these low-resolution spectra, three distinct flow regimes can be identified: a *linear regime* where the boundary layer only displays small-amplitude perturbations associated with at most a single peak in the spectrum; a *weakly nonlinear regime* characterized by a dominant frequency and its harmonics due to nonlinear interactions; and a *fully turbulent regime* where the harmonic peaks have been superseded by a continuous spectrum.

In terms of mean velocities, these three regimes broadly correspond to no, weak, and strong mean-flow deviations from the similarity profile, as shown in Sec. III A. A complete characterization of the different regions of the rotating-disk boundary layer will be discussed in Sec. IV.

2. High-resolution spectra

As described earlier, high-resolution spectra are derived by Fourier analyzing the velocity time-series recorded over long temporal intervals. Plots shown in Figure 5 have a frequency resolution of $\Delta\omega = 0.01$ and are obtained by averaging 50 spectra computed over 100 disk revolutions. Spectra obtained with a frequency resolution of $\Delta\omega = 0.001$ look very similar and are not shown here. Overall, the high-resolution spectra display similar characteristics to their low-resolution counterparts, but a distinctive feature is the existence of discrete peaks at integer multiples of the disk rotation rate. These peaks are smoothed out in the low-resolution spectra. The discrete peaks are more clearly visible in the close-up views shown in Figure 6. The radial evolution of high-resolution spectra in the range $450 \leq R \leq 650$ for $Z = 1$ and $Z = 6$ is illustrated in Figure 7 for $20 < \omega < 40$.

These measurements show that the velocity spectra are made up of both a continuous and a discrete part. The discrete part corresponds to flow components that have exactly the same periodicity as the disk.

It is observed that both the discrete and continuous parts of the spectrum grow with R . However, the discrete component is the dominant feature only in the “weakly nonlinear” regime, while it is hardly developed in both the laminar and in the turbulent regions. Also, it is more prominent for the most amplified frequency, around $\omega \simeq 30$, and its harmonics.

At $R = 350$, the spectrum is essentially background noise and the discrete component appears to be irrelevant. For, say, $450 < R < 510$, the discrete part grows to form a peak around $\omega \simeq 30$. This growth continues up to $R = 530$, but involves a wider band of frequencies and then saturates. From $R = 530$ on, the continuous part grows as the boundary layer approaches the turbulent regime. By $R = 650$, the spectrum corresponds to a fully turbulent flow without any visible discrete component.

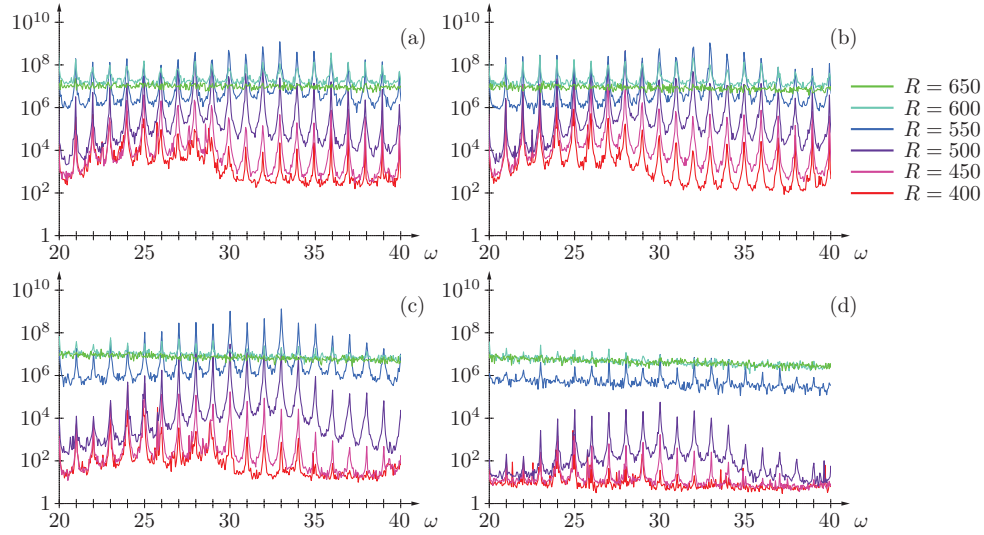


FIG. 6. Closeup view for $20 < \omega < 40$ of high-resolution spectra corresponding to $R = 400, 450, \dots, 650$ and (a) $Z = 0.8$, (b) $Z = 1.5$, (c) $Z = 3.0$, and (d) $Z = 6.0$.

IV. DISCUSSION

In the present experimental investigation of a rotating-disk flow, hot-wire velocity measurements have been carried out to characterize the dynamics of this boundary layer with special emphasis on the near transition region.

As expected, mean velocity profiles follow the self-similar von Kármán solution at low radii, small but significant mean-flow deviations from the similarity profile are obtained for $490 \leq R \leq 540$ and $2 \leq Z \leq 3$, and fully turbulent profiles prevail for $R \geq 550$, characterized by strong mean-flow corrections extending beyond $Z = 15$.

Spectral analyses of velocity-series yield the frequency content of the perturbations that develop in the different regions of the boundary layer. Low-resolution spectra show that the first perturbations to develop with increasing R exhibit characteristic frequencies near $\omega = 30$. This corresponds to the largest spatial growth rate for perturbations that are stationary with respect to the disk. Figure 8 shows the spatial growth rate $-\alpha_i$ as function of frequency ω and azimuthal mode number β , derived from the local linear dispersion relation $\omega = \Omega(\alpha, \beta; R)$. This dispersion relation is obtained by considering perturbations of the form $\exp[i(\alpha r + \beta\theta - \omega t)]$ and numerically implementing a complete stability analysis based on the linearized Navier–Stokes equations, as in Ref. 10. The plot in Figure 8, shows that at $R = 500$ the largest spatial growth rate $-\alpha_i \simeq 0.1$ is obtained for $(\omega, \beta) \simeq (47, 62)$. However, perturbations with $\omega \neq \beta$ are traveling with respect to the disk surface. Considering that fluctuations measured in the convectively unstable range $280 < R < 510$ are mainly

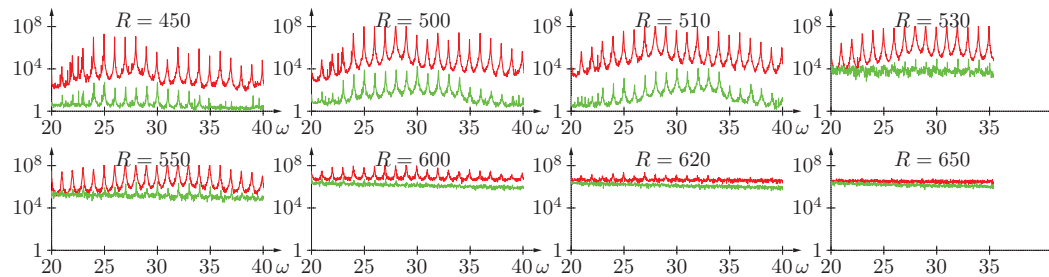


FIG. 7. Radial evolution of high-resolution power spectra in the range $20 \leq \omega \leq 40$, for $450 \leq R \leq 650$ and $Z = 1$ (upper curves) and $Z = 6$ (lower curves).

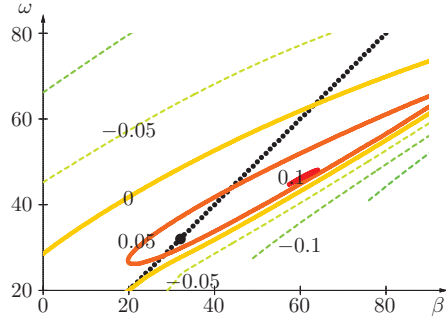


FIG. 8. Isolines of spatial growth rates $-\alpha_i$ at $R = 500$, derived from the exact local linear dispersion relation $\omega = \Omega(\alpha, \beta; R)$, in the ω - β (frequency—azimuthal mode number) plane.

due to imperfections and roughness of the disk surface and are therefore stationary with respect to the disk, they correspond to the line $\omega = \beta$ in Figure 8. For these waves rotating at the same rate as the disk, maximum spatial growth is attained with $\omega = \beta = 32$ (at $R = 500$), indicated by a big dot in Figure 8. It is also found that this maximally amplified frequency hardly depends on R in the convectively unstable region. Thus, by carrying out a systematic computation of the spatio-temporal dispersion relation based on the linearized Navier–Stokes equations, we confirm the origin of the fundamental harmonic peak observed in the spectra from onset of linear instability to transition to turbulence.

With increasing radial distance, the flow enters a weakly nonlinear regime, characterized by a harmonic spectrum made up of the dominant fundamental frequency and its harmonics. Eventually, the boundary layer enters a fully turbulent state associated with the disappearance of the modal peaks, replaced by a broad continuous spectrum. The detailed characteristics of these spectra, such as the number of harmonic peaks that may be identified or the occurrence of a broad spectrum, depend both on the radial and the axial locations of the measurement. Counting of the harmonic peaks can be performed automatically by a post-processing script: for each of the low-resolution spectra (cf. Figure 4), the script first extracts the maxima located approximately at multiples of the fundamental frequency and then retains those that are separated by a sufficiently deep minimum. A detailed map of the flow structures is given in Figure 9(a). Measurements have been systematically carried out for $R = 350, 360, \dots, 650$ and $Z = 0.8, 1.0, 1.5, 2.0, 3.0, 4.0$, and 6.0 . For each of these locations, the symbol in Figure 9(a) depicts the type of spectrum that is obtained: the number of circles corresponds to the number of harmonic peaks that could be identified and a grey background indicates the presence of a broadband component. A single circle on white background thus corresponds to a laminar boundary layer that is at most linearly perturbed. The weakly nonlinear region corresponds to at least two identifiable broad harmonic peaks and thus starts with the double-circle symbols. With increasing radial distance, higher-order harmonics develop; up to six clearly identifiable harmonic peaks have been found at $Z = 3$ and $510 \leq R \leq 520$. Then, a broadband component appears near $R = 530$ (symbols with grey background) that progressively replaces the harmonic spectrum. Eventually a fully turbulent regime is reached with no identifiable harmonic peaks in the spectrum. From this map one sees that the transition from laminar to turbulent flow is relatively sharp far from the disk surface (say $Z > 5$), while a nonlinear region of considerable extent is observed in the near-disk region. This nonlinear region can be considered to start as early as $R \simeq 450$ and to survive up to $R \simeq 570$, well beyond a single transition location near $R \simeq 530$.

Velocity spectra with high frequency resolution have been obtained from velocity signals recorded over long time-periods. These high-resolution spectra reveal the existence of narrow peaks located at integer values of the frequency. Since these discrete peaks appear every integer multiple of disk rotation rate, they are associated with the flow components that have the same periodicity as the disk and that are probably stationary with respect to the disk surface. It should be noted that these discrete peaks are not an experimental artifact, for otherwise they would also be present at low and high values of R . In order to map out the regions where this discrete part of the spectrum is

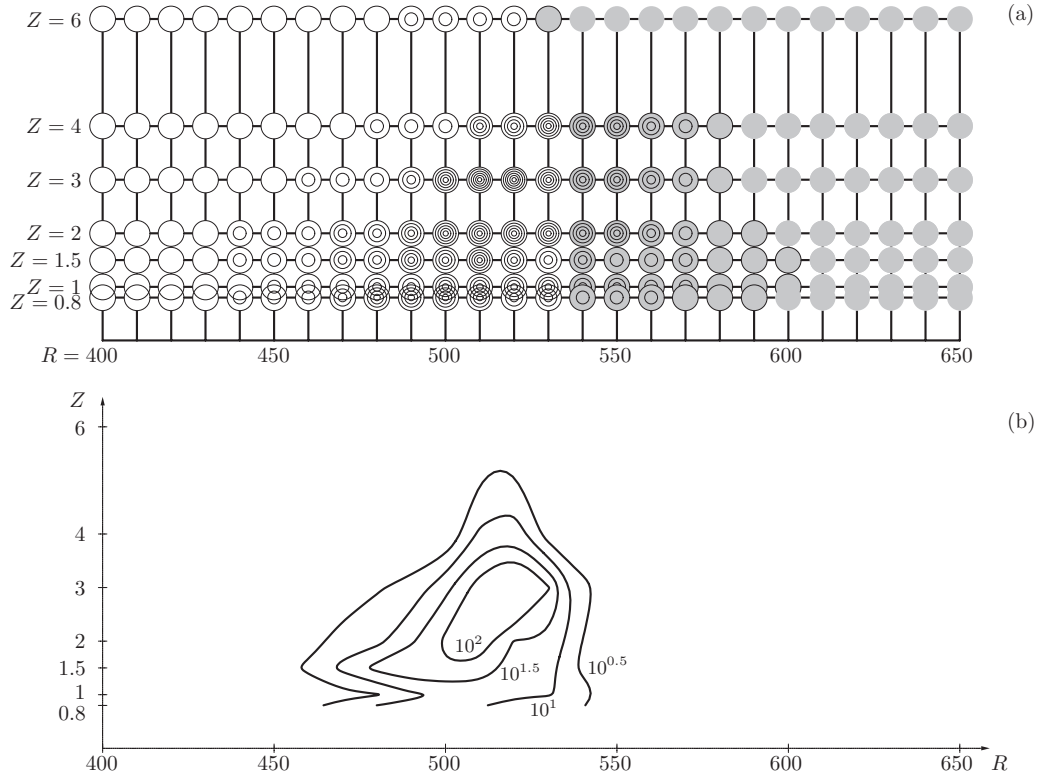


FIG. 9. (a) Detailed map of the local boundary-layer features, based on the low-resolution spectra recorded at $R = 400, 410, \dots, 650$ and $Z = 0.8, 1, 1.5, 2, 3, 4$, and 6. The symbols depict the type of spectrum that prevails at a given location: the number of circles corresponds to the number of harmonic peaks that could be identified and a grey background indicates the presence of a broadband component. (b) Contour plot measuring the importance of the discrete component in the high-resolution velocity spectra. The measure is based on the mean ratio between the integer-frequency maxima and the semi-integer-frequency minima of the high-resolution spectra.

important, another post-processing script has been developed: for each of the high-resolution spectra, the script extracts the maxima located at integer frequencies and the minima located at half-integer frequencies, and then computes the average separation of these alternating extrema, on a logarithmic scale. The result represents a measure of the amplitude of the discrete spectral component and is shown as a contour plot with equispaced iso-levels in the (R, Z) -plane in Figure 9(b). Comparing Figures 9(a) and 9(b) clearly demonstrates that the presence of this discrete component coincides with the existence of a weakly nonlinear regime. Moreover, the discrete component has maximal strength around $R = 520$ and $Z = 3$, which is also where the largest number of harmonic peaks have been identified. It should also be observed that this radial position nearly coincides with the onset of local absolute instability at $R = 507$. To our knowledge, despite much previous research on the rotating-disk boundary-layer flow, the only previous discussion of the discrete part of the velocity spectra is to be found in Refs. 13 and 14, though it is visible in the results of Ref. 15. One reason for the poor documentation of this feature may be the fact that it is only observable using high-resolution spectra and thus requires measurement of velocity time-series over long time periods.

Traditionally, the rotating-disk boundary layer is considered as an example of a flow exhibiting a transition from the laminar to the turbulent regime much shorter than the case for other boundary layers, such as the flat plate boundary layer. However, measurements close to the disk surface indicate that an intermediate nonlinear regime is present over a considerable range of R . In a recent study, Imayama *et al.*¹² have characterized the evolution of the boundary layer by measuring the probability density function of the fluctuating azimuthal disturbance velocity. In the present investigation, by systematically acquiring low- and high-resolution spectra over a range of narrowly spaced radial and

axial positions, further light is shed on the detailed structure of the complex transition region close to the disk surface.

ACKNOWLEDGMENTS

The invaluable technical assistance by Alexandre Azouzi, Horacio Correia, Roger Michelet, Christian Nicot, and Bruno Poirel is gratefully acknowledged.

This research was financially supported by *Agence nationale de la recherche* (Project “Microsillon”).

- ¹ Th. von Kármán, “Über laminare und turbulente Reibung,” *Z. Angew. Math. Mech.* **1**, 233–252 (1921).
- ² N. Gregory, J. T. Stuart, and W. S. Walker, “On the stability of three-dimensional boundary layers with application to the flow due to a rotating disk,” *Philos. Trans. R. Soc. London, Ser. A* **248**, 155–199 (1955).
- ³ R. Kobayashi, Y. Kohama, and C. Takamadate, “Spiral vortices in boundary layer transition regime on a rotating disk,” *Acta Mechanica* **35**, 71–82 (1980).
- ⁴ M. R. Malik, S. P. Wilkinson, and S. A. Orszag, “Instability and transition in rotating disk flow,” *AIAA J.* **19**, 1131–1138 (1981).
- ⁵ S. P. Wilkinson and M. R. Malik, “Stability experiments in the flow over a rotating disk,” *AIAA J.* **23**, 588–595 (1985).
- ⁶ R. J. Lingwood, “An experimental study of absolute instability of the rotating-disk boundary-layer flow,” *J. Fluid Mech.* **314**, 373–405 (1996).
- ⁷ H. Othman and T. Corke, “Experimental investigation of absolute instability of a rotating-disk boundary layer,” *J. Fluid Mech.* **565**, 63–94 (2006).
- ⁸ R. J. Lingwood, “Absolute instability of the boundary layer on a rotating disk,” *J. Fluid Mech.* **299**, 17–33 (1995).
- ⁹ C. Davies and P. W. Carpenter, “Global behaviour corresponding to the absolute instability of the rotating-disk boundary layer,” *J. Fluid Mech.* **486**, 287–329 (2003).
- ¹⁰ B. Pier, “Finite-amplitude crossflow vortices, secondary instability and transition in the rotating-disk boundary layer,” *J. Fluid Mech.* **487**, 315–343 (2003).
- ¹¹ J. J. Healey, “Model for unstable global modes in the rotating-disk boundary layer,” *J. Fluid Mech.* **663**, 148–159 (2010).
- ¹² S. Imayama, P. H. Alfredsson, and R. J. Lingwood, “A new way to describe the transition characteristics of a rotating-disk boundary-layer flow,” *Phys. Fluids* **24**, 031701 (2012).
- ¹³ M. E. Siddiqui, “Experimental study of natural and forced instabilities and transition of a rotating-disk boundary-layer flow,” Ph.D. dissertation (École centrale de Lyon, Écully, France, 2011).
- ¹⁴ M. E. Siddiqui, B. Pier, J. Scott, A. Azouzi, and R. Michelet, “Experimental characterization and control of transition region in rotating-disk boundary layer,” in *Seventh IUTAM Symposium on Laminar–Turbulent Transition*, edited by P. Schlatter and D. S. Henningson (Springer, Stockholm, Sweden, 2010), pp. 573–576.
- ¹⁵ S. Imayama, P. H. Alfredsson, and R. J. Lingwood, “An experimental study of laminar–turbulent transition of a rotating-disk flow,” in *EUROMECH Colloquium 525, Instabilities and Transition in Three-Dimensional Flows with Rotation* (Écully, France, 2011), pp. 29–30, see <http://hal.archives-ouvertes.fr/EC525/hal-00600333>.

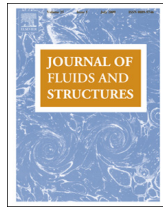
[A14]

Periodic and quasiperiodic vortex shedding in the wake of a rotating sphere

B. Pier

Journal of Fluids and Structures **41**, 43–50 (2013)

doi:10.1016/j.jfluidstructs.2012.09.002
<https://hal.archives-ouvertes.fr/hal-00733514>



Periodic and quasiperiodic vortex shedding in the wake of a rotating sphere



Benoît Pier

Laboratoire de mécanique des fluides et d'acoustique, École centrale de Lyon — CNRS — Université Claude-Bernard Lyon 1 — INSA Lyon,
36 avenue Guy-de-Collongue, 69134 Écully Cedex, France

ARTICLE INFO

Article history:

Received 30 March 2012

Received in revised form

5 September 2012

Accepted 18 September 2012

Available online 23 October 2012

Keywords:

Wake

Vortex shedding

Drag

Lift

Quasiperiodic

Bifurcation

Instability

ABSTRACT

The flow past a sphere rotating about an axis aligned with the streamwise direction is numerically investigated. The dynamics is governed by the incompressible Navier-Stokes equations and depends on two control parameters: the Reynolds number Re and rotation rate Ω . The present investigation systematically covers the range $Re \leq 350$ and $\Omega \leq 2$. First, the axisymmetric steady base flow (whether stable or not) is computed for all values of the control parameters. Then, after linearisation of the equations about the base flow, the growth rates and frequencies of the leading eigenmodes are obtained. Fully nonlinear direct numerical simulations yield the detailed flow fields and hydrodynamic forces acting on the sphere. Different wake modes (low-frequency periodic helical, quasi-periodic shedding and high-frequency periodic helical) are identified and their characteristic frequencies precisely determined.

© 2012 Elsevier Ltd. All rights reserved.

1. Introduction

At moderate Reynolds numbers, our understanding of the wake dynamics for a fixed sphere in uniform upstream flow is by now fairly complete. More complex scenarios prevail when additional effects are taken into account, such as shear in the oncoming flow, the presence of a wall, rotation of the obstacle or non-spherical shapes. Most of these configurations break the axisymmetry of the formulation. The purpose of the present investigation is to shed new light on the dynamics prevailing in a situation governed by two control parameters but preserving the axisymmetry of the problem: the wake of a sphere rotating about an axis aligned with the incident flow.

The bifurcation scenario followed by the wake of a fixed sphere in uniform upstream flow is now fairly well established, both experimentally and numerically (Ghidersa and Duček, 2000; Johnson and Patel, 1999; Nakamura, 1976; Sakamoto and Haniu, 1995; Schouwiler and Provansal, 2002; Thompson et al., 2001): at low Reynolds numbers a steady, axisymmetric flow prevails; beyond a first critical Reynolds number, $Re_1 \approx 212$, the flow bifurcates and a steady non-axisymmetric wake with planar symmetry is selected; beyond a second critical Reynolds number, $Re_2 \approx 272$, periodic shedding sets in, but conserves the symmetry plane. At still larger Reynolds numbers, the planar symmetry is broken (Mittal, 1999), and the wake becomes progressively disordered and turbulent (Constantinescu and Squires, 2004; Ormières and Provansal, 1999; Tomboulides and Orszag, 2000). Careful measurements of the hydrodynamic forces (drag, lift, torque) acting on the sphere allow characterisation of these different flow regimes (Benjamin, 1993; Bouchet et al., 2006; Maxworthy, 1965).

E-mail address: benoit.pier@ec-lyon.fr

In many situations of practical interest, the incoming flow is not perfectly uniform. In the presence of shear (Bagchi and Balachandar, 2002a; Dandy and Dwyer, 1990; Kurose and Komori, 1999; Kim et al., 2005; Kim, 2006), strain (Bagchi and Balachandar, 2002b) or stratification (Hanazaki, 1988), the lack of axisymmetry modifies the bifurcation scenario and the hydrodynamic forces. If the obstacle is not fixed but allowed to interact with the flow, it may rotate and rise or fall under the action of torque and gravity (Bagchi and Balachandar, 2002a; Ern et al., 2012; Fernandes et al., 2007; Jenny and Dušek, 2004; Jenny et al., 2003, 2004; Veldhuis et al., 2005). Numerous studies have also addressed the wake of deformable bodies such as bubbles or droplets (Kurose et al., 2001; Legendre and Magnaudet, 1997; Legendre et al., 2006; Magnaudet et al., 2003; Rastello et al., 2009, 2011; Sugioka and Komori, 2007).

Of particular interest in the present context are the flows around axisymmetric but non-spherical bodies. When the symmetry axis of disks or ellipsoids is aligned with the incident flow, the problem remains axisymmetric and the wake dynamics depend not only on the Reynolds number but also on the aspect ratio. For the extreme case of an infinitely thin disk, Fabre et al. (2008) have identified new vortex shedding modes and introduced a symmetry-based model to explain this scenario and predict the evolution of the lift force. For a thicker disk, yet more regimes have been found (Auguste et al., 2010). Meliga et al. (2009) use the leading eigenmodes derived from global stability theory and develop a weakly nonlinear model that accurately predicts the sequence of bifurcations for a thin disk. The efficiency of this model relies, among other things, on the fact that the leading eigenmodes have very similar growth rates, favouring (weak) nonlinear interactions which control the complex bifurcation scenario. Inspired by these findings, the present investigation revisits the configuration used by Kim and Choi (2002): the wake of a sphere rotating about a streamwise oriented axis. The rotation of the sphere introduces a chirality in the problem but does not break the axisymmetry. The growth rates of the leading eigenmodes depend on two parameters, Reynolds number and rotation rate, and competition between these is expected to lead to rich dynamics, possibly amenable to weakly nonlinear interaction models.

The paper is organised as follows. After formulating the problem and presenting the numerical methods in Section 2, axisymmetric base flows and their linear stability properties are discussed in Section 3. The different finite-amplitude vortex shedding regimes and associated hydrodynamic forces are presented in Section 4. Finally, Section 5 summarises the results.

2. Problem formulation and numerical method

The study is carried out using the incompressible Navier–Stokes equations. The Reynolds number is defined as $\text{Re} = U_\infty D/v$, where U_∞ is the free-stream velocity, D the sphere diameter and v the kinematic viscosity.

Throughout this investigation, cylindrical coordinates are used with r , θ and z (u , v and w) denoting radial, azimuthal and axial coordinates (velocities), respectively. The z -axis is aligned with the free-stream velocity and the origin is at the centre of the sphere. For later use, a Cartesian (x,y,z) -frame is also defined. Using non-dimensional variables based on U_∞ and D , the total velocity and pressure fields are denoted by $\mathbf{u}(r,\theta,z,t)$ and $p(r,\theta,z,t)$, respectively and are governed by the momentum and continuity equations

$$\partial_t \mathbf{u} + (\mathbf{u} \cdot \nabla) \mathbf{u} + \nabla p = \frac{1}{\text{Re}} \Delta \mathbf{u} + \mathbf{f}, \quad (1)$$

$$\nabla \cdot \mathbf{u} = 0, \quad (2)$$

with boundary conditions

$$u = v - \Omega r = w = 0 \quad \text{for } r^2 + z^2 = 1/4, \quad (3)$$

$$u = v = w - 1 = 0 \quad \text{for } r \rightarrow \infty \text{ or } z \rightarrow \pm \infty. \quad (4)$$

Here Ω is the non-dimensional rotation rate (based on U_∞ and D) of the sphere about the z -axis. The dynamics of the rotating-sphere wake are then completely determined by two control parameters, Re and Ω .

The numerical method closely follows the technique successfully implemented for studying the non-rotating sphere wake (Pier, 2008). An immersed boundary method (Fadlun et al., 2000; Mittal and Iaccarino, 2005; Zhang and Zheng, 2007) is used, whereby the presence of the sphere is enforced through the externally applied volume force \mathbf{f} in the momentum Eq. (1). Thus, the entire space is assumed to be filled with fluid and the body force ensures that the boundary conditions (3) of a rotating sphere are met. All flow fields are Fourier-expanded in the azimuthal coordinate θ , while the (r,z) -plane is discretised on a Cartesian grid using finite-differences in z and Chebyshev collocation points in r . The time-marching algorithm uses a second-order accurate predictor–corrector fractional-step method, similar to Hugues and Randriamampianina (1998).

3. Axisymmetric base flows and linear stability

Axisymmetric wakes have been computed by retaining only the axisymmetric component in the azimuthal Fourier expansions. For all Reynolds numbers and rotation rates considered in the present study, the sphere wakes were found to approach a steady state when time-marching the governing Eqs. (1) and (2).

The structure of the basic axisymmetric wake for different values of the control parameters is illustrated in Fig. 1 by isolines of the azimuthal vorticity $\omega_\theta = \partial_z u - \partial_r w$.

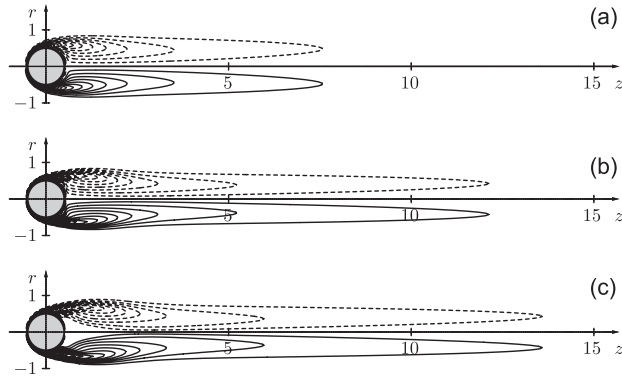


Fig. 1. Flow structure of the basic axisymmetric wake for (a) $Re = 150$ and $\Omega = 1$, (b) $Re = 250$ and $\Omega = 1$, (c) $Re = 250$ and $\Omega = 2$. Solid (dashed) isolines correspond to positive (negative) values of azimuthal vorticity, spaced by 0.5.

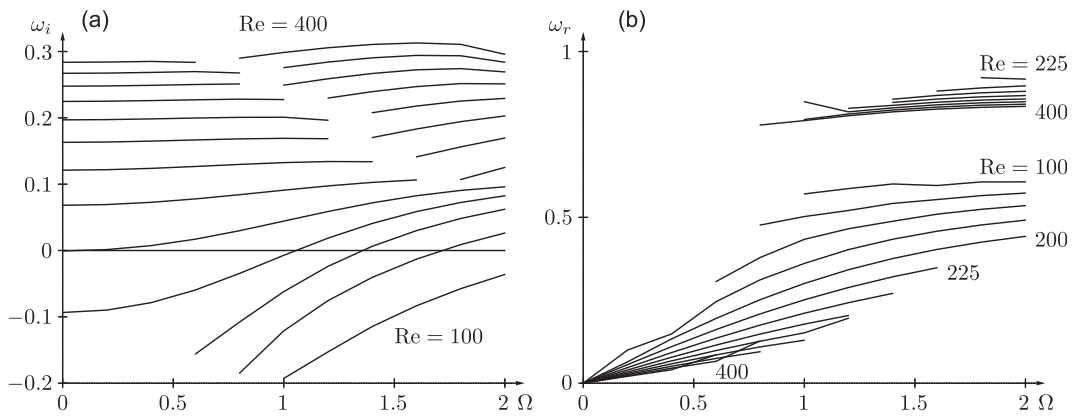


Fig. 2. (a) Growth rate ω_i and (b) frequency ω_r of the leading eigenmode for axisymmetric basic wakes, computed for $\Omega = 0.0, 0.2, \dots, 2.0$ and $Re = 100, 125, \dots, 400$.

The linear stability of these axisymmetric wakes is probed by computing the response to a non-axisymmetric perturbation. Here only a single non-axisymmetric azimuthal Fourier component is retained in the expansions of the flow fields, and the Navier-Stokes equations are linearised around the previously computed basic flow. Growth rates and frequencies of the most unstable modes are then derived from the time-series of selected flow components, recorded at a fixed spatial location. Such a flow component f is expected to evolve as $f \propto \exp(-i\omega t)$, where ω is the complex eigenvalue associated with the mode. The growth rate ω_i is then obtained by a linear fit of $\log |f|$, while the frequency ω_r is obtained by spectral analysis of the compensated $f \exp(-\omega_i t)$. Thus, the growth rates ω_i and frequencies ω_r are obtained for the most unstable mode at each setting of the control parameters Re and Ω . These values are shown in Fig. 2. It is observed that two distinct mode types lead to instability, depending on the control parameters: at moderate rotation rates and low Reynolds numbers, the instability is dominated by a “slow” mode, the frequency of which scales nearly linearly with the sphere rotation rate Ω . In contrast, at higher parameter values, a “fast” mode dominates, whose frequency is approximately independent of Ω . Similar behaviour is observed for the nonlinear dynamics, as discussed below.

4. Nonlinear dynamics

To investigate the nonlinear dynamics, a finite number of azimuthal Fourier harmonics are retained and the direct numerical simulations take into account the nonlinear coupling between all these modes. When starting integration, the initial condition is chosen as the previously computed axisymmetric base flow with a small non-axisymmetric perturbation. In situations where this axisymmetric flow is unstable, the non-axisymmetric perturbation starts to grow exponentially in time. After a transient growth phase, nonlinear effects come into play that limit the amplitude growth. At large times, the system is found to approach a periodic or quasi-periodic regime, or to display irregular behaviour.

Monitoring the temporal evolution of the energy E_1 contained in the first azimuthal harmonic illustrates the development of non-axisymmetric components in the sphere wake. In Fig. 3, the energy content E_1 is plotted for $0 \leq \Omega \leq 2$ and $Re = 250$ and 325. For the wakes corresponding to these plots, after entering a finite-amplitude regime, the energy E_1 is seen to reach either a constant value or to converge towards a state of periodic oscillations. At larger values of the Reynolds number, irregular oscillations may also be found to persist indefinitely.

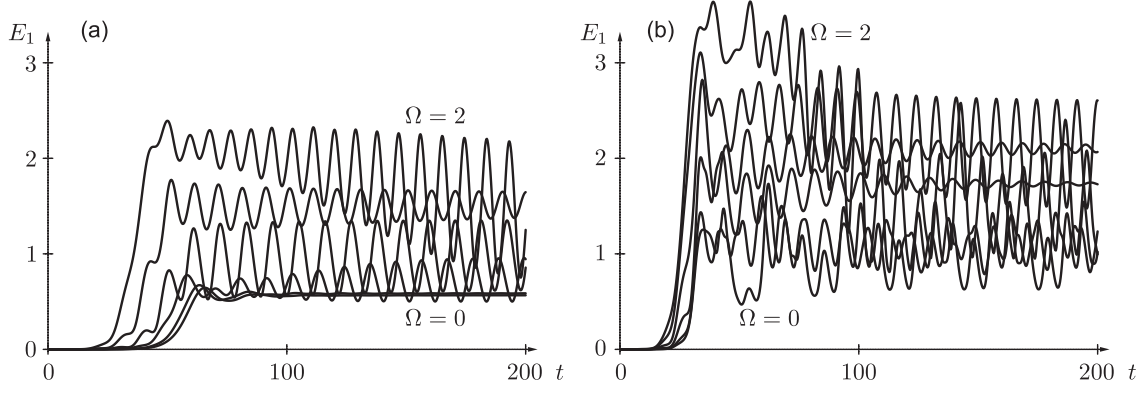


Fig. 3. Temporal evolution of energy E_1 (arbitrary units) contained in first azimuthal harmonic for $\Omega = 0.0, 0.4, \dots, 2.0$ and $Re = 250$ (a), $Re = 325$ (b).

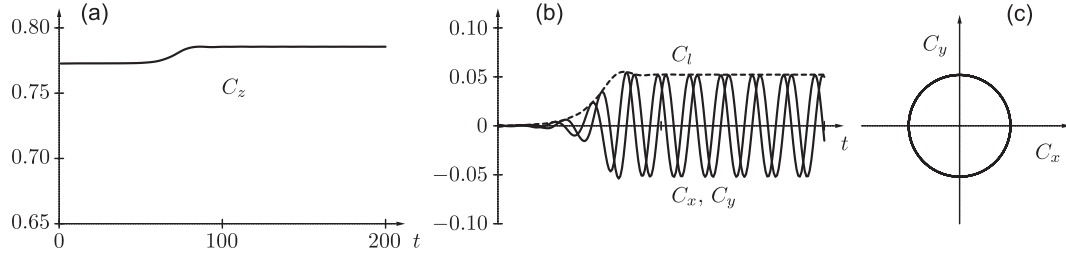


Fig. 4. Temporal evolution of hydrodynamic forces for $Re = 225$ and $\Omega = 1$. C_z : drag; C_x and C_y : lift forces; C_l : transverse force. Initial condition consists of the axisymmetric base flow with a small-amplitude non-axisymmetric perturbation.

To further characterise the flow dynamics, the hydrodynamic forces acting on the sphere have been computed. These forces are obtained by spatial integration of the volume force used in the immersed boundary method; there is no need to evaluate components of the stress tensor at the sphere surface. The drag coefficient C_z measures, in non-dimensional units, the component of the force acting in the z -direction aligned with the outer flow. The lift coefficients C_x and C_y are obtained by projection onto the x - and y -axes, respectively, while the lateral force coefficient C_l is defined as $C_l = \sqrt{C_x^2 + C_y^2}$.

For axisymmetric wakes, all coefficients vanish except the drag C_z . In configurations where the axisymmetric base flow is unstable, the development of finite non-axisymmetric flow components is accompanied by a similar development of transverse forces, characterised by C_x and C_y (and C_l). The constant, periodic, quasi-periodic or irregular values taken by these hydrodynamic force coefficients characterise the associated wake dynamics.

4.1. Helical regime

The wake behaviour observed for $Re = 225$ and $\Omega = 1$ is typical of the dynamics prevailing after the first destabilisation of the axisymmetric flow. Fig. 4 illustrates the temporal evolution of the force coefficients, starting from the slightly perturbed (and unstable) axisymmetric base flow. After a transient regime characterised by growth of transverse force components, the wake is seen to approach a state of constant drag, slightly higher than for the base flow (Fig. 4a). Lift coefficients C_x and C_y display harmonic oscillations, out of phase by a quarter-period, while the magnitude of the lateral force C_l is observed to tend to a constant value (Fig. 4b). This is further illustrated by the time-trace in the (C_x, C_y) -plane (Fig. 4c): beyond the transient phase, a perfect circle is described at a constant angular speed.

The spatial structure of the wake flow is illustrated in Fig. 5, where isolines of the azimuthal vorticity are plotted for two orthogonal (x, z) - and (y, z) -planes.

Temporal spectral analysis of the force coefficients (as well as of any other flow components) demonstrates that this regime is characterised by a single frequency. For $Re = 225$ and $\Omega = 1$, the periodicity of the lift coefficients is obtained as $\omega_x = \omega_y = 0.31$. In fact, it can be shown that the entire wake is in a *helical* state, characterised by “solid-body” rotation of the flow field about the z -axis at constant angular speed. This means that the flow is steady in a frame of reference rotating about the z -axis at $\omega_x (= \omega_y)$. Note that the angular speed $\omega_x = \omega_y$ is well below the sphere rotation rate $\Omega = 1$.

4.2. Quasi-periodic vortex shedding

For $Re = 275$ and $\Omega = 0.8$, a different behaviour is obtained. Again, the development of non-axisymmetric components is accompanied by an increase in drag. But here, no steady state is reached: the drag coefficient continues to oscillate

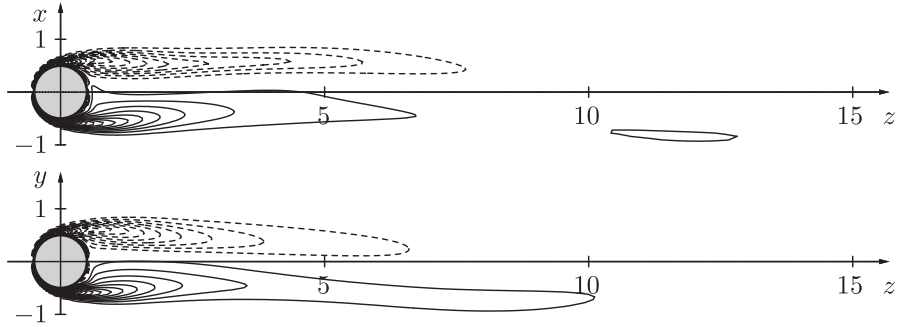


Fig. 5. Snapshot of vorticity fields in the helical regime at $Re = 225$ and $\Omega = 1$. Isolines of azimuthal vorticity in two orthogonal planes.

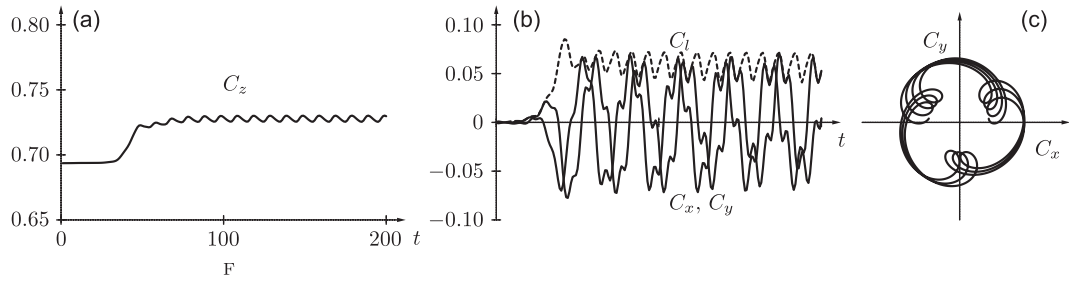


Fig. 6. Temporal evolution of hydrodynamic forces for $Re = 275$ and $\Omega = 0.8$.

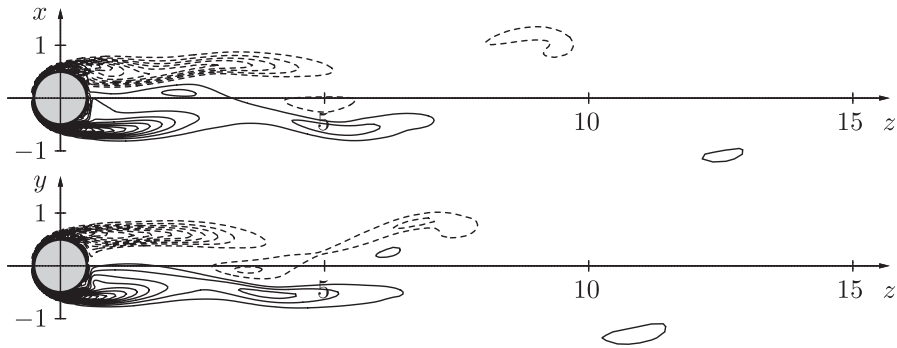


Fig. 7. Snapshot of vorticity fields in the quasiperiodic regime at $Re = 275$ and $\Omega = 0.8$.

(Fig. 6a). Lift coefficients C_x and C_y display quasiperiodic oscillations while the lateral force C_l fluctuates with the same periodicity as the drag (Fig. 6b). This behaviour leads to a more complex pattern in the (C_x, C_y) -plane, see Fig. 6(c). Temporal spectral analyses show that these signals are characterised by two distinct (and incommensurate) frequencies: $\omega_x = \omega_y = 0.21$ and $\omega_z = \omega_l = 0.62$. Indeed, C_z and C_l are periodic (with same frequency $\omega_z = \omega_l$) while C_x and C_y are quasiperiodic (displaying a combination of ω_z and ω_x).

A snapshot of the spatial structure of the associated vorticity fields is given in Fig. 7. This dynamics can be interpreted as a quasiperiodic vortex shedding regime, corresponding to the combination of a helical mode (“solid-body rotation” about the z-axis at ω_x) and vortex shedding waves travelling axially downstream (frequency ω_z).

4.3. High-frequency helical regime

For $Re = 300$ and $\Omega = 1$ a further wake behaviour is observed, representative of a third class of flow dynamics. After a relatively long transient, the system approaches a (single-frequency) periodic state. The drag C_z and the lateral force C_l reach constant values, while the lift coefficients C_x and C_y display harmonic oscillations in quadrature, leading to a circular time-trace in the (C_x, C_y) -plane (Fig. 8). This regime is again of periodic helical vortex shedding type, characterised by a single frequency $\omega_x = \omega_y = 0.90$. Note that the frequency of this “solid-body” rotation is quite closer to the sphere rotation rate Ω . Hence, this regime could be termed “high-frequency helical vortex shedding”.

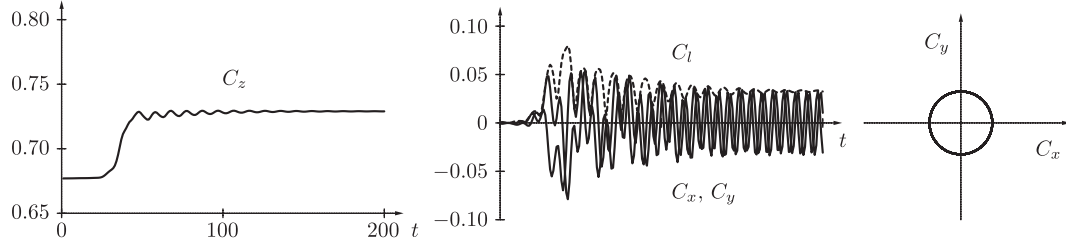


Fig. 8. Temporal evolution of hydrodynamic forces for $Re = 300$ and $\Omega = 1$.

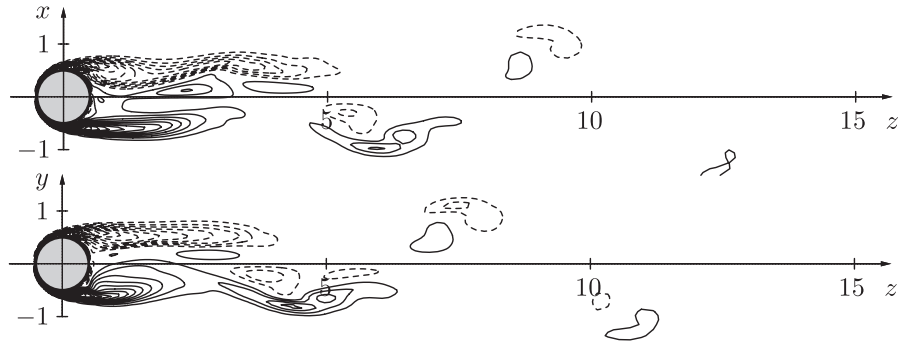


Fig. 9. Snapshot of vorticity fields in the high-frequency helical regime at $Re = 300$ and $\Omega = 1$.

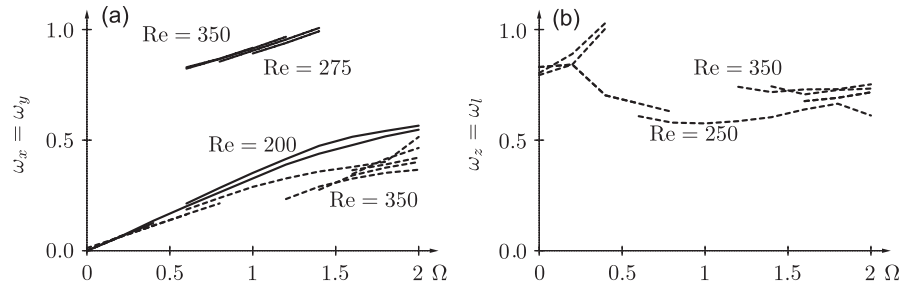


Fig. 10. Characteristic frequencies prevailing in the rotating-sphere wake. (a) Frequencies $\omega_x = \omega_y$ dominating the fluctuations of the lift coefficients C_x and C_y . (b) Frequencies $\omega_z = \omega_l$ governing the oscillations of the drag and lateral force coefficients C_z and C_l . Solid curves correspond to low- or high-frequency helical regimes. Dashed curves indicate quasiperiodic vortex-shedding (or disordered) regimes.

The corresponding vorticity fields are illustrated for two orthogonal planes in Fig. 9. Although this regime is periodic and the flow fields would be steady in a frame rotating at ω_x around the z -axis, these vorticity fields closely resemble those prevailing in the quasiperiodic regime (see Fig. 7) and are rather different from those of the low-frequency helical regime (see Fig. 5). It is as if the axial vortex shedding and the helical “solid-body” rotation were locked together, or “frozen” (Kim and Choi, 2002).

4.4. Characteristic frequencies

For each Reynolds number and sphere rotation rate, the characteristic frequencies have been determined via temporal Fourier analyses of long time series of the force coefficients. The helical frequencies $\omega_x (= \omega_y)$ are plotted in Fig. 10(a), while the axial frequencies $\omega_z (= \omega_l)$ are shown in Fig. 10(b). In these plots, solid curves correspond to low- and high-frequency modes while dashed curves indicate quasiperiodic (or disordered) vortex shedding. Note that helical frequencies dominating the fluctuations of the lift coefficients C_x and C_y are obtained for any non-axisymmetric flow, while the axial vortex-shedding frequencies governing the oscillations of the drag and lateral force coefficients C_z and C_l are only relevant in the quasiperiodic shedding regimes.

In Fig. 10(a), it is seen that ω_x displays an almost linear dependence on Ω in the low-frequency helical and quasiperiodic regimes. Transition from low-frequency helical to quasiperiodic vortex shedding hardly affects these values. In the high-frequency helical regimes, however, order of magnitude larger values for ω_x are obtained. The axial frequencies ω_z shown in 10(b), correspond more specifically to axially travelling vortex shedding waves and display only weak dependence on the rotation rate Ω .

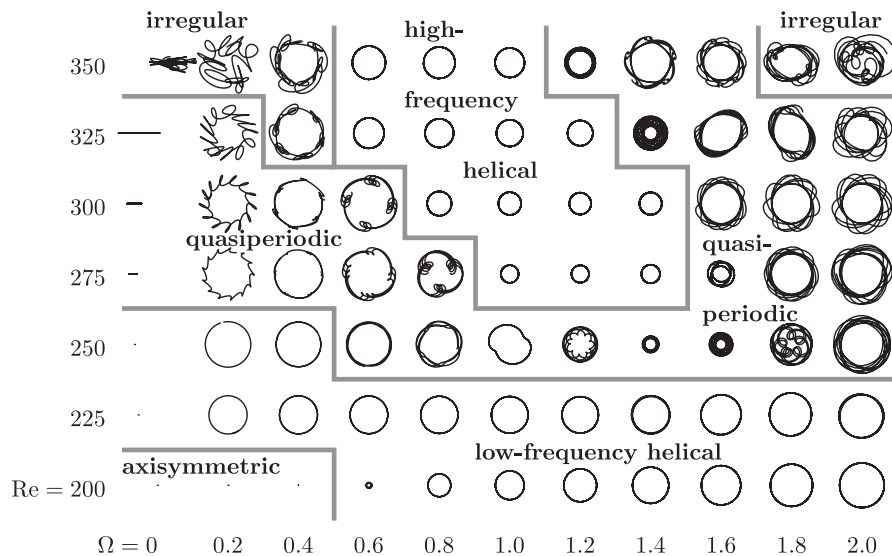


Fig. 11. Map of the different regimes as a function of the control parameters.

5. Conclusion and discussion

Direct numerical simulations have been carried out in order to systematically cover the governing parameter space for sphere rotation rates $\Omega \leq 2$ and Reynolds numbers up to $Re = 350$. Fig. 11 presents a map of the observed regimes characterised by the associated time-traces of the lift coefficients in the (C_x, C_y) -plane.

At low Reynolds numbers, the axisymmetric wake is stable. When the Reynolds number is increased, a low-frequency helical regime takes over, characterised by constant values of drag (C_z) and transverse force (C_l). The flow field is found to rotate around the z-axis at constant frequency $\omega_x = \omega_y$ without deformation. Indeed, in such a rotating frame, the flow field would be time-independent. The rate ω_x at which the wake rotates around the axis is found to increase almost linearly with the sphere rotation rate Ω , and this regime can be viewed as a continuous deformation, through axial rotation, of the well-documented steady planar symmetric state for non-rotating spheres in the range $Re_1 < Re < Re_2$, with $Re_1 \simeq 212$ and $Re_2 \simeq 272$ (Ghidersa and Duček, 2000; Johnson and Patel, 1999; Mittal, 1999; Schouwiler and Provansal, 2002).

A second bifurcation occurs when the Reynolds number is increased, leading to a quasiperiodic state which can be interpreted as a modulation (at a second incommensurate frequency ω_z) of the previous helical regime. A rotating frame in which the flow field would be steady no longer exists. Again, this regime can be viewed as the continuation through axial rotation of the periodic vortex shedding regime that prevails for $Re > Re_2 \simeq 272$ for a non-rotating sphere. In the non-rotating case, onset of vortex shedding occurs through a Hopf bifurcation (Schouwiler and Provansal, 2002). Here, our results indicate that this remains true along the entire boundary separating the low-frequency helical wakes from the quasiperiodic wakes. However, many more computations would be necessary to prove that the amplitude of the second-frequency component scales as the square-root of the distance to this critical boundary.

The third type of behaviour, termed the high-frequency helical regime, occurs at still larger Reynolds numbers. This periodic regime does not have an analogue in the non-rotating $\Omega = 0$ case. While the transition from the low-frequency helical to the quasiperiodic regime is a continuous process, the switching from quasiperiodic to high-frequency helical regimes is discontinuous in the control parameters. Indeed, the dominant ω_x -frequency prevailing in the wake abruptly increases while the amplitude of the transverse forces (C_l) suddenly drops. The nature of the associated bifurcation remains unclear. Despite several attempts at slowly modifying one of the control parameters, no hysteresis was found.

At yet larger Reynolds numbers, irregular states have been observed. No systematic survey of the parameter space beyond $Re = 350$ has been attempted since this would require much finer spatial meshes to obtain reliable results.

In future work, it would be interesting to address the nature of the bifurcations between the different regimes in more detail and to test whether the theory of Meliga et al. (2009) can be adapted to the present configuration.

Acknowledgements

Computing resources from Fédération lyonnaise de calcul hautes performances (FLCHP) and Institut national de physique nucléaire et de physique des particules (IN2P3) are gratefully acknowledged.

References

- Auguste, F., Fabre, D., Magnaudet, J., 2010. Bifurcations in the wake of a thick circular disk. *Theoretical and Computational Fluid Dynamics* 24, 305–313.
- Bagchi, P., Balachandar, S., 2002a. Effect of free rotation on the motion of a solid sphere in linear shear flow at moderate Re. *Physics of Fluids* 14, 2719–2737.
- Bagchi, P., Balachandar, S., 2002b. Steady planar straining flow past a rigid sphere at moderate Reynolds number. *Journal of Fluid Mechanics* 466, 365–407.
- Benjamin, T.B., 1993. Note on formulas for the drag of a sphere. *Journal of Fluid Mechanics* 246, 335–342.
- Bouchet, G., Mebarek, M., Dušek, J., 2006. Hydrodynamic forces acting on a rigid fixed sphere in early transitional regimes. *European Journal of Mechanics—B/Fluids* 25, 321–336.
- Constantinescu, G., Squires, K., 2004. Numerical investigations of flow over a sphere in the subcritical and supercritical regimes. *Physics of Fluids* 16, 1449–1466.
- Dandy, D.S., Dwyer, H.A., 1990. A sphere in shear flow at finite Reynolds number: effect of shear on particle lift, drag, and heat transfer. *Journal of Fluid Mechanics* 216, 381–410.
- Ern, P., Rocco, F., Fabre, D., Magnaudet, J., 2012. Wake-induced oscillatory paths of bodies freely rising or falling in fluids. *Annual Review of Fluid Mechanics* 44, 97–121.
- Fabre, D., Auguste, F., Magnaudet, J., 2008. Bifurcations and symmetry breaking in the wake of axisymmetric bodies. *Physics of Fluids*, 051702.
- Fadlun, E.A., Verzicco, R., Orlandi, P., Mohd-Yusof, J., 2000. Combined immersed-boundary finite-difference methods for three-dimensional complex flow simulations. *Journal of Computational Physics* 161, 35–60.
- Fernandes, P.C., Rocco, F., Ern, P., Magnaudet, J., 2007. Oscillatory motion and wake instability of freely rising axisymmetric bodies. *Journal of Fluid Mechanics* 573, 479–502.
- Ghidersa, B., Dušek, J., 2000. Breaking of axisymmetry and onset of unsteadiness in the wake of a sphere. *Journal of Fluid Mechanics* 423, 33–69.
- Hanazaki, H., 1988. A numerical study of three-dimensional stratified flow past a sphere. *Journal of Fluid Mechanics* 192, 393–419.
- Hugues, S., Randriamampianina, A., 1998. An improved projection scheme applied to pseudospectral methods for the incompressible Navier–Stokes equations. *International Journal of Numerical Methods in Fluids* 28, 501–521.
- Jenny, M., Bouchet, G., Dušek, J., 2003. Nonvertical ascension or fall of a free sphere in a Newtonian fluid. *Physics of Fluids* 15, L9–L12.
- Jenny, M., Dušek, J., 2004. Efficient numerical method for the direct numerical simulation of the flow past a single light moving spherical body in transitional regimes. *Journal of Computational Physics* 194, 215–232.
- Jenny, M., Dušek, J., Bouchet, G., 2004. Instabilities and transition of a sphere falling or ascending freely in a Newtonian fluid. *Journal of Fluid Mechanics* 508, 201–239.
- Johnson, T.A., Patel, V.C., 1999. Flow past a sphere up to a Reynolds number of 300. *Journal of Fluid Mechanics* 378, 19–70.
- Kim, D., Choi, H., 2002. Laminar flow past a sphere rotating in the streamwise direction. *Journal of Fluid Mechanics* 461, 365–386.
- Kim, D., Choi, H., Choi, H., 2005. Characteristics of laminar flow past a sphere in uniform shear. *Physics of Fluids* 17, 103602.
- Kim, I., 2006. Forces on a spherical particle in shear flow at intermediate Reynolds numbers. *International Journal of Computational Fluid Dynamics* 20, 137–141.
- Kurose, R., Komori, S., 1999. Drag and lift forces on a rotating sphere in a linear shear flow. *Journal of Fluid Mechanics* 384, 183–206.
- Kurose, R., Misumi, R., Komori, S., 2001. Drag and lift forces acting on a spherical bubble in a linear shear air flow. *International Journal of Multiphase Flow* 27, 1247–1258.
- Legendre, D., Magnaudet, J., 1997. A note on the lift force on a spherical bubble or drop in a low-Reynolds-number shear flow. *Physics of Fluids* 9, 3572–3574.
- Legendre, D., Merle, A., Magnaudet, J., 2006. Wake of a spherical bubble or a solid sphere set fixed in a turbulent environment. *Physics of Fluids* 18, 048102.
- Magnaudet, J., Takagi, S., Legendre, D., 2003. Drag, deformation and lateral migration of a buoyant drop moving near a wall. *Journal of Fluid Mechanics* 476, 115–157.
- Maxworthy, T., 1965. Accurate measurements of sphere drag at low Reynolds numbers. *Journal of Fluid Mechanics* 23, 369–372.
- Meliga, P., Chomaz, J.-M., Sipp, D., 2009. Global mode interaction and pattern selection in the wake of a disk: a weakly nonlinear expansion. *Journal of Fluid Mechanics* 633, 159–189.
- Mittal, R., 1999. Planar symmetry in the unsteady wake of a sphere. *AIAA Journal* 37, 388–390.
- Mittal, R., Iaccarino, G., 2005. Immersed boundary methods. *Annual Review of Fluid Mechanics* 37, 239–261.
- Nakamura, I., 1976. Steady wake behind a sphere. *Physics of Fluids* 19, 5–8.
- Ormières, D., Provansal, M., 1999. Transition to turbulence in the wake of a sphere. *Physical Review Letters* 83, 80–83.
- Pier, B., 2008. Local and global instabilities in the wake of a sphere. *Journal of Fluid Mechanics* 603, 39–61.
- Rastello, M., Marié, J.-L., Grosjean, N., Lance, M., 2009. Drag and lift forces on interface-contaminated bubbles spinning in a rotating flow. *Journal of Fluid Mechanics* 624, 159–178.
- Rastello, M., Marié, J.-L., Lance, M., 2011. Drag and lift forces on clean spherical and ellipsoidal bubbles in a solid-body rotating flow. *Journal of Fluid Mechanics* 682, 434–459.
- Sakamoto, H., Hanju, H., 1995. The formation mechanism and shedding frequency of vortices from a sphere in uniform shear flow. *Journal of Fluid Mechanics* 287, 151–171.
- Schouwiler, L., Provansal, M., 2002. Self-sustained oscillations in the wake of a sphere. *Physics of Fluids* 14, 3846–3854.
- Sugioka, K.-I., Komori, S., 2007. Drag and lift forces acting on a spherical water droplet in homogeneous linear shear air flow. *Journal of Fluid Mechanics* 570, 155–175.
- Thompson, M.C., Leweke, T., Provansal, M., 2001. Kinematics and dynamics of sphere wake transition. *Journal of Fluids and Structures* 15, 575–585.
- Tomboulides, A.G., Orszag, S.A., 2000. Numerical investigation of transitional and weak turbulent flow past a sphere. *Journal of Fluid Mechanics* 416, 45–73.
- Veldhuis, C., Biesheuvel, A., van Wijngaarden, L., Lohse, D., 2005. Motion and wake structure of spherical particles. *Nonlinearity* 18, C1–C8.
- Zhang, N., Zheng, Z.C., 2007. An improved direct-forcing immersed-boundary method for finite difference applications. *Journal of Computational Physics* 221, 250–268.

[A15]

Temporal stability of eccentric Taylor–Couette–Poiseuille flow

C. Leclercq, B. Pier & J. Scott

Journal of Fluid Mechanics **733**, 68–99 (2013)

doi:10.1017/jfm.2013.437

<https://hal.archives-ouvertes.fr/hal-00865631>

Temporal stability of eccentric Taylor–Couette–Poiseuille flow

Colin Leclercq[†], Benoît Pier and Julian F. Scott

Laboratoire de mécanique des fluides et d'acoustique, École centrale de Lyon – CNRS – Université Claude-Bernard Lyon 1 – INSA Lyon, 36 avenue Guy-de-Collongue, 69134 Écully CEDEX, France

(Received 23 February 2013; revised 27 June 2013; accepted 16 August 2013)

The combined effects of axial flow and eccentricity on the temporal stability properties of the Taylor–Couette system are investigated using a pseudospectral method. Eccentricity is found to stabilize the Couette flow regardless of axial advection intensity. As the axial Reynolds number Re_z is increased for any fixed eccentricity $e \leq 0.7$, the critical mode switches from deformed toroidal Taylor vortices to helical structures with an increasing number of waves, and with helicity opposed to the inner-cylinder rotation. For a wide-gap configuration of radius ratio $\eta = 0.5$, increasing axial advection has a stabilizing effect for low Re_z , then a weak destabilizing effect for high enough Re_z . Centrifugal effects are always destabilizing, but axial shear is responsible for the dominance of helical modes of increasing azimuthal complexity. The modes localize in the converging gap region, and the energy concentrates increasingly into axial motion for larger Re_z . Critical quantities are also computed for a small-gap case, and similar trends are observed, even though no destabilizing effect of advection is observed within the range of Re_z considered. Comparison with the experiment of Coney & Mobbs (*Proc. Inst. Mech. Engrs*, vol. 184 Pt 3L, 1969–70, pp. 10–17) for $\eta = 0.89$ shows good agreement, despite small discrepancies attributed to finite length effects.

Key words: convection, instability, Taylor–Couette flow

1. Introduction

More than 40 years ago, Coney & Mobbs (1969–70) wrote: ‘a linear stability theory solution for the case of eccentric rotating cylinders with a superimposed axial flow [...] is not available and the difficulties in the way of such a solution are formidable’. Indeed, while the flow between rotating cylinders has been one of the benchmarks of hydrodynamic stability since the path-breaking work of Taylor (1923), the computational cost associated with more complex versions of this flow has long been considered a showstopper, and still remains a major challenge as we try to bridge the gap with engineering applications. In this paper, we study the temporal stability of cylindrical Couette flow with two additional effects: eccentricity of the cylinder axes and axial flow. Taken separately, the two effects have already been the subject of numerous studies, which we will briefly review in this introductory section. But to the

[†]Email address for correspondence: colin.leclercq@ec-lyon.fr

best of our knowledge, no one has yet undertaken the complete theoretical study of the combination of both, and very limited experimental data are available in this case.

1.1. Control parameters

This problem is governed by four control parameters. The geometry is defined by the ratio of radii $0 < \eta \equiv a/b < 1$ and eccentricity $0 \leq e \equiv c/(b-a) \leq 1$, where a and b are the inner and outer cylinder radii and c is the distance between centres. Introducing the clearance $d = b - a$, one can also use the clearance ratio $\delta \equiv d/a = (1 - \eta)/\eta$ instead of η .

The azimuthal Reynolds number $Re_\Omega = a\Omega d/\nu$, based on the inner-cylinder rotation rate Ω , compares centrifugal and viscous effects, while the axial Reynolds number $Re_z = \bar{w}d/\nu$, based on the mean axial velocity \bar{w} , measures the importance of axial advection.

1.2. Industrial applications: wellbore drilling and high-speed journal bearings

This model flow is of interest to the oil industry as a first step towards understanding the dynamics of the complex annular flow of mud in wellbore drilling operations. For drilling applications, a drillstring is rotated inside the well in order to drive a drill bit that cuts the rock at the bottom of the well. Mud is injected through the drillstring and flows back to the surface through the annular gap, ensuring several engineering functions, among which are the following (Escudier, Oliveira & Pinho 2002): carrying the rock cuttings out of the well, cooling and cleaning the drill bit, supporting the wellbore, avoiding inflow of formation fluids and preventing settling of the cuttings when circulation is stopped. The annular flow of mud can be modelled in a first approximation by an eccentric Taylor–Couette–Poiseuille flow because of the rotation of the drillstring, the pressure-driven axial flow and eccentricity caused by flexibility of the drillstring.

For typical industrial configurations (Escudier *et al.* 2002; Guo & Liu 2011), the ratio between drillstring and outer-wall radii ranges from 0.2 at the top to 0.8 at the bottom, and the eccentricity can go all the way to the limit of touching cylinders. The gap between the drillstring and the outer wall is of order 10^{-2} – 10^{-1} m. The velocity of the inner cylinder in rotation is comparable to the mean axial velocity of the flow, of the order of 1 m s^{-1} . Finally, the mud density is of order 10^3 kg m^{-3} , with an equivalent dynamic viscosity in the range 10^{-3} – 10^{-1} Pa s (note that viscosity is a function of local strain rate for non-Newtonian fluids). As a result, equivalent Reynolds numbers Re_Ω and Re_z of the order of 10^2 – 10^5 are expected.

Limitations of the model for this application include non-Newtonian effects (viscoelasticity and thixotropicity), motion of the inner-cylinder position inside the well, contamination of the fluid by cuttings and ‘formation fluid’, variable eccentricity and outer-wall radius with depth, and imperfect circularity of the wellbore wall. However, the consideration of both eccentricity and axial flow in a systematic way is already a significant improvement on existing theory.

Eccentric Taylor–Couette–Poiseuille flow is also of interest in the field of high-speed journal bearings, where ‘the damaging effect of impurities contained in oil can be considerably reduced when they are quickly removed from the friction contact area [...] by intensifying axial oil flow’ (Sep 2008). In high-speed journal bearings, Huggins (1966–67) quotes a value of $Re_z = 100$ during tests on a 24 in diameter journal bearing. And instabilities are expected to arise, as noted by Coney & Mobbs (1969–70): ‘in the large-diameter journal bearings, which may be expected to operate

in the Taylor vortex régime, there is [...] a considerable superimposed axial flow of lubricant'.

1.3. Eccentric Taylor–Couette flow

The effect of eccentricity on the Taylor–Couette flow has been investigated by many researchers, covering a wide range of ratio of radii and eccentricities, starting with the experimental work of Cole (1957). Using torque measurements, flow visualization (dye injection, aluminum flakes etc.) and hot-wire probes, Cole (1957, 1967, 1969), Kamal (1966), Vohr (1968), Koschmieder (1976) and later Karasudani (1987), Xiao, Lim & Chew (1997) and Lim & Lim (2008) found a stabilizing effect of eccentricity on the appearance of Taylor vortices. On the other hand, Castle & Mobbs (1967), Versteegen & Jankowski (1969) and Frêne & Godet (1971) found a slight destabilization at weak eccentricities, followed by stabilization at higher values. The vortices of the first type, confined to the neighbourhood of the inner cylinder, were later found to be caused by endwall effects by Mobbs & Ozogan (1984) and El-Dujaily & Mobbs (1990). For the second type of vortices, an increase in critical wavenumber at higher eccentricities was reported in the early work of Cole (1967) and quantified by subsequent authors.

The first theoretical analyses were made by DiPrima (1963) and Ritchie (1968), using local stability theory (as implied by the parallel-flow approximation in the ‘pseudo-azimuthal’ direction) and asymptotic analyses in the small-gap, small-eccentricity limit. The first global stability analyses of the problem, considering fully two-dimensional basic flows, were performed a decade later by DiPrima & Stuart (1972b), DiPrima & Stuart (1975) and Eagles, Stuart & DiPrima (1978), demonstrating a stabilizing effect of eccentricity and the weakness of the local approach to model this flow. More recently, Oikawa, Karasudani & Funakoshi (1989a,b) and Dai, Dong & Szeri (1992) were able to relax the small-gap and small-eccentricity constraint (e up to 0.6–0.7, η as low as 0.5), using numerical methods to solve the two-dimensional stability problem.

Finally, most recent numerical and experimental stability analyses seem to have been concerned mostly with the effect of non-Newtonian fluids (e.g. Chawda & Avgousti 1996; Dris & Shaqfeh 1998), with applications to oil drilling and polymeric processing.

1.4. Taylor–Couette–Poiseuille flow

The effect of a pressure-driven axial flow on the concentric Taylor–Couette system with a fixed outer cylinder has been the object of even more investigations. The first analytical studies were restricted to the narrow-gap limit and axisymmetric perturbations (e.g. Chandrasekhar 1960; DiPrima 1960), reaching (after some controversy) the conclusion that advection stabilizes the Couette flow. The first correct numerical studies of the finite-gap geometry, with non-axisymmetric disturbances, are due to Takeuchi & Jankowski (1981) and Ng & Turner (1982). For a wide-gap configuration $\eta = 0.5$, Takeuchi & Jankowski (1981) confirmed numerically and experimentally (for respectively $Re_z \leq 100$ and $Re_z \leq 150$) the results from Snyder (1962, 1965)’s experiments showing that toroidal vortices are replaced by helical vortices for larger advection rates. Ng & Turner (1982) extended the results to $Re_z \leq 6000$ for $\eta = 0.77$ and $\eta = 0.95$, with fair agreement with experiments. They also considered axisymmetric disturbances for $\eta = 0.95$ up to the value of $Re_z = 7739.5$, where annular Poiseuille flow becomes unstable with respect to Tollmien–Schlichting (TS) like disturbances. They showed a connection between the

centrifugal instability and the shear instability at high advection rates, as conjectured by Reid (1961). More recently, Cotrell & Pearlstein (2004) and Cotrell, Sarma & Pearlstein (2004) extended the analysis of Ng & Turner (1982) to non-axisymmetric disturbances for $\eta = 0.5, 0.77, 0.95$. Before the transition to shear instability, these authors noted the existence of a plateau in critical Re_Ω , for which the associated critical axial wavenumber drops with increasing Re_z . For the case $\eta = 0.5$, they also noticed the existence of a maximum critical Re_Ω for a specific value of Re_z . Heaton (2008) complemented their analyses by assessing the importance of non-modal effects, and showed their relevance at moderate and large $Re_z \sim 10^2–10^4$. Other recent studies concern rotation of the outer cylinder (Meseguer & Marques 2002), absolute/convective instabilities (Altmeyer, Hoffmann & Lücke 2011), supercritical states (Hwang & Yang 2004), time-periodic flow (Marques & Lopez 2000), additional radial flow (e.g. Martinand, Serre & Lueptow 2009) and so on. A comprehensive review of the large panel of work on this topic, though not completely up to date, is available in Cotrell & Pearlstein (2004).

1.5. Eccentric Taylor–Couette–Poiseuille flow

As already mentioned, some experimental data are available in the case of combined eccentricity and axial flow. To the best of the authors' knowledge, only one experiment has been undertaken, at a radius ratio of $\eta = 0.89$ (Coney & Mobbs 1969–70; Coney 1971; Younes 1972; Younes, Mobbs & Coney 1972; Mobbs & Younes 1974; Coney & Atkinson 1978). In Coney & Mobbs (1969–70) and Younes *et al.* (1972), the critical Taylor number is reported as a function of $e \leq 0.8$ and Re_z up to 125, using flow visualization and torque measurements. It is found that axial flow always stabilizes the Couette flow. At fixed eccentricity, stabilization due to advection is less marked than in the concentric case. The critical curves have complicated forms for $Re_z \geq 75$, but the effect of eccentricity is generally stabilizing. However, the results display considerable scatter and are very sensitive to the instability criterion, as shown in Coney & Atkinson (1978). Moreover, attempts at determining the critical wavenumber of the perturbations proved abortive, because of the complex flow structure observed. For $e > 0.2$, $Re_z > 20$, there seems to be coexistence of two helical structures winding in opposite directions, with ‘fluctuations in the number of vortex cells occupying the length of the apparatus at any instant or in the number of turns in the vortex spirals’ (Coney & Mobbs 1969–70; Mobbs & Younes 1974). These experiments will be discussed further in § 4.

On the theoretical side, apart from the semi-empirical local stability theory of Coney & Mobbs (1969–70), inspired by the work of DiPrima (1963), no stability analysis has been attempted so far. Modal stability analysis is the object of the present paper and is a first step towards understanding the complex behaviour exhibited by this flow.

1.6. Plan of the paper

The paper is organized into four sections. Section 2 introduces the linear stability problem, including governing equations and numerical methods for basic-flow and normal-mode computations. The main properties of the basic flow and dominant eigenmodes are presented. In § 3, a parametric temporal stability study is performed for $\eta = 0.5$: critical quantities are computed and stability diagrams are given. The instability mechanism is investigated by examining the spatial structure of the critical modes, and variations of growth rates with control parameters. In § 4, critical values are computed for a small-gap case $\eta = 0.89$, for which comparison with experimental

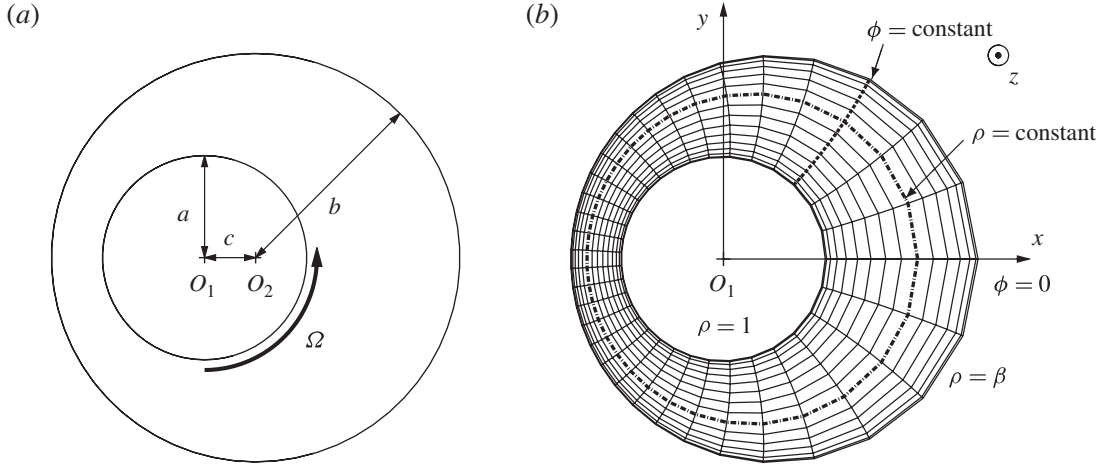


FIGURE 1. The eccentric annular domain for radius ratio $\eta = 0.5$ and eccentricity $e = 0.5$. (a) Definition of the geometry. (b) A typical bipolar mesh used for calculations with $N_\xi = K_\phi = 16$.

data is possible. A concluding section then summarizes our main findings and paves the way for future work.

2. Linear stability framework

Recall that a , b are the inner and outer cylinder radii, $d = b - a$ is the clearance and Ω is the rotation rate of the inner cylinder, while ρ and ν are the density and the kinematic viscosity. In the following, quantities will be made non-dimensional with respect to the reference scales $L \equiv d$, $V \equiv a\Omega$ and $P \equiv \rho V^2$ for length, velocity and pressure.

An azimuthal/rotational Reynolds number, defined as $Re_\Omega \equiv VL/\nu = a\Omega d/\nu$, will be used to measure competition between centrifugal effects and viscosity. Note that this type of definition is preferred in recent numerical work (e.g. Oikawa *et al.* 1989a; Feng, Li & Fu 2007; Martinand *et al.* 2009) rather than using Taylor numbers of the form $Ta \sim \delta Re_\Omega^2$, which naturally appeared in the pioneering analytical studies of the small-gap limit $\delta \rightarrow 0$ (e.g. Taylor 1923; DiPrima 1959; Chandrasekhar 1981).

Axial advection is characterized by an axial Reynolds number $Re_z \equiv \bar{w}d/\nu$, based on the mean axial velocity \bar{w} . The ratio Re_z/Re_Ω represents the mean axial velocity in units of rotation velocity, and conveniently measures competition between advection and rotation. Because of this, the use of an azimuthal Reynolds number instead of a ‘classical’ Taylor number seems particularly appropriate when axial flow is considered.

Finally, the geometry is characterized by the ratio of radii $0 < \eta \equiv a/b < 1$ or, equivalently, the clearance ratio $\delta \equiv d/a = (1 - \eta)/\eta$. The eccentricity is measured by the non-dimensional number $0 \leq e = c/d \leq 1$, where c is the distance between centres (cf. figure 1).

2.1. Governing equations

The incompressible Navier–Stokes equations governing velocity \mathbf{u} and pressure p read

$$\left. \begin{aligned} \partial_t \mathbf{u} + \mathbf{u} \cdot \nabla \mathbf{u} &= -\nabla p + Re_\Omega^{-1} \nabla^2 \mathbf{u}, \\ \nabla \cdot \mathbf{u} &= 0, \end{aligned} \right\} \quad (2.1)$$

with impermeability and no-slip boundary conditions at the walls (rotating inner cylinder, fixed outer one). Basic flows for stability analyses are axially invariant, steady solutions of (2.1). Because of the vanishing derivatives in the axial direction e_z , velocity components $\mathbf{u}_\perp = \mathbf{u} - w\mathbf{e}_z$ perpendicular to the axis are decoupled from the axial component w . Letting the subscript ‘ \perp ’ denote projection perpendicular to e_z , \mathbf{u}_\perp satisfies

$$\left. \begin{aligned} \partial_t \mathbf{u}_\perp + \mathbf{u}_\perp \cdot \nabla_\perp \mathbf{u}_\perp &= -\nabla_\perp p + Re_\Omega^{-1} \nabla_\perp^2 \mathbf{u}_\perp, \\ \nabla_\perp \cdot \mathbf{u}_\perp &= 0. \end{aligned} \right\} \quad (2.2)$$

Steady solutions of (2.2), with boundary conditions, yield ‘in-plane’ components $\mathbf{u}_{B,\perp}$ of basic flows, denoted in what follows as $\mathbf{u}_B = (\mathbf{u}_{B,\perp}, w_B)$. The basic axial velocity can then be calculated by simply solving a linear system

$$\mathbf{u}_{B,\perp} \cdot \nabla_\perp w_B = -G + Re_\Omega^{-1} \nabla_\perp^2 w_B, \quad (2.3)$$

where G is the imposed axial pressure gradient. Wood (1957)’s modified bipolar coordinate system (ρ, ϕ) , fitting the annular domain (see figure 1) with the following conformal transformation, is appropriate for the present configuration

$$x + iy = \frac{1}{\delta} \frac{\rho e^{i\phi} + \gamma}{1 + \gamma \rho e^{i\phi}}, \quad (2.4)$$

with constants γ and β depending on the geometry through δ and e :

$$\gamma = \left\{ \left(\frac{2 + \delta(1 - e^2)}{2e} \right)^2 - 1 \right\}^{1/2} - \frac{2 + \delta(1 - e^2)}{2e} \quad \text{if } e \neq 0, \text{ else } \gamma = 0, \quad (2.5)$$

$$\beta = \frac{1 + \delta(1 + e) - \gamma}{1 - \gamma(1 + \delta(1 + e))}. \quad (2.6)$$

Unlike classical bipolar coordinates, this system is non-singular in the concentric limit, allowing computations in the axisymmetric case. Local orthogonality ensures separation of the variables in the expression of the Laplacian operator. An additional transformation maps the non-dimensional ‘pseudo-radius’ $1 \leq \rho \leq \beta$ to $-1 \leq \xi \leq 1$, with $\xi = (2\rho - \beta - 1)/(\beta - 1)$. In the local frame, the in-plane velocity is decomposed as $\mathbf{u}_\perp = ue_\xi + ve_\phi$. Expressions for operators in (2.2)–(2.3), written in the (ξ, ϕ) coordinate system, are given in the Appendix.

Linear stability theory predicts the behaviour of small-amplitude perturbations $\mathbf{X}'(\xi, \phi, z, t) \equiv (u', v', w', p')^t$ superimposed on the basic flow, $\mathbf{X}_B(\xi, \phi) \equiv (u_B, v_B, w_B, p_B)^t$. The system being homogeneous along the axial direction z , small perturbations can be written in normal-mode form:

$$\mathbf{X}'(\xi, \phi, z, t) = \mathbf{X}(\xi, \phi) \exp[i(kz - \omega t)]. \quad (2.7)$$

As usual in temporal stability analyses, the axial wavenumber k is real, and the frequency is a complex number $\omega = \omega_r + i\omega_i$. The phase speed $c \equiv \omega_r/k$ characterizes axial propagation, and the growth rate ω_i indicates temporal growth/decay (respectively, $\omega_i > 0$ and $\omega_i < 0$). Linearization of the Navier–Stokes equations about the basic flow and use of the normal-mode form (2.7) gives the system of differential equations $\mathbf{AX} = i\omega \mathbf{BX}$, expressed in the (ξ, ϕ) coordinate system

as follows:

$$\mathbf{A} = \begin{bmatrix} A_{11} & A_{12} & 0 & D_\xi \\ A_{21} & A_{22} & 0 & D_\phi \\ D_\xi w_B & D_\phi w_B & A_{33} & ik \\ D_\xi + A & D_\phi - B & ik & 0 \end{bmatrix}, \quad \mathbf{B} = \begin{bmatrix} 1 & 0 & 0 & 0 \\ 0 & 1 & 0 & 0 \\ 0 & 0 & 1 & 0 \\ 0 & 0 & 0 & 0 \end{bmatrix}, \quad (2.8)$$

$$\left. \begin{aligned} A_{11} &= (u_B D_\xi + D_\xi u_B) + v_B (D_\phi - B) + ik w_B - Re_\Omega^{-1} (\nabla_\perp^2 - k^2 + C), \\ A_{22} &= (v_B D_\phi + D_\phi v_B) + u_B (D_\xi + A) + ik w_B - Re_\Omega^{-1} (\nabla_\perp^2 - k^2 + C), \\ A_{33} &= (u_B D_\xi + v_B D_\phi) + ik w_B - Re_\Omega^{-1} (\nabla_\perp^2 - k^2), \\ A_{12} &= -2Av_B + (D_\phi - B)u_B + 2Re_\Omega^{-1} (AD_\phi + BD_\xi), \\ A_{21} &= 2Bu_B + (D_\xi + A)v_B - 2Re_\Omega^{-1} (AD_\phi + BD_\xi). \end{aligned} \right\} \quad (2.9)$$

The symbols D_ξ , D_ϕ are differential operators given in the [Appendix](#), together with the spatially dependent factors A , B and C . At the walls, impermeability $u = 0$, no-slip $v = w = 0$ and incompressibility $D_\xi u = 0$ conditions apply. For each value of k , the solution of this eigenvalue problem yields a spectrum of temporal modes $\omega = \Omega(k; \eta, e, Re_z, Re_\Omega)$. The critical azimuthal Reynolds number is such that the mode with the largest growth rate is at most neutrally stable ($\omega_{i,max} = 0$). The value of k for which it is neutrally stable is called the critical wavenumber.

The eigenvalue problem is invariant under complex conjugation (denoted by \star) $(k, \omega, X) \mapsto (-k, -\omega^\star, X^\star)$, so only $k > 0$ need be considered. In the absence of axial flow, the problem is also invariant to axial reflection, implying, with conjugation symmetry, that the spectrum is symmetric with respect to the imaginary axis ($\omega \mapsto -\omega^\star$). When axial flow is added, mirror symmetry of the system in the axial direction and the resulting symmetry of the spectrum are lost.

2.2. Numerical method

A spectral decomposition of the fields was implemented, as in Oikawa *et al.* (1989a) and Chawda & Avgousti (1996), using a Fourier–Chebyshev decomposition:

$$u(\xi, \phi) = \sum_{i=0}^{N_\xi-1} \sum_{j=-K_\phi}^{K_\phi} \hat{u}_{ij} e^{ij\phi} T_i(\xi), \quad (2.10)$$

where T_i is the Chebyshev polynomial of order i . A pseudospectral collocation method is used in the pseudo-radial direction, employing a Gauss–Lobatto distribution $\xi_i = \cos[i\pi/(N_\xi - 1)]$, with $0 \leq i \leq N_\xi - 1$. K_ϕ is the number of Fourier components, corresponding to $N_\phi = 2K_\phi + 1$ points on the physical grid (figure 1), after inverse discrete Fourier transform.

Steady solutions $\mathbf{u}_{B,\perp}$ of (2.2) are calculated using a time-marching procedure, then the axial flow w_B is obtained by solving the linear system (2.3). Thanks to the linearity of (2.3) with respect to w_B , the axial pressure gradient G is just a multiplying factor on the axial velocity, so G can be set to 1 without loss of generality. w_B is then rescaled to yield the required axial Reynolds number Re_z .

Integration of (2.2) is performed using a projection method enhanced with a preliminary pressure-prediction step (Goda 1979; Raspo *et al.* 2002). A simple and robust first-order temporal scheme is used since only steady solutions are of interest here. The stiff viscous terms of the vectorial Laplacian operator involving the scalar Laplacian ∇_\perp^2 (see the [Appendix](#)) are treated implicitly, while all other terms are extrapolated from the previous time step. The Poisson and Helmholtz problems involve

block pentadiagonal matrices, and are efficiently solved using the Thomas algorithm. The choice of time step was automated in order to achieve convergence. When velocity residuals in the physical space $\max_{i,j} |u_{i,j}^n - u_{i,j}^{n-1}|$ or $\max_{i,j} |v_{i,j}^n - v_{i,j}^{n-1}|$ diverged, the time step was divided by 2: the resulting time steps ranged from 1 for the concentric case to 10^{-2} for $Re_\Omega = 250$, $e \geq 0.8$, and $N_\xi = K_\phi = 32$. The convergence tolerance on the residuals was set to 10^{-8} .

Approximating normal modes (2.7) with the same Fourier–Chebyshev expansion as the basic flow leads to a generalized eigenvalue problem, with matrix versions of linear operators (2.8)–(2.9), of size $4N_\phi N_\xi$. This generalized eigenvalue problem can be reduced to a standard eigenvalue problem $\tilde{\mathbf{A}}\tilde{\mathbf{X}} = i\omega\tilde{\mathbf{X}}$ of size $2N_\phi(N_\xi - 3)$, after eliminating w , p and boundary points of u and v . The reduction is performed numerically and allows significant time savings in full-spectrum calculation, as well as avoiding spurious eigenvalues. A similar approach seems to have been used in Oikawa *et al.* (1989a).

Full-spectrum computations were performed using the standard QR procedure available in the free software package LAPACK (www.netlib.org/lapack). When the region of interest in the spectrum was known beforehand, we used the Arnoldi (1951) method to compute a few eigenvalues efficiently. The shift–invert spectral transformation was used to enhance convergence, where the initial problem was replaced by $(\tilde{\mathbf{A}} - \sigma\mathbf{I})^{-1}\tilde{\mathbf{X}} = v\tilde{\mathbf{X}}$. The eigenvalues $v = 1/(\lambda - \sigma)$ of largest magnitude give the corresponding eigenvalues $\lambda = i\omega$ of the original problem closest to the given shift σ . The eigenvectors $\tilde{\mathbf{X}}$ of the new problem are those of the initial one. The method requires solving linear systems involving the non-sparse matrix $\tilde{\mathbf{A}} - \sigma\mathbf{I}$, which is factorized in LU form in an initialization step. The calculations were performed using the ARPACK++ class for non-sparse matrices (www.caam.rice.edu/software/ARPACK), based on LAPACK routines.

For a given mode, critical curves were calculated using a Newton–Raphson iteration: k and Re_Ω were varied simultaneously so as to reach $|\omega_i|$ and $|\partial_k\omega_i|$ less than 10^{-6} . Initial estimates for the critical k and Re_Ω were obtained by linear extrapolation with respect to Re_z . Identification of the most unstable modes is discussed in § 2.5.

2.3. Spatial resolution

A systematic grid refinement study was performed for the basic flow with $16 \leq N_\xi \leq 64$ and $0 \leq K_\phi \leq 128$ ($K_\phi = 0$ for $e = 0$), for $e \leq 0.99$ and $Re_\Omega \leq 250$. The minimal resolution achieving convergence of six significant digits of a number of integral quantities (forces and torque on inner cylinder, Fanning friction factor $f \equiv d|G|/(1/2\rho\bar{w}^2)$, azimuthal volume flux) was found for each set of parameters, and used for the computations in § 2.4. It appears that refining the number of collocation points much above $N_\xi = 32$ is unnecessary for $Re_\Omega \leq 250$, and the dependence on eccentricity is weak. On the other hand, if eccentricities close to 1 are considered, ϕ varies extremely slowly in the wide gap and a large number of Fourier modes is required. For $e = 0.98$ and $Re_\Omega = 223.61$, a resolution of $N_\xi \times K_\phi = 32 \times 128$ achieves excellent results, as can be seen in figure 2, which shows a comparison with Escudier *et al.* (2000)'s calculations.

In parametric stability analyses, however (§§ 3 and 4), a fixed resolution of $N_\xi = K_\phi = 16$ was systematically used for both basic-flow and normal modes, for practical reasons and because of the computational cost. Tests were performed *a posteriori* to check that these values provided reliable results, and are reported in table 1. With the chosen resolution, three significant digits of the critical Re_Ω are

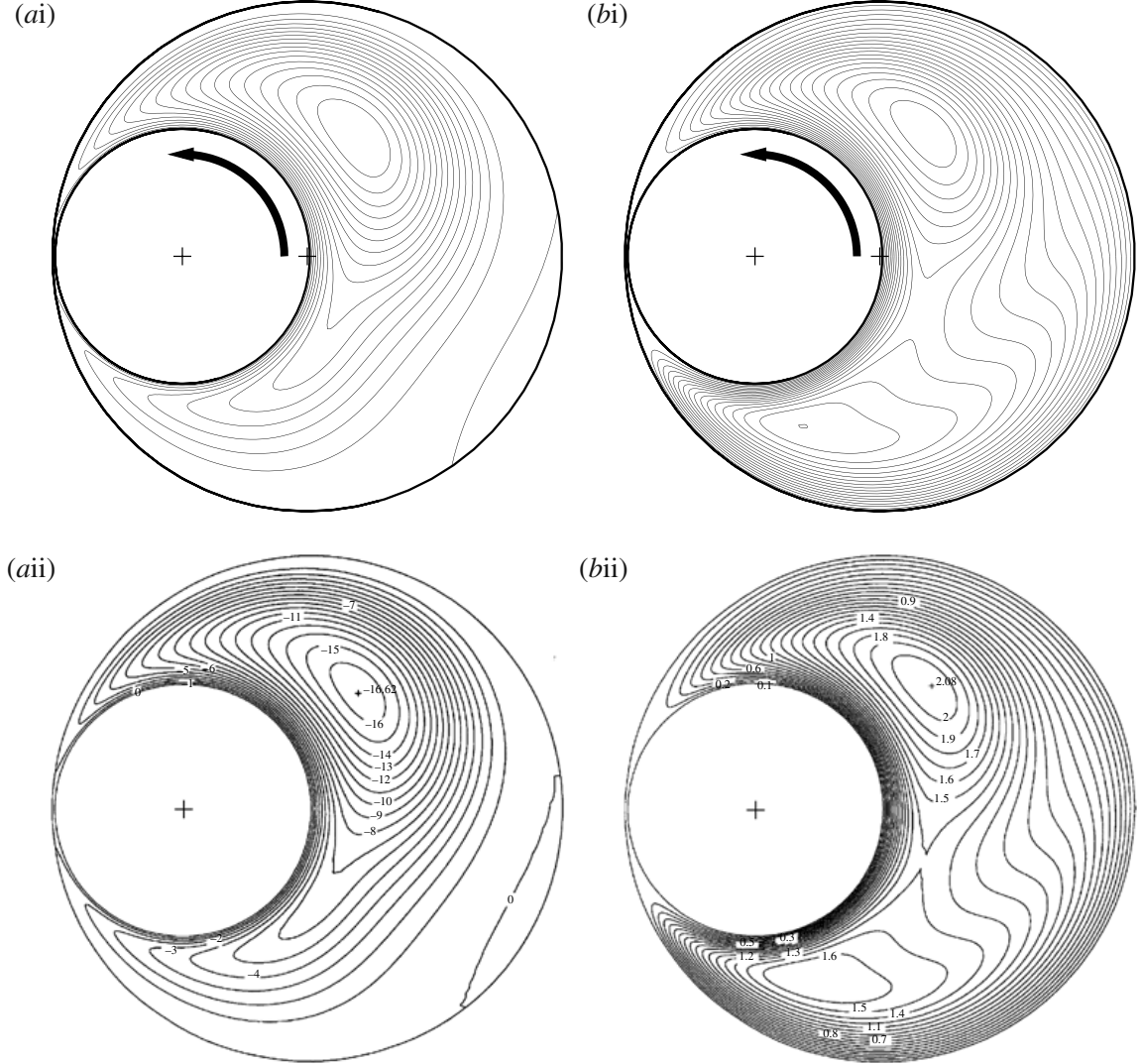


FIGURE 2. The basic flow for $\eta = 0.5$, $e = 0.98$ and $Re_\Omega = 223.61$: (i) the present calculation using $N_\xi \times N_\phi = 32 \times 257$ ($K_\phi = 128$); (ii) Escudier *et al.* (2000) with a 40×256 grid – (a) streamlines; (b) isolines of axial velocity normalized by mean velocity \bar{w} . The calculation recovers the secondary recirculation region in the wide gap and the two distorted maxima in the axial velocity. The numerical values of the isolines match those of Escudier *et al.* (2000).

converged in most cases. However, larger inaccuracies occur for high e and Re_z , and critical curves are truncated below $Re_\Omega = 200$ (respectively, $Re_\Omega = 250$) for $\eta = 0.5$ (respectively, $\eta = 0.89$), as remeshing above this limit quickly becomes prohibitive.

2.4. Basic flow

The most striking feature of the basic flow is the occurrence of a recirculation eddy for eccentricities larger than a certain threshold value of ~ 0.3 for $\eta = 0.5$ (see figure 3), which only depends weakly on Re_Ω . This behaviour exists even for Stokes flow and Kamal (1966) was the first to study the influence of inertial effects. The recirculation is due to the adverse pressure gradient caused by the large expansion of annulus clearance, downstream of the ‘bottleneck’ at $\phi = \pi$. Figure 4(d) represents

η	$N_\xi \times K_\phi$	0.5		0.6		0.7	
		Re_z	Re_Ω	Re_z	Re_Ω	Re_z	Re_Ω
0.5	50	127.41	3.34	127.41	3.35	147.52	3.45
	100	151.61	3.17	151.63	3.17	171.59	2.67
	150	156.73	2.86	156.76	2.86	187.61	2.76
	180	156.91	2.78	157.02	2.79	191.58	2.53
	200	156.15	2.53	156.28	2.54	194.73	2.42
	32	247.82	2.98	247.82	2.98	—	—
0.8907	50	296.19	2.74	296.20	2.74	—	—
	17	—	—	—	—	247.40	3.40
	30	—	—	—	—	283.26	3.11
	—	—	—	—	—	284.04	3.13

TABLE 1. Resolution tests for $\eta = 0.5$ and $\eta = 0.8907$, with $N_\xi \times K_\phi = 16 \times 16, 32 \times 32$. Critical Re_Ω and k are given for various e and Re_z .

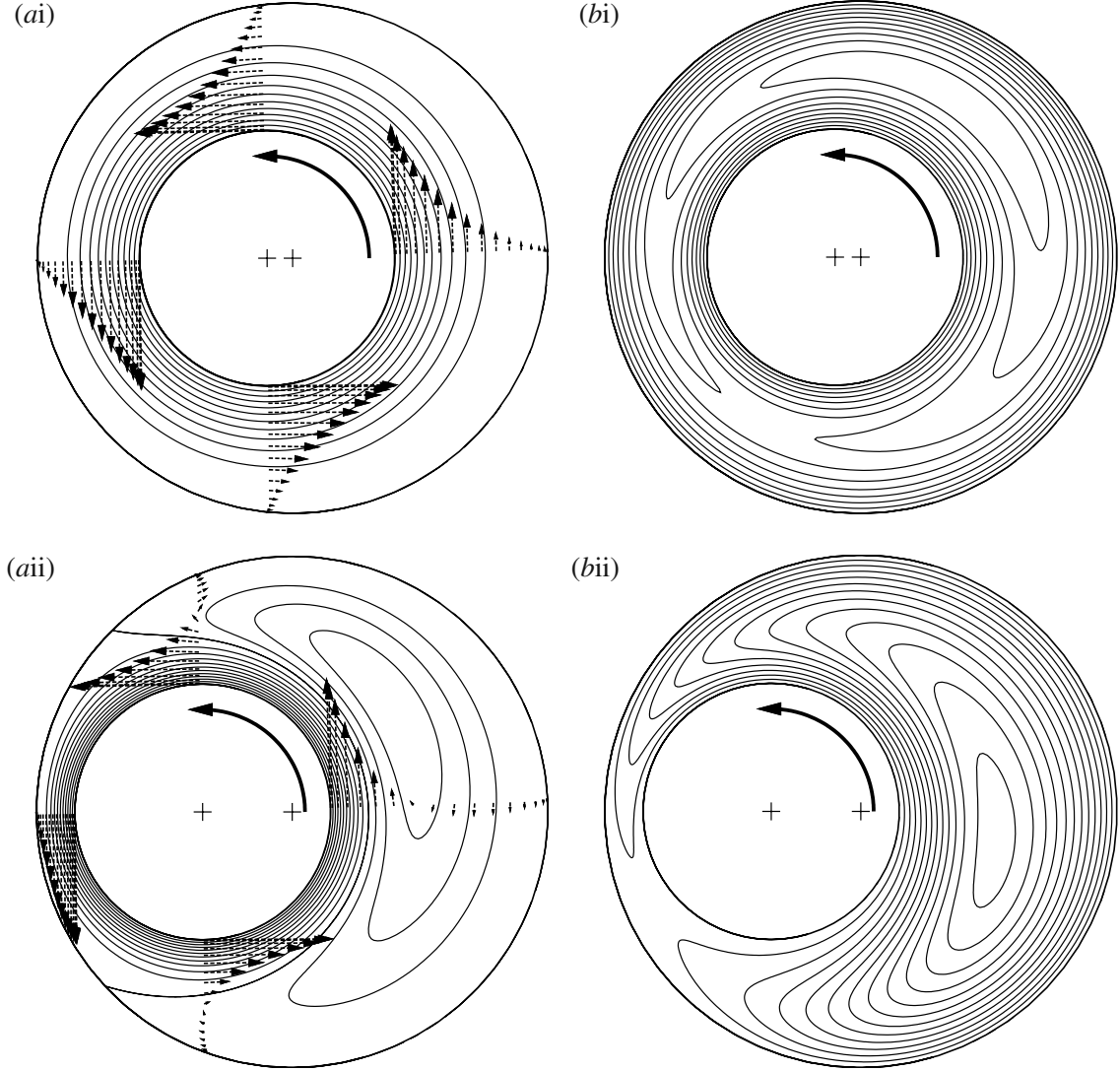


FIGURE 3. Basic flows for $\eta = 0.5$, $Re_\Omega = 100$: (i) weak eccentricity $e = 0.2$; (ii) high eccentricity $e = 0.7$ – (a) contours of equispaced in-plane streamfunction with superimposed in-plane velocity profiles at $\theta = 0, \pi/2, \pi, 3\pi/2$ (polar angle with respect to the inner cylinder); (b) equispaced contours of axial velocity.

the evolution of the azimuthal volume flux (per unit length) Q_ϕ with eccentricity, for $\eta = 0.5$ and azimuthal Reynolds numbers Re_Ω up to 250. Q_ϕ is obtained by integration of the azimuthal velocity along the radial path $\phi = 0$ joining the cylinders. As the inner cylinder gets closer to the outer one, the azimuthal flow becomes progressively ‘choked’, and Q_ϕ seems to be controlled by the smaller gap width. Indeed, the flow in the vicinity of the inner cylinder resembles a circular Couette flow of clearance ratio controlled by the smaller gap, while the wide-gap region hosts a low-velocity recirculation zone contributing no net azimuthal volume flux. A comparison is made with the value of Q_ϕ in the Stokes régime, using Wannier (1950)’s exact formula for the in-plane stream function. Inertial effects only have a weak impact on Q_ϕ , which could be expected from the fact that the fluid is entrained in rotation by viscous forces.

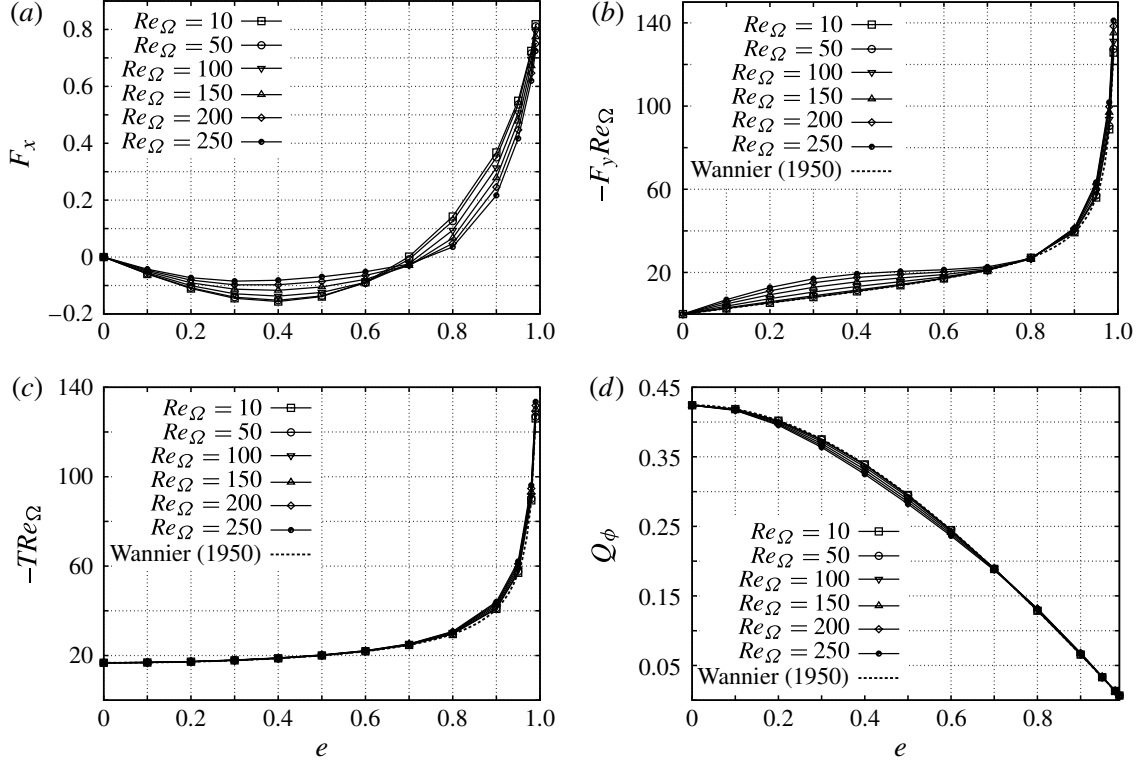


FIGURE 4. The forces, torque and azimuthal flow rate (per unit length) for $e = 0, \dots, 0.7$ and $Re_\Omega = 10, \dots, 250$: (a) the x -component F_x ; (b) the y -component F_y of the force on the inner cylinder; (c) the torque T on the inner cylinder; (d) the azimuthal flow rate Q_ϕ . The dotted lines in (b–d) correspond to the exact value in the Stokes régime, taken from Wannier (1950).

Maximum axial velocity occurs in the wide-gap region. Indeed, in the absence of rotation, eccentric annular Poiseuille flow is nearly parabolic in the pseudo-radial direction, and for any fixed value of ϕ , the maximum velocity scales as the ‘local clearance’ squared. However, the position of the maximum axial velocity is not exactly located at $\phi = 0$, because of convective transport of w_B by cross-flow components $\mathbf{u}_{B,\perp}$ (see (2.3)). In fact, these nonlinear effects distort the whole flow field, and Escudier *et al.* (2000) performed a thorough computational/experimental analysis of the effects of eccentricity and inner-cylinder rotation, on annular Poiseuille flow. At low eccentricity, the maximum axial velocity was shown to be advected towards the narrowing-gap region, inducing a slight increase in Fanning friction factor (defined in § 2.3) with e . For moderate eccentricities $0.3 \leq e \leq 0.8$, the maximum moves back to the wide-gap region, with a subsequent decrease in friction factor. For larger eccentricities, the maximum is located in the diverging-gap region, and the friction factor increases again. At very high eccentricities and rotation rates, a second peak in axial velocity appears in the wide gap, while a secondary recirculation is observed at the outer cylinder wall. This complex pattern is successfully obtained with our code, as illustrated in figure 2.

The forces on the inner cylinder can be easily computed by integration of the pressure and viscous stresses at the wall. The expressions for the strain tensor components in our coordinate system are given in the Appendix. Figure 4 shows a systematic study of the effect of Re_Ω and e on the loads, for $\eta = 0.5$. A comparison is made with the Stokes régime, using analytical formulas derived by Wannier (1950). In

this limit, the velocity and pressure distributions are antisymmetric with respect to the symmetry plane of the annulus. Therefore, the x -component of the force is exactly 0. At the inner-cylinder surface, the pressure increases with ϕ on the wide-gap side up to $0 < \phi_{max} < \pi$, and decreases on the small-gap side up to $\phi_{min} = -\phi_{max}$. As e increases, the pressure extrema both tend to the same limit $\phi_{min/max} \rightarrow \pi$. Because $0 < \phi_{max} < \pi$, the y -component of the force F_y is negative. The viscous torque T is obviously opposed to the sense of rotation, so $T < 0$. In the Stokes limit, T and F_y both scale as Re_Ω^{-1} . Indeed, the torque T is induced by shear stresses τ , which scale as $\tau \sim \mu V/L$ in dimensional form, where μ is the dynamic viscosity. Non-dimensionalizing with respect to the pressure scale $P \equiv \rho V^2$, one obtains $T \sim \tau \sim Re_\Omega^{-1}$. In the absence of inertial terms, the pressure p_B also scales as τ , so $F_y \sim p_B \sim \tau \sim Re_\Omega^{-1}$.

When inertial effects are added, this scaling still holds and only small deviations to the Stokes limit are observed. Larger variations occur for an eccentricity of ~ 0.3 – 0.4 , where the value of $F_y Re_\Omega$ at $Re_\Omega = 250$ is almost twice the purely viscous one. At $e \approx 0.8$, variations of $F_y Re_\Omega$ with Re_Ω are almost non-existent. Similarly, the formula for the torque in the Stokes régime applies quite robustly for all the range of eccentricities and Re_Ω up to 250. Again, this close agreement is attributed to the fact that the flow in the vicinity of the inner cylinder is similar to a circular Couette flow where inertial effects are weak (and non-existent in the purely axisymmetric case). For e close to 1, F_y and T increase sharply because of lubrication effects.

When $Re_\Omega \neq 0$, the flow antisymmetry is broken, and F_x is non-zero. For low eccentricities, F_x is negative, but for high e , F_x is positive, as expected from lubrication theory. The change of sign of F_x is located about a critical eccentricity of $e \approx 0.7$ – 0.75 for $\eta = 0.5$ and $Re_\Omega \leq 250$, as already discussed by Feng *et al.* (2007) and Podryabinkin & Rudyak (2011). Small-eccentricity perturbations about this point tend to push the inner cylinder back to its initial position. However, pressure-induced precession prevents any stable equilibrium for this value of eccentricity, explaining the complex motion of drillstrings in wellbores. The intensity of F_x is determined by the magnitude of the convective term, so the pressure scaling $P \equiv \rho V^2$ is appropriate in this case.

2.5. Critical modes

The first step in linear stability analysis is to identify a reduced set of leading modes, with the largest growth rates. Full-spectrum computations were used to find the most unstable eigenvalue at each point of a coarse grid in (e, Re_Ω, Re_z) , for $\eta = 0.5$. k was varied between 1 and 7, a range containing all the critical wavenumbers for the concentric case with $Re_z \leq 200$ ($1.5 \lesssim k \lesssim 4.5$ from the graph in Cotrell & Pearlstein 2004), with large steps of 0.5 for computational efficiency. Approximate critical curves were obtained, and it was found that the modes at criticality are always either propagating ‘Taylor-like’ vortices or deformed left-handed helical modes. These pseudo-toroidal and pseudo-helical modes correspond to the same family of critical modes found in Taylor–Couette–Poiseuille flow (Takeuchi & Jankowski 1981), but distorted by eccentricity (cf. figure 10). In the axisymmetric case, these modes can be assigned an integer azimuthal wavenumber m corresponding to a normal-mode decomposition of the form $X' = X(r) \exp[i(kz + m\theta - \omega t)]$, using the usual cylindrical coordinates (r, θ, z) . Considering $k > 0$, $m = 0$ correspond to Taylor vortices and $m > 0$ (respectively, $m < 0$) are left-handed (respectively, right-handed) helical vortices, with helicity opposed to (respectively, matching) that of the basic flow. Following these modes by continuity, pseudo-helices are also assigned a ‘pseudo-azimuthal wavenumber’ equal to the corresponding value of m in the concentric case. Henceforth,

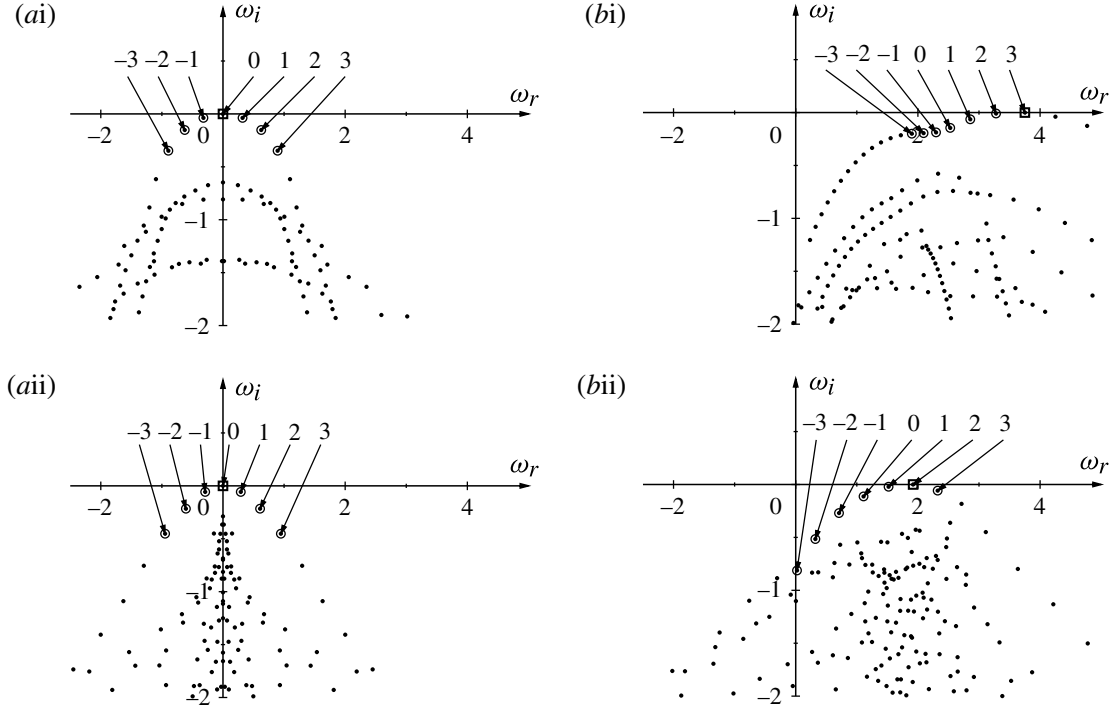


FIGURE 5. Spectra of eigenvalues $\omega = \Omega(k; e, Re_\Omega, Re_z)$ with (k, Re_Ω) at critical conditions. Rows: (i) $e = 0$; (ii) $e = 0.5$. Columns: (a) $Re_z = 0$; (b) $Re_z = 50$. Numbers indicate the azimuthal wavenumber m of the eigenmode (or pseudo-wavenumber if eccentric). Positive ω_i indicates instability. Positive (negative) m correspond to left- (right-)handed helix-like modes. The eigenvalue in the square box corresponds to the most unstable mode.

TV will denote ‘Taylor-like’ vortices, while LH $|m|$ and RH $|m|$ will correspond to left-handed (respectively, right-handed) helical vortices of order m . The symmetry of the spectrum for $Re_z = 0$ implies that LH and RH of equal order m have the same growth rate and oppositely signed phase speeds. As Re_z is increased, LH modes become more unstable than TV and RH, and form the family of critical modes, as in the axisymmetric case (cf. figure 5). The critical value of m increases steadily with Re_z .

Additional families of modes, such as wall modes related to a shear instability mechanism, were not found to be critically unstable in the range of parameters considered. Centre modes of *Sp* type, such as described by Merzari *et al.* (2008), and critical in highly eccentric annular Poiseuille flow for high values of Re_z , were not found to be critical in our configuration either.

In axisymmetric Taylor–Couette–Poiseuille flow with $\eta = 0.5$, the maximum value of m at criticality is 7 (Cotrell & Pearlstein 2004). Hence, in the subsequent parametric study at $\eta = 0.5$ (§ 3), critical curves were calculated for TV, LH modes with $m \leq 7$, and RH of order one and two, as a check.

2.6. Validation

Extensive validations of basic-flow and stability calculations have been performed. In the Stokes limit $Re_\Omega \ll 1$, Wannier (1950) derived analytical expressions for torque and forces on the inner cylinder, that were matched by our code up to machine precision. Using his analytical solution of the stream function, azimuthal volume flux Q_ϕ calculations were also successfully validated. Escudier *et al.* (2000) calculated

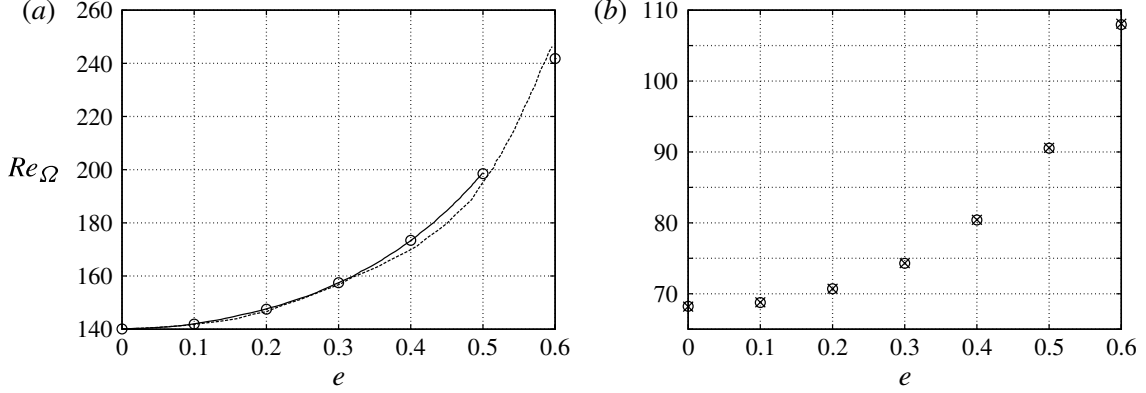


FIGURE 6. Validation of critical azimuthal Reynolds number Re_{Ω} against eccentricity e . (a) $\eta = 0.912$, $k = 3.17$: solid line, Chawda & Avgousti (1996); dotted line, Dai et al. (1992), \circ , present calculation. (b) $\eta = 0.5$: \times , Oikawa et al. (1989a); \circ , present calculation.

the Fanning friction factor (defined in § 2.3) in the eccentric Taylor–Couette flow, for $10 \leq Re_{\Omega} \leq 223.61$ and eccentricities up to 0.98. The present numerical results all lay within 0.67 % of their values. Feng et al. (2007) gave numerical values for the pressure and stress contributions to the x and y components of the force on the inner cylinder for $Re_{\Omega} = 125$ and eccentricities up to $e = 0.98$. For these parameters, our calculations match their results, with less than 1.80 % of relative difference, and 0.76 % on average when at least four significant digits were provided by the authors.

In the axisymmetric configuration with axial throughflow, Takeuchi & Jankowski (1981) performed the first numerical prediction of the critical curves for Re_z up to 100. In their paper, they provide data for the critical values of Re_{Ω} , k and wave speed $c = \omega_r/k$ for $Re_z = 0, 10, \dots, 100$. The critical values are exactly matched by our code in all cases except for $Re_z = 90$, where only the last significant digit given by the authors for k and c differs from our values by one.

In the eccentric configuration with no axial flow, Oikawa et al. (1989a) reported a critical azimuthal Reynolds number of 307.59 for an axial wavenumber of 4.126 and $\delta = 0.1$, $e = 0.7$. With the same spatial resolution $N_{\xi} \times K_{\phi} = 21 \times 24$, our corresponding critical values are $Re_{\Omega} = 307.71$ and $k = 4.127$, which gives relative errors of 0.04 and 0.02 %, respectively. Additional tests were performed using a graph of critical Re_{Ω} versus eccentricity for $\eta = 0.5$ from a second paper of Oikawa et al. (1989b), and for $\eta = 0.912$ and $k = 3.17$ against graphical results from Dai et al. (1992) and Chawda & Avgousti (1996). Figure 6 shows excellent agreement with the data of Oikawa et al. (1989b) and Chawda & Avgousti (1996), who both used the same spectral decomposition of the modes as us. Values from Dai et al. (1992) are close, but discrepancies may be attributed to their relatively coarse meshing ($N_{\phi} = 16$ points only in the ‘pseudo-azimuthal’ direction) and to the use of piecewise polynomials to approximate the fully nonlinear fields in their bifurcation analysis.

3. Parametric study for a wide gap $\eta = 0.5$

In this section, we give results for the case $\eta = 0.5$, representative of industrial configurations in oil-well drilling. A resolution of $N_{\xi} = K_{\phi} = 16$ allows satisfactory accuracy for $e \leq 0.7$ and Re_{Ω} , Re_z up to 200, as shown in the previous section.

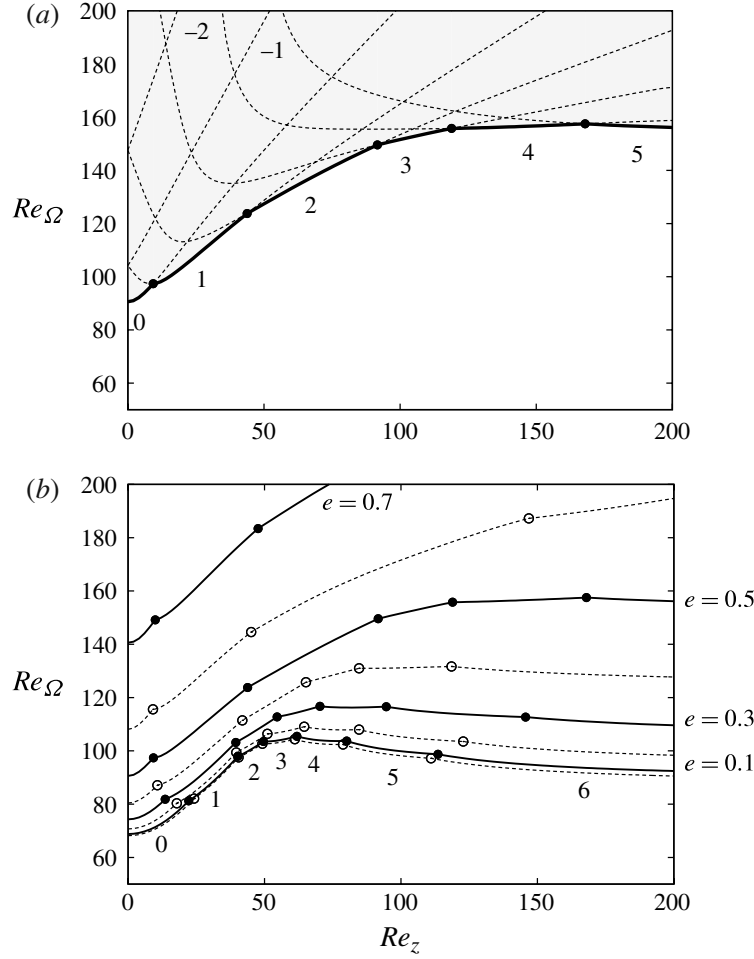


FIGURE 7. (a) Critical curves $Re_\Omega = f(Re_z)$ for $e = 0.5$ and modes $m = -2, \dots, 5$. The thick solid line indicates the instability threshold taking all the modes into account. The shaded area corresponds to instability. (b) Solid (respectively, dotted) lines: critical curves taking all the modes into account, for $e = 0.1, 0.3, 0.5, 0.7$ (respectively, $e = 0, 0.2, 0.4, 0.6$). In both (a) and (b), filled/open circles indicate a switch in critical m , and the associated ‘pseudo-azimuthal’ wavenumber is indicated by annotation.

3.1. Critical azimuthal Reynolds number

For an eccentricity of $e = 0.5$, figure 7(a) shows the critical curves of the TV ($m = 0$), LH ($m > 0$) and RH ($m < 0$) modes labelled from $m = -2$ to 5. The solid thick line indicates the stability boundary, switching from one m to the next as Re_z is increased. Similar behaviour was found in the axisymmetric case by Takeuchi & Jankowski (1981).

Similar results were obtained for all eccentricities and figure 7(b) superimposes on a single figure all the results concerning the stability boundary for $e = 0, 0.1, \dots, 0.7$. The main result of this study is clear from this figure: eccentricity always has a stabilizing effect, regardless of axial advection. The origin of this stabilization, as hinted at by Karasudani (1987) for the eccentric Taylor–Couette flow without axial flow, seems to lie in the weakening of centrifugal effects by eccentricity. Indeed, as already mentioned in § 2.4, azimuthal flow gets ‘choked’ with increasing eccentricity (see Q_ϕ in figure 4d), and the basic flow becomes similar to an axisymmetric Couette flow of clearance ratio δ' , controlled by the small gap $\delta' \sim \delta(1 - e)$, next to a ‘dead’

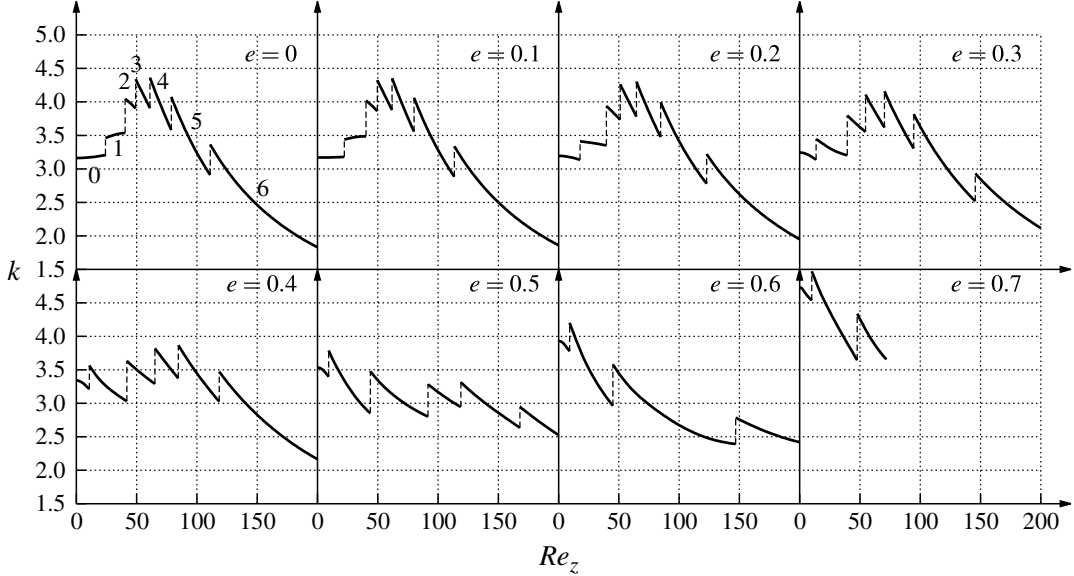


FIGURE 8. The critical wavenumber k against the axial Reynolds number Re_z for eccentricities $e = 0, 0.1, \dots, 0.7$. Discontinuities correspond to a switch in critical m (values indicated by annotation for $e = 0$).

recirculating flow zone. Decreasing the clearance ratio or, equivalently, increasing the radius ratio of a circular Couette flow, reduces curvature effects and has a stabilizing effect, as shown by DiPrima, Eagles & Ng (1984).

The effect of axial advection on the axisymmetric case is twofold: first, it stabilizes the Couette flow up to $Re_z = 61.08$; and then it slightly destabilizes it as Re_z is further increased, while maintaining the threshold above the value for $Re_z = 0$. The change in behaviour corresponds exactly to the intersection between the increasing critical curve corresponding to mode $m = 3$ and the decreasing curve for $m = 4$; hence maximal stability is achieved when the two modes exchange stability. The value of Re_z corresponding to the maximum in critical Re_Ω increases with eccentricity. Above $e = 0.5$, maximum stability occurs beyond $Re_z = 200$.

At fixed Re_z above 50, increasing eccentricity tends to select critical modes of lower m : the stabilizing effect of eccentricity is even more important for higher azimuthal wavenumbers. On the contrary, at small Re_z , eccentricity favours the dominance of the LH1 over TV. For large enough eccentricities, one can expect helices with $m = 1$ to dominate TV even without axial flow. In the absence of axial flow, this feature was found experimentally by Vohr (1968) ($\delta = 0.099$ and $e > 0.707$) and Karasudani (1987) ($\eta = 0.83$, $e > 0.6$). Oikawa *et al.* (1989a) found a complex conjugate pair of eigenvalues $\lambda = i\omega$ at criticality for $\delta = 0.1$, $e = 0.7$ (LH and RH), confirming numerically Vohr (1968)'s findings.

3.2. Critical axial wavenumber

Figure 8 shows the evolution of the critical wavenumber. The curves display jumps at points where modes exchange stability, and these discontinuities always correspond to a positive jump in k . When axial flow is increased, k usually decreases as long as the critical mode does not switch. The order of magnitude of k is always the same regardless of eccentricity, and remains between 1.5 and 5, which indicates that the axial wavelength of the critical perturbations is always of the same order of magnitude

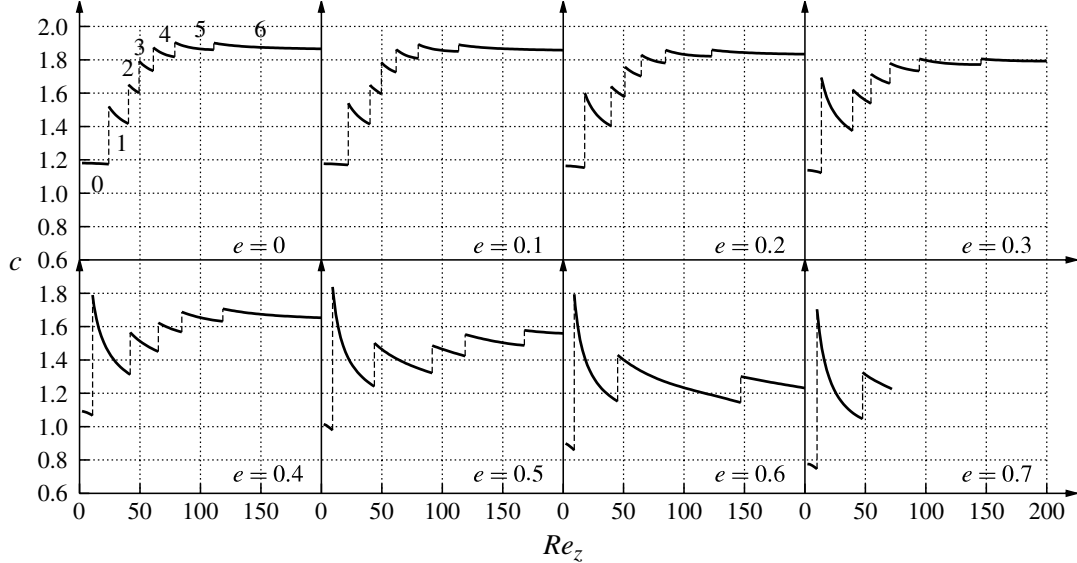


FIGURE 9. The critical phase speed c against the axial Reynolds number Re_z at critical conditions for eccentricities $e = 0, 0.1, \dots, 0.7$. Discontinuities correspond to a switch in m (values indicated by annotation for $e = 0$). The unit is the average axial basic-flow velocity \bar{w}_B .

as the clearance $d = b - a$. These observations may explain the pattern selection process: increasing Re_z tends to elongate the modes in the axial direction, so a switch to a higher ‘pseudo-azimuthal’ wavenumber mode occurs to reach a vortical structure that fits the annular domain better, and is thus amplified faster.

3.3. Critical phase speed

Figure 9 shows the evolution of the phase speed at criticality. As in figure 8, the curves are discontinuous as critical m switches with increasing Re_z . The phase speed always remains between 0.6 times and twice the average axial velocity of the basic flow. It decreases with increasing Re_z for each mode, but discontinuities always correspond to a jump to a larger value. Interestingly, except for LH1 (LH with $m = 1$) at the point of stability exchange with TV, all the critical modes see their phase speed decrease with eccentricity, this effect being more noticeable for $e \geq 0.3$. Most critical perturbations propagate somewhat faster than the average axial flow velocity, but see their propagation hindered by increasing Re_z .

3.4. Critical eigenmodes structure

A systematic study of the spatial structure of the critical eigenmodes has been performed. Figure 10 shows a deformed LH1 for $e = 0.5$, $Re_z = 40$. Figure 10(e) clearly represents the helical structure, while figure 10(b) shows the $m = 1$ azimuthal order. In-plane motion of the mode (figure 10(a)) can be quite complicated and difficult to interpret for higher-order modes.

It is interesting to look at the disturbance kinetic energy distribution to see where the mode localizes within the annulus. Figure 10(c) shows concentration of the energy in the converging gap region, consistent with observations of Oikawa for TV perturbations in both the small- and wide-gap eccentric Taylor–Couette flow (and the numerous theoretical and experimental studies cited in the introduction, either calculating or observing the so-called ‘maximum vortex activity’ in the saturated

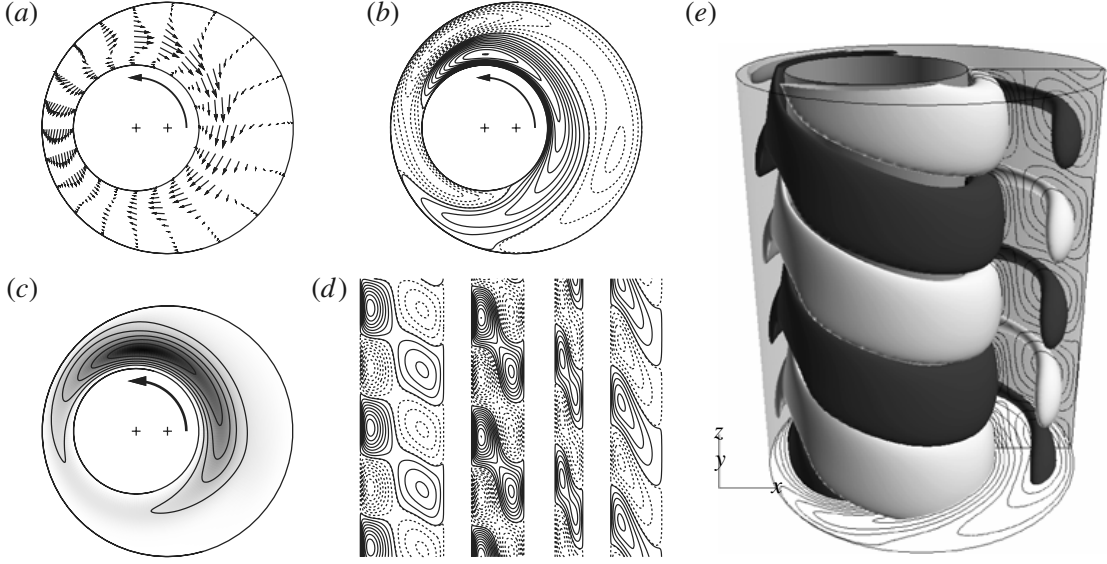


FIGURE 10. The structure of the critical eigenmode for $e = 0.5$, $Re_z = 40$. (a) The real part of the in-plane perturbation velocity $\mathbf{u}_\perp = (u, v)$. (b) Equispaced contours of the real part of the axial perturbation velocity w : solid (dotted) lines indicate positive (negative) values. (c) Map and (equispaced) contours of the disturbance energy density $\frac{1}{2}(|u|^2 + |v|^2 + |w|^2)$ dark grey corresponds to high values. (d) Vertical cuts (equispaced contours) of the real part of the axial perturbation velocity w for $\theta = 0, \pi/2, \pi, 3\pi/2$ (from left to right) in a polar coordinate system centred on the inner cylinder. (e) Isosurfaces of $Re(w)$, showing the three-dimensional structure of the mode: dark (light) shades of grey indicate positive (negative) values, respectively.

régime). It is also possible to track the position of the maximum of the total disturbance energy. It is found that both in the axisymmetric and the $e = 0.5$ cases, the perturbation localizes closer and closer to the inner wall as advection is increased, at a radius (with respect to the inner cylinder) of ~ 1.2 – 1.5 times the inner-cylinder radius. In the eccentric case, this maximum also moves azimuthally to the small-gap region, with jumps as the critical mode switches. At $Re_z = 0$ ($m = 0$), it is located at a polar angle (centred on the inner cylinder) of $\theta = 79^\circ$, while at $Re_z = 200$ ($m = 5$), it is at $\theta = 121^\circ$. From the energy density maps, it is also clear that as Re_z is increased, the energy is less and less spread out in the annular region and peaks around some radial position. For $Re_z = 0$, the ratio between the maximum of the total disturbance energy and the average is 5.7, whereas it is 16.3 for $Re_z = 200$.

Let us define the in-plane and axial disturbance energy contributions of a mode as the integral quantities over the annular domain \mathcal{A} :

$$E_\perp = \frac{1}{2} \int_{\mathcal{A}} (|u|^2 + |v|^2) d\mathcal{A}, \quad E_z = \frac{1}{2} \int_{\mathcal{A}} |w|^2 d\mathcal{A}. \quad (3.1)$$

Figure 11 shows the contributions to the total disturbance energy of the critical mode as a function of Re_z for $e = 0$ and $e = 0.5$. In both cases, the graphs show how the energy transfers from dominantly in-plane motion to dominantly axial motion as advection is increased, regardless of the ('pseudo-')azimuthal wavenumber involved. There is a tendency for the modes to become more and more two-dimensional with suppressed spanwise (here azimuthal) motion, as for TS waves on a flat plate or in channel flow. This suggests that viscosity plays an important role in the destabilization

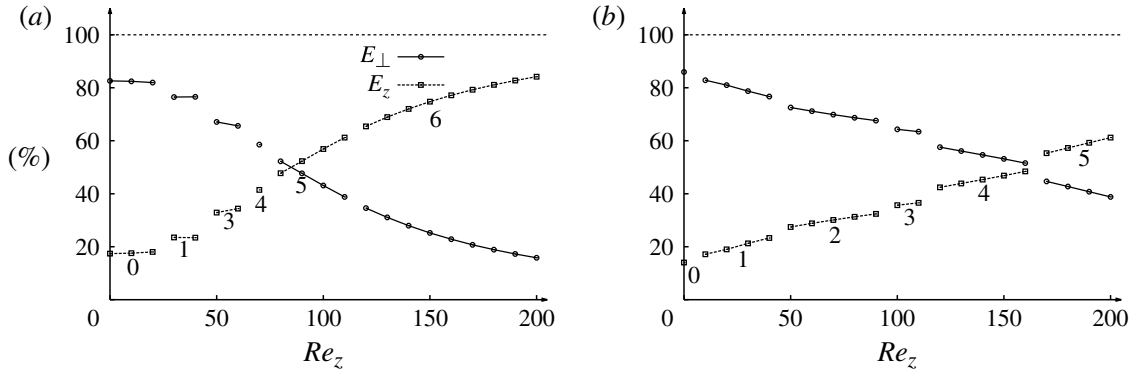


FIGURE 11. In-plane E_{\perp} and axial E_z contributions to the total disturbance energy of the critical mode as a function of Re_z : (a) $e = 0$; (b) $e = 0.5$. Numbers indicate the ('pseudo')azimuthal wavenumber of the critical mode.

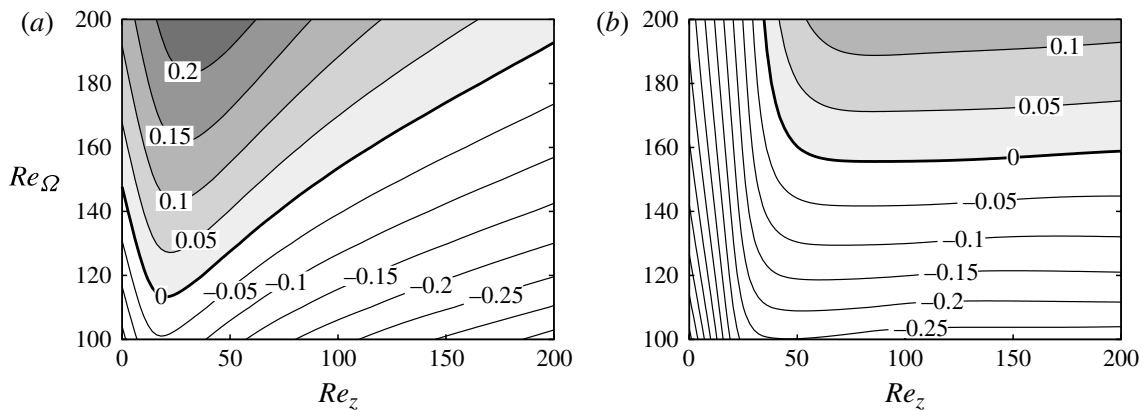


FIGURE 12. Growth rate maps for an eccentricity of $e = 0.5$: (a) mode $m = 2$; (b) mode $m = 4$.

of the modes at high Re_z . This hypothesis is consistent with the fact that the modes localize more and more in high-shear regions: closer to the inner wall at smaller clearance. It is also consistent with the decrease in critical axial wavenumber k with increasing Re_z (figure 8). Interestingly, in the case $e = 0.5$, the critical axial Reynolds number above which advection becomes destabilizing corresponds to the switch from dominantly in-plane disturbance energy to dominantly axial disturbance energy (this is less clear for $e = 0$). Note, however, that these modes are distinct from the ‘pure’ viscous wall modes referred to as modes A in Merzari *et al.* (2008) for eccentric Poiseuille flow, or TS-like modes in axisymmetric Taylor–Couette–Poiseuille flow (Cotrell & Pearlstein 2004). Those latter modes are localized about critical layers, and are expected to become critical at higher values of Re_z , typically of the order of 10^4 in the axisymmetric Taylor–Couette–Poiseuille flow with $\eta = 0.5$ (Cotrell & Pearlstein 2004).

3.5. Growth rate maps and stability diagrams

In the concentric and $e = 0.5$ cases, a more complete study of the dispersion relation was carried out. Figure 12 shows maps of the maximum growth rate $\omega_{i,\max}$ in the (Re_{Ω}, Re_z) space for modes 2 and 4 and $e = 0.5$. For ‘higher-order’ modes such

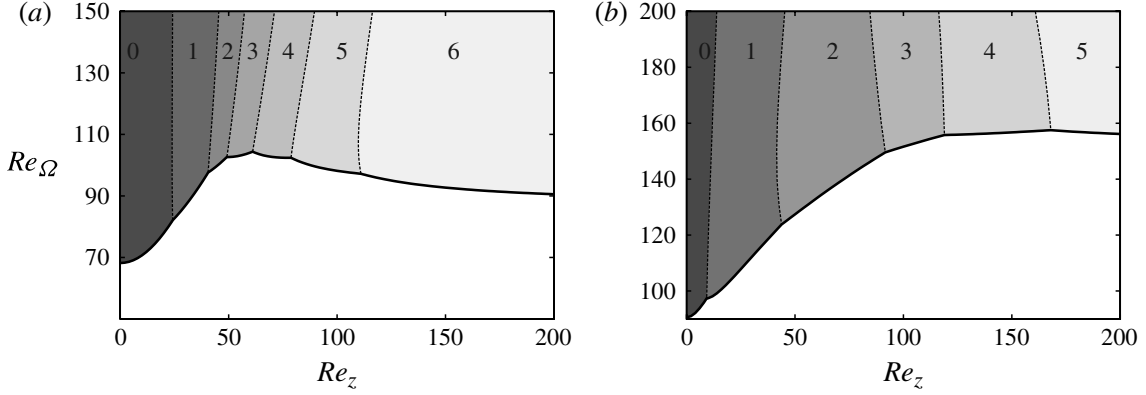


FIGURE 13. Dominant unstable modes in (Re_z, Re_Ω) space with and without eccentricity: (a) $e = 0$; (b) $e = 0.5$. Numbers indicate the azimuthal or ‘pseudo-azimuthal’ wavenumber of the fastest growing mode.

as $m = 4$, one can clearly distinguish two zones. For low Re_z , there is a sharp increase in $\omega_{i,\max}$ with advection and rotation has only a minor effect on stability. For higher axial flow rates, the tendency is reversed: advection has only a weak effect on stability and centrifugal effects govern the stability of the mode. This trend was also observed in the concentric case for high-order left helices. For ‘low-order’ modes such as $m = 2$, the separation of the two effects is less clear: the increase of $\omega_{i,\max}$ for weak axial advection is also observed, though less markedly, and at higher axial flow rates, the stabilizing effect of advection is comparable in magnitude to the destabilizing effect of rotation.

It is also possible to calculate the regions in which each m dominates the instability, as shown in figure 13. In the cases of both no eccentricity and of $e = 0.5$, it appears that frontiers between these regions are always close to straight lines parallel to the Re_Ω -axis. This again illustrates the importance of advection in the destabilization of the helical modes. While the instability mechanism is centrifugal in nature, there is a need for a minimum axial flow rate for this instability to operate on higher-order LH modes.

This importance of both shear and centrifugal effects in the destabilization process at high Re_z as noticed here and in the preceding subsection, is not a complete surprise. Indeed, as pointed out in Meseguer & Marques (2002), Hagen–Poiseuille flow is linearly stable for any Re_z ; however, a slow rotation may destabilize the basic flow (Mackrodt 1976). Conversely, rigid-body rotation is linearly stable for any rotation rate, but the superposition of axial flow can also destabilize the flow. The same mechanism was observed for an axisymmetric Couette flow (Meseguer & Marques 2000) with axial motion of the inner cylinder, where both shear and centrifugal effects were needed to make the basic flow unstable. It is clear from figure 12(b) that here this is the case for higher-order helical modes: the region of instability is bounded by a threshold in both rotation and advection rates.

4. Parametric study for a small gap $\eta = 0.89$

As mentioned in the introduction, very little work has been done on the experimental study of eccentric Taylor–Couette–Poiseuille flow. However, some experimental data are available for radius ratios close to $\eta = 0.9$. We study the case $\eta = 0.89$ ($\eta = 0.8907$ to be exact), corresponding to the sharp entry apparatus in

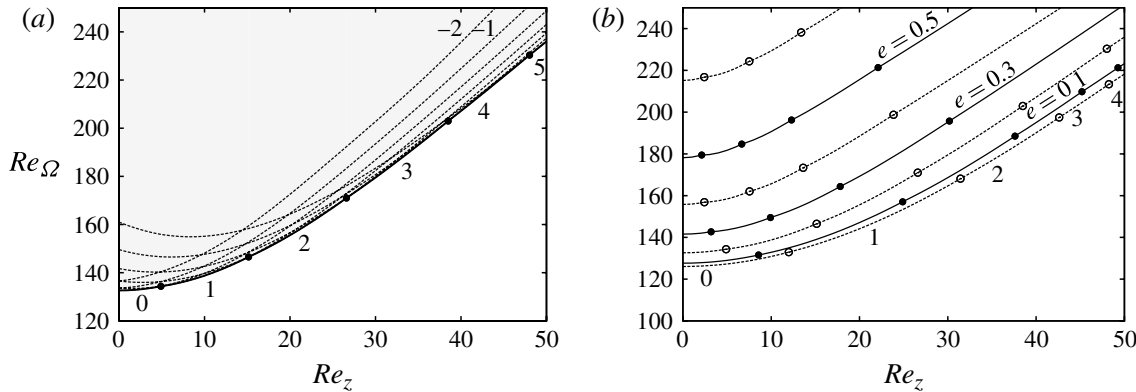


FIGURE 14. (a) Critical curves $Re_\Omega = f(Re_z)$ for $\eta = 0.8907$, $e = 0.2$ and modes $m = -2, \dots, 5$: the thick solid line indicates the instability threshold taking all the modes into account; the shaded area corresponds to instability. (b) Critical curves taking all the modes into account, for different eccentricities $e = 0, 0.1, \dots, 0.6$ and $\eta = 0.8907$. In both (a) and (b), dots indicate a switch in critical m , and the associated ‘pseudo-azimuthal’ wavenumber is indicated below.

Coney & Mobbs (1969–70) (comparable results were obtained for the smooth entry). In the same fashion as in § 3, we obtain results for e up to 0.6, Re_z up to 50 and Re_Ω up to 250, reaching reasonable accuracy with $N_\xi = K_\phi = 16$, as indicated in table 1.

4.1. Critical azimuthal Reynolds number

Compared to the wide-gap case, the critical Re_Ω are higher, which is as expected because the curvature of the gap is less important. The transition to higher-order LH modes happens at much lower advection rates, and $m = 5$ becomes critical before $Re_z = 50$ for some eccentricities. Unlike for $\eta = 0.5$, increasing the eccentricity at a fixed Re_z results in the selection of higher-order m . For the wide gap, this was the case only for TV and LH1 (for low e), and otherwise selection of lower-order m was observed. Figure 14(a) shows how the critical curves for the different m lie close to each other ($e = 0.2$ here), including the first RH modes. Complex behaviour is expected in the supercritical régime from the competition of the different helices. Note that no weak destabilizing effect of advection is noticed for any value of $Re_z \leq 50$ at any eccentricity. Indeed, this effect is expected to be pushed towards much higher values of Re_z , as in the concentric case. In this case, Ng & Turner (1982) found such an effect to occur at about $Re_z \sim 10^3$ for $\eta = 0.77$ (extremely weak effect), and did not observe it at all for $\eta = 0.95$ and $Re_z \leq 6000$.

4.2. Critical axial wavenumber

The range of critical axial wavenumbers (figure 15) is almost the same as in the wide-gap case. This means that the clearance is still controlling the size of the vortices. The most noticeable difference with $\eta = 0.5$ is the fact that for weak eccentricities ($e \leq 0.2$) and low-order modes, k increases continuously with Re_z . This was observed only for TV and LH1 in the previous case, but is now seen for more modes. This observation, together with the previous subsection, shows that the behaviour is globally the same as for $\eta = 0.5$, but variation in critical m is much faster as Re_z increases and more modes are involved. This behaviour is consistent with the results of Ng & Turner

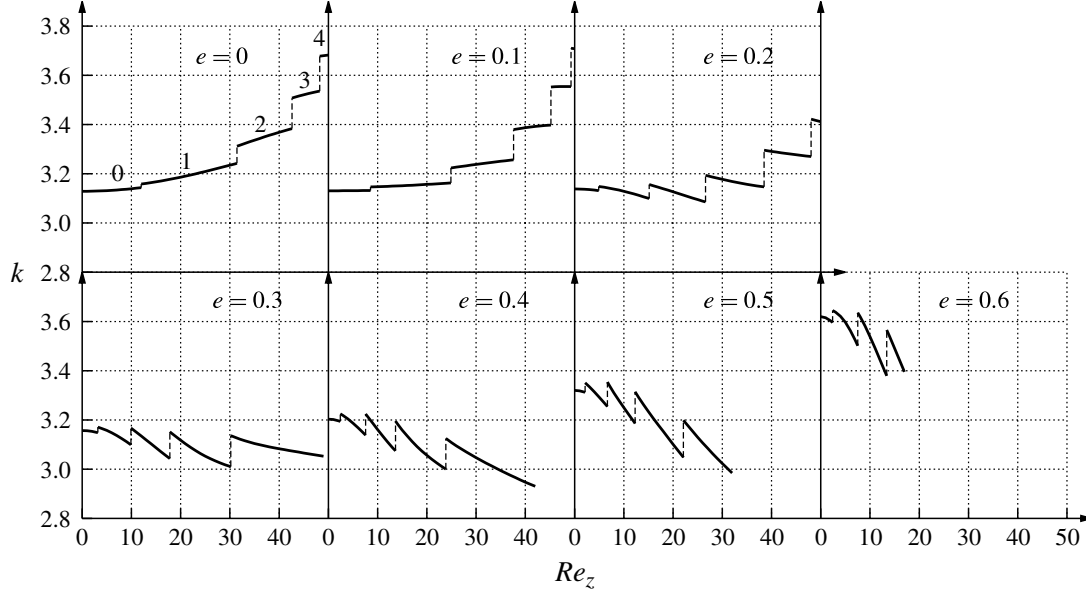


FIGURE 15. The critical wavenumber k against the axial Reynolds number Re_z for eccentricities $e = 0, 0.1, \dots, 0.6$. Discontinuities correspond to a switch in critical m (values indicated by annotation for $e = 0$).

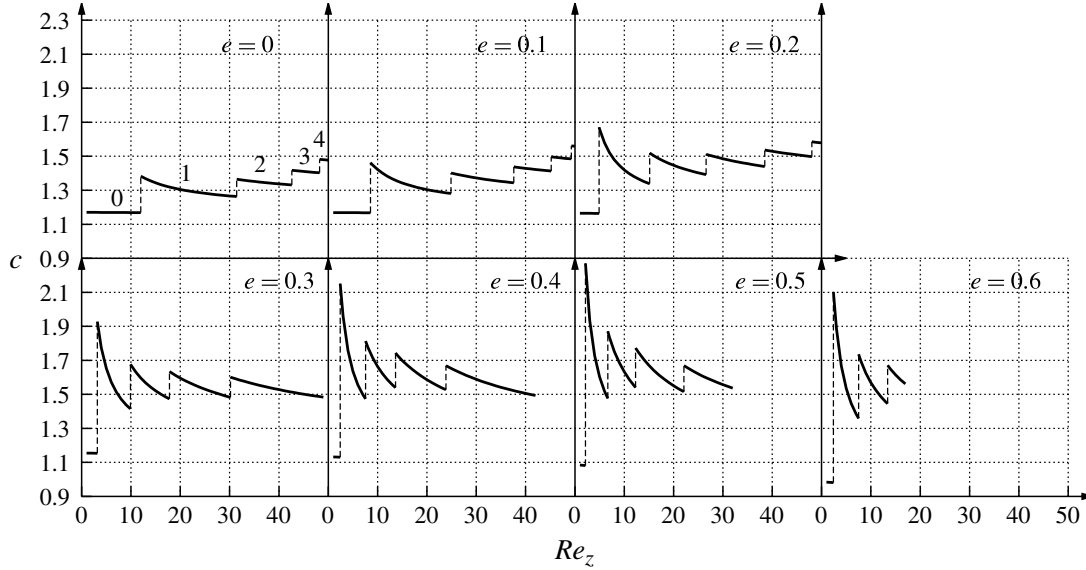


FIGURE 16. The critical phase speed c (in base flow axial speed unit \bar{w}_B) against the axial Reynolds number Re_z for eccentricities $e = 0, 0.1, \dots, 0.6$. Discontinuities correspond to a switch in critical m (values indicated by annotation for $e = 0$).

(1982) who found a critical azimuthal wavenumber of 12 at $Re_z = 100$ for $\eta = 0.77$, and of 35 for $\eta = 0.95$.

4.3. Critical phase speed

As for the case $\eta = 0.5$, the phase speed is around 1–2 times the average axial speed of the base flow (figure 16). As the eccentricity is increased, the jump in phase speed

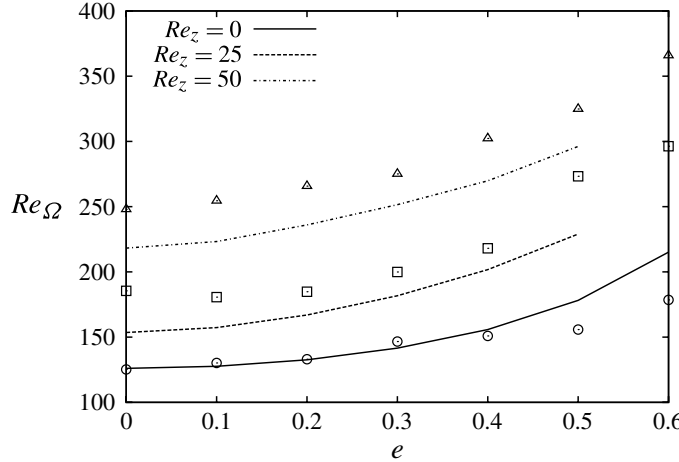


FIGURE 17. Comparison of the critical curves $Re_\Omega = f(e)$ for $Re_z = 0, 25, 50$: the present results (lines) and the experimental results (points) of Coney & Mobbs (1969–70) for the sharp entry apparatus.

between consecutive critical modes becomes larger. For high enough eccentricities, the peak phase speed is that of the LH1.

4.4. Comparison with experiments

In this section, we compare the numerical results with a series of experiments performed on a single apparatus of radius ratio $\eta = 0.89$ and aspect ratio (length over clearance) $L = 71.8$. Figure 17 compares experimental data from Coney & Mobbs (1969–70) (sharp entry case) against our calculations, after converting their graphical data into our system of control parameters. The agreement is quite good when there is no axial flow, and for $e < 0.5$. At higher eccentricities, though, we predict transition at higher rotation rates. It is likely that the difference is due to boundary effects, causing early transition to a Taylor ‘pre-vortex’ flow as reported in Mobbs & Ozgan (1984).

As soon as axial flow is added, the predicted critical Re_Ω is significantly lower than the experimental values, at any eccentricity, though the trends are the same. The experimental data lie between 10 and 20 % above the calculated threshold. Discrepancies as high as 20 % were also noticed between the numerical predictions of Ng & Turner (1982) and the experimental data of Nagib (1972) for the Taylor–Couette–Poiseuille flow of radius ratio $\eta = 0.77$. Takeuchi & Jankowski (1981) reported divergent trends between theoretical predictions and experimental data for $\eta = 0.5$ and Re_z as low as 40. Takeuchi & Jankowski (1981) claimed that the length of the apparatus was responsible for the supercritical Taylor numbers. Indeed, they invoked the idea of a ‘vortex development length’, defined as ‘the length needed for a moving disturbance to reach an amplitude that is observable by the visualization method’. With more recent theory, it would be said that the instability is convective and is triggered by noise at the inlet of the apparatus (sharp or smooth). Indeed, the apparatus used by Coney & Mobbs (1969–70) is quite compact compared to other experiments. The length to gap ratio L is 71.8, whereas it was 160 for Nagib (1972) and 110 for Takeuchi & Jankowski (1981), respectively. In comparison, for a radius ratio of $\eta = 0.95$ and a length to gap ratio of 290, Snyder (1962) obtained experimental data that match those of Ng & Turner (1982) very closely, supporting the idea of the importance of the vortex development length. As advection is increased,

Re_z	Torque (1)	Visual (1)	Visual (1)	Visual (2)	Visual (3)	Present work
0	145	175	166	162	164	178
25	208	269	219	249	301	229
50	281	349	303	334	319	296

TABLE 2. Critical Re_Ω for $e = 0.5$, $\eta = 0.89$: (1), Younes (1972); (2), Coney & Mobbs (1969–70) and Coney (1971); (3), Coney & Atkinson (1978).

m	k	$\omega_{i,max}$	c	c_g	$-k_i$	$\exp[-k_i L]$
-1	2.60	1.95×10^{-4}	0.89	1.08	0.0010	1.1
0	2.70	9.04×10^{-3}	1.03	1.09	0.0455	26.3
1	2.82	1.55×10^{-2}	1.16	1.10	0.0774	258.3
2	2.94	2.00×10^{-2}	1.28	1.12	0.0986	1187.6
3	3.08	2.28×10^{-2}	1.39	1.13	0.1112	2943.3
4	3.21	2.43×10^{-2}	1.50	1.14	0.1169	4429.7
5	3.37	2.46×10^{-2}	1.60	1.16	0.1171	4488.0
6	3.53	2.40×10^{-2}	1.69	1.17	0.1131	3356.9

TABLE 3. Properties of the unstable modes $m = -1, \dots, 6$ for $e = 0.3$, $Re_z = 50$ and $Re_\Omega = 275$. k and $\omega_{i,max}$ are calculated from the temporal stability problem. The phase speed c and the group velocity c_g are relative to the average axial flow velocity \bar{w}_B . k_i is the spatial amplification rate from Gaster (1962)'s relation. $\exp[-k_i L]$ is the amplification factor from the inlet to the outlet of the apparatus (Coney & Mobbs 1969–70).

perturbations travel faster as they grow, and might not be detected for large Re_z , which also explains why the results diverge for larger Re_z .

In table 2, numerical values are given for the critical Re_Ω at $e = 0.5$, from visual observations and torque measurements, compared to our values. The table shows significant scatter of the experimental data, even when using the same technique; for example, visual observations. Values obtained via torque measurements always give lower values than those from visualization, as the method is essentially more sensitive to the ‘pre-vortex’ flow located near the inner cylinder and difficult to visualize. Overall, the theoretical values always lie within (or very close to) the bounds given by the experiments.

4.5. The ‘double-vortex’ pattern

More surprising are the complex patterns observed by Coney & Mobbs (1969–70), with an apparently random axial wavenumber. For an eccentricity of $e = 0.3$ and an axial Reynolds number of $Re_z = 50$, they described a system of two vortices coexisting in the annulus: a left and a right helix, respectively. Looking at their graph, the azimuthal Reynolds number associated with this state has a supercritical value of $Re_\Omega \approx 275$. For this set of parameters, it is possible to calculate the maximum growth rate of all unstable modes. The results are reported in table 3, including the axial wavenumber, the phase speed and the group velocity $c_g \equiv \partial \omega_r / \partial k$. Modes $m = -1$ to 6 are all linearly unstable, so theory allows for a RH to grow at these operating conditions. However, the growth rates associated with higher-order LH are much higher, and $m = 5$ is dominant, closely followed by $m = 4$. The wavenumbers of these

latter modes lie in the lower range of what was experimentally observed: 3.25–5.20. Temporal stability theory offers no obvious explanation for the larger wavenumber perturbations observed in the experiment.

In table 3, we also give the equivalent spatial amplification properties of the unstable modes, following Gaster (1962). For near-critical perturbations, the spatial amplification rate $-k_i$ can be related to the temporal growth rate ω_i , via the group velocity of the perturbation, with the simple relation $-k_i \approx \omega_i/c_g$. In the spatial stability framework (meaningful for convective instabilities), the resulting amplification of the perturbations over the length L of the apparatus is given by $\exp[-k_i L]$. According to this theory, the spatial amplification of higher-order spirals is very fast due to the large growth rate and the moderate group velocity. On the other hand, RH spiral $m = -1$ is barely amplified through the apparatus and is very unlikely to saturate before exiting the system.

One could then think of this unexpected pattern as a consequence of transient growth due to non-modal effects (for a review, see Chomaz 2005). Heaton (2008) assessed the importance of these effects in axisymmetric Taylor–Couette–Poiseuille flow, and showed that they could also potentially explain deviations from modal stability predictions at moderate Re_z , typically of the order of a few hundreds. For lower Re_z , however, transient growth is not significant, and modal theory alone was shown (Cotrell *et al.* 2004) to match the experimental results accurately. Hence, for $Re_z = 50$, it seems unlikely that transient effects might be important, even though no results are currently available for the eccentric case.

Owing to the supercritical operating conditions and the variety of unstable modes, nonlinear simulations would surely help us to understand the double-vortex pattern. As in the case with no advection, end effects might also have an impact on the stability properties. Finally, phase noise may prevent a clear identification of the convectively amplified pattern (Babcock, Ahlers & Cannell 1991; Babcock, Cannell & Ahlers 1992).

5. Conclusions and perspectives

The temporal stability of eccentric Taylor–Couette–Poiseuille flow with a fixed outer cylinder has been investigated for a large range of parameter space. Parametric studies have been performed for a wide-gap case $\eta = 0.5$ with $Re_z \leq 200$ and $e \leq 0.7$, and a small-gap case $\eta = 0.89$ with $Re_z \leq 50$ and $e \leq 0.6$. Taylor vortices give way to helical structures of increasing azimuthal complexity as advection is increased. The helicity of these structures is always opposed to the inner-cylinder rotation, and are termed left helices, as in Taylor–Couette–Poiseuille flow. Broken axisymmetry changes the thresholds and distorts the critical modes, but was not found to trigger any new instability mechanism for the parameter range considered.

Eccentricity is always stabilizing, regardless of the axial flow rate, and this effect becomes even more important for higher values of e . Indeed, centrifugal effects are weakened at $e \geq 0.3$, as a low-speed recirculation region forms in the base flow and less fluid is driven in rotation around the inner cylinder. The effect of axial advection at fixed eccentricities is more subtle. For the small-gap case, the critical Re_Ω increases steadily with Re_z . For the wide-gap case $\eta = 0.5$, the critical Re_Ω increases for weak values of Re_z , but decreases slightly as axial advection is increased further. The maximum value of the critical Re_Ω is obtained for a value of Re_z that increases with eccentricity. Despite the destabilizing effect of advection above this specific value of Re_z , the case with no advection always remains the most unstable. For the wider

gap $\eta = 0.5$, increasing e at fixed Re_z tends to lower the critical pseudo-azimuthal wavenumber m (except for LH1 over TV), whereas ‘higher-order’ modes seem to be selected for $\eta = 0.89$. The critical axial wavelength is always of the order of the clearance d . For $\eta = 0.5$, the axial wavenumber k decreases continuously for a given m (except for TV and LH1 at small eccentricities) with increasing Re_z , but positive jumps are seen as higher and higher pseudo-azimuthal wavenumber m are selected at criticality. For $\eta = 0.89$, the behaviour is similar except that the increase of k for small m and small e is seen for more modes. For both radius ratios, the critical phase speed c of the travelling waves varies between 0.8 and 2.2 times the axial mean velocity of the base flow. c decreases with Re_z , except when the critical azimuthal wavenumber switches, in which case there is a discontinuous jump to a higher phase speed. For the small-gap case $\eta = 0.89$, the range of Re_z for which a critical fixed m dominates is much smaller than for $\eta = 0.5$ and transition to higher-order modes happens in a smoother way as Re_z increases. Mode competition is more pronounced for the small-gap case because modes of different m lie closer to each other in the (Re_Ω, Re_z) plane.

Whereas the instability mechanism for TV is only centrifugal, with a stabilizing effect of Re_z , the destabilization of helical modes $m > 0$ is strongly influenced by axial advection. Indeed, higher-order LH modes require a minimum amount of axial shear to become unstable, and this effect dominates the centrifugal mechanism for low Re_z . For large enough Re_z , the effect of axial advection becomes minor, compared to centrifugal destabilization with increasing Re_Ω . Maximum vortex activity, measured here by the maximum of the disturbance kinetic energy, is localized in the converging gap and moves towards the small gap and inner cylinder as Re_z is increased. At the same time, the disturbance energy concentrates increasingly into axial motion, recalling the two-dimensional structure of TS waves generated by axial shear. However, the so-called TS-like disturbances, involving a critical layer close to the wall, are not found in the range of the computations and are only expected to appear at larger advection rates (Cotrell & Pearlstein 2004). Centre modes of *Sp* type, found in eccentric annular Poiseuille flow by Merzari *et al.* (2008), are expected to exist in eccentric Taylor–Couette–Poiseuille flow at sufficiently large values of Re_z , but would require prohibitively fine meshing to be explored thoroughly with the method used here.

Comparison with the experiment of Coney & Mobbs (1969–70) for the small-gap case shows agreement within 20 % and matching trends. However, transition is found to occur below the linear threshold for $e \geq 0.5$ and $Re_z = 0$, and above for $Re_z = 25$ and 50 regardless of e . These differences are thought to be due to finite-length effects. In the eccentric case with no axial flow, end effects may be responsible for the onset of toroidal vortices below the limit of infinite-cylinder theory. When axial flow is added, delayed onset is probably caused by the ‘vortex development length’ invoked by Takeuchi & Jankowski (1981). In the framework of convective instabilities, the system needs to be of appropriate length for the perturbations to reach an amplitude detectable by experiments. The apparatus being quite compact, it is plausible that high rotation rates would be needed to amplify perturbations before they exit the system. Despite encouraging results overall, modal stability analysis cannot fully explain the complex pattern observed for $e = 0.3$, $Re_z = 50$, involving a double-vortex structure. Non-modal effects, potentially responsible for transient amplification of this unexpected structure, are likely to be weak for such a low advection rate. According to Heaton (2008), these effects become important for Re_z of the order of a few hundreds in the concentric case, and might contribute to discrepancies in onset

of instability. Assuming that non-modal effects are also important at high Re_z for the eccentric case, we leave the calculation of optimal perturbations as a perspective. The double-vortex structure may result from nonlinear interactions between modes, and fully nonlinear simulations, including end effects and inlet noise, would be very helpful in understanding the formation of this pattern. More experimental data would also be appreciated to ensure reproducibility of the observations.

Although the experiments of Coney & Mobbs (1969–70) suggest that instability is triggered by noise at the inlet and amplified convectively, the effect of eccentricity on absolute instabilities (Huerre & Monkewitz 1985, 1990) remains an open problem. This aspect is currently being investigated and will be addressed in a future paper. A weakly nonlinear study is also required to determine whether the bifurcation remains supercritical over the whole parameter space, or if subcritical transition can occur. Possible steps towards a better understanding of annular flows of drilling muds include non-Newtonian effects and motion of the inner cylinder, as complex effects are expected (Escudier *et al.* 2002; Feng & Fu 2007; Feng *et al.* 2007). To fully document the linear stability properties of this flow, it would also be interesting to investigate the connection with eccentric annular Poiseuille flow at high Re_z , analysed by Cotrell & Pearlstein (2004) and Cotrell *et al.* (2004) in the concentric case. At high Re_z , three families of modes of very different structure are expected to compete (Merzari *et al.* 2008) and make the problem even more computationally challenging.

Appendix

This appendix contains, in non-dimensional form, the expression of some differential operators using Wood (1957)'s modified bipolar coordinate system defined by (2.4)–(2.6). As in § 2.2, the ‘stretched’ variable defined by $\xi = (2\rho - \alpha - 2)/\alpha$ (where $\alpha = \beta - 1$) is used instead of ρ to transform the flow domain to $-1 \leq \xi \leq 1$. Following DiPrima & Stuart (1972a), the infinitesimal length element ds in (ξ, ϕ, z) is as follows:

$$ds^2 = \frac{\alpha^2}{4\delta^2 J} d\xi^2 + \frac{\rho^2}{\delta^2 J} d\phi^2 + dz^2, \quad (\text{A } 1)$$

where J the Jacobian of the transformation (2.4), given by

$$J = \frac{(1 + 2\gamma\rho \cos \phi + \gamma^2\rho^2)^2}{(1 - \gamma^2)^2}. \quad (\text{A } 2)$$

Introducing the inverse scale factors μ_ξ and μ_ϕ associated to the coordinates ξ and ϕ , respectively,

$$\mu_\xi = \frac{2\delta\sqrt{J}}{\alpha}, \quad \mu_\phi = \frac{\delta\sqrt{J}}{\rho}, \quad (\text{A } 3)$$

one can define the operators

$$D_\xi \equiv \mu_\xi \partial_\xi, \quad D_\phi \equiv \mu_\phi \partial_\phi, \quad (\text{A } 4)$$

and factors

$$A \equiv \mu_\phi - \partial_\xi \mu_\xi, \quad B \equiv \partial_\phi \mu_\phi, \quad C \equiv D_\xi A - D_\phi B. \quad (\text{A } 5)$$

Using Whitham (1963)'s general orthogonal coordinate formulas, the different terms in (2.2)–(2.3) can be written (recall that $\partial_z \equiv 0$ for the basic flow) as follows:

$$\nabla_{\perp} p \equiv \begin{bmatrix} D_{\xi} p \\ D_{\phi} p \end{bmatrix}, \quad (\text{A } 6)$$

$$\nabla_{\perp} \cdot \mathbf{u}_{\perp} \equiv (D_{\xi} + A)u + (D_{\phi} - B)v, \quad (\text{A } 7)$$

$$\mathbf{u}_{\perp} \cdot \nabla_{\perp} \mathbf{u}_{\perp} \equiv (uD_{\xi} + vD_{\phi}) \mathbf{u} + (Av + Bu) \begin{bmatrix} -v \\ u \end{bmatrix}, \quad (\text{A } 8)$$

$$\mathbf{u}_{\perp} \cdot \nabla_{\perp} w \equiv (uD_{\xi} + vD_{\phi}) w, \quad (\text{A } 9)$$

$$\nabla_{\perp}^2 \mathbf{u}_{\perp} \equiv \begin{bmatrix} \nabla_{\perp}^2 u \\ \nabla_{\perp}^2 v \end{bmatrix} + \begin{bmatrix} Cu - 2(AD_{\phi} + BD_{\xi})v \\ Cv + 2(AD_{\phi} + BD_{\xi})u \end{bmatrix}, \quad (\text{A } 10)$$

where the scalar Laplacian has the expression

$$\nabla_{\perp}^2 \equiv D_{\xi}^2 + D_{\phi}^2 + (AD_{\xi} - BD_{\phi}). \quad (\text{A } 11)$$

Finally, we give the expression for the rate-of-strain tensor in-plane components used for force/torque calculations:

$$\begin{cases} e_{\xi\xi} = D_{\xi}u - Bv, \\ e_{\phi\phi} = D_{\phi}v + Au, \\ e_{\phi\xi} = e_{\xi\phi} = \frac{1}{2}(D_{\xi}v + D_{\phi}u + Bu - Av). \end{cases} \quad (\text{A } 12)$$

REFERENCES

- ALTMAYER, S., HOFFMANN, C. & LÜCKE, M. 2011 Islands of instability for growth of spiral vortices in the Taylor–Couette system with and without axial through flow. *Phys. Rev. E* **84**, 046308.
- ARNOLDI, W. E. 1951 The principle of minimized iterations in the solution of the matrix eigenvalue problem. *Q. Appl. Maths* **9**, 17–29.
- BABCOCK, K. L., AHLERS, G. & CANNELL, D. S. 1991 Noise-sustained structure in Taylor–Couette flow with through flow. *Phys. Rev. Lett.* **67**, 3388–3391.
- BABCOCK, K. L., CANNELL, D. S. & AHLERS, G. 1992 Stability and noise in Taylor–Couette flow with through-flow. *Physica D* **61** (1), 40–46.
- CASTLE, P. & MOBBS, F. R. 1967 Hydrodynamic stability of the flow between eccentric rotating cylinders: visual observations and torque measurements (paper 6). In *Institution of Mechanical Engineers, Conference Proceedings*, vol. 182, pp. 41–52.
- CHANDRASEKHAR, S. 1960 The hydrodynamic stability of viscous flow between coaxial cylinders. *Proc. Natl Acad. Sci. USA* **46**, 141–143.
- CHANDRASEKHAR, S. 1981 *Hydrodynamic and Hydromagnetic Stability*. Dover.
- CHAWDA, A. & AVGOUTI, M. 1996 Stability of viscoelastic flow between eccentric rotating cylinders. *J. Non-Newtonian Fluid Mech.* **63**, 97–120.
- CHOMAZ, J.-M. 2005 Global instabilities in spatially developing flows: non-normality and nonlinearity. *Annu. Rev. Fluid Mech.* **37**, 357–392.
- COLE, J. A. 1957 Experiments on the flow in rotating annular clearances (paper 15). In *Proceedings of the Conference on Lubrication and Wear*, pp. 16–19. Institution of Mechanical Engineers.
- COLE, J. A. 1967 Taylor vortices with eccentric rotating cylinders. *Nature* **216**, 1200–1202.
- COLE, J. A. 1969 Taylor vortices with eccentric rotating cylinders. *Nature* **221**, 253–254.
- CONEY, J. E. R. 1971 Taylor vortex flow with special reference to rotary heat exchangers. PhD thesis, University of Leeds.

- CONEY, J. E. R. & ATKINSON, J. 1978 The effect of Taylor vortex flow on the radial forces in an annulus having variable eccentricity and axial flow. *Trans. ASME: J. Fluids Engng* **100**, 210–214.
- CONEY, J. E. R. & MOBBS, F. R. 1969–70 Hydrodynamic stability of the flow between eccentric rotating cylinders with axial flow: visual observations (paper 2). *Proc. Inst. Mech. Engrs* **184 Pt 3L**, 10–17.
- COTRELL, D. L. & PEARLSTEIN, A. J. 2004 The connection between centrifugal instability and Tollmien–Schlichting-like instability for spiral Poiseuille flow. *J. Fluid Mech.* **509**, 331–351.
- COTRELL, D. L., SARMA, L. R. & PEARLSTEIN, A. J. 2004 Computational assessment of subcritical and delayed onset in spiral Poiseuille flow experiments. *J. Fluid Mech.* **509**, 353–378.
- DAI, R.-X., DONG, Q. & SZERI, A. Z. 1992 Flow between eccentric rotating cylinders: bifurcation and stability. *Intl J. Engng Sci.* **30**, 1323–1340.
- DiPRIMA, R. C. 1959 The stability of viscous flow between rotating concentric cylinders with a pressure gradient acting round the cylinders. *J. Fluid Mech.* **6**, 462–468.
- DiPRIMA, R. C. 1960 The stability of a viscous fluid between rotating cylinders with an axial flow. *J. Fluid Mech.* **9**, 621–631.
- DiPRIMA, R. C. 1963 A note on the stability of flow in loaded journal bearings. *Trans. Am. Soc. Lubric. Engrs* **6**, 249–253.
- DiPRIMA, R. C., EAGLES, P. M. & NG, B. S. 1984 The effect of radius ratio on the stability of Couette flow and Taylor vortex flow. *Phys. Fluids* **27**, 2403–2411.
- DiPRIMA, R. C. & STUART, J. T. 1972a Flow between eccentric rotating cylinders. *J. Lubric. Tech.* **94**, 266–274.
- DiPRIMA, R. C. & STUART, J. T. 1972b Non-local effects in the stability of flow between eccentric rotating cylinders. *J. Fluid Mech.* **54**, 393–415.
- DiPRIMA, R. C. & STUART, J. T. 1975 The nonlinear calculation of Taylor vortex flow between eccentric rotating cylinders. *J. Fluid Mech.* **67**, 85–111.
- DRIS, I. M. & SHAQFEH, E. S. G. 1998 Experimental and theoretical observations of elastic instabilities in eccentric cylinder flows: local versus global instability. *J. Non-Newtonian Fluid Mech.* **80**, 1–58.
- EAGLES, P. M., STUART, J. T. & DiPRIMA, R. C. 1978 The effects of eccentricity on torque and load in Taylor-vortex flow. *J. Fluid Mech.* **87**, 209–231.
- EL-DUJAILY, M. J. & MOBBS, F. R. 1990 The effect of end walls on subcritical flow between concentric and eccentric rotating cylinders. *Intl J. Heat Fluid Flow* **11**, 72–78.
- ESCUDIER, M. P., GOULDSON, I. W., OLIVEIRA, P. J. & PINHO, F. T. 2000 Effects of inner cylinder rotation on laminar flow of a Newtonian fluid through an eccentric annulus. *Intl J. Heat Fluid Flow* **21**, 92–103.
- ESCUDIER, M. P., OLIVEIRA, P. J. & PINHO, F. T. 2002 Fully developed laminar flow of purely viscous non-Newtonian liquids through annuli, including the effects of eccentricity and inner-cylinder rotation. *Intl J. Heat Fluid Flow* **23**, 52–73.
- FENG, S. & FU, S. 2007 Influence of orbital motion of inner cylinder on eccentric Taylor vortex flow of Newtonian and power-law fluids. *Chin. Phys. Lett.* **24**, 759–762.
- FENG, S., LI, Q. & FU, S. 2007 On the orbital motion of a rotating inner cylinder in annular flow. *Intl J. Numer. Meth. Fluids* **54**, 155–173.
- FRÊNE, J. & GODET, M. 1971 Transition from laminar to Taylor vortex flow in journal bearings. *Tribology* **4**, 216–217.
- GASTER, M. 1962 A note on the relation between temporally-increasing and spatially-increasing disturbances in hydrodynamic stability. *J. Fluid Mech.* **14**, 222–224.
- GODA, K. 1979 A multistep technique with implicit difference schemes for calculating two- or three-dimensional cavity flows. *J. Comput. Phys.* **30**, 76–95.
- GUO, B. & LIU, G. 2011 *Applied Drilling Circulation Systems – Hydraulics, Calculations, Models*. Elsevier.
- HEATON, C. J. 2008 Optimal linear growth in spiral Poiseuille flow. *J. Fluid Mech.* **607**, 141–166.
- HUERRE, P. & MONKEWITZ, P. A. 1985 Absolute and convective instabilities in free shear layers. *J. Fluid Mech.* **159**, 151–68.

- HUERRE, P. & MONKEWITZ, P. A. 1990 Local and global instabilities in spatially developing flows. *Annu. Rev. Fluid. Mech.* **22**, 473–537.
- HUGGINS, N. J. 1966–67 Tests on a 24-in diameter journal bearing: transition from laminar to turbulent flow. In *Symposium on Journal Bearings for Reciprocating and Turbo Machinery*, *Proc. Inst. Mech. Engrs*, vol. 181 (Pt 3B), p. 81.
- HWANG, J. Y. & YANG, K. S. 2004 Numerical study of Taylor–Couette flow with an axial flow. *Comput. Fluids* **33**, 97–118.
- KAMAL, M. M. 1966 Separation in the flow between eccentric rotating cylinders. *Trans. ASME J. Basic Engng* **88**, 717–724.
- KARASUDANI, T. 1987 Non-axis-symmetric Taylor vortex flow in eccentric rotating cylinders. *J. Phys. Soc. Japan* **56**, 855–858.
- KOSCHMIEDER, E. L. 1976 Taylor vortices between eccentric cylinders. *Phys. Fluids* **19**, 1–4.
- LIM, T. T. & LIM, S. S. 2008 Modified expression for critical Reynolds number in eccentric Taylor–Couette flow. *AIAA J.* **46**, 277–280.
- MACKRODT, P. A. 1976 Stability of Hagen–Poiseuille flow with superimposed rigid rotation. *J. Fluid Mech.* **73**, 153–164.
- MARQUES, F. & LOPEZ, J. M. 2000 Spatial and temporal resonances in a periodically forced hydrodynamic system. *Physica D* **136**, 340–352.
- MARTINAND, D., SERRE, E. & LUEPTOW, R. M. 2009 Absolute and convective instability of cylindrical Couette flow with axial and radial flows. *Phys. Fluids* **21**, 104102.
- MERZARI, E., WANG, S., NINOKATA, H. & THEOFILIS, V. 2008 Biglobal linear stability analysis for the flow in eccentric annular channels and a related geometry. *Phys. Fluids* **20**, 114104.
- MESEGUER, A. & MARQUES, F. 2000 On the competition between centrifugal and shear instability in spiral Couette flow. *J. Fluid Mech.* **402**, 33–56.
- MESEGUER, A. & MARQUES, F. 2002 On the competition between centrifugal and shear instability in spiral Poiseuille flow. *J. Fluid Mech.* **455**, 129–148.
- MOBBS, F. R. & OZOGAN, M. S. 1984 Study of sub-critical Taylor vortex flow between eccentric rotating cylinders by torque measurements and visual observations. *Intl J. Heat Fluid Flow* **5**, 251–253.
- MOBBS, F. R. & YOUNES, M. A. M. A. 1974 The Taylor vortex regime in the flow between eccentric rotating cylinders. *Trans. ASME: J. Lubric. Tech.* 127–134.
- NAGIB, H. 1972 On instabilities and secondary motions in swirling flows through annuli. PhD thesis, Illinois Institute of Technology.
- NG, B. S. & TURNER, E. R. 1982 On the linear stability of spiral flow between rotating cylinders. *Proc. R. Soc. Lond. A Mat.* **382**, 83–102.
- OIKAWA, M., KARASUDANI, T. & FUNAKOSHI, M. 1989a Stability of flow between eccentric rotating cylinders. *J. Phys. Soc. Japan* **58**, 2355–2364.
- OIKAWA, M., KARASUDANI, T. & FUNAKOSHI, M. 1989b Stability of flow between eccentric rotating cylinders with a wide gap. *J. Phys. Soc. Japan* **58**, 2209–2210.
- PODRYABINKIN, E. V. & RUDYAK, V. Y. 2011 Moment and forces exerted on the inner cylinder in eccentric annular flow. *J. Engng Thermophys.* **20**, 320–328.
- RASPO, I., HUGUES, S., SERRE, E., RANDRIAMAMPIANINA, A. & BONTOUX, P. 2002 A spectral projection method for the simulation of complex three-dimensional rotating flows. *Comput. Fluids* **31**, 745–767.
- REID, W. H. 1961 Review of The hydrodynamic stability of viscous flow between coaxial cylinders by S. Chandrasekhar (*Proc. Natl Acad. Sci. USA* **46**, 141–143, 1960). *Math. Rev.* **22**, 565.
- RITCHIE, G. S. 1968 On the stability of viscous flow between eccentric rotating cylinders. *J. Fluid Mech.* **32**, 131–144.
- SEP, J. 2008 Journal bearing with an intensive axial oil flow—experimental investigation. *Scientific Problems of Machines Operation and Maintenance* **43**, 21–29.
- SNYDER, H. A. 1962 Experiments on the stability of spiral flow at low axial Reynolds numbers. *Proc. R. Soc. Lond. A Mat.* **265**, 198–214.
- SNYDER, H. A. 1965 Experiments on the stability of two types of spiral flow. *Ann. Phys.* **31**, 292–313.

- TAKEUCHI, D. I. & JANKOWSKI, D. F. 1981 Numerical and experimental investigation of the stability of spiral Poiseuille flow. *J. Fluid Mech.* **102**, 101–26.
- TAYLOR, G. I. 1923 Stability of a viscous liquid contained between two rotating cylinders. *Phil. Trans. R. Soc. Lond.* **223**, 289–343.
- VERSTEEGEN, P. L. & JANKOWSKI, D. F. 1969 Experiments on the stability of viscous flow between eccentric rotating cylinders. *Phys. Fluids* **12**, 1138–1143.
- VOHR, J. A. 1968 An experimental study of Taylor vortices and turbulence in flow between eccentric rotating cylinders. *Trans. ASME: J. Lubric. Tech.* **90**, 285–296.
- WANNIER, G. H. 1950 A contribution to the hydrodynamics of lubrication. *Q. Appl. Maths* **8**, 1–32.
- WHITHAM, G. B. 1963 The Navier–Stokes equations of motion. In *Laminar boundary layers* (ed. L. Rosenhead), chap. III, Clarendon.
- WOOD, W. W. 1957 The asymptotic expansions at large Reynolds numbers for steady motion between noncoaxial rotating cylinders. *J. Fluid Mech.* **3**, 159–175.
- XIAO, Q., LIM, T. T. & CHEW, Y. T. 1997 Experimental investigation on the effect of eccentricity on Taylor–Couette flow. In *Transport Phenomena in Thermal Science and Process Engineering*, pp. 685–689. Kyoto, Japan.
- YOUNES, M. A. M. A. 1972 The hydrodynamic stability of spiral flow between eccentric rotating cylinders. PhD thesis, University of Leeds.
- YOUNES, M. A. M. A., MOBBS, F. R. & CONEY, J. E. R. 1972 Hydrodynamic stability of the flow between eccentric rotating cylinders with axial flow: torque measurements (paper C76/72). In *Tribology Convention, Institution of Mechanical Engineers*, pp. 14–19.

[A16]

Transition near the edge of a rotating disk

B. Pier

Journal of Fluid Mechanics **737**, R1 (9 pages) (2013)

doi:10.1017/jfm.2013.578

<https://hal.archives-ouvertes.fr/hal-00907846>



Transition near the edge of a rotating disk

Benoît Pier[†]

Laboratoire de mécanique des fluides et d'acoustique, École centrale de Lyon – CNRS – Université de Lyon 1 – INSA Lyon, 36 avenue Guy-de-Collongue, 69134 Écully CEDEX, France

(Received 4 October 2013; revised 23 October 2013; accepted 28 October 2013)

The rotating-disk boundary layer is generally considered as an example of a flow that displays a robust transition from laminar to turbulent régimes. By taking into account disks of finite radius, Healey (*J. Fluid Mech.*, vol. 663, 2010, pp. 148–159) has predicted a stabilizing effect of the boundary condition, but Imayama *et al.* (*J. Fluid Mech.*, vol. 716, 2013, pp. 638–657) were unable to confirm this prediction experimentally. Following these contradictory results, the present experimental investigation revisits the rotating-disk boundary layer, without any artificially imposed excitation, and studies in further detail the dynamics prevailing in the region closely surrounding the edge of the disk, as well as the flow beyond the disk. Azimuthal mean velocities and fluctuation amplitudes are recorded with small steps in radial and axial directions for a wide range of disk sizes. An objective criterion is used to define the onset of fluctuations consistently over a large data set. Two distinct mechanisms for the onset of fluctuations are identified. In particular, it is found that the flow over the edge of the disk acts as a strong source of fluctuations. Explanations and suggestions for a possible reconciliation of previous studies are given.

Key words: boundary layer stability, instability, transition to turbulence

1. Context

Ever since the pioneering work of von Kármán (1921), the boundary layer due to a disk rotating in otherwise still fluid has served as the archetypical three-dimensional boundary layer (Reed & Saric 1989; Saric, Reed & White 2003; Launder, Poncet & Serre 2010). This flow is known for its robust laminar–turbulent transition occurring at a radial position closely corresponding to the onset of local absolute instability (Lingwood 1995, 1996).

Assuming a disk of infinite extent, previous studies have established the global linear stability of the base boundary-layer flow (Garrett 2002; Davies & Carpenter

[†]Email address for correspondence: benoit.pier@ec-lyon.fr

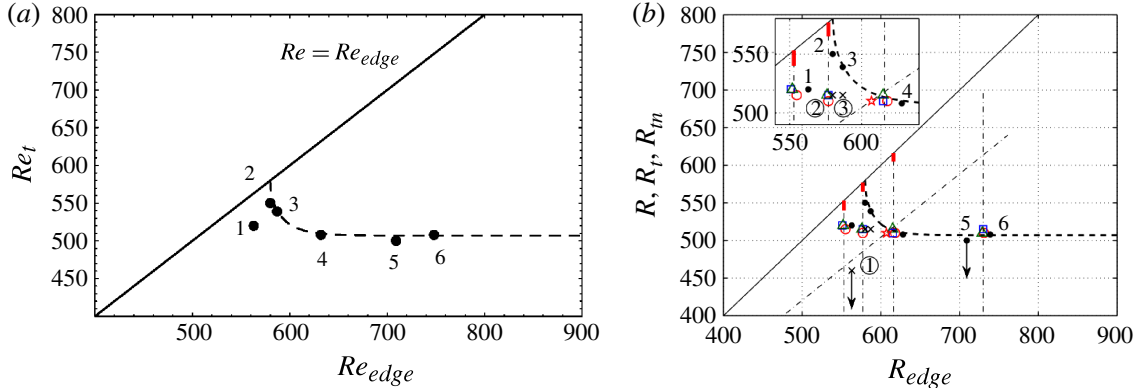


FIGURE 1. Dependence of transition radius (Re_t or R_t) on the size of the disk (Re_{edge} or R_{edge}): (a) reproduced from Healey (2010), figure 7(a); (b) reproduced from Imayama *et al.* (2013), figure 8. The numbers 1–6 refer to transition data from different experiments used in both papers.

2003), while the nonlinear behaviour can be explained by a scenario involving both local primary and secondary absolute instabilities (Pier 2003). Local absolute instability is only a necessary but not a sufficient condition for global linear instability (Huerre & Monkewitz 1990). In contrast, nonlinear global modes (aka ‘elephant’ global modes (Pier & Huerre 2001)) are triggered by a sharp front at the transition from local convective to absolute instability; thus, the existence of local absolute instability is a necessary and sufficient condition for global nonlinear instability (Pier, Huerre & Chomaz 2001). It turns out that the rotating-disk flow precisely falls into the category of linearly stable but nonlinearly unstable systems.

By considering spatially varying systems of finite extent, a recent theoretical study by Healey (2010) has shown that the presence of a downstream boundary condition may have a destabilizing effect on the base state and a stabilizing effect on the nonlinear state. Using a simple nonlinear model, Healey (2010) has shown that the front which appears at the onset of absolute instability when the boundary is far from the front, moves slightly downstream when the boundary approaches the front. For the rotating-disk configuration, the transition radius is thus expected to increase when the size of the disk is reduced. This prediction may be supported by plotting experimentally observed transition radii found in the literature; see figure 7(a) of Healey (2010), reproduced here as figure 1(a), where the numbers 1–6 refer to transition data from different experiments. However, this theory is unable to quantitatively assess this stabilizing effect for the rotating disk since the nonlinear interaction terms are difficult to quantify for this flow.

Following these theoretical predictions, the edge effects on rotating-disk transition have been experimentally studied by Imayama, Alfredsson & Lingwood (2013). Three different edge conditions and a range of edge Reynolds numbers have been investigated. The authors concluded that no obvious variation in the transition location due to the proximity to the edge of the disk had been observed in the study; see figure 8 of Imayama *et al.* (2013), reproduced here as figure 1(b). Note, however, that data measured within 10 boundary-layer units from the edge were removed in that study since the mean flow was seen to deviate from the Kármán similarity solution in this region, and that the values of the transition radii already used by Healey (2010) were reinterpreted in Imayama *et al.* (2013), using different definitions of onset.

In view of these contradictory results, there is clearly a need for new measurements covering a wide range of disk radii and for an unbiased criterion to define the transition location consistently over a large data set. From a long history of rotating-disk experiments (Theodorsen & Regier 1944; Smith 1947; Gregory, Stuart & Walker 1955; Chin & Litt 1972; Fedorov *et al.* 1976; Kobayashi, Kohama & Takamadate 1980; Malik, Wilkinson & Orszag 1981; Wilkinson & Malik 1985; Lingwood 1996; Othman & Corke 2006; Imayama, Alfredsson & Lingwood 2012; Imayama *et al.* 2013; Siddiqui *et al.* 2013), the reported radii for onset of transition display significant scatter. This scatter may be attributable to edge effects, but also to the use of different definitions of onset radius. Although the rotating-disk boundary layer is usually associated with a sharp laminar–turbulent transition, detailed measurements by Siddiqui *et al.* (2013) have shown that there exists a significant intermediate nonlinear régime, and that the extent of this intermediate region (of the order of 50 units) also depends on disk-normal distance. This observation again calls for new measurements and for the use of a consistent criterion.

Therefore the present investigation aims to make a contribution to our understanding of the dynamics prevailing near the edge, as well as the flow behaviour beyond the disk. By considering a wide range of non-dimensional disk sizes, the aim is to perform measurements with small steps in radial and normal directions and to use an objective criterion to gain further insight into the role played by the edge region in the global dynamics.

2. Experimental setup and procedure

The experimental facility (see figure 2) used in the present investigation has been improved following Siddiqui (2011)'s thesis and consists of a synthetic resin disk of $R_e^* = 250$ mm radius that is rotated at constant angular velocity, up to 2000 r.p.m. The disk surface topography was characterized using by a linear variable differential transducer (LVDT) and adjustments were made so as to achieve best alignment with a plane normal to the rotation axis. The residual out-of-flatness was less than 20 μm (i.e. the entire disk surface is within two parallel planes that are no more than 20 μm apart) and the azimuthal imbalance is less than 10 μm (i.e. below any fixed point in the laboratory frame, the surface of the disk travels by less than 10 μm under rotation). The edge of the disk is a sharp right angle (see figure 2b), and the disk protrudes 23 mm above the aluminium plate that holds it. Since a typical boundary-layer thickness is less than 0.5 mm, it is thus reasonable to assume that this setup is a good approximation of a disk of finite radius and infinite thickness.

Following Siddiqui (2011), local velocity measurements are carried out via constant-temperature hot-wire anemometry, which is particularly suitable for measuring flows with fast fluctuations at fixed points in space. A single Dantec hot wire of type 55P01 is used, positioned parallel to the disk surface and aligned in the radial direction so as to measure the azimuthal flow component. A high-precision computer-controlled traversing mechanism is used for positioning the probe in the radial and axial directions with precisions of 20 μm and 2 μm respectively. The accessible range of radial positions is such that measurements up to 20 mm beyond the edge of the disk are possible. In the axial direction, the hot wire can reach down to 9 mm below the disk surface. Due to the size of the hot-wire probe (5 mm), it is safe to measure below the disk surface only for $R^* \geq 253$ mm.

Here, the constant boundary-layer thickness is proportional to $\delta = \sqrt{\nu/\Omega}$, where ν is the kinematic viscosity and Ω the disk rotation rate. Since all distances are non-

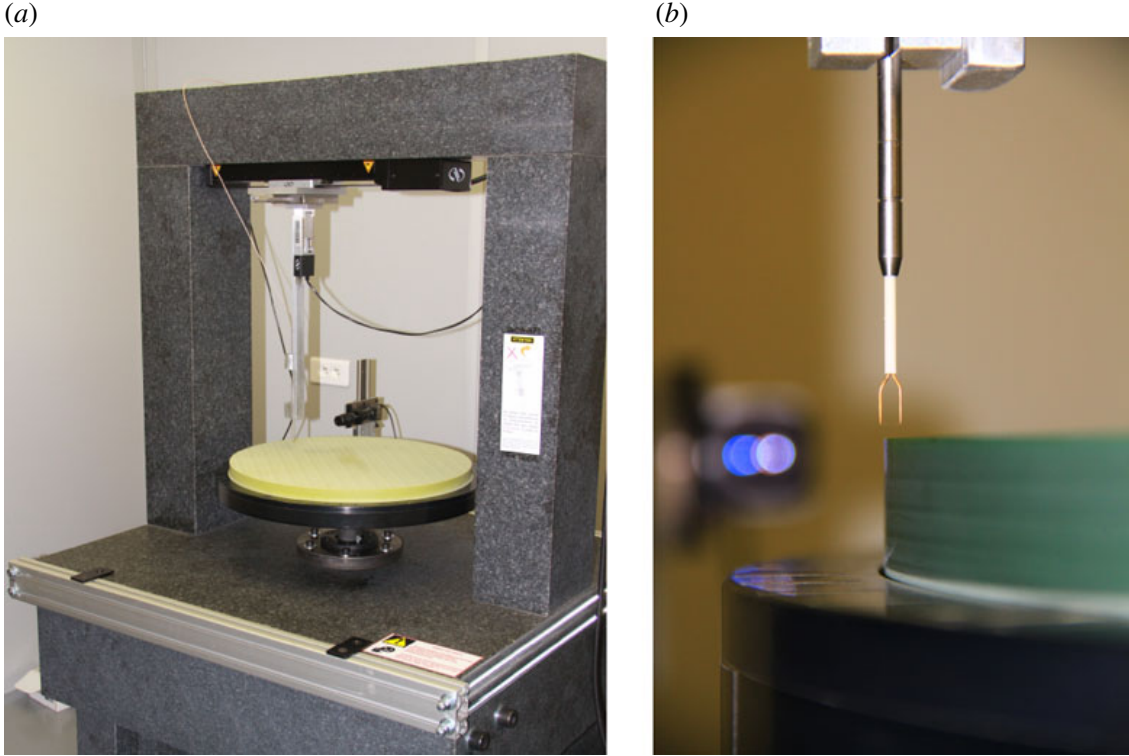


FIGURE 2. Experimental setup. (a) General view of disk and two-axes traversing mechanism for computer-controlled measurements. (b) Hot-wire probe above the sharp edge of the disk, protruding 23 mm out of the aluminium plate.

dimensionalized by δ , the non-dimensional disk-edge radius $R_e = R_e^*/\delta$ may be varied by adjusting the disk rotation rate. Then, velocity measurements are automatically performed over specified ranges of non-dimensional radial and axial positions, R and Z ; at each position, data are typically acquired over 100 disk revolutions. Velocities are always non-dimensionalized by the local disk velocity: $V = V^*/(R\delta\Omega)$.

3. Results

Mean azimuthal velocity profiles are shown in figure 3 for $R_e = 400, 500, 550$ and 600 . Symbols correspond to measurements, while the solid curve indicates the von Kármán similarity solution. These plots show that the azimuthal velocities depart from the Kármán profile either when transition starts ($R \gtrsim 500$) or when the edge is approached ($R \gtrsim R_e$). Strong azimuthal shear prevails in the boundary layer over the entire disk ($R < R_e$ and $0 < Z < 4$). Beyond the disk edge ($R > R_e$), the azimuthal shear rapidly decays and the velocity profiles flatten out over the entire Z -range, above and below the disk surface. Even when the flow is expected to remain laminar up to the edge of the disk (e.g. $R_e = 400$, figure 3a), the presence of the boundary is felt about 10 boundary-layer units inboard. For this reason, Imayama *et al.* (2013) removed all data measured close to the outer edge from their results and discussions. While Healey (2010)'s theory assumes a point-like boundary condition and vanishing fluctuations at this point, the cross-over from the boundary layer prevailing over the

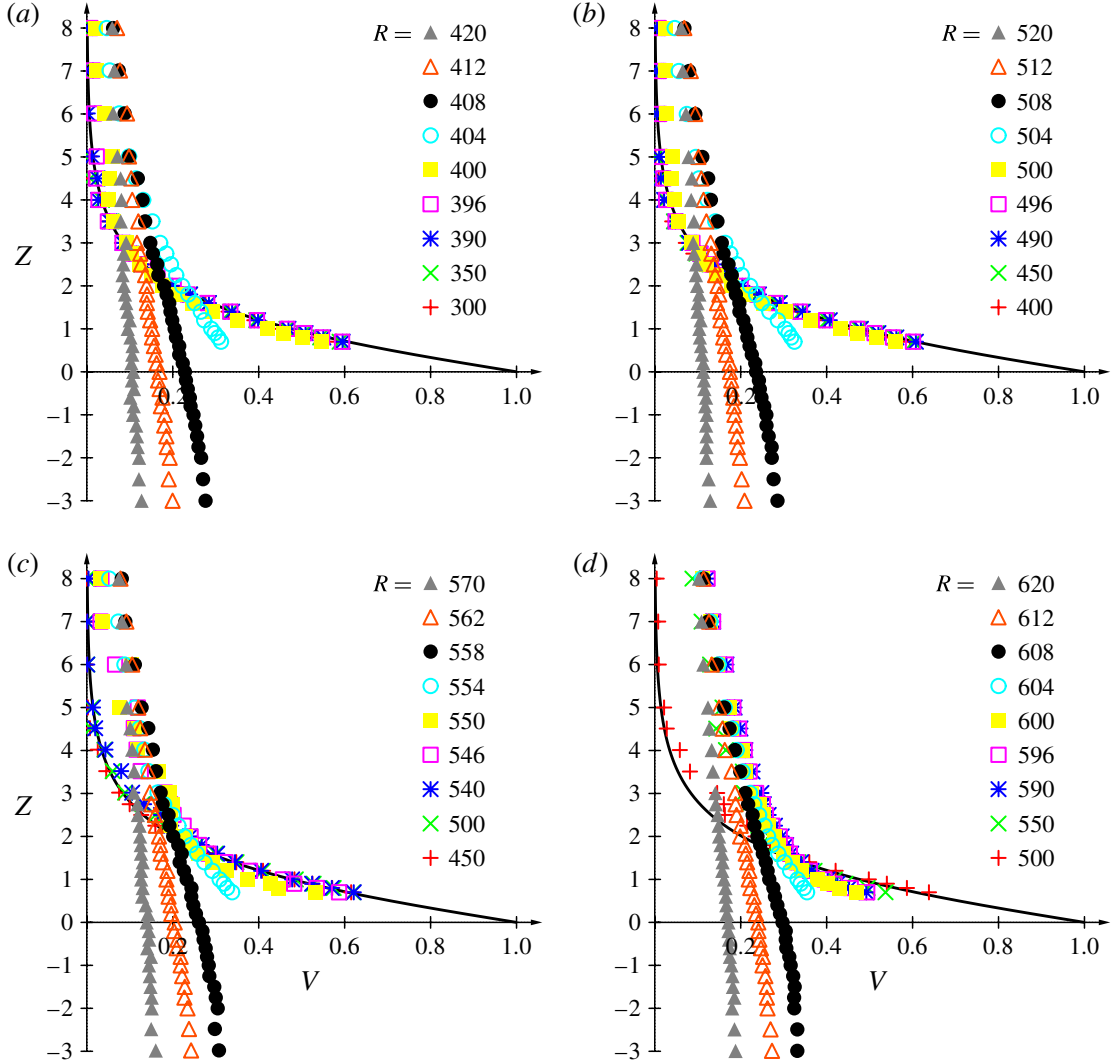


FIGURE 3. Mean azimuthal velocity profiles obtained with (a) $R_e = 400$, (b) $R_e = 500$, (c) $R_e = 550$, (d) $R_e = 600$. The solid curve indicates the Kármán similarity profile and symbols correspond to measurements at the specified non-dimensional radial positions.

disk surface to the low-velocity region beyond the disk clearly occurs in a more gradual way. We believe therefore that an investigation of the edge effects should precisely take into account this cross-over region.

The structure of this cross-over region is more clearly illustrated in figure 4, where radial sections of the mean azimuthal velocity are plotted for different edge radii and different normal distances. For $R < R_e$ and $R < 500$ all plots are almost horizontal lines, which shows that they closely follow the Kármán similarity solution, whatever the disk-normal distance Z . Beyond the edge, $R > R_e$, the velocities depend much less on Z and rapidly drop with increasing radial distance. It is only for larger edge radii ($R_e > 550$) that a significant departure from the Kármán solution occurs before the disk edge is reached.

The amplitude of the fluctuations around the basic flow has been characterized by V_{rms} , the root-mean-square (r.m.s.) value of the velocity. Figure 5 shows the radial

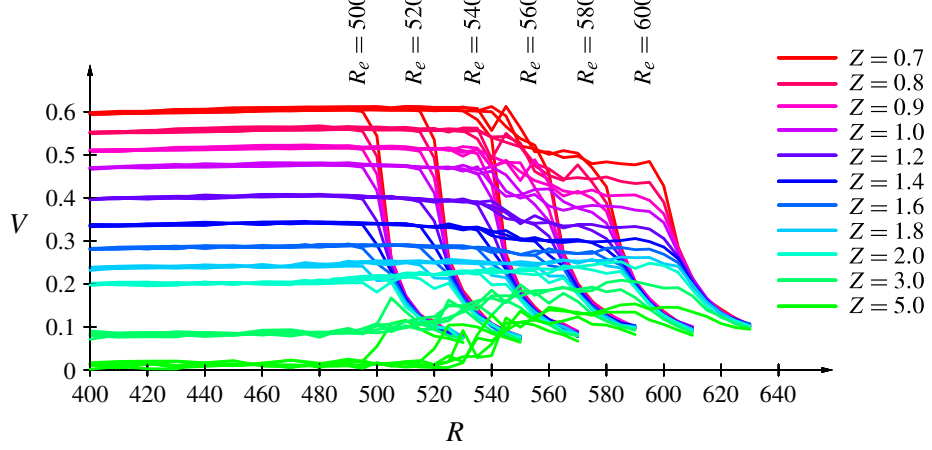


FIGURE 4. Radial traverses of mean azimuthal velocity for a range of disk-normal distances Z and edge radii R_e .

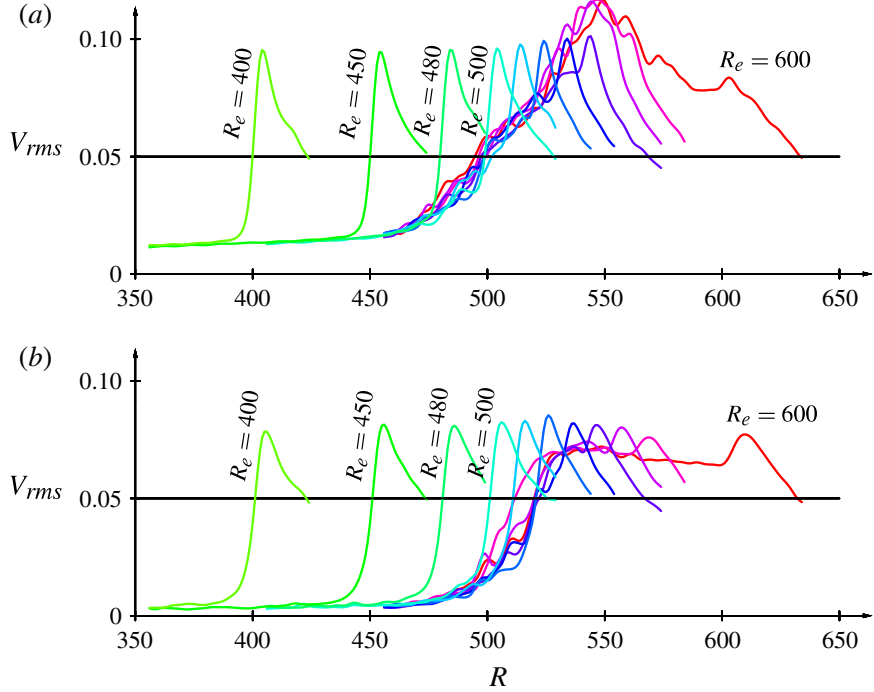


FIGURE 5. Radial evolution of V_{rms} at $Z = 1$ (a) and $Z = 3$ (b) for $R_e = 400, 450, 480, 500, 510, 520, 530, 540, 550, 560$ and 600.

evolution of the fluctuating amplitude for a range of R_e , measured at $Z = 1$ (figure 5a) and $Z = 3$ (figure 5b). These plots show two distinct features. For $R_e \lesssim 500$, the boundary layer remains unperturbed over most of the disk surface and the r.m.s. values rapidly increase near the edge of the disk to reach a maximum value near $R_e + 5$ beyond which they decay again. For $R_e \gtrsim 500$, fluctuations start to rise as $R = 500$ is approached and continue for the rest of the boundary layer.

These measurements clearly indicate that the near-edge region acts as a strong source of noise, even at very low R_e (i.e. at very low disk rotation rates). At a given disk-normal distance Z , this sudden increase of fluctuations in the vicinity of

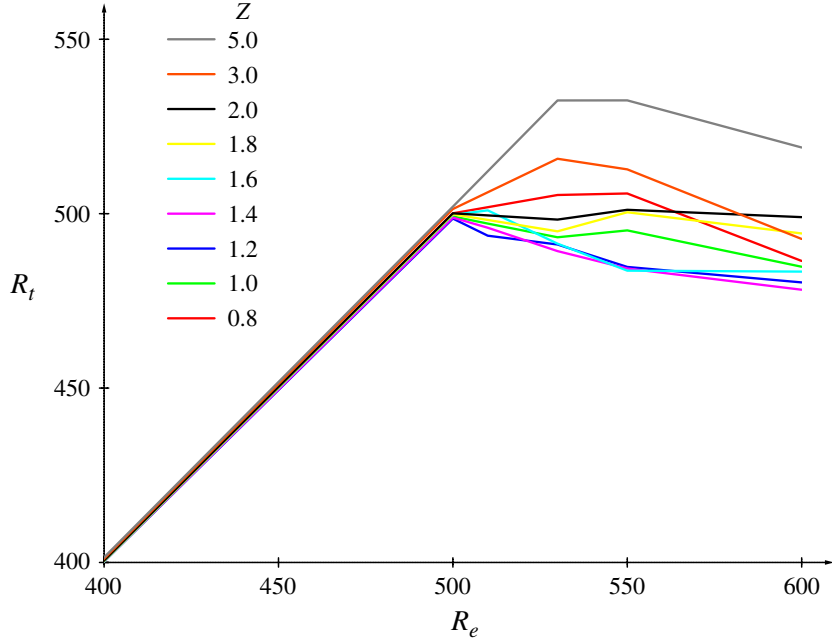


FIGURE 6. Dependence of onset radius R_t on edge location R_e for different values of disk-normal distance Z .

the edge has a characteristic shape that hardly depends on the value of R_e , provided that $R_e < 500$. For larger disks, $R_e > 500$, a slow increase of fluctuation amplitude is observed to start around $R = 450$ and to saturate around $R = 550$. This more gradual development of fluctuation amplitude does not seem to be much affected by the value of the edge radius. For much larger disks (see plots corresponding to $R_e = 600$ in figure 5), large-amplitude fluctuations are fully developed before the edge is reached, and the r.m.s. values display only a weak peak at the edge before decaying beyond the edge.

In order to characterize more precisely the influence of the edge, an objective criterion for the onset of finite-amplitude fluctuations is required. Here we define R_t as the radial position where the above r.m.s. values cross the value 0.05 (thin horizontal lines in figure 5). Note that, due to the steep slope of the curves in figure 5, this criterion yields onset values that are largely insensitive to the precise threshold value used (here 0.05). Applying this criterion to the data acquired over a large number of experimental runs yields the dependence of the onset radius R_t on the edge location R_e and disk-normal distance Z , shown in figure 6. These plots show that for all $R_e \leq 500$ and $Z \leq 5$, onset always occurs at the disk edge: $R_t = R_e$. For $R_e > 500$, the onset radius R_t no longer linearly increases with R_e and eventually reaches a nearly constant value. The onset radius moreover significantly depends on the disk-normal distance Z : earliest onset is observed for $Z \approx 1.4$, while it is delayed in the regions further above the disk. Since for most of these curves the onset radius R_t slightly decreases with increasing R_e for $R_e > 500$, this could be interpreted as pointing towards a weakly stabilizing edge effect, as predicted by Healey (2010). However, considering only curves derived from measurements at $Z = 2.0$ and $Z = 1.8$, which are nearly flat, one could also argue that the stabilizing edge effect is negligible at these disk-normal distances.

4. Summary and discussion

In the present investigation, the near-edge region of the rotating-disk boundary layer has been characterized in detail for a wide range of non-dimensional disk radii. Mean azimuthal velocity measurements reveal how the cross-over from the boundary layer prevailing over the disk surface to the low-velocity region beyond the disk occurs.

Detailed measurements of the spatial development of fluctuating amplitudes have been carried out, using small steps in R and Z for a range of disk radii R_e . The onset radius R_t has then been obtained via automatic data processing, using the same criterion consistently across a large data set. It has been found that for small disks, i.e. $R_e < 500$, onset always occurs at the disk edge: $R_t = R_e$ independently of Z . For large disks, i.e. $R_e > 500$, it is observed that the onset radius R_t depends weakly on R_e and also significantly on Z , and no stabilizing trend can be clearly established.

In view of these results, it seems that Healey (2010)'s theory cannot be confirmed and also that any attempt to compare data obtained via different experiments and criteria cannot be justified. Indeed, the present investigation has shown that the scatter of R_t due to different values of Z is of the same order as the data given by Healey (2010) or Imayama *et al.* (2013) (see figure 1).

Two distinct mechanisms have been identified for the onset of fluctuations:

Larger disks (typically $R_e > 500$) display a gradual increase of fluctuating amplitude for $450 < R < 550$, which is mostly independent of disk size. This may be interpreted as a self-sustained boundary-layer global mode (Pier 2003), triggered by absolute instability near $R = 500$ and largely insensitive to edge effects.

Smaller disks (typically $R_e < 500$) display a sharp increase of fluctuating amplitude in the vicinity of the edge. This shows that, even at low rotation rates, the flow over the edge of the disk is strongly unstable. The flow over the edge is a combination of a radial wall jet (shooting over the edge) and an azimuthal shear layer that rapidly decay with radial distance. We conjecture that this flow over the edge is locally absolutely unstable, thus triggering another self-sustained global mode that cannot be suppressed.

By masking any stabilization due to the zero-fluctuation outlet condition, this strong source of fluctuations could provide an explanation for the inapplicability of the theory (Healey 2010). A possible reconciliation between Healey (2010)'s theory and Imayama *et al.* (2013)'s interpretation might be achieved if the theory could be modified so as to model the downstream boundary condition as a source of random noise rather than by vanishing fluctuating amplitude.

Further theoretical investigations are planned to obtain the base flow solutions prevailing beyond the disk and their stability characteristics, in order to study the possible existence of a self-sustained edge global mode and its competition with the boundary-layer global mode.

Acknowledgements

The author thanks J. J. Healey, S. Imayama, P. H. Alfredsson and R. J. Lingwood for stimulating discussions and for convincing him to undertake the present work. Invaluable technical assistance by A. Azouzi, H. Correia, R. Michelet, C. Nicot and B. Poirel is gratefully acknowledged. This research was partially supported by *Agence nationale de la recherche* (Project 'Microssillon').

References

- CHIN, D.-T. & LITT, M. 1972 An electrochemical study of flow instability on a rotating disk. *J. Fluid Mech.* **54**, 613–625.
- DAVIES, C. & CARPENTER, P. W. 2003 Global behaviour corresponding to the absolute instability of the rotating-disk boundary layer. *J. Fluid Mech.* **486**, 287–329.
- FEDOROV, B. I., PLAVNIK, G. Z., PROKHOROV, I. V. & ZHUKHOVITSKII, L. G. 1976 Transitional flow conditions on a rotating disk. *J. Engng Phys.* **31**, 1448–1453.
- GARRETT, S. J. 2002 The stability and transition of the boundary layer on rotating bodies. PhD thesis, University of Cambridge.
- GREGORY, N., STUART, J. T. & WALKER, W. S. 1955 On the stability of three-dimensional boundary layers with application to the flow due to a rotating disk. *Phil. Trans. R. Soc. Lond. A* **248**, 155–199.
- HEALEY, J. J. 2010 Model for unstable global modes in the rotating-disk boundary layer. *J. Fluid Mech.* **663**, 148–159.
- HUERRE, P. & MONKEWITZ, P. A. 1990 Local and global instabilities in spatially developing flows. *Annu. Rev. Fluid Mech.* **22**, 473–537.
- IMAYAMA, S., ALFREDSSON, P. H. & LINGWOOD, R. J. 2012 A new way to describe the transition characteristics of a rotating-disk boundary-layer flow. *Phys. Fluids* **24**, 031701.
- IMAYAMA, S., ALFREDSSON, P. H. & LINGWOOD, R. J. 2013 An experimental study of edge effects on rotating-disk transition. *J. Fluid Mech.* **716**, 638–657.
- VON KÁRMÁN, TH. 1921 Über laminare und turbulente Reibung. *Z. Angew. Math. Mech.* **1**, 233–252.
- KOBAYASHI, R., KOHAMA, Y. & TAKAMADATE, C. 1980 Spiral vortices in boundary layer transition regime on a rotating disk. *Acta Mechanica* **35**, 71–82.
- LAUNDER, B., PONCET, S. & SERRE, E. 2010 Laminar, transitional, and turbulent flows in rotor-stator cavities. *Annu. Rev. Fluid Mech.* **42**, 229–248.
- LINGWOOD, R. J. 1995 Absolute instability of the boundary layer on a rotating disk. *J. Fluid Mech.* **299**, 17–33.
- LINGWOOD, R. J. 1996 An experimental study of absolute instability of the rotating-disk boundary-layer flow. *J. Fluid Mech.* **314**, 373–405.
- MALIK, M. R., WILKINSON, S. P. & ORSZAG, S. A. 1981 Instability and transition in rotating disk flow. *AIAA J.* **19**, 1131–1138.
- OTHMAN, H. & CORKE, T. 2006 Experimental investigation of absolute instability of a rotating-disk boundary layer. *J. Fluid Mech.* **565**, 63–94.
- PIER, B. 2003 Finite-amplitude crossflow vortices, secondary instability and transition in the rotating-disk boundary layer. *J. Fluid Mech.* **487**, 315–343.
- PIER, B. & HUERRE, P. 2001 Nonlinear synchronization in open flows. *J. Fluids Struct.* **15**, 471–480.
- PIER, B., HUERRE, P. & CHOMAZ, J.-M. 2001 Bifurcation to fully nonlinear synchronized structures in slowly varying media. *Physica D* **148**, 49–96.
- REED, H. L. & SARIC, W. S. 1989 Stability of three-dimensional boundary layers. *Annu. Rev. Fluid Mech.* **21**, 235–284.
- SARIC, W. S., REED, H. L. & WHITE, E. B. 2003 Stability and transition of three-dimensional boundary layers. *Annu. Rev. Fluid Mech.* **35**, 413–440.
- SIDDIQUI, M. E. 2011 Experimental study of natural and forced instabilities and transition of a rotating-disk boundary-layer flow. PhD thesis, École centrale de Lyon, Écully, France.
- SIDDIQUI, M. E., MUKUND, V., SCOTT, J. & PIER, B. 2013 Experimental characterization of transition region in rotating-disk boundary layer. *Phys. Fluids* **25**, 034102.
- SMITH, N. H. 1947 Exploratory investigation of laminar-boundary-layer oscillations in a rotating disk. *NACA Tech. Rep.* TN 1227.
- THEODORSEN, T. & REGIER, A. 1944 Experiments on drag of revolving disks, cylinders, and streamline rods at high speeds. *NACA Tech. Rep.* 793.
- WILKINSON, S. P. & MALIK, M. R. 1985 Stability experiments in the flow over a rotating disk. *AIAA J.* **23**, 588–595.

[A17]

Absolute instabilities in eccentric Taylor–Couette–Poiseuille flow

C. Leclercq, B. Pier & J. Scott

Journal of Fluid Mechanics **741**, 543–566 (2014)

doi:10.1017/jfm.2013.646

<https://hal.archives-ouvertes.fr/hal-00948589>

Absolute instabilities in eccentric Taylor–Couette–Poiseuille flow

Colin Leclercq[†], Benoît Pier and Julian F. Scott

Laboratoire de mécanique des fluides et d’acoustique, École centrale de Lyon – CNRS – Université Claude-Bernard Lyon 1 – INSA Lyon, 36 avenue Guy-de-Collongue, 69134 Écully CEDEX, France

(Received 18 July 2013; revised 13 November 2013; accepted 30 November 2013)

The effect of eccentricity on absolute instabilities (AI) in the Taylor–Couette system with pressure-driven axial flow and fixed outer cylinder is investigated. Five modes of instability are considered, characterized by a pseudo-angular order m , with here $|m| \leq 2$. These modes correspond to toroidal ($m = 0$) and helical structures ($m \neq 0$) deformed by the eccentricity. Throughout the parameter range, the mode with the largest absolute growth rate is always the Taylor-like vortex flow corresponding to $m = 0$. Axial advection, characterized by a Reynolds number Re_z , carries perturbations downstream, and has a strong stabilizing effect on AI. On the other hand, the effect of the eccentricity e is complex: increasing e generally delays AI, except for a range of moderate eccentricities $0.3 \lesssim e \lesssim 0.6$, where it favours AI for large enough Re_z . This striking behaviour is in contrast with temporal instability, always inhibited by eccentricity, and where left-handed helical modes of increasing $|m|$ dominate for larger Re_z . The instability mechanism of AI is clearly centrifugal, even for the larger values of Re_z considered, as indicated by an energy analysis. For large enough Re_z , critical modes localize in the wide gap for low e , but their energy distribution is shifted towards the diverging section of the annulus for moderate e . For highly eccentric geometries, AI are controlled by the minimal annular clearance, and the critical modes are confined to the vicinity of the inner cylinder. Untangling the AI properties of each m requires consideration of multiple pinch points.

Key words: absolute/convective instability, Taylor–Couette flow

1. Introduction

The flow between rotating cylinders has attracted attention since the end of the 19th century, starting with the experiments of Couette (1888a,b) and Mallock (1888), and the landmark work by Taylor (1923), who first predicted theoretically the threshold for centrifugal instability. Taylor characterized centrifugal effects using a non-dimensional number appropriate in the limit of small clearance, $d = (b - a) \ll a$, with a and b the inner and outer cylinder radii (see figure 1). In this paper, a wide gap geometry with radii ratio $\eta = a/b = 0.5$ will be considered, and centrifugal effects will be conveniently measured by an azimuthal Reynolds number $Re_\Omega = a\Omega d/\nu$, with Ω the inner cylinder rotation rate and ν the kinematic viscosity.

[†] Email address for correspondence: colin.leclercq@ec-lyon.fr

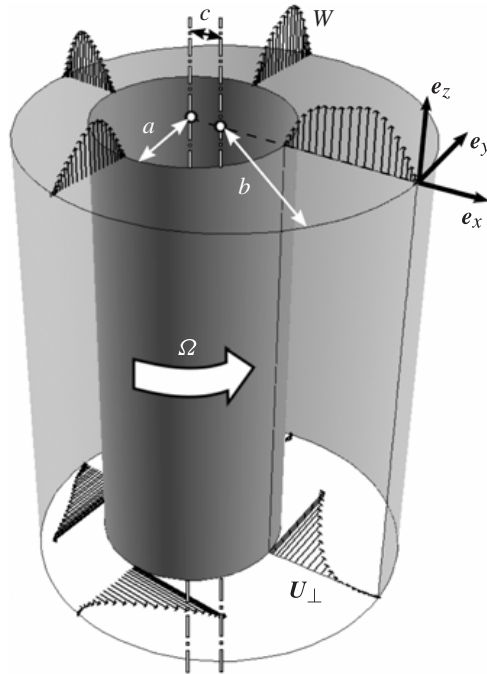


FIGURE 1. Eccentric annulus of radius ratio $\eta = a/b = 0.5$ and basic flow $U = U_{\perp} + We_z$.

Adding axial flow to this system, one obtains a simple prototype for the study of pattern formation in real open flows. The effect of axial advection can also be measured by a Reynolds number $Re_z = \bar{W}d/\nu$, based on the mean axial velocity \bar{W} . First theoretical predictions of the absolute instability (AI) threshold were obtained by Tsameret & Steinberg (1991a) with a criterion based on a one-dimensional Ginzburg–Landau equation (with coefficients determined by two-dimensional numerical simulations), and then by Babcock, Ahlers & Cannell (1991), Babcock, Cannell & Ahlers (1992), using the full set of hydrodynamic equations and a saddle-point criterion (Briggs 1964; Bers 1983) that will be discussed in §2.3. They showed that upon crossing the AI threshold, periodic self-sustained vortices appear, in contrast with the irregular patterns emerging from noise amplification in the convectively unstable régime. In these papers and subsequent work (Tsameret & Steinberg 1991b; Babcock *et al.* 1992; Lücke & Recktenwald 1993; Babcock, Ahlers & Cannell 1994; Swift, Babcock & Hohenberg 1994; Tsameret & Steinberg 1994), effort was dedicated to identifying the noise sources (inlet noise versus thermal noise) which sustain the convective instability (CI). These studies were restricted to small axial Reynolds numbers Re_z , typically below 4, and it was found that the most unstable (fastest growing) perturbations were in the form of propagating Taylor vortices. For higher values of axial advection, Takeuchi & Jankowski (1981) and Ng & Turner (1982) had previously shown numerically (and also experimentally for the former reference) that critical modes consisted of propagating helical vortices, with helicity opposite that of the basic flow, and with azimuthal order m increasing with Re_z . However, the concept of AI was not widespread in fluid mechanics back then, and these studies were restricted to CI.

Theoretical prediction of AI of helical modes was investigated only recently (Pinter, Lücke & Hoffmann 2003; Altmeier, Hoffmann & Lücke 2011). In these papers, the authors studied the effect of axial through-flow on the spatio-temporal properties of

toroidal and helical wavepackets with angular orders $|m| \leq 2$, for $Re_z \leq 20$. For $|m| \leq 1$, it was shown that critical azimuthal Reynolds numbers Re_Ω are higher for AI than for CI, and that the difference between the two thresholds increases with Re_z . For $|m| = 2$ and a stationary outer cylinder, AI was found to occur in a closed region of the Re_z – Re_Ω plane, considering only the saddle point originating at the critical conditions for CI with $Re_z = 0$ (detailed in § 2.4). However, the authors mentioned other saddle points expected to destabilize these modes in other regions of parameter space and which will be taken into account in the present article. More recent work on AI in the Taylor–Couette–Poiseuille flow concerned the effect of radial flow at the inner cylinder, representative of filtration devices (Martinand, Serre & Lueptow 2009). In this analysis, it was shown that axisymmetric modes become absolutely unstable for inward radial flow, while helical modes with helicity identical to that of the basic flow dominate at high enough Re_z , for outward radial flow.

When the two cylinder axes do not coincide, axisymmetry is broken and the stability properties of the flow are modified. Eccentricity is generally measured by the non-dimensional distance between the two cylinders $e = c/d$ (see figure 1). Adding eccentricity to the Taylor–Couette flow with axial advection, one obtains a basic model for annular mud flows in oil-well drilling, or lubrication flows present in high-speed journal bearings. In the first case, mud is injected in a rotating drillstring, and flows back to the surface through the annular domain between the drillstring and the rock face, with several engineering functions: carry the rock cuttings out, lubricate, prevent inflow of formation gases and wellbore collapse, etc. (Escudier, Oliveira & Pinho 2002; Guo & Liu 2011). For deep wells, the drillstring inevitably bends along its axis, on a typical length scale much larger than the well diameter. As a result, a parallel-flow assumption is reasonable, and the flow can be locally described as a Taylor–Couette–Poiseuille flow between eccentric cylinders. In high-speed turbomachinery, a similar configuration is found: oil is contained in eccentric journal bearings for lubrication purposes, and a pressure gradient is imposed along the shaft to evacuate damaging impurities (Sep 2008).

Aside from its fundamental interest, these industrial applications motivate the present analysis. In both applications, transition to complex hydrodynamic régimes would result in increased frictional losses, detrimental to the system efficiency. If the basic flow advection is weak compared to the rotation rate, hydrodynamic resonance may occur and the entire flow would bifurcate to an undesired self-sustained oscillatory state. This specific behaviour, called *absolute instability*, is particularly ‘dangerous’, because it does not require a permanent forcing: once the instability is triggered, it will propagate in both the downstream and upstream directions, and amplify using energy from the basic flow. On the other hand, *convective instabilities* correspond to wavepackets propagating only in the downstream direction: in the absence of forcing, the system eventually relaxes to its initial state at any fixed location, after perturbations have been ‘blown away’ from the source. The most temporally amplified perturbations are given by a classical temporal stability analysis, and such a study was recently carried out for this flow (Leclercq, Pier & Scott 2013). It was shown that the physics is essentially similar to the axisymmetric case (Takeuchi & Jankowski 1981; Ng & Turner 1982), with propagating toroidal vortices replaced by helical structures of increasing azimuthal complexity as Re_z is increased.

Eccentricity deforms the critical modes, but does not introduce new instabilities to the problem. The effect of eccentricity is stabilizing for all values of Re_z , and this result is interpreted as a consequence of the reduction of centrifugal effects in the basic flow. Indeed, as eccentricity increases, the azimuthal flow rate decreases

for a fixed inner cylinder rotation rate, resulting in weaker driving of the instability. This is a consequence of the appearance of a recirculation region in the wide gap which does not contribute to the net azimuthal flow rate. Outside this zone, in the vicinity of the inner cylinder, the flow resembles an axisymmetric Taylor–Couette flow with clearance scaling with the inner gap $d(1 - e)$. The reduction of the ‘effective’ clearance ratio $\delta = d/a$ with eccentricity, or increase in ‘effective’ radius ratio η , also explains stabilization; see DiPrima (1960) for the effect of η on the Taylor–Couette flow. To date, it is, to the authors’ knowledge, the only available theoretical study of eccentric Taylor–Couette–Poiseuille flow. The only known series of experiments were performed by Coney & Mobbs (1969), Coney (1971), Younes (1972), Younes, Mobbs & Coney (1972), Mobbs & Younes (1974), Coney & Atkinson (1978) and show good agreement with our *a posteriori* predictions, despite small discrepancies attributed to finite-length effects. For a brief review of other theoretical and experimental results on eccentric Taylor–Couette flow on the one hand, and axisymmetric Taylor–Couette–Poiseuille flow on the other hand, we refer to Leclercq *et al.* (2013).

The present paper extends this previous linear stability analysis by considering the case of AI. In § 2, the linear stability framework is presented. The governing equations and numerical methods are briefly described, and the main properties of the basic flow and normal modes are recalled. In § 2.3, the methods used to investigate AI, based on the Briggs (1964)–Bers (1983) pinching criterion, are described. In § 3, results are presented for the five modes of instability with angular orders $|m| \leq 2$, which include the fastest growing temporally unstable modes for $Re_z \leq 50$.

2. Linear stability framework

In the following, the geometry will be described using the ratio $0 < \eta = a/b < 1$ between the inner and outer cylinder radii a and b (see figure 1), and the eccentricity $0 \leq e = c/(b - a) < 1$, based on the distance c between centres, divided by the clearance $d = b - a$. The gap varies azimuthally between $d(1 - e)$ and $d(1 + e)$. The radii ratio will be fixed at the value $\eta = 0.5$ throughout this paper. Rotation and axial advection will be quantified using the two Reynolds numbers given in the introduction: $Re_\Omega = a\Omega d/\nu$ and $Re_z = \bar{W}d/\nu$, with Ω the inner cylinder rotation rate, \bar{W} the basic-flow mean axial velocity and ν the kinematic viscosity.

The velocity u will be made non-dimensional with the rotation speed $V \equiv a\Omega$. The clearance d will be taken as the reference length scale L . Finally, the pressure p will be in units of $P \equiv \rho V^2$, with ρ the density of the fluid. All equations and physical quantities will be written in non-dimensional form, using V , L and P .

2.1. Basic flow

The velocity u can be decomposed into a component w parallel to the axis e_z , and a component $u_\perp = u - we_z$ in a plane perpendicular to the axis. The axial flow is driven by a pressure gradient G in the z -direction. Denoting the in-plane pressure gradient as $\nabla_\perp p = \nabla p - Ge_z$, the incompressible Navier–Stokes equations read:

$$\left. \begin{aligned} (\partial_t + u \cdot \nabla) \begin{bmatrix} u_\perp \\ w \end{bmatrix} &= - \begin{bmatrix} \nabla_\perp p \\ G \end{bmatrix} + Re_\Omega^{-1} \nabla^2 \begin{bmatrix} u_\perp \\ w \end{bmatrix}, \\ \nabla \cdot u &= 0, \end{aligned} \right\} \quad (2.1)$$

with impermeability and no-slip boundary conditions on the fixed outer cylinder and on the inner cylinder, whose rotational velocity is 1. In-plane and axial derivatives

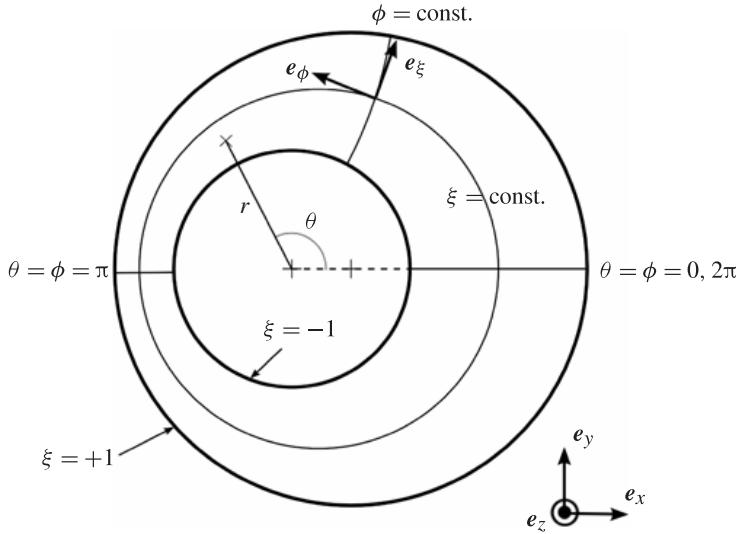


FIGURE 2. Modified bipolar coordinate system (ξ, ϕ) fitting the eccentric annular domain. Polar coordinates (r, θ) are centred on the inner cylinder, with $\theta = \phi = 0$ along the line joining the cylinder axes.

can be separated, using convenient notation: $u_{\perp} \cdot \nabla_{\perp} \equiv u \cdot \nabla - w\partial_z$, $\nabla_{\perp}^2 \equiv \nabla^2 - \partial_z^2$ and $\nabla_{\perp} \cdot u_{\perp} \equiv \nabla \cdot u - \partial_z w$. Assuming an axially invariant flow, the problem is two-dimensional and u_{\perp} becomes independent of w :

$$\left. \begin{aligned} \partial_t u_{\perp} + u_{\perp} \cdot \nabla_{\perp} u_{\perp} &= -\nabla_{\perp} p + Re_{\Omega}^{-1} \nabla_{\perp}^2 u_{\perp}, \\ \nabla_{\perp} \cdot u_{\perp} &= 0. \end{aligned} \right\} \quad (2.2)$$

Basic flows $Q \equiv (U, P)$, denoted with capital letters, are defined as axially invariant, steady solutions of (2.1). Such solutions are found by integrating forwards in time (2.2) until convergence of U_{\perp} is attained, and then solving for the corresponding axial velocity W , given by:

$$U_{\perp} \cdot \nabla_{\perp} W = -G + Re_{\Omega}^{-1} \nabla_{\perp}^2 W. \quad (2.3)$$

Equations are expressed using locally orthogonal, body-fitted coordinates (ξ, ϕ) , with $-1 \leq \xi \leq 1$ and $0 \leq \phi < 2\pi$ the pseudo-radial and pseudo-azimuthal coordinates respectively (see figure 2). In this modified bipolar coordinate system, a Fourier–Chebyshev pseudospectral projection method is implemented, with $N_{\phi} = 2K_{\phi} + 1$ Fourier modes, and N_{ξ} Gauss–Lobatto collocation points. For more details on the numerical procedure, the reader is referred to Leclercq *et al.* (2013).

For an axisymmetric flow, the basic in-plane motion results from diffusion of axial vorticity from the rotating inner cylinder to the fixed outer cylinder. In cylindrical coordinates (r, θ) , it takes the well-known form $U_{\perp} = (0, Ar + B/r)$, with A and B two constants depending on the geometry. For low eccentricities, the result is quite similar, as can be seen in figure 3(ai). However, for higher eccentricities, a low-speed recirculation region forms in the wide gap (figure 3(aii)). For the relatively high value of $Re_{\Omega} = 500$ presented here, small recirculation can already be seen for $e = 0.2$, whereas in Leclercq *et al.* (2013), figure 3, it was not present for $Re_{\Omega} = 100$ and appeared around $e \approx 0.3$ for that lower value of Re_{Ω} .

In the axisymmetric case, W is independent of U_{\perp} , and the axial flow is very similar to a parabolic Poiseuille flow, with small corrections due to the annular geometry. As

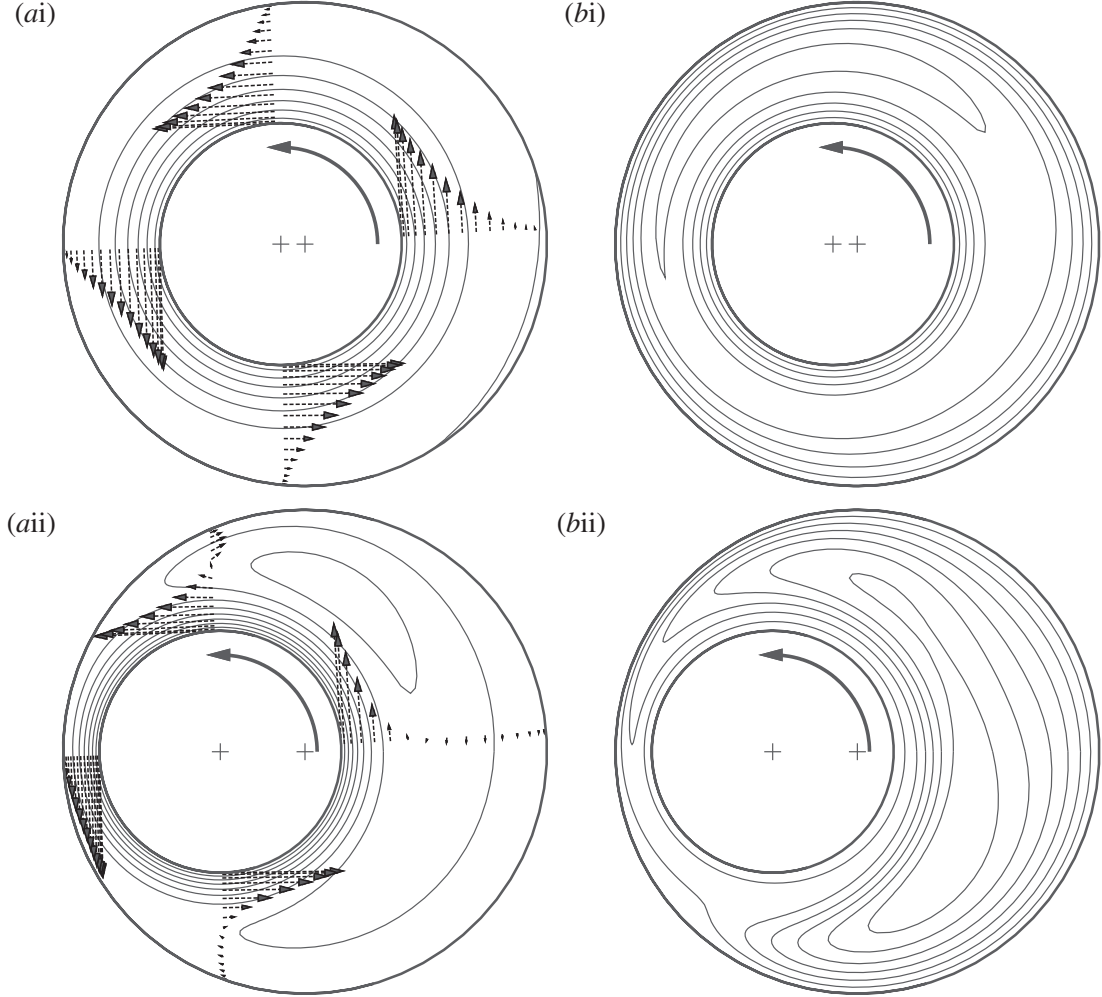


FIGURE 3. Basic flows for $Re_\Omega = 500$: (i) weak eccentricity $e = 0.2$, (ii) high eccentricity $e = 0.7$. (a) Contours of equispaced in-plane streamfunction with superimposed U_\perp profiles at $\theta = 0, \pi/2, \pi, 3\pi/2$ (polar angle with respect to the inner cylinder). (b) Equispaced contours of W .

eccentricity is increased, W decreases in the small gap, because of viscous effects, and most of the volume flux passes through the wide gap (see figure 3bii). Distortion also occurs, due to coupling with U_\perp , and the peak velocity is no longer in the symmetry plane. For high rotation rates, the nonlinear interaction term $U_\perp \cdot \nabla_\perp W$ can locally dominate the viscous term $Re_\Omega^{-1} \nabla_\perp^2 W$, and there is significant transport of W by in-plane components.

2.2. Normal modes

Let $q' \equiv q - Q$ be three-dimensional perturbations of small amplitude superimposed onto the two-dimensional basic flow, and satisfying the linearized Navier–Stokes equations with no-slip boundary conditions. Because of temporal and axial invariance of the basic flow, perturbations are sought in the form of normal modes

$$q' = \tilde{q}(\xi, \phi) \exp i(kz - \omega t) + \text{c.c.}, \quad (2.4)$$

where c.c. denotes the complex conjugate. In a general framework, k is the complex axial wavenumber and ω is the complex frequency. As usual, $\omega_r \equiv \text{Re}(\omega)$ is the

temporal frequency and $\omega_i \equiv \text{Im}(\omega)$ is the temporal growth rate. Equivalently, $k_r \equiv \text{Re}(k)$ is the wavenumber of the mode, and $-k_i \equiv -\text{Im}(k)$ is the spatial growth rate. Injecting the modal form (2.4) into the linearized Navier–Stokes equations with boundary conditions, one obtains a problem of the form $(\mathcal{A} - i\omega\mathcal{B})\tilde{q} = 0$, where $(\mathcal{A}, \mathcal{B})$ are two linear operators, with \mathcal{A} depending on k . Expressions for \mathcal{A} and \mathcal{B} are given in Leclercq *et al.* (2013), in the modified bipolar coordinate system. The wavenumbers k and frequencies ω satisfying this problem for non-zero \tilde{q} define the dispersion relation $D(k, \omega) = 0$. Using the same Fourier–Chebyshev decomposition as for the basic flow, the linear problem is converted into a generalized eigenvalue problem for ω and \tilde{q} that can be solved numerically, using LAPACK (www.netlib.org/lapack) or ARPACK++ (Lehoucq, Sorensen & Yang 1997) routines. For more information on the numerical procedure, the reader is referred to Leclercq *et al.* (2013).

In that previous study, a temporal stability analysis was carried out to predict the fastest growing perturbations with k real and ω complex. It was found that among the large set of temporal modes $\omega(k)$, the most unstable ones were in the form of deformed toroidal vortices for low Re_z , or complex helical structure for higher Re_z . The modes were labelled according to a pseudo-azimuthal integer wavenumber m , or angular order. The labelling was done in accordance with the axisymmetric case, where normal modes can be written as $q' = \tilde{q}(r) \exp i(kz + m\theta - \omega t)$ in polar coordinates (r, θ) (see figure 2). Restricting attention to positive k , because of symmetry arguments to be discussed in the next paragraph, positive values of m (resp. negative) correspond to helical structures winding clockwise (resp. counter-clockwise) around the inner cylinder, and were called left-helical (resp. right-helical), or LH $|m|$ (resp. RH $|m|$) modes. The case $m = 0$ corresponds to the classical toroidal Taylor vortex flow (TV). By following these modes as eccentricity is continuously varied, one obtains the corresponding pseudo-angular order m for $e \neq 0$. Figure 4 shows the structure of modes $m = -2, \dots, 2$ for the classical Taylor–Couette flow.

Note that the symmetry $\Pi_0 \equiv (m, \omega, w) \rightarrow (-m, -\omega^*, -w)$ (with $*$ denoting the complex conjugate) between RH and LH in figure 4 is broken when axial flow is added, or when k is complex. Indeed, by taking the complex conjugate of the axisymmetric modal form, the general symmetry $\Pi_1 \equiv (k, m, \omega) \rightarrow (-k^*, -m, -\omega^*)$ appears, also valid for $e \neq 0$. By considering the mirror image of the system ($z \rightarrow -z$), one obtains another symmetry: $\Pi_2 \equiv (Re_z, k, w) \rightarrow (-Re_z, -k, -w)$. Combining Π_1 and Π_2 , one gets

$$\Pi_3 \equiv (Re_z, k, m, \omega, w) \rightarrow (-Re_z, k^*, -m, -\omega^*, -w). \quad (2.5)$$

Setting Re_z to zero and k real in Π_3 , one recovers Π_0 . In the general case, because of Π_3 , one can choose to study only $m \geq 0$, or only $Re_z \geq 0$, without loss of generality. Π_1 also indicates that it is possible to restrict computations to $k_r \geq 0$.

2.3. Absolute instability threshold

Absolute instability occurs when the impulse response wavepacket is temporally growing at any fixed axial position z . The asymptotic dynamics of the wavepacket is dominated by the normal mode which satisfies the pinching criterion of Briggs (1964)–Bers (1983) and has the largest temporal growth rate. This mode has zero group velocity $\partial\omega/\partial k(k_0) = 0$ for the complex absolute wavenumber k_0 . This condition indicates the presence of a *saddle point* of $\omega(k)$ at k_0 . This saddle point is

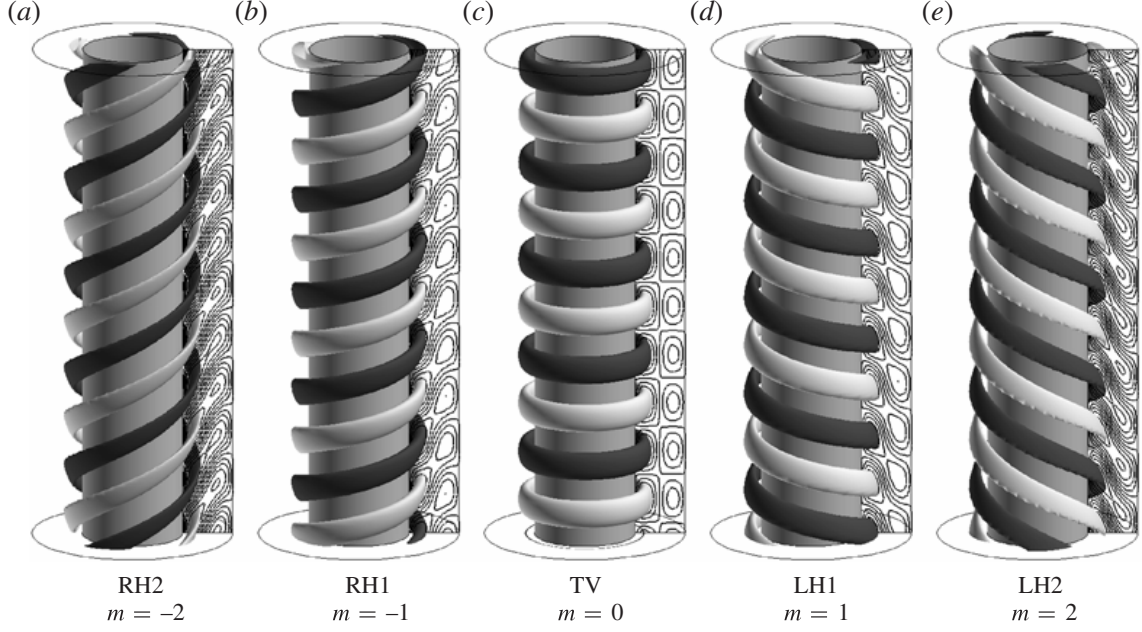


FIGURE 4. Structure (isovales of axial velocity) of the five modes of interest $m = -2, \dots, 2$, from left to right. For this example, $e = 0$, $Re_\Omega = 68.19$, $Re_z = 0$ and $k = 3.16$, corresponding to the critical conditions for temporal instability of the axisymmetric Taylor–Couette flow (see DiPrima & Swinney 1985 for a review).

associated to a branch-point singularity at the complex absolute frequency $\omega_0 = \omega(k_0)$. Additionally, the saddle point must comply with causality and result from the collision between downstream- and upstream-propagating spatial branches, respectively denoted $k^+(\omega)$ and $k^-(\omega)$. The flow is absolutely unstable if and only if the most unstable pinch point has positive absolute growth rate $\omega_{0,i}$. Otherwise, the flow is either stable or convectively unstable. In the latter case, the wavepacket grows while being advected away from the impulse location so the system eventually relaxes to its initial state at any axial position. For a comprehensive review of these concepts, the reader is referred to Huerre & Monkewitz (1990), Huerre (2000), Chomaz (2005).

The border of the absolutely unstable domain is determined by following all the neutrally stable saddle points in parameter space. This is done by performing Newton–Raphson iterations at each point, varying simultaneously k_r , k_i and Re_Ω until $|\omega_i|$, $|\text{Re}(\partial\omega/\partial k)|$ and $|\text{Im}(\partial\omega/\partial k)|$ are all below 10^{-6} . Estimated values for the independent variables are obtained by linear extrapolation with respect to the parameter being varied, e.g. e , Re_Ω or Re_z . For $|m| = 2$, critical curves display folds, and it is necessary to implement a continuation scheme based on an arclength variable (Keller 1977).

However, not all saddle points are valid and only the ones satisfying the pinching criterion are relevant. In order to discard invalid saddle points, extensive tests are carried out, where the two spatial branches $k(\omega)$ coalescing at k_0 are tracked numerically as ω_i is increased from ω_0 . The saddle point is a genuine pinch only when the spatial branches separate into the upper and lower half- k -planes for large enough ω_i . Indeed, causality demands that this be true for $\omega_i > \omega_{i,\max}$, where $\omega_{i,\max}$ is the maximum temporal growth rate for real k . Spatial branches are obtained by numerically inverting the relation $\omega(k)$ with a Newton–Raphson iteration.

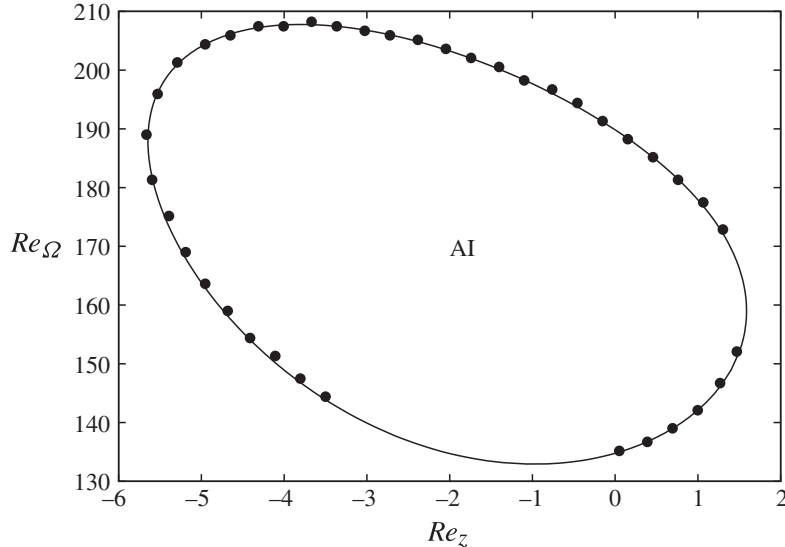


FIGURE 5. ‘Island’ of AI in the axisymmetric case, for mode LH2. Line: present calculation; dots: figure 8(b) in Altmeyer *et al.* (2011).

2.4. Validation

To validate the numerical procedure, critical curves in the axisymmetric case were computed and compared with literature results. For $m=0$ and 1 , Pinter *et al.* (2003) provide the coefficients of fourth-order polynomials f_m fitting their data in the range $-20 \leq Re_z \leq 20$, with step $\delta Re_z = 1$. The same procedure was applied here, and our calculated values \tilde{g}_m at the same points were fitted by polynomials g_m . To compare our results, the residual $\sum_{-20}^{20} |f_m(Re_z) - g_m(Re_z)|^2$ between the two fits was divided by the residual $\sum_{-20}^{20} |g_m(Re_z) - \tilde{g}_m(Re_z)|^2$ between our fit and our calculated values. For $m=0$ and 1 , this ratio is respectively 1.16×10^{-2} and 1.10×10^{-2} , showing agreement with the Pinter *et al.*’s calculations. For $m=2$, only graphical data were available, and figure 5 shows excellent agreement with the ‘island’ of instability found by Altmeyer *et al.* (2011) in the Re_Ω – Re_z plane.

In their analysis, those authors considered only the saddle points originating at the real critical wavenumber k_c of temporal instability with $Re_z = 0$, as will be explained now. For Re_Ω above the temporal instability threshold $Re_{\Omega,c}$, the medium is unstable, and the growing part of the wavepacket is bounded by two spatio-temporal rays referred to as *leading* and *trailing fronts*, respectively $z/t = V^+$ and $z/t = V^-$ with $V^- < V^+$. The fronts are defined by the conditions $\partial\omega/\partial k(k_*^\pm) = V^\pm$ and $\omega_i(k_*^\pm) - V^\pm k_{*,i}^\pm = 0$ (see Huerre 2000 for more details). At critical conditions for temporal instability, $Re_\Omega = Re_{\Omega,c}$ and $k = k_c$, the constraint $\partial\omega_i/\partial k = 0$ for k real defines two degenerate fronts propagating at the group velocity V_{max} of the most rapidly amplified temporal mode: $V^\pm = V_{max} = \partial\omega/\partial k(k_c)$. For Re_Ω just above $Re_{\Omega,c}$, $V^+ \neq V^-$ so the fronts are properly defined and the now complex wavenumbers k_*^\pm are close to k_c so $V^\pm \approx V_{max}$. In general, $V_{max} > 0$, so the wavepacket is advected downstream and the flow is only convectively unstable. But when Re_Ω is further increased, one front may eventually change propagation direction, which translates into the saddle-point condition $\partial\omega/\partial k = 0$ defining the AI threshold. In Altmeyer *et al.* (2011), only the two fronts bounding the convectively unstable wavepacket at Re_Ω slightly above $Re_{\Omega,c}$ and $Re_z = 0$ were considered. These specific fronts were followed as Re_Ω and Re_z were varied, and the AI boundary in figure 5 corresponds

m	0	1	-1	2	-2					
e	0.3	0.7	0.3	0.7	0.45	0.7	0.45	0.7		
16 × 8	402.59	283.22	475.66	285.22	431.88	300.21	465.54	305.73	472.77	347.83
16 × 16	402.59	283.32	475.66	285.70	431.88	300.22	465.54	306.79	472.77	347.90
32 × 32	402.59	283.33	475.65	285.71	431.88	300.29	465.52	306.80	472.46	348.34

TABLE 1. Critical azimuthal Reynolds number Re_Ω for $Re_z = 50$ and different resolutions $N_\xi \times K_\phi$.

to points where one of the fronts was stationary. Saddle points corresponding to other stationary fronts were ignored in figure 5, even though the authors mentioned the existence of more. Note that validation for $m \geq 0$ is sufficient because of the Π_3 -symmetry (2.5).

In this study, only values of $|m| \leq 2$ will be considered and a small number of Fourier modes $K_\phi = 8$ is deemed satisfactory, as can be seen in table 1. A higher number of collocation points $N_\xi = 16$ is however required for accuracy at large Re_Ω .

3. Results

A parametric study has been performed within the ranges $e \leq 0.7$, $0 \leq Re_z \leq 60$ and $0 \leq Re_\Omega \leq 500$. Within these bounds, modes $m = 0, 1, 2$ are always the most temporally unstable, except for a small range $e \leq 0.3$, $50 \leq Re_z \leq 60$, where $m = 3$ has the largest temporal growth rate (Leclercq *et al.* 2013). It will be assumed that the absolute growth rate of these modes will be higher than that of $|m| \geq 3$. However, right helical modes RH1 and RH2 will be retained in the analysis, as RH are known to be more absolutely unstable than TV and LH in some cases (e.g. high- Re_z , outward radial flow, $e = 0$, cf. Martinand *et al.* 2009). Because we are considering both positive and negative m , it is unnecessary to consider negative Re_z , because of the Π_3 -symmetry (2.5).

3.1. Reference saddle point

The bifurcation to (pseudo-)toroidal vortices without axial flow is a steady one, $\omega_r(m=0) = 0$, so CI and AI thresholds, respectively denoted here $Re_{\Omega,c}$ and $Re_{\Omega,c-a}$, coincide in this case. For modes $m \neq 0$, CI occurs through Hopf bifurcations at $Re_z = 0$, so AI only occurs above a higher threshold: $Re_{\Omega,c-a} > Re_{\Omega,c}$. For these modes, $Re_{\Omega,c-a}(Re_z = 0)$ is found by locating the saddle point with k_0 closest to k_c , the real critical wavenumber of CI. This neutral saddle point corresponds to a stationary front of the impulse response wavepacket for Re_Ω just above $Re_{\Omega,c}$, as explained in detail in § 2.4. For $m = 1, 2$, the stationary front is the trailing one: $V_- = 0$, $k_{0,i} < 0$. For negative m , $k_{0,i} > 0$ because of the Π_3 -symmetry (2.5), and the stationary front is the leading one: $V_+ = 0$. The present subsection defines the *reference saddle point* for each m , obtained for $Re_z = 0$ and $e = 0$. These saddle points are systematically followed in parameter space to define critical curves of AI. However, as will be seen in the next subsection, other saddle points are also relevant to the spatio-temporal dynamics and must be considered.

3.2. Multiplicity of saddle points

Pinch points corresponding to other stationary fronts can be identified using the geometric method described in § 3.2 of Juniper (2006). The same approach is used

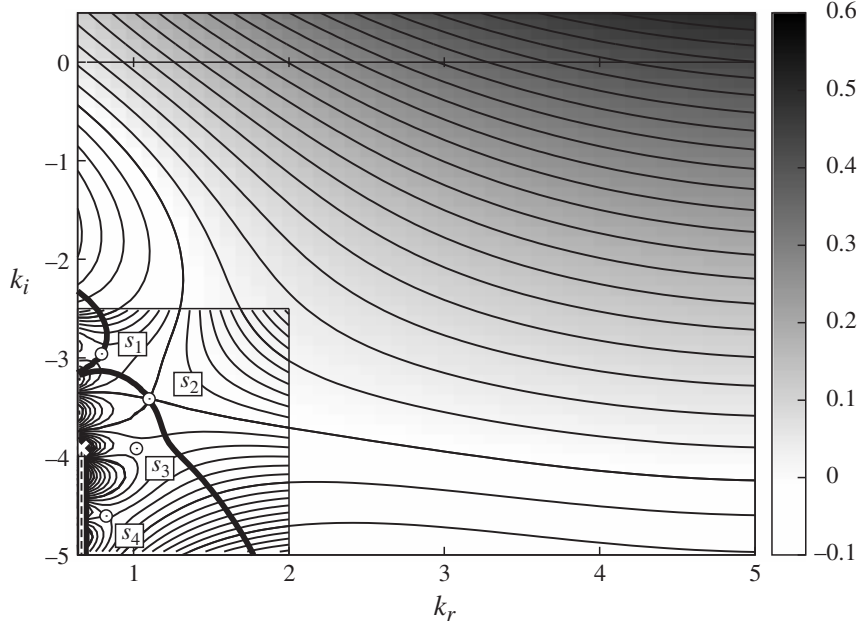


FIGURE 6. Contours of temporal growth rate at criticality for $m=0$, $e=0.3075$ and $Re_z=60$ ($Re_\Omega=472.24$). Saddles are indicated by white circles. The thick line indicates the steepest descent path associated with the pinch points s_1 and s_2 . The white cross indicates a branch point $\partial k/\partial \omega=0$ from which originates a branch cut (vertical dotted line). The temporal growth rate of s_2 is larger than that of s_1 : the pinch s_2 dominates the impulse response.

here to study the dispersion relation of mode $m=0$ in the presence of strong axial advection, $Re_z=60$, for three eccentricities around $e=0.3$. Figure 6, similar to figure 2 in Juniper (2006), shows isocontours of $\omega_i(k)$ for complex values of k . The thick black line indicates a contour in the complex k -plane including the steepest descent paths of all genuine pinch points, here s_1 and s_2 (s_3 and s_4 are ‘spurious’ k^-/k^- saddle points). The impulse response can be obtained at any time using a classical inverse Laplace transform formula (see Huerre 2000 for instance), which is easily evaluated at large time using this integration contour. The asymptotic response is indeed dominated by the pinch point of largest temporal growth rate, which here is s_2 . With this geometrical approach, genuine pinch points and invalid saddle points are easily identified.

If the eccentricity is varied by a small amount, the nature of the saddle points may change: valid saddle points may become invalid and vice versa. This is illustrated in figure 7: in case (b), s_1 and s_2 are the two pinch points, but in case (a), only s_1 is a pinch, and in case (c), s_1 , s_2 and s_3 are all three valid. Since the growth rate of each saddle point also varies with the control parameters, the dominant pinch may either be s_1 , s_2 or s_3 , and a careful analysis is required when parameters are varied.

Maps similar to figure 6 are drawn for each value of m , and a large number of saddle points are identified each time. Saddle points with growth rate close to the reference-saddle-point’s are systematically followed in parameter space. Over the whole range of parameters, three different ‘pinch points’ are found to be relevant for TV, two for LH1, LH2 and RH2, but surprisingly, just one for RH1, despite numerous candidate saddle points.

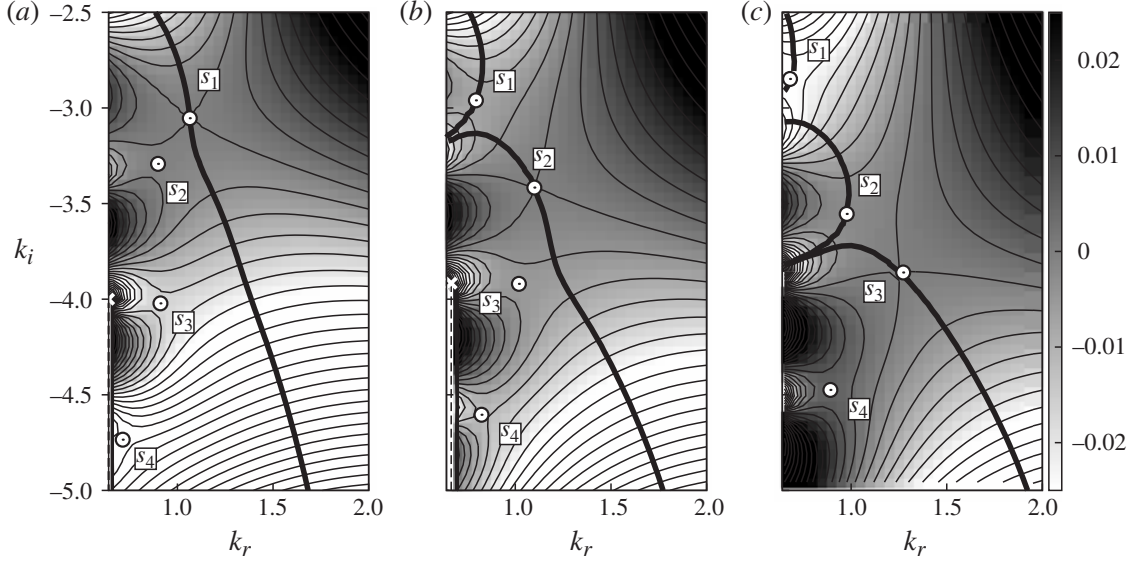


FIGURE 7. Zoom of the bottom-left corner of figure 6 for the same value of Re_z , three eccentricities around $e \approx 0.3$ and their associated critical Re_Ω : (a) $e = 0.285$, $Re_\Omega = 471.65$, s_1 is the dominating pinch; (b) zoom of figure 6, s_2 dominates; (c) $e = 0.33$, $Re_\Omega = 468.00$, s_3 dominates.

3.3. Critical azimuthal Reynolds number

In figure 8, the critical azimuthal Reynolds number is represented as a function of eccentricity, for $Re_z = 0, 10, \dots, 60$. We start by describing the curves in terms of m . Solid lines correspond to $m \geq 0$, and dotted lines are for $m < 0$. Changes of critical saddle point are indicated with a filled (resp. open) circle for $m \geq 0$ (resp. $m < 0$). The most important result is that for any value of e and Re_z , $m = 0$ always has the lowest critical Re_Ω , followed by $|m| = 1$, and finally $|m| = 2$. This observation gives credence to the assumption that modes with $|m| \geq 3$ can be ignored in the analysis. Curves in figures 8(b) and 8(c) also prove the importance of considering both positive and negative m , as LH are not always more absolutely unstable than RH. Indeed, for low eccentricities, RH1 is slightly more unstable than LH1, but the converse is true for high eccentricities. The dynamics is even more subtle for $|m|=2$, as LH2 are generally more unstable than RH2, except for a small range of eccentricities that varies with Re_z .

The effect of axial advection is to stabilize all the modes. For high enough Re_z , the critical Re_Ω seems to increase almost linearly with Re_z . The rate of increase is much stronger for low eccentricities than for high eccentricities, regardless of the value of m , as already mentioned. Critical Re_Ω are typically one order of magnitude higher than Re_z , which means that the inner cylinder must be rotated much faster than the mean axial velocity to have self-sustained oscillations. Indeed, axial flow prevents AI by carrying perturbations downstream while rotation amplifies them.

The effect of eccentricity is more complex than that of Re_z . For low eccentricities, Re_Ω increases slowly for $m=0, 1$, but decreases for all other modes. For high enough e , all the curves have the same shape: Re_Ω decreases before reaching a minimum and then increases again beyond this minimum. TV and LH1 display another similarity: they switch critical saddle point between $0.2 \leq e \leq 0.4$, for high enough Re_z . This change of saddle point coincides with the change in sign of the slope: critical Re_Ω

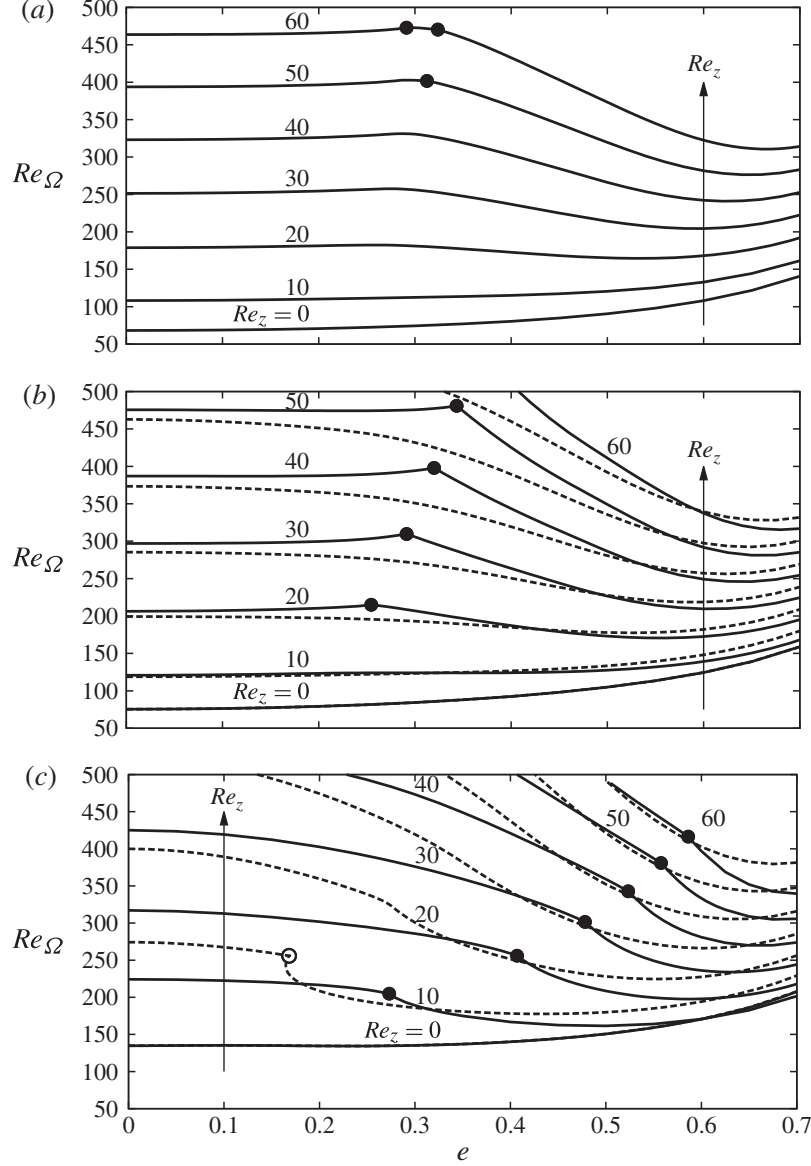


FIGURE 8. Critical azimuthal Reynolds number Re_Q versus eccentricity e for (a) $m=0$, (b) $|m|=1$ and (c) $|m|=2$. Curves are drawn for $Re_z=0, 10, \dots, 60$. Solid lines are for $m \geq 0$, and dashed lines for $m < 0$. Filled/open dots indicate a change of saddle point.

increases with e for the first saddle point, but decreases for the second one. As was already mentioned in §3.2, TV even changes pinch point twice for $Re_z = 60$. On the other hand, the critical curves for RH1 are smooth, because they are obtained by continuously following a single saddle point. Finally, two saddle points define the critical curves of LH2 and RH2. For low values of Re_z and e , the AI threshold is quite complex, and the curves display folds. Folds in the critical curves mean that there are finite ranges of AI in parameter space, surrounded by CI. This unusual behaviour has already been pointed out by Altmeyer *et al.* (2011) in the concentric case, but it seems important here to underline the fact that for high enough Re_Q , all the modes eventually become absolutely unstable, regardless of any ‘island’ of AI occurring at lower Re_Q (cf. figure 5).

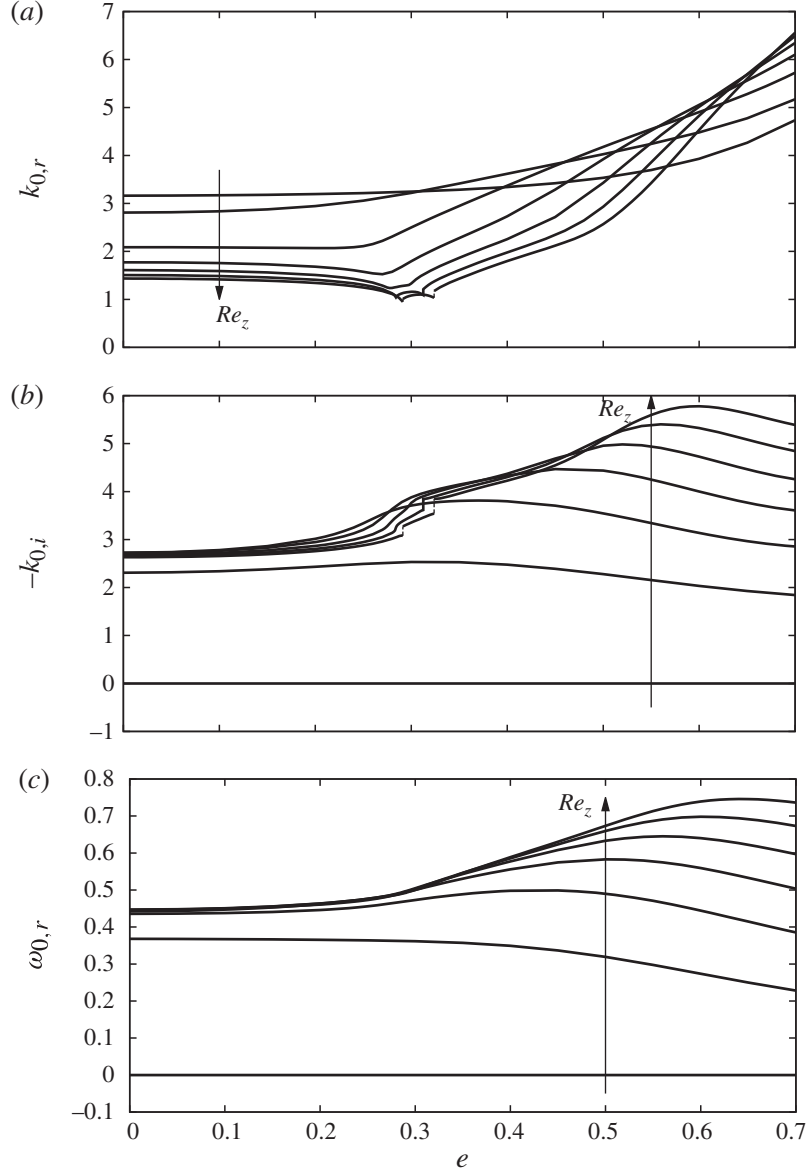


FIGURE 9. (a) Absolute wavenumber $k_{0,r}$, (b) spatial growth rate $-k_{0,i}$ and (c) frequency $\omega_{0,r}$ for $m = 0$ at critical conditions, versus eccentricity e . Curves are given for $Re_z = 0, 10, \dots, 60$.

3.4. Critical absolute wavenumber $k_{0,r}$

Figure 9 shows the evolution of the absolute wavenumber $k_{0,r}$, spatial growth rate $-k_{0,i}$ and frequency $\omega_{0,r}$ associated with the dominant mode $m = 0$, at critical conditions. As before, curves are plotted as functions of e , for $Re_z = 0, 10, \dots, 60$. The absolute wavenumber $k_{0,r}$ (figure 9a) evolves in different ways below and above $e \approx 0.3$. Below $e \approx 0.3$, critical modes have longer wavelengths as Re_z increases, spanning up to 6 times the clearance for $Re_z = 60$ and $e \approx 0.3$. When e is high enough, the trend is the opposite, and critical modes have shorter wavelengths as Re_z increases. Below $e \approx 0.3$, $k_{0,r}$ is almost constant, or slightly decreasing with e , whereas above $e \approx 0.3$, it is clearly increasing with e . For large enough e , the critical wavelength seems to be controlled by the smaller clearance $d(1 - e)$. Small discontinuities in $k_{0,r}$ around $e \approx 0.3$ indicate a change of critical saddle point.

Comments on the curves obtained for other m , although not displayed here for clarity, can be made. First, curves of $k_{0,r}$ for LH1 are very similar to those of TV, except that LH1 only changes saddle point once for $Re_z = 60$ instead of twice for TV. Ignoring the change of saddle point, they are also qualitatively similar to those of RH1. For all m , $k_{0,r}$ always increases with e for high enough eccentricities, showing that all modes scale with the small gap at critical conditions. For $|m| = 2$, large values of $k_{0,r}$ up to 8 and more are obtained for low eccentricities as well, provided Re_z is high enough. This behaviour is not found for other modes, where $k_{0,r}$ is always between 1 and 3.5 when $e \lesssim 0.3$. For LH2 and RH2, a large discontinuity of axial wavenumber is observed upon switching saddle point. For example, $k_{0,r}$ of LH2 varies from ~ 7.5 to ~ 3.5 for $Re_z = 60$ and $e \approx 0.6$.

3.5. Critical absolute spatial growth rate $-k_{0,i}$

The absolute spatial growth rate $-k_{0,i}$ (figure 9b) measures the ‘steepness’ of the stationary front of the impulse response wavepacket. For $e \lesssim 0.3$, it is slightly increasing with e . It varies quickly for $Re_z \lesssim 20$, and then slowly varies in the range $2.5 \lesssim -k_{0,i} \lesssim 4$ for higher Re_z . For $e \gtrsim 0.3$, $-k_{0,i}$ increases with e , reaches a maximum value, and then decreases again. For high enough e , $-k_{0,i}$ increases steadily with Re_z .

Similar trends are noticed for LH1 and RH1, with comparable ranges of values. For LH2 and RH2 however, the curves are quite different. For low eccentricities, $-k_{0,i}$ increases significantly with Re_z , whereas it is almost constant for other m . Therefore, extreme front steepness occurs for LH2 at low e , with $-k_{0,i} > 12$ for $Re_z = 60$.

For RH1 and RH2 at low Re_z , $-k_{0,i}$ can be negative over the whole range of eccentricities. Physically, this means that the stationary front is the leading one in this case $V_+ = 0$ (cf. section § 2.4), and that the most temporally unstable RH wave has a negative group velocity.

Finally, a common feature of all m is that $-k_{0,i}$ has a maximum as a function of e .

3.6. Critical absolute frequency $\omega_{0,r}$

The absolute frequency $\omega_{0,r}$ (figure 9c) is given here for reference. After nonlinear saturation of the instability, self-sustained oscillations with frequency close to $\omega_{0,r}$ are expected for a supercritical transition. Therefore, the values of $\omega_{0,r}$ can be used as a good estimate of the hydrodynamic resonance frequency of the flow, and may be of interest for engineering applications. The trends of the curves are very similar to those obtained for the spatial growth rate. The frequency range is shifted towards higher values as m increases. For RH1 and RH2, $\omega_{0,r}$ can be negative (always the case for RH2), indicating that the absolute phase speed $c_0 \equiv \omega_{0,r}/k_{0,r}$ of the mode is negative in this case. Finally, discontinuities in the absolute frequency occur for all modes but RH1, because of changes in critical saddle point. Discontinuities are not clearly visible for $m = 0$ and the change of saddle point is ‘smooth’, as will be discussed later in § 4.3.

3.7. Absolute temporal growth rate $\omega_{0,i}$ maps

Critical curves in § 3.3 indicate the AI domain for each m . However, they do not indicate which mode will be the most absolutely unstable if Re_Ω is above two or more thresholds. Indeed, the mode which bifurcates first as Re_Ω is increased does not necessarily have the highest absolute growth rate $\omega_{0,i}$ for larger driving. Figure 10

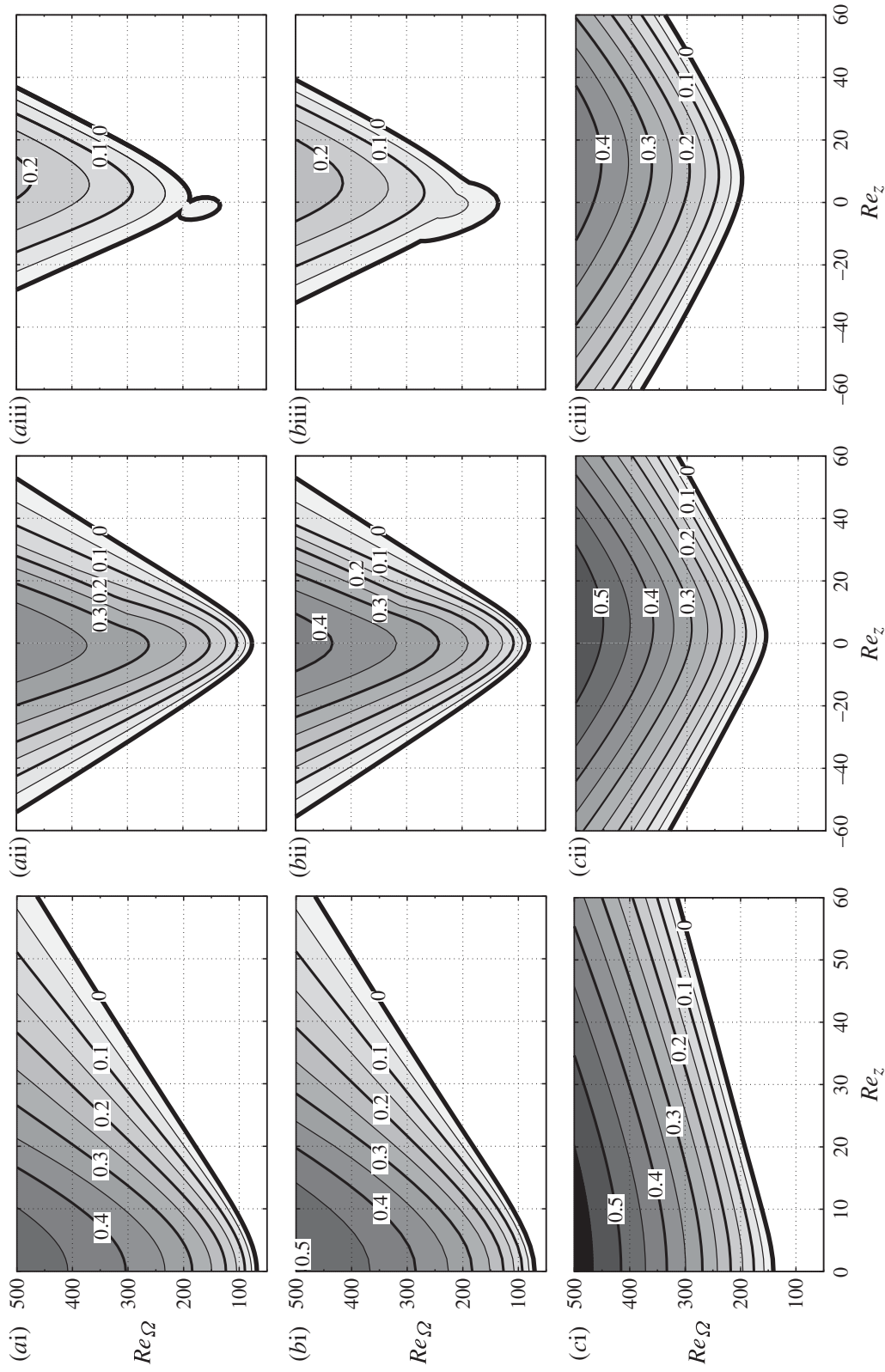


FIGURE 10. Absolute growth rate $\omega_{0,i}$ maps for (a) $e = 0$, (b) 0.2, (c) 0.7; and (i) $m = 0$, (ii) 1, (iii) 2.

represents isocontours of $\omega_{0,i}$ in the Re_Ω – Re_z plane for $m=0, 1, 2$, and $e=0, 0.2, 0.7$. Curves for $m=-1, -2$ can be recovered upon applying the Π_3 -symmetry (2.5).

The first conclusion is that $m=0$ remains the most unstable mode over the whole range of parameters. However, for $e=0.7$, isocontours of $m=1$ are very close to those for $m=0$, and one may expect LH1 to become more absolutely unstable than TV for larger eccentricities and large Re_z .

Isocontours of $\omega_{0,i}$ for $m=1$ and $m=-1$ (using Π_3 -symmetry) are generally close. For low eccentricity, RH1 is always more unstable than LH1, but for high eccentricity, the converse is true. For a moderate eccentricity of $e \approx 0.5$ (not shown here), the dominant mode depends on the specific values of Re_Ω and Re_z .

For $m=1, 2$, some isocontours have discontinuous slopes, as a consequence of a change of dominant saddle point. In figure 10(aiii), the ‘island’ of instability previously presented in figure 5 is shown to be connected to a ‘continent’, for higher values of Re_Ω , via a change of critical saddle point. Indeed, in their analysis of $m=2$ in the axisymmetric case, Altmeyer *et al.* (2011) restricted their analysis to the reference saddle point defined in § 3.1, even though the authors mentioned the existence of other saddle points. Figure 10(aiii) gives the complete AI boundary for this case. For higher eccentricities, the ‘continent’ of instability absorbs the ‘island’, and for $e=0.7$, the saddle point associated with the ‘island’ is always sub-dominant. When considering the saddle point associated with the ‘continent’, LH2 is generally more unstable than RH2. On the other hand, for low e and very low Re_z , RH2 can be more unstable than LH2 because of the ‘island’ of instability. For moderate eccentricities, the ordering depends on the specific values of Re_Ω and Re_z .

4. Discussion

In this section, we study the critical modes and the production of perturbation kinetic energy. We discuss the results and the instability mechanism in the light of these elements.

4.1. Critical modes

In figure 11, we examine the spatial distribution of the mode $m=0$ at critical conditions for $Re_z=60$ and three representative eccentricities: $e=0.2, 0.4, 0.7$. The three-dimensional distribution of axial velocity is shown, together with the corresponding time-averaged distribution of perturbation kinetic energy $\mathcal{E}=\frac{1}{2}(\|\tilde{u}_\perp\|^2+|\tilde{w}|^2)/2$ (the $\exp[-k_i z]$ dependence of the mode amplitude is omitted).

Consider the polar angle θ of the maximum of energy, with respect to the inner cylinder centre, indicated in figure 2. For low eccentricities or low Re_z , the mode is localized in the wide gap, at positive θ . However, for larger e or Re_z , this maximum is shifted upstream to the region $-90^\circ \leq \theta \leq 0^\circ$. For $e=0.7$, the mode is concentrated in the vicinity of the inner cylinder, on the wide gap side, but has a radial extent scaling with the small gap. When e increases for $Re_z=60$, the ratio between the maximum, and the average value increases from less than 2 for $e=0$ to almost 14 for $e=0.7$, indicating confinement of the mode into a smaller region of the annulus. Finally, the only contribution of \tilde{u}_\perp to \mathcal{E} accounts for 65% to 85% of the total perturbation energy when e increases from 0 to 0.7.

Similar behaviour is found for LH1 at $Re_z=60$. For RH1 however, the energy is less tightly concentrated. The maximum of \mathcal{E} still occurs at negative angles, but does not go beyond -45° in this case. It is concluded that the appearance of the peak of perturbation energy at large negative angles is associated with the change of saddle point occurring for both TV and LH1.

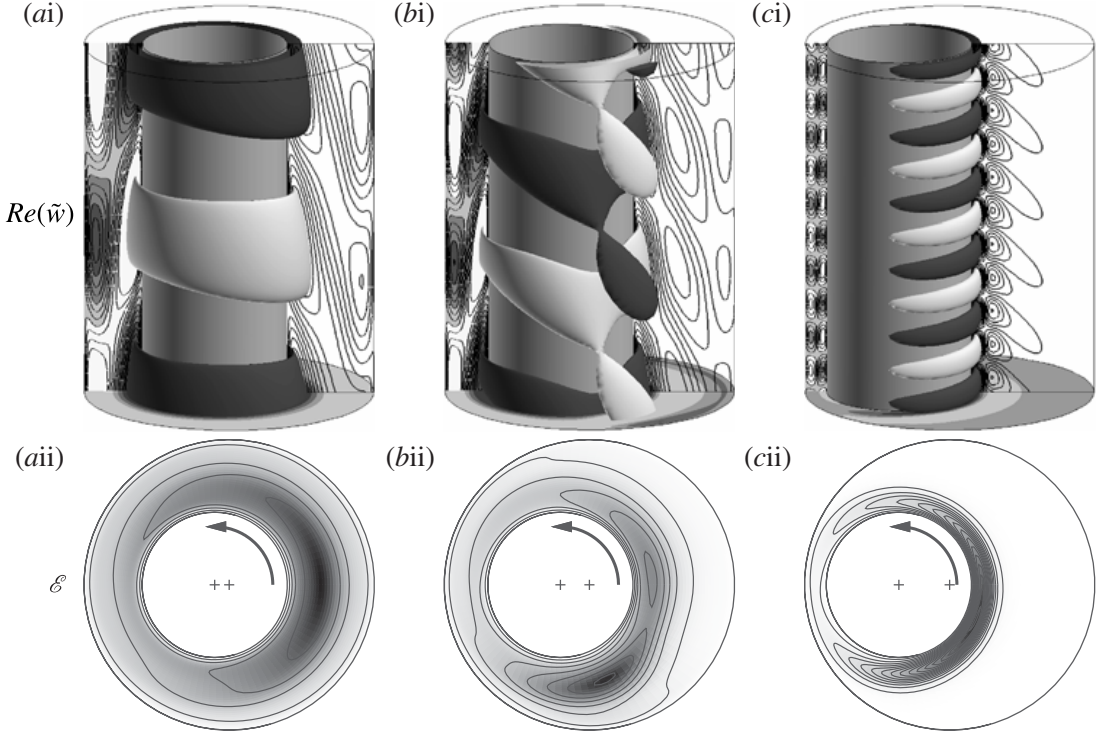


FIGURE 11. Critical mode $m = 0$ for $Re_z = 60$: (a) $e = 0.2$, $Re_\Omega = 465.82$, (b) $e = 0.4$, $Re_\Omega = 432.74$, (c) $e = 0.7$, $Re_\Omega = 314.16$. (i) Distribution of axial perturbation velocity $Re(\tilde{w})$. Dark (resp. light) grey is for positive (resp. negative) values. (ii) Distribution of perturbation kinetic energy $\mathcal{E} = \frac{1}{2}(\|\tilde{u}_\perp\|^2 + |\tilde{w}|^2)$. Dark grey indicates high values, and isocontours are equispaced.

Surprisingly, the critical modes of AI and CI peak in completely different regions of the annulus for moderate eccentricities and high Re_z . In comparison (cf. Leclercq *et al.* 2013), the maximum energy of the critical mode of CI for $e = 0.5$ is always localized at large positive angles. No direct comparison should be made with AI because critical modes of CI are obtained for different threshold values of Re_Ω . It is nonetheless interesting to observe that modes can be localized at either positive or negative polar angles depending on the situation.

Finally, we enumerate characteristics common to all m . First, in-plane motion accounts for the larger contribution to the total perturbation kinetic energy of all m for $Re_z = 60$. Also, as e approaches 0.7 for $Re_z = 60$, all m tend to have similar distributions of energy, with strong localization close to the inner cylinder, over a radial extent scaling with the small gap. In addition, we recall that the critical wavenumber of all modes takes on large values $k_{0,r} \sim 6.5\text{--}8$ when $e = 0.7$ and $Re_z = 60$. These observations indicate that for high eccentricities, the critical modes for all m scale with the small gap.

4.2. Production of perturbation kinetic energy

To further investigate the instability mechanism, the production of perturbation kinetic energy is calculated. In the well-known Reynolds–Orr equation, the local rate of production of \mathcal{E} is given by $-u' \cdot (u' \cdot \nabla U)$. Averaging in time and separating velocities into in-plane and axial components, one can define two contributions

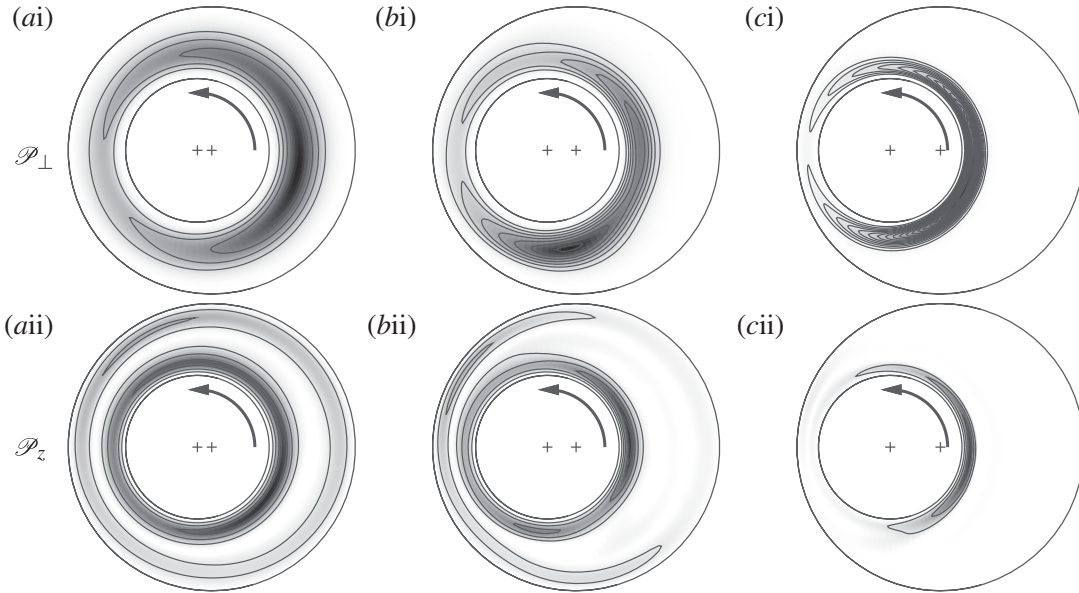


FIGURE 12. Distribution of kinetic energy production for $m = 0$ and $Re_z = 60$, at critical conditions. (i) \mathcal{P}_\perp and (ii) \mathcal{P}_z . (a) $e = 0.2$, $Re_\Omega = 465.82$, (b) $e = 0.4$, $Re_\Omega = 432.74$, (c) $e = 0.7$, $Re_\Omega = 314.16$. Dark grey indicates large contributions and white corresponds to zero or negative contribution. Isocontours are equispaced.

(the spatial growth of the mode amplitude along z is ignored again)

$$\mathcal{P}_\perp = -\frac{1}{2}\text{Re} \left\{ \tilde{u}_\perp^* \cdot (\tilde{u}_\perp \cdot \nabla_\perp U_\perp) \right\} \quad \text{and} \quad \mathcal{P}_z = -\frac{1}{2}\text{Re} \left\{ \tilde{w}^* (\tilde{u}_\perp \cdot \nabla_\perp W) \right\}, \quad (4.1)$$

corresponding to the work of the Reynolds stresses against the in-plane and axial shear respectively. Expressions for the nonlinear terms in the modified bipolar coordinate system are given in Leclercq *et al.* (2013). Because the basic flow is axially invariant, these two terms are the only contributions to the production of \mathcal{E} .

Figure 12 represents the distribution of \mathcal{P}_\perp and \mathcal{P}_z for $m = 0$ and $Re_z = 60$, at $e = 0.2, 0.4, 0.7$, as in figure 11. Only positive contributions are shown in grey shades, as negative contributions inhibit temporal growth. Distributions of \mathcal{P}_\perp and \mathcal{E} look very similar: \mathcal{P}_\perp is maximum in the wide gap for low e , then at negative polar angles for moderate e , then close to the inner cylinder on the wide gap side for e close to 1. The dominant contribution to \mathcal{P}_\perp comes from the Reynolds stress term involving the pseudo-radial derivative of the azimuthal velocity V . The same calculation of \mathcal{P}_\perp and \mathcal{P}_z has been performed for the critical mode of CI at $Re_z = 60$ and $e = 0.5$ ($m = 2$). \mathcal{P}_\perp was also found to account for most of the kinetic energy production (81 %), but the peak was located at a positive polar angle of 92°.

Distributions of \mathcal{P}_z show larger contributions near the walls, where $\|\nabla_\perp W\|$ is larger. As eccentricity increases, production of kinetic energy close to the outer cylinder decreases, as the mode is concentrated in the vicinity of the inner cylinder. For $e = 0.7$, \mathcal{P}_z peaks almost in the same region as \mathcal{P}_\perp and \mathcal{E} , namely close to the inner cylinder in the wide gap.

Integration of \mathcal{P}_\perp and \mathcal{P}_z over the annular domain for $Re_z = 60$ indicates that in-plane shear dominates the production of kinetic energy, \mathcal{P}_\perp always accounting for more than 85 % of the total amount, and even more than 97 % for $e = 0.7$.

The dominant contribution comes from the term involving pseudo-radial variations of pseudo-azimuthal velocity, characteristic of a centrifugal instability.

4.3. Instability mechanism

The striking destabilization occurring at moderate eccentricities remains difficult to explain even after examining the basic flow, the critical mode and the production of kinetic energy. The transition from a stabilizing to a destabilizing effect of eccentricity occurs around $0.2 \leq e \leq 0.4$ for both TV and LH1, through a change of critical saddle point when Re_z is large enough. The recirculation region appears for $e \approx 0.2$ for $Re_\Omega \approx 500$ so it seems that the change of behaviour occurs after the recirculation zone has reached a critical size. The basic flow is then significantly different from a classical Couette flow. Indeed, while energy of the mode mostly localizes in the vicinity of the inner cylinder, it also partially spans over the recirculation region for moderate eccentricities (cf. figure 11b). Surprisingly, a region of the flow located at negative polar angles seems to drive AI for moderate eccentricities, whereas kinetic energy production always peaks at positive angles for CI at criticality. Arguments based on local stability of the flow, however tempting in a quest for explanation, should be avoided here because of strong non-parallelism of the basic flow in the pseudo-azimuthal direction. Indeed, assuming the flow to be locally parallel in ϕ leads to completely wrong predictions of instability thresholds of eccentric Taylor–Couette flow (DiPrima 1963; Ritchie 1968). The most temporally unstable velocity profile, theoretically located at $\phi = \theta = 0^\circ$, does not coincide with the location of maximum vortex activity found in the experiments (Vohr 1968). On the other hand, global analyses yield good results in this geometry (DiPrima & Stuart 1972, 1975; Eagles, Stuart & DiPrima 1978), showing the limits of the local approach. Therefore, localization of the modes and kinetic energy production at moderate eccentricities should be regarded as a global property of the entire flow field.

The consecutive switchovers of dominant saddle point for $e \approx 0.3$ and $Re_z = 60$ occur very near collisions of the distinct pinches into third-order saddle points (Davies 1989) or ‘super branch points’ (Healey 2004), satisfying simultaneously $\partial\omega/\partial k = 0$, $\partial^2\omega/\partial k^2 = 0$ and $\omega_i = 0$. Indeed, s_1 and s_2 collide while being neutral for $e = 0.2839$, $Re_z = 50.115$, $Re_\Omega = 403.21$ while s_2 and s_3 coalesce with $\omega_i = 0$ for $e = 0.3032$ and $Re_z = 43.188$, $Re_\Omega = 353.60$. As a result, the saddle points swap dominance but the absolute wavenumber, frequency, and spatial growth rate vary almost continuously through the exchange (see figure 9a–c). Consequently, the spatial distribution of the critical mode is little changed and the physical reason for the switchover remains unclear.

As e approaches 1, all m tend to behave in a similar way. After reaching a minimum value, the critical Re_Ω increases again as e becomes larger. Instability thresholds of all $m \geq 0$, and even their respective absolute growth rate for any Re_z – Re_Ω combination, become close at high e and less sensitive to variations of Re_z . More similarities are found by inspecting the critical modes. For $Re_z = 60$, all m have absolute wavenumbers $k_{0,r}$ in the range 6.5–8, indicating a similar length scale. Indeed, the kinetic energy of all these modes is localized around the inner cylinder, on a radial extent of the order of the smallest gap $d(1 - e)$, consistent with a small wavelength. The localization is so strong that the difference between toroidal and helical structure of the modes is partially ‘blurred’. These similarities between m at high e is reminiscent of small gap Taylor–Couette–Poiseuille flow, where critical thresholds associated with different m are very close (Ng & Turner 1982; Leclercq *et al.* 2013). Indeed, as eccentricity increases, the Couette-like flow associated with rotation of the inner cylinder scales as $d(1 - e)$, curvature effects become less important, and m behaves more and more like

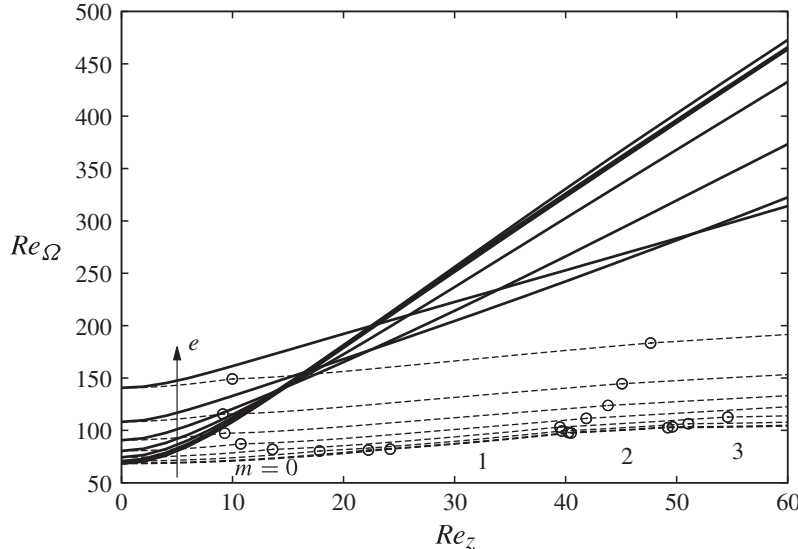


FIGURE 13. Absolute (solid lines) and convective (dashed lines) instability thresholds: critical Re_Ω versus Re_z , for $e=0, 0.1, \dots, 0.7$. Open circles indicate a change of critical m for CI. For AI, the critical mode is always $m=0$.

a continuous real wavenumber, as when $\eta \rightarrow 1$. Matching between localization of the modes and the Couette-like part of the basic flow may also explain the weaker effect of axial advection on the instability thresholds. Indeed, for large eccentricities, most of the axial volume flux passes through the wide gap, and the maximum value of W is located in the recirculation region, far from the inner cylinder. Hence, the region where perturbations are most amplified is spatially separated from the region where they are most rapidly ‘blown away’. This observation could explain why critical Re_Ω are less sensitive to Re_z for e close to 1.

4.4. Convective versus absolute instability

We conclude this section by comparing the thresholds of CI (Leclercq *et al.* 2013) and AI in the eccentric Taylor–Couette–Poiseuille flow. Figure 13 represents the critical Re_Ω for CI (dashed lines), and for AI (solid lines), as a function of Re_z for $e = 0, 0.1, \dots, 0.7$. For $Re_z = 0$, the two thresholds for $m = 0$ coincide, as expected for a steady bifurcation. The critical Re_Ω increases with Re_z for both CI and AI, but with a much larger rate for AI. This was expected as axial advection tends to carry the perturbations away from the source, so a larger driving is required to reach AI. The critical mode is always $m = 0$ for AI, corresponding to closed pseudo-toroidal Taylor vortices, propagating when $Re_z \neq 0$. For CI, LH modes of increasing m become critically unstable as Re_z increases. Open circles indicate a change of critical m on the CI thresholds. The effect of eccentricity is clearly stabilizing for CI, but the effect on AI is more complex. For high enough Re_z , as eccentricity increases, the critical Re_Ω of AI slightly increases for low e , but then decreases before reaching a minimum and increases again for larger values of e .

5. Conclusions

In this paper, an absolute instability analysis has been performed for the flow between eccentric cylinders, with rotation of the inner one and a superimposed

pressure-driven axial flow. The ratio between cylinder radii was fixed at $\eta = 0.5$, a value representative of an oil-well-drilling configuration. Five modes of instability have been considered, $m = -2, -1, 0, 1, 2$, thus including the most temporally unstable modes up to $Re_z = 50$ found in Leclercq *et al.* (2013). Throughout the range of Re_z and e considered in the present study, the mode with the largest absolute growth rate is always the pseudo-toroidal vortex flow corresponding to $m = 0$. Unlike the temporal growth rate, the absolute growth rate of left-handed pseudo-helical modes ($m > 0$) is not always larger than that of right-handed ones ($m < 0$).

Increasing Re_z tends to hinder absolute instability because axial flow sweeps perturbations downstream. As a rule of thumb, the rotational velocity of the inner cylinder needs to be approximately one order of magnitude larger than the mean axial velocity to trigger absolute instability.

The effect of eccentricity is more complex and increasing e can result in destabilization for large enough Re_z and moderate eccentricities $0.3 \lesssim e \lesssim 0.6$. In this case, the critical mode has a complex structure, and the production of kinetic energy peaks at a well-defined region of the annulus, located in the diverging gap region. Outside this range of eccentricities, increasing e has a stabilizing effect, increasingly so as the limit of touching cylinders is approached.

The instability mechanism is purely centrifugal in nature and the critical-mode axial wavelength and radial extent scale as the smallest gap $d(1 - e)$. For large eccentricities, all the modes localize in the vicinity of the inner cylinder, and their spatial distributions become more and more similar. The effect of Re_z on absolute instability thresholds becomes weaker, and the distance between thresholds associated with different m diminishes.

Overall, many valid saddle points were found for the different instability modes, and the critical pinch point switches upon varying the flow parameters. The physical interpretation of the switchovers of saddle point occurring near $e \approx 0.3$ for $m = 0$ and $Re_z = 60$ is unclear, because the saddle points are associated with modes having almost the same spatial distribution and spatio-temporal properties. Indeed, when they swap, the saddle points almost collide into third-order saddle points, where they would be impossible to distinguish.

We believe that the most crucial outlook of this work is additional experiments to confirm our findings on convective and absolute instabilities, since the last measurements made on such a configuration are older than the introduction of absolute instability theory to fluid mechanics (Huerre & Monkewitz 1985)! Even in the convectively unstable régime, the literature is very lean, and only one apparatus seems to have ever existed, whereas the domain of application is vast. From a theoretical viewpoint, it would be particularly interesting to investigate the properties of nonlinear global modes, partly based on local absolute instability properties (Pier, Huerre & Chomaz 2001), when eccentricity varies slowly along the axis. Indeed, bending of the long drillstring results in axially varying eccentricity. Moreover, such weakly non-parallel open flows are believed to be good candidates to confirm the potential existence of *hat modes* (Pier & Huerre 1996, 2001), theoretically predicted for model equations, but yet to be identified in a real configuration.

REFERENCES

- ALTMAYER, S., HOFFMANN, C. & LÜCKE, M. 2011 Islands of instability for growth of spiral vortices in the Taylor–Couette system with and without axial through flow. *Phys. Rev. E* **84**, 046308.
 BABCOCK, K. L., AHLERS, G. & CANNELL, D. S. 1991 Noise-sustained structure in Taylor–Couette flow with through flow. *Phys. Rev. Lett.* **67**, 3388–3391.

- BABCOCK, K. L., AHLERS, G. & CANNELL, D. S. 1994 Noise amplification in open Taylor–Couette flow. *Phys. Rev. E* **50**, 3670–3692.
- BABCOCK, K. L., CANNELL, D. S. & AHLERS, G. 1992 Stability and noise in Taylor–Couette flow with through-flow. *Physica D* **61**, 40–46.
- BERS, A. 1983 Space-time evolution of plasma instabilities—absolute and convective. In *Handbook of Plasma Physics* (ed. M. Rosenbluth & R. Sagdeev), pp. 451–517. North-Holland.
- BRIGGS, R. J. 1964 *Electron-stream Interactions with Plasmas*, pp. 1–46. MIT Press.
- CHOMAZ, J.-M. 2005 Global instabilities in spatially developing flows: non-normality and nonlinearity. *Annu. Rev. Fluid Mech.* **37**, 357–392.
- CONEY, J. E. R. 1971 Taylor vortex flow with special reference to rotary heat exchangers. PhD thesis, Leeds University.
- CONEY, J. E. R. & ATKINSON, J. 1978 The effect of Taylor vortex flow on the radial forces in an annulus having variable eccentricity and axial flow. *Trans. ASME: J. Fluids Engng* **100**, 210–214.
- CONEY, J. E. R. & MOBBS, F. R. 1969–70 Hydrodynamic stability of the flow between eccentric rotating cylinders with axial flow: visual observations (paper 2). *Proc. Inst. Mech. Engrs Pt 3L* **184**, 10–17.
- COUETTE, M. 1888a La viscosité des liquides. *Bull. Sci. Phys.* **4**, 40–62 123–133, 262–278.
- COUETTE, M. 1888b Sur un nouvel appareil pour l'étude du frottement des fluides. *C. R. Acad. Sci. Paris* **107**, 388–390.
- DAVIES, J. A. 1989 Conditions for absolute instability in the cyclotron resonance maser. *Phys. Fluids B* **1**, 663–669.
- DiPRIMA, R. C. 1960 The stability of a viscous fluid between rotating cylinders with an axial flow. *J. Fluid Mech.* **9**, 621–631.
- DiPRIMA, R. C. 1963 A note on the stability of flow in loaded journal bearings. *Trans. Am. Soc. Lubric. Engrs* **6**, 249–253.
- DiPRIMA, R. C. & STUART, J. T. 1972 Non-local effects in the stability of flow between eccentric rotating cylinders. *J. Fluid Mech.* **54**, 393–415.
- DiPRIMA, R. C. & STUART, J. T. 1975 The nonlinear calculation of Taylor vortex flow between eccentric rotating cylinders. *J. Fluid Mech.* **67**, 85–111.
- DiPRIMA, R. C. & SWINNEY, H. L. 1985 Instabilities and transition in flow between concentric rotating cylinders. In *Hydrodynamic Instabilities and the Transition to Turbulence* (ed. H. L. Swinney & J. P. Gollub), pp. 139–180. Springer.
- EAGLES, P. M., STUART, J. T. & DiPRIMA, R. C. 1978 The effects of eccentricity on torque and load in Taylor-vortex flow. *J. Fluid Mech.* **87**, 209–231.
- ESCUDIER, M. P., OLIVEIRA, P. J. & PINHO, F. T. 2002 Fully developed laminar flow of purely viscous non-Newtonian liquids through annuli, including the effects of eccentricity and inner-cylinder rotation. *Intl J. Heat Fluid Flow* **23**, 52–73.
- GUO, B. & LIU, G. 2011 *Applied Drilling Circulation Systems – Hydraulics, Calculations, Models*. Elsevier.
- HEALEY, J. J. 2004 On the relation between the viscous and inviscid absolute instabilities of the rotating-disk boundary layer. *J. Fluid Mech.* **511**, 179–199.
- HUERRE, P. 2000 Open shear flow instabilities. In *Perspectives in Fluid Dynamics* (ed. G. K. Batchelor, H. K. Moffat & M. G. Worster), pp. 159–229. Cambridge University Press.
- HUERRE, P. & MONKEWITZ, P. A. 1985 Absolute and convective instabilities in free shear layers. *J. Fluid Mech.* **159**, 151–168.
- HUERRE, P. & MONKEWITZ, P. A. 1990 Local and global instabilities in spatially developing flows. *Annu. Rev. Fluid. Mech.* **22**, 473–537.
- JUNIPER, M. P. 2006 The effect of confinement on the stability of two-dimensional shear flows. *J. Fluid Mech.* **565**, 171–195.
- KELLER, H. B. 1977 Numerical solution of bifurcation and nonlinear eigenvalue problems. In *Applications of Bifurcation Theory* (ed. P. Rabinowitz), pp. 359–384. Academic.
- LECLERCQ, C., PIER, B. & SCOTT, J. F. 2013 Temporal stability of eccentric Taylor–Couette–Poiseuille flow. *J. Fluid Mech.* **733**, 68–99.

- LEHOUcq, R. B., SORENSEN, D. C. & YANG, C. 1997 *ARPACK Users' Guide: Solution of Large-scale Eigenvalue Problems with Implicitly Restarted Arnoldi Methods*.
- LÜCKE, M. & RECKTENWALD, A. 1993 Amplification of molecular fluctuations into macroscopic vortices by convective instabilities. *Europhys. Lett.* **22**, 559–564.
- MALLOCK, A. 1888 Determination of the viscosity of water. *Proc. R. Soc. Lond.* **45**, 126–132.
- MARTINAND, D., SERRE, E. & LUEPTOW, R. M. 2009 Absolute and convective instability of cylindrical Couette flow with axial and radial flows. *Phys. Fluids* **21**, 104102.
- MOBBS, F. R. & YOUNES, M. A. M. A. 1974 The Taylor vortex regime in the flow between eccentric rotating cylinders. *Trans. ASME: J. Lubric. Tech.* 127–134.
- NG, B. S. & TURNER, E. R. 1982 On the linear stability of spiral flow between rotating cylinders. *Proc. R. Soc. Lond. A* **382**, 83–102.
- PIER, B. & HUERRE, P. 1996 Fully nonlinear global modes in spatially developing media. *Physica D* **97**, 206–222.
- PIER, B. & HUERRE, P. 2001 Nonlinear synchronization in open flows. *J. Fluids Struct.* **15**, 471–480.
- PIER, B., HUERRE, P. & CHOMAZ, J.-M. 2001 Bifurcation to fully nonlinear synchronized structures in slowly varying media. *Physica D* **148**, 49–96.
- PINTER, A., LÜCKE, M. & HOFFMANN, C. 2003 Spiral and Taylor vortex fronts and pulses in axial through flow. *Phys. Rev. E* **67**, 026318.
- RITCHIE, G. S. 1968 On the stability of viscous flow between eccentric rotating cylinders. *J. Fluid Mech.* **32**, 131–144.
- SEP, J. 2008 Journal bearing with an intensive axial oil flow—experimental investigation. *Sci. Prob. Mach. Oper. Maintenance* **43**, 21–29.
- SWIFT, J. B., BABCOCK, K. L. & HOHENBERG, P. C. 1994 Effects of thermal noise in Taylor–Couette flow with corotation and axial through-flow. *Physica A* **204**, 625–649.
- TAKEUCHI, D. I. & JANKOWSKI, D. F. 1981 Numerical and experimental investigation of the stability of spiral Poiseuille flow. *J. Fluid Mech.* **102**, 101–126.
- TAYLOR, G. I. 1923 Stability of a viscous liquid contained between two rotating cylinders. *Phil. Trans. R. Soc. Lond.* **223**, 289–343.
- TSAMERET, A. & STEINBERG, V. 1991a Convective vs. absolute instability in Couette–Taylor flow with an axial flow. *Europhys. Lett.* **14**, 331–336.
- TSAMERET, A. & STEINBERG, V. 1991b Noise-modulated propagating pattern in a convectively unstable system. *Phys. Rev. Lett.* **67**, 3392–3395.
- TSAMERET, A. & STEINBERG, V. 1994 Absolute and convective instabilities and noise-sustained structures in the Couette–Taylor system with an axial flow. *Phys. Rev. E* **49**, 1291–1308.
- VOHR, J. A. 1968 An experimental study of Taylor vortices and turbulence in flow between eccentric rotating cylinders. *Trans. ASME: J. Lubric. Tech.* **90**, 285–296.
- YOUNES, M. A. M. A. 1972 The hydrodynamic stability of spiral flow between eccentric rotating cylinders. PhD thesis, Leeds University.
- YOUNES, M. A. M. A., MOBBS, F. R. & CONEY, J. E. R. 1972 Hydrodynamic stability of the flow between eccentric rotating cylinders with axial flow: torque measurements (paper C76/72). In *Tribology Convention, Institution of Mechanical Engineers* pp. 14–19.

[A18]

Global stability analysis of flow through a fusiform aneurysm : steady flows

S. S. Gopalakrishnan, B. Pier & A. Biesheuvel

Journal of Fluid Mechanics **752**, 90–106 (2014)

doi:10.1017/jfm.2014.292

<https://hal.archives-ouvertes.fr/hal-01084523>

Global stability analysis of flow through a fusiform aneurysm: steady flows

Shyam Sunder Gopalakrishnan[†], Benoît Pier and Arie Biesheuvel

Laboratoire de Mécanique des Fluides et d'Acoustique, CNRS – École Centrale de Lyon,
Université Claude-Bernard Lyon 1, INSA de Lyon, 36 Avenue Guy de Collongue, 69134 Écully, France

(Received 11 July 2013; revised 12 May 2014; accepted 21 May 2014)

The global linear stability of steady axisymmetric flow through a model fusiform aneurysm is studied numerically. The aneurysm is modelled as a Gaussian-shaped inflation on a vessel of circular cross-section. The fluid is assumed to be Newtonian, and the flow far upstream and downstream of the inflation is a Hagen–Poiseuille flow. The model aneurysm is characterized by a maximum height H and width W , non-dimensionalized by the upstream vessel diameter, and the steady flow is characterized by the Reynolds number of the upstream flow. The base flow through the model aneurysms is determined for non-dimensional heights and widths in the physiologically relevant ranges $0.1 \leq H \leq 1.0$ and $0.25 \leq W \leq 2.0$, and for Reynolds numbers up to 7000, corresponding to peak values recorded during pulsatile flows under physiological conditions. It is found that the base flow consists of a core of relatively fast-moving fluid, surrounded by a slowly recirculating fluid that fills the inflation; for larger values of the ratio H/W , a secondary recirculation region is observed. The wall shear stress (WSS) in the inflation is vanishingly small compared to the WSS in the straight vessels. The global linear stability of the base flows is analysed by determining the eigenfrequencies of a modal representation of small-amplitude perturbations and by looking at the energy transfer between the base flow and the perturbations. Relatively shallow aneurysms (of relatively large width) become unstable by the lift-up mechanism and have a perturbation flow which is characterized by stationary, growing modes. More localized aneurysms (with relatively small width) become unstable at larger Reynolds numbers, presumably by an elliptic instability mechanism; in this case the perturbation flow is characterized by oscillatory modes.

Key words: biological fluid dynamics, instability

1. Introduction

Following the observation of transition to turbulence in the human aorta by Nerem, Seed & Wood (1972), the stability of blood flow in the arterial system has been studied extensively. Shortis & Hall (1999), Boiron, Deplano & Pelissier (2007) and Trip *et al.* (2012), among others, have analysed the stability of pulsatile flow in straight and curved tubes of circular cross-section under physiological conditions.

[†]Email address for correspondence: shyam-sunder.gopalakrishnan@univ-lyon1.fr

Recently, because of its association with atherosclerosis, the stability of flow through arterial blockages (stenoses) has been the subject of much research (Sherwin & Blackburn 2005; Blackburn & Sherwin 2007; Peterson & Plesniak 2008; Blackburn, Sherwin & Barkley 2008; Griffith *et al.* 2009; Mao, Sherwin & Blackburn 2011). The structure and stability of flow through arterial inflations (fusiform aneurysms, or abdominal arterial aneurysms), on the other hand, has attracted less attention. Some notable exceptions are the papers by Finol & Amon (2001), Yip & Yu (2001), Finol & Amon (2002b), Salsac *et al.* (2006) and Sheard (2009); other work is discussed in the reviews by Lasheras (2007) and Humphrey & Taylor (2008).

Faced with the complexity of analysing pulsatile flows in arterial blockages or inflations, it is sensible to first consider the stability of steady flows in such geometries. Obviously, the results are not physiologically realistic, although they may be relevant for clinical practice and will certainly be helpful in setting up experiments. Thus, the stability of steady flow through arterial stenoses has been addressed by Sherwin & Blackburn (2005), Griffith *et al.* (2007), Blackburn *et al.* (2008), Griffith *et al.* (2008), Vétel *et al.* (2008) and Griffith *et al.* (2013). This paper concentrates on the stability of steady flow through fusiform aneurysms. The velocity field and wall shear stress (WSS) distribution in steady flow through fusiform aneurysms have been studied earlier by, for example, Peattie *et al.* (1994), Bluestein *et al.* (1996), Peattie *et al.* (1996) and Finol & Amon (2002a).

The model aneurysms studied here are axisymmetric with an inflation of the wall that takes a Gaussian shape. This shape has an advantage over the sinusoidal shapes used in other studies (Sheard 2009) in that its spatial derivatives are continuous to all orders – this is a desirable feature, particularly in the context of studies of hydrodynamic stability; moreover, it is what one would expect to be the case in real aneurysms.

The fluid mechanical problem and the methods of analysis are introduced in § 2, where we also describe the numerical procedures and verification of the code. The results are presented in § 3, i.e. the structure of the steady basic flows through the model aneurysms, the conditions for linear global stability and the structure of the critical amplitude functions. Conclusions are given in § 4.

2. Methods

2.1. Problem formulation

The model aneurysm considered in this paper is shown schematically in figure 1. Let r denote the distance from the centreline of the vessel and z the distance along the centreline, with the origin placed at the axial midpoint of the inflation; then the vessel wall $r = R(z)$ is defined by

$$R(z) = \frac{1}{2}D + H \exp\left(-\frac{1}{2}\frac{z^2}{W^2}\right). \quad (2.1)$$

Here D is the vessel diameter far upstream and downstream of the inflation, H is the maximum height of the inflation and W is a measure of the width of the inflation. For comparison, the vessel with a sinusoidally shaped inflation studied by Sheard (2009), or Model 3 in Salsac *et al.* (2006), is indicated in figure 1 by the dotted lines. It is important to note that the parameter W is a measure of the length of the abdominal arterial aneurysm, and is not the wavelength of the sinusoidal function used to model the aneurysm dilatation in Sheard (2009). To cover different stages of development of an aneurysm, the following parameter ranges are considered: $0.25 \leq W/D \leq 2$ and

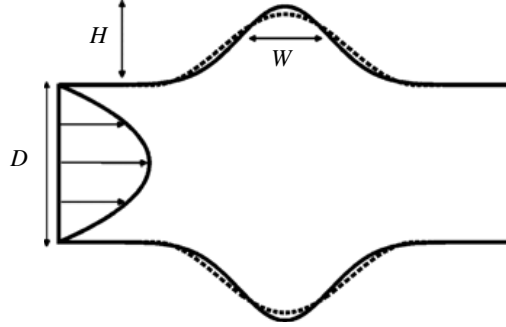


FIGURE 1. The cylindrical geometry considered in the present study, with the radius described by a Gaussian function. In this example $W/D = 0.5$ and $H/D = 0.5$. The sinusoidal shape used in Sheard (2009) and Model 3 of Salsac *et al.* (2006) is shown by the dotted lines.

$0.1 \leq H/D \leq 1$. The latter corresponds to a dilatation ratio of $1.2 \leq D_R \leq 3$, where $D_R = 1 + 2H/D$ is the ratio of the maximum diameter of the inflation to the diameter of the non-inflated vessel.

The fluid motion is assumed to be incompressible and governed by the Navier–Stokes equations. The no-slip condition prevails at the vessel wall, which is assumed to be rigid. The fluid velocity distribution is taken to converge to that of a Hagen–Poiseuille flow far upstream and downstream of the inflation. The Reynolds number of the flow is defined as $Re = \bar{U}D/\nu$, where ν is the kinematic viscosity of the fluid and \bar{U} is the (specified) cross-sectionally averaged velocity in the vessel. Reynolds numbers up to $Re = 7000$ are considered, in view of the fact that typical peak Reynolds numbers of pulsatile blood flow in the abdominal region of the aorta may vary from 600 at rest up to 6000 under exercise conditions (Ku 1997). In what follows, all lengths and velocities are non-dimensionalized by the vessel diameter D and the mean velocity \bar{U} , respectively.

2.2. Stability analysis

Using cylindrical coordinates, the radial velocity $U_r(r, z)$, the axial velocity $U_z(r, z)$ and the pressure $P(r, z)$ of the steady axisymmetric flow through the aneurysms are governed by

$$U_r \frac{\partial U_r}{\partial r} + U_z \frac{\partial U_r}{\partial z} = -\frac{\partial P}{\partial r} + \frac{1}{Re} \left[\frac{1}{r} \frac{\partial}{\partial r} \left(r \frac{\partial U_r}{\partial r} \right) + \frac{\partial^2 U_r}{\partial z^2} - \frac{U_r}{r^2} \right], \quad (2.2a)$$

$$U_r \frac{\partial U_z}{\partial r} + U_z \frac{\partial U_z}{\partial z} = -\frac{\partial P}{\partial z} + \frac{1}{Re} \left[\frac{1}{r} \frac{\partial}{\partial r} \left(r \frac{\partial U_z}{\partial r} \right) + \frac{\partial^2 U_z}{\partial z^2} \right], \quad (2.2b)$$

$$\frac{\partial U_r}{\partial r} + \frac{U_r}{r} + \frac{\partial U_z}{\partial z} = 0, \quad (2.2c)$$

with the no-slip condition $U_r = U_z = 0$ along the wall

$$r = R(z) \equiv \frac{1}{2} + H \exp \left(-\frac{1}{2} z^2 / W^2 \right) \quad (2.3)$$

and with the following conditions far upstream and downstream ($z \rightarrow \pm\infty$):

$$U_r = 0, \quad U_z = 2(1 - 4r^2). \quad (2.4a,b)$$

The linear stability of the base flow (\mathbf{U} , P) is investigated by superimposing a three-dimensional small-amplitude perturbation (\mathbf{u}' , p'). The linearized Navier–Stokes equations governing the behaviour of the perturbation are

$$\frac{\partial \mathbf{u}'}{\partial t} + (\mathbf{U} \cdot \nabla) \mathbf{u}' + (\mathbf{u}' \cdot \nabla) \mathbf{U} = -\nabla p' + \frac{1}{Re} \Delta \mathbf{u}', \quad (2.5a)$$

$$\nabla \cdot \mathbf{u}' = 0. \quad (2.5b)$$

The steadiness and axisymmetry of the base flows allow us to write the perturbations in the modal form

$$[\mathbf{u}', p'](r, \theta, z, t) = [\hat{u}_r, \hat{u}_\theta, \hat{u}_z, \hat{p}](r, z) e^{i(m\theta - \omega t)}, \quad (2.6)$$

where m is the (integer) azimuthal wavenumber and $\omega \equiv \omega_r + i\omega_i$ is the complex eigenfrequency. The perturbation is stationary when $\omega_r = 0$ and oscillatory when $\omega_r \neq 0$; when the growth rate ω_i is positive, the perturbation grows exponentially in time.

Substitution of (2.6) into the linearized Navier–Stokes equations (2.5) yields a generalized eigenvalue problem of the form

$$\mathbf{A}\hat{\mathbf{u}} = -i\omega \mathbf{B}\hat{\mathbf{u}}, \quad (2.7)$$

where $\hat{\mathbf{u}} = (\hat{u}_r, \hat{u}_\theta, \hat{u}_z, \hat{p})$ is a vector consisting of the amplitude functions and \mathbf{A} and \mathbf{B} are the matrices associated with (2.5). A discussion of methods of global linear instability analysis, together with many examples, can be found in Theofilis (2011).

2.3. Energy transfer analysis

The rate of change of the kinetic energy of the perturbation flow is governed by the Reynolds–Orr energy equation

$$\frac{d}{dt} \left(\int_V \frac{1}{2} u'_i u'_i dV \right) = -\frac{1}{Re} \int_V \left(\frac{\partial u'_i}{\partial x_j} \right) dV - \int_V \frac{1}{2} u'_i u'_j \left(\frac{\partial U_i}{\partial x_j} + \frac{\partial U_j}{\partial x_i} \right) dV, \quad (2.8)$$

where contributions due to advection of kinetic energy through the domain boundaries have been neglected. The first term on the right-hand side of (2.8) represents the viscous dissipation of kinetic energy, and the second term represents the transfer of kinetic energy from the base flow to the perturbations. This equation has proven to be helpful in deciding which instability mechanisms are involved in the evolution of the perturbations.

Following Lanzerstorfer & Kuhlmann (2012), the perturbation velocity \mathbf{u}' is decomposed into components \mathbf{u}'_{\parallel} and \mathbf{u}'_{\perp} which are, respectively, parallel and perpendicular to the base velocity \mathbf{U} :

$$\mathbf{u}'_{\parallel} = \frac{(\mathbf{u}' \cdot \mathbf{U}) \mathbf{U}}{\mathbf{U} \cdot \mathbf{U}}, \quad \mathbf{u}'_{\perp} = \mathbf{u}' - \mathbf{u}'_{\parallel}, \quad (2.9a,b)$$

such that the local energy transfer from the base flow to the perturbations may be written as

$$\sum_{i=1}^4 E_{p,i} = -[\mathbf{u}'_{\perp} \cdot (\mathbf{u}'_{\perp} \cdot \nabla \mathbf{U}) + \mathbf{u}'_{\parallel} \cdot (\mathbf{u}'_{\perp} \cdot \nabla \mathbf{U}) + \mathbf{u}'_{\perp} \cdot (\mathbf{u}'_{\parallel} \cdot \nabla \mathbf{U}) + \mathbf{u}'_{\parallel} \cdot (\mathbf{u}'_{\parallel} \cdot \nabla \mathbf{U})]. \quad (2.10)$$

Here, the index i numbers all terms on the right-hand side consecutively. The use of coordinates which are locally aligned with the flow direction is appropriate because locally no other distinguished direction exists. Each of the terms $E_{p,i}$ may be viewed as representing a different energy transfer process. For example, $E_{p,2}$ represents the local rate of change of the energy density of the perturbations due to convective transport by the cross-stream perturbation velocity component \mathbf{u}'_\perp of the basic-state momentum per unit mass, \mathbf{U} . Hence, if $\mathbf{u}'_\perp \cdot \nabla \mathbf{U}$ has a component parallel to and in the direction of \mathbf{u}'_\parallel , kinetic energy is locally transferred from the base flow to the perturbations. When $E_{p,2} < 0$, the perturbations locally lose energy to the base flow.

2.4. Numerical methods

The flow problem (2.2)–(2.4) and the generalized eigenvalue problem (2.5)–(2.7) are solved numerically by a finite element method. The spatial discretization is a mixed finite element formulation using P2 and P1 Taylor–Hood elements, i.e. six-node quadratic triangular elements with quadratic interpolation for velocities (P2) and three-node linear triangular elements for pressure (P1). The meshes and the discrete matrices resulting from the variational formulation of the problems are generated with the software FreeFem++ (<http://www.freefem.org>).

The base flows are computed as in Marquet *et al.* (2009). First, a steady solution of the full time-dependent Navier–Stokes equations is computed, for a small Reynolds number such that the flow is stable. Next, a Newton–Raphson iteration method is used to compute a solution of the steady Navier–Stokes equations, starting with the small-Reynolds-number solution as a first guess, and approaching the required large-Reynolds-number solution by incrementing the Reynolds number in small steps.

Once a base flow has been computed, the associated linear global stability problem is solved. To compute the eigenfrequencies with largest imaginary part, first a shift-and-invert strategy is used, as in Ehrenstein & Gallaire (2005) and Marquet *et al.* (2009), to single out the region of interest in the complex frequency plane. The result is an eigenvalue problem, which is then solved with the implicitly restarted Arnoldi algorithm provided by the UMFPACK software library. The method is discussed in detail in Sorensen (1992) and Nayar & Ortega (1993).

2.5. Code validation

To validate the computation of the base flows, grid convergence and independence of the size of the computational domain were addressed. Table 1 gives information on the meshes M used for the vessel geometry with $W = 0.5$ and $H = 0.5$, representative of the tests that were carried out. The size of the computational domain is characterized by Ω , which gives the axial extension measured in vessel diameters with respect to the origin. The number of nodes associated with the P2 and P1 elements of a mesh are denoted by N_2 and N_1 , respectively. The subscript b indicates that the mesh is associated with the computation of a base flow; the subscripts s and l indicate that the computational domain is, respectively, smaller or larger than the ‘standard domain’ $(-10, 10)$.

To check for convergence when computing the base flow fields, the WSS is used as a sensitive measure of the overall grid resolution. The WSS distribution follows from evaluation of the expression

$$2 \left(\frac{\partial U_r}{\partial r} - \frac{\partial U_z}{\partial z} \right) \cos \alpha \sin \alpha - \left(\frac{\partial U_r}{\partial z} + \frac{\partial U_z}{\partial r} \right) [\cos^2 \alpha - \sin^2 \alpha] \quad (2.11)$$

Mesh	Ω	N_2	N_1
M_b	(−10, 10)	183 061	46 516
M_{b1}	(−10, 10)	152 449	38 788
M_{b2}	(−10, 10)	66 398	17 050
M_{b3}	(−10, 10)	17 058	4 490
M_{bs}	(−5, 5)	136 049	34 613
M_{bl}	(−20, 20)	229 558	58 515

TABLE 1. Meshes used to validate the computation of the base flow for $H = 0.5$ and $W = 0.5$.

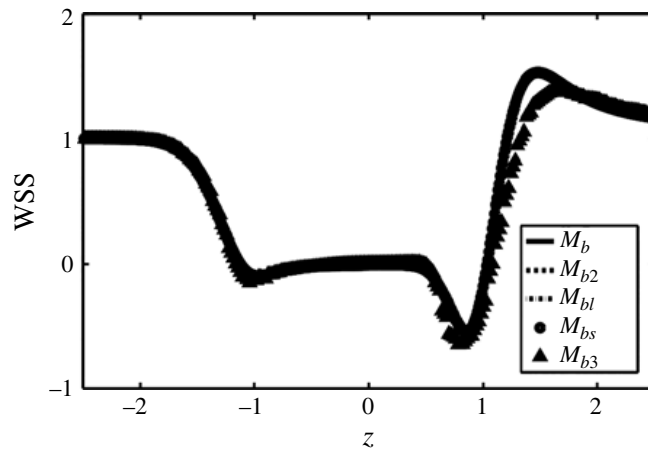


FIGURE 2. The distribution of WSS computed using the different meshes listed in table 1. The parameter settings are $H = 0.5$, $W = 0.5$ and $Re = 2500$.

at the vessel wall $r = R(z)$. In this expression $\alpha(z)$ denotes the local angle of wall slope, defined by $\tan \alpha = dR/dz$. A negative value of the WSS corresponds to reversed flow.

Figure 2 presents the results of the computation of the WSS distribution in a vessel inflation using the meshes listed in table 1. This distribution is normalized by the value of the WSS exerted by the associated Hagen–Poiseuille flow. The Reynolds number is 2500. It is observed that where the vessel is inflated, corresponding roughly to the range $-1 < z < 1$, the WSS is reduced significantly; in fact, it becomes vanishingly small. Near the downstream end of the inflation, however, a sudden change occurs, from a negative relative value of one-half to a positive relative value of one-and-a-half. Similar observations on WSS distributions were made by Budwig *et al.* (1993) and Bluestein *et al.* (1996). With the exception of the computations done with the rather coarse mesh M_{b3} , all the computations match perfectly with those carried out on the fine mesh M_{bl} .

Next, we consider the validation of the stability calculations. As before, the results of tests carried out for the values $W = 0.5$, $H = 0.5$ and $Re = 2500$ are presented. The meshes used in this case are specified in table 2, which also reports the computed values of the real and imaginary parts of ω_1 , the eigenfrequency with the largest imaginary part associated with wavenumber $m = 1$. With the exception of the coarse mesh M_{s3} , all meshes yield values for the eigenfrequencies which agree up to the fourth digit. This finding permits us to use mesh M_{s2} for the stability computations.

Mesh	Ω	N_2	N_1	ω_{1i}	ω_{1r}
M_{s1}	(−10, 10)	124 566	31 742	−0.030 1923	0.031 0782
M_{s2}	(−10, 10)	66 398	17 050	−0.030 1750	0.031 1178
M_{s3}	(−10, 10)	17 058	4 490	−0.029 3571	0.030 4471
M_{s0}	(−10, 10)	152 449	38 788	−0.030 2183	0.031 0903
M_{bs}	(−5, 5)	136 049	34 613	−0.030 2199	0.031 0871

TABLE 2. Size of the computational domain, as characterized by Ω , and the number of nodes N_1 and N_2 used in convergence tests of the stability analysis; ω_{1i} and ω_{1r} are the computed imaginary and real parts of the eigenfrequency of the wavenumber $m = 1$. Here the parameter values are $H = 0.5$, $W = 0.5$ and $Re = 2500$.

(a)						(b)					
L_o	b	Re	m	N_2	N_1	ω_{1i}	L_o	b	Re	m	ω_{1i}
40	0.500	2000	2	114 578	29 470	−0.014 909 38	40	0.500	2000	2	−0.014 783
20	0.500	2350	2	28 310	7 478	0.000 257 31	40	0.500	2350	2	0.000 00
20	0.750	770	1	8 258	31 230	−0.000 141 51	40	0.750	770	1	0.000 00

TABLE 3. (a) Results of the global stability calculations of steady flow through a stenosis; Re is based on the inlet diameter D and the cross-sectionally averaged velocity \bar{U} , and the growth rate ω_{1i} has been normalized by \bar{U}/D . (b) Corresponding results from Griffith *et al.* (2008).

Extensive validation tests have been performed at higher Reynolds numbers and for a range of bulge heights, which are discussed in detail in Gopalakrishnan (2014).

We have also performed computations of flow through model arterial stenoses, to verify our numerical results against those of Griffith *et al.* (2008). Flow through a stenosis presents different numerical challenges than flow through an aneurysm. Large regions of recirculating flow occur downstream of a stenosis, which makes the proper choice of the length of the straight vessel outlet an important issue. In flow through an aneurysm, the recirculating flow, as well as the extent of the critical amplitude functions, is limited to the region of vessel inflation. Table 3 presents a comparison between our results and some of those from Griffith *et al.* (2008). Here the parameter b is the stenosis degree, defined as

$$b = 1 - \left(\frac{d}{D} \right)^2, \quad (2.12)$$

where d is the diameter of the vessel at the centre of the blockage and L_0 denotes the length of the vessel outlet in units of vessel diameter.

3. Results

3.1. Base flows

Streamlines and distributions of azimuthal vorticity of the steady axisymmetric base flows through inflated vessels are shown in figures 3–5. In these figures the values of the dimensionless width W and Reynolds number Re are: $W = 2.0$ and $Re = 4000$ for figure 3; $W = 0.5$ and $Re = 5500$ for figure 4; and $W = 0.25$ and $Re = 5500$ for

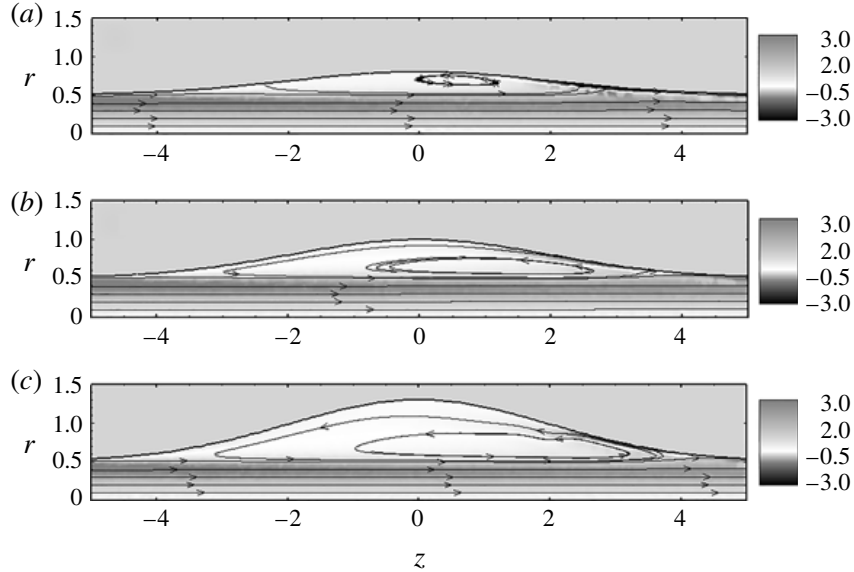


FIGURE 3. Basic flow visualized by the vorticity and streamlines at $Re = 4000$ for $W = 2.0$. The parameter settings are: (a) $H = 0.3$; (b) $H = 0.5$; (c) $H = 0.8$.

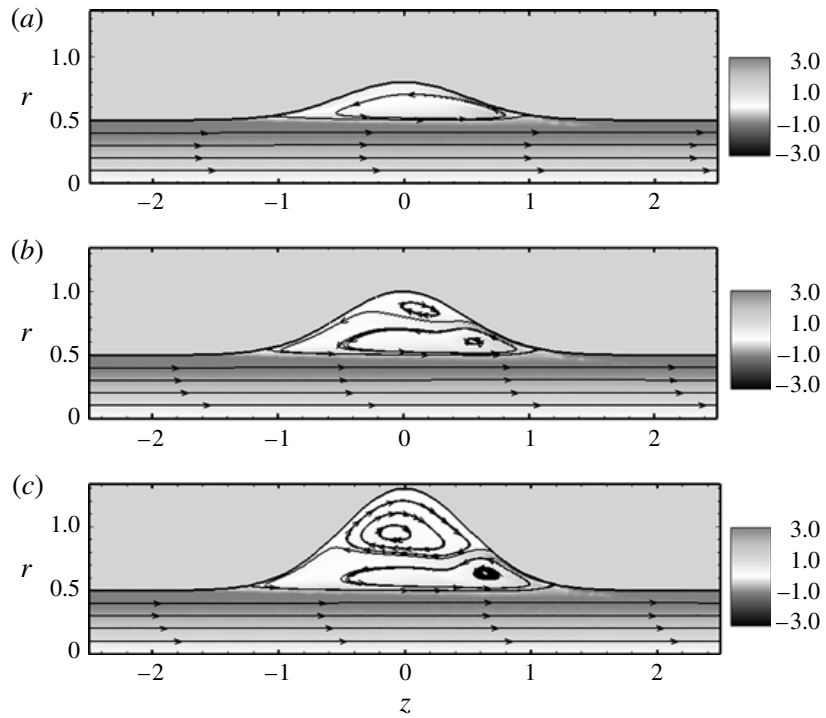


FIGURE 4. As figure 3, but with $Re = 5500$ and $W = 0.5$.

figure 5. In each of these figures the dimensionless height is $H = 0.3$ in (a), $H = 0.5$ in (b) and $H = 0.8$ in (c). Note that, to bring out details, the scales in the figures have been chosen differently. We would like to remind the reader that the peak Reynolds numbers in the abdominal aorta can vary from 600 at rest up to 6000 under exercise conditions (Ku 1997).

The flow through the model aneurysms is qualitatively similar for all parameter values such that H/W is relatively small, consisting of a jet-like core of diameter

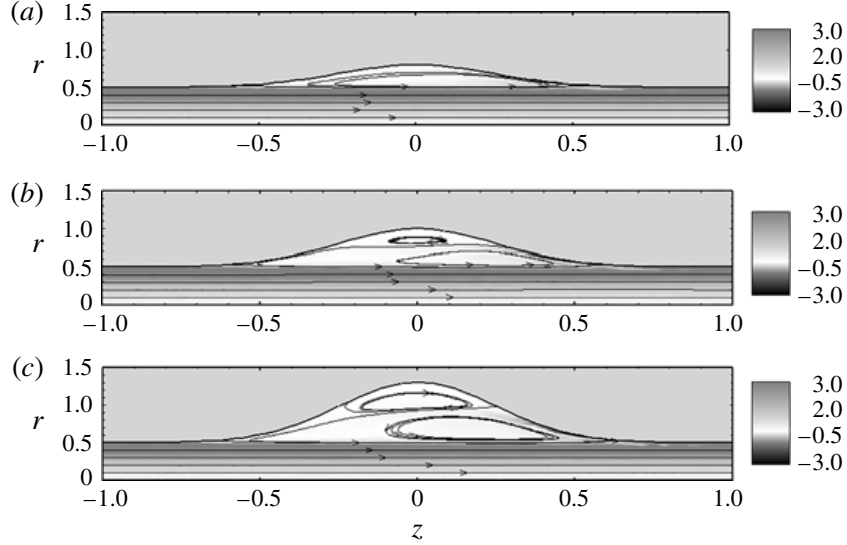


FIGURE 5. As figure 3, but with $Re = 5500$ and $W = 0.25$.

roughly that of the non-inflated vessel, surrounded by slowly recirculating fluid in the inflation. In the recirculation region, the radial velocity is at least two orders of magnitude smaller than the axial velocity, except near the downstream end of the inflation, where it is approximately one order of magnitude smaller. The vorticity distribution in the core region is uniform, with magnitude similar to that in the Hagen–Poiseuille flow far upstream and downstream. The vorticity distribution in the recirculation region is also approximately uniform, but of opposite sign and smaller magnitude. Near the stagnation point at the downstream end of the inflation, there is a small region in which the vorticity is vanishingly small. This flow structure has been observed by Budwig *et al.* (1993) and Bluestein *et al.* (1996) in their experiments and numerical calculations.

The migration with increasing Reynolds number of the centre of the recirculation zone towards the distal end, resulting in a concentration of vorticity at the downstream end, was reported in Bluestein *et al.* (1996). However, it has not been reported before that a secondary recirculation region appears, with weak vorticity of opposite sign to that in the primary recirculation zone, as the ratio H/W or the Reynolds number Re is increased. The centre of the primary recirculation zone is displaced towards the distal end of the inflation as H/W or Re is increased further, while the centre of the secondary recirculation zone is displaced towards the proximal end of the inflation.

3.2. Critical modes and stability boundaries

A typical eigenfrequency spectrum in the complex ω -plane is shown in figure 6. In this example $W = 0.5$, $H = 0.5$ and $Re = 5500$, parameter values for which the basic flow is shown in figure 4(b). Two modes with a positive temporal growth rate ω_i can be observed; they are associated with the azimuthal wavenumbers $m = 4$ and $m = 5$. The real parts ω_r of these eigenfrequencies are non-zero, so that the unstable modes represent three-dimensional oscillations which grow in amplitude.

With each azimuthal wavenumber m a ‘leading mode’ can be associated; this is the mode with the largest imaginary part ω_i of the eigenfrequency. The variation of the temporal growth rate ω_i of these leading modes with Reynolds number is shown in figure 7(a), again for $W = 0.5$ and $H = 0.5$. Figure 7(b) shows the real part ω_r of the

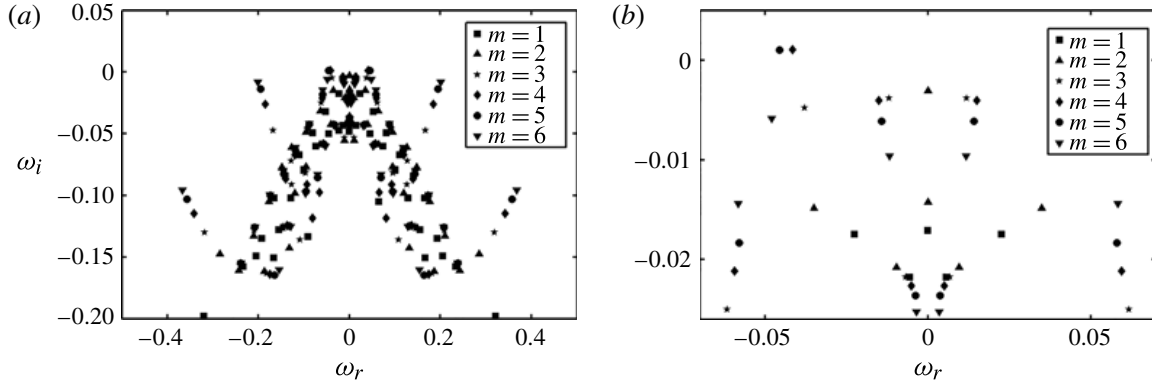


FIGURE 6. (a) Eigenfrequency spectrum for different azimuthal wavenumbers m , in the setting where $W = 0.5$, $H = 0.5$ and $Re = 5500$. (b) A close-up view of the eigenfrequency spectrum, showing the unstable modes corresponding to $m = 4$ and $m = 5$.

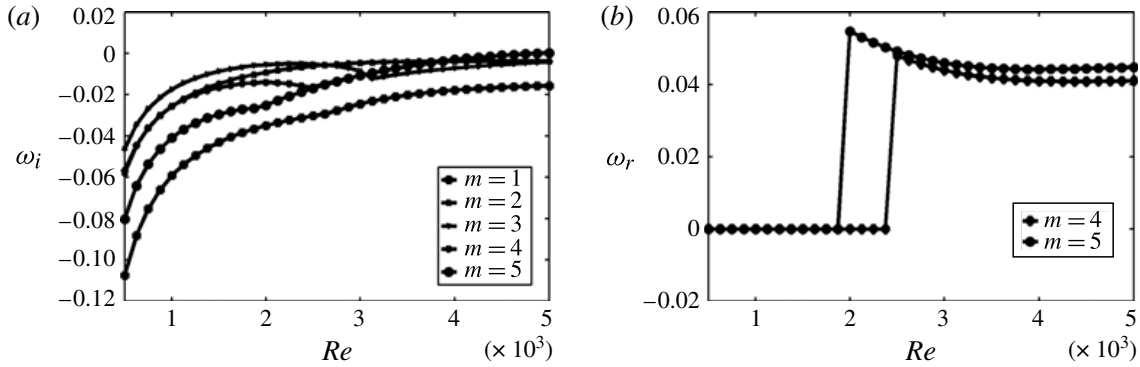


FIGURE 7. Plots as a function of the Reynolds number Re of the leading modes associated with different azimuthal wavenumbers m , in the setting where $W = 0.5$ and $H = 0.5$: (a) temporal growth rates ω_i ; (b) oscillation frequencies ω_r .

leading modes associated with wavenumbers $m = 4$ and $m = 5$. The temporal growth rates of both of these modes become positive at $Re \approx 4875$; both modes are found to switch abruptly from stationary to oscillatory at much smaller Reynolds numbers.

The stability boundaries in the $Re-H$ plane for different azimuthal wavenumbers m are shown in figure 8, for four values of the bulge width: (a) $W = 2.0$; (b) $W = 1.0$; (c) $W = 0.5$; (d) $W = 0.25$. For small values of the height H , the aneurysm can be viewed as a small perturbation to a fully developed flow in a circular pipe; that flow is linearly stable for all Reynolds numbers. Although a critical value cannot be given, it is fair to say that the base flow is linearly stable for bulge heights $H < 0.2$ (for Reynolds numbers $Re < 7000$). As the height H is increased, the base flow becomes unstable to stationary critical modes; these are indicated by the dotted curves in figure 8. The azimuthal wavenumbers that correspond to these critical modes differ according to the width W . No trend is observed, although the wavenumbers $m = 2$ and $m = 5$ seem to be involved most often. As the bulge height is increased further, the base flow also becomes unstable to oscillatory modes, as indicated by the solid curves in figure 8. With regard to the influence of the width of the inflation, we find that as the width is reduced from $W = 2.0$ to $W = 0.5$, the base flow becomes unstable at smaller values of the Reynolds number and of the height of the inflation.

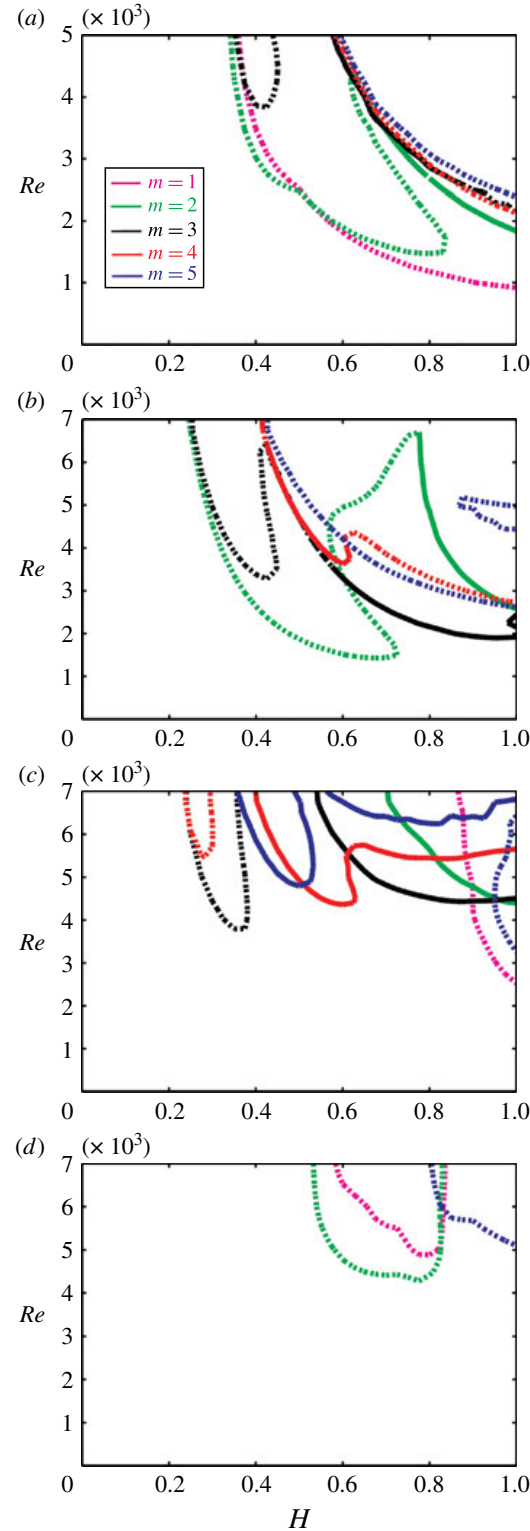


FIGURE 8. (Colour online) Critical curves associated with different azimuthal wavenumbers m in the Re - H plane, where the width of the inflation is: (a) $W = 2.0$; (b) $W = 1.0$; (c) $W = 0.5$; (d) $W = 0.25$. The solid curves indicate oscillatory modes and the dotted curves stationary modes.

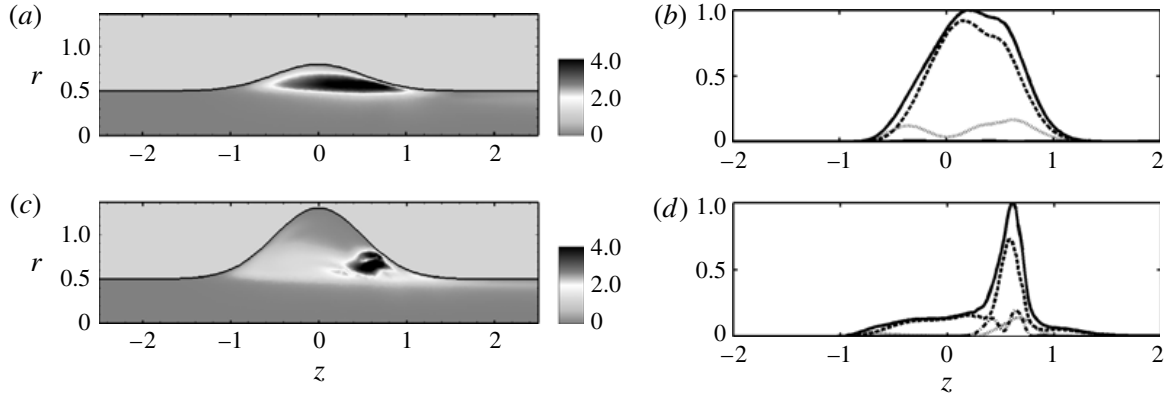


FIGURE 9. (a,c) Amplitude of the global mode defined as the square root of the perturbation energy density field. (b,d) Variation with axial distance z of the magnitude of the velocity of the global mode and of its components integrated over r , all normalized by the maximum value of $\int |\hat{\mathbf{u}}|^2 dr$: $\int |\hat{\mathbf{u}}|^2 dr$ (solid); $\int |\hat{u}_z|^2 dr$ (dashed); $\int |\hat{u}_r|^2 dr$ (dot-dash); $\int |\hat{u}_\theta|^2 dr$ (dotted). The parameter values are $Re = 5500$, $m = 3$, $W = 0.5$ and (a,b) $H = 0.3$; (c,d) $H = 0.8$.

However, a further reduction of the width improves the linear stability of the base flows significantly.

3.3. Instability mechanisms

The analysis of the energy transfer processes that take place suggest that different instability mechanisms are involved when the base flow has just a single recirculation region versus when it also includes a secondary recirculation region. To see this, one can compare two flows at $Re = 5500$ through a model aneurysm of width $W = 0.5$, where in one case the bulge height is $H = 0.3$ and in the other case it is $H = 0.8$. From figure 8(c) it can be seen that a stationary mode with wavenumber $m = 3$ is unstable for $H = 0.3$, whereas for $H = 0.8$ this mode is oscillatory.

Figure 9 presents the perturbation energy density distribution associated with the amplitude function $(\hat{u}_r, \hat{u}_\theta, \hat{u}_z)$ for two different cases: (a,b) the basic flow with a single recirculation region ($H = 0.3$); (c,d) the basic flow with also a secondary recirculation region. We observe (see figure 9a,c) that in the first case the disturbance energy is distributed all along the axis of the inflation, while in the second case it is localized in a small region at the downstream end. This can be seen even more clearly from the cross-sectional averages of the energy density associated with the individual perturbation velocity components (figure 9b,d). Note also that in both cases, most of the perturbation energy is in the axial perturbation velocity component, and that in the second case there is also a small contribution of the radial velocity component, which is totally absent in the first case; in the first case, then, the disturbance motion takes place in circular planes.

That different mechanisms are involved in the instability of the two basic flows is also clear from figures 10 and 11, which provide information on the energy transfer between the basic flow and the perturbation flow. In each figure, the total energy transfer rate is shown in panel (d), and the three separate contributions $E_{p,1}$, $E_{p,2}$ and $E_{p,4}$, which were defined in (2.10), are shown in panels (a), (b) and (c), respectively. The global picture is the same as that which emerges from figure 9, but here we can further see that the main energy transfer mechanism in both cases is the one

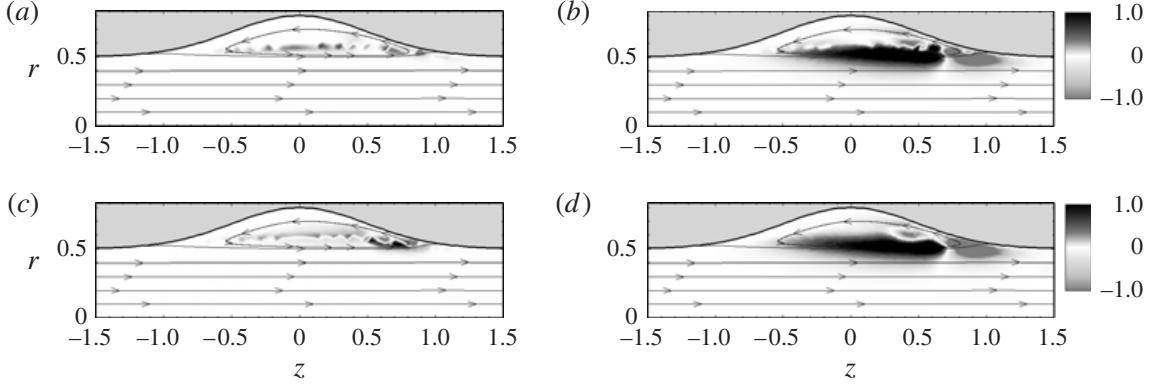


FIGURE 10. Basic streamlines and local energy production rates for $H=0.3$ at $Re=5500$ and for an azimuthal mode number $m=3$: (a) $E_{p,1}$; (b) $E_{p,2}$; (c) $E_{p,4}$; (d) $\sum_{i=1}^4 E_{p,i}$.

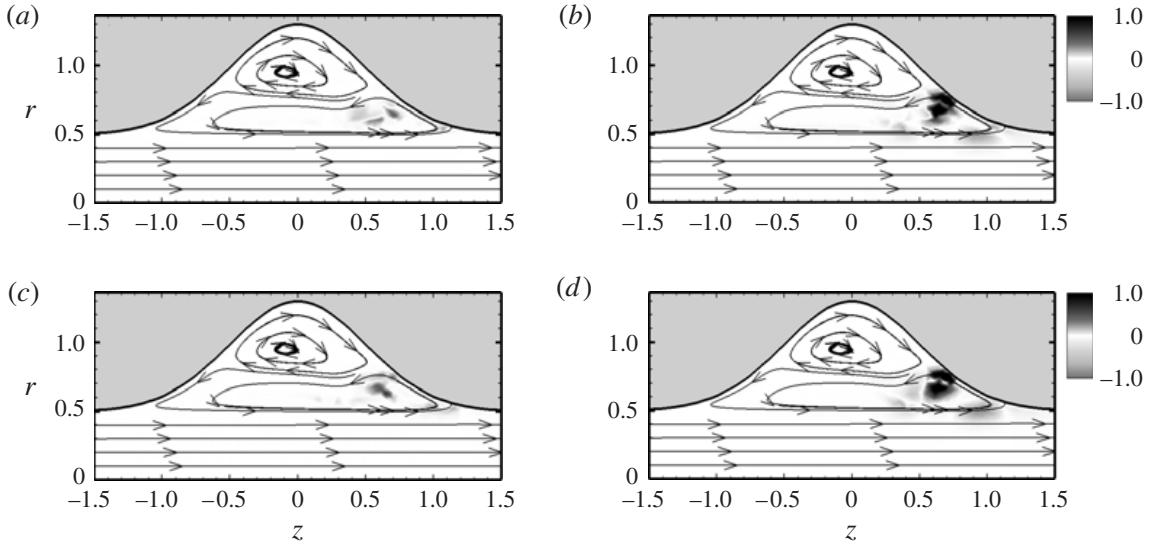


FIGURE 11. Basic streamlines and local energy production rates for $H=0.8$ at $Re=5500$ and for an azimuthal mode number $m=3$: (a) $E_{p,1}$; (b) $E_{p,2}$; (c) $E_{p,4}$; (d) $\sum_{i=1}^4 E_{p,i}$.

represented by $E_{p,2}$; the locations at which this mechanism is active are different, though.

What are the instability mechanisms? Although this cannot be established rigorously, we consider two typical cases, corresponding to a shallow cavity with $H=0.3$ and a deeper cavity with $H=0.8$, for which our computations suggest the following: in the case with a relatively shallow inflation ($H=0.3$), the unstable mode is stationary and the disturbance motion primarily takes place on cylindrical planes. Figures 12 and 13 provide a more detailed view of this perturbation velocity field. The picture that emerges is one of a flow with alternating slow and fast streamwise streaks (figure 12) and an arrangement of alternatingly rotating vortices distributed in the layer between the core and the recirculation zone (figure 13). These vortices transport low-velocity fluid to high-speed regions within the perturbation flow. This is the familiar lift-up mechanism, first described by Orr in 1907. The lift-up mechanism has also been identified by Lanzerstorfer & Kuhlmann (2012) as being the mechanism

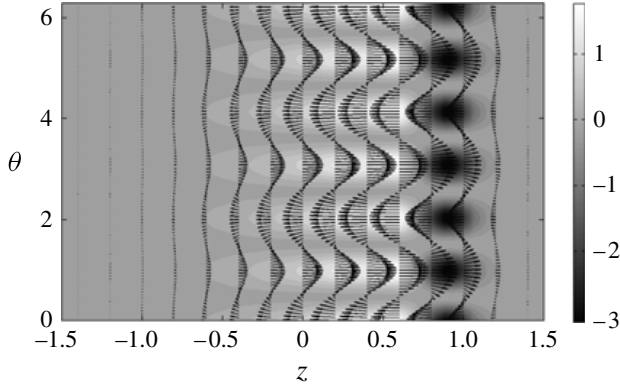


FIGURE 12. Velocity distribution at $r = 0.5$ of the most unstable mode associated with wavenumber $m = 3$ in the form of streaks (arrows) and the total local energy production $\sum_{i=1}^4 E_{p,i}$ (grey shading). The parameter values are $H = 0.3$, $W = 0.5$ and $Re = 5500$.

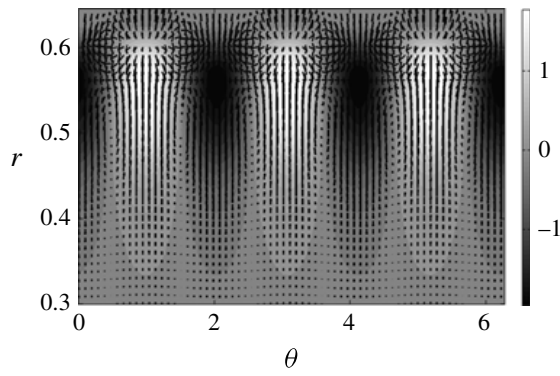


FIGURE 13. Velocity distribution (arrows) and streamwise perturbation velocity u'_z (grey shading) at the axial location of maximum perturbation energy of the most unstable mode associated with wavenumber $m = 3$. The parameter values are $H = 0.3$, $W = 0.5$ and $Re = 5500$.

that governs the instability of two-dimensional flow past a backward-facing step with small expansion ratio; compare their figure 20 with our figure 10(d).

For the more localized inflations (with $H = 0.8$), it can be seen from figure 11(d) that the energy transfer to the perturbation occurs only in a small region, namely at the centre of the primary vortex. This is typical of an elliptical instability mechanism. Lanzerstorfer & Kuhlmann (2012) have also demonstrated that the elliptical instability mechanism is involved in the global instability of flow past a two-dimensional backward-facing step of moderately large expansion rate; note the close correspondence between our figure 11(d) and their figures 13 and 14. This is further exemplified in figure 14(a), where the total local energy production for $H = 0.5$ at Reynolds number $Re = 5500$ for an azimuthal mode number $m = 4$ is shown along with the critical velocity field vectors and the basic flow streamlines. We can see that the perturbation flow is strongest where the energy transfer is maximal, which is entirely localized in the core region of the primary recirculation region, and that they are aligned with the principal direction of strain. Figure 14(b) shows the resulting perturbation flow that arises as a sequence of counter-rotating vortices in the azimuthal plane. The same features are observed at larger bulge heights, which indicates that the instability mechanism is of elliptic type. Although we have demonstrated that the

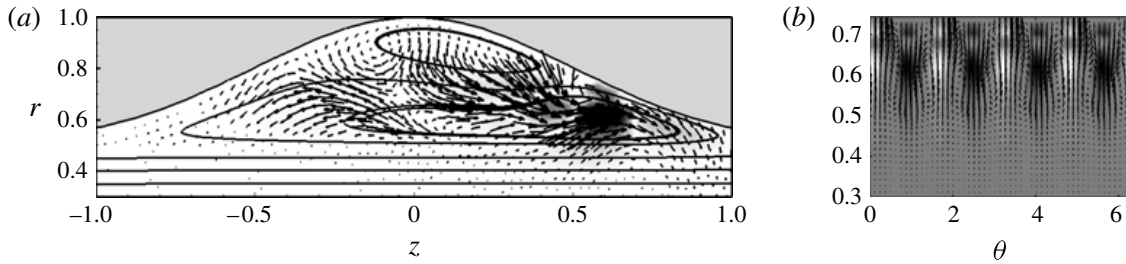


FIGURE 14. (a) Base flow streamlines (continuous lines), critical velocity fields (arrows) and total local energy production $\sum_{i=1}^4 E_{p,i}$. (b) Critical velocity fields (arrows) and the total local energy production $\sum_{i=1}^4 E_{p,i}$ (grey shading) at an axial location where the energy transfer reaches its maximum. The parameter settings are $H = 0.5$, $Re = 5500$ and $m = 4$.

instability mechanism is of an elliptic nature at $H = 0.5$, the exact regimes where the lift-up mechanism or elliptic mechanism dominate cannot be established rigorously, and the value of the bulge height at which the transition occurs is not well-defined.

4. Conclusion

It may be tempting to draw conclusions concerning the pathophysiology of abdominal aortic aneurysms from the results found in this study. However, in our opinion this idealized model is too far removed from reality to allow one to draw such conclusions. The motivation for the present study is to provide a basis for further, more realistic studies, which should enable us to quantify the effects of pulsatility of the flow (as will be done in a sequel to this paper), non-axisymmetry and other characteristics of the geometry of aneurysms, as well as the presence of the iliac bifurcation and other vasculature downstream of the aneurysm. Nevertheless, the present study does suggest that in inflated arteries, regions of slowly recirculating fluid occur, with very low WSS, which alternate in direction during a flow pulsation.

The steady axisymmetric flow through the model aneurysm studied here is unstable for Reynolds numbers that correspond to the peak values observed under physiological conditions. This instability occurs for dimensionless aneurysm ‘heights’ of approximately $H = 0.3$. Also, the flow in relatively shallow aneurysms (i.e. with large widths W) is more susceptible to instability than that through more localized aneurysms. The base flow in these shallow aneurysms is characterized by a single large recirculation region; this flow becomes unstable to a stationary mode by the lift-up mechanism. Steady flows through more localized aneurysms also include a secondary recirculation zone; these flows become unstable to oscillatory modes which involve energy transfer from the base flow to perturbations in a small region at the downstream end of the aneurysm, presumably by an elliptical instability mechanism.

REFERENCES

- BLACKBURN, H. M. & SHERWIN, S. J. 2007 Instability modes and transition of pulsatile stenotic flow: pulse-period dependence. *J. Fluid Mech.* **573**, 57–88.
- BLACKBURN, H. M., SHERWIN, S. J. & BARKLEY, D. 2008 Convective instability and transient growth in steady and pulsatile stenotic flows. *J. Fluid Mech.* **607**, 267–277.
- BLUESTEIN, D., NIU, L., SCHOEPHOERSTER, R. T. & DEWANJEE, M. K. 1996 Steady flow in an aneurysm model: correlation between fluid dynamics and blood platelet deposition. *Trans. ASME: J. Biomed. Engng* **118**, 280–286.

- BOIRON, O., DEPLANO, V. & PELISSIER, R. 2007 Experimental and numerical studies on the starting effect on the secondary flow in a bend. *J. Fluid Mech.* **574**, 109–129.
- BUDWIG, R., ELGER, D., HOOPER, H. & SLIPPY, J. 1993 Steady flow in abdominal aortic aneurysm models. *Trans. ASME: J. Biomed. Engng* **115**, 418–423.
- EHRENSTEIN, U. & GALLAIRE, F. 2005 On two-dimensional temporal modes in spatially evolving open flows: the flat-plate boundary layer. *J. Fluid Mech.* **536**, 221–233.
- FINOL, E. A. & AMON, C. H. 2001 Blood flow in abdominal aortic aneurysms: pulsatile flow haemodynamics. *Trans. ASME: J. Biomech. Engng* **123**, 474–484.
- FINOL, E. A. & AMON, C. H. 2002a Flow-induced wall shear stress in abdominal aortic aneurysm: part I – steady flow haemodynamics. *Comput. Meth. Biomed. Engng* **5**, 309–318.
- FINOL, E. A. & AMON, C. H. 2002b Flow-induced wall shear stress in abdominal aortic aneurysm: part II – pulsatile flow haemodynamics. *Comput. Meth. Biomed. Engng* **5**, 319–328.
- GOPALAKRISHNAN, S. S. 2014 Dynamics and stability of flow through an abdominal aortic aneurysm. PhD thesis, Université de Lyon, <http://hal.archives-ouvertes.fr/tel-00954202>.
- GRIFFITH, M. D., LEWEKE, T., THOMPSON, M. C. & HOURIGAN, K. 2008 Steady inlet flow in stenotic geometries: convective and absolute instabilities. *J. Fluid Mech.* **616**, 111–133.
- GRIFFITH, M. D., LEWEKE, T., THOMPSON, M. C. & HOURIGAN, K. 2009 Pulsatile flow in stenotic geometries: flow behaviour and stability. *J. Fluid Mech.* **622**, 291–320.
- GRIFFITH, M. D., LEWEKE, T., THOMPSON, M. C. & HOURIGAN, K. 2013 Effect of small asymmetries on axisymmetric stenotic flow. *J. Fluid Mech.* **721**, R1.
- GRIFFITH, M. D., THOMPSON, M. C., LEWEKE, T., HOURIGAN, K. & ANDERSON, W. P. 2007 Wake behaviour and instability of flow through a partially blocked channel. *J. Fluid Mech.* **582**, 319–340.
- HUMPHREY, J. D. & TAYLOR, C. A. 2008 Intracranial and abdominal aortic aneurysms: similarities, differences, and need for a new class of computational models. *Annu. Rev. Biomed. Engng* **10**, 221–246.
- KU, D. N. 1997 Blood flow in arteries. *Annu. Rev. Fluid Mech.* **29**, 399–434.
- LANZERSTORFER, D. & KUHLMANN, H. C. 2012 Global stability of the two-dimensional flow over a backward-facing step. *J. Fluid Mech.* **693**, 1–27.
- LASHERAS, J. C. 2007 The biomechanics of arterial aneurysms. *Annu. Rev. Fluid Mech.* **39**, 293–319.
- MAO, X., SHERWIN, S. J. & BLACKBURN, H. M. 2011 Transient growth and bypass transition in stenotic flow with a physiological waveform. *Theor. Comput. Fluid Dyn.* **25**, 31–42.
- MARQUET, O., LOMBARDI, M., CHOMAZ, J. M., SIPP, D. & JACQUIN, L. 2009 Direct and adjoint global modes of a recirculation bubble. *J. Fluid Mech.* **622**, 1–21.
- NAYAR, N. & ORTEGA, J. M. 1993 Computation of selected eigenvalues of generalized eigenvalue problems. *J. Comput. Phys.* **108**, 8–14.
- NEREM, R. M., SEED, W. A. & WOOD, N. B. 1972 An experimental study of the velocity distribution and transition to turbulence in the aorta. *J. Fluid Mech.* **52**, 137–160.
- PEATTIE, R. A., ASBURY, C. L., BLUTH, E. I. & RUBERTI, J. W. 1996 Steady flow in models of abdominal aortic aneurysms. Part I: investigation of the velocity patterns. *J. Ultrasound Med.* **15**, 679–688.
- PEATTIE, R. A., SCHRADER, T., BLUTH, E. I. & COMSTOCK, C. E. 1994 Development of turbulence in steady flow through models of abdominal aortic aneurysms. *J. Ultrasound Med.* **13**, 467–472.
- PETERSON, S. D. & PLESNIAK, M. 2008 The influence of inlet velocity profile and secondary flow on pulsatile flow in a model artery with stenosis. *J. Fluid Mech.* **616**, 263–301.
- SALSAC, A.-V., SPARKS, S. R., CHOMAZ, J.-M. & LASHERAS, J. C. 2006 Evolution of the wall shear stresses during the progressive enlargement of symmetric abdominal aortic aneurysms. *J. Fluid Mech.* **560**, 19–51.
- SHEARD, G. J. 2009 Flow dynamics and wall shear stress variation in a fusiform aneurysm. *J. Engng Maths* **64**, 379–390.
- SHERWIN, S. J. & BLACKBURN, H. M. 2005 Three-dimensional instabilities and transition of steady and pulsatile axisymmetric stenotic flows. *J. Fluid Mech.* **533**, 297–327.
- SHORTIS, T. A. & HALL, P. 1999 On the nonlinear stability of the oscillatory viscous flow of an incompressible fluid in a curved pipe. *J. Fluid Mech.* **379**, 145–163.

- SORENSEN, D. C. 1992 Implicit application of polynomial filters in a k -step Arnoldi method. *SIAM J. Matrix Anal. Applics.* **13**, 357–385.
- THEOFILIS, V. 2011 Global linear instability. *Annu. Rev. Fluid Mech.* **43**, 319–352.
- TRIP, R., KUIK, D. J., WESTERWEEL, J. & POELMA, C. 2012 An experimental study of transitional pulsatile pipe flow. *Phys. Fluids* **24**, 014103.
- VÉTEL, J., GARON, A., PELLETIER, D. & FARINAS, M. I. 2008 Asymmetry and transition to turbulence in a smooth axisymmetric constriction. *J. Fluid Mech.* **607**, 351–386.
- YIP, T. H. & YU, S. C. M. 2001 Cyclic transition to turbulence in rigid abdominal aortic aneurysm models. *Fluid Dyn. Res.* **29**, 81–113.

[A19]

Dynamics of pulsatile flow through modal abdominal aortic aneurysms

S. S. Gopalakrishnan, B. Pier & A. Biesheuvel

Journal of Fluid Mechanics **758**, 150–179 (2014)

doi:10.1017/jfm.2014.535

<https://hal.archives-ouvertes.fr/hal-01084537>

Dynamics of pulsatile flow through model abdominal aortic aneurysms

Shyam Sunder Gopalakrishnan^{1,†}, Benoît Pier¹ and Arie Biesheuvel¹

¹Laboratoire de mécanique des fluides et d'acoustique, CNRS – École centrale de Lyon – Université Claude-Bernard Lyon 1 – INSA Lyon, 36 avenue Guy-de-Collongue, F-69134 Écully, France

(Received 9 April 2014; revised 8 July 2014; accepted 9 September 2014;
first published online 7 October 2014)

To contribute to the understanding of flow phenomena in abdominal aortic aneurysms, numerical computations of pulsatile flows through aneurysm models and a stability analysis of these flows were carried out. The volume flow rate waveforms into the aneurysms were based on measurements of these waveforms, under rest and exercise conditions, of patients suffering abdominal aortic aneurysms. The Reynolds number and Womersley number, the dimensionless quantities that characterize the flow, were varied within the physiologically relevant range, and the two geometric quantities that characterize the model aneurysm were varied to assess the influence of the length and maximal diameter of an aneurysm on the details of the flow. The computed flow phenomena and the induced wall shear stress distributions agree well with what was found in PIV measurements by Salsac *et al.* (*J. Fluid Mech.*, vol. 560, 2006, pp. 19–51). The results suggest that long aneurysms are less pathological than short ones, and that patients with an abdominal aortic aneurysm are better to avoid physical exercise. The pulsatile flows were found to be unstable to three-dimensional disturbances if the aneurysm was sufficiently localized or had a sufficiently large maximal diameter, even for flow conditions during rest. The abdominal aortic aneurysm can be viewed as acting like a ‘wavemaker’ that induces disturbed flow conditions in healthy segments of the arterial system far downstream of the aneurysm; this may be related to the fact that one-fifth of the larger abdominal aortic aneurysms are found to extend into the common iliac arteries. Finally, we report a remarkable sensitivity of the wall shear stress distribution and the growth rate of three-dimensional disturbances to small details of the aneurysm geometry near the proximal end. These findings suggest that a sensitivity analysis is appropriate when a patient-specific computational study is carried out to obtain a quantitative description of the wall shear stress distribution.

Key words: biological fluid dynamics, instability

1. Introduction

An abdominal aortic aneurysm (figure 1) is a localized dilatation of the infrarenal aortic wall, between the renal arteries and the iliac bifurcation. A dilatation of the aorta is considered to be an aneurysm when its maximal diameter is greater

† Email address for correspondence: shyam-sunder.gopalakrishnan@univ-lyon1.fr

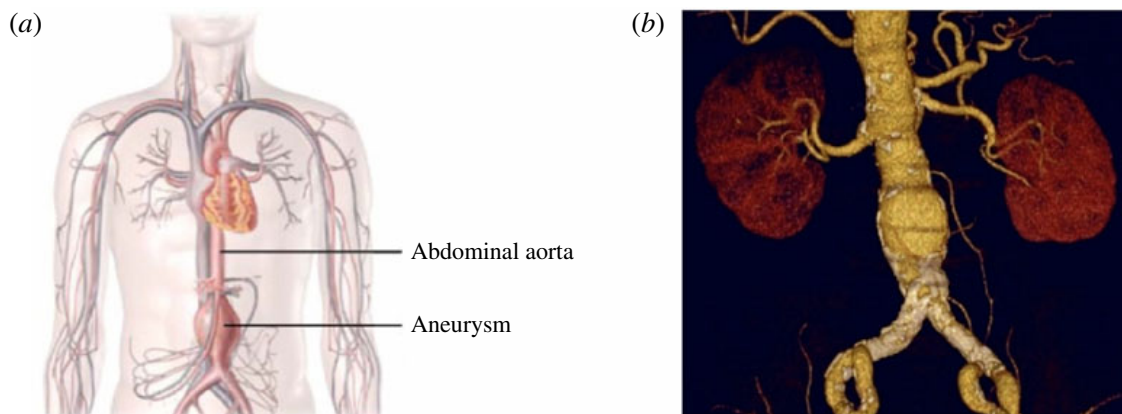


FIGURE 1. (Colour online) (a) Sketch of an abdominal aortic aneurysm that is confined to the infrarenal aorta (Lasheras 2007). (b) Image of an abdominal aortic aneurysm observed *in vivo* (courtesy: P. Feugier, Hôpital Édouard-Herriot).

than 1.5 times the local diameter of the healthy aorta (Johnston *et al.* 1991), which is approximately 2 cm in the abdominal parts of the aorta. One-fifth of large abdominal aneurysms are not limited to the infrarenal aorta, but also extend into one or both of the common iliac arteries (Armon *et al.* 1998).

When the mechanical stress in the vessel wall exceeds a critical value the dilated vessel ruptures, which leads to a bleeding that is often lethal. Presently, clinical intervention is recommended if the maximum diameter reaches 5.0 cm in women and 5.5 cm in men or if the maximal diameter increases by more than 0.5–1 cm in one year (Grootenboer *et al.* 2009). Yet, as observed by Vorp (2007), many smaller lesions rupture (13 % of those of less than 5 cm), while larger lesions may not rupture over long periods (54 % of those of over 7 cm). This leaves physicians to face the dilemma of either subjecting patients to a complex surgery with high morbidity and complications or to an unknown risk of rupture, to paraphrase Lasheras (2007). As pointed out by Humphrey & Taylor (2008) and Humphrey & Holzapfel (2012), there is a pressing need to better understand the mechanobiology, pathophysiology and treatment of abdominal aortic aneurysm; an understanding that should result from combining advances in vascular biology, medical imaging, biofluid mechanics and biosolid mechanics.

To provide a background and motivation for the present study, we briefly mention some of the recent work on the haemodynamics of abdominal aortic aneurysms; for a more elaborate discussion the reader is referred to the reviews by Lasheras (2007) and Humphrey & Taylor (2008). A highly advanced approach, which has increasingly become the standard, is the experimental and computational study of blood flow in models of the cardiovascular system obtained from patient-specific anatomical data acquired by medical imaging. An introduction to this approach can be found in Taylor & Draney (2004) and Taylor & Figueroa (2009). Recent studies of the haemodynamics of abdominal aortic aneurysms using this approach include Les *et al.* (2010), Sheidaei *et al.* (2011), Stamatopoulos *et al.* (2011) and Suh *et al.* (2011). Such studies can provide a quantitative description of the flow in an aneurysm and the distribution of shear stress along the vessel wall, and may even incorporate the presence of atherosclerotic plaque. There is no question that in the near future these computational tools will be sufficiently developed that they will be important for decisions on medical intervention. Yet, given the complexity of the geometries used

in these studies, it will prove very difficult to develop an understanding of the fluid mechanical phenomena that occur and of the relation between these phenomena and the geometrical details. It seems that there will remain a need for detailed studies of the flow in simplified ‘unrealistic’ models of aneurysms. This paper presents a study of pulsatile (physiological) flow through an axisymmetric model aneurysm with a wall that is described by a Gaussian function. In doing so, we follow, to a certain extent, the ‘simplified approach’ of the work by Taylor & Yamaguchi (1994), Finol, Keyhani & Amon (2002), Yip & Yu (2002), Salsac, Sparks & Lasheras (2004), Deplano *et al.* (2007) and Sheard (2009). Regarding the assumption of an axisymmetric geometry, it may be added that it has been observed that aneurysms tend to be symmetric during the early stages of the disease, only becoming non-axisymmetric during the later stages, as reported in Salsac (2005). This means that our results may have a direct bearing on what can be observed during the early stages. To this we should add that in our work we focus on the fluid flow dynamics and assume rigid boundaries, ignoring any compliance of the arterial wall or of an endoluminal thrombus. The idealized geometry used in this study should be understood as the boundaries of the fluid domain (where the blood is in contact either with the arterial wall or with a thrombus).

A question that has received some attention in recent years is the connection between cardiovascular flow and conditions of physical activity, in particular the differences between the conditions of rest and exercise. Here, the articles by Egelhoff *et al.* (1999), Taylor, Hughes & Zarins (1999), Deplano *et al.* (2007), Les *et al.* (2010) and Suh *et al.* (2011) should be mentioned. It has been hypothesized that prolonged physical exercise may eventually slow the growth of aneurysms, but supporting arguments are indecisive. What has been established is that during part of the cardiac cycle the blood flow in the abdominal aorta becomes weakly turbulent during exercise, but it remains laminar during rest conditions (Les *et al.* 2010). A local dilatation of the abdominal aorta may be expected to promote instability of the blood flow, and it is not unlikely that flashes of turbulence may occur during part of the cardiac cycle even during rest conditions (Yip & Yu 2001). This is believed to be beneficial, on the grounds that the presence of turbulence reduces the size of regions of flow stasis and the existence of a correlation between the presence of such regions and thrombus formation (Reininger *et al.* 1994; Vorp *et al.* 2001; Salsac *et al.* 2004). Although we have no support for this, we believe that the repeated occurrence of a vessel wall loading with random small-scale fluctuations in time and space, due to the fact that during part of the cardiac cycle the flow becomes turbulent, may have a detrimental effect on the structure of the vessel wall, and thereby enhance the growth and rupture of aneurysms. To the best of our knowledge, a study of the stability of flow through abdominal aneurysms, even using a simple model configuration, has not yet been published. The present paper provides a first look into this complex problem.

The paper is organized as follows. The geometry of the model aneurysm, the parameters and structure of the pulsatile flow at the inlet of the aneurysm, as well as the numerical methods used to analyze the flow in the aneurysm are described in § 2. It will appear that two geometrical dimensionless quantities, representative of the length and the maximum diameter of the dilatation, and two dimensionless physical flow quantities, the Reynolds number and the Womersley number, characterize the problem. The results of numerical computations of the flow through the model aneurysm are presented in § 3, where we also discuss how the characteristics of this flow change as the geometrical and physical parameters vary in a physiologically

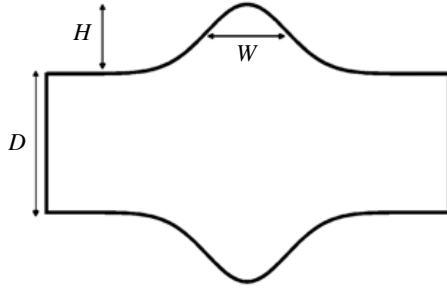


FIGURE 2. The Gaussian vessel wall configuration used in the present study. In this figure $W/D = 0.5$, $H/D = 0.5$.

realistic range. Most of the discussion is centred on a blood flow rate waveform that is observed during rest, with a brief discussion of what has been found for a flow rate waveform that is typical for an exercise condition. Section 4 describes the first results of a global stability analysis of pulsatile flow through a model aneurysm, and how these results change with the values of the geometrical and dynamical flow parameters. In § 5 we report a remarkable sensitivity of the flow to details of the aneurysm geometry. Finally, § 6 summarizes the main conclusions. Some physiological implications are mentioned, even though these are highly speculative.

2. Methodology

2.1. Geometry

The axisymmetric model dilatation that is considered in the present study is shown in figure 2. The vessel wall is described by a Gaussian function

$$r(z) = \left[\frac{D}{2} + H \exp\left(-\frac{z^2}{2W^2}\right) \right], \quad (2.1)$$

where z and r denote the axial and radial coordinates with the origin taken at the centre of the dilatation. Thus, the geometrical quantities that characterize the model aneurysm are the inlet diameter D , the height H and the width W . The length of an aneurysm depends on how it is defined; in most definitions the length will involve both parameters H and W . The so-called dilatation ratio D_R , the ratio of the maximum diameter to the inlet diameter, is here given by $D_R = 1 + 2H/D$. In what follows, lengths are non-dimensionalized by the inlet diameter D , so that the model aneurysm is characterized by two geometrical dimensionless quantities H and W . To study the effects of variations in the size of aneurysms or, to put it differently, the change in the hydrodynamic loading of the vessel wall at different stages of the development of an aneurysm, two values of W are chosen, 0.5 and 1, and H is varied in the range $0.3 \leq H/D \leq 1$ (this corresponds to $1.6 \leq D_R \leq 3$). Most of the geometrical parameters considered in the present study correspond to limited size aneurysms (except for the case where $H = 1$) which are clinically shown to be devoid of an endoluminal thrombus (Harter *et al.* 1982).

2.2. Fluid flow

The velocity distribution of the unperturbed blood flow, taken to be a Newtonian fluid, is considered as solenoidal and axisymmetric, with zero velocity in the azimuthal

direction. The governing equations in cylindrical coordinates are then

$$\frac{\partial U_r}{\partial t} + \left(U_r \frac{\partial U_r}{\partial r} + U_z \frac{\partial U_r}{\partial z} \right) = -\frac{\partial P}{\partial r} + \frac{1}{Re} \left[\frac{1}{r} \frac{\partial}{\partial r} \left(r \frac{\partial U_r}{\partial r} \right) + \frac{\partial^2 U_r}{\partial z^2} - \frac{U_r}{r^2} \right], \quad (2.2a)$$

$$\frac{\partial U_z}{\partial t} + \left(U_r \frac{\partial U_z}{\partial r} + U_z \frac{\partial U_z}{\partial z} \right) = -\frac{\partial P}{\partial z} + \frac{1}{Re} \left[\frac{1}{r} \frac{\partial}{\partial r} \left(r \frac{\partial U_z}{\partial r} \right) + \frac{\partial^2 U_z}{\partial z^2} \right], \quad (2.2b)$$

$$\frac{\partial U_r}{\partial r} + \frac{U_r}{r} + \frac{\partial U_z}{\partial z} = 0, \quad (2.2c)$$

where $U_r(r, z)$ and $U_z(r, z)$ are the radial and axial velocity components, respectively, and $P(r, z)$ is the pressure distribution. The Reynolds number Re is based on the vessel diameter and the mean flow velocity, $Re = 4\bar{Q}/\pi Dv$, with \bar{Q} the volume flow rate averaged over a cardiac pulse cycle and v the kinematic viscosity of the fluid. According to Ku (1997), the peak Reynolds number, based on the maximum volume flow rate during a cycle, can vary from 600 at rest up to 6000 under exercise conditions in the abdominal aorta.

The governing equations have been solved imposing the no-slip condition at the vessel wall, assumed to be rigid, a standard no-stress condition at the outlet of the vessel, and the usual symmetry conditions at the axis. The inlet velocity distribution is the Womersley solution for the time-dependent flow in a cylindrical vessel of constant circular cross-section (Pedley 1979). This velocity distribution is determined completely by specifying the radian frequency ω and the Fourier components Q_n of the imposed flow rate waveform,

$$Q(t) = \sum_{n=-\infty}^{\infty} Q_n e^{in\omega t}. \quad (2.3)$$

Writing this inlet condition in dimensionless form introduces a second dimensionless physical quantity that characterizes the fluid flow, namely the Womersley number $Wo = D(\omega/4v)^{1/2}$ (Pedley 1979). The two physiological flow rate waveforms that have been used in the present study are discussed in the following section.

2.3. Physiological flow rate waveforms

Blood flow rate waveforms differ between rest and exercise conditions. Recently, several studies have been carried out to elucidate how these differences may affect the pathogenesis of abdominal aneurysms. The studies of Salsac *et al.* (2006) and Sheard (2009) were based on a flow rate waveform obtained from a healthy male subject at rest. The difficulty is that the flow rate waveform varies significantly with the location in the aorta. Moreover, during the progression of the pathology the flow rate waveform may change in response to the alterations of the blood vessel geometry. In our study, we have used data presented in a recent article by Suh *et al.* (2011), who recorded blood flow rate waveforms of 10 subjects (nine male, one female) suffering from abdominal aortic aneurysms. The recordings were made at an infrarenal location just upstream of the aneurysm, and during both rest and exercise conditions.

The waveforms, the one corresponding to rest conditions denoted $Q1$ and the one corresponding to exercise conditions denoted $Q2$, are shown in figure 3(a); in figure 3(b) the non-dimensionalized value of the mean flow rate \bar{Q} has been given the

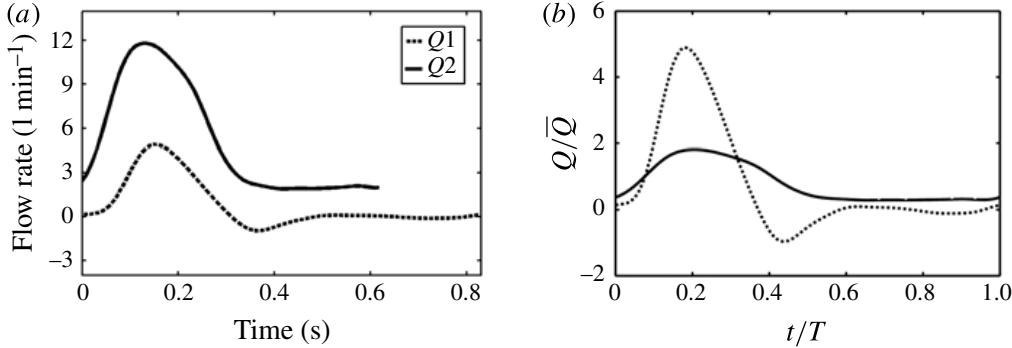


FIGURE 3. (a) Flow rate waveforms corresponding to rest (Q_1) and exercise (Q_2) conditions, as recorded by Suh *et al.* (2011) at an infrarenal location just above an abdominal aortic aneurysm. (b) The two flow rate waveforms when non-dimensionalized by the cycle-averaged volume flow rate.

Waveform	D (cm)	\bar{Q} (1 min ⁻¹)	Heart rate (min ⁻¹)	μ (Pa s)	Re	Wo
Q_1 (rest)	1.7	0.8	72	0.004	264	12
Q_2 (exercise)	1.7	5.1	95	0.004	1700	13.8

TABLE 1. Values of flow parameters related to the flow rate waveforms recorded by Suh *et al.* (2011).

value one. Details of the two waveforms are given in table 1. In Suh *et al.* (2011) blood is considered to be a Newtonian fluid with a density of 1.06 g cm⁻³ and a viscosity of 0.004 Pa s. To convert the recorded volume flow rates to non-dimensional quantities, one also needs to know the diameters of the abdominal aorta at the locations of the recording. These values are not given in Suh *et al.* (2011). The values of the Reynolds number and Womersley number in table 1, for example $Re = 256$ and $Wo = 12$ for waveform Q_1 , are based on a vessel diameter of 1.7 cm, which seems to be a typical value of the inlet diameter of an abdominal aneurysm. The same waveform Q_1 in a blood vessel with diameter 2.0 cm would correspond to $Re = 250$ and $Wo = 15$. The coefficients Q_n of a Fourier series representation of the waveforms, using 10 Fourier coefficients, are listed in table 2.

Given the fact that it is often easier to determine the blood flow rate waveform at a particular location than the values of the blood viscosity and the local arterial diameter, we have studied the characteristics of the pulsatile flow through the model aneurysm with the flow rate waveform Q_1 at the inlet, for three values of the Womersley number (10, 12 and 15) and for Reynolds numbers between 200 and 500. The characteristics of the flow with waveform Q_2 at inlet conditions that are mentioned in § 3 are for $Re = 1700$ and $Wo = 13.8$, as mentioned in table 1. However, it proved to be convenient for the study of the stability of the flow to set the Reynolds number to 500, while keeping 13.8 as the value of the Womersley number.

2.4. Stability analysis

To study the stability of the axisymmetric time-periodic flow to three-dimensional perturbations, the Navier–Stokes equations (2.2) are linearized around the axisymmetric time-periodic base flow. Let base flows be time periodic with period T such that

Q_0	1.0	1.0
Q_1	$0.4461 - i0.9481$	$0.0203 - i0.4735$
Q_2	$-0.7231 - i0.5638$	$-0.1923 - i0.0389$
Q_3	$-0.3046 + i0.3181$	$-0.0392 + i0.0068$
Q_4	$0.0042 + i0.1447$	$-0.0405 + i0.0103$
Q_5	$0.0469 + i0.1112$	$-0.0054 + i0.0170$
Q_6	$0.0780 + i0.0169$	$-0.0026 + i0.0008$
Q_7	$0.0256 - i0.0184$	$-0.0009 + i0.0023$
Q_8	$0.0192 - i0.0104$	$0.0013 + i0.0003$
Q_9	$-0.0021 - i0.0119$	$-0.0002 - i0.0022$
	(a)	(b)

TABLE 2. The coefficients Q_n of the Fourier series representation of the waveforms shown in figure 3. (a) Rest: $Q1$, (b) exercise: $Q2$.

$\mathbf{U}(r, z, t) = \mathbf{U}(r, z, t + T)$. Then, to this flow a three-dimensional perturbation velocity field $\mathbf{u}'(r, z, \theta, t)$ is added to form the composite velocity field:

$$\mathbf{u}(r, z, \theta, t) = \mathbf{U}(r, z, t) + \mathbf{u}'(r, z, \theta, t). \quad (2.4)$$

Substitution of this expression into (2.2) and retaining terms that are linear in the perturbation velocities then yields the equations

$$\frac{\partial \mathbf{u}'}{\partial t} + (\mathbf{U} \cdot \nabla) \mathbf{u}' + (\mathbf{u}' \cdot \nabla) \mathbf{U} = -\nabla p' + \frac{1}{Re} \Delta \mathbf{u}', \quad (2.5a)$$

$$\nabla \cdot \mathbf{u}' = 0. \quad (2.5b)$$

The perturbations are taken to have the form

$$\begin{bmatrix} u'_r(r, \theta, z, t) \\ u'_\theta(r, \theta, z, t) \\ u'_z(r, \theta, z, t) \\ p'(r, \theta, z, t) \end{bmatrix} = \begin{bmatrix} \hat{u}_r(r, z, t) \\ \hat{u}_\theta(r, z, t) \\ \hat{u}_z(r, z, t) \\ \hat{p}(r, z, t) \end{bmatrix} \exp i(m\theta) + \text{c.c.}, \quad (2.6)$$

where m is the azimuthal mode number. For the computations, a plane of symmetry for the perturbations is chosen by considering $\hat{u}_r(r, z, t)$, $\hat{u}_z(r, z, t)$ and $\hat{p}(r, z, t)$ to be purely real and $\hat{u}_\theta(r, z, t)$ to be purely imaginary. This permits one to rewrite the above equations in terms of purely real variables, thereby reducing the computational cost.

The numerical analysis of the stability of the time-periodic flows is carried out by time-marching (2.5) for a suitable number of pulse cycles and monitoring the perturbation fields until they converge. Once the perturbations have converged, the evolution of the perturbation velocity fields at specific points in the computational domain is recorded to determine the Floquet multiplier. According to Floquet theory (Herbert 1988), the velocity and pressure perturbations grow or decay exponentially from period to period, thus

$$\hat{u}(r, z, t + T) = \exp(\sigma T) \hat{u}(r, z, t), \quad (2.7)$$

where T is again the period of the pulsatile flow and σ is the (complex) growth rate. The coefficient $\mu = \exp(\sigma T)$ is the so-called Floquet multiplier. The absolute value $|\mu|$ of the Floquet multiplier is computed as

$$|\mu| = E_k(t + T)/E_k(t), \quad (2.8)$$

with $E_k(t)$ defined as

$$E_k(t) = \left\{ \int_{\Omega} [u_r'(t)^2 + u_\theta'(t)^2 + u_z'(t)^2] d\Omega \right\}^{1/2}. \quad (2.9)$$

For $|\mu| > 1$ the flow is unstable, and for $|\mu| < 1$ the flow is stable; a value $|\mu| = 1$ represents neutral stability. Further, modes can be classified according to the value of the Floquet multiplier. A real bifurcation ($\mu = 1$) has the same period as the base flow, a subharmonic bifurcation ($\mu = -1$) has a period of twice that of the base flow. Such a period-doubling bifurcation can be detected by investigating the perturbation field, which will alternate between opposite values from one period to the next. Complex-conjugate Floquet multipliers correspond to perturbation fields in the form of standing or travelling waves. A complex-conjugate bifurcation can be identified from the evolution of the absolute value of the Floquet multiplier. An oscillation around a mean value signifies that the Floquet multiplier is complex (Robichaux, Balachandar & Vanka 1999; Sheard, Thompson & Hourigan 2005).

2.5. Numerical procedure

The flow problem given by the equations and boundary conditions mentioned in § 2.2 has been solved numerically by a finite-element method. The spatial discretization is a mixed finite-element formulation using P2–P1 Taylor–Hood elements: six-node quadratic triangular elements with quadratic interpolation for velocities (P2) and three-node linear triangular elements for pressure (P1). The meshes, as well as the discrete matrices resulting from the variational formulation of the problem, are generated with the software FreeFem++ (<http://www.freefem.org>).

An inlet length of $10D$ units and an outlet length of $20D$ units have been used in the simulations. At the start of the calculation, the velocity field is considered to be given by the Womersley solution within the cylindrical domain corresponding to a straight vessel of constant cross-section, and a zero velocity field within the dilatation inflation. The flows are time-marched for a sufficient number of cycles for the mean flow to pass through the computational domain. Time traces of the velocities at various points within the domain are then checked at specific phases in the cycle, to confirm that the flows have converged to a time-periodic state. For the parameter conditions explored in the present study, the flow needed to be integrated in time for 10 cycles to attain periodicity. To these axisymmetric base flows, three-dimensional disturbances were added of the form given by (2.6), and the linearized Navier–Stokes equations (2.5) were time-marched for a sufficient number of pulse cycles to obtain the Floquet multipliers. The mesh and the numerical procedure are the same as used in the computation of the time-periodic basic flows.

Extensive validation tests have been performed, the details of which can be found in Gopalakrishnan (2014). Here, we merely present the results of validation tests that consisted of a computational study of pulsatile flow through model arterial stenoses, to verify our results against those presented by Griffith (2007). Table 3 presents a comparison between some of our results and those of Griffith (2007). The parameter b is the stenosis degree, defined as

$$b = 1 - (d/D)^2, \quad (2.10)$$

with d the diameter of the vessel at the centre of the blockage; L_0 denotes the length of the vessel outlet in units of the vessel diameter and A is the amplitude of the harmonic flow rate pulsation.

L_0	b	A	m	$ \mu $	$ \mu _g$
30	0.50	1.25	1	1.0648	—
40	0.50	1.25	1	1.1741	1.1708
30	0.60	1.00	1	1.3495	—
50	0.60	1.00	1	1.3757	1.3761

TABLE 3. Comparison between the magnitude of the Floquet multiplier associated with mode $m=1$ of a perturbed pulsatile flow through a stenosis, as calculated by us, $|\mu|$, and by Griffith (2007), $|\mu|_g$.

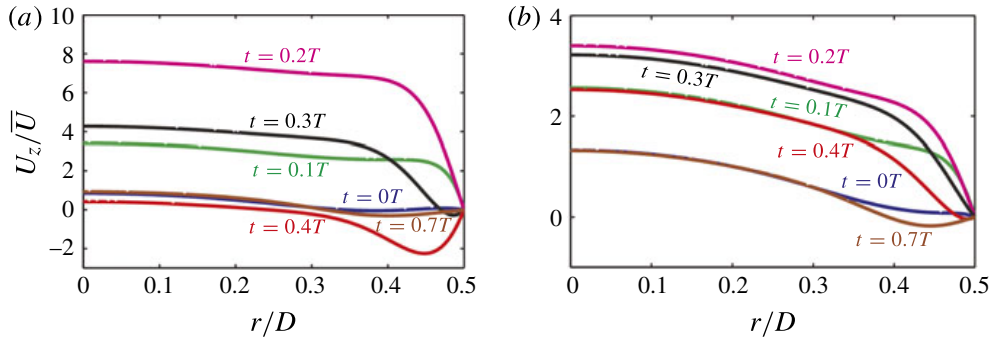


FIGURE 4. (Colour online) Evolution of the axial velocity profile in a straight vessel during one cardiac cycle: (a) $Q1$ (rest); (b) $Q2$ (exercise).

3. The pulsatile flow

3.1. Flow through a vessel with constant cross-sectional area

Before discussing flow through aneurysms, we look at some details of the imposed physiological waveforms.

As can be seen in figure 3(b), under resting conditions ($Q1$) the peak flow rate during systole ($t = 0.18T$) goes up to five times the mean value. After peak systole the flow rate is reduced and even becomes negative during peak diastole ($t = 0.44T$). At the end of the diastole, the flow rate becomes positive again and relaxes to zero during the resting period, before increasing once again at the beginning of the next cardiac cycle. Under exercise conditions ($Q2$) the flow rate remains positive during the entire cardiac cycle: already at the beginning of the cardiac cycle there is a significant flow rate and the flow does not reverse during diastole. Interestingly, the instantaneous velocity profiles during exercise are very similar to the instantaneous velocity profiles, at the same phase within the cycle, during rest; the difference essentially consists in the velocity distribution of a steady Poiseuille flow. This implies that the relative magnitude of the oscillatory component during rest is larger than during exercise conditions.

During the acceleration phase of the systole, the flow develops into a characteristic top-hat velocity profile, as can be seen in figure 4. Thin boundary layers are observed which scale as D/Wo . In line with what was said above, the velocity profiles observed under exercise conditions are more parabolic. The axial velocity also remains positive throughout the cardiac cycle except for a short duration during diastole, when negative velocities are found close to the wall.

The wall shear stress is generally considered as the primary fluid mechanical parameter with regard to the physiological response of the endothelial cells lining the

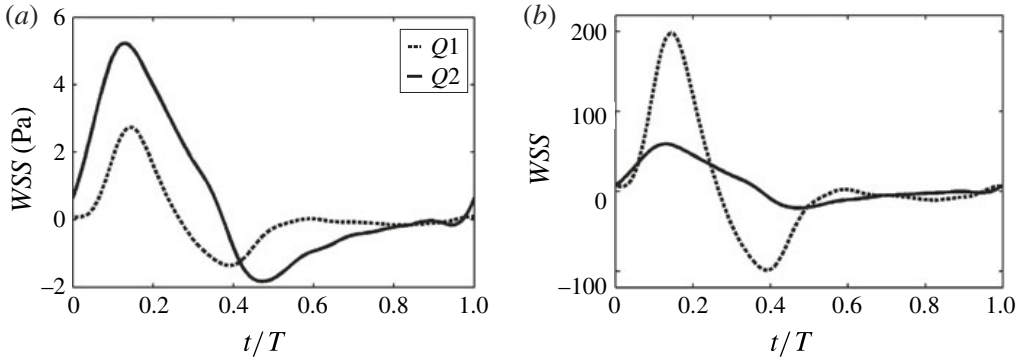


FIGURE 5. Evolution of the wall shear stress during one cardiac cycle, as calculated from the Womersley solution corresponding to the volume flow rate waveforms Q_1 (during rest) and Q_2 (during exercise). (a) Physical values based on the data given in table 1, (b) non-dimensionalized by multiplying by $D/\mu\bar{U}$.

arterial wall (Ku 1997). The time variation of the wall shear stress can be determined from the velocity profiles described above by evaluating

$$WSS(z, t) = -\mu \frac{\partial U_z}{\partial r} \Big|_{r=wall}. \quad (3.1)$$

Here, μ represents the dynamic viscosity of blood. The convention is to assign a negative value to the function WSS in the case of reversed flow. Various quantities have been introduced by different authors to investigate the response of endothelial cells to wall shear stress variations. Examples are the cycle-averaged wall shear stress and the cycle-averaged magnitude of that stress, quantities that are defined as in Salsac *et al.* (2006),

$$\overline{WSS} = \frac{1}{T} \int_0^T WSS dt, \quad |\overline{WSS}| = \frac{1}{T} \int_0^T |WSS| dt, \quad (3.2a,b)$$

respectively. For later comparison, the temporal evolution of the wall shear stress under rest and exercise conditions in a healthy vessel is shown in figure 5; it simply follows the evolution of the flow rate. The peak wall shear stress under exercise conditions is almost twice that during rest conditions. The minimum value of the wall shear stress, however, does not change drastically under varying conditions. The time-averaged wall shear stress is roughly seven times higher during exercise than during rest, but the peak-to-mean ratio is almost four times higher under resting conditions than during exercise.

3.2. Flow in abdominal aneurysms during rest

3.2.1. Phenomenology

We consider a model aneurysm with $W = 0.5$ and $H = 0.5$ for a discussion of the typical flow features; the flow conditions are given by $Re = 264$ and $Wo = 12$. Figure 6 shows the azimuthal vorticity component at various time instants during a pulse cycle. As can be seen in frame (iii), by the time the flow rate reaches peak systole a layer of (positive) vorticity has been formed. Subsequently, as the flow rate decreases, this layer of vorticity detaches from the wall and rolls up into a ring-like vortex structure

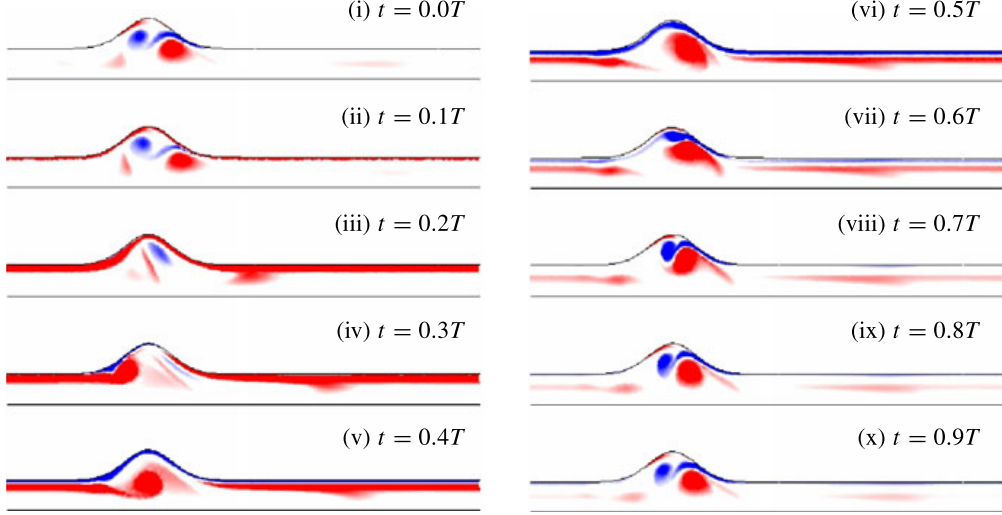


FIGURE 6. (Colour online) Evolution of the azimuthal vorticity distribution during one pulse cycle of the flow rate waveform Q_1 (rest conditions). The dimensionless vorticity values range from -20 (blue) to $+20$ (red). The axial range is $-3 < z < 7$ and the flow parameters and geometrical parameters have values $Re = 264$, $Wo = 12$, $W = 0.5$, $H = 0.5$.

in the centre of the aneurysm, frames (iv) and (v), which moves towards the distal end of the dilatation, frames (vi)–(x). As a consequence, vorticity of opposite (negative) sign is produced at the wall, frames (v) and (vi). As this vorticity is torn off the wall it rolls up in a second ring-like vortex structure, frames (vii)–(x). The two ring-like vortex structures of opposite sign persist for a short period at the end of the cycle, frames (x) and (i), but as the flow rate increases again at the beginning of a new cycle, the primary (positively signed) vortex is washed away downstream, while the second (negatively signed) vortex is annihilated by the newly produced positively signed vorticity at the wall, frames (ii) and (iii). The process then repeats.

Differences between the wall shear stress distribution of a healthy artery and that of an artery with a local dilatation can be deduced by comparing figure 5 with figure 7. In the latter figure, the axial variation of the cycle-averaged wall shear stress and the cycle-averaged magnitude of the wall shear are plotted. It will be seen that significant deviations from the values found for a healthy artery are limited to the central part of the dilatation, roughly in the range $-1 < z < 1$. The minimum and maximum values of the cycle-averaged wall shear stress magnitude in the dilated artery are 36 % and 197 %, respectively, of the values found for the healthy artery. However, with regard to the cycle-averaged wall shear stress itself, it has a positive peak value for the inflated vessel that is 2.8 times the cycle-averaged shear stress in a healthy vessel, and, at another location, a negative peak with a level 4.8 times the mean shear stress in a healthy vessel. It should be noted that these oppositely signed peak values of the mean stress are located within a short distance of each other.

3.2.2. Variations of the geometry

The effect of varying the geometry, as represented by the dilatation ratio $D_R = 1 + 2H/D$, the ratio of the maximum diameter to the inlet diameter, is investigated by varying the non-dimensional bulge height H for a fixed value of W . As a first example we take $W = 0.5$. Figure 8 presents the vorticity distribution of the flow in the model aneurysm at various time instants during a cycle for the

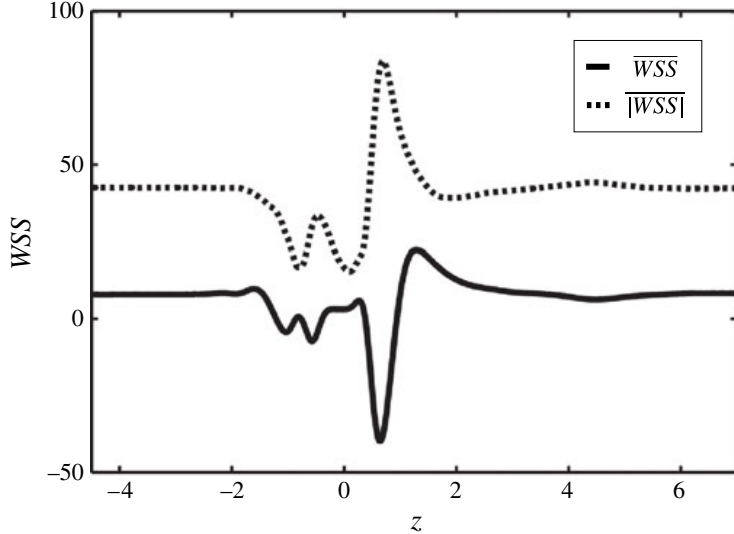


FIGURE 7. Axial variation of the cycle-averaged wall shear stress (\overline{WSS} ; solid line) and cycle-averaged magnitude of the wall shear stress ($|\overline{WSS}|$; dotted line) in the model aneurysm, calculated for the flow rate waveform $Q1$ (rest conditions) and with values of the flow parameters and geometrical parameters as in figure 6: $Re = 264$, $Wo = 12$, $W = 0.5$, $H = 0.5$.

values $H = 0.3$ and $H = 1.0$; the waveform and values of the Reynolds number and Womersley parameter are the same as in figure 6. It should be noted that the flow phenomenology described in the previous section for $H = 0.5$ is also found for a value of the dilatation ratio as low as $D_R = 1.6$ ($H = 0.3$). However, in this shallow dilatation the primary vortex occupies a relatively larger volume and is more readily washed away and convected downstream. As a consequence, the secondary oppositely signed vortex structure occupies less volume and its formation is delayed. In a more developed dilatation, as characterized by $H = 1.0$, the vortices remain trapped during a longer phase of the cycle and the secondary vortex persists throughout the whole cycle.

As a second example, we consider $W = 1$, which is representative of a longer aneurysm than in the first example ($W = 0.5$), for the same value of H . Figure 9 presents the vorticity distribution in the dilatation, again for $H = 0.3$ and $H = 1.0$, and for the same waveform $Q1$, Reynolds number and Womersley parameter as in figure 6. The differences are remarkable: the layer of vorticity at the wall remains attached for a much larger part of the cycle, and, as a result, the primary ring-like vortex structure forms much later during the deceleration phase after peak systole and remains much weaker. The interaction with the wall is so weak that the primary vortex does not move towards the distal wall and no secondary oppositely signed vortex structure is formed during diastole.

The distributions of the cycle-averaged wall shear stress associated with the examples just given are summarized in figure 10, where results for $H = 0.7$ have also been added. A first conclusion from these plots is that the peak value of the cycle-averaged wall shear stress does not seem to be a significant quantity to monitor to decide on the growth of an aneurysm, as it varies very little with changes of H . A similar conclusion could be drawn regarding the distribution itself, since that also remains qualitatively similar as H increases while W is kept fixed. It should be noted,

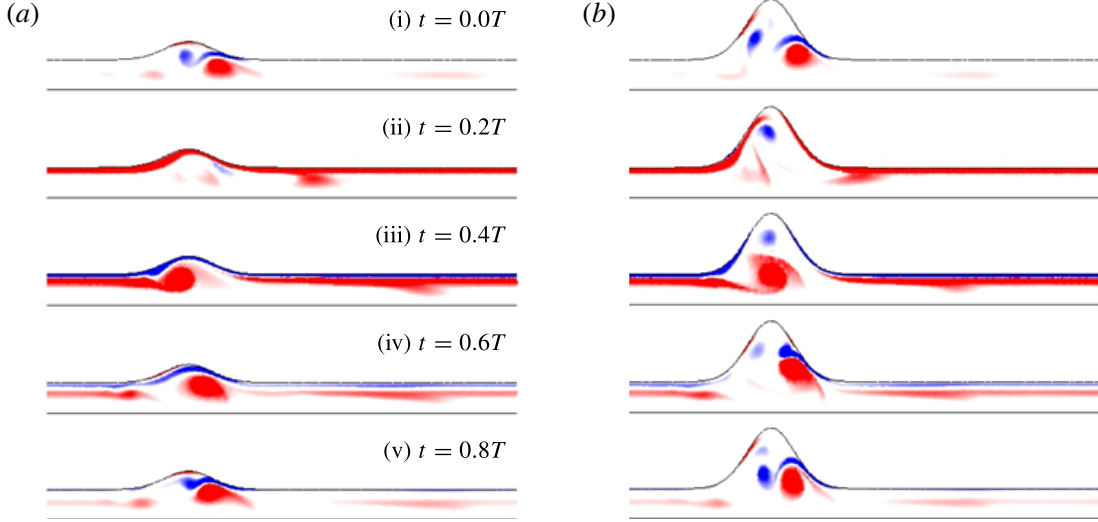


FIGURE 8. (Colour online) Evolution of the azimuthal vorticity distribution during one pulse cycle of the flow rate waveform $Q1$ (rest conditions). The dimensionless vorticity values range from -20 (blue) to $+20$ (red). The axial range is $-3 < z < 7$ and the flow parameters and geometrical parameters have values $Re = 264$, $Wo = 12$, $W = 0.5$; $H = 0.3$ in (a) and $H = 1.0$ in (b).

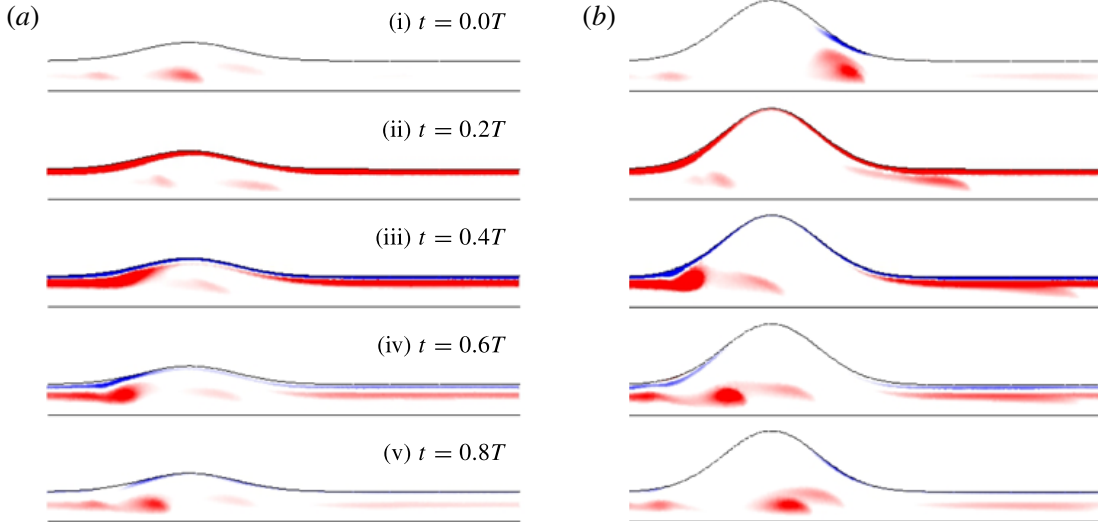


FIGURE 9. (Colour online) Evolution of the azimuthal vorticity distribution during one pulse cycle of the flow rate waveform $Q1$ (rest conditions). The dimensionless vorticity values range from -20 (blue) to $+20$ (red). The axial range is $-3 < z < 7$. The flow parameters and geometrical parameters have the same values as in figure 8: $Re = 264$, $Wo = 12$, $H = 0.3$ in (a) and $H = 1.0$ in (b), but here $W = 1.0$.

however, that much stronger spatial gradients of the cycle-averaged wall shear stress are found for $W = 0.5$ than for $W = 1.0$.

3.2.3. Variations of the flow parameters

In this section we consider the effects of varying the Reynolds number and Womersley number. The geometry is characterized by $W = 0.5$ and $H = 0.5$, values

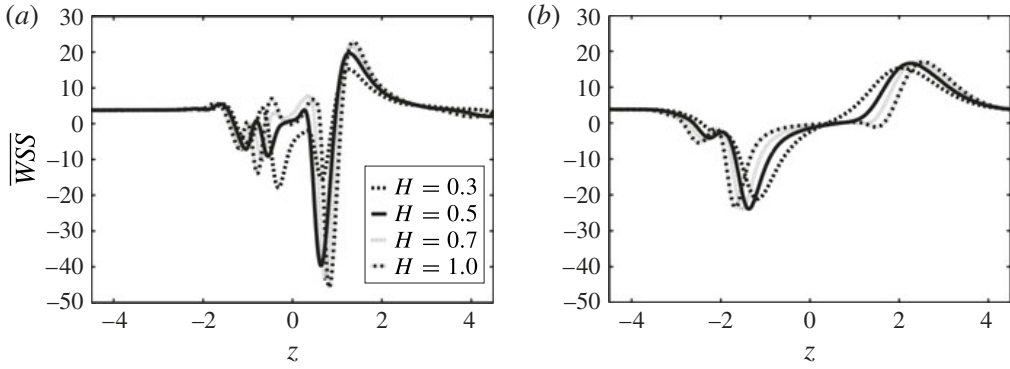


FIGURE 10. Axial variation of the cycle-averaged wall shear stress (\overline{WSS}) in the model aneurysm, as calculated for the flow rate waveform $Q1$ (rest conditions) and with values of the flow parameters as in figure 7: $Re = 264$, $Wo = 12$, but here $W = 0.5$ in (a) and $W = 1.0$ in (b), while the values of H vary between 0.3 and 1.0.

for which the vorticity distribution and cycle-averaged wall shear stress have already been shown in figures 6 and 7, for $Re = 264$ and $Wo = 12$.

In the first example the value of the Reynolds number is kept fixed at 264, but the Womersley number has the values 10 and 15. Figure 11 presents the vorticity distribution at various instants during the pulse cycle. It shows that the flow characteristics for $Wo = 12$ are very different from those for $Wo = 15$. It should be noted, however, that with all other parameters kept fixed, an increase in the Womersley number corresponds to an increase of the square of the frequency of pulsation ($\omega \propto Wo^2$), so that a change from $Wo = 10$ to $Wo = 15$ means that the pulse frequency increases by more than a factor of two. The phenomenology for $Wo = 10$ is similar to that for $Wo = 12$, with a layer of vorticity that separates from the wall and rolls up to form a ring-like vortex structure. For $Wo = 15$ the wall shear layer remains attached for a longer part of the cycle and the rolling up of the vorticity is less prominent. Moreover, the vorticity in the structure that is formed is weaker and the structure does not move towards the distal wall of the inflation; as a result also no oppositely signed vortex structure is formed.

In the second example, the values of the Reynolds number are 200 and 500, while the value of the Womersley number is kept at 12. Figure 12 indicates that the principal effect of increasing the Reynolds number is that the magnitude of the vorticity is larger in the primary vortex structure that forms during the deceleration phase after peak systole. Flow separation occurs at an earlier moment in the cycle, the vortex impinges at the distal wall and induces the formation of various vortices of alternating sign everywhere in the dilatation.

These observations are reflected in figure 13, where the corresponding cycle-averaged wall shear stress distributions are presented. Figure 13(a,b) show that the peak values of the cycle-averaged wall shear stress are reduced as the Womersley number is increased, and figure 13(c,d) show that an increase of the Reynolds number results in stronger spatial variations in the cycle-averaged stress.

3.3. Flow in abdominal aneurysms during exercise

To follow up on the remark just made, this section presents a few results for the waveform $Q2$ (figure 3). The geometry is characterized by $H = 0.5$ and $W = 0.5$, and

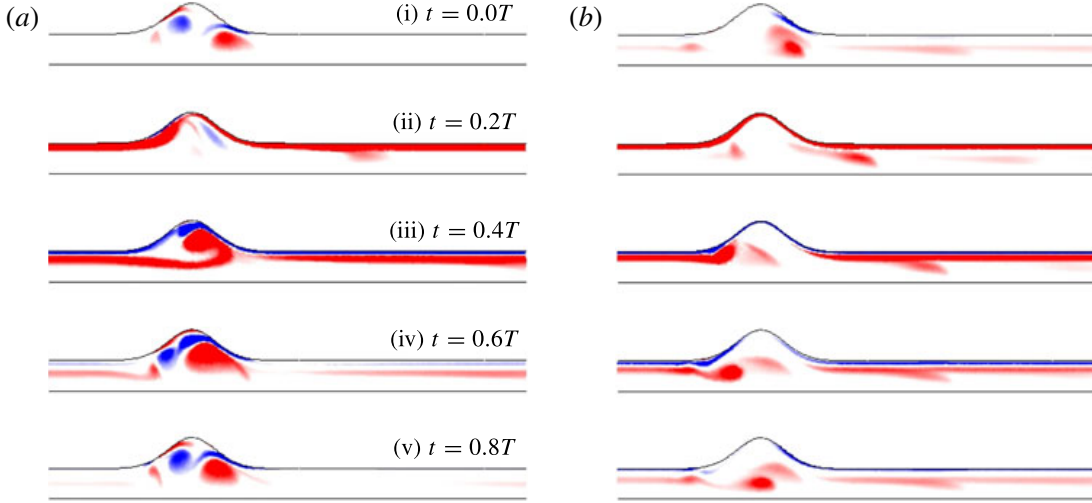


FIGURE 11. (Colour online) Evolution of the azimuthal vorticity distribution during one pulse cycle of the flow rate waveform $Q1$ (rest conditions). The dimensionless vorticity values range from -20 (blue) to $+20$ (red). The axial range is $-3 < z < 7$. The flow parameters and geometrical parameters have the same values as in figure 6: $Re = 264$, $W = 0.5$, $H = 0.5$, but here $Wo = 10$ in (a) and $Wo = 15$ in (b).

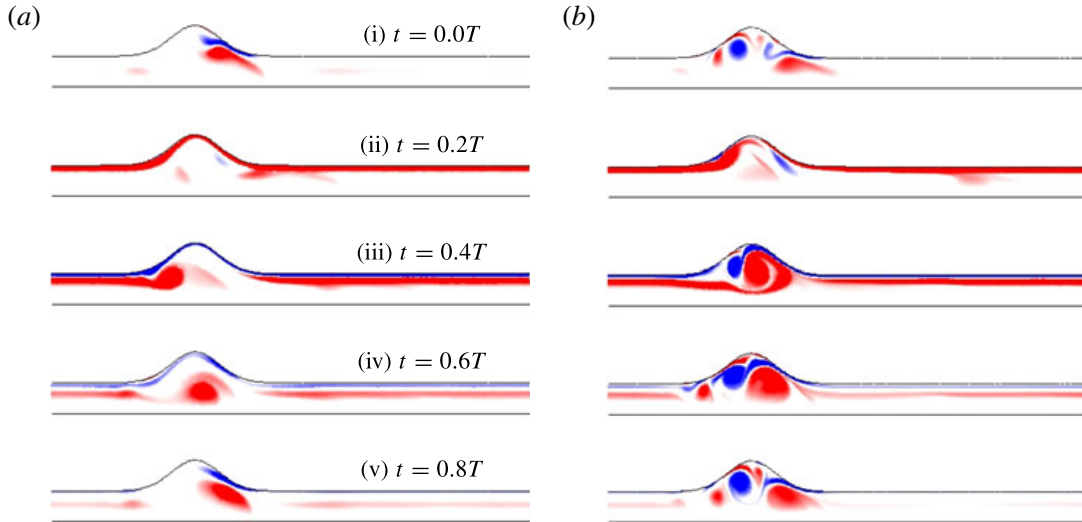


FIGURE 12. (Colour online) Evolution of the azimuthal vorticity distribution during one pulse cycle of the flow rate waveform $Q1$ (rest conditions). The dimensionless vorticity values range from -20 (blue) to $+20$ (red). The axial range is $-3 < z < 7$. The flow parameters and geometrical parameters have the same values as in figure 6: $Wo = 12$, $W = 0.5$, $H = 0.5$, but here $Re = 200$ in (a) and $Re = 500$ in (b).

the flow by $Wo = 13.8$ and $Re = 1700$. Figure 14 shows the vorticity distribution during various instants in a pulse cycle. At this high Reynolds number an intense separated shear layer is formed at the proximal end of the aneurysm during flow deceleration after peak systole. This shear layer rolls up and impinges at the distal end, where subsequently an oppositely signed secondary vortex structure is formed. This is similar to what was observed earlier for the waveform $Q1$, typical of rest conditions, but in

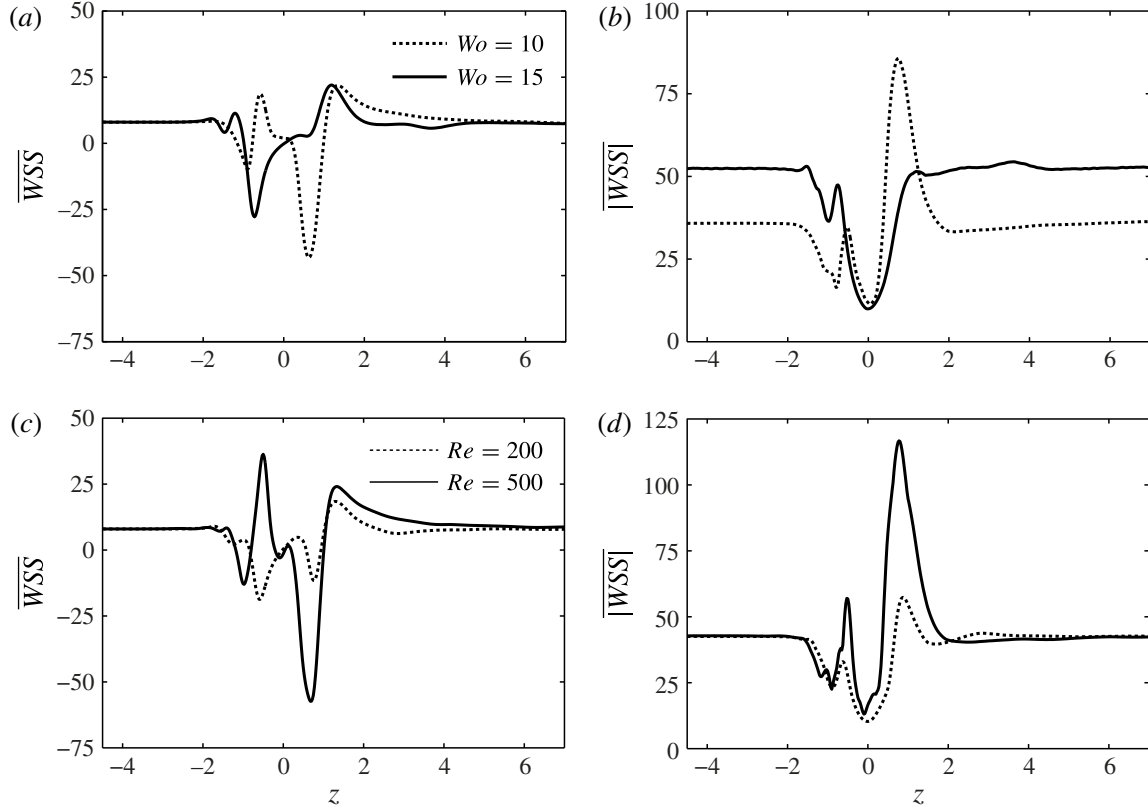


FIGURE 13. (a,c) Axial variation of the cycle-averaged wall shear stress (\overline{WSS}) and (b,d) cycle-averaged magnitude of the wall shear stress ($|WSS|$) in the model aneurysm, as calculated for the flow rate waveform $Q1$ (rest conditions) and with values of the geometrical parameters as in figure 7: $W = 0.5$, $H = 0.5$. The flow parameters have the values (a,b) $Re = 264$, $W_o = 10$ or $W_o = 15$; (c,d) $Re = 200$ or $Re = 500$, $W_o = 12$.

the present case, because the vortices are much stronger, a tertiary vortex with the same sign as the primary vortex is induced inside the dilatation during the diastolic phase. This can be seen clearly in frame (vi), where the (negatively signed) secondary vortex pulls (positively signed) vorticity out of the shear layer, which then rolls up to become a positively signed tertiary vortex. The secondary and tertiary vortices then move together and collide with the proximal wall of the dilatation. The vortices are found to persist during most of the pulse cycle, but gradually weaken by diffusive effects.

Similar flows are observed for other values of H and W . The features of the flows are reflected in the cycle-averaged wall shear stress distributions presented in figure 15. The height H appears to have a relatively weak influence, except for with regard to the minimum value of the averaged wall shear stress. As the aneurysms grow in size, as represented by larger values of H , the secondary vorticity structure persists longer inside the dilatation; this appears to correlate with higher absolute values of the wall shear stress. Variations of the length of aneurysms, as represented by variations in the width W , correspond to shifts in the locations of the maximum and minimum values of the cycle-averaged wall shear stress.

Perhaps the most significant result from these observations is that at elevated Reynolds numbers the flow fields are highly complex, with vortices of alternating

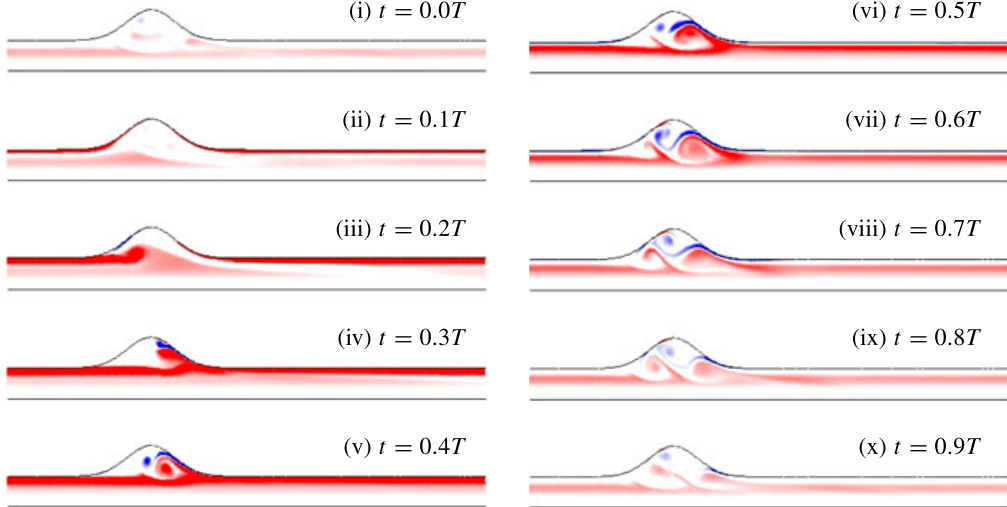


FIGURE 14. (Colour online) Evolution of the azimuthal vorticity distribution during one pulse cycle of the flow rate waveform $Q2$ (exercise conditions). The dimensionless vorticity values range from -20 (blue) to $+20$ (red). The axial range is $-3 < z < 7$. The flow parameters and geometrical parameters have values $Re = 1700$, $Wo = 13.8$, $W = 0.5$, $H = 0.5$.

sign present throughout the aneurysm. As mentioned in § 1, we believe that if such flow conditions persist, this may have a detrimental effect on the vessel wall.

4. Stability characteristics

4.1. Flow in abdominal aneurysms during rest

4.1.1. Variations of the flow parameters

We begin this discussion of the stability of pulsatile flows in a model aneurysm by looking at the flow associated with the pulse waveform $Q1$. The parameters have values $H = 0.5$, $W = 0.5$, $Wo = 15$, while three values of the Reynolds number have been investigated: $Re = 200$, $Re = 250$ and $Re = 300$. The results are summarized in figure 16. The pulsatile flow is stable at $Re = 200$ and $Re = 250$, but at $Re = 300$ it is unstable to perturbations with mode numbers $m = 2$, $m = 3$ and $m = 4$. The most unstable mode is that with $m = 3$. In figure 16 the modes that are classified as subharmonic (period-doubling) are indicated by filled circles. The unstable modes can be seen to arise from two different sets of eigenmodes: the subharmonic modes dominate at small mode numbers, the harmonic modes at higher values of the mode number. It may be noted that something similar was observed for stenotic flows (Sherwin & Blackburn 2005; Griffith *et al.* 2009), where the mode $m = 1$ was found to correspond to a period-doubling bifurcation.

The vorticity distributions of the perturbations associated with modes $m = 1$ and $m = 3$ at various instants in a pulse cycle are shown in figure 17 for $Re = 300$. They are arranged in bands and, although the modes are dominant inside the dilatation, they extend far downstream. This is especially the case for mode $m = 1$, but appears to be a characteristic feature of all subharmonic modes. Such structures of the vorticity perturbations are very different from those that have been found for steady flows through similarly shaped model aneurysms (Gopalakrishnan, Pier & Biesheuvel 2014); in that case these vorticity perturbations are confined to the dilatation.

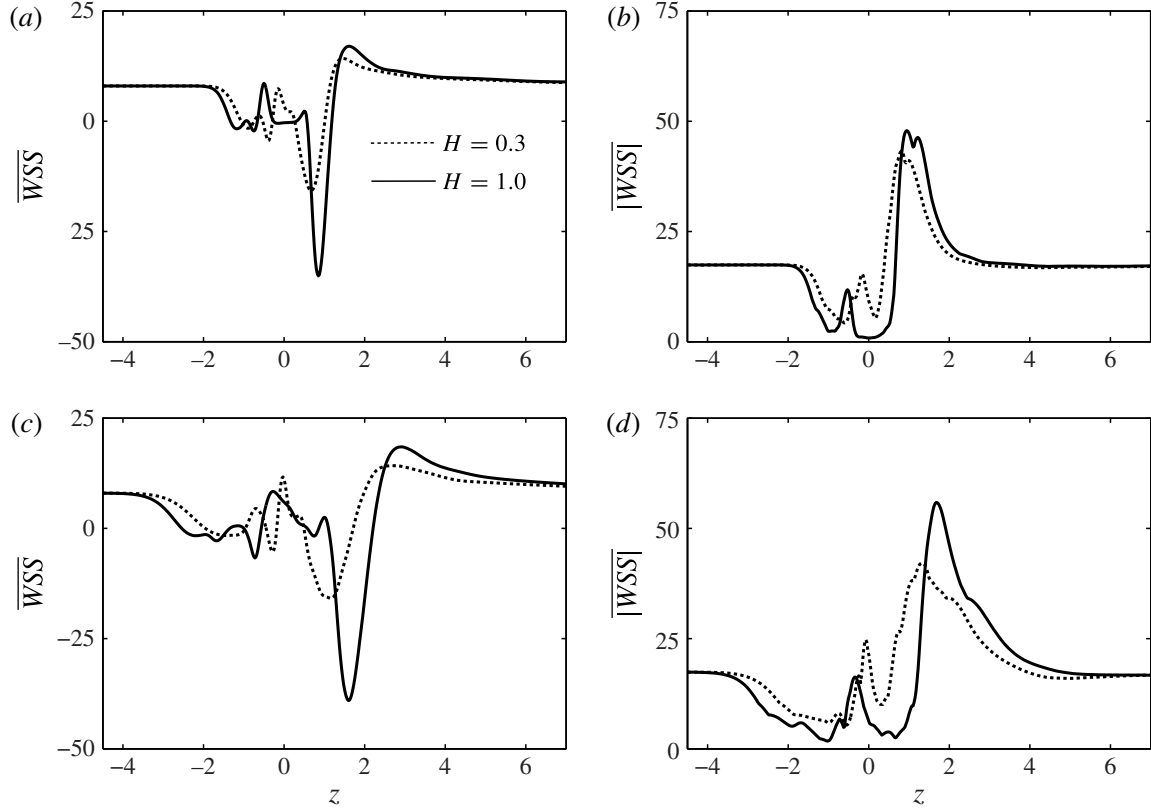


FIGURE 15. (a,c) Axial variation of the cycle-averaged wall shear stress (\bar{WSS}) and (b,d) cycle-averaged magnitude of the wall shear stress ($|WSS|$) in the model aneurysm, as calculated for the flow rate waveform $Q2$ (exercise conditions). The values of the flow parameters and geometrical parameters are $Re = 1700$, $Wo = 13.8$, $H = 0.3$ or $H = 1.0$, $W = 0.5$ (a,b) and $W = 1.0$ (c,d).

These observations imply that the presence of an abdominal aortic aneurysm may create, for certain flow conditions, disturbed flows which extend far downstream into healthy sections of the arterial system. The result is that healthy vessel walls become exposed to sustained abnormal flow velocity conditions, which eventually may damage these vessel walls. This, in turn, may lead to atherosclerosis (Barakat 2013), or to the formation of a secondary aortic aneurysm. This might explain why about one-fifth of large abdominal aortic aneurysms are accompanied by aneurysms of the common iliac arteries.

Figure 18 summarizes the results of a stability analysis of the pulsatile flow at the same values of the parameters as in figure 16, except that now $Wo = 10$ (a) and $Wo = 12$ (b). The most significant observation seems to be that as the Womersley number is reduced, the flows become unstable at lower values of the Reynolds number. As already mentioned, the flows at $Wo = 10$ and $Wo = 12$ are rather different from that at $Wo = 15$. The most unstable mode appears to be the mode $m = 2$, which in the majority of cases can be classified as period-doubling. The absolute values $|\mu|$ of the Floquet multipliers are much higher for $Wo = 10$ and $Wo = 12$ than for $Wo = 15$. It should be noted, however, that the time periods $T \propto Wo^{-2}$ are longer too at Womersley numbers 10 and 12, in comparison with 15. Since the temporal growth rate σ ($= \ln \mu/T$) is inversely proportional to the time period T , the growth rates at $Wo = 10, 12$ are not

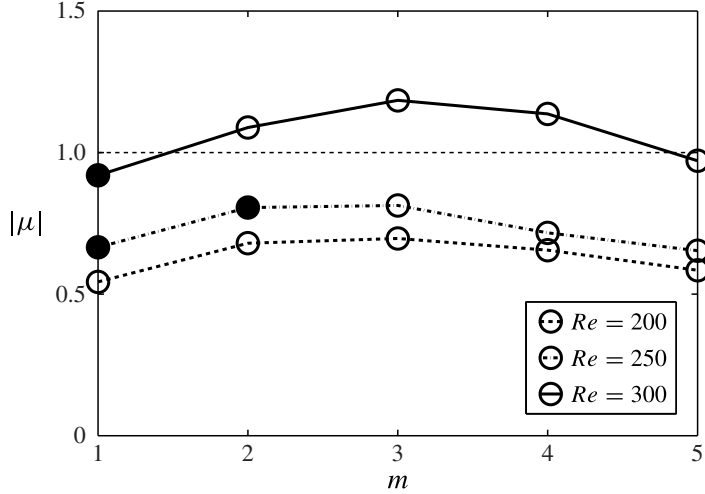


FIGURE 16. Variation of the absolute value of the Floquet multiplier μ with azimuthal mode number m for pulsatile flow through a model aneurysm, for three different values of the Reynolds number. The flow rate waveform is $Q1$ (rest) and the other parameters have the values $Wo = 15$, $H = 0.5$ and $W = 0.5$. Subharmonic modes are indicated by filled circles. The dotted line for $|\mu| = 1$ is the stability boundary.

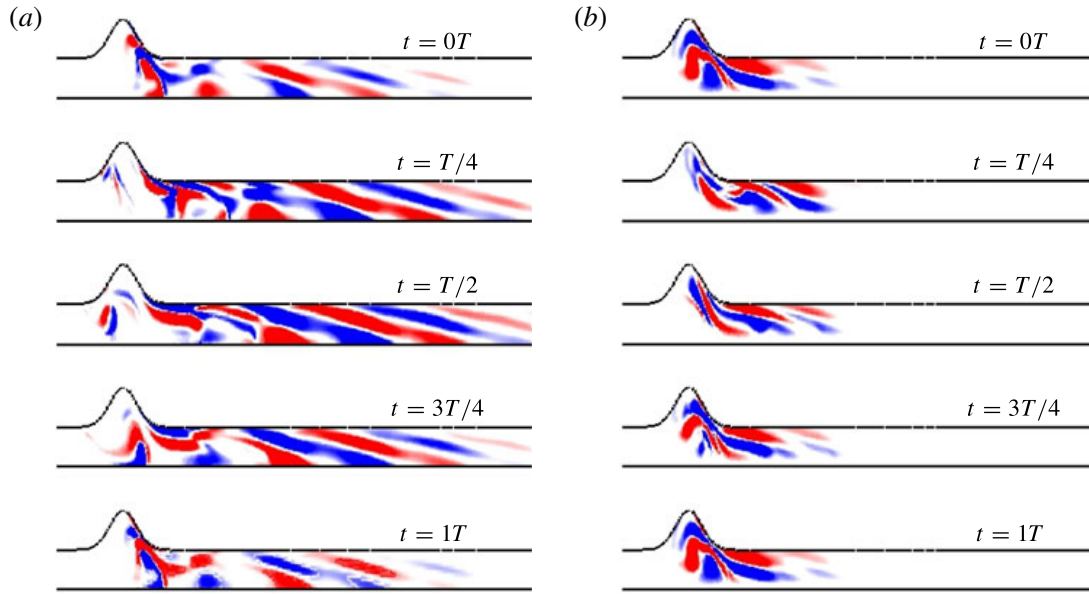


FIGURE 17. (Colour online) Evolution during one pulse cycle of the azimuthal vorticity distributions of the perturbed flows associated with the azimuthal modes $m = 1$ (a) and $m = 3$ (b). The basic flow is that of the pulse waveform $Q1$ (rest) and the values of the flow parameters and geometrical parameters are $Re = 300$, $Wo = 15$, $H = 0.5$, $W = 0.5$.

significantly higher than at $Wo = 15$, as the amplification of the perturbations takes place over a longer time.

4.1.2. Response to harmonic forcing

The presence of vorticity perturbations downstream of the aneurysm, examples of which are shown in figure 17, suggests that an abdominal aortic aneurysm can be

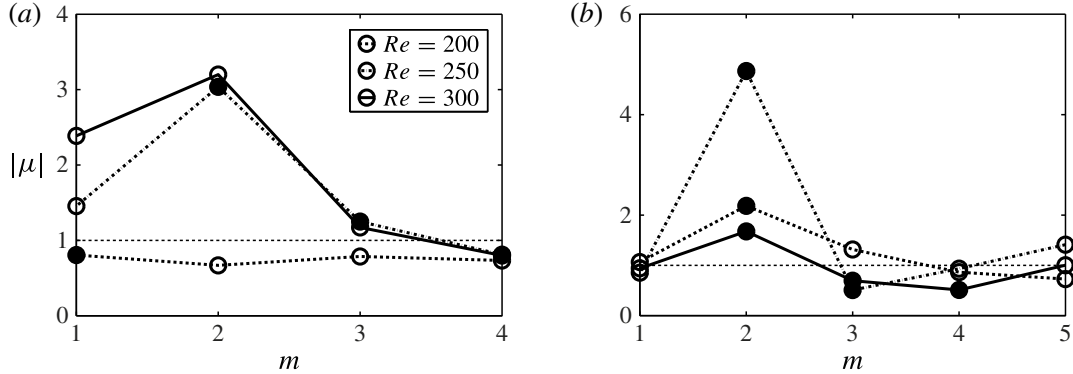


FIGURE 18. Variation of the absolute value of the Floquet multiplier μ with azimuthal mode number m for pulsatile flow through a model aneurysm, for three different values of the Reynolds number. The flow rate waveform is $Q1$ (rest) and the geometrical parameters have the same values as in figure 16, $H = 0.5$ and $W = 0.5$, but here $Wo = 12$ (a) and $Wo = 10$ (b). Subharmonic modes are indicated by filled circles and the dotted line for $|\mu| = 1$ is the stability boundary.

viewed as acting as a wavemaker which forces the flow in the vessels downstream. To verify this, we consider a straight circular vessel of sufficient length, and apply a harmonic forcing and observe the linear response. The unperturbed flow in the circular vessel is the Womersley solution. The external forcing is modelled as a body force $f(x, t)$ added to the linearized Navier–Stokes equations (2.5),

$$\frac{\partial \mathbf{u}'}{\partial t} + (\mathbf{U} \cdot \nabla) \mathbf{u}' + (\mathbf{u}' \cdot \nabla) \mathbf{U} = -\nabla p' + \frac{1}{Re} \Delta \mathbf{u}' + f(\mathbf{x}, t), \quad (4.1a)$$

$$\nabla \cdot \mathbf{u}' = 0, \quad (4.1b)$$

where

$$f(\mathbf{x}, t) = \psi(\mathbf{x}) \exp(-i\sigma_i t). \quad (4.2)$$

Here, the weight function $\psi(\mathbf{x})$ is chosen such that the forcing is restricted to a small region of space. The forcing frequency σ_i is taken as the imaginary part of the complex growth rate obtained from the linear stability analysis of the flow through the model aneurysm.

Figure 19(b,d) shows the response of pulsatile flow in a straight circular vessel to harmonic forcing in comparison with the associated aneurysm flow (figure 19a,c) at two different flow conditions: (a,b) $Re = 200$, $Wo = 15$, $m = 1$ and (c,d) $Re = 300$, $Wo = 15$, $m = 3$ ($H = 0.5$, $W = 0.5$). The region of application of the forcing is the black circular spot. The perturbed flow downstream of the aneurysm (figure 19a,c) compares very well with the forced flow in (b,d).

4.1.3. Variations of the geometry

Figure 20 summarizes the results of a stability analysis of the pulsatile flow at $Re = 264$ and $Wo = 12$, for various values of H , while the value of W is kept fixed at $W = 0.5$ in (a) and at $W = 1.0$ in (b). The radial extent of the dilatation, as represented by the value of H , is found to be of significance for the stability of the flow. For $W = 0.5$, the flow is unstable for $H \geq 0.4$, the dominant mode in all cases being a subharmonic mode of azimuthal mode number 2. An additional calculation at $H = 0.4$ was carried out because of the substantial variation that was observed of the values of

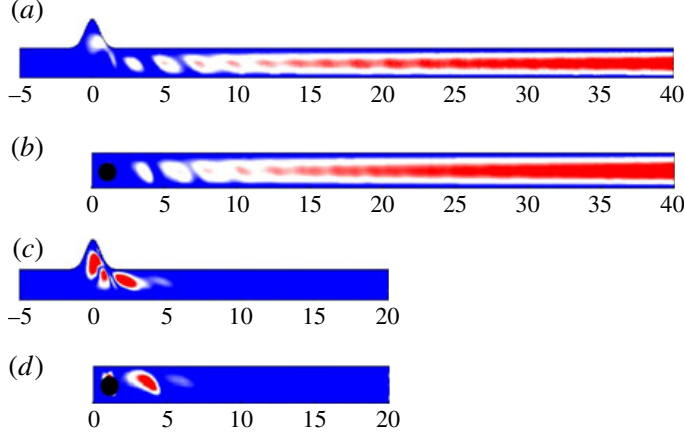


FIGURE 19. (Colour online) (a,c) Energy distribution of the axial velocity component of the leading critical mode for pulsatile flow through a model aneurysm; (b,d) energy distribution of the axial velocity component of the perturbation flow set up by a harmonic forcing at the same frequency applied in the domain shown by a black circle of the pulsatile flow through a straight vessel at the same values of the Reynolds number and Womersley number. Parameter settings: $W = 0.5$, $H = 0.5$, (a,b) $Re = 200$, $Wo = 15$, $m = 1$, (c,d) $Re = 300$, $Wo = 15$, $m = 3$.

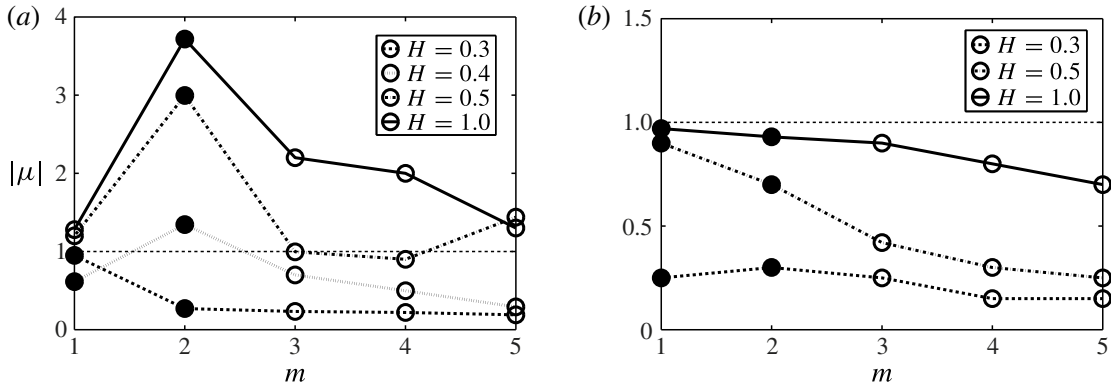


FIGURE 20. Variation of the absolute value of the Floquet multiplier μ with azimuthal mode number m for pulsatile flow through a model aneurysm, for various values of the depth of the aneurysm, as represented by H . The flow rate waveform is $Q1$ (rest) and the other parameters have the values $Re = 264$, $Wo = 12$, $W = 0.5$ (a) and $W = 1.0$ (b). Subharmonic modes are indicated by filled circles and the dotted line for $|\mu| = 1$ is the stability boundary.

the Floquet multipliers as H was changed from 0.3 to 0.5. As expected, and confirmed in figure 20(b), the flow in a long aneurysm, as represented by the value of W , is less prone to becoming unstable than that in a short aneurysm.

The azimuthal vorticity distributions associated with the least stable modes of the flows in figure 20(a) are presented in figure 21. It is remarkable that already at the small value of $H = 0.3$, the dominant mode extends downstream of the dilatation. Similar features are observed for $W = 1$ in figure 22. We have already mentioned the observation that an aneurysm may initiate disturbed flow conditions in healthy segments of the arteries downstream of the aneurysm; the results shown in figures 21 and 22 now suggest that this will already occur in the incipient stages of an aneurysm.

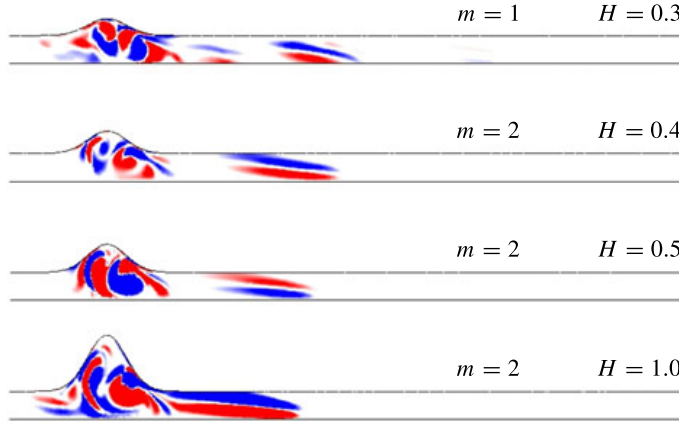


FIGURE 21. (Colour online) Azimuthal vorticity distributions of the perturbed flows associated with the least stable mode m for pulsatile flow through a model aneurysm. The axial range shown is $-1.5D \leq z \leq 7D$ and the flow parameters and geometrical parameters have the values $Re = 264$, $Wo = 12$, $W = 0.5$ and from top to bottom $H = 0.3, 0.5, 1.0$. The flow rate waveform is $Q1$ (rest).

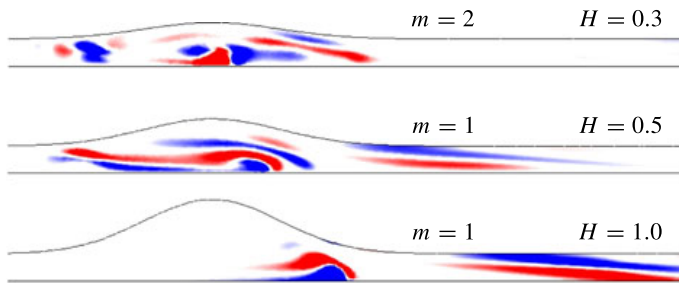


FIGURE 22. (Colour online) Azimuthal vorticity distributions of the perturbed flows associated with the least stable mode m for pulsatile flow through a model aneurysm. The axial range shown is $-1.5D \leq z \leq 10D$ and the flow parameters and geometrical parameters have the values $Re = 264$, $Wo = 12$, $W = 1.0$ and from top to bottom $H = 0.3, 0.4, 0.5, 1.0$. The flow rate waveform is $Q1$ (rest).

Clearly, this study is not conclusive, since the presence of the iliac artery bifurcation downstream of an abdominal aortic aneurysm can be expected to interact with the flow inside the aneurysm. Yet, what it does show is that the iliac bifurcation and segment of the common iliac arteries needs to be included in the computational domain when carrying out realistic, patient-specific simulations of flows in abdominal aortic aneurysms.

4.2. Flow in abdominal aneurysms during exercise

To conclude, we briefly consider the stability of pulsatile flow in the model aneurysm under exercise conditions. The waveform $Q2$, recorded by Suh *et al.* (2011) and shown in figure 3(b), corresponds to a Reynolds number of 1700 and a Womersley number of 13.8, if the vessel diameter at the location of the recording is 1.7 cm. However, to simplify the computations and to focus on the influence of the waveform, we have chosen the lower value $Re = 500$ and kept the value $Wo = 13.8$. Nevertheless, we believe that the results provide a qualitative picture of the flow perturbations

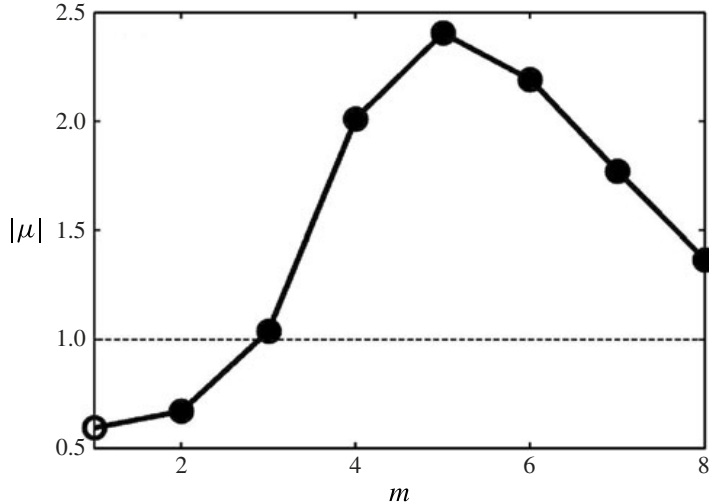


FIGURE 23. Variation of the absolute value of the Floquet multiplier μ with the azimuthal mode number m for pulsatile flow through a model aneurysm. The flow parameters and geometrical parameters have the values $Re = 500$, $Wo = 13.8$, $W = 0.5$, $H = 0.5$. The Womersley number corresponds to the flow rate waveform $Q2$ (exercise), but the Reynolds number is reduced from 1700 to 500. Subharmonic modes are indicated by filled circles and the dotted line for $|\mu|=1$ is the stability boundary.

prevailing for exercise waveforms at larger Reynolds numbers. In all calculations, the geometrical parameters have the values $W = 0.5$ and $H = 0.5$.

The absolute values of the Floquet multipliers associated with the first eight azimuthal modes of the flow perturbations are given in figure 23. All Floquet multipliers are real; the most dominant mode is $m = 5$. Moreover, all modes with $m \geq 2$ can be classified as period-doubling, as indicated by the filled circles.

The azimuthal vorticity distributions of the perturbations are shown in figure 24 for various mode numbers. Here, the modes $m = 1$ and $m = 2$ are stable, and the modes $m = 3$, $m = 4$ and $m = 5$ are unstable. The vorticity distributions associated with $m = 6$, $m = 7$ and $m = 8$ are not shown, because they resemble closely that associated with mode $m = 5$. It will be observed that in this case the perturbation fields associated with the stable modes $m = 1$ and $m = 2$ and the marginally unstable mode $m = 3$ extend downstream of the dilatation, but that the perturbation fields associated with the higher-valued unstable modes are much more localized inside the dilatation; these more localized modes have the largest growth rate.

5. Sensitivity to geometrical details

During the tests that were conducted to validate our numerical tools we noticed a remarkable sensitivity of the results to details of the model geometry. Here, we take the opportunity to report these observations. We compare the results of numerical computations using the Gaussian shaped vessel of the present paper with results obtained for a sinusoidally shaped vessel wall, the model aneurysm studied in the recent work of Sheard & Ryan (2008) and Sheard (2009). For this comparison the same value of H is taken, while W is chosen such that the areas traced out in an axial plane by the vessel walls are the same. The two geometries, with the ‘wavelength’ of the sinusoidally shaped wall denoted L , are shown in figure 25.

The pulsatile flow rate waveform in this comparison is that used by Salsac *et al.* (2006) and Sheard (2009), which is called $Q3$ here and is shown in figure 26.

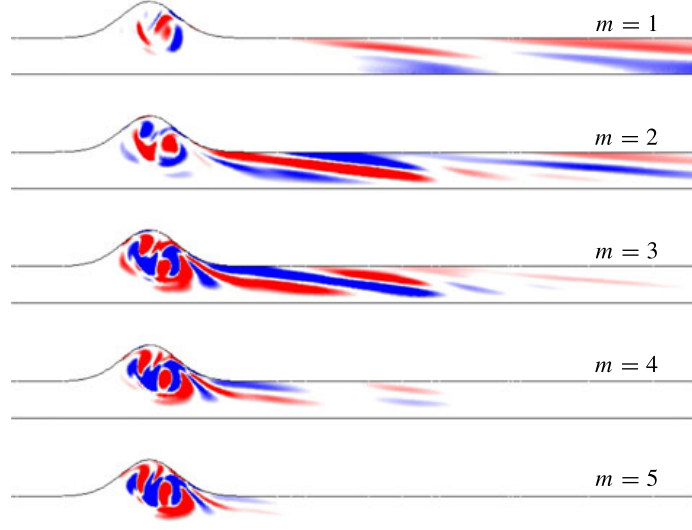


FIGURE 24. (Colour online) Azimuthal vorticity distributions of the perturbed flows associated with modes $m = 1, \dots, 5$ for pulsatile flow through a model aneurysm. The axial range shown is $-2.5D \leq z \leq 10D$ and the flow parameters and geometrical parameters have the values $Re = 500$, $Wo = 13.8$, $W = 0.5$, $H = 0.5$. The Womersley number corresponds to the flow rate waveform $Q2$ (exercise), but the Reynolds number is reduced from 1700 to 500.

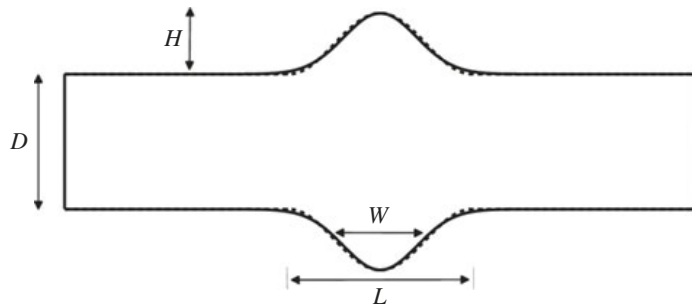


FIGURE 25. The sinusoidal geometry used in the studies by Sheard & Ryan (2008) and Sheard (2009) is shown by the dotted curves and the Gaussian shaped geometry used in the present study is shown by the solid curves. Both model aneurysms have the same area in a plane through the symmetry axis. Parameter values: $H = 0.45$, $W = 0.58$, $L = 2.9$.

The flow parameters have the values $Re = 330$ and $Wo = 10.7$. An important difference between waveforms $Q1$ and $Q3$ is that much larger negative flow rates occur for $Q3$.

Figure 27 presents the evolution of the azimuthal vorticity distribution during one pulse cycle of the pulsatile flow of $Q3$ through a model aneurysm with sinusoidal shape (*a*) and with Gaussian shape (*b*). Qualitatively, the flow phenomena in the two geometries are similar, but closer inspection reveals that there is a slight time delay in the evolution of the vorticity distribution in the Gaussian shaped aneurysm with respect to that in the sinusoidally shaped aneurysm. This may be attributed to the fact that the sinusoidal wall, where it connects to the straight vessel, is not as well rounded-off as the vessel with the Gaussian shaped wall. As a result, flow separation occurs at a slightly earlier stage during systole. This phenomenon can be seen best by comparing the frames (ii) which correspond (roughly) to peak systole.

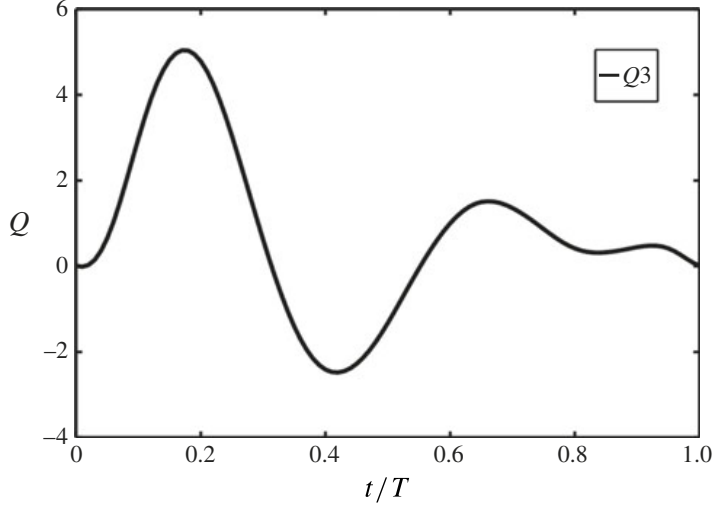


FIGURE 26. The waveform considered in the study by Salsac *et al.* (2006) and Sheard (2009).

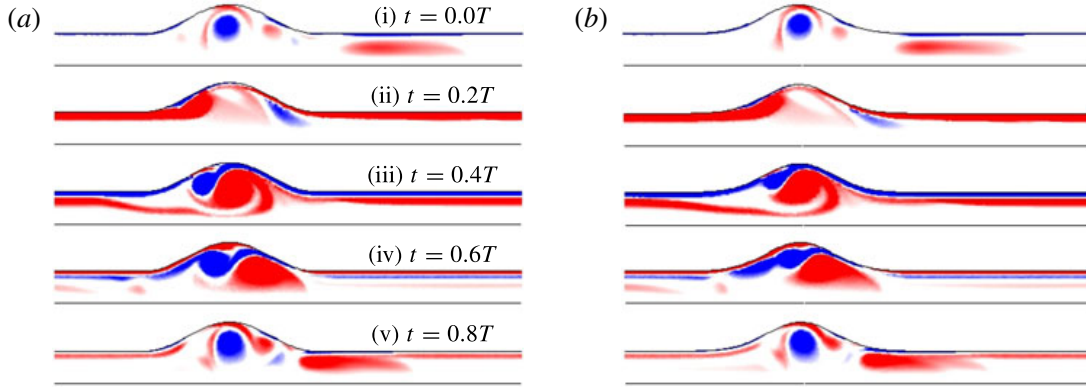


FIGURE 27. (Colour online) Evolution of the azimuthal vorticity distribution during one pulse cycle of the flow rate waveform Q_3 in aneurysms modelled by a sinusoidal (a) and a Gaussian (b) wall function. The dimensionless vorticity values range from -20 (blue) to $+20$ (red). The axial range is $-3D \leq z \leq 5D$. The values of the flow parameters and geometrical parameters are $Re = 330$, $Wo = 10.7$, $H = 0.45$, $W = 0.58$, $L = 2.9$.

The wall shear stress distribution has been found to be rather sensitive to the details of the vorticity distribution in an aneurysm, cf. § 3.2, so that one would expect that the slight time delay just mentioned would be visible in plots of the wall shear stress. This is indeed the case. As figure 28 shows, the most prominent differences are found at the proximal and distal ends of the dilatation, i.e. close to the location where there is a difference in differentiability of the functions that describe the vessel wall shapes.

It will now not come as a surprise that the slight differences in the vorticity distributions of the pulsatile flows are also reflected in the stability characteristics of these flows. Figure 29 compares the absolute value of the Floquet multiplier associated with the azimuthal modes $m = 1, \dots, 5$ in the two geometries; here the flow parameters are $Re = 330$ and $Wo = 10.7$. Qualitatively, the characteristics are the same: all Floquet multipliers are complex and in both cases the mode $m = 3$ is the least stable mode; this was found also by Sheard & Ryan (2008). The absolute

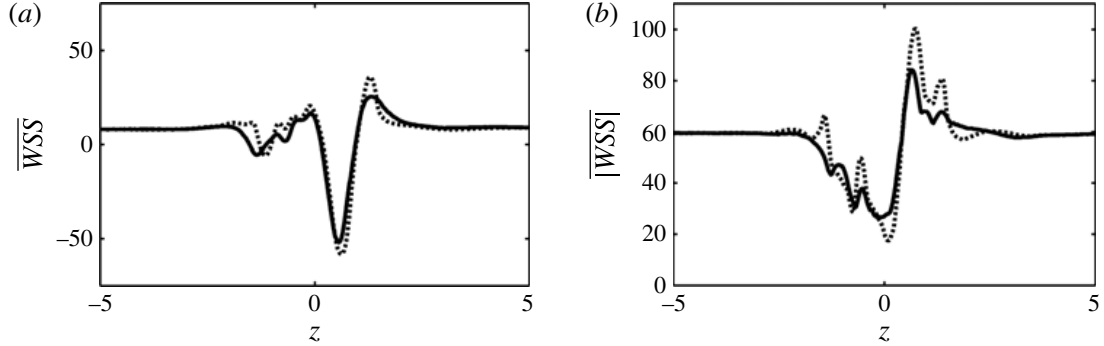


FIGURE 28. Axial variation of the cycle-averaged wall shear stress \overline{WSS} (a) and cycle-averaged magnitude of the wall shear stress $|\overline{WSS}|$ (b) in aneurysms modelled by a sinusoidal (dotted curves) and a Gaussian (solid curves) wall function. The flow rate waveform is $Q3$ and the values of the flow parameters and geometrical parameters are $Re = 330$, $Wo = 10.7$, $H = 0.45$, $W = 0.58$, $L = 2.9$.

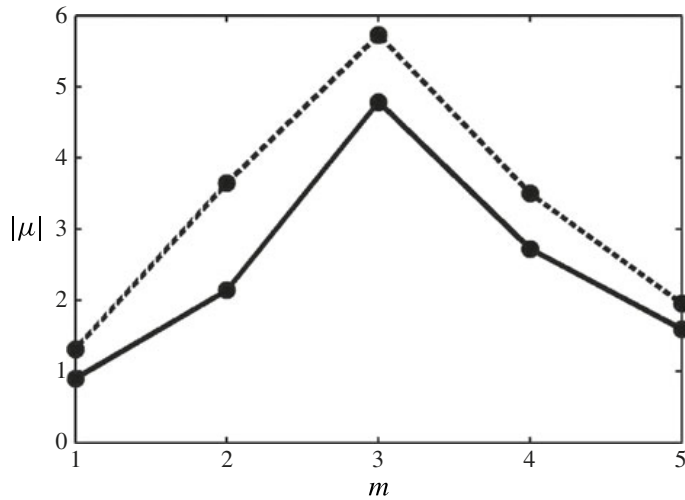


FIGURE 29. Variation of the absolute value of the Floquet multiplier μ with the azimuthal mode number m for pulsatile flow through a model aneurysm with the wall described by a sinusoidal function (dotted curve) and a Gaussian function (solid curve). The flow parameters and geometrical parameters have the values $Re = 330$, $Wo = 10.7$, $H = 0.45$, $W = 0.58$, $L = 2.9$.

values of the Floquet multipliers, though, are significantly larger for pulsatile flow through the sinusoidally shaped aneurysm, the mode $m=1$ even being unstable while it is stable for the Gaussian shaped wall.

The azimuthal vorticity distributions of the perturbed flows associated with the various modes are shown in figure 30, for the sinusoidally shaped wall in (a) and for the Gaussian shaped wall in (b). Again, these vorticity distributions may seem similar; however, they are not indistinguishable. As found earlier, the higher mode numbers $m=2, 3, 4, 5$ are localized within the dilatation, but the (most stable) mode $m=1$ extends far downstream.

This example shows that the details of pulsatile flow through aneurysms, the wall shear stress distribution in particular, can be extremely sensitive to geometrical details. The conclusion is that care must be taken when interpreting results from

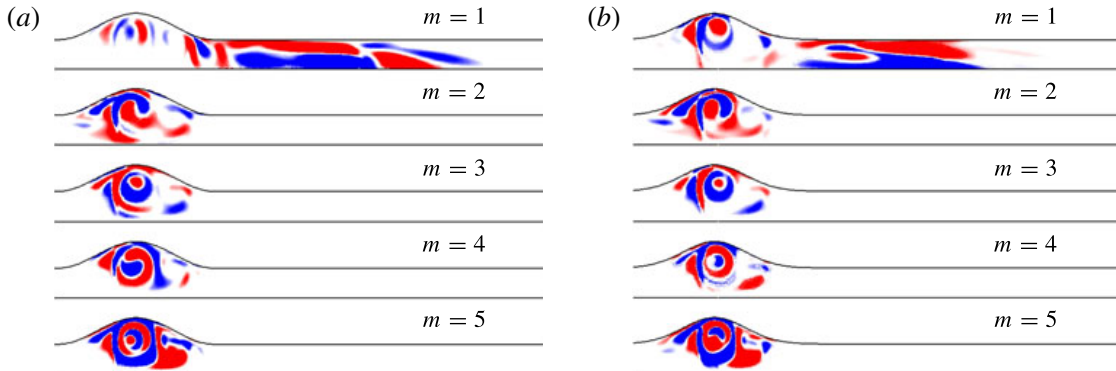


FIGURE 30. (Colour online) Azimuthal vorticity distributions of the perturbed flows associated with modes $m = 1, \dots, 5$ for pulsatile flow through a model aneurysm of sinusoidal shape (a) and Gaussian shape (b). The axial range shown is $-2.5D \leq z \leq 10D$. The flow rate waveform is $Q3$, and the flow parameters and geometrical parameters have the values $Re = 330$, $Wo = 10.7$, $H = 0.45$, $W = 0.58$, $L = 2.9$.

(‘patient-specific’) computations of the flow in an aneurysm geometry that is constructed from medical imaging data.

6. Conclusions

In this paper we have presented the results of numerical computations of pulsatile flow through a model abdominal aortic aneurysm, and of an analysis of the hydrodynamic stability of this flow. The aneurysm is modelled as a circular cylindrical vessel with a radius described by a Gaussian function. The flow at the inlet of the calculational domain is the Womersley solution for pulsatile flow in a cylindrical vessel. This solution is a Fourier–Bessel series; the coefficients of the series were deduced from measurements by Suh *et al.* (2011) of the blood flow rate waveform at the inlet of the infrarenal aorta, during rest and exercise conditions, of patients suffering from an abdominal aortic aneurysm.

For a given flow rate waveform, the problem is characterized by four dimensionless quantities: the Reynolds number Re and Womersley number Wo of the fluid flow, and the ‘height’ H and ‘width’ W which specify the Gaussian geometry of the dilatation. In the present study, the Reynolds number was varied between 200 and 500 and the Womersley number between 10 and 15, for the flow rate waveform of the rest condition. The flow structure corresponding to an exercise condition was studied for $Re = 1700$ and $Wo = 13.8$, but it turned out to be easier to use the value $Re = 500$ in the stability analysis. To learn about the influence of the aneurysm geometry on the flow characteristics, the geometrical dimensionless quantities were varied in the ranges $0.3 \leq H \leq 1.0$ and $0.5 \leq W \leq 1.0$.

Typical flow phenomena that can be observed in pulsatile flow through an aneurysm are the creation of vorticity at the vessel wall during the acceleration phase of systole, followed by detachment of this wall-bounded shear layer at the proximal end of the dilation during the deceleration phase of systole; this leads to the formation of a cylindrical layer of concentrated vorticity with a radius comparable with that of the vessel upstream of the dilatation. For ‘sufficiently localized’ aneurysms, for Reynolds numbers and Womersley numbers in the physiological range, the shear layer rolls up and forms a ring-like vortex structure which interacts with the vessel wall and collides

with it near the distal end of the dilatation. During this vortex–wall interaction, new vorticity of opposite sign is produced at the vessel wall; this eventually detaches and forms a secondary vortex ring with vorticity of opposite sign to that of the primary vortex ring. During the final stages of diastole, the primary vortex is washed downstream with the flow, while the secondary opposite signed vortex decays. This process then repeats in a new cardiac cycle. An increase of the Reynolds number and/or an increase in the height of the dilatation yields more vigorous vortex dynamics, in the sense that the vortices are more intense and approach the distal vessel wall at higher speed, and that further ring-like vortex structures are formed. The computations with the flow rate waveform corresponding to exercise conditions show that at high Reynolds number a highly complex vorticity distribution emerges.

This description of the flow phenomena in pulsatile flow through a Gaussian shaped model aneurysm agrees very well with what was found in experiments by Salsac *et al.* (2006). These authors also observed that the vortex motions within the dilatation induce strong spatial and temporal variations of the wall shear stress, especially near the distal end. Again, this agrees with what was found by us. Our computational approach allowed us to investigate a somewhat larger range of parameter values than Salsac *et al.* (2006). Our results support the conclusion of Salsac *et al.* (2006) that longer aneurysms are less pathological than short ones. Moreover, our results suggest that physical activity is harmful for a patient with an abdominal aortic aneurysm; the more-localized or well-developed aneurysms again being the most pathological.

Yip & Yu (2001) and Salsac *et al.* (2006) mention that during part of the cardiac cycle the flow in an aneurysm may become weakly turbulent. Since this repetitive occurrence of disturbed flow conditions seems especially harmful, we have investigated the hydrodynamic stability of pulsatile flows through a model aneurysm. It appears that such flows are unstable to small-amplitude three-dimensional disturbances for flow conditions within the physiological range, flows through well-developed aneurysms being the most susceptible. Our findings support the idea that patients suffering from abdominal aortic aneurysms might want to avoid physical exercise. A second important observation is that the vorticity structures associated with the flow disturbances are not confined to the dilatation, but rather extend far downstream. The abdominal aortic aneurysm acts as a ‘wavemaker’ which generates disturbed flow conditions in the healthy section of the arterial system downstream of the aortic aneurysm. This may be related to the fact that one-fifth of larger abdominal aortic aneurysms are accompanied by an aneurysm in one or both of the common iliac arteries (Armon *et al.* 1998). It also leads to the conclusion that patient-specific computational studies of the biomechanics of abdominal aortic aneurysms should include the iliac bifurcation and the common iliac arteries as part of the computational domain.

Finally, during various numerical tests we observed a remarkable sensitivity of the flow to geometrical details of the model aneurysm. This became clear by carrying out the calculations of Sheard (2009), who modelled the aneurysm wall by a sinusoidal function, using a Gaussian function with the same maximal vessel radius and which encloses the same area in a plane through the axis of symmetry. The volume flow rate waveform was that used by Salsac *et al.* (2006) and Sheard (2009), obtained from a healthy male subject at rest, and so were the dimensionless flow quantities: $Re = 330$ and $Wo = 10.7$. What was observed was that the exceedingly small difference in the differentiability of the shape functions, where the sinusoidal dilatation connects to the inlet vessel, leads to small, but still significant, differences in the wall shear stress distribution and the growth rate of three-dimensional flow perturbations. If the aim is

to make a quantitative analysis through a patient-specific computational study it seems wise to carry out a sensitivity analysis to assess the influence of unavoidable minor errors that occur when transforming medical images into a computational domain.

Acknowledgements

The authors wish to express their gratitude to Professor P. Feugier of the Université Claude-Bernard Lyon 1, and vascular surgeon at Hôpital Édouard-Herriot in Lyon, for many useful discussions.

REFERENCES

- ARMON, M. P., WENHAM, P. W., WHITAKER, S. C., GREGSON, R. H. S. & HOPKINSON, B. R. 1998 Common iliac artery aneurysms in patients with abdominal aortic aneurysms. *Eur. J. Vasc. Endovasc. Surg.* **15**, 255–257.
- BARAKAT, A. I. 2013 Blood flow and arterial endothelial dysfunction: mechanisms and implications. *C. R. Phys.* **14**, 479–496.
- DEPLANO, V., KNAPP, Y., BERTRAND, E. & GAILLARD, E. 2007 Flow behaviour in an asymmetric compliant experimental model for abdominal aortic aneurysm. *J. Biomech.* **40**, 2406–2413.
- EGELHOFF, C. J., BUDWIG, R. S., ELGER, D. F., KHRAISHI, T. A. & JOHANSEN, K. H. 1999 Model studies of the flow in abdominal aortic aneurysms during resting and exercise conditions. *Biorheology* **32**, 1319–1329.
- FINOL, E. A., KEYHANI, K. & AMON, C. H. 2002 The effect of asymmetry in abdominal aortic aneurysms under physiologically realistic pulsatile flow conditions. *Trans. ASME J. Biomech. Engng* **125**, 207–217.
- GOPALAKRISHNAN, S. S. 2014 Dynamics and stability of flow through an abdominal aortic aneurysm. PhD thesis, Université de Lyon.
- GOPALAKRISHNAN, S. S., PIER, B. & BIESHEUVEL, A. 2014 Global stability analysis of flow through a fusiform aneurysm: steady flows. *J. Fluid Mech.* **752**, 90–106.
- GRIFFITH, M. D. 2007 Stabilité et dynamique des écoulements en géométrie de sténose. PhD thesis, Université de Provence, Aix-Marseille and Monash University, Melbourne.
- GRIFFITH, M. D., LEWEKE, T., THOMPSON, M. C. & HOURIGAN, K. 2009 Pulsatile flow in stenotic geometries: flow behaviour and stability. *J. Fluid Mech.* **622**, 291–320.
- GROOTENBOER, N., BOSCH, J. L., HENDRIKS, J. M. & VAN SAMBEEK, M. R. H. M. 2009 Epidemiology, aetiology, risk of rupture and treatment of abdominal aortic aneurysms. *Eur. J. Vasc. Endovasc. Surg.* **38**, 278–284.
- HARTER, L. P., GROSS, B. H., CALLEN, P. W. & BARTH, R. A. 1982 Ultrasonic evaluation of abdominal aortic thrombus. *J. Ultrasound Med.* **1**, 315–318.
- HERBERT, T. 1988 Secondary instability of boundary layers. *Annu. Rev. Fluid Mech.* **20**, 487–526.
- HUMPHREY, J. D. & HOLZAPFEL, G. A. 2012 Mechanics, mechanobiology, and modeling of human abdominal aorta and aneurysms. *J. Biomech.* **45**, 805–814.
- HUMPHREY, J. D. & TAYLOR, C. A. 2008 Intracranial and abdominal aortic aneurysms: similarities, differences, and need for a new class of computational models. *Annu. Rev. Biomed. Engng* **10**, 221–246.
- JOHNSTON, K. W., RUTHERFORD, R. B., TILSON, M. D., SHAH, D. M., HOLLIER, L. & STANLEY, J. C. 1991 Suggested standards for reporting on arterial aneurysms. *J. Vascu. Surg.* **13**, 452–458.
- KU, D. N. 1997 Blood flow in arteries. *Annu. Rev. Fluid Mech.* **29**, 399–434.
- LASHERAS, J. C. 2007 The biomechanics of arterial aneurysms. *Annu. Rev. Fluid Mech.* **39**, 293–319.
- LES, A. S., SHADDEN, S. C., FIGUEROA, C. A., PARK, J. M., TEDESCO, M. M., HERFKENS, R. J., DALMAN, R. L. & TAYLOR, C. A. 2010 Quantification of hemodynamics in abdominal aortic aneurysms during rest and exercise using magnetic resonance imaging and computational fluid dynamics. *Ann. Biomed. Engng* **38**, 1288–1313.

- PEDLEY, T. J. 1979 *The Fluid Mechanics of Large Blood Vessels*. Cambridge University Press.
- REININGER, A. J., HEINZMANN, U., REININGER, C. B., FRIEDRICH, P. & WURZINGER, L. J. 1994 Flow-mediated fibrin thrombus formation in an endothelium-lined model of arterial branching. *Thrombosis Res.* **74** (6), 629–641.
- ROBICHAUX, J., BALACHANDAR, S. & VANKA, S. P. 1999 Three-dimensional Floquet instability of the wake of a square cylinder. *Phys. Fluids* **11**, 560–578.
- SALSAC, A. V. 2005 Évolution des contraintes hémodynamiques lors de la croissance des anévrismes aortiques abdominaux. PhD thesis, École Polytechnique.
- SALSAC, A. V., SPARKS, S. R., CHOMAZ, J. M. & LASHERAS, J. C. 2006 Evolution of the wall shear stresses during the progressive enlargement of symmetric abdominal aortic aneurysms. *J. Fluid Mech.* **560**, 19–51.
- SALSAC, A. V., SPARKS, S. R. & LASHERAS, J. C. 2004 Hemodynamic changes occurring during the progressive enlargement of abdominal aortic aneurysms. *Ann. Vascu. Surg.* **18**, 14–21.
- SHEARD, G. J. 2009 Flow dynamics and wall shear stress variation in a fusiform aneurysm. *J. Engng Maths* **64**, 379–390.
- SHEARD, G. J. & RYAN, K. 2008 Wall shear stress and flow stability in a model fusiform aneurysm. *ANZIAM J.* **50**, C1–C15.
- SHEARD, G. J., THOMPSON, M. C. & HOURIGAN, K. 2005 Subharmonic mechanism of the mode C instability. *Phys. Fluids* **17**, 111702.
- SHEIDAEI, A., HUNLEY, S. C., ZEINALI-DAVARANI, S., RAGUIN, L. G. & BAEK, S. 2011 Simulation of abdominal aortic aneurysm growth with updating hemodynamic loads using a realistic geometry. *Med. Engng Phys.* **33**, 80–88.
- SHERWIN, S. J. & BLACKBURN, H. M. 2005 Three-dimensional instabilities and transition of steady and pulsatile axisymmetric stenotic flows. *J. Fluid Mech.* **533**, 297–327.
- STAMATOPOULOS, C., MATHIOULAKIS, D. S., PAPAHARILAOU, Y. & KATSAMOURIS, A. 2011 Experimental unsteady flow study in a patient-specific abdominal aortic aneurysm model. *Exp. Fluids* **50**, 1695–1709.
- SUH, G. Y., LES, A. S., TENFORDE, A. S., SHADDEN, S. C., SPILKER, R. L., YEUNG, J. J., CHENG, C. P., HERFKENS, R. J., DALMAN, R. L. & TAYLOR, C. A. 2011 Hemodynamic changes quantified in abdominal aortic aneurysms with increasing exercise intensity using MR exercise imaging and image-based computational fluid dynamics. *Ann. Biomed. Engng* **39**, 2186–2202.
- TAYLOR, C. A. & DRANEY, M. T. 2004 Experimental and computational methods in cardiovascular fluid mechanics. *Annu. Rev. Fluid Mech.* **36**, 197–231.
- TAYLOR, C. A. & FIGUEROA, C. A. 2009 Patient-specific modeling of cardiovascular mechanics. *Annu. Rev. Biomed. Engng* **11**, 109–134.
- TAYLOR, C. A., HUGHES, T. J. R. & ZARINS, C. K. 1999 Effect of exercise on hemodynamic conditions in the abdominal aorta. *J. Vascu. Surg.* **29**, 1077–1089.
- TAYLOR, C. A. & YAMAGUCHI, T. 1994 Three-dimensional simulation of blood flow in an abdominal aortic aneurysm – steady and unsteady flow cases. *Trans. ASME J. Biomech. Engng* **116**, 89–97.
- VORP, D. A. 2007 Biomechanics of abdominal aortic aneurysm. *J. Biomech.* **40**, 1887–1902.
- VORP, D. A., LEE, P. C., WANG, D. H. J., MAKAROUN, M. S., NEMOTO, E. M., OGAWA, S. & WEBSTER, M. W. 2001 Association of intraluminal thrombus in abdominal aortic aneurysm with local hypoxia and wall weakening. *J. Vascu. Surg.* **34**, 291–299.
- YIP, T. H. & YU, S. C. M. 2001 Cyclic transition to turbulence in rigid abdominal aortic aneurysm models. *Fluid Dyn. Res.* **29**, 81–113.
- YIP, T. H. & YU, S. C. M. 2002 Oscillatory flows in straight tubes with an axisymmetric bulge. *Exp. Therm. Fluid Sci.* **26**, 947–961.

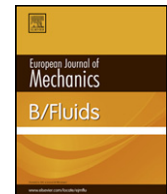
[A20]

Global modes with multiple saddle points

B. Pier & N. Peake

European Journal of Mechanics B-Fluids **49**, 335–344 (2015)

doi:10.1016/j.euromechflu.2014.03.006
<https://hal.archives-ouvertes.fr/hal-01084705>



Global modes with multiple saddle points



Benoît Pier^{a,*}, Nigel Peake^b

^a Laboratoire de mécanique des fluides et d'acoustique, École centrale de Lyon – CNRS – Université de Lyon 1 – INSA Lyon, 36 avenue Guy-de-Collongue, 69134 Écully, France

^b Department of Applied Mathematics and Theoretical Physics, Center for Mathematical Sciences, University of Cambridge, Wilberforce Road, Cambridge CB3 0WA, UK

ARTICLE INFO

Article history:

Available online 3 April 2014

Keywords:

Absolute instabilities
Global modes
Complex saddle points

ABSTRACT

Significant progress has been made towards understanding the global stability of slowly-developing shear flows. The WKBJ theory developed by Patrick Huerre and his co-authors has proved absolutely central, with the result that both the linear and the nonlinear stability of a wide range of flows can now be understood in terms of their local absolute/convective instability properties. In many situations, the local absolute frequency possesses a single dominant saddle point in complex X -space (where X is the slow streamwise coordinate of the base flow), which then acts as a single wavemaker driving the entire global linear dynamics. In this paper we consider the more complicated case in which multiple saddles may act as the wavemaker for different values of some control parameter. We derive a frequency selection criterion in the general case, which is then validated against numerical results for the linearized third-order Ginzburg–Landau equation (which possesses two saddle points). We believe that this theory may be relevant to a number of flows, including the boundary layer on a rotating disk and the eccentric Taylor–Couette–Poiseuille flow.

© 2014 Elsevier Masson SAS. All rights reserved.

1. Introduction

Over the last twenty to thirty years, the investigation of the long-time response of a shear flow to impulsive forcing has become one of the most active areas of fluid mechanics research. In these developments Patrick Huerre has played a huge and seminal role.

In the parallel-flow case, the theory of [1,2] leads to the distinction between convective instability, in which disturbances grow at the same time as being swept out of the system, and absolute instability, in which an unstable Fourier mode with zero group velocity grows *in situ* and eventually dominates the whole fluid domain. This theory has been successfully applied to a wide range of flows which exhibit a transition from convective to absolute instability as some control parameter is varied, including plane mixing layers [3], heated jets [4], and the boundary layer on a rotating disk [5,6].

For non-parallel flow, much attention has focused on the case in which the base flow evolves only slowly in space, allowing the separation of scales between slow, X , and fast, x , streamwise coordinates. We then have the concept of local convective and

absolute instability, in which the base flow at a given value of X is used to compute a local absolute frequency as if for parallel flow, $\omega_0(X)$ say. Many flows contain regions of local absolute instability, where¹ $\omega_{0,i} > 0$, and adjacent regions of local convective instability or local stability, where $\omega_{0,i} < 0$. An example of such a flow is the wake of a bluff body, as noted by [7], with a pocket of local absolute instability close to the body and a region of local convective instability downstream. The key question here, however, is how the local stability properties can be connected to the behaviour of the whole system, and in particular how one can construct from the local data a global mode, in which the whole system oscillates with the same frequency, ω_G say. A significant step forward in this regard was made by [8], who showed how ω_G is given by the saddle point of $\omega_0(X)$ in the complex X -plane: the saddle point is then the effective location of a wavemaker which drives the global oscillation of the whole flow. These ideas are presented in detail in [9,10], while applications to the wake flow in particular are given in [11,12]. Situations with more complicated branch structures have been investigated by [13]. At this point we should also mention that while the above analysis has been

* Corresponding author.

E-mail address: benoit.pier@ec-lyon.fr (B. Pier).

¹ Throughout this paper, subscripts i and r denote imaginary and real parts of a complex quantity.

concerned with linearized unsteady flow, the same ideas also pertain in nonlinear systems. In particular, [14] shows that the global nonlinear dynamics are again driven by a wavemaker, now located close to the transition station from local convective to local absolute instability, with solutions in the two regions connected across a relatively sharp front region.

To date much of the work on the global stability of weakly non-parallel flow has concentrated on the case in which there exists just a single saddle point $\omega_0(X)$ which controls the dynamics. In terms of a simple model, this behaviour is replicated by the second-order linearized Ginzburg–Landau equation. However, there are other flows in which several saddle points are present, with the possibility of the dynamics being driven by different saddles depending on the value of some control parameter. We mention two cases here. First, [15] shows that the rotating-disk boundary layer possesses two separate branches of saddle points, which for a particular Reynolds number (equivalently a particular disk radius) collide at what is termed as a ‘super branch point’. The role of these two saddle points in determining the linear global behaviour of the rotating disk remains an open question. Second, it has recently been shown [16] that the dispersion relation of the eccentric Taylor–Couette–Poiseuille flow displays several saddle points and that the absolute instability may switch between these saddles when control parameters are varied. In typical oil-drilling applications the eccentricity slowly changes with axial distance: a global stability analysis of such a configuration is thus expected to involve multiple saddle points.

In the light of the issues described in the previous paragraph, our aim in this paper is to develop a linear global mode selection criterion for problems containing multiple saddle points, and to test this criterion on the simple model problem of the linearized third-order Ginzburg–Landau equation (which possesses two saddle points). The paper is set out as follows. The problem formulation and basic theory is given in Section 2. In Section 3 we present our global frequency selection criterion, which is then applied in Section 4 to the third-order Ginzburg–Landau equation. Comparisons between our criterion and the results of a full numerical integration are presented in Section 5, and excellent agreement is found.

2. Problem formulation

Consider a system governed by a one-dimensional linear partial differential equation that is first-order in time of the form

$$\partial_t \psi = \mathcal{L}(\partial_x; X)\psi, \quad (1)$$

where x and t represent space and time coordinates, respectively. The differential operator \mathcal{L} depends on the space through a slow coordinate X to be defined shortly. The basic state is assumed to be $\psi = 0$, and the complex-valued function $\psi(x, t)$ represents fluctuations riding on this basic state. Solutions to the linear governing equation (1) may be sought as a superposition of global modes of the form

$$\psi(x, t) = \phi(x; \omega) \exp(-i\omega t), \quad (2)$$

where the spatial functions ϕ and the complex frequencies ω obey the eigenvalue problem

$$-i\omega\phi = \mathcal{L}(\partial_x; X)\phi, \quad (3)$$

derived from (1). Many global modes are in general possible, and the medium governed by (1) is stable if $\omega_i < 0$ for all global modes or unstable if $\omega_i > 0$ for at least one global mode.

A crucial assumption of the present investigation is the slow spatial development as exemplified by the introduction of the slow spatial variable X in the operator \mathcal{L} . The weak non-uniformity hypothesis is fulfilled if the ratio $\epsilon = \lambda/L$ between the typical

instability length scale λ and the inhomogeneity length scale L is small. As a result of this scale separation, the weak spatial variations of the medium properties are described through the slow variable

$$X = \epsilon x \quad \text{with } \epsilon \ll 1, \quad (4)$$

and the time-periodic global-mode solutions may be sought as WKB approximations.

Such a line of thought has been successfully implemented in situations where the entire medium is governed by a single local absolute frequency $\omega_0(X)$, with a dominant saddle point in the complex X -plane [9,10]. The purpose of the present investigation is to address more complex situations involving higher-order dispersion relations and a competition between several saddle points.

3. Theoretical analysis

3.1. Local characteristics

Under the assumption that the governing equation only depends on space through the slow variable X , local characteristics may be derived from (1) by freezing X to some arbitrary value and studying the corresponding strictly uniform system. At this local level of analysis, X and x may then be considered to be independent: the fast x is involved in spatial differentiation whereas the slow X plays the role of an independent control parameter.

Any perturbation can then be sought as a superposition of elementary waves $e^{i(kx-\omega t)}$ where the wavenumber k and the frequency ω satisfy the local linear dispersion relation

$$\omega = \Omega(k; X) \equiv i\mathcal{L}(ik; X). \quad (5)$$

This dispersion relation is assumed to be an analytic function of the complex wavenumber k and it may be thought of as a polynomial in k . (It is also assumed analytic in slow space X , but the parametric dependence in X will be ignored in this section for simplicity.) Solving (5) for a given frequency ω yields a set of spatial branches $k^n(\omega)$ indexed by n ; with $n = 1, 2, \dots, N$ in the situation where $\Omega(k)$ is an N -order polynomial in k .

By invoking causality and assuming that the temporal growth rates are bounded, the spatial branches may be labelled as either k^{n+} or k^{n-} branches according to whether they are confined to the upper or lower complex k -planes for sufficiently large imaginary parts of ω . When ω_i is lowered, branch switching occurs when two spatial branches meet at $k = k_0$ for a frequency $\omega = \omega_0$. Such a wavenumber–frequency pair is defined by the saddle criterion

$$\frac{\partial \Omega}{\partial k}(k_0) = 0 \quad \text{and} \quad \omega_0 = \Omega(k_0). \quad (6)$$

In the situation where the dispersion relation (5) is an N -th order polynomial in k , the criterion (6) yields a set of $N - 1$ solutions $k = k_0^n$ ($1 \leq n \leq N - 1$) each associated with the corresponding frequency $\omega_0^n \equiv \Omega(k_0^n)$.

Let us assume here that the frequencies ω_0^n are sorted by decreasing imaginary part: $\omega_{0,i}^1 > \omega_{0,i}^2 > \dots$. Then, when lowering ω_i , the first branch switching occurs for $\omega = \omega_0^1$ where two spatial branches, say $k^{n_1}(\omega)$ and $k^{n_2}(\omega)$, meet at k_0^1 . If this collision is between a + and a – branch, e.g. between $k^{n_1+}(\omega)$ and $k^{n_2-}(\omega)$, it corresponds to the absolute instability of the system: absolute frequency ω_{abs} and absolute wavenumber k_{abs} are then given by

$$\omega_{abs} = \omega_0^1 \quad \text{and} \quad k_{abs} = k_0^1. \quad (7)$$

However, the branch switching at ω_0^1 may be between two branches of the same label, i.e., between $k^{n_1+}(\omega)$ and $k^{n_2+}(\omega)$

or between $k^{n_1}(\omega)$ and $k^{n_2}(\omega)$. In that situation, the (k_0^1, ω_0^1) -saddle of the dispersion relation is not a genuine pinch point and lowering of the imaginary part of ω may be continued until, at one of the frequencies ω_0^n , say $\omega_0^{n_0}$, pinching between a k^+ and a k^- eventually occurs. In any case, this procedure unambiguously yields the absolute frequency and wave number as

$$\omega_{abs} = \omega_0^{n_0} \quad \text{and} \quad k_{abs} = k_0^{n_0}, \quad (8)$$

associated with one of the saddle points of the dispersion relation defined by (6).

The above analysis can be carried out for each X . Thus the spatial branches $k^{n\pm}(X, \omega)$ are obtained by solving the local dispersion relation (5) for a given frequency ω , while the saddle-point wavenumbers $k_0^n(X)$ and frequencies $\omega_0^n(X)$ are derived from the condition

$$\frac{\partial \Omega}{\partial k}(k_0; X) = 0 \quad \text{and} \quad \omega_0(X) = \Omega(k_0; X). \quad (9)$$

Among the frequencies $\omega_0^n(X)$, the local absolute frequency $\omega_{abs}(X)$ equals the one with largest imaginary part that corresponds to pinching between downstream and upstream spatial branches. Note that the frequencies $\omega_0^n(X)$ are analytic functions of the complex X -variable, while the local absolute frequency $\omega_{abs}(X)$ is not necessarily an analytic function of X since it may jump from one ω_0^n branch to another as X is varied.

3.2. Global modes

The long-time response of (1) can be sought as a linear superposition of *global modes* which are time-harmonic solutions of the form (2) of complex global frequency ω_G . Under the assumption of weak spatial inhomogeneity (4) and resorting to classical WKBJ approximations [17] such a global mode may be obtained as

$$\psi(x, t) \sim A(X) \exp \left(\frac{i}{\epsilon} \int^x k(u; \omega_G) du - i\omega_G t \right), \quad (10)$$

where the slowly-varying local wavenumber $k(X; \omega_G)$ is governed by the local dispersion relation (5), and the slowly-varying amplitude $A(X)$ can be obtained by higher-order expansions.

The boundary conditions for this eigenproblem are that the mode (10) follows an upstream k^- -branch for $X \rightarrow -\infty$ and a downstream k^+ -branch for $X \rightarrow +\infty$. This corresponds to the fact that the modes are self-sustained and not triggered by boundary conditions, *i.e.* their selection takes place in the central region and the waves that propagate towards $X = \pm\infty$ are the consequences of this self-sustained process. As shown by [9,10] in the context of the spatially inhomogeneous complex Ginzburg–Landau equation, the necessary connection of a k^- -branch prevailing near $X = -\infty$ to a k^+ -branch prevailing near $X = +\infty$ can be achieved at a saddle point of the absolute frequency in the complex X -plane. This necessarily involves a dispersion relation which is second-order in the spatial wavenumber. We will now show how to generalize this theory to the case of a higher-order dispersion relation.

In the previous section we described how the saddle point frequencies $\omega_0^n(X)$ may be defined via a local analysis of the dispersion relation for each value of X in the complex plane. Each mapping $X \mapsto \omega_0^n(X)$ is analytic and may be thought of as a polynomial of order N_n . Then there are N_n pre-images, say $\omega \mapsto X^{(n,p)}(\omega)$ for $1 \leq p \leq N_n$, in the complex X -plane, obtained as the inverse mapping $(\omega_0^n)^{-1}$ of a given contour in the complex ω -plane. We assume, as is standard, that the medium is stable, or at most convectively unstable, towards $X \rightarrow \pm\infty$, which means that $\max_n \operatorname{Im} \omega_0^n(X)$ for X on the real axis exists. Now consider a horizontal L -contour in the complex ω -plane (see Fig. 1b), above

all $\omega_0^n(X)$ for X along the real axis (M -contour). Then the associated contours $X^{(n,p)}(\omega)$ do not cross the real axis (the M -contour) for ω along the L -contour and may therefore be labelled as $X^{(n,p)+}$ or $X^{(n,p)-}$ depending on whether they are confined to the upper or lower half X -planes respectively (see Fig. 1a). When the L -contour is lowered, it approaches the $\omega_0^n(X)$ curves in the ω -plane, and the $X^{(n,p)\pm}$ -curves move in closer to the M -contour in the X -plane. As the L -contour is lowered further, it may be necessary to deform the M -contour to avoid a collision with one of the X -branches, and the $\omega_0^n(X)$ -curves in the ω -plane are then deformed accordingly. Eventually, however, this process cannot be continued as the M -contour gets pinched between an X^+ -branch and an X^- -branch (Fig. 1c); this pinching in the X -plane corresponds, in the ω -plane, to the L -contour passing through a cusp of one of the ω_0^n -curves (Fig. 1d).

The arrangement of the $\omega_0^n(X)$ and $X^{(n,p)\pm}(\omega)$ curves for X along the M -contour and ω along the L -contour is then as follows. In the complex ω -plane (Fig. 1d), the horizontal L -contour lies above all $\omega_0^n(X)$ -curves and passes through a cusp at, say, ω_s^1 of the ω_0^1 -curve. In the complex X -plane (Fig. 1c), the deformed M -contour is pinched at, say, X_s^1 between the curves $X^{(1,1)+}$ and $X^{(1,2)-}$. All other $\omega_0^n(X)$ -curves (for $n \neq 1$) are below the L -contour in the ω -plane, and all other $X^{(n,p)+}$ -curves (respectively $X^{(n,p)-}$ -curves) are above (respectively below) the M -contour in the X -plane. This saddle point is characterized by X_s^1 and ω_s^1 and obeys the condition

$$\frac{d\omega_0^1}{dX}(X_s^1) = 0 \quad \text{and} \quad \omega_s^1 = \omega_0^1(X_s^1), \quad (11)$$

or equivalently

$$\frac{\partial \Omega}{\partial X}(k_s^1, X_s^1) = \frac{\partial \Omega}{\partial k}(k_s^1, X_s^1) = 0 \quad \text{and} \quad \omega_s^1 = \Omega(k_s^1, X_s^1), \quad (12)$$

where k_s^1 is the wavenumber value at which two spatial branches $k(X; \omega_s^1)$ pinch when $X = X_s^1$ along the M -contour, and no other connection between spatial branches is possible along the M -contour.

If this connection at X_s^1 is between a k^+ - and a k^- -branch, then a global mode of the form (10) and frequency $\omega_G = \omega_s^1$ has been found. This is the classical result. It may, however, happen that this connection is between two k^+ - or between two k^- -branches, which does not lead to a global mode solution. Therefore, the above saddle-point criterion in the complex X -plane yields a global mode solution only if the associated $\omega_0^1(X)$ indeed corresponds to the absolute frequency of the system for $X = X_s^1$, *i.e.*, if

$$\omega_{abs}(X_s^1) = \omega_0^1(X_s^1). \quad (13)$$

When condition (13) is not fulfilled, another saddle point must be sought to connect a k^- -branch to a k^+ -branch. Then, the process is continued by lowering the L -contour further in the ω -plane (except in a small region around ω_s^1). Via a similar scenario to previously, this eventually leads to a new pinching of the deformed M -contour at, say, X_s^2 between the curves $X^{(2,1)+}$ and $X^{(2,2)-}$, while the L -contour passes through a cusp at, say, ω_s^2 of the $\omega_0^2(X)$ -curve (see Fig. 1e,f). This new saddle point obeys a criterion similar to (12). Again, a connection between k^+ - and k^- -branches has been found if the additional condition similar to (13) is met. If not, the process goes on by lowering the L -contour even further in the ω plane (except in small regions around ω_s^1 and ω_s^2) until, eventually, a saddle point associated with the local absolute frequency is found.

A systematic implementation of this strategy leads to the following criterion for the global mode frequency ω_G :

$$\omega_G = \omega_{abs}(X_s), \quad (14)$$

$$\frac{\partial \Omega}{\partial X}(k_s, X_s) = \frac{\partial \Omega}{\partial k}(k_s, X_s) = 0 \quad \text{and} \quad \Omega(k_s, X_s) = \omega_{abs}(X_s).$$

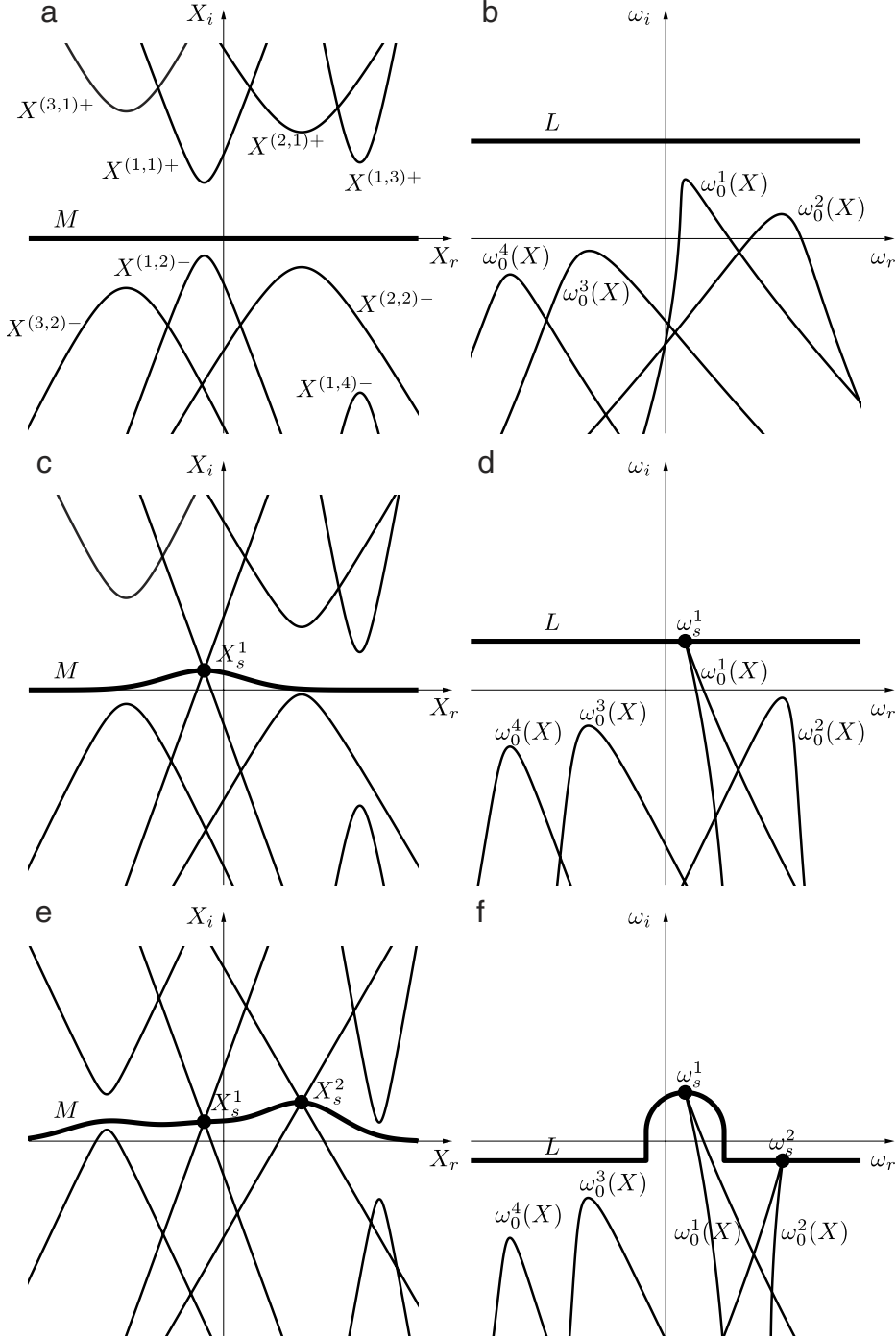


Fig. 1. (b,d,f) Loci of $\omega_0^n(X)$ in the complex ω -plane for X along corresponding L -contour in the complex X -plane. (a,c,e) Loci of $X^{(n,p)\pm}(\omega)$ in the complex X -plane for ω along corresponding M -contour in the complex X_i -plane.

The subtle difference between our new criterion (14) and the classic result

$$\omega_G = \omega_{abs}(X_s) \quad \text{and} \quad \frac{d\omega_{abs}}{dX}(X_s) \quad (15)$$

lies in the fact that, in this more general case, there is no guarantee that the local absolute frequency $\omega_{abs}(X)$ is an analytic function over the entire complex plane, even if the dispersion relation $\mathcal{Q}(k, X)$ is analytic in both k and X .

In the next section we will illustrate our general result by designing the simplest possible partial differential equation exhibiting a local dispersion relation with two saddle points.

4. Toy model

The requirement of more than one saddle point in the dispersion relation leads us to consider a partial differential equation with third-order spatial derivatives

$$\frac{\partial \psi}{\partial t} = a_0(X)\psi + a_1(X)\frac{\partial \psi}{\partial x} + a_2(X)\frac{\partial^2 \psi}{\partial x^2} + a_3(X)\frac{\partial^3 \psi}{\partial x^3}, \quad (16)$$

which corresponds to the dispersion relation

$$\mathcal{Q}(k, X) \equiv ia_0(X) - a_1(X)k - ia_2(X)k^2 + a_3(X)k^3. \quad (17)$$

In the following subsections we will identify the possible choices of the complex coefficients $a_0(X), \dots, a_3(X)$, and discuss a range

of interesting possible behaviours. Our theory will be confirmed by comparison with direct numerical simulation of (16).

4.1. Local dispersion relation

Let us first consider the *local* situation, by assuming a spatially homogeneous configuration where the coefficients a_0, \dots, a_3 do not depend on X .

Causality requires that temporal growth rates are bounded above, i.e. $\Omega_i(k)$ is bounded above when $k \rightarrow \pm\infty$. This condition is met when a_3 is real and $a_{2,r} > 0$. Without loss of generality, we will use $a_3 = 1$ from now on, which corresponds to a rescaling of the temporal coordinate. Thus the dispersion relation is entirely determined by the three complex parameters a_0, a_1 and a_2 (with $a_{2,r} > 0$).

Since the dispersion relation is a third-order polynomial in k , there are two saddle points that satisfy $\partial_k \Omega = 0$. The frequencies and wavenumbers of these saddle points may be written as

$$\omega_0^1 = \omega_0 + \delta\omega_0 \quad \text{and} \quad k_0^1 = k_0 + \delta k_0, \quad (18)$$

$$\omega_0^2 = \omega_0 - \delta\omega_0 \quad \text{and} \quad k_0^2 = k_0 - \delta k_0. \quad (19)$$

Since only three of these four parameters are independent, the local dispersion relation may be entirely specified by the three complex parameters ω_0, k_0 and δk_0 as

$$\omega - \omega_0 = (k - k_0)^3 - 3(\delta k_0)^2(k - k_0), \quad (20)$$

which corresponds to

$$a_0 = i[k_0^3 - 3(\delta k_0)^2 k_0 - \omega_0], \quad (21)$$

$$a_1 = 3[(\delta k_0)^2 - k_0^2], \quad (22)$$

$$a_2 = -3ik_0, \quad (23)$$

$$a_3 = 1. \quad (24)$$

The fourth (dependent) parameter follows as $\delta\omega_0 = -2(\delta k_0)^3$, and the causality condition $a_{2,r} > 0$ is fulfilled for $k_{0,i} > 0$.

In this section we will not consider the detailed local behaviour, in terms of local absolute/convective instability, which depends in a complicated way on the local values of the complex coefficients a_0, \dots, a_3 . However, in the Appendix we will derive the Green's function for the constant-coefficient third-order equation with general complex a_0, \dots, a_3 , which we will then use to find implicit conditions for local stability in the simplified case of real coefficients.

4.2. Local absolute frequency

The dispersion relation (20) is characterized by the two saddle points $\omega_0 \pm \delta\omega_0$ at $k_0 \pm \delta k_0$ (18) and (19), with $\delta\omega_0 = -2(\delta k_0)^3$. In order to work out which one of these saddle points yields the local absolute frequency, the method outlined in the previous section may be used.

The asymptotic behaviour of the dispersion relation (20) is that $\omega \sim k^3$ as $|k| \rightarrow \infty$. Hence, for sufficiently large $\omega_i > 0$, frequencies along a horizontal line $\omega_i = \text{const}$ in the complex ω -plane are associated with two spatial k^+ -branches and one spatial k^- -branch in the complex k -plane: say k^{1+}, k^{2+} and k^{3-} with $\text{Arg}(k^n) \rightarrow (n-1)2\pi/3$ for $\omega_r \rightarrow \infty$.

We will now show that the choice of the local absolute frequency, i.e. $\omega_{abs} = \omega_0^1$ or $\omega_{abs} = \omega_0^2$, only depends on the value of δk_0 . We write $\delta k_0 = \kappa e^{i\phi}$ with $\kappa > 0$, so that $\delta\omega_0 = 2\kappa^3 e^{i(3\phi+\pi)}$, and consider the different ranges of values of ϕ as follows:

- (i) First consider the case $0 < \phi < \pi/3$, which gives $\omega_{0,i}^1 < \omega_{0,i}^2$. When lowering the horizontal line $\omega_i = \text{const}$ in the complex ω -plane, the first saddle-point frequency to be crossed is $\omega_0^2 \equiv \omega_0 - \delta\omega_0$ (see Fig. 2a). For $\omega = \omega_0^2$, two spatial branches meet at $k_0^2 \equiv k_0 - \delta k_0$. Since $\pi < \text{Arg}(-\delta k_0) < 4\pi/3$, the pinch at k_0^2 is between the k^{3-} and the k^{2+} branches (see Fig. 2b). Therefore, $\omega_{abs} = \omega_0^2$ and $k_{abs} = k_0^2$, in this case.
- (ii) Next consider the case $\pi/3 < \phi < 2\pi/3$, which corresponds to $\omega_{0,i}^2 < \omega_{0,i}^1$. When lowering the horizontal line $\omega_i = \text{const}$ in the complex ω -plane, the first saddle-point frequency to be crossed is ω_0^1 (see Fig. 2c). For $\omega = \omega_0^1$, two spatial branches meet at $k_0^1 \equiv k_0 + \delta k_0$. Since $\pi/3 < \text{Arg}(+\delta k_0) < 2\pi/3$, the saddle at k_0^1 is between the k^{1+} and k^{2+} branches (see Fig. 2d). Thus, the (k_0^1, ω_0^1) -saddle does not yield the absolute frequency of the system, and the lowering of the contour $\omega_i = \text{const}$ may be continued until ω_0^2 is reached. For $\omega = \omega_0^2$, two spatial branches meet at $k_0^2 \equiv k_0 - \delta k_0$. The pinch at k_0^2 is between the k^{3-} -branch and a branch that results from the recombination of the two k^+ -branches. Therefore, one has again that $\omega_{abs} = \omega_0^2$ and $k_{abs} = k_0^2$.
- (iii) The case $2\pi/3 < \phi < \pi$ is similar to the case $0 < \phi < \pi/3$, and yields $\omega_{abs} = \omega_0^2$ and $k_{abs} = k_0^2$ by pinching of k^{1+} and k^{3-} .
- (iv) Analysing in turn the three remaining cases $\pi < \phi < 4\pi/3$, $4\pi/3 < \phi < 5\pi/3$ and $5\pi/3 < \phi < 2\pi$, it can be shown that they all yield $\omega_{abs} = \omega_0^1$ and $k_{abs} = k_0^1$.

In summary, for dispersion relation (20) the absolute frequency is obtained by the following criterion:

$$\omega_{abs} = \omega_0^1 \quad \text{when } \delta k_{0,i} < 0, \quad (25)$$

$$\omega_{abs} = \omega_0^2 \quad \text{when } \delta k_{0,i} > 0. \quad (26)$$

Note also that the absolute frequency is the saddle-point frequency of larger imaginary part, unless $\pi/3 < \text{Arg}(\delta k_0) < 2\pi/3$ or $4\pi/3 < \text{Arg}(\delta k_0) < 5\pi/3$ (in which cases the saddle point corresponding to the saddle-point frequency with larger imaginary part is not a pinch point).

4.3. Global modes

For weakly inhomogeneous systems, the coefficients of the governing Eq. (16) depend on the slow spatial variable X . As shown in the previous section, the selection criterion of self-sustained global-mode solutions is based on the double saddle-point criterion (14) in the complex k - and X -planes for the local dispersion relation. We will now further specify the spatial variation of the coefficients (21)–(24) so as to check this criterion for different situations.

For the application of the spatial saddle-point criterion it is convenient to use

$$\omega_0^1(X) = \omega_s^1 + \frac{1}{2}\omega_{s,XX}^1(X - X_s^1)^2, \quad (27)$$

$$\omega_0^2(X) = \omega_s^2 + \frac{1}{2}\omega_{s,XX}^2(X - X_s^2)^2, \quad (28)$$

so that each of $\omega_0^{1,2}(X)$ displays exactly one saddle point at $X_s^{1,2}$ with frequency $\omega_s^{1,2}$. The use of second-order polynomials in X for $\omega_0^{1,2}(X)$ guarantees that the associated $\omega_0(X)$ and $\delta\omega_0(X)$ are also second-order polynomials.

After specifying the frequencies (27) and (28), the spatial distribution of $\delta k_0(X)$ follows from $\delta\omega_0(X) = -2[\delta k_0(X)]^3$, and so evaluation of $\delta k_0(X)$ involves a third-order root. Since $\delta\omega_0(X)$ is a second-order polynomial in X , it displays two zeroes in the complex X -plane, which correspond to two branch points for

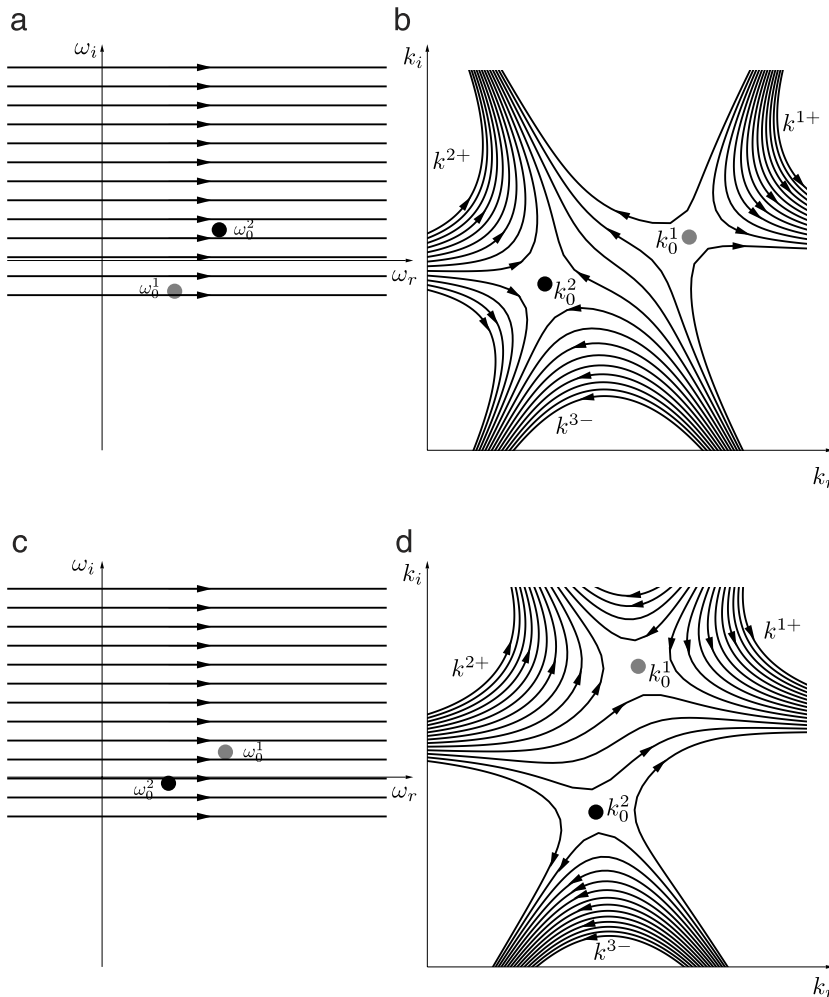


Fig. 2. Temporal branches in complex frequency plane (a,c) and spatial branches in complex wavenumber plane (b,d) for local third-order dispersion relation. (a,b) Configuration with $0 < \text{Arg}(\delta k_0) < \pi/3$, (c,d) with $\pi/3 < \text{Arg}(\delta k_0) < 2\pi/3$.

$\delta k_0(X)$. After choosing the associated branch cuts to lie away from the real X -axis, Eqs. (27) and (28) completely specify the three possible analytic distributions of $\delta k_0(X)$ along the real X -axis, and, for simplicity, the remaining unspecified parameter $k_0(X)$ will be chosen to be a constant in this study.

Tackling the problem the other way round, *i.e.*, by specifying an analytic distribution of $\delta k_0(X)$, would have led to complicated expressions for $\omega_0^{1,2}(X)$, preventing the closed-form determination of saddle points in the complex X -plane. Thus the introduction of a third-order root for $\delta k_0(X)$ seems a small price to pay to retain the simplest possible model. It would have been even more complicated to have started by writing down analytic expressions for the coefficients $a_0(X), \dots, a_3(X)$, and we therefore assert that our approach of starting with quadratic expressions for $\omega_0^{1,2}(X)$ is the best way to understand the behaviour of our system.

So in summary, we have ended up with a particular class of spatially inhomogeneous system (16) that is entirely determined by the seven complex parameters

$$\omega_s^1, \omega_s^2, X_s^1, X_s^2, \omega_{s,XX}^1, \omega_{s,XX}^2 \quad \text{and} \quad k_0, \quad (29)$$

and by the additional choice of one among the three possible $\delta k_0(X)$ -branches. Causality requires that $k_{0,i} > 0$, and the conditions $\text{Im } \omega_{s,XX}^{1,2} < 0$ prevent the medium from being locally absolutely unstable when $X_r \rightarrow \pm\infty$. The method outlined in the previous subsection and based on $\text{Arg}(\delta k_0(X))$ is then used to determine the different regions of the complex X -plane where

the local absolute frequency $\omega_{abs}(X)$ equals either $\omega_0^1(X)$ or $\omega_0^2(X)$. Then, according to the theoretical result (14), the frequencies ω_s^1 and ω_s^2 are possible global mode frequencies if $\omega_s^1 = \omega_{abs}(X_s^1)$ or $\omega_s^2 = \omega_{abs}(X_s^2)$. If both are possible, the mode of larger growth rate is expected to dominate in the long term. In the next section we will confirm these results by comparison with direct numerical simulation.

5. Numerical confirmation

In order to confirm the theoretical results of Section 3, direct numerical simulations of the third-order partial differential equation discussed in Section 4 were carried out for a variety of parameter settings.

The simulations presented below were performed with saddle point frequencies $\omega_0^{1,2}(X)$ determined by

$$\omega_s^1 = 1 + i, \quad X_s^1 = -i, \quad \omega_{s,XX}^1 = -0.02 - 0.10i, \quad (30)$$

and

$$\omega_s^2 = 2, \quad X_s^2 = -2 + i, \quad \omega_{s,XX}^2 = -0.05i. \quad (31)$$

Using $k_0 = i$, each of the three possible $\delta k_0(X)$ -branches was investigated.

Fig. 3 shows isolines of $\omega_{0,i}^{1,2}(X)$ in the complex X -plane. For this configuration, the branch points of $\delta k_0(X)$ (where $\omega_0^1(X) =$

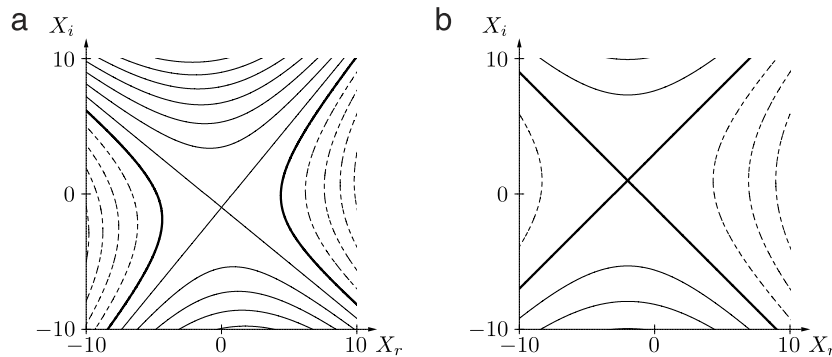


Fig. 3. Isolines of (a) $\omega_{0,i}^1$ and (b) $\omega_{0,i}^2$ in the complex X -plane. Thick line: $\omega_{0,i} = 0$, thin solid lines: $\omega_{0,i} = 1, 2, \dots$, thin dashed lines: $\omega_{0,i} = -1, -2, \dots$

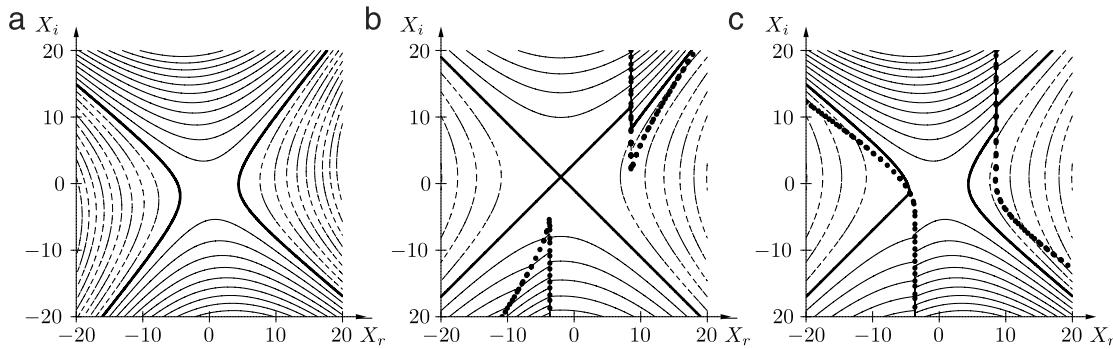


Fig. 4. Isolines of $\omega_{abs,i}(X)$ for (a) branch A, (b) branch B and (c) branch C. Thick line: $\omega_{0,i} = 0$, thin solid lines: $\omega_{0,i} = 2, 4, \dots$, thin dashed lines: $\omega_{0,i} = -2, -4, \dots$. Thick dotted curve represents boundary where the local absolute frequency $\omega_{abs}(X)$ switches between $\omega_0^1(X)$ and $\omega_0^2(X)$.

$\omega_0^2(X)$) are located at $X \simeq 8.51 + 0.95i$ and $X \simeq -3.68 - 5.02i$. Upon choosing the associated branch cuts away from the real X -axis, there are three possible choices for $\delta k_0(X)$ along the real axis (hereafter called branches A, B and C). For each case, the resulting local absolute frequency $\omega_{abs}(X)$ is illustrated by isolines of its imaginary part in the complex X -plane in Fig. 4.

For branch A, it is seen in Fig. 4(a) that $\omega_{abs}(X) = \omega_0^1(X)$ in the entire domain although ω_0^1 is the dominant saddle only in the central region. In this situation, the expected global mode frequency is therefore ω_s^1 .

For branch B (Fig. 4b), the local absolute frequency $\omega_{abs}(X)$ is seen to follow $\omega_0^2(X)$ over a large domain including the real X -axis and both saddles X_s^1 and X_s^2 . It is only in the two wedge-shape regions, starting at the two branch points, that the local absolute frequency equals $\omega_0^1(X)$. The expected global mode frequency is therefore ω_s^2 .

For branch C (Fig. 4c), it is seen that the complex X -plane is partitioned into three regions: $\omega_{abs}(X)$ follows $\omega_0^1(X)$ in the central region and $\omega_0^2(X)$ in the regions extending towards $X = \pm\infty$. Since $\omega_{abs}(X_s^1) = \omega_s^1$, the expected global mode frequency is ω_s^1 in this configuration.

A numerical simulation of (16) performed with coefficient settings corresponding to branch A leads to the global mode shown in Fig. 5(a). Here, the inhomogeneity parameter (4) was chosen as $\epsilon = 0.1$; therefore the interval $-100 < x < 50$ corresponds to $-10 < X < 5$. The numerically determined global frequency $\omega_G = 0.98 + 0.97i$ is very close to the expected $\omega_s^1 = 1 + i$. Numerically, the local wavenumber is computed as $-i\partial_x\psi/\psi$, and its real and imaginary parts are plotted as thick dashed lines in Fig. 5(b) and (c) respectively. The three analytical spatial branches associated with the frequency ω_s^1 are shown by thin lines in the same plots. It is seen that the local wavenumber obtained by direct numerical simulation very closely follows the expected analytical

branches. The imaginary parts of $\omega_{abs}(X)$, $\omega_0^1(X)$ and $\omega_0^2(X)$ along the real X -axis are plotted in Fig. 5(d).

Numerical results corresponding to branch B are shown in Fig. 6. The mode plotted in Fig. 6(a) is synchronized to a global frequency $\omega_G = 2.01 - 0.02i$, in close agreement with the expected $\omega_s^2 = 2$. Its numerically derived local wavenumber follows the associated analytical branches, as shown in Fig. 6(b,c). For this configuration, the local absolute frequency follows $\omega_0^2(X)$ over the entire real X -axis, see Fig. 6(d).

Numerical results corresponding to branch C are shown in Fig. 7. The mode plotted in Fig. 7(a) is synchronized to a global frequency $\omega_G = 1.01 + 0.98i$, again in close agreement with the expected $\omega_s^1 = 1 + i$. Its numerically derived local wavenumber follows the associated analytical branches, as shown in Fig. 7(b,c). For this configuration, the local absolute frequency switches between $\omega_0^1(X)$ and $\omega_0^2(X)$ along the real X -axis, as shown in Fig. 7(d).

In order to study the influence of the inhomogeneity parameter, simulations were carried out for a range of ϵ -values, while keeping the same dependence of the complex coefficients $a_n(X)$ on the slow spatial variable $X = \epsilon x$. Reducing ϵ while keeping the same X -interval thus corresponds to simulations over larger x -intervals. For all three configurations, Table 1 indicates the numerically obtained global mode frequencies ω_G as a function of ϵ and demonstrates that they nicely converge to the theoretical value as $\epsilon \rightarrow 0$.

Finally, results are presented for a configuration where the global frequency is determined by ω_s^2 , while the local absolute frequency is largely dominated by $\omega_0^1(X)$. Using $\omega_s^1 = 0.5 + i$, $X_s^1 = 10 - 8i$, $\omega_{s,XX}^1 = -0.02 - 0.10i$, $\omega_s^2 = 1 + 2i$, $X_s^2 = -5$, $\omega_{s,XX}^2 = 0.02 - 0.05i$ and $k_0 = i$, the absolute frequency distribution shown in Fig. 8 is obtained. The saddle X_s^1 lies within the region where $\omega_{abs}(X) = \omega_0^1(X)$ and the X_s^2 lies within the region where $\omega_{abs}(X) = \omega_0^2(X)$. Since $\omega_{s,i}^2 > \omega_{s,i}^1$, the theory predicts a dominant global mode of frequency $\omega_G \simeq \omega_s^2 = 1 + 2i$. Plotting the local

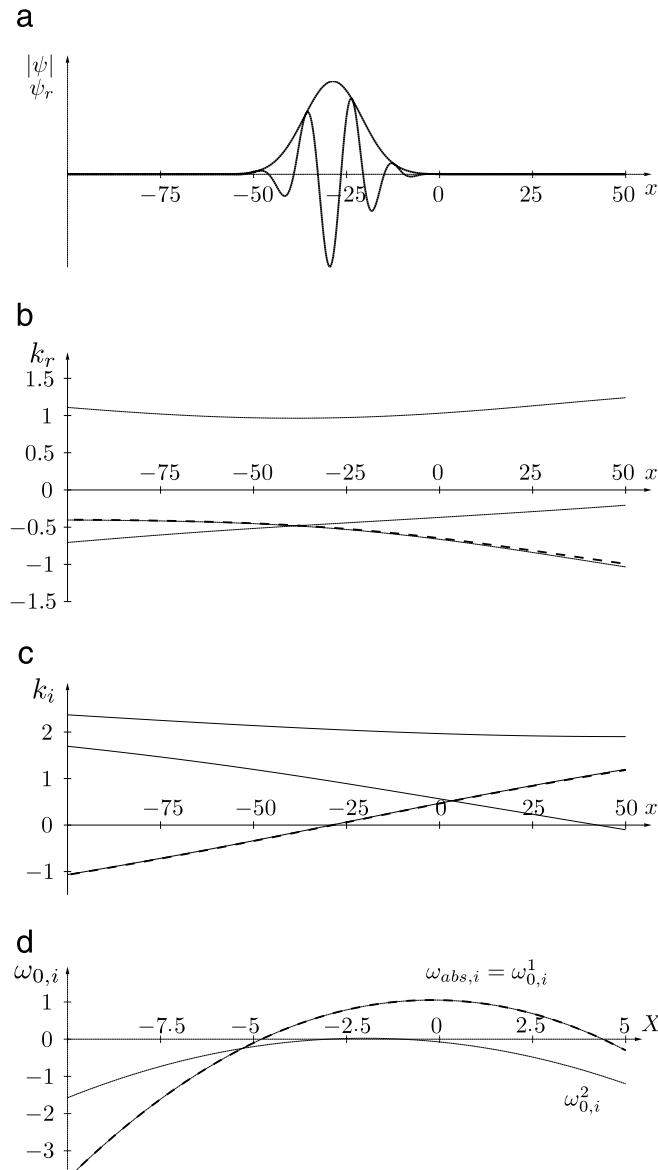


Fig. 5. Structure of global mode obtained by direct numerical simulations for configuration A. (a) Envelope $|\psi|$ and real part ψ_r as functions of streamwise distance. (b) Real part of analytically computed spatial branches (thin lines) together with local wavenumber of simulation (thick dashed line). (c) Imaginary part of analytically computed spatial branches together with local wavenumber of simulation. (d) Imaginary parts of $\omega_{abs}(X)$ (thick dashed line), together with $\omega_0^{1,2}(X)$ (thin lines).

Table 1
Dependence of numerically obtained global mode frequency ω_G on inhomogeneity parameter ϵ .

ϵ	Branch A	Branch B	Branch C
1.0	$0.818 + 0.683i$	$2.133 - 0.217i$	$1.125 + 0.754i$
0.5	$0.924 + 0.833i$	$2.064 - 0.108i$	$1.059 + 0.878i$
0.2	$0.969 + 0.934i$	$2.026 - 0.042i$	$1.025 + 0.952i$
0.1	$0.984 + 0.967i$	$2.013 - 0.021i$	$1.013 + 0.977i$
0.05	$0.992 + 0.984i$	$2.007 - 0.011i$	$1.007 + 0.990i$
0.02	$0.997 + 0.994i$	$2.003 - 0.004i$	$1.003 + 0.998i$
ω_s	$1 + i$	2	$1 + i$

absolute growth rate along the real X -axis (Fig. 8b) shows that the absolute instability of this system is largely dominated by the ω_0^1 -branch. Nevertheless, a direct numerical simulation confirms that a global mode of frequency $\omega_G \simeq 0.92 + 1.97i$ is indeed selected in this configuration (with $\epsilon = 0.2$).

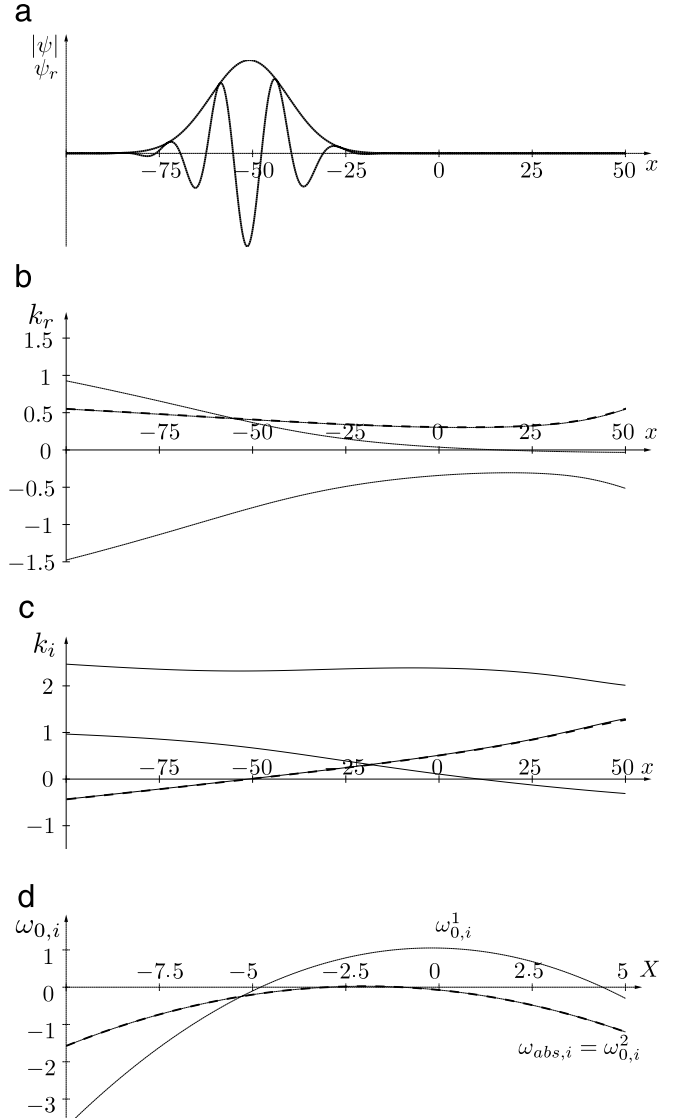


Fig. 6. Same as Fig. 5, using coefficient settings corresponding to branch B.

6. Concluding remarks

In this paper we have developed a global frequency selection criterion, Eq. (14), for weakly non-parallel systems whose local dynamics are controlled by more than one pinch point. Our result differs from the classical condition (e.g. [8]) in that when more than one pinch point must be considered the local absolute frequency, $\omega_{abs}(X)$, is no longer necessarily an analytic function. Of course, our condition has been derived within the context of asymptotically slow variation of the base flow ($\epsilon \rightarrow 0$), whereas in practice ϵ will be small, but nonzero. For the third-order linearized Ginzburg–Landau equation we have therefore compared our criterion with a full numerical solution, and excellent agreement has been obtained for small ϵ (and qualitative agreement even for $\epsilon = 1$).

There are a number of possibilities for further investigation. First, our criterion can be applied to a range of fluid flows, including the rotating-disk boundary layer and the eccentric Taylor–Couette–Poiseuille, as mentioned in the introduction. Second, interesting questions arise about the behaviour of the equivalent signalling problem, in which waves emitted by a fixed-frequency source propagate through the spatially-developing medium. [18] has shown that for the case of a single X -saddle (second-order Ginzburg–Landau) the system response depends on the size of the

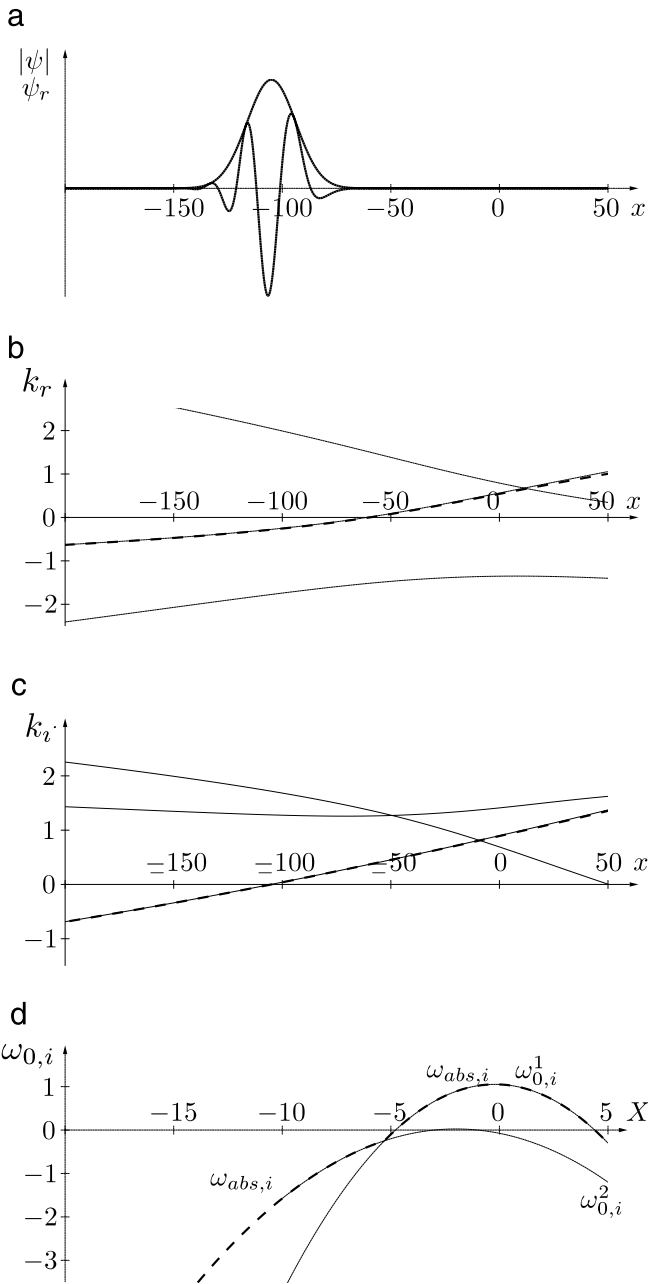


Fig. 7. Same as Fig. 5, using coefficient settings corresponding to branch C.

forcing frequency relative to the marginal frequencies at either end of the single region (if it exists) of local absolute instability. As soon as more than one saddle is present, even richer dynamics are presumably possible. Third, nonlinear analysis in the style of [19] could also be considered. In the nonlinear case, the dynamics are controlled by the local absolute frequency on the real X -axis, but again richer behaviour is presumably possible when multiple regions of local absolute instability are present, especially when those regions become closely spaced relative to the spatial extent of the nonlinear global modes.

It is a great pleasure to dedicate this article to Professor Patrick Huerre. Patrick's contribution to fluid mechanics and to the fluid mechanics community has been, and continues to be, enormous. In particular, his work on hydrodynamic instability theory has shaped the development of the subject for a generation. We also wish to record our gratitude to Patrick for his great personal kindness to us, stretching over many years.

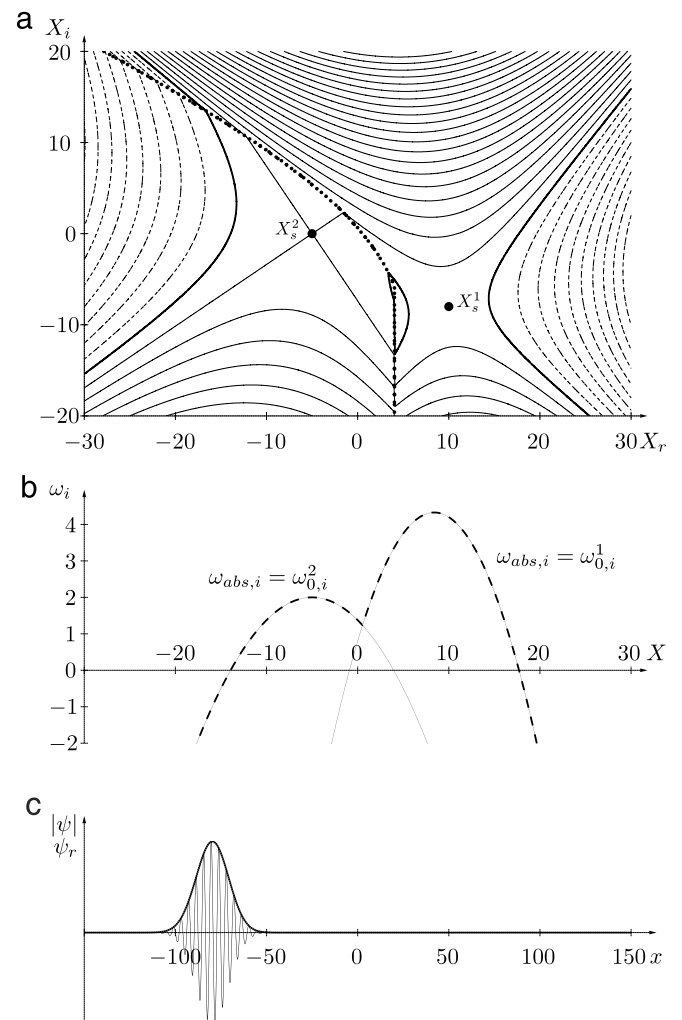


Fig. 8. (a) Isolines of local absolute growth rates in complex X -plane. Thick line: $\omega_{abs,i} = 0$, thin solid lines: $\omega_{abs,i} = 2, 4, \dots$, thin dashed lines: $\omega_{abs,i} = -2, -4, \dots$. Thick dotted curve represents boundary where the local absolute frequency $\omega_{abs}(X)$ switches between $\omega_0^1(X)$ and $\omega_0^2(X)$. (b) Cut along the real X -axis. (c) Structure of numerically selected global mode, for $\epsilon = 0.2$.

Appendix. Green's function

In this Appendix we will derive the Green's function of the forced constant-coefficient third-order equation

$$\frac{\partial \psi}{\partial t} = a_0 \psi + a_1 \frac{\partial \psi}{\partial x} + a_2 \frac{\partial^2 \psi}{\partial x^2} + a_3 \frac{\partial^3 \psi}{\partial x^3} + \delta(x)\delta(t). \quad (\text{A.1})$$

We will then use the Green's function to investigate the local stability of the system.

By taking the Fourier transform of Eq. (A.1) in x , which is defined by

$$\bar{\psi}(k, t) = \int_{-\infty}^{\infty} \psi(x, t) \exp(-ikx) dx, \quad (\text{A.2})$$

and noting that $\bar{\psi}(k, +0) = 1$, thanks to the presence of the $\delta(t)$ term in Eq. (A.1), it is easy to show that the Green's function is given as a Fourier inversion integral in the form

$$\psi(x, t)$$

$$= \frac{\exp(a_0 t)}{2\pi} \int_{-\infty}^{\infty} \exp[(ika_1 - k^2 a_2 - ik^3 a_3)t + ikx] dk. \quad (\text{A.3})$$

In order for this integral to converge, we note that we require a_3 to be real and the real part of a_2 to be positive – these are exactly the necessary causality conditions already set out in Section 4.1.

The trick now is to complete the cube within the exponential. This is done by making the substitution $k = z + c$, for some constant c , and then choosing c so that the coefficient of z^2 within the exponential is zero. This leads to

$$\psi(x, t) = \frac{\exp(a_0 t + At)}{2\pi} \times \int_C \exp\left(iz\left\{x + a_1 t - \frac{a_2^2 t}{3a_3}\right\} - ia_3 t z^3\right) dz, \quad (\text{A.4})$$

where

$$A = \left(\frac{2a_2^3}{27a_3^2} - \frac{a_1 a_2}{3a_3}\right) - \frac{a_2 x}{3a_3 t}, \quad (\text{A.5})$$

and the contour C runs parallel to the z axis. Finally, deforming the contour back to the real axis, we can write the Green's function in terms of the well-known Airy function (see [20] page 447, 10.4.32),

$$\psi(x, t) = \frac{\exp(a_0 t + At)}{(3|a_3|t)^{1/3}} \text{Ai} \times \left\{ -\frac{\text{sgn}(a_3)\left(x + \left[a_1 - \frac{a_2^2}{3a_3}\right]t\right)}{(3|a_3|t)^{1/3}} \right\}. \quad (\text{A.6})$$

This is our closed-form expression for the Green's function—note that here we have taken a_3 to be real, but the remaining coefficients may be complex. In what follows we set $a_3 = 1$, as was done earlier in the paper.

The limiting behaviour of the Green's function follows from the well-known asymptotic behaviour of $\text{Ai}(s)$ for large $|s|$ (see [20] page 448, 10.4.59, 60):

$$\begin{aligned} \text{Ai}(s) &\sim \frac{\exp(-2s^{3/2}/3)}{2\sqrt{\pi}s^{1/4}} \quad \text{as } s \rightarrow \infty \text{ with } |\arg(s)| < \pi, \\ \text{Ai}(-s) &\sim \frac{\sin\left(\frac{2s^{3/2}}{3} + \frac{\pi}{4}\right)}{\sqrt{\pi}s^{1/4}} \end{aligned}$$

as $s \rightarrow \infty$ with $|\arg(s)| < 2\pi/3$. (A.7)

For fixed t the Green's function decays exponentially as $x \rightarrow \infty$ and oscillates and decays algebraically (like $|x|^{-1/4}$) as $x \rightarrow -\infty$. The behaviour for large t is more complicated, but can be determined by setting $x = Vt$ and sending $t \rightarrow \infty$ with V fixed (for simplicity we now consider the special case of the coefficients a_0, a_1, a_2 being real). We define

$$\chi = \frac{a_2^2}{3} - a_1 - V. \quad (\text{A.8})$$

There are then two separate cases to be considered:

1. If $\chi < 0$ then the Airy function oscillates as $t \rightarrow \infty$ (i.e. the second asymptotic behaviour in (A.7)), and the stability of the Green's function is determined only by the exponential term $\exp(a_0 t + At)$ in (A.6). It then follows that the Green's function grows exponentially in time if

$$a_2 \chi > \frac{a_2^3}{9} - 3a_0. \quad (\text{A.9})$$

2. If $\chi > 0$ then the Airy function decays exponentially as $t \rightarrow \infty$ (i.e. the first asymptotic behaviour in (A.7)), and the growth or otherwise of the Green's function is then determined by the behaviour of the product of the exponential term $\exp(a_0 t + At)$

and the Airy function in (A.6). After some algebra it follows that the Green's function grows exponentially in time if

$$a_2 \chi - \frac{2\chi^{3/2}}{\sqrt{3}} > \frac{a_2^3}{9} - 3a_0. \quad (\text{A.10})$$

This provides a sufficient condition for instability when $\chi > 0$, but a necessary condition can be found by noting that the maximum value of the left hand side of (A.10) over all χ is $a_2^3/9$, which occurs when $\chi = a_2^2/3$. This then leads to the necessary condition

$$a_0 > 0 \quad (\text{A.11})$$

for instability.

To summarize, the condition for the Green's function to grow exponentially as $t \rightarrow \infty$ for a given value of observer velocity V is given by the combination of conditions (A.9) and (A.10). In order to detect the occurrence of absolute instability, we simply need to use conditions (A.9) and (A.10) in the case $V = 0$; when this is done, the results are identical to what is obtained using the standard Briggs-Bers procedure of locating the k pinch point and requiring the imaginary part of the corresponding pinch frequency to be positive.

Finally, we note that the Green's function we have derived is only valid in the case of constant coefficients, and is therefore only relevant to the local properties of a spatially inhomogeneous system. Ideally, one would like to be able to determine the Green's function in a spatially-varying case so as to analyse global behaviour, as was done by [21] for the usual second-order linearized Ginzburg Landau equation with linear and quadratic spatial variation of the criticality parameter. Unfortunately, this has not proved possible to date for our third-order equation.

References

- [1] R.J. Briggs, Electron-stream Interaction with Plasmas, M.I.T. Press, Cambridge, Mass., 1964.
- [2] A. Bers, Space-time evolution of plasma instabilities – absolute and convective, in: M.N. Rosenbluth, R.Z. Sagdeev) (Eds.), Handbook of Plasma Physics, North-Holland, Amsterdam, 1983, pp. 451–517.
- [3] P. Huerre, P.A. Monkewitz, Absolute and convective instabilities in free shear layers, J. Fluid Mech. 159 (1985) 151–168.
- [4] P.A. Monkewitz, K.D. Sohn, Absolute instability of hot jets, AIAA J. 26 (1988) 911–916.
- [5] R.J. Lingwood, Absolute instability of the boundary layer on a rotating disk, J. Fluid Mech. 299 (1995) 17–33.
- [6] R.J. Lingwood, An experimental study of absolute instability of the rotating-disk boundary-layer flow, J. Fluid Mech. 314 (1996) 373–405.
- [7] W. Koch, Local instability characteristics and frequency determination on self-excited wake flows, J. Sound Vib. 99 (1985) 53–83.
- [8] P.A. Monkewitz, P. Huerre, J.-M. Chomaz, Global linear stability analysis of weakly non-parallel shear flows, J. Fluid Mech. 251 (1993) 1–20.
- [9] P. Huerre, P.A. Monkewitz, Local and global instabilities in spatially developing flows, Annu. Rev. Fluid Mech. 22 (1990) 473–537.
- [10] J.-M. Chomaz, P. Huerre, L.G. Redekopp, A frequency selection criterion in spatially developing flows, Stud. Appl. Math. 84 (1991) 119–144.
- [11] B.M. Woodley, N. Peake, Global linear stability analysis of thin aerofoil wakes, J. Fluid Mech. 339 (1997) 239–260.
- [12] B. Pier, On the frequency selection of finite-amplitude vortex shedding in the cylinder wake, J. Fluid Mech. 458 (2002) 407–417.
- [13] S. Le Dizès, P. Huerre, J.-M. Chomaz, P.A. Monkewitz, Linear global modes in spatially developing media, Phil. Trans. R. Soc. Lond. A 354 (1996) 169–212.
- [14] B. Pier, P. Huerre, Nonlinear synchronization in open flows, J. Fluids Struct. 15 (2001) 471–480.
- [15] J.J. Healey, On the relation between the viscous and inviscid absolute instabilities of the rotating-disk boundary layer, J. Fluid Mech. 511 (2004) 179–199.
- [16] C. Leclercq, B. Pier, J. Scott, Absolute instabilities in eccentric Taylor-Couette-Poiseuille flow, J. Fluid Mech. 741 (2014) 543–566.
- [17] C.M. Bender, S.A. Orszag, Advanced Mathematical Methods for Scientists and Engineers, McGraw-Hill, New York, 1978.
- [18] B. Pier, Signalling problem in absolutely unstable systems, Theor. Comput. Fluid Dyn. 25 (2011) 7–17.
- [19] B. Pier, P. Huerre, J.-M. Chomaz, Bifurcation to fully nonlinear synchronized structures in slowly varying media, Physica D 148 (2001) 49–96.
- [20] M. Abramowitz, I. Stegun, Handbook of Mathematical Functions, Dover, 1965.
- [21] R.E. Hunt, D.G. Crighton, Instability of flows in spatially developing media, Proc. R. Soc. Lond. A 435 (1991) 109–128.

[A21]

The structural sensitivity of open shear flows calculated with a local stability analysis

M. P. Juniper & B. Pier

European Journal of Mechanics B-Fluids **49**, 426–437 (2015)

doi:10.1016/j.euromechflu.2014.05.011
<https://hal.archives-ouvertes.fr/hal-01084708>



The structural sensitivity of open shear flows calculated with a local stability analysis



Matthew P. Juniper^{a,*}, Benoit Pier^b

^a Department of Engineering, University of Cambridge, Trumpington Street, Cambridge, CB2 1PZ, UK

^b Laboratoire de mécanique des fluides et d'acoustique, École centrale de Lyon - CNRS - Université Claude-Bernard Lyon 1 - INSA Lyon, 36 avenue Guy-de-Collongue, 69134, Écully, France

ARTICLE INFO

Article history:

Available online 5 June 2014

Keywords:

Stability
Structural sensitivity
Adjoint
Global modes

ABSTRACT

The structural sensitivity shows where an instability of a fluid flow is most sensitive to changes in internal feedback mechanisms. It is formed from the overlap of the flow's direct and adjoint global modes. These global modes are usually calculated with 2D or 3D global stability analyses, which can be very computationally expensive. For weakly non-parallel flows the direct global mode can also be calculated with a local stability analysis, which is orders of magnitude cheaper. In this theoretical paper we show that, if the direct global mode has been calculated with a local analysis, then the adjoint global mode follows at little extra cost. We also show that the maximum of the structural sensitivity is the location at which the local k^+ and k^- branches have the same imaginary value. Finally, we use the local analysis to derive the structural sensitivity of two flows: a confined co-flow wake at $Re = 400$, for which it works very well, and the flow behind a cylinder at $Re = 50$, for which it works reasonably well. As expected, we find that the local analysis becomes less accurate when the flow becomes less parallel.

© 2014 Elsevier Masson SAS. All rights reserved.

1. Introduction

Many open flows have a steady solution to the Navier–Stokes equations that becomes unstable above a critical Reynolds number. Usually this instability is driven by one region of the flow, which is called the wavemaker region. The rest of the flow merely responds to forcing from this region. The shape, linear growth rate, and frequency of the instability can be calculated by considering the evolution of small perturbations about the steady solution. This is known as the direct global mode. The direct global mode emanates from the wavemaker region and grows spatially downstream, reaching a maximum at the streamwise location where the spatial growth rate is zero. For example, in the case of the flow behind a cylinder, this direct global mode is a sinuous flapping motion, whose nonlinear development is the familiar Kármán vortex street [1].

The receptivity of the direct global mode to harmonic open loop forcing is given by the last term in Eq. (9) of Ref. [2] and Eq. (7) of Ref. [3]. This term is proportional to the adjoint global mode, which is calculated in the same way as the direct global mode,

but from the adjoint (rather than direct) linearized Navier–Stokes equations. If the perturbation magnitude is measured by the perturbation kinetic energy, which is the conventional approach, then there are only two significant differences between the direct and adjoint equations [2,4]. The first is the sign of the convection term, $V_j \partial v_i / \partial x_j$, and is called *convective non-normality*. The second is the appearance of a transconjugate operator, $v_j \partial V_i / \partial x_j$, and is called *component-type non-normality*. For the flows in this paper, the non-normality is almost entirely convective [4]. In a manner analogous to the direct global mode, the adjoint global mode emanates from the wavemaker region but grows spatially upstream, reaching a maximum at the streamwise location where the adjoint spatial growth rate is zero, or when it meets the upstream boundary. Physically, this reflects the fact that an open loop forcing signal will have most influence on the flow if it impinges on the wavemaker region, and if it is amplified by the flow before it does so.

The sensitivity of the direct global mode to changes in the linearized Navier–Stokes (LNS) equations is given by the penultimate term in Eq. (9) of Ref. [2]. This term is proportional to the overlap between the direct and adjoint global modes and is known as the structural sensitivity. It is equivalent to the sensitivity of the direct global mode to closed-loop feedback between the perturbation and the governing equations in the special case where the sensor and actuator are co-located. For example, in the case of the

* Corresponding author. Tel.: +44 1223 332 585.
E-mail address: mpj1001@cam.ac.uk (M.P. Juniper).

flow behind a cylinder, it can quantify the sensitivity of the flow to the presence of a small control cylinder that produces a small force on the flow in the opposite direction to the velocity perturbation [5,6]. Given that the direct global mode grows downstream of the wavemaker region and that the adjoint global mode grows upstream, the structural sensitivity is clearly maximal in the wavemaker region itself. Indeed, the wavemaker region is often defined as the position of maximum structural sensitivity, although alternative definitions exist [4, Section 4.2.1]. Physically, this reflects the fact that, for a closed loop feedback mechanism to be effective, it requires firstly that the perturbation has significant amplitude at that point, which is quantified by the direct global mode, and secondly that the flow has significant receptivity at that point, which is quantified by the adjoint global mode.

The above concepts were first introduced for the flow behind a cylinder at $Re = 50$ by Hill [5] and Giannetti and Luchini [6,7] and have been extended to include the sensitivity to steady forcing and modifications to the base flow [8–10]. They have also been applied to recirculation bubbles [11] bluff bodies, both incompressible [12] and compressible [13], backward-facing steps [14], forward-facing steps [15], confined wakes [16,17], and a recirculation bubble in a swirling flow [18].

The direct global mode is usually found with a global stability analysis. This typically proceeds in three steps: (i) the Navier–Stokes (N–S) equations are linearized around a steady laminar flow, which is called the base flow and which is usually unstable; (ii) the equations are discretized and expressed as a 2D or 3D matrix eigenvalue problem; (iii) the most unstable eigenmodes are calculated with an iterative technique, such as an Arnoldi algorithm or power iteration. Each eigenmode consists of a complex eigenvalue, which describes the frequency and growth rate, and an eigenfunction, which describes the 2D or 3D shape that grows on top of the base flow until nonlinear effects become significant. As more elaborate configurations are examined, the number of degrees of freedom rapidly approaches millions, so global stability analyses can be extremely computationally expensive [4].

If the base flow varies slowly in the streamwise direction then the global stability analysis can be replaced with a local stability analysis [19]. The WKBJ approximation reduces the LNS equations over the entire domain into a series of local LNS or Orr–Sommerfeld (O–S) equations at each streamwise location. Each local equation can be discretized and expressed as a small matrix eigenvalue problem, which represents the dispersion relation between the complex frequency, ω , and the complex wavenumber, k . At each streamwise location, the value of ω is found for which the dispersion relation is satisfied and for which $d\omega/dk = 0$. This is known as the absolute complex frequency, ω_0 and its imaginary part, ω_{0i} , is the absolute growth rate. The flow is absolutely unstable in regions in which ω_{0i} is positive. These regions exist in every flow that is globally unstable due to hydrodynamic feedback. The frequency and growth rate of the linear global mode can be derived from the streamwise distribution of ω_0 . This also gives a specific spatial position for the region of the flow that, in the context of the local analysis, is known as the wavemaker [20]. Local stability analyses are much quicker and require much less computer memory than global stability analyses because they convert one large matrix eigenvalue problem into several small independent matrix eigenvalue problems. This is why they have been used so widely in the past and why they are still used for flows that are beyond the range of global analyses [21–23].

In all existing papers, the adjoint global mode is calculated with a global stability analysis. The purpose of this paper is to show that, if a local stability analysis is used to calculate the direct global mode, then the adjoint global mode follows at almost no extra cost. This means that, for weakly nonparallel flows, adjoint global modes and structural sensitivities can be estimated quickly and cheaply,

without deriving the adjoint equations. After defining the form of the direct and adjoint equations in Section 2, we derive this result rigorously in Section 3 for the Ginzburg–Landau equation (G–L), which is often used as a simple model for slowly-developing flows. We then apply this to the linearized N–S equations in Section 4 and demonstrate this on two flows in Section 5: a slowly-developing confined wake, and the flow behind a cylinder at $Re = 50$.

2. General form of the direct and adjoint equations

Many different conventions are used to describe direct and adjoint global modes. The convention used here is similar to that used for local stability analysis, so that it is easy to compare the local and global approaches. It differs from that used in Hill [5,24] and Giannetti and Luchini [6] in three ways. The direct and adjoint governing equations (1) and (2) have the same form so that their k^+ and k^- branches in the local analysis have the same physical meaning. The adjoint variables are denoted with \dagger , rather than $+$ or $*$, so that they are not confused with the k^+ branch or with the complex conjugate. The inner product contains a complex conjugate so that the inner product of a complex state variable with itself is a real number.

The linearized governing equations are expressed in terms of the direct state variable, $\psi(x, t)$, the adjoint state variable, $\psi^\dagger(x, t)$, the direct linear spatial operator L , and the adjoint linear spatial operator L^\dagger :

$$\frac{\partial \psi}{\partial t} - L\psi = 0, \quad (1)$$

$$\frac{\partial \psi^\dagger}{\partial t} - L^\dagger\psi^\dagger = 0. \quad (2)$$

(The relationship between the direct and adjoint quantities will be specified in (8), after the inner product (7) has been defined.) Solutions to the initial value problems defined by (1) and (2) can be expressed for $t \in [0, \infty)$ as the sum of the direct and adjoint global modes:

$$\psi(x, t) = \sum_m \hat{\psi}_m(x) \exp(-i\omega_m t), \quad (3)$$

$$\psi^\dagger(x, t) = \sum_n \hat{\psi}_n^\dagger(x) \exp(-i\omega_n t). \quad (4)$$

Substituting (3) into (1) and (4) into (2) gives, for each mode,

$$-i\omega_m \hat{\psi}_m - L\hat{\psi}_m = 0, \quad (5)$$

$$-i\omega_n \hat{\psi}_n^\dagger - L^\dagger \hat{\psi}_n^\dagger = 0. \quad (6)$$

An inner product between state variables f and g is defined as

$$\langle f, g \rangle \equiv \int_{-\infty}^{+\infty} f^* g \, dx. \quad (7)$$

If boundary terms are assumed to be zero, as in Giannetti and Luchini [6], Hill [5], then the relationship between the direct operator, L , and its adjoint, L^\dagger , is given by

$$\langle L\hat{\psi}_m, \hat{\psi}_n^\dagger \rangle = \langle \hat{\psi}_m, L^\dagger \hat{\psi}_n^\dagger \rangle. \quad (8)$$

These definitions determine the relationship between ω_m and ω_n :

$$\langle L\hat{\psi}_m, \hat{\psi}_n^\dagger \rangle = \langle \hat{\psi}_m, L^\dagger \hat{\psi}_n^\dagger \rangle, \quad (9)$$

$$\langle -i\omega_m \hat{\psi}_m, \hat{\psi}_n^\dagger \rangle = \langle \hat{\psi}_m, -i\omega_n \hat{\psi}_n^\dagger \rangle, \quad (10)$$

$$i\omega_m^* \langle \hat{\psi}_m, \hat{\psi}_n^\dagger \rangle = -i\omega_n \langle \hat{\psi}_m, \hat{\psi}_n^\dagger \rangle, \quad (11)$$

$$(\omega_m^* + \omega_n) \langle \hat{\psi}_m, \hat{\psi}_n^\dagger \rangle = 0. \quad (12)$$

This is the bi-orthogonality condition: every adjoint mode is orthogonal to every direct mode, except for the pairs that satisfy $\omega_n = -\omega_m^*$.

2.1. Structural sensitivity

We would like to find the change in the direct eigenvalue, $\delta\omega_m$, when there is a small change, δL , in the direct linear operator, L :

$$\delta\omega_m = \lim_{\epsilon \rightarrow 0} \left(\frac{\omega_m(L + \epsilon\delta L) - \omega_m(L)}{\epsilon} \right). \quad (13)$$

This perturbation causes perturbed eigenvalues, $\omega_m + \epsilon\delta\omega_m$, perturbed direct eigenmodes, $\hat{\psi}_m + \epsilon\delta\hat{\psi}_m$, and perturbed adjoint eigenmodes, $\hat{\psi}_n^\dagger + \epsilon\delta\hat{\psi}_n^\dagger$. We premultiply (5) by $\hat{\psi}_n^\dagger$ and substitute in the perturbed variables:

$$\begin{aligned} & (\langle \hat{\psi}_n^\dagger + \epsilon\delta\hat{\psi}_n^\dagger, (i\omega_m + i\epsilon\delta\omega_m)(\hat{\psi}_m + \epsilon\delta\hat{\psi}_m) \rangle \\ & + \langle (\hat{\psi}_n^\dagger + \epsilon\delta\hat{\psi}_n^\dagger), (L + \epsilon\delta L)(\hat{\psi}_m + \epsilon\delta\hat{\psi}_m) \rangle) = 0. \end{aligned} \quad (14)$$

Retaining terms at order ϵ and making use of (5), (6), and the bi-orthogonality condition (12) leads to

$$\delta\omega_m = i \frac{\langle \hat{\psi}_m^\dagger, \delta L \hat{\psi}_m \rangle}{\langle \hat{\psi}_m^\dagger, \hat{\psi}_m \rangle}. \quad (15)$$

This is the penultimate term in Eq. (9) of [2], but expressed in the notation of this paper. The operator δL describes a generic perturbation to the operator, L . If one considers a perturbation that is localized in space then the structural sensitivity [6, Section 8] is defined as:

$$\nabla_L \omega_m \equiv i \frac{\hat{\psi}_m^* \hat{\psi}_m^\dagger}{\langle \hat{\psi}_m^\dagger, \hat{\psi}_m \rangle}, \quad (16)$$

where the numerator is a function of x and the eigenfunctions are usually normalized such that the denominator is 1. This is shown graphically in [2, Fig 5 a,b].

3. Local analysis of the direct and adjoint Ginzburg–Landau equations

For the Ginzburg–Landau (G–L) equation, the operator L acting on $\psi(x, t)$ in (1) is:

$$\frac{\partial \psi}{\partial t} = L\psi \equiv a_0(x)\psi + a_1(x)\frac{\partial \psi}{\partial x} + a_2(x)\frac{\partial^2 \psi}{\partial x^2}, \quad (17)$$

where a_0 , a_1 and a_2 are complex coefficients that depend on the spatial coordinate, x . The aim of this section is to perform WKBJ analysis on the direct and adjoint G–L equations in order to determine ω_n^\dagger in terms of ω_m and k_n^\dagger in terms of k_m , and to confirm that higher-order terms in the WKBJ analysis do not need to be considered. In this section, the subscripts m and n will be dropped because the adjoint mode constructed in Section 3.6 is always the bi-orthogonal counterpart of the direct mode constructed in Section 3.5.

3.1. Local dispersion relation of the direct G–L equation

In slowly-evolving flows, the coefficients a_0 , a_1 and a_2 in (17) depend only on a slow spatial coordinate $X = \epsilon x$. The small parameter $\epsilon \ll 1$ measures the ratio between typical instability and typical inhomogeneity length scales. Implementing a WKBJ analysis, a global-mode solution of (17) is sought in the form

$$\psi \sim A(X) \exp \left(\frac{i}{\epsilon} \int^X k(u) du - i\omega t \right), \quad (18)$$

where the local complex wavenumber $k(X)$ is a solution of the local dispersion relation:

$$\omega = \Omega(k, X) \equiv ia_0(X) - a_1(X)k - ia_2(X)k^2. \quad (19)$$

The dispersion relation can also be written in terms of the local absolute frequency, $\omega_0(X)$, the local absolute wavenumber, $k_0(X)$, and the local curvature, $\omega_{kk}(X)$:

$$\Omega(k, X) = \omega_0(X) + \frac{1}{2} \omega_{kk}(X) (k - k_0(X))^2, \quad (20)$$

where $\omega_0 = ia_0 - ia_1^2/4a_2$, $k_0 = ia_1/2a_2$, and $\omega_{kk} = -2ia_2$. (Equivalently, $a_0 = -i\omega_0 - i\omega_{kk}k_0^2/2$, $a_1 = \omega_{kk}k_0$, and $a_2 = i\omega_{kk}/2$.) This shows how the coefficients of the G–L equation can be derived from the dispersion relation associated with a given weakly developing shear flow by taking a Taylor expansion around the saddle point, which is at (ω_0, k_0) and by definition has $d\omega/dk = 0$. Eq. (20) can be rearranged to give k as an explicit function of ω :

$$k^\pm(X, \omega) = k_0(X) \pm \sqrt{2 \frac{\omega - \omega_0(X)}{\omega_{kk}(X)}}. \quad (21)$$

Here, branch cuts of (21) are taken along positive real values of the argument of the square root. This choice of branch cut ensures that, in stable or convectively unstable regions of the complex X -plane, the above definition coincides with the usual labelling of spatial branches based on causality considerations, for which a k^+ -branch corresponds to a downstream response to localized harmonic forcing, and a k^- -branch corresponds to an upstream response.

3.2. Calculation of the adjoint of the G–L equation

For the G–L equation, the adjoint operator, L^\dagger , is found by expanding $\langle \hat{\psi}^\dagger, L\hat{\psi} \rangle$, using (7), and then integrating by parts:

$$\begin{aligned} \langle \hat{\psi}^\dagger, L\hat{\psi} \rangle &= \int_{-\infty}^{+\infty} \hat{\psi}^{\dagger *} \left(a_0 \hat{\psi} + a_1 \frac{\partial \hat{\psi}}{\partial x} + a_2 \frac{\partial^2 \hat{\psi}}{\partial x^2} \right) dx \\ &= \int_{-\infty}^{+\infty} \left(a_0 \hat{\psi}^{\dagger *} - \frac{\partial}{\partial x} (a_1 \hat{\psi}^{\dagger *}) + \frac{\partial^2}{\partial x^2} (a_2 \hat{\psi}^{\dagger *}) \right) \times \hat{\psi} dx, \end{aligned} \quad (22)$$

in which the boundary terms have been set to zero with appropriate boundary conditions. The adjoint operator is found by noting that, from (8), $\langle \hat{\psi}^\dagger, L\hat{\psi} \rangle = \langle L^\dagger \hat{\psi}^\dagger, \hat{\psi} \rangle$, and therefore that

$$L^\dagger \hat{\psi}^\dagger = a_0^* \hat{\psi}^\dagger - \frac{\partial}{\partial x} (a_1^* \hat{\psi}^\dagger) + \frac{\partial^2}{\partial x^2} (a_2^* \hat{\psi}^\dagger) \quad (24)$$

$$= a_0^\dagger \hat{\psi}^\dagger + a_1^\dagger \frac{\partial \hat{\psi}^\dagger}{\partial x} + a_2^\dagger \frac{\partial^2 \hat{\psi}^\dagger}{\partial x^2}, \quad (25)$$

where $a_0^\dagger \equiv a_0^* - \partial a_1^*/\partial x + \partial^2 a_2^*/\partial x^2$, $a_1^\dagger \equiv -a_1^* + 2\partial a_2^*/\partial x$, and $a_2^\dagger \equiv a_2^*$. These expressions are general and do not necessarily assume weak spatial inhomogeneities.

3.3. Local dispersion relation of the adjoint problem

Under the quasi-parallel-flow assumption, the coefficients of the direct G–L equations depend only on the slow spatial coordinate $X = \epsilon x$. Eq. (24) becomes:

$$\begin{aligned} L^\dagger \hat{\psi}^\dagger &= a_0^* \hat{\psi}^\dagger - a_1^* \frac{\partial \hat{\psi}^\dagger}{\partial x} - \hat{\psi}^\dagger \epsilon \frac{\partial a_1^*}{\partial X} \\ &\quad + a_2^* \frac{\partial^2 \hat{\psi}^\dagger}{\partial X^2} + 2\epsilon \frac{\partial a_2^*}{\partial X} \frac{\partial \hat{\psi}^\dagger}{\partial x} + \hat{\psi}^\dagger \epsilon^2 \frac{\partial^2 a_2^*}{\partial X^2}. \end{aligned} \quad (26)$$

When performing a WKBJ analysis of the adjoint G–L equation (2), the adjoint operator (24) must be expanded in powers of ϵ as

$$\begin{aligned} L^\dagger \left(\frac{\partial}{\partial X}; X \right) &= L_0^\dagger \left(\frac{\partial}{\partial X}; X \right) \\ &\quad + \epsilon L_1^\dagger \left(\frac{\partial}{\partial X}; X \right) + \epsilon^2 L_2^\dagger \left(\frac{\partial}{\partial X}; X \right), \end{aligned} \quad (27)$$

By inspection of (26), L_0^\dagger , L_1^\dagger , and L_2^\dagger are:

$$L_0^\dagger \left(\frac{\partial}{\partial X}; X \right) = a_0^*(X) - a_1^*(X) \frac{\partial}{\partial X} + a_2^*(X) \frac{\partial^2}{\partial X^2}, \quad (28)$$

$$L_1^\dagger \left(\frac{\partial}{\partial X}; X \right) = -\frac{\partial a_1^*(X)}{\partial X} + 2 \frac{\partial a_2^*(X)}{\partial X} \frac{\partial}{\partial X}, \quad (29)$$

$$L_2^\dagger \left(\frac{\partial}{\partial X}; X \right) = \frac{\partial^2 a_2^*(X)}{\partial X^2}. \quad (30)$$

A solution of the adjoint problem is then sought in the form

$$\begin{aligned} \psi^\dagger \sim & \left(A_0^\dagger(X) + \epsilon A_1^\dagger(X) + \epsilon^2 A_2^\dagger(X) + \dots \right) \\ & \times \exp \left(\frac{i}{\epsilon} \int^X k(u) du - i\omega^\dagger t \right). \end{aligned} \quad (31)$$

Substituting (28)–(31) into the governing adjoint equation (2) gives, at leading-order,

$$-i\omega^\dagger = a_0^*(X) - a_1^*(X)ik(X) - a_2^*(X)k^2(X) = L_0^\dagger(ik; X). \quad (32)$$

In a manner similar to the direct problem, the adjoint dispersion relation can be rewritten as

$$\omega^\dagger = \Omega_0^\dagger(k, X) \equiv ia_0^*(X) + a_1^*(X)k(X) - ia_2^*(X)k^2(X) \quad (33)$$

$$= \omega_0^\dagger(X) + \frac{1}{2} \omega_{kk}^\dagger(X) (k - k_0^\dagger(X))^2, \quad (34)$$

where

$$\omega_0^\dagger(X) = ia_0^*(X) - \frac{i}{4} a_1^{*2}(X)/a_2^*(X) = -\omega_0^*(X), \quad (35)$$

$$k_0^\dagger(X) = -\frac{i}{2} a_1^*(X)/a_2^*(X) = k_0^*(X), \quad (36)$$

$$\omega_{kk}^\dagger(X) = -2ia_2^*(X) = -\omega_{kk}^*(X). \quad (37)$$

The higher-order terms L_1^\dagger and L_2^\dagger do not appear in this adjoint dispersion relation, because it is obtained at leading order in the WKBJ analysis. The L_1^\dagger component enters only when working out, at $O(\epsilon^1)$, the solvability condition that governs the leading-order amplitude term $A_0^\dagger(X)$ in (31). This amplitude equation is

$$\begin{aligned} \Omega_{0,k}^\dagger(k(X), X) \frac{dA_0^\dagger}{dX} + \frac{1}{2} \Omega_{0,kk}^\dagger(k(X), X) \frac{dk}{dX} A_0^\dagger(X) \\ + i\Omega_1^\dagger(k(X), X) A_0^\dagger(X) = 0, \end{aligned} \quad (38)$$

where $\Omega_1^\dagger(k, X) \equiv iL_1^\dagger(ik, X)$. Higher-order expansions will not be derived further, however, because the results of this paper require only the local dispersion relations. Turning points, where $d\Omega_0^\dagger/dk = 0$, are not affected by the higher-order expansions.

The key point of this section is that, at leading order, the dispersion relation of the adjoint G-L equation is the same as that of the direct G-L equation but with the substitutions (35)–(37).

3.4. Adjoint of a generic polynomial PDE

The development in Sections 3.1–3.3 is for a parabolic PDE but holds for any polynomial PDE in one spatial dimension, as shown in this section. For a generic polynomial PDE, the direct operator (17) can be written as

$$\frac{\partial \psi}{\partial t} = L\psi \equiv \sum_j a_j(x) \frac{\partial^j \psi}{\partial x^j}, \quad (39)$$

and, after integration by parts, the adjoint operator can be written as

$$\frac{\partial \psi^\dagger}{\partial t} = L^\dagger \psi^\dagger \equiv \sum_j (-1)^j \frac{\partial^j}{\partial x^j} (a_j^*(x) \psi^\dagger). \quad (40)$$

If the coefficients a_j^* do not depend on x then $L^\dagger \psi^\dagger = \sum_j (-1)^j a_j^* \frac{\partial^j}{\partial x^j} \psi^\dagger$ and (35)–(37) follow immediately. If the coefficients a_j^* depend on x , then the x -derivatives of $a_j^*(x) \psi^\dagger$ produce extra terms:

$$L^\dagger \psi^\dagger = \left(a_0^*(x) - \frac{\partial a_1^*(x)}{\partial x} + \frac{\partial^2 a_2^*(x)}{\partial x^2} - \frac{\partial^3 a_3^*(x)}{\partial x^3} + \dots \right) \psi^\dagger \quad (41)$$

$$+ \left(-a_1^*(x) + 2 \frac{\partial a_2^*(x)}{\partial x} - 3 \frac{\partial^2 a_3^*(x)}{\partial x^2} + \dots \right) \frac{\partial \psi^\dagger}{\partial x} \quad (42)$$

$$+ \left(a_2^*(x) - 3 \frac{\partial a_3^*(x)}{\partial x} + \dots \right) \frac{\partial^2 \psi^\dagger}{\partial x^2} \quad (43)$$

$$+ \left(-a_3^*(x) + \dots \right) \frac{\partial^3 \psi^\dagger}{\partial x^3} + \dots \quad (44)$$

However, under the assumption of slow spatial development, the n^{th} derivatives of the coefficients a_j are of order ϵ^n , so the local dispersion relation that is obtained at leading order is the same as that obtained for constant coefficients. This proves that the relations $\omega_0^\dagger(X) = -\omega_0^*(X)$, $k_0^\dagger(X) = k_0^*(X)$ and $\omega_{kk}^\dagger(X) = -\omega_{kk}^*(X)$ in (35)–(37) hold for systems governed by any dispersion relation that is polynomial in k . We therefore expect this result to remain generally valid in the case of dispersion relations that are analytic in k over large parts of the complex k -plane. We assume that dispersion relations derived from the linearized Navier–Stokes equations in slowly-varying flows fall into this category.

3.5. Global mode of the direct G-L equation with a local analysis

A linear global mode is a global solution of the governing equation (1) with the form $\psi(x, t) \sim \exp(-i\omega_g t)$ for a complex global frequency ω_g . Assuming that the slowly-varying coefficients $\omega_0(X)$, $k_0(X)$ and $\omega_{kk}(X)$ are known along the real X -axis, a WKBJ approximation of the global mode can be sought as in (18) with $\omega = \omega_g$. This integral is most easily evaluated in the complex X -plane, as shown in the top half of Fig. 1a. (The bottom half is for the adjoint mode.) The point X_s is a saddle point of $\omega_0(X)$ and the diagonal lines have the same value of ω_{0i} as the saddle point. Huerre and Monkewitz [19] have shown that the frequency of the dominant global mode, ω_g , is equal to $\omega_s + O(\epsilon)$, where $\omega_s = \omega_0(X_s)$.

At a given ω_g , there are two valid solutions to k , known as the k^+ and k^- spatial branches, and there are therefore two independent WKBJ approximations

$$\psi^+ \sim A^+(X) \exp \left(\frac{i}{\epsilon} \int_{X_s}^X k^+(u, \omega_g) du - i\omega_g t \right) \quad (45)$$

and

$$\psi^- \sim A^-(X) \exp \left(\frac{i}{\epsilon} \int_{X_s}^X k^-(u, \omega_g) du - i\omega_g t \right). \quad (46)$$

These two WKBJ approximations are singular at the saddle point X_s , which is a double turning point of the dispersion relation. From this double turning point, four Stokes lines emerge, defined by

$$\text{Im} \int_{X_s}^X [k^+(u, \omega_s) - k^-(u, \omega_s)] du = 0. \quad (47)$$

Along these Stokes lines both WKBJ approximations remain of the same order of magnitude, while inside the sectors delimited by

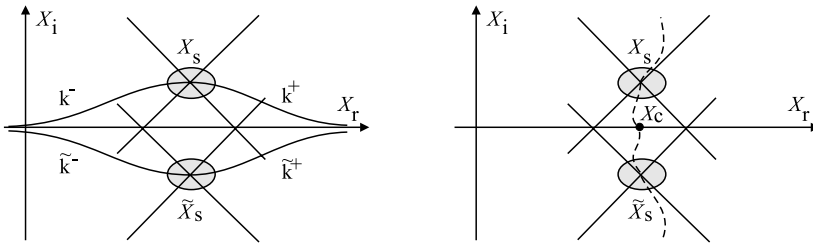


Fig. 1. (a) Left frame: integration paths in the complex X -plane for the direct (top) and adjoint (bottom) cases. The diagonal lines represent the boundaries between valleys (left and right of the lines) and hills (above and below the lines). The integration paths must pass through the valleys in order to obey causality. (b) Right frame: branch cuts (dashed lines) in the complex X -plane.

the Stokes lines one approximation is exponentially larger than the other. Following classical WKBJ theory [25] the global mode must be sought as a linear combination of the two independent solutions, $\psi = C^+ \psi^+ + C^- \psi^-$, within each sector delimited by these Stokes lines.

When $X \rightarrow +\infty$, the solution must be dominated by a k^+ branch and is therefore made up of the subdominant ψ^+ approximation. The global mode is therefore of the form $\psi = C^+ \psi^+$ (with $C^- = 0$) in the region starting from the Stokes lines issuing from X_s and extending to $X = +\infty$. (See Pier [26] for a detailed analysis of a similar case.) For similar reasons, the global mode is of the form $\psi = C^- \psi^-$ (with $C^+ = 0$) in the region starting from the Stokes lines issuing from X_s and extending to $X = -\infty$.

Consequently, the global mode is approximated by the WKBJ approximation $C^- \psi^-$ along the semi-infinite path from X_s to $-\infty$, and by $C^+ \psi^+$ along the semi-infinite path from X_s to $+\infty$. Since the global mode must be continuous at X_s , the coefficient C^+ on the path from X_s to $+\infty$ must equal C^- on the path from X_s to $-\infty$ (this includes higher-order terms; asymptotic matching of the two WKBJ-expansions prevailing on each side of the saddle point can be rigorously carried out via an inner layer). After rescaling the solution so that $C^+ = C^- = 1$, the direct global mode is approximated by ψ^+ along the semi-infinite path from X_s to $X = +\infty$ and by ψ^- along the semi-infinite path from X_s to $X = -\infty$.

Finally, the approximations of the direct global mode obtained along the path from $X = -\infty$ to $X = +\infty$, passing through the saddle point X_s , must be continued onto the real X -axis. When crossing a Stokes line, a subdominant WKBJ solution becomes dominant but remains a valid asymptotic approximation. Therefore the global mode is approximated by ψ^- in the sectors adjacent to the sector extending to $X = -\infty$, and by ψ^+ in the sectors adjacent to the sector extending to $X = +\infty$. Since there are four Stokes lines and two branch cuts emanating from the saddle point, X_s , one may safely assume that one branch cut crosses the real axis at X_c and that no more than one Stokes line crosses the real axis on either side of X_c . It follows that the global mode is approximated by ψ^- for $X < X_c$ along the real axis and by ψ^+ for $X > X_c$. At X_c there is a smooth relabelling of the k -branches, but otherwise nothing special happens across the branch cut. This division of the integration path becomes important in Section 3.7.

3.6. Global mode of the adjoint G-L equation with a local analysis

Following the same development as Section 3.5, the adjoint global mode is sought as

$$\psi^\dagger \sim A^\dagger(X) \exp \left[\frac{i}{\epsilon} \int_{X_s}^X k^\dagger(u; \omega_g^\dagger) du - i\omega_g^\dagger t \right]. \quad (48)$$

We again assume that the coefficients $\omega_0(X)$, $k_0(X)$ and $\omega_{kk}(X)$ can be continued analytically into the complex plane and use the relationships (35)–(37). This is represented in the bottom half of Fig. 1(a). We obtain the result that $\omega_g^\dagger = \omega_s^\dagger + O(\epsilon)$, where $\omega_s^\dagger =$

$\omega_0^\dagger(X_s^\dagger)$ with $d\omega_0^\dagger/dX|_{X_s^\dagger} = 0$. The local wavenumber in (48) follows the $k^{+/-}$ branch for $X \rightarrow -\infty$ and the $k^{+/-}$ branch for $X \rightarrow +\infty$. Here, these branches are obtained from the local adjoint dispersion relation (36) as

$$k^{\pm\pm}(X, \omega_g^\dagger) = k_0^\dagger(X) \pm \sqrt{2 \frac{\omega_g^\dagger - \omega_0^\dagger(X)}{\omega_{kk}^\dagger(X)}}. \quad (49)$$

For real values of X , substituting (35)–(37) into (49) leads to the following relationship between the local branches of the adjoint and the direct global modes:

$$k^{\pm\pm}(X; \omega_g^\dagger) = (k^\mp(X; \omega_g))^*. \quad (50)$$

This relationship guarantees that a branch cut of the adjoint $k^{\pm\pm}$ crosses the real X -axis at the same location, X_c , as a branch cut of the direct $k^{\pm\pm}$.

The two adjoint spatial branches $k^{\pm\pm}$ lead to two independent WKBJ approximations

$$\psi^{\dagger+} \sim A^{\dagger+}(X) \exp \left(\frac{i}{\epsilon} \int_{X_s^\dagger}^X k^{\dagger+}(u, \omega_g^\dagger) du - i\omega_g^\dagger t \right) \quad (51)$$

and

$$\psi^{\dagger-} \sim A^{\dagger-}(X) \exp \left(\frac{i}{\epsilon} \int_{X_s^\dagger}^X k^{\dagger-}(u, \omega_g^\dagger) du - i\omega_g^\dagger t \right). \quad (52)$$

Following similar arguments to those in the previous section, it can be shown that the adjoint global mode is approximated along the real axis by $\psi^{\dagger-}$ for $X < X_c$ and by $\psi^{\dagger+}$ for $X > X_c$. For $X < X_c$, the direct global mode follows k^- and the adjoint global mode follows k^+ , which is $(k^+)^*$. For $X > X_c$, the direct global mode follows k^+ and the adjoint global mode follows k^+ , which is $(k^-)^*$. At X_c , there is a smooth re-labelling of the k -branches.

The final result, that the adjoint mode follows $(k^+)^*$ upstream of the wavemaker and $(k^-)^*$ downstream, is simple and may seem trivial. However, we are not aware of this result being stated or used before in stability analysis, despite its potential usefulness.

3.7. Calculating the structural sensitivity of the G-L equation with a local analysis

The structural sensitivity (16) is the product of the direct and adjoint global modes. For X along the real axis, the direct global mode found from the local analysis takes the form

$$\psi \sim \begin{cases} A^+(X) \exp \left[\frac{i}{\epsilon} \int_{X_s}^X k^+ du \right] & \text{for } X > X_c, \\ A^-(X) \exp \left[\frac{i}{\epsilon} \int_{X_s}^X k^- du \right] & \text{for } X < X_c. \end{cases} \quad (53)$$

After splitting the integrals from X_s to X into two integrals from X_s to X_c and from X_c to X , and using the fact that the k^+ -branch on the

right of the branch cut is identical to the k^- -branch on the left of the branch cut, the linear global mode may be renormalized as

$$\psi \sim \begin{cases} A^+(X) \exp \left[\frac{i}{\epsilon} \int_{X_c}^X k^+ du \right] & \text{for } X > X_c, \\ A^-(X) \exp \left[\frac{i}{\epsilon} \int_{X_c}^X k^- du \right] & \text{for } X < X_c. \end{cases} \quad (54)$$

Similarly, the adjoint global mode found from the local analysis takes the following form along the real axis

$$\psi^\dagger \sim \begin{cases} A^{\dagger+}(X) \exp \left[\frac{i}{\epsilon} \int_{X_c}^X k^{\dagger+} du \right] & \text{for } X > X_c, \\ A^{\dagger-}(X) \exp \left[\frac{i}{\epsilon} \int_{X_c}^X k^{\dagger-} du \right] & \text{for } X < X_c. \end{cases} \quad (55)$$

With the identity (50), it follows that

$$\psi^\dagger \sim \begin{cases} A^{\dagger+}(X) \exp \left[\frac{i}{\epsilon} \int_{X_c}^X k^{-*} du \right] & \text{for } X > X_c, \\ A^{\dagger-}(X) \exp \left[\frac{i}{\epsilon} \int_{X_c}^X k^{+*} du \right] & \text{for } X < X_c. \end{cases} \quad (56)$$

The structural sensitivity $\nabla_L \omega_m$ from (16) may now be obtained by computing the product $\psi^* \psi^\dagger$. Noting that $(\exp(iz))^* = \exp(-iz^*)$ yields

$$\nabla_L \omega_m \propto \begin{cases} A^{\dagger+}(X) [A^+(X)]^* \exp \left[\frac{i}{\epsilon} \int_{X_c}^X (k^- - k^+)^* du \right] & \text{for } X > X_c, \\ A^{\dagger-}(X) [A^-(X)]^* \exp \left[\frac{i}{\epsilon} \int_{X_c}^X (k^+ - k^-)^* du \right] & \text{for } X < X_c. \end{cases} \quad (57)$$

The magnitude of the structural sensitivity is therefore obtained as

$$|\nabla_L \omega_m| \propto \begin{cases} B(X) \exp \left[\frac{1}{\epsilon} \int_{X_c}^X \operatorname{Im}(k^- - k^+) du \right] & \text{for } X > X_c, \\ B(X) \exp \left[\frac{1}{\epsilon} \int_{X_c}^X \operatorname{Im}(k^+ - k^-) du \right] & \text{for } X < X_c, \end{cases} \quad (58)$$

where $B(X)$ is a slowly varying coefficient.

The wavenumbers k^+ and k^- are given by (21) with $\omega = \omega_s$. In a configuration that, when $X \rightarrow \pm\infty$, is stable or at most convectively unstable, $\operatorname{Im}(k^+ - k^-) > 0$ for sufficiently large $|X|$ on the real axis. Therefore the structural sensitivity necessarily decays for $X \rightarrow \pm\infty$ and the maximum structural sensitivity corresponds to the location where $\operatorname{Im}(k^+ - k^-) = 0$. For the G-L equation, $\operatorname{Im}(k^+ - k^-)$ is always positive, due to our definition of the branch cut, and vanishes only at X_c . This means that $|\nabla_L \omega_m|$ is a maximum at X_c . In general, it is true that the maximum structural sensitivity is found where $\operatorname{Im}(k^+ - k^-) = 0$. However, it is not necessarily located on the branch cut, because the location where $\operatorname{Im}(k^+ - k^-) = 0$ does not necessarily coincide with the (arbitrary) choice of branch cut.

This result, which is for flows with infinite streamwise extent, should not be confused with the Kulikovskii criterion [27, Section 65], which is for flows with finite streamwise extent. In those flows, the downstream travelling waves, k^+ , reflect off the downstream boundary and the upstream travelling waves, k^- , reflect off the upstream boundary. The function describing the wave must be singly-valued between the boundaries, which means that only certain combinations of k^+ and k^- are permitted. For long (but streamwise-confined) systems, this constraint reduces to $\operatorname{Im}(k^+ - k^-) = 0$. In those flows, the permitted global mode frequen-

cies are then calculated by combining this constraint with the local dispersion relation. For flows with finite extent, the relation $\operatorname{Im}(k^+ - k^-) = 0$ therefore serves as an additional constraint on the global complex frequency, ω_g , of the flow. For flows with infinite extent, on the other hand, there is no corresponding restriction on ω_g and the point where $\operatorname{Im}(k^+ - k^-) = 0$ merely indicates the centre of the structural sensitivity.

The wavemaker in a local analysis and the structural sensitivity in a global analysis differ both in concept and in outcome. Nevertheless, the two regions lie close to each other and there is a link between the two, which can be summarized as follows. The complex frequency of the global mode, ω_g , is the absolute frequency at the saddle point X_s of $\omega_0(X_s)$ in the complex X -plane. The region around the saddle point in the complex X -plane is the wavemaker region in the local sense given by Huerre and Monkewitz [19]. It could be tempting to assume that the *real* component of X_s has physical significance. However, this is only an approximation to the position of the maximum of the structural sensitivity (i.e. the global concept) in cases where $\operatorname{Im}(X_s)$ is small. Instead, to work out the position of maximum structural sensitivity from a local analysis, the spatial branches, k^+ and k^- , must be calculated at the global mode frequency, ω_g . Because $\operatorname{Im}(\omega_g) < \operatorname{Im}(\omega_0)$ along the real X axis, the point of maximum structural sensitivity, in the global sense given by [6], is the point at which $\operatorname{Im}(k^+ - k^-) = 0$.

4. Local analysis of the direct and adjoint Linearized Navier-Stokes equations

The planar linearized Navier-Stokes (LNS) equations for a perturbation $\tilde{\mathbf{q}}(x, z, t) \equiv [\tilde{v}_1(x, z, t), \tilde{v}_2(x, z, t), \tilde{p}(x, z, t)]^T$ are expressed as three PDEs in the three primitive variables, $(\tilde{v}_1, \tilde{v}_2, \tilde{p})$. The WKBJ analysis is performed, reducing these three PDEs to three ODEs for the Fourier/Laplace modes $\hat{\mathbf{q}}_m(z) \exp\{i(k_m x - \omega_m t)\}$. These ODEs are then expressed as the generalized eigenvalue problem:

$$-i\omega_m B \hat{\mathbf{q}}_m - A \hat{\mathbf{q}}_m = 0. \quad (59)$$

The problem is discretized by replacing the operators $A(k_m)$ and $B(k_m)$, which act on the continuous field $\hat{\mathbf{q}}_m(z)$, with matrices $A(k_m)$ and $B(k_m)$, which act on a state vector φ_m . This state vector holds the values of $\hat{\mathbf{q}}_m$ at N gridpoints at $z_j, j \in [1, N]$. The local direct LNS equations (59) are thereby expressed as the generalized matrix eigenvalue problem

$$-i\omega_m B \varphi_m - A \varphi_m = 0, \quad (60)$$

which serves as the dispersion relation for the calculation of $\omega_0(X)$, (ω_s, X_s) , ω_g , $k^+(X)$ and $k^-(X)$. Computing the dispersion relation for the Navier-Stokes problem is technically more difficult than for the Ginzburg-Landau problem, for which it is explicit. However, once the dispersion relation is expressed numerically, the subsequent calculations and derivations of quantities such as spatial branches and local absolute frequencies are carried out in a similar manner.

The direct global mode is constructed with the technique described in Section 3.5 and [28]. In summary, the absolute complex frequency, $\omega_0(X)$, is calculated by finding the valid saddle point of $\omega(k)$ at each streamwise location, X . An 8th order Padé polynomial is fitted to $\omega_0(X)$ and then extrapolated into the complex X -plane, as will be described in Section 5.1. The saddle point of $\omega_0(X)$ is identified in the complex X -plane and its value of ω_0 gives the global mode complex frequency, ω_g . Then, at the streamwise location of the saddle point in the X -plane, two values of $k(\omega_g)$ are found on either side of the saddle point ω_0 in the k -plane. These are labelled k^+ and k^- and they are followed upstream and downstream from this point. The local values of $k^+(X)$ and $k^-(X)$ are then integrated according to (54) in order to obtain the amplitude

and phase of the global mode in the X -direction. The eigenfunctions of $k^+(X)$ and $k^-(X)$ are required in order to obtain the z -dependence of the global mode. At this point there is an apparent contradiction: the local eigenfunctions can be multiplied by any arbitrary constant, yet the amplitude and phase of the global mode in the X -direction should be dictated by (54). To avoid this contradiction, the eigenfunctions must be normalized consistently. This is analogous to the normalization required when handling the Parabolized Stability Equation [29, Eq. (9a,b)]. In this paper, the eigenfunctions are normalized such that the v_2 -eigenfunctions have the same amplitude and phase at $z = 0$. This is chosen because, for the sinuous perturbations considered here, the v_2 -eigenfunction always has a large absolute value at $z = 0$. In principle, any value of z could be chosen, and for flows that are nearly parallel, such as that in Section 5.1, the choice of z has only a small effect on the predicted shapes of the direct and adjoint global modes.

The adjoint global mode is calculated using the substitution derived in Section 3.3 for a parabolic dispersion relation and in Section 3.4 for a generic polynomial PDE: $\omega_g^\dagger = -\omega_g^*$, $k^{\dagger+} = (k^-)^*$ and $k^{\dagger-} = (k^+)^*$. This substitution requires the base flow to vary slowly in the streamwise direction. In this paper, this result has been shown for a generic PDE with one spatial dimension and it can be generalized (after lengthy developments) to a PDE with two spatial dimensions. For the z -dependence, however, the eigenfunctions of $k^{\dagger+}$ and $k^{\dagger-}$ are not the same as those of k^- and k^+ , and need to be calculated from the discrete adjoint of the LNS equations. To do this, the generalized matrix eigenvalue problem (60) is post-multiplied by the adjoint eigenfunction φ_n^\dagger and re-arranged using the discretized version of the inner product: $\langle \varphi_m, \varphi_n^\dagger \rangle \equiv \varphi_m^H M \varphi_n^\dagger$, where H denotes the Hermitian transpose and M is the mass matrix, whose diagonal elements are the volume of space attributed to each gridpoint:

$$\begin{aligned} -i\omega_m B \varphi_m - A \varphi_m &= 0, \\ \langle -i\omega_m B \varphi_m, \varphi_n^\dagger \rangle - \langle A \varphi_m, \varphi_n^\dagger \rangle &= 0, \\ \langle \varphi_m, M^{-1}(i\omega_m^*) B^H M \varphi_n^\dagger \rangle - \langle \varphi_m, M^{-1} A^H M \varphi_n^\dagger \rangle &= 0, \\ i\omega_m^* (M^{-1} B^H M) \varphi_n^\dagger - (M^{-1} A^H M) \varphi_n^\dagger &= 0. \end{aligned} \quad (61)$$

The local adjoint LNS equations are written as

$$-i\omega_n B^\dagger \varphi_n^\dagger - A^\dagger \varphi_n^\dagger = 0, \quad (62)$$

so, by comparing (61) and (62),

$$\omega_n = -\omega_m^*, \quad (63)$$

$$A^\dagger = M^{-1} A^H M, \quad (64)$$

$$B^\dagger = M^{-1} B^H M, \quad (65)$$

and it can be shown that the bi-orthogonality condition becomes $(\omega_n - \omega_m^*) \varphi_m^H B^H M \varphi_n^\dagger = 0$. The adjoint eigenvalue, ω_n , is known from (63), so there is no need to solve (62) as a generalized eigenvalue problem. The fastest method is to calculate the adjoint matrices of the discretized problem with (64)–(65) and then to find the null space of $-i\omega_n B^\dagger - A^\dagger$ with a QR decomposition.

5. Demonstrations

5.1. Slowly-developing confined wake flow

We test the procedure described in Section 4 on a slowly-developing flow, using the planar linearized Navier–Stokes equations. Fig. 2(a) shows the streamlines and vorticity of a confined co-flow wake at $Re = 400$, with perfect slip at the top and bottom boundaries. The flow is identical to that in [28], except that it

has a sharper inlet velocity profile, which makes it slightly more unstable. It is similar to the flows studied by Tammisola [17].

Fig. 2(b) shows the absolute growth rate $\omega_{0i}(X)$. This is calculated at each axial station, X , by finding saddle points of $\omega(k)$ in the complex k -plane, using the dispersion relation formed from the matrix eigenvalue problem (60). This flow has a recirculation bubble between $2.26 < X < 22.42$ and is absolutely unstable over the slightly wider range of $0.05 < X < 28.70$.

In order to find the complex frequency of the linear global mode, ω_g , the saddle point of $\omega_0(X)$ must be found in the complex X -plane. Its position is labelled (ω_s, X_s) . For the G–L equation (17), the coefficients were expressed in terms of this saddle point position via (20), but for the LNS equation there is no such analytical solution. Instead, 8th order Padé polynomials are fitted to $\omega_0(X)$ using the procedure described in [28]. Saddle points of this polynomial are then found in the complex plane, as shown in Fig. 2(c). There are several saddle points but the main one is easy to identify because it lies close to the real X -axis and moves very little as the order of the polynomials increases. The range of $\omega_0(X)$ over which the points are fitted must encompass the peak of $\omega_0(X)$ but is otherwise arbitrary. We performed eight calculations, fitting between all points that satisfied $\omega_{0i} > 0.15, 0.10, 0.05, 0.00, -0.05, -0.10, -0.25, -0.20$ and found that ω_s varied by less than 1% between all these calculations.

For this flow, the polynomial is fitted through all points that have $\omega_{0i} > 0.00$; i.e. the absolutely unstable region. The saddle point is at $\omega_s = 0.6570 + 0.1409i$, $X_s = 11.05 + 4.251i$. As explained in Section 3.5, ω_s equals ω_g to within order ϵ , which is the degree of non-parallelism in the flow. For this flow, a global analysis gives $\omega_g = 0.6631 + 0.1239i$. The local analysis is seen to over-predict the growth rate of the linear global mode, which is a common feature of local analyses of wake flows [6,28]. In order to investigate the influence of this discrepancy on the direct and adjoint global modes, we calculate the k^+ and k^- branches at both values of ω_g . These branches are shown in Fig. 2(d,e) for forcing at $\omega_g(\text{loc})$ and $\omega_g(\text{glob})$. They can be compared with the local wavenumbers, k and k^\dagger , extracted from the direct and adjoint global modes from the global analysis. These were extracted from the v_1 -eigenfunction at $z = 0.79$, where the global mode has the highest absolute value. There are four important points.

Firstly, we confirm that the wavenumber of the direct global mode, k (solid black line), follows k^- upstream of X_c and k^+ downstream, as already known, and that the wavenumber of the adjoint global mode, k^\dagger (dashed black line), follows k^+ upstream of X_c and k^- downstream, as predicted in Section 3.6.

Secondly, the match is closest where the flow is more parallel. For example, when the flow is forced at $\omega_g(\text{glob})$, k^+ and k^- follow k and k^\dagger very closely for $X > 22.4$, where the flow is nearly parallel, but follow k and k^\dagger less closely for $X < 22.4$, where the flow is less parallel. Also, the local analysis predicts that the crossing point of the k^+ and k^- branches is slightly further upstream than that given by the global analysis. This is the case whether or not the flow is forced at $\omega_g(\text{loc})$ or $\omega_g(\text{glob})$ so is due to the flow's non-parallelism, or to the effect described next, and not due to the discrepancy in ω_g .

Thirdly, k^- and k^+ diverge from k and k^\dagger around the upstream boundary. This is not a defect in the local analysis. It is because the global analysis has a Dirichlet boundary condition at $X = 0$, while the local analysis assumes that the flow is homogeneous to $X = -\infty$.

Fourthly, the position of maximum structural sensitivity, where $k_i^+ - k_i^- = 0$, is at $X = 10.50$ when using $\omega_g(\text{loc})$ and $X = 10.30$ when using $\omega_g(\text{glob})$. These values differ from 11.05, which is the streamwise position of the saddle point in the complex X -plane. This small difference is to be expected, for the reasons given in Section 3.7.

The direct global modes obtained from the local analysis at $\omega_g(\text{loc})$ are compared with those obtained from the global analysis

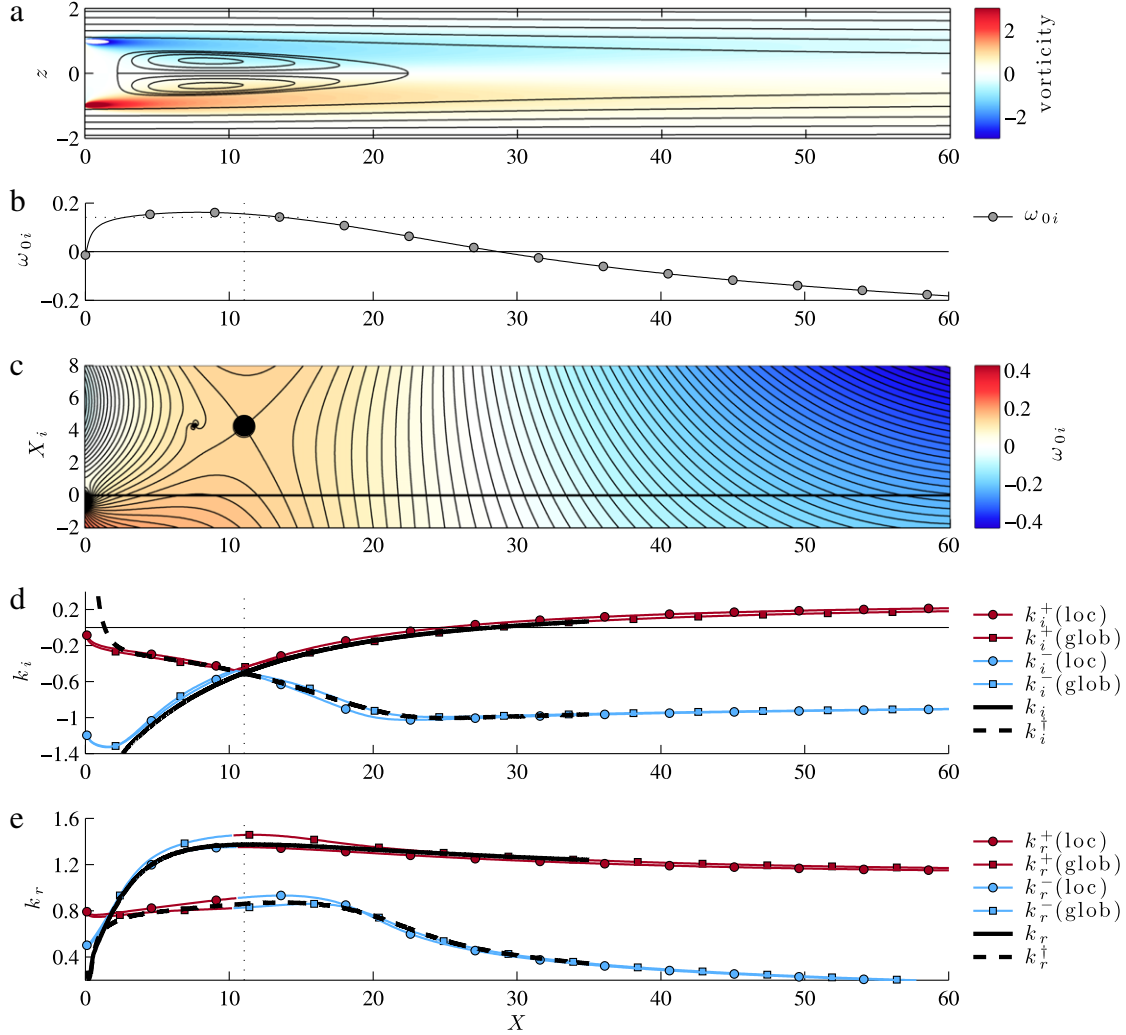


Fig. 2. (Colour online) (a) Streamlines (black lines) and vorticity (colour) of a confined co-flow wake at $Re = 400$ with perfect slip at the top and bottom boundaries. (b) Absolute growth rate, ω_{0i} . (c) Contours of ω_{0i} in the complex X -plane, formed by fitting an 8th order Padé polynomial to the points in (b) for which $\omega_{0i} > 0$. The saddle point (black dot) is at $\omega_s = 0.6570 + 4.251i$, $X_s = 11.05 + 2.451i$. (d) The imaginary component of the local wavenumber (i) calculated from the local analysis performed with ω_g equal to the saddle point position ω_s , labelled $k_i^+(\text{loc})$ and $k_i^-(\text{loc})$; (ii) calculated from the local analysis performed with ω_g taken from the global analysis, labelled $k_i^+(\text{glob})$ and $k_i^-(\text{glob})$; (iii) extracted from the direct global mode, labelled k_i and from the adjoint global mode, labelled k_i^\dagger . (e) The real component of the local wavenumber with the same nomenclature as (d).

in Fig. 3(a)–(c). Their structure is identical but the local analysis predicts that the maximum amplitude is reached slightly further upstream than it is in the global analysis. This is due to the over-prediction of the growth rate, ω_g , as noted by [28]. This can be seen in Fig. 2(d) by the fact that the k^+ branch from the local analysis at $\omega_g(\text{loc})$ crosses the k_i axis before the k branch from the global analysis, while that at $\omega_g(\text{glob})$ crosses at the same place.

The adjoint global modes obtained from the local analysis are compared with those obtained from the global analysis in Fig. 3(d)–(f). They have a similar structure to each other but there are some clear differences around $X = 0$, which are due to the different boundary condition there.

The structural sensitivity, as defined by [6] is shown in 3(g). From the global analysis, the maximum of the structural sensitivity is at the position where $\text{Im}(k - k^\dagger) = 0$, which is at $X = 11.00$. From the local analysis, the maximum of the structural sensitivity is at the position where $\text{Im}(k^+ - k^-) = 0$, which is at $X = 10.50$. The local analysis predicts the maximum of the structural sensitivity to be slightly further upstream than is predicted by the global analysis. This is the case for both $\omega_g(\text{loc})$ and $\omega_g(\text{glob})$ and is therefore due to the non-parallelism of the flow or the effect of the upstream boundary condition, and not due to the discrepancy

between $\omega_g(\text{loc})$ and $\omega_g(\text{glob})$. Apart from this small difference, the structural sensitivities are almost indistinguishable. This shows that, for this slowly-developing flow, the structural sensitivity can be estimated easily and accurately with a local stability analysis. If the direct global mode has been calculated with the local analysis, then, apart from a quick calculation to find the eigenfunction in the cross-stream direction, the adjoint has already been calculated.

5.2. The flow behind a cylinder at $Re = 50$

Hill [5] and Giannetti and Luchini [6] calculated the direct and adjoint global modes of the two-dimensional flow around a circular cylinder at $Re = 50$, based on the cylinder diameter. This is another good test case for the local analysis because there are several published results and it is less parallel than the previous test case.

Fig. 4(a) shows the streamlines and vorticity of this flow and Fig. 4(b) shows the absolute growth rate ω_{0i} as a function of downstream distance. Fig. 4(c) shows the position of the saddle point ω_s in the complex X -plane, which was calculated by fitting Padé polynomials through all points downstream of the cylinder with $\omega_{0i} > 0.03$. The saddle point is at $\omega_s = 0.791 + 0.083i$, $X_s = 1.297 +$

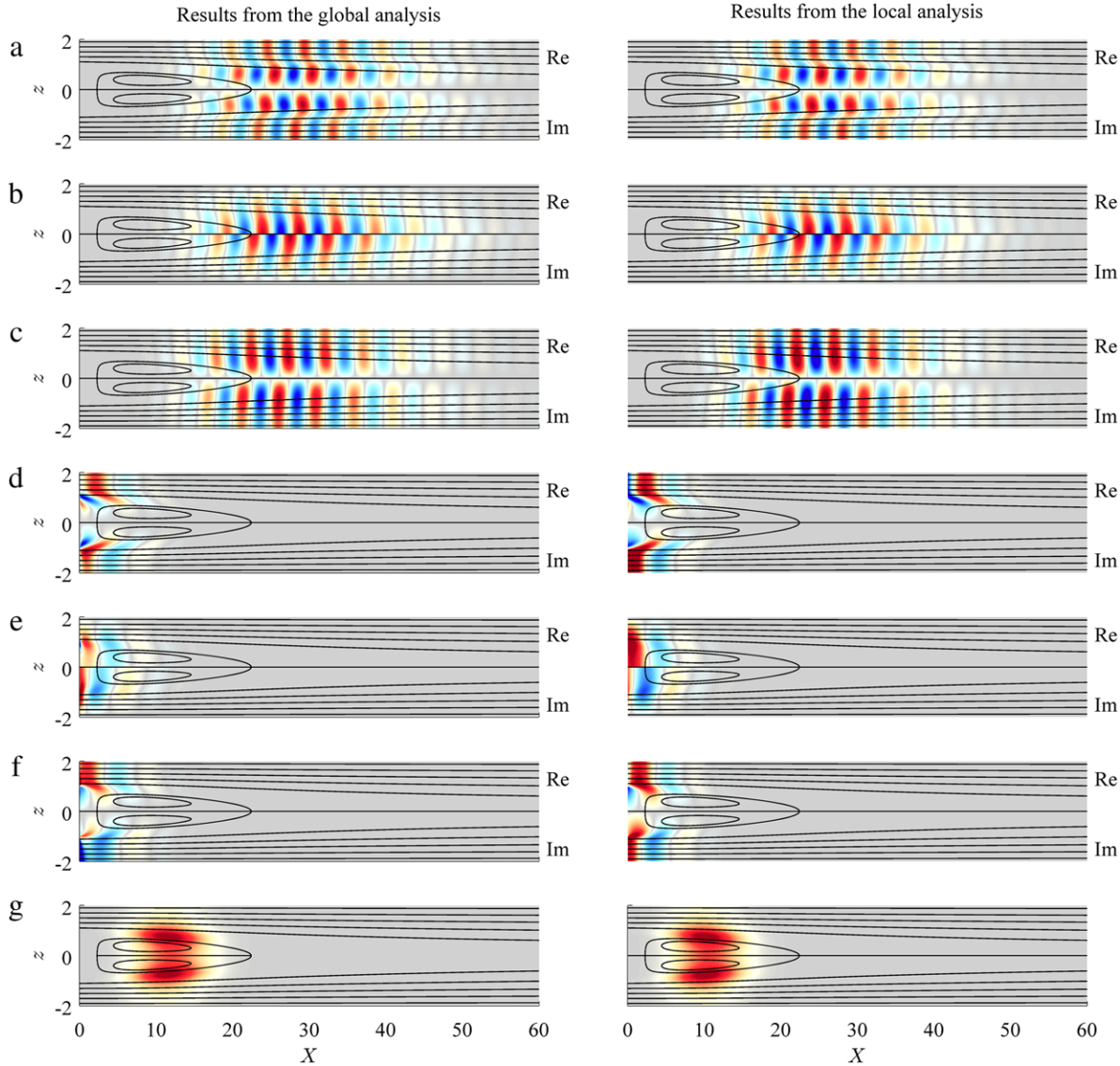


Fig. 3. (Colour online) Direct and adjoint global modes calculated from the global analysis (left) and the local analysis (right). The top halves of frames (a-f) show the real component. The bottom halves show the imaginary component. (a) Direct streamwise velocity component, v_1 . (b) Direct cross-stream velocity component, v_2 . (c) Direct pressure, p . (d) Adjoint streamwise velocity component, v_1^\dagger . (e) Adjoint cross-stream velocity component, v_2^\dagger . (f) Adjoint pressure, p^\dagger . (g) Structural Sensitivity $\nabla_L \omega_m = (v_1^2 + v_2^2) \times (v_1^{\dagger 2} + v_2^{\dagger 2})^{1/2}$.

0.699i. The threshold of 0.03 was chosen because a threshold of 0.00 gave rise to too many nearby saddle points. For comparison, the global analysis of [6] gives $\omega_g = 0.750 + 0.013i$ and the local analysis of [30] gives $\omega_g = 0.785 + 0.091i$. The k^+ and k^- branches are shown in Fig. 4(d)–(e) using ω_g (local) and ω_g (global).

Fig. 5(a)–(b) shows the vorticity of the direct global mode obtained from the local analysis and can be compared directly with Fig. 2 of [5], which is obtained from the global analysis. Fig. 5(c)–(d) shows the vorticity of the adjoint global mode obtained from the local analysis and can be compared directly with Fig. 3 of [5]. The local results are close to the global results in the region behind the cylinder but differ in the region around the cylinder. This is not surprising because the flow is strongly non-parallel there.

The structural sensitivity is shown in Fig. 6, and can be compared directly with Fig. 17 of [6]. Both frames are calculated from the local analysis but the left frame is calculated at ω_g (local), while the right frame is calculated at ω_g (global). The local analysis predicts the same features as the global analysis but there are some noticeable differences. Firstly, the centre of the structural sensitivity is too far upstream when ω_g (local) is used. This was also seen for

the wake flow in Section 5.1 and is because the local analysis over-predicts the growth rate. Secondly, the z -dependence of the global mode is poorly predicted in regions where the flow is strongly non-parallel, such as at the end of the recirculation zone. Nevertheless, this shows that the local analysis can estimate the structural sensitivity in this type of flow, at very little computational cost.

It is worth mentioning that we also attempted to use this method to compute the global modes for the swirling vortex breakdown bubble in [31], which is very non-parallel around the vortex breakdown bubble. It was impossible to identify the k^+ and k^- branches in the non-parallel region and therefore impossible to generate direct and adjoint global modes.

6. Conclusions

In an unstable open flow, it is useful to know which regions are most receptive to forcing and which regions are most sensitive to changes in internal feedback. These regions can be found easily if the direct and adjoint global modes have been calculated.

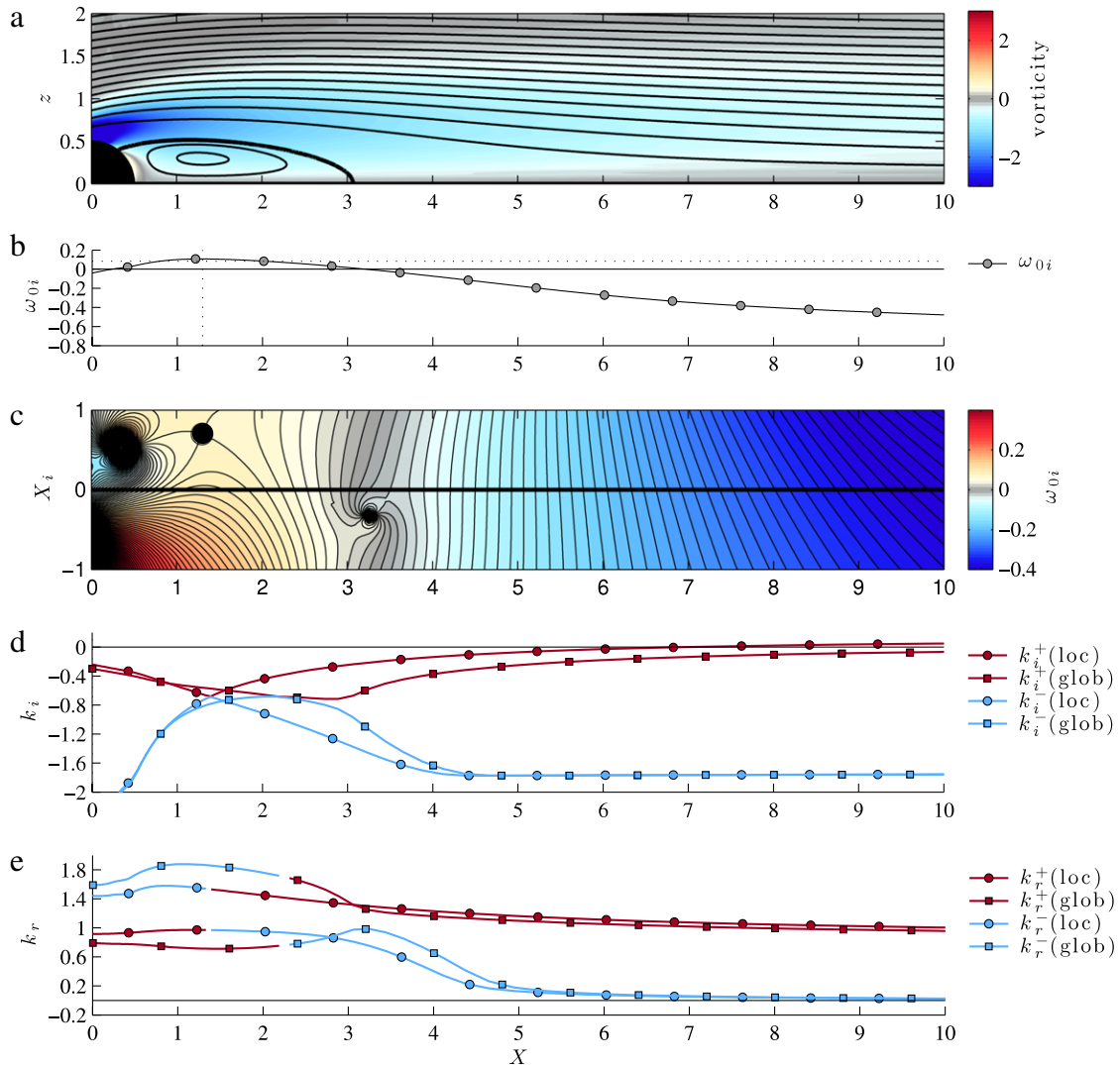


Fig. 4. As for Fig. 2 but for the flow around a cylinder at $Re = 50$.

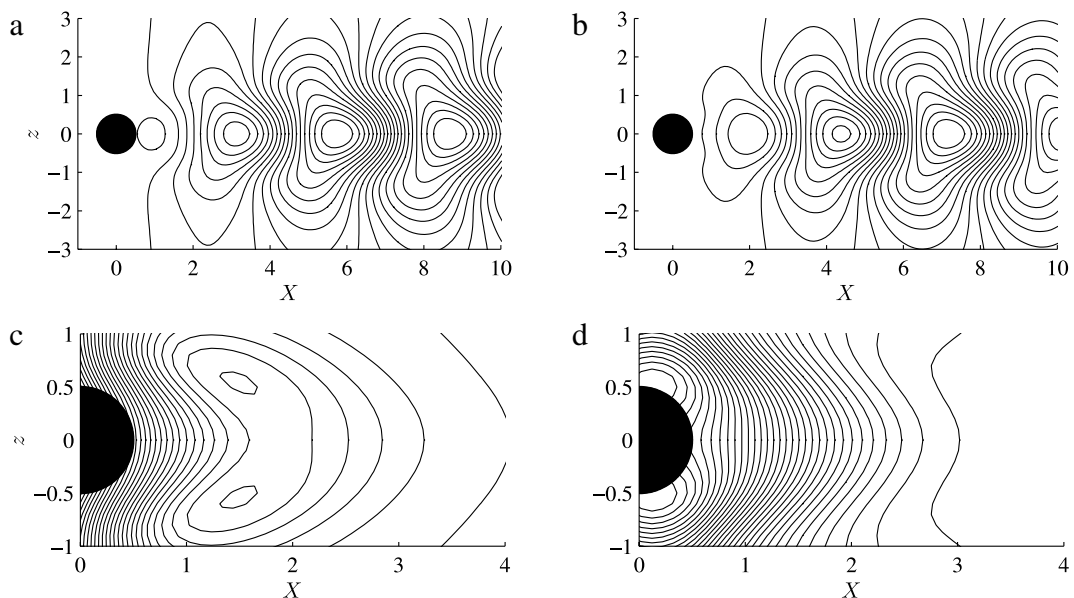


Fig. 5. Direct (top) and adjoint (bottom) global modes calculated from the local analysis at $\omega_g(\text{local})$: (a, c) real component, (b, d) imaginary component. These frames can be compared with Figs. 2 and 3 of [5].

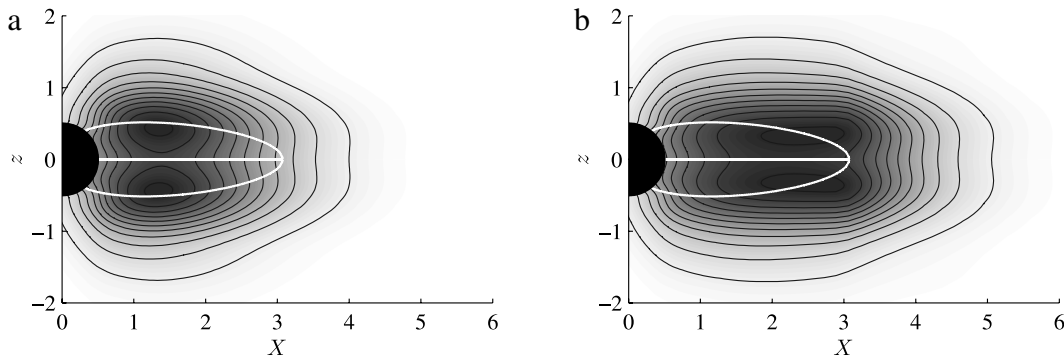


Fig. 6. The structural sensitivity calculated from the local analysis at (a) ω_g (local) and (b) ω_g (global). These frames can be compared with Fig. 17 of [6].

These modes are usually calculated with a global linear stability analysis, meaning that small perturbations on top of a base flow are discretized on a 2D or 3D grid. This creates a generalized matrix eigenvalue problem, which is then solved numerically. These matrices can have millions of degrees of freedom, so this procedure is computationally expensive and is impractical for many flows.

An alternative approach, which is applicable to weakly non-parallel open flows, is to calculate the direct global mode with a local stability analysis. This is orders of magnitude cheaper than a global analysis. The main result of this paper is to show that the adjoint global mode then follows at almost no extra cost. We show this formally for the Ginzburg–Landau equation and find that the direct global mode is formed from the k^- -branch upstream and the k^+ -branch downstream, while the adjoint global mode is formed from the k^+ -branch upstream and the k^- -branch downstream. We include higher order terms of the WKBJ analysis in order to show that these analytical relationships are valid up to order ϵ , which measures the non-parallelism of the flow. Furthermore, we show that the maximum of the structural sensitivity, as defined by [6], is the point at which the spatial branches, k^+ and k^- , have identical imaginary components.

We apply this to the linearized Navier–Stokes (LNS) equations and show that, if the direct global mode has already been calculated, the only extra cost in calculating the adjoint mode is in calculating the adjoint eigenfunction at each point in the flow. This cost is small because the adjoint eigenvalue is already known.

We compare the local and global results for two flows: a confined wake flow at $Re = 400$, and the flow behind a cylinder at $Re = 50$. The procedure works very well for the confined wake flow: the local wavenumbers of the direct and adjoint global modes closely follow the k^+ and k^- branches of the local analysis, as expected, and the structural sensitivity calculated with the local analysis is almost indistinguishable from that calculated with the global analysis. The procedure works less well for the cylinder: although the local and global results are qualitatively similar, the local analysis over-predicts the growth rate and therefore predicts that the wavemaker region lies too far upstream. We conclude that the procedure works less well for the cylinder because the wavemaker sits in a region that is less parallel.

Some flows, such as those in a gas turbine fuel injector [23], contain more than one unstable global mode. Each of these global modes has, in a local analysis, an associated saddle point of $\omega(k)$ in the k -plane and an associated saddle point of $\omega_0(X)$ in the X -plane. Therefore the technique in this paper can be applied to each of these saddle points individually and can identify multiple global modes in a flow, if they exist.

In many real flows, the assumptions underlying the WKBJ approach are not met very closely. Nevertheless, the techniques of local stability analysis have proved to be remarkably robust, probably

because the wavemaker region often lies in a region of nearly parallel flow. In such cases, a local stability analysis will give reasonable estimates of the direct and adjoint global modes at much less computational cost than a global analysis. For example, the global modes of a 3D flow that evolves slowly in the streamwise direction could be calculated by combining the results of several 2D calculations. This opens the door to the application of sensitivity analysis to flows that are currently beyond the reach of global analysis.

Acknowledgements

We gratefully acknowledge the help of Outi Tammisola, who provided the confined wake flow and the corresponding global stability analysis. This work was supported by the European Research Council under Project ALORS 2590620 and by MPJ's visiting Professorship at École centrale de Lyon.

References

- [1] P.A. Monkewitz, The absolute and convective nature of instability in two-dimensional wakes at low Reynolds numbers, *Phys. Fluids* 31 (1998) 999–1006.
- [2] J.-M. Chomaz, Global instabilities in spatially developing flows: non-normality and nonlinearity, *Annu. Rev. Fluid Mech.* 37 (2005) 357–392.
- [3] J.-M. Chomaz, Linear and nonlinear, local and global stability analysis of open flows, in: *Turbulence in Spatially Extended Systems*, Nova, ISBN: 1-56072-120-0, 1993.
- [4] D. Sipp, O. Marquet, P. Meliga, A. Barbagallo, Dynamics and control of global instabilities in open flows: a linearized approach, *Appl. Mech. Rev.* 63 (2010) 030801.
- [5] D.C. Hill, A theoretical approach for analyzing the restabilization of wakes, *AIAA Paper 92-0067*, and *NASA Tech. Mem. 103858*, 1992.
- [6] F. Giannetti, P. Luchini, Structural sensitivity of the first instability of the cylinder wake, *J. Fluid Mech.* 581 (2007) 167–197.
- [7] F. Giannetti, P. Luchini, Receptivity of the circular cylinders first instability, in: *5th Eur. Fluid Mech. Conf.*, Toulouse, 2003.
- [8] P. Luchini, F. Giannetti, J.O. Pralits, Structural sensitivity of linear and nonlinear global modes, *AIAA Paper 2008-4227*, 2008.
- [9] O. Marquet, D. Sipp, L. Jacquin, J.-M. Chomaz, *Multiple Time Scale Analysis and Sensitivity Analysis for the Passive Control of the Cylinder Flow*, AIAA, 2008, pp. 2008–4228.
- [10] O. Marquet, D. Sipp, L. Jacquin, Sensitivity analysis and passive control of cylinder flow, *J. Fluid Mech.* 615 (2008) 221–252.
- [11] O. Marquet, M. Lombardi, J.-M. Chomaz, D. Sipp, L. Jacquin, Direct and adjoint global modes of a recirculation bubble: lift-up and convective nonnormalities, *J. Fluid Mech.* 622 (2009) 1–21.
- [12] P. Meliga, J.-M. Chomaz, D. Sipp, Unsteadiness in the wake of disks and spheres: Instability, receptivity and control using direct and adjoint global stability analyses, *J. Fluids Struct.* 25 (2009) 601–616.
- [13] P. Meliga, D. Sipp, J.-M. Chomaz, Open-loop control of compressible afterbody flows using adjoint methods, *Phys. Fluids* 22 (2010) 054109.
- [14] A. Barbagallo, G. Dergham, D. Sipp, P. Schmid, J.-C. Robinet, Closed-loop control of unsteadiness over a rounded backward-facing step, *J. Fluid Mech.* 703 (2012) 326–362.
- [15] L. Marino, P. Luchini, Adjoint analysis of the flow over a forward-facing step, *Theor. Comput. Fluid Dyn.* 23 (2009) 37–54.
- [16] O. Tammisola, F. Lundell, P. Schlatter, A. Wehrfritz, L.D. Söderberg, Global linear and nonlinear stability of viscous confined plane wakes with co-flow, *J. Fluid Mech.* 675 (2011) 397–434.

- [17] O. Tammisola, Oscillatory sensitivity patterns for global modes in wakes, *J. Fluid Mech.* 701 (2012) 251–277.
- [18] P. Meliga, F. Gallaire, J.-M. Chomaz, A weakly nonlinear mechanism for mode selection in swirling jets, *J. Fluid Mech.* (2012) <http://dx.doi.org/10.1017/jfm.2012.93>.
- [19] P. Huerre, P.A. Monkewitz, Local and global instabilities in spatially developing flows, *Annu. Rev. Fluid Mech.* 22 (1990) 473–537.
- [20] P.A. Monkewitz, P. Huerre, J.-M. Chomaz, Global linear stability analysis of weakly non-parallel shear flows, *J. Fluid Mech.* 251 (1993) 1–20.
- [21] B. Pier, Local and global instabilities in the wake of a sphere, *J. Fluid Mech.* 603 (2008) 39–61.
- [22] K. Oberleithner, M. Sieber, C.N. Nayeri, C.O. Paschereit, C. Petz, H.-C. Hege, B.R. Noack, Three-dimensional coherent structures in a swirling jet undergoing vortex breakdown: stability analysis and empirical mode construction, *J. Fluid Mech.* 679 (2011) 383–414.
- [23] M.P. Juniper, Absolute and convective instability in gas turbine fuel injectors, ASME Turbo Expo. June 2012, Copenhagen, Denmark, GT2012-68253, 2012.
- [24] D.C. Hill, Adjoint systems and their role in the receptivity problem for boundary layers, *J. Fluid Mech.* 292 (1995) 183–284.
- [25] C.M. Bender, S.A. Orszag, *Advanced Mathematical Methods for Scientists and Engineers: Asymptotic Methods and Perturbation Theory*, Springer, 1978.
- [26] B. Pier, Signalling problem in absolutely unstable systems, *Theor. Comput. Fluid Dyn.* 25 (2011) 7–17.
- [27] L.D. Landau, E.M. Lifshitz, *Physical Kinetics*, Butterworth-Heinemann, 1981.
- [28] M.P. Juniper, O.L. Tammisola, F. Lundell, The local and global stability of confined planar wakes at intermediate Reynolds number, *J. Fluid Mech.* 686 (2011) 218–238.
- [29] T. Herbert, Parabolized stability equations, *Annu. Rev. Fluid Mech.* 29 (1997) 245–283.
- [30] B. Pier, On the frequency selection of finite-amplitude vortex shedding in the cylinder wake, *J. Fluid Mech.* 458 (2002) 407–417.
- [31] U. Qadri, D. Mistry, M.P. Juniper, Structural sensitivity of spiral vortex breakdown, *J. Fluid Mech.* 720 (2013) 558–581.

[A22]

Flow around a rotating, semi-infinite cylinder in an axial stream

S. Derebail Muralidhar, B. Pier, J. F. Scott & R. Govindarajan

Proceedings of the Royal Society A **752**, 20150850 (17 pages) (2016)

doi:10.1098/rspa.2015.0850

<https://hal.archives-ouvertes.fr/hal-01330462>

Research



Cite this article: Derebail Muralidhar S, Pier B, Scott JF, Govindarajan R. 2016 Flow around a rotating, semi-infinite cylinder in an axial stream. *Proc. R. Soc. A* **472**: 20150850.

<http://dx.doi.org/10.1098/rspa.2015.0850>

Received: 11 December 2015

Accepted: 9 May 2016

Subject Areas:

fluid mechanics, applied mathematics

Keywords:

rotating body, wall jet, boundary layer, asymptotic analysis

Author for correspondence:

B. Pier

e-mail: benoit.pier@ec-lyon.fr

Flow around a rotating, semi-infinite cylinder in an axial stream

S. Derebail Muralidhar¹, B. Pier¹, J. F. Scott¹ and R. Govindarajan²

¹Laboratoire de mécanique des fluides et d'acoustique (École centrale de Lyon—CNRS—Université de Lyon 1—INSA Lyon), 36 avenue Guy-de-Collongue, 69134 Écully, France

²Centre for Interdisciplinary Sciences, Tata Institute of Fundamental Research, 21 Brundavan Colony, Narsingi, Hyderabad 500075, India

BP, 0000-0001-8663-8694

This paper concerns steady, high-Reynolds-number flow around a semi-infinite, rotating cylinder placed in an axial stream and uses boundary-layer type of equations which apply even when the boundary-layer thickness is comparable to the cylinder radius, as indeed it is at large enough downstream distances. At large rotation rates, it is found that a wall jet appears over a certain range of downstream locations. This jet strengthens with increasing rotation, but first strengthens then weakens as downstream distance increases, eventually disappearing, so the flow recovers a profile qualitatively similar to a classical boundary layer. The asymptotic solution at large streamwise distances is obtained as an expansion in inverse powers of the logarithm of the distance. It is found that the asymptotic radial and axial velocity components are the same as for a non-rotating cylinder, to all orders in this expansion.

1. Introduction

When a semi-infinite rotating cylindrical body is placed in a high-Reynolds-number axial flow (figure 1), an axisymmetric boundary layer develops along the cylinder. Initially thin, this layer becomes of thickness comparable with, then larger than the cylinder radius at sufficiently large axial distances. Our original motivation for studying this flow was to undertake a stability analysis. However, it soon became clear that there are very few existing studies of the underlying flow, despite its interesting features, e.g. the appearance of

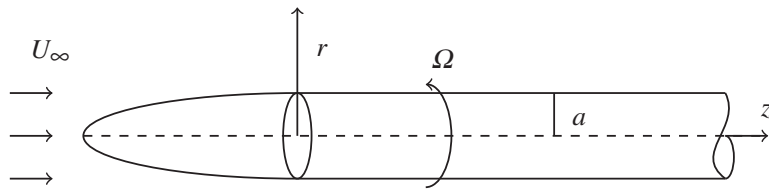


Figure 1. Schematic diagram of the problem.

an axial wall jet beyond a certain threshold value of the rotation rate. The presence of curvature and rotation means that the classical Prandtl equations need to be generalized to allow for these effects. In particular, rotation leads to a centrifugal term which couples all three velocity components. This results in significant qualitative changes in the flow structure, e.g. the wall jet, compared with Blasius flow on a flat plate.

The non-rotating version of this problem was studied analytically by Seban & Bond [1] using a series solution in powers of $z^{1/2}$, where z is the axial coordinate, non-dimensionalized using the cylinder radius. This series solution was limited to order 3, and thus only applicable close to the inlet. Kelly [2] showed that the series solution for the displacement thickness provided by Seban & Bond [1] was erroneous, and obtained the correct result. Glauert & Lighthill [3] extended this work to obtain a solution at all z using the Pohlhausen approximation. At large z , Glauert & Lighthill [3] also showed that the velocity profile had an asymptotic expansion in inverse powers of $\log(z)$. Jaffe & Okamura [4] were the first to solve the boundary-layer equations for this problem numerically, thus covering the entire range of z , from small to large values. Boundary-layer velocity profiles have also been numerically determined by Tutty *et al.* [5] and Vinod & Govindarajan [6] in the context of stability analysis.

Petrov [7] appears to be the first to have studied the rotating case. Axial velocity profiles were obtained in the limit of small z and show the existence of a wall jet for sufficiently strong rotation, though this interesting feature was not explained in the paper. Motivated as we were by stability analysis of the flow, Kao & Chow [8] and Herrada *et al.* [9] solved the present problem numerically. However, both papers limit themselves to a range of rotation rates insufficiently large to produce a wall jet. Furthermore, the centrifugal term is missing in the boundary-layer equations of Kao & Chow [8], and so they are incapable of yielding a wall jet even at large rotation rates.

In §2, we define the two non-dimensional control parameters of the problem, Re and S , the Reynolds number and non-dimensional rotation rate. The boundary-layer equations, valid for large Re , and allowing for boundary-layer thickness to be comparable with the cylinder radius are given. These equations generalize the Prandtl equations and apply for arbitrary (not necessarily small) ratios of boundary-layer thickness to cylinder radius. Suitable rescaling of the variables renders the problem independent of Re , leaving only S as control parameter. Section 3 describes the numerical scheme and its verification, while §4 gives results and discussion, in particular focusing on the wall jet. Finally, §5 gives asymptotic analyses of the limits of large $Z = z/Re$ and large S . The boundary layer on the nose is discussed in the appendices. It is found that the precise shape of the nose is unimportant: the input to the boundary-layer equations of §2 being the Blasius flat-plate flow (generalized to include the azimuthal component due to rotation), independent of the nose shape.

2. Boundary-layer equations

A semi-infinite cylinder of radius a rotates about its axis with angular velocity Ω and is placed in an axial stream of incompressible fluid of velocity U_∞ and viscosity ν (figure 1). Assuming large Reynolds number, an initially thin boundary layer develops along the cylinder. If the cylinder were sharply truncated at the nose, flow separation would occur as is usually the case at a salient

edge [10]. To avoid this scenario, we assume that there is a smooth nose, as shown in figure 1. Another way to avoid flow separation would be to consider a thin hollow cylinder. The boundary-layer equations formulated in this section hold good for both these cases. A detailed analysis of the nose region is given in appendix B.

The natural length and velocity scales are a and U_∞ . These scales are used to non-dimensionalize the axisymmetric, steady Navier–Stokes equations in cylindrical coordinates, z, r, θ . There are two non-dimensional parameters, namely the Reynolds number

$$Re = \frac{U_\infty a}{\nu}, \quad (2.1)$$

and the rotation rate

$$S = \frac{\Omega a}{U_\infty}. \quad (2.2)$$

Assuming a large Reynolds number, the length scale for axial variation of the flow is much longer than that for radial variation. This separation of scales leads to the boundary-layer approximation. Thus,

$$u_z \frac{\partial u_z}{\partial z} + u_r \frac{\partial u_z}{\partial r} = -\frac{\partial p}{\partial z} + \frac{1}{Re} \left(\frac{\partial^2 u_z}{\partial r^2} + \frac{1}{r} \frac{\partial u_z}{\partial r} \right), \quad (2.3)$$

$$\frac{u_\theta^2}{r} = \frac{\partial p}{\partial r}, \quad (2.4)$$

$$u_z \frac{\partial u_\theta}{\partial z} + u_r \frac{\partial u_\theta}{\partial r} + \frac{u_\theta u_r}{r} = \frac{1}{Re} \left(\frac{\partial^2 u_\theta}{\partial r^2} + \frac{1}{r} \frac{\partial u_\theta}{\partial r} - \frac{u_\theta}{r^2} \right) \quad (2.5)$$

and

$$\frac{\partial u_z}{\partial z} + \frac{1}{r} \frac{\partial r u_r}{\partial r} = 0 \quad (2.6)$$

are obtained by dropping terms of higher order from the Navier–Stokes equations in the usual manner. Note that we have not assumed the boundary layer to be thin compared with the radius. The boundary conditions are

$$u_z = 0, \quad u_r = 0, \quad u_\theta = S \quad z > 0, \quad r = 1 \quad (2.7)$$

and

$$u_z \rightarrow 1, \quad u_\theta \rightarrow 0, \quad p \rightarrow 0 \quad z > 0, \quad r \rightarrow \infty. \quad (2.8)$$

The above equations contain the azimuthal component, u_θ , of the velocity. This is due to rotation of the cylinder, which induces the centrifugal term on the left-hand side of equation (2.4), leading to a significant radial pressure gradient. Such an effect is not present in classical boundary-layer theory, which predicts near constancy of the pressure across the layer. Compared to the Prandtl equations of a classical boundary layer, equations (2.3)–(2.6) allow for the additional effects of both rotation and curvature. Near the nose the boundary layer is thin compared with the cylinder radius and curvature effects are negligible. But at large z , boundary-thickening eventually makes the thickness comparable to, then larger compared with the radius, and the full set of equations is required.

The above problem needs to be completed by inlet conditions. At distances from the nose of $O(a)$, the boundary layer is thin compared with the radius and is described by the axisymmetric Prandtl equations given in appendix B. On the cylinder (after leaving the nose), these equations become the flat-plate Prandtl equations, and as z increases, we expect the flow to forget the precise initial conditions and to approach the Blasius solution, independent of the nose shape (here, we implicitly suppose the nose length to be of the same order as its diameter). There are, in fact, two asymptotic regions, $z = O(1)$, where the equations of appendix B apply, and $z = O(Re)$, where the boundary-layer thickness is comparable to the cylinder radius and equations (2.3)–(2.8) hold. Matching between these regions requires that the inlet condition be the Blasius solution

(generalized to include the azimuthal component due to rotation). The same is true for the case of the hollow cylinder. In either case, equations (2.3)–(2.8) are supplemented by Blasius initial conditions as $z \rightarrow 0$.

Introducing the scaled variables

$$R = r, \quad Z = \frac{z}{Re}, \quad (2.9)$$

and

$$U_z = u_z, \quad U_r = Ru_r Re, \quad U_\theta = Ru_\theta, \quad P = R^2 p, \quad (2.10)$$

equations (2.3)–(2.8) become

$$U_z \frac{\partial U_z}{\partial Z} + \frac{U_r}{R} \frac{\partial U_z}{\partial R} = -\frac{1}{R^2} \frac{\partial P}{\partial Z} + \frac{\partial^2 U_z}{\partial R^2} + \frac{1}{R} \frac{\partial U_z}{\partial R}, \quad (2.11)$$

$$U_\theta^2 = R \frac{\partial P}{\partial R} - 2P, \quad (2.12)$$

$$U_z \frac{\partial U_\theta}{\partial Z} + \frac{U_r}{R} \frac{\partial U_\theta}{\partial R} = \frac{\partial^2 U_\theta}{\partial R^2} - \frac{1}{R} \frac{\partial U_\theta}{\partial R}, \quad (2.13)$$

$$\frac{\partial U_z}{\partial Z} + \frac{1}{R} \frac{\partial U_r}{\partial R} = 0, \quad (2.14)$$

$$U_z = U_r = 0, \quad U_\theta = S \quad R = 1 \quad (2.15)$$

and

$$U_z \rightarrow 1, \quad U_\theta = 0, \quad P = 0 \quad R \rightarrow \infty. \quad (2.16)$$

It is apparent that, using these scalings, Re has disappeared from the problem, leaving S as the only non-dimensional parameter. This result indicates, among other things, that the natural scaling of the axial coordinate is $z = O(Re)$. Thus, as noted earlier, the distance needed for the boundary-layer thickness to become comparable with the radius is Re times the radius. The factors of R appearing in equation (2.10) have been introduced to improve numerical convergence.

3. Numerical scheme and validation

The boundary-layer thickness goes to zero like $Z^{1/2}$ and $U_r \rightarrow \infty$ like $Z^{-1/2}$ as $Z = 0$ is approached. To maintain numerical accuracy in the presence of such singular behaviour, we introduce the variables

$$\zeta = (2Z)^{1/2}, \quad \sigma = \frac{R - 1}{\zeta}, \quad V_r = \zeta U_r, \quad V_z = U_z, \quad V_\theta = U_\theta. \quad (3.1)$$

Here, the boundary-layer thickness is prevented from going to zero in the radial coordinate σ by dividing $R - 1$ by ζ . V_r is kept finite by use of the factor ζ , and ζ is used in place of Z to make the solution a smooth function of the axial coordinate. Using these variables in the boundary-layer equations (2.11)–(2.16) results in

$$\zeta V_z \frac{\partial V_z}{\partial \zeta} + \left(\frac{V_r - \zeta}{R} - \sigma V_z \right) \frac{\partial V_z}{\partial \sigma} = \frac{1}{R^2} \left(\sigma \frac{\partial P}{\partial \sigma} - \zeta \frac{\partial P}{\partial \zeta} \right) + \frac{\partial^2 V_z}{\partial \sigma^2}, \quad (3.2)$$

$$\frac{\zeta}{R} (V_\theta^2 + 2P) = \frac{\partial P}{\partial \sigma}, \quad (3.3)$$

$$\zeta V_z \frac{\partial V_\theta}{\partial \zeta} + \left(\frac{V_r + \zeta}{R} - \sigma V_z \right) \frac{\partial V_\theta}{\partial \sigma} = \frac{\partial^2 V_\theta}{\partial \sigma^2} \quad (3.4)$$

and $\zeta \frac{\partial V_z}{\partial \zeta} - \sigma \frac{\partial V_z}{\partial \sigma} + \frac{1}{R} \frac{\partial V_r}{\partial \sigma} = 0, \quad (3.5)$

with the boundary conditions

$$V_z = V_r = 0, \quad V_\theta = S \quad \sigma = 0 \quad (3.6)$$

and

$$V_z \rightarrow 1, \quad V_\theta = 0, \quad P = 0 \quad \sigma \rightarrow \infty. \quad (3.7)$$

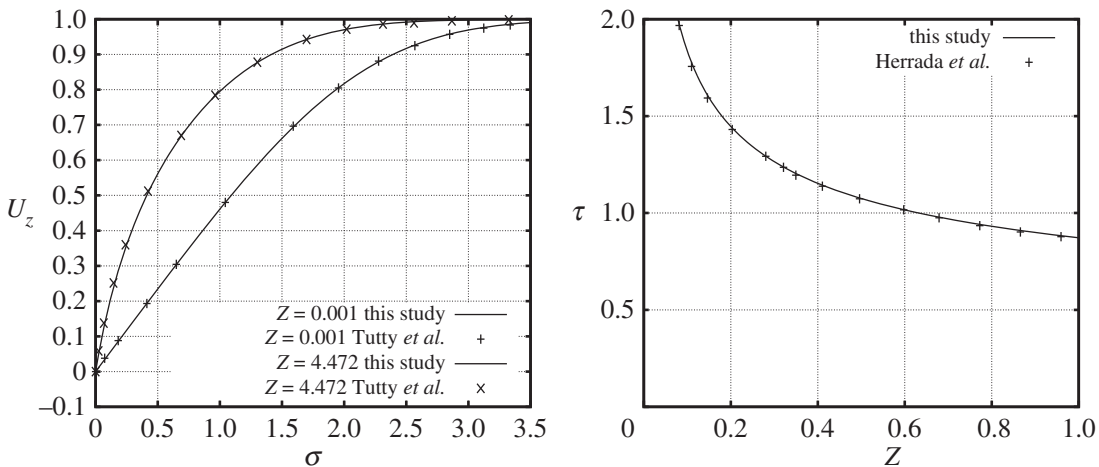


Figure 2. Comparison of U_z for $S = 0$ at two values of Z with [5] and comparison of skin friction τ for $S = 1$ with [9].

These equations govern the axial evolution of the flow. The inlet condition (Blasius solution) is obtained by setting $\zeta = 0$ and solving the resulting equations.

The radial coordinate σ is discretized using Chebyshev collocation points:

$$x_n = \cos\left(\frac{n\pi}{N-1}\right) \quad 0 \leq n < N \quad (3.8)$$

and

$$\sigma_n = \frac{\hat{\sigma}(1+x_n)}{1-x_n}, \quad x \in [-1, 1] \rightarrow \sigma \in [0, \infty]. \quad (3.9)$$

The parameter $\hat{\sigma}$ controls the distribution of points such that half of them lie between $0 \leq \sigma \leq \hat{\sigma}$. The velocities V_z and V_θ are represented by their values at all collocation points. However, since there is no boundary condition for the pressure at the surface, it is represented at all points except $\sigma = 0$. Similarly, there is no boundary condition for V_r at $\sigma = \infty$ and so it is represented at all points apart from $\sigma = \infty$. The Chebyshev derivative matrices for P and V_r are correspondingly modified (e.g. appendix A in [11]).

The coordinate ζ is discretized using small, equally spaced steps, $\zeta_i = i\Delta$, and the variables V_z, V_r, V_θ, P are represented by their values at ζ_i . Equations (3.2), (3.4) and (3.5) are evaluated at mid-step, $\zeta_{i+1/2}$, using an implicit scheme that employs centred finite differencing to represent the ζ -derivatives. Equation (3.3) is evaluated at the step position ζ_i , rather than at the midstep. At each step, the equations are solved using Newton–Raphson iteration, thus allowing forward marching. The inlet solution is obtained from equations (3.2)–(3.7) using $\zeta = 0$. Following discretization in σ using the collocation points, the result is again obtained by Newton–Raphson iteration.

The code was first tested by changing the numerical parameters $N, \hat{\sigma}, \Delta$, and observing the dependence of the solution on these parameters. Based on the convergence results, we decided to use $N = 128$, $\hat{\sigma} = 5$, $\Delta = 0.001$ in our computations. These values gave convergence to better than seven decimal places. The code was also tested using the volume-flux and momentum balance equations. The results respect these equations to seven decimal places. Although use of the Blasius solution at the inlet has earlier been justified by an asymptotic argument, it is interesting to see the effect of a change in inlet profile on the solution. Thus, we modified the inlet profile to be $U_z^* = U_z + A\sigma \exp(-0.5\sigma)$, where U_z is the Blasius profile. Taking $A = 2$, it was found that the change in U_z at $Z = 2$ was in the sixth decimal place. This illustrates the fact that the flow forgets the initial condition as Z increases and becomes insensitive to the precise inlet profile used.

We also validated the code by comparing our results with the existing literature. Tutty *et al.* [5] studied the case without rotation. The axial (x_t) and radial (σ_t) coordinates used by Tutty *et al.* [5] are related to those used here via $x_t/Re = Z$ and $\sigma_t = \sqrt{2}\sigma$. Figure 2 shows good agreement with our results for $Re = 10^4$, $x_t = 0.01$ and $x_t = 10^5$. Herrada *et al.* [9] considered the problem of the

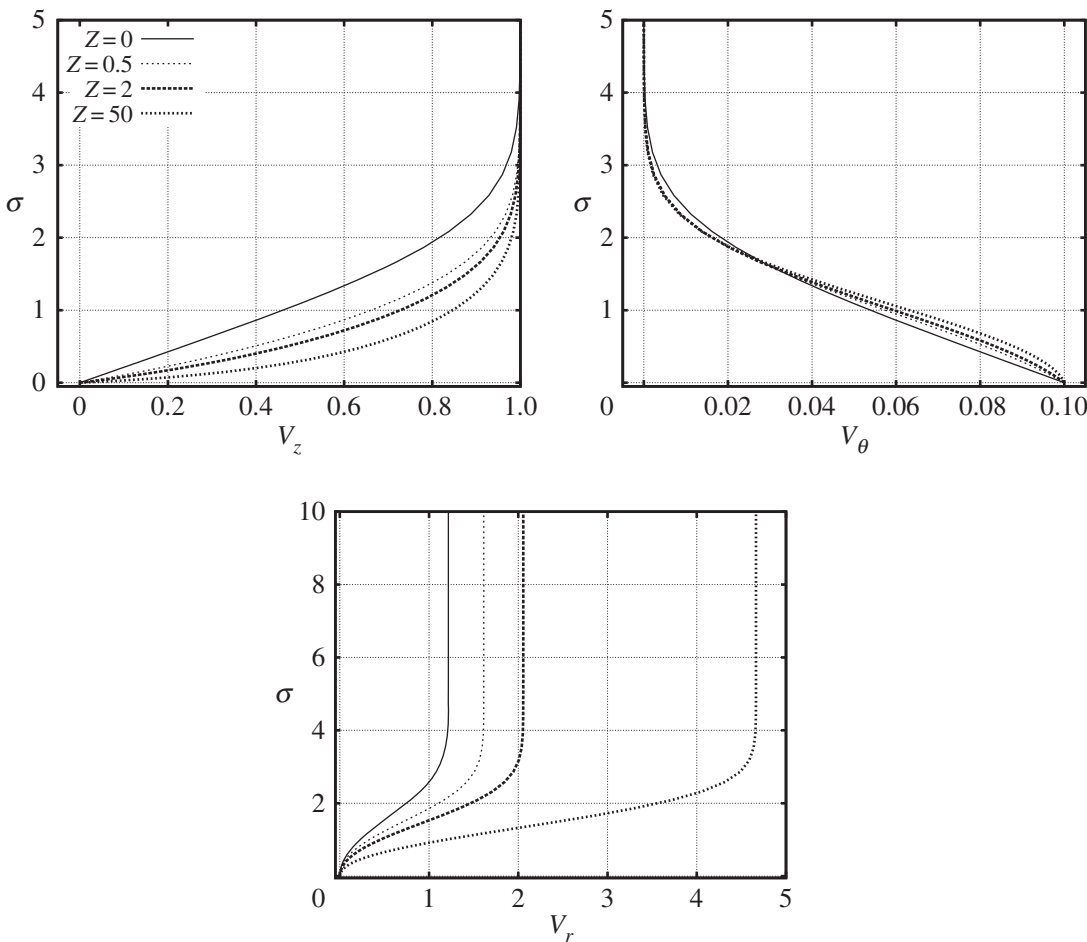


Figure 3. Velocity profiles $V_z(\sigma)$, $V_\theta(\sigma)$ and $V_r(\sigma)$ for different axial positions Z at $S = 0.1$.

rotating cylinder. They do not give velocity profiles, but rather the skin friction on the cylinder:

$$\tau = \frac{\partial U_z(Z)}{\partial R} \Big|_{R=1} = \frac{1}{\zeta} \frac{\partial V_z(\zeta)}{\partial \sigma} \Big|_{\sigma=0}. \quad (3.10)$$

Figure 2 shows τ as a function of Z for $S = 1$ and good agreement is apparent.

4. Results

Flow profiles were obtained for different values of S and Z . Figure 3 shows velocity profiles for $S = 0.1$ and different values of Z . For $Z = 0$, $V_z(\sigma)$ corresponds to the Blasius flat-plate solution. As Z increases, $V_z(\sigma)$ deviates from the Blasius profile due to cylinder curvature and rotation. It should be borne in mind that the boundary-layer thickness increases with Z , although this is not apparent in the figure because the scaled radial coordinate $\sigma = (R - 1)/\zeta$ has been used. Note that the azimuthal velocity at $Z = 0$ is $V_\theta(\sigma) = S(1 - V_z(\sigma))$. As Z increases, small departures from this profile arise. Figures 4 and 5 show results for $Z = 0.5$ and different values of S . When $S \lesssim 1$, $V_z(\sigma)$ is a modified Blasius profile. However, for $S \gtrsim 4$, $V_z(\sigma)$ is no longer monotonic having a maximum at finite σ . At large S , the maximum is large and the profile is better described as an axial wall jet, rather than a boundary layer. At first sight, it is perhaps surprising that increasing the rotation rate leads to a stronger and stronger axial flow. Increasing S causes V_θ to increase (figure 4). This in turn produces an increasing radial pressure gradient due to the centrifugal force. Since the pressure is constant outside the boundary layer, the pressure within the layer drops (figure 5) with Z . The development of the flow means that the axial pressure gradient becomes

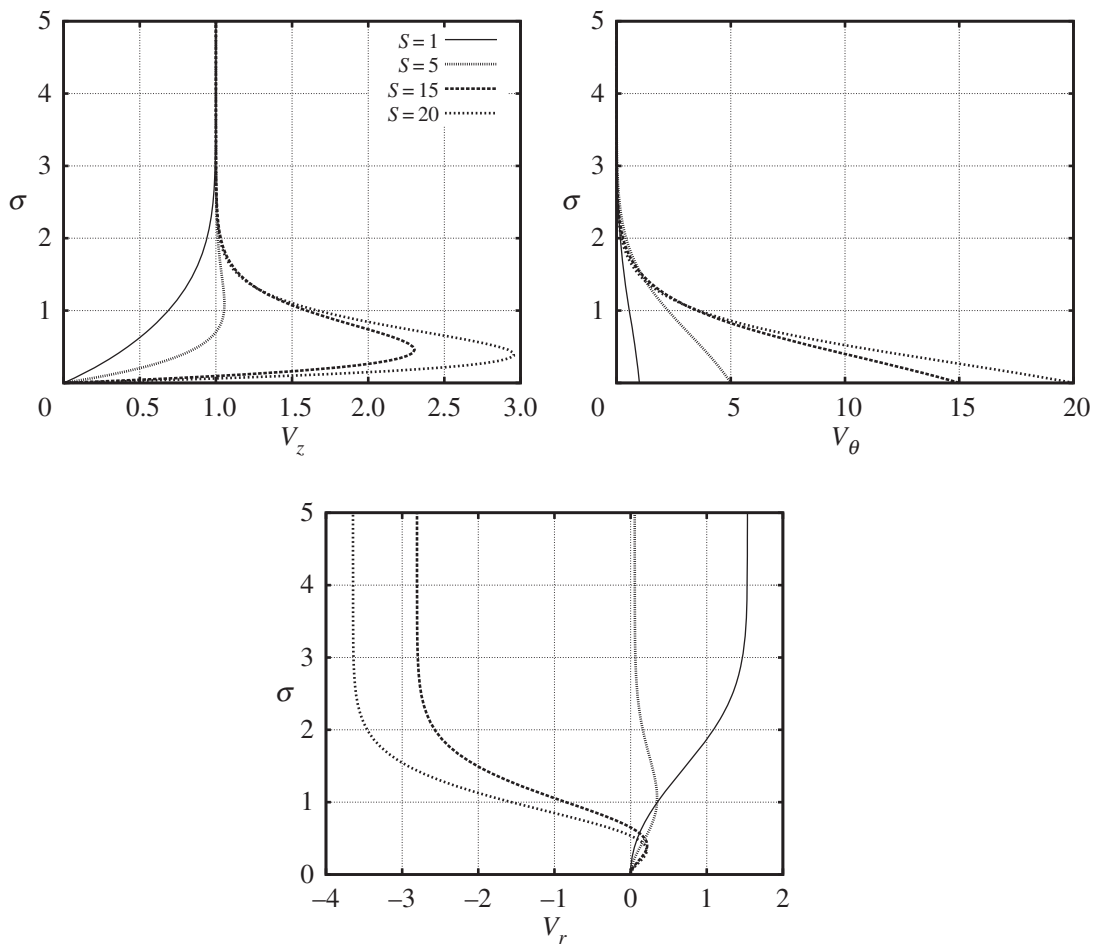


Figure 4. Velocity profiles $V_z(\sigma)$, $V_\theta(\sigma)$ and $V_r(\sigma)$ at $Z = 0.5$ for different values of rotation rate S .

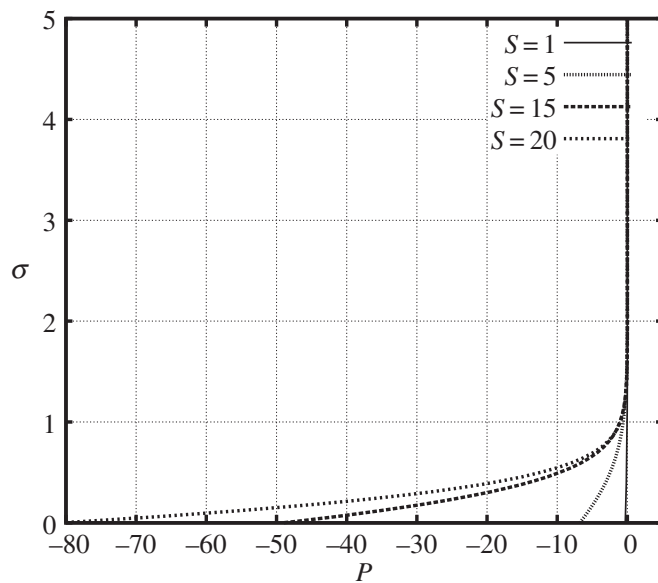


Figure 5. Pressure profile $P(\sigma)$ at $Z = 0.5$ for different values of S .

larger and larger, thus driving a strong axial wall jet. Whereas for lower values of S , boundary-layer thickening leads to positive V_r , at large S entrainment by the wall jet gives negative V_r outside the layer (figure 4).

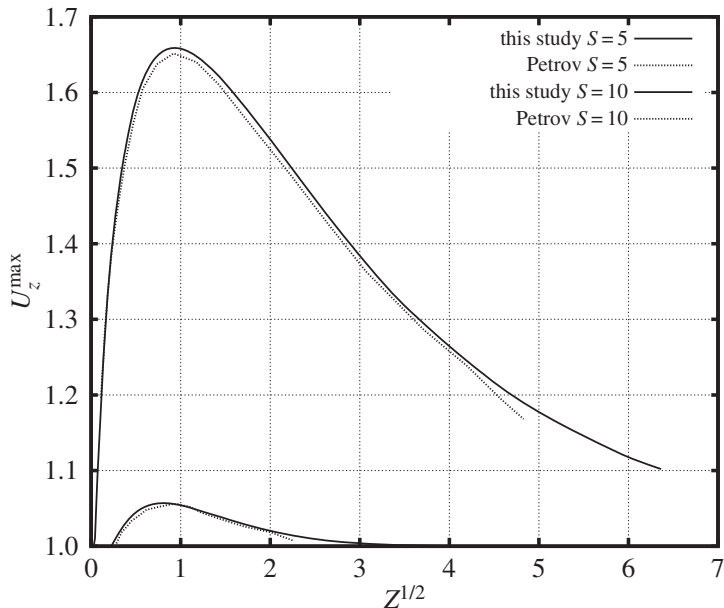


Figure 6. Comparison of U_z^{\max} as a function of $Z^{1/2}$ obtained by the present study with [7] for the case of $S = 5$ and $S = 10$.

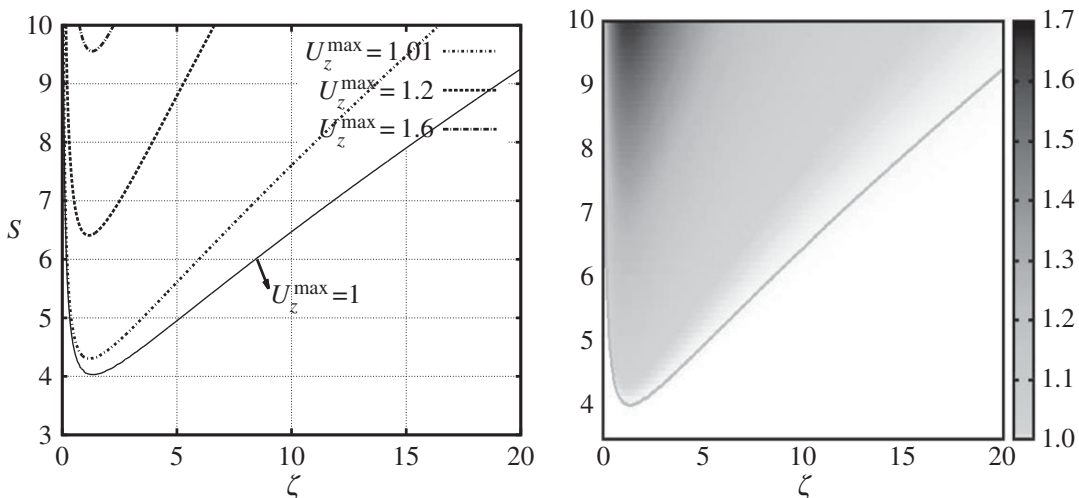


Figure 7. Greyscale plot of U_z^{\max} alongside a contour plot of U_z^{\max} . The figure also shows the boundary (solid line) between $U_z^{\max} = 1$ and $U_z^{\max} > 1$.

The existence of a wall jet at large S is apparent in the axial velocity profiles given by Petrov [7]. However, that article only gives such profiles for the case of small Z (thin boundary layer) and no explanation is provided. Petrov [7] also gives the maximum axial velocity $U_z^{\max} = \max_R(U_z(R))$ as a function of Z . Figure 6 shows a comparison with our results. A small difference is apparent, the origin of which is unclear.

Figure 7 shows contours of constant U_z^{\max} in the (S, ζ) -plane as well as the boundary (solid line) separating the region in which $U_z^{\max} = 1$ from that in which $U_z^{\max} > 1$ (which we interpret as indicating a wall jet). It will be seen that there is a threshold, $S = 4.15$, below which $U_z^{\max} = 1$. Above this value, the wall jet exists for some range of axial position. Note that, whatever the strength of rotation, the wall jet eventually disappears sufficiently far downstream.

The thickness of the boundary layer/wall jet can be measured using

$$\delta = \frac{1}{U_z^{\max}} \int_1^\infty |1 - U_z| dR. \quad (4.1)$$

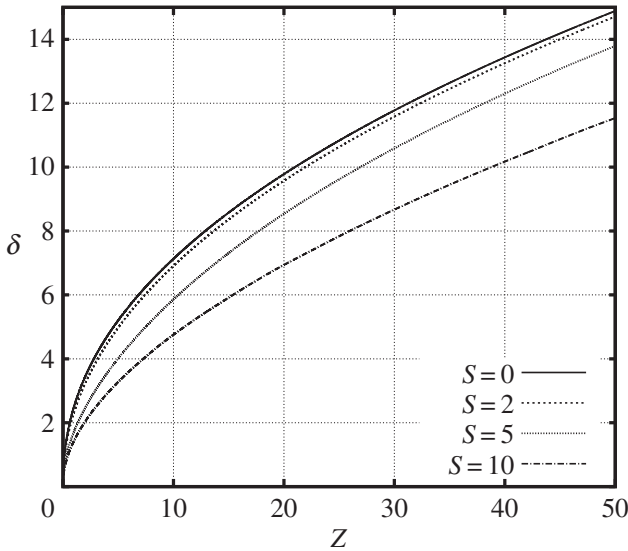


Figure 8. Boundary-layer/wall-jet thickness δ versus Z for different values of S .

The absolute value is taken to make the integral always positive and the division by U_z^{\max} allows for the strong wall jets which arise at large S . Figure 8 shows $\delta(Z)$ for different values of S . The layer thickness is seen to increase with Z in a roughly parabolic manner (recall that the thickness behaves as $Z^{1/2}$ for small Z). Thickening of the layer is due to viscous diffusion in the usual manner. Increasing S causes the layer to become thinner. At large S , the wall jet is of increasing strength. Viscous diffusion competes with axial convection, the latter being of growing importance, hence the decrease of δ with increasing S .

5. Asymptotic analysis

(a) Large-Z asymptotics

Suitable coordinates are

$$\eta = \frac{R}{\zeta}, \quad \chi = \ln(\zeta). \quad (5.1)$$

Here, we have followed Glauert & Lighthill [3], who used a logarithmic axial coordinate for the non-rotating cylinder problem. This coordinate reflects slower and slower evolution of the flow in the streamwise direction as Z increases. Using these coordinates, equations (2.11)–(2.16) become

$$U_z \left(\frac{\partial U_z}{\partial \chi} - \eta \frac{\partial U_z}{\partial \eta} \right) + \frac{U_r}{\eta} \frac{\partial U_z}{\partial \eta} = \frac{e^{-2\chi}}{\eta^2} \left(\eta \frac{\partial P}{\partial \eta} - \frac{\partial P}{\partial \chi} \right) + \frac{\partial^2 U_z}{\partial \eta^2} + \frac{1}{\eta} \frac{\partial U_z}{\partial \eta}, \quad (5.2)$$

$$U_\theta^2 + 2P = \eta \frac{\partial P}{\partial \eta}, \quad (5.3)$$

$$U_z \left(\frac{\partial U_\theta}{\partial \chi} - \eta \frac{\partial U_\theta}{\partial \eta} \right) + \frac{U_r}{\eta} \frac{\partial U_\theta}{\partial \eta} = \frac{\partial^2 U_\theta}{\partial \eta^2} - \frac{1}{\eta} \frac{\partial U_\theta}{\partial \eta}, \quad (5.4)$$

$$\frac{\partial U_z}{\partial \chi} - \eta \frac{\partial U_z}{\partial \eta} + \frac{1}{\eta} \frac{\partial U_r}{\partial \eta} = 0, \quad (5.5)$$

$$U_z = U_r = 0, \quad U_\theta = S \quad \eta = e^{-\chi} \quad (5.6)$$

and

$$U_z \rightarrow 1, \quad U_\theta \rightarrow 0, \quad P \rightarrow 0 \quad \eta \rightarrow \infty. \quad (5.7)$$

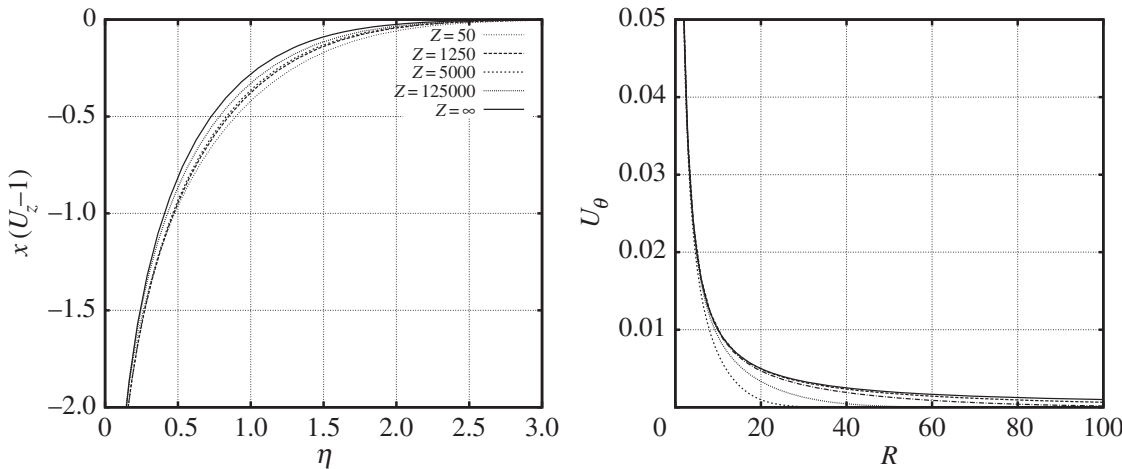


Figure 9. Comparison of $\chi(U_z - 1)$ and $u_\theta = U_\theta/R$ for different values of Z at $S = 0.1$ with the $Z \rightarrow \infty$ solution.

It is shown in appendix A that U_z , U_r , U_θ and P have asymptotic expansions in powers of χ^{-1} . The factor of $e^{-2\chi}$ in equation (5.2) is exponentially small and is hence negligible at all algebraic orders. Without the corresponding term in equation (5.2), U_z and U_r decouple from U_θ and P , though the latter depends on the former. Thus, we expect such decoupling to hold at all orders. This is indeed what is found in appendix A, where the governing equations for the coefficients of the expansions in powers of χ^{-1} are obtained for all orders. Given decoupling, rotation does not enter into the asymptotics of U_z and U_r , which are consequently the same as for the non-rotating case.

Glauert & Lighthill [3] studied the case without rotation and obtained the expansions of U_z and U_r . Appendix A extends the analysis to include rotation and gives detailed results up to order 5. At first order, the asymptotic solution can be obtained analytically and is given by

$$U_z \sim 1 - \chi^{-1} \int_{\eta}^{\infty} \frac{e^{-\xi^2/2}}{\xi} d\xi, \quad (5.8)$$

$$U_r \sim \chi^{-1} (1 - e^{-\eta^2/2}), \quad (5.9)$$

$$U_\theta \sim S e^{-\eta^2/2} \quad (5.10)$$

and

$$P \sim -S^2 \eta^2 \int_{\eta}^{\infty} \frac{e^{-\xi^2}}{\xi^3} d\xi. \quad (5.11)$$

In figure 9, the results for U_z show convergence to the asymptotic form (5.8), while those for $u_\theta = U_\theta/R$ converge to $u_\theta \sim S/R$, which is the flow due to a rotating cylinder, infinite in both axial directions (rather than semi-infinite) and without axial flow.

(b) Large- S asymptotics

As we saw in the previous section, the numerical results show the existence of a wall jet at large S . In this limit, appropriate scaled variables are

$$Z^* = \frac{Z}{S}, \quad R^* = R \quad (5.12)$$

and

$$U_z^* = \frac{U_z}{S}, \quad U_r^* = U_r, \quad U_\theta^* = \frac{U_\theta}{S}, \quad P^* = \frac{P}{S^2}. \quad (5.13)$$

The scaling of Z reflects the increasing distance required for flow development as the rotation rate increases. The scaling of U_z and U_θ indicates the strengthening flow velocity as S increases.

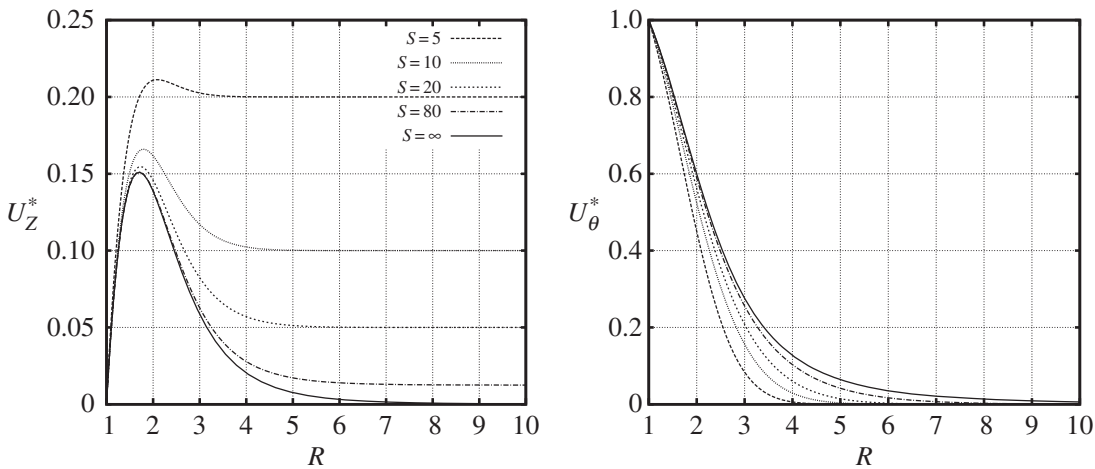


Figure 10. Comparison of U_z^* and U_θ^* for different values of S and $Z^* = 0.1$ with the $S \rightarrow \infty$ asymptotic solution.

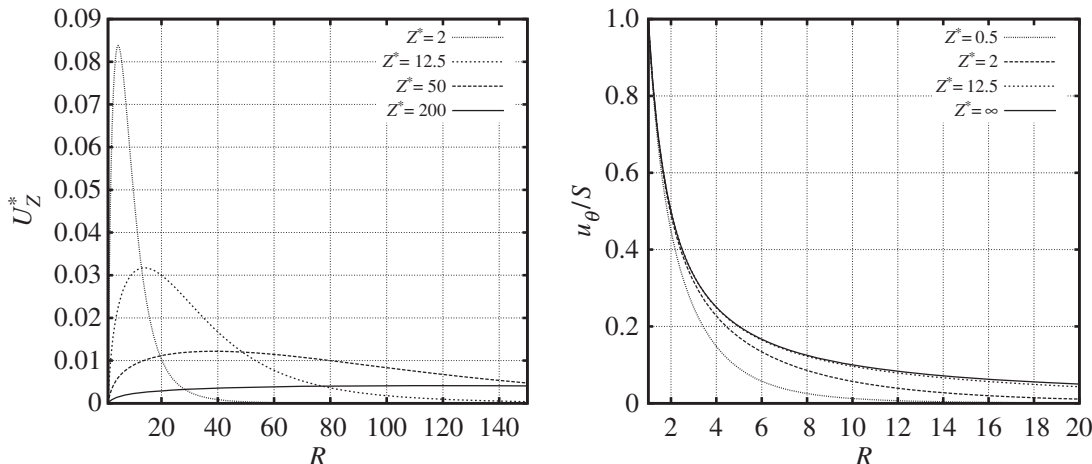


Figure 11. $u_z/S = U_z^*$ and u_θ/S at different values of Z^* for a rotating cylinder in the limit $S \rightarrow \infty$.

The large- S asymptotic expansions of U_z^* , U_r^* , U_θ^* and P^* proceed as powers of S^{-1} . At leading order (S^0), we find

$$U_z^* \frac{\partial U_z^*}{\partial Z^*} + \frac{U_r^*}{R^*} \frac{\partial U_z^*}{\partial R^*} = -\frac{1}{R^{*2}} \frac{\partial P^*}{\partial Z^*} + \frac{\partial^2 U_z^*}{\partial R^{*2}} + \frac{1}{R^*} \frac{\partial U_z^*}{\partial R^*}, \quad (5.14)$$

$$U_\theta^{*2} = R^* \frac{\partial P^*}{\partial R^*} - 2P^*, \quad (5.15)$$

$$U_z^* \frac{\partial U_\theta^*}{\partial Z^*} + \frac{U_r^*}{R^*} \frac{\partial U_\theta^*}{\partial R^*} = \frac{\partial^2 U_\theta^*}{\partial R^{*2}} - \frac{1}{R^*} \frac{\partial U_\theta^*}{\partial R^*} \quad (5.16)$$

and

$$\frac{\partial U_z^*}{\partial Z^*} + \frac{1}{R^*} \frac{\partial U_r^*}{\partial R^*} = 0, \quad (5.17)$$

with the following inlet and boundary conditions:

$$U_z^* = 0, \quad U_\theta^* = 0 \quad Z^* = 0, \quad (5.18)$$

$$U_z^* = 0, \quad U_r^* = 0, \quad U_\theta^* = 1 \quad R^* = 1 \quad (5.19)$$

and

$$U_z^* = 0, \quad U_\theta^* = 0, \quad P^* = 0 \quad R^* \rightarrow \infty. \quad (5.20)$$

Figure 10 shows the solution of the above problem (solid line) compared with the numerical results discussed before for $Z^* = 0.1$ and different values of S . It is apparent that the asymptotics

are indeed approached as $S \rightarrow \infty$. Figure 11 shows the leading-order asymptotic solution for different values of Z^* . We see that the large- Z limit ($u_\theta \sim SR^{-1}$) is approached by u_θ as $Z^* \rightarrow \infty$.

Note that the limit $S \rightarrow \infty$ can be reached in two ways: either by increasing the rotation rate, or by decreasing the velocity U_∞ to zero. Note also that u_z/S and u_θ/S are the velocity components non-dimensionalized by Ωa , rather than U_∞ , and that $Z^* = z/Re_\Omega$, where $Re_\Omega = \Omega a^2/\nu$ is the Reynolds number based on the rotational velocity Ωa . Thus, figure 11 can be interpreted as showing the flow due to a rotating, semi-infinite cylinder in a still fluid ($U_\infty = 0$). It can be shown that the separation of radial and axial length scales, which underlies the boundary-layer type approximation we have used, is valid if either of the Reynolds numbers, Re or Re_Ω , is large.

6. Conclusion

In this paper, we have presented a study of the flow around a rotating cylinder in an axial stream. We have assumed a smooth nose to avoid flow separation. The two non-dimensional control parameters of the problem are: Reynolds number (Re) and rotation rate (S). The flow equations are formulated using a boundary-layer type approximation, appropriate at large Reynolds numbers and in which the flow is assumed to evolve slowly in the streamwise direction in comparison to the radial direction. The resulting equations are not limited to the case in which the boundary layer is thin compared with the cylinder radius. By using appropriate scalings, we remove Re from the problem.

The results show that the boundary-layer thickness increases with axial distance, becoming comparable with the cylinder radius a at distances of $O(Re a)$. Prior to this, the layer is thin compared with the radius and the flow is close to the Blasius profile of a flat plate. However, it differs from the Blasius solution due to the effects of curvature and rotation at larger downstream distances. As S increases, the centrifugal force creates an increasing radial pressure gradient, which combined with axial development, implies an increasing axial gradient of pressure. Above $S = 4.15$, the maximum velocity exceeds the free-stream velocity for a range of Z and we say that a wall jet exists. This jet becomes stronger and stronger as $S \rightarrow \infty$.

In the limit of large Z , we find that the axial and radial components of velocity decouple from the azimuthal velocity component and pressure. All these quantities are found to have asymptotic expansions in inverse powers of $\ln(Z)$, a result already obtained for the non-rotating case by Glauert & Lighthill [3], and here extended to include rotation. The leading-order term in the u_θ expansion is $u_\theta \sim SR^{-1}$, which is the flow expected for a rotating cylinder, infinite in both directions. Because U_θ becomes independent of Z , the same is true of the pressure field resulting from the centrifugal force, hence the absence of an axial pressure gradient to drive the axial/radial flow. This is the reason for the decoupling.

When S is large, we introduce appropriate scalings for Z , U_z , U_θ and P . The asymptotic expansions of the scaled velocity and pressure proceed as inverse powers of S , beginning with S^0 . The leading-order term describes an axial wall jet due to a rotating cylinder in a fluid at rest.

Data accessibility. No new data were collected in the course of this research.

Authors' contributions. S.D.M. has carried out the research as part of his PhD, supervised by B.P. and J.F.S.; B.P. and R.G. have formulated the problem as part of the longer term Franco-Indian collaboration; S.D.M. has started on this work with R.G.

Competing interests. We have no competing interests.

Funding. The authors are grateful to the French Ministry of Education and Research and the Indo-French Centre for the Promotion of Advanced Research-CEFIPRA for financial support.

Appendix A. Large Z asymptotic expansions

The flow variables are expressed as asymptotic expansions in inverse powers of χ :

$$U_z \sim 1 + \sum_{n=1}^{\infty} \chi^{-n} U_z^{(n)}(\eta), \quad (\text{A } 1)$$

$$U_r \sim \sum_{n=1}^{\infty} \chi^{-n} U_r^{(n)}(\eta), \quad (\text{A } 2)$$

$$U_\theta \sim S \sum_{n=1}^{\infty} \chi^{-n+1} U_\theta^{(n)}(\eta) \quad (\text{A } 3)$$

$$\text{and} \quad P \sim S^2 \sum_{n=1}^{\infty} \chi^{-n+1} P^{(n)}(\eta). \quad (\text{A } 4)$$

Introducing these expansions into equations (5.2)–(5.5) gives

$$\frac{1}{\eta} \frac{d}{d\eta} \left(\eta \frac{dU_z^{(n)}}{d\eta} \right) + \eta \frac{dU_z^{(n)}}{d\eta} = \phi_z^{(n)}, \quad (\text{A } 5)$$

$$\eta^3 \frac{d}{d\eta} \left(\frac{P^{(n)}}{\eta^2} \right) = \psi^{(n)}, \quad (\text{A } 6)$$

$$\eta \frac{d}{d\eta} \left(\frac{1}{\eta} \frac{dU_\theta^{(n)}}{d\eta} \right) + \eta \frac{dU_\theta^{(n)}}{d\eta} = \phi_\theta^{(n)} \quad (\text{A } 7)$$

$$\text{and} \quad \frac{1}{\eta} \frac{dU_r^{(n)}}{d\eta} - \eta \frac{dU_z^{(n)}}{d\eta} = \phi_r^{(n)}, \quad (\text{A } 8)$$

where

$$\phi_z^{(n)} = (1-n)U_z^{(n-1)} + \sum_m \left(\left(\frac{U_r^{(m)}}{\eta} - \eta U_z^{(m)} \right) \frac{dU_z^{(n-m)}}{d\eta} - m U_z^{(m)} U_z^{(n-m-1)} \right), \quad (\text{A } 9)$$

$$\phi_\theta^{(n)} = (2-n)U_\theta^{(n-1)} + \sum_m \left(\left(\frac{U_r^{(m)}}{\eta} - \eta U_z^{(m)} \right) \frac{dU_\theta^{(n-m)}}{d\eta} - (m-1) U_\theta^{(m)} U_z^{(n-m-1)} \right) \quad (\text{A } 10)$$

$$\text{and} \quad \phi_r^{(n)} = (n-1)U_z^{(n-1)}, \quad \psi^{(n)} = \sum_m U_\theta^{(m)} U_\theta^{(n-m+1)}. \quad (\text{A } 11)$$

Equations (A 5)–(A 8) are to be solved, along with appropriate boundary conditions (which will be derived shortly), for the n th-order coefficients of the expansions, $U_z^{(n)}$, $U_r^{(n)}$, $U_\theta^{(n)}$ and $P^{(n)}$ ($n \geq 1$). It should be noted that, in equations (A 9)–(A 11), $U_z^{(m)}$, $U_r^{(m)}$ and $U_\theta^{(m)}$ are to be interpreted as zero when $m \leq 0$. The governing equations for $U_z^{(n)}$ and $U_r^{(n)}$ are independent of $U_\theta^{(n)}$ and $P^{(n)}$. Thus, the asymptotics of $U_z^{(n)}$ and $U_r^{(n)}$ are the same as for a non-rotating cylinder and are governed by equations (A 5), (A 8), (A 9) and the first of the equations (A 11). $U_\theta^{(n)}$ is determined by equations (A 7) and (A 10), while $P^{(n)}$ follows from equation (A 6) and the second of the equations (A 11). Note that $\phi_z^{(n)}$, $\phi_r^{(n)}$ and $\phi_\theta^{(n)}$ depend only on the solution at lower orders than n , suggesting a method which proceeds from $n = 1$ to successively higher values of n .

The boundary conditions at $\eta \rightarrow \infty$ are

$$U_z^{(n)} = U_\theta^{(n)} = P^{(n)} = 0. \quad (\text{A } 12)$$

Application of the boundary conditions (2.15) at the cylinder surface requires the introduction of an inner region, $R = O(1)$, represented by the expansions

$$U_z \sim \sum_{n=1}^{\infty} \chi^{-n} \hat{U}_z^{(n)}(R), \quad (\text{A } 13)$$

$$U_r \sim \sum_{n=1}^{\infty} \chi^{-n} \hat{U}_r^{(n)}(R), \quad (\text{A } 14)$$

$$U_{\theta} \sim S \sum_{n=1}^{\infty} \chi^{-n+1} \hat{U}_{\theta}^{(n)}(R) \quad (\text{A } 15)$$

and

$$P \sim S^2 \sum_{n=1}^{\infty} \chi^{-n+1} \hat{P}^{(n)}(R). \quad (\text{A } 16)$$

Equations (2.11), (2.13) and (2.14) are rewritten using the axial coordinate χ in place of Z . Equation (2.14) yields

$$\frac{\partial \hat{U}_r^{(n)}}{\partial R} = 0, \quad (\text{A } 17)$$

which, together with the boundary conditions (2.15) gives $\hat{U}_r^{(n)} = 0$. Equations (2.11) and (2.13) imply

$$\frac{\partial^2 \hat{U}_z^{(n)}}{\partial R^2} + \frac{1}{R} \frac{\partial \hat{U}_z^{(n)}}{\partial R} = 0 \quad (\text{A } 18)$$

and

$$\frac{\partial^2 \hat{U}_{\theta}^{(n)}}{\partial R^2} - \frac{1}{R} \frac{\partial \hat{U}_{\theta}^{(n)}}{\partial R} = 0, \quad (\text{A } 19)$$

hence

$$\hat{U}_z^{(n)}(R) = A_n \ln R + B_n \quad (\text{A } 20)$$

and

$$\hat{U}_{\theta}^{(n)}(R) = C_n R^2 + D_n. \quad (\text{A } 21)$$

The boundary conditions (2.15) imply $B_n = 0$, $C_1 + D_1 = 1$, and $C_n + D_n = 0$ for $n > 1$.

Recalling that $R = \xi \eta = e^{\chi} \eta$, the inner expansions give

$$U_z \sim A_1 + \sum_{n=1}^{\infty} \chi^{-n} (A_n \ln \eta + A_{n+1}), \quad (\text{A } 22)$$

$$U_{\theta} \sim S \left(1 + \sum_{n=1}^{\infty} C_n \chi^{-n} (e^{2\chi} \eta^2 - 1) \right) \quad (\text{A } 23)$$

and

$$U_r \sim 0, \quad (\text{A } 24)$$

when expressed in terms of the outer coordinate, η . Matching requires $A_1 = 1$, $C_n = 0$ and

$$U_z^{(n)} \sim A_n \ln \eta + A_{n+1}, \quad (\text{A } 25)$$

$$U_{\theta}^{(1)} \rightarrow 1 \quad \text{and} \quad U_{\theta}^{(n)} \rightarrow 0 \text{ for } n > 1 \quad (\text{A } 26)$$

and

$$U_r^{(n)} \rightarrow 0, \quad (\text{A } 27)$$

as $\eta \rightarrow 0$. It follows from (A 25) that

$$\eta \frac{dU_z^{(n)}}{d\eta} \rightarrow A_n \quad (\text{A } 28)$$

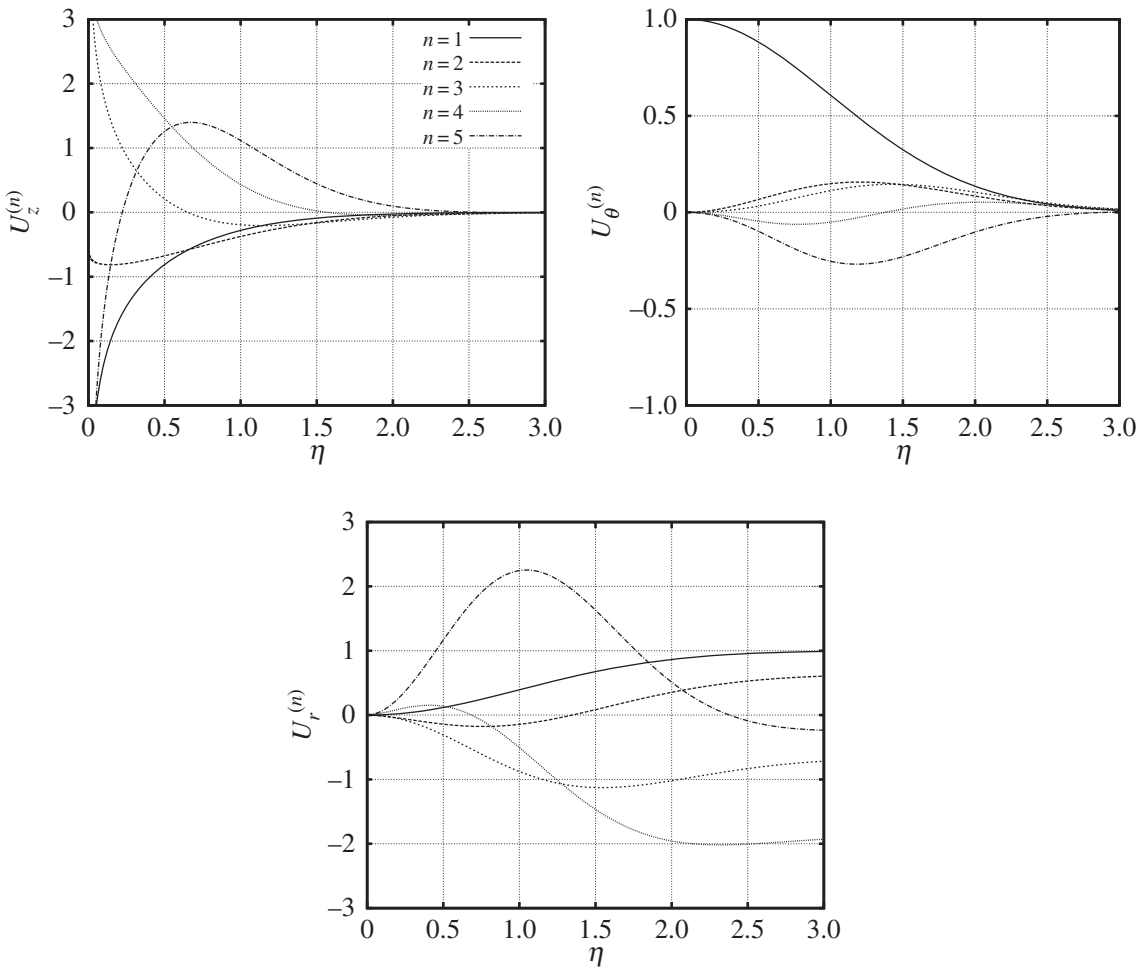


Figure 12. First five coefficients of the large- Z asymptotic expansions of U_z , U_θ and U_r .

and

$$A_{n+1} = \lim_{\eta \rightarrow 0} (U_z^{(n)} - A_n \ln \eta). \quad (\text{A } 29)$$

Assuming A_n is known, equations (A 5)–(A 11) and the boundary conditions (A 12) and (A 26)–(A 28) can be solved for $U_z^{(n)}$, $U_r^{(n)}$, $U_\theta^{(n)}$ and $P^{(n)}$. $A_1 = 1$ gets the process started and leads to the leading-order outer solution, (5.8)–(5.11), in agreement with [3]. Equation (A 29) gives A_n at the next order, allowing solution at successively higher orders. It can be shown that

$$U_z^{(n)} = A_n \ln \eta + A_{n+1} + O(\eta^2 \ln^{p_n} \eta), \quad U_\theta^{(n)} = 1 - q_n + O(\eta^2), \quad U_r^{(n)} = O(\eta^2 \ln^{q_n} \eta), \quad (\text{A } 30)$$

as $\eta \rightarrow 0$, where $q_n = p_{n+1} - 1$, $p_1 = 0$, $p_2 = 1$ and $p_n = 2$ for $n \geq 3$. The terms in (A 30) indicated by the $O()$ notation are exponentially small in the inner region, while the remaining ones reproduce the inner solution. Thus, the outer expansions in fact apply in the inner region.

The above procedure has been implemented numerically and results up to $n = 5$ are presented in figure 12. Figure 13 shows the comparison of numerical solution of U_z at $Z = 5000$ and $S = 1$ with the asymptotic solution obtained by truncating at different orders n . Although this result shows good convergence, and therefore further confirms both numerical and analytical results, it should be borne in mind that the expansions (A 1)–(A 4) are, in fact, asymptotic as $Z \rightarrow \infty$, rather than necessarily convergent at any finite Z .

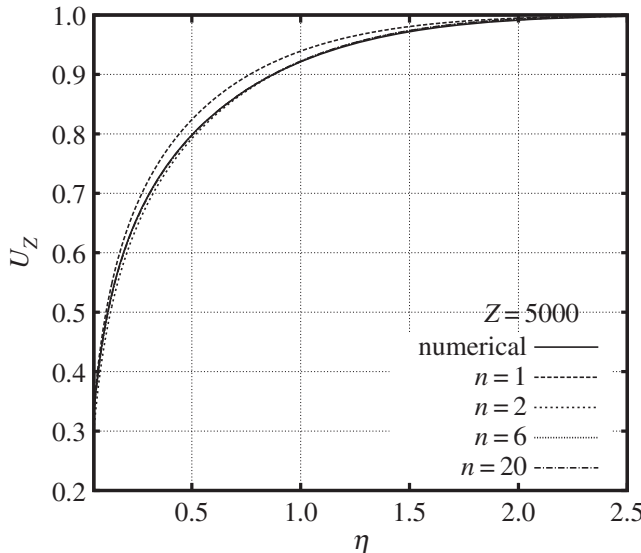


Figure 13. Comparison of the numerical solution of U_z with the large- Z asymptotic solution truncated at different orders for $Z = 5000$ at $S = 1$.

Appendix B. Flow over the nose

Large Reynolds number implies a thin boundary layer over the nose. Schlichting [12] gives the axisymmetric boundary-layer equations in terms of curvilinear coordinates, x, y, θ , where x is distance along the surface, and y is distance normal to the surface. Here, we use the non-dimensional coordinates, velocity components and pressure:

$$\tilde{y} = \frac{Re^{1/2}y}{a}, \quad \tilde{x} = \frac{x}{a} \quad (\text{B } 1)$$

and

$$\tilde{u}_y = \frac{Re^{1/2}u_y}{U_\infty}, \quad \tilde{u}_x = \frac{u_x}{U_\infty}, \quad \tilde{u}_\theta = \frac{u_\theta}{U_\infty}, \quad \tilde{p} = p. \quad (\text{B } 2)$$

The boundary-layer equations in these variables are

$$\tilde{u}_x \frac{\partial \tilde{u}_x}{\partial \tilde{x}} + \tilde{u}_y \frac{\partial \tilde{u}_x}{\partial \tilde{y}} - \frac{\tilde{u}_\theta^2}{\tilde{R}} \frac{d\tilde{R}}{d\tilde{x}} = -\frac{\partial \tilde{p}}{\partial \tilde{x}} + \frac{\partial^2 \tilde{u}_x}{\partial \tilde{y}^2}, \quad (\text{B } 3)$$

$$\tilde{u}_x \frac{\partial \tilde{u}_\theta}{\partial \tilde{x}} + \tilde{u}_y \frac{\partial \tilde{u}_\theta}{\partial \tilde{y}} + \frac{\tilde{u}_\theta \tilde{u}_x}{\tilde{R}} \frac{d\tilde{R}}{d\tilde{x}} = \frac{\partial^2 \tilde{u}_\theta}{\partial \tilde{y}^2} \quad (\text{B } 4)$$

$$\frac{\partial \tilde{p}}{\partial \tilde{y}} = 0$$

and

$$\frac{\partial \tilde{u}_x}{\partial \tilde{x}} + \frac{\tilde{u}_x}{\tilde{R}} \frac{d\tilde{R}}{d\tilde{x}} + \frac{\partial \tilde{u}_y}{\partial \tilde{y}} = 0, \quad (\text{B } 5)$$

with the boundary conditions

$$\tilde{u}_x = \tilde{u}_y = 0, \quad \tilde{u}_\theta = S\tilde{R}(\tilde{x}) \quad \tilde{y} = 0 \quad (\text{B } 6)$$

and

$$\tilde{u}_x \rightarrow U_{\text{ext}}(\tilde{x}), \quad \tilde{u}_\theta \rightarrow 0 \quad \tilde{y} \rightarrow \infty, \quad (\text{B } 7)$$

where the nose geometry is represented by $r = \tilde{R}(\tilde{x})$ and $U_{\text{ext}}(\tilde{x})$ is the velocity just outside the boundary layer. Equations (B 3)–(B 5) can, in principle, be solved to obtain the flow over the nose. Note the centrifugal term in equation (B 3), which will no doubt produce a wall jet on the nose at sufficiently large S . The terms containing $d\tilde{R}/d\tilde{x}$ vanish on the constant-radius cylinder (where \tilde{x}

and z coincide to within an additive constant) and equations (B3)–(B5) then become those of a flat-plate. Thus, we expect the flow to approach the Blasius solution as $\tilde{x} \rightarrow \infty$. There are, in fact, two asymptotic regions, $\tilde{x} = O(1)$ and $\tilde{x} = O(Re)$, the former being described by equations (B3)–(B5) and the latter by equations (2.11)–(2.14). Matching of the regions requires the Blasius flow as inlet conditions to the latter equations, as noted in the main text. Thus, the flow in the region $Z = O(1)$, which is the subject of this paper, is insensitive to the geometry of the nose. Note that a wall jet may appear on the nose, subsequently disappearing on the cylinder, later reappearing in the region $Z = O(1)$.

References

1. Seban RA, Bond R. 1951 Skin-friction and heat-transfer characteristics of a laminar boundary layer on a cylinder in axial incompressible flow. *J. Aeronaut. Sci.* **18**, 671–675. (doi:10.2514/8.2076)
2. Kelly HR. 1954 A note on the laminar boundary layer on a circular cylinder in axial incompressible flow. *J. Aeronaut. Sci.* **21**, 634. (doi:10.2514/8.3151)
3. Glauert MB, Lighthill MJ. 1955 The axisymmetric boundary layer on a long thin cylinder. *Proc. R. Soc. Lond. A* **230**, 188–203. (doi:10.1098/rspa.1955.0121)
4. Jaffe NA, Okamura TT. 1968 The transverse curvature effect on the incompressible laminar boundary layer for longitudinal flow over a cylinder. *Z. Angew. Math. Phys. ZAMP* **19**, 564–574. (doi:10.1007/BF01594964)
5. Tutty OR, Price WG, Parsons AT. 2002 Boundary layer flow on a long thin cylinder. *Phys. Fluids* **14**, 628. (doi:10.1063/1.1427921)
6. Vinod N, Govindarajan R. 1955 Secondary instabilities in incompressible axisymmetric boundary layers: effect of transverse curvature. *J. Fluids Eng. Trans. ASME* **134**, 024503. (doi:10.1115/1.4005767)
7. Petrov GV. 1976 Boundary layer on a rotating cylinder in axial flow. *J. Appl. Mech. Tech. Phys.* **17**, 506–510. (doi:10.1007/BF00852000)
8. Kao KH, Chow CY. 1991 Stability of the boundary layer on a spinning semi-infinite circular cylinder. *J. Spacecraft Rockets* **28**, 284–291. (doi:10.2514/3.26242)
9. Herrada MA, Del Pino C, Fernandez-Feria R. 2008 Stability of the boundary layer flow on a long thin rotating cylinder. *Phys. Fluids* **20**, 034105. (doi:10.1063/1.2885330)
10. Batchelor GK. 1967 *An introduction to fluid dynamics*. Cambridge, UK: Cambridge University Press.
11. Scott JF. 2013 Moffatt-type flows in a trihedral cone. *J. Fluid Mech.* **725**, 446–461. (doi:10.1017/jfm.2013.180)
12. Schlichting H. 1956 Laminar flow about a rotating body of revolution in an axial airstream. *Ingenieur-Arch.* **21**, 227–244. (<http://ntrs.nasa.gov/archive/nasa/20050019631.pdf>).

[A23]

Instability of flow around a rotating, semi-infinite cylinder

S. Derebail Muralidhar, B. Pier & J. F. Scott

Physical Review Fluids **1**, 053602 (15 pages) (2016)

doi:10.1103/PhysRevFluids.1.053602
<https://hal.archives-ouvertes.fr/hal-01368877>

Instability of flow around a rotating, semi-infinite cylinder

Srikanth Derebail Muralidhar, Benoît Pier, and Julian F. Scott

Laboratoire de mécanique des fluides et d'acoustique, CNRS–École centrale de Lyon–Université de Lyon 1–INSA Lyon, 36 avenue Guy-de-Collongue, 69134 Écully, France

(Received 24 June 2016; published 16 September 2016)

Stability of flow around a rotating, semi-infinite cylinder placed in an axial stream is investigated. Assuming large Reynolds number, the basic flow is computed numerically as described by Derebail Muralidhar *et al.* [Proc. R. Soc. London, Ser. A **472**, 20150850 (2016)], while numerical solution of the local stability equations allows calculation of the modal growth rates and hence determination of flow stability or instability. The problem has three nondimensional parameters: the Reynolds number Re , the rotation rate S , and the axial location Z . Small amounts of rotation are found to strongly affect flow stability. This is the result of a nearly neutral mode of the nonrotating cylinder which controls stability at small S . Even small rotation can produce a sufficient perturbation that the mode goes from decaying to growing, with obvious consequences for stability. Without rotation, the flow is stable below a Reynolds number of about 1060 and also beyond a threshold Z . With rotation, no matter how small, instability is no longer constrained by a minimum Re nor a maximum Z . In particular, the critical Reynolds number goes to zero as $Z \rightarrow \infty$, so the flow is always unstable at large enough axial distances from the nose. As Z is increased, the flow goes from stability at small Z to instability at large Z . If the critical Reynolds number is a monotonic decreasing function of Z , as it is for S between about 0.0045 and 5, there is a single boundary in Z , which separates the stable from the unstable part of the flow. On the other hand, when the critical Reynolds number is nonmonotonic, there can, depending on the choice of Re , be several such boundaries and flow stability switches more than once as Z is increased. Detailed results showing the critical Reynolds number as a function of Z for different rotation rates are given. We also obtain an asymptotic expansion of the critical Reynolds number at large Z and use perturbation theory to further quantify the behavior at small S .

DOI: [10.1103/PhysRevFluids.1.053602](https://doi.org/10.1103/PhysRevFluids.1.053602)

I. INTRODUCTION

The stability of three-dimensional boundary layers provides a rich subject of research (see Reed and Saric [1], Saric *et al.* [2], and references therein). Such flows are often due to rotating bodies as, for example, disks [3,4], cones [5,6], or spheres [7]. Here, we consider a semi-infinite cylinder, rotating about its axis and placed in a high-Reynolds-number axial stream, thus inducing a steady, axisymmetric, three-velocity-component boundary layer whose flow field depends on rotation and curvature of the cylinder, as we have already described in an earlier paper [8], henceforth referred to as I. In this paper, we study the stability of this flow for a wide range of parameters, to determine the effects of rotation and curvature.

As noted above, the basic flow around a rotating cylinder in an axial stream (see Fig. 1) has been extensively studied by the authors in preparation for the present stability analysis. To avoid the flow separation typically induced by sharp corners, a smooth nose is assumed at the front of the cylinder. The problem has two nondimensional control parameters: a Reynolds number $Re = U_\infty a / v$, constructed using the incident velocity U_∞ and cylinder radius a , and a rotation rate $S = \Omega a / U_\infty$, where Ω is the angular velocity of the cylinder. Assuming large Reynolds number, the basic flow comprises an axisymmetric boundary layer. Initially thin compared to the cylinder radius, the boundary-layer thickness increases with axial distance, becoming comparable to the cylinder radius at large axial distances of order $a Re$. The thickness nonetheless remains small compared with the downstream distance, leading to a separation of length scales (asymptotic in

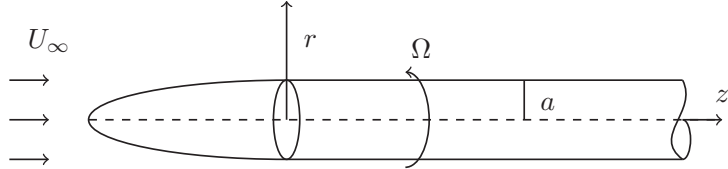


FIG. 1. Schematic diagram of the problem.

the assumed large Reynolds number) between the axial and radial directions and allowing use of a boundary-layer approximation. However, once the thickness is comparable to a , effects of surface curvature and the centrifugal force due to rotation become important and must be included in the boundary-layer equations. The intervention of curvature and rotation at axial distances of order $a \text{ Re}$ is the reason why we focus on this region. Although the basic flow depends on the nose geometry at streamwise distances of order a , boundary-layer development forgets such details and the flow becomes independent of the nose profile at larger distances, in particular those of order $a \text{ Re}$. Interested readers should refer to I for more details of the basic flow, including the appearance of a wall jet for S above about 4 and asymptotic analyses of the limits of large rotation rate and large streamwise distance.

Stability of the Blasius boundary layer on a flat plate has been extensively studied, the primary instability being due to growth of Tollmien-Schlichting waves (see, for example, [9–11]). Stability analysis of a nonrotating cylinder placed in an axial stream was conducted by Tutty [12]. They found that nonaxisymmetric modes have a lower critical Reynolds number than axisymmetric modes and that the flow is stable at all streamwise distances for Reynolds numbers below 1060. Above this critical value, the flow is unstable only for a range of streamwise distance and reverts to being stable at sufficiently large distances. Vinod and Govindarajan [13] studied the secondary instability and also showed that the flow is stable according to inviscid theory.

There have been few studies of the stability of a rotating cylinder placed in an axial stream. Kao and Chow [14] appear to be the first to consider the rotating case, but their basic flow is erroneous because they do not include the centrifugal term in the radial momentum equation. They also studied the nonrotating case, but the results are in disagreement with [12]. This disagreement was noted by Herrada *et al.* [15], who were the first to formulate the correct basic-flow equations. Results were obtained for a range of rotation rates between 0.1 and 1, and are in excellent agreement with our results. They observed that the critical Reynolds numbers were much lower than for the nonrotating case. This motivated us to study the rotating case in a more systematic manner, in particular the range of small rotation rates. To our surprise, we found that the stability characteristics, in particular the critical curves, were significantly dependent on the rotation rate for values of S much lower than the ones covered in Ref. [15]. The elucidation of these differences between the nonrotating case and the rotating case at very low S is one of the main topics of this paper.

To our knowledge, the only published experimental work on a rotating cylinder which matches the geometry of the present study is by Kegelman *et al.* [16]. They give visualizations of different instability modes developing on the cylinder. However, the cylindrical section in their experiments is not long enough to reach distances at which the flow forgets the details of the nose profile (let alone to reach distances at which curvature and rotation become important for the basic flow). Thus, quantitative comparison between our results and [16] is inappropriate and is not attempted.

Formally, the basic-flow and stability equations for the rotating cylinder are the same as those of a vortex core with axial flow (in the quasicylindrical approximation, see [17]). However, the two flows are quite different and it would be rash to draw parallels in terms of stability. In particular, vortex breakdown is associated with an adverse axial pressure gradient of the basic flow, whereas the rotating cylinder has a favorable pressure gradient.

The local stability equations are derived in Sec. II. The numerical scheme is described in Sec. III, along with results of validation. Section IV contains the main results. In Sec. IV C, the limit of low rotation rate is examined in more detail and quantified using a perturbation method.

II. PROBLEM FORMULATION

A semi-infinite cylinder of radius a , which rotates about its axis at angular velocity Ω , is placed in an axial stream of velocity U_∞ (see Fig. 1), the fluid being incompressible and of viscosity ν and density ρ . Lengths, times, velocities, and pressures are nondimensionalized using a , a/U_∞ , U_∞ , and ρU_∞^2 . Adopting cylindrical coordinates (z, r, θ) , the basic (steady and axisymmetric) flow has velocity components U_z, U_r, U_θ and associated pressure denoted by P . As noted in the Introduction, there are two control parameters, namely, the Reynolds number Re and the rotation rate S , given by

$$\text{Re} = \frac{U_\infty a}{\nu}, \quad (1)$$

$$S = \frac{\Omega a}{U_\infty}. \quad (2)$$

To avoid possible confusion, we remark that U_z, U_r, U_θ , and P were denoted by u_z, u_r, u_θ , and p in I, whereas these lower-case quantities are used to represent the flow perturbation in this paper.

We assume large Reynolds number from here on and restrict attention to the flow over the constant-radius part of the cylinder $z > 0$. As discussed in the Introduction, large Reynolds number leads to a separation of length scales in which streamwise evolution of the basic flow is slow compared with its radial variation. Not only does this allow use of the boundary-layer approximation to describe the basic flow, but it is also a prerequisite for local stability analysis. Boundary-layer theory implies that U_r is small compared with U_z and U_θ . Neglect of U_r is the second ingredient of local stability theory.

Under these assumptions, the steady and axisymmetric base-flow components are governed by a generalization of the classical Prandtl boundary-layer equations that allow for the additional effects of both curvature and rotation. Near the nose, the boundary layer is thin compared with the cylinder radius. Thus, in that region, curvature effects are negligible and the flow is close to the Blasius profile of a flat plate. Using a Blasius inlet condition, the entire base flow is then obtained by integrating the boundary-layer equations along the z direction. See I for full theoretical and numerical details about the basic flow.

The linear stability equations are obtained in the usual manner: by adding infinitesimal perturbations (u_z, u_r, u_θ, p) to the basic-flow quantities (U_z, U_r, U_θ, P) , using the nondimensionalized Navier-Stokes equations, and neglecting terms which are nonlinear in the perturbations. The local approximation is then adopted: U_r is neglected, as are variations of U_z and U_θ with respect to z . Invariance with respect to z, θ , and t allows modal solutions of the form

$$\begin{pmatrix} u_z \\ u_r \\ u_\theta \\ p \end{pmatrix} = \begin{pmatrix} v_z(r) \\ v_r(r) \\ v_\theta(r) \\ q(r) \end{pmatrix} e^{i(\alpha z + m\theta - \omega t)}. \quad (3)$$

Here, ω is the complex frequency, while α and m are the axial and azimuthal wave numbers, which are, respectively, real and integer modal parameters. Note that modes occur in complex-conjugate pairs, related by $\alpha \leftrightarrow -\alpha, m \leftrightarrow -m$, and $\omega \leftrightarrow -\omega^*$, where $*$ denotes complex conjugation. It is this conjugation symmetry which allows the construction of physically meaningful (i.e., real) solutions by combining a mode and its conjugate. Conjugation symmetry allows us to restrict attention to $\alpha \geq 0$, while m can take any integer value.

Substituting the modal form for the perturbation in the local stability equations gives

$$i\alpha v_z + v'_r + \frac{1}{r}v_r + \frac{im}{r}v_\theta = 0, \quad (4)$$

$$i\left(\alpha U_z + \frac{m U_\theta}{r} - \omega\right)v_z + U'_z v_r + i\alpha q = \frac{1}{\text{Re}} \left[v''_z + \frac{1}{r}v'_z - \left(\alpha^2 + \frac{m^2}{r^2}\right)v_z \right], \quad (5)$$

$$i\left(\alpha U_z + \frac{mU_\theta}{r} - \omega\right)v_r - \frac{2U_\theta}{r}v_\theta + q' = \frac{1}{\text{Re}}\left[v_r'' + \frac{1}{r}v_r' - \left(\alpha^2 + \frac{m^2+1}{r^2}\right)v_r - \frac{2im}{r^2}v_\theta\right], \quad (6)$$

$$i\left(\alpha U_z + \frac{mU_\theta}{r} - \omega\right)v_\theta + \left(U_\theta' + \frac{U_\theta}{r}\right)v_r + \frac{im}{r}q = \frac{1}{\text{Re}}\left[v_\theta'' + \frac{1}{r}v_\theta' - \left(\alpha^2 + \frac{m^2+1}{r^2}\right)v_\theta + \frac{2im}{r^2}v_r\right], \quad (7)$$

where the primes denote derivatives with respect to r . The boundary conditions are

$$v_z(1) = v_r(1) = v_\theta(1) = 0, \quad (8)$$

$$v_z(\infty) = v_r(\infty) = v_\theta(\infty) = 0. \quad (9)$$

The modes are determined as nonzero solutions of the above boundary-value problem. The problem contains the basic-flow velocity profiles $U_z(r)$ and $U_\theta(r)$, which are determined by solving the boundary-layer equations, as described in I. As noted in the Introduction, the basic flow becomes independent of the nose geometry for streamwise distances much greater than a , i.e., large z , and we focus on this region. As shown in I, $U_z(r)$ and $U_\theta(r)$ then depend only on the parameters $Z = z/\text{Re}$ and S , of which the former is a version of streamwise distance, scaled such that the boundary-layer thickness is of order a when Z is of order 1. Thus, the physical parameters of the problem are Re , Z , and S , while it also contains the modal parameters α and m . The set of differential equations and boundary conditions given above form an eigenvalue problem for determination of possible values of the complex frequency $\omega = \omega_r + i\omega_i$, whose imaginary part gives the modal growth rate. Expressing the eigenvalues in terms of the other parameters of the problem yields the dispersion relation

$$\omega = F(\alpha, m, \text{Re}, Z, S). \quad (10)$$

Numerical solution of the eigenvalue problem is described in the next section. The physical parameters Re , Z , and S and modal parameters α and m are then varied, looking for growing modes, i.e., eigenvalues with $\omega_i > 0$, which are symptomatic of local instability.

III. NUMERICAL METHOD

Prior to numerical discretization, we transform the radial coordinate as in I. Because the boundary-layer thickness goes to zero like $Z^{1/2}$ at small Z , the radial coordinate is first replaced by $\sigma = (r-1)/(2Z)^{1/2}$ to improve the radial resolution in that limit. The semi-infinite range of σ is then transformed to a finite interval using

$$x = \frac{\sigma - \hat{\sigma}}{\sigma + \hat{\sigma}}, \quad \sigma \in [0, \infty] \rightarrow x \in [-1, 1] \quad (11)$$

where $\hat{\sigma} > 0$ is a numerical parameter allowing some control over the distribution of the discrete points introduced below.

Also as in I, rewriting the local stability equations using the coordinate x , Chebyshev collocation is used to discretize the problem. We introduce the N collocation points

$$x_n = \cos\left(\frac{n\pi}{N-1}\right), \quad 0 \leq n < N \quad (12)$$

where, to avoid interpolation, N has the same value as in the calculation of the basic flow. Note that, according to (11), $\hat{\sigma}$ divides the flow into two ranges, $\sigma < \hat{\sigma}$ and $\sigma > \hat{\sigma}$, containing equal numbers of points. The smaller $\hat{\sigma}$, the better the resolution near the cylinder and the worse the resolution at large σ , the opposite being true if $\hat{\sigma}$ is increased. The variables v_z , v_r , and v_θ are represented by their values at all collocation points, whereas only the values of q for $0 < n < N-1$ are used. As is usual in Chebyshev collocation, derivatives are expressed using polynomial fitting: $(N-1)$ th degree polynomials are fitted to the discrete values of v_z , v_r , and v_θ and an $(N-3)$ th one to those of q . This allows approximation of derivatives as matrices obtained by differentiating the polynomials. Equations (4)–(7) are applied at x_n for $0 < n < N-1$, giving $4N-8$ equations for the $4N-2$

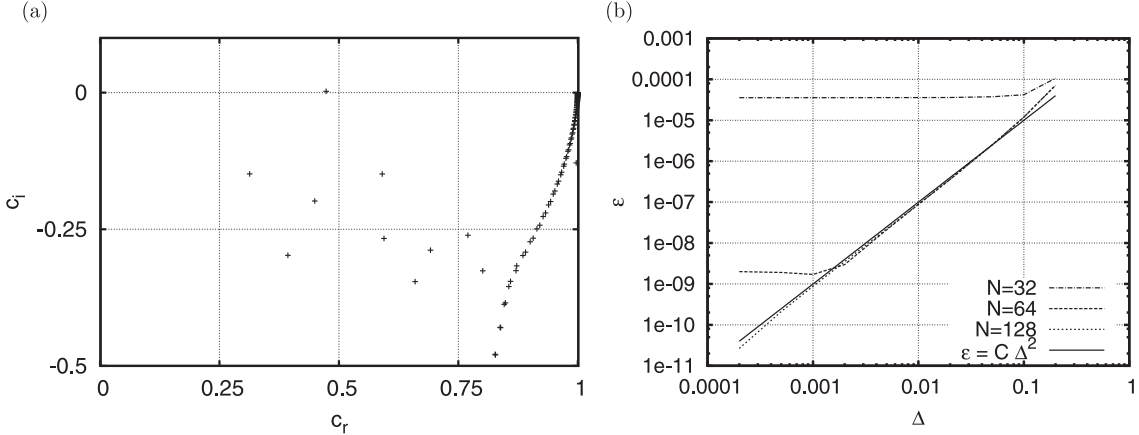


FIG. 2. (a) Eigenspectrum in the complex c plane for $Re = 2000$, $\alpha = 0.2$, $Z = 0.5$, $m = 1$, and $S = 0.01$. (b) Relative error plot as a function of the axial discretization of the basic flow for different values of N .

discrete values of v_z , v_r , v_θ , and q . q is eliminated as described in Appendix C1 of [18], as are the boundary values of v_z , v_r , and v_θ using (8) and (9). The result is a $(3N - 6) \times (3N - 6)$ standard matrix eigenvalue problem with eigenvalue ω and eigenvector whose elements are the discrete values of v_z , v_r , and v_θ at $x = x_n$ for $0 < n < N - 1$.

Figure 2(a) shows an example of a numerically computed eigenspectrum in the complex phase velocity ($c = c_r + i c_i$) plane (where $c = \omega/\alpha$). It consists of a discretized version of the continuous spectrum (which arises because the flow domain is semi-infinite in the radial direction) and a set of discrete eigenvalues, one of which has $c_i > 0$ and therefore represents a growing mode. We conclude that the flow is unstable for the given values of Re , Z , and S . The continuous spectrum can be safely neglected as it always lies in $c_i \leq 0$, originating at $c = 1 - i\alpha/Re$ and extending downwards in the complex c plane (see the asymptotic analysis in Ref. [19]).

The code was tested by observing the sensitivity of the most unstable (largest c_i) discrete eigenvalue (which is the one of principal interest) to changes in the numerical parameters N , $\hat{\sigma}$, and Δ , where Δ is the axial step used in the basic-flow computation [recall from I that the basic flow was obtained by integration of the boundary-layer equations using small steps Δ in $\zeta = (2Z)^{1/2}$]. Figure 2(b) shows a log-log plot of the relative error ϵ of the computed eigenvalue with $\hat{\sigma} = 5$ and the parameters given in Fig. 2(b) as a function of Δ for different values of N . The error is computed by comparison with the case $N = 128$ and $\Delta = 0.0001$. It will be seen that, for $N = 64$ and 128, the accuracy is mainly limited by axial discretization. The results are consistent with the use of a scheme which is second-order accurate in Δ to compute the basic flow, as can be seen by comparison with the reference line on the plot. The mapping parameter $\hat{\sigma}$ was found to affect the precision at only the 10th decimal place when varied between 2–6. After studying such convergence results for numerous sets of parameters, we decided to use $N = 64$, $\hat{\sigma} = 5$, and $\Delta = 0.001$ for the computations. This gives better than eight decimal places of accuracy. Note that, even though the continuous spectrum is not well resolved, this does not significantly affect the accuracy with which the most unstable eigenvalue is computed. The numerical eigenfunctions were also validated by comparing their exponential decay rate at large radial distances with the asymptotic decay rate given by the streamwise wave number α (see [19]). Good agreement was found.

For given m and S , the neutral curve is defined as the boundary of the region in the Re - Z plane for which a growing mode exists. Another way of putting this is that it is the curve of zero maximum growth rate, with the maximum taken over the discrete spectrum and all α . A first approximation to the neutral curves was obtained by plotting the contour of zero maximum growth rate in the Re - Z plane using a rectangular grid of values. This was carried out for different values of m and S . However, obtaining accurate neutral curves with such a method requires a very fine grid, making it computationally expensive. A faster, multivariate Newton-Raphson scheme was developed to obtain

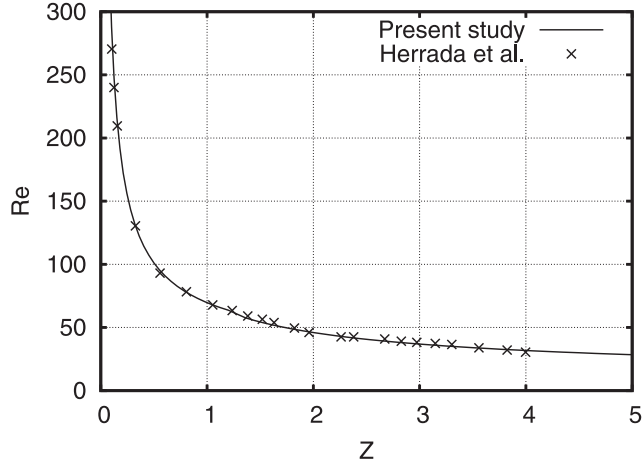


FIG. 3. Comparison of the neutral curve for $m = 1, S = 0.1$ with results of Herrada *et al.* [15].

more precise results with values taken from the contour plot to initialize the iteration. The neutral point α, Re at a given m, Z, S is obtained by simultaneously solving the system of equations

$$\omega_i(\alpha, \text{Re}) = 0, \quad (13)$$

$$\frac{\partial \omega_i}{\partial \alpha}(\alpha, \text{Re}) = 0. \quad (14)$$

The Newton-Raphson scheme requires computation of derivatives of ω_i with respect to α and Re , which were obtained using centered finite differencing. The solution was considered to have converged when the norm of the residuals was less than 10^{-7} . The result was used to initialize the iteration at the next step in Z , and the process continued for a range of values of Z .

The code was validated by comparing the results for the neutral curve with $S = 0.1$ and $m = 1$ with those of [15]. Figure 3 shows good agreement. Since the results of [15] for the nonrotating case are known to be in agreement with those of [12], a comparison of our results with [12] will not be presented, although we did check they agreed.

IV. RESULTS

A. Eigenspectra and growth-rate plots

The eigenspectra for the nonrotating case are qualitatively similar to that of the Blasius boundary layer, there being one distinguished eigenvalue close to the real axis in the complex c plane. This eigenvalue may lie in either $c_i > 0$ or $c_i \leq 0$, the remainder of the discrete spectrum being in $c_i < 0$ and well separated from the real c axis. Similarity with the Blasius flow might be expected because the basic flow without rotation has a velocity profile $U_z(r)$, whose form resembles the Blasius profile, which it approaches in the limit $Z \rightarrow 0$. It is the sign of c_i for the distinguished mode which controls flow stability in the nonrotating case, hence also for sufficiently small values of S .

Figure 2(a) shows an example with small rotation rate ($S = 0.01$): the eigenspectrum is essentially the same as for the nonrotating case at the same values of Re, α, Z , and m . However, because it is close to the real c axis, the slight perturbation of the distinguished mode at small S may suffice for c_i to change sign, with obvious consequences for flow stability. This does, in fact, happen for the values of Re, α, Z , and m used in Fig. 2(a): $c_i < 0$ when $S = 0$ and $c_i > 0$ when $S = 0.01$. This is a reflection of a surprising sensitivity of flow stability to small amounts of rotation, an important theme of this paper which will be further elucidated by later results.

As S is increased to larger values, the eigenspectrum changes character and one can no longer think in terms of a single distinguished mode near the real c axis which controls stability. Figure 4(a)

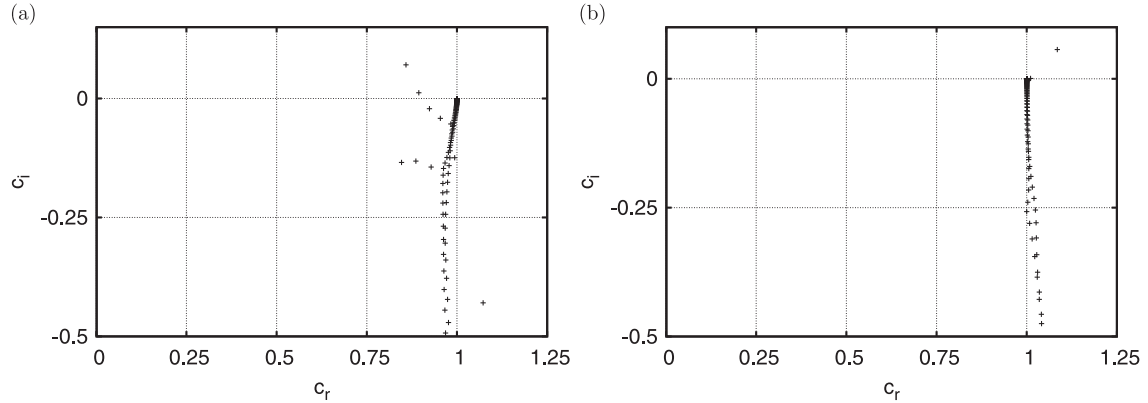


FIG. 4. Eigenspectra for (a) $\text{Re} = 200$, $\alpha = 0.16$, $Z = 12.5$, $m = 3$, and $S = 0.2$, (b) $\text{Re} = 200$, $\alpha = 0.04$, $Z = 12.5$, $m = 1$, and $S = 0.5$.

shows an example in which two discrete modes are unstable. Thus, for the rotating case, there can be more than one growing mode. When this occurs, the mode with the largest c_i is more important because it grows fastest according to the linear theory used here. Figure 4(b) gives an example in which there is a growing mode with $c_r > 1$, despite the fact that the maximum value of $U_z(r)$ is 1. Howard and Gupta [20] have shown that a modified semicircle theorem (which places limits on c_r) can be obtained for general swirling flows, but only for axisymmetric disturbances ($m = 0$) in the inviscid case. We are unaware of any such result for nonaxisymmetric disturbances. The given example shows that the phase velocity of a mode can exceed the maximum of $U_z(r)$ when $S > 0$.

From here on, we focus on the fastest growing discrete mode. Overall instability or stability of the flow is determined by the sign of the maximum growth rate ω_i^{\max} , the maximum being taken over all m and α . However, before taking this step, it is perhaps interesting to consider the behavior of the growth rate ω_i as a function of m and α . We never found a case in which $\omega_i^{\max} > 0$ arose from $m \leq 0$ modes, so we mostly restrict attention to $m > 0$ in what follows.

Figure 5(a) shows an example for which ω_i is plotted as a function of α for different values of m . We see that the m which yields the largest ω_i depends on α and that the overall maximum ω_i^{\max} arises from $m = 1$ (it is given by the peak in the $m = 1$ curve). This is not always the case, as is apparent from Fig. 5(b), for which ω_i^{\max} arises from $m = 2$. In the absence of rotation, we found that ω_i^{\max} was always associated with either $m = 1$ or 2 when the flow was unstable, in agreement with the results of [12] for the particular case $\text{Re} = 15\,000$. However, higher values of m can arise for nonzero S and we found no general rule concerning the m associated with ω_i^{\max} in the presence of rotation. We remark that, for the quite different case of flow in a rotating pipe, Pedley [21] also found that the m yielding the maximum overall growth rate depends on the physical parameters of the flow.

Negative values of m were also examined. In the nonrotating case, reflection symmetry with respect to any plane containing the cylinder axis implies that the growth rates for m are the same as for $-m$. For nonzero S , we found that negative m yields lower growth rates than positive m , as illustrated by Fig. 5(c). Attention is restricted to $m > 0$ from here on.

Figure 5(d) shows cases for which $\omega_i(\alpha)$ has more than one local maximum. As the physical parameters are varied, the overall maximum can jump discontinuously from one local maximum to another, a phenomenon encountered later. The effect of such a jump is apparent in Fig. 6(c) of [15] and in results of the next subsection.

B. Overall maximum growth rate, neutral and critical curves

Contour plots of overall maximum growth rate ω_i^{\max} in the $\text{Re}-Z$ plane are shown for three values of S in Fig. 6. The contours $\omega_i^{\max} = 0$ are the critical curves, which form the boundary between flow stability and instability. (Note that we use the term neutral curve for the stability boundary of

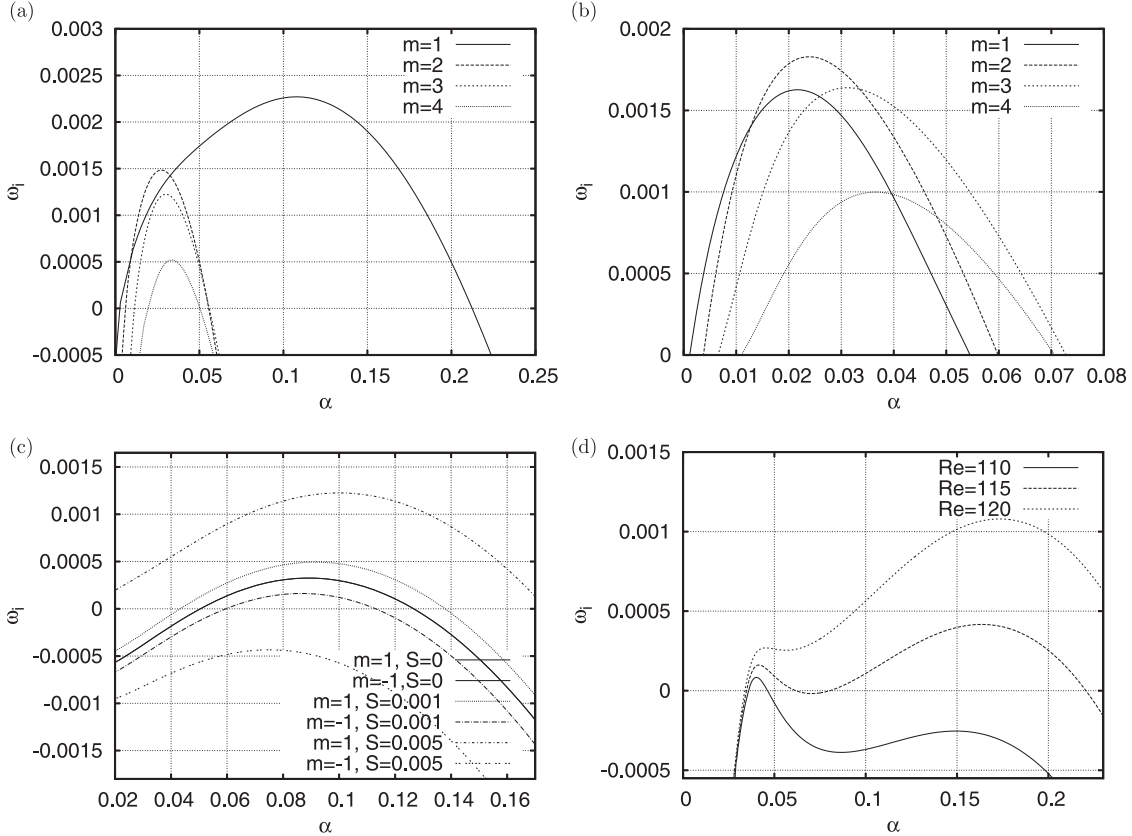


FIG. 5. Plots of temporal growth rate as a function of α : (a) $Re = 2000$, $Z = 0.5$, and $S = 0.01$, (b) $Re = 2000$, $Z = 2$, and $S = 0.01$, (c) $Re = 2000$, $Z = 0.5$ for $m = 1$ and -1 and different (small) values of S , (d) $Z = 0.5$, $S = 0.1$, $m = 1$ for different values of Re .

a single value of m , while a critical curve allows for all m .) Figure 6(a) shows that the nonrotating flow is always stable above a certain value of Z (0.8001), i.e., at sufficiently large downstream distances, and also below a certain value of Re (1059.5, in accord with [12]). The other two cases are quite different: instability has neither an upper limit in Z nor a lower limit in Re . Note the small growth rates in the unstable region for all three cases. This reflects control of small- S stability by a distinguished mode close to the real c axis, as does Fig. 7. Note also the large differences between the contour plots, a result which is perhaps at first surprising, but is, in fact, a logical consequence of a controlling mode close to the real c axis for $S = 0$.

As noted towards the end of Sec. III, obtaining accurate neutral curves using contour plots is computationally expensive compared to Newton-Raphson iteration and varying Z in small steps, and the same is even more true for critical curves because different m must be accounted for. For this reason, we use Newton-Raphson iteration (as described in Sec. III) to follow the neutral curves, then combine the results for different m to obtain the critical curve. This is achieved by minimization of the neutral Reynolds number over m for given Z and S .

Figure 8(a) shows neutral curves for the first three nonaxisymmetric modes and $S = 0.1$. The critical Reynolds number arises from the $m = 1$ mode for $Z > 1.3$ and from $m = 2$ for Z between 0.05–1.3. Higher m take over for Z less than about 0.05. These do not contribute to the plots of Fig. 8(a) because the critical Reynolds number lies above the range shown. As noted earlier, $m = 1$ and 2 control stability in the nonrotating case and here we see that they are the most important modes for small S as well. Indeed, we found that, when $Z > 0.1$, criticality was associated with $m = 1$ or 2 in all cases studied. Figure 8(b) shows plots of the axial wave number corresponding to neutrality. The jumps are a consequence of the existence of two local maxima in $\omega_i(\alpha)$, a scenario discussed

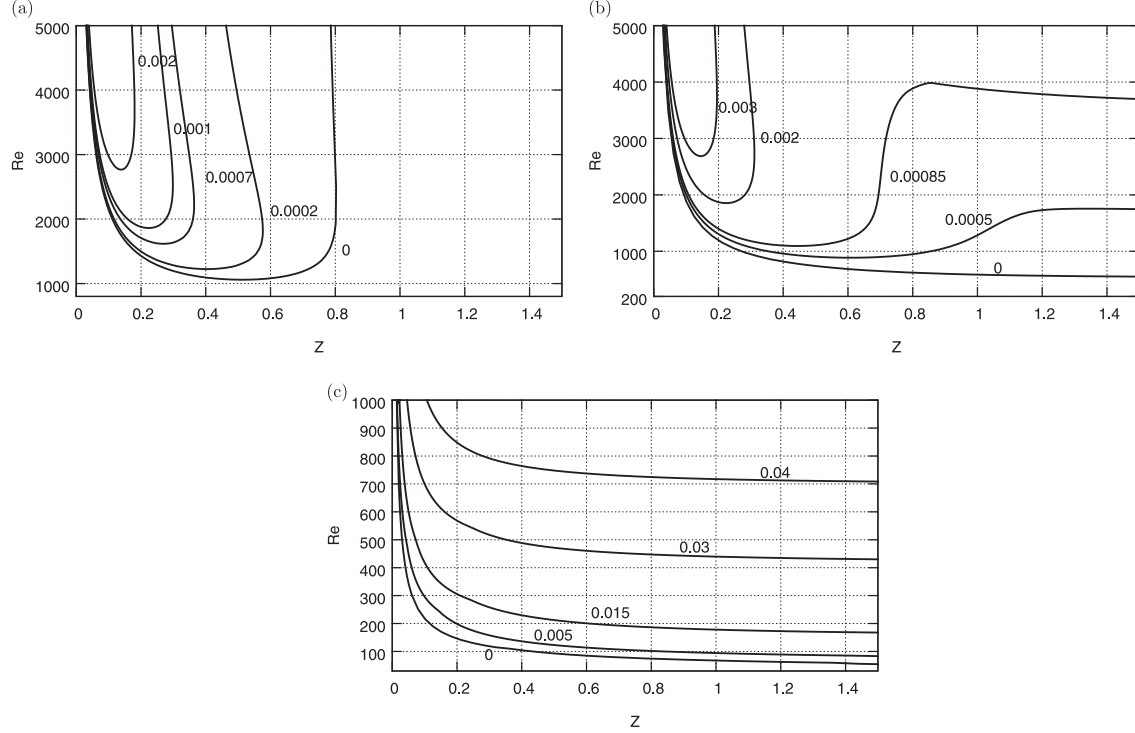


FIG. 6. Contour plots of ω_i^{\max} for (a) $S = 0$, (b) $S = 0.005$, and (c) $S = 0.1$.

earlier and illustrated by Fig. 5(d). As Z is varied, neutrality is controlled first by one of the maxima, then by the other. At the jump, both maxima give $\omega_i = 0$.

Figure 9 shows critical curves and corresponding wave-number plots for values of S between 0–0.012. The sensitivity of flow stability to small amounts of rotation is again apparent. As noted earlier, when $S = 0$ there is a minimal Reynolds number and a maximal Z for instability, neither of which persist to the rotating case. A given value of the Reynolds number corresponds to a horizontal line in Fig. 9(a), whose intersections with the critical curve yield boundaries in Z separating regions of stability and instability. With or without rotation, the flow is stable at sufficiently small Z , but each time the critical curve is crossed, the flow changes stability. In the nonrotating case, stability at small Z can either persist to all Z (if $Re \leqslant 1059.5$) or there is a range of instability, beyond which the flow is again stable. The rotating case is quite different because the critical Reynolds number

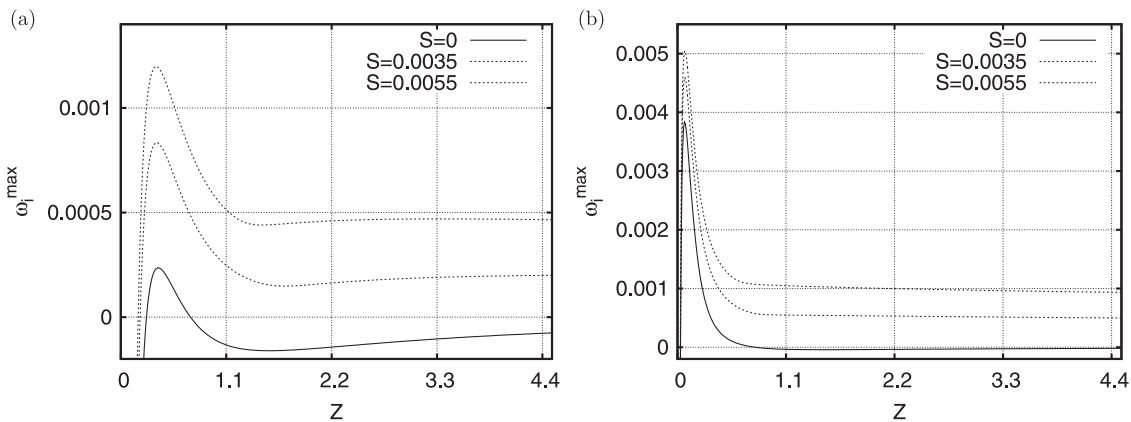
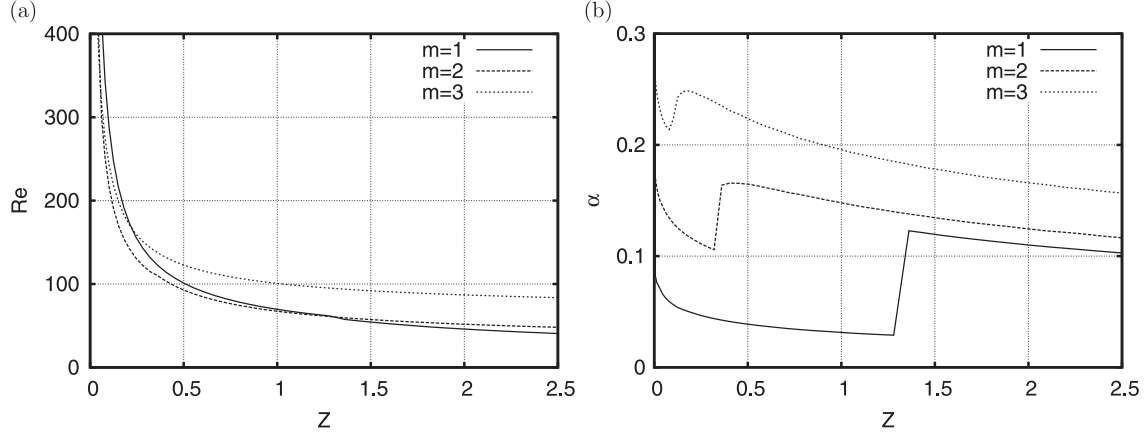


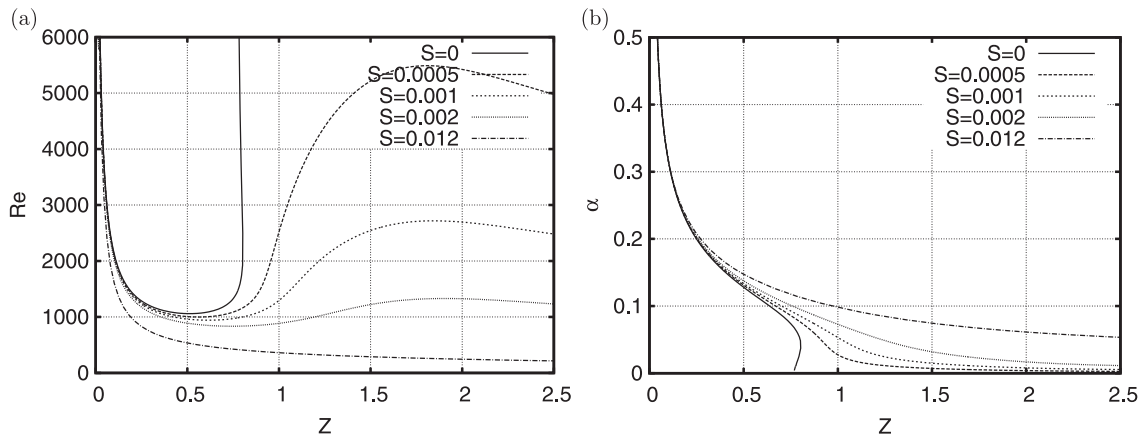
FIG. 7. Plots of ω_i^{\max} as a function of Z for different (small) values of S and (a) $Re = 1250$, (b) $Re = 5000$.

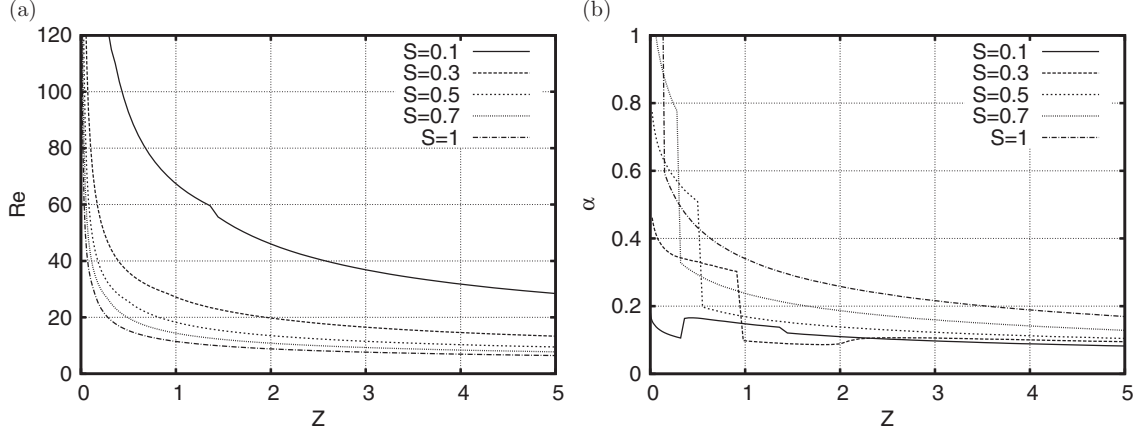
FIG. 8. (a) Neutral curves and (b) corresponding wave-number plots for $m = 1, 2$, and 3 and $S = 0.1$.

decreases to zero at large Z . As a result, the flow is unstable for sufficiently large Z . If the critical Reynolds number is a monotonically decreasing function of Z , as it is for small S above a certain threshold value equal to about 0.0045, there is a single intersection of the critical curve with any given line of constant Re , resulting in stability at small Z , followed by instability once the critical curve is crossed. On the other hand, the critical curve is nonmonotonic for S below the threshold, as illustrated by Fig. 9(a) for three such values of $S > 0$. For values of Re between the local minimum and maximum of the curve, there are then three stability boundaries, hence, four distinct regions in Z : stable, unstable, stable, unstable as Z increases. Note that increasing S lowers the critical Reynolds number, i.e., rotation has a destabilizing effect.

Figure 10 concerns S between 0.1 and 1. According to Fig. 10(a), the critical Reynolds number remains a decreasing function of Z and S , while Fig. 10(b) shows jumps in the critical wave number. Some of these jumps were identified as between local maxima of $\omega_i(\alpha)$ for a single m , while others correspond to jumps between different m .

Figure 11 gives results for higher values of S . Close inspection of Fig. 11(a) reveals that the critical Re is no longer a monotonic decreasing function of Z for $S = 10$ and 15. This is more apparent in Fig. 12, which extends the range of Z to much higher values using a logarithmic scale. For S exceeding a threshold value of about 5, the critical curve is nonmonotonic, as it is for S below the small- S threshold of about 0.0045. This leads to the same qualitative conclusion concerning stability, namely, the possibility, depending on Re , of more than one stability or instability boundary

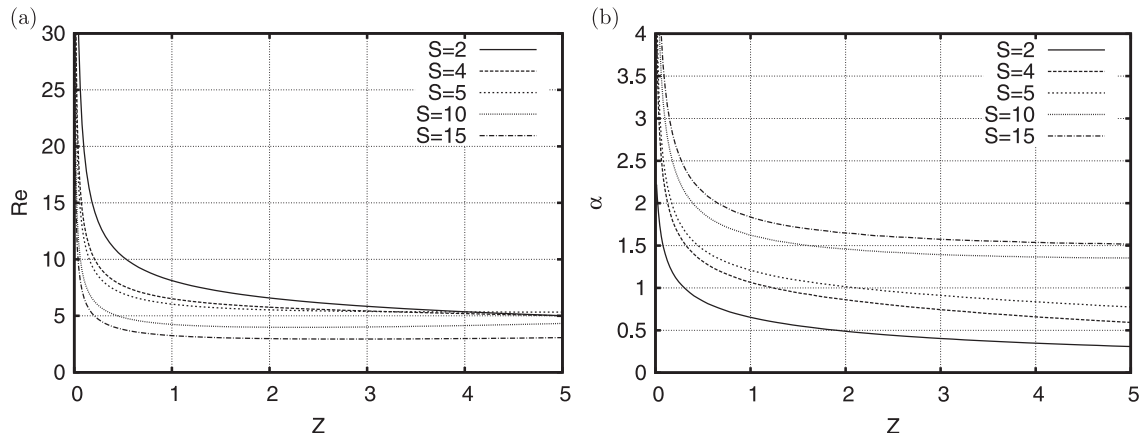
FIG. 9. (a) Critical curves and (b) corresponding wavenumber plots for values of S between 0 and 0.012.

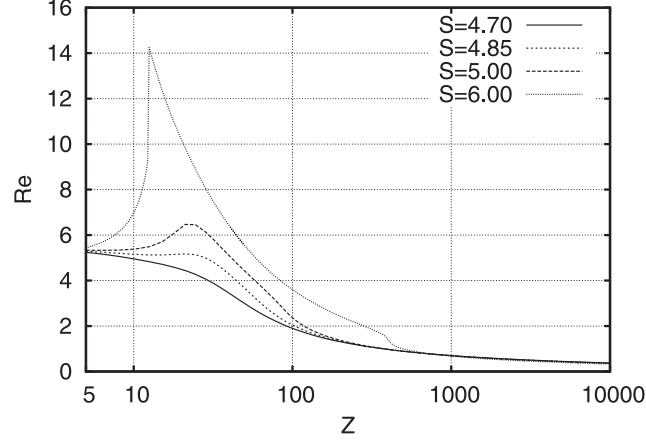
FIG. 10. (a) Critical curves and (b) corresponding wave-number plots for values of S between 0.1 and 1.

in Z . Note the sharp cusp in the critical curve for $S = 6$, apparent in Fig. 12, which is a consequence of a jump between different local maxima of $\omega_i(\alpha)$ for $m = 1$.

Figure 11(a) shows that the critical Re continues to be a decreasing function of S for fixed Z less than about 3. However, as is apparent from Fig. 12, this is no longer the case at larger Z when S exceeds a certain threshold value (which we found to be about 2.5). At such values of S , no general statement, covering all values of Z , concerning the effects of increasing rotation on flow stability can be made.

Figure 13(a) shows critical curves for $5 < Z < 100\,000$ and illustrates the statement, made earlier, that the critical Reynolds number tends to 0 as $Z \rightarrow \infty$. Figure 13(b) shows the same results, but it is $Z^{1/2}Re$, rather than Re , which is plotted as a function of Z . It appears that the curves asymptote to straight lines at large Z , corresponding to the asymptotic expansion $Re \sim Z^{-1/2}(A \ln Z + B)$ for the critical Reynolds number as $Z \rightarrow \infty$. It is interesting to note that the coefficient A (corresponding to the slope of the asymptote in the figure) appears to have the same value (close to 18) for different S . On the other hand, B is a decreasing function of S , so increasing rotation destabilizes the flow at large Z , as it does at small Z . Although asymptotic analysis of the large- Z limit of the stability problem has not been attempted, the form of the expansion given above is a logical consequence of that of the asymptotic expansions of the basic-flow velocity profiles, which were derived in I (Sec. 5a and Appendix A). These expansions proceed in inverse powers of $\ln Z$, hence, the appearance

FIG. 11. (a) Critical curves and (b) corresponding wave-number plots for values of S between 2 and 15.

FIG. 12. Critical curves for $5 < Z < 10\,000$.

of $\ln Z$ in the expansion of the critical Reynolds number. The coefficients of the basic-flow expansions are functions of $r/Z^{1/2}$, leading to the factor of $Z^{-1/2}$.

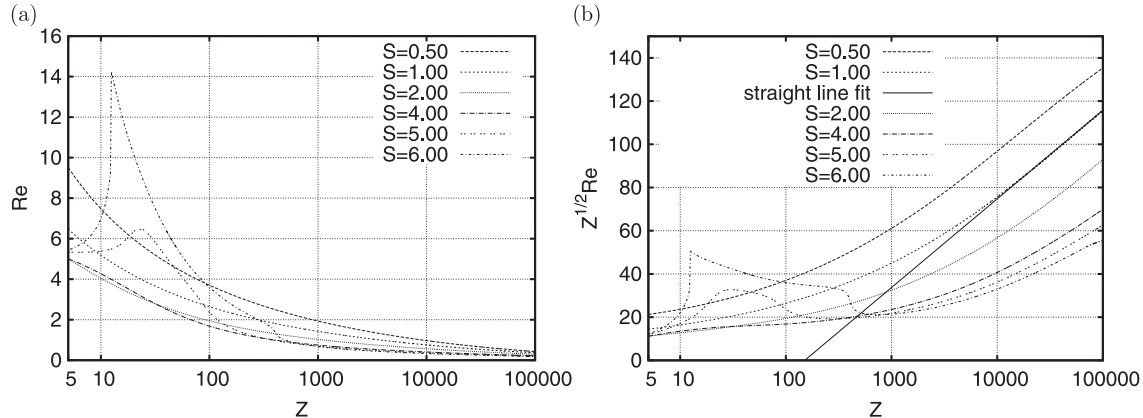
Finally, some caveats concerning the results at large S . Figure 11(a) shows that the critical Reynolds number is rather low (of order 5) except at small Z . Such moderate values of Re raise questions concerning the basis of this work: both the boundary-layer equations used to compute the basic flow and the local stability equations for the perturbation are predicated on the assumption of large Re . Thus, accurate quantitative values of the critical Reynolds number should not be expected at large S . We might, nonetheless, hope that qualitative trends resemble the present results.

C. Small- S perturbation analysis

As we have seen (recall Figs. 6 and 9), flow stability is significantly affected by small amounts of rotation. This suggests using the Taylor's series

$$\omega_i = \omega_{i0} + \frac{\partial \omega_i}{\partial S} S + \frac{1}{2} \frac{\partial^2 \omega_i}{\partial S^2} S^2 + \dots \quad (15)$$

to express the effects of rotation. Here, ω_{i0} and the derivatives of ω_i denote $S = 0$ values for given m , Z , Re , and α . As discussed earlier, small- S stability is controlled by a single distinguished mode, having small ω_{i0} and to which we specialize in this section (as noted earlier, other discrete eigenvalues are well below the real ω axis and hence unimportant).

FIG. 13. Critical curves for $5 < Z < 100\,000$: (a) Re , (b) $Z^{1/2}Re$ as functions of Z .

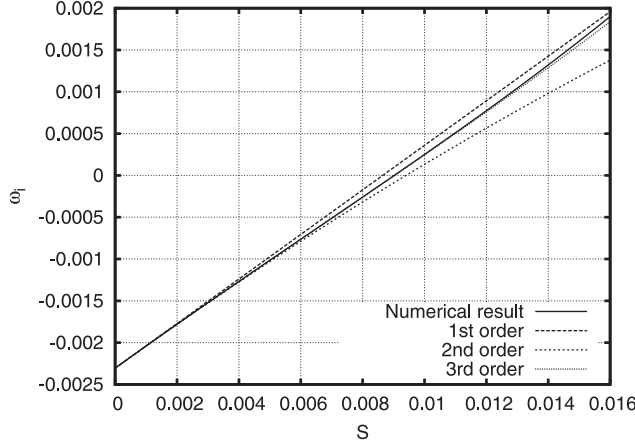


FIG. 14. Comparison of the growth rate of the most unstable mode obtained from the full numerical calculation and perturbation theory of different orders: $m = 1$, $Z = 1$, $\text{Re} = 2000$, $\alpha = 0.1$.

Figure 14 shows a plot of $\omega_i(S)$ for particular values of m , Z , Re , and α . The full numerical results are compared with the Taylor's series truncated at different orders [the derivatives in Eq. (15) being determined using second-order, centered finite differencing). Second- and higher-order terms can be neglected to a first approximation. Note the small value of ω_{i0} , here negative, which is characteristic of the distinguished mode, and the order 1 value of $\partial\omega_i/\partial S$. It is the combination of these two ingredients which makes flow stability sensitive to small amounts of rotation. As noted earlier, increasing small S destabilizes the flow, a result which is a consequence of positive $\partial\omega_i/\partial S$ for the distinguished mode when $S = 0$.

V. CONCLUSION

In this paper, we have studied the local, linear stability of flow around a semi-infinite, rotating cylinder placed in an axial stream. Assuming large values of the Reynolds number, the basic flow is determined numerically using a boundary-layer approximation (as described in I). Large Reynolds number also justifies local stability analysis. The stability problem depends on three nondimensional physical parameters: the Reynolds number Re , the rotation rate S , and the axial location Z . Modal analysis introduces two additional parameters: namely, α , the axial wave number, and m , which is an integer whose value identifies the azimuthal Fourier component of the mode. The local stability equations are solved numerically to obtain the complex frequency $\omega = \omega_r + i\omega_i$ of modes via solution of a matrix eigenvalue problem. The numerics were checked by studying the sensitivity of the results to variations of the numerical parameters of the problem and also by comparison with the few results available in the literature. The eigenspectrum consists of a discrete part and a numerical approximation (many closely spaced eigenvalues lying along a curve in the complex ω plane) of the continuous spectrum. The latter lies in $\omega_i < 0$ and thus represents a decaying contribution which is unimportant from a stability point of view. Discrete eigenvalues in $\omega_i > 0$ represent growing modes and are symptomatic of instability. Let ω_i^{\max} be the maximum growth rate, where only discrete eigenvalues contribute and the maximum is taken over α and m . If $\omega_i^{\max} > 0$, the flow is unstable for the given values of Re , S , and Z . This allows the determination of the stability boundary in physical-parameter space. The most important results of the paper consist of critical curves representing this boundary in the Z - Re plane for different values of S (see Figs. 9–13).

An important conclusion of the paper is that flow stability is surprisingly sensitive to small amounts of rotation. This is apparent in Figs. 6 and 9(a) and is further quantified by the perturbation analysis of Sec. IV C. It is the consequence of a nearly neutral mode for $S = 0$ which controls stability at small S . Even a small amount of rotation can produce a sufficient perturbation that ω crosses

the real axis and flow stability or instability switches for the given values of Re and Z . Rotation is destabilizing for small S , i.e., the critical Reynolds number decreases for fixed Z as S is increased.

As is apparent from Fig. 9(a), in the absence of rotation the flow is stable beyond a certain value of Z (close to 0.8) and also below a Re threshold (close to 1060). No such constraints on instability apply when rotation is added. As for $S = 0$, the critical Reynolds number goes to infinity at small Z , but, for nonzero S , it approaches zero as $Z \rightarrow \infty$. Thus, as in the nonrotating case, the flow is stable at sufficiently small Z , but, with rotation, it is unstable at large enough downstream distances.

Between small and large Z there is at least one boundary separating stable and unstable portions of the flow. The simplest case is when the critical Reynolds number is a monotonic decreasing function of Z . There is then a single stability boundary in Z , below which the flow is stable, and above which it is unstable. On the other hand, a nonmonotonic critical curve implies the possibility, dependent on Re , of more than one stability boundary in Z . We found that the critical curve was monotonic for S between about 0.0045 and 5.

As noted above, rotation is destabilizing at small S . This was found to persist up to about $S = 2.5$, but beyond that there were cases for which the critical Reynolds number increases with increasing S at fixed Z . Even above this threshold, the destabilizing trend continues for Z below about 3 and at sufficiently large values of Z . Destabilization by rotation can thus be considered as the norm.

Finally, the limit of large Z was also examined. We found that the critical Reynolds number has the asymptotic expansion $Re \sim Z^{-1/2}(A \ln Z + B)$, where the factor A has the same value for all S and B is a decreasing function of S . The expansion is consistent with the earlier statement that critical Re goes to zero as $Z \rightarrow \infty$, while decreasing B means that rotation destabilizes the flow at large Z , as stated above.

ACKNOWLEDGMENTS

The authors are grateful to the French Ministry of Education and Research and the Indo-French Centre for the Promotion of Advanced Research-CEFIPRA for financial support.

-
- [1] H. L. Reed and W. S. Saric, Stability of three-dimensional boundary layers, *Annu. Rev. Fluid Mech.* **21**, 235 (1989).
 - [2] W. S. Saric, H. L. Reed, and E. B. White, Stability and transition of three-dimensional boundary layers, *Annu. Rev. Fluid Mech.* **35**, 413 (2003).
 - [3] R. J. Lingwood, Absolute instability of the boundary layer on a rotating disk, *J. Fluid Mech.* **299**, 17 (1995).
 - [4] B. Pier, Primary crossflow vortices, secondary absolute instabilities and their control in the rotating-disk boundary layer, *J. Eng. Math.* **57**, 237 (2007).
 - [5] S. J. Garrett and N. Peake, The absolute instability of the boundary layer on a rotating cone, *Eur. J. Mech. B: Fluids* **26**, 344 (2007).
 - [6] S. J. Garrett, Z. Hussain, and S. O. Stephen, Boundary-layer transition on broad cones rotating in an imposed axial flow, *AIAA J.* **48**, 1184 (2010).
 - [7] B. Pier, Periodic and quasiperiodic vortex shedding in the wake of a rotating sphere, *J. Fluids Struct.* **41**, 43 (2013).
 - [8] S. Derebail Muralidhar, B. Pier, J. F. Scott, and R. Govindarajan, Flow around a rotating, semi-infinite cylinder in an axial stream, *Proc. R. Soc. London, Ser. A* **472**, 20150850 (2016).
 - [9] W. Tollmien, Über die Entstehung der Turbulenz. 1. Mitteilung, Nachr. Ges. Wiss. Goettingen, Math. Phys. Kl. **1929**, 21 (1928).
 - [10] R. Jordinson, The flat plate boundary layer. Part 1. Numerical integration of the Orr-Sommerfeld equation, *J. Fluid Mech.* **43**, 801 (1970).

- [11] L. M. Mack, A numerical study of the temporal eigenvalue spectrum of the Blasius boundary layer, *J. Fluid Mech.* **73**, 497 (1976).
- [12] O. R. Tutty, W. G. Price, and A. T. Parsons, Boundary layer flow on a long thin cylinder, *Phys. Fluids* **14**, 628 (2002).
- [13] N. Vinod and R. Govindarajan, Secondary instabilities in incompressible axisymmetric boundary layers: Effect of transverse curvature, *J. Fluids Eng.* **134**, 024503 (2012).
- [14] K. H. Kao and C. Y. Chow, Stability of the boundary layer on a spinning semi-infinite circular cylinder, *J. Spacecr. Rockets* **28**, 284 (1991).
- [15] M. A. Herrada, C. Del Pino, and R. Fernandez-Feria, Stability of the boundary layer flow on a long thin rotating cylinder, *Phys. Fluids* **20**, 034105 (2008).
- [16] J. T. Kegelman, R. C. Nelson, and T. J. Mueller, The boundary layer on an axisymmetric body with and without spin, *AIAA J.* **21**, 1485 (1983).
- [17] M. G. Hall, Vortex breakdown, *Annu. Rev. Fluid Mech.* **4**, 195 (1972).
- [18] C. Leclercq, Instabilités convectives et absolues dans l'écoulement de Taylor-Couette-Poiseuille excentrique, Ph.D. thesis, École centrale de Lyon, 2013.
- [19] P. J. Schmid and D. S. Henningson, *Stability and Transition in Shear Flows*, Applied Mathematical Sciences (Springer, New York, 2001).
- [20] L. N. Howard and A. S. Gupta, On the hydrodynamic and hydromagnetic stability of swirling flows, *J. Fluid Mech.* **14**, 463 (1962).
- [21] T. J. Pedley, On the instability of viscous flow in a rapidly rotating pipe, *J. Fluid Mech.* **35**, 97 (1969).

[A24]

Linear and nonlinear dynamics of pulsatile channel flow

B. Pier & P. J. Schmid

Journal of Fluid Mechanics **815**, 435–480 (2017)

doi:10.1017/jfm.2017.58

<https://hal.archives-ouvertes.fr/hal-01385093>

Linear and nonlinear dynamics of pulsatile channel flow

Benoît Pier^{1,†} and Peter J. Schmid²

¹Laboratoire de mécanique des fluides et d'acoustique, CNRS, École centrale de Lyon,
Université de Lyon 1, INSA Lyon, 36 avenue Guy-de-Collongue, 69134 Écully, France

²Department of Mathematics, Imperial College, South Kensington Campus, London SW7 2AZ, UK

(Received 14 July 2016; revised 19 January 2017; accepted 19 January 2017;
first published online 21 February 2017)

The dynamics of small-amplitude perturbations, as well as the regime of fully developed nonlinear propagating waves, is investigated for pulsatile channel flows. The time-periodic base flows are known analytically and completely determined by the Reynolds number Re (based on the mean flow rate), the Womersley number Wo (a dimensionless expression of the frequency) and the flow-rate waveform. This paper considers pulsatile flows with a single oscillating component and hence only three non-dimensional control parameters are present. Linear stability characteristics are obtained both by Floquet analyses and by linearized direct numerical simulations. In particular, the long-term growth or decay rates and the intracyclic modulation amplitudes are systematically computed. At large frequencies (mainly $Wo \geq 14$), increasing the amplitude of the oscillating component is found to have a stabilizing effect, while it is destabilizing at lower frequencies; strongest destabilization is found for $Wo \simeq 7$. Whether stable or unstable, perturbations may undergo large-amplitude intracyclic modulations; these intracyclic modulation amplitudes reach huge values at low pulsation frequencies. For linearly unstable configurations, the resulting saturated fully developed finite-amplitude solutions are computed by direct numerical simulations of the complete Navier–Stokes equations. Essentially two types of nonlinear dynamics have been identified: ‘cruising’ regimes for which nonlinearities are sustained throughout the entire pulsation cycle and which may be interpreted as modulated Tollmien–Schlichting waves, and ‘ballistic’ regimes that are propelled into a nonlinear phase before subsiding again to small amplitudes within every pulsation cycle. Cruising regimes are found to prevail for weak base-flow pulsation amplitudes, while ballistic regimes are selected at larger pulsation amplitudes; at larger pulsation frequencies, however, the ballistic regime may be bypassed due to the stabilizing effect of the base-flow pulsating component. By investigating extended regions of a multi-dimensional parameter space and considering both two-dimensional and three-dimensional perturbations, the linear and nonlinear dynamics are systematically explored and characterized.

Key words: biological fluid dynamics, instability, nonlinear instability

† Email address for correspondence: benoit.pier@ec-lyon.fr

1. Introduction

Pulsatile flows occur in a variety of engineering applications as well as in the human body. Over the past fifty years many studies have addressed the linear dynamics of oscillating flows over a flat plate or through channels or pipes, but surprisingly few recent investigations have considered pulsatile flows, and the development of finite-amplitude travelling waves has hardly ever been addressed. While purely oscillatory flows are governed by a single characteristic time, based on the oscillation period, pulsatile flows also depend on a second characteristic time scale, related to the mean flow velocity. Another essential difference is that oscillating configurations undergo global flow reversal and therefore the absolute value of the flow speed increases and decreases twice per period, while pulsating flows generally maintain the same flow direction and display only one phase of increasing flow speed and one phase of decreasing flow speed in each cycle. Hence, the presence of a non-vanishing mean-flow component leads to behaviour distinct from purely oscillating situations. Using the classical channel geometry, the purpose of the present work is to systematically establish both linear and fully nonlinear flow features prevailing for fundamental pulsatile-flow configurations.

Among the few known exact solutions of the Navier–Stokes equations (Drazin & Riley 2006), those which are time periodic and parallel are of particular interest (Davis 1976). The Stokes (1851) layer, i.e. the flow induced in a semi-infinite volume of fluid by an infinite flat plate harmonically oscillating in its own plane, has served as the archetypal configuration for the study of time-periodic flows near a solid boundary. Similar velocity profiles prevail if the fluid is in contact with a fixed plate and is brought into motion by an oscillating pressure gradient parallel to the plate. If the flow is confined between two parallel plates, the exact base-flow profiles are still obtained in terms of exponential functions, while periodic flows through a circular pipe are known as Womersley (1955) solutions and may be expanded in terms of Bessel functions.

All these time-periodic flows develop an oscillating boundary layer of characteristic thickness

$$\delta = \sqrt{\nu/\Omega}, \quad (1.1)$$

where ν is the kinematic viscosity of the fluid and Ω the pulsation frequency. For channels or pipes, the time-periodic flow profiles significantly depend on the ratio of the diameter to the oscillating-boundary-layer thickness, known as the Womersley number Wo . Thus, for large values of Wo , confinement or curvature effects are expected to be negligible and the dynamics similar to that of a semi-infinite Stokes layer. In contrast, at low values of Wo , pulsatile flows may be seen as slowly modulated parabolic Poiseuille profiles. In physiological situations (Ku 1997; Pedley 2000), typical Womersley numbers prevailing in the main blood vessels are in the range 5–15 which is neither small nor very large. Our recent study of flow through model abdominal aortic aneurysms (Gopalakrishnan, Pier & Biesheuvel 2014a,b) has revealed the need to investigate in detail the dynamics of physiological flow conditions even for simple parallel geometries. As will be shown in the present paper, it is precisely in the range $5 < Wo < 20$ that pulsatile channel flow undergoes transitions between different characteristic regimes, both for small-amplitude perturbations as well as fully developed nonlinear propagating waves.

1.1. Literature review

Early theoretical and numerical work is mainly focused on the linear stability of Stokes layers or the equivalent channel and pipe flows. For obvious reasons, experimental investigations almost exclusively consider the flow through circular pipes, but are able to address the fully developed dynamics prevailing in unstable configurations. More recently, the linear stability of a range of time-periodic flows has been revisited, using the now available numerical methods and facilities. Surprisingly, apart from a few recent computations of turbulent periodic flows, the nonlinear regime has not yet attracted much theoretical or numerical attention.

Grosch & Salwen (1968) were among the first to address the linear stability of time-dependent plane Poiseuille flow, by expanding the disturbance streamfunction on a small set of basis functions. They found that for weak pressure gradient modulations, the resulting modulated flow was more stable than the steady flow, while a rather drastic destabilization was observed at higher velocity modulations.

von Kerczek & Davis (1974) studied the linear stability of oscillatory Stokes layers, using quasi-static theories and integration of the linearized time-dependent equations. They were unable to find any unstable modes for the configurations considered. Using semi-analytic methods, Hall (1978) also found this flow to be stable in the parameter range investigated.

Yang & Yih (1977) considered axisymmetric perturbations to harmonic oscillating pipe flow. All configurations for which calculations have been carried out are found to be stable. Later, Fedele, Hitt & Prabhu (2005) also claimed that axisymmetric modes in pulsatile pipe flow are stable, while, more recently, Thomas *et al.* (2011) were able to obtain unstable axisymmetric modes and to establish critical conditions for this flow.

In a landmark study of pulsating plane channel flow, von Kerczek (1982) considered configurations with moderate pulsation amplitudes, mostly near the critical Reynolds number for steady flow, and computed Floquet exponents by a series expansion, using a perturbation analysis in the amplitude of the oscillating base velocity. It was found that the sinusoidally pulsating flow is more stable than the steady plane Poiseuille flow for a range of frequencies greater than approximately $Wo = 12$. Lower or much higher frequencies were found to make the flow unstable, in contrast with the results of Grosch & Salwen (1968). The perturbation analysis also confirmed the result obtained by Hall (1975) that the growth rate depends quadratically on small pulsating amplitudes.

Using numerical simulations, Singer, Ferziger & Reed (1989) found that the effect of oscillation is generally stabilizing. However, at low frequencies, the perturbation energy may vary by several orders of magnitude within each cycle. These authors confirmed the findings by von Kerczek (1982) and suspect that those by Grosch & Salwen (1968) are underresolved. They were also probably the first to attempt a nonlinear simulation.

Rozhdestvenskii, Simakin & Stoinov (1989) appear to be the first to implement a complete Floquet analysis, based on temporal integration of matrices. They were also able to confirm results by von Kerczek (1982).

Using mainly analytical methods, Cowley (1987) and, more recently, Hall (2003), suggested that the Stokes layers do not sustain linearly unstable modes in the limit of very large Reynolds numbers.

In an experimental study, Merkli & Thomann (1975) investigated transition in oscillating pipe flow and showed that turbulence occurs in the form of periodic bursts

which are followed by relaminarization in the same cycle and do not necessarily lead to turbulent flow during the whole cycle.

Using a similar experimental set-up, Hino, Sawamoto & Takasu (1976) identified three types of regimes: weakly turbulent, conditionally turbulent and fully turbulent. Decelerating phases are found to promote turbulence while the laminar flow may recover during accelerating phases.

Adopting a physiological approach, Winter & Nerem (1984) reported similar experimental observations and noted that fully turbulent flow is only found when a mean flow is present.

Stettler & Hussain (1986) further investigated the transition occurring in a pulsatile pipe flow experiment and documented the passage frequency of ‘turbulent plugs’ for a wide range of control parameters and delineated the conditions when plugs occur randomly or are phase locked with the pulsation.

Considering oscillatory pipe flow, Akhavan, Kamm & Shapiro (1991a,b) established experimentally and numerically that turbulence appears explosively towards the end of the acceleration phase and is sustained throughout the deceleration phase while being restricted to the wall region. Using a quasi-steady transient growth analysis, it was suggested that transition may be the result of a secondary instability mechanism.

Straatman *et al.* (2002) derived, by a linear stability analysis, that pulsating a plane Poiseuille flow is always destabilizing. However, they seemed to associate stability with decay throughout the cycle and it is therefore difficult to interpret the marginal curves shown in that paper.

More recently, in a series of theoretical and numerical papers, Blennerhassett and Bassom, with Thomas and Davies, have used Floquet analysis and linear simulation to address the stability of a range of related time-periodic flows due to an oscillating plate (Blennerhassett & Bassom 2002; Thomas *et al.* 2010, 2014, 2015), a streamwise oscillating channel (Blennerhassett & Bassom 2006; Thomas *et al.* 2011) or pipe (Blennerhassett & Bassom 2006; Thomas *et al.* 2011; Thomas, Bassom & Blennerhassett 2012) as well as a torsionally oscillating pipe (Blennerhassett & Bassom 2007; Thomas *et al.* 2012), thereby resolving some of the inconsistencies of previous linear stability analyses and establishing, among others, curves of marginal linear instability for this family of flows. The spatio-temporal impulse response of the Stokes layer was studied by Thomas *et al.* (2014), and the fate of some disturbances when they become nonlinear was also considered.

Luo & Wu (2010) revisited the linear instability of finite Stokes layers, comparing results obtained by instantaneous instability theory in a quasi-steady approach with those from Floquet analysis. It was shown that during its amplification phase, a Floquet mode closely follows the instantaneous unstable mode, and the results by Blennerhassett & Bassom (2002) were confirmed.

Transition to turbulence has been investigated by direct numerical simulations of the Stokes boundary layer by Vittori & Verzicco (1998), Costamagna, Vittori & Blondeaux (2003) and Ozdemir, Hsu & Balachandar (2014). Tuzi & Blondeaux (2008) have addressed the intermittent turbulent regime observed in a pulsating pipe. These studies consider flow in wavy walled channels or pipes and it is observed that turbulence generally appears around flow reversal, and that it displays statistical properties similar to those prevailing in the steady case.

1.2. Objectives and organization of the paper

By considering the fundamental configuration of pulsatile channel flow, the aim of the present study is to systematically document the temporal dynamics of small-amplitude

perturbations and, in unstable situations, to characterize the resulting finite-amplitude regime of travelling nonlinear modulated waves.

Revisiting the linear regime, using both Floquet analyses and linearized numerical simulations, we confirm the earlier findings and analyse in full detail three-dimensional perturbations over large parameter ranges.

The so-far neglected finite-amplitude travelling wave solutions prevailing for linearly unstable base flows are computed by direct numerical simulations of the complete Navier–Stokes equations, at prescribed total pulsating flow rates. Again, the purpose is to identify and analyse the characteristic regimes and to systematically explore a wide parameter space.

To this end, after introducing the governing equations and the geometry in § 2, the base flow and non-dimensional parameters are specified in § 3. The different mathematical approaches used in this work are formulated in § 4, while the associated numerical solution methods and relevant validation steps are discussed in appendix A. The main body of the paper consists of the results pertaining to the linear (§ 5) and nonlinear (§ 6) dynamics. In both cases, we start by discussing the features of characteristic examples, before progressively taking into account variations of more parameters in order to explore how the dynamics unfolds over the complete parameter space. The paper finishes (§ 7) with a summary and some suggestions for future work.

2. Governing equations and geometry

Throughout this study, the fluid flow is described by a vector velocity field $\mathbf{u}(\mathbf{x}, t)$ and a scalar pressure field $p(\mathbf{x}, t)$ that depend on position \mathbf{x} and time t and are governed by the incompressible Navier–Stokes equations

$$\frac{\partial \mathbf{u}}{\partial t} + (\mathbf{u} \cdot \nabla) \mathbf{u} = \nu \Delta \mathbf{u} - \nabla p + \mathbf{f}, \quad (2.1)$$

$$0 = \nabla \cdot \mathbf{u}, \quad (2.2)$$

where ν is the kinematic viscosity of the fluid (and the pressure has been redefined to eliminate the constant fluid density from the equations). In the momentum equation (2.1), the term $\mathbf{f}(\mathbf{x}, t)$ represents an externally applied volume force.

The fluid domain is bounded by two fixed parallel plates, along which no-slip boundary conditions prevail. Using a Cartesian coordinate system, position is given by $\mathbf{x} = x_0 \mathbf{e}_0 + x_1 \mathbf{e}_1 + x_2 \mathbf{e}_2$, where x_0 , x_1 and x_2 (respectively \mathbf{e}_0 , \mathbf{e}_1 and \mathbf{e}_2) denote wall-normal, streamwise and spanwise coordinates (respectively unit vectors), and the domain corresponds to $|x_0| < h$ where $2h$ is the channel width.

3. Base flow and non-dimensional parameters

A pulsatile base flow, of frequency Ω , is an exact solution of the Navier–Stokes equations that is temporally periodic and consists of a velocity field purely in the streamwise direction that only depends on the wall-normal coordinate:

$$\mathbf{U}(\mathbf{x}, t) = U_1(x_0, t) \mathbf{e}_1 \quad \text{with } U_1(x_0, t) = \sum_n U_1^{(n)}(x_0) \exp(in\Omega t). \quad (3.1)$$

Such a base flow is associated with a spatially uniform and temporally periodic streamwise pressure gradient of the form $-G(t)\mathbf{e}_1$, with

$$G(t) = \sum_n G^{(n)} \exp(in\Omega t), \quad (3.2)$$

and corresponds to a temporally periodic flow rate

$$Q(t) = \sum_n Q^{(n)} \exp(in\Omega t). \quad (3.3)$$

In the above expressions, the conditions $Q^{(-n)} = [Q^{(n)}]^\star$, $G^{(-n)} = [G^{(n)}]^\star$, and $U_1^{(-n)}(x_0) = [U_1^{(n)}(x_0)]^\star$ ensure that all flow quantities are real (with \star denoting complex conjugate).

Using these expansions in the Navier–Stokes equations shows that the different harmonics of the base flow are decoupled and yields the linear relationship between the flow-rate components $Q^{(n)}$ and the velocity components $U_1^{(n)}(x_0)$ as

$$U_1^{(n)}(x_0) = \frac{Q^{(n)}}{2h} W\left(\frac{x_0}{h}, \sqrt{n} Wo\right), \quad (3.4)$$

where the Womersley number Wo is defined as

$$Wo \equiv h\sqrt{\Omega/\nu}, \quad (3.5)$$

and the function W determines the profiles of the different velocity components and is defined as

$$W(\xi, w) \equiv \begin{cases} \left(\frac{\cosh(\sqrt{i}\xi w)}{\cosh(\sqrt{i}w)} - 1 \right) / \left(\frac{\tanh(\sqrt{i}w)}{\sqrt{i}w} - 1 \right) & \text{if } w \neq 0 \\ \frac{3}{2}(1 - \xi^2) & \text{if } w = 0, \end{cases} \quad (3.6)$$

for $|\xi| \leq 1$, using $\sqrt{i} \equiv (1 + i)/\sqrt{2}$. These profiles (3.6) are normalized to unit cross-sectionally averaged velocity.

Furthermore, the pressure and flow-rate components are related as

$$\frac{Q^{(n)}}{G^{(n)}} = 2 \frac{h^3}{\nu} \frac{i}{n Wo^2} \left(\frac{\tanh(\sqrt{in} Wo)}{\sqrt{in} Wo} - 1 \right) \quad \text{if } n \neq 0 \quad \text{and} \quad \frac{Q^{(0)}}{G^{(0)}} = \frac{2}{3} \frac{h^3}{\nu}. \quad (3.7a,b)$$

Hence it is obvious that the pulsatile base flow is entirely determined by its frequency Ω and the Fourier components $Q^{(n)}$ of the flow rate (or the components $G^{(n)}$ of the associated pressure gradient).

The mathematical and numerical methods implemented in the present study can handle flow rates of the form (3.3) with an arbitrary number of Fourier components, but this would correspond to a tremendously large multi-dimensional parameter space, impossible to explore exhaustively. Since, the aim here is to systematically analyse the behaviour of fundamental pulsating-flow configurations, the control-parameter space is restricted by investigating only base flow rates with a single oscillating component, i.e. for which $Q^{(n)} = 0$ as $|n| \geq 2$. Without loss of generality, $Q^{(1)}$ may then be restricted to real values. As only flows with a non-vanishing mean-flow component $Q^{(0)}$ will be considered, it is then convenient to write

$$Q(t) = Q^{(0)}(1 + \tilde{Q} \cos \Omega t), \quad (3.8)$$

where the relative amplitude \tilde{Q} of the oscillating flow-rate component is defined as

$$\tilde{Q} \equiv 2Q^{(1)}/Q^{(0)}. \quad (3.9)$$

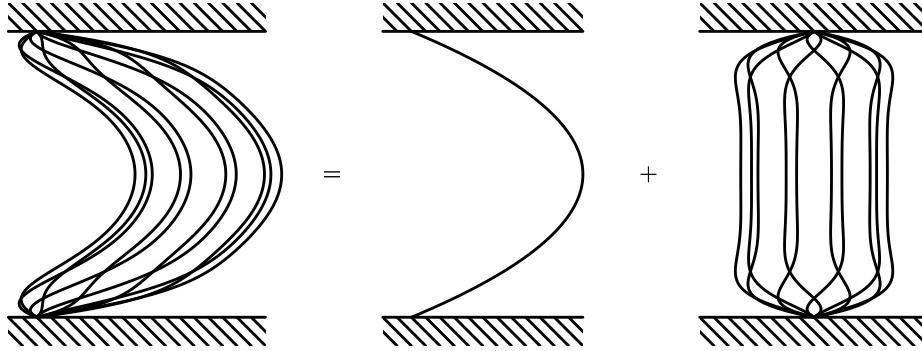


FIGURE 1. Snapshots of typical base-flow profile associated with a flow rate of the form $Q(t)/Q^{(0)} = 1 + \tilde{Q} \cos \Omega t$. In this example, $Wo = 10$ and $\tilde{Q} = 0.6$ and ten profiles over one complete pulsation cycle are shown.

After defining a Reynolds number

$$Re \equiv Q^{(0)}/\nu, \quad (3.10)$$

based on the mean velocity $Q^{(0)}/2h$, the channel width $2h$ and the viscosity ν , the base flow is entirely specified by three non-dimensional control parameters: the Womersley number Wo (3.5), the Reynolds number Re (3.10) and the relative amplitude of the oscillating flow-rate component \tilde{Q} (3.9).

Snapshots of typical base-flow profiles are given in figure 1. Remember that the oscillating profiles develop a boundary layer near the walls of thickness $\delta = \sqrt{\nu/\Omega}$. The relative thickness of this boundary layer is governed by the Womersley number since $Wo = h/\delta$. Throughout this paper, reference is often made to acceleration (respectively deceleration) phases of the base flow, here defined as phases during which the flow rate $Q(t)$ increases (respectively decreases). Note that since the boundary layers near the walls are out of phase with the bulk flow, the actual fluid accelerations or decelerations at different positions in the channel cross-section do not coincide exactly with such a global definition based on the sign of dQ/dt .

4. Mathematical formulation

In this entire study, the total instantaneous flow fields are separated into basic and perturbation quantities as

$$\mathbf{u}_{tot}(\mathbf{x}, t) = U_1(x_0, t)\mathbf{e}_1 + \mathbf{u}(\mathbf{x}, t), \quad (4.1)$$

$$p_{tot}(\mathbf{x}, t) = -G(t)x_1 + p(\mathbf{x}, t), \quad (4.2)$$

whether the perturbation is of small amplitude (for linear stability analyses) or not (for investigating the fully developed nonlinear dynamics). The momentum and continuity equations for the perturbation quantities $\mathbf{u}(\mathbf{x}, t) \equiv u_0(\mathbf{x}, t)\mathbf{e}_0 + u_1(\mathbf{x}, t)\mathbf{e}_1 + u_2(\mathbf{x}, t)\mathbf{e}_2$ and $p(\mathbf{x}, t)$ then read, in dimensional form,

$$\frac{\partial \mathbf{u}}{\partial t} + U_1 \frac{\partial \mathbf{u}}{\partial x_1} + u_0 \frac{\partial U_1}{\partial x_0} \mathbf{e}_1 + (\mathbf{u} \cdot \nabla) \mathbf{u} = \nu \Delta \mathbf{u} - \nabla p + \mathbf{f}, \quad (4.3)$$

$$0 = \nabla \cdot \mathbf{u}. \quad (4.4)$$

The external volume force $\mathbf{f}(\mathbf{x}, t)$ is mainly used in nonlinear evolution problems for maintaining the prescribed total pulsatile flow rate; it will be specified and discussed below (§ 4.3). Also, the initial perturbation in both linear and nonlinear evolution problems is triggered by a small-amplitude impulsive \mathbf{f} , and it has been checked that the resulting dynamics does not depend on the details of this initial impulse.

4.1. Linear temporal evolution problem

When carrying out a linear stability analysis for small-amplitude perturbations, the quadratic terms $(\mathbf{u} \cdot \nabla) \mathbf{u}$ in the previous equation (4.3) may be neglected. Since the base flow is homogeneous in directions parallel to the channel walls, infinitesimally small velocity and pressure disturbances may then be written by resorting to spatial normal modes of the form

$$\mathbf{u}(\mathbf{x}, t) = \mathbf{u}^l(x_0, t) \exp i(\alpha_1 x_1 + \alpha_2 x_2), \quad (4.5)$$

$$p(\mathbf{x}, t) = p^l(x_0, t) \exp i(\alpha_1 x_1 + \alpha_2 x_2), \quad (4.6)$$

where α_1 and α_2 are the streamwise and spanwise wavenumbers, respectively. Substitution of (4.5), (4.6) into the linearized version of the governing equations (4.3), (4.4) yields

$$\partial_t u_0 + i\alpha_1 U_1 u_0 = v(\partial_{00} - \alpha_1^2 - \alpha_2^2) u_0 - \partial_0 p, \quad (4.7)$$

$$\partial_t u_1 + i\alpha_1 U_1 u_1 + (\partial_0 U_1) u_0 = v(\partial_{00} - \alpha_1^2 - \alpha_2^2) u_1 - i\alpha_1 p, \quad (4.8)$$

$$\partial_t u_2 + i\alpha_1 U_1 u_2 = v(\partial_{00} - \alpha_1^2 - \alpha_2^2) u_2 - i\alpha_2 p, \quad (4.9)$$

$$0 = \partial_0 u_0 + i\alpha_1 u_1 + i\alpha_2 u_2, \quad (4.10)$$

with the notation $\partial_t \equiv \partial/\partial t$, $\partial_0 \equiv \partial/\partial x_0$ and $\partial_{00} \equiv \partial^2/\partial x_0^2$. Together with no-slip boundary conditions along the channel walls, this system of partial differential equations consists of a temporal evolution problem for the complex-valued functions u_0 , u_1 , u_2 and p that depend on a single spatial coordinate, x_0 , and is numerically solved using the method outlined in § A.3 of the appendix.

4.2. Floquet analysis

Instead of integrating the previous linear temporal evolution problem by starting with a given initial condition, the linear stability of pulsating channel flow can also be studied by solving the eigenproblems arising from a Floquet analysis, thus obtaining the complete spectrum and the associated eigenfunctions.

Since the base flow is time periodic with pulsation Ω , perturbations are sought in normal-mode form as

$$\mathbf{u}(\mathbf{x}, t) = \left[\sum_n \hat{\mathbf{u}}^{(n)}(x_0) \exp in\Omega t \right] \exp i(\alpha_1 x_1 + \alpha_2 x_2 - \omega t), \quad (4.11)$$

$$p(\mathbf{x}, t) = \left[\sum_n \hat{p}^{(n)}(x_0) \exp in\Omega t \right] \exp i(\alpha_1 x_1 + \alpha_2 x_2 - \omega t), \quad (4.12)$$

where the complex frequency ω is the eigenvalue, and the eigenfunctions

$$\hat{\mathbf{u}}(x_0, t) \equiv \sum_n \hat{\mathbf{u}}^{(n)}(x_0) \exp in\Omega t \quad \text{and} \quad \hat{p}(x_0, t) \equiv \sum_n \hat{p}^{(n)}(x_0) \exp in\Omega t \quad (4.13a,b)$$

have the same temporal periodicity as the base flow.

Substitution of these expansions, with $\hat{\mathbf{u}}^{(n)}(x_0) \equiv \hat{u}_0^{(n)}(x_0)\mathbf{e}_0 + \hat{u}_1^{(n)}(x_0)\mathbf{e}_1 + \hat{u}_2^{(n)}(x_0)\mathbf{e}_2$, into (4.7)–(4.10) yields the Floquet eigenvalue problem. This system of linear coupled

ordinary differential equations in the x_0 -coordinate may be written, for each integer n , as

$$\omega \hat{u}_0^{(n)} = n\Omega \hat{u}_0^{(n)} + \alpha_1 \sum_k U_1^{(k)} \hat{u}_0^{(n-k)} + i\nu(\partial_{00} - \alpha_1^2 - \alpha_2^2) \hat{u}_0^{(n)} - i\partial_0 \hat{p}^{(n)}, \quad (4.14)$$

$$\begin{aligned} \omega \hat{u}_1^{(n)} &= n\Omega \hat{u}_1^{(n)} + \alpha_1 \sum_k U_1^{(k)} \hat{u}_1^{(n-k)} - i \sum_k \partial_0 U_1^{(k)} \hat{u}_0^{(n-k)} \\ &\quad + i\nu(\partial_{00} - \alpha_1^2 - \alpha_2^2) \hat{u}_1^{(n)} + \alpha_1 \hat{p}^{(n)}, \end{aligned} \quad (4.15)$$

$$\omega \hat{u}_2^{(n)} = n\Omega \hat{u}_2^{(n)} + \alpha_1 \sum_k U_1^{(k)} \hat{u}_2^{(n-k)} + i\nu(\partial_{00} - \alpha_1^2 - \alpha_2^2) \hat{u}_2^{(n)} + \alpha_2 \hat{p}^{(n)}, \quad (4.16)$$

$$0 = -i\partial_0 \hat{u}_0^{(n)} + \alpha_1 \hat{u}_1^{(n)} + \alpha_2 \hat{u}_2^{(n)}, \quad (4.17)$$

together with no-slip boundary conditions along the channel walls

$$\hat{u}_0^{(n)} = \hat{u}_1^{(n)} = \hat{u}_2^{(n)} = 0 \quad \text{for } x_0 = \pm h. \quad (4.18)$$

In the above momentum equations (4.14)–(4.16), the coupling of the different Fourier components of the velocity eigenfunctions occurs through the base-flow velocity components. Note that, since $U_1^{(k)} = 0$ for $|k| \geq 2$ in the configurations under investigation (3.8), the coupling of the eigenvelocities through the base flow only occurs between n and $n-1$, n or $n+1$. The numerical solution of this generalized eigenvalue problem (4.14)–(4.18) is outlined in § A.2 of the appendix.

The long-term evolution of a given mode is dictated by the complex frequency ω , or equivalently by the Floquet multiplier $\mu \equiv \exp(-i\omega T)$ which accounts for the gain after one complete pulsation period. The complex frequency of the most unstable or least stable mode depends on all parameters through a linear dispersion relation as

$$\omega = \omega^{lin}(\alpha_1, \alpha_2; Re, Wo, \tilde{Q}). \quad (4.19)$$

Whenever $\omega_i > 0$, or equivalently $|\mu| > 1$, the perturbation is unstable and grows exponentially over a large number of pulsation periods. Note, however, that within a pulsation period the dynamics differs from such an exponential behaviour due to the base-flow pulsation.

4.3. Nonlinear temporal evolution problem

In unstable situations, an initial small-amplitude perturbation of wave vector $\alpha_1 e_1 + \alpha_2 e_2$ may be amplified and eventually reach finite amplitudes so that the nonlinear term in (4.3) can no longer be neglected. Expanding the finite-amplitude disturbance as

$$\mathbf{u}(\mathbf{x}, t) = \sum_n \mathbf{u}^{(n)}(x_0, t) \exp[in(\alpha_1 x_1 + \alpha_2 x_2)], \quad (4.20)$$

$$p(\mathbf{x}, t) = \sum_n p^{(n)}(x_0, t) \exp[in(\alpha_1 x_1 + \alpha_2 x_2)], \quad (4.21)$$

and replacing these expansions with $\mathbf{u}^{(n)}(x_0, t) \equiv u_0^{(n)}(x_0, t)\mathbf{e}_0 + u_1^{(n)}(x_0, t)\mathbf{e}_1 + u_2^{(n)}(x_0, t)\mathbf{e}_2$ into (4.3), (4.4) results in a nonlinear temporal evolution problem consisting of a system of coupled partial differential equations for the different flow components

$$\partial_t u_0^{(n)} + i\alpha_1 U_1 u_0^{(n)} + \sum_k N^{(n,k)} u_0^{(k)} = v \Delta^{(n)} u_0^{(n)} - \partial_0 p^{(n)}, \quad (4.22)$$

$$\partial_t u_1^{(n)} + i\alpha_1 U_1 u_1^{(n)} + (\partial_0 U_1) u_0^{(n)} + \sum_k N^{(n,k)} u_1^{(k)} = v \Delta^{(n)} u_1^{(n)} - i\alpha_1 p^{(n)}, \quad (4.23)$$

$$\partial_t u_2^{(n)} + i\alpha_1 U_1 u_2^{(n)} + \sum_k N^{(n,k)} u_2^{(k)} = v \Delta^{(n)} u_2^{(n)} - i\alpha_2 p^{(n)}, \quad (4.24)$$

$$0 = \partial_0 u_0^{(n)} + i\alpha_1 u_1^{(n)} + i\alpha_2 u_2^{(n)}, \quad (4.25)$$

where the operators $N^{(n,k)}$ and $\Delta^{(n)}$ are defined as

$$N^{(n,k)} \equiv u_0^{(n-k)} \partial_0 + u_1^{(n-k)} ik\alpha_1 + u_2^{(n-k)} ik\alpha_2 \quad \text{and} \quad \Delta^{(n)} \equiv \partial_{00} - n^2 \alpha_1^2 - n^2 \alpha_2^2. \quad (4.26a,b)$$

This is akin to performing a direct numerical simulation in a finite domain with periodic boundary conditions in the wall-parallel coordinates. The initial-value problem of interest here is the temporal development of a streamwise and spanwise-periodic small-amplitude perturbation, characterized by real values of α_1 and α_2 . The initial evolution is dictated by the linear temporal growth rate ω_i , obtained from a linear stability analysis. Whenever $\omega_i > 0$, modulated exponential temporal growth takes place until nonlinear effects come into play. The quadratic nonlinear terms of the Navier–Stokes equations then promote higher spatial harmonics of the form $\mathbf{u}^{(n)}(x_0, t) \exp i(n\alpha_1 x_1 + m\alpha_2 x_2)$ as well as a spatially homogeneous flow correction $\mathbf{u}^{(0)}(x_0, t)$. Terms of the form $\exp i(n\alpha_1 x_1 + m\alpha_2 x_2)$ with $m \neq n$ would only be generated by secondary instabilities; therefore, finite-amplitude flow fields may be expanded here as a single spatial Fourier series (4.20), (4.21) since the aim is to obtain finite-amplitude primary solutions. A complete secondary stability analysis of these primary nonlinear waves is beyond the scope of the present investigation.

The development, through nonlinear interactions, of a spatially homogeneous flow correction $\mathbf{u}^{(0)}(x_0, t)$ results in a modification of the streamwise total flow rate by

$$q_1(t) = \int_{-h}^{+h} u_1^{(0)}(x_0, t) dx_0, \quad (4.27)$$

and three-dimensional oblique waves may also give rise to a non-vanishing spanwise flow rate

$$q_2(t) = \int_{-h}^{+h} u_2^{(0)}(x_0, t) dx_0. \quad (4.28)$$

Since there is no mean pressure gradient associated with a perturbation of the form (4.21), the governing equations (4.3), (4.4) for perturbations of the form (4.20), (4.21) without an external volume force f correspond to a temporal evolution problem at prescribed total pressure gradient. In order to simulate a temporal evolution at prescribed total flow rate, the assumed form of the pressure (4.21) is not sufficiently general: one must allow for the development of a spatially homogeneous pressure gradient, which is equivalent to an external volume force

of the form $f = -g_1(t)\mathbf{e}_1 - g_2(t)\mathbf{e}_2$ and entails the additional terms $-g_1(t)$ and $-g_2(t)$ on the right-hand side of (4.23) and (4.24) when $n = 0$. This additional force, or pressure gradient, in the streamwise and spanwise directions may be tuned so that disturbances develop without modifying the base flow rate, which is purely in the streamwise direction. The numerical computation of the required $g_1(t)$ and $g_2(t)$ will be discussed in § A.3.

5. Linear dynamics

The configurations under investigation are completely determined by three non-dimensional control parameters: the Womersley number Wo (3.5), the Reynolds number Re (3.10) and the relative amplitude of the oscillating flow-rate component \tilde{Q} (3.9). Numerical results, however, depend on the choice of units for space and time. In the sequel, distances are measured in units of the channel diameter (here $2h$) and velocities in units of mean base-flow velocity (here $Q^{(0)}/2h$). The associated time scale of $4h^2/Q^{(0)}$ then leads to a non-dimensional frequency of $\Omega = 4Wo^2/Re$, which corresponds to a pulsation period of $T = \pi Re/2Wo^2$.

With the non-dimensionalization adopted in this work, the steady Poiseuille flow is known to become linearly unstable for $Re > Re_c$ with $Re_c \simeq 7696$, and the marginal perturbation at criticality is two-dimensional with a streamwise wavenumber of $\alpha_{1,c} \simeq 2.041$ and a frequency of $\omega_c \simeq 0.808$ (see e.g. p. 73 of Schmid & Henningson (2001) and references therein).

The approach used here is to investigate how the instability features are influenced by the presence of an additional pulsatile component. Starting from Poiseuille flow, the instability characteristics are monitored as the amplitude \tilde{Q} of the oscillating base flow-rate component is increased. For most results presented below, the reference configuration is the steady Poiseuille flow at $Re = 10\,000$, which is linearly unstable. Depending on the pulsation frequency, measured by the Womersley number, the aim is to work out whether the pulsating component promotes or reduces the instability and how the linear dynamics is affected within a pulsation period and in the long term.

The linear stability analysis is introduced with typical temporal evolution problems, increasing only \tilde{Q} while all other parameters are kept constant. Subsequently, more general situations are considered, varying the Womersley number Wo , streamwise and spanwise wavenumbers α_1 and α_2 and eventually the Reynolds number Re to obtain the critical conditions for onset of linear instability in the most general case.

5.1. Typical temporal evolution problems

To illustrate the temporal dynamics of small-amplitude perturbations developing in pulsatile channel flow, we first consider perturbations of streamwise wavenumber $\alpha_1 = 2$ at $Re = 10\,000$.

Figure 2(a) shows the temporal evolution of a perturbation developing in steady Poiseuille flow (with $\tilde{Q} = 0$), computed by time marching of (4.7)–(4.10). An exponentially growing linear travelling wave is seen to develop, where $\mathbf{u}^l(x_0, t) \sim \exp(-i\omega t)$ with a complex frequency of $\omega = 0.7497 + 0.0067i$. This frequency is numerically determined by computing e.g. $i(\partial_t u_0)/u_0$, and its value is also confirmed by solving the corresponding eigenvalue problem (4.14)–(4.18). The energy contained in the perturbation grows exponentially as $E \sim \exp(2\omega_i t)$, see figure 3. Throughout this section on linear dynamics, the instantaneous energy $E(t)$ of a perturbation is defined as the spatially averaged value of $|\mathbf{u}(\mathbf{x}, t)|^2$ per unit volume.

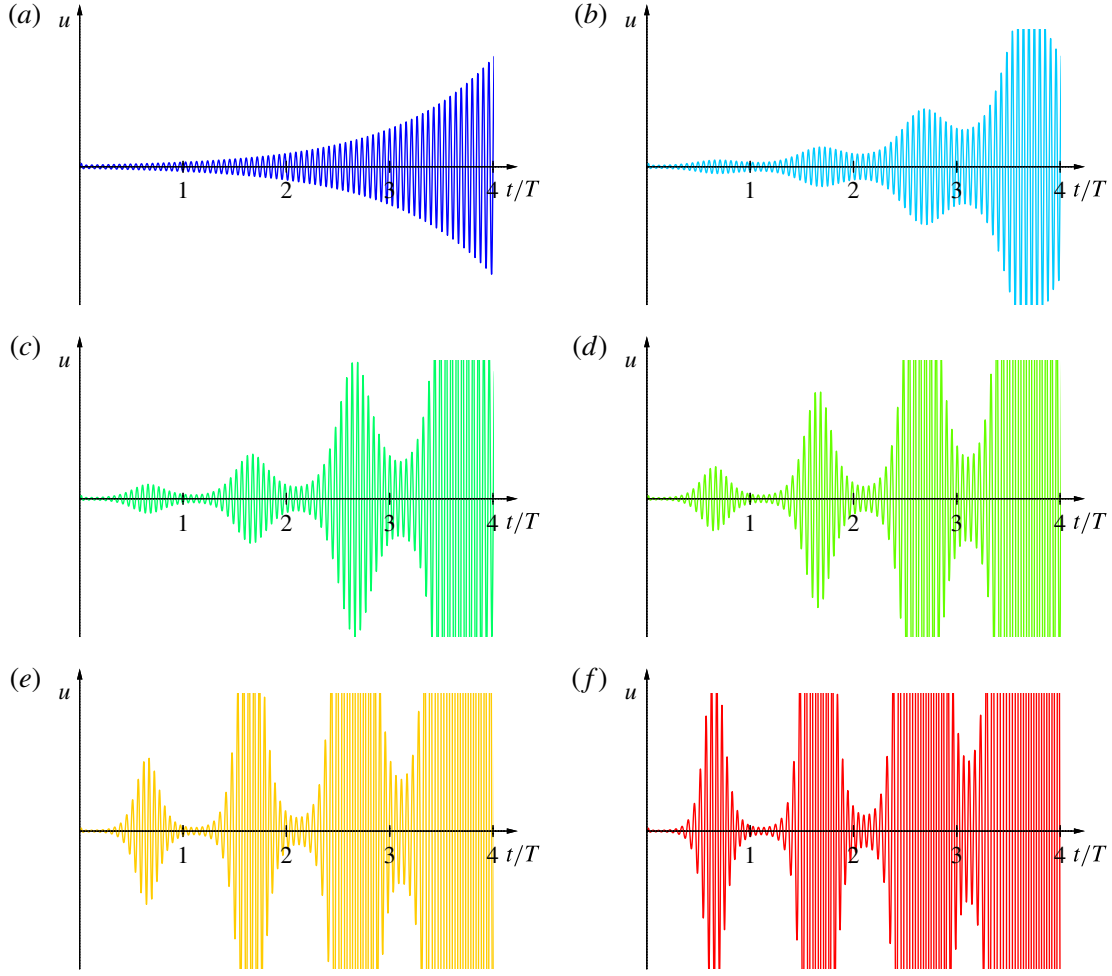


FIGURE 2. (Colour online) Temporal evolution of a small-amplitude perturbation with $\alpha_1 = 2$ at $Re = 10\,000$ and $Wo = 10$. Perturbation velocity time series for base flow with (a) $\tilde{Q} = 0$ (Poiseuille flow), (b) $\tilde{Q} = 0.02$, (c) $\tilde{Q} = 0.04$, (d) $\tilde{Q} = 0.06$, (e) $\tilde{Q} = 0.08$ and (f) $\tilde{Q} = 0.10$ over 4 base-flow pulsation cycles. In this linear dynamics, the velocity scale is arbitrary but identical for all cases shown, and the same initial perturbation has been used throughout to trigger the perturbation.

Adding to this base flow a pulsatile component of different magnitudes $\tilde{Q} = 0.02, 0.04, \dots, 0.10$, at $Wo = 10$, the perturbation is observed to undergo a modulated exponential growth (figure 2b–f), where the modulations occur at the frequency of the base flow. The temporal evolution of the corresponding fluctuating energy is shown in figure 3. The long-term growth of the perturbation is governed by the Floquet multiplier $\mu \equiv \exp(-i\omega T)$ and may be derived in the direct numerical simulations by monitoring e.g. $u_0(x_0, t + T)/u_0(x_0, t)$ (see § A.3 for more details on the numerical implementation). Here, for $\tilde{Q} = 0.02, 0.04, 0.06, 0.08$ and 0.10 , the perturbation grows exponentially according to a complex frequency of $\omega = 0.7495 + 0.0068i$, $\omega = 0.7490 + 0.0072i$, $\omega = 0.7481 + 0.0077i$, $\omega = 0.7468 + 0.0085i$ and $\omega = 0.7852 + 0.0095i$ respectively. Again, these values are confirmed by solving the corresponding Floquet eigenproblems. Thus, the weak periodic component of the base flow is here responsible for a slight increase in growth rate (ω_i).

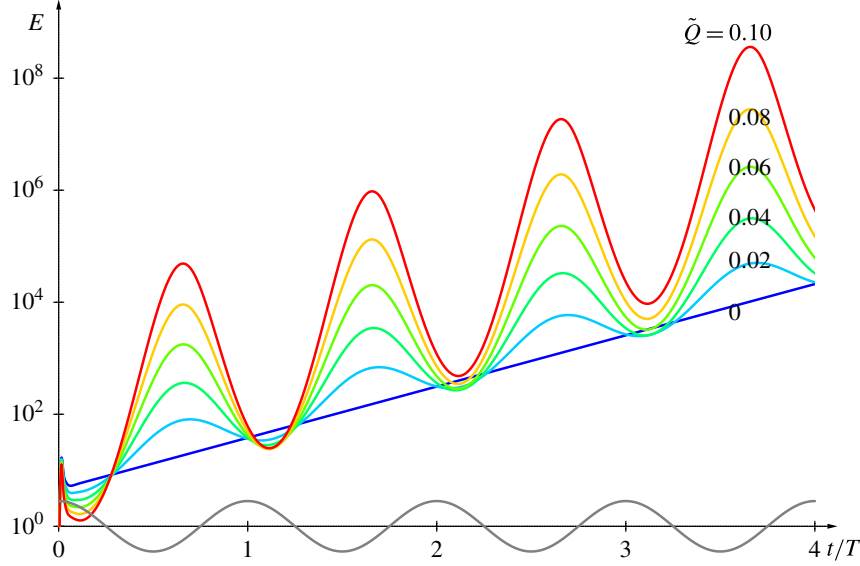


FIGURE 3. (Colour online) Temporal evolution of perturbation energy for $\tilde{Q} = 0.00, 0.02, \dots, 0.08, 0.10$ at $\alpha_1 = 2$, $Re = 10\,000$ and $Wo = 10$ (same configurations as figure 2). Intracyclic modulation amplitude rapidly increases with the pulsation amplitude \tilde{Q} , and it is observed that intracyclic growth (respectively decay) approximately coincides with base-flow deceleration (respectively acceleration) phases, as indicated by solid sinusoidal line representing $Q(t)$ (not to scale).

In these examples, the pulsatile component of the base flow only weakly affects the long-term perturbation growth: all energy curves in figure 3 display a similar mean slope in these logarithmic plots. However, the dynamics within each cycle significantly changes with increasing values of \tilde{Q} . Indeed, the amplitude of the intracyclic modulations increases by approximately three orders of magnitude as \tilde{Q} is increased from 0.02 to 0.1.

Comparison of the energy curves with the base flow rate (solid grey curve in figure 3) shows that enhanced growth occurs in the deceleration phase of the base flow, while decay occurs during the acceleration phase. Although time dependent, this behaviour is similar to what is known for steady boundary layers developing along a flat plate, for which an adverse pressure gradient promotes transition while a favourable pressure gradient delays it (Kachanov 1994). The importance of this intracyclic growth and decay rapidly increases with \tilde{Q} , while the net growth over an entire base-flow cycle in these examples is of the same order as the growth prevailing for the equivalent steady Poiseuille configuration.

In order to characterize the intracyclic dynamics, it is convenient to compensate the computed quantities by removing the asymptotic long-term exponential growth, i.e. to consider

$$\underline{\mathbf{u}}(x_0, t) \equiv \mathbf{u}(x_0, t) \exp(-\omega_i t) \quad \text{and} \quad \underline{E}(t) \equiv E(t) \exp(-2\omega_i t). \quad (5.1a,b)$$

Note that the compensated flow fields $\underline{\mathbf{u}}$, obtained by processing data from direct numerical simulations, differ from the Floquet eigenfunctions only by a phase velocity term $\exp(i\omega_r t)$. The ratio

$$\frac{\underline{E}_{\max}^{max}}{\underline{E}_{\min}^{min}} \equiv \frac{\max_t \underline{E}(t)}{\min_t \underline{E}(t)} \quad (5.2)$$

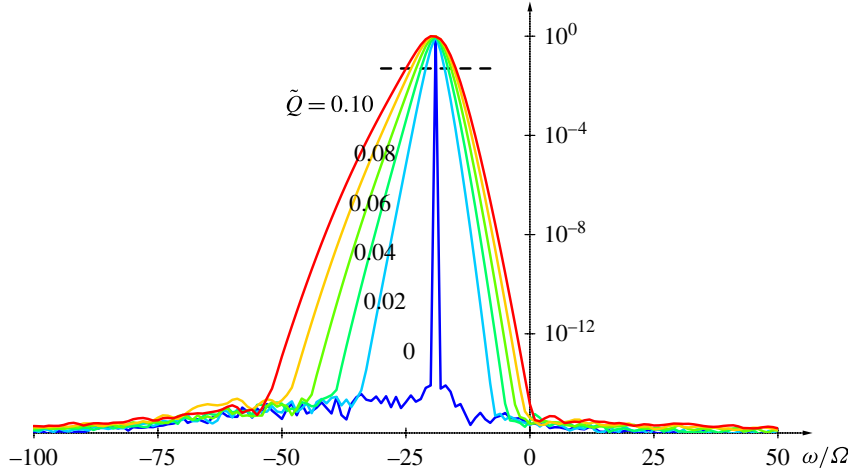


FIGURE 4. (Colour online) Spectra of compensated velocity time series for $\tilde{Q} = 0.00, 0.02, \dots, 0.08, 0.10$ at $\alpha_1 = 2$, $Wo = 10$ and $Re = 10\,000$. The peak in these spectra near $\omega/\Omega = -19$ is associated with the dominant frequency $-\omega_r$ of the travelling fluctuations. The width is related to the number of Fourier modes that are required in a Floquet analysis and is seen to rapidly increase with the base-flow pulsating amplitude \tilde{Q} .

is then a direct measure of the amplitude of the intracyclic modulations. While $E_{min}^{max} = 1$ for steady Poiseuille flow, it rapidly grows with the pulsatile component and reaches $E_{min}^{max} = 8042$ for $\tilde{Q} = 0.10$ in the above example. More results for E_{min}^{max} over a large parameter space are presented below.

The velocity time series shown in figure 2 illustrate that the dynamics is governed by two distinct time scales: fast oscillations (associated with ω_r) are due to the spatially travelling wave, while the slower modulations are tuned to the frequency Ω of the base flow. In these examples, $\omega_r/\Omega \simeq 19$ as $\Omega = 4Wo^2/Re = 0.04$. This discrepancy of frequencies explains why a stability analysis in terms of Floquet eigenmodes (4.13) requires a large number of Fourier components to be successful, and the required number of modes rapidly increases with \tilde{Q} . In theory, a Floquet analysis is preferable to a linearized direct numerical simulation since it yields the entire spectrum and not only the dominant mode. In practice, however, the size of the associated eigenproblems becomes rapidly unmanageable as \tilde{Q} is increased, while the resolution requirements for a direct numerical simulation (DNS) are largely independent of \tilde{Q} .

The number of Floquet harmonics that is required for a sufficient resolution of the modes may be estimated from DNS data. Indeed, a Fourier analysis of the compensated flow fields \underline{u} yields the spectra shown in figure 4. These spectra are centred around the dominant frequency in the signal, which corresponds to $-\omega_r$, and their width (e.g. the number of modes above the dashed line at 1/20 of the maximum) is directly related to the number of Fourier modes required to approximate the intracyclic dynamics. The rapid broadening of the spectra in figure 4 with \tilde{Q} is associated with the increase of the intracyclic modulation amplitude, and highlights the sensitivity of the dynamics to the pulsating component of the base flow.

5.2. Temporal instability at $\alpha_1 = 2$ and $Re = 10\,000$

The influence of the base-flow pulsating magnitude and frequency on disturbance growth has been systematically investigated at $Re = 10\,000$ and $(\alpha_1, \alpha_2) = (2, 0)$ for

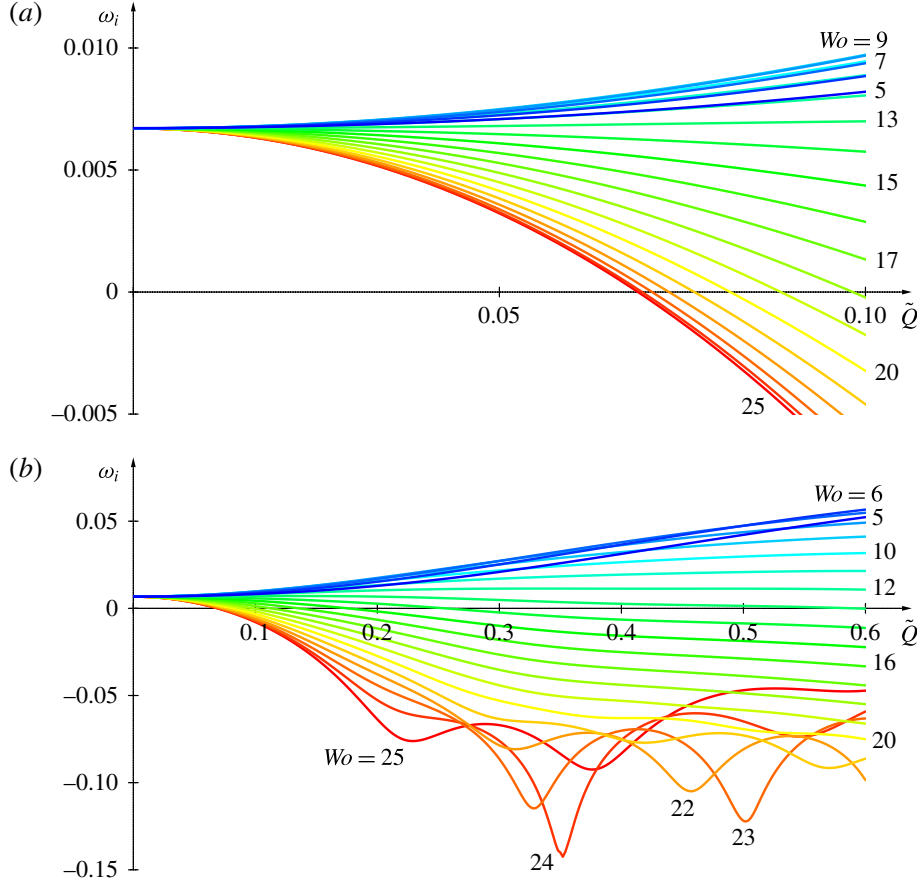


FIGURE 5. (Colour online) Linear temporal growth rate at $Re = 10\,000$ and $\alpha_1 = 2$ for $0 \leq \tilde{Q} \leq 0.6$ and $Wo = 5, 6, \dots, 25$.

$5 \leq Wo \leq 25$ and $0 \leq \tilde{Q} \leq 0.6$. The temporal growth rate ω_i has been computed both by direct numerical simulations of the linearized evolution equations and by solving the Floquet eigenproblems. For each value of the Womersley number $Wo = 5, 6, \dots, 25$, the pulsating magnitude \tilde{Q} has been increased from 0 to 0.6 (in steps of 0.002) to illustrate the effect of an increasing oscillating component, starting with a Poiseuille flow, which is unstable in this configuration. For small values of \tilde{Q} , the growth rate is seen to depend quadratically on the pulsating magnitude (figure 5a), and the instability is enhanced at low frequencies ($Wo = 5, \dots, 13$) while it is reduced at higher frequencies ($Wo = 14, \dots, 25$); strongest destabilization occurs for $Wo = 9$. Note that the quadratic dependence in small values of \tilde{Q} has been analytically established by Hall (1975) and von Kerczek (1982). At larger values of \tilde{Q} , perturbations are found to decay ($\omega_i < 0$) for Womersley numbers beyond $Wo = 14$, and the decay rate may display a non-monotonic dependence on \tilde{Q} (figure 5b).

The intracyclic modulation amplitudes E_{\min}^{\max} computed for the same parameter ranges are given in figure 6. Whatever the Womersley number Wo , the ratio E_{\min}^{\max} increases almost exponentially with \tilde{Q} starting from Poiseuille flow ($\tilde{Q} = 0$). At larger pulsation amplitudes \tilde{Q} , the growth of E_{\min}^{\max} is seen to saturate; however, at low Womersley numbers, the exponential growth of E_{\min}^{\max} continues to astronomical values as \tilde{Q} increases. Since the intracyclic amplification E_{\min}^{\max} is related to the

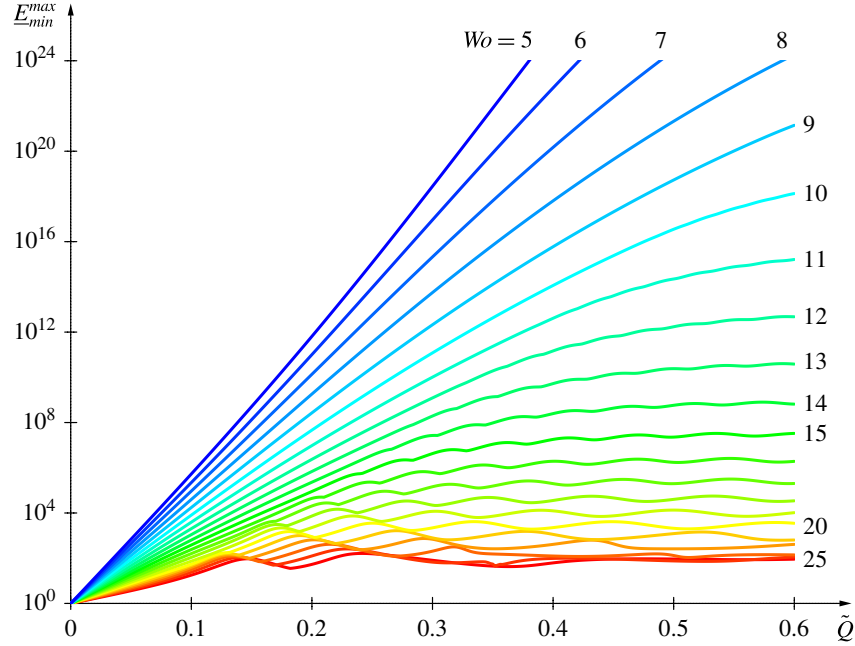


FIGURE 6. (Colour online) Amplitude of intracyclic modulation E_{\min}^{\max} at $Re = 10\,000$ and $\alpha_1 = 2$ for $0 \leq \tilde{Q} \leq 0.6$ and $5 \leq Wo \leq 25$.

deceleration and acceleration phases of the base flow, its growth may be understood in the following manner. Increasing \tilde{Q} at constant Wo , corresponds to stronger deceleration and acceleration of the base flow without modifying their durations and therefore enhances the ratio E_{\min}^{\max} that is reached within each pulsation cycle. Moreover, reducing Wo corresponds to increasing the pulsation period as Wo^{-2} , and therefore stretching the duration of both deceleration and acceleration phases. Hence, E_{\min}^{\max} grows much faster with \tilde{Q} at smaller values of Wo .

As discussed previously, in situations where significant intracyclic modulations take place, a large number of Fourier components is required when carrying out a stability analysis based on Floquet eigenproblems. From the DNS results, after computing Fourier spectra of the compensated velocity fields, the approximate number of Fourier modes required in a Floquet analysis can be determined: the data plotted in figure 7(a) correspond to the number of modes in the compensated spectrum with energy above 1/20 of the maximum (above dashed line in figure 4). This plot may be used as a guideline for estimating the parameter region amenable to Floquet analysis. The relevance of this criterion is demonstrated in figure 7(b), comparing temporal growth rates computed both by linearized DNS (lines) and Floquet analysis (symbols) retaining $N_f = 30$ Fourier components to expand the eigenmodes (4.13). As expected, both methods yield indistinguishable results up to $\tilde{Q} = 0.6$ for moderate to large values of Wo . It is only at lower pulsation frequencies, i.e. lower Wo , that a truncated Floquet method is seen to fail beyond some value of \tilde{Q} .

5.3. Two-dimensional instability analysis at $Re = 10\,000$

A complete two-dimensional instability analysis has been performed by exploring a range of streamwise wavenumbers, $0.5 \leq \alpha_1 \leq 4.0$, for each configuration. This range has been chosen so as to encompass all unstable wavenumbers for $5 \leq Wo \leq 25$ and $0 \leq \tilde{Q} \leq 0.6$ at $Re = 10\,000$.

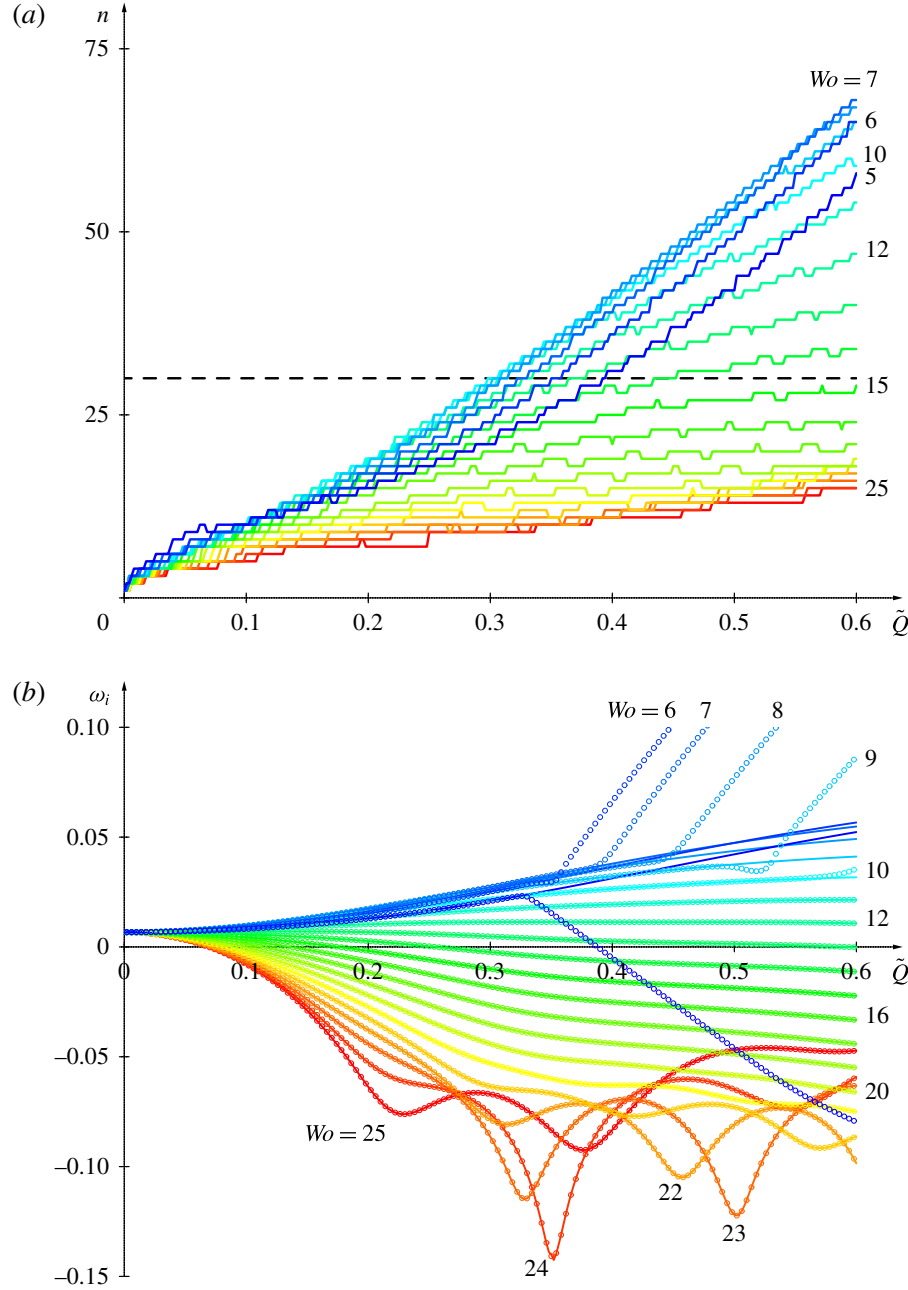


FIGURE 7. (Colour online) Linear dynamics at $Re = 10\,000$ and $\alpha_1 = 2$ for $0 \leq \tilde{Q} \leq 0.6$ and $5 \leq Wo \leq 25$. (a) DNS-based estimate of the number of Fourier modes required for a sufficiently resolved Floquet analysis. (b) Comparison of temporal growth rates, computed by linearized DNS (solid lines) and Floquet eigenproblems (symbols) with $N_f = 30$. Failure of truncated Floquet analysis (symbols off solid lines in b) largely corresponds to curves above dashed line in (a).

Figure 8 shows isolines of positive temporal growth rate for (a) $Wo = 6$, (b) $Wo = 10$, (c) $Wo = 12$ and (d) $Wo = 15$, computed via linearized DNS. For Poiseuille flow ($\tilde{Q} = 0$), unstable wavenumbers range from $\alpha_1 \simeq 1.75$ to $\alpha_1 \simeq 2.19$, and, as the amplitude \tilde{Q} of the pulsating base-flow component is increased, this range evolves as well as the maximum growth rate that is achieved for each \tilde{Q} .

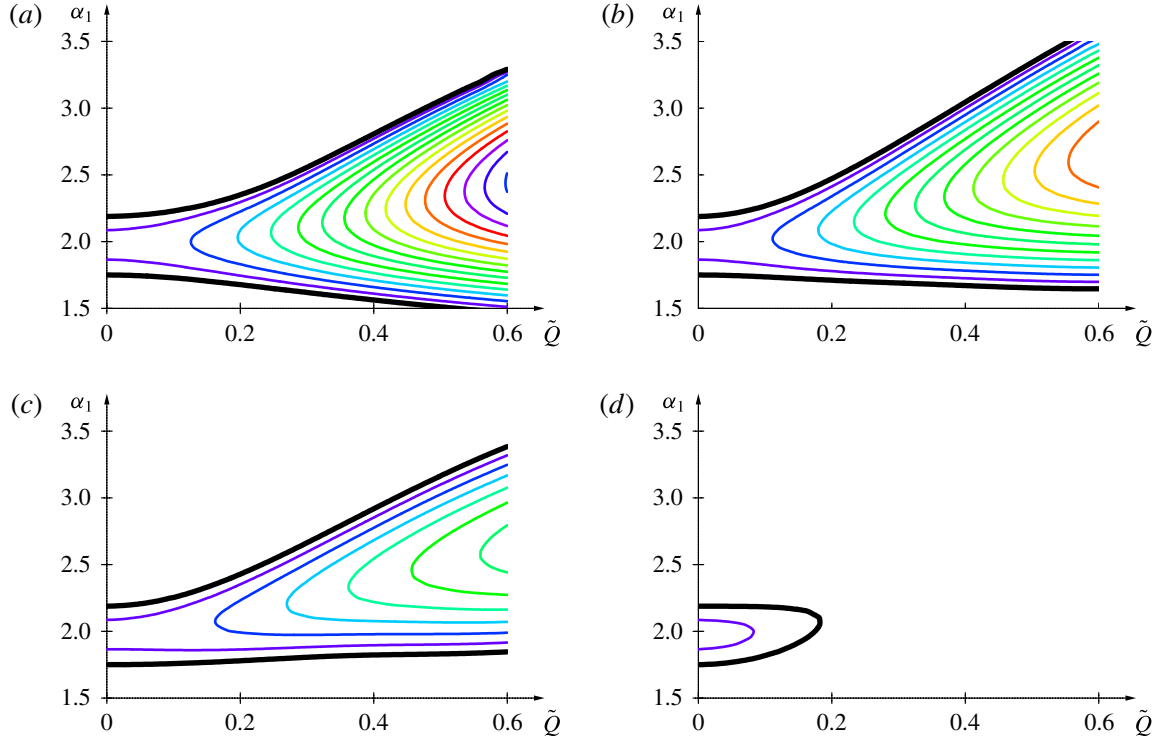


FIGURE 8. (Colour online) Isolines of linear temporal growth rate for two-dimensional perturbations in (α_1, \tilde{Q}) -plane at $Re = 10000$ and (a) $Wo = 6$, (b) $Wo = 10$, (c) $Wo = 12$, (d) $Wo = 15$. Thick black lines correspond to the marginal curve $\omega_i = 0$ and thin coloured lines to positive growth rates $\omega_i = 0.005, 0.010, 0.015, \dots$

As already observed, the instability is enhanced with increasing \tilde{Q} for low to moderate Womersley numbers. Figure 8(a–c), corresponding to $Wo = 6, 10$ and 12 respectively, shows how the upper bound of the unstable wavenumber range increases almost linearly with \tilde{Q} , while the lower bound depends much less on \tilde{Q} . The most unstable wavenumber occurs roughly in the centre of the unstable range, and it is therefore observed that an increasing pulsation amplitude \tilde{Q} favours instabilities at smaller wavelengths (larger α_1). Thus, for these configurations, the maximum temporal growth rate is significantly larger than the values shown in figure 5 corresponding to a fixed $\alpha_1 = 2$.

At larger Womersley numbers (see figure 8d corresponding to $Wo = 15$), the pulsating component has a stabilizing effect and the range of unstable α_1 disappears as \tilde{Q} is increased.

5.4. Three-dimensional instability analysis at $Re = 10000$

According to Squire's theorem, which remains valid for pulsating flows (Conrad & Criminale 1965), a two-dimensional analysis is sufficient to study onset of instability. Nonetheless, it is worth investigating the dynamics of three-dimensional perturbations developing in pulsatile channel flow. Figure 9 shows the temporal growth rate in the (α_1, α_2) -wavevector plane for a range of pulsating amplitudes \tilde{Q} and Womersley numbers Wo , at $Re = 10000$.

At a high pulsation frequency of $Wo = 15$ (figure 9c), the pulsating component reduces the growth rates and base flows are stable at $\tilde{Q} = 0.2$ and beyond. In contrast,

at lower Womersley numbers, the base-flow pulsation enhances the instability and increases the range of unstable wavenumbers. At $Wo = 5$ (figure 9a), the maximum growth rate increases slightly faster with \tilde{Q} than at $Wo = 10$ (figure 9b). While the maximum growth rate follows very similar trends at $Wo = 5$ and 10, the evolution with \tilde{Q} of the entire unstable region in the (α_1, α_2) -wavevector plane shows some differences. Indeed, at $Wo = 5$ (figure 9a), the pulsation promotes spanwise modes associated with a finite α_2 and small α_1 . At $Wo = 10$ (figure 9b), the pulsation rather favours streamwise modes: as \tilde{Q} is increased, the unstable region further extends in the direction of large values of α_1 .

5.5. Critical Reynolds number

Whether a given base flow, characterized by the non-dimensional parameters Re , Wo and \tilde{Q} , is linearly unstable or not depends on the growth rate of its most unstable or least stable mode:

$$\omega_i^{max}(Re, Wo, \tilde{Q}) \equiv \max_{\alpha_1, \alpha_2} \text{Im} \omega^{lin}(\alpha_1, \alpha_2; Re, Wo, \tilde{Q}). \quad (5.3)$$

In accordance with Squire's theorem, it is observed that the maximum growth rate always occurs for $\alpha_2 = 0$. Then, the critical Reynolds number $Re_c(Wo, \tilde{Q})$ for onset of instability at given values of Wo and \tilde{Q} is obtained by the condition of vanishing ω_i^{max} . The evolution of Re_c with \tilde{Q} for a range of Wo is shown in figure 10. Poiseuille flow ($\tilde{Q} = 0$) corresponds to a critical Reynolds number of $Re_c = 7696$. For the configurations investigated here, the pulsating base-flow component is seen to have a stabilizing effect for Womersley numbers beyond 13. This stabilizing effect is very strong for $Wo > 18$: when increasing \tilde{Q} , the critical Reynolds number more than doubles when $\tilde{Q} = 0.2$ is reached. On the other hand, for lower frequencies, the pulsating component has a destabilizing effect, which appears to be strongest around $Wo = 7$.

6. Nonlinear dynamics

In this section the aim is to analyse the fully developed dynamics sustained in linearly unstable base flows, in order to identify and characterize the different regimes that prevail in this configuration. Since fully developed perturbations naturally arise from the temporal development of a small-amplitude initial disturbance, the present approach is based on temporal evolution problems investigated by direct numerical simulations of the complete Navier–Stokes equations. The initial evolution is dictated by linear dynamics, as discussed in the previous section. Whenever the linear temporal growth rate is positive, the perturbation necessarily reaches finite-amplitude levels and nonlinear effects come into play. In the absence of secondary instabilities, a fully developed regime is then reached with spatial periodicity imposed by the prescribed values of streamwise and spanwise wavenumbers α_1 and α_2 .

Subcritical behaviour has been documented for plane Poiseuille flow (Ehrenstein & Koch 1991) and is expected to exist also for pulsatile channel flow. However, it is beyond the scope of the present paper to investigate finite-amplitude regimes that may exist beyond the linearly unstable regions in parameter space.

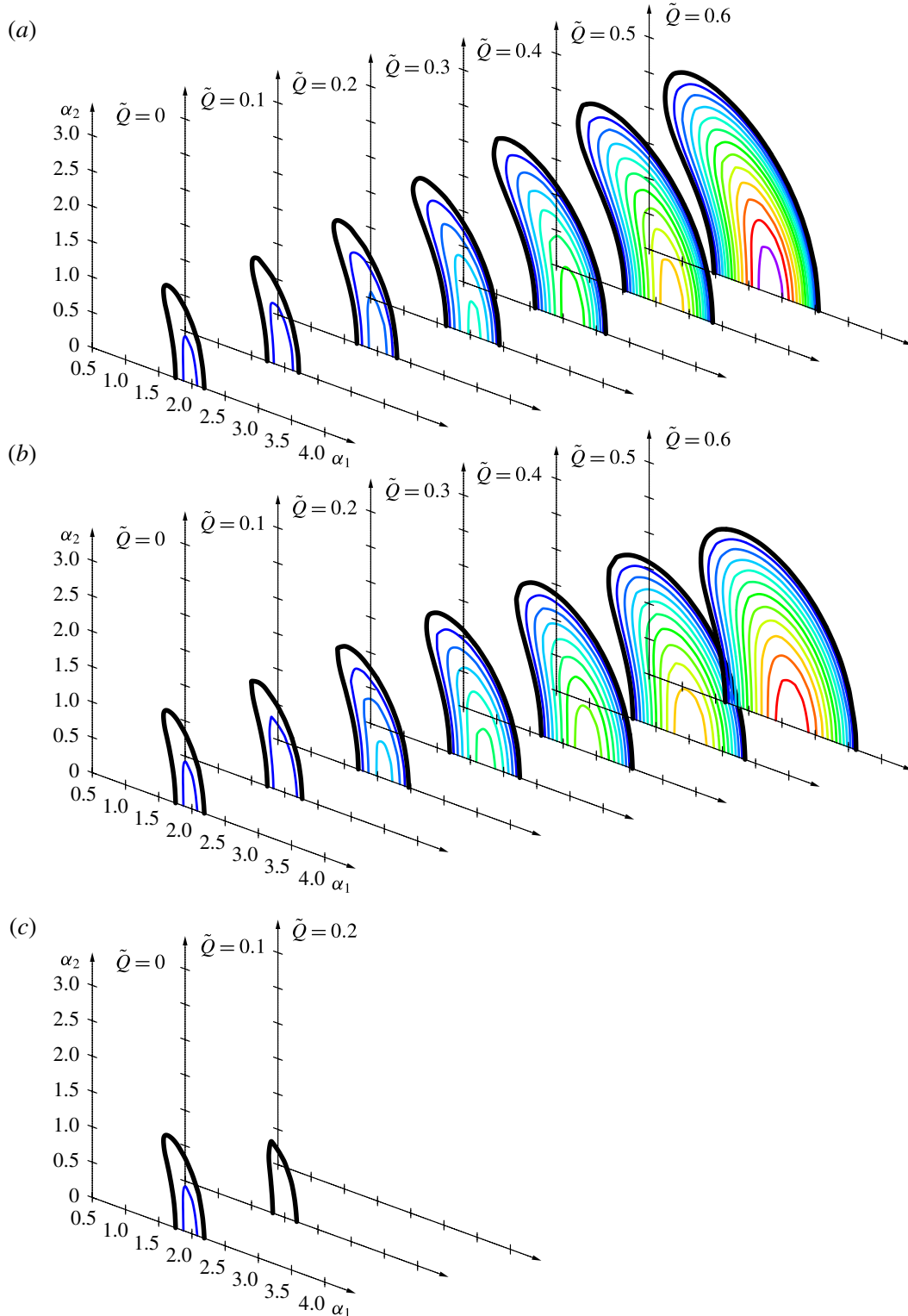


FIGURE 9. (Colour online) Isolines of temporal growth rate ω_i in the (α_1, α_2) -wavevector plane for $\tilde{Q} = 0.0, 0.1, \dots, 0.6$ at (a) $Wo = 5$, (b) $Wo = 10$, (c) $Wo = 15$. Thick black lines correspond to the marginal curve $\omega_i = 0$ and thin coloured lines to positive growth rates $\omega_i = 0.005, 0.010, 0.015, \dots$

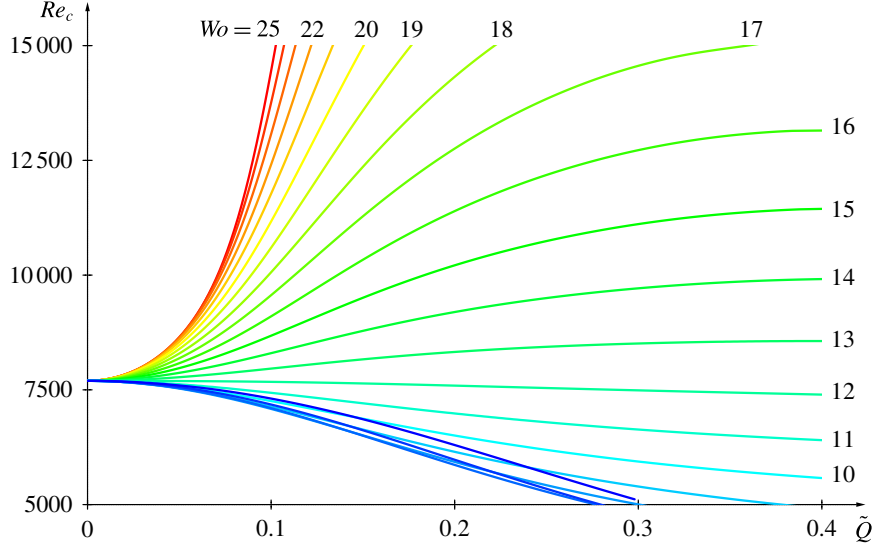


FIGURE 10. (Colour online) Critical Reynolds number for onset of temporal instability as a function of the base-flow pulsation amplitude \tilde{Q} for a range of Womersley numbers: $Wo = 5, 6, \dots, 25$.

6.1. Two characteristic examples of fully developed regimes

While carrying out direct numerical simulations over large regions of a multi-dimensional parameter space, essentially two types of fully developed regimes have been observed: ‘cruising’ regimes for which nonlinearities are sustained throughout the entire pulsation cycle and ‘ballistic’ regimes that are propelled into a nonlinear phase before subsiding again to small amplitudes within every cycle.

These two distinct regimes may be illustrated by analysing perturbations with $\alpha_1 = 2$ developing in a base flow at $Re = 10\,000$ and $Wo = 10$ with two different pulsation amplitudes $\tilde{Q} = 0.08$ and 0.20 .

6.1.1. ‘Cruising’ nonlinear regime

For a pulsatile base flow at $Re = 10\,000$, $Wo = 10$ and $\tilde{Q} = 0.08$, a small-amplitude perturbation of streamwise wavenumber $\alpha_1 = 2$ is linearly unstable and therefore leads to a fully developed regime. Figure 11(a) gives the temporal evolution of the total perturbation energy on a linear scale, while figure 11(b) shows the energy of the different spatial Fourier components on a logarithmic scale. Here, the instantaneous energy $E^{(n)}(t)$ of the n th Fourier component of the perturbation is defined as the spatially averaged value of $|\mathbf{u}^{(n)}(x_0, t)|^2$ per unit volume.

Instantaneous spatially averaged wall shear stress values are plotted in figure 11(c).

During the early stages of the temporal evolution (here approximately $0 < t/T < 10$), a linear regime prevails with a complex frequency of $\omega = 0.7468 + 0.0085i$ and an intracyclic modulation amplitude of $\underline{E}_{min}^{max} = 1.35 \times 10^3$. In this regime, the different Fourier components are classically slaved to the fundamental as $E^{(n)} \propto (E^{(1)})^n$ for $n \geq 2$, and $E^{(0)} \propto (E^{(1)})^2$. The mean slopes of the energy curves are seen to follow these scalings in figure 11(b), and the intracyclic modulations around these mean slopes do the same. It is only the mean-flow correction $E^{(0)}$ that is found to decay more slowly than $(E^{(1)})^2$ during the intracyclic decay phases. This slower decay of the spatially homogeneous component $E^{(0)}$ corresponds to viscous dissipation that is less efficient

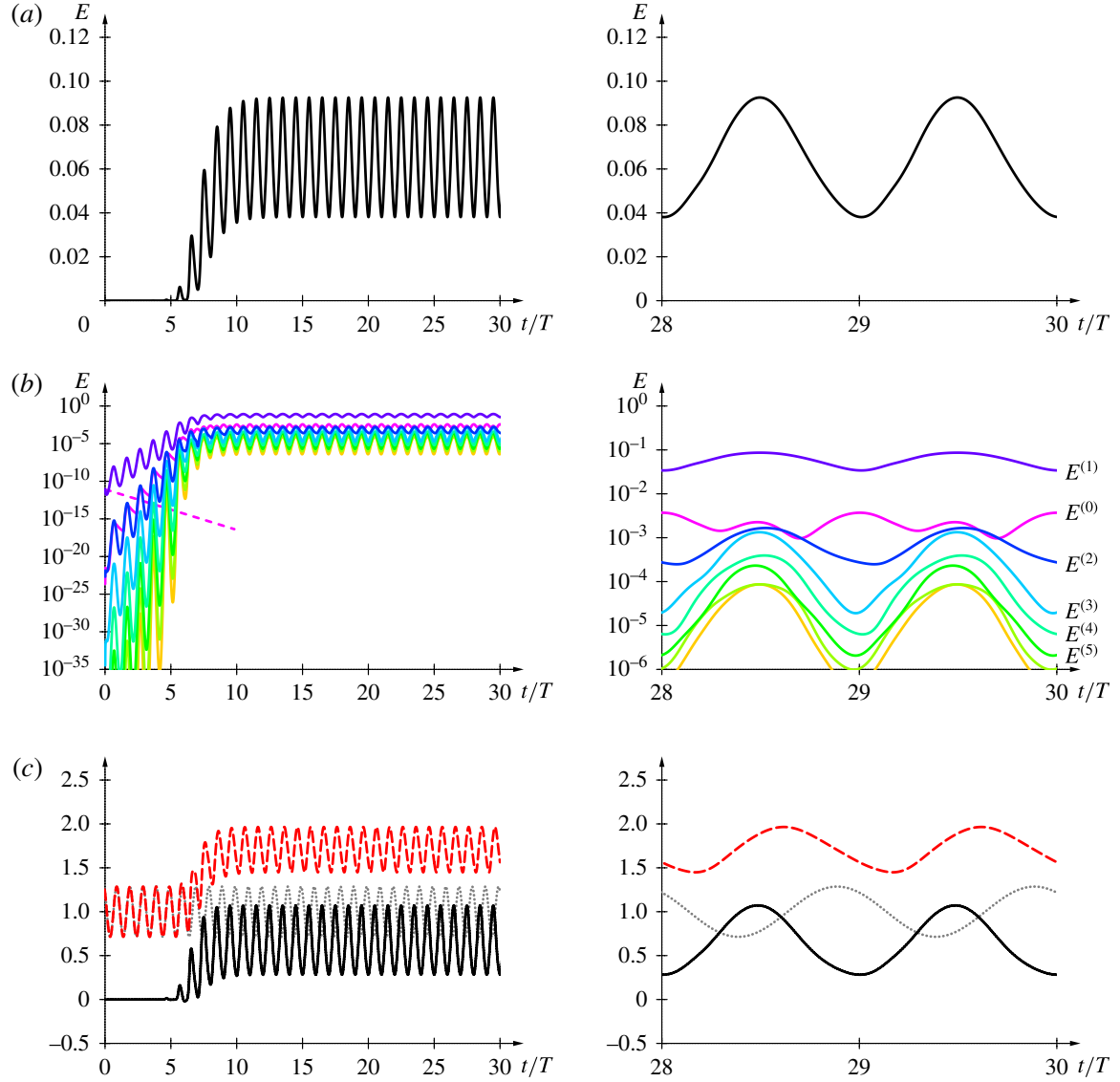


FIGURE 11. (Colour online) ‘Cruising’ nonlinear regime resulting from modulated exponential growth of small-amplitude initial perturbation with $\alpha_1 = 2$ at $Re = 10\,000$, $Wo = 10$ and $\tilde{Q} = 0.08$. (a) Total perturbation energy. (b) Energy of each spatial Fourier component. (c) Spatially averaged wall shear stress of perturbation (black solid), total (red dashed) and base (grey dotted) fields relative to steady Poiseuille flow value.

than the stabilization of the $E^{(1)}$ component during the base-flow acceleration phase. Indeed, for the same base flow, the decay of a spatially homogeneous perturbation with $\alpha_1 = \alpha_2 = 0$ follows the dashed line in figure 11(b), which displays a similar slope as the mean-flow correction $E^{(0)}$ here in its phases of slow decay.

As finite-amplitude levels are reached (here beyond $t/T = 10$), a fully developed regime is entered consisting of a travelling nonlinear wave that is modulated by the pulsating base flow. In this regime, the modulation amplitude is no larger than the average values so that the regime remains fully nonlinear throughout the pulsation cycle and is characterized by a ratio of intracyclic modulation amplitudes of order unity, here $E_{\min}^{\max} = 2.51$.

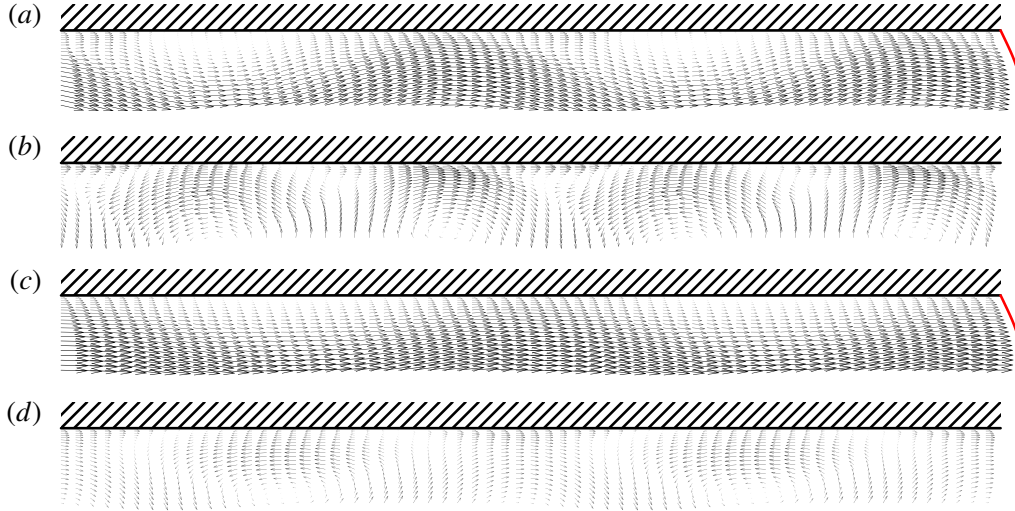


FIGURE 12. (Colour online) Snapshots of velocity fields in cruising nonlinear regime over two wavelengths with $\alpha_1 = 2$ at $Re = 10\,000$, $Wo = 10$ and $\tilde{Q} = 0.08$: (a) total velocity at $t/T = 29.5$, (b) perturbation velocity at $t/T = 29.5$, (c) total velocity at $t/T = 30.0$, (d) perturbation velocity at $t/T = 30.0$. Solid curves to the right of (a) and (c) indicate base-flow profile prevailing at the same instant.

From figure 11(b) it is observed that the total perturbation energy is largely dominated by the fundamental component $E^{(1)}$, even in the nonlinear regime. Higher harmonics are well below the fundamental and follow the same pattern of intracyclic modulation. It is only the mean-flow correction $E^{(0)}$ that displays a different trend: two intracyclic maxima, coinciding with the extrema of the fundamental (or the total) energy. The second maximum of $E^{(0)}$ that occurs when the perturbation is near its lowest is probably due to the continuing transfer of energy from the fundamental to the spatially homogeneous component and due to the fact that this energy is only slowly dissipated so that $E^{(0)}$ continues to build up while $E^{(1)}$ decreases. Monitoring the energy associated with the different Fourier components shows that this fully developed regime may be accurately computed by using only a limited number of components. All of the computations of the present study have been carried out with $N_h = 9$, and for most cases the fully developed dynamics was already well resolved with $N_h = 5$.

The instantaneous spatially averaged wall shear stress (WSS) is plotted in figure 11(c), relative to the value prevailing for a steady Poiseuille flow at the same Reynolds number. The wall shear stress component due to the perturbation (solid black curve) follows a similar evolution to the fluctuating energy (figure 11a), which results in a significant increase of the total WSS (dashed red curve) and departure from the WSS prevailing for the base flow (dotted grey curve). The growth (respectively decay) of the perturbation WSS during the deceleration (respectively acceleration) phases of the base flow, results in a total spatially averaged WSS modulation out of phase with the base flow by approximately a quarter period, similar to what is observed for Stokes layers.

This regime consists of a travelling nonlinear wave that propagates downstream with a temporally modulated amplitude. Snapshots of the flow fields over two wavelengths are shown in figure 12, near maximum energy at $t/T = 29.5$ (a,b) and minimum energy at $t/T = 30.0$ (c,d). The total flow fields (a,c) display the sinuous structure

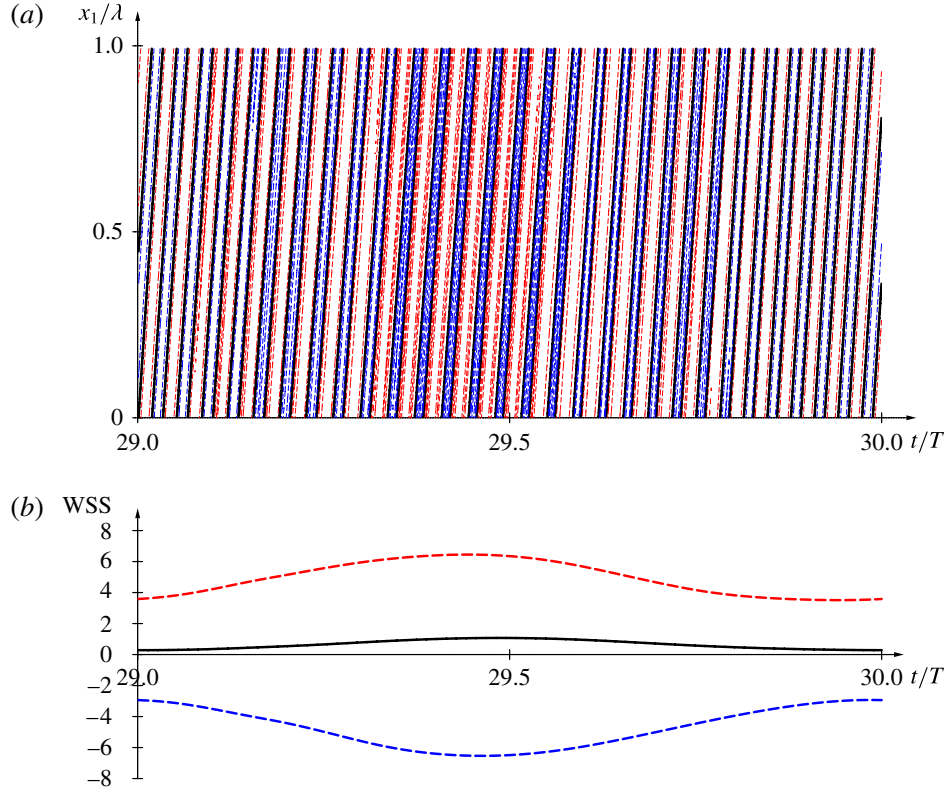


FIGURE 13. (Colour online) (a) Spatio-temporal pattern of the perturbation WSS in cruising regime over one streamwise wavelength $\lambda = 2\pi/\alpha_1$ and one pulsation period. WSS values are relative to a steady Poiseuille flow at the same Reynolds number, and thick solid black isoline corresponding to $WSS = 0$ separates thin dashed red (respectively blue) isolines corresponding to levels $WSS = 2, 4, 6$ (respectively $WSS = -2, -4, -6$). (b) Instantaneous spatially averaged (solid black), minimum (dashed blue) and maximum (dashed red) values of WSS.

of these nonlinear travelling waves, while the perturbation velocity fields (*b,d*) give an idea of the associated propagating vortices.

These modulated travelling nonlinear waves are associated with the spatio-temporal WSS pattern shown in figure 13(*a*) over one streamwise wavelength for one pulsation period. The characteristic oblique lines in this plot are associated with the nonlinear waves travelling at a nearly constant phase velocity. Their amplitude is modulated over the pulsation period, similarly to what has already been observed in figure 11. However, the wave-like nature of the flow structure is associated with local WSS values well above and below their spatial average shown in figure 11(*c*). The temporal evolution of the local maximum and minimum WSS values are shown in figure 13(*b*) together with the instantaneous spatial average. While the spatially averaged perturbation WSS values are of the same order as the base-flow contribution, the local extrema are significantly larger. Also, the modulation of these nonlinear propagating waves results in larger modulation amplitudes for the local extrema than for the spatially averaged values. Thus, this fully developed regime is associated with strong localized stresses in alternating directions travelling along the channel walls.

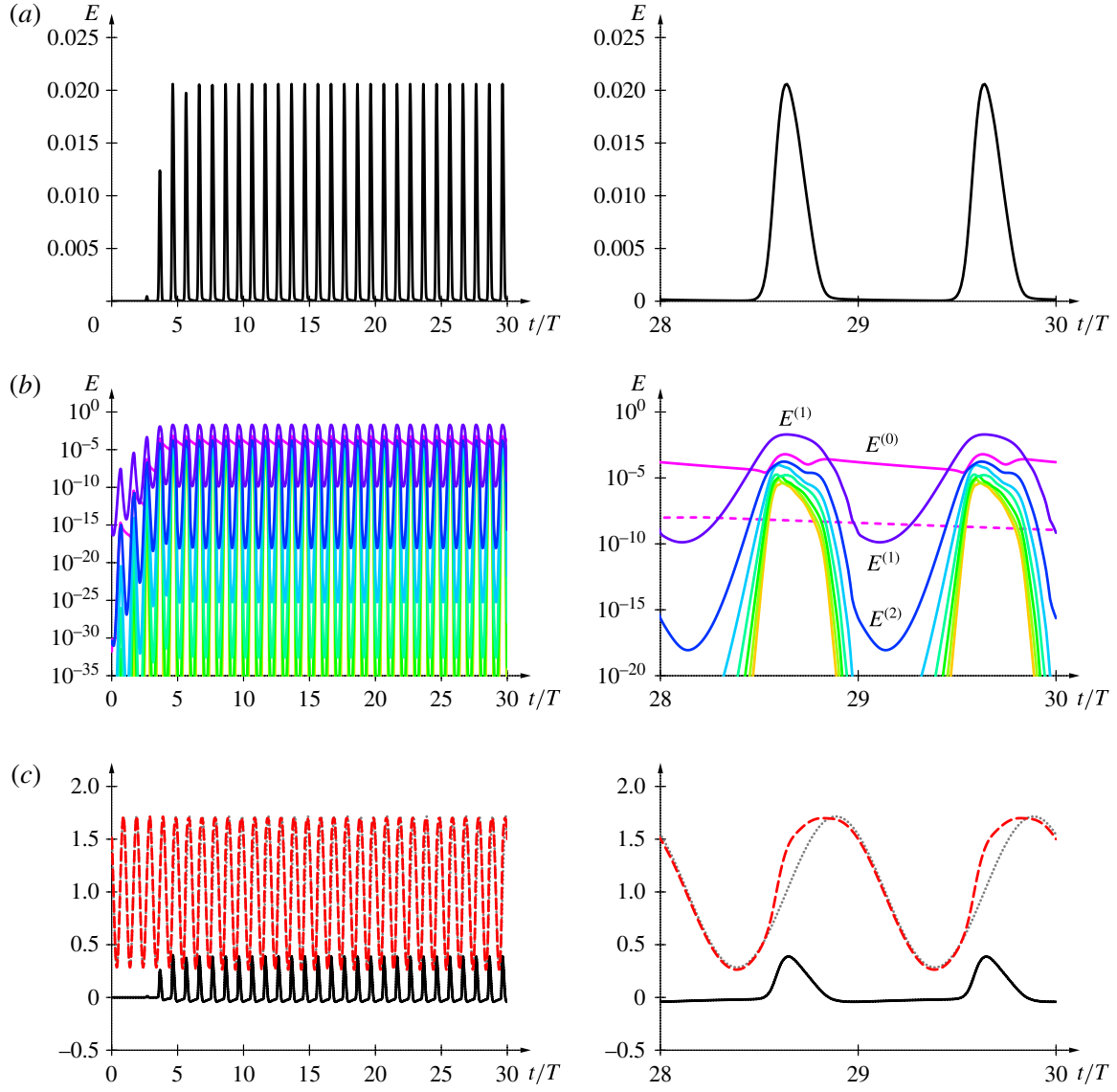


FIGURE 14. (Colour online) ‘Ballistic’ nonlinear regime resulting from modulated exponential growth of small-amplitude initial perturbation with $\alpha_1 = 2$ at $Re = 10\,000$, $Wo = 10$ and $\tilde{Q} = 0.2$. (a) Total perturbation energy. (b) Energy of each spatial Fourier component. (c) Spatially averaged wall shear stress of perturbation (black solid), total (red dashed) and base (grey dotted) fields relative to steady Poiseuille flow value.

6.1.2. ‘Ballistic’ nonlinear regime

The temporal evolution of an initial small-amplitude perturbation for a base flow at a larger pulsating amplitude of $\tilde{Q} = 0.20$ is depicted in figure 14. In this example, the small-amplitude regime prevails approximately for $0 < t/T < 5$, and, in that stage, the perturbation exponentially grows according to a complex frequency of $\omega = 0.8119 + 0.0156i$ with a significantly larger intracyclic modulation amplitude of $\underline{E}_{min}^{max} = 4.61 \times 10^7$.

Once finite amplitudes are reached, the essential difference with the previous configuration is that the nonlinear regime does not prevail throughout the entire pulsation cycle: the fully developed regime consists of regular nonlinear bursts

separated by phases of nearly unperturbed base flow. Thus, the ratio of intracyclic modulation amplitudes is here much larger than unity, $E_{\min}^{\max} = 391$, since the perturbation drops to very small levels during the linear phase of the cycle (figure 14a).

Monitoring the temporal evolution of the energy contained in the different spatial Fourier components (figure 14b), shows that the observations of the previous configuration still hold: during the linear phases, higher harmonics are slaved to the fundamental as $E^{(n)} \propto (E^{(1)})^n$; a few Fourier components are enough to fully resolve the dynamics; during stabilization phases, the mean-flow correction $E^{(0)}$ decays on a slow time scale and therefore becomes un-slaved from the fundamental. Here the un-slaving of the mean-flow correction from the fundamental also occurs in the linear phases of the fully developed regime: the slow decay rate of the mean-flow correction is dictated by viscosity and is equivalent to that of a spatially homogeneous perturbation with $\alpha_1 = \alpha_2 = 0$ indicated by a dashed line in figure 14(b). Again, the total perturbation energy is dominated by the fundamental component, except during the linear phases of the fully developed regime where the fundamental drops to negligible levels while the mean-flow correction lags behind. Note also that due to these alternating linear and nonlinear phases, the energy levels in the ballistic regime are significantly lower than those of the cruising regime.

The temporal evolution of the associated WSS is shown in figure 14(c). Obviously the WSS associated with the perturbation (solid black curve) is only significant during the nonlinear phases. These nonlinear phases are relatively short compared with the pulsation period, therefore the total WSS (dashed red curve) in the fully developed regime only weakly departs from the WSS prevailing for the base flow (dotted grey curve).

This fully developed regime consists of periodic nonlinear bursts that are identically regenerated during every pulsation cycle. Snapshots of the flow fields over two wavelengths are shown in figure 15. Near maximum energy at $t/T = 29.6$, the total flow fields (figure 15a) exhibit the sinuous structure of the finite-amplitude travelling perturbation; this sinuosity is, however, less pronounced than in figure 12(a) since the perturbation is less energetic here. The associated perturbed fields at $t/T = 29.6$ are represented in figure 15(b). In the linear phase, at $t/T = 30.0$, the total flow fields (figure 15c) are indistinguishable from the base flow since the perturbation has negligible amplitude.

These nonlinear bursting travelling waves are associated with the spatio-temporal WSS pattern shown in figure 16(a). As already noted, the perturbation WSS is only significant during the nonlinear phases of the dynamics, here approximately for $29.4 < t/T < 29.8$. While the spatially averaged perturbation WSS (solid black curve in figure 16b) does not exceed half the mean value prevailing for the base flow, the local extrema due the travelling wave structure reach values that are an order of magnitude larger. Thus the ballistic regime is still associated with intense spatially localized WSS events, while the spatially averaged values remain rather weak (see also figure 14c).

6.1.3. Terminology

These two markedly different fully developed dynamics exemplified by the configurations discussed in this section have motivated the terms ‘cruising’ and ‘ballistic’ regimes by analogy with cruising and ballistic flight: the ‘cruising’ perturbations are continuously driven by nonlinearities while the ‘ballistic’ state is characterized by ‘take-off’ and ‘landing’ of the perturbation energy level. More

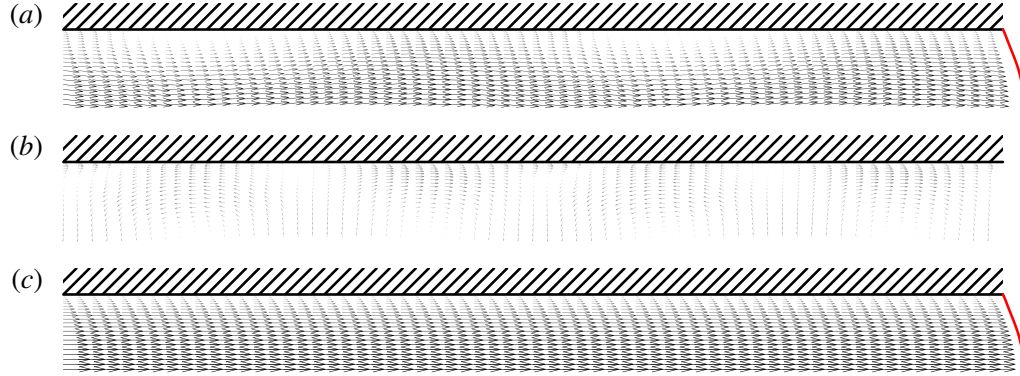


FIGURE 15. (Colour online) Snapshots of velocity fields in ballistic nonlinear regime over two wavelengths with $\alpha_1 = 2$ at $Re = 10\,000$, $Wo = 10$ and $\tilde{Q} = 0.2$: (a) total velocity at $t/T = 29.6$, (b) perturbation velocity at $t/T = 29.6$, (c) total velocity at $t/T = 30.0$ when the perturbation is negligible. Solid curves to the right of (a,c) indicate base-flow profile prevailing at same instant.

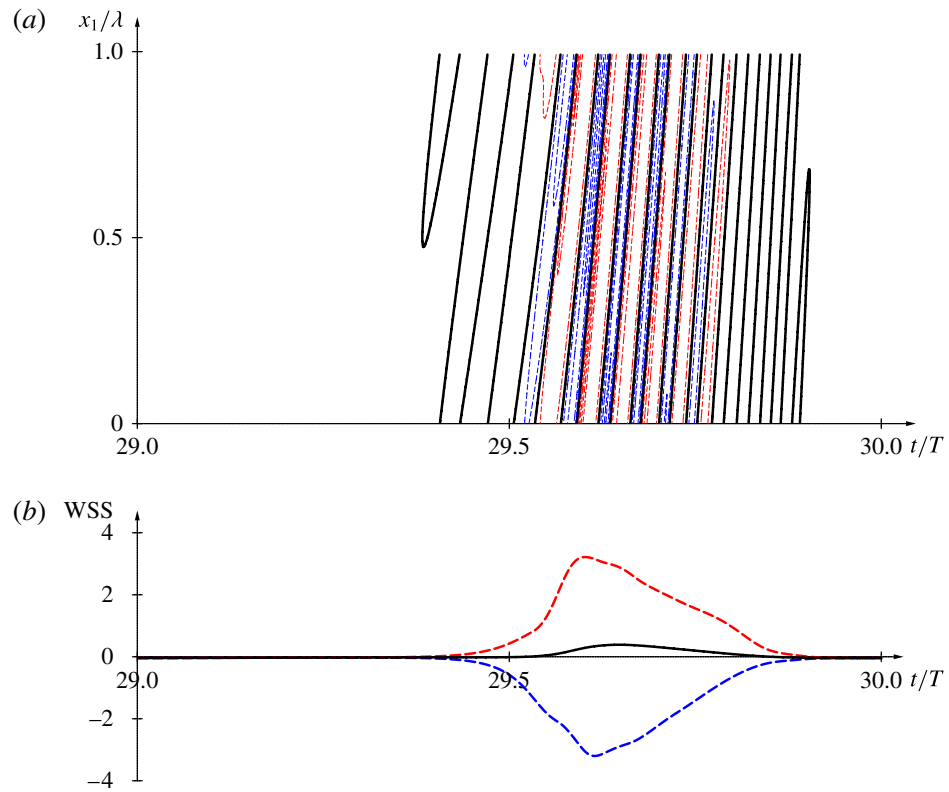


FIGURE 16. (Colour online) (a) Spatio-temporal pattern of the perturbation WSS in ballistic regime over one streamwise wavelength $\lambda = 2\pi/\alpha_1$ and one pulsation period. WSS values are relative to a steady Poiseuille flow at the same Reynolds number, and the thick solid black isoline corresponding to $WSS = 0$ separates the thin dashed red (respectively blue) isolines corresponding to levels $WSS = 1, 2, 3$ (respectively $WSS = -1, -2, -3$). (b) Instantaneous spatially averaged (solid black), minimum (dashed blue) and maximum (dashed red) values of WSS.

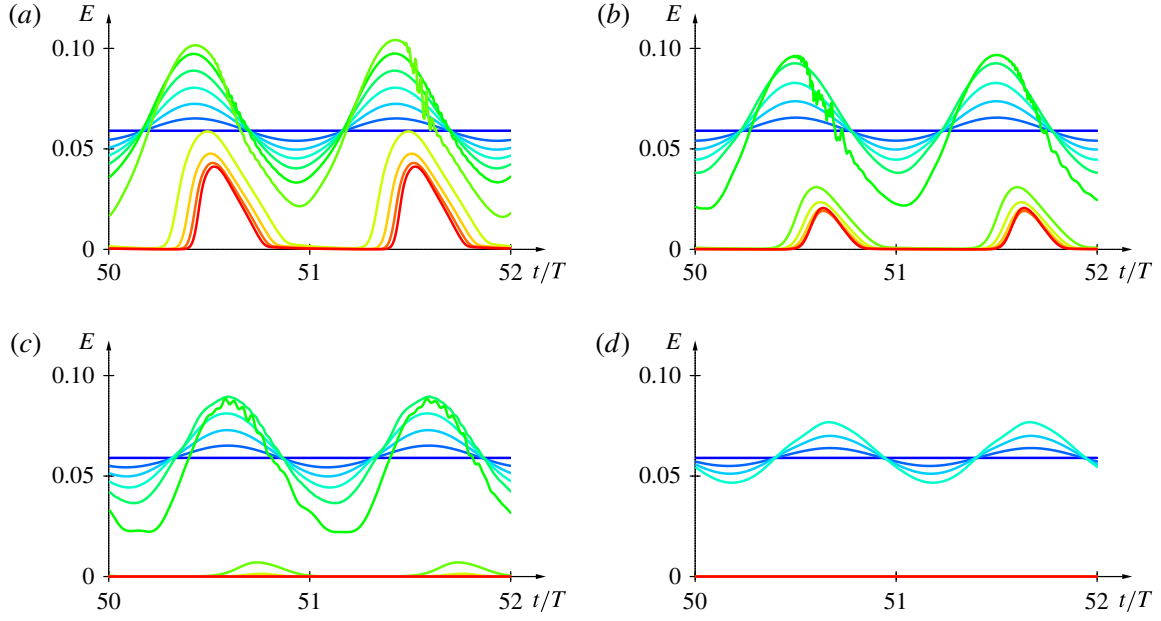


FIGURE 17. (Colour online) Temporal evolution of perturbation energy in fully developed regime at (a) $Wo = 7$, (b) $Wo = 10$, (c) $Wo = 15$, (d) $Wo = 20$, for $\tilde{Q} = 0.00$ (horizontal line), $0.02, 0.04, \dots, 0.20$ and $\alpha_1 = 2$, $Re = 10\,000$.

precisely, in the cruising regime, nonlinearities are sustained throughout the pulsation cycle, resulting in a fully developed regime with a modulated amplitude, that may be interpreted as saturated Tollmien–Schlichting waves undergoing modulations caused by the pulsation of the underlying base flow. In contrast, the ballistic regime consists of linear and nonlinear phases that alternate within every pulsation cycle: from a small-amplitude minimum reached near the middle of the linear phase, strong linear growth thrusts the system into a nonlinear regime that culminates after saturation at finite amplitude, before collapsing again and subsiding towards the next minimum.

6.2. Nonlinear dynamics at $\alpha_1 = 2$ and $Re = 10\,000$

The fully developed regime that prevails after perturbations reach finite amplitudes has been systematically investigated at $\alpha_1 = 2$ and $Re = 10\,000$ for Womersley numbers in the range $5 \leq Wo \leq 25$ and increasing pulsation amplitudes \tilde{Q} . Figure 17 shows the temporal evolution of the perturbation energy in the final regime over two base-flow pulsation periods for $0 \leq \tilde{Q} \leq 0.2$.

For Poiseuille flow, i.e. $\tilde{Q} = 0$, finite-amplitude Tollmien–Schlichting waves with constant energy are selected (dark blue horizontal lines in figure 17).

As the base-flow pulsation amplitude \tilde{Q} is increased, these nonlinear travelling waves display energy modulations around a mean value: in this cruising regime the temporally averaged perturbation energy remains very close to the value prevailing for $\tilde{Q} = 0$. As for the linear dynamics (see figure 3), energy builds up during base-flow deceleration ($n < t/T < n + 0.5$ for integer n) while it declines during base-flow acceleration ($n + 0.5 < t/T < n + 1$); recall that the definition of base-flow acceleration and deceleration phases is based on the sign of dQ/dt .

The amplitude of these perturbation energy modulations grows as \tilde{Q} is increased. Eventually the minimum energy value reached near $t/T = n$ drops to a low level,

and the flow behaviour switches then to a ballistic regime, characterized by linear phases of negligible perturbation amplitudes alternating with finite-amplitude bursts. This transition from cruising to ballistic regimes appears to be rather sudden: curves in figure 17 correspond to constant steps in \tilde{Q} of 0.02, and they display a gap at the transition between these two nonlinear regimes. At larger pulsation frequencies, see figure 17(d) at $Wo = 20$, the base-flow modulation has a stabilizing effect so that the ballistic regime is never selected: as \tilde{Q} is increased, the critical value for stability is reached while the flow is still in a cruising regime. The fully developed modulated Tollmien–Schlichting waves that prevail at the lower values of \tilde{Q} could probably be interpreted as inviscid vorticity waves and described by a Korteweg–de Vries equation, following a similar approach than that proposed by Tutty & Pedley (1994). In that context, the transition from cruising to ballistic regimes may be governed by a similar mechanism than that leading to cnoidal waves in a Korteweg–de Vries model.

Note also that when the critical value of \tilde{Q} for transition from cruising to ballistic regimes is approached, the energy curves display small-scale irregular fluctuations that break the overall periodicity of the flow from one pulsation period to the next and are believed to be the sign of secondary instabilities rather than numerical instabilities since this same behaviour is observed after changing spatial and temporal resolutions of the simulations. These secondary instabilities certainly play a role in the precise transition scenario between the two nonlinear regimes. However, the present numerical implementation was designed to investigate the structure of nonlinear travelling waves of given spatial wavenumbers and does not take into account sufficient degrees of freedom for a full secondary stability analysis, which is left for future investigations.

At larger base-flow modulation amplitudes, the maximum energy reached during the nonlinear bursts in the ballistic regime increases again with \tilde{Q} , as illustrated in figure 18 for $0.2 \leq \tilde{Q} \leq 0.4$ and $Wo = 7$ and 10. Eventually, the nonlinear bursts occurring at every base-flow pulsation period display some variation from one period to the next. Depending on the control parameters, the fluctuations that affect the regular pattern associated with the ballistic regime result either in period doubling or more irregular behaviour. A more detailed characterization of the fully developed regimes prevailing beyond these periodic nonlinear waves has not been attempted.

The phase diagram in figure 19 indicates the nature of the selected regime over the whole range of investigated Womersley numbers: $5 \leq Wo \leq 25$. The cruising regime prevails at low base-flow modulation amplitudes, starting from Poiseuille flow at $\tilde{Q} = 0$. At larger values of \tilde{Q} , to the right of the dashed curve, transition to a ballistic regime occurs. The pulsating base flow is linearly stable above the black curve. The critical value of \tilde{Q} where the transition between the two nonlinear regimes occurs is seen to weakly depend on the Womersley number. It is only at low values of Wo that the cruising regime survives significantly beyond $\tilde{Q} \simeq 0.1$. At larger pulsation frequencies (i.e. larger Wo), the stabilizing effect of the base-flow pulsation competes with its enhancing effect on the perturbation energy modulation. Thus, as already observed in figure 17(d) for $Wo = 20$, the ballistic regime is suppressed and the cruising regime prevails over the entire range of unstable \tilde{Q} , here for $Wo \geq 17$.

The criterion used to distinguish between cruising and ballistic regimes is based on the ratio E_{\min}^{\max} of the energy perturbation in the fully developed regime. This ratio is of order 1 for cruising regimes and increases more than tenfold in the ballistic regime, characterized by vanishing energy levels in its linear phases. Since the transition between both nonlinear regimes occurs rather suddenly, the boundary between both regimes is largely independent of the precise value of the critical ratio E_{\min}^{\max} used.

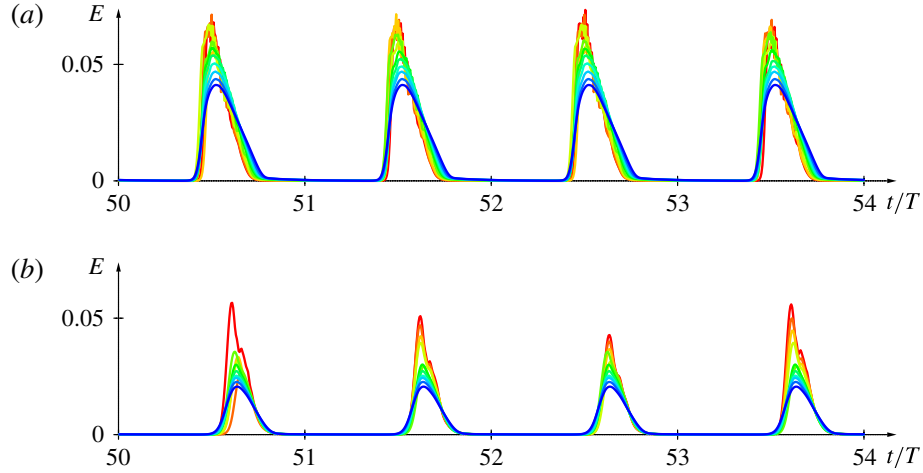


FIGURE 18. (Colour online) Temporal evolution of perturbation energy in fully developed regime at (a) $Wo = 7$, (b) $Wo = 10$, for $\tilde{Q} = 0.20$ (dark blue), $0.22, \dots, 0.38, 0.40$ (red) and $\alpha_1 = 2$, $Re = 10\,000$. The maximum energy of the nonlinear bursts increases with \tilde{Q} and, at larger values of \tilde{Q} , successive peaks culminate at slightly different levels.

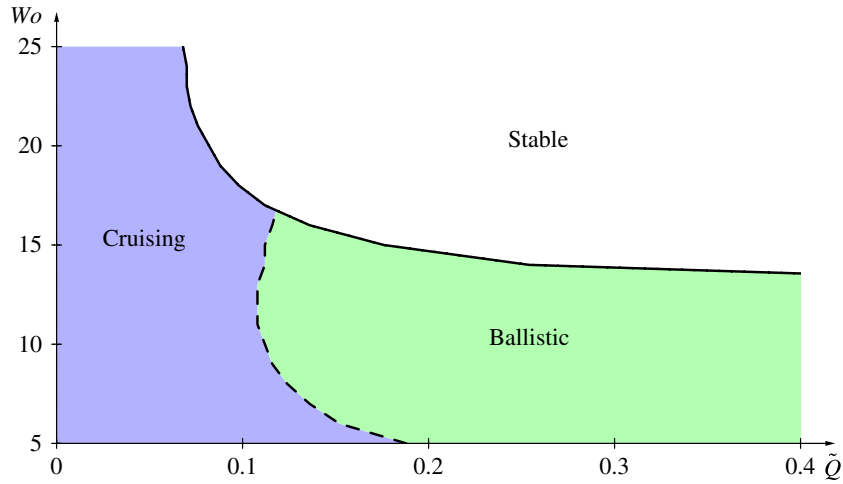


FIGURE 19. (Colour online) Phase diagram of the flow dynamics for $Re = 10\,000$ and $\alpha_1 = 2$. A cruising regime prevails at low base-flow modulation amplitudes \tilde{Q} . At larger \tilde{Q} , to the right of the dashed curve, a ballistic regime takes over. Above the black curve, the pulsating base flow is linearly stable.

6.3. Two-dimensional nonlinear dynamics at $Re = 10\,000$

The complete two-dimensional nonlinear travelling wave solutions have been computed by exploring the whole range of linearly unstable wavenumbers α_1 for $0 \leq \tilde{Q} \leq 0.5$ and $5 \leq Wo \leq 25$ at $Re = 10\,000$.

Figure 20 shows characteristic features of perturbation energy for selected configurations. Panels of the first column (*a1–d1*) in this figure illustrate the temporally averaged energy of the fully developed regime prevailing in the linearly unstable domain of the (α_1, \tilde{Q}) -plane for (a1) $Wo = 6$, (b1) $Wo = 10$, (c1) $Wo = 12$ and

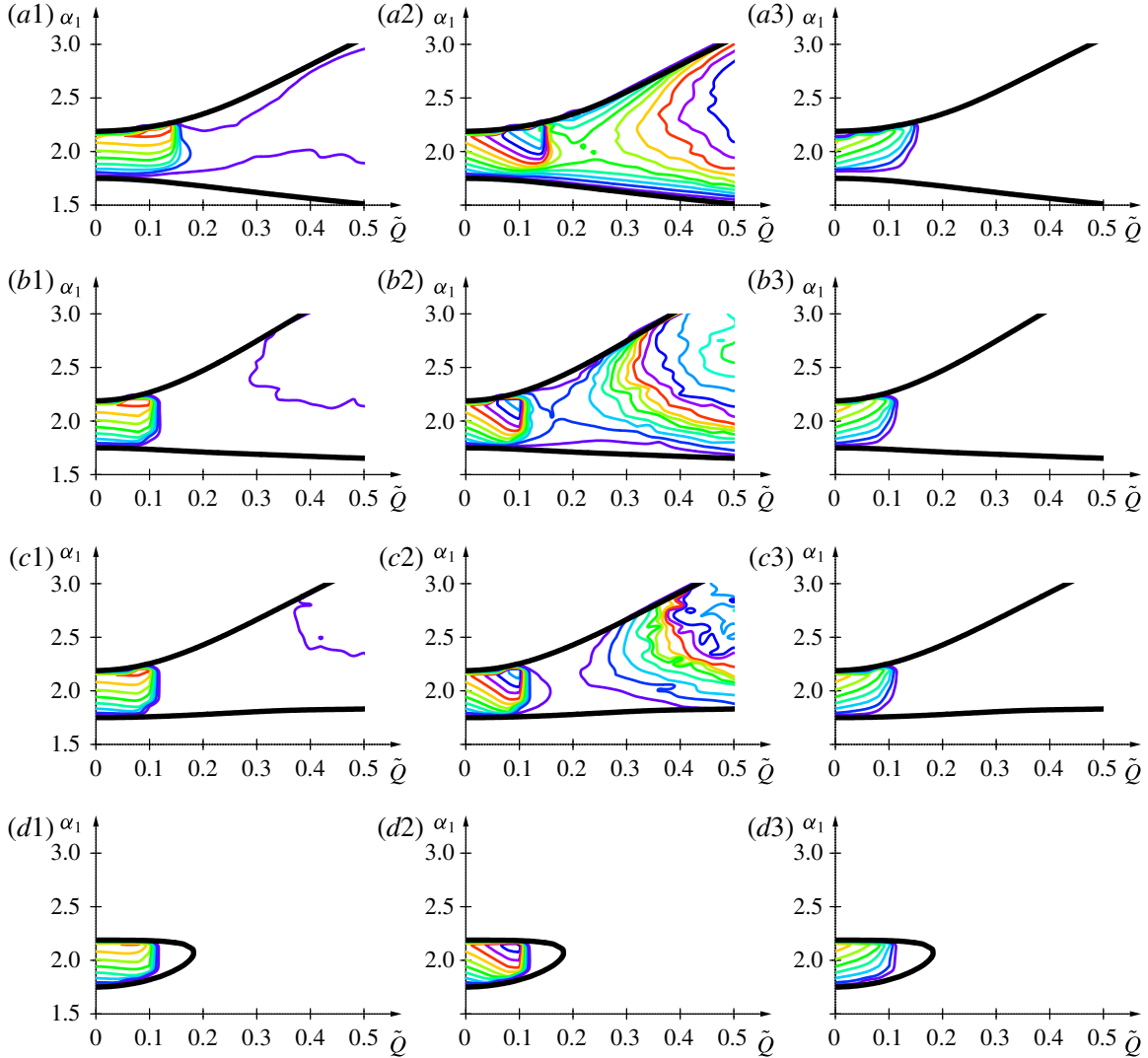


FIGURE 20. (Colour online) Isolines of perturbation energy levels for two-dimensional fully developed nonlinear regimes in (α_1, \tilde{Q}) -plane at $Re = 10000$ and (a) $Wo = 6$, (b) $Wo = 10$, (c) $Wo = 12$, (d) $Wo = 15$. Panels (1) represent temporally averaged energy, while (2) and (3) give maximum and minimum values respectively. Colour isolines correspond to $E = 0.01, 0.02, 0.03, \dots$, and the thick black curve represents the neutral boundary.

(d1) $Wo = 15$. Panels in the second ($a2-d2$) and third ($a3-d3$) columns correspond respectively to maximum and minimum energy values in the same regimes.

For Poiseuille flow, constant-amplitude Tollmien–Schlichting waves are obtained, so that all plots correspond to the same values along the line $\tilde{Q} = 0$.

Increasing the base-flow pulsation amplitude \tilde{Q} results in modulated nonlinear travelling waves with increasing modulation amplitude. For example, considering the case $Wo = 6$ (figure 20a1–a3) and concentrating on $\alpha_1 = 2$ for $0 \leq \tilde{Q} \leq 0.1$, it is seen that the average energy (figure 20a1) remains almost constant while the maximum energy (figure 20a2) increases with \tilde{Q} and the minimum energy (figure 20a3) decreases. The same observation holds for different values of α_1 and Wo : for $0 \leq \tilde{Q} \leq 0.1$, the discrepancy between maximum energy (figure 20a2–d2)

and the corresponding minimum energy (figure 20a3–d3) increases with \tilde{Q} , while the average energy (figure 20a1–d1) remains almost constant in \tilde{Q} . It is found that this cruising regime prevails over all unstable wavenumbers α_1 , and that the modulation amplitude is more pronounced at smaller wave lengths (larger α_1). Note also that the nonlinear regime displays finite-amplitude energy levels up to the upper marginal wavenumber (near $\alpha_1 \simeq 2.2$): it is expected that these nonlinear solutions continue to exist in the linearly stable region for larger values of α_1 , but the investigation of such sub-critical nonlinear modulated solutions by continuation methods has not yet been attempted.

The cruising regime, characterized by energy modulations around a mean value that is rather independent of \tilde{Q} , extends over the entire range of linearly unstable α_1 from $\tilde{Q} = 0$ to $\tilde{Q} \simeq 0.15$ at $Wo = 6$ and to $\tilde{Q} \simeq 0.11$ at $Wo = 10, 12$ and 15 . Thus, the phase diagram of figure 19 remains valid after taking into account the whole range of unstable wavenumbers α_1 .

As already observed, the cruising regime ends rather suddenly when \tilde{Q} is increased. The ballistic regime, that takes over at larger base-flow pulsation amplitudes, is characterized by much lower values of the temporally averaged energy (figure 20a1–c1) and vanishing values of minimum energy levels (figure 20a3–c3). The maximum energy (figure 20a2–c2) prevailing in the ballistic regime displays low values at onset of this regime (near $\tilde{Q} \simeq 0.15$) and increases with \tilde{Q} . The irregular shape of isolines in the ballistic regime is due to the loss of exact periodicity of the nonlinear solutions already observed in the previous section: when the successive nonlinear bursts are not perfectly identical, some scatter results while recording peak values in different realizations. At larger pulsation frequencies, the instabilities are suppressed as \tilde{Q} is increased (figure 20d1–d3), thus avoiding the ballistic regime.

6.4. Three-dimensional nonlinear dynamics at $Re = 10\,000$

For given pulsating base flows, three-dimensional finite-amplitude modulated propagating waves have been computed over the entire linearly unstable region of the (α_1, α_2) -wavevector plane. The linear temporal growth rate of three-dimensional perturbations has been discussed in § 5.4 and illustrated in figure 9.

The task of systematically investigating these fully developed nonlinear solutions has been carried out for $5 \leq Wo \leq 25$ and $0 \leq \tilde{Q} \leq 0.6$ at $Re = 10\,000$. For each base flow, characterized by the non-dimensional control parameters \tilde{Q} , Wo and Re , the nonlinear temporal evolution problem has been simulated for those values of (α_1, α_2) that are associated with a positive linear temporal growth rate. In this process, the (α_1, α_2) -wavevector plane has been covered using steps of 0.05 in both α_1 and α_2 and, for each run, characteristic quantities are derived from the fully developed nonlinear regime.

Figure 21 shows levels of temporally averaged perturbation energy while peak energy levels are plotted in figure 22. In these figures, colour isolines correspond to energy levels $E = 0.01, 0.02, \dots$, and the thick black curve represents the neutral boundary.

At low base-flow modulation amplitudes, $\tilde{Q} = 0.0$ and 0.1 , the fully developed flow is in the cruising regime, characterized by a significant average perturbation energy (figure 21) and slightly larger maximum energy levels (figure 22). In this regime, average and peak energy levels significantly increase with α_1 , starting at low values near the small- α_1 neutral boundary and reaching finite values at the large- α_1 neutral

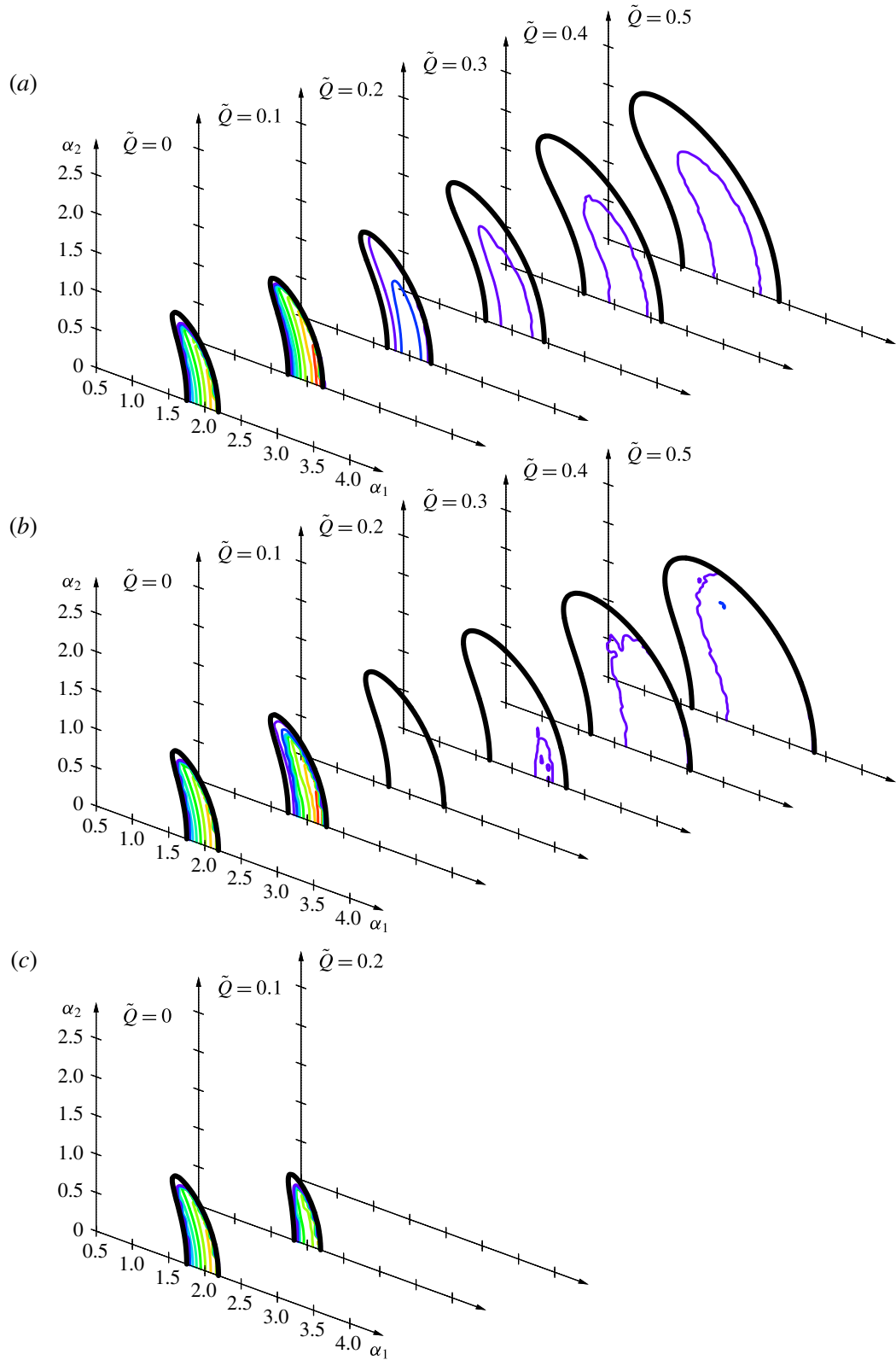


FIGURE 21. (Colour online) Isolines of average energy levels for three-dimensional nonlinear solutions in the (α_1, α_2) -wavevector plane for $\tilde{Q} = 0.0, 0.1, \dots, 0.5$ at (a) $Wo = 5$, (b) $Wo = 10$, (c) $Wo = 15$ and $Re = 10000$. Colour isolines correspond to $E = 0.01, 0.02, 0.03, \dots$, and the thick black curve represents the neutral boundary.

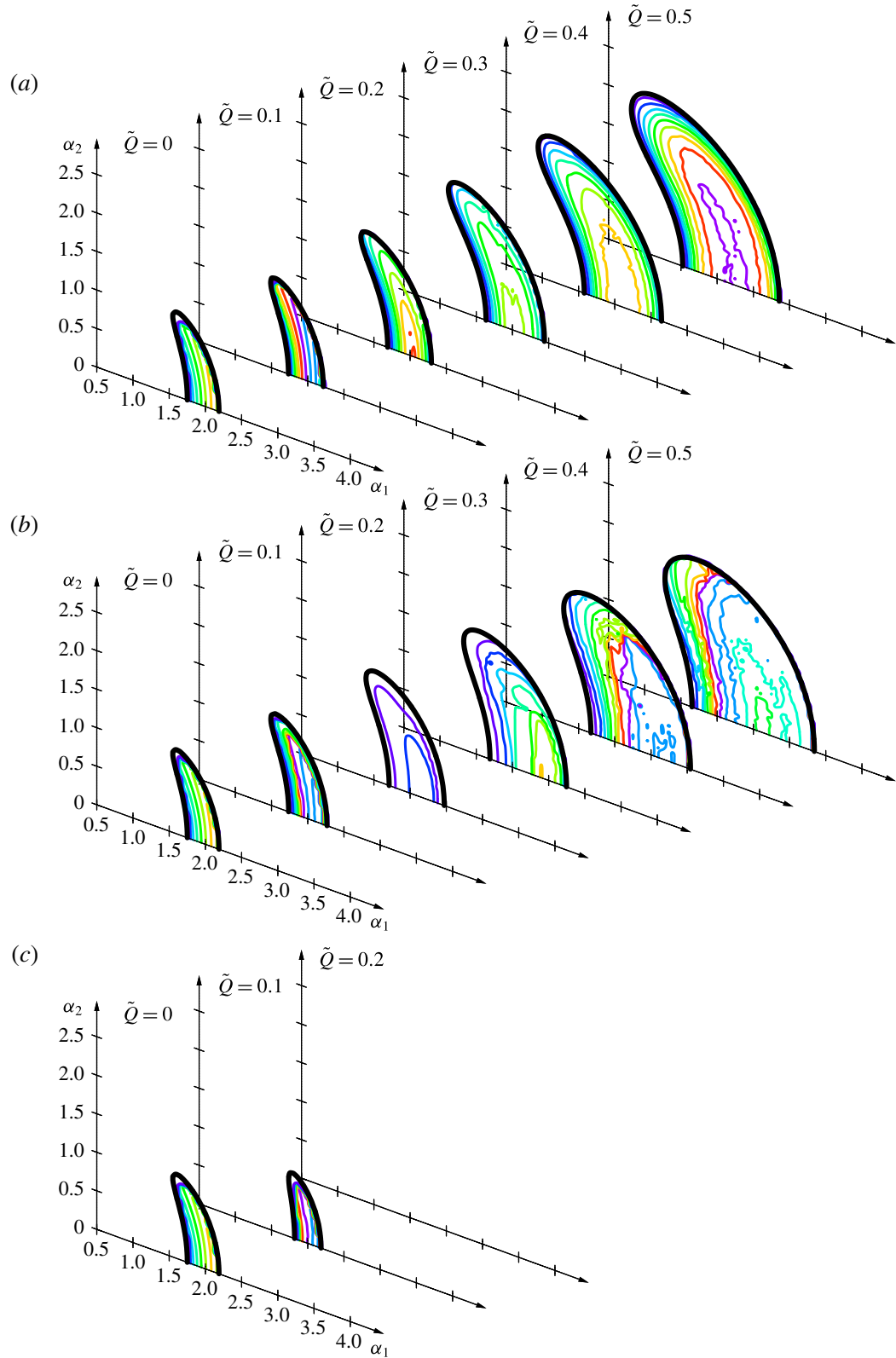


FIGURE 22. (Colour online) Isolines of maximum energy levels for three-dimensional nonlinear solutions in the (α_1, α_2) -wavevector plane for $\tilde{Q} = 0, 0.1, \dots, 0.5$ at (a) $W_0 = 5$, (b) $W_0 = 10$, (c) $W_0 = 15$ and $Re = 10\,000$. Colour isolines correspond to $E = 0.01, 0.02, 0.03, \dots$, and the thick black curve represents the neutral boundary.

boundary. The energy levels depend more weakly on α_2 , so that the isolines remain roughly parallel to the neutral boundaries as α_2 is increased from 0.

Between $\tilde{Q} = 0.1$ and $\tilde{Q} = 0.2$, the flow switches to ballistic regimes, and this transition is accompanied by a sharp drop in energy levels. Beyond $\tilde{Q} = 0.2$, for low to moderate pulsation frequencies, the perturbation energy levels increase again with \tilde{Q} , very weakly on average (figure 21a,b) but significantly for peak values (figure 22a,b). In contrast, at higher Womersley numbers, base-flow pulsation has a stabilizing effect, see figures 21(c) and 22(c) at $Wo = 15$. In the ballistic regime, the energy isolines are more irregular for the same reasons as those mentioned in the previous sub-section, but the general trend of the peak energy levels remains the same, except that the largest values are reached within the linearly unstable region and not near the large- α_1 neutral boundary. Therefore it would be expected that the cruising nonlinear regime is more likely to display subcritical behaviour, i.e. to continue to exist beyond the large- α_1 neutral boundary, than the ballistic regime.

At a given value of \tilde{Q} , the same regime is seen to prevail over the entire linearly unstable region of the (α_1, α_2) -plane. Thus it appears that the phase diagram of figure 19 still remains valid after taking into account all linearly unstable three-dimensional waves.

The maximum localized WSS occurring in the nonlinear regimes is shown in figure 23. In this figure, colour isolines correspond to WSS levels of 0.5, 1.0, 1.5, ..., relative to Poiseuille flow values. These plots follow a similar trend as the peak energy levels shown in figure 22, except that the regime change between $\tilde{Q} = 0.1$ and 0.2 is associated with a less pronounced drop in WSS.

6.5. Nonlinear dynamics at other Reynolds numbers

In order to systematically investigate the nonlinear dynamics prevailing after onset of linear instability, i.e. for Reynolds numbers above the marginal curves plotted in figure 10, two-dimensional nonlinear travelling wave solutions have been computed for linearly unstable configurations in the range $8000 \leq Re \leq 15000$.

The main findings are summarized in figure 24, extending the phase diagram of figure 19 and showing the nature of the selected flow regime in the (\tilde{Q}, Wo) -plane for $Re = 8000, 10000, 12000$ and 15000 . As in figure 19, these curves correspond to a fixed streamwise wavenumber of $\alpha_1 = 2$. In the preceding sections it has been shown, for $Re = 10000$, that this approach yields a good approximation of the boundary between cruising and ballistic regimes without exploring the whole region of linearly unstable three-dimensional waves in the (α_1, α_2) -plane for each base flow. A systematic coverage of the five-dimensional parameter space $(Re, Wo, \tilde{Q}, \alpha_1, \alpha_2)$ would require of the order of 10^6 runs for each value of Re . Nonetheless, it has been checked that the curves of figure 24 are a faithful representation of the dominant flow dynamics prevailing for any linearly unstable wavenumbers.

In agreement with the linear results of § 5, the stable region of the (\tilde{Q}, Wo) -plane shrinks as the Reynolds number is increased: the stability boundary (solid curves in figure 24) moves toward larger values of \tilde{Q} and Wo with increasing Re . In contrast, the boundary between cruising and ballistic regimes remains almost unchanged over the entire range from $Re = 8000$ to $Re = 15000$. For all the base flows considered in this investigation, the transition from cruising to ballistic regimes is found to occur when the base-flow oscillation amplitude exceeds about 10%–15% of the steady flow component.

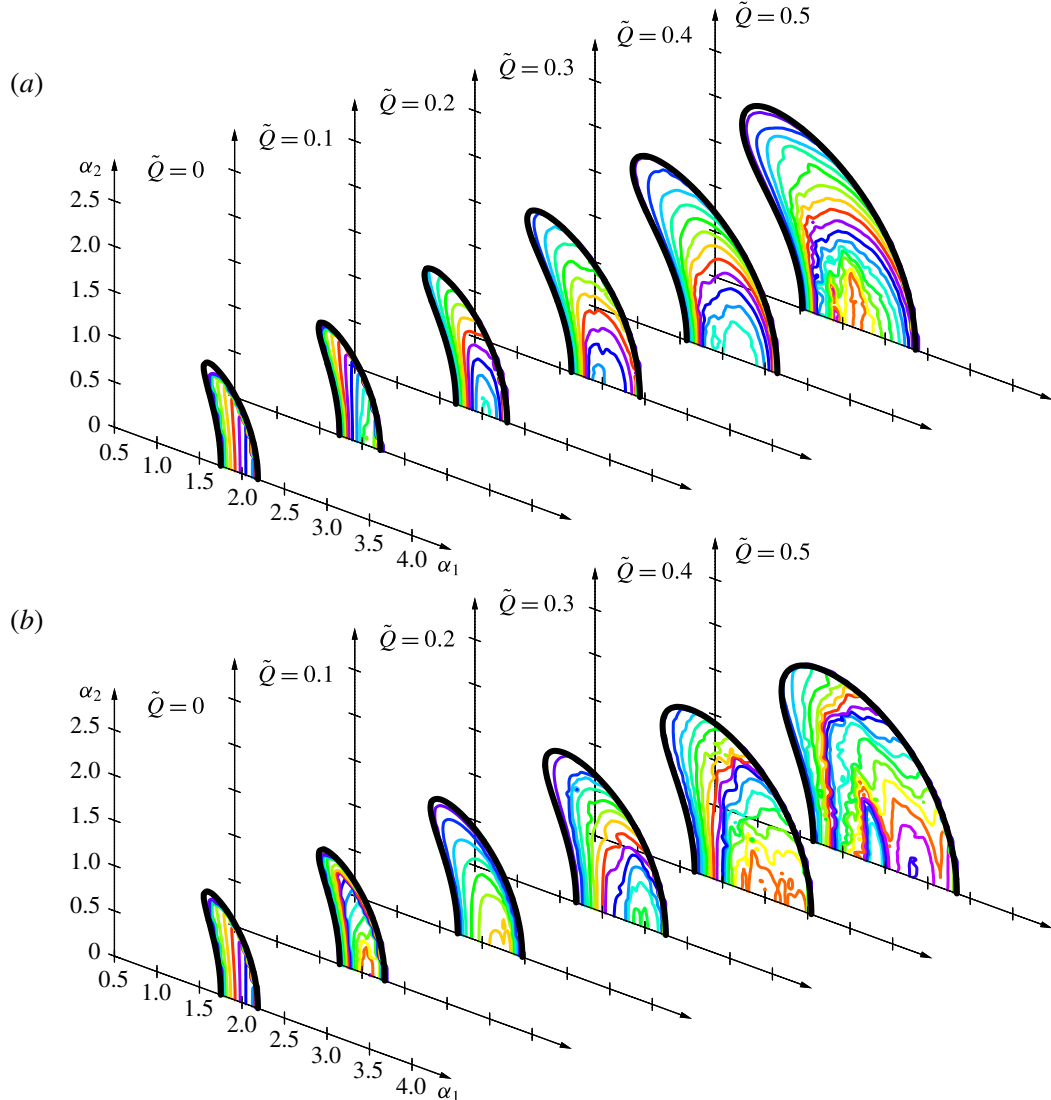


FIGURE 23. (Colour online) Isolines of maximum local WSS levels for three-dimensional nonlinear solutions in the (α_1, α_2) -wavevector plane for $\tilde{Q} = 0.0, 0.1, \dots, 0.5$ at (a) $Wo = 5$, (b) $Wo = 10$ and $Re = 10\,000$. Colour isolines correspond to $WSS = 0.5, 1.0, 1.5, \dots$, relative to Poiseuille value, and the thick black curve represents the neutral boundary.

7. Summary and future work

In this paper, we have systematically investigated the rich dynamics resulting from perturbations developing in harmonically pulsating channel flows, for Womersley numbers in the range $5 \leq Wo \leq 25$.

The temporal dynamics of small-amplitude perturbations consists of travelling waves that grow or decay exponentially in the long term while displaying intracyclic modulations tuned to the base-flow pulsations. Starting from steady Poiseuille flow and increasing the amplitude of the oscillating base-flow component \tilde{Q} at constant Womersley number, it is found that the oscillating component reduces instability for $Wo \gtrsim 13$ while it has a destabilizing effect at lower frequencies. Strongest destabilization occurs near $Wo = 7$. Using Floquet analysis and linearized simulations,

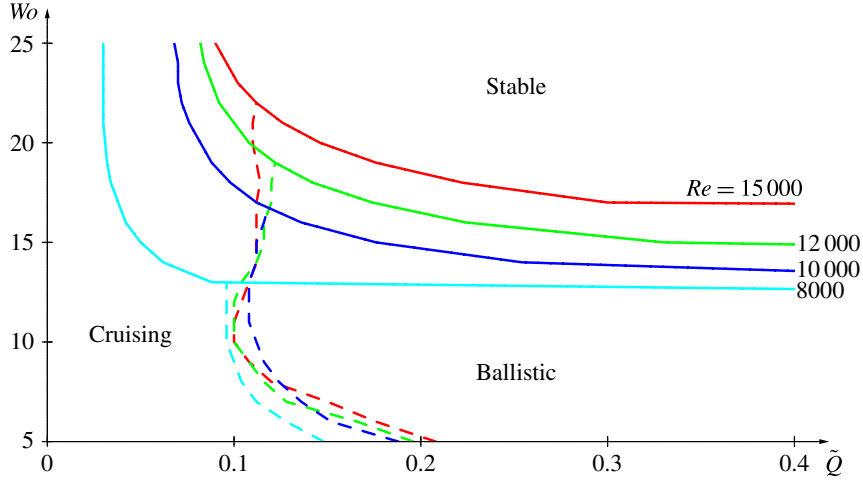


FIGURE 24. (Colour online) Maps in (\tilde{Q}, Wo) -plane indicating nature of the flow dynamics prevailing for a range of Reynolds numbers: $Re = 8000, 10\,000, 12\,000$ and $15\,000$. Dashed curves correspond to boundary between cruising and ballistic regimes. Above the solid curves the base flows are linearly stable.

the present investigation confirms that growth rates depend quadratically on small values of \tilde{Q} , a result analytically obtained by Hall (1975).

While instability (respectively stability) is determined by the net growth (respectively decay) of fluctuations over one complete pulsation cycle, strong transient growth and decay occur within each cycle. At small values of \tilde{Q} , the intracyclic growth and decay phases almost balance so that the long-term growth remains similar to the Poiseuille value despite intracyclic modulation amplitudes that may reach several orders of magnitude. Intracyclic growth and decay mainly occur during base-flow deceleration and acceleration phases respectively, and intracyclic modulation is enhanced at low pulsation frequencies, i.e. for long durations of deceleration and acceleration phases. A side-effect of these strong intracyclic modulations is the requirement of a large number of Fourier modes for a reasonably resolved Floquet analysis. This also probably explains why earlier attempts at linear stability analyses by solving Floquet eigenproblems were fraught with difficulties, and only Thomas *et al.* (2011) were able to locate neutral conditions.

Exploring the whole range of three-dimensional perturbations does not change the general picture derived from two-dimensional stability analysis since Squire's theorem remains valid for pulsating flows (Conrad & Criminale 1965). Nonetheless, it is found that oblique perturbations at finite spanwise and small streamwise mode numbers are more strongly destabilized by low-frequency base-flow pulsation, e.g. at $Wo = 5$, than at frequencies around $Wo = 10$.

Using direct numerical simulations to compute the temporal evolution of fully developed nonlinear propagating waves resulting from linearly unstable situations has shown that there exist two distinct regimes of finite-amplitude dynamics. In the cruising regime, the perturbation evolves nonlinearly throughout the pulsation cycle, while the ballistic regime consists of linear and nonlinear phases that alternate, locked-in with the base-flow pulsation. Nonlinear solutions in the cruising regime may be interpreted as saturated Tollmien–Schlichting waves that are modulated by the base-flow pulsation. These cruising waves are selected for weak base-flow pulsation amplitudes \tilde{Q} and their intracyclic modulation amplitudes increase with \tilde{Q} ,

albeit not as drastically as in the linear regime. For stronger base-flow pulsations, the intracyclic modulation amplitude eventually becomes of the same order as the mean perturbation level. When such strongly modulated waves are no longer able to keep up with the nonlinear regime throughout the cycle, transition to the ballistic regime occurs. In the ballistic regime, the temporal evolution is then governed by the following sequence of steps: during base-flow deceleration phases, small-amplitude fluctuations grow fast, as in a purely linear setting, thus propelling the system into a nonlinear regime where the amplitude saturates at finite level; during subsequent base-flow acceleration, the perturbation amplitude declines until the flow falls back to the linear regime; the fluctuation amplitude then rapidly drops to reach a minimum near the maximum of the basic flow rate, and grows again in the subsequent base-flow deceleration phase. Thus, the ballistic regime follows part of a linear dynamics with high intracyclic modulation amplitude, while nonlinear saturation caps its growth and limits the perturbation level in the high-amplitude phase. These linear and nonlinear mechanisms adjust so that the nonlinear bursts are identically regenerated, resulting in a regime with no net growth or decay over one pulsation cycle. For larger base-flow pulsation amplitudes, these nonlinear bursts prevailing in the ballistic regime display some fluctuations from cycle to cycle, which is the sign of secondary instabilities, beyond the scope of the present investigation.

Computation of spatio-temporal wall shear stress patterns has revealed that both cruising and ballistic regimes are associated with intense spatially localized WSS values, much stronger than the spatially averaged values as well as the base-flow values.

Working out the nonlinear dynamics for the entire parameter space in the range $5 \leq Wo \leq 25$, shows that a cruising regime prevails at low base-flow modulation amplitudes \tilde{Q} , and that transition to a ballistic regime occurs between $\tilde{Q} = 0.1$ and 0.2 , unless the ballistic regime is bypassed because the neutral boundary is crossed while still in the cruising regime.

The present investigation uses a single spatial Fourier series (4.20), (4.21) to compute the saturated wavetrains. This approach yields nonlinear solutions of the Navier–Stokes equations and prevents the development of secondary instabilities that would break the imposed spatial periodicity. Secondary instabilities may play an important part in the fully developed dynamics, and in particular near the transition between cruising and ballistic regimes. Secondary stability properties could be investigated by implementing a technique similar to that used for the rotating-disk flow (Pier 2007), and the resulting dynamics could be computed by simulations allowing for more degrees of freedom, e.g. using a double Fourier expansion in both wall-parallel directions for the flow fields.

The nonlinear travelling waves found in the present investigation display a structure that is reminiscent of solutions to the Korteweg–de Vries equation. Therefore one might expect that an approach similar to that implemented by Tutty & Pedley (1994) could account for the dynamics, and possibly explain the ballistic regime in terms of cnoidal waves. Another line of thought would be to analyse the pulsating channel flow in terms of a Mathieu equation (McLachlan 1964), also known to give rise to similar solutions as the amplitude of the oscillatory term becomes larger.

Having established the existence of nonlinear modulated travelling wave solutions for linearly unstable pulsating channel flows, it would now be worth to investigate the existence of subcritical solutions, i.e. finite-amplitude solutions that prevail in linearly stable base flows. Such subcritical solutions are known to exist for steady Poiseuille flow (Ehrenstein & Koch 1991) and are therefore also expected in its

pulsating counterpart. These subcritical solutions may be sought by continuously varying control parameters in a DNS or by generalizing the continuation technique of Ehrenstein & Koch (1991) to take into account the modulation of these solutions. The findings of the present paper suggest that the cruising regime probably displays such a subcritical behaviour, while it is less likely for the ballistic regime. And indeed, since the ballistic regime continuously regenerates nonlinear pulses on its own, it presumably does not depend on a finite-amplitude perturbation to be selected.

In the context of small-amplitude fluctuations, a question that has not yet been addressed is the nature of pulsating channel-flow instability, i.e. convective or absolute (Huerre & Monkewitz 1990). For purely oscillating boundary layers, as investigated by Blennerhassett & Bassom (2002, 2006) and Thomas *et al.* (2014), the onset of instability is expected to coincide with absolute instability, while steady plane Poiseuille flow is at most convectively unstable. Therefore, transition between convective and absolute instability is likely to occur when the pulsating base-flow component is increased or equivalently the steady component reduced; this could be investigated using the theory discussed by Brevdo & Bridges (1997).

The observation of linear modes exhibiting strong intracyclic growth phases, raises the question of the possibility for even larger transient growth resulting from an optimal initial condition. Current investigations address the computation of transient energy amplifications using non-modal stability theory (see Schmid 2007) applied to time-periodic flows.

In a physiological context, the blood flow rates resulting from the cardiac pulse cannot be described by a single oscillating harmonic component but require a Fourier expansion of the form (3.3) with more modes. All the mathematical methods and numerical tools developed in the present investigation can handle flow rates with an arbitrary number of base-flow Fourier components. Current collaboration with Service de chirurgie vasculaire (Hôpital Édouard-Herriot, Lyon) and Service de Radiologie (Hôpital de la Croix-Rousse, Lyon) aims at obtaining relevant flow-rate waveforms for studying their fluid dynamical properties.

For bioengineering applications as well as for fundamental reasons, the present approach needs to be generalized from plane channel to circular pipe configurations. This work is in progress and requires minor adjustments to take into account the extra terms due to a formulation in cylindrical coordinates. However, the main difficulty arises from the fact that Hagen–Poiseuille flow through a circular pipe is linearly stable at all Reynolds numbers, therefore an approach based on temporally modulating the steady base flow is inappropriate for comprehending a regime of nonlinear waves travelling through a circular pipe. Thomas *et al.* (2011) have found neutrally stable conditions for pulsating pipe flow that could be used as starting points for nonlinear simulations; these conditions, however, correspond to essentially oscillating flow with a weak steady component, thus complicating their continuation toward physiological conditions. Furthermore, pulsatile flow through curved pipes (Siggers & Waters 2008) probably sustains even more complex dynamics.

Acknowledgements

This work was partially supported by a grant ‘PEPS Écoulements biologiques’, Institut des sciences de l’ingénierie et des systèmes (INSIS-CNRS). Part of this work was carried out while B.P. was enjoying a French Government fellowship at Churchill College, Cambridge University. Institut national de physique nucléaire et de physique des particules (IN2P3-CNRS) is gratefully acknowledged for very generously

providing computing resources. Without access to its Centre de calcul allowing to continuously run hundreds of independent single-processor jobs it would not have been possible to carry out the present research requiring the systematic investigation of a multi-dimensional parameter space in great detail and at multiple resolutions.

Appendix A. Numerical solution methods and validation

Following the mathematical formulation of § 4, the governing equations yield systems of coupled partial differential equations of first order in time with spatial derivatives only in the wall-normal coordinate x_0 . The numerical implementation of these one-dimensional multi-component problems is based on the home-spun PackstaB library in C++; it involves a Chebyshev collocation technique for spatial discretization and a predictor–corrector fractional-step method for temporal integration. The essential features used in the present investigation are presented below, more details of the general method may be found in (Pier 2015, § A.6).

A.1. Spatial discretization

The differential problems in the wall-normal coordinate x_0 are solved via a Chebyshev collocation method (Boyd 2001) where the collocation points $\xi_i \equiv -h \cos(i\pi/(N_0 - 1))$ for $0 \leq i < N_0$ span the diameter of the channel.

No-slip boundary conditions apply to the velocity components while there are no boundary conditions for the pressure. Thus the velocity components are discretized using all N_0 collocation points including boundary points, while the pressure components may be discretized using only the $N_0 - 2$ interior points. This amounts to approximating velocity components by polynomials of order $N_0 - 1$ and pressure components by polynomials of order $N_0 - 3$. In this collocation technique, approximations of the x_0 -derivatives are then computed by using $N_0 \times N_0$ or $(N_0 - 2) \times (N_0 - 2)$ matrices, respectively.

Taking into account symmetry/antisymmetry of the different flow fields and using the associated discretized differential operators in the x_0 -coordinate, computations may be restricted to half the channel width and the numerical effort reduced by using only the N_0^* collocation points from the centreline to the boundary instead of the complete set of $N_0 = 2N_0^* - 1$ points covering the entire channel diameter.

A.2. Eigenvalue problems

The Floquet analysis discussed in § 4.2 yields an infinite system of linear coupled ordinary differential equations involving the Fourier components of the velocity and pressure eigenfunctions (4.14)–(4.17).

Truncating the Fourier expansions of the eigenfunctions (4.13) at $|n| \leq N_f$ then yields an algebraic generalized eigenvalue problem of size $(4N_0 - 2)(2N_f + 1)$, since there are N_0 values for each of the three velocity components and $N_0 - 2$ values for the pressure components. This generalized eigenvalue problem may be reduced to a regular eigenvalue problem of size $2(N_0 - 2)(2N_f + 1)$ by eliminating the pressure (taking the divergence of the momentum equations) and one of the velocity components (using the continuity equation) as well as the (homogeneous) velocity boundary conditions. This may be further reduced to $2(N_0^* - 1)(2N_f + 1)$, with $N_0 = 2N_0^* - 1$, by separately solving for sinuous or varicose modes.

Note that for all configurations considered in this study, it has been found that the most unstable or least stable perturbation is a sinuous mode, a confirmation of what was already observed by von Kerczek (1982).

A.3. Temporal evolution problems

In a linear analysis, the equations (4.7)–(4.10) involve three scalar velocity components and one pressure field. In a nonlinear analysis, after truncating the Fourier expansions (4.20), (4.21) at $|n| \leq N_h$, the equations (4.22)–(4.25) involve $3(2N_h + 1)$ velocity components and $2N_h + 1$ pressure components; note that the condition of real fields implies that $2N_h + 1$ complex components are completely described by $2N_h + 1$ independent real components. Time marching of these incompressible Navier–Stokes equations is carried out by a second-order accurate predictor–corrector fractional-step method, derived from the implementations of Goda (1979) and Raspo *et al.* (2002), where the velocity components are obtained at the intermediate time step by solving Helmholtz-type problems, and Poisson-type problems yield the pressure predictions and corrections required to enforce divergence-free velocity fields. Complete details of the numerical method are given in Pier (2015, §A.6.3).

For each simulation, the numerical values of the Floquet multiplier μ and of the associated frequency ω are derived by computing the ratios $u_i(x_{0,j}, t + T)/u_i(x_{0,j}, t)$, where $i = 0, 1$ or 2 and $x_{0,j}$ is any of the collocation points. It is then checked that all these ratios converge to the same constant value and do not depend on the phase with respect to the base-flow pulsation, with at least five significant digits. Since the precision of these ratios is degraded when both the numerator and the denominator approach very small values, a threshold has been set on the magnitude of the denominator (typically 10^{-5}) below which the ratio is not computed. The same strategy has been adopted to produce table 1, but using longer time series than for the rest of the paper in order to obtain the required highly converged numbers.

As mentioned in §4.3, an external volume force $f = -g_1(t)\mathbf{e}_1 - g_2(t)\mathbf{e}_2$ is used in the nonlinear governing equations in order to simulate evolution problems at the prescribed instantaneous total flow rate of the base flow. The purpose of this time-dependent spatially homogeneous body force, or pressure gradient, in the wall-parallel directions is to ensure that the spatially invariant flow corrections $\mathbf{u}^{(0)}(x_0, t)$ due to nonlinearities develop without modifying the base flow rate. In the numerical implementation, the streamwise and spanwise flow-rate corrections $q_1(t)$ and $q_2(t)$, defined in (4.27), (4.28), are driven to vanishing values by applying pressure gradient values governed by

$$\partial_t g_1 = q_1 \left(\frac{G^{(0)}}{\tau Q^{(0)}} \right) \quad \text{and} \quad \partial_t g_2 = q_2 \left(\frac{G^{(0)}}{\tau Q^{(0)}} \right). \quad (\text{A } 1a,b)$$

Using sufficiently small values of the relaxation time τ and solving (A 1) while time marching (4.22)–(4.25) guarantees that the pressure gradients $g_1(t)$ and $g_2(t)$ constantly adjust so as to suppress any departure from the base flow rate.

A.4. Validation

The accuracy of our numerical schemes has been assessed by comparison with known results and by extensive resolution tests.

For steady Poiseuille configurations, the eigenvalues given by Schmid & Henningson (2001, p. 504) have been reproduced to 8 significant digits both by solving the corresponding eigenvalue problem and by linearized direct numerical simulations (DNS); note that in these tables (Schmid & Henningson 2001, p. 504) the third column corresponds to $\alpha = 0.25$ and $\beta = 2$ instead of the mistakenly given $\beta = 3$. The nonlinear time-marching procedure has been checked by reproducing the Tollmien–Schlichting waves obtained by Ehrenstein & Koch (1991).

Floquet	$N_0^* = 16$	24
$N_f = 4$	$0.77226176 + 0.01194734i$	$0.77241812 + 0.01208715i$
8	$0.78504147 + 0.00935444i$	$0.78521143 + 0.00945091i$
12	$0.78504178 + 0.00935423i$	$0.78521176 + 0.00945071i$
16	$0.78504178 + 0.00935423i$	$0.78521176 + 0.00945071i$
20	$0.78504178 + 0.00935423i$	$0.78521176 + 0.00945071i$
	$N_0^* = 32$	40
$N_f = 4$	$0.77241825 + 0.01208730i$	$0.77241825 + 0.01208730i$
8	$0.78521144 + 0.00945111i$	$0.78521144 + 0.00945111i$
12	$0.78521178 + 0.00945092i$	$0.78521178 + 0.00945092i$
16	$0.78521178 + 0.00945092i$	$0.78521178 + 0.00945092i$
20	$0.78521178 + 0.00945092i$	$0.78521178 + 0.00945092i$
DNS	$N_0^* = 16$	24
$N_t = 2 \times 10^3$	$0.78591123 + 0.00945731i$	$0.78604254 + 0.00954315i$
5×10^3	$0.78520420 + 0.00933115i$	$0.78534476 + 0.00946264i$
10^4	$0.78508394 + 0.00929745i$	$0.78524509 + 0.00945350i$
2×10^4	$0.78504068 + 0.00928410i$	$0.78522016 + 0.00945137i$
5×10^4	$0.78501960 + 0.00927863i$	$0.78521309 + 0.00945070i$
10^5	$0.78501341 + 0.00927741i$	$0.78521196 + 0.00945057i$
2×10^5	$0.78501048 + 0.00927694i$	$0.78521160 + 0.00945057i$
5×10^5	$0.78500878 + 0.00927670i$	$0.78521146 + 0.00945061i$
	$N_0^* = 32$	40
$N_t = 2 \times 10^3$	$0.78604246 + 0.00954325i$	$0.78604246 + 0.00954326i$
5×10^3	$0.78534469 + 0.00946274i$	$0.78534468 + 0.00946274i$
10^4	$0.78524501 + 0.00945363i$	$0.78524501 + 0.00945363i$
2×10^4	$0.78522009 + 0.00945157i$	$0.78522009 + 0.00945157i$
5×10^4	$0.78521311 + 0.00945102i$	$0.78521311 + 0.00945102i$
10^5	$0.78521211 + 0.00945094i$	$0.78521211 + 0.00945094i$
2×10^5	$0.78521186 + 0.00945092i$	$0.78521186 + 0.00945092i$
5×10^5	$0.78521179 + 0.00945092i$	$0.78521179 + 0.00945092i$

TABLE 1. Complex frequency ω of most unstable linear perturbation at $Re = 10\,000$, $Wo = 10$, $\tilde{Q} = 0.1$ and $\alpha_1 = 2$. Values computed by solving Floquet eigenproblem (truncated at N_f Fourier components) and linearized DNS (with N_t time steps per pulsation period) for different spatial resolutions.

For pulsating base flows, we have reproduced the growth rates shown in figure 1 of von Kerczek (1982) by computing data similar to those shown in our figure 5(b). By modifying our codes to take into account oscillating boundaries, we have also reproduced the data given in table 1 of Blennerhassett & Bassom (2006), albeit not to 6 significant digits for all of them, and those more recently presented in figure 2b of Thomas *et al.* (2011).

The validation of our numerical methods is further based on thorough resolution-independence studies and, for the linear results, on the consistency between Floquet analysis and linearized DNS.

Table 1 gives values of the complex frequency ω for the most unstable linear perturbation at $Re = 10\,000$, $Wo = 10$, $\tilde{Q} = 0.1$ and $\alpha_1 = 2$. For a range of spatial discretizations $N_0^* = 16, 24, 32$ and 40 , the value of ω is computed by solving Floquet eigenproblems using an increasing number N_f of Fourier modes for the eigenfunctions

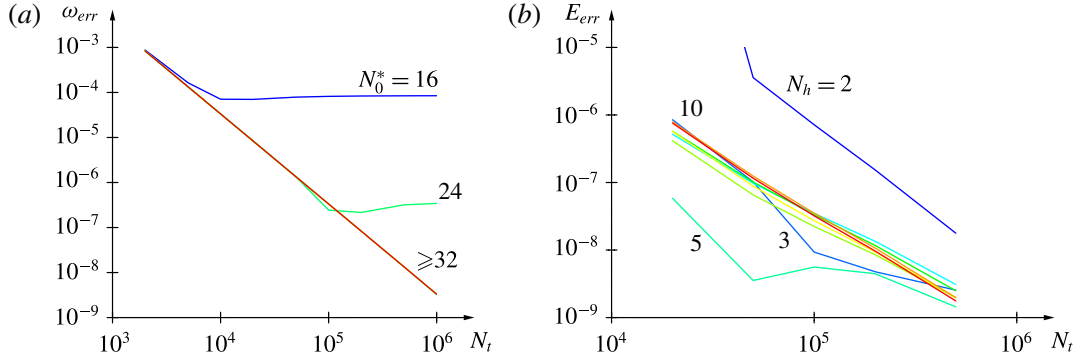


FIGURE 25. (Colour online) (a) Error in ω computed by linearized DNS with increasing number N_t of time steps per pulsation period and $N_0^* = 16, 24, 32, 40, 48$. (b) Error in perturbation energy computed by nonlinear DNS with increasing N_t and $N_h = 2$ (blue), 3, 4, ..., 10 (red) at $N_0^* = 56$.

$N_h = 4$	$N_0^* = 32$	40	48	56
$N_t = 2 \times 10^4$	0.0035969556	0.0035969659	0.0035969656	0.0035969656
5×10^4	0.0035965369	0.0035965454	0.0035965451	0.0035965451
10^5	0.0035964768	0.0035964830	0.0035964826	0.0035964826
2×10^5	0.0035964555	0.0035964615	0.0035964612	0.0035964612
5×10^5	0.0035964290	0.0035964511	0.0035964508	0.0035964508
10^6	0.0035964198	0.0035964480	0.0035964477	0.0035964477
$N_h = 9$	$N_0^* = 32$	40	48	56
$N_t = 2 \times 10^4$	0.0035947566	0.0035945442	0.0035945398	0.0035945397
5×10^4	0.0035941373	0.0035938778	0.0035938737	0.0035938737
10^5	0.0035941337	0.0035937882	0.0035937844	0.0035937847
2×10^5	0.0035942881	0.0035937632	0.0035937600	0.0035937600
5×10^5	0.0035948005	0.0035937528	0.0035937513	0.0035937512
10^6	0.0035953686	0.0035937481	0.0035937493	0.0035937492

TABLE 2. Energy of fully developed nonlinear fluctuation at $Re = 10\,000$, $Wo = 10$, $\tilde{Q} = 0.2$ and $\alpha_1 = 2$. Values computed by DNS with N_t time steps per pulsation period, spatial Fourier expansions truncated at $|n| \leq N_h$ and using a range of resolutions in x_0 coordinate.

and by linearized DNS using an increasing number N_t of time steps per base-flow pulsation period. With both methods, it is found that eight significant digits are achieved for $N_0^* \geq 32$. In this example, the eigenproblem is already very accurately resolved with $N_f \geq 12$, and the temporal simulations reach the same precision with $N_t \geq 5 \times 10^5$. Note that these correspond to approximately $N_t/20$ time steps per perturbation period since $\omega_r/\Omega \simeq 20$ with $\Omega = 4Wo^2/Re = 0.04$. Figure 25(a) plots the error of the values computed by DNS with respect to the converged Floquet results and demonstrates the second-order convergence of the temporal integration scheme; for $N_0^* \geq 32$, curves are indistinguishable in this log-log plot. In practice, linearized simulations with $N_t = 10^4$ and $N_0^* = 32$ yield results of sufficient accuracy over the entire parameter space considered here. In contrast, the number N_f of Fourier modes required for convergence depends on Wo and increases significantly with \tilde{Q} as discussed in § 5.2.

Table 2 gives values of the average perturbation energy in the fully developed regime at $Re = 10\,000$, $Wo = 10$, $\tilde{Q} = 0.2$ and $\alpha_1 = 2$, obtained by DNS with up to $N_t = 10^6$ time steps per pulsation period and different settings of N_h and N_0^* . This configuration is discussed in detail in § 6.1.2. For nonlinear temporal evolution problems, the resolution requirements to achieve a precision of 8 significant digits are more difficult to meet since increasing the number N_h of spatial Fourier modes also requires larger values of N_0^* to fully resolve these higher modes. Nonetheless, figure 25(b), which plots the error with respect to the value computed at highest resolution, shows that second-order convergence is still achieved for the nonlinear simulations. For the parameter ranges considered in this paper, it has been found that nonlinear simulations with $N_t = 10^5$, $N_h = 7$ and $N_0^* = 48$ are generally more than enough to obtain reliable results and plots that do not change at higher resolutions.

REFERENCES

- AKHAVAN, R., KAMM, R. D. & SHAPIRO, A. H. 1991a An investigation of transition to turbulence in bounded oscillatory Stokes flows. Part 1. Experiments. *J. Fluid Mech.* **225**, 395–422.
- AKHAVAN, R., KAMM, R. D. & SHAPIRO, A. H. 1991b An investigation of transition to turbulence in bounded oscillatory Stokes flows. Part 2. Numerical simulations. *J. Fluid Mech.* **225**, 423–444.
- BLENNERHASSETT, P. J. & BASSOM, A. P. 2002 The linear stability of flat Stokes layers. *J. Fluid Mech.* **464**, 393–410.
- BLENNERHASSETT, P. J. & BASSOM, A. P. 2006 The linear stability of high-frequency oscillatory flow in a channel. *J. Fluid Mech.* **556**, 1–25.
- BLENNERHASSETT, P. J. & BASSOM, A. P. 2007 The linear stability of high-frequency oscillatory flow in a torsionally oscillating cylinder. *J. Fluid Mech.* **576**, 491–505.
- BOYD, J. P. 2001 *Chebyshev and Fourier Spectral Methods*. Dover.
- BREVDØ, L. & BRIDGES, T. J. 1997 Absolute and convective instabilities of temporally oscillating flows. *Z. Angew. Math. Phys.* **48**, 290–309.
- CONRAD, P. W. & CRIMINALE, W. O. 1965 The stability of time-dependent laminar flow: parallel flows. *Z. Angew. Math. Phys.* **16**, 233–254.
- COSTAMAGNA, P., VITTORI, G. & BLONDEAUX, P. 2003 Coherent structures in oscillatory boundary layers. *J. Fluid Mech.* **474**, 1–33.
- COWLEY, S. J. 1987 High frequency Rayleigh instability of Stokes layers. In *Stability of Time Dependent and Spatially Varying Flows* (ed. D. L. Dwyer & M. Y. Hussaini), pp. 261–275. Springer.
- DAVIS, S. H. 1976 The stability of time-periodic flows. *Annu. Rev. Fluid Mech.* **8**, 57–74.
- DRAZIN, P. & RILEY, N. 2006 *The Navier-Stokes Equations. A Classification of Flows and Exact Solutions*. Cambridge University Press.
- EHRENSTEIN, U. & KOCH, W. 1991 Three-dimensional wavelike equilibrium states in plane Poiseuille flow. *J. Fluid Mech.* **228**, 111–148.
- FEDELE, F., HITT, D. L. & PRABHU, R. D. 2005 Revisiting the stability of pulsatile pipe flow. *Eur. J. Mech. (B/Fluids)* **24**, 237–254.
- GODA, K. 1979 A multistep technique with implicit difference schemes for calculating two- or three-dimensional cavity flows. *J. Comput. Phys.* **30**, 76–95.
- GOPALAKRISHNAN, S. S., PIER, B. & BIESHEUVEL, A. 2014a Dynamics of pulsatile flow through model abdominal aortic aneurysms. *J. Fluid Mech.* **758**, 150–179.
- GOPALAKRISHNAN, S. S., PIER, B. & BIESHEUVEL, A. 2014b Global stability analysis of flow through a fusiform aneurysm: steady flows. *J. Fluid Mech.* **752**, 90–106.
- GROSCH, C. E. & SALWEN, H. 1968 The stability of steady and time-dependent plane Poiseuille flow. *J. Fluid Mech.* **34**, 177–205.
- HALL, P. 1975 The stability of Poiseuille flow modulated at high frequencies. *Proc. R. Soc. Lond. A* **344**, 453–464.

- HALL, P. 1978 The linear stability of flat Stokes layers. *Proc. R. Soc. Lond. A* **359**, 151–166.
- HALL, P. 2003 On the instability of Stokes layers at high Reynolds numbers. *J. Fluid Mech.* **482**, 1–15.
- HINO, M., SAWAMOTO, M. & TAKASU, S. 1976 Experiments on transition to turbulence in an oscillatory pipe flow. *J. Fluid Mech.* **75**, 193–207.
- HUERRE, P. & MONKEWITZ, P. A. 1990 Local and global instabilities in spatially developing flows. *Annu. Rev. Fluid Mech.* **22**, 473–537.
- KACHANOV, Y. S. 1994 Physical mechanisms of laminar-boundary-layer transition. *Annu. Rev. Fluid Mech.* **26**, 411–482.
- VON KERCZEK, C. & DAVIS, S. H. 1974 Linear stability of oscillatory Stokes layers. *J. Fluid Mech.* **62**, 753–773.
- VON KERCZEK, C. H. 1982 The instability of oscillatory plane Poiseuille flow. *J. Fluid Mech.* **116**, 91–114.
- KU, D. N. 1997 Blood flow in arteries. *Annu. Rev. Fluid Mech.* **29**, 399–434.
- LUO, J. & WU, X. 2010 On the linear instability of a finite Stokes layer: Instantaneous versus Floquet modes. *Phys. Fluids* **22**, 054106.
- MCLACHLAN, M. W. 1964 *Theory and Application of Mathieu Functions*. Dover.
- MERKL, P. & THOMANN, H. 1975 Transition to turbulence in oscillating pipe flow. *J. Fluid Mech.* **68**, 567–575.
- OZDEMIR, C. E., HSU, T.-J. & BALACHANDAR, S. 2014 Direct numerical simulations of transition and turbulence in smooth-walled Stokes boundary layer. *Phys. Fluids* **26**, 045108.
- PEDLEY, T. J. 2000 Blood flow in arteries and veins. In *Perspectives in Fluid Dynamics* (ed. G. K. Batchelor, H. K. Moffatt & M. G. Worster), pp. 105–158. Cambridge University Press.
- PIER, B. 2007 Primary crossflow vortices, secondary absolute instabilities and their control in the rotating-disk boundary layer. *J. Engng Maths* **57**, 237–251.
- PIER, B. 2015. Dynamique des écoulements ouverts : instabilités et transition, courbure et rotation. Habilitation à diriger des recherches, École centrale de Lyon & Université de Lyon.
- RASPO, I., HUGUES, S., SERRE, E., RANDRIAMAMPIANINA, A. & BONTOUX, P. 2002 A spectral projection method for the simulation of complex three-dimensional rotating flows. *Comput. Fluids* **31**, 745–767.
- ROZHDESTVENSKIY, B. L., SIMAKIN, I. N. & STOINOV, M. I. 1989 Investigation of the stability of a pulsating Poiseuille flow in a planar channel. *USSR Comput. Math. Math. Phys.* **29**, 65–73.
- SCHMID, P. J. 2007 Nonmodal stability theory. *Annu. Rev. Fluid Mech.* **39**, 129–162.
- SCHMID, P. J. & HENNINGSON, D. S. 2001 *Stability and Transition in Shear Flows*. Springer.
- SIGGERS, J. H. & WATERS, S. L. 2008 Unsteady flows in pipes with finite curvature. *J. Fluid Mech.* **600**, 133–165.
- SINGER, B. A., FERZIGER, J. H. & REED, H. L. 1989 Numerical simulations of transition in oscillatory plane channel flow. *J. Fluid Mech.* **208**, 45–66.
- STETTLER, J. C. & HUSSAIN, A. K. M. F. 1986 On transition of the pulsatile pipe flow. *J. Fluid Mech.* **170**, 169–197.
- STOKES, G. G. 1851 On the effect of the internal friction of fluids on the motion of pendulums. *Trans. Camb. Phil. Soc.* **9** (2), 8–106.
- STRAATMAN, A. G., KHAYAT, R. E., HAJ-QASEM, E. & STEINMAN, D. A. 2002 On the hydrodynamic stability of pulsatile flow in a plane channel. *Phys. Fluids* **14**, 1938–1944.
- THOMAS, C., BASSOM, A. P. & BLENNERHASSETT, P. J. 2012 The linear stability of oscillating pipe flow. *Phys. Fluids* **24**, 014106.
- THOMAS, C., BASSOM, A. P., BLENNERHASSETT, P. J. & DAVIES, C. 2010 Direct numerical simulations of small disturbances in the classical Stokes layer. *J. Engng Maths* **68**, 327–338.
- THOMAS, C., BASSOM, A. P., BLENNERHASSETT, P. J. & DAVIES, C. 2011 The linear stability of oscillatory Poiseuille flow in channels and pipes. *Proc. R. Soc. Lond. A* **467**, 2643–2662.
- THOMAS, C., BLENNERHASSETT, P. J., BASSOM, A. P. & DAVIES, C. 2015 The linear stability of a Stokes layer subjected to high-frequency perturbations. *J. Fluid Mech.* **764**, 193–218.
- THOMAS, C., DAVIES, C., BASSOM, A. P. & BLENNERHASSETT, P. J. 2014 Evolution of disturbance wavepackets in an oscillatory Stokes layer. *J. Fluid Mech.* **752**, 543–571.

- TUTTY, O. R. & PEDLEY, T. J. 1994 Unsteady flow in a nonuniform channel: A model for wave generation. *Phys. Fluids* **6**, 199–208.
- TUZI, R. & BLONDEAUX, P. 2008 Intermittent turbulence in a pulsating pipe flow. *J. Fluid Mech.* **599**, 51–79.
- VITTORI, G. & VERZICCO, R. 1998 Direct simulation of transition in an oscillatory boundary layer. *J. Fluid Mech.* **371**, 207–232.
- WINTER, D. C. & NEREM, R. M. 1984 Turbulence in pulsatile flows. *Ann. Biomed. Engng* **12**, 357–369.
- WOMERSLEY, J. R. 1955 Method for the calculation of velocity, rate of flow and viscous drag in arteries when pressure gradient is known. *J. Phys.* **127**, 553–563.
- YANG, W. H. & YIH, C.-S. 1977 Stability of time-periodic flows in a circular pipe. *J. Fluid Mech.* **82**, 497–505.

[A25]

Algebraic disturbances and their consequences in rotating channel flow transition

S. Jose, V. Kuzhimparampil, B. Pier & R. Govindarajan

Physical Review Fluids 2, 083901 (25 pages) (2017)

doi:10.1103/PhysRevFluids.2.083901

<https://hal.archives-ouvertes.fr/hal-01578604>

Algebraic disturbances and their consequences in rotating channel flow transition

Sharath Jose,^{1,*} Vishnu Kuzhimparampil,¹ Benoît Pier,² and Rama Govindarajan³

¹TIFR Centre for Interdisciplinary Sciences, Tata Institute of Fundamental Research,

21 Brundavan Colony, Narsingi, Hyderabad 500075, India

²Laboratoire de mécanique des fluides et d'acoustique, CNRS-École centrale de Lyon-Université

Claude-Bernard Lyon 1-INSA, 36 avenue Guy-de-Collongue, F-69134 Écully, France

³International Centre for Theoretical Sciences, Tata Institute of Fundamental Research, Survey 151,

Shivakote, Hesaraghatta Hobli, Bengaluru 560089, India

(Received 19 September 2016; published 14 August 2017)

It is now established that subcritical mechanisms play a crucial role in the transition to turbulence of nonrotating plane shear flows. The role of these mechanisms in rotating channel flow is examined here in the linear and nonlinear stages. Distinct patterns of behavior are found: the transient growth leading to nonlinearity at low rotation rates Ro , a highly chaotic intermediate Ro regime, a localized weak chaos at higher Ro , and complete stabilization of transient disturbances at very high Ro . At very low Ro , the transient growth amplitudes are close to those for nonrotating flow, but Coriolis forces assert themselves by producing distinct asymmetry about the channel centreline. Nonlinear processes are then triggered, in a streak-breakdown mode of transition. The high Ro regimes do not show these signatures; here the leading eigenmode emerges as dominant in the early stages. Elongated structures plastered close to one wall are seen at higher rotation rates. Rotation is shown to reduce nonnormality in the linear operator, in an indirect manifestation of Taylor-Proudman effects. Although the critical Reynolds for exponential growth of instabilities is known to vary a lot with rotation rate, we show that the energy critical Reynolds number is insensitive to rotation rate. It is hoped that these findings will motivate experimental verification and examination of other rotating flows in this light.

DOI: [10.1103/PhysRevFluids.2.083901](https://doi.org/10.1103/PhysRevFluids.2.083901)

I. INTRODUCTION

Rotation of the system, in a number of flow situations, plays an important role in stability and turbulence characteristics. Rotational effects are seen to influence the evolution of several flow phenomena of practical interest ranging from engineering to geophysics. Atmospheric and oceanic flows offer a myriad of not entirely understood phenomena, which are affected by Earth's rotation in addition to other physics [1,2]. In industrial situations, the modeling of rotational effects of flows is a crucial aspect in the design procedure of several technologies: pumps and turbines, for example [3].

The effect of rotation on shear flow instabilities is not immediately obvious, and it depends largely on the strength of the rotation. Rotation introduces a body force which is a function of space and time, and bears some analogy to density stratification. At high Ro , the flow is expected to obey Taylor-Proudman behavior [4,5], by which variations parallel to the rotation axis are strongly suppressed. In the manner of swirling flows, an inviscid criterion for instability in parallel flows of the form $\mathbf{U} = [U(y), 0, 0]$, with the rotation vector $\boldsymbol{\Omega} = (0, 0, \Omega)$ perpendicular to the plane of the flow, was formulated by Bradshaw [6] and Pedley [7]. As per the criterion, an instability can occur if at any point in the flow the absolute vorticity of the base flow and the rotation vector are antiparallel. Subsequent studies have shown that this simple analogue of the

*josesk@tifrh.res.in

Rayleigh criterion provides good predictions in many parallel flows even in the presence of viscous effects [8–12].

One of the most commonly studied systems is the pressure-driven flow between two stationary, parallel plates that is rotated about the spanwise coordinate, which is also the geometry of our interest. This is an appealing system for investigation as it is a simple rotating shear flow which offers regions that are both stable and unstable as per the inviscid criterion given above. Henceforth, this system will be referred to simply as rotating channel flow. This flow is characterized by two parameters, the Reynolds number $Re = U_0 d / \nu$ and the rotation number $Ro = \Omega d / U_0$, where U_0 is the centerline velocity in the channel, d is its half-width, Ω is the rotation rate, and ν is the kinematic viscosity of the fluid.

It was found experimentally that the critical Reynolds number Re_{cr} , below which no exponential instabilities exist, may be up to two orders magnitude lower than that of a nonrotating channel [8,11]. This critical Reynolds number shows a nonmonotonic variation with the strength of rotation and is very sensitive to it. Just past Re_{cr} , the first unstable mode corresponds to a stationary streamwise-invariant disturbance. As we move further into the unstable part of the parameter space, we may find oblique modes that have growth rates comparable to the streamwise-invariant mode [13]. At high Ro , Taylor-Proudman behavior sets in and these streamwise-invariant rotation modes are suppressed. The two-dimensional spanwise-invariant Tollmien-Schlichting (TS) mode can be triggered even for values of Re above the critical value 5772 for nonrotating channels [14,15]. But in the regime where both the TS mode and the rotation mode are present, the rotation mode is expected to win over due to a much larger growth rate [13].

Secondary instabilities of the traveling wave type with short and long wavelengths which eventually broke down to turbulence had been observed in experiments [11]. Merging and splitting of vortex pairs through a nonlinear wavelength selection process was also seen. These types of motions were further confirmed by numerical studies [16–18]. Matsubara and Alfredsson attribute the secondary instability to the spanwise inflectional profile resulting from the saturation of the primary disturbance [19]. The existence of secondary and tertiary saturated solutions of rotating shear flows has also been investigated [13,20,21]. The turbulent rotating channel flow has been studied extensively for a wide range of Reynolds numbers through experiments and simulations [9,22–25].

For the rotating channel flow, the effect of nonmodal (algebraic) growth of disturbances has not been previously investigated to our knowledge, despite extensive studies on instabilities and turbulence in the system. In a different geometry, namely on the rotating asymptotic suction boundary layer, transient growth effects were studied [26]. The effect of subcritical mechanisms in nonmagnetized accretion disks modeled as plane shear flows with rotation have been studied [27–29]. Given that it has been firmly established that subcritical linear processes arising from nonmodal dynamics play a pivotal role in determining the conditions of transition to turbulence in a variety of shear flows [30,31], it is important to ask how rotation will modify the role of nonmodal dynamics.

In some range of rotation numbers, the critical Reynolds number is very low and exponential growth of instabilities may be expected to dominate. However, given that the rotation number is independent of the Reynolds number and that the critical Reynolds number is a sensitive function of Ro , it is necessary to investigate algebraic growth in the modally stable region of the Re - Ro plane. Second, in the unstable region as well, algebraic growth can affect the transition process in spite of coexisting exponential modes of growth. In this article, we seek to characterize the role played by algebraically growing disturbances in different rotation regimes, modally stable and unstable, within the purview of the transition processes.

II. SYSTEM

Our system, consisting of a pressure driven flow between parallel fixed walls, is subjected to rotation about the spanwise direction with a constant angular velocity $\Omega = (0, 0, \Omega)$ (Fig. 1). For the

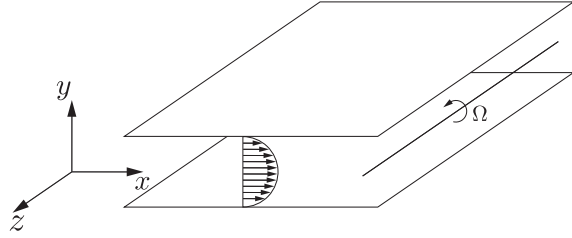


FIG. 1. The rotating channel, with a parabolic streamwise velocity ($U = 1 - y^2$) and a rotation rate Ω about the spanwise coordinate.

purposes of the analysis to follow, we consider the two parallel walls to extend infinitely; i.e., there are no end walls. It is also convenient to work in a frame of reference that is rotating along with the channel. Then the governing equations for the velocity $\mathbf{u}^* = (u^*, v^*, w^*)$ and pressure p^* are the incompressible Navier-Stokes equations in the rotating frame given by

$$\partial_t \mathbf{u}^* + \mathbf{u}^* \cdot \nabla^* \mathbf{u}^* = -\frac{1}{\rho} \nabla^* p^* + \nu \Delta^* \mathbf{u}^* - 2\Omega \times \mathbf{u}^*, \quad (1)$$

$$\nabla^* \cdot \mathbf{u}^* = 0. \quad (2)$$

Here ρ is constant density of the fluid. The centrifugal force has been absorbed into the pressure term. With U_0 and d as the velocity and length scales respectively, the Reynolds and rotation numbers as defined in the previous section, and \hat{z} being the unit vector along the spanwise coordinate, the governing equations in the nondimensional form are as follows:

$$\partial_t \mathbf{u} + \mathbf{u} \cdot \nabla \mathbf{u} = -\nabla p + \frac{1}{Re} \Delta \mathbf{u} - 2Ro \hat{z} \times \mathbf{u}, \quad (3)$$

$$\nabla \cdot \mathbf{u} = 0. \quad (4)$$

When the effects of the end walls are neglected, the base flow adopts a parabolic streamwise velocity profile $U = (1 - y^2)$ [10]. Note that we use uppercase to denote base flow. The transverse and wall-normal velocity components are zero. In a real system with end walls, a secondary flow in the form of a double vortex is set up [32]. As is standard for rotating flows, a mean pressure gradient is sustained in the wall-normal direction y , balancing Coriolis forces, and may be obtained from Eq. (3) as

$$\partial_y P = -2URo. \quad (5)$$

Tritton and Davies [33], using an elegant displaced particle argument, describe the instability mechanism in rotating plane shear flows in terms of the imbalance of centrifugal force and force due to this wall-normal pressure gradient. Their argument recovers the inviscid criterion derived by Bradshaw [6] and Pedley [7]. In nondimensionalized form, the criterion for instability has the following form:

$$\phi(y) = 2Ro \left(-\frac{\partial U}{\partial y} + 2Ro \right) < 0. \quad (6)$$

Examining our system in this context, we see that for a given sense of rotation, one side of the channel is inviscidly stable and the other is unstable. Since we have a base flow which is symmetric about the centerline, if the sense of rotation were to be reversed, we would merely have a switch in which side is unstable, and all results would merely be mirror images. We therefore fix our rotation to be anticyclonic, i.e., $Ro > 0$. However, we caution that for asymmetric shear flows, positive and negative Ro would need to be studied separately [26,33,34].

III. LINEAR ANALYSIS

A. Governing equations and methodology

On introducing perturbations that are nominally small compared to the base state quantities, and by linearizing the governing equations, we can study linear stability characteristics of the base flow. In the current setting where the channel extends infinitely in the streamwise and the spanwise directions, we can consider the disturbances to be periodic in these directions with a specific wavenumber $\mathbf{k} = (\alpha, \beta)$, with α the streamwise wavenumber and β the spanwise wavenumber, so disturbances take on the form $f = \hat{f}(y, t)e^{i(\alpha x + \beta z)}$. In terms of the wall-normal velocity disturbance $[v = \hat{v}(y, t)e^{i(\alpha x + \beta z)}]$ and the wall-normal vorticity disturbance $[\eta = \hat{\eta}(y, t)e^{i(\alpha x + \beta z)}]$, the resulting system of linear equations is

$$\frac{\partial \hat{\mathbf{q}}}{\partial t} = \mathbf{L}\hat{\mathbf{q}}, \quad \hat{\mathbf{q}}(t=0) = \hat{\mathbf{q}}_0, \quad (7)$$

$$\text{where } \hat{\mathbf{q}} = \begin{bmatrix} \hat{v} \\ \hat{\eta} \end{bmatrix}, \quad \text{and } \mathbf{L} = \begin{bmatrix} D^2 - k^2 & 0 \\ 0 & 1 \end{bmatrix}^{-1} \begin{bmatrix} L_{OS} & -2iRo\beta \\ -i\beta U' + 2iRo\beta & L_{SQ} \end{bmatrix}.$$

Here $D(\cdot) = \partial(\cdot)/\partial y$, a prime denotes $d(\cdot)/dy$, and $k^2 = \alpha^2 + \beta^2$. L_{OS} and L_{SQ} are the Orr-Sommerfeld and Squire operators given by

$$L_{OS} = i\alpha U'' - i\alpha U(D^2 - k^2) + \frac{1}{Re}(D^2 - k^2)^2, \quad (8)$$

$$L_{SQ} = -i\alpha U + \frac{1}{Re}(D^2 - k^2). \quad (9)$$

The perturbation pressure can then be obtained as the solution of a Poisson equation. The boundary conditions for the above system of equations are

$$\hat{v}(\pm 1, t) = D\hat{v}(\pm 1, t) = \hat{\eta}(\pm 1, t) = 0. \quad (10)$$

For the rest of the article, we simply refer to wall-normal components of velocity and vorticity as normal components unless suggested otherwise.

If the spectrum of the linearized operator \mathbf{L} in Eq. (7) contains an eigenvalue with a positive real part, then there is an exponentially growing mode that causes the base flow to transition to another state. If there is no such growing eigenmode, we may conclude that the flow is asymptotically stable. In the present system, exponential instabilities are known to set in fairly low values of Re .

The linearized problem governed by Eq. (7) may also be addressed as an initial value problem with a view of finding the initial condition that maximizes an objective functional, i.e., in this case the disturbance kinetic energy [30]. The maximum possible gain at a given time $G(t)$ and its global maximum G_{\max} can be defined for a set of fixed values of parameters Re and Ro as follows:

$$G(t; \alpha, \beta) = \sup_{\hat{\mathbf{q}}_0} \frac{\|\hat{\mathbf{q}}(t)\|_E^2}{\|\hat{\mathbf{q}}_0\|_E^2} \quad \text{and} \quad G_{\max} = \sup_{t \geq 0, \alpha, \beta} G(t; \alpha, \beta). \quad (11)$$

The disturbance kinetic energy norm that is to be maximized is defined in terms of the normal velocity v and normal vorticity η as

$$\|\hat{\mathbf{q}}(t)\|_E^2 = \frac{1}{2k^2} \int_{-1}^1 \hat{\mathbf{q}}^H(t) \begin{bmatrix} k^2 - D^2 & 0 \\ 0 & 1 \end{bmatrix} \hat{\mathbf{q}}(t) dy. \quad (12)$$

For a given Re and Ro , the streamwise wavenumber α , spanwise wavenumber β , and time t that yield G_{\max} are said to be optimal for maximizing the disturbance energy. These values are denoted as the optimal streamwise wavenumber α_{opt} , optimal spanwise wavenumber β_{opt} , and optimal time T_{opt} .

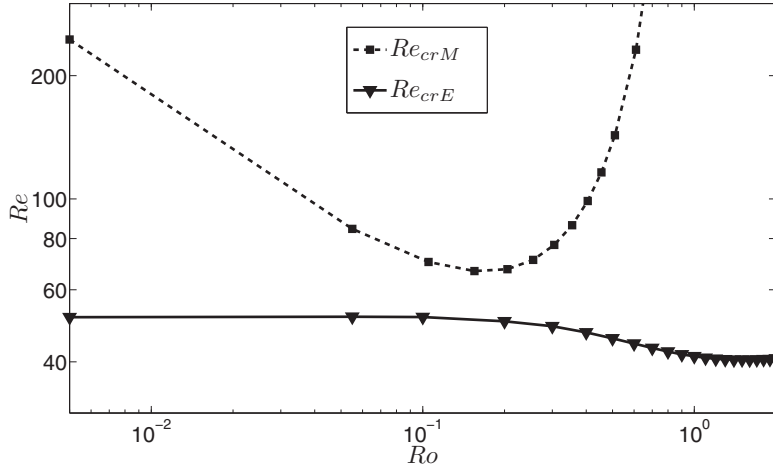


FIG. 2. The stability boundaries as per the energy and the eigenvalue methods.

For obtaining the optimal initial condition, the eigenvectors of the linearized operators can be used as a basis as they are complete in the present bounded geometry [35]. Upon inspecting the pseudospectra of the linearized operator, we find that a resolution of $N = 65$ Chebyshev collocation points in the normal direction is sufficient to form a complete basis of eigenvectors. Calculations performed with $N = 81$ or 121 produce the same result up to at least nine decimal places. Defining $\mathbf{\Lambda}$ as the diagonal matrix consisting of eigenvalues of the operator \mathbf{L} , and $\tilde{\mathbf{q}}$ as the corresponding set of eigenvectors of \mathbf{L} , we may express solutions of Eq. (7) in variable separable form as

$$\hat{\mathbf{q}}(y, t) = \tilde{\mathbf{q}}(y)\mathbf{k}(t). \quad (13)$$

This allows us to deal with a computationally simpler problem as we now have $\mathbf{k}(t) = e^{\mathbf{\Lambda}t}\mathbf{k}(0)$. Eigenfunctions which decay extremely rapidly have no consequence to the evolution of the transient disturbance and may be ignored. We choose a decay rate of -3 as the cutoff and find disturbances that are linear combinations of eigenfunctions with slower decay rate.

The computations were performed in MATLAB. Our code uses a differentiation suite for the Chebyshev grid developed by Weideman and Reddy [36]. The objective functional was maximized by using the MATLAB generic nonlinear constrained optimization package FMINCON. The code has been validated by confirming the eigenspectra for the nonrotating channel flow at $Re = 2000$ up to eight significant digits (Appendix A.7 in Ref. [30]).

B. Stability boundaries

The stability of a flow to small perturbations may be determined by either modal analysis or from the point of growth of perturbation energy. As mentioned earlier, the asymptotic stability of the flow is determined by the spectrum of the linearized operator. If the energy of any small disturbance decays monotonically for all time, then the flow is considered to be stable from an energy point of view. A flow which is asymptotically stable but not energy stable may display a transiently growing feature, which, but for nonlinear effects, will eventually decay [37]. This growth of disturbances can sometimes be sufficient to trigger nonlinearities, in which case the flow need not return to the initial base state. In shear flows, typically there is a stark difference in the critical Reynolds numbers obtained by the two measures. This is due to the nonnormal nature of the linearized operator \mathbf{L} .

We denote the critical Reynolds number, below which no disturbance mode grows exponentially, as Re_{crM} (where M stands for modal), and the energy critical Reynolds number as Re_{crE} , above which G_{\max} first exceeds 1. In Fig. 2, we show how these critical values vary with the Ro . It can be seen that Re_{crM} obtained by modal analysis is highly sensitive to the rotation rate. Lezius and Johnston [10] first accurately derived the modal neutral curve by noting the analogy of the present

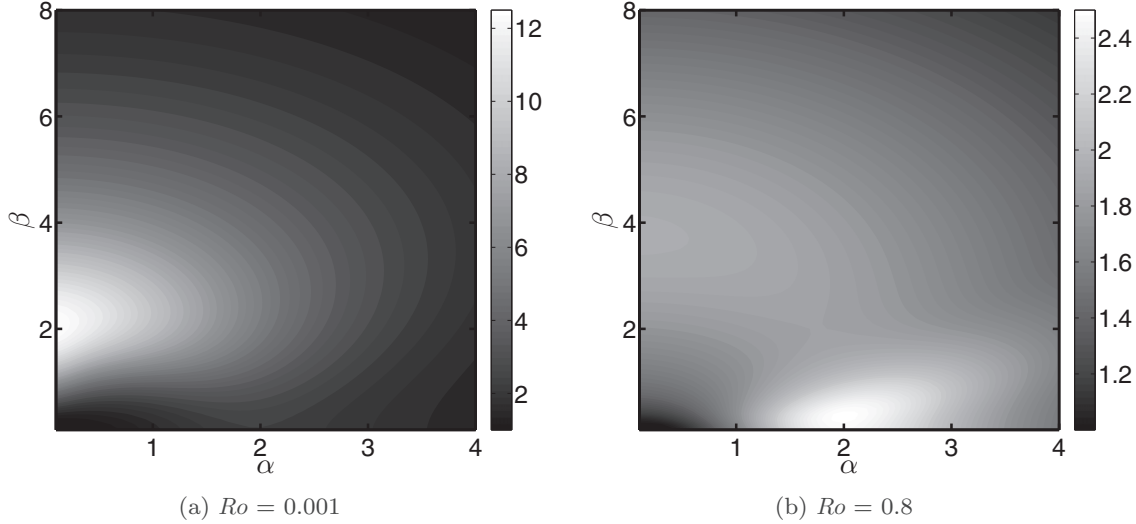


FIG. 3. The G_{\max} contours for $Re = 250$ for different Ro . The optimal parameters are (a) $T_{\text{opt}} = 18.72$, $\alpha_{\text{opt}} = 0.0$, $\beta_{\text{opt}} = 2.05$, $G_{\max} = 12.64$; (b) $T_{\text{opt}} = 4.85$, $\alpha_{\text{opt}} = 2.00$, $\beta_{\text{opt}} = 0.36$, $G_{\max} = 2.52$.

problem to the flow between two rotating cylinders in the narrow gap limit. The mode corresponding to the marginal state is seen to be streamwise independent. When the rotation rate is low, the spanwise wavenumber of the critical mode is around 2. As the rotation rate is increased, the corresponding critical mode has larger spanwise wavenumbers.

From Fig. 2, we see that Re_{crE} is far less sensitive to changes in the rotation rate; it changes from 51.43 to 41.16 over three decades of magnitude of Ro . In configurations between the neutral curves obtained by the two methods, disturbances may grow in energy for some time by a linear mechanism. We shall discuss the role of algebraic disturbances in the region in parameter space above the energy critical Reynolds number. It is also to be noted that the energy critical Reynolds numbers obtained for low rotation rates are close to 49.60, a value obtained by Joseph and Carmi [38] for the nonrotating channel flow (also see Ref. [37]).

C. Modally stable regime

We next study the transient growth characteristics in different regions of the Re - Ro parameter space where exponential instabilities are absent. In Fig. 3 we demonstrate by a typical example that transient growth is qualitatively different to the left and to the right of the neutral stability boundary. For a fixed Re ($=250$), the figure shows contours of G_{\max} for representative low and high rotation rates. The $Ro = 0.001$ case is not markedly different from the corresponding results for a stationary channel at this Reynolds number. There, too, the disturbances that yield the largest growths are streamwise invariant [39]. They form rolls that evolve into streaks as a consequence of the vortex tilting lift-up mechanism [40]. On the other hand, at $Ro = 0.8$, the optimal disturbances are almost aligned along streamwise direction with a very small dependence on the spanwise coordinate. This suggests that the Orr mechanism is likely to be the more dominant energy amplification mechanism [41]. It may be noticed that the maximum achievable algebraic growth is lower when compared to the situation at low Ro .

In Fig. 4, we show level curves of G_{\max} in the Re - Ro plane (outside the linearly unstable region). Two findings are immediately apparent. As in the example above, transient growth levels are much smaller everywhere on the right of the neutral boundary as compared to a corresponding Reynolds number on the left. Second, on a given side of the neutral boundary, G_{\max} depends primarily on Re and is rather insensitive to changes in Ro . We can gain insight into these observations by examining

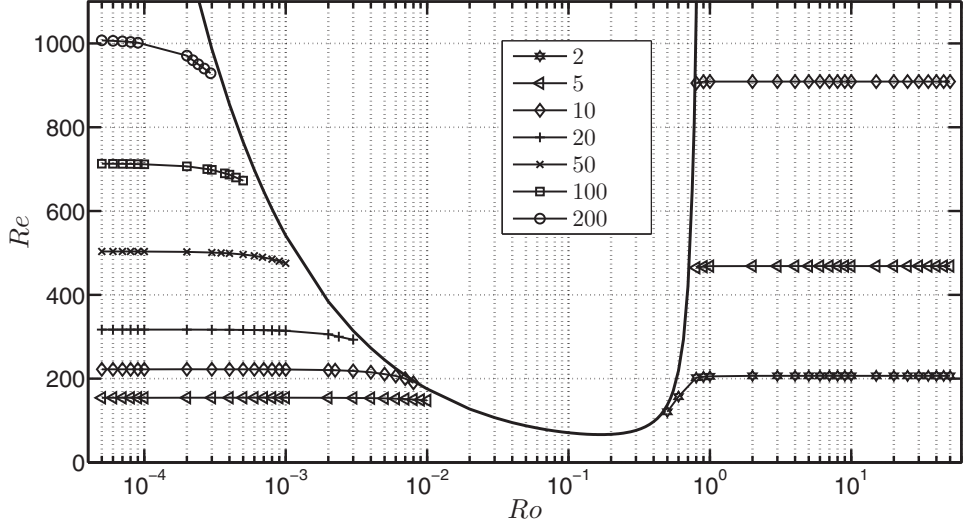


FIG. 4. Level curves of G_{\max} are given. For low Ro , the behavior resembles that of the optimal disturbances of the nonrotating channel. A large drop in the amplification levels is seen at high Ro .

the different sources of nonnormality in the linearized equations [Eq. (7)]. The strength of the rotation then determines which of the sources of nonnormality will emerge stronger.

The major source of nonnormality is the forcing due to the normal velocity \hat{v} in the normal vorticity equation, and it is this term that is responsible for the lift-up mechanism. An examination of the structure of the stability operator makes it evident that, at a given β , the departure from normality due to these operators decreases as the rotation rate increases. As in the nonrotating case, the largest amplifications are seen for disturbances that are streamwise independent at low rotation rates. For low rotation rates, the terms involving Ro serve to act as small corrections to the linearized operator. Hence, the growth in disturbance energies is similar to the growth seen in the nonrotating case. This translates to the lack of the dependence on Ro of G_{\max} in the low rotation regime in Fig. 4.

The other source of nonnormality in the linearized equations is that the Orr-Sommerfeld operator L_{OS} itself is not self-adjoint. This gives rise to a much weaker transient growth in two dimensions, which is completely independent of the rotation rate. As the rotation rate is increased, consistent with Taylor-Proudman arguments, the motion of the fluid is restricted to the plane perpendicular to the rotation axis. Thus, while disturbances favoring the lift-up mechanism are suppressed strongly, the disturbances amplified by Orr mechanism can still be excited at higher rotation rates. Disturbances initially having spanwise variation rapidly evolve to become two-dimensional with no flow along the axis of rotation. Thus the optimal disturbances in this regime evolve transiently only due to the Orr mechanism; i.e., $\beta_{\text{opt}} = 0$. Evidence of the Orr mechanism leading to the largest amplifications can be seen in Fig. 4 at high Ro , where the level curves become horizontal and thus display insensitivity to the rotation rate.

In Fig. 5, we have plotted the G_{\max} for specific values of Ro in different rotation regimes as a function of Re . The values obtained at higher Ro are shown to be at times an order of magnitude lower than for a small Ro for a given Re . It is seen here as well that G_{\max} does not vary too much as the Ro is varied in different rotation regimes for large ranges of Re . At low rotation rates, as long as Re is not sufficiently close to the critical value at given Ro , the energy amplification obtained is found to obey the scaling laws due to Gustavsson's results [42] as the different curves coincide. It can be seen that for $Ro = 2.5 \times 10^{-4}$, as we increase Re , deviations from the $Ro = 0$ curve start to appear. This is a result of the values of Re approaching the neutral boundary. Thus, it would be of interest to examine the regions close to the stability boundary in more detail.

In the high-rotation-rate modally stable regime, very close to the stability boundary, it can be seen in Fig. 4 that the level curves rise very slightly with Ro . This implies that the value of Re which

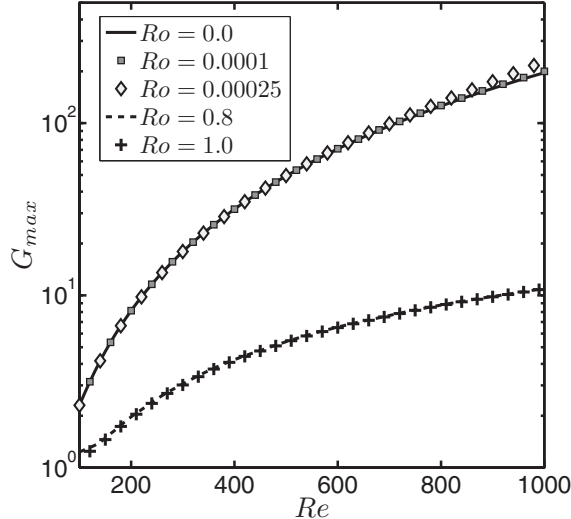


FIG. 5. A contrast between maximum transient energy growth at high and low rotation numbers.

yields a given energy growth increases with the rotation rate. It is important to note that if β were to be identically zero, there would be no effect of the rotation on transient growth, since Ro would completely drop out of Eq. (7) (Ro appears in the linearized equation only in the form βRo). The independence of the Orr mechanism on rotation was also demonstrated for the rotating Couette flow in the thesis of Daly [43]. Thus, the level curves not being perfectly horizontal near the stability boundary implies an oblique optimal structure; i.e., $\beta_{opt} \neq 0$. As we move to a region in Re - Ro parameter space further away from the stability boundary, the optimal amplification corresponds to that of the disturbance best amplified by the Orr mechanism at a given Re as the spanwise variation is suppressed, consistent with Taylor-Proudman theory.

As we approach the neutral stability curve from the low Ro side, we see in Fig. 4 that the level curves of G_{max} noticeably dip toward a lower Re . This means that for a fixed Re , we have an increase in G_{max} as we approach the stability boundary. The typical behavior of optimal growth with Ro (for $Re = 1000$) is shown in Fig. 6. The corresponding time at which this optimal growth is attained is also shown. The first modes that go linearly unstable are streamwise independent. The least stable modes have smaller decay rates as we approach the neutral boundary from the left, and hence the time before the modes individually decay is slightly longer. This allows for the lift-up effect to persist for a slightly longer time.

As mentioned earlier, the optimal structures obtained at low rotation rates are streamwise rolls that develop into streaks. This is similar to the nonrotating case in the sense that streaks are formed. However, due to the additional Coriolis force, the streaks are not symmetric about the centerline, with one side of the channel displaying a stronger streak than the other. This feature is more pronounced close to the stability boundary. Figure 7 shows the optimal structure for a typical low rotation ($Ro = 0.0002$) and compares this to the nonrotating case. The velocities in the two cases are comparable.

The optimal disturbance is given in Fig. 8 for $Re = 1000$ and $Ro = 0.8$. We can see that the rotation does not bias the occurrence of a secondary disturbance velocity toward any particular wall despite the high rotation rates. The strong rotation does little to alter the features of a flow that is largely confined to the plane normal to the rotational axis, i.e., the x - y plane. Hence, disturbances may evolve by the Orr mechanism unhindered by the rotation.

D. Modally unstable regime

If there exists an exponentially growing linear mode for a given wavenumber vector, then an optimal analysis to determine the maximum amplification attainable over all time would not yield a

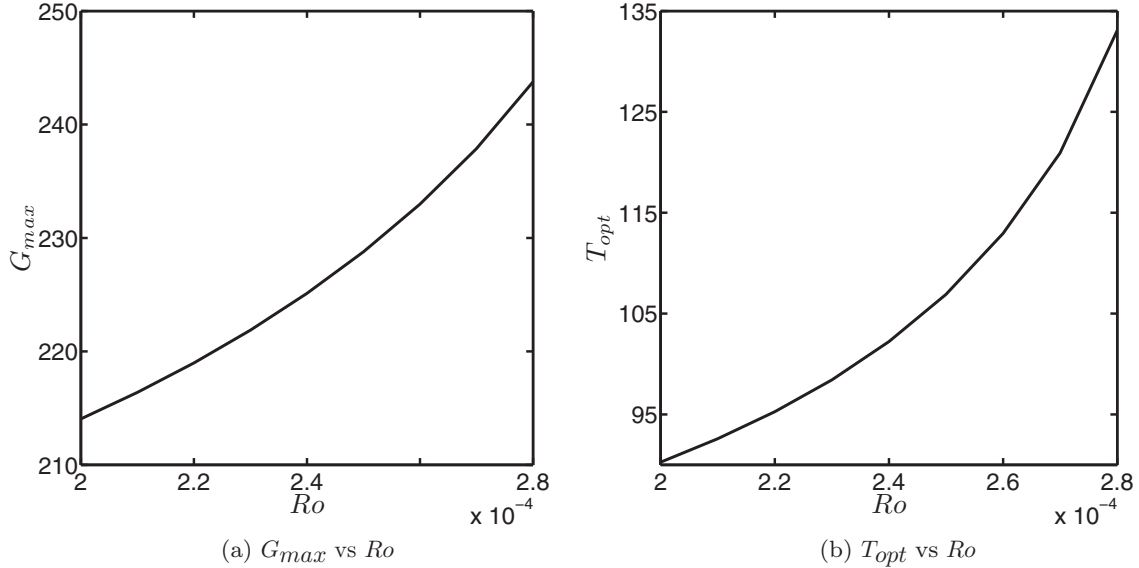


FIG. 6. Optimal growth G_{\max} and optimal time T_{opt} when the neutral boundary is approached with $Re = 1000$.

finite value. Does this mean transient growth is inconsequential here? That remains to be verified. For the nonrotating channel flow, it was shown that algebraic growth can raise the energy of the disturbance before exponential instability definitively takes over the dynamics [39].

As the parameter space to be explored is vast, we shall limit our analysis to $Re = 1500$ and some typical values of Ro where unstable modes exist; we have verified that our findings below are valid over a range of Re . The same set of pairs of Re and Ro have also been used for nonlinear analysis using direct numerical simulations; the results will be presented in the next section. Hence, the discussion presented in this subsection will provide the necessary context for the results from the nonlinear simulations.

1. Modal instabilities

As we are considering parameters within the unstable regime, it would be instructive to see what region in wavenumber space modal instabilities exist. In Fig. 9(a), the curves represent the neutral

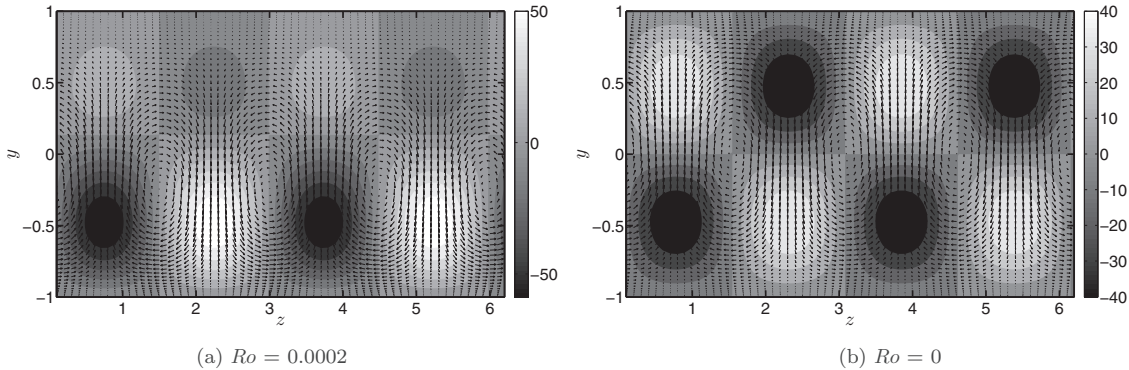


FIG. 7. The optimal structures for $Re = 1000$ for low Ro (a), and for the nonrotating case (b), at the optimal times. The contours depict the magnitude of the streamwise velocity component. The velocity field (v, w) are expressed through the vectors. The optimal parameters are (a) $T_{\text{opt}} = 90.27$, $\alpha_{\text{opt}} = 0$, $\beta_{\text{opt}} = 2.10$, $G_{\max} = 214.05$; (b) $T_{\text{opt}} = 75.68$, $\alpha_{\text{opt}} = 0$, $\beta_{\text{opt}} = 2.04$, $G_{\max} = 196.17$.

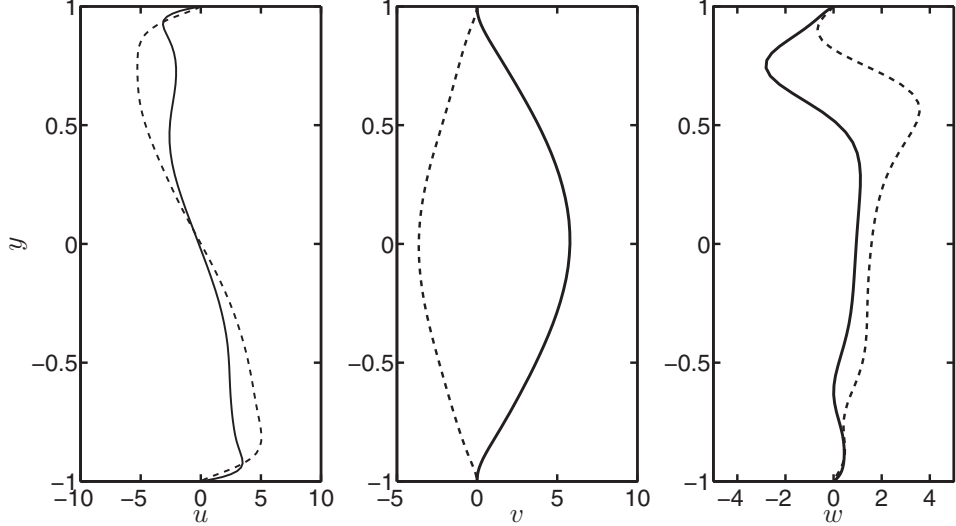


FIG. 8. The velocity components of the optimal disturbance at the optimal time when $Ro = 0.8$ and $Re = 1000$. The real and the imaginary parts are given by the solid line and the dashed line respectively. The optimal parameters are $T_{\text{opt}} = 8.52$, $\alpha_{\text{opt}} = 1.75$, $\beta_{\text{opt}} = 0.169$, and $G_{\text{max}} = 11.03$.

boundaries in the α - β plane for different Ro when $Re = 1500$. The wavenumber space bounded by each curve and the $\alpha = 0$ axis are the modally unstable regions for the given rotation rate. Thus, the introduction of rotation brings in a large class of instabilities that was absent in the case of the nonrotating channel flow.

The largest growth rates correspond to modes that are streamwise independent. In Fig. 9(b), we show the exponential growth rate of the least stable streamwise-independent mode as a function of the spanwise wavenumber for different rotation rates; the growth rate is given by the real part of the eigenvalue (λ_r). The growth rate associated with these unstable modes are large when compared to that of the Tollmien-Schlichting mode in the nonrotating channel. The spanwise wavenumber corresponding to the most unstable of these streamwise-independent modes does not remain constant; at larger rotation rates, the spanwise wavenumber of the most unstable mode increases. The observed trend is consistent with what is observed for the marginally stable modes along the neutral curve as the rotation rate is increased.

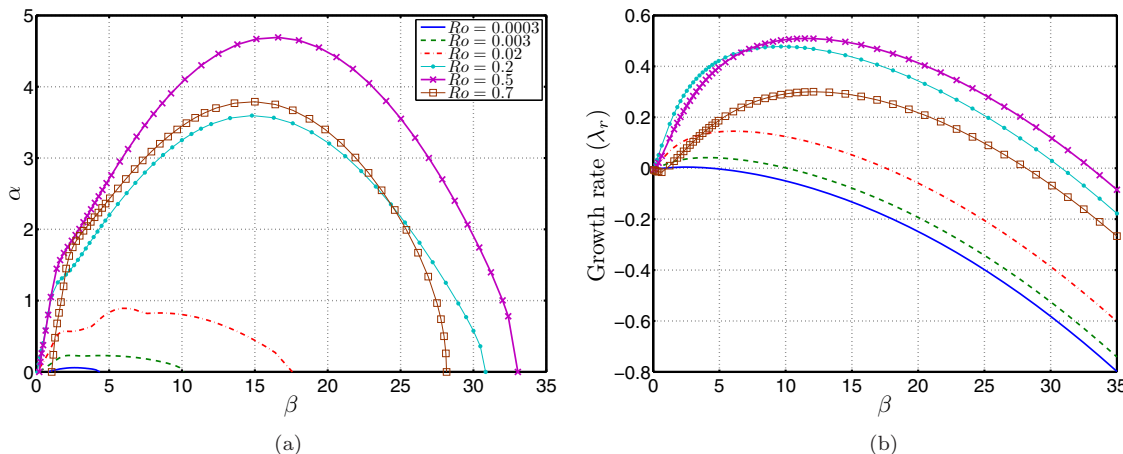


FIG. 9. $Re = 1500$. (a) The marginal stability curves for various Ro . (b) The exponential growth rate λ_r of the least stable mode (with $\alpha = 0$) as a function of β for various Ro .

2. Transient analysis

We turn our attention back to the issue of characterizing algebraic growth mechanisms. As we are dealing with cases within the linearly unstable regime, we have to examine the extent of the role played by the unstable mode during the evolution of the disturbance. Now for a given rotation rate, we shall denote the most unstable eigenmode as $\hat{\mathbf{q}}_u$. We shall analyze the evolution of the initial perturbation for different rotation rates in the linearized setting governed by Eq. (7). $\hat{\mathbf{q}}(t)$ denotes the disturbance state vector at different times during the linear evolution of the perturbation. At this juncture, for every time, we define a vector $\hat{\mathbf{p}}(t)$ that is obtained by normalizing $\hat{\mathbf{q}}(t)$ to have unit kinetic energy as per Eq. (12). Thus, for $\hat{\mathbf{p}}(t)$, we simply have

$$\hat{\mathbf{p}}(t) = \frac{\hat{\mathbf{q}}(t)}{\|\hat{\mathbf{q}}(t)\|_E}. \quad (14)$$

To see if $\hat{\mathbf{q}}(t)$ is indeed coincident with the unstable mode $\hat{\mathbf{q}}_u$, we now take advantage of Eq. (12) and define a new quantity M as

$$M(t) = \frac{1}{2k^2} \int_{-1}^1 \hat{\mathbf{p}}^H(t) \begin{bmatrix} k^2 - D^2 & 0 \\ 0 & 1 \end{bmatrix} \hat{\mathbf{q}}_u dy. \quad (15)$$

We can interpret M simply as a measure of the projection of the disturbance onto the unstable eigenmode. When $M = 1$, the disturbance has evolved such that it exactly coincides with the unstable eigenmode. It follows that M will remain at 1 for all subsequent times after this point while the system behaves linearly.

We have already noted the limitations of doing a linear optimal perturbation analysis within unstable regime. However, our aim is to maximize growth at early times, so by specifying a target time T_{tar} , we can find the best possible initial condition with a particular wavenumber that maximizes the gain [given by Eq. (12)] obtained at that particular time; we denote this gain as $G_{\text{opt},t}$. On obtaining the optimal initial conditions, we can find the extent of coincidence between the disturbance and the unstable mode at the initial and optimal times using Eq. (15). In addition to fixing Re at 1500, we shall also restrict the subsequent discussion to results for disturbances with wavenumber vector $\mathbf{k} = (0, 2)$. The results do not qualitatively change on varying Re and the disturbance wavenumbers within the modally unstable regime, and do not have a bearing on the overall conclusions.

In Fig. 10, we have plotted the maximum gain $G_{\text{opt},t}$ obtained and the corresponding projection measures at different rotation rates for a range of values of T_{tar} . For a comparison, we also plot the gain had the initial condition been the unstable mode; this gain is given by $G_{\text{uns},t}$. We see that the maximum gain due to introduction of the optimal disturbances is greater than the corresponding gain seen when the unstable mode is used as the initial condition for all choices of the target time. In other words, if the initial conditions are the optimal ones, we get an initial spurt in disturbance kinetic energy followed by exponential growth, so the total disturbance kinetic energy is greater with algebraic growth than without. It is also telling that the unstable mode is never seen to be the optimal initial condition. This is a direct consequence of the nonnormal nature of the linearized operator. In the evolution of these optimals, the initial evolution is algebraic and this elevates the energy of the unstable mode that will continue evolving as per its associated growth rate after the other modes die out.

At this point, we can define a quantity $G_{\text{a/e}}$ as follows:

$$G_{\text{a/e}}(t) = \frac{G_{\text{opt},t}}{G_{\text{uns},t}}. \quad (16)$$

Going back to Fig. 10, we see that beyond a certain target time (τ^*), the $G_{\text{opt},t}$ and $G_{\text{uns},t}$ are directly proportional to each other. This suggests that the ratio $G_{\text{a/e}}$ is a constant (\mathcal{G}^*) for all target times larger than this threshold value. This “saturated” ratio can serve as a measure of the nonmodal growth as it indicates the extent to which the energy of the unstable mode is enhanced by initial algebraic growth.

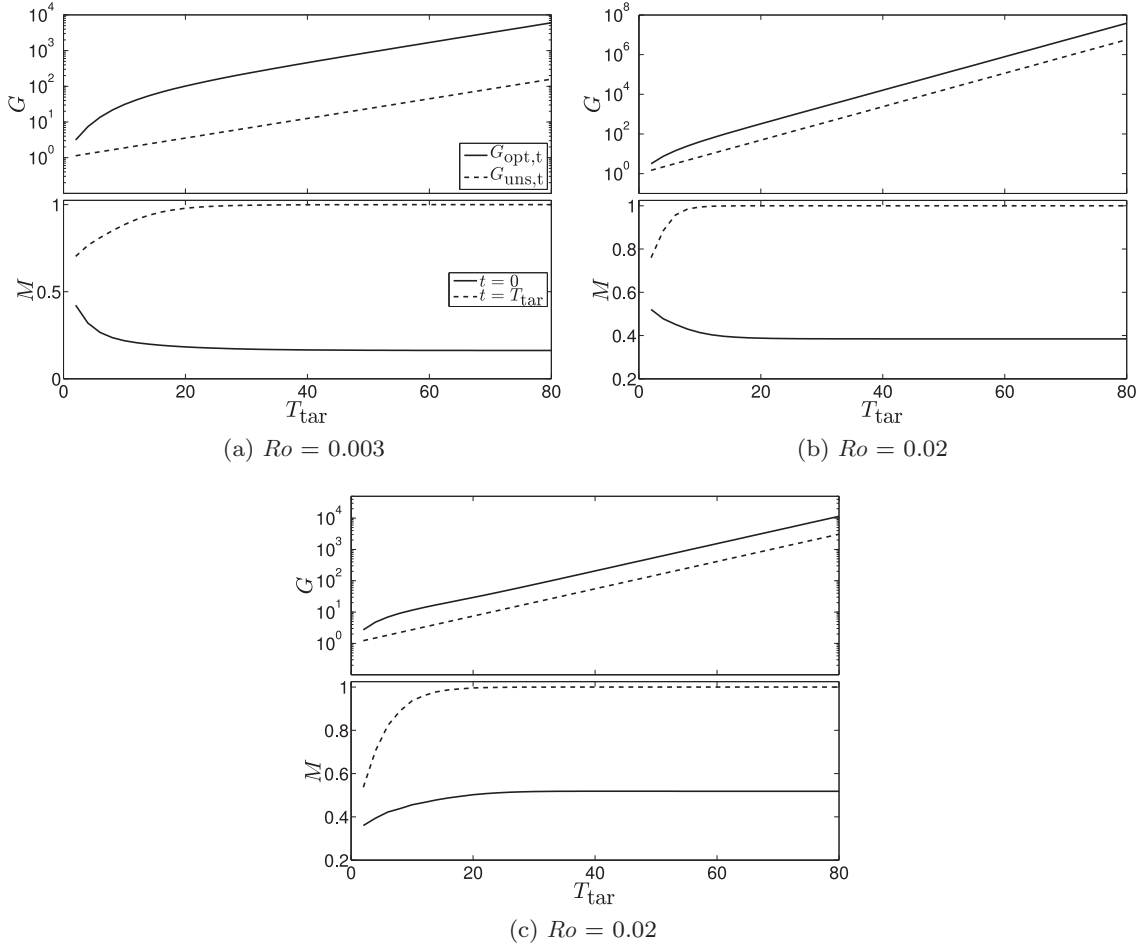


FIG. 10. The gains $G_{\text{opt,t}}$ and $G_{\text{uns,t}}$, and the projection measures M when T_{tar} is varied for different rotation rates. $Re = 1500$, $\alpha = 0$, and $\beta = 2$.

We plot \mathcal{G}^* and τ^* as a function of the rotation number Ro in Fig. 11. The values of \mathcal{G}^* cover a wide range and are seen to be nonmonotonic in Ro . The lowest values of \mathcal{G}^* [$\sim O(1)$] are obtained when we are well away from the neutral stability boundary on both the low and high rotation portion

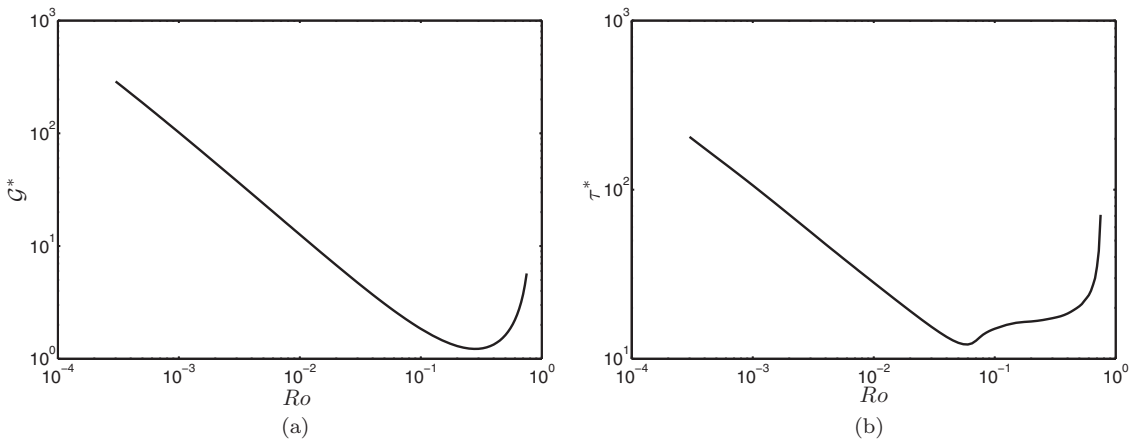


FIG. 11. (a) \mathcal{G}^* and (b) τ^* at different Ro . $Re = 1500$, $\alpha = 0$, and $\beta = 2$.

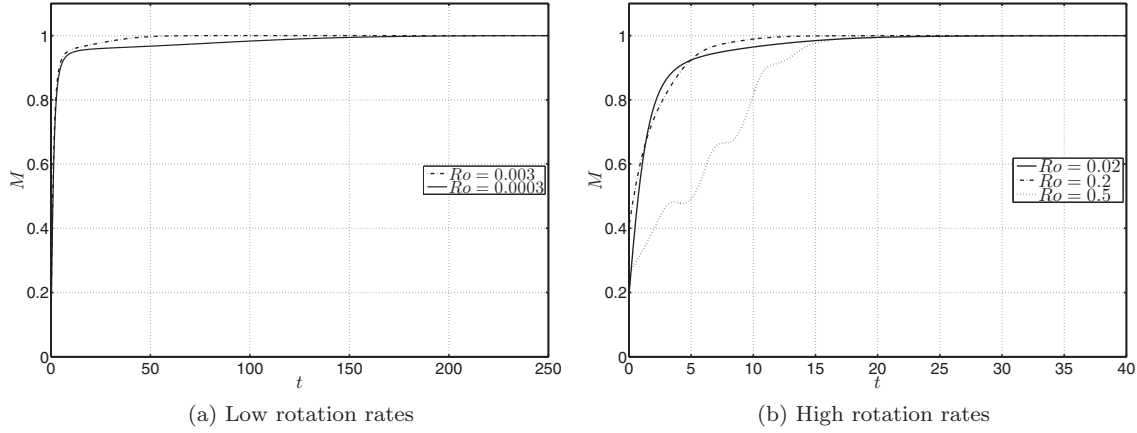


FIG. 12. The evolution of the projection measure M defined in Eq. (15) for different rotation rates. $Re = 1500$, $\alpha = 0$, and $\beta = 2$.

of the Re - Ro phase space. This is consistent with the fact that exponential instabilities in this range of Ro are readily excited. On the other hand, there is also a significant window in the low rotation range (nearly two decades of values of Ro), where $G_{\text{opt},t}$ and $G_{\text{uns},t}$ differ by well over an order of magnitude.

We estimate by τ^* the time at which the disturbance evolution is taken over by the unstable mode, which then drives the dynamics entirely. When the rotation rate is increased, i.e., when we go further into the linearly unstable regime, the time period before the unstable mode takes over and the dynamics becomes shorter. As our interest is in the relevance of algebraic growth, we see a range of Ro for which τ^* is not too small. This essentially suggests a window for the different nonnormal modes to interact with each other to produce a transient phenomenon. From the trends observed, for this set of rotation rates, there is a strong suggestion that nonmodal mechanisms are capable of playing a role in the transition process.

Thus far, the discussion involved finding an optimal perturbation for each value of the rotation rate while specifying a target time. We can also compare the extent to which the algebraic growth is prevalent at different Ro by fixing the initial condition. A suitable initial condition for the present study would be one that would evolve transiently in the absence of rotation. Once again with $Re = 1500$ and $\mathbf{k} = (0, 2)$, we choose the optimal perturbation when $Ro = 1 \times 10^{-4}$ as our initial condition; $Ro = 1 \times 10^{-4}$ belongs the modally stable region of Re - Ro phase plane, and therefore there is no trouble evaluating the optimal perturbation over all time. The method used here ties in with the conditions under which the nonlinear simulations discussed in the next section were performed.

We will start by examining when the values of Ro are small. So now we examine the projection measure M defined by Eq. (15) for the two rotation rates that fall in the linearly unstable regime. We see in Fig. 12(a) at later times $M = 1$, indicating that the disturbance has come to comprise the unstable mode alone. During the early stages of the evolution, the secondary flow evolves in a manner to form streaks in the flow as is in the nonrotating channel flow. At higher rotation rates, the unstable mode is excited relatively quickly as can be surmised from Fig. 12(b), where the projection measure M [Eq. (15)] is plotted. Therefore, at higher rotation rates, the initial condition serves as a background out of which the unstable mode emerges.

The measures of \mathcal{G}^* , τ^* , and M calculated in this section offer some preliminary insight what might transpire in the transition picture for different Ro . For a more complete picture, we now turn our attention to results obtained from nonlinear simulations.

IV. NONLINEAR SIMULATIONS

In cases where a modal perturbation grows exponentially, or where transient growth is large, a nonlinear study is imperative to understand the next stage of evolution. We carry this out by direct

numerical simulations of the three-dimensional Navier-Stokes equations in this flow, to characterize the transition to a new (steady or unsteady) state of the channel flow at different rotation rates. As discussed above, the rotational channel flow is a well-studied problem from both numerical and experimental points of view. In these studies, typically transitions away from the parabolic profile are achieved by the introduction of noise at a sufficiently high level such that instabilities are triggered, and the flow is allowed to evolve nonlinearly [18,44]. These studies were interested in the linearly unstable regime. In the present, we discuss results from nonlinear simulations with a wide range of Ro , encompassing both regimes that are modally stable and those that are unstable. To make the discussion simpler, we present results at a Reynolds number of 1500, deeming them to be typical of the simulations we have carried out at other Reynolds numbers.

A. Methodology

The simulations were performed using the SIMSON code developed by KTH Mechanics, Stockholm [45]. A pseudospectral method is employed with Fourier expansions in the streamwise and spanwise directions, and a Chebyshev discretization is employed in the normal direction. For the results to follow, the horizontal directions are discretized using 64 Fourier modes each, and 81 Chebyshev polynomials are used for discretizing the normal coordinate. A second-order Crank-Nicolson scheme was used to discretize the linear terms, and the nonlinear terms were discretized by a four-stage Runge-Kutta (RK3) scheme. Periodic boundary conditions are used in the streamwise and spanwise directions, and at the walls, no slip and no penetration are imposed. In addition, all the simulations are performed with the mass flux through the channel kept fixed.

For validating the code, we imposed the least stable eigenmode as the initial condition at a very low amplitude (10^{-6} times the centerline base velocity) and found that the disturbance growth rates agrees with those predicted by linear stability theory for both the rotating and the nonrotating channel flows. For the rotating case, where the flow has undergone transition, we also verified that the total shear stress (sum of viscous and Reynolds stresses) varies linearly with the normal coordinate. The code has also previously been employed for numerous studies with the plane channel flow geometry (see Chevalier *et al.* [45]).

Here we wish to specify initial conditions that are favorable for algebraic evolution of the secondary flow. When the rotation rates are low, a streamwise independent initial disturbance is likely to grow transiently. Within the unstable regime as well, it was shown in the previous section that there is scope for algebraic amplification before the unstable modes dominates. For all the results here we fix $Re = 1500$, a value where subcritical transition was previously observed in the nonrotating case [46]. The main results to follow are obtained with the optimal disturbance with wavenumber vector $\mathbf{k} = (\alpha, \beta) = (0, 2)$ for $Ro = 10^{-4}$ provided as the initial condition. Within the regime of linear instability, we continue to use these initial conditions.

The computational box employed for all the cases is $x_l \times y_l \times z_l = 2\pi \times 2 \times 2\pi$. Since our interest here is largely on the period leading up to transition, this is sufficient. However, it is to be noted that when one is interested in finding secondary instabilities (of twisting and wavy types), a much larger extent in the streamwise direction is desired [18]. We have ascertained that the short-time evolution of the flow varies insignificantly upon changing the streamwise extent of the computational domain. The computational box measures two wavelengths of the perturbation in the spanwise coordinate.

The initial kinetic energy has an amplitude of 25×10^{-6} per box of size 1 wavelength of the disturbance in both streamwise and spanwise directions. In case of a zero wavenumber in either direction, an arbitrary length is fixed in that direction to define the box. The initial amplitude chosen is the lowest that leads to transition in the nonrotating case, and this is in agreement with the threshold values obtained in previous studies [46]. For cases that fall within the linearly unstable regime, we can also start with lower initial perturbation energy.

Particular care must be taken when the initial perturbation is streamwise independent, since these perturbations, through the nonlinear term in the governing equation, would act to excite only higher

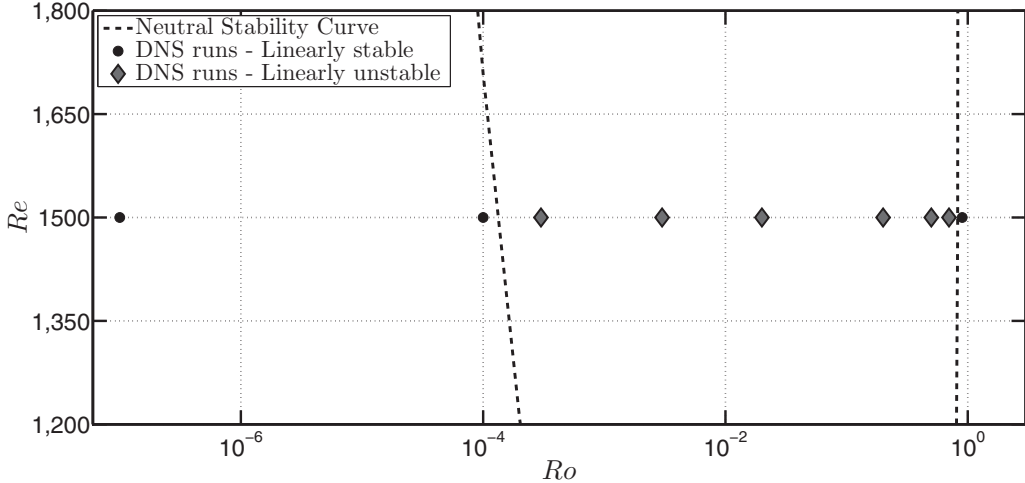


FIG. 13. The nonlinear simulations presented here are for the parameter values denoted by the symbols. Re is fixed at 1500.

harmonics of the initial spanwise wavenumber while remaining independent of the streamwise coordinate. In order to excite other streamwise spatial frequencies, we also introduce noise at a very low level at the start of the simulation [30,46]. The noise is introduced in the form of Stokes modes for a few nonzero streamwise wavenumbers. The total energy content of the noise is prescribed to be half a percent of that of the optimal perturbation, which ensures that noise is not the dominant factor in the dynamics and serves to trigger secondary instabilities. We have verified that the flow does not undergo transition to a new state when noise alone is introduced. The noise is added primarily to excite secondary instabilities.

The rotation rate is varied across some decades of Ro to clearly elucidate what happens in different regimes. In Fig. 13, we show the different cases considered and where they lie in the Re - Ro space with respect to the neutral stability boundary. The lowest Ro we choose is 1×10^{-7} , and this practically corresponds to the nonrotating case. On the low rotation side, we also study $Ro = 1 \times 10^{-4}$, which is just outside the stability boundary. Within the region where exponential instabilities may occur, we choose several points. The highest Ro we study is 0.9, which does not yield exponentially growing disturbances at $Re = 1500$; i.e., it lies to the right of the stability boundary. For ease of discussion, we shall refer to cases with $Ro \leq 0.003$ as low rotation cases and to higher Ro as high rotation cases.

To get a measure of whether the transitioned flow is chaotic, we define an entropy Q as follows:

$$Q = \frac{1}{2x_l z_l} \int_{\text{box}} [\omega_x(x, y, z, \tau + \Delta t) - \omega_x(x, y, z, \tau)]^2 dx, \quad (17)$$

where x_l and z_l are the streamwise and spanwise lengths of the box, and $2x_l z_l$ is the volume of the periodic box. Streaks that have evolved from streamwise vortices have been seen as precursors to the transition process in several shear flows [47,48]. Hence, we define Q based on the streamwise vorticity, as this gives us a picture of the fluid motion in the y - z . A similar approach had been employed by previously to quantify chaotic motion due to a flow past an inline oscillating cylinder [49]. On defining Q by using other vorticity or velocity components, qualitatively similar results are obtained. We choose the reference time τ to be later than the time at which the initial transient behavior dies down. At $\Delta t = 0$, we have $Q = 0$. In a strictly periodic flow with period T , Q will return to zero when $\Delta t = nT$, where n is any positive integer.

In Table I, we have specified that the growth rates of the least stable eigenmodes with wavenumber vector $\mathbf{k} = (\alpha, \beta) = (0, 2)$ when $Re = 1500$ to serve as a reference.

TABLE I. The exponential growth rates of the least stable mode with $\mathbf{k} = (\alpha, \beta) = (0, 2)$ when $Re = 1500$ at different rotation rates.

Ro	Growth rate	Ro	Growth rate	Ro	Growth rate
1×10^{-7}	-0.00431158	0.003	0.03165619	0.5	0.19551277
1×10^{-4}	-0.00087845	0.02	0.09718189	0.7	0.05017800
3×10^{-4}	0.00398466	0.2	0.25758712	0.9	-0.01717999

B. Nonlinear results: Low rotation rates

To start off, we shall first consider the cases where the rotation rates are small. As a measure of transition, we examine the time evolution of the root mean square (rms) values of the different components of the velocity for all the cases. For all the cases, there is an initial period where there is transient amplification of the disturbance. Several wavenumbers then start to gain energy (not shown) through the nonlinear terms aided by the initial noise. The transient amplification seen at early times is then inhibited by nonlinear effects. For both low and high rotation cases, we seek to describe the flow characteristics well after the initial transients have run their course, and the resulting flow is fully nonlinear.

It can be seen in Fig. 14 that the rms values of the streamwise velocity u settle within a range of amplitudes not very dependent on the rotation rate. A transient spurt in rms values of the various velocity components is followed by a settling down into a time-dependent state at a lower mean energy level than the maximum transient. In this state, the rms values show an apparently chaotic signal for all the cases with similar time-averaged behavior. The observations when other components of the velocity are considered offer similar trends. We emphasize that this is the case regardless of the fact that some of the configurations here ($Ro = 3 \times 10^{-4}, 0.003$) can support exponential instabilities. We also show in Fig. 14(b) that the initial evolution of the secondary flow appears to be similar while the nonlinear terms have not fully come into play. Departures from this type of behavior are seen when the rotation rate is increased. This prepares us for pronouncedly different behavior at high rotation rates.

The rms values do not, however, tell us about where the secondary flow is set up and what the dominant structures are. The linear stability results lead us to expect that the Coriolis force biases the flow toward stronger secondary flow near the high-pressure side of the channel. In Fig. 15, we show vortex core regions identified by use of the λ_2 criterion [50]. λ_2 is the second eigenvalue of the tensor $\mathbf{S}^2 + \mathbf{R}^2$, where \mathbf{S} is the strain rate tensor and \mathbf{R} is the antisymmetric part of the velocity

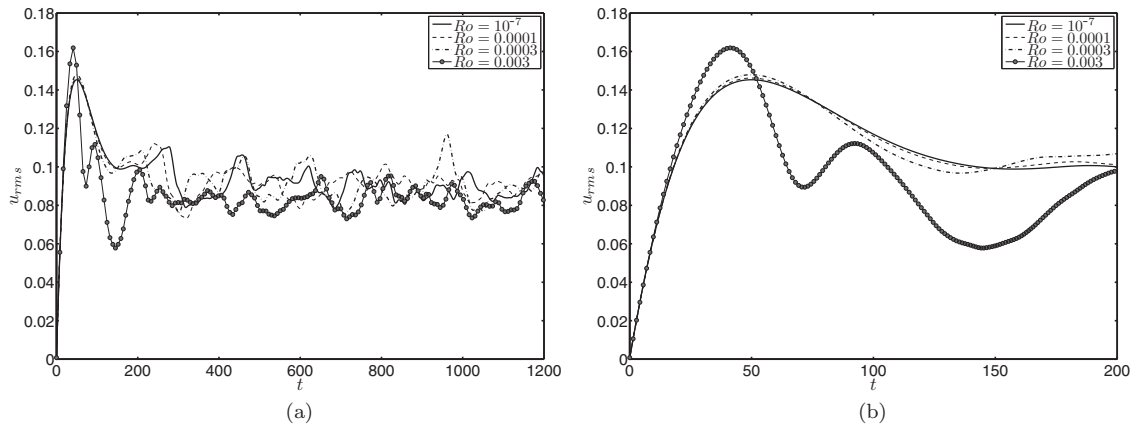


FIG. 14. (a) Evolution of root mean square (rms) values of the streamwise velocity component. (b) A magnified portion of panel (a) highlighting the early stages of the evolution of the secondary flow.

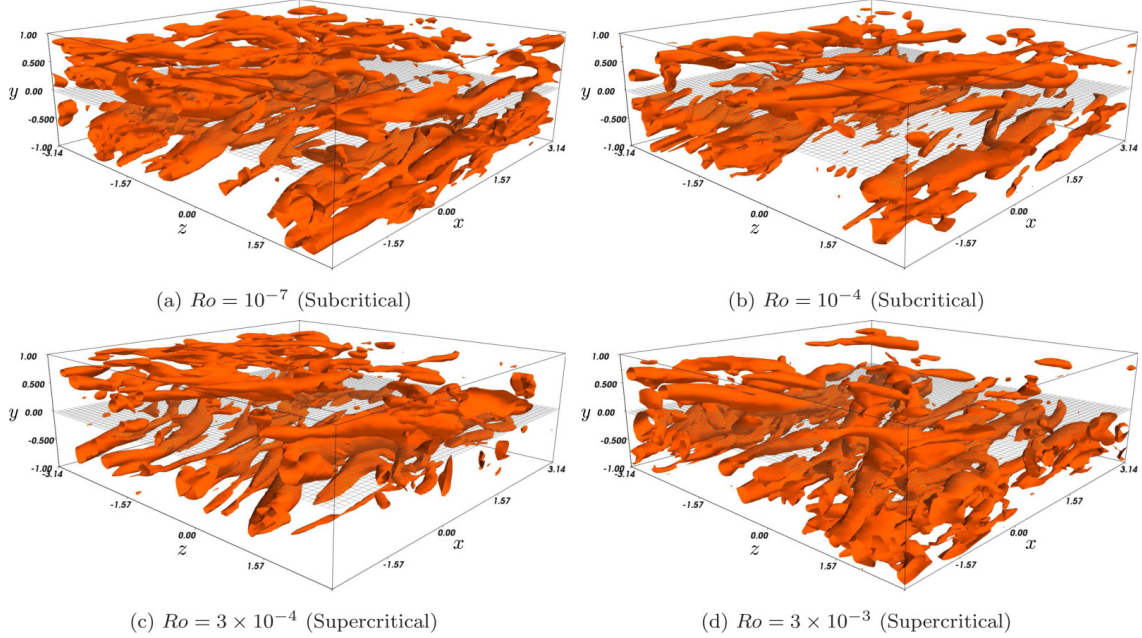


FIG. 15. The isocontours of constant $\lambda_2 = -0.05$ at various rotation rates. The vortex cores are identified in each of the cases at $t = 500$, a characteristic time after the initial transient behavior has died out.

gradient tensor (the rotation tensor multiplied by 0.5). We choose a characteristic time $t = 500$ for comparing the different cases such that the initial transient behavior has run its course and the flow is fully nonlinear.

When the rotation rate is low, we see the vortex structures to be distributed across the channel and to be disordered. The behavior is qualitatively similar in all cases and similar to that in a stationary channel. At early times (not shown), the secondary flow initially gets set up as aligned in the streamwise direction and then breaks down to give a seemingly chaotic flow [46]. Thus, the flow at low Ro , even if within the linearly unstable regime, can undergo transition via mechanisms by which subcritical transition occurs in the nonrotating channel flow. At this point, no clear indication of the role of the unstable mode is seen.

In Fig. 16 are shown mean flow profiles of the present simulation for different values of Ro considered. The mean flow is derived by averaging in the streamwise and spanwise coordinates and in time. The profiles obtained resemble that of nonrotating turbulent channel flow. It was seen in earlier work that the mean flow in the rotating channel is no longer symmetric about the centerline due to the Coriolis force when the flow becomes turbulent [22,23]. Despite being in the linearly unstable regime, here we do not see strong manifestations of the asymmetry in the mean flows despite the Coriolis force being capable of exciting instabilities in a couple of the cases.

The rms values in Fig. 14 suggest a strongly fluctuating velocity field. To get a sense of how chaotic each of the resulting flows are, we now turn to the entropy measure Q defined in Eq. (17). Setting the reference time τ as 500, in Fig. 17, we plot the evolution of Q for the different cases considered. The plots make it evident that we have chaotic flow, since in no case do we have Q returning to zero. In addition, the range of values of Q seen for the different cases is not drastically different.

Thus far, there has been no indication of whether the unstable mode plays a significant role during the transition process. The results from the linear analysis in the previous section suggest that the disturbance initially grows algebraically despite the presence of the unstable mode (for the unstable configurations considered here). The nonlinearity in the governing equations act to limit the linear growth once the secondary flow has become sufficiently strong. Then the peak of the rms values in Fig. 14 can be considered a marker for when the flow has become fully nonlinear; this is seen to

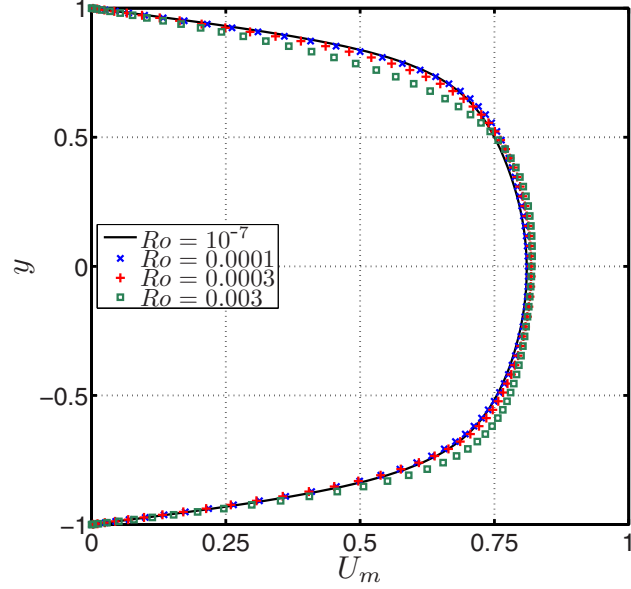


FIG. 16. The temporally and spatially averaged mean flow profiles for different rotation rates. The familiar profile of a turbulent channel flow is obtained for low rotation rates.

occur at $t \approx 50$ for all the cases. At the same stage in the linear evolution, the unstable mode has not yet come to dominate the dynamics [see Fig. 12(a)]. The algebraic evolution of the disturbance has been so strong such that the flow becomes fully nonlinear without the linear unstable mode having completely emerged.

In the case of the nonrotating channel flow, the optimal perturbation eventually decays if the nonlinear terms are not triggered. This happens when the energy content of the perturbation is initially very low, and the algebraic linear amplification is not strong enough to render the nonlinear terms important. If we were to introduce the perturbation at lower energy levels, the secondary flow can evolve linearly for long enough to coincide with the unstable mode. This is clearly depicted in Fig. 18 when $Ro = 3 \times 10^{-4}$. As we increase rotation such that we are further away from the

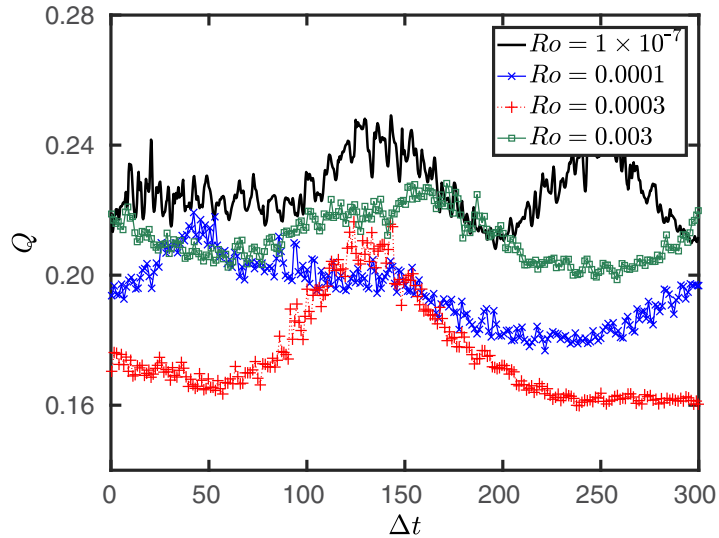


FIG. 17. The evolution for the measure of chaos Q for different Ro . For all the cases, a departure from the initial state is shown. Here we choose $\tau = 500$ as the starting state.

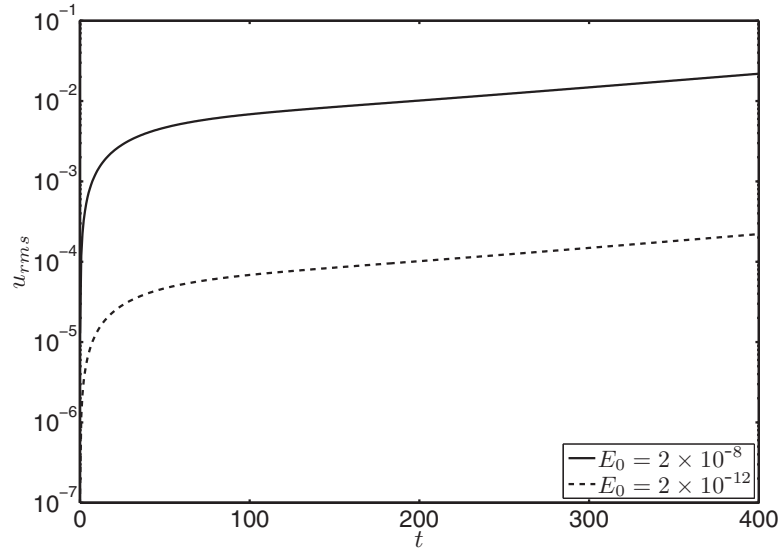


FIG. 18. The unstable mode is eventually excited in the full nonlinear setting when initial perturbation energy is low ($Ro = 3 \times 10^{-4}$). Algebraic growth is seen at early times before the unstable mode becomes dominant.

stability boundary, the time taken for the unstable mode to emerge becomes shorter. Upon exciting the unstable mode, the flow would evolve as dictated by the exponential growth rate from linear theory until the nonlinear terms become important.

From Fig. 18, we also see that the initial rise in the rms values happen at a much faster rate than the growth rate specified by the unstable mode. Eventually the unstable mode alone is seen to dominate. At the stage where the unstable mode alone survives, the secondary flow is seen to have already attained a kinetic energy that is larger than what would have achieved had we started with an unstable mode alone. We can then say that given a class of initial conditions with the same kinetic energy, algebraic disturbances can enhance the energy content of the unstable mode and make the flow nonlinear at earlier times.

So in the cases considered above at low rotation rates, algebraically growing disturbances have been shown to be capable of triggering transition in two ways. First, the algebraic growth can be strong enough such that the nonlinear terms come into play. The transition is triggered by the vortex stretching and tilting mechanisms that lead to the formation of streaky structures. Alternatively, if we impose the initial energy content of the disturbance to be very low, we end up with the situation where the unstable mode is eventually excited and transition occurs by the secondary instabilities of the saturated flow. However, in contrast to noisy environments, the unstable mode emerges with much higher energy due to the algebraic amplification of the disturbance. With regard to that point when the evolution transition has occurred, the nonmodal mechanisms are more dominant at short times. However, if the flow has not undergone transition by subcritical mechanisms, the unstable mode will trigger the nonlinearity at later stages.

C. Nonlinear results: Intermediate and higher rotation rates

As the rotation is increased, we are now very much within the modally unstable regime. In the previous subsection, we already saw signs of the unstable mode emerging in the dynamics provided that the flow has not become fully nonlinear until a certain time. The range of rotation rates considered here are more in line with earlier studies where strong instabilities and transition to turbulence have been observed. The question then posed here would be to see if the nonnormal nature

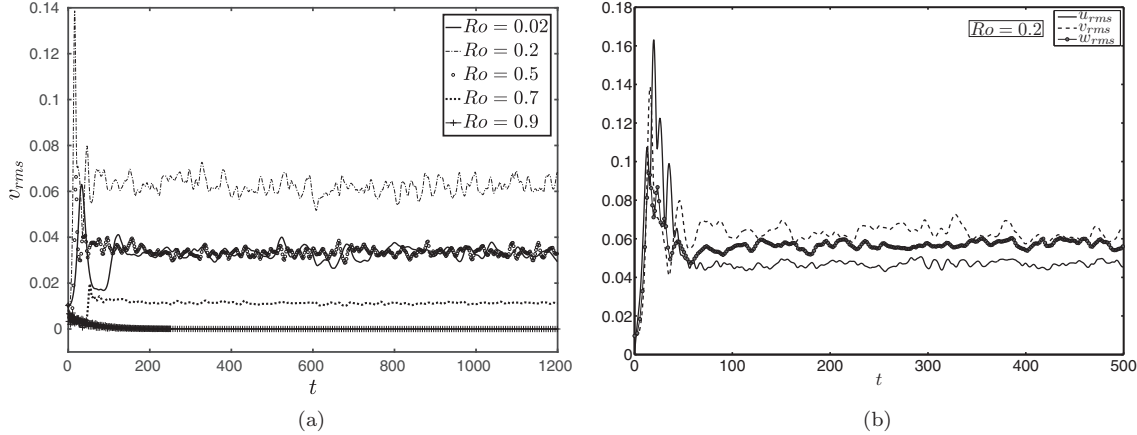


FIG. 19. (a) For the high rotation cases, the evolution of the root mean square (rms) values of the normal velocity component. (b) The rms values of the different velocity components when $Ro = 0.2$. The secondary flow becomes more isotropic when the rotation rate is increased.

of the governing equations and algebraic disturbances have any significant effect on the dynamics of the flow.

As before, we first examine the rms values of the resulting flow at various rotation rates in Fig. 19. A notable algebraic behavior, as was evident at lower values of Ro (Fig. 14), is not very apparent here. In Fig. 19(a), for certain cases ($Ro = 0.2$, for instance), the rms value (perturbation energy) rises drastically in a short period, and consequently the flow rapidly becomes nonlinear. One must remember that the exponential growth rates of modes for these values of Ro are fairly high, and the linear regime lasts for a very short window. For the values of Ro considered here, the results from the linear analysis also do not predict pronounced algebraic growth effects (see Subsec. III D).

The rms values of the streamwise velocity get suppressed to a greater extent (not shown). For the other velocity components, the rms behavior is not monotonic as we increase the rotation rate [see Fig. 19(a)]. What was initially a more streamwise dominant flow in the case of low rotation rate cases now has comparable rms values of velocity in all directions; the $Ro = 0.2$ case displays this the best [see Fig. 19(b)]. Inside the linearly unstable region, the rms values of the spanwise and normal velocity components increase in a range of Ro . These values once again get suppressed as the rotation is further increased, and the region of linear stability is approached. Also to be noted is that on increasing the rotation rates, the rms values display smaller deviations from their long time average [for instance, compare the cases with $Ro = 0.2, 0.7$ in Fig. 19(a)].

From Fig. 19(a), the flow has undergone a transition to an unsteady state at all rotation rates except $Ro = 0.9$. For this case, the high rotation rates effectively kill all the fluctuations very quickly, in keeping with Taylor-Proudman arguments. The resulting flow then quickly reverts back to the parabolic flow. For the parameters considered here, in the rapidly rotating case, both exponential and algebraic growths of perturbations are suppressed. One must keep in mind that when $Re > 5772$, transition due to the breakdown of the two-dimensional TS waves, which is unaffected by rotation, is still possible [15].

When we consider the λ_2 structures in Fig. 20, they are found to be increasingly concentrated at the lower, high-pressure side of the channel. The structures appear to be far more disordered when the rotation rate is far from either linear stability boundary ($Ro = 0.2$, for example). The vortex structures formed also appear to be more ordered along the streamwise coordinate as the rotation is further increased. The conspicuous absence of vortical structures on the low-pressure side of the channel suggests that the flow remains largely ordered and laminar in that region. Thus, the Coriolis force acts to effectively laminarize at least one side of the channel flow. Such behavior was seen in Ref. [10], where the authors found a reduction in the turbulent intensities near the low-pressure wall. As we increase the rotation rates further, the Coriolis force acts to confine the secondary

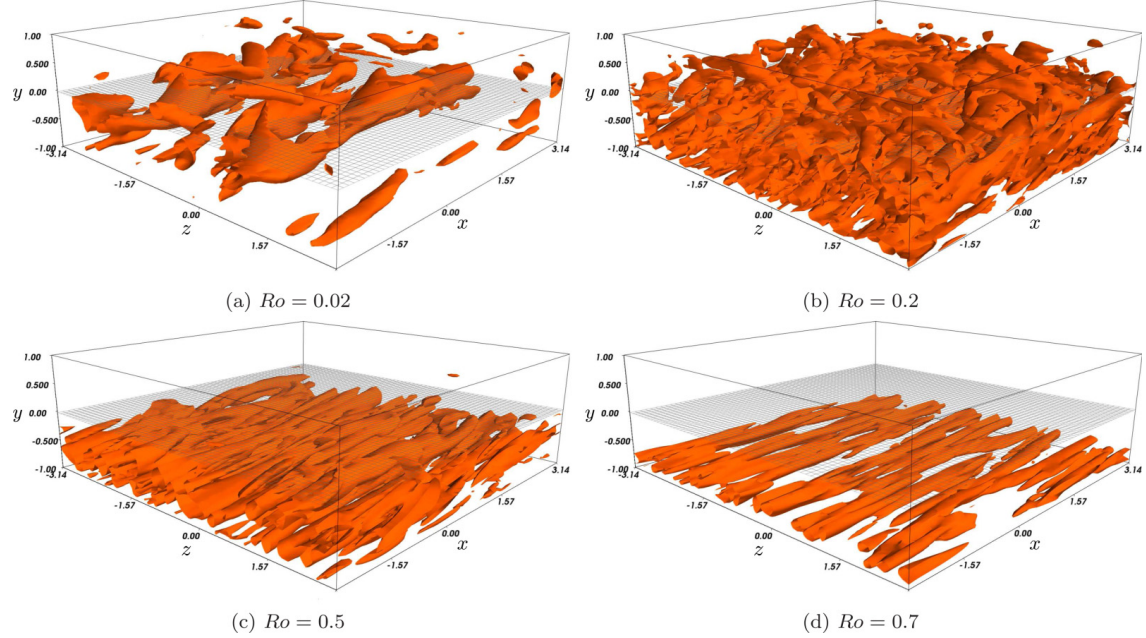


FIG. 20. The isocontours of constant $\lambda_2 = -0.05$ at different rotation rates. All cases are supercritical. The vortex cores are identified at $t = 500$, same as in Fig. 15.

motion to smaller regions in the channel. Thus, the secondary flow set up is much weaker, as can be seen for the $Ro = 0.7$ case in Fig. 20.

The mean flow obtained for these rotation rates are given in Fig. 21. The case of $Ro = 0.2$ displays clear departure from symmetry about the centerline. It is noticed that the velocity profile is linear over a significant portion of the channel width. This portion is the region where the strong vortical structures seen in Fig. 20 exist. A similar correspondence of linear velocity profiles and strong

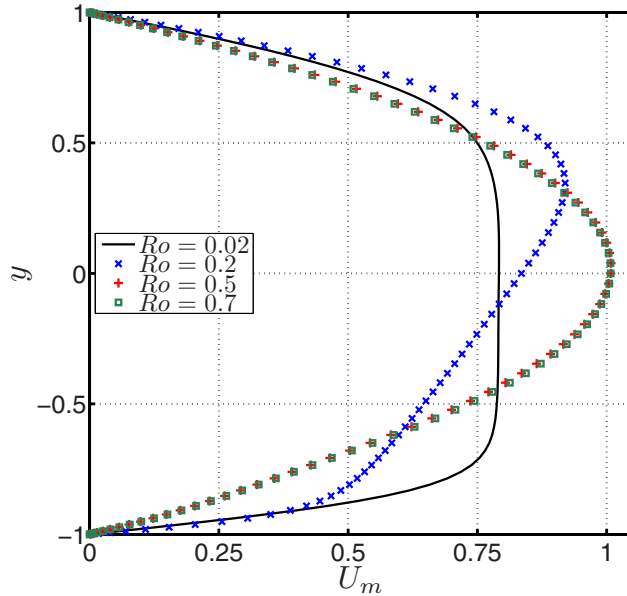


FIG. 21. The temporally and spatially averaged mean flow profiles for different rotation rates. Prominent asymmetry is seen at higher rotation rates.

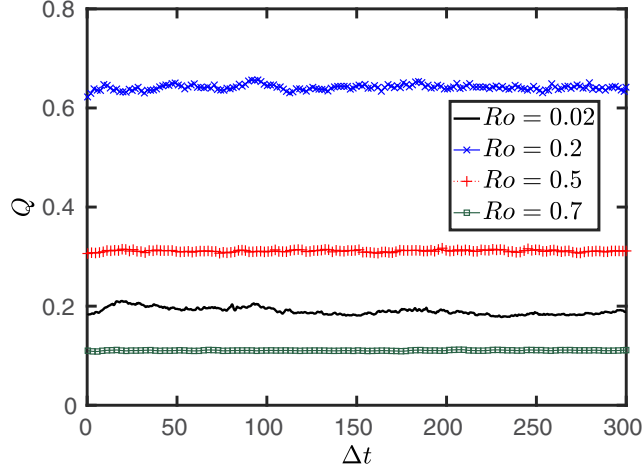


FIG. 22. The evolution for the measure of chaos Q for different Ro . For all the cases, a departure from the initial state is shown. Here we choose $\tau = 500$ as the starting state.

structures has been reported earlier for turbulent rotating shear flows [23,51–53]. We comment here that the resulting mean flow is not different from the case if we induce transition using the unstable mode.

To get a picture of how chaotic the resulting flows are after transition, we plot entropy Q in Fig. 22. It is seen that for none of the cases does Q go to zero, and hence the resulting flows are chaotic. Additionally it must be noted that Q defined in Eq. (17) is an integral measure over the computational box. At these rotations, we are seeing one side of the channel getting laminarized with the vortex structures concentrated on the other side. This means that the contribution to Q in these cases is not very significant in the laminarized side of the channel. Despite such a situation, the values of Q are fairly high when compared to the low rotation cases. This suggests that the regions where the secondary flow does persist offer extremely chaotic dynamics.

V. CONCLUSION

In this article, we focus on the role of algebraic disturbances in the transition scenario of the rotating channel in various rotation regimes. We show that the critical modal Reynolds number for the rotating channel flow does not coincide the energy critical Reynolds number for all rotation regimes. As a consequence, transient amplification of disturbances is observed in modally stable regions in the Re - Ro phase plane. Interestingly, we show that the energy critical Reynolds number is only feebly sensitive to the rotation rate, in stark contrast to the modal behavior. On a given side of the modally stable region (i.e., at low and high Ro) at a given Reynolds number, the optimal transient growth does not vary much with the rotation rate at a given Re . However, the insensitivity to rotation on either side of the neutral curve has very different origins. It is only in the vicinity of the neutral boundary in Re - Ro parameter space that discernible changes in the optimal characteristics are observed.

At low rotation rates, the transient growth of disturbance kinetic energy is due to the lift-up effect and is subsequently shown to be important while considering transition. The optimal transient growth amplitudes and the corresponding optimal wavenumbers obtained are close to those for the nonrotating channel. It is a consequence of rotation serving as a correction to the dynamics of the channel flow. However, even at extremely low rotation rates, the optimal structure breaks centerline symmetry due to the Coriolis force, with larger asymmetry closer to the neutral boundary. At extremely large rotation rates, consistent with the Taylor-Proudman theorem, all variation along the axis of rotation is inhibited. The streamwise-independent disturbances which yield the largest transient growth at low Ro are therefore now suppressed. Thus, we see only weakly growing

perturbations that evolve transiently due to the Orr mechanism that is completely unaffected by the strength of the rotation.

Within the modally unstable regime, we have shown that initial disturbances can grow algebraically before the most unstable mode alone emerges. While it is impractical to perform an optimization over all wavenumbers and time, we can deal with a more tractable problem by specifying a target time T_{tar} , where we are interested in the initial condition yielding the largest gain. Beyond a particular target time τ^* , the initial condition that gives the best gain in comparison to when the unstable mode is alone introduced becomes invariant. This suggests τ^* defines a window where nonmodal behavior prevails before the unstable mode becomes dominant. For a wide range of values of Ro within the unstable regime, this algebraic gain suggests that linear nonmodal mechanisms are still important as they raise the energy of the unstable mode and accelerate the transition process.

We solve the incompressible Navier-Stokes equations using direct numerical simulations for better understanding the processes in the modally unstable regime. When the rotation rate is low, both modally stable and unstable, we have shown that transition occurs similarly to the subcritical manner of the nonrotating case. The transient amplification of the disturbance triggers nonlinearity, and transition ensues. Vortical structures fill the entire domain, and the nonlinear statistical steady states obtained resemble that of the turbulent nonrotating channel flow. This behavior is observed over a wide range of initial disturbance amplitudes, except at extremely low initial energy of the disturbance where the unstable mode emerges after the transients boost the disturbance energy, and the secondary flow grows exponentially until the nonlinear terms become important. Similar features in Görtler flow have also been observed where transition can be aided by the boosting of the unstable mode energy by algebraic mechanisms [54,55]. This suggests that algebraic nonmodal mechanisms are likely to be relevant even when exponential instabilities exist in certain parameter regimes due to the inherent nonnormal nature of the dynamics in shear flows.

On increasing the rotation rate to moderate levels ($Ro \sim 0.2$), the Coriolis force expectedly manifests itself in a more pronounced manner. Initial disturbances rapidly evolve into the most unstable eigenmode, and the resulting transitioned flow is strongly vortical with no characteristic structure or organization. This is in sharp contrast to the elongated structures seen at both lower and higher rotation rates. With further increase in rotation rate, the secondary (chaotic) flow is increasingly localized toward one wall, becoming smaller until it finally disappears. At high rotation rates, the base flow is extremely stable to nonmodal disturbances, as expected. At such values of Ro , the effect of algebraic processes is negligible.

In summary, for the rotating channel flow, we have shown distinct behavior patterns at low, intermediate, and higher rotation rates, and the switchover between these is gradual with change in rotation rate. It is clear that algebraic growth can contribute decisively toward the transition in the rotating channel flow in a range of rotation rates.

ACKNOWLEDGMENTS

The Indo-French Centre for the Promotion of Advanced Research (IFCPAR)/Centre Franco-Indien pour la Promotion de la Recherche Avancée (CEFIPRA) is gratefully acknowledged for its financial support. S.J. would like to thank Prof. Luca Brandt at KTH Mechanics, Stockholm, for his help with understanding the SIMSON code. We are also grateful to the anonymous referees for their suggestions.

- [1] A. E. Gill, *Atmosphere-Ocean Dynamics*, International Geophysics Series Vol. 30 (Academic Press, San Diego, USA, 1982).
- [2] G. K. Vallis, *Atmospheric and Oceanic Fluid Dynamics: Fundamentals and Large-Scale Circulation* (Cambridge University Press, Cambridge, UK, 2006).

- [3] P. R. N. Childs, *Rotating Flow* (Elsevier, Oxford, UK, 2011).
- [4] G. I. Taylor, Motion of solids in fluids when the flow is not irrotational, *Proc. R. Soc. London, Ser. A* **93**, 99 (1917).
- [5] J. Proudman, On the motion of solids in a liquid possessing vorticity, *Proc. R. Soc. London, Ser. A* **92**, 408 (1916).
- [6] P. Bradshaw, The analogy between streamline curvature and buoyancy in turbulent shear flow, *J. Fluid Mech.* **36**, 177 (1969).
- [7] T. J. Pedley, On the instability of viscous flow in a rapidly rotating pipe, *J. Fluid Mech.* **35**, 97 (1969).
- [8] J. E. Hart, Instability and secondary motion in a rotating channel flow, *J. Fluid Mech.* **45**, 341 (1971).
- [9] J. P. Johnston, R. M. Halleen, and D. K. Lezius, Effects of spanwise rotation on the structure of two-dimensional fully developed turbulent channel flow, *J. Fluid Mech.* **56**, 533 (1972).
- [10] D. K. Lezius and J. P. Johnston, Roll-cell instabilities in rotating laminar and turbulent channel flows, *J. Fluid Mech.* **77**, 153 (1976).
- [11] P. H. Alfredsson and H. Persson, Instabilities in channel flow with system rotation, *J. Fluid Mech.* **202**, 543 (1989).
- [12] S. Yanase, C. Flores, O. Métais, and J. J. Riley, Rotating free-shear flows, I: Linear stability analysis, *Phys. Fluids A* **5**, 2725 (1993).
- [13] D. P. Wall and M. Nagata, Nonlinear secondary flow through a rotating channel, *J. Fluid Mech.* **564**, 25 (2006).
- [14] P. G. Drazin and W. H. Reid, *Hydrodynamic Stability* (Cambridge University Press, Cambridge, UK, 2004).
- [15] S. Wallin, O. Grundestam, and A. V. Johansson, Laminarization mechanisms and extreme-amplitude states in rapidly rotating plane channel flow, *J. Fluid Mech.* **730**, 193 (2013).
- [16] W. H. Finlay, Transition to oscillatory motion in rotating channel flow, *J. Fluid Mech.* **215**, 209 (1990).
- [17] W. H. Finlay, Transition to turbulence in a rotating channel, *J. Fluid Mech.* **237**, 73 (1992).
- [18] K.-S. Yang and J. Kim, Numerical investigation of instability and transition in rotating plane Poiseuille flow, *Phys. Fluids A* **3**, 633 (1991).
- [19] M. Matsubara and P. H. Alfredsson, Secondary instability in rotating channel flow, *J. Fluid Mech.* **368**, 27 (1998).
- [20] D. P. Wall and M. Nagata, Three-dimensional exact coherent states in rotating channel flow, *J. Fluid Mech.* **727**, 533 (2013).
- [21] C. A. Daly, T. M. Schneider, P. Schlatter, and N. Peake, Secondary instability and tertiary states in rotating plane Couette flow, *J. Fluid Mech.* **761**, 27 (2014).
- [22] R. Kristoffersen and H. I. Andersson, Direct simulations of low-Reynolds-number turbulent flow in a rotating channel, *J. Fluid Mech.* **256**, 163 (1993).
- [23] E. Lamballais, O. Métais, and M. Lesieur, Spectral-dynamic model for large-eddy simulations of turbulent rotating channel flow, *Theor. Comp. Fluid Dyn.* **12**, 149 (1998).
- [24] O. Grundestam, S. Wallin, and A. V. Johansson, Direct numerical simulations of rotating turbulent channel flow, *J. Fluid Mech.* **598**, 177 (2008).
- [25] Z. Xia, Y. Shi, and S. Chen, Direct numerical simulation of turbulent channel flow with spanwise rotation, *J. Fluid Mech.* **788**, 42 (2016).
- [26] P. Yecko and M. Rossi, Transient growth and instability in rotating boundary layers, *Phys. Fluids* **16**, 2322 (2004).
- [27] P. A. Yecko, Accretion disk instability revisited-transient dynamics of rotating shear flow, *Astron. Astrophys.* **425**, 385 (2004).
- [28] G. D. Chagelishvili, J-P. Zahn, A. G. Tevzadze, and J. G. Lominadze, On hydrodynamic shear turbulence in Keplerian disks: Via transient growth to bypass transition, *Astron. Astrophys.* **402**, 401 (2003).
- [29] B. Mukhopadhyay, N. Afshordi, and R. Narayan, Growth of hydrodynamic perturbations in accretion disks: Possible route to non-magnetic turbulence, *Adv. Space Res.* **38**, 2877 (2006).
- [30] P. J. Schmid and D. S. Henningson, *Stability and Transition in Shear Flows* (Springer-Verlag, Berlin, 2001).
- [31] P. J. Schmid, Nonmodal stability theory, *Ann. Rev. Fluid Mech.* **39**, 129 (2007).

- [32] C. G. Speziale and S. Thangam, Numerical study of secondary flows and roll-cell instabilities in rotating channel flow, *J. Fluid Mech.* **130**, 377 (1983).
- [33] D. J. Tritton and P. A. Davies, Instabilities in geophysical fluid dynamics, in *Hydrodynamic Instabilities and the Transition to Turbulence*, edited by H. L. Swinney and J. P. Gollub (Springer, Berlin, 1985), pp. 229–270.
- [34] S. Sipp, E. Lauga, and L. Jacquin, Vortices in rotating systems: Centrifugal, elliptic, and hyperbolic type instabilities, *Phys. Fluids* **11**, 3716 (1999).
- [35] R. C. Prima and G. J. Habetler, A completeness theorem for non-self-adjoint eigenvalue problems in hydrodynamic stability, *Arch. Rat. Mech. Anal.* **34**, 218 (1969).
- [36] J. A. Weideman and S. C. Reddy, A MATLAB differentiation matrix suite, *ACM Trans. Math. Software* **26**, 465 (2000).
- [37] D. D. Joseph, *Stability of Fluid Motions I* (Springer-Verlag, Berlin, 1976).
- [38] D. D. Joseph and S. Carmi, Stability of Poiseuille flow in pipes, annuli, and channels, *Q. Appl. Math.* **26**, 575 (1969).
- [39] S. C. Reddy and D. S. Henningson, Energy growth in viscous channel flows, *J. Fluid Mech.* **252**, 209 (1993).
- [40] M. T. Landahl, A note on an algebraic instability of inviscid parallel shear flows, *J. Fluid Mech.* **98**, 243 (1980).
- [41] W. M'F. Orr, The stability or instability of the steady motions of a perfect liquid and of a viscous liquid. Part I: A perfect liquid, *Proc. R. Irish Acad. A* **27**, 9 (1907).
- [42] L. H. Gustavsson, Energy growth of three-dimensional disturbances in plane Poiseuille flow, *J. Fluid Mech.* **224**, 241 (1991).
- [43] C. A. Daly, Nonlinear and non-modal stability of structures evolving in shear flows, Ph.D. thesis, University of Cambridge, Cambridge, UK, 2014.
- [44] S. Yanase and Y. Kaga, Zero-mean-absolute-vorticity state and vortical structures in rotating channel flow, *J. Phys. Soc. Jpn.* **73**, 1419 (2004).
- [45] M. Chevalier, P. Schlatter, A. Lundbladh, and D. S. Henningson, SIMSON: A pseudo-spectral solver for incompressible boundary layer flows, Tech. Rep. (KTH Mechanics, Stockholm, Sweden, 2007).
- [46] S. C. Reddy, P. J. Schmid, J. S. Baggett, and D. S. Henningson, On stability of streamwise streaks and transition thresholds in plane channel flows, *J. Fluid Mech.* **365**, 269 (1998).
- [47] P. A. Elofsson, M. Kawakami, and P. H. Alfredsson, Experiments on the stability of streamwise streaks in plane Poiseuille flow, *Phys. Fluids* **11**, 915 (1999).
- [48] B. G. B. Klingmann, On transition due to three-dimensional disturbances in plane Poiseuille flow, *J. Fluid Mech.* **240**, 167 (1992).
- [49] T. Srikanth, H. N. Dixit, R. Tatavarti, and R. Govindarajan, Vortex shedding patterns, their competition, and chaos in flow past inline oscillating rectangular cylinders, *Phys. Fluids* **23**, 073603 (2011).
- [50] J. Jeong and F. Hussain, On the identification of a vortex, *J. Fluid Mech.* **285**, 69 (1995).
- [51] K. H. Bech and H. I. Andersson, Turbulent plane Couette flow subject to strong system rotation, *J. Fluid Mech.* **347**, 289 (1997).
- [52] E. Lamballais, M. Lesieur, and O. Métais, Effects of spanwise rotation on the vorticity stretching in transitional and turbulent channel flow, *Int. J. Heat Fluid Flow* **17**, 324 (1996).
- [53] M. Tanaka, S. Kida, S. Yanase, and G. Kawahara, Zero-absolute-vorticity state in a rotating turbulent shear flow, *Phys. Fluids* **12**, 1979 (2000).
- [54] L.-U. Schrader, L. Brandt, and T. A. Zaki, Receptivity, instability, and breakdown of Görtler flow, *J. Fluid Mech.* **682**, 362 (2011).
- [55] J.-M. Lucas, O. Vermeersch, and D. Arnal, Transient growth of Görtler vortices in two-dimensional compressible boundary layers: Application to surface waviness, *Eur. J. Mech. B* **50**, 132 (2015).

[A26]

Nonlinear travelling waves in rotating Hagen–Poiseuille flow

B. Pier & R. Govindarajan

Fluid Dynamics Research **50**, 031402 (14 pages) (2018)

doi:10.1088/1873-7005/aaaa9f
<https://hal.archives-ouvertes.fr/hal-01693277>

Nonlinear travelling waves in rotating Hagen–Poiseuille flow

Benoît Pier^{1,3}  and Rama Govindarajan²

¹ Laboratoire de mécanique des fluides et d'acoustique, CNRS—École centrale de Lyon—Université de Lyon 1—INSA de Lyon, 36 avenue Guy-de-Collongue, F-69134, Écully, France

² International Centre for Theoretical Sciences, Tata Institute of Fundamental Research, Survey No. 151, Shivakote, Hesaraghatta Hobli, Bengaluru 560 089, India

E-mail: benoit.pier@ec-lyon.fr

Received 17 July 2017, revised 4 January 2018

Accepted for publication 25 January 2018

Published 29 March 2018



Communicated by Yasuhide Fukumoto

Abstract

The dynamics of viscous flow through a rotating pipe is considered. Small-amplitude stability characteristics are obtained by linearizing the Navier–Stokes equations around the base flow and solving the resulting eigenvalue problems. For linearly unstable configurations, the dynamics leads to fully developed finite-amplitude perturbations that are computed by direct numerical simulations of the complete Navier–Stokes equations. By systematically investigating all linearly unstable combinations of streamwise wave number k and azimuthal mode number m , for streamwise Reynolds numbers $Re_z \leqslant 500$ and rotational Reynolds numbers $Re_\Omega \leqslant 500$, the complete range of nonlinear travelling waves is obtained and the associated flow fields are characterized.

Keywords: pipe flow, instabilities, nonlinearity, rotation

(Some figures may appear in colour only in the online journal)

1. Introduction

The axial flow through a rotating pipe has been studied over decades, both for its fundamental importance and for its wide application in turbomachinery and other fluid machines. Rotation changes the basic nature of the instability of the laminar Hagen–Poiseuille flow (Pedley 1968, 1969, Mackrodt 1976, Cotton and Salwen 1981, Fernandez-Feria and del Pino 2002, Rusak and

³ Author to whom any correspondence should be addressed.

Wang 2014, Miranda-Barea *et al* 2016) and the subsequent route towards turbulence. The final turbulent state too is rather different from that in the non-rotating pipe (Imao *et al* 1996).

The laminar flow through a non-rotating pipe is linearly stable at all Reynolds numbers in that all eigenmodes are exponentially decaying. The transition to turbulence takes place by means of a subcritical route, due to the non-normality of the stability operator, and the consequent algebraic growth of disturbances. In contrast, when the pipe wall is in rotation about the pipe axis, exponentially growing disturbances are supported, and the nonlinear evolution is supercritical. Pedley (1968) showed that the inviscid flow in the limit of strong pipe rotation and weak axial flow is linearly unstable to long wave disturbances. He extended his study to viscous flow in the following year (Pedley 1969) to show that rotating Hagen–Poiseuille flow (RHPF) in the same strong rotation limit is linearly unstable to long waves above a critical Reynolds number of 82.9. The mode that was found to be least stable was a corkscrew mode which propagates axially in the direction of the flow but rotates in a sense opposite to that of the walls of the pipe. Given the symmetries in the problem, this mode is equivalent to one which propagates axially in a sense opposite to the axial mean flow but rotates in the same sense as the pipe. Mackrodt (1976) extended this study to lower rotation rates and showed that the flow can still be linearly unstable at fairly low rotation rates. This work also showed experimentally that residual swirl in the entry region can trigger instabilities. A comprehensive study of the linear stability of the RHPF was carried out by Cotton and Salwen (1981), extending the earlier results to higher axial wave-numbers and a range of azimuthal mode numbers. By deriving neutral stability curves, they noticed that the critical Reynolds number is only weakly dependent on the rotation number provided that the latter is large enough, and that similarly the critical rotation number is only weakly dependent on the Reynolds number provided that the Reynolds number is large enough. In other words, the unstable region is approximately delimited by lines of either constant Reynolds number or constant rotation number. An asymptotic theory for the draining bathtub vortex was given by Foster (2014), and there are a host of such studies of swirling flows where the pipe walls are stationary, which we do not discuss here. Analogously, Rusak and Wang (2014) conducted an inviscid study of solid body rotation accompanied by uniform axial flow and found a critical swirl ratio, above which there are two kinds of nonlinear states.

Given that a Hagen–Poiseuille flow through a stationary pipe is linearly stable to all convective modes, this flow can obviously never be absolutely unstable. In contrast, RHPF can display modes of absolute instability, as was shown by Fernandez-Feria and del Pino (2002). These modes of absolute instability were obtained experimentally in the recent study of Miranda-Barea *et al* (2016). They applied a spin-down to the pipe and could thus obtain the critical rotation rate for the switch from absolute instabilities to convective.

Some studies of the nonlinear evolution of disturbances have been carried out on the RHPF. Toplosky and Akylas (1988) resolved a controversy as to whether the nonlinear evolution is supercritical or subcritical, and found no subcritical nonlinearities. All subsequent nonlinear studies to our knowledge, and also the present study, find only supercritical growth of perturbations in the nonlinear regime. In fact the boundary of linear neutral stability also marks the onset of nonlinear evolution of wave trains. This was seen explicitly in the study of Yang and Leibovich (1991) which focused on the close vicinity of the neutral stability boundary. The predicted linear and nonlinear modes were confirmed qualitatively in the experiments of Imao *et al* (1992). Furthermore, these experiments have shown how the initially sinusoidal perturbations adopted a saw-tooth form in their nonlinear state. Far downstream, perturbations other than the least stable linear mode were triggered, and the disturbance spectrum became broadband. Landman (1990) imposed the constraint of helical symmetry, and demonstrated that the nonlinear state goes through several bifurcations and results in a time-dependent flow. Barnes and Kerswell (2000) found three-dimensional travelling waves which appeared after a bifurcation from the solutions found by Toplosky and Akylas (1988).

A range of studies focus on pipes where the flow is not streamwise independent. One situation is of course when the pipe is finite, so entry and exit flows dictate the dynamics, see e.g. Sanmiguel-Rojas and Fernandez-Feria (2005). Dennis *et al* (2014) created a vortex breakdown in a pipe where one part was rotating faster than a critical rate. The fully turbulent flow through a rotating pipe is not a topic of the present study, but it is of interest to note that while rotation acts to destabilise the laminar flow and provide a supercritical route to turbulence, the resulting turbulence may be suppressed by rotation (Imao *et al* 1996).

The objective of the present investigation is to systematically derive and characterize the family of nonlinear travelling-wave solutions sustained in RHPF. Therefore we study the nonlinear evolution of a class of travelling waves over a range of the relevant parameters in a periodic box. We show that the dynamics saturates into a nonlinear state of a system of travelling waves. In all cases, the most energetic nonlinear state has longer wavelength than that of the corresponding fastest growing linear eigenmode.

2. Problem formulation

In this study, the fluid flow is described by a vector velocity field $\mathbf{u}(\mathbf{x}, t)$ and a scalar pressure field $p(\mathbf{x}, t)$ that depend on position \mathbf{x} and time t and are governed by the incompressible Navier–Stokes equations

$$\frac{\partial \mathbf{u}}{\partial t} + (\mathbf{u} \cdot \nabla) \mathbf{u} = \nu \Delta \mathbf{u} - \nabla p, \quad (1)$$

$$\nabla \cdot \mathbf{u} = 0, \quad (2)$$

where ν is the kinematic viscosity of the fluid, and the pressure has been redefined to eliminate the constant fluid density from the equations. The flow occurs inside a pipe of radius R which is rotating at rate Ω about its axis and no-slip boundary conditions prevail along the pipe walls. A fixed cylindrical coordinate system will be used where r, θ and z denote radial, azimuthal and axial coordinates respectively, and $r = 0$ coincides with the pipe axis.

In the RHPF configuration, the flow is driven by the combination of two factors: a constant axial pressure gradient and the rotating pipe walls. The resulting steady, axisymmetric and axially invariant base flow is then an exact superposition of an axial parabolic velocity profile U_z and an azimuthal solid-body rotation U_θ depending only on the radial coordinate r as

$$U_z(r) = 2\bar{U} \left(1 - \frac{r^2}{R^2}\right) \quad \text{and} \quad U_\theta(r) = \Omega r, \quad (3)$$

where \bar{U} is the mean axial velocity, associated with an axial pressure gradient of magnitude $G_z = 8\nu\bar{U}/R^2$. This flow is governed by two non-dimensional control parameters, the streamwise and azimuthal (or rotational) Reynolds numbers defined as

$$Re_z \equiv 2\bar{U}R/\nu \quad \text{and} \quad Re_\Omega \equiv 2\Omega R^2/\nu \quad (4)$$

respectively. With this definition, the ratio Re_Ω/Re_z corresponds to the ratio of the azimuthal pipe wall velocity to the mean axial flow velocity. In the sequel, units used for giving numerical results are based on the pipe diameter $2R$ and the mean axial velocity \bar{U} .

Throughout this investigation, the total instantaneous flow fields are separated into basic and perturbation quantities as

$$u_r^{\text{tot}}(r, \theta, z, t) = u_r(r, \theta, z, t), \quad (5)$$

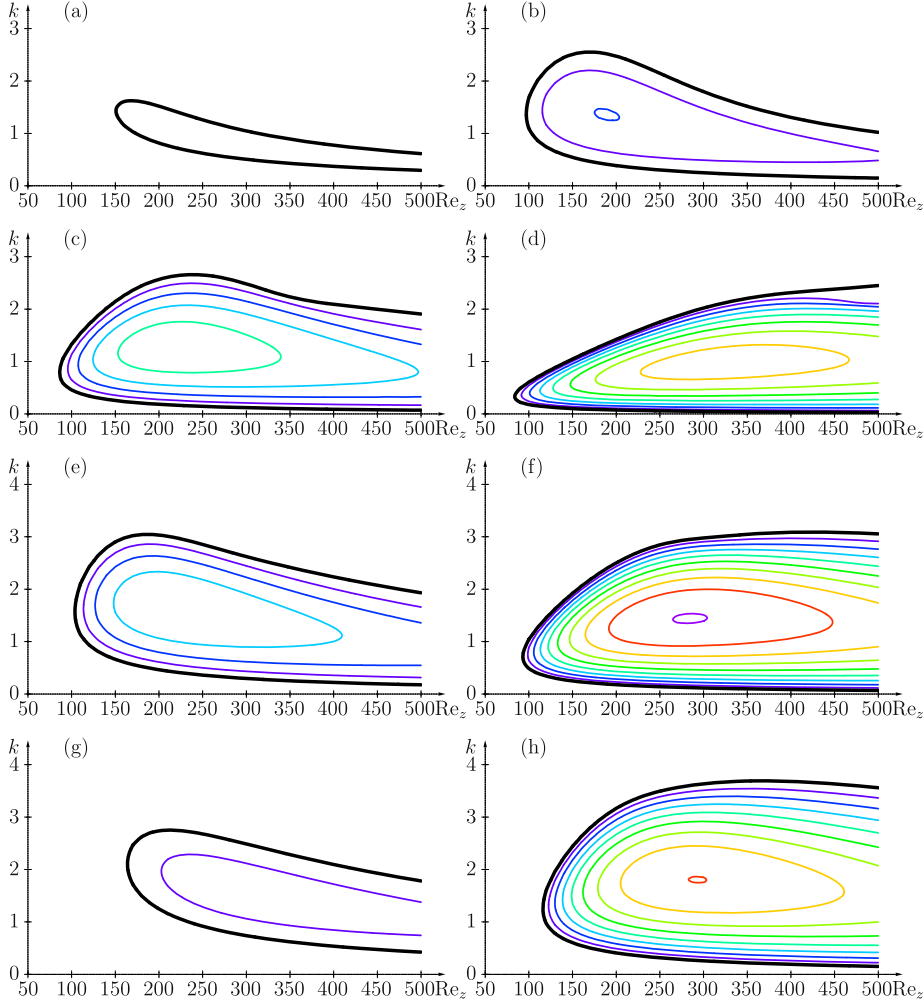


Figure 1. Temporal growth rate ω_i in (Re_z, k) -plane for (a) $m = -1$, $Re_\Omega = 60$, (b) $m = -1$, $Re_\Omega = 100$, (c) $m = -1$, $Re_\Omega = 200$, (d) $m = -1$, $Re_\Omega = 500$, (e) $m = -2$, $Re_\Omega = 200$, (f) $m = -2$, $Re_\Omega = 500$, (g) $m = -3$, $Re_\Omega = 200$ and (h) $m = -3$, $Re_\Omega = 500$. Thick black lines correspond to the marginal curve $\omega_i = 0$ and thin coloured lines to positive growth rates $\omega_i = 0.1, 0.2, 0.3, 0.4, \dots$

$$u_\theta^{\text{tot}}(r, \theta, z, t) = U_\theta(r) + u_\theta(r, \theta, z, t), \quad (6)$$

$$u_z^{\text{tot}}(r, \theta, z, t) = U_z(r) + u_z(r, \theta, z, t), \quad (7)$$

$$p^{\text{tot}}(r, \theta, z, t) = -G_z z + p(r, \theta, z, t), \quad (8)$$

whether the perturbation is of small amplitude or not. Replacing these expansions into the Navier–Stokes equations (1) and (2) then yields the governing equations for the perturbation flow fields u_r , u_θ , u_z and p .

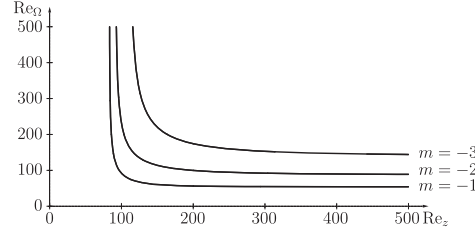


Figure 2. Neutral curves in (Re_z, Re_Ω) -plane for $m = -1, -2, -3$.

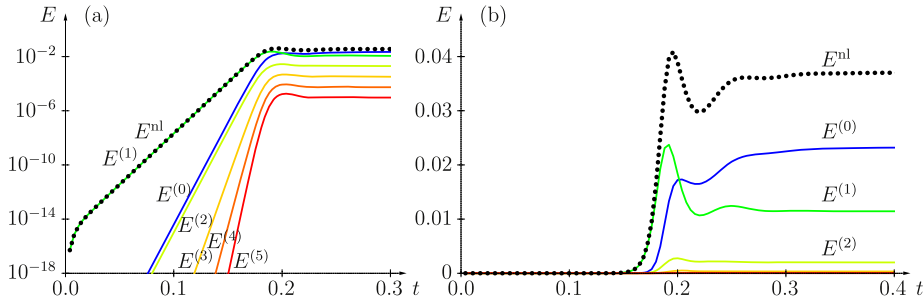


Figure 3. Temporal evolution of $E^{(n)}$, kinetic energy contained in each spatial Fourier component, and of total E^{nl} , resulting from a small-amplitude initial perturbation at $k = 1$ and $m = -1$ for $Re_z = 250$ and $Re_\Omega = 200$, plotted on (a) logarithmic and (b) linear scales.

When analysing the dynamics of small-amplitude perturbations, the disturbances may be written in normal-mode form as

$$u_r(r, \theta, z, t) = \hat{u}_r(r) \exp i(kz + m\theta - \omega t), \quad (9)$$

$$u_\theta(r, \theta, z, t) = \hat{u}_\theta(r) \exp i(kz + m\theta - \omega t), \quad (10)$$

$$u_z(r, \theta, z, t) = \hat{u}_z(r) \exp i(kz + m\theta - \omega t), \quad (11)$$

$$p(r, \theta, z, t) = \hat{p}(r) \exp i(kz + m\theta - \omega t), \quad (12)$$

where k is an axial wave number, m an azimuthal mode number and ω a (complex) frequency. Linearization of the governing equations then leads to eigenvalue problems, the solution of which yields the ω -eigenvalue spectrum together with the associated eigenfunctions $\hat{u}_r(r)$, $\hat{u}_\theta(r)$, $\hat{u}_z(r)$ and $\hat{p}(r)$, for each setting of k , m , Re_z and Re_Ω . Usually, the spectrum is dominated by a single eigenvalue and its identification then yields the linear dispersion relation as

$$\omega = \omega^{\text{lin}}(k, m; Re_z, Re_\Omega). \quad (13)$$

In unstable situations, characterized by positive growth rates $\omega_i \equiv \text{Im } \omega$, an initial spatially periodic small-amplitude perturbation may be exponentially amplified in time and eventually reach finite amplitudes, thus be governed by the full nonlinear equations. The resulting nonlinear dynamics is then investigated by using spatial Fourier series of the form

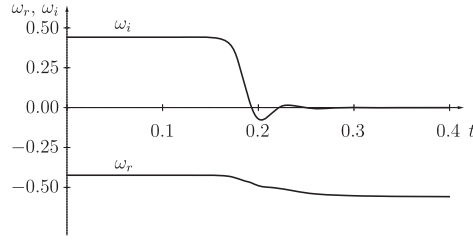


Figure 4. Temporal evolution of instantaneous frequency $\omega = \omega_r + i\omega_i$ from the linear growth phase ($\omega^{\text{lin}} = -0.42 + 0.44i$) to the saturation regime ($\omega^{\text{nl}} = -0.56$). Same configuration as figure 3.

$$u_r(r, \theta, z, t) = \sum_n u_r^{(n)}(r, t) \exp in(kz + m\theta), \quad (14)$$

$$u_\theta(r, \theta, z, t) = \sum_n u_\theta^{(n)}(r, t) \exp in(kz + m\theta), \quad (15)$$

$$u_z(r, \theta, z, t) = \sum_n u_z^{(n)}(r, t) \exp in(kz + m\theta), \quad (16)$$

$$p(r, \theta, z, t) = \sum_n p^{(n)}(r, t) \exp in(kz + m\theta), \quad (17)$$

and integrating in time the nonlinear temporal evolution problem consisting in a system of coupled partial differential equations for the components $u_r^{(n)}(r, t)$, $u_\theta^{(n)}(r, t)$, $u_z^{(n)}(r, t)$ and $p^{(n)}(r, t)$. This is equivalent to considering a finite domain with periodic boundary conditions and investigating the dynamics of finite-amplitude disturbances at prescribed total axial pressure gradient. The numerical implementation of this time-marching problem uses a second-order accurate predictor–corrector fractional-step method, similar to the one described in detail in Pier and Schmid (2017). Complete expressions and derivations of the linear and nonlinear governing equations as well as numerical solution methods may be found in Pier (2015).

It should be emphasized that the use of single spatial Fourier series in expansions (14)–(17), instead of double series using terms of the form $\exp i(nkz + lm\theta)$ with $n \neq l$, is motivated by our objective of computing primary nonlinear travelling wave solutions, rather than studying their stability with respect to secondary perturbations. Indeed, starting from a linearly unstable small-amplitude initial perturbation of the form $\exp i(kz + m\theta)$, the nonlinearities of the Navier–Stokes equations only promote spatial harmonics of the form $\exp in(kz + m\theta)$, while terms of the form $\exp i(nkz + lm\theta)$ with $n \neq l$ would only be generated by secondary instabilities.

3. Results

3.1. Linear dynamics

The dynamics of small-amplitude perturbations is governed by the dispersion relation (13) derived from a normal-mode analysis of the Navier–Stokes equations linearized around the base flow (3). In this subsection we repeat some of the results obtained by previous authors to

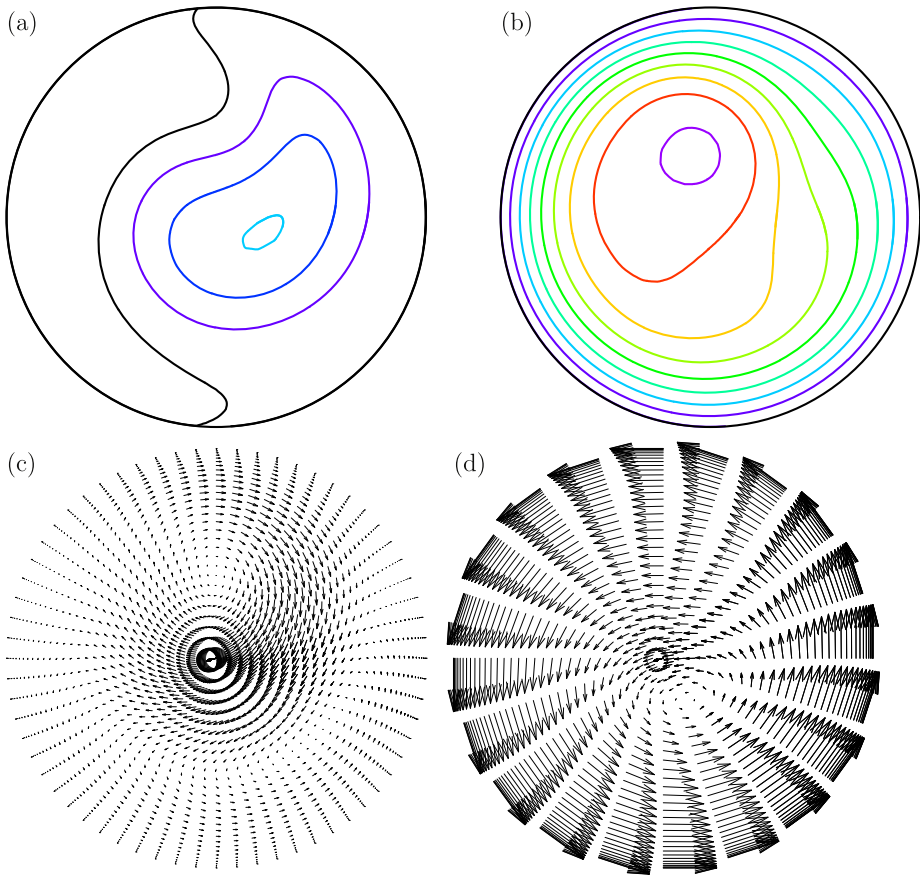


Figure 5. Velocity fields of saturated nonlinear travelling wave at $k = 1$ and $m = -1$ for $Re_z = 250$ and $Re_\Omega = 200$: (a), (b) axial component and (c), (d) in-plane velocity for ((a), (c)) perturbation and ((b), (d)) total flow. In (a), coloured lines correspond to negative velocities -0.2 , -0.4 and -0.6 . In (b), coloured lines correspond to positive velocities 0.2 , ..., 1.6 . Black lines indicate vanishing values.

validate our approach and identify the parameter space of interest for the subsequent investigation of nonlinear travelling-wave solutions.

Temporal growth rates ω_i corresponding to the most unstable mode are shown in figure 1 over the (Re_z, k) -plane for $Re_z \leq 500$ and different values of Re_Ω and m . For $m = -1$ (figures 1(a)–(d)), the RHPF becomes already unstable at $Re_\Omega = 60$, while higher values of Re_Ω are required for $m = -2$ (figures 1(e)–(f)) and $m = -3$ (figures 1(g)–(h)). These results fully agree with those obtained by Cotton and Salwen (1981).

The critical curves for onset of instability in the (Re_z, Re_Ω) -plane are shown in figure 2 for $m = -1, -2$ and -3 . As already noticed by Cotton and Salwen (1981), these critical curves asymptote towards constant values of Re_z or of Re_Ω . Except for low values of both Re_z and Re_Ω , onset of instability thus only depends on the lowest of these two control parameters. For parameter values within the linearly unstable regions, growing perturbations lead to a fully developed regime, analysed in detail in the rest of this paper.

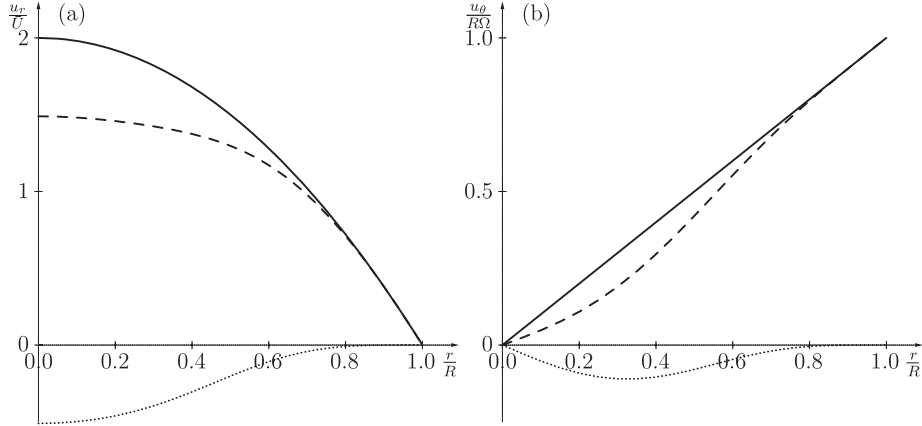


Figure 6. (a) Axial and (b) azimuthal mean velocity profiles prevailing for the fully developed nonlinear travelling wave: comparison of base profile (solid), mean flow correction (dotted) and total mean profile (dashed). Same parameter settings as in figures 3 and 5.

3.2. Nonlinear travelling waves

In configurations where the base flow displays linear temporal instability, a small-amplitude perturbation with a positive growth rate is exponentially amplified and eventually reaches finite-amplitude levels. The nonlinear terms in the Navier–Stokes equations can then no longer be neglected and the dynamics is governed by the complete nonlinear equations. The aim of this investigation is to systematically derive and characterize the resulting fully developed travelling wave solutions for $Re_z \leq 500$ and $Re_\Omega \leq 500$.

The approach is here based on temporal evolution problems investigated by direct numerical simulations of the Navier–Stokes equations. Starting from a small-amplitude initial perturbation, the evolution is first dictated by linear dynamics before nonlinear effects come into play. In the absence of secondary instabilities, a fully developed regime is reached with spatial periodicity imposed by the prescribed values of streamwise wave number k and azimuthal mode number m . As already mentioned in the Introduction, no sign of a subcritical transition has been found. This approach is therefore deemed to yield all nonlinear wave solutions that may prevail in the RHPF, for the control-parameter region under consideration.

A typical scenario may be illustrated by considering the temporal evolution of a perturbation at $k = 1$ and $m = -1$ for $Re_z = 250$ and $Re_\Omega = 200$. At these parameter values the linear dispersion relation yields a complex frequency of $\omega^{\text{lin}} = -0.42 + 0.44i$, with a positive temporal growth rate. Figure 3 shows the temporal evolution of the energy $E^{(n)}$ contained in each spatial harmonic together with the total $E^{\text{nl}} \equiv \sum_{n \geq 0} E^{(n)}$, both on logarithmic and linear scales; the energy $E^{(n)}$ is here defined as the spatially averaged kinetic energy per unit volume associated with the Fourier component corresponding to n and $-n$ of the expansions (14)–(16).

In the first stage of the evolution, here approximately for $t < 0.15$, the perturbation is seen to grow exponentially: the energy $E^{(1)}(t)$ in the fundamental component is amplified as $e^{2\omega_l t}$, while the higher harmonics ($n \geq 2$) are slaved by nonlinear interaction to the fundamental as $E^{(n)}(t) \propto [E^{(1)}(t)]^n$ and the mean-flow correction as $E^{(0)}(t) \propto [E^{(1)}(t)]^2$, see figure 3(a). The nonlinearities are stabilizing and therefore lead to saturation at finite

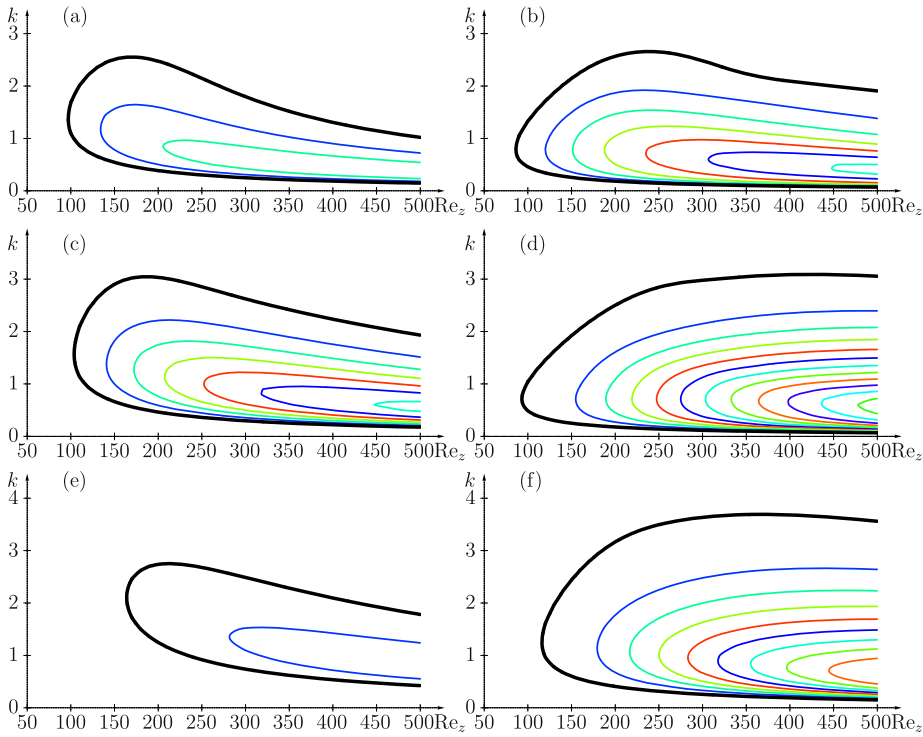


Figure 7. Levels of total disturbance energy E^{nl} in the (Re_z, k) -plane for (a) $m = -1$, $Re_\Omega = 100$, (b) $m = -1$, $Re_\Omega = 200$, (c) $m = -2$, $Re_\Omega = 200$, (d) $m = -2$, $Re_\Omega = 500$, (e) $m = -3$, $Re_\Omega = 200$, (f) $m = -3$, $Re_\Omega = 500$. Thick black lines correspond to the marginal curve and thin coloured lines to levels $E^{\text{nl}} = 0.005, 0.010, 0.015, \dots$

amplitude levels. In the absence of secondary instabilities, a fully nonlinear travelling-wave solution is then reached in the long-time limit with spatial periodicity imposed by the prescribed values of k and m and constant energy levels, see figure 3(b). For the final perturbation velocity and pressure fields (14)–(17) associated with this nonlinear travelling solution, each of the n th spatial Fourier components is found to depend on time as $\exp(-in\omega^{\text{nl}}t)$ for some real frequency ω^{nl} . This means that the flow fields are 2π -periodic functions of $kz + m\theta - \omega^{\text{nl}}t$, which is characteristic of three-dimensional solutions that travel without deforming. The nonlinear frequency ω^{nl} is related to the axial wave propagation speed as ω^{nl}/k and to the azimuthal wave rotation rate as ω^{nl}/m . Its value is obtained by the numerical simulations, which therefore yield the nonlinear dispersion relation

$$\omega^{\text{nl}}(k, m; Re_z, Re_\Omega). \quad (18)$$

In the example illustrated here, $\omega^{\text{nl}} = -0.56$. Monitoring the temporal evolution of the instantaneous complex frequency, figure 4 shows how the growth rate varies from $\omega_i = 0.44$ in the linear growth phase to a vanishing value in the saturation regime, while the real part of the frequency decreases from $\omega_r = -0.42$ to $\omega_r = -0.56$. As shown below (see figure 6(a)), this frequency reduction in the nonlinear régime is associated with the development of a negative mean-flow correction.

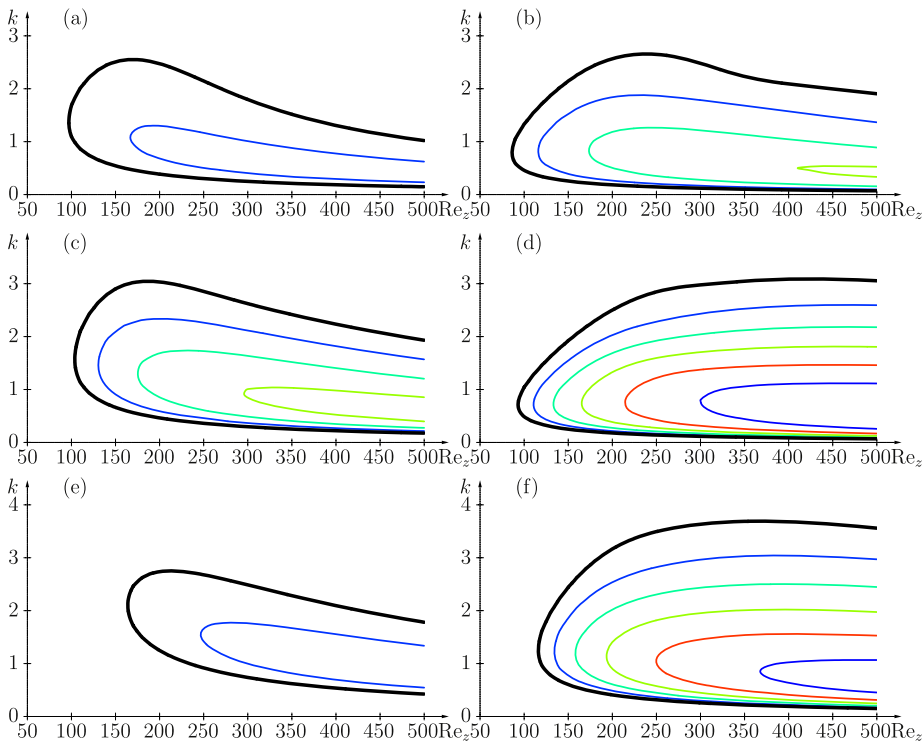


Figure 8. Relative axial mean flow-rate corrections for (a) $m = -1$, $Re_\Omega = 100$, (b) $m = -1$, $Re_\Omega = 200$, (c) $m = -2$, $Re_\Omega = 200$, (d) $m = -2$, $Re_\Omega = 500$, (e) $m = -3$, $Re_\Omega = 200$, (f) $m = -3$, $Re_\Omega = 500$. Thick black lines correspond to the marginal curve and thin coloured lines to levels $Q/Q_{bf} = -0.05, -0.10, -0.15, \dots$

Note that the fully developed nonlinear travelling waves could have been obtained by an iterative Newton–Raphson search procedure, a technique that we have used and implemented in a similar context for the three-dimensional rotating-disk boundary layer (Pier 2007). For the RHPF, however, that was not necessary since for the parameter space under consideration the time-marching procedure outlined in section 2 was always found to converge towards the desired finite-amplitude travelling wave solutions and, moreover, provides information about the transition from the linear growth phase to the saturated regime.

The velocity fields of this nonlinear travelling-wave solution are given in figure 5. Iso-lines of the axial velocity are shown in figures 5(a) and (b) for the nonlinear perturbation and the total flow respectively. The velocity field in a cross-section of the pipe is shown in figures 5(c) and (d), again for the perturbation and total flow. Due to the travelling-wave structure of this solution, plots at a different axial position z or different time t only differ from those shown in figure 5 by rotation in θ . The axial disturbance velocity component (figure 5(a)) is mostly negative and non-axisymmetric. Thus the resulting total axial velocity (figure 5(b)) is significantly reduced in comparison with the base Poiseuille profile and displays a maximum value slightly in excess of 1.6 off axis. Recall that the maximum axial Poiseuille velocity is 2 since the mean velocity \bar{U} is used as unit.

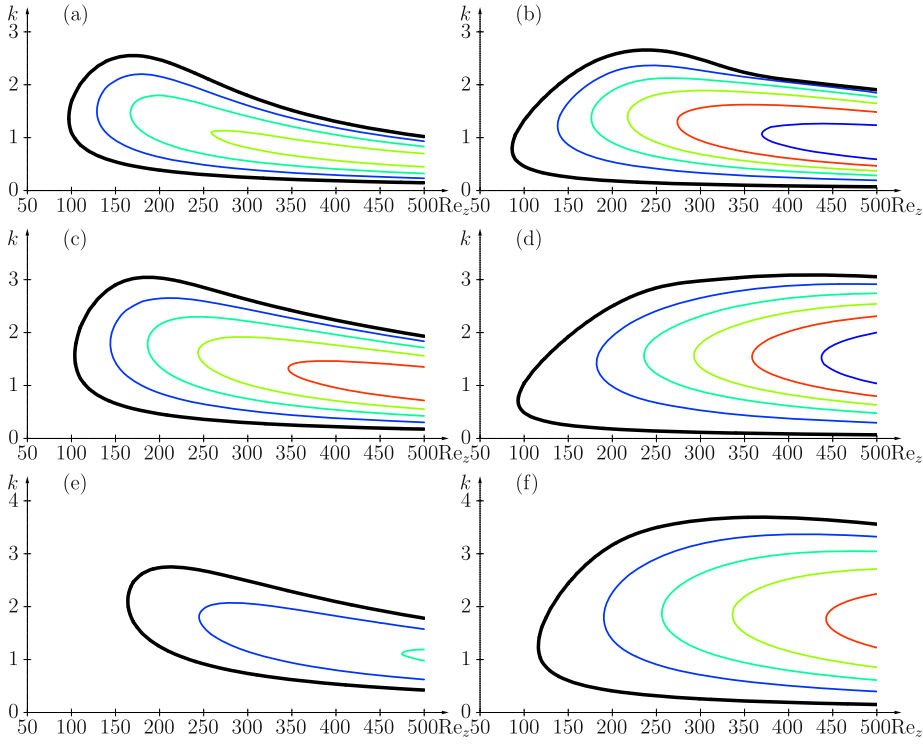


Figure 9. Relative mean angular momentum corrections for (a) $m = -1$, $Re_\Omega = 100$, (b) $m = -1$, $Re_\Omega = 200$, (c) $m = -2$, $Re_\Omega = 200$, (d) $m = -2$, $Re_\Omega = 500$, (e) $m = -3$, $Re_\Omega = 200$, (f) $m = -3$, $Re_\Omega = 500$. Thick black lines correspond to the marginal curve and thin coloured lines to levels $M/M_{bf} = -0.01, -0.02, -0.03 \dots$

The development of nonlinearities produce higher harmonics as well as an axisymmetric mean flow correction associated with the non-periodic component of the perturbation. Figure 6 compares the mean profiles prevailing in the fully developed regime with those of the unperturbed base flow, both for the axial (figure 6(a)) and the azimuthal (figure 6(b)) components. The effect of this mean flow correction is to reduce the total axial flow rate Q_{tot} as well as the total angular momentum M_{tot} of the flow: here $Q_{\text{tot}}/Q_{\text{bf}} = 0.88$ and $M_{\text{tot}}/M_{\text{bf}} = 0.97$, where Q_{bf} and M_{bf} refer to flow rate and momentum prevailing for the unperturbed base flow.

By varying the disturbance wave numbers k and m and the base flow control parameters Re_z and Re_Ω , the complete set of nonlinear travelling waves may be systematically computed. In the present investigation we have covered the full range of nonlinear solutions for $Re_z \leq 500$ and $Re_\Omega \leq 500$.

Isolines of the total disturbance energy E^{nl} associated with the nonlinear travelling waves are plotted in figure 7 in the (Re_z, k) -plane for selected values of m and Re_Ω . For $m = -1$ and $Re_\Omega = 100$, comparison of the linear temporal growth rates shown in figure 1(b) with the energy levels of the nonlinear saturated travelling waves shown in figure 7(a) clearly demonstrates the supercritical nature of the nonlinearities: the amplitude of nonlinear travelling waves vanishes as the critical curve for instability is approached. However, the largest values of E^{nl} do not coincide

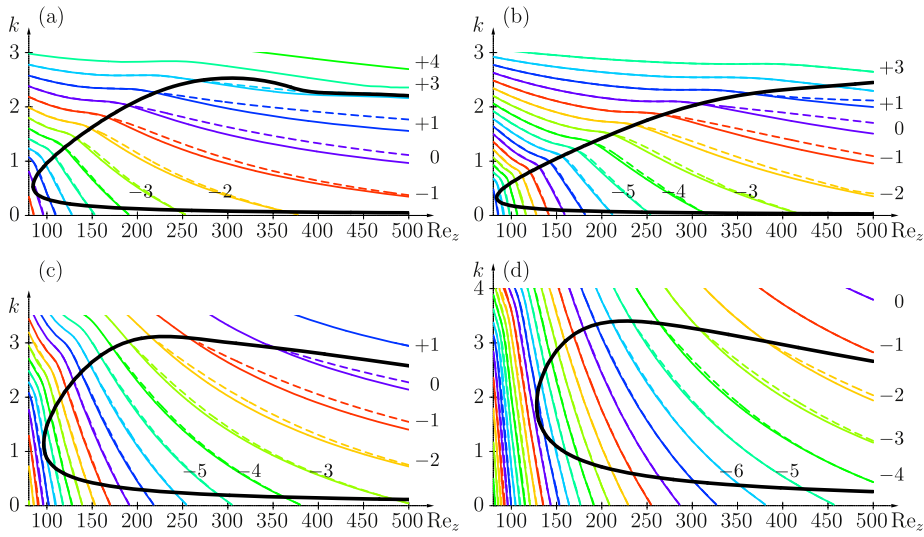


Figure 10. Frequencies of linear (solid coloured lines) and nonlinear (dashed lines) waves in the (Re_z, k) -plane for (a) $m = -1$, $Re_\Omega = 300$, (b) $m = -1$, $Re_\Omega = 500$, (c) $m = -2$, $Re_\Omega = 300$, (d) $m = -3$, $Re_\Omega = 300$. The thick black lines indicate the curve of marginal stability.

with the strongest linear temporal growth rates. Indeed, for a given value of Re_z , the strongest temporal growth rate occurs approximately in the centre of the unstable k -range, while the largest nonlinear amplitudes are found towards lower values of k . Similar conclusions hold for all configurations investigated here, comparing figures 1(c) with 7(b), 1(e) with 7(c), 1(f) with 7(d), 1(g) with 7(e) and 1(h) with 7(f), respectively.

The mean axial flow rate corrections and angular momentum corrections due to the fully developed nonlinear travelling waves are shown in figures 8 and 9, respectively. In these figures, mean-flow-correction quantities are shown relative to the values prevailing for the underlying base flows.

As expected by the supercritical nature of the instabilities, the flow-rate correction curves shown in figure 8 follow very similar trends to the energy curves of figure 7. Comparison of panels corresponding to the same settings of m and Re_Ω reveals that the largest flow-rate corrections approximately correspond to the largest disturbance energy levels.

Monitoring the mean angular momentum corrections as the control parameters are varied a slightly different pattern emerges (figure 9): while the values obviously still decay towards the critical curves, it is found that largest contributions prevail for axial wavenumbers in the centre of the unstable k -range. These computations thus reveal that the strength of axial and azimuthal mean-flow corrections significantly depend on the wavenumber k and that the axial corrections are more important for long wavelength perturbations. Thus the evolution of the relative angular momentum shown in figure 9 more closely follows that of the linear temporal growth rate (figure 1) than that of the saturated energy levels (figure 7). Unlike the linear temporal growth rates that display a maximum when Re_z is varied (see figure 1), both the flow-rate and angular momentum corrections continue to increase with the axial Reynolds number Re_z over the range investigated (see figures 8 and 9).

Finally, the frequencies of the linear and nonlinear travelling waves are compared in figure 10. For linear waves, the real part of the complex frequency ω_r^{lin} is derived from the

linear dispersion relation (13) over the entire (Re_z, k) -plane, and plotted with solid coloured lines in the panels of figure 10. Nonlinear waves exist within the regions of linear instability (delimited by thick black curves), and the dashed coloured lines indicate their associated frequency ω^{nl} (18). These results show that the nonlinear waves always display a lower frequency than their linear counterparts. Due to the supercritical nature of the present instabilities, linear and nonlinear frequencies converge to the same values along the curves of marginal stability. The departure between linear and nonlinear frequencies is seen to increase with Re_z and to be most significant towards the larger values of k .

4. Conclusions

In this paper, we have systematically investigated the fully developed dynamics prevailing in RHPF, for streamwise Reynolds numbers up to $Re_z = 500$ and azimuthal Reynolds numbers up to $Re_\Omega = 500$.

In the small-amplitude regime, perturbations are governed by the Navier–Stokes equations linearized about the steady axisymmetric base flow and the relevant linear stability characteristics are derived by solving the associated eigenvalue problems for given values of the streamwise wavenumber k and azimuthal modenumber m . The resulting dispersion relation has confirmed previously known results.

In unstable situations, small-amplitude perturbations may display exponential temporal growth and the resulting saturated fully developed regimes have been computed by direct numerical simulations of the complete Navier–Stokes equations. Over the entire control parameter space considered in this study, $Re_z \leq 500$ and $Re_\Omega \leq 500$, the flow fields have been found to evolve towards a nonlinear regime consisting of finite-amplitude travelling (i.e. spiralling) waves, characterised by constant values of energy levels, axial mean flow corrections and mean angular momentum corrections. The general effect of nonlinearities is to reduce the mean flow as well as the angular momentum. The strength of the axial mean-flow correction is directly related to the perturbation energy levels, and the highest levels occur for axial wavenumbers below those exhibiting strongest linear instability. The development of nonlinearities has always been found to result in a lower (or more negative) frequency of the nonlinear waves than of their linear counterparts.

Some secondary instabilities have been observed at larger values of Re_z or Re_Ω than those reported here. However, a complete study of secondary instability features is left for future investigation. Such secondary stability properties could be investigated by implementing a Floquet analysis similar to that used for the rotating-disk boundary-layer flow (Pier 2007), and the resulting dynamics could be computed by simulations allowing for more degrees of freedom, e.g., replacing the single Fourier series in (14)–(17) by a double series expansion in both axial and azimuthal coordinates for the flow fields.

Since the RHPF is known to display absolute instabilities (Fernandez-Feria and del Pino 2002), it would also be interesting to consider domains of large streamwise extent as Sanmiguel-Rojas and Fernandez-Feria (2005) to analyse the development of nonlinear global modes in terms of local nonlinear spiralling waves or for comparison with experimental observations (Miranda-Barea *et al* 2016). Carrying out direct numerical simulations in axially extended domains would also allow a detailed investigation of inlet conditions and entry flow properties, which are known to have non-trivial effects for the non-rotating case (Sahu and Govindarajan 2007). Presumably, an approach similar to that presented in Juniper and Pier (2015) could also shed light on how the global dynamics is influenced by the entry flow region.

Acknowledgments

The Indo-French Centre for the Promotion of Advanced Research/Centre franco-indien pour la promotion de la recherche avancée (IFCPAR/CEFIPRA) is gratefully acknowledged for its financial support.

ORCID iDs

Benoît Pier  <https://orcid.org/0000-0001-8663-8694>

References

- Barnes D R and Kerswell R R 2000 *J. Fluid Mech.* **417** 103–26
Cotton F W and Salwen H 1981 *J. Fluid Mech.* **108** 101–25
Dennis D J C, Seraudie C and Poole R J 2014 *Phys. Fluids* **26** 053602
Fernandez-Feria R and del Pino C 2002 *Phys. Fluids* **14** 3087–97
Foster M R 2014 *J. Fluid Mech.* **749** 113–44
Imao S, Itoh M and Harada T 1996 *Int. J. Heat Fluid Flow* **17** 444–51
Imao S, Itoh M, Yamada Y and Zhang Q 1992 *Exp. Fluids* **12** 277–85
Juniper M P and Pier B 2015 *Eur. J. Mech. B* **49** 426–37
Landman M J 1990 *J. Fluid Mech.* **221** 289–310
Mackrodt P A 1976 *J. Fluid Mech.* **73** 153–64
Miranda-Barea A, Fabregas-García C, Parras L and del Pino C 2016 *J. Fluid Mech.* **793** 316–34
Pedley T J 1968 *J. Fluid Mech.* **31** 603–7
Pedley T J 1969 *J. Fluid Mech.* **35** 97–115
Pier B 2007 *J. Eng. Math.* **57** 237–51
Pier B 2015 Habilitation à diriger des recherches École centrale de Lyon & Université de Lyon (<https://hal.archives-ouvertes.fr/tel-01107517>)
Pier B and Schmid P J 2017 *J. Fluid Mech.* **815** 435–80
Rusak Z and Wang S 2014 *J. Fluid Mech.* **759** 321–59
Sahu K C and Govindarajan R 2007 *J. Fluids Eng.* **129** 1277–80
Sammiguel-Rojas E and Fernandez-Feria R 2005 *Phys. Fluids* **17** 014104
Toplosky N and Akylas T R 1988 *J. Fluid Mech.* **190** 39–54
Yang Z and Leibovich S 1991 *J. Fluid Mech.* **233** 329–47

[A27]

Optimal energy growth in pulsatile channel and pipe flows

B. Pier & P. J. Schmid

Journal of Fluid Mechanics **926**, A11 (34 pages) (2021)

doi:10.1017/jfm.2021.702

<https://hal.archives-ouvertes.fr/hal-03084366>



Optimal energy growth in pulsatile channel and pipe flows

Benoît Pier¹,† and Peter J. Schmid²

¹Laboratoire de mécanique des fluides et d'acoustique, CNRS, École centrale de Lyon, Université de Lyon 1, INSA Lyon, 36 avenue Guy-de-Collongue, 69134 Écully, France

²Department of Mathematics, Imperial College, South Kensington Campus, London SW7 2AZ, UK

(Received 25 March 2021; revised 30 July 2021; accepted 30 July 2021)

Pulsatile channel and pipe flows constitute a fundamental flow configuration with significant bearing on many applications in the engineering and medical sciences. Rotating machinery, hydraulic pumps or cardiovascular systems are dominated by time-periodic flows, and their stability characteristics play an important role in their efficient and proper operation. While previous work has mainly concentrated on the modal, harmonic response to an oscillatory or pulsatile base flow, this study employs a direct–adjoint optimisation technique to assess short-term instabilities, identify transient energy-amplification mechanisms and determine their prevalence within a wide parameter space. At low pulsation amplitudes, the transient dynamics is found to be similar to that resulting from the equivalent steady parabolic flow profile, and the oscillating flow component appears to have only a weak effect. After a critical pulsation amplitude is surpassed, linear transient growth is shown to increase exponentially with the pulsation amplitude and to occur mainly during the slow part of the pulsation cycle. In this latter regime, a detailed analysis of the energy transfer mechanisms demonstrates that the huge linear transient growth factors are the result of an optimal combination of Orr mechanism and intracyclic normal-mode growth during half a pulsation cycle. Two-dimensional sinuous perturbations are favoured in channel flow, while pipe flow is dominated by helical perturbations. An extensive parameter study is presented that tracks these flow features across variations in the pulsation amplitude, Reynolds and Womersley numbers, perturbation wavenumbers and imposed time horizon.

Key words: shear-flow instability

† Email address for correspondence: benoit.pier@ec-lyon.fr

1. Introduction

Pulsatile flows are a common phenomenon in a variety of engineering flows, and they are ubiquitous in physiological configurations. The pulsatile flow through tubular geometries plays a key role in the haemodynamic system of many species as it is responsible for the transport of oxygenated blood to the organs and muscular tissue (Ku 1997; Pedley 2000). While in many of these configurations inertial effects are too weak to cause and sustain turbulent fluid motion, a variety of cardiovascular diseases can be linked to flow instabilities in the arteries (Chiu & Chien 2011). In addition, geometric modifications of the standard fluid-carrying vessels, such as stenoses, aneurysms or other pathologies, further amplify adverse flow effects and aggravate physiological consequences. For these reasons, a better understanding of pulsatile flows, and the perturbation dynamics they support, would be beneficial, if not mandatory, for improved diagnostics as well as the design of advanced medical devices.

Despite their importance in medical and engineering applications, pulsatile flows – and in particular their stability characteristics – have received far less attention than their steady analogues. Pulsatile flows comprise a steady as well as a time-periodic component. This is in contrast to oscillatory flows which consist of a harmonic part, but lack a steady background flow. The periodic time dependence precludes a standard modal approach, based on temporal Fourier normal modes, and instead calls for more complex methods, such as Floquet analysis. Furthermore, pulsatile flows are governed by a far larger suite of parameters than steady flows: besides the common Reynolds number Re and the wavenumbers of the perturbations, pulsatile flows depend on the pulsation amplitudes and the non-dimensional frequency (the Womersley number Wo). For a non-modal analysis, the time horizon over which growth or decay is measured and the phase shift of the perturbation within a base-flow cycle have to be accounted for as well. Within this high-dimensional parameter space, a rich and varied perturbation dynamics can be observed, with important transitions between distinct flow behaviours.

The stability of pulsatile flow has been addressed by a few key studies that laid the foundation for our current understanding of its perturbation dynamics. An account of the pertinent body of literature has been presented in Pier & Schmid (2017) with emphasis on the modal treatment via Floquet analysis. A resume of earlier work on general time-periodic flows has been presented in Davis (1976). Further notable work by von Kerczek (1982) has built on this foundation and established a framework for the analysis of flows with a harmonic base flow. Generic configurations such as a Stokes layer (Blennerhassett & Bassom 2002) or channel and pipe flow with time-periodic pressure gradients (Thomas *et al.* 2011), have been investigated with modal techniques and have been mapped out as to their stability characteristics across a range of governing parameters. The influence of wall modifications, such as stenoses or aneurysms, on the overall stability behaviour has been addressed via numerical simulations (see, e.g. Blackburn, Sherwin & Barkley 2008; Gopalakrishnan, Pier & Biesheuvel 2014).

The role of pulsation in the transition from laminar to turbulent pipe flow has been recently investigated by Xu *et al.* (2017) and Xu & Avila (2018). These studies in particular concentrated on the emergence and life cycle of localised ‘puffs’, together with their role in triggering transition in the presence of a pulsating flow component, since the occurrence of turbulent bursts in each cycle has been found to be sensitive on flow parameters and configuration details. A strong influence of the Womersley number has been reported, and a distinct regime-switching across three proposed parameter regions has been observed (Xu *et al.* 2017). These experimental findings have been further corroborated by direct numerical simulations initiated by a localised perturbation (Xu & Avila 2018). The earlier

numerical study by Tuzi & Blondeaux (2008) concluded that at moderate but subcritical Reynolds numbers only parts of the harmonic cycle (around flow reversal) support turbulent flow via an instability and an associated break of the flow's symmetry.

While the early body of literature on time-periodic flows has concentrated on a modal (Floquet) approach, more recent studies have employed an initial-value perspective on the analysis of perturbation dynamics and energy growth. Biau (2016) has analysed the generic oscillatory Stokes layer as to its potential to support transiently growing perturbations over a forcing cycle. This study isolated the Orr mechanism as the dominant process by which energy amplification could be achieved efficiently for sufficiently high unsteady amplitudes. In particular the decelerating part of the forcing cycle has been identified as prone to strong non-modal growth. Complementary nonlinear simulations further verified that triggering by these mechanisms can yield subcritical transition to turbulence. A similar technique has been applied in a recent study by Xu, Song & Avila (2021) for oscillatory and pulsating pipe flow. Among others, they have reported that pulsating pipe flows are generally dominated by helical perturbations. In accordance with Biau (2016), a strong Orr-type mechanism has been found to dominate, once a threshold pulsation amplitude has been exceeded. Again, only half of the forcing cycle supported growth of the kinetic perturbation energy; disturbances have been observed to rapidly reach energy levels that facilitate a transition to turbulent fluid motion, often via localised disturbances.

These latter studies advocate the treatment of pulsatile flow as a generally time-dependent flow, distinct from a periodic Floquet ansatz. Over the past decades, the application of these non-modal techniques to hydrodynamic stability calculations has resulted in a more complete understanding of shear-driven instability phenomena. The generality of this approach (Schmid 2007) is well-suited for assessing pulsatile flow over a range of time scales, thus mapping out the optimal perturbation dynamics over partial and multiple pulsation cycles. This non-modal approach for time-dependent flows is based on a variational principle arising from a partial-differential-equation-constrained optimisation problem. It results in a direct–adjoint system of equations (Luchini & Bottaro 2014) that produce the maximum energy growth of perturbations over a prescribed time horizon. Time-dependent base flows are treated naturally within this formalism, and short-term energy amplification mechanisms, for example over a partial pulsation cycle, can be detected and extracted effectively. Over the past years, this computational framework has been successfully brought to bear on a variety of complex flow configurations (see, e.g. Magri (2019) and Qadri *et al.* (2021) for applications in reactive flows), and has furnished quantitative stability measures beyond the time-asymptotic limit and without the need for simplifying assumptions.

This article follows up on and extends earlier work (Pier & Schmid 2017) that demonstrated the influence of a pulsating flow component on the stability of channel flow via a linear (Floquet) and nonlinear analysis. In this present study, we focus on non-modal effects and the occurrence of transient energy amplification mechanisms under conditions that are asymptotically stable, both for rectangular channel and cylindrical pipe flows. The unsteady nature of the base flow lends itself to a formulation as a partial-differential-equation-constrained optimisation problem for the maximum energy gain which is subsequently solved by a variational approach based on direct–adjoint looping.

The main finding, and significance, of our investigation consists of the quantification of extremely large transient growth, brought on by the unsteady nature of the base flow. By considering both channel and pipe flows and carefully studying energy transfer mechanisms, we identify the fundamental mechanisms responsible for this huge growth,

common to both geometries. This amplification potential translates directly into a strong sensitivity for the rise of coherent structures over one or many pulsatile cycles. While this feature of pulsatile flows has been observed and reported in previous studies, an encompassing treatment of this phenomenon, including its presence in parameter space and its manifestation in dominant spatial structures, is still missing in the literature on unsteady flows. Our findings also have a direct connection to classifying transition scenarios in wall-bounded flows under the influence of cyclic base flow variations, thus extending the classical scenarios for steady flows and potential routes for the transition to turbulence occurring during part of the cycle.

Despite our attempt to analyse pulsating channel and pipe flows comprehensively, judicious choices had to be made to arrive at an emerging picture for the perturbation dynamics prevailing in these configurations. The ensuing parameter ranges have been selected to capture the most compelling and representative flow phenomena, while limiting our focus to flows encountered in physiological and medical situations. Haemodynamic applications, across a range of blood vessel geometries, are well covered by our choice of parameters. Nonetheless, configurations outside this parameter range are touched upon as well, to establish continuity or bifurcations in flow behaviour and to connect to other studies that investigate such parameter regimes in more detail, e.g. Xu *et al.* (2021).

The present paper represents the culmination of several years of work; a preliminary version of the main results has been presented at the 12th European Fluid Mechanics Conference in Vienna (Pier & Schmid 2018).

2. Flow configurations and governing equations

This investigation considers viscous incompressible flow through infinite channels and pipes of constant diameter. In this context, a flow is characterised by a velocity vector field $\mathbf{u}(x, t)$ and a scalar pressure field $p(x, t)$ that depend on position x and time t and are governed by the Navier–Stokes equations

$$\frac{\partial \mathbf{u}}{\partial t} + (\mathbf{u} \cdot \nabla) \mathbf{u} = \nu \Delta \mathbf{u} - \nabla p, \quad (2.1)$$

$$0 = \nabla \cdot \mathbf{u}, \quad (2.2)$$

where ν is the kinematic viscosity of the fluid, and the pressure has been redefined to eliminate the constant fluid density.

The channel-flow configuration calls for a formulation using Cartesian coordinates, while cylindrical coordinates are appropriate for pipe flows. In order to address both configurations with similar mathematical and numerical tools, we adopt a general formalism using three spatial coordinates x_0, x_1, x_2 and associated velocity components u_0, u_1, u_2 . When analysing channel flow with respect to a Cartesian reference frame, the variables x_0, x_1 and x_2 denote wall-normal, streamwise and spanwise coordinates, respectively, while they stand for radial, streamwise and azimuthal coordinates when studying pipe flow in a cylindrical setting. Whatever the configuration, the flow domain corresponds to $|x_0| < D/2$ where D is the channel or the pipe diameter, and no-slip boundary conditions prevail along the solid walls at $|x_0| = D/2$.

A formulation of the incompressible Navier–Stokes equations ((2.1) and (2.2)) in cylindrical coordinates comprises more terms than one in Cartesian coordinates. Nevertheless, the resulting equations have a very similar structure, and the above notations allow us to cast the governing equations into a single general system of partial differential equations, pertaining to both channel and pipe configurations, the details of which are given in [Appendix A](#).

3. Base flows and non-dimensional control parameters

Pulsatile base flows driven by a spatially uniform and temporally periodic streamwise pressure gradient are obtained as exact solutions of the Navier–Stokes equations and consist of a velocity field in the streamwise x_1 -direction with profiles that only depend on time t and on the wall-normal/radial coordinate x_0 . Denoting by Ω the pulsation frequency, the base velocity profiles may be expanded as temporal Fourier series,

$$U_1(x_0, t) = \sum_n U_1^{(n)}(x_0) \exp(in\Omega t), \quad (3.1)$$

and are associated with a periodic flow rate

$$Q(t) = \sum_n Q^{(n)} \exp(in\Omega t). \quad (3.2)$$

In the above expressions, the conditions $Q^{(-n)} = [Q^{(n)}]^\star$ and $U_1^{(-n)}(x_0) = [U_1^{(n)}(x_0)]^\star$ ensure that all flow quantities are real (with \star denoting a complex conjugate).

By invariance of these base flows in the streamwise x_1 -direction, the different harmonics in the expansion (3.1) are not coupled through the nonlinear terms of the Navier–Stokes equations and the velocity components $U_1^{(n)}(x_0)$ are analytically obtained by solving simple differential equations derived for each harmonic component. The mean-flow component $U_1^{(0)}(x_0)$ displays a parabolic Poiseuille profile. For $n \neq 0$, following Womersley (1955), the profiles $U_1^{(n)}(x_0)$ are obtained in terms of Bessel functions in cylindrical coordinates corresponding to pipe flows, while they are obtained in terms of exponential functions in Cartesian coordinates corresponding to channel flows.

Pulsatile channel or pipe flows are characterised by the Womersley number

$$Wo \equiv \frac{D}{2} \sqrt{\frac{\Omega}{\nu}}, \quad (3.3)$$

which is a non-dimensional measure of the pulsation frequency, and may be interpreted as the ratio of the pipe radius (or the channel half-diameter) to the thickness $\delta = \sqrt{\nu/\Omega}$ of the oscillating boundary layers developing near the walls. A pulsatile base flow is then completely specified by the Fourier components $Q^{(n)}$ of its flow rate (3.2), and the velocity profiles of the different harmonics (3.1) are obtained as

$$U_1^{(n)}(x_0) = \frac{Q^{(n)}}{A} W\left(\frac{x_0}{D/2}, \sqrt{n} Wo\right). \quad (3.4)$$

In the above expression, A denotes the relevant measure of the cross-section ($A = D$ for channels and $A = \pi D^2/4$ for pipes) and the function W is the normalised velocity profile pertaining to each harmonic component. The analytic expressions of W for channel and pipe flows are given in [Appendix B](#).

In this investigation, we only consider pulsatile flows with a non-vanishing mean flow rate $Q^{(0)}$. Thus, the definition of the Reynolds number may be based on mean velocity

$Q^{(0)}/A$, diameter D and viscosity ν , leading to

$$Re \equiv \frac{Q^{(0)}}{\nu} \text{ for channels and } Re \equiv \frac{Q^{(0)}}{\nu} \frac{4}{\pi D} \text{ for pipes.} \quad (3.5)$$

Moreover, using $Q^{(0)}$ as reference, the flow rate waveform is completely determined by the non-dimensional ratios

$$\tilde{Q}^{(n)} \equiv \frac{Q^{(n)}}{Q^{(0)}}, \quad (3.6)$$

corresponding to the amplitude (and phase) of the oscillating flow rate components ($n > 0$) relative to the mean flow.

In order to reduce the dimensionality of the control-parameter space for the rest of this paper, we will only consider base flow rates with a single oscillating component

$$Q(t) = Q^{(0)}(1 + \tilde{Q} \cos \Omega t), \quad (3.7)$$

where the pulsation amplitude $\tilde{Q} \equiv 2\tilde{Q}^{(1)}$ may be assumed real without loss of generality. Note that the theoretical and numerical methods developed for the present investigation are also suitable for studying the dynamics of pulsating base flows with higher harmonic content.

4. Mathematical formulation

This entire study considers the dynamics of small-amplitude perturbations developing in the basic pulsatile channel and pipe flows specified in the previous section. The incompressible Navier–Stokes equations are, therefore, linearised about these base flows. Considering that the base flows do not depend on the streamwise coordinate x_1 nor on the spanwise/azimuthal coordinate x_2 , infinitesimally small velocity and pressure perturbations may thus be written as spatial normal modes of the form

$$\mathbf{u}^d(x_0, t) \exp i(\alpha_1 x_1 + \alpha_2 x_2), \quad (4.1)$$

$$p^d(x_0, t) \exp i(\alpha_1 x_1 + \alpha_2 x_2), \quad (4.2)$$

where α_1 and α_2 are streamwise and spanwise/azimuthal wavenumbers, respectively. Separation of total flow fields into basic and perturbation quantities and substitution of the expansions (4.1) and (4.2) into the governing equations (2.1) and (2.2) linearised about the relevant time-periodic base flow then yields a system of coupled linear partial differential governing equations of the form

$$\mathbf{A} \partial_t \mathbf{q}(x_0, t) = \mathbf{L}(x_0, t) \mathbf{q}(x_0, t), \quad (4.3)$$

where

$$\mathbf{q}(x_0, t) \equiv \begin{pmatrix} u_0^d(x_0, t) \\ u_1^d(x_0, t) \\ u_2^d(x_0, t) \\ p^d(x_0, t) \end{pmatrix} \quad \text{and} \quad \mathbf{A} \equiv \begin{pmatrix} 1 & 0 & 0 & 0 \\ 0 & 1 & 0 & 0 \\ 0 & 0 & 1 & 0 \\ 0 & 0 & 0 & 0 \end{pmatrix}. \quad (4.4a,b)$$

Here, the superscript d refers to components of the direct problem, to be distinguished from the adjoint variables below (4.6). The spatial differential operator $\mathbf{L}(x_0, t)$ in (4.3) is a 4-by-4 matrix and its coefficients involve ∂_0 -differentiation, depend on the wavenumbers

α_1 and α_2 as well as on the base velocity profiles $U_1(x_0, t)$; see [Appendix C](#) for explicit expressions of all these terms.

When studying transient growth effects and searching for optimal initial perturbations that are maximally amplified over a finite-time horizon, it is necessary to choose an appropriate measure of disturbance size ([Schmid 2007](#)). Using a classical energy-based inner product, the adjoint governing equations associated with the direct problem [\(4.3\)](#) are routinely obtained as

$$A\partial_t \mathbf{q}^\dagger(x_0, t) = \mathbf{L}^\dagger(x_0, t)\mathbf{q}^\dagger(x_0, t), \quad (4.5)$$

and the adjoint differential operator $\mathbf{L}^\dagger(x_0, t)$ is explicitly given in [Appendix D](#). In contrast with the direct [\(4.3\)](#), the adjoint equations [\(4.5\)](#) have negative diffusion coefficients and the adjoint fields

$$\mathbf{q}^\dagger(x_0, t) \equiv \begin{pmatrix} u_0^a(x_0, t) \\ u_1^a(x_0, t) \\ u_2^a(x_0, t) \\ p^a(x_0, t) \end{pmatrix}, \quad (4.6)$$

are integrated backwards in time.

Denoting by $\{\mathbf{q}(x_0, t_i), |x_0| < D/2\}$ an initial perturbation at time t_i , the evolution of this disturbance at subsequent times $t > t_i$ and the associated perturbation energy $E(t)$ are then obtained by solving the initial-value problem corresponding to [\(4.3\)](#) with $\mathbf{q}(x_0, t_i)$ specified for $|x_0| < D/2$. The temporal evolution of the perturbation amplitude is then characterised by the ratio $E(t)/E(t_i)$, for $t > t_i$.

The maximum possible amplification of a disturbance over the interval $t_i < t < t_f$ is obtained as

$$G(t_i, t_f) = \max_{\{\mathbf{q}(x_0, t_i)\}} \frac{E(t_f)}{E(t_i)}, \quad (4.7)$$

by optimising over all possible initial conditions at $t = t_i$. Note that, since the base flow is time-periodic, the amplification factor depends not only on the duration $t_f - t_i$ of the temporal evolution but also on the phase of its starting point t_i within the pulsation cycle.

The particular initial condition at $t = t_i$ that achieves the largest amplification at $t = t_f$ is referred to as the optimal perturbation and the resulting flow fields at $t = t_f$ as the optimal response. In practice, the amplification factors $G(t_i, t_f)$ and associated optimal perturbations and responses are iteratively computed by successive direct–adjoint loops, consisting of temporal integration of the direct [\(4.3\)](#) from t_i to t_f and of the adjoint equations [\(4.5\)](#) from t_f to t_i , using the numerical methods described in the next section.

In linearly stable configurations, all perturbations eventually decay and the maximal transient growth for given wavenumbers α_1 and α_2 ,

$$G^{max}(\alpha_1, \alpha_2) = \max_{t_i, t_f} G(t_i, t_f; \alpha_1, \alpha_2), \quad (4.8)$$

is well defined and takes finite values. Obviously, $G^{max}(\alpha_1, \alpha_2)$ also depends on the base flow configuration and its control parameters. For a given pulsating base flow, the largest possible transient amplification that may be achieved is obtained as

$$G_{max}^{max} = \max_{\alpha_1, \alpha_2} G^{max}(\alpha_1, \alpha_2), \quad (4.9)$$

by considering all possible wavenumbers.

5. Numerical implementation

The direct and adjoint temporal evolution problems (4.3) and (4.5) are first order in time and involve spatial differential operators in the wall-normal x_0 -coordinate.

For spatial discretisation we use a Chebyshev spectral method with collocation points spanning the whole diameter of the channel or the pipe. Whether considering channel or pipe flows, all computations are restricted to half of the domain, $0 \leq x_0 \leq D/2$, by taking into account the symmetry or antisymmetry of the different flow fields and using the associated discretised differential operators of corresponding symmetry. For channel flow calculations carried out in Cartesian coordinates, the parity of the different flow fields depends on the sinuous or varicose nature of the perturbation under consideration. Note that for all the channel flow configurations considered in this paper, the dynamics is dominated by sinuous perturbations. For pipe flow calculations carried out in cylindrical coordinates, it is the value (even or odd) of the azimuthal mode number that determines the parity of each of the different flow fields. Note that the singularities in the differential operators at the pipe axis ($x_0 = 0$) are only ‘apparent’ (Boyd 2001): the exact solution is analytic at the axis even though the coefficients of the differential equations are not. Thus a consistent implementation of the symmetry/antisymmetry conditions at the axis removes any apparent singularities and guarantees that the spectral method yields smooth solutions.

Time-marching of the direct and adjoint incompressible Navier–Stokes equations uses a second-order accurate predictor–corrector fractional-step method, derived from Raspo *et al.* (2002). In classical fashion, the maximal gain $G(t_i, t_f)$, together with optimal initial perturbation and final response, is then obtained by direct–adjoint loops, maximising the energy growth from $t = t_i$ to $t = t_f$. All subsequent quantities G^{\max} and G_{\max}^{\max} are derived from the gain G , by maximising over t_i and t_f , and over α_1 and α_2 .

Resorting to the general formulation of the governing equations detailed in the Appendix A and taking advantage of the relevant symmetry properties of the different flow fields thus leads to a numerical implementation capable of handling all configurations of the present investigation.

This entire numerical solution procedure is a generalisation of an approach already used in our previous investigation (Pier & Schmid 2017), and its implementation in C++ is based on the ‘home-spun’ PackstaB library (Pier 2015, § A.6). The interested reader is referred to these references for further details of the general method.

6. Pulsating channel flow

The objective of the present section, which is the core part of the paper, is to investigate how the well known transient-growth properties of steady channel flow are modified by the presence of a pulsating base flow component. Starting with a steady Poiseuille flow, the approach consists of studying the influence of pulsation as the amplitude \tilde{Q} is increased from 0 for different values of the Womersley number Wo .

First, we consider the growth rates G of streamwise-invariant and spanwise-periodic streaks since they display the largest transient growth for Poiseuille flow. Then, the strikingly different behaviour observed for two-dimensional (spanwise-invariant) flows calls for a systematic computation of all possible three-dimensional perturbations. Having established the optimal amplification rates G^{\max} that prevail over the whole wavenumber plane, we are then in a position to derive the maximal achievable energy amplification G_{\max}^{\max} for a given pulsating base flow and to document its dependence on the pulsation amplitude \tilde{Q} , the Womersley number Wo and the Reynolds number Re . Finally, a detailed discussion of the energy transfer mechanisms allows us to highlight the various growth

mechanisms that come into play during the different stages of the evolution and to explain the huge growth factors that are observed for pulsating flows, already for moderate pulsation amplitudes. We recall that sinuous perturbations prevail for all the situations investigated here; thus, all the results presented in this section correspond to flow fields of sinuous symmetry.

The vast parameter space of the problem requires a systematic exploration of the flow physics and a concentration on essential characteristics by a progressive compression of the governing parameters. To this end, we successively investigate the growth of streaks, two-dimensional and three-dimensional disturbances, before focusing on transient energy growth and the energy transfer mechanisms that accompany the observed amplifications. We conclude by isolating the shape and dynamics of the two- and three-dimensional structures that optimally exploit the unsteady background flow and thus exhibit maximal energy growth. Along this analysis, we present a sequential reduction of the parameter space, starting from the effect of cycle length and cycle phase, via spatial scales to the time horizon for optimal growth. Within each step, the essential features of the transient instability will be presented, before reducing the parameter dependency for the subsequent analysis. This section then culminates in the detailed examination of the most amplified disturbances, for the two- and three-dimensional case, under the influence of a pulsatile background flow.

6.1. Growth of streaks

In steady channel Poiseuille flow, largest transient growth is known to occur for initial conditions which are spanwise periodic and consist of streamwise aligned vortices, thus corresponding to perturbations with $\alpha_1 = 0$ and $\alpha_2 \neq 0$. Figure 1(a) shows the optimal transient amplification at $Re = 1000, 2000, \dots, 5000$ computed for $\alpha_2 = 4$, which is near the most transiently amplified spanwise wavenumber. (Throughout this paper, length scales are non-dimensionalised with respect to the channel (or pipe) diameter D .) For a steady base flow, the energy growth factor $G(t_i, t_f)$ only depends on the duration $t_f - t_i$, here measured in mean-flow advection units $\tau_Q \equiv D^2/Q^{(0)}$. Replotting these data for G/Re^2 and measuring the duration $t_f - t_i$ in diffusion units $\tau_v \equiv D^2/v = Re\tau_Q$, the curves in figure 1(b) confirm the known scaling laws, leading to a maximum transient growth of $G^{\max} \simeq 1.1 \times 10^{-4} Re^2$ at $t^{\max}/\tau_Q \simeq 1.9 \times 10^{-2} Re$.

Adding to this steady base flow a pulsatile component of given amplitude and frequency, the transient growth properties are characterised by $G(t_i, t_f)$ which then depends both on the phase of the initial perturbation t_i within the pulsation period $T \equiv 2\pi/\Omega$ and on the duration $t_f - t_i$ of the temporal evolution. For $Re = 2000$ and $Re = 5000$, figure 2 shows plots of the growth factors $G(t_i, t_f)$ for pulsation amplitudes $\tilde{Q} = 0.4$ and 1.0 at $Wo = 10$. It is found that the amplitude \tilde{Q} of the base flow modulation only weakly influences the streak growth. Even increasing \tilde{Q} to values larger than unity (corresponding to negative flow rates during part of the pulsation cycle), does not significantly alter the distribution of $G(t_i, t_f)$: the maximum amplification remains at the same level and the growth hardly depends on the phase t_i/T . Thus streamwise-invariant ($\alpha_1 = 0$) perturbations appear to be almost unaffected by the time-dependent component of the base flow and to display a dynamics predominantly dictated by the time-averaged base flow. The discussion of energy transfer mechanisms in § 6.5 below will shed further light on this observation. Comparing figure 2(a) with 2(c), and 2(b) with 2(d), the similarity observed between plots at different Re and same \tilde{Q} also indicates that the scaling of G with Re^2 remains valid for the transient growth of streaks in pulsating base flows.

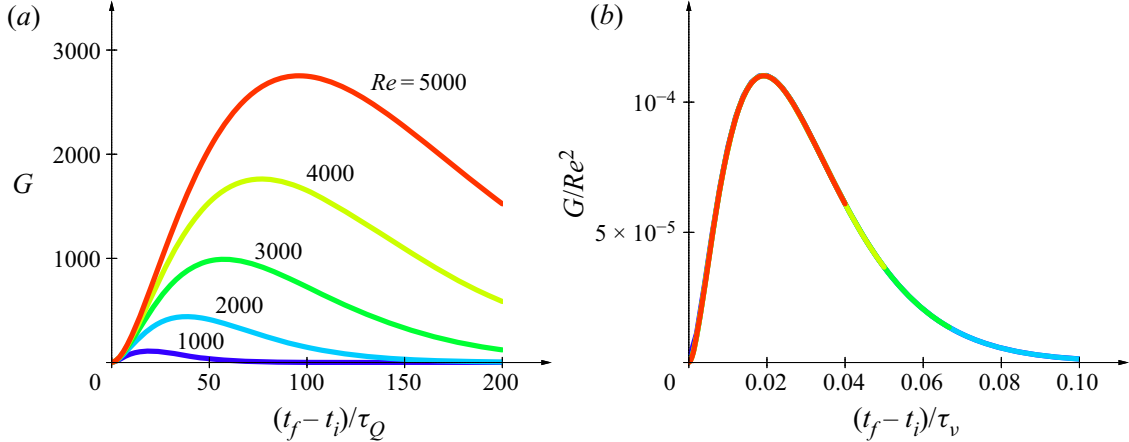


Figure 1. Optimal energy growth for streaks with $\alpha_2 = 4$ and $\alpha_1 = 0$ in steady channel Poiseuille flow at $Re = 1000, 2000, \dots, 5000$. (a) Duration $t_f - t_i$ of growth phase measured in mean-flow advection time scale τ_Q . (b) Rescaled growth factors G/Re^2 and $t_f - t_i$ measured in diffusion time scale $\tau_v = Re\tau_Q$.

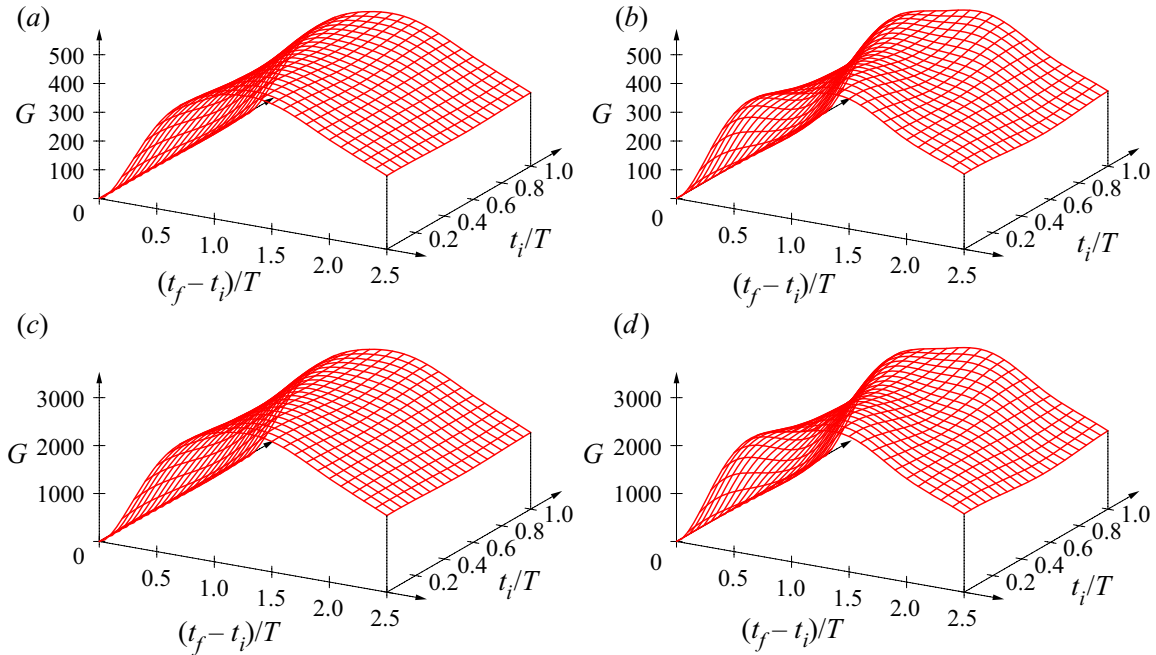


Figure 2. Optimal transient amplification for streaks with $\alpha_2 = 4$ and $\alpha_1 = 0$ at (a,b) $Re = 2000$ and (c,d) $Re = 5000$. Pulsating channel flow at $Wo = 10$ and (a,c) $\tilde{Q} = 0.4$ and (b,d) $\tilde{Q} = 1.0$.

6.2. Growth of two-dimensional perturbations

Two-dimensional spanwise invariant perturbations, corresponding to $\alpha_2 = 0$ and $\alpha_1 \neq 0$, exhibit much weaker transient amplification than streaks for the same steady Poiseuille flow. Figure 3 plots the transient growth properties prevailing for Poiseuille flow at $Re = 1000, 2000, \dots, 5000$ for perturbations with $\alpha_1 = 2$ and $\alpha_2 = 0$, near the most unstable two-dimensional perturbation. Here, the maximal amplification G^{max} scales linearly with the Reynolds number and reaches much lower values than those corresponding to streaks (see figure 1a); note that this maximal amplification is also reached for a much shorter time horizon.

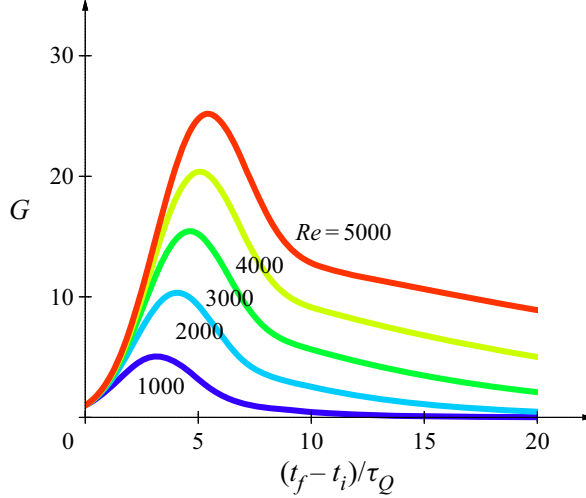


Figure 3. Optimal energy growth for two-dimensional perturbations $\alpha_1 = 2$ and $\alpha_2 = 0$ in channel Poiseuille flow at $Re = 1000, 2000, \dots, 5000$.

The evolution of two-dimensional transient growth properties as the amplitude \tilde{Q} of the pulsating component is increased is given in figure 4. After increasing \tilde{Q} , a second maximum emerges in the plot of G , located around $t_i/T = 0.2$ and $(t_f - t_i)/T = 0.5$. In contrast with the situation prevailing for streaks, this second maximum is seen to rapidly grow with \tilde{Q} and to become the dominant feature, here already for $\tilde{Q} \simeq 0.1$. While streaks display much larger transient growth for steady Poiseuille flow, these two-dimensional perturbations are found to become the most efficient optimal perturbations for pulsatile base flows, beyond some threshold value of the pulsating amplitude \tilde{Q} . This overwhelming growth of two-dimensional perturbations for pulsatile conditions will be explained in § 6.5, below, by detailed monitoring of the amplification process in comparison with the dynamics of temporal Floquet eigenmodes.

6.3. Growth of three-dimensional perturbations

The very different transient growth behaviour observed for streaky and two-dimensional perturbations calls for a systematic investigation in the entire (α_1, α_2) -wavenumber plane. For a given pulsating base flow, the optimal energy amplification $G^{max}(\alpha_1, \alpha_2)$ (4.8) is obtained by maximising the transient growth $G(t_i, t_f; \alpha_1, \alpha_2)$ over all values of t_i and t_f at each prescribed wavenumber. We have systematically explored the control-parameter space spanning the ranges $1000 \leq Re \leq 5000$, $5 \leq Wo \leq 15$ and $0 \leq \tilde{Q} \leq 1$, and a few characteristic results are presented below.

The plot of G^{max} for steady Poiseuille flow ($\tilde{Q} = 0$) at $Re = 4000$ (figure 5a) confirms that strongest transient growth occurs for streaks (with $\alpha_1 = 0$) and that the largest value of $G^{max} \simeq 1763$ is reached at $\alpha_2 \simeq 4.09$ (indicated by a black dot). Two-dimensional perturbations (with $\alpha_2 = 0$) experience growth factors that are two orders of magnitude smaller, with $G^{max} \simeq 30$ for $\alpha_1 = 3.1$.

The distribution of maximal amplification factors G^{max} in the (α_1, α_2) -plane evolves significantly as the amplitude \tilde{Q} of the pulsating component is increased for a given pulsation frequency. Figure 5(b–g) reveal that, as \tilde{Q} is increased, the maximum energy growth (indicated by a black dot) rapidly switches over from streaks to two-dimensional perturbations that experience growth factors sharply increasing with \tilde{Q} while those

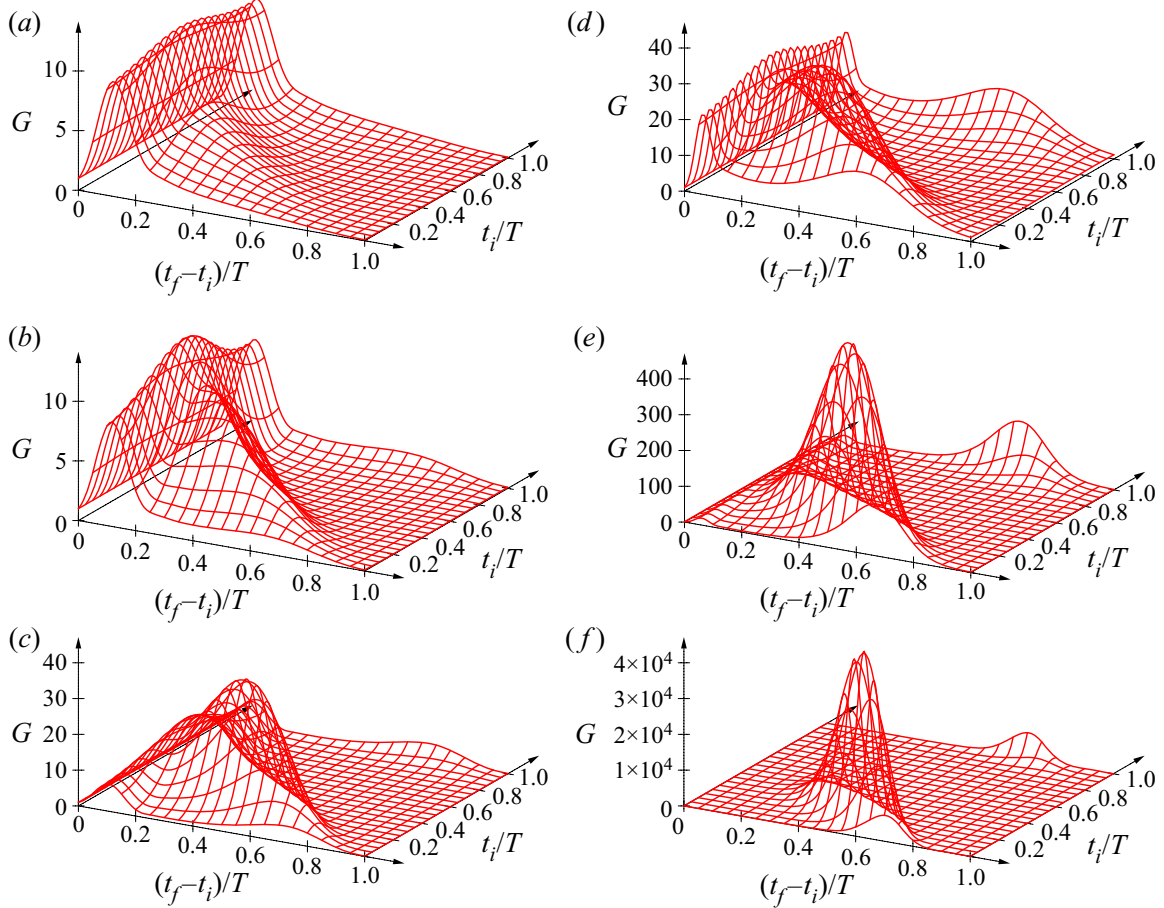


Figure 4. Optimal transient amplification for two-dimensional perturbations with $\alpha_2 = 0$ and $\alpha_1 = 2$ at (a–c) $Re = 2000$ and (d–f) $Re = 5000$. Pulsating base flow at $Wo = 10$ and (a,d) $\tilde{Q} = 0.04$, (b,e) $\tilde{Q} = 0.10$ and (c,f) $\tilde{Q} = 0.20$.

experienced by streaks (along the α_2 -axis) do not much depend on \tilde{Q} nor on Wo . Comparison of the results obtained with $Wo = 8$ (figure 5b,c), $Wo = 10$ (figure 5d,e) and $Wo = 12$ (figure 5f,g) demonstrates that the rate of increase of G^{max} with \tilde{Q} varies significantly with Wo and is larger for lower values of the Womersley number.

Figures 5(h–j) illustrate the behaviour at $Re = 2000$. For steady Poiseuille flow (figure 5h), the isolines of G^{max} display a similar structure as for $Re = 4000$ (figure 5a) but with lower levels. After increasing the amplitude \tilde{Q} of the pulsating flow component at $Wo = 10$, figures 5(i,j) show that two-dimensional perturbations again eventually dominate the response. However, at this lower Reynolds number, a larger value of \tilde{Q} is required for the two-dimensional perturbations to emerge, and the increase of G^{max} with \tilde{Q} also occurs at a lower rate. Thus G^{max} is found to reach values of the order of 10^5 at $Re = 2000$ for $\tilde{Q} = 0.5$ and $Wo = 10$ (figure 5j), while at $Re = 4000$ values in excess of 10^{11} are observed (figure 5e).

6.4. Maximal transient growth

The maximal transient energy amplification achievable for a given base flow has been defined as G_{max}^{max} (4.9) and is derived by maximising $G^{max}(\alpha_1, \alpha_2)$ over the entire wavenumber plane.

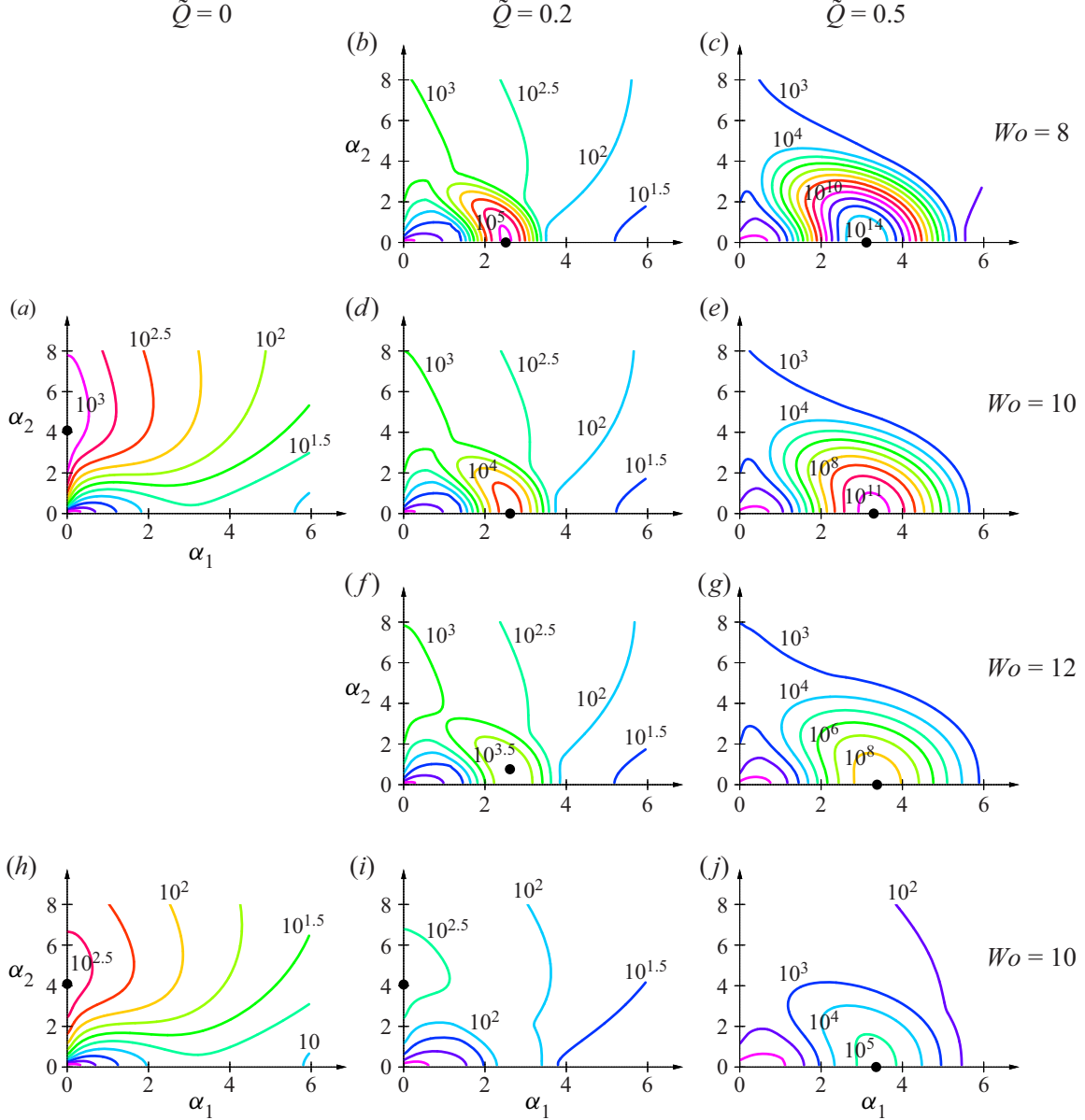


Figure 5. Isolines of maximum energy growth G^{max} in (α_1, α_2) -wavenumber plane for base flows with $Re = 4000$ (a–g) and $Re = 2000$ (h–j). (a,h) Steady Poiseuille flow ($\tilde{Q} = 0$), (b,d,f,i) pulsating base flows with $\tilde{Q} = 0.2$, (c,e,g,j) pulsating base flows with $\tilde{Q} = 0.5$. Womersley numbers: $Wo = 8$ in panels (b,c), $Wo = 10$ in panels (d,e,i,j), $Wo = 12$ in panels (f,g). The black dots indicate the wavenumbers where G^{max} reaches its largest value.

Figure 6 plots the evolution of G_{max}^{max} as the pulsation amplitude \tilde{Q} is continuously increased for Womersley and Reynolds numbers in the range $5 \leq Wo \leq 15$ and $1000 \leq Re \leq 5000$, respectively. At low values of \tilde{Q} , the pulsating flow component has a very weak influence and G_{max}^{max} remains near the value prevailing for steady Poiseuille flow at the same Reynolds number. For these low pulsation amplitudes, the optimal initial perturbation corresponds to streaks (with $\alpha_1 = 0$) and the associated growth duration $t_f - t_i$ remains very close to that prevailing for the equivalent mean Poiseuille flow (see also figure 8, below).

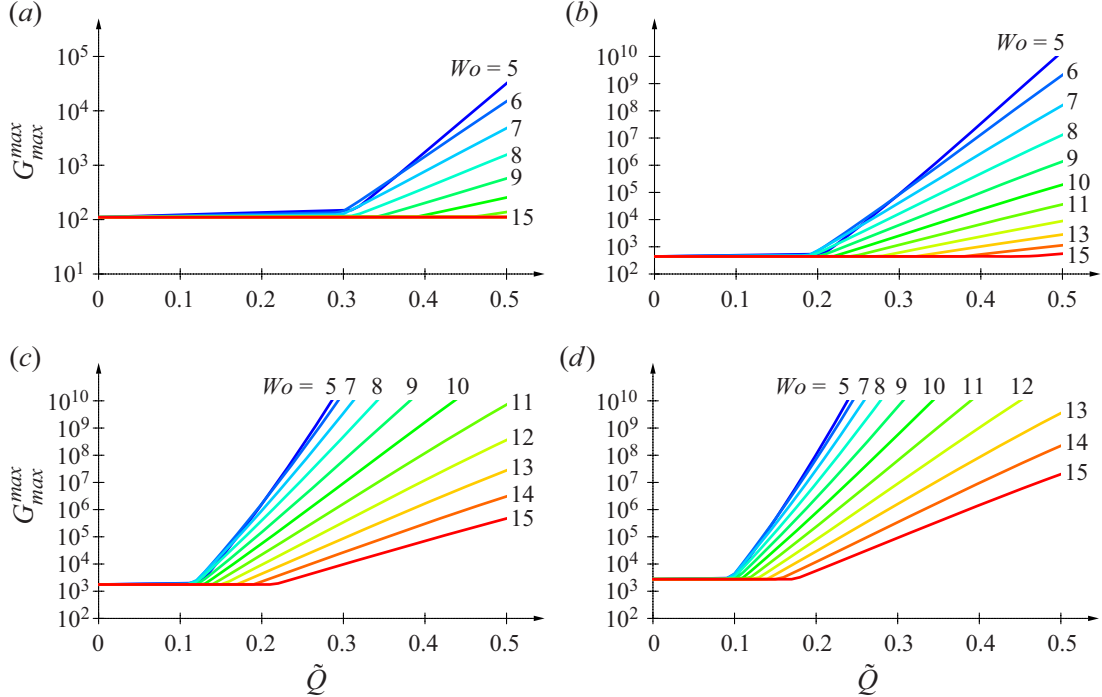


Figure 6. Evolution of maximal transient energy amplification G_{\max}^{\max} with \tilde{Q} for $5 \leq Wo \leq 15$ at (a) $Re = 1000$, (b) $Re = 2000$, (c) $Re = 4000$ and (d) $Re = 5000$.

Beyond some critical value of \tilde{Q} , the amplification factor G_{\max}^{\max} starts to increase exponentially with \tilde{Q} , as illustrated by the nearly constant slopes in the logarithmic plots of figure 6 (note the different vertical scale used in figure 6a for $Re = 1000$). This critical value \tilde{Q}_c of the pulsation amplitude depends on Wo and Re as shown in figure 7(a): increasing the Reynolds number is found to promote the two-dimensional perturbations which become the dominant feature already for $\tilde{Q} > 0.1$ around $Re = 5000$. For $\tilde{Q} > \tilde{Q}_c$, the rate of the exponential growth of G_{\max}^{\max} with \tilde{Q} corresponds to the slopes seen in figure 6 and significantly increases as the Womersley number decreases. As a result, G_{\max}^{\max} rapidly reaches ‘astronomical’ values, several orders of magnitude beyond the amplification rates prevailing for the corresponding steady Poiseuille flows. These exponential rates have been computed as

$$\kappa \equiv \frac{1}{G_{\max}^{\max}} \frac{\partial G_{\max}^{\max}}{\partial \tilde{Q}}, \quad (6.1)$$

and their variation with Re and Wo is given in figure 7(b). In this plot the values of κ have been computed by taking the average over $\tilde{Q}_c < \tilde{Q} < \tilde{Q}_c + 0.1$, but note that the growth rate remains nearly constant over much larger intervals of \tilde{Q} in the two-dimensional regime. Obviously, the growth rates are enhanced with the Reynolds number and they also significantly increase towards the lower Womersley numbers, corresponding to longer pulsation periods.

The regime change in the transient growth behaviour occurring for $\tilde{Q} = \tilde{Q}_c$ is further illustrated in figure 8 at $Re = 4000$. The evolution with pulsation amplitude \tilde{Q} of the streamwise α_1 and spanwise α_2 wavenumbers associated with the maximally amplified optimal perturbations display a sharp transition from streaky ($\alpha_1 = 0, \alpha_2 \neq 0$) to two-dimensional ($\alpha_1 \neq 0, \alpha_2 = 0$) perturbations. For $Wo = 6$ and 8 , the spanwise

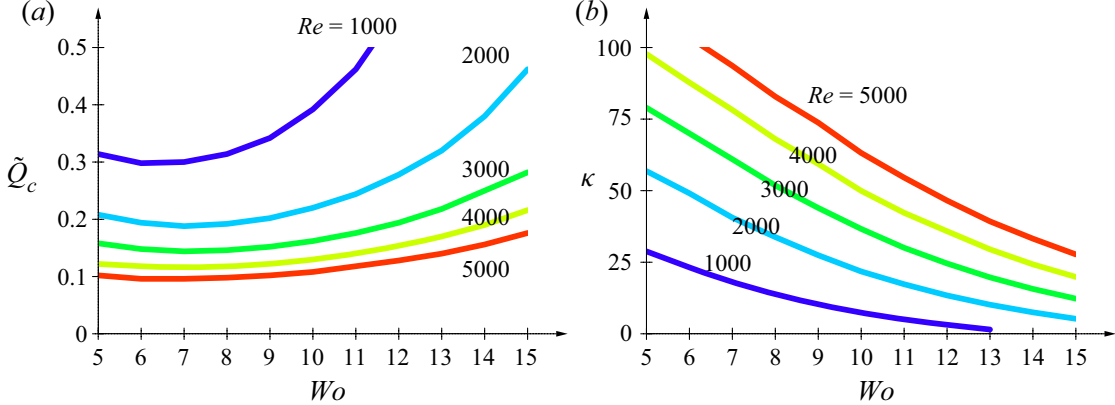


Figure 7. (a) Critical values \tilde{Q}_c for transition between streaky and two-dimensional maximally amplified perturbations. (b) Exponential growth rate κ of G_{\max}^{max} with \tilde{Q} in the two-dimensional regime.

wavenumber here directly switches from $\alpha_2 \simeq 4$ to 0. For higher values of Wo , however, a small range in \tilde{Q} is observed where the maximally amplified perturbations consist of oblique waves with small but finite values of α_2 . This corresponds to configurations where the amplification of two-dimensional perturbations is still in competition with streaks, so that the maximum of G^{\max} in the (α_1, α_2) -plane occurs slightly off the α_1 -axis, as illustrated by the black dot in figure 5(f) and corresponding dots in figure 8(a,b). It is then only for higher values of \tilde{Q} that purely two-dimensional ($\alpha_2 = 0$) perturbations prevail.

The transition from streaky to two-dimensional maximally amplified perturbations is also accompanied by a significant change in the duration of the growth phase $t_f - t_i$, shown in figure 8(c) in mean-flow advection units τ_Q and in figure 8(d) in units of the pulsation period T . These two time scales are associated with different dynamical features and related as $Wo^2 T = (\pi/2) Re \tau_Q$. At weak pulsation amplitudes \tilde{Q} , the duration $t_f - t_i$ remains very close to the value prevailing for streaks developing in the equivalent steady Poiseuille flow, here approximately $75\tau_Q$ at $Re = 4000$ (compare with figure 1). At higher pulsation amplitudes, when two-dimensional perturbations dominate, maximal amplification occurs over intervals $t_f - t_i$ that approximately correspond to half a pulsation period, $T/2$. Thus, the transition from streaky to two-dimensional perturbations also coincides with a change in the dynamical time scale: from streak growth essentially dictated by the mean flow to two-dimensional perturbations strongly amplified over half a pulsation cycle.

6.5. Discussion of energy transfer mechanisms

In this final subsection on channel flows, we investigate the energy production and dissipation mechanisms in order to explain the different transient-growth scenarios that have been identified.

Following the notations introduced in § 4, we consider a perturbation of the form

$$\mathbf{u}(x_0, t) \exp i(\alpha_1 x_1 + \alpha_2 x_2) + \text{c.c.} \quad \text{with } \mathbf{u}(x_0, t) \equiv \begin{pmatrix} u_0(x_0, t) \\ u_1(x_0, t) \\ u_2(x_0, t) \end{pmatrix}, \quad (6.2)$$

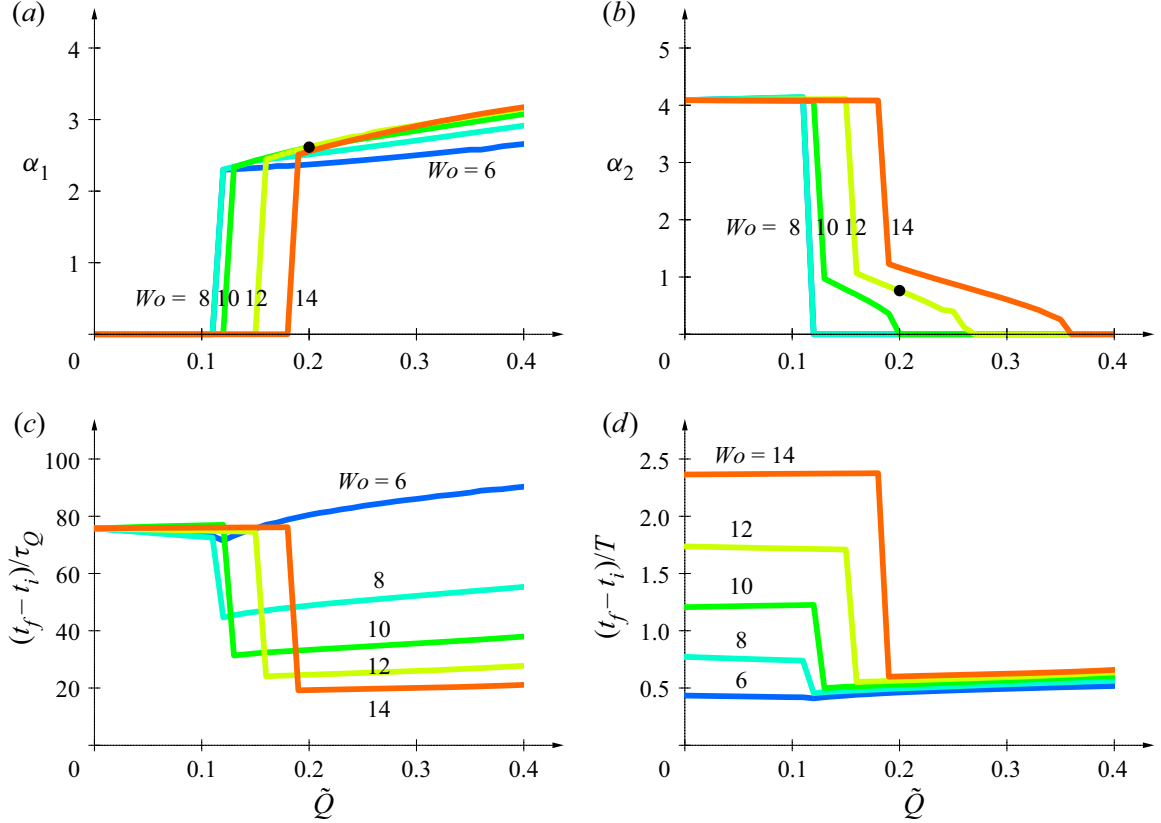


Figure 8. Characterisation of the maximally amplified optimal perturbations as the pulsation amplitude \tilde{Q} is increased for $Wo = 6, 8, 10, 12, 14$ at $Re = 4000$. (a) Streamwise wavenumber α_1 , (b) spanwise wavenumber α_2 , (c) duration of transient growth $t_f - t_i$ measured in mean-flow advection units τ_Q and (d) in pulsation periods T .

using a complex-valued three-dimensional velocity vector $\mathbf{u}(x_0, t)$. Such a perturbation is associated with an instantaneous kinetic energy per unit volume of

$$E(t) = \frac{1}{D} \int_{-D/2}^{+D/2} e(x_0, t) dx_0, \quad (6.3)$$

where

$$e(x_0, t) = \|\mathbf{u}(x_0, t)\|^2 \equiv \mathbf{u}(x_0, t) \cdot [\mathbf{u}(x_0, t)]^*, \quad (6.4)$$

represents the local energy density. Thus, the temporal energy variation,

$$\frac{dE(t)}{dt} = \frac{1}{D} \int_{-D/2}^{+D/2} (\partial_t \mathbf{u}(x_0, t) \cdot [\mathbf{u}(x_0, t)]^* + \mathbf{u}(x_0, t) \cdot [\partial_t \mathbf{u}(x_0, t)]^*) dx_0, \quad (6.5)$$

follows from the dynamics of $\mathbf{u}(x_0, t)$, governed by the Navier–Stokes equations linearised about the pulsating base flow (4.3). Separating terms due to interaction with the base flow from those involving viscous dissipation leads to

$$\frac{dE(t)}{dt} = \Pi(t) - \Theta(t), \quad (6.6)$$

where

$$\Pi(t) = \frac{1}{D} \int_{-D/2}^{+D/2} \pi(x_0, t) dx_0 \quad \text{and} \quad \Theta(t) = \frac{1}{D} \int_{-D/2}^{+D/2} \theta(x_0, t) dx_0, \quad (6.7a,b)$$

with

$$\pi(x_0, t) = -\frac{\partial U_1(x_0, t)}{\partial x_0} (u_0(x_0, t)[u_1(x_0, t)]^* + [u_0(x_0, t)]^* u_1(x_0, t)) \quad (6.8)$$

and

$$\theta(x_0, t) = 2\nu(\|\partial_0 \mathbf{u}(x_0, t)\|^2 + (\alpha_1^2 + \alpha_2^2)\|\mathbf{u}(x_0, t)\|^2). \quad (6.9)$$

The term $\pi(x_0, t)$ accounts for energy transfer between the pulsating base flow and the perturbation: it essentially represents energy production due to base-flow shear, but negative values may occur and its profile across the channel crucially depends on the relative phases of $u_0(x_0, t)$ and $u_1(x_0, t)$.

Another quantity of interest is the instantaneous growth rate

$$\sigma(t) \equiv \frac{1}{2E(t)} \frac{dE(t)}{dt} = \frac{\Pi(t) - \Theta(t)}{2E(t)}, \quad (6.10)$$

particularly relevant during phases of near-exponential amplification.

Close monitoring of the spatiotemporal development of the base-flow interaction $\pi(x_0, t)$ and the dissipation $\theta(x_0, t)$ terms will clarify the amplification mechanisms that govern the different stages of the dynamics.

We focus on two characteristic configurations that have already been discussed: pulsating base flows at $Re = 4000$ and $Wo = 10$ with two different pulsation amplitudes, $\tilde{Q} = 0.1$ and $\tilde{Q} = 0.2$, associated with streaky and two-dimensional maximally amplified perturbations, respectively.

6.5.1. Streaky maximally amplified optimal perturbation

For the lower pulsation amplitude of $\tilde{Q} = 0.1$, a maximal amplification of $G_{max}^{max} = 1.77 \times 10^3$ is achieved from $t_i = 0.166T$ to $t_f = 1.389T$ for streamwise invariant and spanwise periodic perturbations with $\alpha_1 = 0$ and $\alpha_2 = 4.073$. The associated temporal evolution of the perturbation energy $E(t)$ is shown in figure 9(a), with the corresponding instantaneous growth rate $\sigma(t)$ in figure 9(b). Here, the transient growth is seen to follow the classical pattern prevailing for steady Poiseuille flow: a strong and very short initial boost for $t_i < t < t_* = 0.175T$ (blue parts of the curves), followed by a phase of gradually weakening growth for $t_* < t < t_f$ (in red) towards the maximum response. And indeed, these curves in figure 9(a,b) are almost identical to the accompanying insets that correspond to the maximally amplified perturbations for steady Poiseuille flow at the same Reynolds number, characterised by $\alpha_1 = 0$, $\alpha_2 = 4.088$, $G_{max}^{max} = 1.76 \times 10^3$. This evolution is the result of energy production $\Pi(t)$ and dissipation $\Theta(t)$, shown in figure 9(c). As can be seen by plotting these quantities relative to the instantaneous energy in figure 9(d), viscous dissipation plays here a minor part in the transient growth throughout the entire process from t_i to t_f .

The temporal evolution of the spatial structure of the maximally amplified streaky perturbation is illustrated in figure 10. Selected snapshots correspond to the thick black dots in figure 9: $t_i = 0.166T$ optimal initial perturbation (thick blue curves); $t = 0.169T$ (thin blue curves); $t_* = 0.175T$ at maximal instantaneous growth (thick green curves); $t = 0.500T$ (thin red curves); $t_f = 1.389T$ optimal response (thick red curves). In order to enable comparison of these profiles throughout the temporal evolution, they have here all been normalised to unit total energy. As expected, the initial perturbation consists in streamwise aligned vortices, that fill the entire channel cross-section, with a vanishing streamwise velocity component: see thick blue curves in figure 10(a–c) and corresponding

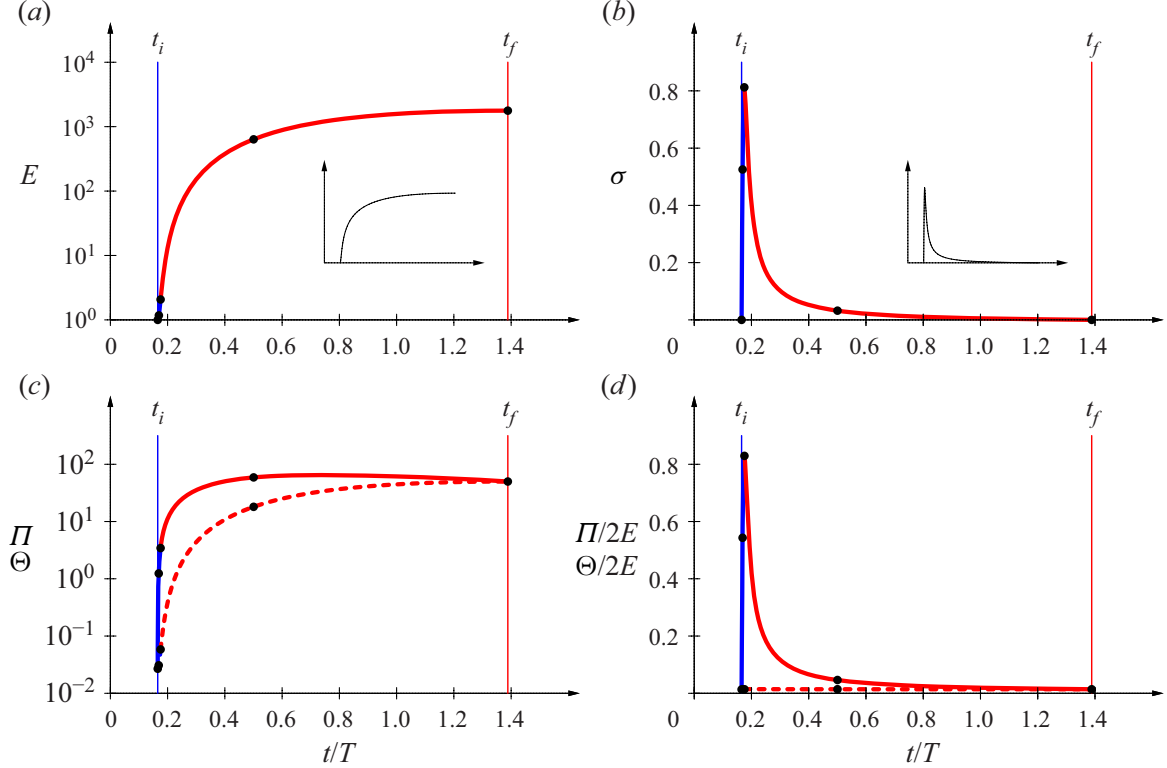


Figure 9. Temporal development of maximally amplified perturbation at $Re = 4000$, $Wo = 10$ and $\tilde{Q} = 0.1$. Optimal perturbation is streamwise invariant with $\alpha_1 = 0$ and $\alpha_2 = 4.073$. (a) Evolution of energy $E(t)$ from $t_i = 0.166T$ to $t_f = 1.389T$, leading to $G_{\max}^{max} = 1.77 \times 10^3$. (b) Corresponding instantaneous growth rate $\sigma(t)$. (c) Energy production $\Pi(t)$ (solid line) and dissipation $\Theta(t)$ (dashed line). (d) Production and dissipation terms relative to instantaneous energy. Insets in panels (a) and (b) correspond to maximally amplified streaks for steady Poiseuille flow at same Reynolds number.

vector plot in figure 10(e). Transient amplification promotes streamwise velocity while reducing wall-normal and spanwise velocity components, leading to a final response that solely consists of streamwise velocity: see thick red curves in figure 10(a–c) and u_1 -isolines in figure 10(f). The energy production profiles π shown in figure 10(d) result from the interaction of base flow shear with u_0 and u_1 , and are therefore significant only around $t_\star = 0.175T$ (green curve), while displaying vanishing levels near t_i and t_f . Dissipation profiles θ (not shown) remain at small values throughout the entire evolution.

Clearly, in this regime, the oscillating component of the base flow has a very weak influence, the amplification process operates as for the equivalent steady Poiseuille flow by redistributing streamwise momentum by streamwise vortices, and the dynamics is essentially dictated by the lift-up effect. This insensitivity to the pulsating base-flow component explains why the maximal growth factors G_{\max}^{max} prevailing for streaky optimal perturbations remain at nearly constant level as \tilde{Q} is increased, as observed in figure 6.

6.5.2. Two-dimensional maximally amplified optimal perturbation

A markedly different scenario prevails at higher pulsation amplitudes when the largest transient amplification is achieved for two-dimensional (streamwise periodic and spanwise invariant) perturbations.

As already shown in figure 5(d), for a pulsation amplitude of $\tilde{Q} = 0.2$, the maximally amplified optimal initial perturbation at $Re = 4000$ and $Wo = 10$ occurs for $\alpha_1 = 2.619$

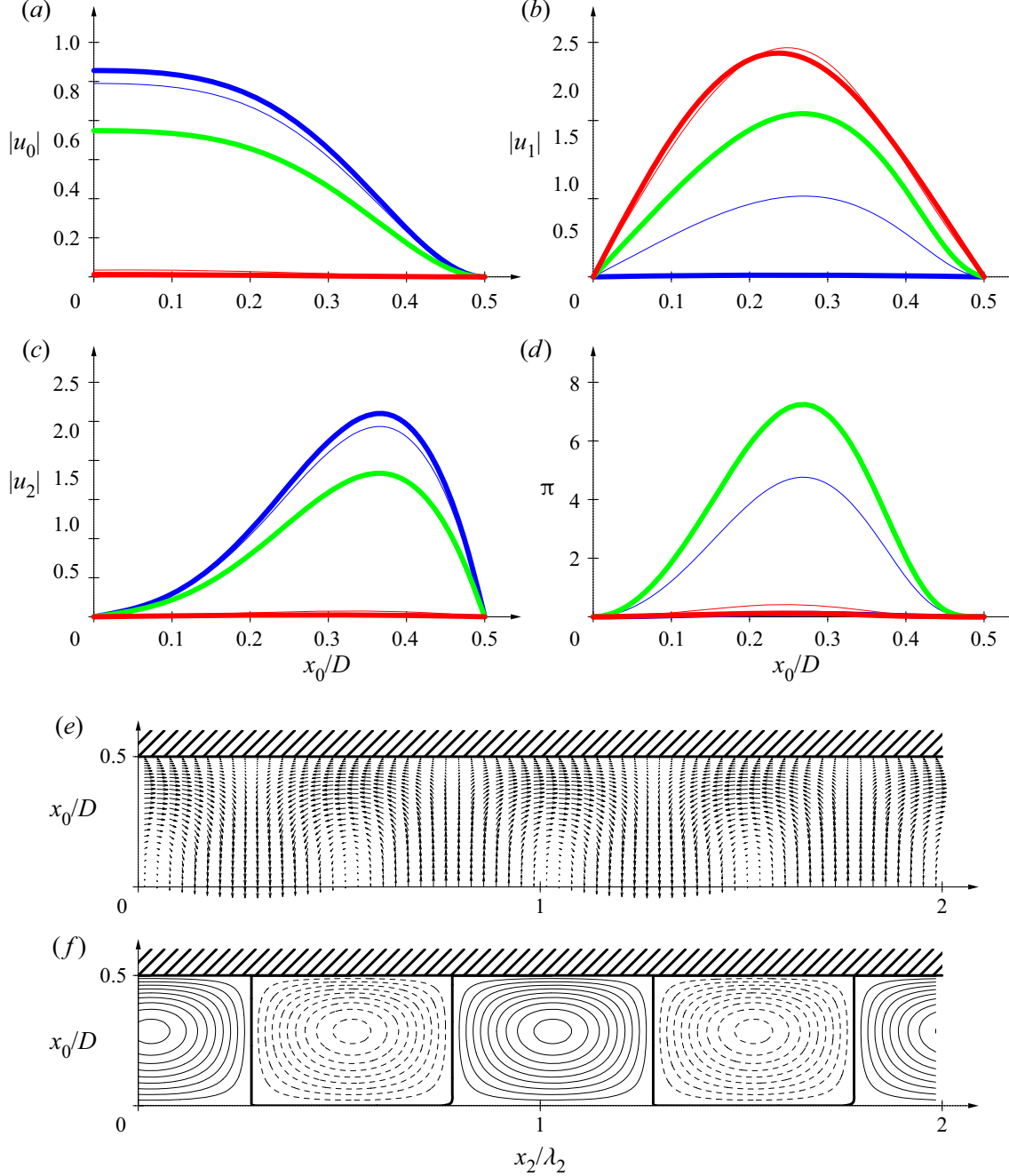


Figure 10. Evolution of spatial structure of maximally amplified streaks for $Re = 4000$, $Wo = 10$ and $\tilde{Q} = 0.1$. Spatial profiles of flow fields (normalised to unit total energy) over half-channel $0 \leq x_0 \leq D/2$ at different snapshots: $t_i = 0.166T$ optimal initial perturbation (thick blue lines); $t = 0.169T$ (thin blue lines); $t_\star = 0.175T$ at maximum growth rate (thick green lines); $t = 0.500T$ (thin red lines); $t_f = 1.389T$ optimal response (thick red lines). Envelope of (a) wall-normal $|u_0(x_0, t)|$, (b) streamwise $|u_1(x_0, t)|$ and (c) spanwise $|u_2(x_0, t)|$ velocity perturbations. (d) Energy production $\pi(x_0, t)$ terms. Snapshots of velocity fields in half-channel over two spanwise wavelengths ($\lambda_2 = 2\pi/\alpha_2$): (e) vector plot of (u_0, u_2) for initial perturbation at t_i and (f) equispaced isolines of streamwise component u_1 of response at $t = t_f$.

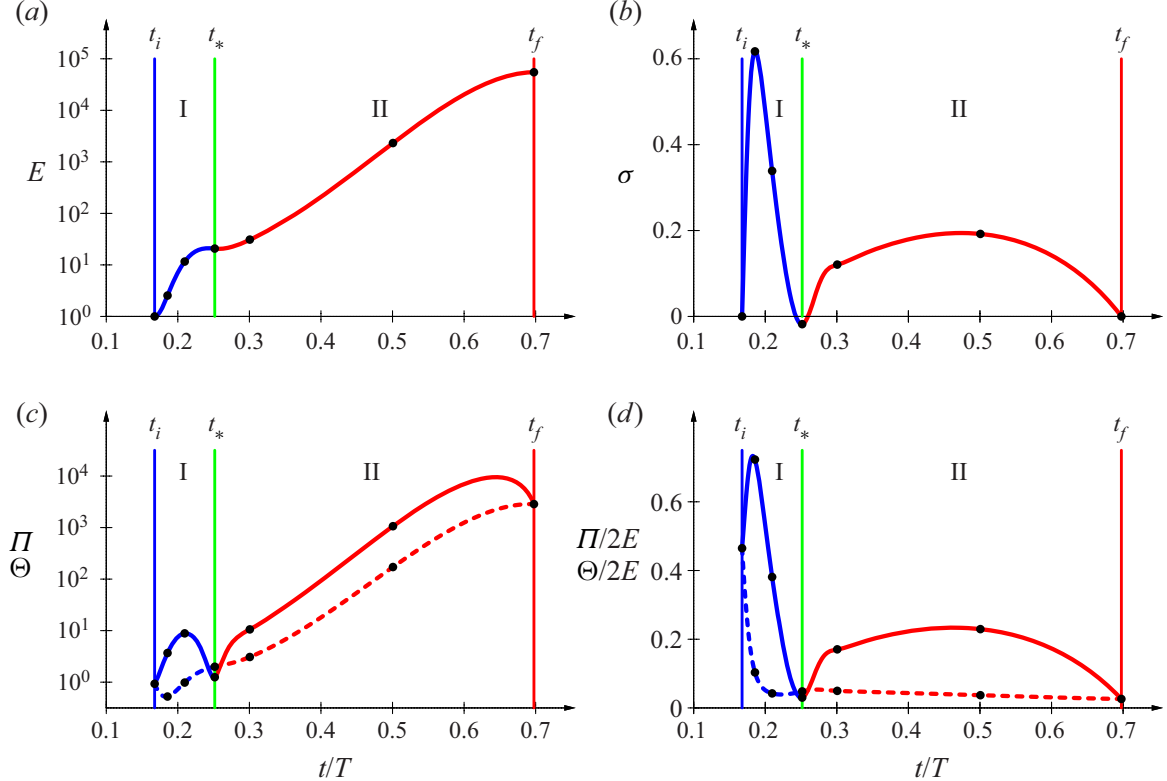


Figure 11. Temporal development of maximally amplified perturbation at $Re = 4000$, $Wo = 10$ and $\tilde{Q} = 0.2$. Optimal perturbation is two-dimensional with $\alpha_1 = 2.619$ and $\alpha_2 = 0$. (a) Evolution of energy $E(t)$ from $t_i = 0.168T$ to $t_f = 0.698T$, leading to $G_{max}^{max} = 5.48 \times 10^4$. (b) Corresponding instantaneous growth rate $\sigma(t)$. (c) Energy production $\Pi(t)$ (solid line) and dissipation $\Theta(t)$ (dashed line). (d) Production and dissipation terms relative to instantaneous energy. Growth occurs in two stages: phase I (in blue) for $t_i < t < t_*$ and phase II (in red) for $t_* < t < t_f$, separated by stall at $t_* = 0.251T$ (green vertical line).

and $\alpha_2 = 0$ and leads to an amplification of $G_{max}^{max} = 5.48 \times 10^4$ from $t_i = 0.168T$ to $t_f = 0.698T$. The temporal evolution of the perturbation energy is given in figure 11(a), with the associated instantaneous growth rate in figure 11(b). The transient growth that occurs over the interval $t_i < t < t_f$ is here seen to develop in two stages: first a relatively short period (phase I, blue curves) of rapid growth followed by a longer interval (phase II, red curves) of weaker but almost constant growth. Between these two stages, the amplification stalls and the instantaneous growth displays a minimum value, which is here slightly negative around $t_* = 0.251T$. This two-stage evolution results from production and dissipation contributions, as illustrated in figure 11(c,d): a first peak in $\Pi(t)$ during phase I is responsible for the rapid growth of the perturbation, followed by a sustained nearly exponential increase during phase II. The contribution of the relative dissipation $\Theta(t)/2E(t)$ is significant only at the very beginning, before rapidly dropping to low values.

The mechanisms responsible for the growth of the perturbation differ in both phases, as illustrated by the profiles in figure 12. These plots show the evolution of the spatial distribution of various fields by selected snapshots, corresponding to the thick black dots in figure 11. Note that the perturbation profiles have again been normalised to unit total energy. The envelopes of wall-normal $|u_0|$ and streamwise $|u_1|$ velocity components in figure 12(a,b) show that the initial perturbation at t_i (thick blue curves) is localised toward the wall with maximum amplitude around $x_0 = 0.4D$, before spreading over the entire channel cross-section in the subsequent evolution. The spatial distribution of the base-flow

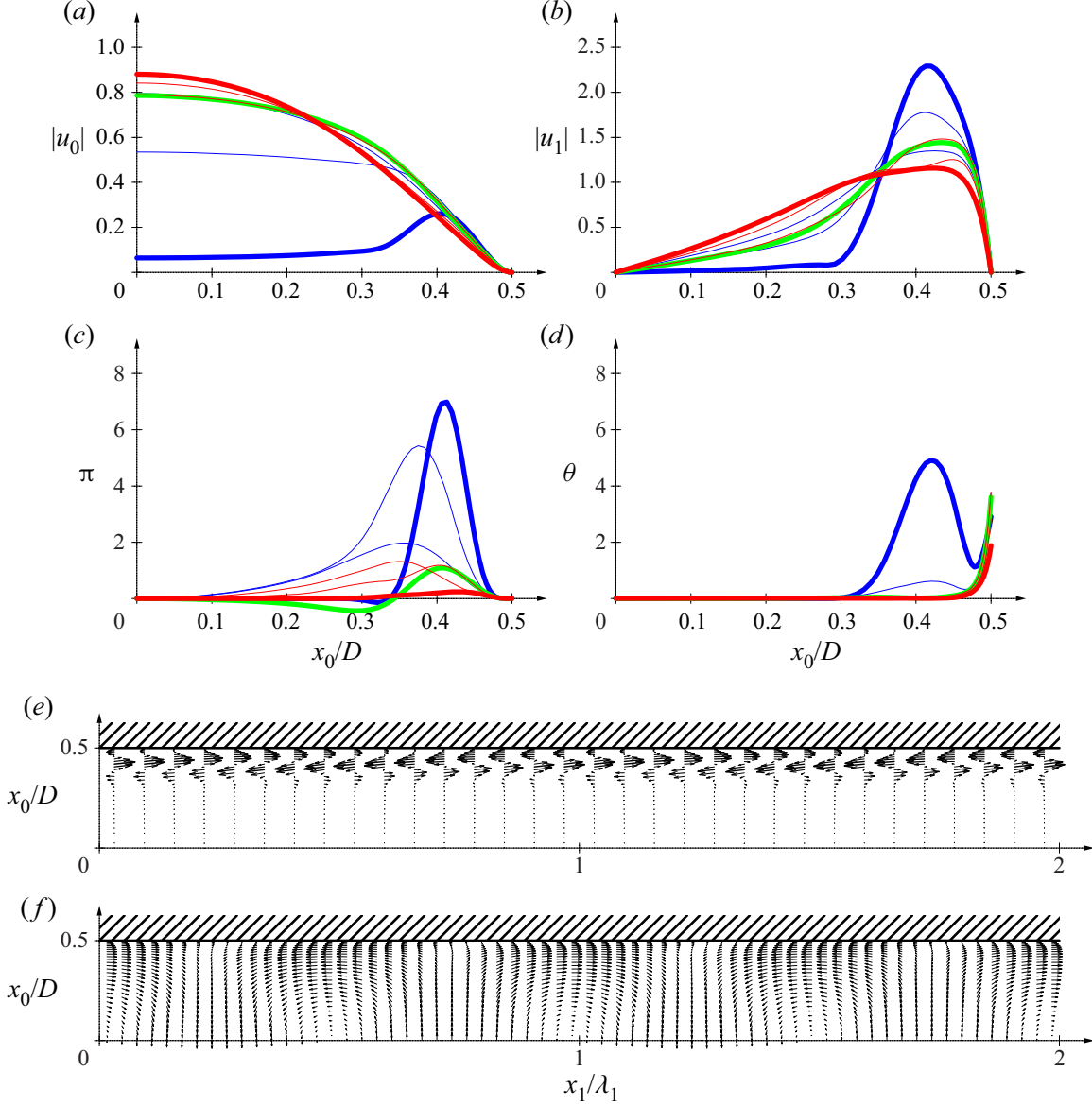


Figure 12. Evolution of spatial structure of maximally amplified (two-dimensional) optimal perturbation for $Re = 4000$, $Wo = 10$ and $\tilde{Q} = 0.2$. Spatial profiles of flow fields (normalised to unit total energy) over half-channel $0 \leq x_0 \leq D/2$ at different snapshots: $t_i = 0.168T$ optimal initial perturbation (thick blue lines); $t = 0.186T$ and $t = 0.210T$ in phase I (thin blue lines); $t_* = 0.251T$ at stall (thick green lines); $t = 0.300T$ and $t = 0.500T$ in phase II (thin red lines); $t_f = 0.698T$ optimal response (thick red lines). (a) Envelope of wall-normal $|u_0(x_0, t)|$ and (b) streamwise $|u_1(x_0, t)|$ velocity perturbations. (c) Energy production $\pi(x_0, t)$ and (d) dissipation $\theta(x_0, t)$ terms. Snapshots of (u_0, u_1) velocity fields in half-channel over two streamwise wavelengths ($\lambda_1 = 2\pi/\alpha_1$): (e) initial perturbation at $t = t_i$ and (f) response at $t = t_f$.

interaction terms $\pi(x_0, t)$ (shown in figure 12c) reveals that the driving mechanism is strong and concentrated around $x_0 = 0.4D$ in phase I (blue curves) while weaker and evenly spread out in phase II (red curves). In contrast, plots of $\theta(x_0, t)$ (figure 12d) show that dissipation is only significant in the initial stages for $t \simeq t_i$ and reduced to a very thin boundary layer near the wall throughout the rest of the evolution. The vector plot of the initial perturbation in a streamwise channel cross-section (figure 12e) highlights the flow structures concentrated near the wall and characteristically tilted upstream. In contrast, the final response (figure 12f) fills the entire channel.

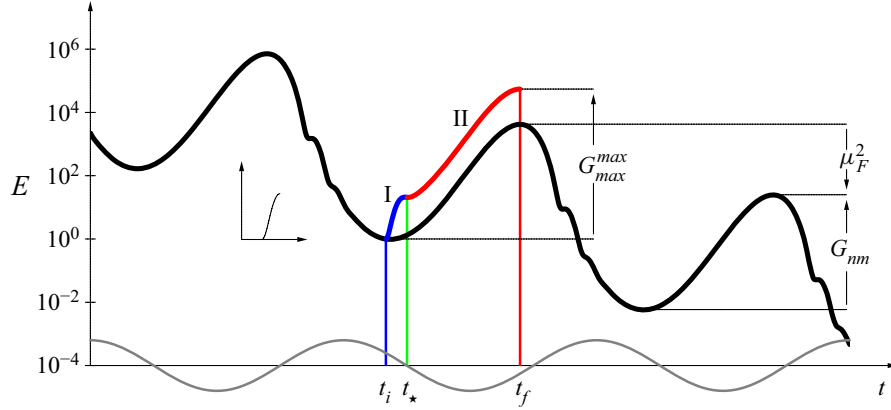


Figure 13. Temporal energy evolution of maximally amplified perturbation (blue and red curves) compared with least stable normal mode (thick black curve), at $Re = 4000$, $Wo = 10$ and $\tilde{Q} = 0.2$, for $\alpha_1 = 2.619$. Normal-mode energy exponentially decays in the long term, according to a Floquet multiplier of $\mu_F = 0.0766$, but displays intracyclic amplification by a factor of $G_{nm} = 4.30 \times 10^3$, approximately during half a pulsation period. Optimal perturbation is amplified by $G_{\max}^{\max} = 5.48 \times 10^4$. Phase II (in red) closely follows normal mode while phase I (in blue) is very similar to optimal growth prevailing for steady Poiseuille flow at same parameters (inset). Grey sinusoidal curve represents base flow rate $Q(t)$ (not to scale).

Finally, we compare the dynamics of the present maximally amplified optimal perturbation with the development of the temporal normal mode prevailing for the same pulsating base flow at the same spatial wavenumbers. Such normal modes have been extensively computed and characterised in our previous investigation (Pier & Schmid 2017), using both Floquet eigenproblems and linearised direct numerical simulations.

All pulsatile base flows under consideration here are linearly stable so that temporal eigenmodes decay in the long term. The thick black curve in figure 13 shows the temporal evolution of perturbation energy for the least stable normal mode at $Re = 4000$, $Wo = 10$ and $\tilde{Q} = 0.2$, with $\alpha_1 = 2.619$ and $\alpha_2 = 0$. The negative mean slope in this logarithmic plot confirms the decay, governed by a Floquet multiplier of $\mu_F = 0.0766$. Thus, the perturbation energy of this normal mode is reduced by a factor of μ_F^2 after each pulsation period. However, within each pulsation cycle, significant modulation occurs. This intracyclic growth and decay has been shown to approximately coincide with base-flow deceleration and acceleration phases (Pier & Schmid 2017), as indicated by the grey sinusoidal line representing $Q(t)$. Here, the normal mode displays an intracyclic amplification of $G_{nm} = 4.30 \times 10^3$.

Comparison of optimal-perturbation and normal-mode energy curves reveals that, during phase II ($t_* < t < t_f$, red part of curve in figure 13), the optimal perturbation closely follows the normal-mode dynamics. And, indeed, optimal perturbation and normal mode also display very similar flow fields during that interval.

In the initial phase I ($t_i < t < t_*$, blue part of curve in figure 13), however, the maximally amplified perturbation takes advantage of the optimal initial condition responsible for the initial boost in the response through the Orr mechanism. The amplification during phase I is almost identical to the maximal growth experienced by a two-dimensional optimal initial condition for steady Poiseuille flow at the same Reynolds number and same streamwise wavenumber, shown in the inset in figure 13.

These considerations reveal that the maximally amplified two-dimensional perturbation is an optimal combination of Orr mechanism (phase I) and intracyclic normal-mode growth over half a pulsation cycle (phase II). Growth during phase I is essentially determined by the equivalent steady Poiseuille base flow: the resulting amplification factor

therefore scales approximately linearly on Re while being largely independent of Wo and \tilde{Q} . In contrast, growth during phase II closely follows the intracyclic amplification of the associated temporal eigenmodes, and the magnitude of this intracyclic growth has been shown to strongly depend on Wo and \tilde{Q} : whatever the Womersley number, it increases almost exponentially with \tilde{Q} , and the increase is fastest at the lower values of Wo (Pier & Schmid 2017). This exponential growth with \tilde{Q} explains why two-dimensional optimal perturbations always eventually prevail over streaky perturbations, as observed in figure 6.

The maximal growth factor G_{max}^{max} is obviously always larger than either contribution of phase I or of phase II to the total growth. But while the contribution of phase I remains at moderate levels (one or two orders of magnitude, as for steady Poiseuille flow), it is phase II that is responsible for the huge amplification factors prevailing as the modulation amplitude \tilde{Q} increases. As a result, except for weak pulsation amplitudes, the Orr mechanism only contributes a small factor to the maximal growth G_{max}^{max} , while most of the amplification process is due to modal growth during base-flow deceleration.

7. Pulsating pipe flow

After having presented detailed results for channel flows, we now turn to the transient growth properties of pulsating flows through circular pipes. The organisation of this section is similar to the previous one. However, since most features are equivalent, many details may be omitted here.

By adopting the general formulation appropriate for both Cartesian and cylindrical coordinates, the analysis of pulsating pipe flows is carried out with the same numerical codes as previously used for pulsating channel flows. Due to periodicity in the azimuthal coordinate, the wavenumber α_2 only takes integer values, but otherwise the numerical implementation proceeds as for a Cartesian formulation. Recall that the apparent singularity at the pipe axis ($x_0 = 0$) resolves itself by taking advantage of the symmetry properties relevant for each flow component, since all flow fields are either symmetric or antisymmetric in the radial coordinate x_0 .

7.1. Transient growth of streaks and helical perturbations

Since for steady Hagen–Poiseuille flow, streamwise invariant streaks with $\alpha_2 = 1$ and $\alpha_1 = 0$ undergo the largest non-modal growth, we first consider the transient amplification features prevailing for the same type of perturbations developing in pulsating pipe flows. Figure 14 shows the amplification factors $G(t_i, t_f)$ obtained at $Wo = 10$, for $Re = 2000$ and 5000 , $\tilde{Q} = 0.4$ and 1.0 . The control parameters are the same as those used in figure 2 for pulsating channel flow, and it is observed that the transient growth properties are very similar.

For streamwise periodic ($\alpha_1 \neq 0$) perturbations, the least stable temporal modes correspond to helical perturbations with $\alpha_2 = 1$. Investigation of transient growth characteristics for $\alpha_1 \neq 0$ also confirms that perturbations with $\alpha_2 = 1$ dominate over axisymmetric perturbations ($\alpha_2 = 0$) as well as over those of higher azimuthal order ($\alpha_2 \geq 2$).

Figure 15 illustrates the transient growth properties for $\alpha_2 = 1$ and $\alpha_1 = 2$ at $Wo = 10$ and $Re = 2000$ and $Re = 5000$ as the amplitude \tilde{Q} of the pulsating base flow component is increased. As for pulsating channel flow, a second maximum emerges that rapidly dominates the dynamics beyond some value of the base flow modulation amplitude.

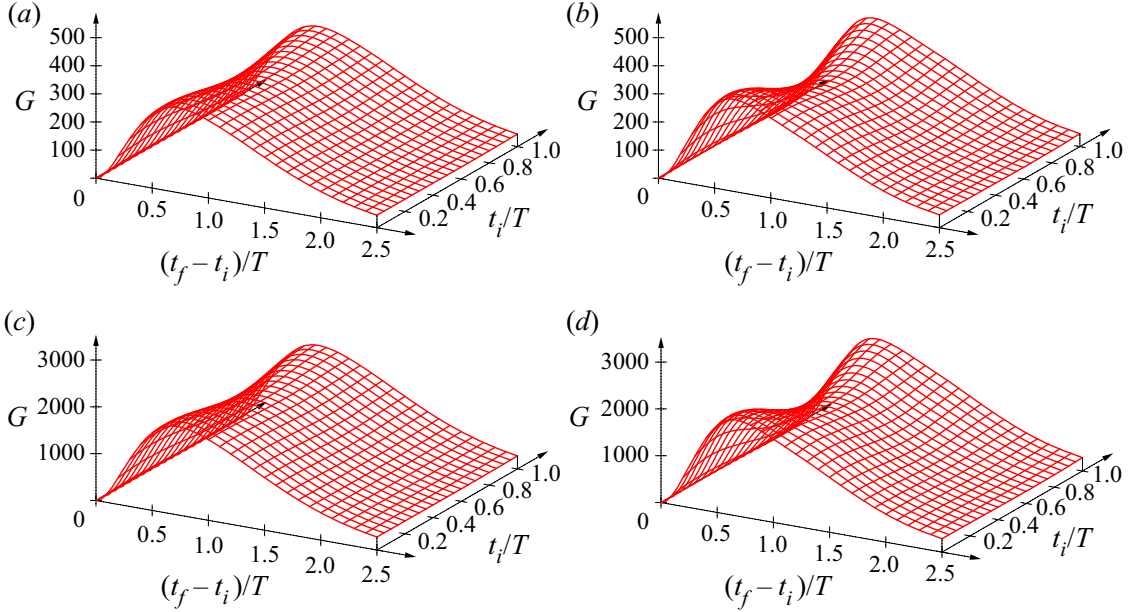


Figure 14. Optimal transient amplification for streaks with $\alpha_2 = 1$ and $\alpha_1 = 0$ at (a,b) $Re = 2000$ and (c,d) $Re = 5000$. Pulsating pipe flow at $Wo = 10$ and (a,c) $\tilde{Q} = 0.4$ and (b,d) $\tilde{Q} = 1.0$.

This maximum is again located near $t_i/T = 0.2$ and $(t_f - t_i)/T = 0.5$ and corresponds thus to amplification over half a pulsation cycle.

7.2. Optimal growth at given wavenumbers

The maximal transient growth G^{max} , computed by optimisation of $G(t_i, t_f)$ over all values of t_i and t_f for fixed wavenumbers α_1 and α_2 , is shown in figure 16. In each plot the evolution of G^{max} curves for $0 < \alpha_1 < 6$ is illustrated as \tilde{Q} is increased from $\tilde{Q} = 0$ to $\tilde{Q} = 1$ in steps of 0.1. Panels (a–c) compare the growth of axisymmetric perturbations, $\alpha_2 = 0$ in panel (a), with that of helical perturbations, $\alpha_2 = 1$ in panel (b) and $\alpha_2 = 2$ in panel (c). Clearly, under pulsating flow conditions, axisymmetric initial conditions undergo transient amplification that is not much larger than for the equivalent steady Poiseuille flow, as demonstrated by the nearly overlapping curves in figure 16(a). Non-axisymmetric perturbations, however, experience transient amplification that rapidly grows with \tilde{Q} , and strongest growth occurs for $\alpha_2 = 1$ (figure 16b). Computation of G^{max} for all $\alpha_2 \leq 6$ (results not shown) reveals that the same scenario prevails at higher azimuthal order, but the rate of increase of G^{max} with \tilde{Q} is significantly weaker for higher α_2 .

Evolution of the growth characteristics for $Re = 4000$ with different Womersley numbers, $Wo = 8$ in panel (d), $Wo = 12$ in panel (e) and $Wo = 14$ in panel (f), confirms again that largest amplification factors occur for lower pulsation frequencies, i.e., longer pulsation cycles.

Finally, values obtained at lower $Re = 2000$ for $Wo = 8$ in panel (g), 10 in panel (h) and 14 in panel (i) show that the general trend is similar but with lower values of G^{max} , as expected for lower Re .

7.3. Maximal amplification

Finally, the maximal amplification G_{max}^{max} achievable for a given pulsating pipe flow is obtained by optimising $G^{max}(\alpha_1, \alpha_2)$ over all streamwise wavenumbers α_1 and

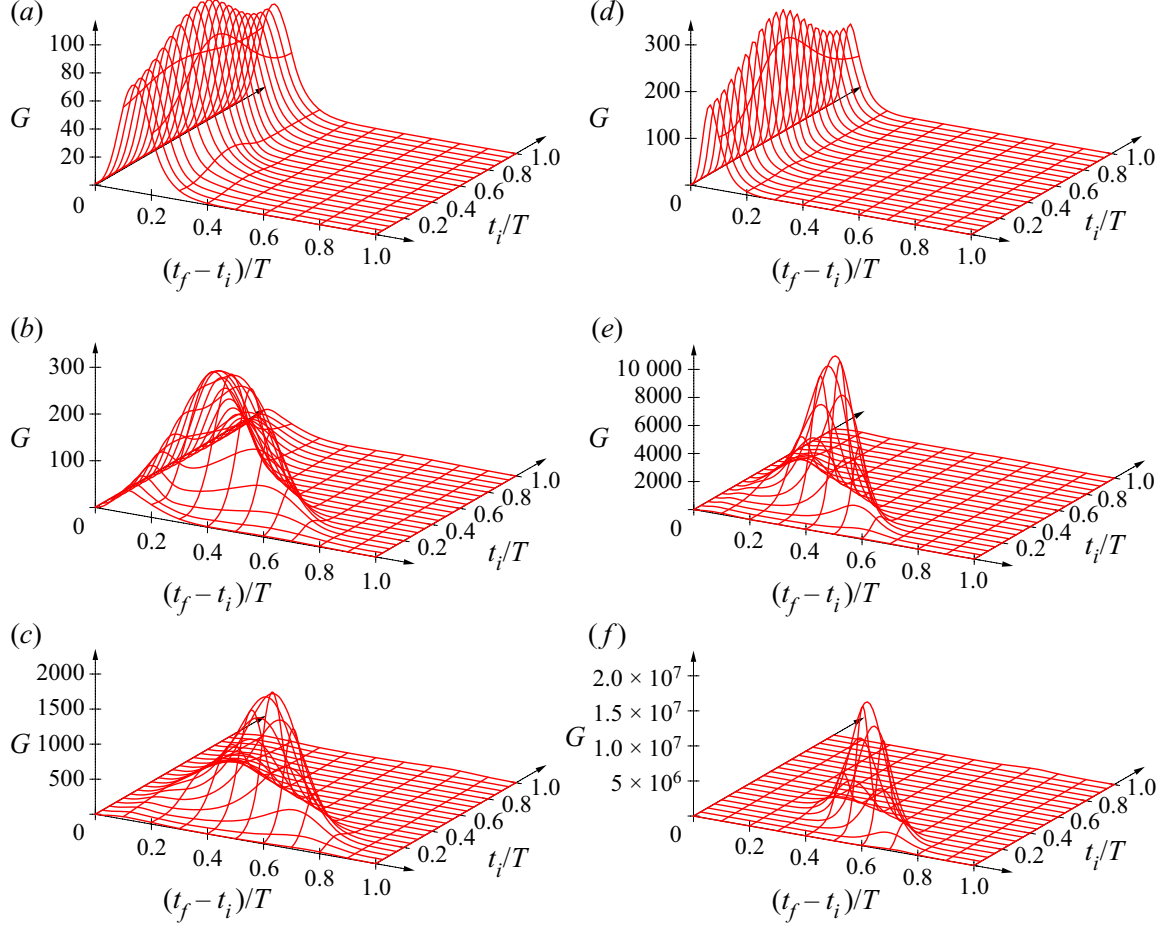


Figure 15. Optimal transient amplification for helical perturbations with $\alpha_2 = 1$ and $\alpha_1 = 2$ at (a–c) $Re = 2000$ and (d–f) $Re = 5000$. Pulsating pipe flow at $Wo = 10$ and (a,d) $\tilde{Q} = 0.1$, (b,e) $\tilde{Q} = 0.4$ and (c,f) $\tilde{Q} = 0.6$.

azimuthal mode numbers α_2 . Figure 17 shows the variation of G_{\max}^{max} as the pulsation amplitude \tilde{Q} is increased for Womersley numbers in the range $5 \leq Wo \leq 15$ and $Re = 2000, 3000, 4000$ and 5000 . The behaviour is again found to be similar to that prevailing for pulsating channel flows: at low pulsation amplitudes, G_{\max}^{max} hardly departs from the value corresponding to the equivalent steady Poiseuille flow; beyond a critical value \tilde{Q}_c of the pulsation amplitude \tilde{Q} , transition to approximately exponential growth of G_{\max}^{max} with \tilde{Q} takes over. The results shown in figure 17(a) perfectly match those of figure 4(a) of Xu *et al.* (2021), for the subset of control parameter values that is common to both studies. This agreement further validates our methods.

The variation with Wo and Re of the critical value \tilde{Q}_c for crossover between the two regimes is shown in figure 18(a). In the exponential regime prevailing for $\tilde{Q} \geq \tilde{Q}_c$, the growth rates κ corresponding to the slopes in figure 17 are given in figure 18(b), computed according to (6.1). For a given Reynolds number, the curves of \tilde{Q}_c in figure 18(a) are seen to display a minimum for moderate values of the Womersley number, while they increase both for large and small values of Wo . The increase of \tilde{Q}_c with Wo for $Wo \geq 10$ is strongest at lower values of the Reynolds number. In contrast, for $Wo \leq 10$ the values of \tilde{Q}_c depend much less on Re .

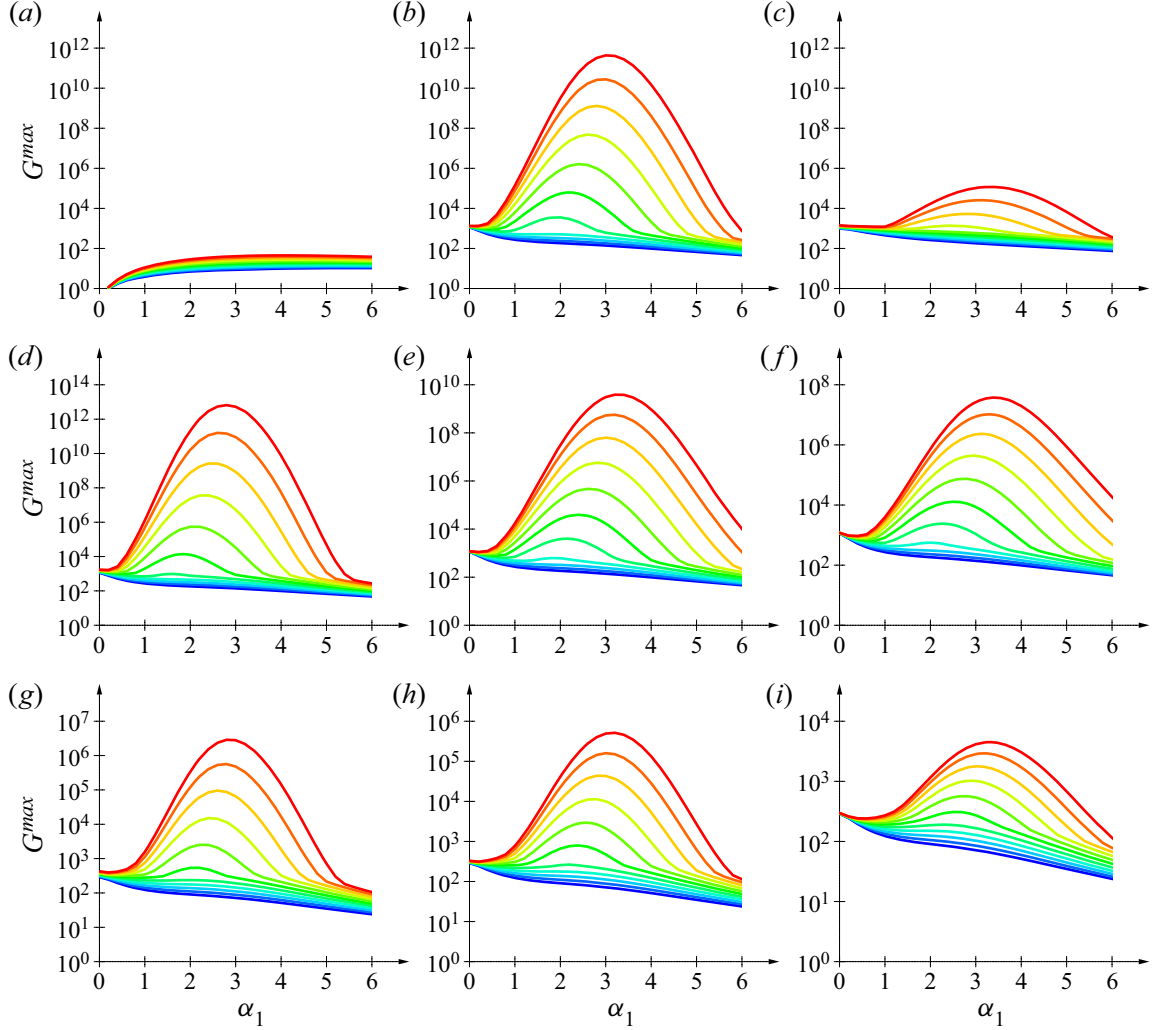


Figure 16. Maximum energy growth G^{max} for pulsating pipe flows, over $0 < \alpha_1 < 6$ at $\tilde{Q} = 0.0, 0.1, 0.2, \dots, 1.0$. Here (a–f) $Re = 4000$ and (g–i) $Re = 2000$; (a–c,h) $Wo = 10$, (d,g) $Wo = 8$, (e) $Wo = 12$ and (f,i) $Wo = 14$; (a) $\alpha_2 = 0$, (b,d–i) $\alpha_2 = 1$ and (c) $\alpha_2 = 2$.

Comparison of the values of \tilde{Q}_c and κ for pipe flows (figure 18) with those prevailing for channel flows shown in figure 7, reveals that pipe flows require larger pulsation amplitudes to switch to the regime with exponentially growing amplification factors G_{max}^{max} . This is especially true for lower Womersley numbers (see also figure 20 below with additional data for $Wo = 3$). Also, while the growth rates κ display very similar trends for both channel (figure 7b) and pipe configurations (figure 18b), the values for pipe flows are approximately half those of channel flows.

The streamwise wavenumber α_1 associated with the most amplified perturbation as the pulsation amplitude \tilde{Q} is varied for a range of Womersley numbers is monitored in figures 19(a) and 19(b) for $Re = 2000$ and $Re = 4000$, respectively. These plots demonstrate that the regime change occurring at \tilde{Q}_c is indeed associated with a jump in streamwise wavenumber from $\alpha_1 = 0$ for $\tilde{Q} < \tilde{Q}_c$ to finite α_1 -values for $\tilde{Q} > \tilde{Q}_c$. In contrast with channel flows, however, for all pulsating pipe flow configurations investigated here, the optimal perturbations always occur with azimuthal mode number $\alpha_2 = 1$. Thus the critical value \tilde{Q}_c always corresponds to a transition from streaky ($\alpha_1 = 0, \alpha_2 = 1$) to helical ($\alpha_1 \neq 0, \alpha_2 = 1$) optimal perturbations, at the same azimuthal mode number.

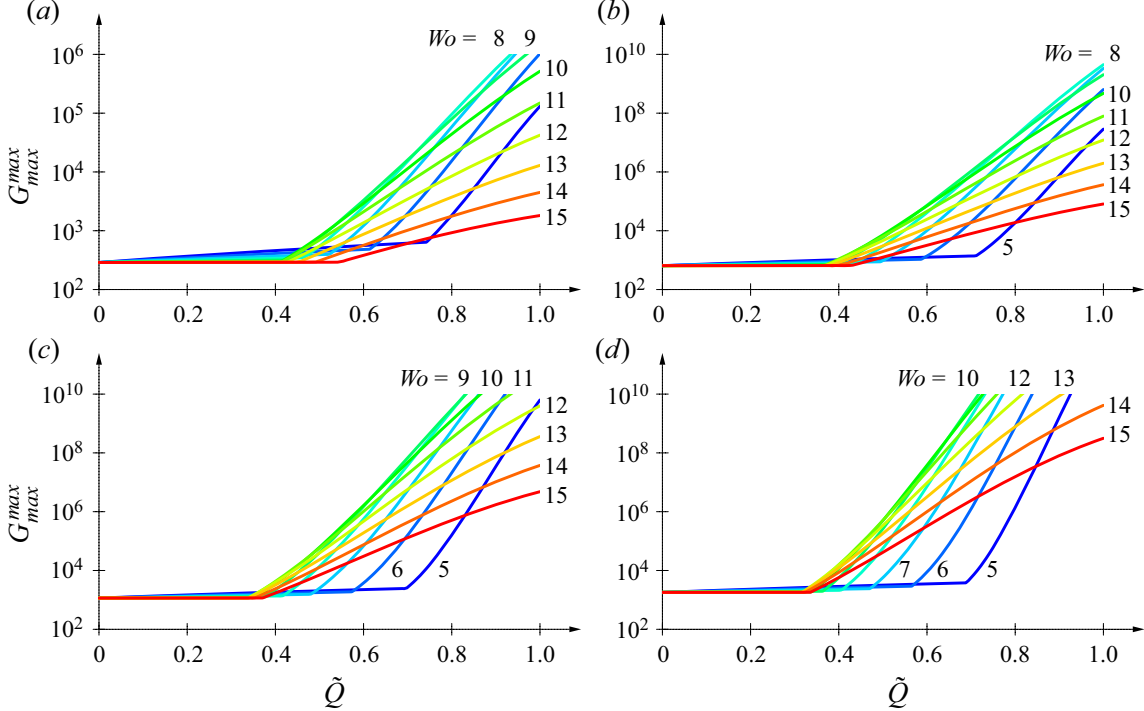


Figure 17. Evolution of maximal transient energy amplification G_{\max}^{\max} for pulsating pipe flows with \tilde{Q} for $W_o = 5, 6, 7, \dots, 15$ at (a) $Re = 2000$, (b) $Re = 3000$, (c) $Re = 4000$ and (d) $Re = 5000$.

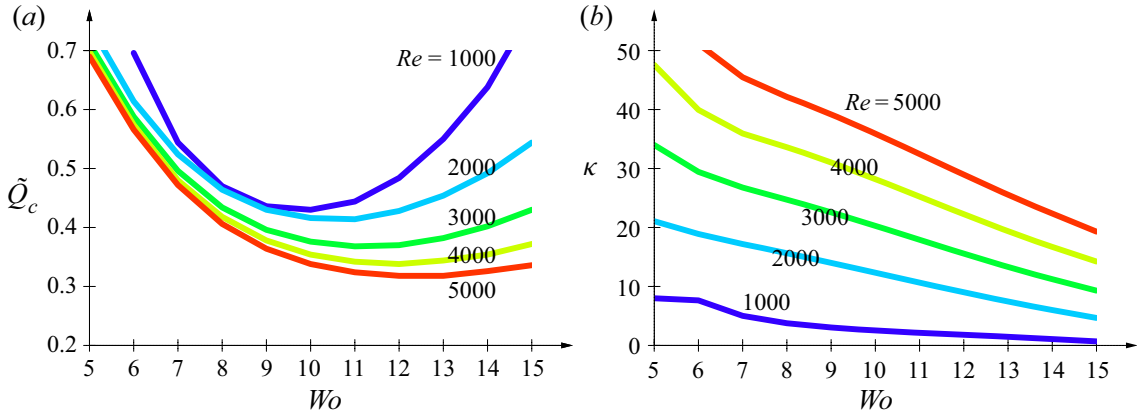


Figure 18. (a) Critical values \tilde{Q}_c for transition between streaky and helical maximally amplified perturbations in pulsating pipe flows. (b) Exponential growth rate κ of G_{\max}^{\max} with \tilde{Q} in the helical regime.

This regime change is also associated with a discontinuity in the duration of the growth phase $t_f - t_i$ for the optimal amplification process, as illustrated in figure 19(c,d) for $Re = 4000$. The optimised duration $t_f - t_i$ is given in mean-flow advection units τ_Q in figure 19(c) and in units of the pulsation period T in figure 19(d). These plots illustrate that pulsating pipe flows display similar transient dynamics as channel flows: for $\tilde{Q} < \tilde{Q}_c$, the optimal duration $t_f - t_i$ remains close to the value prevailing for the average parabolic flow profile; for $\tilde{Q} > \tilde{Q}_c$, when helical perturbations dominate, maximal amplification occurs over intervals corresponding approximately to half a pulsation period. Thus our results confirm the findings of Xu *et al.* (2021) that helical perturbations dominate the transient growth at large pulsation amplitudes. By our detailed comparison of channel and

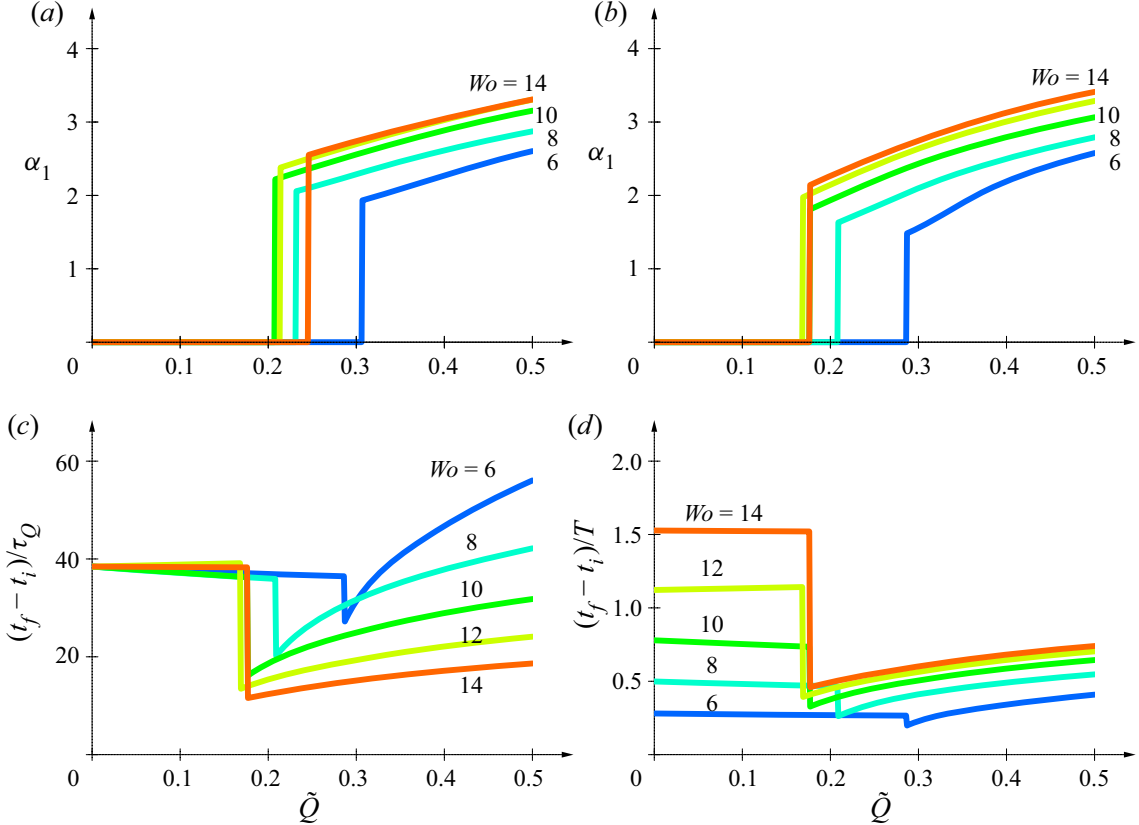


Figure 19. Characterisation of the maximally amplified optimal perturbations as the pulsation amplitude \tilde{Q} is increased for $Wo = 6, 8, 10, 12, 14$. Streamwise wavenumber α_1 at (a) $Re = 2000$ and (b) $Re = 4000$. Duration of transient growth $t_f - t_i$ at $Re = 4000$ (c) measured in mean-flow advection units τ_Q and (d) in pulsation periods T .

pipe configurations at moderate pulsation frequencies, we have been able to highlight the fundamental growth mechanisms, which are common to both geometries.

8. Conclusion

Considering pulsating flows through both channels and pipes, we have investigated the non-modal transient energy amplification resulting from optimal initial conditions. Our study has systematically covered the pulsating base flows for $1000 \leq Re \leq 5000$, $5 \leq Wo \leq 15$ and $0 \leq \tilde{Q} \leq 1$.

While channel and pipe flows display quite different linear modal stability characteristics, their non-modal transient growth features are found to be very similar in situations that are linearly stable. Optimal energy growth occurs according to two distinct scenarios. At weak pulsation amplitudes \tilde{Q} , the behaviour is similar to that resulting from the equivalent steady Poiseuille flow, and the oscillating flow component appears to have only a small effect. Beyond a critical value of \tilde{Q} , however, transient growth increases exponentially with \tilde{Q} and reaches astronomical values, already for moderate pulsation amplitudes. In this latter regime, optimal growth mainly occurs over half a pulsation period, during the slow part of the pulsation cycle, and closely follows the intracyclic amplification of the associated Floquet eigenmodes. We have previously shown (Pier & Schmid 2017) that the intracyclic modulation amplitudes derived from temporal normal modes may be huge, even for linearly decaying eigenmodes. The maximal transient

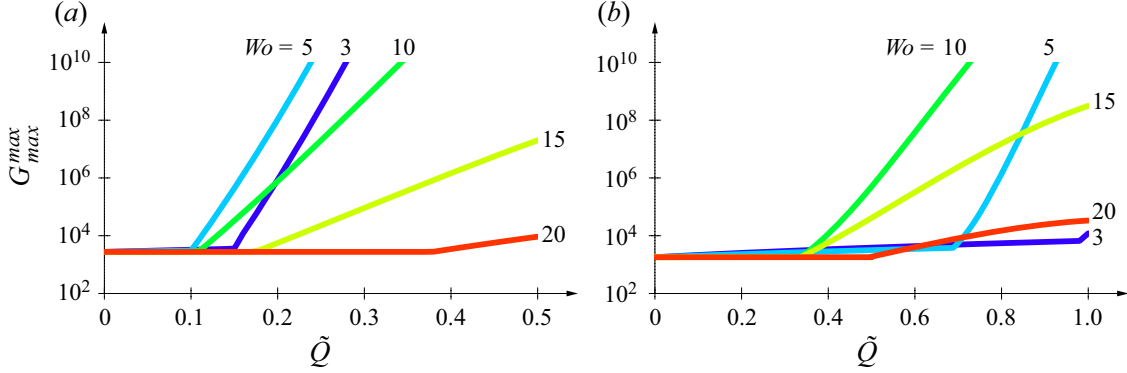


Figure 20. Evolution of maximal transient energy amplification G_{\max}^{\max} with \tilde{Q} for $Wo = 3, 5, 10, 15$ and 20 at $Re = 5000$, for (a) channel and (b) pipe configurations.

amplification factors G_{\max}^{\max} computed in the present investigation are even larger since they take advantage of both this normal-mode intracyclic growth and non-modal Orr-type amplification, which contributes in the early stage of the growth process.

These findings have been firmly established by a comprehensive investigation of pulsating flows over the range $5 \leq Wo \leq 15$, deemed to be the most relevant for applications in the haemodynamic context. In order to explore the expected behaviour beyond that frequency range, figure 20 shows the maximal achievable transient growth G_{\max}^{\max} for channel and pipe flows at $Re = 5000$, extending the results of figures 6(d) and 17(d) by including data at lower and higher pulsation frequencies, $Wo = 3$ and $Wo = 20$, respectively. At high pulsation frequencies, it is observed that the pulsating component is rather inefficient in producing G_{\max}^{\max} factors beyond those prevailing for steady base flows, a result closely related to the fact that high-frequency pulsation also has a strong stabilising effect on modal temporal growth rates. In the low frequency regime, the curves for $Wo = 3$ indicate that strong growth is still possible but requires larger pulsation amplitudes \tilde{Q} . When lowering Wo , the critical value \tilde{Q}_c for onset of the exponential regime increases moderately for channel flows and significantly for pipe flows ($\tilde{Q}_c \simeq 0.98$ for $Wo = 3$). These plots are in agreement with observations already made by Xu *et al.* (2021) for pulsating pipe flows. Concerning the spatial structure of the optimal perturbations, the results of figure 20 follow the same scenario as previously discussed: while streaky perturbations prevail for $\tilde{Q} < \tilde{Q}_c$, at larger pulsation amplitudes two-dimensional and helical perturbations dominate, respectively, in channel and pipe flows.

It should be noted that a major difference between channel and pipe flows concerns their linear modal instability features. Indeed, for channel flows there exists a critical Reynolds number beyond which linear instability occurs. This is well known for steady Poiseuille channel flow, and the dependence of this critical Reynolds number with the pulsating flow parameters has been extensively discussed in our previous work (Pier & Schmid 2017). By contrast, steady pipe Poiseuille flow remains linearly stable, whatever the Reynolds number. For time-periodic base flows, linear instability has been found for purely oscillating pipe flows (Thomas *et al.* 2011). However, the presence of a non-vanishing mean flow rate appears to have a stabilising effect and all pulsating pipe flows considered in the present study are far from temporal instability.

Another difference is that two-dimensional (spanwise invariant and streamwise periodic) perturbations are the most unstable or the least stable for channel flows, whereas the leading linear instability for pipe flows occurs for helical modes with $\alpha_2 = 1$ and $\alpha_1 \neq 0$, which dominate over perturbations of higher azimuthal order ($\alpha_2 \geq 2$) as well

as over axisymmetric ($\alpha_2 = 0$) ones. It is found that this remains true for pulsating pipe flows.

While channel flows are rapidly dominated by two-dimensional sinuous perturbations, pipe flows are dominated by helical perturbations in similar pulsating flow regimes. For pipe flows, axisymmetric perturbations never prevail. But note that the Cartesian equivalent of axisymmetric perturbations are two-dimensional perturbations of varicose symmetry, which never prevail either. The closest equivalent to a two-dimensional sinuous perturbation in a cylindrical geometry is a helical perturbation (with $\alpha_2 = 1$).

This study gives a detailed and comprehensive perspective on the perturbation dynamics in pulsatile channel and pipe flow, treating these configurations within a time-dependent, initial-value problem formalism and thus avoiding restrictive assumptions of a modal, time-asymptotic approach. This analysis identified a rich perturbation behaviour driven by parametric and transient excitation over one or multiple forcing cycles and the dominance of an Orr-type amplification mechanism at early times that acts efficiently and selectively across a significant parameter range, once a critical pulsation amplitude has been surpassed.

Our study lays the foundation for a future analysis of pulsating base flows with higher harmonic content, such as blood flow rates resulting from the cardiac pulse. The present approach could also be generalised to take into account compliant walls or to address nonlinear fluid effects.

Acknowledgements. Institut national de physique nucléaire et de physique des particules (IN2P3-CNRS) is warmly thanked for very generously providing computing resources. Without access to its Centre de calcul allowing us to run thousands of independent single-processor jobs, it would have been very difficult to carry out the present research.

Early stages of this work were carried out while B.P. was visiting the BP Institute, enjoying a French Government Fellowship at Churchill College, Cambridge University.

Funding. The Royal Society is gratefully acknowledged for its financial support through an International Exchanges Cost Share award (IEC/R2/170133).

Declaration of interests. The authors report no conflict of interest.

Author ORCIDs.

- ④ Benoît Pier <https://orcid.org/0000-0001-8663-8694>;
- ④ Peter J. Schmid <https://orcid.org/0000-0002-2257-8490>.

Appendix A. General formulation of the Navier–Stokes equations

In order to handle both Cartesian and cylindrical formulations of the governing Navier–Stokes equations ((2.1) and (2.2)), a general set of spatial coordinates x_0, x_1, x_2 and associated velocity components u_0, u_1, u_2 is used. These correspond to either wall-normal, streamwise and spanwise directions for channel flows, or radial, streamwise and azimuthal directions for pipe flows, respectively. Using these coordinates and velocity fields, the components of the incompressible Navier–Stokes equations become

$$\partial_t u_0 + (\mathbf{u} \cdot \nabla) u_0 - \left[\frac{1}{x_0} u_2^2 \right] = \nu \left(\Delta u_0 + \left[\frac{1}{x_0^2} (-u_0 - 2\partial_2 u_2) \right] \right) - \partial_0 p, \quad (\text{A1})$$

$$\partial_t u_1 + (\mathbf{u} \cdot \nabla) u_1 = \nu \left(\Delta u_1 \right) - \partial_1 p, \quad (\text{A2})$$

$$\partial_t u_2 + (\mathbf{u} \cdot \nabla) u_2 + \boxed{\frac{1}{x_0} u_0 u_2} = \nu \left(\Delta u_2 + \boxed{\frac{1}{x_0^2} (-u_2 + 2\partial_2 u_0)} \right) - \boxed{\frac{1}{x_0}} \partial_2 p, \quad (\text{A3})$$

$$0 = \partial_0 u_0 + \boxed{\frac{1}{x_0} u_0} + \partial_1 u_1 + \boxed{\frac{1}{x_0}} \partial_2 u_2, \quad (\text{A4})$$

with the notations

$$\partial_0 \equiv \partial_{x_0}, \quad \partial_1 \equiv \partial_{x_1}, \quad \partial_2 \equiv \partial_{x_2}, \quad (\text{A5a-c})$$

and

$$\mathbf{u} \cdot \nabla \equiv u_0 \partial_0 + u_1 \partial_1 + \boxed{\frac{1}{x_0} u_2 \partial_2}, \quad (\text{A6})$$

$$\Delta \equiv \partial_{00} + \boxed{(1/x_0) \partial_0} + \partial_{11} + \boxed{(1/x_0^2) \partial_{22}}. \quad (\text{A7})$$

In these expressions, the terms enclosed in boxes are only present in the formulation using cylindrical coordinates and pertaining to the pipe flow configuration. Resorting to such a general formalism is particularly useful when developing numerical codes to solve both channel and pipe flows: the boxed terms may be switched on or off depending on the flow configuration.

Appendix B. Analytic expressions of the pulsating base flow profiles

For pulsating base flows prevailing in infinite channels or pipes, the harmonic components $U_1^{(n)}(x_0)$ of the streamwise velocity fields (3.1) display profiles following the shape function $W(\xi, \omega)$ with $\xi = 2x_0/D$ and $\omega = \sqrt{n}Wo$.

When considering channel flows in Cartesian coordinates, the oscillating velocity profiles are analytically obtained in terms of hyperbolic functions

$$W(\xi, \omega) \equiv \left(\frac{\cosh(\sqrt{i}\xi\omega)}{\cosh(\sqrt{i}\omega)} - 1 \right) \Bigg/ \left(\frac{\tanh(\sqrt{i}\omega)}{\sqrt{i}\omega} - 1 \right), \quad (\text{B1})$$

for $|\xi| \leq 1$ and $\omega \neq 0$, while the steady component is parabolic,

$$W(\xi, \omega = 0) \equiv \frac{3}{2}(1 - \xi^2). \quad (\text{B2})$$

When considering pipe flows in cylindrical coordinates, the velocity profiles involve Bessel functions

$$W(\xi, \omega) \equiv \left(\frac{J_0(\sqrt{-i}\xi\omega)}{J_0(\sqrt{-i}\omega)} - 1 \right) \Bigg/ \left(\frac{2}{\sqrt{-i}\omega} \frac{J_1(\sqrt{-i}\omega)}{J_0(\sqrt{-i}\omega)} - 1 \right), \quad (\text{B3})$$

with J_0 and J_1 denoting the classic Bessel functions of the first kind. The steady component is again parabolic,

$$W(\xi, \omega = 0) \equiv 2(1 - \xi^2). \quad (\text{B4})$$

All the profiles above are normalised so that their cross-sectional average equals unity. Thus, the pulsating base flow velocity components (3.4) are simply obtained by multiplying these profiles with the flow rate coefficients $Q^{(n)}$.

Appendix C. Linear governing equations of direct problem

In the direct formulation of the incompressible Navier–Stokes equations (4.3), the spatial differential operator $\mathbf{L}(x_0, t)$ is a 4-by-4 matrix of the form

$$\mathbf{L}(x_0, t) \equiv \begin{pmatrix} L_{00}(x_0, t) & 0 & L_{02}(x_0, t) & -\partial_0 \\ L_{10}(x_0, t) & L_{11}(x_0, t) & 0 & -i\alpha_1 \\ L_{20}(x_0, t) & 0 & L_{22}(x_0, t) & -\boxed{\frac{1}{x_0}} i\alpha_2 \\ -\partial_0 - \boxed{\frac{1}{x_0}} & -i\alpha_1 & -\boxed{\frac{1}{x_0}} i\alpha_2 & 0 \end{pmatrix}, \quad (\text{C1})$$

Its coefficients involve ∂_0 -differentiation, depend on the spatial wavenumbers as well as on the base flow velocity profiles. Their explicit expressions are the following:

$$L_{00}(x_0, t) = -i\alpha_1 U_1(x_0, t) + v \left(\Delta - \boxed{\frac{1}{x_0^2}} \right), \quad (\text{C2})$$

$$L_{11}(x_0, t) = -i\alpha_1 U_1(x_0, t) + v \Delta, \quad (\text{C3})$$

$$L_{22}(x_0, t) = -i\alpha_1 U_1(x_0, t) + v \left(\Delta - \boxed{\frac{1}{x_0^2}} \right), \quad (\text{C4})$$

$$L_{10}(x_0, t) = -\partial_0 U_1(x_0, t), \quad (\text{C5})$$

$$L_{20}(x_0, t) = -L_{02}(x_0, t) = \boxed{2v \frac{i\alpha_2}{x_0^2}}, \quad (\text{C6})$$

with

$$\Delta \equiv \partial_{00} + \boxed{\frac{1}{x_0} \partial_0} - \alpha_1^2 - \boxed{\frac{1}{x_0^2}} \alpha_2^2. \quad (\text{C7})$$

Appendix D. Adjoint problem

In the adjoint formulation of the incompressible Navier–Stokes equations (4.5), the spatial differential operator $\mathbf{L}^\dagger(x_0, t)$ is obtained as

$$\mathbf{L}^\dagger(x_0, t) \equiv \begin{pmatrix} L_{00}^\dagger(x_0, t) & L_{01}^\dagger(x_0, t) & L_{02}^\dagger(x_0, t) & -\partial_0 \\ 0 & L_{11}^\dagger(x_0, t) & 0 & -i\alpha_1 \\ L_{20}^\dagger(x_0, t) & 0 & L_{22}^\dagger(x_0, t) & -\boxed{\frac{1}{x_0}} i\alpha_2 \\ -\partial_0 - \boxed{\frac{1}{x_0}} & -i\alpha_1 & -\boxed{\frac{1}{x_0}} i\alpha_2 & 0 \end{pmatrix}, \quad (\text{D1})$$

with

$$L_{00}^\dagger(x_0, t) = -i\alpha_1 U_1(x_0, t) - \nu \left(\Delta - \boxed{\frac{1}{x_0^2}} \right), \quad (\text{D2})$$

$$L_{11}^\dagger(x_0, t) = -i\alpha_1 U_1(x_0, t) - \nu \Delta, \quad (\text{D3})$$

$$L_{22}^\dagger(x_0, t) = -i\alpha_1 U_1(x_0, t) - \nu \left(\Delta - \boxed{\frac{1}{x_0^2}} \right), \quad (\text{D4})$$

$$L_{01}^\dagger(x_0, t) = \partial_0 U_1(x_0, t), \quad (\text{D5})$$

$$L_{20}^\dagger(x_0, t) = -L_{02}^\dagger(x_0, t) = \boxed{2\nu \frac{i\alpha_2}{x_0^2}}. \quad (\text{D6})$$

REFERENCES

- BIAU, D. 2016 Transient growth of perturbations in Stokes oscillatory flows. *J. Fluid Mech.* **794**, R4.
- BLACKBURN, H.M., SHERWIN, S.J. & BARKLEY, D. 2008 Convective instability and transient growth in steady and pulsatile stenotic flows. *J. Fluid Mech.* **607**, 267–277.
- BLENNERHASSETT, P.J. & BASSOM, A.P. 2002 The linear stability of flat Stokes layers. *J. Fluid Mech.* **464**, 393–410.
- BOYD, J.P. 2001 *Chebyshev and Fourier Spectral Methods*. Dover.
- CHIU, J.-J. & CHIEN, S. 2011 Effects of disturbed flow on vascular endothelium: pathophysiological basis and clinical perspectives. *Physiol. Rev.* **91**, 327–387.
- DAVIS, S.H. 1976 The stability of time-periodic flows. *Annu. Rev. Fluid Mech.* **8**, 57–74.
- GOPALAKRISHNAN, S.S., PIER, B. & BIESHEUVEL, A. 2014 Dynamics of pulsatile flow through model abdominal aortic aneurysms. *J. Fluid Mech.* **758**, 150–179.
- VON KERCZEK, C.H. 1982 The instability of oscillatory plane Poiseuille flow. *J. Fluid Mech.* **116**, 91–114.
- KU, D.N. 1997 Blood flow in arteries. *Annu. Rev. Fluid Mech.* **29**, 399–434.
- LUCHINI, P. & BOTTARO, A. 2014 Adjoint equations in stability analysis. *Annu. Rev. Fluid Mech.* **46**, 493–517.
- MAGRI, L. 2019 Adjoint methods as design tools in thermoacoustics. *Appl. Mech. Rev.* **71**, 020801.
- PEDLEY, T.J. 2000 Blood flow in arteries and veins. In *Perspectives in Fluid Dynamics* (ed. G.K. Batchelor, H.K. Moffatt & M.G. Worster), pp. 105–158. Cambridge University Press.
- PIER, B. 2015 Dynamique des écoulements ouverts: instabilités et transition, courbure et rotation. Habilitation à diriger des recherches, École centrale de Lyon & Université de Lyon. Available at: <https://hal.archives-ouvertes.fr/tel-01107517>.
- PIER, B. & SCHMID, P.J. 2017 Linear and nonlinear dynamics of pulsatile channel flow. *J. Fluid Mech.* **815**, 435–480.
- PIER, B. & SCHMID, P.J. 2018 Optimal energy growth in pulsatile channel and pipe flows. In *12th European Fluid Mechanics Conference (EFMC12)*.
- QADRI, U., MAGRI, L., IHME, M. & SCHMID, P.J. 2021 Using adjoint-based optimization to enhance ignition in non-premixed jets. *Proc. R. Soc. A* **477**, 20200472.
- RASPO, I., HUGUES, S., SERRE, E., RANDRIAMAMPIANINA, A. & BONTOUX, P. 2002 A spectral projection method for the simulation of complex three-dimensional rotating flows. *Comput. Fluids* **31**, 745–767.
- SCHMID, P.J. 2007 Nonmodal stability theory. *Annu. Rev. Fluid Mech.* **39**, 129–162.
- THOMAS, C., BASSOM, A.P., BLENNERHASSETT, P.J. & DAVIES, C. 2011 The linear stability of oscillatory Poiseuille flow in channels and pipes. *Proc. R. Soc. Lond. A* **467**, 2643–2662.
- TUZI, R. & BLONDEAUX, P. 2008 Intermittent turbulence in a pulsating pipe flow. *J. Fluid Mech.* **599**, 51–79.
- WOMERSLEY, J.R. 1955 Method for the calculation of velocity, rate of flow and viscous drag in arteries when pressure gradient is known. *J. Physiol.* **127**, 553–563.

B. Pier and P.J. Schmid

- XU, D. & AVILA, M. 2018 The effect of pulsation frequency on transition in pulsatile pipe flow. *J. Fluid Mech.* **857**, 937–951.
- XU, D., SONG, B. & AVILA, M. 2021 Non-modal transient growth of disturbances in pulsatile and oscillatory pipe flows. *J. Fluid Mech.* **907**, R5.
- XU, D., WARNECKE, S., SONG, B., MA, X. & HOF, B. 2017 Transition to turbulence in pulsating pipe flow. *J. Fluid Mech.* **831**, 418–432.

[A28]

Revisiting the linear instabilities of plane channel flow between compliant walls

S. Lebbal, F. Alizard & B. Pier

Physical Review Fluids 7, 023903 (32 pages) (2022)

doi:10.1103/PhysRevFluids.7.023903
<https://hal.archives-ouvertes.fr/hal-03337441>

Revisiting the linear instabilities of plane channel flow between compliant walls

Smail Lebbal ¹, Frédéric Alizard ^{2,*} and Benoît Pier ¹

¹*Univ Lyon, Ecole Centrale de Lyon, CNRS, Univ Claude Bernard Lyon 1, INSA Lyon, LMFA, UMR5509, 69130 Ecully, France*

²*Univ Lyon, Univ Claude Bernard Lyon 1, CNRS, Ecole Centrale de Lyon, INSA Lyon, LMFA, UMR5509, 69622 Villeurbanne France*



(Received 4 September 2021; accepted 19 January 2022; published 11 February 2022)

The present investigation revisits the linear stability of Poiseuille channel flow interacting with compliant walls. The results obtained include the dynamics of Tollmien-Schlichting (TS) modes as well as flow-induced surface-instability (FSI) modes, in the form of both traveling-wave flutter (TWF) and divergence modes. The compliant wall model consists of a spring-backed plate with a viscous substrate deformable in the vertical direction [C. Davies and P. W. Carpenter, *J. Fluid Mech.* **352**, 205 (1997)]. At the interface between the fluid and the walls, the continuity of velocities and stresses, including both viscous and pressure contributions, are taken into account. The FSI modes (both varicose and sinuous) and TS modes are then reinterpreted in the light of the two principal nondimensional control parameters: the Reynolds number (Re), which characterizes the base flow, and the reduced velocity (V_R), which measures the response of the flexible wall to hydrodynamic loading [E. De Langre, *La Houille Blanche*, 3, 14 (2000)]. The characteristics of TS and FSI modes are systematically investigated over a large control-parameter space, including wall dissipation, spring stiffness, and flexural rigidity. We observe that TWF modes are primarily governed by V_R and largely independent of the Reynolds number. It is found that the instability is generally dominated by the TWF mode of varicose symmetry. Divergence and TS modes are both affected by V_R and Re , confirming that these modes belong to a different class. The onset of the divergence mode is mainly observed for the sinuous motion, when increasing the dissipation. To provide physical insight into the mechanisms driving these instabilities, the perturbative energy equations for both FSI and TS modes are analyzed for a wide range of wall parameters and wavenumbers.

DOI: [10.1103/PhysRevFluids.7.023903](https://doi.org/10.1103/PhysRevFluids.7.023903)

I. INTRODUCTION

The constant scientific interest to extend the laminar regime for industrial applications has led to the development of compliant walls since the beginning of the 20th century. In particular, researchers focused on finding optimum wall properties, aiming to delay the laminar-turbulent transition.

In the biological context, interactions between fluid and elastic forces associated with a deformable channel or tube lead to a variety of physiologically significant phenomena. In particular, deformability plays a prominent role in blood flow as well as peristaltic transport, for example, through the intestines and the urogenital tract (see [1,2] for a review).

Such interest arose from Gray's paradox [3]. Gray showed that, to overcome the friction drag of a swimming dolphin subjected to a turbulent flow around its body, the muscles have to be capable

*frederic.alizard@univ-lyon1.fr

of generating a power at least seven times greater than that of other kinds of mammalian muscle. Hence, Gray has suggested that the dolphin skin is able to delay the laminar-turbulent transition. In the laminar regime, indeed, the power developed by muscles would still conform to that of other types of mammalian muscle.

Kramer [4] in the 1950s developed a compliant coating trying to mimic the dolphin's skin. The author claimed that he was able to reduce the drag of a torpedolike model by as much as 60%. Later, the conclusions of both Gray's hypotheses and Kramer's experiments were in part questioned. Russian and American experiments since the 1980s failed to reproduce results provided by Kramer. In addition, scientists observed that the lower turbulence level around the dolphin's swimming body could also be attributed to local pressure gradients. It was also suggested that a reduction in the friction drag may result from the fact that the dolphin leaps out of the water for breathing (see [5–7] for reviews).

However, Gaster's experiments in 1988 [8] gave new hope in using compliant walls to delay laminar-turbulent transition. He showed that the growth rates of artificially generated Tollmien-Schlichting (TS) waves are inhibited when using appropriate coatings. These experiments have given a strong impulse to theoretical developments aiming to tackle this problem.

A major difficulty arises from the design of compliant wall models that are able to couple fluid and solid dynamics. These models may be separated into two categories: surface based and volume based (see [7,9] for a review). The first class of models is less computationally demanding and considers an infinitely thin wall interacting with the fluid through an interface condition. In this case, the wall is defined as a thin plate mounted on springs and dampers. The wall parameters are classically the spring stiffness, the tension, the bending stiffness, its mass, and the damping coefficient.

For the second family of models (i.e., volume based), the wall material is fully described to include single- or multilayer coatings (see [10] and [9] for recent reviews). However, Duncan [11] has shown that a surface model can be used to quantitatively describe many aspects of instabilities and wave propagation on the surface of an elastic and incompressible coating.

Here, the surface-based approach is adopted. Within this approach and following the lead of Benjamin [12–14], which relies on the theory developed by Miles for water waves [15], Carpenter and Garrad [16,17] focused on the stability of boundary-layer flows over Kramer-type compliant walls. They provided some confirmation of the transition-delaying potential of compliant coatings. According to Carpenter and Garrad [16,17], instability modes can be classified into two categories: fluid based (TS mode) and solid based (flow-induced surface instabilities, or fluid-structure instabilities, referenced as FSI hereafter). The last category includes both the traveling-wave flutter (TWF) modes and the (almost static) divergence modes. For the divergence mode, scientists are still arguing about its precise nature. It is either interpreted as an absolute instability [18] or it may also result from a modal instability with a nearly vanishing phase velocity when increasing the wall dissipation [19].

While the surface-based model has been extensively used for external flows such as boundary layers, very few studies have been conducted on internal flows (see, for instance, the recent review of Kumaran [9]). Among them, Davies and Carpenter [20,21] investigated linear instability waves that emerge when a viscous incompressible flow interacts with infinite or finite spring-backed plates in a plane channel.

Considering only sinuous perturbations, Davies and Carpenter [20] derived a theory for the motion of the walls and obtained neutral stability curves for both FSI and TS modes and some values of flexural rigidity of the plate, spring stiffness, and damping. The same year, these authors investigated the dynamics of TS waves that propagate over a compliant panel of finite length, using linearized numerical simulations [21]. For low external disturbances, Davies and Carpenter [21] then suggested that the use of multiple-panel compliant walls could maintain the laminar flow regime at all Reynolds numbers in a plane channel flow. This seminal work was also limited to the sinuous symmetry. These prior analyses have been extended to the varicose motion of the walls for the same case with infinite compliant walls by Nagata and Cole [22]. Despite the fact that this

investigation focused only on a narrow region of the parameter space to make definite statements, the authors found that the varicose TWF mode can be amplified prior to its sinuous counterpart. A similar analysis was recently conducted to address the effect of pulsatile Poiseuille flow through a compliant channel [23] for modal and nonmodal instabilities. Although the latter extended results discussed above to pulsatile flows and short-time perturbations, it has not brought new elements for the asymptotic regime of the steady flow case. Finally, Gajjar and Sibanda [24] investigated a viscous flow in a channel in which only one wall is compliant. The same spring-plate model is used by the authors and the nonlinear evolution of disturbances have been obtained in the limit of large Reynolds numbers within the nonlinear critical layer theory.

The aforementioned analyses address the amplification of FSI and TS modes for compliant channel flows but it should be noted that the models used above have some limitations. First, these analyses use the Reynolds number as a control parameter for both FSI and TS modes. This approach is not entirely satisfactory because a change in the Reynolds number also leads to a change in the compliant wall characteristics. Therefore, the reduced velocity, defined as the ratio between the characteristic time of the solid and that of the fluid, has been advocated by de Langre [25] to measure the strength of the fluid-structure interactions independently of the Reynolds number. Second, a rigorous treatment of the pressure at the wall is key for a complete analysis of fluid-structure interaction problems. On one hand, a consistent formulation was indeed derived by Davies and Carpenter [20] under the form of an Orr-Sommerfeld-like equation accounting for compliant walls. However, this formulation only applies to perturbations of sinuous symmetry. On the other hand, Nagata and Cole [22] and Tsigklifis and Lucey [23] used a primitive formulation combined with a spectral collocation method without any specific treatments for the pressure and the additional boundary conditions arising from the wall equation. In this case, spurious eigenvalues are likely to occur [26]. Third, as suggested by Nagata and Cole [22], the varicose symmetry is as important as the sinuous one for FSI modes. Nevertheless, as far as we know, existing studies of varicose modes only explore a narrow parameter range. As a consequence, the potential gain in using compliant walls to delay laminar-turbulent transition in a plane channel flow could be challenged significantly.

The purpose of the present paper is therefore to revisit the instability modes that emerge when a viscous flow interacts with two parallel spring-backed plates and hope to address the inherent limitations mentioned above. Thus, we reconsider this problem by using the reduced velocity to describe FSI modes. A general formulation is implemented, free of spurious modes, suitable for both sinuous and varicose symmetries, and taking into account the exact hydrodynamic forces acting on the walls. A wide range of wall parameters has been explored to highlight their influence on both FSI and TS modes. Only two-dimensional perturbations are considered since the Squire theorem holds for compliant walls [27].

The paper is organized as follows. Section II presents the model and governing equations used for the fluid-structure interaction problem. In particular, the dimensionless parameters and linearized equations will be introduced. After the numerical methods are presented in Sec. III, Sec. IV provides some physical insight into the influence of wall parameters onto FSI and TS modes for both the sinuous and varicose symmetries. For that purpose, kinetic energy budgets are also computed. Conclusions and prospects are given in the last section.

II. PROBLEM FORMULATION

A. Fluid-structure interaction model and interface conditions

In the entire paper, we restrict our analysis to the two-dimensional problem. Using a Cartesian coordinate system (x, y) with unit vectors $(\mathbf{e}_x, \mathbf{e}_y)$, we consider an incompressible Newtonian fluid with dynamic viscosity μ and density ρ between two spring-backed deformable plates located at $y = \zeta^\pm(x, t)$, which are allowed to move only in the y direction. A schematic diagram of the configuration is shown in Fig. 1.

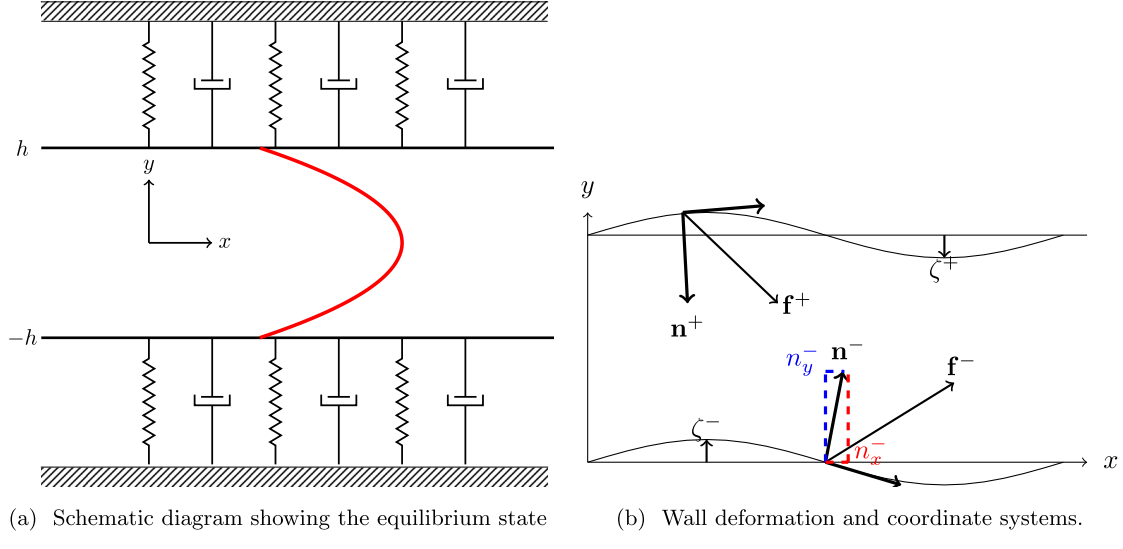


FIG. 1. Channel flow with infinite spring-backed flexible walls.

The flow between the walls is governed by the Navier-Stokes equations:

$$\frac{\partial \mathbf{u}}{\partial t} + \mathbf{u} \cdot \nabla \mathbf{u} = -\frac{1}{\rho} \nabla p + \nu \Delta \mathbf{u},$$

$$\nabla \cdot \mathbf{u} = 0, \quad (1)$$

where $\mathbf{u} = (u, v)$ and p represent the velocity and pressure fields, u (v) denotes the streamwise (wall-normal) velocity component, and $\nu \equiv \mu/\rho$ is the kinematic viscosity of the fluid.

The movement of the flexible plates obeys the following equations, derived through Newton's second law:

$$m \frac{\partial^2 \zeta^\pm}{\partial t^2} + d \frac{\partial \zeta^\pm}{\partial t} + \left(B \frac{\partial^4}{\partial x^4} - T \frac{\partial^2}{\partial x^2} + K \right) \zeta^\pm = f^\pm. \quad (2)$$

Here, m denotes the mass per unit area of the plates, d their damping coefficient, B the flexural rigidity, T the wall tension, K the spring stiffness, and f^\pm represents the y component of the forces acting on the plates. These forces are obtained as

$$f^\pm = \mathbf{e}_y \cdot \mathbf{f}^\pm \quad \text{with} \quad \mathbf{f}^\pm = (\bar{\tau}^\pm - \delta p^\pm \mathbf{I}) \cdot \mathbf{n}^\pm. \quad (3)$$

Here $\bar{\tau}^\pm$ denotes the viscous stress tensor at the walls and δp^\pm the transmural surface pressure, i.e., the difference between the surface pressure inside and outside of the channel, and \mathbf{n}^\pm is the unit vector normal to the walls pointing towards the fluid.

The viscous stress tensor at the walls has the following expression:

$$\bar{\tau}^\pm = \begin{pmatrix} 2\mu \frac{\partial u}{\partial x} & \mu \left(\frac{\partial u}{\partial y} + \frac{\partial v}{\partial x} \right) \\ \mu \left(\frac{\partial u}{\partial y} + \frac{\partial v}{\partial x} \right) & 2\mu \frac{\partial v}{\partial y} \end{pmatrix} \Bigg|_{y=\zeta^\pm}, \quad (4)$$

and the normal vectors to the interface $\mathbf{n}^\pm = (n_x^\pm, n_y^\pm)$ are obtained as

$$n_x^\pm = \pm \frac{\partial \zeta^\pm}{\partial x} \frac{1}{\sqrt{1 + \left(\frac{\partial \zeta^\pm}{\partial x}\right)^2}} \quad \text{and} \quad n_y^\pm = \mp \frac{1}{\sqrt{1 + \left(\frac{\partial \zeta^\pm}{\partial x}\right)^2}}. \quad (5)$$

Combining Eqs. (3)–(5) yields the y component of the hydrodynamic forces acting on the compliant walls,

$$f^\pm = \left[\pm \mu \left(\frac{\partial u}{\partial y} \Big|_{y=\zeta^\pm} + \frac{\partial v}{\partial x} \Big|_{y=\zeta^\pm} \right) \zeta_x^\pm \mp 2\mu \frac{\partial v}{\partial y} \Big|_{y=\zeta^\pm} \pm \delta p^\pm \right] \Bigg/ \sqrt{1 + \left(\frac{\partial \zeta^\pm}{\partial x}\right)^2}, \quad (6)$$

which governs the wall dynamics (2) since the wall movement is constrained to occur only in the y direction. Note that in this approach there are no hydrodynamic forces acting on the plate from the outside, except for a pressure.

Finally, the no-slip conditions on both walls lead to the kinematic conditions prevailing at the moving boundaries:

$$u = 0 \quad \text{and} \quad v = \frac{\partial \zeta^\pm}{\partial t} \quad \text{for} \quad y = \zeta^\pm. \quad (7)$$

Thus, the fluid-structure interaction problem is completely determined by the coupling of the fluid equations (1), the wall equations (2), and boundary conditions (7).

B. Dimensionless control parameters

The present compliant-channel flow configuration is characterized by nine dimensional parameters: the volumetric flow rate Q ($\text{m}^3 \text{s}^{-1}$); the half height h (m) of the channel; the fluid density ρ (kg m^{-3}); the kinematic viscosity ν ($\text{m}^2 \text{s}^{-1}$); the mass of the plate per unit area, m (kg m^{-2}); the damping coefficient of the wall, d ($\text{kg m}^{-2} \text{s}^{-1}$); the bending stiffness of the plate, B ($\text{kg m}^2 \text{s}^{-2}$); the wall tension T (kg s^{-2}); and the spring stiffness K ($\text{kg m}^{-2} \text{s}^{-2}$). Hence, this system may be described by six dimensionless parameters. A useful parameter to characterize fluid-structure interaction phenomena is the reduced flow velocity V_R , defined [25] as the ratio of a characteristic time of the structure to a characteristic time of the flow. Using time scales based on spring stiffness,

$$\tau_K = \sqrt{\frac{m}{K}},$$

and flow advection,

$$\tau_Q = \frac{4h^2}{Q},$$

the reduced velocity is obtained as $V_R = \tau_K / \tau_Q$. Other choices based on different characteristic times would be possible. For $V_R \ll 1$, the influence of the wall compliance is negligible, while $V_R \gg 1$ corresponds to very soft walls. Hence, the resulting six nondimensional control parameters are

$$\begin{cases} \text{Re} = \frac{Q}{\nu}, & V_R = \frac{Q}{4h^2} \sqrt{\frac{m}{K}}, & \Gamma = \frac{m}{\rho h}, \\ d_\star = \frac{d}{\sqrt{mK}}, & B_\star = \frac{B}{Kh^4}, & T_\star = \frac{T}{h^2 K}. \end{cases} \quad (8)$$

Here Re is the Reynolds number based on channel diameter and average flow velocity, and Γ is the mass ratio between the compliant walls and the fluid. The three nondimensional wall parameters d_\star , B_\star , and T_\star are all relative to the spring stiffness K , which serves as reference for the reduced velocity V_R . One may notice that in several previous studies [20,22,28] fluid quantities are used to

build nondimensional parameters for the wall. As underlined by Domaradzki and Metcalfe [29], this may correspond to nonphysical situations where at each Reynolds number a different compliant wall and a different fluid are considered. In the present work, the Reynolds number may be modified using ν and/or Q without changing the wall properties. Hereafter, the mass ratio is kept constant at $\Gamma = 2$ and we only consider walls without tension, $T = 0$. We fix the three dimensional parameters at $\rho = 1$, $h = 1$, and $\tau_Q = 1$.

C. Formulation of the linearized model

This entire study considers the dynamics of small-amplitude perturbations, obeying the linearized version of the governing equations around a steady base state. The unperturbed base configuration thus consists of a parabolic Poiseuille flow $\mathbf{U}(y) = (U_b(y), 0)$ between parallel walls located at $y = \pm h$ [see Fig. 1(a)]. This flow is driven by a pressure $P_b(x) = P_0 - Gx$ of constant streamwise gradient, and we assume a pressure outside the channel walls always equal to $P_b(x)$, so as to equilibrate the forces acting on both sides of the walls for unperturbed conditions.

The total flow fields are then decomposed as $\mathbf{u}(x, y, t) = \mathbf{U}(y) + \mathbf{u}'(x, y, t)$ and $p(x, y, t) = P_b(x) + p'(x, y, t)$. The wall displacement is written as $\zeta^\pm(x, t) = \pm h + \eta^\pm(x, t)$.

Considering that the perturbation components \mathbf{u}' , p' , and η^\pm are of small amplitude, the governing equations may be linearized about the base state.

Since the base state is steady and homogenous in the streamwise direction, the perturbation to the velocity fields, pressure fields, and normal displacements are expressed in normal-mode form as

$$\mathbf{u}'(x, y, t) = \hat{\mathbf{u}}(y)e^{i(\alpha x - \omega t)}, \quad p'(x, y, t) = \hat{p}(y)e^{i(\alpha x - \omega t)}, \quad \text{and} \quad \eta^\pm(x, t) = \hat{\eta}^\pm e^{i(\alpha x - \omega t)}, \quad (9)$$

with α the streamwise wavenumber and ω the frequency. Hereafter, we adopt a temporal viewpoint where $\alpha \in \mathbb{R}$ and $\omega = \omega_r + i\omega_i \in \mathbb{C}$, with ω_i the temporal amplification rate of the mode and ω_r its circular frequency. Substitution of this decomposition into the Navier-Stokes equations and linearization about the base flow leads to

$$\begin{cases} -i\omega\rho\hat{u} + \rho i\alpha\hat{u}U_b + \rho\hat{v}\frac{dU_b}{dy} = -i\alpha\hat{p} + \mu\left(\frac{d^2}{dy^2} - \alpha^2\right)\hat{u}, \\ -i\omega\rho\hat{v} + \rho i\alpha\hat{v}U_b = -\frac{d\hat{p}}{dy} + \mu\left(\frac{d^2}{dy^2} - \alpha^2\right)\hat{v}, \end{cases} \quad (10)$$

together with the divergence-free condition

$$i\alpha\hat{u} + \frac{d\hat{v}}{dy} = 0. \quad (11)$$

Linearization of the wall equations (2) and (6) yields

$$\begin{cases} -\omega^2m\hat{\eta}^+ - i\omega d\hat{\eta}^+ + (B\alpha^4 + T\alpha^2 + K)\hat{\eta}^+ = +\hat{p}(h) + \mu\left(i\alpha\frac{dU_b}{dy}\Big|_h\right)\hat{\eta}^+ - 2\mu\frac{d\hat{v}}{dy}\Big|_h, \\ -\omega^2m\hat{\eta}^- - i\omega d\hat{\eta}^- + (B\alpha^4 + T\alpha^2 + K)\hat{\eta}^- = -\hat{p}(-h) - \mu\left(i\alpha\frac{dU_b}{dy}\Big|_{-h}\right)\hat{\eta}^- + 2\mu\frac{d\hat{v}}{dy}\Big|_{-h}. \end{cases} \quad (12)$$

Following Shankar and Kumaran [30], the boundary conditions at the perturbed interface are implemented using Taylor series about the base state at $y = \pm h$. At linear order, the flow velocity at the walls reads

$$\mathbf{u}(x, y = \zeta^\pm, t) = \mathbf{u}'(x, y = \pm h, t) + \eta^\pm\frac{dU_b}{dy}\Big|_{\pm h}\mathbf{e}_x. \quad (13)$$

Thus, the kinematic boundary conditions (7) become

$$\hat{u}(\pm h) + \hat{\eta}^\pm \frac{dU_b}{dy} \Big|_{\pm h} = 0 \quad \text{and} \quad \hat{v}(\pm h) = -i\omega \hat{\eta}^\pm. \quad (14)$$

Then, by using Eqs. (14) and the divergence-free condition, the right-hand side of Eqs. (12) can be further simplified, leading to

$$\begin{cases} -\omega^2 m \hat{\eta}^+ - i\omega d \hat{\eta}^+ + (B\alpha^4 + T\alpha^2 + K) \hat{\eta}^+ = +\hat{p}(h) - \mu \frac{d\hat{v}}{dy} \Big|_h, \\ -\omega^2 m \hat{\eta}^- - i\omega d \hat{\eta}^- + (B\alpha^4 + T\alpha^2 + K) \hat{\eta}^- = -\hat{p}(-h) + \mu \frac{d\hat{v}}{dy} \Big|_{-h}. \end{cases} \quad (15)$$

Equations (10), (11), and (15) completely govern the dynamics of small-amplitude perturbations and take into account the linearized fluid-structure coupling as derived from the exact hydrodynamic forces.

III. NUMERICAL METHODS

In this work, we follow the general framework described by Manning *et al.* [26] for avoiding spurious eigenvalues. First of all, we rewrite Eqs. (15) using velocity components at the boundaries. For illustration purposes, only the upper wall is here considered.

Using the condition $-i\omega \hat{\eta}^+ = \hat{v}(h)$, we obtain

$$-i\omega \hat{v}(h) = W_1 \hat{v}(h) + W_2 \hat{u}(h) + \frac{1}{m} p(h), \quad (16)$$

with

$$W_1 = -\frac{d}{m} - 2 \frac{\mu}{m} \frac{d}{dy} \quad \text{and} \quad W_2 = \frac{(B\alpha^4 + T\alpha^2 + K)}{m \frac{dU_b}{dy} \Big|_h} - \frac{\mu}{m} i\alpha.$$

The kinematic condition $\hat{u}(h) + \hat{\eta}^+ \frac{dU_b}{dy} \Big|_h = 0$ is recast as

$$-i\omega \hat{u}(h) + \hat{v}(h) \frac{dU_b}{dy} \Big|_h = 0. \quad (17)$$

The velocity components and pressure are discretized in the y -direction using a Chebyshev collocation method. To avoid spurious pressure modes, we consider the so-called $\mathbb{P}_N - \mathbb{P}_{N-2}$ approximation in which the pressure is approximated with a polynomial of degree $N - 2$ while the velocity is discretized with a polynomial of degree N [31]. From this point, we note the vectors con-

taining the unknowns: $\mathbf{V} = (\overbrace{\hat{u}_0, \hat{u}_N, \hat{v}_0, \hat{v}_N, \hat{u}_1, \dots, \hat{u}_{N-1}, \hat{v}_1, \dots, \hat{v}_{N-1}}^{\mathbf{V}_{BC}}, \overbrace{\hat{v}_2, \dots, \hat{v}_{N-2}}^{\mathbf{V}_I})$ and $\mathbf{P}_I = (\hat{p}_1, \dots, \hat{p}_{N-1})$, where we separate the boundary values (\mathbf{V}_{BC}) from the interior points (\mathbf{V}_I). Hence, the discretized counterpart of the previous continuous model [Eqs. (10), (15), and (14)] reads

$$\left[\begin{array}{ccc} \overbrace{\mathbf{A}_1, \mathbf{B}_1, \mathbf{0}}^4 & \overbrace{\mathbf{A}_2, \mathbf{B}_2, \mathbf{C}_2}^{2(N-2)} & \overbrace{\mathbf{A}_3, \mathbf{B}_3, \mathbf{0}}^{N-2} \\ \end{array} \right] \left[\begin{array}{c} \mathbf{V}_{BC} \\ \mathbf{V}_I \\ \mathbf{P}_I \end{array} \right]$$

$$= i\omega \begin{bmatrix} \mathbf{I} & \mathbf{0} & \mathbf{0} \\ \mathbf{0} & \mathbf{I} & \mathbf{0} \\ \mathbf{0} & \mathbf{0} & \mathbf{0} \end{bmatrix} \begin{bmatrix} \mathbf{V}_{BC} \\ \mathbf{V}_I \\ \mathbf{P}_I \end{bmatrix} \} \begin{array}{l} 4 \\ 2(N-2) \\ N-2 \end{array}, \quad (18)$$

where the divergence-free condition is imposed on the interior points and \mathbf{I} denotes the identity matrix. The derivative matrices based on Chebyshev polynomials are either expressed on the interior points only (for the pressure) or all the nodes (for the velocity components) [31]. Note that the boundary equations involve the pressure at $y = \pm h$: these values are readily obtained by polynomial interpolation with spectral accuracy, corresponding to matrix \mathbf{A}_3 .

The discrete counterpart of the divergence-free condition reads $\mathbf{C}_2 \mathbf{V}_I = \mathbf{0}$. Hence, from

$$\mathbf{0} = \mathbf{C}_2(i\omega \mathbf{V}_I) = \mathbf{C}_2 \mathbf{B}_1 \mathbf{V}_{BC} + \mathbf{C}_2 \mathbf{B}_2 \mathbf{V}_I + \mathbf{C}_2 \mathbf{B}_3 \mathbf{P}_I,$$

the vector \mathbf{P}_I can be expressed as a function of \mathbf{V}_I and \mathbf{V}_{BC} :

$$\mathbf{P}_I = \underbrace{-(\mathbf{C}_2 \mathbf{B}_3)^{-1} \mathbf{C}_2 \mathbf{B}_1}_{\mathbf{M}_{BC}} \mathbf{V}_{BC} \underbrace{-(\mathbf{C}_2 \mathbf{B}_3)^{-1} \mathbf{C}_2 \mathbf{B}_2}_{\mathbf{M}_I} \mathbf{V}_I.$$

Thus eliminating the pressure, the system (18) is recast as

$$\begin{bmatrix} \mathbf{A}_1 + \mathbf{A}_3 \mathbf{M}_{BC} & \mathbf{A}_2 + \mathbf{A}_3 \mathbf{M}_I \\ \mathbf{B}_1 + \mathbf{B}_3 \mathbf{M}_{BC} & \mathbf{B}_2 + \mathbf{B}_3 \mathbf{M}_I \end{bmatrix} \begin{bmatrix} \mathbf{V}_{BC} \\ \mathbf{V}_I \end{bmatrix} = i\omega \begin{bmatrix} \mathbf{I} & \mathbf{0} \\ \mathbf{0} & \mathbf{I} \end{bmatrix} \begin{bmatrix} \mathbf{V}_{BC} \\ \mathbf{V}_I \end{bmatrix}. \quad (19)$$

System (19) still contains $N - 2$ null eigenvalues due to the divergence-free constraint. We can further reduce Eq. (19) by eliminating the streamwise velocity components at the interior points

[26]. Indeed, using $\mathbf{V}_I = (\hat{u}_1, \dots, \hat{u}_{N-1}, \hat{v}_1, \dots, \hat{v}_{N-1})$, the divergence-free condition $\mathbf{C}_2 \mathbf{V}_I = 0$ becomes $i\alpha \mathbf{U} + \mathbf{C}_2 \mathbf{v} \mathbf{V} = 0$. Thus, for $\alpha \neq 0$, the streamwise velocity \mathbf{U} is obtained as a function of \mathbf{V} . This then leads to a discrete version of the Orr-Sommerfeld equation for the fluid-structure interaction problem of the form

$$\begin{bmatrix} \mathbf{U} & \mathbf{V} \\ \vdots & \vdots \end{bmatrix} \begin{bmatrix} \mathbf{V}_{BC} \\ \mathbf{V} \end{bmatrix} = i\omega \begin{bmatrix} \mathbf{V}_{BC} \\ \mathbf{V} \end{bmatrix}. \quad (20)$$

This system may be further reduced [32], by considering perturbations of either sinuous or varicose symmetry and using only half of the channel together with derivative operators appropriate for the symmetry of each component of the different flow fields.

Apart from the fact that the above algebraic transformations remove spurious eigenvalues, they also drastically reduce the computational effort. The system is either solved using the QZ algorithm from the LAPACK library or an Arnoldi technique provided by the ARPACK software. The numerical procedure is validated and discussed in the Appendix. The number of collocation points is varied from 100 to 300 as the Reynolds number is increased.

IV. LINEAR STABILITY RESULTS

After the formulation of the linear fluid-structure interaction problem and the presentation of the numerical methods, we are now in a position to analyze its dynamics. The different classes of modes and their dependence on the control parameters are investigated in detail. Specific attention is devoted to provide physical insight through total energy budget analyses.

A. Spectra and classes of modes

A typical spectrum is shown in Fig. 2, corresponding to a base configuration at $Re = 7000$, $V_R = 1$, $B_\star = 4$, $d_\star = 0.2$, and perturbations with wavenumber $\alpha = 0.6$. Since the base state is symmetric in y , the entire spectrum consists of the same number of modes of either varicose (red symbols) or sinuous (blue) symmetry. The Orr-Sommerfeld modes (\times and $+$) are essentially due to the base

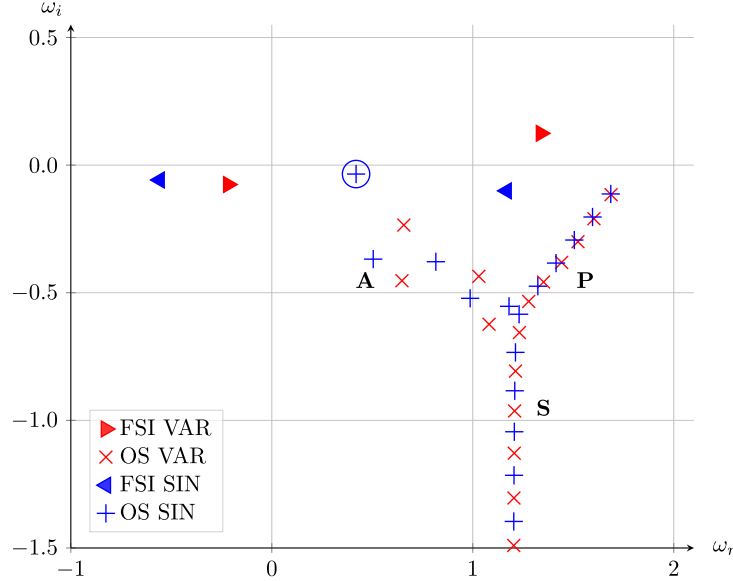


FIG. 2. Eigenvalue spectrum for perturbations with $\alpha = 0.6$ at $\text{Re} = 7000$, $V_R = 1$, $B_* = 4$, and $d_* = 0.2$. Orr-Sommerfeld modes (+, sinuous; \times , varicose) are located on three main branches (A, P, and S) and dominated by TS mode (circle); four modes (\triangleleft and \triangleright) are due to fluid-structure interactions. Modes of varicose and sinuous symmetry are shown in red and blue, respectively.

Poiseuille flow and organized in three branches (classically labeled A, P, and S [33]), as for rigid channels. This part of the spectrum is dominated by the TS mode (indicated by the circle in Fig. 2) of sinuous symmetry. In the present configuration, the coupling between the fluid and wall equations leads to four additional eigenvalues (indicated by \triangleleft and \triangleright) and referenced hereafter as FSI modes. Two of these FSI modes travel upstream ($\omega_r < 0$), while the other pair of FSI modes propagates along the flow direction ($\omega_r > 0$); each of these pairs consists of a sinuous and a varicose mode.

To gain a better understanding of these eigenmodes, we monitor changes in the spectrum resulting from the variation of some control parameters. A few typical scenarios are shown in Fig. 3.

FSI modes strongly depend on the reduced velocity V_R , as shown in Fig. 3(a). When $V_R \rightarrow 0$, which corresponds to approaching the rigid-walls case, the growth rates of the FSI modes reach neutrality ($\omega_i \rightarrow 0$) while their phase velocities tend to infinity ($\omega_r \rightarrow \pm\infty$). For the range of base state configurations shown here, the upstream propagating FSI modes are always stable, albeit with a weak decay rate, and their (negative) phase velocities reach very small values as V_R is increased: this behavior is characteristic of divergence modes, as observed for boundary-layer flows along highly damped walls [19]. On the other hand, the downstream propagating FSI modes are strongly destabilized as V_R is increased; these modes are identified as TWF modes. In contrast with the FSI mode dynamics, the TS mode only weakly depends on V_R since it is mainly driven by the shear flow [see inset in Fig. 3(a)]. Consistently with the definition of V_R , the eigenvalue corresponding to the TS mode matches the one found for the rigid case when $V_R \rightarrow 0$. The other Orr-Sommerfeld modes on the A branch also display only a weak dependence on V_R , while those on the P and S branches appear to be mostly unaffected.

The influence of the wall-damping parameter d_* is shown in Figs. 3(b) and 3(c) for $V_R = 1$ and $V_R = 2$, respectively. The growth rate ω_i of the downstream propagating TWF modes is seen to significantly decrease with wall dissipation d_* . Thus wall damping has a strongly stabilizing effect on both sinuous and varicose TWF modes. For $V_R = 1$, Fig. 3(b) shows that wall damping has a similar stabilizing effect on the upstream propagating FSI modes. However, at the larger value $V_R = 2$ of the reduced velocity [Fig. 3(c)], these FSI modes are nearly stationary divergence modes. In that regime, an increase in wall damping d_* results in an increase of their negative growth rate, and the phase velocity is seen to vanish in the limit of large wall damping d_* . Here destabilization of

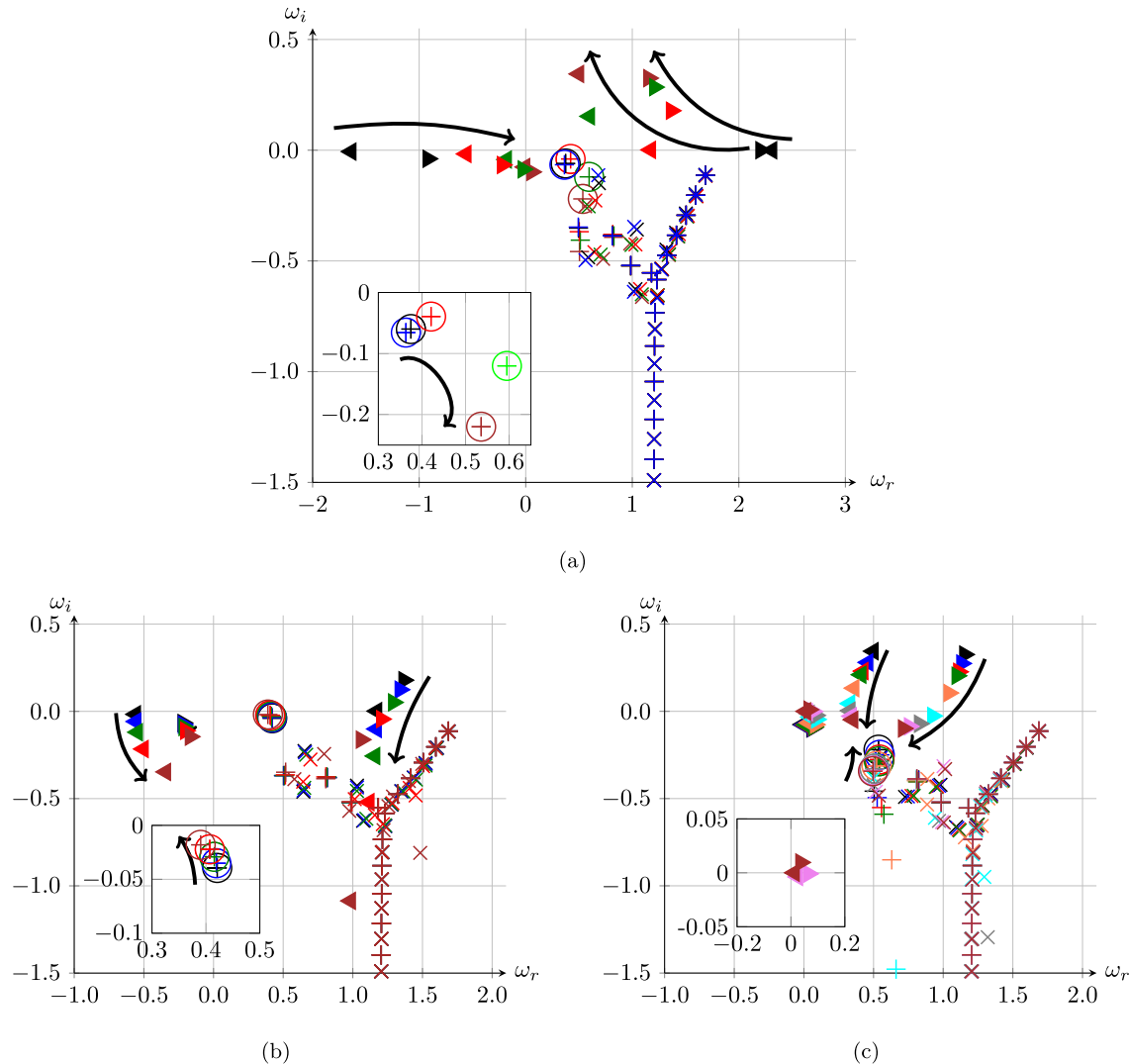


FIG. 3. Influence of V_R and d_* on eigenspectra for $\alpha = 0.6$ at $Re = 7000$ and $B_* = 4$. (a) $V_R = 0.01, 0.5, 1, 1.5$, and 2 (in blue, black, red, green, and brown, respectively) at $d_* = 0$. (b) $d_* = 0, 0.2, 0.5, 1$, and 2 (in black, blue, green, red, and brown, respectively) at $V_R = 1$. (c) $d_* = 0, 0.4, 0.8, 1, 2, 4, 6, 10$, and 20 (in black, blue, red, green, orange, light blue, grey, pink, and brown, respectively) at $V_R = 2$. Some mode trajectories are also represented.

the divergence modes occurs for large values of d_* . One may recall that while the sinuous TWF and divergence modes were investigated numerically by Davies and Carpenter [20], the varicose TWF and divergence modes have not been explored for the plane channel flow.

Thus, the influence of the various control parameters may be summarized as follows: the TS mode is temporally damped by an increase of V_R , but its temporal amplification rate may be amplified with an increase in wall damping for a certain range of streamwise wavenumbers. A different behavior is found when the TWF modes are considered: their growth rate increases with V_R , while it decreases with d_* . This is consistent with the mode classification given by Benjamin [14] (i.e., class A for TS modes and class B for TWF modes). Moreover, the divergence mode is seen to be amplified for high values of wall-damping parameter. Finally, the effect of the wall compliance is seen to be negligible for both P and S branches.

To further identify the different types of modes with respect to Benjamin's classification, the eigenfunctions of a few selected modes are shown in Fig. 4.

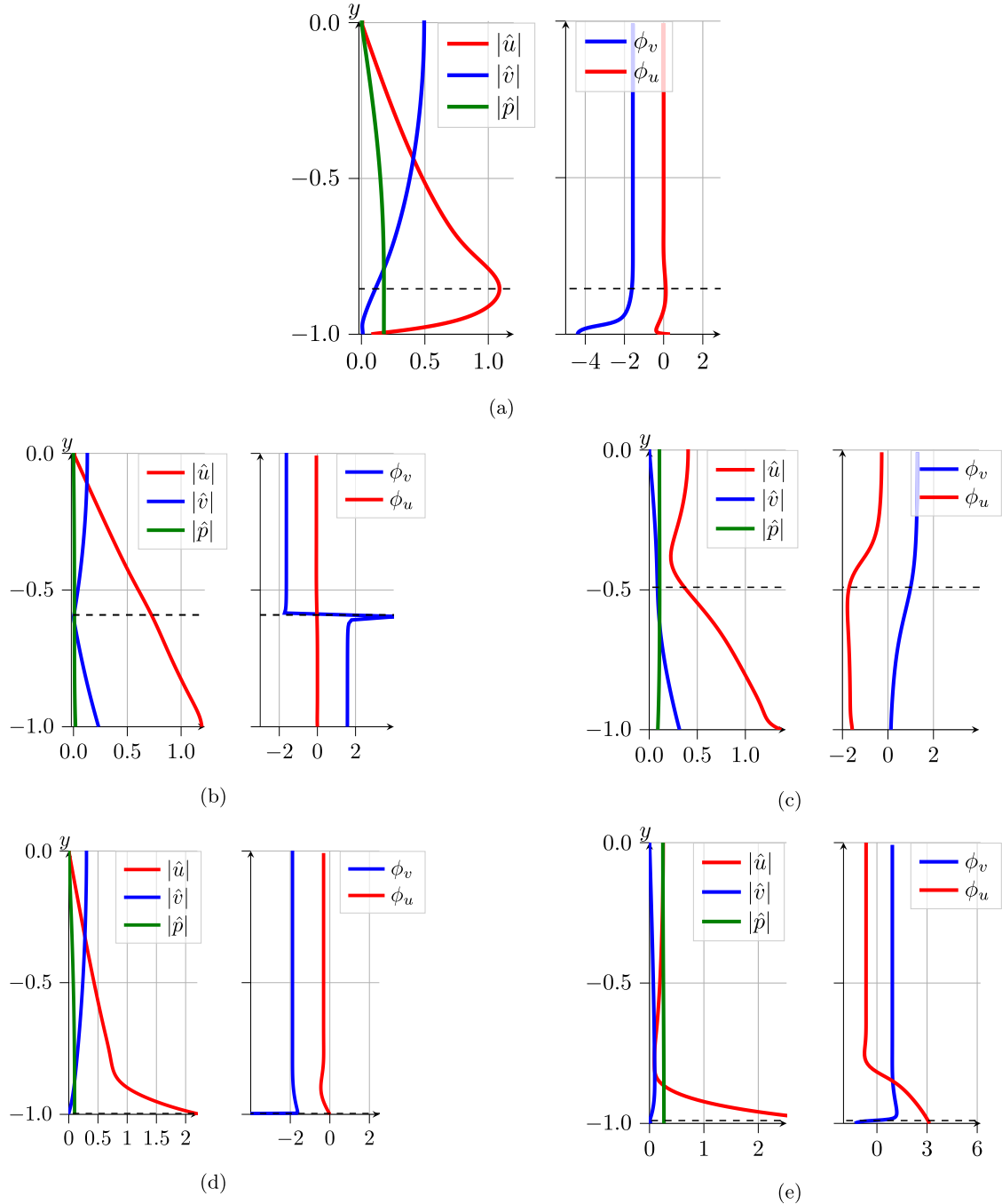


FIG. 4. Eigenfunctions for $\text{Re} = 7000$ and $B_* = 4$. (a) TS (sinuous) mode for $\alpha = 1$, $d_* = 4$, and $V_R = 0.5$. (b) Sinuous TWF mode for $\alpha = 0.6$, $d_* = 0$, and $V_R = 1$. (c) Varicose TWF mode for $\alpha = 0.6$, $d_* = 0$, and $V_R = 1$. (d) Sinuous divergence mode for $\alpha = 0.6$, $d_* = 20$, and $V_R = 2$. (e) Varicose divergence mode for $\alpha = 0.6$, $d_* = 20$, and $V_R = 2$. The phase angles of eigenfunctions are denoted as ϕ_u and ϕ_v for u' and v' , respectively. The eigenfunctions are normalized to the unit kinetic energy norm.

One may recall that the mechanism whereby both TWF modes and TS modes grow involves the action of the streamwise velocity base flow gradient along the wall-normal position working against the Reynolds stresses. In the absence of an inflection point, both modes involve a phase shift of the disturbance velocity at some distance from the wall [34]. However, mechanisms are quite different

for each of these modes. Within a large-Reynolds-number asymptotic theory, viscous effects are only present in the vicinity of the viscous wall layer or the critical layer, located at the wall-normal position y_c where $U_b(y_c) = \omega_r/\alpha$ [34]. The inviscid approximation is therefore accurate in the other regions of the flow. For the TWF mode, the instability mechanism is essentially driven by the wall. Indeed, the instability is amplified if the work done by the pressure disturbance on the wall is positive when averaged over one period [12]. As first proven by Miles [15] for water waves, Benjamin [13] shows for the boundary-layer-flow case that it results from a phase shift between disturbance wall pressure and wall displacement. In particular, Benjamin [13] proves that the pressure at the wall is associated with the integrated effect of the velocity perturbations along the wall direction and is a consequence of a phase shift for velocity components near the critical layer. We note hereafter ϕ_u and ϕ_v as the phases of the respective velocity components \hat{u} and \hat{v} of the associated eigenfunctions. For TWF modes [see Figs. 4(b) and 4(c)], the essential phase shift (i.e., $\phi_u - \phi_v \neq \pi/2$) occurs near the critical layer in the limit of large Reynolds numbers (class B modes). For the TS mode [Fig. 4(a)], the phase shift is rather associated with the viscous wall layer. They belong to class A modes and are stabilized through a transfer of energy to the wall. Hence it is essential, when addressing the different classes of modes, to monitor the phases of the perturbation components. Figure 4(b) shows that the sinuous TWF mode exhibits a clear phase shift near the critical layer in agreement with class B modes. It is consistent with the theoretical investigation of Davies and Carpenter [20] for the same flow case. The linear behavior along with the wall-normal position of \hat{u} is associated with a displacement of the Poiseuille solution when the walls are shifted with η . It is easily verified that the small deviation from the Poiseuille solution due to sinuous motion of the walls is proportional to $-2\hat{\eta}y$ (see also [35]). Interestingly, the varicose case [Fig. 4(c)], not studied by Davies and Carpenter [20], also exhibits a phase shift.

Finally, the divergence mode [Figs. 4(d) and 4(e)] exhibits a phase shift in the viscous wall layer. Nevertheless, due to the low velocity phase, the viscous wall layer and the critical layer are not well separated. As a consequence, the theoretical framework derived by Davies and Carpenter [20] cannot be applied for these modes.

For all FSI modes (both TWF and divergence), velocity and pressure fluctuations are concentrated near the wall. For the TS mode, as for the rigid case, the streamwise velocity component peaks at the critical layer.

B. Temporal growth and instability onset

The stability features of compliant channel flow configurations depend on a large number of parameters. In the previous section we have shown that the reduced velocity V_R is the main control parameter governing fluid-structure interactions, but growth rates of the different classes of modes may also depend significantly on Reynolds number Re , wall dissipation d_* , and flexural rigidity B_* . In the present section, we will map out the stability characteristics by monitoring the dispersion relation in the (V_R, α) plane for selected values of the other relevant control parameters. By taking advantage of the base flow symmetry, sinuous and varicose perturbations may be efficiently computed and their properties are here discussed separately. We first consider perturbations of varicose symmetry, which are generally the modes most amplified by fluid-structure interactions.

Figure 5(a) shows isolines of the temporal growth rate ω_i of the leading varicose eigenmode in the (V_R, α) plane at $Re = 5000$, $d_* = 10$, and $B_* = 4$. The neutral curve ($\omega_i = 0$) exhibits two distinct minima at $V_R \approx 1.6$ and $V_R \approx 3.9$. Beyond onset, a finite range of wavenumbers α display positive temporal growth rates. The associated phase speeds ω_r/α are given in Fig. 5(b). It is found that near the first minimum $V_R \approx 1.6$, modes travel with vanishingly small phase speeds. In contrast, near the second minimum $V_R \approx 3.9$, modes travel with phase speeds of the order of the mean base flow velocity. This behavior is characteristic of divergence and TWF modes, which are thus each found to dominate the perturbation dynamics in distinct regions of the (V_R, α) plane for these parameter settings. Figure 6 illustrates the influence of wall dissipation d_* , for the same values of Re and B_* . It is observed that energy dissipation in the wall only weakly influences the temporal growth

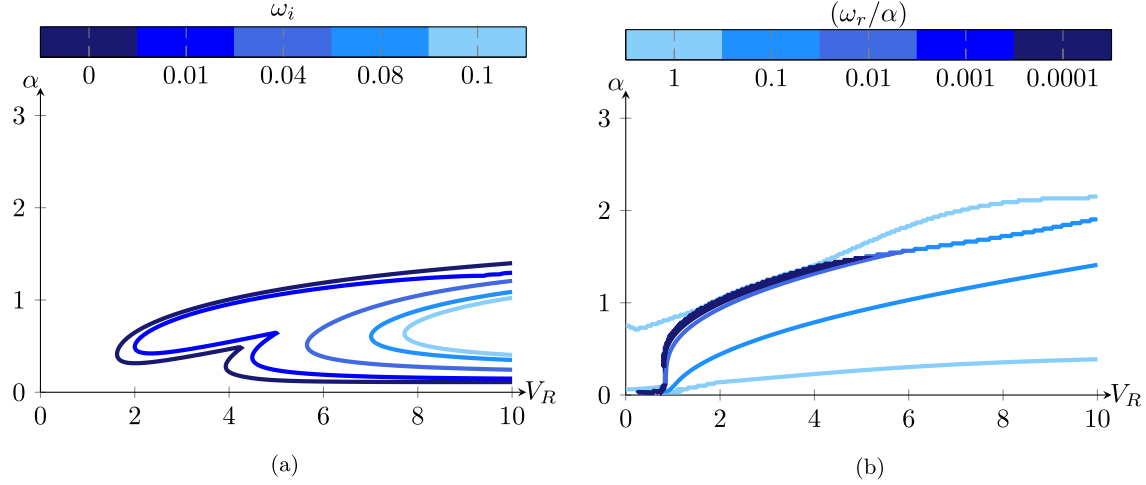


FIG. 5. Dispersion relation for leading varicose mode in (V_R, α) plane for $Re = 5000$, $d_* = 10$, and $B_* = 4$: contours of (a) growth rate ω_i and (b) phase velocity ω_r/α .

rate for $0 \leq d_* \leq 1$, while stronger stabilization occurs for $d_* > 1$. At these high dissipation rates, the growth rate and the range of unstable wavenumbers are greatly reduced; however, the critical value of V_R for onset of instability (denoted V_R^c hereafter) remains of the same order of magnitude. Monitoring the neutral curves more precisely reveals that V_R^c increases from $V_R^c \simeq 0.45$ for $d_* = 0$ to reach a maximal value of about $V_R^c \simeq 1.6$ for $d_* = 10$ and decreases again for larger values of d_* ($V_R^c \simeq 1.0$ for $d_* = 100$). This nonmonotonous effect of wall dissipation on instability onset is due to a change of the nature of the leading eigenmode: while the instability is dominated by the TWF mode at low values of d_* , the unstable dynamics is governed by the divergence mode for strong dissipation in the compliant wall as already suggested by Fig. 5.

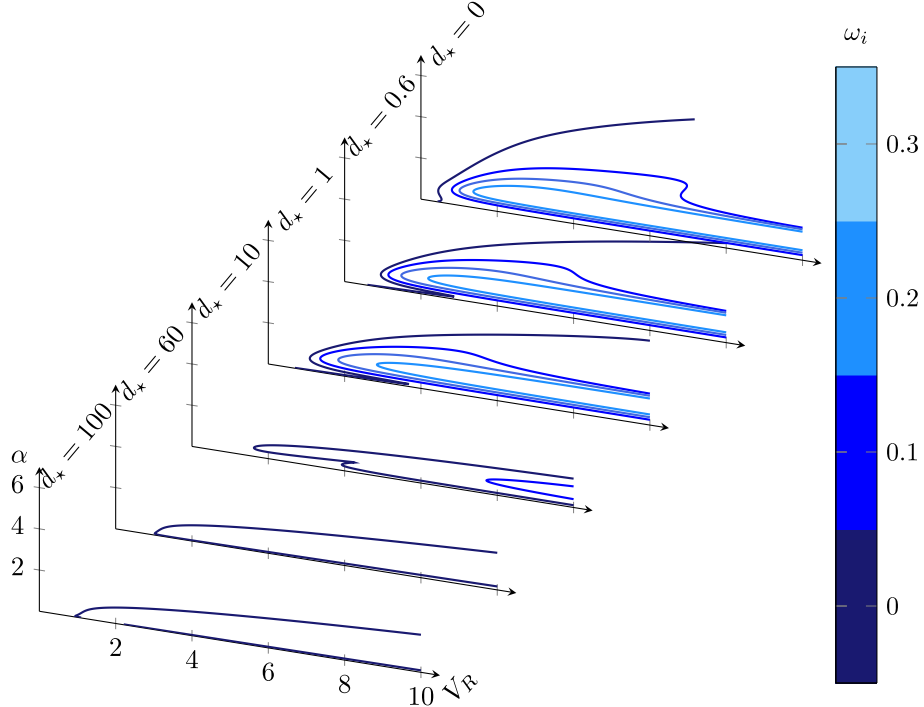


FIG. 6. Temporal growth rates ω_i for the varicose instability at $Re = 5000$ and $B_* = 4$ for $d_* = 0, 0.6, 1, 10, 60$, and 100 . The contour levels are 0, 0.1, 0.2, and 0.3.

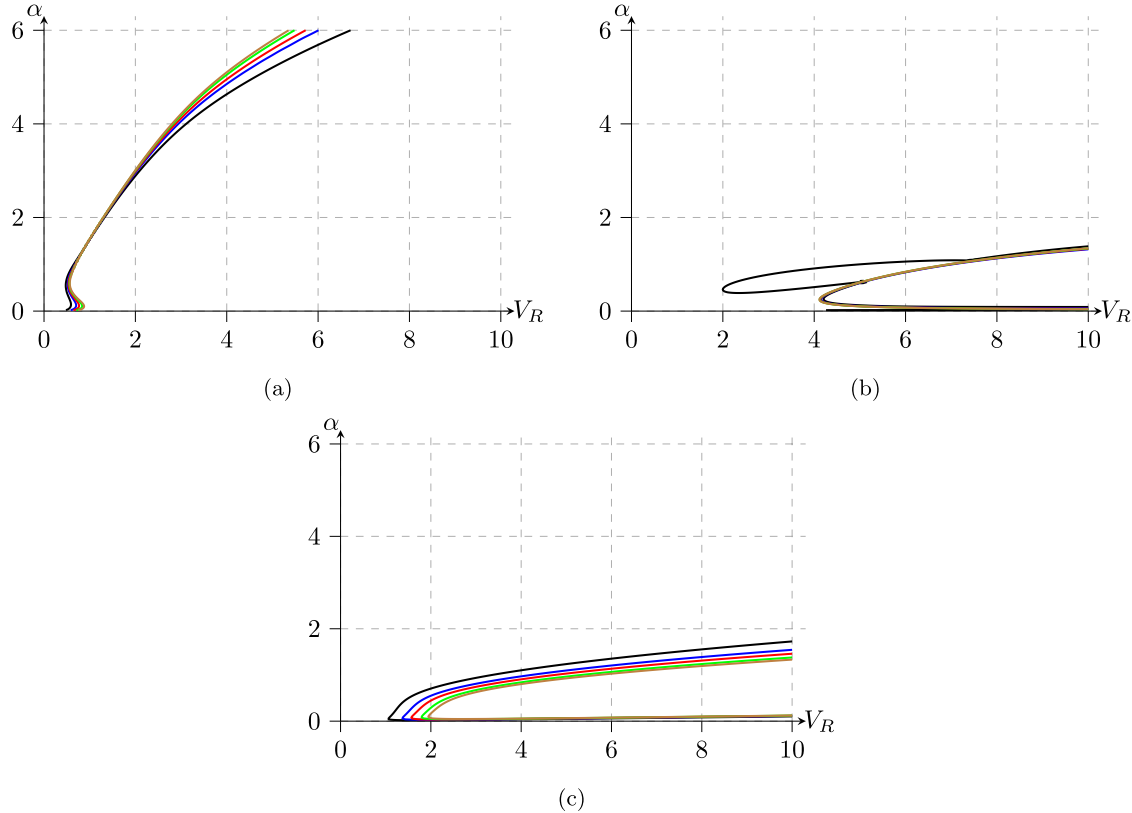


FIG. 7. Marginal curves for onset of varicose instability at $B_* = 4$ for $\text{Re} = 10000, 40000, 80000, 160000$, and 240000 (in black, blue, red, green, and brown respectively) and (a) $d_* = 0$, (b) $d_* = 10$, and (c) $d_* = 100$.

This observation is further illustrated in Fig. 7, where neutral curves are shown for various Reynolds numbers and wall dissipations. In particular, for $\text{Re} = 10000$ and $d_* = 10$ [Fig. 7(b)], we observe the coexistence of the divergence and TWF modes. The critical reduced velocities V_R^c for the divergence and TWF modes are ≈ 2 and ≈ 4 , respectively. Neutral curves associated with the TWF mode [Fig. 7(a)] are seen to be almost independent of the Reynolds number. For the divergence mode, we observe a destabilizing effect of viscosity [Fig. 7(c)]: the critical value V_R^c for onset of instability is seen to increase with Reynolds number, which is consistent with the fact that divergence modes are intimately connected to the viscous wall layer. Nevertheless, in the regime dominated by divergence modes, the temporal amplification rates reach much lower values than those prevailing for TWF modes at low values of d_* (see Fig. 6).

After the previous extensive discussions of results for varicose perturbations we now focus on the sinuous symmetry. The linear dynamics of sinuous eigenmodes is very similar to that of their varicose counterpart, except that the (sinuous) Tollmien-Schlichting modes may also display positive growth rates.

The growth-rate isolines in the (V_R, α) plane of Fig. 8(a) are obtained for $\text{Re} = 8000$, $B_* = 4$, and $d_* = 10$. This Reynolds number (based on channel diameter and mean fluid velocity) is slightly in excess of the critical value $\text{Re}_c \simeq 7696$ for Tollmien-Schlichting instability developing in rigid channel flow. As for the varicose case, the neutral curve exhibits two minima. The first appears near $V_R \approx 0$ while the second minimum is close to $V_R \approx 2$. The associated phase speeds ω_r/α given in Fig. 8(b) indicate that divergence, TWF, and TS modes can be involved in this regime.

Figure 9 shows the evolution of sinuous temporal instability characteristics with the wall dissipation parameter d_* . For $d_* = 0$ and low values of V_R , corresponding to near-rigid compliant walls, there exists a narrow band of unstable wavenumbers near $\alpha = 1$ associated with unstable

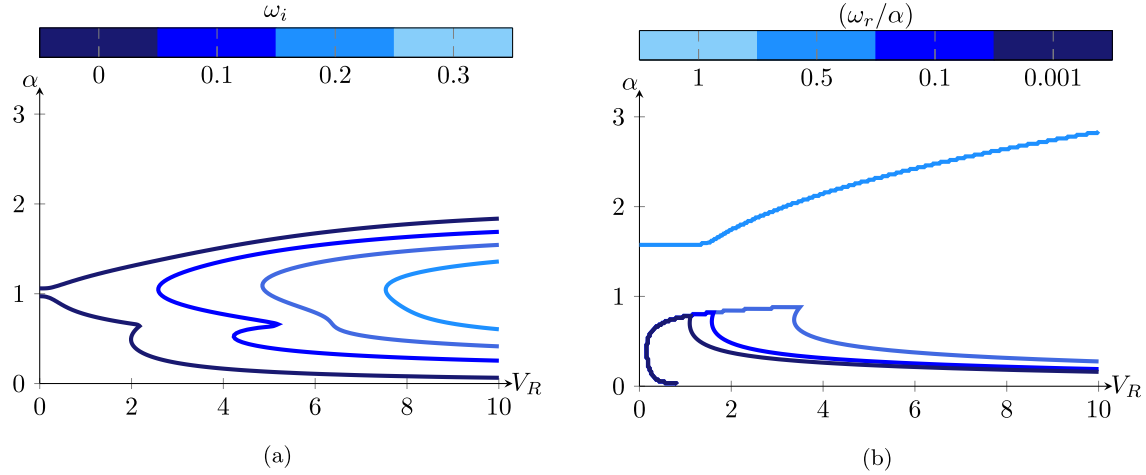


FIG. 8. Dispersion relation for leading sinuous mode in (V_R, α) plane for $\text{Re} = 8000$, $d_* = 10$, and $B_* = 4$: contours of (a) growth rate ω_i and (b) phase velocity ω_r/α .

Tollmien-Schlichting modes. At larger values of V_R , stronger fluid-structure coupling leads to the destabilization of (sinuous) TWF modes: the temporal growth rates ω_i and the range of unstable wavenumbers rapidly increase with V_R . Note that there exists a narrow region near $V_R = 1$ where both TS and TWF modes are stable. As d_* is increased from 0 to 0.6, it is observed that the regions corresponding to unstable TS and TWF modes merge, giving rise to the so-called transition mode.

Except for the merging of TS and TWF instabilities, the instability features of sinuous perturbations shown in Fig. 9 are very similar to those observed for varicose perturbations. For $d_* > 1$,

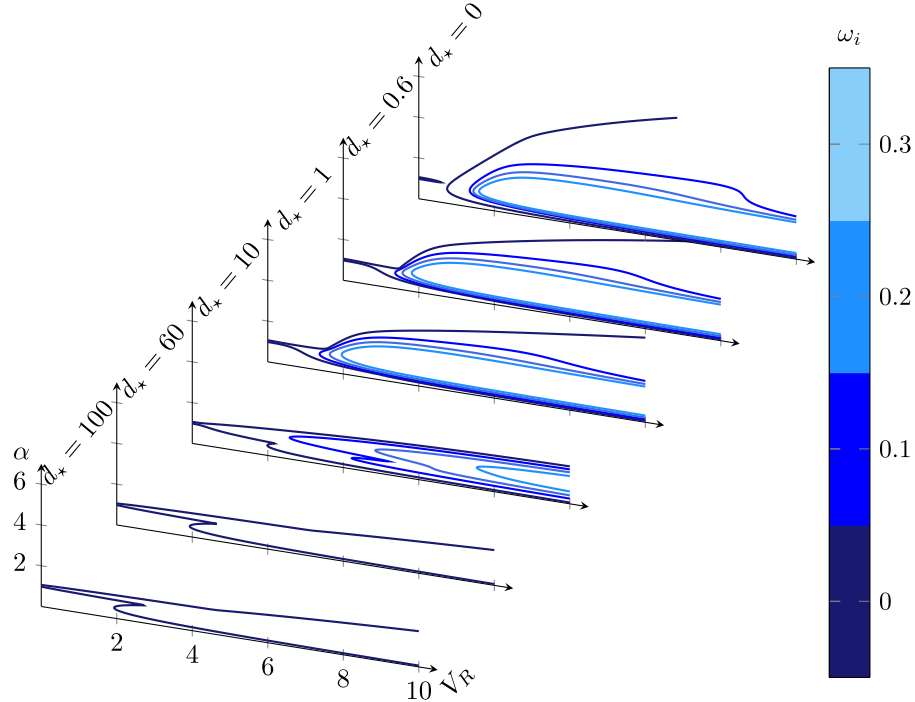


FIG. 9. Temporal growth rates ω_i for the sinuous instability at $\text{Re} = 8000$ and $B_* = 4$ for $d_* = 0, 0.6, 1, 10, 60$, and 100 . The contour levels are 0, 0.1, 0.2, and 0.3.

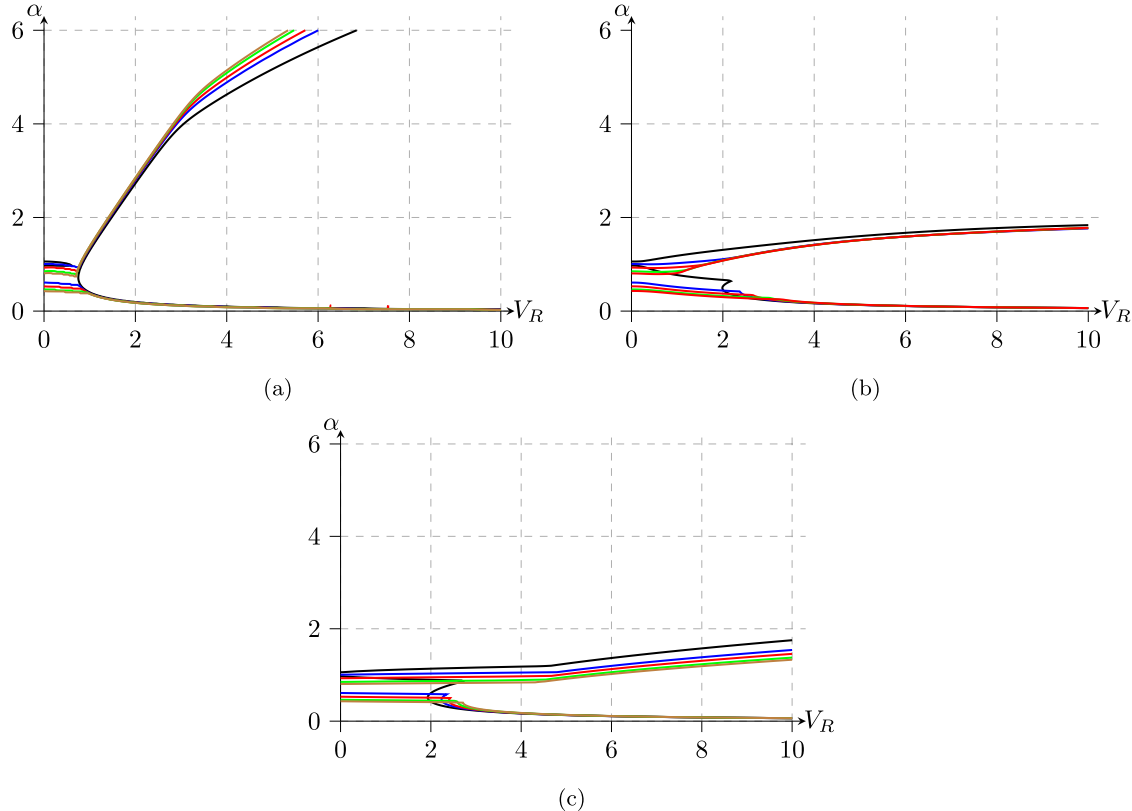


FIG. 10. Marginal curves for onset of sinuous instability at $B_*=4$ for $\text{Re} = 10000, 40000, 80000, 160000$, and 240000 (in black, blue, red, green, and brown respectively) and (a) $d_*=0$, (b) $d_*=10$, and (c) $d_*=100$.

wall dissipation d_* significantly reduces the temporal growth rates and the range of unstable wavenumbers. For $d_* \geq 10$, Fig. 9 shows that divergence and transition modes coexist. In addition, the critical reduced velocity V_R^c for the onset of the divergence mode is only weakly influenced by the wall dissipation ($V_R^c \approx 2$). The critical curves shown in Fig. 10 correspond to marginal ($\omega_i = 0$) sinuous instability for a range of Reynolds numbers and $d_* = 0, 10$, and 100 . Due to the fact that, for $\text{Re} > 7696$, TS instability prevails at low values of V_R , down to $V_R = 0$, a critical value of reduced velocity V_R^c cannot be defined for onset of sinuous instability. For the sinuous instability, it may be hard to distinguish between TS or TWF modes since branch switching occurs as some parameters are continuously varied. To better illustrate this phenomenon, Fig. 11 shows the dispersion relation for both branches in the range $0.55 < \alpha < 1.05$ for $d_* = 0.10, 0.13$, and 0.16 , at $\text{Re} = 10000$, $B_*=1$, and $V_R = 1$. For $\alpha < 0.8$, the branches with largest temporal growth rate [upper branches in Fig. 11(a)] are of TS type while the other branches are always stable in that wavenumber range and can be identified as TWF modes. For $\alpha > 0.8$, the unstable branch displays a growth rate ω_i rapidly increasing with α , and is found to correspond to a mode of the TWF type, while the other branch is strongly stabilized at these wavenumbers. Due to the branch switching that occurs near $\alpha = 0.8$ and $d_* = 0.13$, the unstable TWF branch prevailing for $\alpha > 0.8$ is continuously connected to the TS branch when $d_* > 0.13$ while it is continued as a stable TWF mode for $\alpha < 0.8$ when $d_* < 0.13$. This behavior is further illustrated in Fig. 12. For a small amount of wall dissipation, the TS mode is seen to be damped as V_R is increasing [Fig. 12(a)], for all the Reynolds numbers considered. In particular, for $d_* = 0$, the critical reduced velocity of TS mode suppression is varying from $V_R \approx 0.8$ for $\text{Re} = 10000$ to $V_R \approx 4$ for $\text{Re} = 40000$. However, as d_* is increased beyond 0.13 , a transition mode emerges and it is no longer possible to distinguish between TWF and TS modes [Figs. 12(b)–(d)].

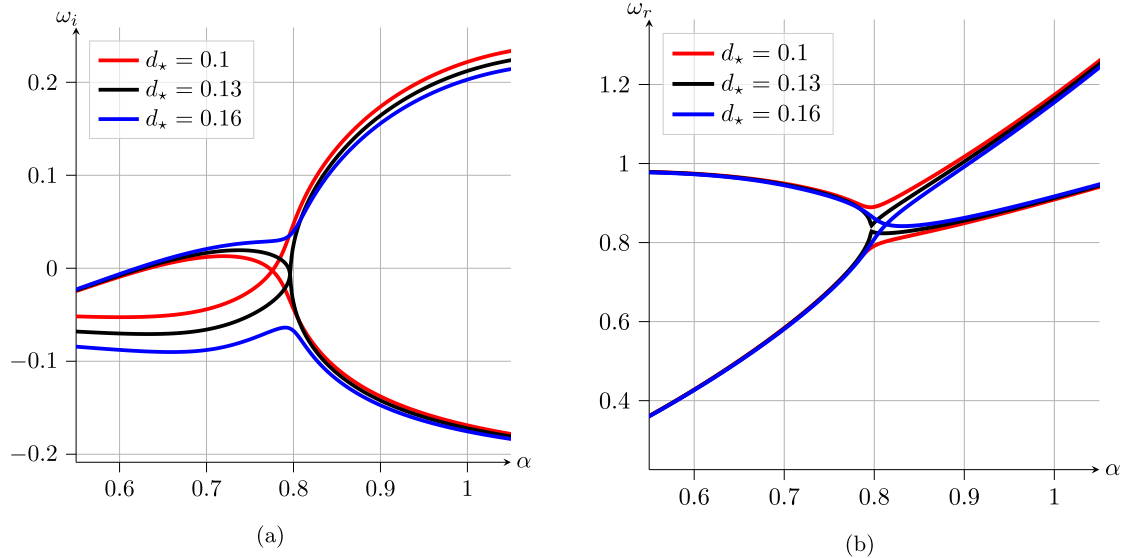


FIG. 11. Dispersion relation for the two leading sinuous modes at $\text{Re} = 10000$, $B_\star = 1$, and $V_R = 1$: (a) temporal growth rate ω_i and (b) frequency ω_r . Branch switching occurs near $\alpha = 0.8$ and $d_\star = 0.13$.

Finally, we present some results for the destabilization of the divergence mode and its dependence on wall dissipation d_\star and Reynolds number Re . We compute the critical value V_R^c for onset of instability in the (V_R, α) plane at fixed values of the other control parameters. A Newton-Raphson search algorithm with an adaptive step has been implemented to automatically identify the start of the neutral curve in the (V_R, α) plane for different values of d_\star and Re . The critical value V_R^c (and associated wavenumber α^c) for onset of instability is then obtained when $\frac{dV_R}{d\alpha}$ vanishes along the neutral curve.

Critical curves as functions of d_\star for different Re values are plotted in Figs. 13(a) and 13(b), respectively, for the divergence modes of varicose and sinuous symmetry. Flexural rigidity is kept constant at $B_\star = 1$. Both sets of curves clearly indicate the stabilizing effect of the Reynolds number on the divergence mode, for both the varicose and sinuous cases. For the varicose case, unstable divergence modes only occur at relatively high wall dissipation, $d_\star > 6$ for $\text{Re} = 5000$ and $d_\star > 9.5$ for $\text{Re} = 80000$. For the sinuous case, divergence mode instability already starts for d_\star in the range 2–4, with a weaker Reynolds number dependence. In both varicose and sinuous cases, the critical V_R^c appears to asymptote towards a finite limit for large values of d_\star .

As discussed above, the combined effects of the different wall parameters are conveniently summarized by monitoring either the variations of the critical reduced velocity V_R^c or the critical Reynolds number Re^c depending on whether the FSI or TS mode is considered. First, we focus on FSI instability modes of varicose symmetry. To that purpose, we consider a high value of the Reynolds number in order to investigate only the influence of the wall properties.

Results are reported in Fig. 14 for $0 \leq d_\star \leq 60$ and $0.2 \leq B_\star \leq 10$. The inset in the figure shows that for small values of d_\star , flexural rigidity has a moderately stabilizing effect on TWF modes: V_R^c increases as B_\star is increased for fixed d_\star . In the range $5 < d_\star < 15$, onset of instability is seen to display an almost universal behavior with a linear relationship between V_R^c and d_\star , almost independent of B_\star . In this regime, instability always occurs by a TWF mode. For larger wall dissipation rates, $d_\star > 20$, the dynamics is dominated by the divergence modes, associated with vanishing phase velocities. In this latter regime, the critical values V_R^c weakly depend on flexural rigidity B_\star and decrease with increasing wall dissipation d_\star . For large values of d_\star , a limit value of $V_R^c \simeq 2.85$ is asymptotically reached, independently of B_\star . Note that the crossover from

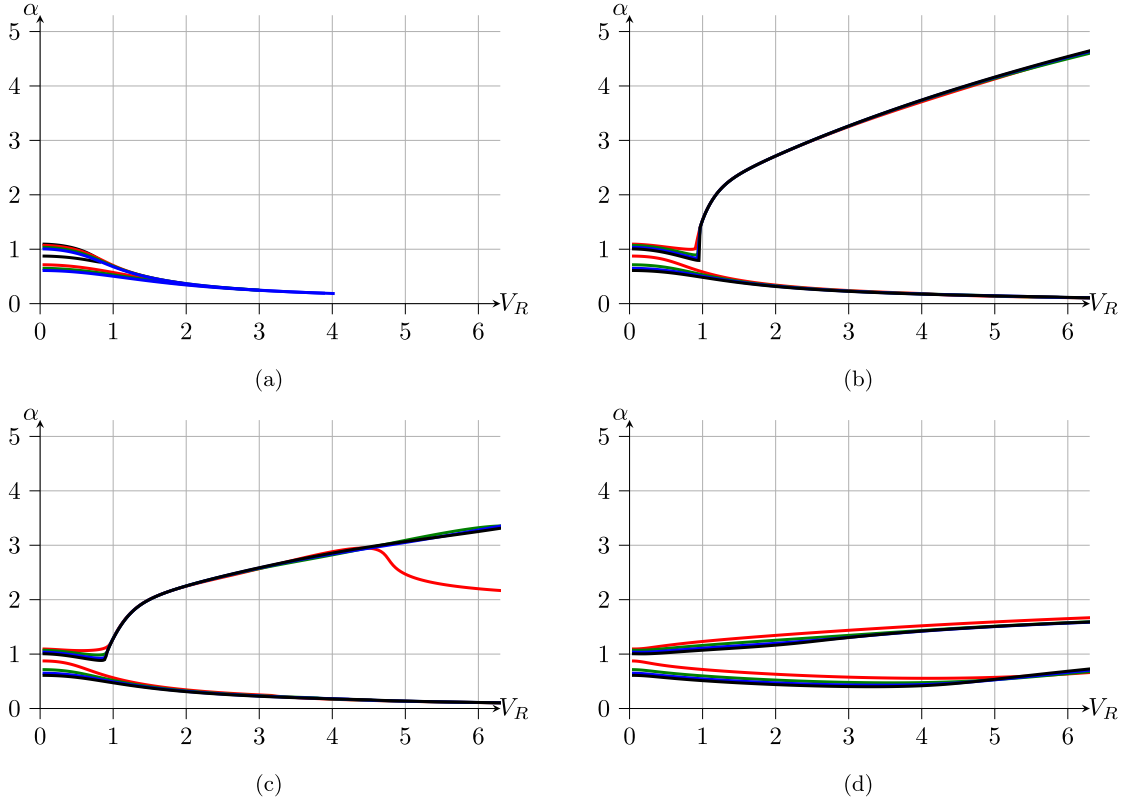


FIG. 12. Neutral curves for the TS mode for $\text{Re} = 10000, 20000, 30000$, and 40000 (in black, red, green, and blue, respectively) and $B_* = 1$ in the plane (α, V_R) . (a) $d_* = 0$, (b) $d_* = 0.5$, (c) $d_* = 1$, and (d) $d_* = 10$.

the TWF-dominated instabilities (low d_*) to the divergence-dominated instabilities (high d_*) also depends on B_* .

Finally, we address the influence of the wall properties on the stability of TS modes by monitoring the critical Re^c . We restrict our analysis to the case without wall damping. Results are summarized in Fig. 15, where the critical Reynolds number for the TS mode is displayed as a function of V_R for $B_* = 1, 2$, and 4 . The figure shows that the TS mode is significantly stabilized with increasing wall compliance (i.e., increasing V_R), and this stabilizing effect is enhanced at low flexural rigidity B_* . In

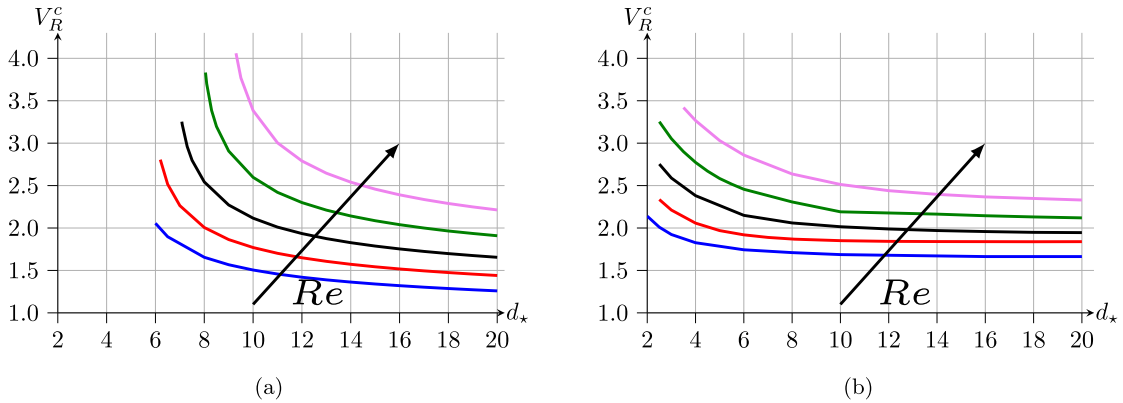


FIG. 13. Divergence mode. Critical reduced velocity distribution V_R^c with the wall-damping parameter and for $\text{Re} = 5000, 10000, 20000, 40000$, and 80000 with $B_* = 1$: (a) the varicose case and (b) the sinuous case.

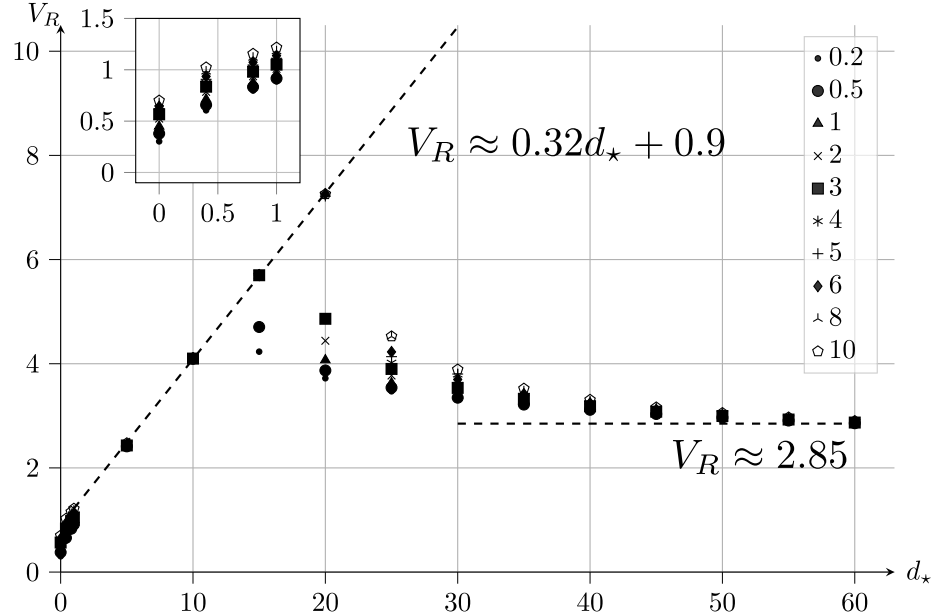


FIG. 14. Evolution of critical reduced velocity V_R^c with wall-damping parameter d_* , for a range of flexural rigidity values B_* (from 0.2 to 10). Perturbations of varicose symmetry are considered.

the figure, onset of TWF instability is indicated by the nearly vertical lines; recall that these modes are almost independent of the Reynolds number. Dotted lines correspond to sinuous TWF modes while dashed lines have been computed for varicose TWF modes. It is immediately apparent from the figure that the potential effect of a compliant wall regarding transition delay is clearly limited by the destabilization of TWF modes. Indeed, the region of the (V_R, Re) plane corresponding to stable configurations is located below the Re^c curves for onset of TS instability and delimited at large values of V_R by onset of TWF instability. The results of the present investigation reveal that the extent of the stable region is drastically reduced by taking into account TWF perturbations of varicose symmetry, which display growth rates in excess of their sinuous counterparts. For instance,

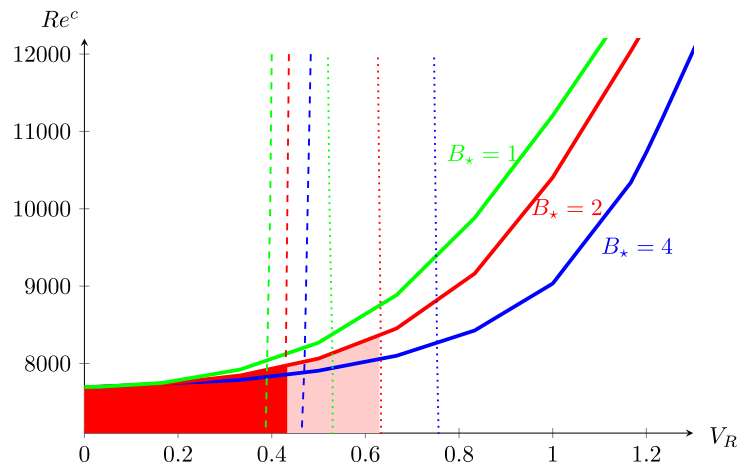


FIG. 15. The critical Reynolds number associated with TS instability is plotted as a function of V_R for $B_* = 1, 2$, and 4 in solid lines. Nearly vertical lines indicate onset of TWF instability for perturbations of sinuous (dotted lines) and varicose (dashed lines) symmetry. The colored regions correspond to stable configurations at $B_* = 2$, allowing only sinuous perturbations (light red) or all types of perturbations (solid red).

when only sinuous perturbations are taken into account, the upper right corner of the shaded region in Fig. 15 indicates that stable configurations would be possible up to $\text{Re} = 8370$, for $B_\star = 2$. However, when perturbations of all symmetries are allowed, the stable domain is reduced to the solid red region, with maximal Reynolds number of $\text{Re} = 7970$, only marginally larger than the critical Reynolds number of $\text{Re} = 7696$ corresponding to the rigid case. Similar conclusions hold for different values of B_\star . Moreover, since it has been shown that wall dissipation has a destabilizing effect on TS waves, it is not expected that using $d_\star > 0$ could increase the extent of the stable regions in parameter space. Thus it seems impossible to significantly delay instability onset by wall compliance.

C. Comparison with asymptotic theories for $d_\star = 0$

Davies and Carpenter [20] derived an analytical expression for the wall pressure for $d_\star = 0$ in the limit of small α and high Reynolds numbers, for modes of sinuous symmetry. This pressure, denoted $\hat{p}(\alpha, c, U_{\text{ref}})$, is obtained as a function of the wavenumber α , the phase velocity $c = \omega_r/\alpha$, and a reference value for the fluid velocity, $U_{\text{ref}} = Q/2h$, and includes the effects of both the critical and viscous layers. The wall pressure is obtained as an expansion in α up to α^2 : $\hat{p} = p_0 + \alpha^2 p_1$, where only the term p_1 includes the effect of viscous and critical layers. For the viscous layer, the approximation is carried out up to $O((\alpha \text{Re})^{-1/2})$. Neglecting the viscous stress at the wall, they obtain the dispersion relation:

$$m(c^2 - c_0^2) + \hat{p}(\alpha, c, U_{\text{ref}}) + i\left(\frac{c}{\alpha}\right)d = 0, \quad (21)$$

with $c_0 = \sqrt{\frac{1}{m}(B\alpha^2 + T + \frac{K}{\alpha^2})}$ the free wave speed for the wall. Davies and Carpenter [20] express the onset of instability with the Reynolds number. Here, we suggest that it is more appropriate to use the reduced velocity V_R . The resulting neutral curves are shown in Fig. 16 for $B_\star = 4$. For the sinuous case, Fig. 16(a) shows a very good agreement between the analytical model and complete numerical resolution of the full system up to $\alpha \approx 3$. In order to remove the Reynolds number effect, a numerical solution for $\text{Re} = 1 \times 10^6$ has been carried out. For the latter case, the grid mesh is increased up to $N = 300$ in order to correctly capture both viscous and critical layers. Figure 16(a) shows that the departure from the theoretical model is due to the expansion in terms of streamwise wavenumber up to α^2 ; hence this approximation is no longer valid for α greater than 3.5 (not shown in [16]). In addition, one observes that neglecting the viscous stress at the wall and in the analytical expression of the pressure yields an almost perfect approximation of the exact dispersion relation. In Fig. 16(b), comparisons with varicose cases are shown. While the theoretical model is derived only for the sinuous symmetry, it is interesting to notice that in the limit of high Reynolds numbers, the model associated with merely the critical layer gives a quite accurate description of the varicose symmetry for α varying from 0.8 to 3. For streamwise wavenumbers greater than 4, the varicose and sinuous neutral curves fall in one single curve for all Reynolds numbers. For $\alpha < 0.8$, the varicose case exhibits a more complex Reynolds number dependence. Since the varicose mode always dominates over the sinuous mode, the critical value V_R^c for onset of instability is associated with a varicose perturbation for all configurations that have been considered in the present study. The latter observation is also in agreement with results provided by Nagata and Cole [22]. In addition, it is found that the Reynolds number has a slight stabilizing effect. In Fig. 16, we provide a comparison with the theoretical model derived by Huang [36] for the varicose symmetry, only based on the critical layer. The figure shows a good agreement for moderate values of α between the model and the numerical simulation.

D. Energy budgets

This final section addresses the energy transfer mechanisms between the different components of the compliant channel flow configurations, in order to shed further light on the dynamics and on

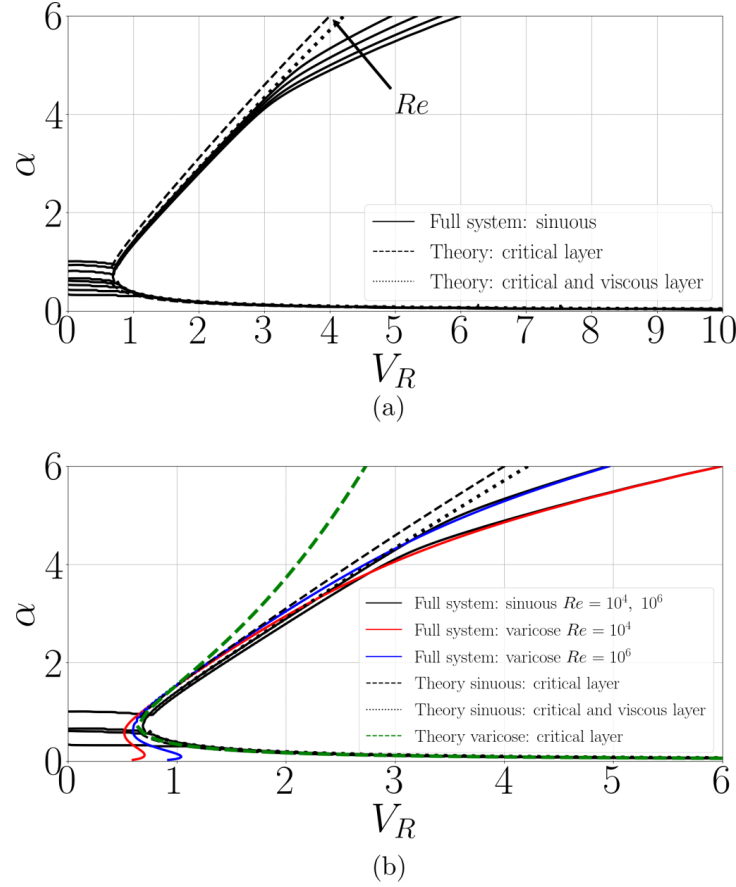


FIG. 16. Neutral curves for $d_* = 0$ and $B_* = 4$. For the full system of equations, the Reynolds numbers are fixed to $Re = 4 \times 10^4, 8 \times 10^4, 2.4 \times 10^5$, and 1×10^6 . For the analytical dispersion relation Re is fixed to 1×10^6 . (a) Sinuous case and (b) sinuous and varicose cases comparison.

the fundamental mechanisms promoting instability. This section is greatly influenced by the work of Domaradski and Metcalfe [29] and Carpenter and Morris [37].

For the compliant channel flow configuration under consideration, the total energy of the system is the sum of three components:

$$E_{tot} = E_{FK} + E_{WK} + E_{WP}, \quad (22)$$

where E_{FK} represents the fluid kinetic energy, while the wall energy consists of both kinetic and potential contributions, E_{WK} and E_{WP} , respectively.

The global fluid kinetic energy is obtained by integration over the channel diameter:

$$E_{FK} = \int_{-h}^{+h} e(y) dy, \quad (23)$$

where

$$e(y) = \rho \hat{\mathbf{u}}(y) \cdot \hat{\mathbf{u}}(y)^* \equiv \rho [\hat{u}(y)\hat{u}(y)^* + \hat{v}(y)\hat{v}(y)^*] \quad (24)$$

denotes the local kinetic energy of the flow, averaged over x at a given wall-normal position y , using the notations introduced in Sec. II C. The temporal variation of the local kinetic energy then follows

from the governing equation (10) as

$$\begin{aligned}
2\omega_i e(y) = & -\underbrace{\rho[\hat{u}(y)\hat{v}(y)^* + \hat{u}(y)^*\hat{v}(y)]\frac{dU_b(y)}{dy}}_{\mathcal{P}: \text{Reynolds stress work against the mean shear}} - \underbrace{\frac{d}{dy}[\hat{p}(y)\hat{v}(y)^* + \hat{p}(y)^*\hat{v}(y)]}_{\Pi: \text{pressure diffusion}} \\
& - \underbrace{2\mu \left[\frac{d\hat{u}(y)}{dy} \frac{d\hat{u}(y)^*}{dy} + \frac{d\hat{v}(y)}{dy} \frac{d\hat{v}(y)^*}{dy} + \alpha^2 (\hat{u}(y)\hat{u}(y)^* + \hat{v}(y)\hat{v}(y)^*) \right]}_{\varepsilon: \text{viscous dissipation}} \\
& + \underbrace{\mu \frac{d}{dy} \left[\hat{u}(y) \frac{d\hat{u}(y)^*}{dy} + \hat{u}(y)^* \frac{d\hat{u}(y)}{dy} + \hat{v}(y) \frac{d\hat{v}(y)^*}{dy} + \hat{v}(y)^* \frac{d\hat{v}(y)}{dy} \right]}_{\mathcal{D}: \text{viscous diffusion}} \quad (25)
\end{aligned}$$

and is the result of four distinct mechanisms as indicated in the above equation. Integration of this expression over the channel diameter leads to the equivalent equation governing the evolution of the total fluid kinetic energy:

$$\begin{aligned}
2\omega_i E_{FK} = & - \int_{-h}^{+h} \rho[\hat{u}(y)\hat{v}(y)^* + \hat{u}(y)^*\hat{v}(y)]\frac{dU_b(y)}{dy} dy - [\hat{p}(y)\hat{v}(y)^* + \hat{p}(y)^*\hat{v}(y)]_{-h}^{+h} \\
& - 2\mu \int_{-h}^{+h} \left[\frac{d\hat{u}(y)}{dy} \frac{d\hat{u}(y)^*}{dy} + \frac{d\hat{v}(y)}{dy} \frac{d\hat{v}(y)^*}{dy} + \alpha^2 (\hat{u}(y)\hat{u}(y)^* + \hat{v}(y)\hat{v}(y)^*) \right] dy \\
& + \mu \left[\hat{u}(y) \frac{d\hat{u}(y)^*}{dy} + \hat{u}(y)^* \frac{d\hat{u}(y)}{dy} + \hat{v}(y) \frac{d\hat{v}(y)^*}{dy} + \hat{v}(y)^* \frac{d\hat{v}(y)}{dy} \right]_{-h}^{+h}. \quad (26)
\end{aligned}$$

While interaction with the base shear flow and viscous dissipation prevails throughout the channel cross section, pressure and viscous diffusion only contribute at the boundaries and transfer energy between the fluid and the compliant walls.

The kinetic and potential energies associated with the walls are obtained as

$$E_{WK} = m|\omega|^2(|\hat{\eta}^+|^2 + |\hat{\eta}^-|^2) \quad \text{and} \quad E_{WP} = (B\alpha^4 + T\alpha^2 + K)(|\hat{\eta}^+|^2 + |\hat{\eta}^-|^2), \quad (27)$$

respectively. Using wall equations (15), together with boundary conditions (14), yields the temporal variation of the wall energy as

$$\begin{aligned}
2\omega_i(E_{WK} + E_{WP}) = & - \underbrace{2d|\omega|^2(|\hat{\eta}^+|^2 + |\hat{\eta}^-|^2)}_{E_0} + \underbrace{[\hat{p}(y)\hat{v}(y)^* + \hat{p}(y)^*\hat{v}(y)]_{-h}^{+h}}_{E_1} \\
& - \underbrace{\mu \left[\hat{v}(y) \frac{d\hat{v}(y)^*}{dy} + \hat{v}(y)^* \frac{d\hat{v}(y)}{dy} \right]_{-h}^{+h}}_{E_2}. \quad (28)
\end{aligned}$$

Thus, changes in total wall energy are seen to be the result of either dissipation within the wall (E_0) or energy exchange at the interface between the fluid and the compliant walls: work done by the pressure force (E_1) or the normal viscous stress (E_2). Both terms E_1 and E_2 also appear in Eq. (26) but with opposite sign; these fluid-structure interaction terms only account for an exchange of energy between the fluid and the walls but do not modify the total energy of the system.

The temporal variation of the total energy (22) is then obtained by adding (26) and (28), which leads to the following integrated total energy budget:

$$\begin{aligned}
2\omega_i E_{tot} = & - \underbrace{\int_{-h}^{+h} \rho[\hat{u}(y)\hat{v}(y)^* + \hat{u}(y)^*\hat{v}(y)]\frac{dU_b(y)}{dy} dy}_{C_1: \text{energy exchange with the base flow}}
\end{aligned}$$

$$\begin{aligned}
 & -\mu \underbrace{\left[\left(\frac{d\hat{u}(y)}{dy} \hat{\eta}^* + \frac{d\hat{u}(y)^*}{dy} \hat{\eta} \right) \frac{dU_b(y)}{dy} \right]_{-h}^{+h}}_{C_2: \text{energy exchange with the base flow at the walls}} \\
 & -2\mu \underbrace{\int_{-h}^{+h} \left[\frac{d\hat{u}(y)}{dy} \frac{d\hat{u}(y)^*}{dy} + \frac{d\hat{v}(y)}{dy} \frac{d\hat{v}(y)^*}{dy} + \alpha^2 (\hat{u}(y)\hat{u}(y)^* + \hat{v}(y)\hat{v}(y)^*) \right] dy}_{C_3: \text{viscous dissipation}} \\
 & -2d|\omega|^2(|\hat{\eta}^+|^2 + |\hat{\eta}^-|^2). \underbrace{\quad}_{C_4: \text{wall damping}}
 \end{aligned} \tag{29}$$

Hence, the only mechanisms that contribute to variations of the total energy are interactions with the base flow and dissipation (see also [19,35]). Energy transfer from or to the base flow occurs in the bulk (C_1) as well as at the boundaries (C_2), and energy dissipation takes place both in the fluid (C_3) and in the compliant walls (C_4). Note that the kinematic boundary conditions (14) have been used to bring to the fore the role of the base flow shear in the exchange term C_2 . As underlined by Carpenter and Morris [37], the contribution C_2 arises from the interaction of the displaced mean flow and shear stress. In the literature, the terms C_1 and C_2 are often labeled as irreversible energy transfer from the base flow to the perturbation; depending on the signs and phases of the different components in C_1 and C_2 , they may have a destabilizing or a stabilizing influence.

The energy budget (29) may be used to recover the temporal growth rate as

$$\omega_i = \underbrace{\hat{C}_1 + \hat{C}_2 + \hat{C}_3 + \hat{C}_4}_{\Sigma}, \tag{30}$$

where the different contributions have been renormalized by the total energy, $\hat{C}_i \equiv C_i/(2E_{tot})$.

Now that we have identified the different components that contribute to the variation of the perturbation energy, we proceed to analyze their role in the dynamics of the different classes of modes that prevail in the present configuration. In sequence we will address TS, divergence, and TWF modes and discuss the corresponding total energy budget as well as the spatial structure of the different contributions.

First we consider the stabilization mechanism of the TS mode as the reduced velocity V_R is increased. To that purpose, we investigate configurations with $Re = 10000$, $B_\star = 1$, and $d_\star = 0$. For these typical control parameter values, the TS mode is stable for V_R in excess of approximately 0.85, as shown by the black curve in Fig. 12(a). To study the influence of V_R on the energy transfer mechanisms, the most unstable TS mode is considered as V_R is varied; i.e., the streamwise wavenumber α is chosen to maximize the temporal growth rate ω_i for each value of V_R .

Figure 17(a) plots the components of the total energy budget as V_R is increased. The associated growth rate ω_i is also reported in the same figure. The excellent agreement between the curves of ω_i , derived from the eigenvalue problem, and of Σ , right-hand side of Eq. (30), gives confidence that the computation of the different energy terms is correctly implemented. The curves in Fig. 17(a) show that for the range of V_R considered here, the major destabilizing contribution is due to the action of the basic velocity gradient working against the Reynolds stress (\hat{C}_1). However, as V_R is increased, this production term \hat{C}_1 is observed to decrease and to be partially balanced by \hat{C}_2 . This suggests two stabilizing mechanisms associated with the compliant wall: one reducing the bulk production term \hat{C}_1 and due to a modification of the perturbation velocity profiles, and another one directly connected to the wall term \hat{C}_2 and due to the displaced mean flow that acts as a dissipative term here. The viscous dissipation (\hat{C}_3) is seen to weaken as V_R is increased, but the overall stabilizing influence dominates for increasing V_R .

The relative importance of the different components of the total energy (22) are displayed in Fig. 17(b) as V_R is varied, using the notation $\hat{E}_{FK} = E_{FK}/E_{tot}$, $\hat{E}_{WK} = E_{WK}/E_{tot}$, $\hat{E}_{WP} = E_{WP}/E_{tot}$, and $\hat{E}_W = \hat{E}_{WK} + \hat{E}_{WP}$. This plot shows that, as V_R is increased, a small part of the fluid kinetic

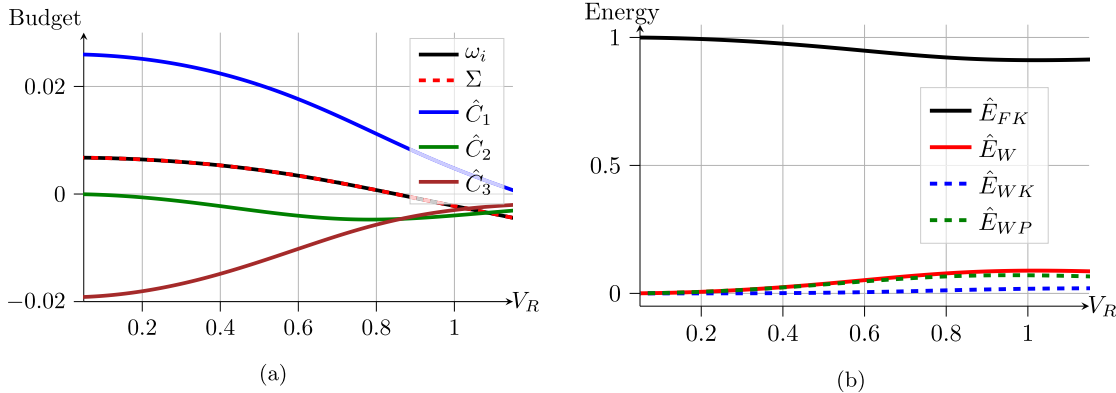


FIG. 17. Energy of most unstable TS mode as V_R is increased at $Re = 10000$, $B_* = 1$, and $d_* = 0$. (a) Evolution of the integrated total energy budget and comparison with temporal growth rate ω_i . (b) Different contributions to the total energy for $d_* = 0$.

energy is indeed transferred to the wall, mainly as potential energy. This is consistent with a class A mode.

We now analyze the spatial structure of the fluid kinetic energy budget (25). Figure 18 shows the wall-normal profiles of the different contributions for the most unstable TS mode computed at different values of V_R and d_* . Note that these profiles have been normalized to unit fluid kinetic energy E_{FK} . Figures 18(a) and 18(b), corresponding to $V_R = 0$ and $V_R = 0.03$ at $d_* = 0$, show that the production term \mathcal{P} is significantly modified by an increase of V_R . In particular, the amplitude of \mathcal{P} decreases with V_R and it exhibits a small region of negative production above the critical layer. In this region, the energy is transferred from the wave to the mean flow leading to a decrease of the total energy associated with the fluctuation. A similar observation is made by Metcalfe and Domaradzki [29] for the case of a laminar boundary layer stabilized by a compliant membrane. Comparison of Figs. 18(a) and 18(b) also illustrates the importance of the viscous diffusion term \mathcal{D} in redistributing energy produced by the Reynolds stress as V_R is increased, whereas the pressure diffusion term Π has a minor influence. This shows that under the action of the viscous diffusion term, the energy produced by the work of the Reynolds stress is transferred towards the wall where it is dissipated by viscosity (ε). Figure 18(a) also reveals that the production term \mathcal{P} increases near the wall with the emergence of a second peak as V_R is increased. Due to the pressure diffusion and viscous diffusion terms, which are negatively correlated with \mathcal{P} , this additional production does not result in a destabilizing effect.

The influence of the dissipation within the compliant wall is illustrated in Figs. 18(b)–(d) for $V_R = 1$. When d_* is increased from 0 [Fig. 18(b)] to 0.14 [Fig. 18(c)], the TS mode is destabilized (not shown here for the sake of conciseness). In Fig. 18(c), the pressure-diffusion term Π is positive across the entire channel, which leads to work of the pressure force at the walls; the viscous diffusion profile \mathcal{D} is mostly unchanged, but the peak near the wall of the production term \mathcal{P} becomes the dominant feature. The increase of the dissipation leads to an increase in the production term in the viscous layer which is consistent with the TS mode (i.e., the phase shift mainly occurs in this region).

Finally, for a stronger wall damping $d_* = 0.2$ [Fig. 18(d)], the pressure diffusion term Π is almost identical to the production term \mathcal{P} , in contrast with what is observed for $d_* = 0.14$ and $d_* = 0$. In particular, Π exhibits positive values near the wall which are associated with work of the pressure at the wall. This indicates that the mode is then in strong interaction with the wall and could probably be classified as a TWF mode. In particular, at $d_* = 0.15$, a branch switching occurs and a collapse between TS and TWF modes is observed. This behavior is illustrated in Fig. 19. In the figure, α is chosen to maximize ω_i for each value of d_* . On one hand, for $d_* < 0.15$ where the TS mode exists, the production term \hat{C}_1 is increasing with the dissipation. It has as a consequence to increase the

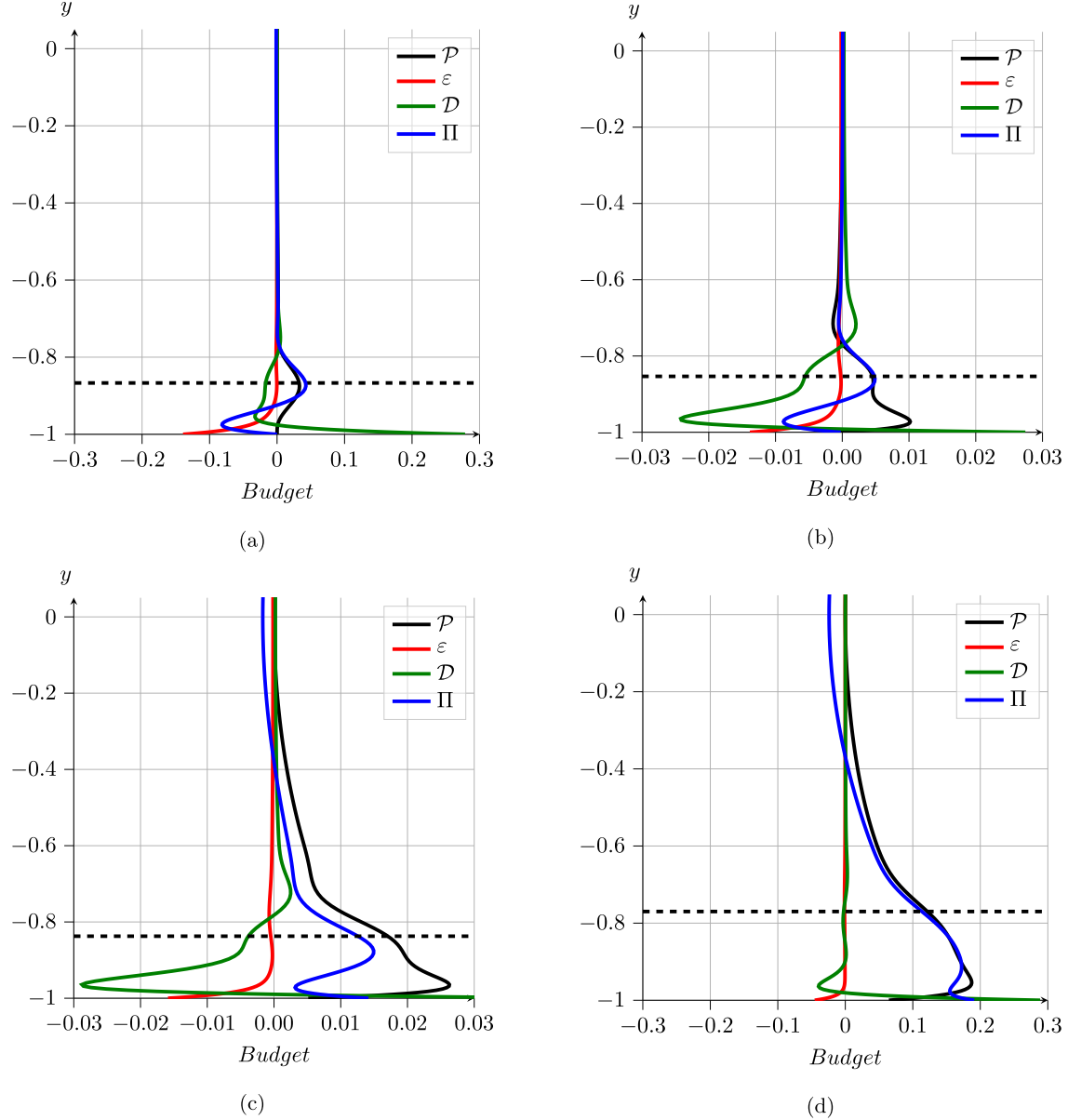


FIG. 18. Fluid kinetic energy budget profiles for most unstable TS mode at $\text{Re} = 10000$, $B_* = 1$, and (a) $d_* = 0$, $V_R = 0.03$, (b) $d_* = 0$, $V_R = 1$, (c) $d_* = 0.14$, $V_R = 1$, and (d) $d_* = 0.2$, $V_R = 1$. The wall-normal position of the critical layer is shown as a dashed line.

temporal amplification rate of the TS mode in agreement with class A modes. On the other hand, for $d_* > 0.15$, the temporal amplification rate is decreasing with the wall dissipation. This further indicates that beyond $d_* = 0.15$, the mode is mainly associated with a TWF instability.

After the discussion of the TS modes, we now address the total energy budgets prevailing for divergence modes, of both sinuous and varicose symmetry. The evolution of the energy transfer mechanisms is monitored as d_* is varied, since this is the main control parameter influencing the dynamics of divergence modes. Figure 20 shows data computed over the range $0 < d_* < 10$ at $\text{Re} = 10000$, $B_* = 1$, and $V_R = 2$. The evolution with d_* of the different terms of the energy budget for sinuous [Fig. 20(a)] and varicose [Fig. 20(c)] modes reveals that the term \hat{C}_2 dominates for both symmetries. This term accounts for the energy exchange with the base flow due to wall displacement, which is therefore identified as the main mechanism promoting instability of the

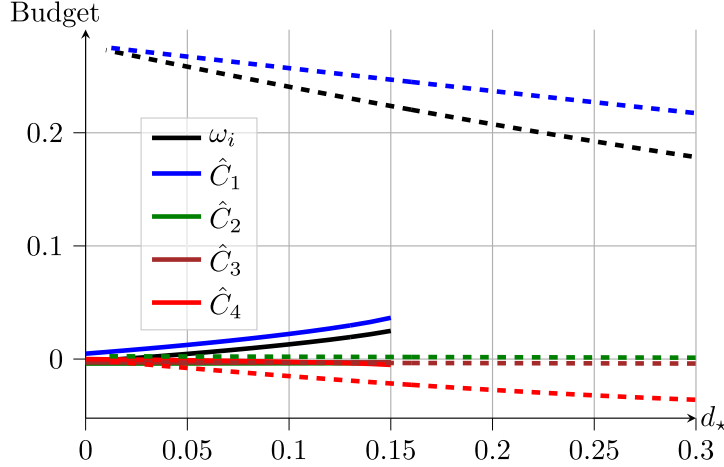


FIG. 19. Energy of most unstable sinuous modes. Evolution of the integrated total energy budget with d_* for $V_R = 1$. TS mode is shown as solid lines. Sinuous TWF mode is shown in dashed lines. At $d_* \approx 0.15$ modes collapse.

divergence modes. It also confirms the influence of the Reynolds number onto the divergence mode as observed in the previous section. The importance of viscous effects for divergence modes has also been observed by Carpenter and Morris [37] for the boundary-layer flow case. The destabilizing effect of \hat{C}_2 is partially balanced by the work of the Reynolds stress against the basic shear \hat{C}_1 , the viscous dissipation \hat{C}_3 , and the wall dissipation \hat{C}_4 . Hence, it illustrates the dual nature of viscous effects for the divergence mode. On one hand, it promotes the instability by propagating the

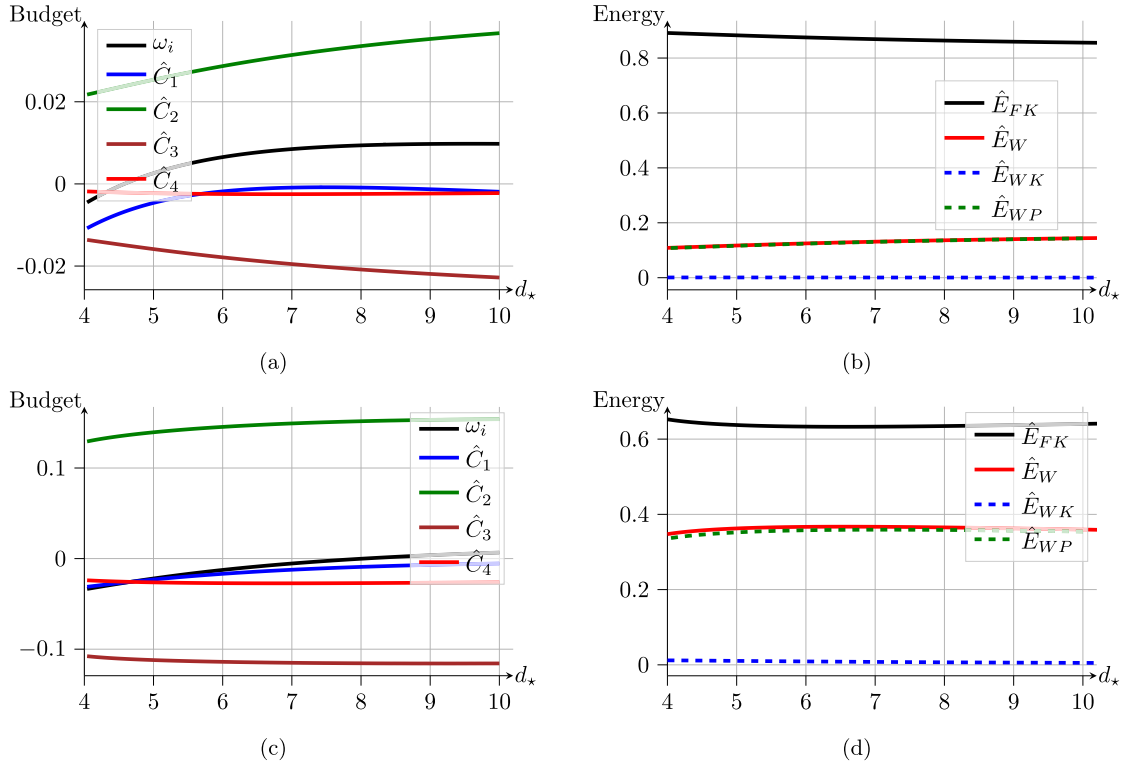


FIG. 20. Energy of most unstable divergence mode as d_* is increased at $Re = 10000$, $B_* = 1$, and $V_R = 2$. (a, c) Evolution of integrated total energy budget and (b, d) breakdown of total energy into its components for (a, b) sinuous and (c, d) varicose modes.

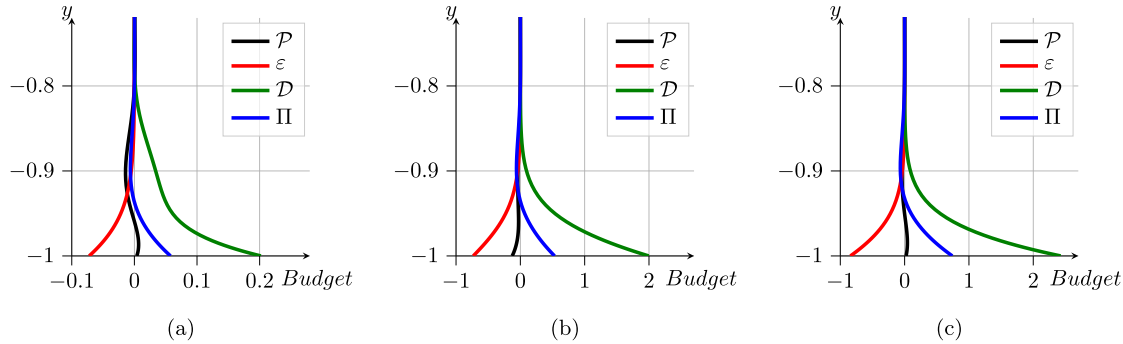


FIG. 21. Fluid kinetic energy budget profiles for most unstable divergence mode at $\text{Re} = 10000$, $B_* = 1$, and $V_R = 2$ and (a) $d_* = 5$ sinuous mode, (b) $d_* = 5$ varicose mode, and (c) $d_* = 9$ varicose mode.

energy production from the wall displacement into the flow domain, but on the other hand, viscosity also plays its usual dissipative role. Inspection of the different contributions to the total energy [Figs. 20(b) and 20(d)] shows that while the fluid energy remains the main factor in both situations, the varicose modes involve significantly more wall energy than their sinuous counterparts. Due to the slow dynamics of these modes, the wall energy is almost entirely made up of potential energy for both symmetries. It should also be mentioned that due to the long wavelengths of the divergence modes, the main contribution to the wall potential energy E_{WP} [Eq. (27)] is here due to the stiffness while the flexural rigidity only plays a marginal role.

The cross-channel profiles of the fluid kinetic energy budgets for the divergence modes are shown in Fig. 21. The figure demonstrates that the production, diffusion, and dissipation contributions are all localized in the near-wall region. Comparison of Figs. 21(a) and 21(b) reveals a notable difference between sinuous and varicose modes at $d_* = 5$: while the production term \mathcal{P} is negative throughout the channel cross section for the varicose mode, the sinuous mode exhibits a small region near the wall with positive values of the production \mathcal{P} . Interestingly, when d_* is further increased up to $d_* = 9$, the plots in Fig. 21(c) show that then the varicose production term \mathcal{P} also exhibits a weakly positive region near the wall. This change of sign of the production term appears to approximately coincide with the onset of divergence instability, i.e., change of sign of the growth rate ω_i plotted in Fig. 20(c). Hence, while the energy budget is dominated by the term $\hat{\mathcal{C}}_2$, it seems that the instability is also significantly influenced by \mathcal{P} .

Finally we consider TWF modes. For this final class of modes, we restrict our analysis to the varicose symmetry which has been observed to always dominate over the sinuous symmetry. The evolution of the total energy budgets with V_R is shown in Fig. 22(a) for $\text{Re} = 10000$, $B_* = 1$, and $d_* = 0$. These plots indicate that the budget is driven by the production term $\hat{\mathcal{C}}_1$, in agreement with previous analyses [20,29]. However, it is interesting to notice that energy transfer $\hat{\mathcal{C}}_2$ from the base flow to the perturbation via the boundaries also promotes the instability. Both contributions $\hat{\mathcal{C}}_1$ and $\hat{\mathcal{C}}_2$ have a destabilizing influence. The distribution of the total energy among its different components plotted in Fig. 22(b) shows that for small values of V_R the wall is the most energetic component of this fluid-structure system, but for $V_R > 1.6$ the kinetic energy of the fluid overcomes the wall contribution. Thus, the present scenario appears to be exactly opposite of the situation prevailing for TS modes: as V_R is increased, the ratio E_{FK}/E_W decreases for TS modes while it increases for TWF modes. This is in accordance with the classification of TS modes as class A and TWF modes as class B modes. Finally, monitoring the potential and kinetic components of the wall energy (E_{WP} and E_{WK} , respectively) shows that the wall energy is essentially due to the kinematic contribution for TWF modes, which is in contrast to the situation prevailing for divergence modes.

In Fig. 22(c), the fluid kinetic energy profile is shown across the channel diameter for $V_R = 3$. The role of viscosity is found to be mainly concentrated in two distinct areas. The viscous diffusion term \mathcal{D} exhibits a first shallow peak around the critical layer (indicated by the dashed line), while

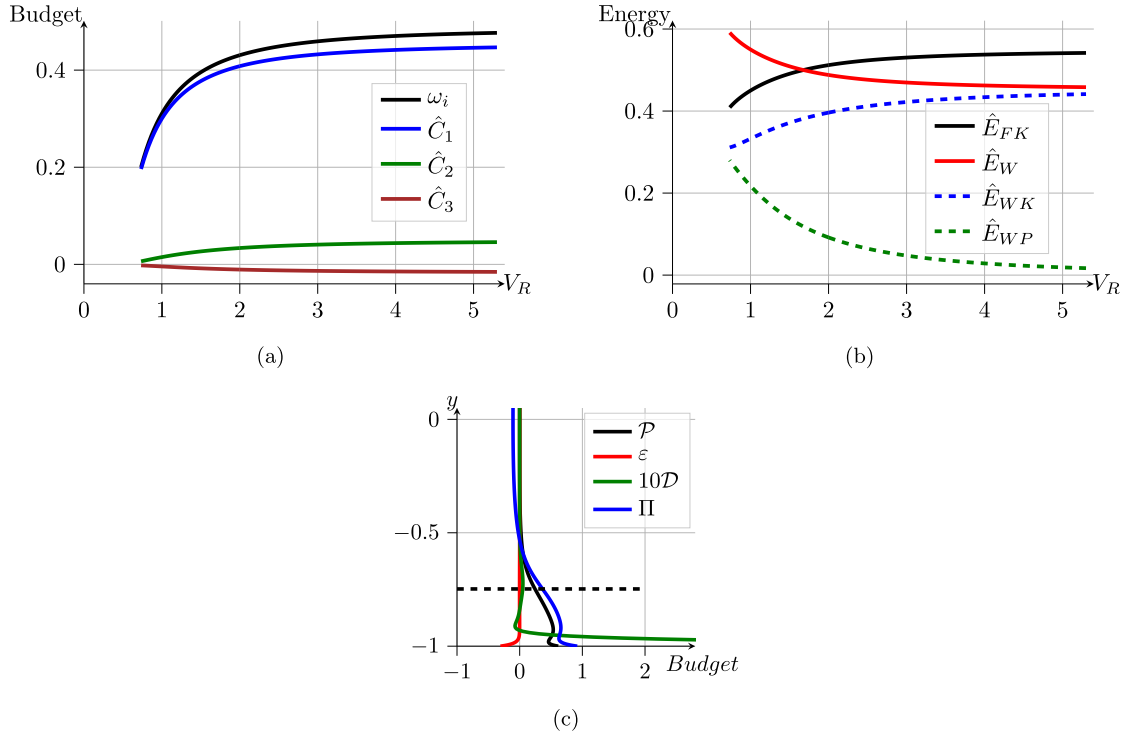


FIG. 22. Energy of most unstable varicose TWF mode as V_R is increased at $Re = 10000$, $B_* = 1$, and $d_* = 0$. (a) Evolution of integrated total energy budget. (b) Distribution of total energy as fluid and wall contributions. (c) Cross-channel profile of the fluid kinetic energy budget for $V_R = 3$. The wall-normal position of the critical layer is shown as a dashed line.

a second stronger peak emerges near the wall due to the viscous layer. This is consistent with the theoretical model developed by Davies and Carpenter [20]. However, the dominant production term \mathcal{P} is associated with the work of the Reynolds stress against the mean shear and does not exhibit a maximum near the critical layer. Its profile presents rather an inflection point near the critical layer, which is in contrast with observations by Metcalfe and Domaradski [29] for the flat plate boundary layer. We also observe that both pressure diffusion Π and viscous diffusion \mathcal{D} display large positive values near the wall. Thus the energy production due to the basic shear flow is transferred to the wall through the action of both diffusion processes.

To conclude this section on energy transfer mechanisms, the influence of wall dissipation d_* is reported in Fig. 23 for the most unstable varicose TWF modes at $Re = 10000$, $B_* = 1$, and $V_R = 3$. The plots in Fig. 23(a) show that for small values of d_* the stabilization of the TWF mode is essentially due to the increasing energy dissipation \hat{C}_4 in the compliant walls. For larger values of d_* , both the work of the Reynolds stress against the basic shear \hat{C}_1 and the wall dissipation \hat{C}_4 evolve so as to stabilize the TWF mode. This illustrates that two distinct mechanisms are at play to diminish the growth rate for the TWF mode. The curves in Fig. 23(b) illustrate the redistribution of the total energy due to wall dissipation: as d_* is increased, the wall contribution (essentially kinetic energy) to the total energy decreases almost linearly in favor of the fluid contribution. The effect of the wall damping on the wall-normal profiles of the fluid kinetic energy is shown in Fig. 23(c). While these profiles at $d_* = 4$ are similar to those prevailing without wall dissipation [see Fig. 22(c)], it is observed that the production \mathcal{P} exhibits a lower amplitude than the pressure diffusion term Π . As d_* increases, the energy transfer from the fluid towards the wall is no longer sufficient to balance the higher wall dissipation and, as a result, the proportion of fluid energy increases in the total energy of the perturbation.

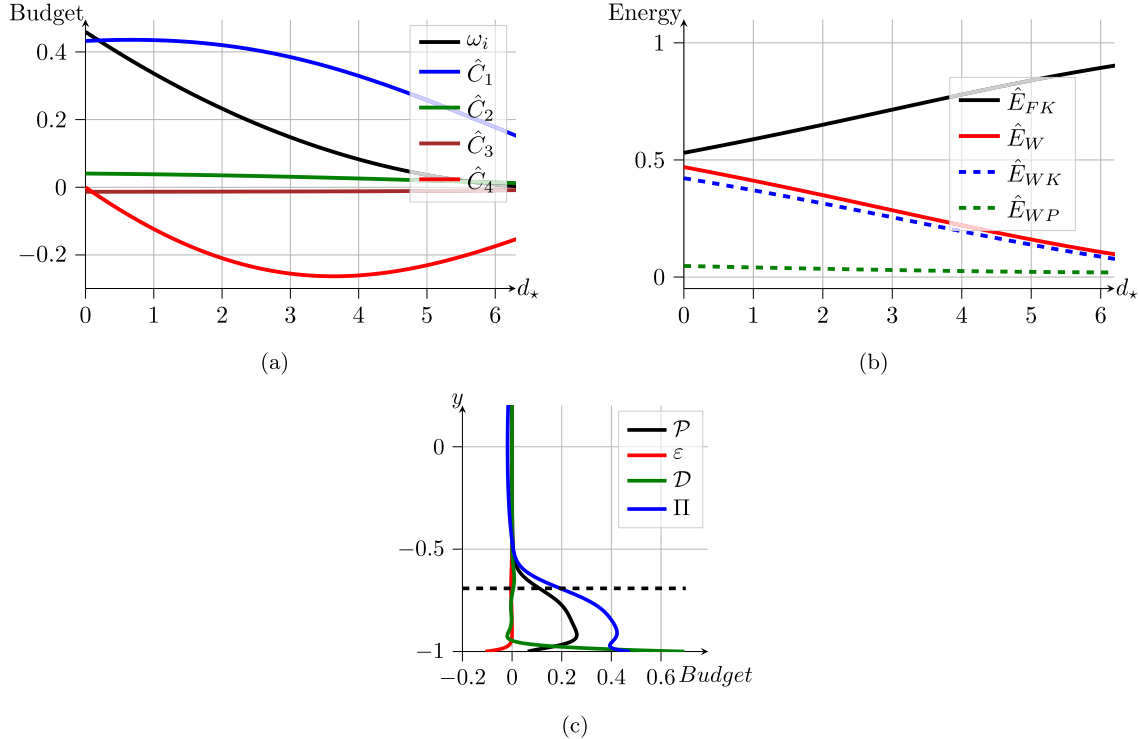


FIG. 23. Energy of most unstable varicose TWF mode as d_* is increased at $Re = 10000$, $B_* = 1$, and $V_R = 3$. (a) Evolution of integrated total energy budget. (b) Distribution of total energy as fluid and wall contributions. (c) Cross-channel profile of the fluid kinetic energy budget for $d_* = 4$. The wall-normal position of the critical layer is shown as a dashed-line.

V. CONCLUDING REMARKS

In this paper, we have revisited the linear stability problem of a fluid interacting with a compliant channel. The walls are modeled as spring-backed deformable plates including a damping mechanism. A general numerical method free of spurious modes is derived to tackle this problem. By taking advantage of the base flow symmetries, varicose and sinuous eigenmodes are computed separately and efficiently. A dimensional analysis has been carried out to identify the most physically relevant control parameters. Traveling wave flutter (TWF), divergence, and Tollmien-Schlichting (TS) modes are then recovered. The main conclusions of the current study are as follows:

(1) TWF waves are mainly driven by the reduced velocity V_R which measures the strength of the coupling between the fluid and the compliant walls. The Reynolds number effect is not significant for these modes.

(2) For TWF modes, the perturbations of varicose symmetry are observed to be destabilized first when increasing V_R . While a decrease in the flexural rigidity is accompanied by a stabilization of the TS mode, it enhances the amplification of TWF modes. This is especially true for the varicose TWF modes. In particular, we show that the compliant wall potential for laminar-turbulent transition delay is almost negligible when the varicose symmetry is taken into account. This finding extends the previous linear stability results obtained for the same flow case but either limited to the sinuous modes [20,21] or focusing on a quite narrow region of parameter space [22].

(3) For the varicose symmetry, a linear relationship is found between the critical reduced velocity and the wall dissipation, independently of the flexural rigidity. For large values of V_R , the dynamics is eventually dominated by divergence modes for a certain amount of wall dissipation and for both symmetries. While a stabilizing effect is observed for the divergence mode when increasing the Reynolds number, sinuous perturbations are amplified at a lower wall dissipation

than their varicose counterpart. Such a distinction between varicose and sinuous symmetries was not identified in previous studies.

We have also uncovered physical mechanisms responsible for the amplification of the different categories of modes. This was accomplished by evaluating total energy budgets. First, for $d_\star = 0$, kinetic energy budgets indicate that the TS mode is stabilized as V_R is increasing under the action of two mechanisms. On one hand, the work of the Reynolds stress against the mean flow exhibits a region above the critical layer which is negative. Here, energy is transferred from the wave to the base flow. The second mechanism is associated with an irreversible energy transfer from the fluctuation to the mean flow due to the mean flow displacement near the walls. On the other hand, the vertical distribution of the production term associated with the TWF mode is observed to peak near the walls and exhibits an inflection point close to the critical layer for both symmetries. Hence, it shows some differences with results provided by Domaradzki and Metcalfe [29] for the boundary layer where a peak is observed near the critical layer position. Furthermore, the energy transfer from the wall to the fluid is mainly attributed to a pressure diffusion term.

Second, the dominant term for divergence modes appears to be associated with an irreversible energy exchange due to the interaction of the displaced mean flow and shear stress.

Extension of the present study to nonmodal stability analyses can be considered in a future work. Hœpffner *et al.* [35] have investigated the same problem for three-dimensional perturbations but numerical oscillations were observed by the authors when increasing the number of eigenmodes used to compute transient growth. The formulation adopted here is free of spurious modes and we believe that the problem can be solved using the numerical procedure developed in the present analysis. In addition, the role of the reduced velocity has not been investigated by Hœpffner *et al.* [35]. Finally, it should also be interesting to extend our study to pulsatile flow [38,39] and the pipe geometry, which cover more biologically significant phenomena.

ACKNOWLEDGMENTS

Fédération lyonnaise de modélisation et sciences numériques (FLMSN) is gratefully acknowledged for providing access to high-performance computing resources.

APPENDIX: VALIDATION AND INFLUENCE OF BOUNDARY CONDITIONS

For validation purposes, we adopt choices made by Davies and Carpenter [20] for dimensionless wall equations. Here, the Reynolds number is based on h , v , and the centerline velocity. The dimensionless wall parameters are

$$\Gamma = \frac{m}{\rho h}, \quad B_\star = \frac{B}{h \rho v^2}, \quad K_\star = \frac{Kh^3}{\rho v^2}, \quad d_\star = \frac{dh}{\rho v}.$$

Davies and Carpenter [20] used an Orr-Sommerfeld equation for solving the fluid-structure interaction problem. The pressure at the lower wall is recovered through

$$p(-1) = \frac{1}{2} \left(-i\omega \int_{-1}^1 \hat{v} dy + i\alpha \int_{-1}^1 U_b \hat{v} dy \right),$$

where the viscous terms have been neglected. For consistency, the authors have also neglected the effect of the viscous stress at the wall for the coupling between the fluid and the walls. We recall that this formulation is correct only for the sinuous configuration. Guaus and Bottaro [28] used a primitive formulation for the same problem and considered only the pressure at the wall for the force associated with the fluid acting at the walls. However, the pressure is computed without neglecting the viscous stress along the wall-normal direction. In the present study, we have not neglected the effect of the viscous stress on both the pressure and the force acting on the walls. In Fig. 24, we show the neutral curve for the sinuous TWF mode for $K_\star = 10^7$, $B_\star = 4K$, $d_\star = 0$, and $\Gamma = 2$. The figure shows an almost perfect agreement between our approach and the one given by Davies

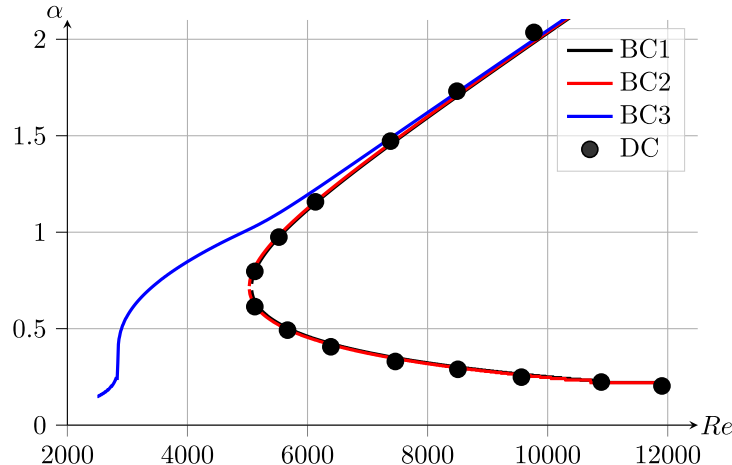


FIG. 24. Neutral curves. Sinuous configuration. Effects of the boundary conditions. $K_* = 10^7$, $B_* = 4K_*$, $d_* = 0$, and $\Gamma = 2$. DC, results extracted from [20]; BC1, the formulation adopted in the present paper; BC2, the pressure at the wall is expressed as in [20] and we neglect the viscous stress at the walls; BC3, formulation adopted in [28].

and Carpenter [20]. It supports the hypotheses made by the previous authors. Nevertheless, our approach is more general because it also allows to deal with the varicose symmetry. In addition, the system also reduces to an Orr-Sommerfeld problem with only one velocity component. Figure 24 also shows that the formulation made by Guaus and Bottaro [28] is not consistent and leads to discrepancies near the critical Reynolds number.

-
- [1] J. B. Grotberg and O. E. Jensen, Biofluid mechanics in flexible tubes, *Annu. Rev. Fluid Mech.* **36**, 121 (2004).
 - [2] P. G. Larose and J. B. Grotberg, Flutter and long-wave instabilities in compliant channels conveying developing flows, *J. Fluid Mech.* **331**, 37 (1997).
 - [3] J. Gray, Studies in animal locomotion. VI. The propulsive powers of the dolphin, *J. Exp. Biol.* **13**, 192 (1936).
 - [4] M. Kramer, Boundary layer stabilization by distributed damping, *J. Aeronaut. Sci.* **24**, 459 (1957).
 - [5] D. M. Bushnell and K. J. Moore, Drag reduction in nature, *Annu. Rev. Fluid Mech.* **23**, 65 (1991).
 - [6] F. E. Fish and G. V. Lauder, Passive and active flow control by swimming fishes and mammals, *Annu. Rev. Fluid Mech.* **38**, 193 (2006).
 - [7] M. Gad-el-Hak, Boundary layer interactions with compliant coatings: An overview, *Appl. Mech. Rev.* **39**, 511 (1986).
 - [8] M. Gaster, Is the dolphin a red herring? in *Turbulence Management and Relaminarisation* (Springer-Verlag, Berlin, 1988), pp. 285–304.
 - [9] V. Kumaran, Stability and the transition to turbulence in the flow through conduits with compliant walls, *J. Fluid Mech.* **924**, P1 (2021).
 - [10] R. Patne and V. Shankar, Stability of flow through deformable channels and tubes; implications of consistent formulation, *J. Fluid Mech.* **860**, 837 (2019).
 - [11] J. H. Duncan, A comparison of wave propagation on the surfaces of simple membrane walls and elastic coatings bounded by a fluid flow, *J. Sound Vib.* **119**, 565 (1987).
 - [12] B. T. Benjamin, Shearing flow over a wavy boundary, *J. Fluid Mech.* **6**, 161 (1959).
 - [13] B. T. Benjamin, Effects of a flexible boundary on hydrodynamics stability, *J. Fluid Mech.* **9**, 513 (1960).
 - [14] B. T. Benjamin, The threefold classification of unstable disturbances in flexible surfaces bounding inviscid flows, *J. Fluid Mech.* **16**, 436 (1963).

- [15] J. W. Miles, On the generation of surface waves by shear flows, *J. Fluid Mech.* **3**, 185 (1957).
- [16] P. W. Carpenter and A. D. Garrad, The hydrodynamic stability of flow over Kramer-type compliant surfaces. Part 1. Tollmien-Schlichting instabilities, *J. Fluid Mech.* **155**, 465 (1985).
- [17] P. W. Carpenter and A. D. Garrad, The hydrodynamic stability of flow over Kramer-type compliant surfaces. Part 2. Flow-induced surface instabilities, *J. Fluid Mech.* **170**, 199 (1986).
- [18] O. Wiplier and U. Ehrenstein, Numerical simulation of linear and nonlinear disturbance evolution in a boundary layer with compliant walls, *J. Fluids Struct.* **14**, 157 (2000).
- [19] M. Malik, M. Skote, and R. Bouffanais, Growth mechanisms of perturbations in boundary layers over a compliant wall, *Phys. Rev. Fluids* **3**, 013903 (2018).
- [20] C. Davies and P. W. Carpenter, Instabilities in a plane channel flow between compliant walls, *J. Fluid Mech.* **352**, 205 (1997).
- [21] C. Davies and P. W. Carpenter, Numerical simulation of the evolution of Tollmien-Schlichting waves over finite compliant panels, *J. Fluid Mech.* **335**, 361 (1997).
- [22] M. Nagata and T. R. Cole, On the stability of plane Poiseuille flow between compliant boundaries, in *Proceedings of the International Conference on Computational Methods and Experimental Measurements IX*, edited by G. M. Carlomagno, University of Naples di Napoli, Italy and C.A. Brebbia, Wessex Institute of Technology, United Kingdom (WIT Press, 1999), pp. 231–240.
- [23] K. Tsigklifis and A. D. Lucey, Asymptotic stability and transient growth in pulsatile Poiseuille flow through a compliant channel, *J. Fluid Mech.* **820**, 370 (2017).
- [24] J. S. B. Gajjar and P. Sibanda, The hydrodynamic stability of channel flow with compliant boundaries, *Theor. Comput. Fluid Dyn.* **8**, 105 (1996).
- [25] E. de Langre, *Fluides et Solides* (École polytechnique, 91120 Palaiseau).
- [26] M. L. Manning, B. Bamieh, and J. M. Carlson, Descriptor approach for eliminating spurious eigenvalues in hydrodynamic equations, [arXiv:0705.1542](https://arxiv.org/abs/0705.1542).
- [27] J. M. Rotenberry and P. G. Saffman, Effect of compliant boundaries on weakly nonlinear shear waves in channel flow, *SIAM J. Appl. Math.* **50**, 361 (1990).
- [28] A. Guaus and A. Bottaro, Instabilities of the flow in a curved channel with compliant walls, *Proc. R. Soc. A* **463**, 2201 (2007).
- [29] J. A. Domaradzki and R. W. Metcalfe, Stabilization of laminar boundary layers by compliant membranes, *Phys. Fluids* **30**, 695 (1987).
- [30] V. Shankar and V. Kumaran, Stability of wall modes in fluid flow past a flexible surface, *Phys. Fluids* **14**, 2324 (2002).
- [31] R. Peyret, *Spectral Methods for Incompressible Viscous Flow* (Springer, Berlin, 2002).
- [32] L. Trefethen, *Spectral Methods in MATLAB* (Society for Industrial and Applied Mathematics, Philadelphia, 2000).
- [33] P. J. Schmid and D. S. Henningson, *Stability and Transition in Shear Flows*, Applied Mathematical Sciences Vol. 142 (Springer, Berlin, 2001).
- [34] P. G. Drazin and W. H. Reid, *Hydrodynamic Stability* (Cambridge University Press, Cambridge, U.K., 1981).
- [35] J. Höpffner, A. Bottaro, and J. Favier, Mechanisms of non-modal energy amplification in channel flow between compliant walls, *J. Fluid Mech.* **642**, 489 (2010).
- [36] L. Huang, Reversal of the Bernoulli effect and channel flutter, *J. Fluids Struct.* **12**, 131 (1998).
- [37] P. W. Carpenter and P. J. Morris, The effect of anisotropic wall compliance on boundary-layer stability and transition, *J. Fluid Mech.* **218**, 171 (1990).
- [38] B. Pier and P. J. Schmid, Linear and nonlinear dynamics of pulsatile channel flow, *J. Fluid Mech.* **815**, 435 (2017).
- [39] B. Pier and P. J. Schmid, Optimal energy growth in pulsatile channel and pipe flows, *J. Fluid Mech.* **926**, A11 (2021).

[A29]

Residence time distributions for in-line chaotic mixers

N. Poumaëre, F. Raynal & B. Pier

Physical Review E **106**, 015107 (13 pages) (2022)

doi :10.1103/PhysRevE.106.015107
<https://hal.archives-ouvertes.fr/hal-03727867>

Residence time distributions for in-line chaotic mixers

Nelson Poumaëre , Benoît Pier , and Florence Raynal *

Laboratoire de Mécanique des Fluides et d'Acoustique, Université de Lyon,

École centrale de Lyon, INSA Lyon, Université Claude Bernard Lyon 1, CNRS, F-69134 Écully, France



(Received 11 January 2022; revised 11 May 2022; accepted 1 July 2022; published 19 July 2022)

We investigate the distributions of residence time for in-line chaotic mixers; in particular, we consider the Kenics, the F-mixer, and the multilevel laminating mixer and also a synthetic model that mimics their behavior and allows exact mathematical calculations. We show that whatever the number of elements of mixer involved, the distribution possesses a t^{-3} tail, so that its shape is always far from Gaussian. This t^{-3} tail also invalidates the use of second-order moment and variance. As a measure for the width of the distribution, we consider the mean absolute deviation and show that, unlike the standard deviation, it converges in the limit of large sample size. Finally, we analyze the performances of the different in-line mixers from the residence-time point of view when varying the number of elements and the shape of the cross section.

DOI: 10.1103/PhysRevE.106.015107

I. INTRODUCTION

Efficient stirring is the key ingredient of good mixing. This mechanism is generally associated with a turbulent flow, but even when the flow field is laminar, dynamical systems theory allows chaotic trajectories by stretching and folding of fluid elements, a process called chaotic advection [1–3]. Chaotic advection arises in a large diversity of natural or industrial flows. Extreme examples are mixing in geophysical flows (in the oceans [4] or magma in the earth mantle [5]), where the typical length scale reaches hundreds of kilometers, and microfluidics [6,7], with typical length scale of the order of 100 μm , that is, nine orders of magnitude smaller.

In this article, we are interested in in-line mixers, consisting of a succession of identical elements, which have applications from millifluidics [8,9] to microfluidics [10]. Although solving the concentration field is not easy to achieve because of their complicated geometry [11,12], it is well known that those mixers achieve a very good mixing by reproducing the baker's map. Thus they can indeed be considered as ideal mixers.

The present investigation focuses on another aspect of in-line mixers, their residence-time distributions (RTD) [13,14]: An ideal mixer is characterized by a very narrow Gaussian or a Dirac centered on the mean travel time. However, when considering only one element of an in-line mixer, the histogram of residence time is very broad and often monotonously decaying, with a maximum equal (or very close) to the minimum time involved to cross the element [15]: a behavior very far from that of an ideal mixer. Our goal is thus to study how the histogram evolves when increasing the number of elements.

Residence time distribution is a complex feature, not always correctly comprehended. Indeed, let us consider the case of the flow in a cylindrical pipe with circular cross section. The parallel flow field in the x direction is a parabolic profile

of equation:

$$v_x(r) = 2 v_m (1 - r^2/R^2), \quad (1)$$

where r is the radial distance to the center of the section, R is the radius of the pipe, and v_m the mean velocity over the section. Because of the cylindrical symmetry, the residence time t depends only on r as

$$t(r) = L/v_x(r), \quad (2)$$

for a section of length L . Suppose now that we calculate the mean residence time t_m just by sampling randomly M particles at the inlet section at $t = 0$ (what Danckwerts named a “pulse signal” [14]) and measure the mean of the M corresponding residence times t . The result should be the same as what is obtained from the continuous equation:

$$t_m = \frac{1}{\pi R^2} \int_0^R t(r) 2\pi r dr, \quad (3)$$

$$= \frac{L}{2v_m} \int_0^R \frac{1}{1 - r^2/R^2} \frac{2r dr}{R^2}, \quad (4)$$

$$= \frac{L}{2v_m} \int_0^1 \frac{1}{1 - u} du, \quad (5)$$

where we have used Eq. (2) and set $u = r/R$. Finally t_m diverges logarithmically when u approaches 1 (r approaches R), so that the mean time calculated this way is not defined. The reason lies in the way the mean time is calculated: When considering the inlet section during a lapse of time dt , many more particles cross at the center (where the velocity is maximal) than near the walls (where the velocity is very weak). As expressed by Danckwerts [13], “there is a variation in velocity from the axis to the wall of the pipe, so that the central ‘core’ of fluid moves with a velocity greater than the mean, while the fluid near the wall lags behind.” In order to calculate a mean time, this nonuniform flux of particles must be taken into account by properly weighting the statistics [15–17]. As the quantity of particles that cross a section during dt is proportional to the crossing velocity, the weight must also be chosen proportional to this velocity, i.e., v_\perp/v_m where

*Corresponding author: florence.raynal@ec-lyon.fr

v_{\perp} is the component of the velocity perpendicular to the cross section. Now calculating again the mean time t_m using this weight, with $v_{\perp} = v_x$, leads to the trivial expression

$$t_m = \frac{1}{\pi R^2} \int_0^R \frac{v_x(r)}{v_m} t 2\pi r dr = L/v_m \quad (6)$$

because of Eq. (2). We finally obtain the desired result,

$$t_m = \frac{\mathcal{V}}{Q}, \quad (7)$$

where \mathcal{V} is the volume of an element and Q the flow rate.

In a former article [15], we proposed to use the time of flight in order to obtain statistics of residence time. The time of flight is the lapse of time between the inlet and outlet of a given element when following a single fluid particle. Unlike RTD, the time of flight is a Lagrangian quantity, very close to the time of first return [18], or to the waiting time (time spent by a particle in a given domain \mathcal{D}) [19], both introduced for dynamical systems. Obviously, a particle trajectory is more likely to enter a given element in regions of high velocity than near the walls, so that there is no need for weighting the statistics as for RTD: When averaged, the time of flight converges naturally toward the mean time $t_m = \mathcal{V}/Q$ [15].

In the following, we will use time of flight to construct residence time distributions. The flow field is laminar, and we mostly consider nondiffusive particles, which corresponds to flows at high Péclet numbers on short times, for which the effects of molecular diffusion are negligible. The mean residence time in n elements is denoted by $t_m^{(n)} = n \times t_m$, where $t_m \equiv t_m^{(1)}$ is the mean residence time in a single element of mixer; similarly, $t_{\min}^{(n)} = n \times t_{\min}$ denotes the minimal time taken by a particle to cross n elements; the maximum time is infinite, due to the zero-velocity field on the walls. The density probability of residence time in n elements is denoted by $f_n(t)$.

This paper is organized as follows: In the next section we present the different mixers studied. We begin with the real mixers and show that their autocorrelation coefficient decreases very rapidly with the number of elements. This allows us to introduce a kinematic model that mimics the residence time distributions in a single element. In the following section we vary the number of mixing elements from 1 to n . In particular, we show that t^{-3} tail that exists for 1 element persists when the number of elements is increased. Then we explain how, because of this t^{-3} tail, the use of the classic standard deviation is forbidden. We thus discuss how to measure the stretching of RTD and choose the mean absolute deviation; we can therefore compare the different in-line mixers. Finally, in the last section we use this tool to discuss the influence of the cross-section geometry of mixing elements in the stretching of RTD.

II. MIXERS STUDIED

The mixers studied here—the Kenics, the F-mixer, and the multilevel laminating mixer (MLLM)—enable global chaos [15]; they are constituted of n identical elements. For each mixer we calculate the RTD using time of flight: We follow a fluid particle over time and record the time taken to cross each element. For the calculation of the time of flight in n elements, we sum the n individual times of flight corresponding to n elements in a row.

A. Real mixers

The numerical treatment of the velocity field by finite-element method and integration of the trajectories by a fourth-order Runge-Kutta method for the mixers studied here was explained in detail in Ref. [15]; we use the same numerical data here.

The computational geometries for three mixers are depicted in Fig. 1. The corresponding Poincaré sections and Lyapunov exponents are not shown here but can be found in Ref. [15]. A particle which exits at the outlet cross section of a computational geometry is reintroduced at the same location in the inlet cross section. This enables us to follow a particle on a very long number of elements, and we note the consecutive residence time in each element. Note that the number of elements involved in the computational geometries is not significant in this study.

For each mixer four long trajectories were calculated. A trajectory is terminated when the point ends in a wall, which may happen due to intrinsically limited numerical accuracy, or when a point is so close to a wall that the time taken to escape the element is too high. For this work the loss of particles is less than 1% [15].

The Kenics mixer [20] is composed of a series of identical internal blades inside a circular pipe; each blade has a helical shape, alternately right or left handed, and the leading edge of a given blade is at right angle of the trailing edge of the preceding blade. The computational geometry used here is shown in Fig. 1(a): Note that six elements are represented, so that the periodicity of the flow arises after two elements.

The MLLM [21–23] has a three-dimensional configuration intended to mimic the baker's map. The computational geometry used is shown in Fig. 1(b), with six elements represented. The successive elements are inverted so as to break the symmetry of the flow and avoid small residual nonchaotic regions [22]. Therefore here again, the structure has a periodicity of two elements.

Finally, the F-mixer [24,25] has a similar topological behavior as the MLLM, although its geometry is simpler; compared to the former, it is less symmetric, which is not a problem for Stokes flows. Indeed, its Lyapunov exponent is, as for the MLLM, equal to $\ln 2$ [15]. Its computational geometry is represented in Fig. 1(c), with eight elements. However, compared to the former, a mixing element represents a whole spatial period of the mixer. This property will be taken into account later.

B. Autocorrelation coefficient

How is a time of flight of a given element correlated to the time of flight in an element further away? It can be estimated through the autocorrelation coefficient,

$$R(i) = \frac{M}{M-i} \frac{\sum_{j=1}^{M-i} (t_j - t_m)(t_{j+i} - t_m)}{\sum_{j=1}^M (t_j - t_m)^2}; \quad (8)$$

here $i = 1$ corresponds to the correlation between two consecutive elements. In Fig. 2 we have plotted the autocorrelation coefficient for the three mixers depicted above. As can be seen the time of flight decorrelates very rapidly with the number of elements.

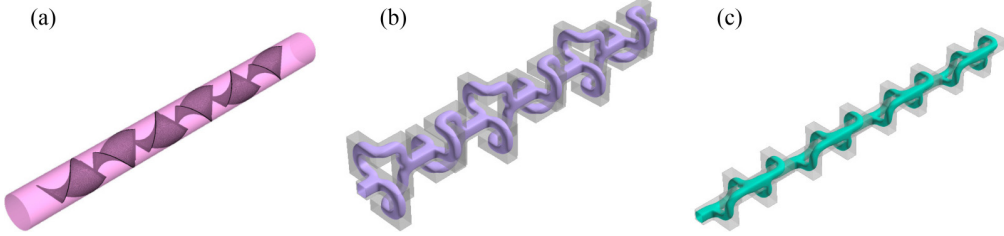


FIG. 1. Computational geometry of the different mixers studied: (a) the Kenics mixer (six elements); (b) the MLLM (six elements); (c) the F-mixer (eight elements). For (b) and (c) an isosurface of velocity modulus for a Stokes flow is plotted in color.

The decorrelation is the fastest for the F-mixer. Indeed, unlike the MLLM, its asymmetry leads to very different times of flight depending on the branch chosen in an element. Furthermore, as already noted, one element of the F-mixer corresponds to a full spatial period, in contrast to the two other mixers. But, even when considering this particularity, the decorrelation is still the fastest, since $R(1)$ is nearly zero, thus below $R(2)$ for the two other mixers.

Overall, for all mixers, the time of flight is totally decorrelated after only four basic elements. This rapid decorrelation of time of flight justifies *a priori* the model that we present hereafter.

C. A residence time model

We propose to model residence time in such mixers using the time of flight between inlet and outlet of an element with simple geometry. Such a model was previously used to model the distribution of time of flight in a single element of mixer [15]. It can be described as follows:

(i) the flow through one element of the mixer is modeled by a nonchaotic flow possessing no-slip boundaries (for instance a piece of pipe with circular cross section);

(ii) the effect of global chaos on the trajectory of the fluid particle is modeled by random reinjection at the entry to the next element with a probability density taking into account the fact that the particle randomly samples the whole section but less near the walls;

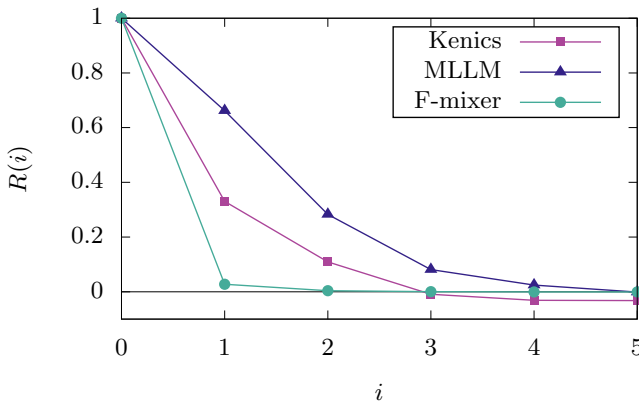


FIG. 2. Evolution of the correlation coefficient $R(i)$ between residence time values in elements that are i elements away for the three real mixers.

(iii) in order to conserve mass, as explained in the Introduction, the probability density function of the location of reinjection is taken proportional to the local velocity [see Eq. (9) below for a pipe with circular cross section].

In the following, we mostly focus on the case of a circular cross section (other shapes are also considered, see Sec. V). In practice we generate random numbers with a parabolic probability density using an inversion method [26], see Appendix A.

The circular cross section enables indeed an analytical expression for the probability density $f_1(t)$ to have a time of flight of duration t for 1 element: The probability to have a duration of time in between t and $t + dt$ is equal to that of having a particle reinjected in between r and $r + dr$, where t and r are linked by relation (2):

$$f_1(t) dt = \frac{v_x(r)}{v_m} \frac{2\pi r dr}{\pi R^2}, \quad (9)$$

where $v_x(r)$ verifies Eq. (1). When differentiating Eq. (2), we obtain

$$-\frac{2r dr}{R^2} = -\frac{L}{2v_m t^2} dt, \quad (10)$$

which, when combined with Eqs. (9), (2), and (6), leads to

$$f_1(t) = \frac{t_m^2}{2t^3}. \quad (11)$$

This is indeed the profile obtained numerically for one element, see Fig. 3(a). Not surprisingly, the expression derived by Danckwerts [13] is recovered. This t^{-3} tail was also found for the three mixers in the case of a single element ($n = 1$). Because large times of flight correspond to points located near the wall where the velocity is weak, this behavior was related to the region of constant shear near the wall [15]. An indirect proof can be found when considering the plane Couette flow, where the shear is constant everywhere: For this flow also, the probability density follows Eq. (11) [15].

In the following, we propose to use this model for n consecutive elements of an in-line mixer.

III. RESIDENCE TIME DISTRIBUTIONS: FROM 1 TO n MIXING ELEMENTS

For a single-element of mixer, the RTD is characterized by the following properties [15]:

the existence of a t^{-3} tail and a maximum close to $t = t_{\min}$.

As already stated, our idea is now to go further and explore the more realistic case of multiple elements.

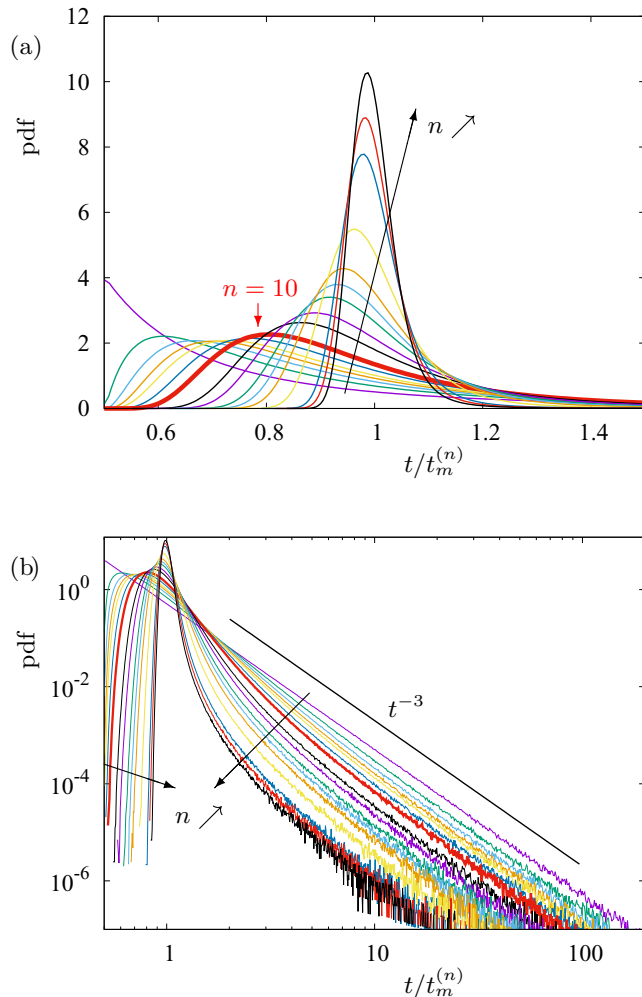


FIG. 3. Residence time distribution f_n for the model chaotic flow (Poiseuille flow with circular cross section) for different numbers of sections, $n = 1, 2, 3, 4, 5, 7, 10, 14, 20, 30, 50, 70, 100, 140, 200, 300, 500, 700$, and 1000 . By way of comparison with real mixers, the case $n = 10$ is drawn thicker. Each distribution was built with $M = 10^8$ data; the data are the sum of n independent residence times. (a) Linear scale; (b) logarithmic scale. Even for a very large number of sections n , the probability density function (pdf) is far from Gaussian, and exhibits a t^{-3} power-law tail. For the large number of elements, the tails are slightly more scattered, because more points are in the peak [Fig. 3(a)].

A. Model

The model is of particular interest since, because of its intrinsic simplicity, it allows to increase arbitrarily the number of elements. In Fig. 3(a) we show the nondimensional time distributions [built as a nondimensional probability density function (pdf)] for a number of elements varying from $n = 1$ to $n = 1000$. Of course, 1000 elements is not a realistic configuration in practice, but it allows us to visualize theoretically the rate of convergence toward the “perfect” mixer.

The first notable point is that for $n \geq 2$ the distribution is actually a bell curve, with a maximum different from $t = t_{\min}$, therefore a much improved shape compared to the $n = 1$ case. When n increases the curve becomes more peaked, and the

position of the maximum tends to the mean time of flight $t_m^{(n)} = n \times t_n^{(1)}$. However, the convergence is very slow. The case $n = 10$, that can be considered as a reasonable maximum number of elements in a real mixer, is shown as a thicker line (in red): As can be seen, the distribution is still very broad; furthermore, even for $n = 1000$, the maximum of the distribution is still not completely centered on the mean time.

The second notable point is visible in the log-log plot of the same distributions [Fig. 3(b)]: The t^{-3} tail that was found for $n = 1$ persists at all higher values of n , and the distributions remain very asymmetric. In the model, all residence times in an element are completely independent of each other. It can be shown that the distribution of the sum of two decorrelated data with an algebraic tail also possesses an algebraic tail [27,28]. In Appendix B, we apply this result and prove the existence of this t^{-3} tail when summing n independent data taken from the same distribution with a t^{-3} tail.

In real mixers, two consecutive times are not completely decorrelated as in the model (Fig. 2). However, because the correlation is weak, quite similar results are expected.

B. Mixers

Figure 4 shows the RTD for the three mixers. Due to a much reduced number of data points for the real mixers compared to the model, the histograms are limited to distributions for $n = 10$ elements; in any case, most in-line mixers have fewer than 10 mixing elements.

As expected, the distributions are quite similar to what was obtained with the model, although not as smooth, due to the much smaller sample of data. As for the model, the distributions are still broad for $n = 10$ and quite far from the desired Gaussian shape. Another important point is the persistence of the t^{-3} tail, visible on the log-log plot. This is not surprising: We demonstrated that summing n independent variables with a t^{-3} tail led to a distribution with a similar tail. These real-mixer data are poorly correlated (see Fig. 2), so that the variables may be considered as nearly independent. The assumption of uncorrelated data is almost exact for the F-mixer, for which the autocorrelation coefficient has fallen to negligible values after only one element. Moreover, the least noisy tail is that of the MLLM [Fig. 4(d)], for which we have twice as much data as for the two other mixers but that also corresponds to the more correlated mixer. Finally, note that El Omary *et al.* [29] also found a t^{-3} tail when properly weighting their statistics.

A distribution with an algebraic tail $t^{-\alpha}$ (also called Pareto distribution) belongs to the family of “heavy-tailed” distributions [30]. This type of distribution is well known in economy [31], finance [32], physics [33], maths [34], and even bibliometry [35].

IV. A MEASUREMENT TOOL FOR THE STRETCHING OF RESIDENCE TIME DISTRIBUTION

A. Why not use the standard deviation?

When dealing with distributions it is natural to measure the histogram width. Because many distributions in fluid mechanics are Gaussian, or close to Gaussian, it is usual to use

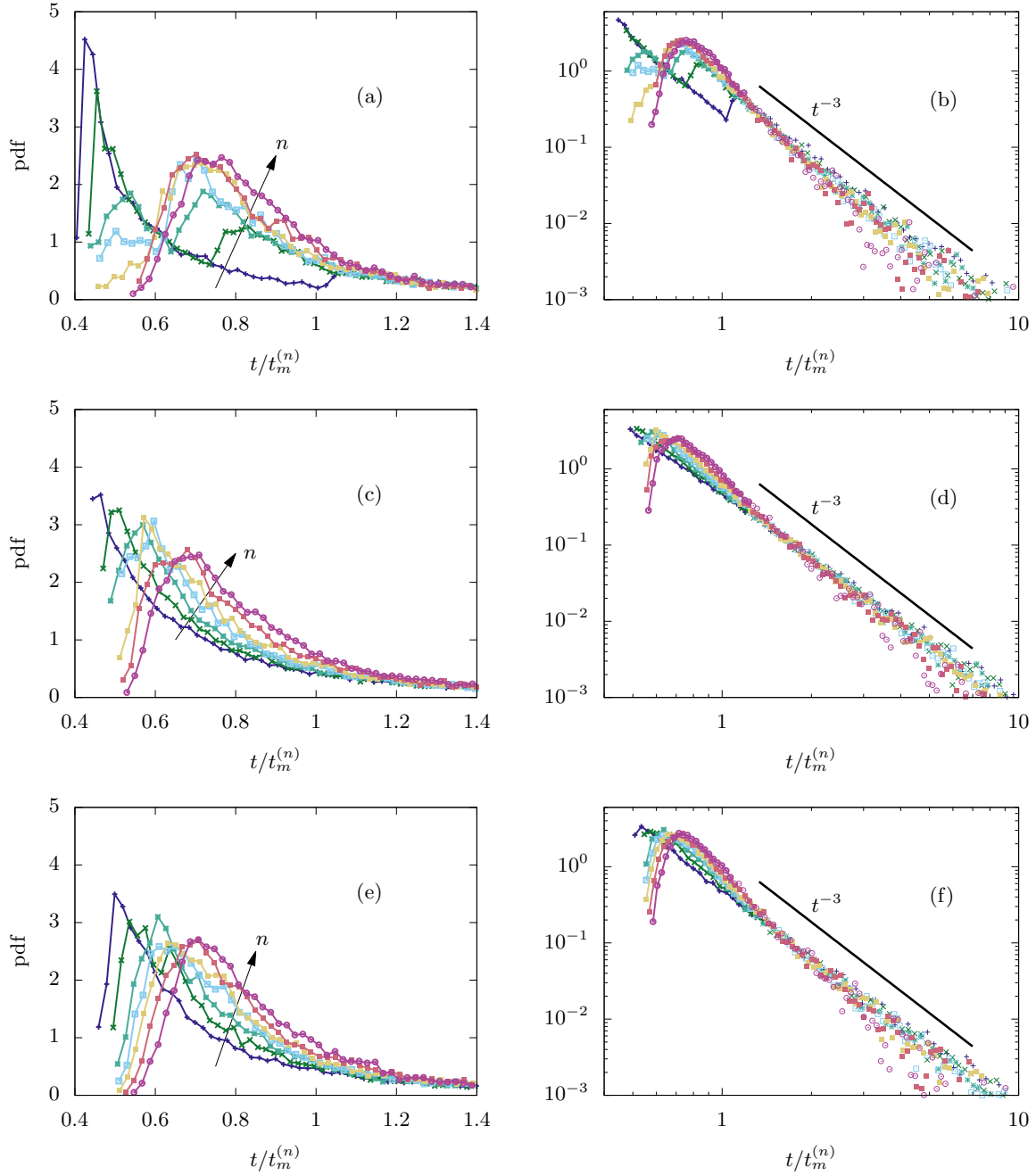


FIG. 4. Residence time distributions for the three real mixers for different numbers of elements, $n = 1, 2, 3, 4, 5, 7, 10$. From top to bottom: Kenics, MLLM, and F-mixer. For each mixer, four trajectories were calculated, corresponding to a total of 16 886 times of flight for the Kenics, 33 570 for the MLLM, and 18 987 for the F-mixer. We used a sliding average, so that the number of points are roughly the same for the different values of n . Left: linear scale; right: logarithmic scale. As for the model, the tail is more noisy for the highest values of n ($n \geq 7$): The weight (integral under the curve) of the bell-shaped part is more significant, which implies that the proportion of points in the tail is less important.

the standard deviation, or even higher moments. In our case, the standard deviation for n consecutive elements is denoted by $\sigma_2^{(n)}$ and defined as:

$$\sigma_2^{(n)} = \sqrt{\int_{t_{\min}^{(n)}}^{\infty} f_n(t) \left[\frac{t}{t_m^{(n)}} - 1 \right]^2 dt}. \quad (12)$$

However, because of the t^{-3} tail, the integral diverges and this quantity is clearly not well defined.

It is always possible in practice to calculate a standard deviation from a series of M values of time of flight as:

$$\sigma_2^{(n)} = \sqrt{\frac{1}{M} \sum_{j=1}^M \left[\frac{t_j}{t_m^{(n)}} - 1 \right]^2}. \quad (13)$$

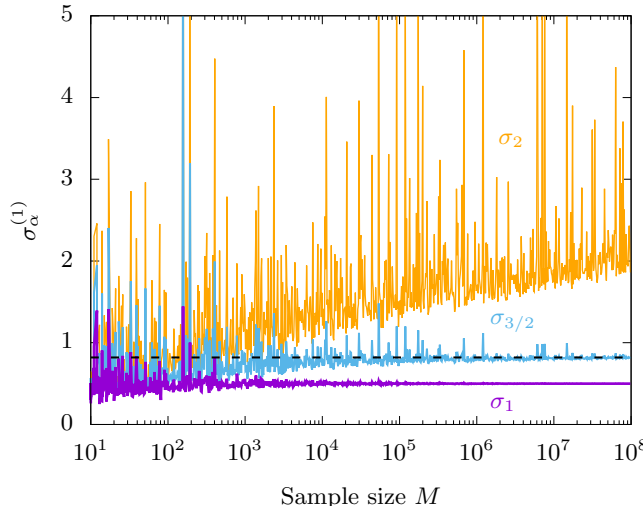


FIG. 5. Evolution of the standard deviation σ_2 (orange), centered absolute moment of order $3/2$ $\sigma_{3/2}$ (light blue), and mean absolute deviation σ_1 (purple) for one element of the Poiseuille flow model and for independent samples of increasing size M . The horizontal dotted line denotes the analytically computed value $\sigma_{3/2}^{(1)} \approx 0.820$. In the case $\alpha = 1$ we have $\sigma_1^{(1)} = 1/2$. Note that the figure was truncated with a maximum of 5 for the ordinate, while the standard deviation showed incursions up to 100.

Note again that, because we deal with times of flight (resulting from a single trajectory), the weighting is here naturally included in the statistics.

We propose to use the model (that allows for very large samples) in the simple case $n = 1$ to evaluate the reliability of this quantity: Figure 5 shows the evolution of the standard deviation $\sigma_2^{(1)}$ for increasing sample size M . For each sample we draw M times of flight, so that the samples are totally independent. As expected, the standard deviation does not converge but continues to increase with the sample size M , so that there is no limit value for this quantity, even if the divergence is very slow. What is more surprising is the fact that the signal is incredibly noisy: Indeed, while we show only data in the reduced vertical range $[0 : 5]$, values of up to 100 are present. Finally, although the fact that the different samples are independent may explain part of the randomness of the curve, we could expect at least the noise to decay when M increases. This is obviously not the case, which means that the standard deviation cannot even be used to compare two different laminar mixers using the same sample size. This point has to be stressed since, because of turbulent flows where distributions are close to Gaussian, nearly all RTD studies in fluid mechanics use this parameter (and sometimes higher moments) [36–40]. The difficulty lies indeed in the fact that a logarithmic divergence is extremely difficult to detect from a series of points. For an experiment also, the algebraic decay is impossible to monitor in practice, so that the tail—responsible for the logarithmic divergence—will not be fully taken into account, hiding the problem.

Since the moment of order 2, related to the standard deviation, is mathematically ill posed, we propose to use a centered

absolute moment of order α defined as

$$\sigma_\alpha^{(n)} = \left[\int_{t_{\min}^{(n)}}^\infty f_n(t) \left| \frac{t}{t_m^{(n)}} - 1 \right|^\alpha dt \right]^{1/\alpha}, \quad (14)$$

where α is strictly less than 2 and can be fractional; fractional moments are indeed frequently used in physics for evaluation of heavy-tailed distributions [33]. In practice, it can also be calculated from a finite series of M values of time of flight, as done for the standard deviation. We obtain:

$$\sigma_\alpha^{(n)} = \left[\frac{1}{M} \sum_{j=1}^M \left| \frac{t_j}{t_m^{(n)}} - 1 \right|^\alpha \right]^{1/\alpha}. \quad (15)$$

Here again, the weighting is already contained in the Lagrangian nature of the time of flight. Evaluating this quantity from points uniformly distributed at inlet is described later [see Eq. (22)].

B. Choice of α

In our case, taking $\alpha = 1.99$ would do fine in theory, since the integral would converge. However, as seen in Fig. 5, the signal is very noisy for $\alpha = 2$, and we expect the chosen quantity to converge reasonably rapidly with increasing M . We therefore propose to test two different values of α , namely $\alpha = 3/2$ and $\alpha = 1$. The moment of order 1 [41] is more specifically named “mean absolute deviation” in statistics. As for the usual standard deviation, we wish to evaluate the reliability of these quantities using one element of the model ($n = 1$). We denote $\sigma_\alpha \equiv \sigma_\alpha^{(1)}$: We will check that the series in Eq. (15) actually converge when increasing the size M of the sample, and compare how fast they converge toward the limit σ_α for the two values of α . We thus need an analytical expression of σ_α from the model flow, calculated from Eq. (14).

The case $\alpha = 1$ is straightforward and leads to $\sigma_1 = 1/2$ for the model flow. Matsui and Pawlas calculated existing fractional moments of Pareto functions using Laplace transforms [42]; the results are expressed in terms of the β function and the Gauss hypergeometric function. We give in Appendix C a classic analytical calculation: We obtain $\sigma_{3/2} \approx 0.820$ for the model flow, and we expect to find the same value numerically.

In Fig. 5 we show the evolution of these quantities as a function of the sample size M , using the same set of data already used for the standard deviation $\sigma_2^{(1)}$. While both moments converge toward the desired limits, the convergence is far more rapid in the case $\alpha = 1$. The signal is also much less noisy for the mean absolute deviation, obviously much less sensitive to the presence of very large residence times in the sample. Note finally that σ_1 is reasonably converged for a quite low sample size ($M \geq 10^3$ – 10^4).

C. Influence of molecular diffusion

Since the reason for the divergence of the standard deviation σ_2 is linked to the existence of arbitrary long residence times, we could wonder whether this phenomenon would be effectively observed when molecular diffusion is taken into account. Indeed, molecular diffusion would allow the fluid particle to change streamline, preventing very long residence times from being observed. In numerical simulations also,

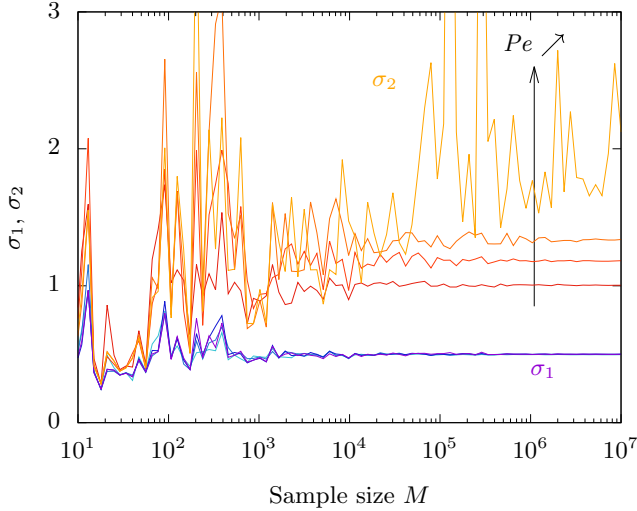


FIG. 6. Evolution of the standard deviation σ_2 (from red to yellow) and mean absolute deviation σ_1 (from blue to purple) for diffusing species in one element of the Poiseuille model flow, and independent samples of increasing size M . The Péclet numbers are $\text{Pe} = 10^6, 10^7, 10^8, +\infty$. The number of points is here much less than in Fig. 5, typically 15 samples in a decade compared to 150 in Fig. 5. Because molecular diffusion should not play a significant role in a single element of mixer, the different plateaus obtained for σ_2 are clearly artificial and show again that the standard deviation is ill posed here. In contrast, the mean absolute deviation σ_1 is nearly insensitive to molecular diffusion, proving that σ_1 is a robust measure of the width of RTD for a given mixer.

even without diffusion, the calculations would be stopped in the case of too-large residence times. This cutoff could enable the convergence of the standard deviation, and render this parameter acceptable for calculating the width of distributions. In order to evaluate how molecular diffusion would modify the preceding result, we proceed as follows: As for Fig. 5, we consider one element of the Poiseuille model flow, with length $L = D$, where D is the diameter of the entrance section. We define the Péclet number of the flow as $\text{Pe} = v_m D/D_s$, where D_s is the molecular diffusion of the species considered. The displacement of a given diffusing species obeys to

$$\frac{dx}{dt} = \mathbf{v}(x, y, z, t) + \zeta(t), \quad (16)$$

where $\zeta(t)$ is a Gaussian decorrelated process such that $\langle \zeta_i(t) \zeta_j(t') \rangle = 2D_s \delta_{ij} \delta(t - t')$ [43]. For the model \mathbf{v} is simply given by Eq. (1). As done in Fig. 5, for an abscissa M we generate M random initial locations with a parabolic probability. For those M initial points we solve Eq. (16) between $x = 0$ and $x = L$ for different realistic finite Péclet numbers ($\text{Pe} = 10^6, 10^7$, and 10^8), and also in the case without diffusion ($\text{Pe} = +\infty$); for each case we plot the standard deviation σ_2 and the mean absolute deviation σ_1 of the resulting RTD. As is visible in Fig. 6, σ_2 converges for finite Péclet number. However, the convergence is slow; even more important, the value of the plateau depends significantly on the Péclet number. Although we could expect a small dependence for a long mixer, those large differences for a single piece of mixer at high Péclet numbers are not physical, which shows that the

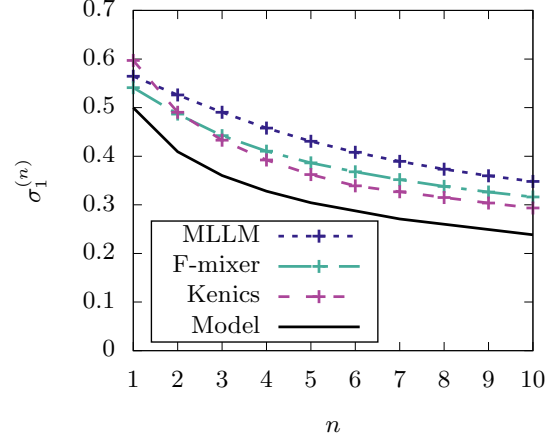


FIG. 7. Evolution of the mean absolute deviation $\sigma_1^{(n)}$ with the number of elements $n = 1, 2, 3, 4, 5, 7, 10$, for the three mixers and the model.

converged value obtained for σ_2 is artificial. In the case of σ_1 , the curves merge for quite small samples, and, as expected in that situation, converge toward the theoretical value $\sigma_1 = 1/2$, whatever the Péclet number. This clearly shows that, unlike the standard deviation, the mean absolute deviation is a robust measure of the width of the distributions.

D. Application to the different mixers

Because the number of numerical data points used for the different mixers is in between 17 000 and 34 000, from the analysis above we have enough data to calculate reasonably accurately the mean absolute deviation,

$$\sigma_1^{(n)} = \frac{1}{M} \sum_{j=1}^M \left| \frac{t_j}{t_m^{(n)}} - 1 \right|. \quad (17)$$

Figure 7 shows $\sigma_1^{(n)}$ as a function of the number of elements for the three mixers and the model. In Appendix D, we show the same evolution for $\sigma_{3/2}^{(n)}$; we can check that the hierarchy between the different mixers is the same for the two different values of α , which definitely reinforces the choice $\alpha = 1$.

Without surprise, the totally uncorrelated model is the most efficient. As expected also, the reduced moment of the MLLM, which is the most correlated mixer, decreases less rapidly than the others; the Kenics is the best of the three mixers from the RTD point of view.

Although $\sigma_1^{(n)}$ is a decreasing function of n for all cases considered, there is no obvious analytical fit for the decay even in the case of the decorrelated model. The decrease is the most rapid at the beginning, for small values of n : The width of the distributions [measured with $\sigma_1^{(n)}$] has decreased by 25% (for the MLLM) to 40% (for the model) after $n = 5$ elements, but the decrease is only 40 to 52% for $n = 10$. Hence from the RTD point of view there is no interest in adding many elements in a row, provided that a good mixing is reached after a few number of elements.

V. INFLUENCE OF THE CROSS-SECTION GEOMETRY

In this section we would like to understand the reason for the differences in values of $\sigma_1^{(n)}$. Since large times of flight are linked to the presence of walls, one could wonder whether the shape of the mixer is of importance. As noted by Mortensen *et al.* [44], a shape can be characterized by a perimeter \mathcal{P} and an area \mathcal{A} , that can be combined in a dimensionless compactness number \mathcal{C} , defined as

$$\mathcal{C} = \frac{\mathcal{P}^2}{\mathcal{A}}. \quad (18)$$

This quantity is not easy to measure for the mixers considered here. We thus propose to consider model flows as the one proposed in Sec. II C. We formerly took the case of a circular cross section, which allowed for analytical exact results easily comparable to numerical simulations. But it is relatively simple to investigate different compactness by varying the shape of the cross section (ellipse, square, or rectangle rather than a circle), as done in Mortensen *et al.* [44]. Because $\sigma_1^{(n)}$ decays roughly similarly with n for all mixers (Fig. 7), we focus on the value $n = 1$.

In the following we keep the area \mathcal{A} , length L and the flow rate \mathcal{Q} constant, so that all different shapes correspond to the same mean time t_m .

A. Ellipse

There is no exact expression for the perimeter of an ellipse; however, it can be approximated using Ramanujan's second formula [45]:

$$\mathcal{P} \approx \pi(a+b) \left(1 + \frac{3\lambda^2}{10 + \sqrt{4 - 3\lambda^2}} \right) \text{ with } \lambda = \frac{a-b}{a+b}, \quad (19)$$

where a and b are the large and small semiaxes, respectively. This expression is very accurate, even for very elongated ellipses [46]. The parameter λ varies from 0 (circle) to 1 (very elongated ellipses). If $\mathcal{A} = \pi ab$ is kept constant, then $a+b = a+\mathcal{A}/(\pi a)$ is minimum for the circle; the bracketed expression in Eq. (19) is also a growing function of a , so that the perimeter is always increasing with a . The area \mathcal{A} being kept constant, the compactness number \mathcal{C} also increases with a .

However, as shown in Appendix E, the probability density of time duration for a pipe of length L is identical for a circular or elliptic cross section, whatever λ . This implies that all moments derived (including $\sigma_1^{(1)}$) are identical. In this case the compactness \mathcal{C} plays no role on the distribution of duration times. Nevertheless, $\sigma_1^{(1)}$ may depend on the geometry, number of angles, etc.

B. Square and rectangles

Let us consider the Hagen-Poiseuille flow with rectangular cross section. The rectangle has a width a , a height b , and is characterized by its area $\mathcal{A} = a \times b$ and aspect ratio $\beta = b/a$. For this configuration, Spiga and Morino [47] proposed the

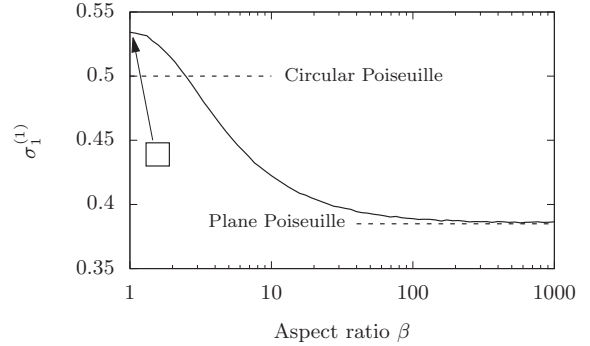


FIG. 8. Evolution of the mean absolute deviation for the Hagen-Poiseuille flow in rectangular ducts of varying aspect ratio β . Dashed lines indicate values of $\sigma_1^{(1)}$ for the circular and plane Poiseuille flow configurations, respectively, $\sigma_1^{(1)} = 1/2$ and $\sigma_1^{(1)} = 2/(3\sqrt{3}) \simeq 0.385$. As β increases, the configuration tends to that of the plane Poiseuille flow.

following expression for the velocity field:

$$v(y, z) = \frac{16a^2b^2G}{\mu\pi^4} \sum_{n \text{ odd}}^{\infty} \sum_{m \text{ odd}}^{\infty} \frac{\sin[n\pi(y/a - 1/2)] \sin[m\pi(z/b - 1/2)]}{nm(b^2n^2 + a^2m^2)} \quad (20)$$

for $-a/2 \leq y \leq a/2$ and $-b/2 \leq z \leq b/2$, with G the imposed pressure gradient and μ the dynamic viscosity of the fluid. The mean velocity v_m is therefore:

$$v_m = \frac{64a^2b^2G}{\mu\pi^6} \sum_{n \text{ odd}}^{\infty} \sum_{m \text{ odd}}^{\infty} \frac{1}{n^2m^2(b^2n^2 + a^2m^2)}. \quad (21)$$

In practice, this series converges rather rapidly, and we checked that truncating the sums such that $0 \leq n, m \leq 1000$ was enough for our calculation. The aspect ratio is varied from $\beta = 1$ (square cross section) to $\beta = 1000$ (very elongated rectangle), the limit $\beta \rightarrow +\infty$ being the plane Poiseuille flow. Finally, all times are made nondimensional using the mean time $t_m = L/v_m$, where L is the length of the pipe section.

Due to the complexity of the expression of the velocity field, the inversion method is of no use in this situation. We can nonetheless compute the mean absolute deviation corresponding to this velocity field by taking points uniformly distributed in the rectangle and weighting the values using the velocity, which modifies expression (17) as follows:

$$\sigma_1^{(1)} = \frac{1}{M} \sum_{j=1}^M \frac{v_j}{v_m} \left| \frac{t_j}{t_m^{(1)}} - 1 \right|. \quad (22)$$

This approach was tested on the circular Poiseuille flow by taking points uniformly distributed on the disk and using the expression (22), and the same value of 0.5 was obtained for $\sigma_1^{(1)}$, confirming the validity of the method.

Figure 8 represents the evolution of $\sigma_1^{(1)}$ with the aspect ratio β . For each value of β , three samples of 100 000 points were computed, leading to slightly different values of $\sigma_1^{(1)}$ due to the randomness of the process. However, because of the rapid convergence of σ_1 with the sample size, the three

values are very close to each other, with a typical variation of order 0.5%; the quantity plotted in Fig. 8 is the mean for those three sets.

We observe that the mean absolute deviation decreases as the aspect ratio increases, converging to the value corresponding to the plane Poiseuille flow.

Note finally that in microfluidics, most microchannels have rectangular cross section; the case of the circular cross section, better than the square from the residence time point of view, is very close to the 3-1 rectangle, a geometry quite common in microfluidics.

VI. SUMMARY AND CONCLUSION

In this article we have studied the statistics of residence time distributions for n elements of an in-line mixer, using numerical data for three mixers and a model flow. We have shown that those types of mixers are not perfect from the RTD point of view and that the t^{-3} tail found for one element of mixer persists when increasing the number of elements. This algebraic decay, signature of a “heavy-tailed” distribution, has an important consequence in practice: The second-order moment of the distributions—and therefore higher moments—do not exist, so that the standard deviation cannot be used to characterize the width of the histogram.

Therefore we proposed to use the first-order absolute moment, also called mean absolute deviation, given by Eq. (17): This moment exists and converges with increasing sample size in numerical simulations and should also be used in experiments, where the tail is difficult to obtain in practice.

The mean absolute deviation is then used to compare the different mixers and how the typical width of the distribution decreases with n . It is also applied to discriminate between different shapes of cross section. We show that this parameter is higher for a square than for a circle but also that a rectangular cross section, very common in microfluidics, is a better mixer than a square from the RTD point of view.

One could wonder how the results for a mixer consisting of n elements would be affected by molecular diffusion. In fact, molecular diffusion has negligible effects as long as the Batchelor scale is not reached [48]. Since such in-line mixers reproduce the baker’s map, the width of a given heterogeneity at the exit of the n th element is typically $\ell_n \sim w/2^n$, where w is the width of the cross section. Such an heterogeneity is mixed on a timescale $\tau_n \sim \ell_n^2/D_s$, where D is the molecular diffusion of the species to be mixed. Thus the scalar is mixed at the exit of the $(n+1)$ -th element if τ_n is of the order of the mean travel time in one element $t_m = L/v_m$. When equating $\tau_n \sim t_m$, we obtain

$$2n \ln 2 \sim \ln \left(\frac{v_m w}{D_s} \frac{w}{L} \right), \quad (23)$$

where we recognize the Péclet number $\text{Pe} = v_m w / D_s$. In an in-line mixer, the length L is a few times the width w (see Fig. 1), while the Péclet number is typically of the order of 10^6 , so that $\ln(w/L)$ can be neglected in front of $\ln \text{Pe}$. We finally obtain

$$n \approx \frac{\ln \text{Pe}}{2 \ln 2}. \quad (24)$$

For $\text{Pe} = 10^6$, we obtain $n \approx 10$, so that in that case the effects of diffusion are negligible until the outlet of the mixer. In any case, even if the diffusion effects became important in the very last elements, this would not significantly change the statistics of the residence time on the whole mixer, so that our results should apply even if diffusion is taken into account.

ACKNOWLEDGMENTS

The support from the PMCS2I of École centrale de Lyon for the numerical calculations is gratefully acknowledged. We also thank an anonymous referee for interesting suggestions and challenging comments.

APPENDIX A: GENERATION OF A RANDOM VARIABLE WITH PARABOLIC DENSITY

This basic technique is described in Ref. [26]. The goal is to derive a two-dimensional pdf that is proportional to the velocity field, here in the case of circular cross section:

$$f(M) \propto v(M) = v(r). \quad (A1)$$

By cylindrical symmetry, this is readily reduced to finding a one-dimensional pdf of the variable r , that has, however, to be proportional to the velocity field and the perimeter corresponding to the position considered:

$$f(r) \propto 2\pi r v(r) = 2\pi r \times 2v_m(1 - (r/R)^2). \quad (A2)$$

Since the integral of f over $[0, R]$ has to be 1, we easily obtain:

$$f(r) = \frac{4r}{R^2} \left(1 - \frac{r^2}{R^2} \right). \quad (A3)$$

We then compute the corresponding cumulative density function F , primitive of f :

$$F(r) = \frac{2r^2}{R^2} \left(1 - \frac{r^2}{2R^2} \right). \quad (A4)$$

Finally, the inverse function of F is expressed as:

$$F^{-1}(p) = R \sqrt{1 - \sqrt{1 - p}}, \quad \forall p \in [0, 1]. \quad (A5)$$

From here, the inversion method consists in generating a sample $(p_i)_{1 \leq i \leq M}$ of reals uniformly distributed between 0 and 1; in practice, we use a pseudorandom numbers generator (PRNG) to produce the uniform distribution, here the xoshiro256** PRNG of the gfortran compiler. We then apply F^{-1} to the sample produced. The result is a new sample of radii $(r_i)_{1 \leq i \leq M} = [F^{-1}(p_i)]_{1 \leq i \leq M}$ which follows the distribution law described by f .

APPENDIX B: TAIL OF RTD FOR n IDENTICAL ELEMENTS

Suppose that the RTD of 1 element of a mixer possesses a t^{-3} tail. Then, if the elements are decorrelated from the residence time point of view, then the tail of the distribution of n elements also has a t^{-3} tail.

Proof. We will proceed by recurrence. We denote by $f_m(t)$ the pdf associated to the crossing time for m sections. We

suppose that for all $m \leq (n - 1)$, we have

$$f_m(t) = \frac{g_m(t)}{(t + t_\epsilon)^{-3}}, \quad (\text{B1})$$

where t_ϵ is an arbitrary positive time and $g_m(t)$ a smooth function such as

$$g_m(t < m \times t_{\min}) = 0 \text{ and } \lim_{t \rightarrow \infty} g_m(t) = C_m \neq 0. \quad (\text{B2})$$

The assertion (B2) is true for $n = 1$; we suppose that it is also true for $n - 1$ and prove that it is true for n . Providing that the events are sufficiently decorrelated, the pdf for n elements is the convolution product of f_1 with f_{n-1} :

$$\begin{aligned} f_n(t) &= \int_{-\infty}^{+\infty} f_1(t) f_{n-1}(t_n - t) dt \\ &= \int_{t_{\min}}^{t_n - (n-1)t_{\min}} \frac{g_1(t)}{(t + t_\epsilon)^3} \frac{g_{n-1}(t_n - t)}{(t_n + t_\epsilon - t)^3} dt. \end{aligned} \quad (\text{B3})$$

We make the change of variable $x = t/t_n$, so that $dt = t_n dx$:

$$\begin{aligned} f_n(t) &= \int_{t_{\min}/t_n}^{1-(n-1)t_{\min}/t_n} \frac{g_1(t_n x)}{(t_n x + t_\epsilon)^3} \frac{g_{n-1}[t_n(1-x)]}{[t_\epsilon + t_n(1-x)]^3} t_n dx \\ &\underset{t_n \rightarrow \infty}{\sim} \int_0^1 t_n^{1-3-3} \frac{g_1(t_n x)}{(x + t_\epsilon/t_n)^3} \frac{g_{n-1}[t_n(1-x)]}{(t_\epsilon/t_n + 1-x)^3} dx \\ &\underset{t_n \rightarrow \infty}{\sim} t_n^{-5} \int_0^1 \frac{g_1(t_n x)}{(x + t_\epsilon/t_n)^3} \frac{g_{n-1}[t_n(1-x)]}{(t_\epsilon/t_n + 1-x)^3} dx \end{aligned} \quad (\text{B4})$$

because of the presence of the constant t_ϵ , the function to integrate remains smooth on $[0; 1]$. Let us focus on Eq. (B4): When $t_n \rightarrow \infty$, we have $t_\epsilon/t_n \rightarrow 0$, and we have two important contributions, one at $x = 0$ and the other at $x = 1$. We thus neglect other contributions: In the vicinity of $x = 0$, the function to integrate is equivalent to $A_0(x + t_\epsilon/t_n)^{-3}$, and in the vicinity of $x = 1$, is equivalent to $A_1(t_\epsilon/t_n + 1-x)^{-3}$, where the functions that do not tend to infinity have been approximated by constants. We obtain:

$$f_n(t) \underset{t_n \rightarrow \infty}{\sim} t_n^{-5} \left[\frac{A_0}{2(t_\epsilon/t_n)^2} + \frac{A_1}{2(t_\epsilon/t_n)^2} \right], \quad (\text{B5})$$

$$\underset{t_n \rightarrow \infty}{\sim} C_n t_n^{-3}. \quad (\text{B6})$$

We have shown that $f_n(t)$ also has a t^{-3} tail and, by recurrence, the property is true for all n .

APPENDIX C: CALCULATION OF THE REDUCED MOMENT $\sigma_{3/2}^{(1)}$ FOR THE MODEL FOR ONE ELEMENT OF A CYLINDRICAL PIPE

The reduced moment $\sigma_{3/2}^{(1)}$ for one element of the model writes:

$$\sigma_{3/2}^{(1)} = \left(\frac{\sqrt{t_m}}{2} \int_{t_m/2}^{\infty} \frac{|t - t_m|^{3/2}}{t^3} dt \right)^{2/3}. \quad (\text{C1})$$

Because of the absolute value, the integral is divided, one integral for $t \leq t_m$ (denoted by I_1) and the other for $t \geq t_m$

(denoted by I_2), such that

$$\sigma_{3/2}^{(1)} = (I_1 + I_2)^{2/3}. \quad (\text{C2})$$

Calculation of $I_1(t \leq t_m)$

We set $u^2 = (1 - t/t_m)$. I_1 satisfies

$$I_1 = \int_0^{1/\sqrt{2}} \frac{u^4}{(1 - u^2)^3} du. \quad (\text{C3})$$

We use formula 2.147(4) from Gradshteyn and Ryzhik [49]:

$$\begin{aligned} \int \frac{x^m dx}{(1 - x^2)^n} &= \frac{1}{2n - 2} \frac{x^{m-1}}{(1 - x^2)^{n-1}} \\ &- \frac{m - 1}{2n - 2} \int \frac{x^{m-2} dx}{(1 - x^2)^{n-1}} \end{aligned} \quad (\text{C4})$$

first with $m = 4$ and $n = 3$, next with $m = n = 2$ and obtain:

$$I_1 = -\frac{1}{4\sqrt{2}} + \frac{3}{8} \ln(\sqrt{2} + 1). \quad (\text{C5})$$

Calculation of $I_2(t \geq t_m)$

We set $u^2 = (t/t_m - 1)$ and obtain:

$$I_2 = \int_0^{\infty} \frac{u^4}{(1 + u^2)^3} du. \quad (\text{C6})$$

We next use formula 3.241(4) from Gradshteyn and Ryzhik [49]:

$$\int_0^{\infty} \frac{x^{\mu-1} dx}{(p + qx^\nu)^{\mu+1}} = \frac{1}{\nu p^{\mu+1}} \left(\frac{p}{q} \right)^{\mu/\nu} \frac{\Gamma(\mu/\nu) \Gamma(1+n-\mu/\nu)}{\Gamma(1+n)} \quad (\text{C7})$$

with $\mu = 5$, $\nu = 2$, $p = q = 1$, and $n = 2$:

$$I_2 = \frac{1}{2} \frac{\Gamma(5/2) \Gamma(1/2)}{\Gamma(3)}, \quad (\text{C8})$$

$$= \frac{3\pi}{16}. \quad (\text{C9})$$

We finally obtain:

$$\begin{aligned} \sigma_{3/2}^{(1)} &= \left[-\frac{1}{4\sqrt{2}} + \frac{3}{8} \ln(\sqrt{2} + 1) + \frac{3\pi}{16} \right]^{2/3} \\ &\approx 0.820. \end{aligned} \quad (\text{C10})$$

Ramsay [34] calculated fractional moments of this type of distribution using Laplace transforms, and gave the result in the form of an infinite series. We checked that the series indeed converged toward the same value.

APPENDIX D: EVOLUTION OF THE REDUCED MOMENT $\sigma_{3/2}^{(1)}$ WITH THE NUMBER OF ELEMENTS

The evolution of the reduced moment of order 3/2 with the number n of elements is shown in Fig. 9. When compared to Fig. 7, the hierarchy between the different mixers is preserved; the decay with n is also similar.

APPENDIX E: FROM CIRCULAR TO ELLIPTIC CROSS SECTION: CALCULATION OF RTD FOR ONE ELEMENT OF MODEL MIXER

The velocity field for an ellipse of semiaxes a and b writes:

$$v_x(y, z) = 2v_m \left(1 - \frac{y^2}{a^2} - \frac{z^2}{b^2} \right), \quad (\text{E1})$$

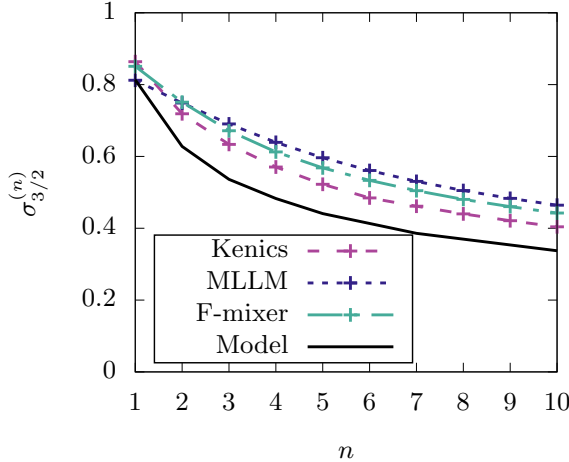


FIG. 9. Evolution of $\sigma_{3/2}^{(n)}$ with the number of elements $n = 1, 2, 3, 4, 5, 7, 10$, for the three real mixers and the model.

where v_m denotes the mean velocity. We denote by $g(t)$ the density probability to have a time of flight of duration t for an element of size L , with

$$t = L/v_x(y, z). \quad (\text{E2})$$

Let us consider the points that verify

$$\frac{y^2}{a^2} + \frac{z^2}{b^2} = \alpha^2, \quad 0 \leq \alpha \leq 1. \quad (\text{E3})$$

They describe an ellipse of axes αa and αb . From Eqs. (E1), (E2), and (E3) we obtain

$$v_x(\alpha) = 2v_m(1 - \alpha^2) = L/t, \quad (\text{E4})$$

that differentiates into

$$4\alpha d\alpha v_m = L dt/t^2. \quad (\text{E5})$$

Because the density probability is proportional to the velocity, we now write that the probability that t is in between t and $t + dt$ is the same as that for v_x to be in between $v_x(\alpha)$ and

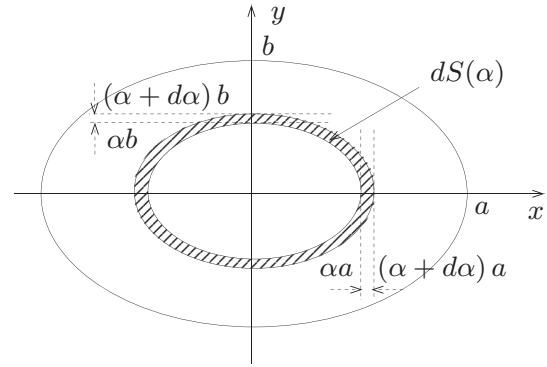


FIG. 10. Elliptic case: The hatched area represents the surface between the two ellipses corresponding to values α and $\alpha + d\alpha$ in Eq. (E4).

$v_x(\alpha + d\alpha)$:

$$g(t) dt = \frac{v_x(\alpha)}{v_m} \frac{dS(\alpha)}{\pi ab}, \quad (\text{E6})$$

with $dS(\alpha)$ the surface difference between ellipses corresponding to $\alpha + d\alpha$ and α , see Fig. 10. We thus have:

$$\begin{aligned} dS(\alpha) &= \pi ab[(\alpha + d\alpha)^2 - \alpha^2] \\ &\approx 2\pi ab\alpha d\alpha. \end{aligned} \quad (\text{E7})$$

By combining equations (E4), (E5), (E6), and (E7), we obtain

$$g(t) = \frac{L}{v_m t} 2\alpha \frac{d\alpha}{dt}, \quad (\text{E8})$$

$$= \frac{L^2}{2v_m^2 t^3}. \quad (\text{E9})$$

The mean time t_m verifies

$$t_m = \frac{1}{\pi ab} \int_{\alpha=0}^{\alpha=1} \frac{v_x(\alpha)}{v_m} \times \frac{L}{v_x(\alpha)} dS(\alpha), \quad (\text{E10})$$

$$= \frac{L}{v_m}. \quad (\text{E11})$$

We finally obtain

$$g(t) = \frac{t_m^2}{2t^3}, \quad (\text{E12})$$

that is, the same expression as for the circle Eq. (11).

-
- [1] J. M. Ottino, Mixing, chaotic advection, and turbulence, *Annu. Rev. Fluid Mech.* **22**, 207 (1990).
 - [2] H. Aref, J. R. Blake, M. Budišić, S. S. S. Cardoso, J. H. E. Cartwright, H. J. H. Clercx, K. El Omari, U. Feudel, R. Golestanian, E. Gouillart, G. F. van Heijst, T. S. Krasnopolskaya, Y. Le Guer, R. S. MacKay, V. V. Meleshko, G. Metcalfe, I. Mezić, A. P. S. de Moura, O. Piro, M. F. M. Speetjens, R. Sturman, J.-L. Thiffeault, and I. Tuval, *Frontiers of chaotic advection*, *Rev. Mod. Phys.* **89**, 025007 (2017).
 - [3] E. Gouillart, O. Dauchot, and J.-L. Thiffeault, Measures of mixing quality in open flows with chaotic advection, *Phys. Fluids* **23**, 013604 (2011).
 - [4] M. V. Budyansky, M. Yu. Uleysky, and S. V. Prants, Detection of barriers to cross-jet lagrangian transport and its destruction in a meandering flow, *Phys. Rev. E* **79**, 056215 (2009).
 - [5] S. Rossi, M. Petrelli, D. Morgavi, D. González-García, L. A. Fischer, F. Vetere, and D. Perugini, Exponential decay of concentration variance during magma mixing: Robustness of a volcanic chronometer and implications for the homogenization

- of chemical heterogeneities in magmatic systems, *Lithos* **286**, 396 (2017).
- [6] S. Wiggins and J. M. Ottino, Foundations of chaotic mixing, *Phil. Trans. R. Soc. Lond. A* **362**, 937 (2004).
- [7] H. Bruus, *Theoretical Microfluidics*, Vol. 18 (Oxford University Press, Oxford, 2008).
- [8] M. Creyssels, S. Prigent, Y. Zhou, X. Jianjin, C. Nicot, and P. Carrière, Laminar heat transfer in the “MLLM” static mixer, *Int. J. Heat Mass Transf.* **81**, 774 (2015).
- [9] S. A. Bahrani, L. Humberset, R. Osipian, L. Royon, K. Azzouz, and A. Bontemps, How thermally efficient are chaotic advection mixers? An experimental assessment, *Int. J. Therm. Sci.* **145**, 106046 (2019).
- [10] A. D. Stroock, S. K. W. Dertinger, A. Ajdari, I. Mezic, H. A. Stone, and G. M. Whitesides, Chaotic mixer for microchannels, *Science* **295**, 647 (2002).
- [11] O. Gorodetskyi, M. F. M. Speetjens, P. D. Anderson, and M. Giona, Analysis of the advection–diffusion mixing by the mapping method formalism in 3D open-flow devices, *AIChE J.* **60**, 387 (2014).
- [12] A. Borgogna, M. A. Murmura, M. C. Annesini, M. Giona, and S. Cerbelli, A hybrid numerical approach for predicting mixing length and mixing time in microfluidic junctions from moderate to arbitrarily large values of the Péclet number, *Chem. Eng. Sci.* **196**, 247 (2019).
- [13] P. V. Danckwerts, Continuous flow systems: Distribution of residence times, *Chem. Eng. Sci.* **2**, 1 (1953).
- [14] P. V. Danckwerts, Local residence-times in continuous-flow systems, *Chem. Eng. Sci.* **9**, 78 (1958).
- [15] F. Raynal and P. Carrière, The distribution of “time of flight” in three dimensional stationary chaotic advection, *Phys. Fluids* **27**, 043601 (2015).
- [16] F. Raynal, A. Beuf, and P. Carrière, Numerical modeling of DNA-chip hybridization with chaotic advection, *Biomicrofluidics* **7**, 034107 (2013).
- [17] L. Oteski, Y. Duguet, and L. R. Pastur, Lagrangian chaos in confined two-dimensional oscillatory convection, *J. Fluid Mech.* **759**, 489 (2014).
- [18] J.-P. Eckmann and D. Ruelle, Ergodic theory of chaos and strange attractors, in *The Theory of Chaotic Attractors* (Springer Science+Business Media, New York, 1985).
- [19] R. Artuso, L. Cavallasca, and G. Cristadoro, Dynamical and transport properties in a family of intermittent area-preserving maps, *Phys. Rev. E* **77**, 046206 (2008).
- [20] D. M. Hobbs, P. D. Swanson, and F. J. Muzzio, Numerical characterization of low Reynolds number flow in the Kenics static mixer, *Chem. Eng. Sci.* **53**, 1565 (1998).
- [21] B. L. Gray, D. Jaeggi, N. J. Mourlas, B. P. van Drieënhuizen, K. R. Williams, N. I. Maluf, and G. T. A. Kovacs, Novel interconnection technologies for integrated microfluidic systems, *Sens. Actuat.* **77**, 57 (1999).
- [22] P. Carrière, On a three-dimensional implementation of the baker’s map, *Phys. Fluids* **19**, 118110 (2007).
- [23] Z. Anzionnaz-Minvielle, P. Tochon, R. Couturier, C. Magallon, F. Théron, M. Cabassud, and C. Gourdon, Implementation of ‘chaotic’ advection for viscous fluids in heat exchanger/reactors, *Chem. Eng. Process.: Process Intensif.* **113**, 118 (2017).
- [24] H. Chen and J.-S. Meiners, Topologic mixing on a microfluidic chip, *Appl. Phys. Lett.* **84**, 2193 (2004).
- [25] Z. Chen, M. R. Bown, B. O’Sullivan, J. M. MacInnes, R. W. K. Allen, M. M. M. Blom, and R. van’t Oever, Performance analysis of a folding flow micromixer, *Microfluid. Nanofluid.* **6**, 763 (2009).
- [26] L. Devroye, *Non-Uniform Random Variate Generation* (Springer-Verlag, Berlin, 1986).
- [27] W. Feller, *An Introduction to Probability Theory and Its Applications*, 2nd ed. (John Wiley & Sons, New York, 1971).
- [28] C. Wilke, S. Altmeyer, and T. Martinetz, Large-scale evolution and extinction in a hierarchically structured environment, in *Proceedings of the 6th International Conference on Artificial Life* (MIT Press, Cambridge, MA, 1998), pp. 266–274.
- [29] K. El Omari, E. Younes, T. Burghelea, C. Castelain, Y. Moguen, and Y. Le Guer, Active chaotic mixing in a channel with rotating arc-walls, *Phys. Rev. Fluids* **6**, 024502 (2021).
- [30] L. B. Klebanov, *Heavy Tailed Distributions*, Vol. 488 (Matfyzpress, Prague, 2003).
- [31] V. Pareto, *Cours d’Économie Politique*, Vol. 1 (Librairie Droz, Geneva, 1964).
- [32] S. T. Rachev, *Handbook of Heavy Tailed Distributions in Finance: Handbooks in Finance, Book 1* (Elsevier, Amsterdam, 2003).
- [33] T. Srokowski, Fractional Fokker-Planck equation for Lévy flights in nonhomogeneous environments, *Phys. Rev. E* **79**, 040104(R) (2009).
- [34] C. M. Ramsay, The distribution of sums of certain I.I.D. pareto variates, *Commun. Stat. Theory Methods* **35**, 395 (2006).
- [35] V. Larivière, V. Kiermer, C. J. MacCallum, M. McNutt, M. Patterson, B. Pulverer, S. Swaminathan, S. Taylor, and S. Curry, A simple proposal for the publication of journal citation distributions, *bioRxiv* 062109 (2016).
- [36] J.-H. Ham and B. Platzer, Semi-empirical equations for the residence time distributions in disperse systems—Part 1:Continuous phase, in *Chemical Engineering & Technology: Industrial Chemistry, Plant Equipment, Process Engineering, and Biotechnology*, Vol. 27 (WILEY-VCH Verlag GmbH & Co. KGaA, Weinheim, 2004), 1172.
- [37] F. Trachsel, A. Günther, S. Khan, and K. F. Jensen, Measurement of residence time distribution in microfluidic systems, *Chem. Eng. Sci.* **60**, 5729 (2005).
- [38] J. T. Adeosun and A. Lawal, Numerical and experimental studies of mixing characteristics in a T-junction microchannel using residence-time distribution, *Chem. Eng. Sci.* **64**, 2422 (2009).
- [39] D. Bošković, S. Loebbecke, G. A. Gross, and J. M. Koehler, Residence time distribution studies in microfluidic mixing structures, *Chem. Eng. Technol.* **34**, 361 (2011).
- [40] A. E. Rodrigues, Residence time distribution (RTD) revisited, *Chem. Eng. Sci.* **230**, 116188 (2021).
- [41] U. Khair, H. Fahmi, S. Al. Hakim, and R. Rahim, Forecasting error calculation with mean absolute deviation and mean absolute percentage error, *J. Phys.: Conf. Ser.* **930**, 012002 (2017).
- [42] M. Matsui and Z. Pawlas, Fractional absolute moments of heavy tailed distributions, *Braz. J. Probab. Stat.* **30**, 272 (2016).
- [43] H. Aref and S. W. Jones, Enhanced separation of diffusing particles by chaotic advection, *Phys. Fluids* **1**, 470 (1989).
- [44] N. A. Mortensen, F. Okkels, and H. Bruus, Reexamination of hagen-poiseuille flow: Shape dependence of the hydraulic resistance in microchannels, *Phys. Rev. E* **71**, 057301 (2005).
- [45] S. Ramanujan, *Ramanujan’s Collected Works* (Chelsea, New York, 1962).

- [46] M. B. Villarino, Ramanujan's perimeter of an ellipse [<https://arxiv.org/abs/math/0506384>].
- [47] M. Spiga and G. L. Morino, A symmetric solution for velocity profile in laminar flow through rectangular ducts, *Int. Commun. Heat Mass Transf.* **21**, 469 (2006).
- [48] F. Raynal and J.-N. Gence, Energy saving in chaotic laminar mixing, *Int. J. Heat Mass Transf.* **40**, 3267 (1997).
- [49] I. S. Gradshteyn and I. M. Ryzhik, *Table of Integrals, Series, and Products*, 7th ed. (Elsevier/Academic Press, Amsterdam, 2007).

[A30]

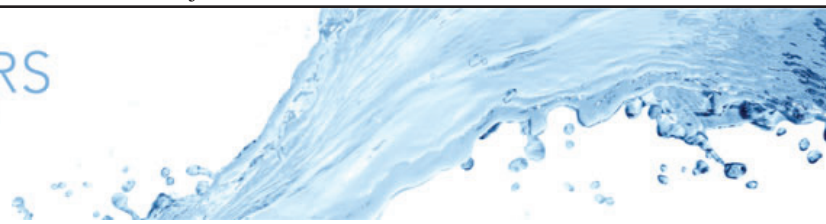
Linear instabilities of pulsatile plane channel flow between compliant walls

S. Lebbal, F. Alizard & B. Pier

Journal of Fluid Mechanics **948**, A15 (32 pages) (2022)

doi:10.1017/jfm.2022.658

<https://hal.archives-ouvertes.fr/hal-03559481>



Linear instabilities of pulsatile plane channel flow between compliant walls

Smail Lebbal¹, Frédéric Alizard¹ and Benoît Pier^{1,†}

¹Laboratoire de mécanique des fluides et d'acoustique, CNRS, École centrale de Lyon, Université de Lyon 1, INSA Lyon, 36 avenue Guy-de-Collongue, 69134 Écully, France

(Received 8 February 2022; revised 21 June 2022; accepted 27 July 2022)

The linear dynamics of perturbations developing in an infinite channel with compliant walls is investigated for pulsatile flow conditions. Two-dimensional modal perturbations are considered for Womersley-type pulsating base flows and the wall motion is only allowed in the normal direction. It is found that the flow dynamics is mainly governed by four control parameters: the Reynolds number Re , the reduced velocity V_R , the Womersley number Wo and the amplitude of the base-flow modulation \tilde{Q} . Linear stability analyses are carried out within the framework of Floquet theory, implementing an efficient approach for removing spurious eigenmodes. The characteristics of flow-based (Tollmien–Schlichting) and wall-based (both travelling-wave flutter and divergence) modes are investigated over a large control-parameter space. It is shown that travelling-wave flutter (TWF) modes are predominantly influenced by the reduced velocity and that the Reynolds number has only a marginal effect. The critical reduced velocity (corresponding to onset of linear instability) is demonstrated to depend both on the Womersley number and modulation amplitude for a given set of wall parameters. Similarly to the steady flow case, the Tollmien–Schlichting (TS) mode is also found to be only weakly affected by the flexibility of the wall in pulsatile flow conditions. Finally, the classification given by Benjamin (*J. Fluid Mech.*, vol. 16, 1963, pp. 436–450) is found to be too restrictive in the case of pulsatile base flows. In particular, a new type of mode is identified that shares characteristics of two distinct Floquet eigenmodes: TS and TWF modes. Due to coupling of the different Floquet harmonics, a phenomenon specific to time-periodic base flows, this two-wave mode exhibits a beating over the intracyclic dynamics.

Key words: flow-vessel interactions

† Email address for correspondence: benoit.pier@cnrs.fr

1. Introduction

Pulsating flows in pipe or channel flows are laminar provided that the Reynolds numbers are sufficiently low, as is largely the case for vast parts of the cardiovascular system. In the large arteries, however, blood flow may experience instability, generating large fluctuating shear stresses, which are a possible cause for cardiovascular diseases (Chiu & Chien 2011). The compliance of arteries plays a major role in blood transport, such as maintaining blood pressure and regularising the flow rate (Ku 1997). The flexibility of the aorta is also a key element in minimising pressure fluctuations of blood provided by the left ventricle and distributing oxygen-rich blood through capillaries (O'Rourke & Hashimoto 2007). For these reasons, both flexible walls and pulsatile flow are ubiquitous in the physiological context. When a pulsatile flow interacts with compliant walls, a better analysis of the development of instabilities is therefore required in order to improve our understanding of the link between wall-shear-stress distributions and flow dynamics.

The theory of viscous flow interacting with compliant walls has come a long way from Gray's (1936) initial observations of the outstanding performance of dolphin skins in delaying turbulence, to the recent review of Kumaran (2021) enlightening us on the various instability mechanisms. In the 1950s, Kramer conducted pioneering tests in water by towing a dolphin-shaped object covered with viscoelastic materials of varying compliance (Kramer 1957). The author shows that the compliant coating leads to a significant drag reduction and suggests that the dolphin's secret originates in the laminarisation of the flow due to its skin material.

On one hand, several researchers tried and failed to replicate Kramer's experiments; see Gad-el-Hak (1986, 1996) for reviews. On the other hand, theoretical results of Carpenter & Garrad (1985) extend the first analytical studies developed by Benjamin (1959, 1960, 1963) and Landahl (1962) and demonstrate that a suitable choice of wall properties could control the onset of the primary instability mode of a flat-plate boundary layer, the so-called Tollmien–Schlichting (TS) mode. However, it is also suggested that the emergence of wall-based instability modes due to fluid–structure interactions (also referenced as flow–structure instabilities, FSI) can limit the potential of laminarisation of the flow (Carpenter & Garrad 1986). The FSI modes can be divided into two categories: the travelling-wave flutter (TWF) modes and the (almost static) divergence (DIV) modes. The onset of the DIV mode only occurs for a certain amount of wall dissipation (see Lebbal, Alizard & Pier (2022) for a recent investigation). While the physics of TWF modes is fairly well understood using an analogy with the onset of water waves (Miles 1957), scientists are still arguing about the physical mechanism behind the DIV mode (either absolute or convective instabilities with a low phase velocity). The first successful experiment to reproduce Kramer's findings was given by Gaster (1988).

Several attempts to classify instability modes in the presence of fluid–structure interactions were made since the seminal study of Benjamin (1963) for a boundary-layer flow developing on either a wavy boundary or an elastic material with given stiffness, mass and damping. In particular, three types of instability mechanism have been considered: TS modes belong to class A, TWF modes are associated with class B and class C modes correspond to almost steady waves, i.e. the DIV mode (see Davies & Carpenter (1997a,b) for the channel-flow case). Apart from these modes, a transition mode is also found by Sen & Arora (1988), resulting from the coalescence between a TS mode and a TWF mode. For instance, Davies & Carpenter (1997a) have shown that the transition mode could develop inside a flow between a compliant channel for a sufficiently high level of wall damping. For the same flow case, we have recently shown that, while class B modes are mainly driven by the reduced velocity, which corresponds to the ratio of characteristic wall and

advection time scales, the class C mode is influenced by both the Reynolds number and the reduced velocity (Lebbal *et al.* 2022).

Independently of studies assessing the optimal properties of wall coating to delay transition to turbulence in wall-bounded flows, the stability of pulsatile flow with respect to viscous shear instability modes has been theoretically addressed since the middle of the 1970s (Davis 1976). In comparison with steady flows, pulsatile flows are governed by additional control parameters: the pulsation amplitudes and the pulsating frequency, of which the Womersley number Wo is a non-dimensional measure (see its definition in (3.6a–c) below). In physiological situations, typical Womersley numbers for large blood vessels are in the range 5–15 (Ku 1997). Within a Floquet theory framework, von Kerczek (1982) shows that the sinusoidally pulsating flow developing between two flat plates is more stable than the steady plane Poiseuille flow for Womersley numbers in excess of $Wo = 12$. This result was confirmed by direct numerical simulations carried out by Singer, Ferziger & Reed (1989). Using linear Floquet stability analyses and nonlinear numerical simulations, Pier & Schmid (2017) explored a large parameter space for the same flow configuration, confirming and extending the earlier results given by von Kerczek (1982).

On the other hand, several authors (Straatman *et al.* 2002; Blennerhassett & Bassom 2006) have found that the perturbations may experience a strong increase in kinetic energy during the deceleration phase of the pulsatile base flow. This suggests that transient growth mechanisms and nonlinear effects likely come into play during this part of the pulsation cycle and that the flow could possibly break down to turbulence. Recently, such a scenario has been further supported by non-modal stability analyses, experiments and direct numerical simulations for both pipe and channel flows (Xu *et al.* 2020b; Pier & Schmid 2021; Xu, Song & Avila 2021).

In spite of major successes achieved so far in the understanding of the dynamics prevailing for either pulsatile base flows or wall flexibility, only few studies address these two effects in combination. Among of them, Tsigklifis & Lucey (2017) investigated numerically the asymptotic linear stability and transient growth for a pulsatile flow in a compliant channel where both vertical and horizontal displacements are allowed. Using Floquet stability analyses, Tsigklifis & Lucey (2017) show that wall flexibility has a stabilising effect for the Womersley number varying from 5 to 50. The combined effect of wall damping and Womersley number is illustrated by these authors for TS and TWF modes. The authors also found that the tangential motion of the wall could be neglected and that the most dangerous perturbation for the asymptotic regime is always two-dimensional. The non-modal transient growth is shown to be increased by wall compliance. However, the symmetry of the perturbation is not discussed by these authors, and it is therefore not clear whether the sinuous or the varicose TWF modes are investigated. In addition, the DIV mode was not considered by Tsigklifis & Lucey (2017). For a steady channel flow and similar compliant walls, the DIV mode has been characterised by Lebbal *et al.* (2022) and is therefore also expected to occur for the pulsatile flow case.

Finally, the influence of the reduced velocity on TWF modes has not yet been considered when the pulsatile base-flow component comes into play and it is not completely clear if the classification made by Benjamin (1963) still holds for the pulsatile flow case.

To provide further understanding of the above points, the present study addresses the linear stability properties of small-amplitude perturbations developing in pulsatile flows through compliant channels. This paper is organised as follows. In § 2, we introduce the coupled fluid–structure system, and the base flow and non-dimensional control parameters are given in § 3. The mathematical formulation of the linear stability problem is presented in § 4. The numerical methods to solve and reduce the generalised eigenvalue

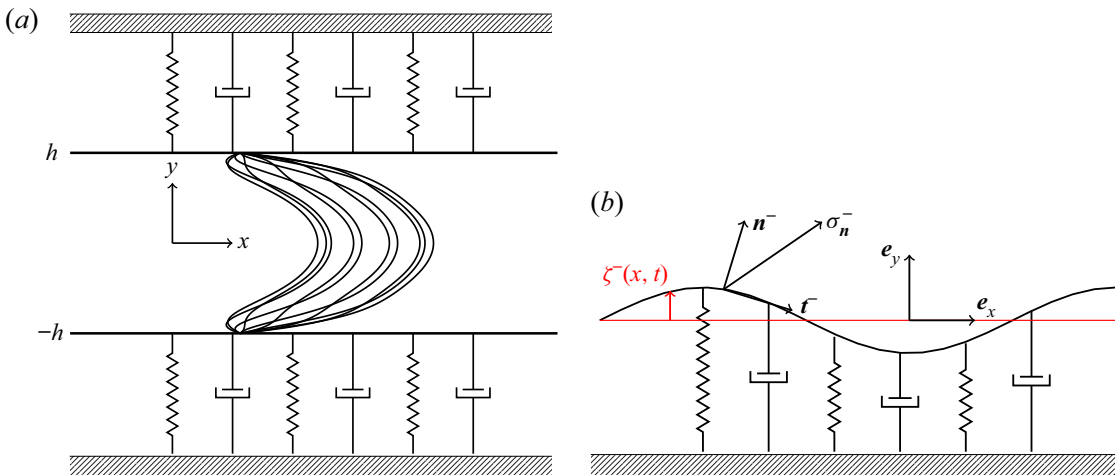


Figure 1. Channel flow with infinite spring-backed flexible walls. (a) Schematic diagram showing the equilibrium state configuration and (b) wall deformation and coordinate system.

problem are explained in § 5. Section 6 is devoted to the results and constitutes the main contribution of the paper: discussion of the spectra, influence of the control parameters and spatio-temporal structure of the eigenmodes. In particular, specific attention will be given to providing critical parameters for the onset of instabilities for the different types of modes (TWF, DIV and TS) and symmetries (sinuous and varicose). In that respect, the extension of the classification made by Benjamin (1963) for the steady flow to the pulsatile flow case will be discussed. Finally, in § 7 the conclusions are summarised, an attempt is made to assess the relevance of the critical parameter values in practical contexts, and some prospects for future work are given.

2. Fluid–structure interaction model and interface conditions

In the present study, the analysis is restricted to the two-dimensional case. We introduce the Cartesian coordinate system (x, y) with unit vectors $(\mathbf{e}_x, \mathbf{e}_y)$ and consider an incompressible Newtonian fluid with dynamic viscosity μ and density ρ between two spring-backed deformable plates located at $y = \zeta^\pm(x, t)$ which are allowed to move only in the wall-normal direction (see figure 1). As suggested by previous theoretical analyses carried out by Larose & Grotberg (1997) and Tsigklifis & Lucey (2017) for steady and pulsatile flow cases, respectively, horizontal wall motion only plays a minor role in the dynamics and is therefore not considered in the present investigation for simplicity of the model.

The flow between the walls is governed by the incompressible Navier–Stokes equations

$$\rho \frac{\partial \mathbf{u}}{\partial t} + \rho (\mathbf{u} \cdot \nabla) \mathbf{u} = -\nabla p + \mu \Delta \mathbf{u}, \quad (2.1)$$

$$0 = \nabla \cdot \mathbf{u}, \quad (2.2)$$

where $\mathbf{u} = u\mathbf{e}_x + v\mathbf{e}_y$ is the velocity field, with streamwise (u) and wall-normal (v) velocity components and p the pressure field.

The movement of the flexible plates obeys the following equations:

$$m \frac{\partial^2 \zeta^\pm}{\partial t^2} + d \frac{\partial \zeta^\pm}{\partial t} + \left(B \frac{\partial^4}{\partial x^4} - T \frac{\partial^2}{\partial x^2} + K \right) \zeta^\pm = f^\pm, \quad (2.3)$$

where m denotes the mass per unit area of the plates, d their damping coefficient, B the flexural rigidity, T the wall tension, K the spring stiffness and f^\pm represents the y -component of the hydrodynamic forces acting on the plates. These forces are obtained as

$$f^\pm = \mathbf{e}_y \cdot \mathbf{f}^\pm \quad \text{with } \mathbf{f}^\pm = (\bar{\tau}^\pm - \delta p^\pm \mathbf{I}) \cdot \mathbf{n}^\pm. \quad (2.4)$$

Here, $\bar{\tau}^\pm$ denotes the viscous stress tensor at the walls, δp^\pm the transmural surface pressure and $\mathbf{n}^\pm = (n_x^\pm, n_y^\pm)$ is the unit vector normal to the walls pointing towards the fluid. The y -component of the normal forces acting on the plate then reads

$$f^\pm = \mu \left(\frac{\partial u}{\partial y} \Big|_{y=\zeta^\pm} + \frac{\partial v}{\partial x} \Big|_{y=\zeta^\pm} \right) n_x^\pm + 2\mu \frac{\partial v}{\partial y} \Big|_{y=\zeta^\pm} n_y^\pm - \delta p^\pm n_y^\pm, \quad (2.5)$$

with

$$n_x^\pm = \pm \frac{\partial \zeta^\pm}{\partial x} \frac{1}{\sqrt{1 + \left(\frac{\partial \zeta^\pm}{\partial x}\right)^2}} \quad \text{and} \quad n_y^\pm = \mp \frac{1}{\sqrt{1 + \left(\frac{\partial \zeta^\pm}{\partial x}\right)^2}}. \quad (2.6a,b)$$

Finally, since only vertical displacements are allowed, the no-slip conditions on both walls lead to the kinematic conditions (Wiplier & Ehrenstein 2000)

$$u = 0 \quad \text{and} \quad v = \frac{\partial \zeta^\pm}{\partial t} \quad \text{for } y = \zeta^\pm. \quad (2.7)$$

The fluid–structure interaction problem is thus fully defined by the coupling of the fluid equations (2.1) and (2.2), the wall equations (2.3) and (2.5) and the boundary conditions (2.7).

3. Base flows and non-dimensional control parameters

A pulsatile base flow, of frequency Ω , is considered. Such a flow is driven by a spatially uniform and temporally periodic streamwise pressure gradient and is obtained as an exact solution of the Navier–Stokes equations, assuming a vanishing transmural pressure difference for the unperturbed state. The base-state solution then consists of undeformed parallel walls and of a velocity field in the streamwise direction with profiles that only depend on the wall-normal coordinate and time. It can be expanded as a temporal Fourier series

$$U(y, t) = U(y, t)\mathbf{e}_x \quad \text{with } U(y, t) = \sum_{-\infty < n < +\infty} U^{(n)}(y) \exp(in\Omega t). \quad (3.1)$$

Similarly, the pressure gradient that drives the flow is expanded as

$$G(t) = \sum_{-\infty < n < +\infty} G^{(n)} \exp(in\Omega t), \quad (3.2)$$

and is associated with a pulsatile flow rate

$$Q(t) = \sum_{-\infty < n < +\infty} Q^{(n)} \exp(in\Omega t). \quad (3.3)$$

In the above expressions, the conditions $Q^{(n)} = [Q^{(-n)}]^\star$, $G^{(n)} = [G^{(-n)}]^\star$ and $U^{(n)}(y) = [U^{(-n)}(y)]^\star$ ensure that all flow quantities are real (with \star denoting complex conjugation).

The velocity profile is analytically obtained for each harmonic component. The mean-flow component $U^{(0)}(y)$ corresponds to a parabolic steady Poiseuille flow solution. For $n \neq 0$, the profiles $U^{(n)}(y)$ are obtained in terms of exponential functions (Womersley 1955). Analytical expressions as well as the relationship between $U^{(n)}(y)$ and $Q^{(n)}$ are detailed in the appendix of Pier & Schmid (2021). In this work, we focus on pulsatile base flows with a single oscillating component: $-1 \leq n \leq 1$ in (3.1)–(3.3). Without loss of generality, $Q^{(1)}$ may then be assumed real, and the flow rate is obtained as

$$Q(t) = Q^{(0)}(1 + \tilde{Q} \cos \Omega t), \quad (3.4)$$

with the relative pulsating amplitude \tilde{Q} defined as

$$\tilde{Q} = 2 \frac{Q^{(1)}}{Q^{(0)}}. \quad (3.5)$$

The problem is then characterised by 11 dimensional parameters: the mean flow rate $[Q^{(0)}] = \text{m}^2 \text{s}^{-1}$, the half-channel width $[h] = \text{m}$, the fluid density $[\rho] = \text{kg m}^{-3}$, the viscosity $[\mu] = \text{kg s}^{-1} \text{m}^{-1}$, the mass of the plate per unit area $[m] = \text{kg m}^{-2}$, the damping coefficient of the wall $[d] = \text{kg m}^{-2} \text{s}^{-1}$, the bending stiffness of the plate $[B] = \text{kg m}^2 \text{s}^{-2}$, the wall tension $[T] = \text{kg s}^{-2}$, the spring stiffness $[K] = \text{kg m}^{-2} \text{s}^{-2}$, the pulsation frequency $[\Omega] = \text{s}^{-1}$ and the amplitude of the oscillating flow component $[Q^{(1)}] = \text{m}^2 \text{s}^{-1}$. Hence, the present configuration may be described by eight non-dimensional control parameters.

The base flow is characterised by three non-dimensional parameters

$$Re = \frac{Q^{(0)}}{\nu}, \quad Wo = h \sqrt{\frac{\Omega}{\nu}} \quad \text{and} \quad \tilde{Q} = 2 \frac{Q^{(1)}}{Q^{(0)}}. \quad (3.6a-c)$$

Here, the Reynolds number Re is based on the average fluid velocity, the channel diameter and the kinematic viscosity $\nu = \mu/\rho$; the Womersley number Wo is a measure of the pulsation frequency and can be interpreted as the ratio of the channel half-diameter h to the thickness $\delta = \sqrt{\nu/\Omega}$ of the oscillating Stokes boundary layers.

The parameters associated with the walls are non-dimensionalised with respect to the spring stiffness K , which leads to

$$B_* = \frac{B}{Kh^4}, \quad T_* = \frac{T}{Kh^2} \quad \text{and} \quad d_* = \frac{d}{\sqrt{mK}}. \quad (3.7a-c)$$

Finally, two non-dimensional parameters account for the coupling between the fluid and the compliant walls

$$V_R = \frac{Q^{(0)}}{4h^2} \sqrt{\frac{m}{K}} \quad \text{and} \quad \Gamma = \frac{m}{\rho h}. \quad (3.8a,b)$$

The reduced velocity V_R represents the ratio of the wall characteristic time scale $\tau_K = \sqrt{m/K}$, associated with the spring stiffness, to the characteristic flow advection time scale $\tau_Q = 4h^2/Q^{(0)}$ (de Langre 2000). The parameter Γ is the mass ratio between the walls and the fluid.

Unperturbed base configurations are thus completely specified by the 8 non-dimensional control parameters (3.6a–c)–(3.8a,b). We further use $\rho = 1$, $h = 1$ and $Q^{(0)} = 1$ to uniquely determine dimensional quantities. Hereafter, to reduce the dimensionality of control-parameter space, the mass ratio is kept constant at $\Gamma = 2$ and we consider walls without tension $T = 0$.

4. Linear stability analysis

For the stability analysis, the total flow fields are decomposed as the superposition of base and small-amplitude perturbation fields

$$\mathbf{u}(x, y, t) = \mathbf{U}(y, t) + \mathbf{u}'(x, y, t), \quad (4.1)$$

$$p(x, y, t) = G(t)x + p'(x, y, t). \quad (4.2)$$

The wall displacement is similarly written as

$$\zeta^\pm(x, t) = \pm h + \eta^\pm(x, t). \quad (4.3)$$

Since the base configuration is homogeneous in x , perturbation fields may be expressed as spatial normal modes

$$\mathbf{u}'(x, y, t) = \tilde{\mathbf{u}}(y, t)e^{i\alpha x} + \text{c.c.}, \quad (4.4)$$

$$p'(x, y, t) = \tilde{p}(y, t)e^{i\alpha x} + \text{c.c.}, \quad (4.5)$$

$$\eta^\pm(x, t) = \tilde{\eta}^\pm(t)e^{i\alpha x} + \text{c.c.}, \quad (4.6)$$

where α denotes the streamwise wavenumber and c.c. stands for the complex conjugate. Introducing this decomposition into the governing equations (2.1)–(2.3) and neglecting the quadratic terms leads to the following system of coupled linear partial differential equations:

$$\frac{\partial \tilde{u}}{\partial t} = -i\alpha U(y, t)\tilde{u} - \frac{\partial U}{\partial y}(y, t)\tilde{v} - \frac{1}{\rho}i\alpha\tilde{p} + \nu \left(\frac{\partial^2}{\partial y^2} - \alpha^2 \right) \tilde{u}, \quad (4.7)$$

$$\frac{\partial \tilde{v}}{\partial t} = -i\alpha U(y, t)\tilde{v} - \frac{1}{\rho} \frac{\partial \tilde{p}}{\partial y} + \nu \left(\frac{\partial^2}{\partial y^2} - \alpha^2 \right) \tilde{v}, \quad (4.8)$$

$$0 = i\alpha\tilde{u} + \frac{\partial \tilde{v}}{\partial y}, \quad (4.9)$$

$$m \frac{\partial \tilde{\gamma}^\pm}{\partial t} = -d\tilde{\gamma}^\pm - (B\alpha^4 + T\alpha^2 + K)\tilde{\eta}^\pm \pm \tilde{p}(y, t)|_{\pm h} \mp \mu \frac{d\tilde{v}}{dy} \Big|_{\pm h}, \quad (4.10)$$

where we have introduced the additional functions $\tilde{\gamma}^\pm = \partial_t \tilde{\eta}^\pm$ in order to reduce the system to first-order differential equations in time. Note that the wall equations (4.10) assume a pressure outside the channel walls always equal to the unperturbed pressure $G(t)x$ prevailing inside (see Lebbal *et al.* (2022) for further details). The same assumption has been made by Davies & Carpenter (1997a,b), Tsigklifis & Lucey (2017) and many others. The effect of the transmural pressure for collapsible channels has been investigated by Luo & Pedley (1996) and Xu *et al.* (2020a) and is out the scope of the present study.

The boundary conditions at the perturbed interface are expanded in a Taylor series about their equilibrium values at $y = \pm h$ (Domaradzki & Metcalfe 1986; Davies & Carpenter 1997a; Shankar & Kumaran 2002). At linear order, the flow velocities at the walls are

obtained as

$$\mathbf{u}(x, y = \zeta^\pm, t) = \mathbf{u}'(x, y = \pm h, t) + \eta^{\pm'}(x, t) \frac{dU}{dy} \Big|_{(y=\pm h, t)} \mathbf{e}_x. \quad (4.11)$$

Thus, the boundary conditions (2.7) become

$$\tilde{u}(y = \pm h, t) + \tilde{\eta}^\pm(t) \frac{dU}{dy} \Big|_{(y=\pm h, t)} = 0 \quad \text{and} \quad \tilde{v}(y = \pm h, t) = \tilde{\gamma}^\pm(t). \quad (4.12a,b)$$

Since the base flow is time periodic, the linear stability analysis proceeds by following Floquet theory, where the eigenfunctions are assumed to have the same temporal periodicity as the base flow. The perturbations are therefore further decomposed as

$$\tilde{u}(y, t) = \left[\sum_n \hat{u}^{(n)}(y) \exp(in\Omega t) \right] \exp(-i\omega t), \quad (4.13)$$

$$\tilde{p}(y, t) = \left[\sum_n \hat{p}^{(n)}(y) \exp(in\Omega t) \right] \exp(-i\omega t), \quad (4.14)$$

$$\tilde{\eta}^\pm(t) = \left[\sum_n \hat{\eta}^{\pm(n)} \exp(in\Omega t) \right] \exp(-i\omega t), \quad (4.15)$$

$$\tilde{\gamma}^\pm(t) = \left[\sum_n \hat{\gamma}^{\pm(n)} \exp(in\Omega t) \right] \exp(-i\omega t), \quad (4.16)$$

where the complex frequency $\omega = \omega_r + i\omega_i$ is the eigenvalue, with ω_i the growth rate and ω_r the circular frequency. After substitution of these expansions, the linearised equations governing the dynamics of small perturbations take the following form, for each integer n :

$$\begin{aligned} \omega \hat{u}^{(n)}(y) &= [n\Omega + iv(\partial_{yy} - \alpha^2)] \hat{u}^{(n)}(y) + \frac{\alpha}{\rho} \hat{p}^{(n)}(y) \\ &\quad + \sum_k \left[\alpha U^{(k)}(y) \hat{u}^{(n-k)}(y) - i \frac{dU^{(k)}}{dy} \hat{v}^{(n-k)}(y) \right], \end{aligned} \quad (4.17)$$

$$\begin{aligned} \omega \hat{v}^{(n)}(y) &= [n\Omega + iv(\partial_{yy} - \alpha^2)] \hat{v}^{(n)}(y) + \frac{1}{\rho} \frac{d\hat{p}^{(n)}}{dy} \\ &\quad + \sum_k [\alpha U^{(k)}(y) \hat{v}^{(n-k)}(y)], \end{aligned} \quad (4.18)$$

$$0 = i\alpha \hat{u}^{(n)}(y) + \frac{\partial \hat{v}^{(n)}}{\partial y}, \quad (4.19)$$

$$\omega \hat{\eta}^{\pm(n)} = n\Omega \hat{\eta}^{\pm(n)} + i\hat{\gamma}^{\pm(n)}, \quad (4.20)$$

$$\begin{aligned} \omega \hat{\gamma}^{\pm(n)} &= n\Omega \hat{\gamma}^{\pm(n)} - i \frac{d}{m} \hat{\gamma}^{\pm(n)} - \frac{i}{m} (B\alpha^4 + T\alpha^2 + K) \hat{\eta}^{\pm(n)} \\ &\quad \pm \frac{i}{m} \left(\hat{p}^{(n)}(\pm h) - \mu \frac{d\hat{v}^{(n)}}{dy} \Big|_{\pm h} \right), \end{aligned} \quad (4.21)$$

together with the kinematic wall conditions

$$\hat{u}^{(n)}(\pm h) = - \sum_k \frac{dU^{(k)}}{dy} \Big|_{\pm h} \hat{\eta}^{\pm(n-k)}, \quad (4.22)$$

$$\hat{v}^{(n)}(\pm h) = \hat{\gamma}^{\pm(n)}. \quad (4.23)$$

Note that, in (4.17), (4.18) and (4.22), the summation only involves $-1 \leq k \leq +1$ for harmonically pulsating base flows.

The system of coupled linear differential equations (4.17)–(4.21) with boundary conditions (4.22) and (4.23) forms the generalised eigenvalue problem that governs the dynamics of small-amplitude perturbations developing in this time-periodic fluid–structure interaction system.

5. Numerical methods

In this section, we outline the numerical strategy that has been implemented for solving the generalised Floquet eigenvalue problem derived in the previous section. The main objectives in this implementation are the elimination of spurious (non-physical) eigenvalues and the reduction of the required computational effort. To that purpose, we follow the general framework described by Manning, Bamieh & Carlson (2007), who have also suggested an interest in the proposed method for handling fluid–structure interaction problems.

The velocity and pressure components are discretised in the wall-normal direction using a Chebyshev collocation method. To suppress spurious pressure modes, we consider the $(\mathbb{P}_N, \mathbb{P}_{N-2})$ -formulation, where the pressure is approximated with a polynomial of degree $N - 2$ while the velocity is discretised with a polynomial of degree N (Schumack, Schultz & Boyd 1991; Boyd 2001; Peyret 2002). In classical fashion, velocity fields are therefore represented by their values over N Gauss–Lobatto collocation points spanning the entire channel diameter and including the boundary points, while the pressure fields use only the $N - 2$ interior points. We note the vectors containing the unknown velocity and pressure components at the interior points for each Fourier mode

$$\mathbf{V}_I^{(n)} = (\hat{u}_2^{(n)}, \dots, \hat{u}_{N-1}^{(n)}, \hat{v}_2^{(n)}, \dots, \hat{v}_{N-1}^{(n)}), \quad (5.1)$$

$$\mathbf{P}_I^{(n)} = (\hat{p}_2^{(n)}, \dots, \hat{p}_{N-1}^{(n)}).$$

Similarly, wall displacements and wall velocities are denoted by

$$\mathbf{W}^{(n)} = (\hat{\eta}_1^{(n)}, \hat{\eta}_N^{(n)}, \hat{\gamma}_1^{(n)}, \hat{\gamma}_N^{(n)}).$$

The kinematic conditions (4.22) and (4.23) may be used to express the velocity values at the boundaries in terms of the wall variables. As a consequence, the variables $\hat{u}_1^{(n)}, \hat{v}_1^{(n)}, \hat{u}_N^{(n)}$ and $\hat{v}_N^{(n)}$ may be directly eliminated from the problem together with the boundary conditions. Then, using

$$\hat{\mathbf{X}}^{(n)} = (\mathbf{V}_I^{(n)}, \mathbf{P}_I^{(n)}, \mathbf{W}^{(n)}) \quad (5.4)$$

for each harmonic of the Floquet eigenvector, the system (4.17)–(4.21) is recast as a generalised algebraic eigenvalue problem of the form

$$\hat{\mathbf{A}}^{(n)} \hat{\mathbf{X}}^{(n)} + \sum_k \hat{\mathbf{S}}^{(k)} \hat{\mathbf{X}}^{(n-k)} = i\omega \hat{\mathbf{B}}^{(n)} \hat{\mathbf{X}}^{(n)}. \quad (5.5)$$

Here, the square matrices $\hat{A}^{(n)}$, $\hat{S}^{(k)}$ and $\hat{B}^{(n)}$ are of size $(3N - 2)^2$ and may be written in block structure as

$$\begin{aligned}\hat{A}^{(n)} &= \begin{pmatrix} \hat{A}_{VV}^{(n)} & \hat{G}_V & \hat{A}_{VW} \\ \hat{D}_V & \mathbf{0} & \hat{D}_W \\ \hat{A}_{WV} & \hat{G}_W & \hat{A}_{WW}^{(n)} \end{pmatrix}, \quad \hat{S}^{(k)} = \begin{pmatrix} \hat{S}_{VV}^{(k)} & \mathbf{0} & \hat{S}_{VW}^{(k)} \\ \mathbf{0} & \mathbf{0} & \mathbf{0} \\ \mathbf{0} & \mathbf{0} & \mathbf{0} \end{pmatrix} \quad \text{and} \\ \hat{B}^{(n)} &= \begin{pmatrix} \mathbb{I}_{VV} & \mathbf{0} & \mathbf{0} \\ \mathbf{0} & \mathbf{0} & \mathbf{0} \\ \mathbf{0} & \mathbf{0} & \mathbb{I}_{WW} \end{pmatrix}. \end{aligned} \quad (5.6a-c)$$

Their decomposition in terms of square blocks along the diagonal and rectangular blocks off diagonal reflects the structure of the vectors $\hat{X}^{(n)}$ (5.4), with $2N - 4$ variables for $V_I^{(n)}$, $N - 2$ variables for $P_I^{(n)}$ and 4 variables for $W^{(n)}$. Note that the wall equations involve the pressure at $y = \pm h$; since the pressure is represented on the $N - 2$ interior collocation points, these boundary values are obtained by polynomial interpolation with spectral accuracy, corresponding to two lines of the rectangular block \hat{G}_W . In the above expressions, n may in theory take all integer values (positive and negative) but in practice the Fourier series are truncated at $|n| \leq N_f$ for some cutoff value N_f (i.e. the number of complex Fourier components is then $2N_f + 1$).

Note also that the blocks for which the superscript (n) is not indicated in (5.6a–c) do not depend on a specific harmonic and that the matrix $\hat{B}^{(n)}$ only consists of two identity blocks. The matrices $\hat{S}^{(k)}$ account for the advection terms due to the pulsating base-flow component $U^{(k)}(y)$ and are responsible for the coupling of the different Fourier components of the Floquet eigenfunctions. Since we consider pulsating flows with only a single oscillating component $U^{(\pm 1)}(y)$, only the matrices $\hat{S}^{(k)}$ with $|k| \leq 1$ are here non-zero. As a result, the eigenvalue problem (5.5) has block-tridiagonal structure, which allows the use of efficient solution methods such as a generalised form of the Thomas algorithm.

The next step consists in eliminating the pressure by using the discrete version of the divergence-free condition

$$\hat{D}_V V_I^{(n)} + \hat{D}_W W^{(n)} = \mathbf{0}. \quad (5.7)$$

Hence, applying this divergence operator to the parts of the algebraic system (5.5) corresponding to the momentum equations yields

$$\begin{aligned}-(\hat{D}_V \hat{G}_V + \hat{D}_W \hat{G}_W) P_I^{(n)} &= (\hat{D}_V \quad \hat{G}_V) \begin{pmatrix} \hat{A}_{VV}^{(n)} & \hat{A}_{VW} \\ \hat{A}_{WV} & \hat{A}_{WW}^{(n)} \end{pmatrix} \begin{pmatrix} V_I^{(n)} \\ W^{(n)} \end{pmatrix} \\ &\quad + \hat{D}_V \sum_k (\hat{S}_{VV}^{(k)} V_I^{(n-k)} + \hat{S}_{VW}^{(k)} W^{(n-k)}). \end{aligned} \quad (5.8)$$

The operator $(\hat{D}_V \hat{G}_V + \hat{D}_W \hat{G}_W)$ is a square matrix of size $(N - 2)^2$, independent of the harmonic n and non-singular. By inverting it, the pressure components $P_I^{(n)}$ are obtained as the result of linear operators acting on the components $V_I^{(k)}$ and $W^{(k)}$.

Thus eliminating the pressure, the system (5.5) is recast as

$$\mathbf{A}^{(n)} \mathbf{X}^{(n)} + \sum_k \mathbf{S}^{(k)} \mathbf{X}^{(n-k)} = i\omega \mathbf{X}^{(n)}. \quad (5.9)$$

Now, the components of the eigenvector

$$\mathbf{X}^{(n)} = (\mathbf{V}_I^{(n)}, \mathbf{W}^{(n)}) \quad (5.10)$$

contain $2N$ variables and the new matrices $\mathbf{A}^{(n)}$ and $\mathbf{S}^{(k)}$ are of size $(2N)^2$. Note also that, through the elimination of the pressure, the generalised eigenproblem (5.5) has been transformed into a regular eigenproblem.

The system (5.9) may be further reduced when $\alpha \neq 0$. Indeed, using the discretised version of the divergence-free condition $\tilde{u} = (i/\alpha)\partial_y \tilde{v}$, allows us to eliminate the longitudinal velocity components by expressing them in terms of the wall-normal velocities. This leads to an eigenvalue problem of the same form as (5.9) where the components of the eigenvector are of size $N + 2$, with $N - 2$ wall-normal velocity values and 4 wall variables. In practice, this system is solved using an Arnoldi algorithm that exploits the block-tridiagonal structure of the matrices.

The transformations that have led from the initial generalised eigenvalue problem of size $3N + 2$ to a regular eigenproblem of size $N + 2$ may appear tedious. However, it is largely worth the effort: the final formulation is not only free of spurious eigenmodes, it is also drastically more efficient in terms of numerical computations. Finally, the method may be further improved by considering separately perturbations of sinuous or varicose symmetries and using only half of the channel together with derivative operators appropriate for the symmetry of each component of the different flow fields. Thus the complete problem may be addressed by carrying out two eigenvalue computations (sinuous and varicose) of half-size, which further speeds up the process and directly provides the information about the symmetry of the different modes.

The numerical method has been validated using the results given by Pier & Schmid (2017) for the pulsatile flow inside a rigid channel and those provided by Davies & Carpenter (1997a) for the steady base flow between compliant walls.

6. Stability analysis

The purpose of the present study is to identify the effect of the pulsating base flow on instability modes in the presence of compliant walls for a wide range of flow and wall parameters. We first discuss how the eigenvalue spectra are modified due to the time-periodic flow component. Then, the influence of the main control parameters on the dominant modes is investigated, with special attention given to possible cross-over between different mode types (i.e. TS, TWF and DIV modes). Finally, the multi-dimensional parameter space is mapped out using a variety of critical curves for instability onset.

6.1. The Floquet eigenspectrum

The linear stability properties of time-periodic flow configurations is addressed by resorting to Floquet theory, as explained in § 4. In order to introduce the specific features of Floquet eigenspectra that are essential to this entire investigation, we illustrate them for a situation with small pulsation amplitude \tilde{Q} , and compare them with the corresponding steady case.

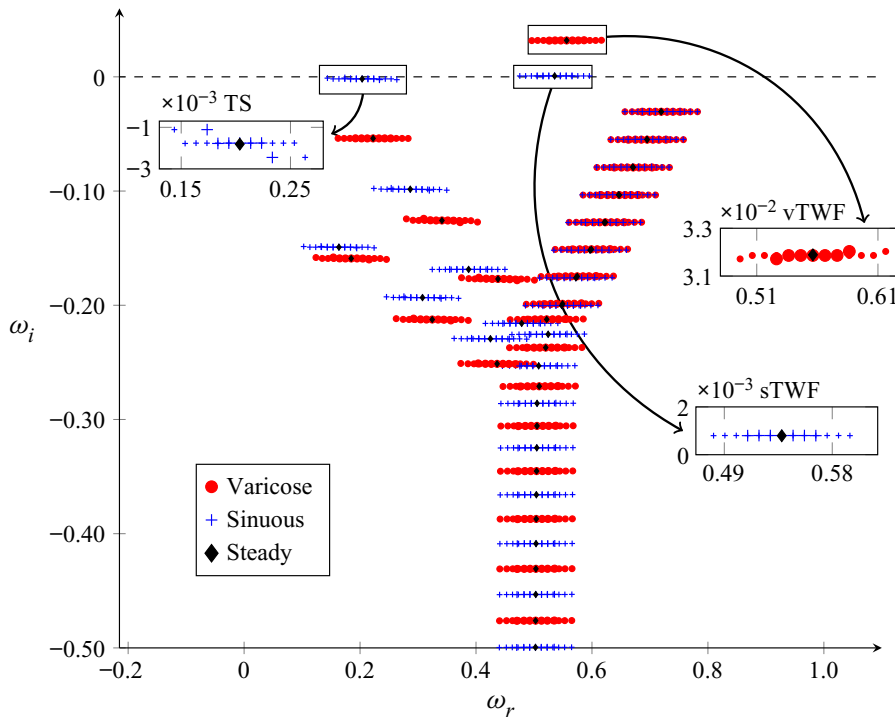


Figure 2. Spectrum for $\tilde{Q} = 0.02$, $Wo = 10$, $V_R = 1$, $Re = 10\,000$, $\alpha = 1$, $B_* = 4$ and $d_* = 0$. The steady case corresponds to $\tilde{Q} = 0$. In the insets, small symbols correspond to eigenvalues computed with $N_f = 6$ and large symbols are obtained with $N_f = 3$.

Figure 2 shows the eigenvalue spectrum computed with $\alpha = 1$ for a pulsating base configuration characterised by $V_R = 1$, $Wo = 10$, $\tilde{Q} = 0.02$, $Re = 10\,000$, $B_* = 4$ and $d_* = 0$. In the figure, the corresponding steady configuration is also reported (i.e. $\tilde{Q} = 0$).

This plot reveals the characteristic feature of any Floquet spectrum: multiple eigenvalues of the same growth rate ω_i and frequencies ω_r separated by integer multiples of the base frequency Ω . This is due to the fact that, if ω is a complex eigenvalue associated with an eigenfunction of the form (4.13)–(4.16), then all frequencies $\omega_* = \omega + k\Omega$ (for any positive or negative integer k) are also among the eigenvalues and their associated eigenfunctions are simply obtained by similarly shifting the Fourier components in the Floquet expansion as, for example, $\hat{\mathbf{u}}_*^{(n)}(y) = \hat{\mathbf{u}}^{(n-k)}(y)$. In theory, the Fourier expansions (4.13)–(4.16) are an infinite series, and the infinite number of eigenvalues $\omega + k\Omega$ all correspond to the same physical perturbation. In practice, however, the Fourier expansions are truncated to a finite number of components, leading to a finite set of eigenvalues ω_* . These are then no longer exactly equal to $\omega + k\Omega$ and the associated normal modes also differ since they correspond to different truncations of the Fourier series. To illustrate this truncation effect, two spectra are shown, computed with $N_f = 3$ and $N_f = 6$, thus corresponding to $2N_f + 1 = 7$ and 13 Fourier components, respectively, and associated with sets of 7 or 13 eigenvalues each.

The superposition of flow cases $\tilde{Q} = 0$ and $\tilde{Q} = 0.02$ illustrates the close similarity of steady and pulsating spectra and reveals that each of the steady eigenvalues is located very near one of the Floquet eigenvalues (see insets). Here, the Floquet spectrum corresponds to a weakly modulated base flow, for which the oscillating base-flow component $U^{(\pm 1)}(y)$ is much smaller than the Poiseuille component $U^{(0)}(y)$. Thus, the magnitude of the off-diagonal blocks $S^{(\pm 1)}$ in the Floquet eigenproblem (5.9) is small in comparison with

the diagonal blocks and the adjacent Fourier components in the Floquet eigenfunction are therefore only weakly coupled. As a result, the growth rates in the eigenspectrum here closely follow those prevailing for the equivalent steady flow. For weakly modulated base flows, as is the case in figure 2, it thus seems natural to choose the eigenvalue $\omega + k\Omega$ nearest its steady counterpart as the most representative frequency of the Floquet normal mode.

Insets in figure 2 reveal slight variations in ω_i for the eigenvalues towards the edges (especially visible for the TS mode and to a lesser extent for the varicose TWF mode). This indicates that the corresponding Floquet modes suffer from truncation errors, while the eigenvalues sufficiently far from the edges are well resolved. Note also that the eigenvalues nearest their steady counterpart are located in the central region and therefore the first to be sufficiently well resolved when increasing N_f .

For larger pulsation amplitudes \tilde{Q} , however, this similarity with the steady spectrum no longer holds and a more robust criterion is required to lift the formal degeneracy of the Floquet eigenspectrum. It seems suitable to consider the frequency associated with the most energetic Fourier component in the Floquet expansion. In order to identify this most representative frequency among the multiple Floquet eigenvalues for each normal mode, we consider the magnitude of the different Fourier components of the Floquet eigenfunctions, defined as

$$E_n = \rho \int_{-h}^{+h} |\hat{\mathbf{u}}^{(n)}(y)|^2 dy + m(|\hat{\gamma}^{+(n)}|^2 + |\hat{\gamma}^{-(n)}|^2) + (B\alpha^4 + T\alpha^2 + K)(|\hat{\eta}^{+(n)}|^2 + |\hat{\eta}^{-(n)}|^2). \quad (6.1)$$

By using this energy-based norm, it is possible to single out the dominant component in the eigenfunction Fourier expansion and also to check if the truncation contains enough harmonics for an accurate representation of the normal mode. This process is illustrated in figure 3, for $N_f = 100$, where the magnitudes E_n are plotted for five consecutive eigenvalues corresponding to the varicose TWF mode associated with $\alpha = 0.8$, $Re = 10\ 000$, $\tilde{Q} = 0.2$, $Wo = 10$, $V_R = 1$, $B_* = 4$ and $d_* = 0$. It is observed that the E_n -distribution peaks at $n = 0$ for the eigenvalue $\omega = 0.415 + 0.046i$, while the distributions associated with the surrounding eigenfrequencies $\omega + k\Omega$ peak at $n = k$ since they correspond to similarly shifted Fourier components. It follows that $\omega = 0.415 + 0.046i$ is the dominant frequency of this eigenmode. Throughout this paper we will therefore always consider that, for a given mode, the dominant frequency is derived by this energy-based criterion and choose the eigenvalue for which the Fourier series is dominated by the $n = 0$ component, i.e. for which E_0 is largest. For the rigid wall case, this method has been proven to be effective in recovering the TS mode frequency obtained using linearised direct numerical simulation (results are given in Pier & Schmid 2017). Note also that the plots in figure 3 demonstrate that we are using more than enough harmonics to fully resolve the Floquet eigenfunctions, since the energy associated with the higher harmonics is almost negligible.

The Floquet eigenfunctions correspond to either sinuous or varicose modes, depending on the symmetry or antisymmetry of the different flow fields with respect to the mid-plane $y = 0$. As explained in § 5, they may be efficiently computed by taking advantage of these symmetry properties. In the spectrum of figure 2, the sinuous eigenfrequencies are given in blue and the varicose frequencies in red. Despite the multiplicity of the eigenvalues due to the time-periodic base flow, the spectrum still displays the familiar structure made of a large number of Orr–Sommerfeld modes (as A, P and S branches) together with two

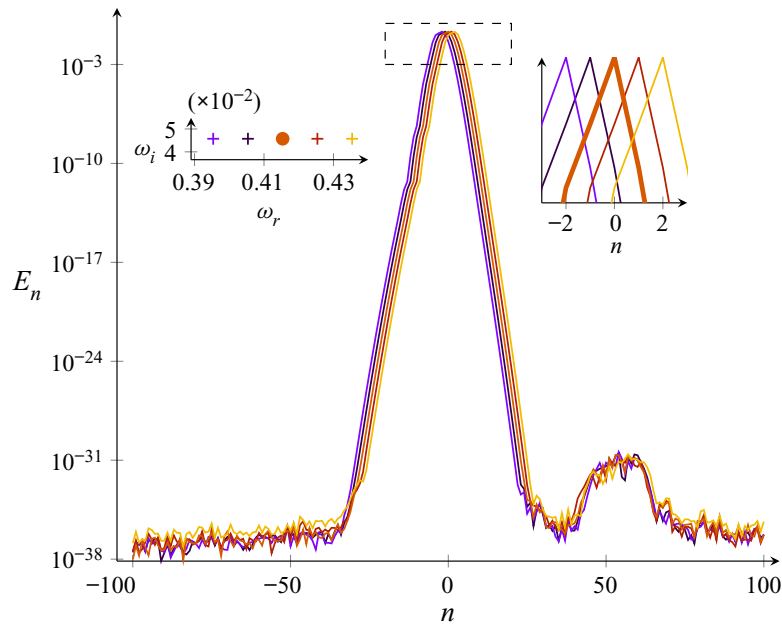


Figure 3. Fourier density for FSI varicose mode associated with $\alpha = 0.8$, $Re = 10\,000$, $\tilde{Q} = 0.2$, $Wo = 10$, $V_R = 1$, $B_* = 4$ and $d_* = 0$. The numerical eigenproblem is solved with $N_f = 100$.

isolated TWF modes (one sinuous and one varicose). Note that the two DIV modes are here out of the range of this plot.

6.2. Influence of some parameters on the spectrum

Figure 4(a) displays spectra for $V_R = 1$, $Wo = 10$, $d_* = 0$ and \tilde{Q} varying from 0 (i.e. the steady flow case) to $\tilde{Q} = 0.2$. **Figure 4(b)** illustrates the effect of the base-flow frequency by varying Wo from 10 to 20 for $\tilde{Q} = 0.8$. Note that the significant increase in N_f for **figure 4(b)** is required due to a broadening of the Fourier density distribution when \tilde{Q} increases. As discussed in the previous section, the figure shows modes that exhibit equispaced eigenfrequencies where the gap between two successive frequencies corresponds to the base frequency Ω , which scales as the square root of the Womersley number. In **figure 4**, the bold eigenvalues are associated with the dominant frequency for each mode, obtained by considering the magnitude of the Floquet harmonics, as explained in the previous subsection. Concentrating on FSI modes, dominant frequencies for both sinuous and varicose symmetries have finite ω_r values. These FSI modes are thus connected to TWF instability waves. They are referenced hereafter as sTWF (sinuous TWF) or vTWF (varicose TWF) depending on their symmetry with respect to the midplane $y = 0$.

For the flow and wall parameters that are considered and $\tilde{Q} = 0$, the most amplified TWF mode is of varicose type (see **figure 4a**). For this steady base-flow case, the sTWF is seen to be marginally stable and the temporal growth rate of the TS mode is damped. For $Wo = 10$, an increase of \tilde{Q} tends to destabilise the TS wave (see **figure 4a**). This is reminiscent of the results of Pier & Schmid (2017), where TS modes for a pulsatile base flow between rigid walls have been computed. By contrast, the TWF modes exhibit distinct behaviours whether the sinuous or varicose symmetry is considered. While an increase of \tilde{Q} up to 0.2 leads to a reduction of the temporal amplification rate for the varicose type,

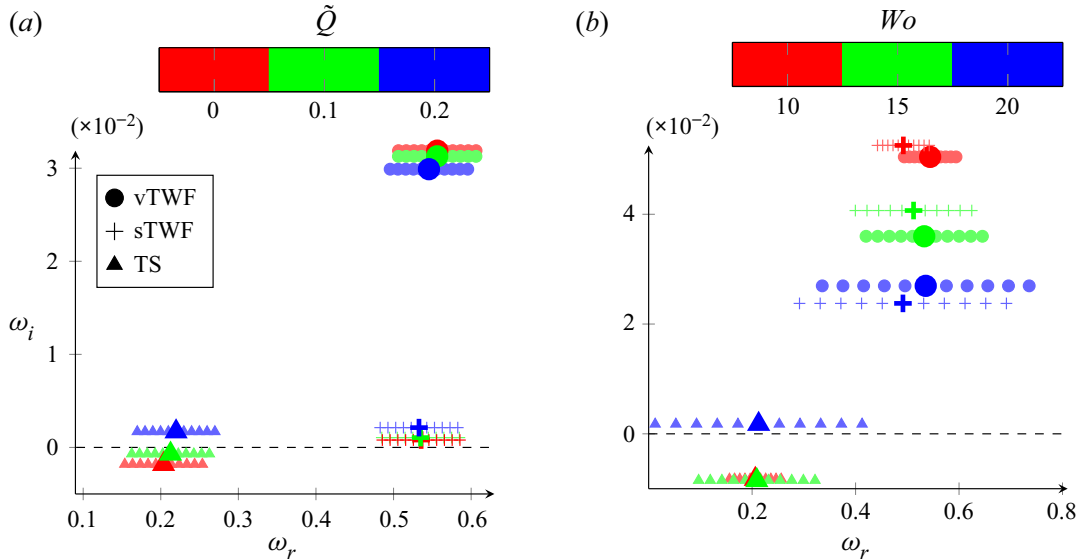


Figure 4. Spectra with $V_R = 1$, $Re = 10\,000$, $\alpha = 1$, $B_* = 4$ and $d_* = 0$. For each branch, 11 eigenvalues are shown centred around the dominant frequency (large symbols). The numerical eigenproblem is solved with $N_f = 20$ in (a) and $N_f = 150$ in (b); (a) $Wo = 10$ and (b) $\tilde{Q} = 0.8$.

the opposite behaviour is observed for the sTWF mode. Figure 4(b) shows the effect of the Womersley number Wo on TS and TWF modes for the same case at $\tilde{Q} = 0.8$. An increase of Wo has a stabilising effect on TWF modes for both symmetries. The opposite role of Wo is seen for the TS mode. This reflects the richness of physical processes that are involved, in comparison with the rigid wall case.

Finally, figure 5 shows the effect of wall compliance on TS and TWF modes for $\tilde{Q} = 0.2$, $Wo = 10$, $Re = 10\,000$, $B_* = 4$ and $\alpha = 1$. Only Floquet modes that match the dominant frequency for each mode are shown. As V_R is approaching zero, the phase speed of TWF modes tends to infinity, which is consistent with the rigid wall case. An increase of V_R has a stabilising effect on the TS mode. The opposite behaviour is observed for TWF modes, whatever the symmetry considered. However, the figure suggests a preferred varicose symmetry for large V_R . Parenthetically, one can see in figure 5(a) that the phase speed tends to a finite value (≈ 0.5) for both sTWF and vTWF as wall compliance increases. The influence of the wall dissipation is illustrated in figure 5(b) for small values of d_* . The figure shows that the temporal amplification rate of the TS mode is slightly enhanced by increasing d_* . In contrast, growth rates of both sTWF and vTWF modes are significantly reduced by wall dissipation.

When increasing the wall dissipation d_* , the onset of a DIV mode is expected as documented for steady base flows (see Davies & Carpenter (1997a) and Lebbal *et al.* (2022) for a recent investigation). The effects of the pulsatile base-flow components for different values of d_* are shown in figure 6. We restrict here the analysis to the varicose case since the sinuous symmetry is much more complicated due to the competition between the transition and DIV modes (Lebbal *et al.* 2022). The effect of \tilde{Q} , illustrated in panel (a), shows that, for moderate values of d_* , the dynamics is driven by the TWF mode (i.e. the phase velocity ω_r/α is of the order of the mean base-flow velocity). As d_* is increased, the TWF mode is temporally damped. For large values of d_* , we observe a different regime for all \tilde{Q} . The most unstable mode is shifted towards lower frequencies and its temporal growth rate increases again, a behaviour characteristic of the DIV mode.

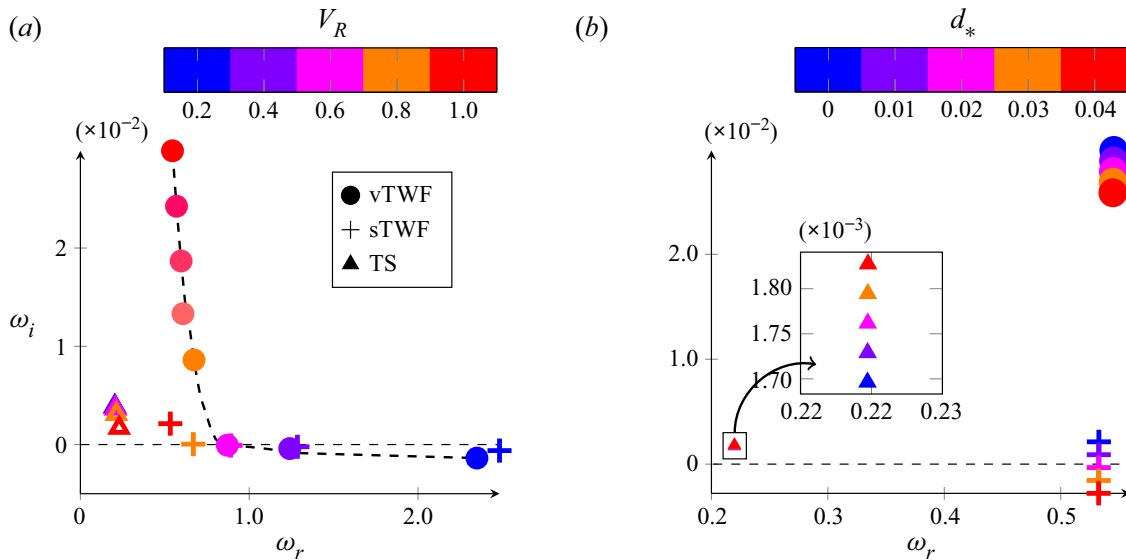


Figure 5. Spectra with $\tilde{Q} = 0.2$, $Wo = 10$, $Re = 10\,000$, $\alpha = 1$ and $B_* = 4$; (a) $d_* = 0$ and (b) $V_R = 1$.

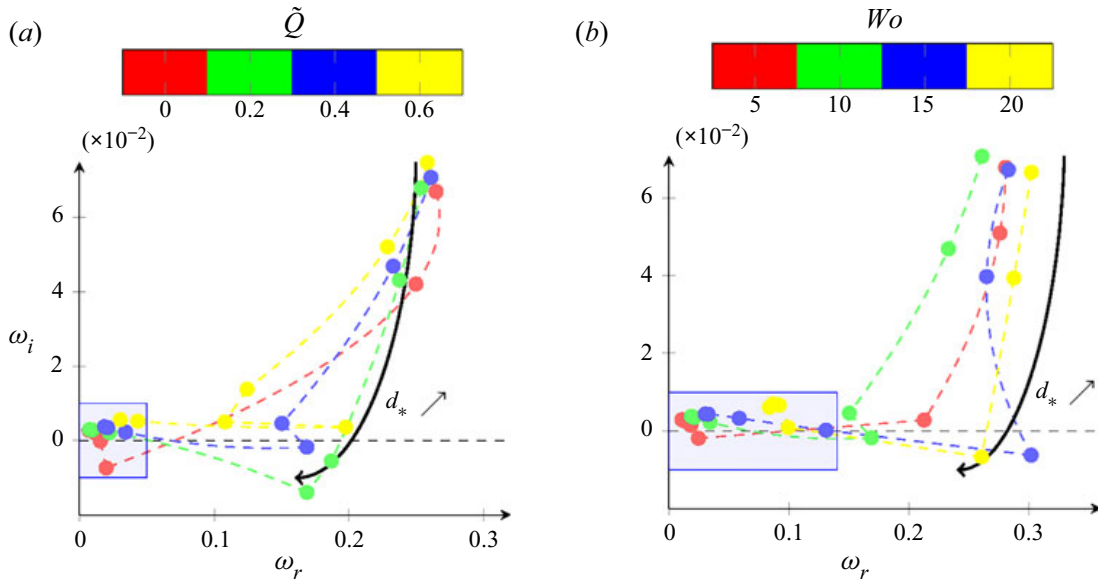


Figure 6. Spectra for the varicose symmetry with $Re = 10\,000$, $\alpha = 0.5$, $B_* = 4$ and $V_R = 2$; (a) $Wo = 10$ and $0 \leq \tilde{Q} \leq 0.6$, (b) $\tilde{Q} = 0.4$ and $5 \leq Wo \leq 20$ for $d_* = 0, 1, 5, 10, 15, 20$ and 25 . The mode trajectories are displayed by dashed lines. The shaded region indicates the regime dominated by the DIV mode.

The critical value of d_* for this regime change is seen to increase with \tilde{Q} : $5 \leq d_* \leq 10$ for $\tilde{Q} = 0$ and $15 \leq d_* \leq 20$ for $\tilde{Q} = 0.6$. As soon as the regime is driven by the DIV mode, its temporal amplification rate ω_i is seen to increase with \tilde{Q} . The effect of Wo is illustrated in panel (b). The figure shows that the onset of the DIV mode for the range of Womersley numbers investigated occurs for $10 \leq d_* \leq 15$. It also shows that ω_i and ω_r increase with Wo for the DIV mode.

Although the dynamics of the different modes is influenced by the pulsatile base-flow parameters, the above discussion suggests similarities between the steady case and our results. In particular, for the parameters that have been considered, the distinction

made between class A and B modes by Benjamin (1963), Landahl (1962) and Carpenter & Garrad (1985) still holds for our pulsatile flow case. However, we will see in the next section that this classification is clearly too restrictive for pulsatile base flows.

6.3. Wave superposition for sinuous Floquet mode

The Fourier density distributions for a sinuous Floquet mode associated with $V_R = 1$, $Wo = 10$, $Re = 10\,000$, $\alpha = 1$, $B_* = 4$ and $d_* = 0$ are shown in figure 7 together with the associated eigenvalues for $\tilde{Q} = 0.349$ and 0.350 . Both series of eigenvalues have positive growth rates. The figure shows the existence of two distinct peaks in the Fourier density distribution. This suggests that two different mechanisms influence this mode. To further illustrate this scenario, the different contributions of the total energy per Fourier mode are also reported in figure 7. For the E_n -distribution at $\tilde{Q} = 0.349$ (left curves), the main peak is due to the fluid kinetic energy contribution, associated with a dominant frequency of $\omega_r \simeq 0.26$. In contrast, for $\tilde{Q} = 0.350$, the wall contributions take over, leading to a dominant frequency of $\omega_r \simeq 0.52$. For both cases, the E_n -distributions are very similar, but the exchange in dominant peaks due to a continuous modification of the distribution results in a sudden jump of the dominant frequency. This behaviour indicates that the intracyclic mechanism involves the interference between fluid-based (TS) and wall-based (TWF) modes. By contrast with the steady base-flow case, we can therefore no longer distinguish here between class A and class B modes. Moreover, figure 7 also shows that for $\tilde{Q} < 0.35$, the Floquet mode is mainly driven by its TS component. When \tilde{Q} is increased up to 0.35, the intracyclic growth is mainly due to its sTWF part. This new type of mode will be called hereafter a two-wave mode. For the same set of parameters, the influence of \tilde{Q} on the stability of the system is shown in figure 8. For comparison purposes, the rigid case is also reported. We restrict our analysis to the sinuous symmetry. For the compliant wall case, the evolution of both temporal growth rates and circular frequencies are displayed for the first and second most amplified Floquet modes. The dominant Floquet frequency for each mode is selected using the methodology mentioned in the previous section. The TS mode distribution is seen to closely follow its rigid wall counterpart up to $\tilde{Q} = 0.3$. When \tilde{Q} exceeds this value, however, its E_n -distribution exhibits two peaks and the mode consists of the superposition of TS and TWF waves (as illustrated in figure 7). For \tilde{Q} greater than 0.35 the energy peak is connected to the TWF wave. At this point, the dominant frequency for this mode is associated with the wall dynamics, as shown by the energy contributions in figure 7. For \tilde{Q} up to 0.5, we observe the co-existence of TWF and two-wave modes. For $0.5 < \tilde{Q} < 0.6$, the two-wave mode is seen to be temporally damped. By contrast, the growth rate of TWF mode is increased for this range of \tilde{Q} . For larger values of \tilde{Q} , the spectrum features a single unstable mode that shares the main characteristics of TWF modes.

In the next section, we will describe the spatio-temporal behaviour of Floquet eigenfunctions, for TWF, TS and two-wave modes.

6.4. Spatial structure of eigenmodes

The structure of TS and FSI Floquet modes are investigated in more detail by monitoring the wall-normal distribution of their flow kinetic energy. To that end, we define the fluid

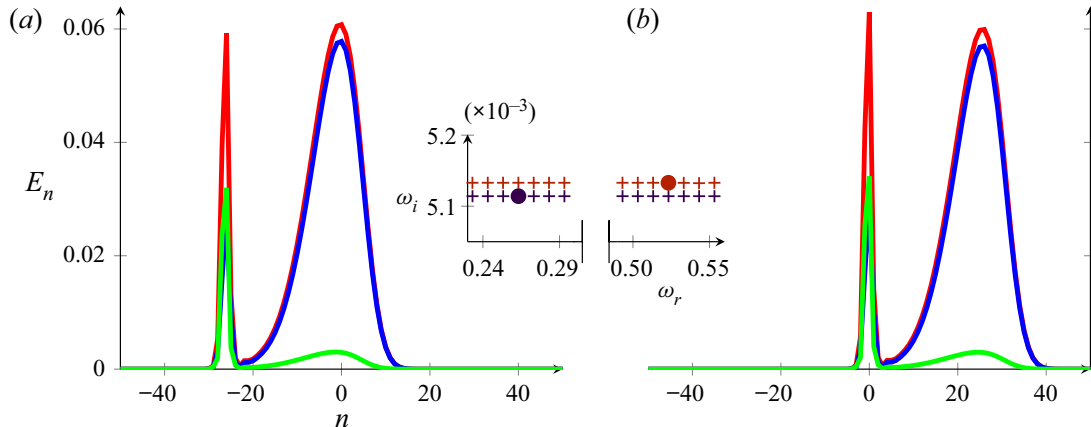


Figure 7. Energy per Floquet modes (red for total energy, blue for fluid kinetic energy, green for the wall potential and kinetic energy) at $\tilde{Q} = 0.349$ (left) and $\tilde{Q} = 0.350$ (right) with $V_R = 1$, $Wo = 10$, $Re = 10\,000$, $\alpha = 1$, $B_* = 4$ and $d_* = 0$. The frequency associated with the dominant peak is indicated by \bullet .

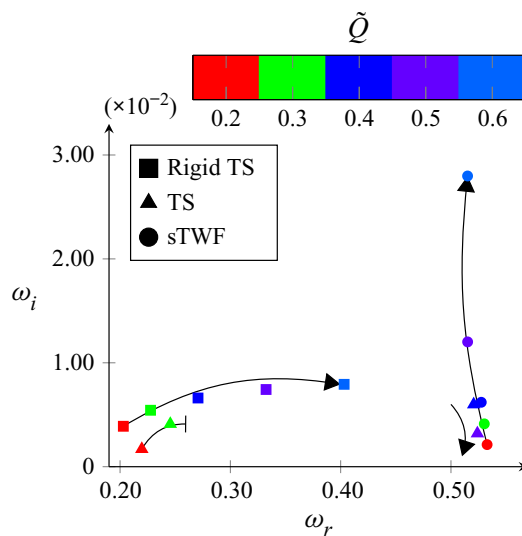


Figure 8. Spectra for different \tilde{Q} with $V_R = 1$, $Wo = 10$, $Re = 10\,000$, $\alpha = 1$, $B_* = 4$ and $d_* = 0$.

kinetic energy of the Floquet mode (4.13)–(4.16) as

$$\hat{E}(y, t) = \frac{1}{2}\rho \left| \sum_n \hat{\mathbf{u}}^{(n)}(y) \exp(in\Omega t) \right|^2, \quad (6.2)$$

which is periodic in time and may be used to characterise the intracyclic dynamics, since it does not contain the long-term exponential growth (or decay) part.

First, we will discuss the temporally averaged energy distribution, obtained as

$$\bar{E}(y) = \frac{1}{T} \int_0^T \hat{E}(t, y) dt. \quad (6.3)$$

In figure 9(b), $\bar{E}(y)$ is shown for the TS mode for $Wo = 10$, $\tilde{Q} = 0.2$, $Re = 10\,000$, $\alpha = 1$, $B_* = 4$, $d_* = 0$ and $V_R = 1$. For comparison purposes, the rigid wall and steady base-flow cases are also reported in figure 9(a).

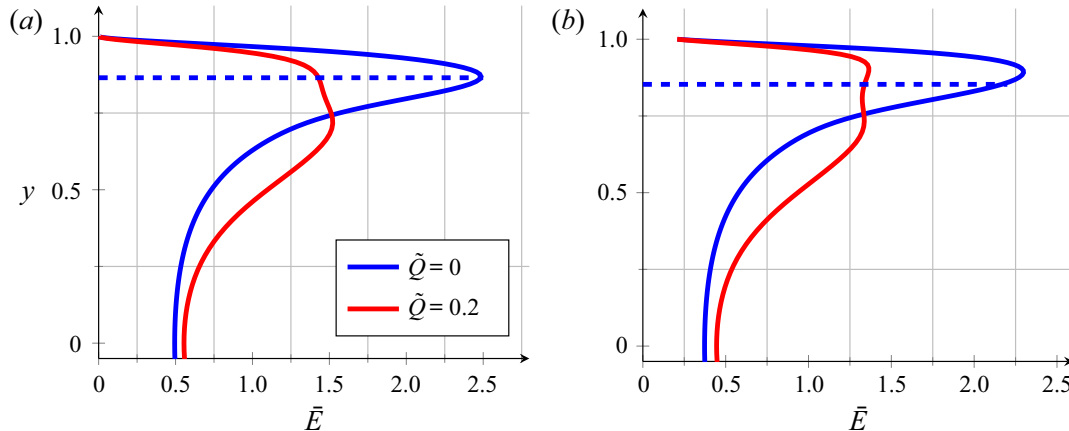


Figure 9. The wall-normal distribution $\bar{E}(y)$ of averaged kinetic energy for the TS perturbations with $\tilde{Q} = 0, 0.2$, $Wo = 10$, $Re = 10\,000$, $\alpha = 1$, $B_* = 4$ and $d_* = 0$. The critical layer position is indicated by blue dashed lines. (a) Rigid channel and (b) compliant channel with $V_R = 1$.

We recall that, for the case of a Poiseuille flow between flat rigid walls, $\bar{E}(y)$ should peak around the critical layer, i.e. the wall-normal position where the phase speed equals the base-flow velocity (Drazin & Reid 1981), as shown in figure 9(a). For compliant walls and the steady flow case, a similar behaviour is observed (Davies & Carpenter 1997a), see figure 9(b). However, a slight shift near the wall is observed for the peak in kinetic energy as a consequence of the stabilising effect of the compliant wall on TS modes.

The distribution of $\bar{E}(y)$ for the time-periodic base flow exhibits a double peak structure for both the rigid wall and compliant wall cases (see red curves in figure 9). This behaviour has also been observed by Singer *et al.* (1989) for the same flow case by using linearised direct numerical simulations and assuming rigid walls. They have shown that, in a certain moment of the cycle, the mean-flow profile exhibits an inflection point. These authors came to the conclusion that this second peak is a consequence of changes in the base-flow profile during the cycle. Interestingly, figure 9 shows that the wall compliance favours the first peak over the second one. More recently, Tsigklifis & Lucey (2017) have observed that both peaks are enhanced during the cycle by wall compliance. However, since the eigenfunction does not vanish at $y = \pm h$ for a compliant channel, comparisons between rigid and compliant configurations are not straightforward. We also observe that the inner peak is shifted closer to the wall due to wall compliance (figure 9). This suggests that the stabilising effect of elastic walls on TS modes still holds for pulsatile base flows.

The wall-normal distributions of $\bar{E}(y)$ for both varicose and sinuous TWF modes are shown in figure 10 for the same set of parameters. While for the sinuous symmetry, the TWF mode exhibits no significant changes in comparison with the steady flow case, the vTWF mode displays clearly a different structure near the walls. Indeed, the amplitude of vTWF mode peaks near $y = 0.9$ for the pulsatile base-flow case, while it exhibits its maximum at the wall for the steady case. The consequences for the stability properties will be discussed in the next sections.

6.5. Temporal dynamics of Floquet eigenmodes

In this section, we investigate the intracyclic dynamics of the perturbations for the same configurations as in the previous section. For that purpose, we consider the instantaneous

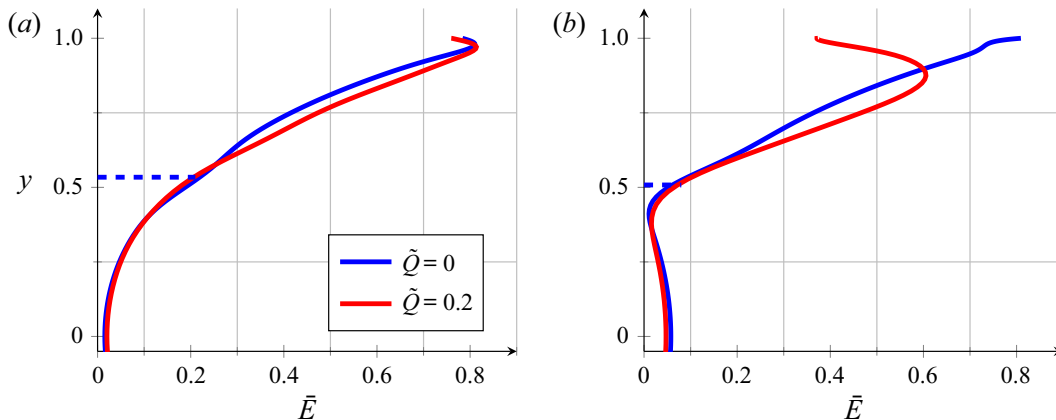


Figure 10. The wall-normal distribution of energy for TWF modes are shown for $\tilde{Q} = 0$ and 0.2 , $V_R = 1$, $Wo = 10$, $Re = 10\,000$, $\alpha = 1$, $B_* = 4$ and $d_* = 0$. (a) The sTWF mode and (b) the vTWF mode.

total perturbation energy, defined as

$$\tilde{E}(t) = \frac{1}{2h} \int_{-h}^h \hat{E}(y, t) dy + \tilde{E}_{WK}(t) + \tilde{E}_{WP}(t). \quad (6.4)$$

This quantity $\tilde{E}(t)$ is the sum of the instantaneous fluid kinetic energy and the kinetic and potential energies of the walls

$$\tilde{E}_{WK}(t) = m \left| \sum_n \hat{\gamma}^{\pm(n)} \exp(in\Omega t) \right|^2, \quad (6.5)$$

$$\tilde{E}_{WP}(t) = (B\alpha^4 + T\alpha^2 + K) \left| \sum_n \hat{\eta}^{\pm(n)} \exp(in\Omega t) \right|^2. \quad (6.6)$$

Recall that all these quantities are temporally periodic (with period Ω) since the complex exponential term $\exp(-i\omega t)$ has been removed. We first consider the TS mode. Figure 11 shows the different contributions to $\tilde{E}(t)$ for $Wo = 10$, $\tilde{Q} = 0.2$, $Re = 10\,000$, $B_* = 4$, $d_* = 0$ and $\alpha = 1$ for both the rigid case and compliant walls with $V_R = 1$. As noted by Pier & Schmid (2017) for the rigid case, the growth of $\tilde{E}(t)$ occurs in the deceleration phase of the base flow (indicated by regions hatched in red along the t -axis), while decay occurs during the acceleration phase (hatched in blue). This remains true for the compliant wall configuration (figure 11b). Here, the definition of base-flow acceleration or deceleration phases is based on the sign of dQ/dt . In particular, the dynamics of the perturbation is mainly driven by the flow kinetic energy while the wall energy is almost negligible. A similar behaviour has also been observed by Tsigklifis & Lucey (2017), who have shown that the kinetic energy of the flow mostly contributes to the total energy of the system for the TS mode.

The intracyclic dynamics associated with TWF disturbances exhibits a markedly different behaviour, as shown in figure 12. In contrast to the TS mode, the growth in total energy occurs during the acceleration phase of the base flow for both symmetries. In particular, walls mainly contribute to the total energy growth whatever the symmetry that is considered. However, the contribution to the total perturbation energy of the fluid kinetic energy is lower for the varicose case than the sinuous one.

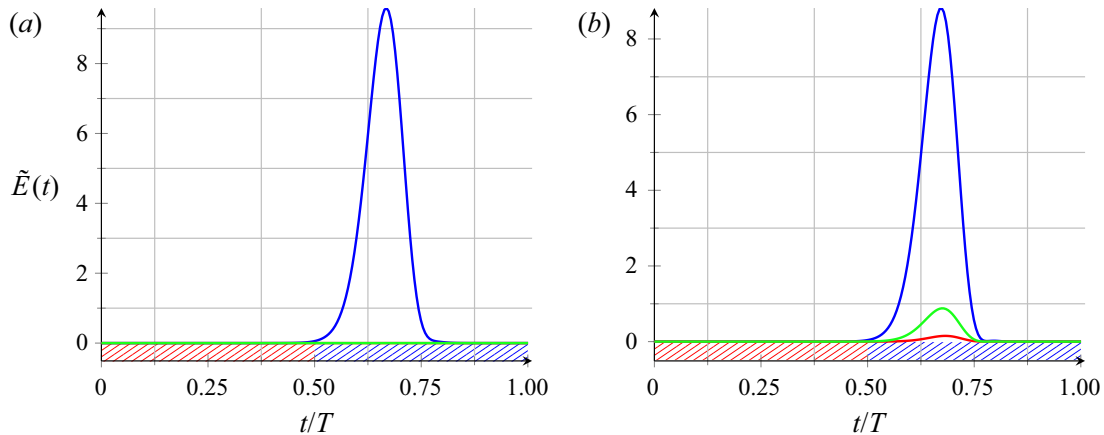


Figure 11. The intracyclic modulation of energy for the TS perturbations with $\tilde{Q} = 0.2$, $Wo = 10$, $Re = 10\,000$ and $\alpha = 1$. Colours: blue for the fluid kinetic energy, green for the wall kinetic energy, red for wall potential energy. (a) Rigid channel, (b) compliant channel with $B_* = 4$, $d_* = 0$ and $V_R = 1$.

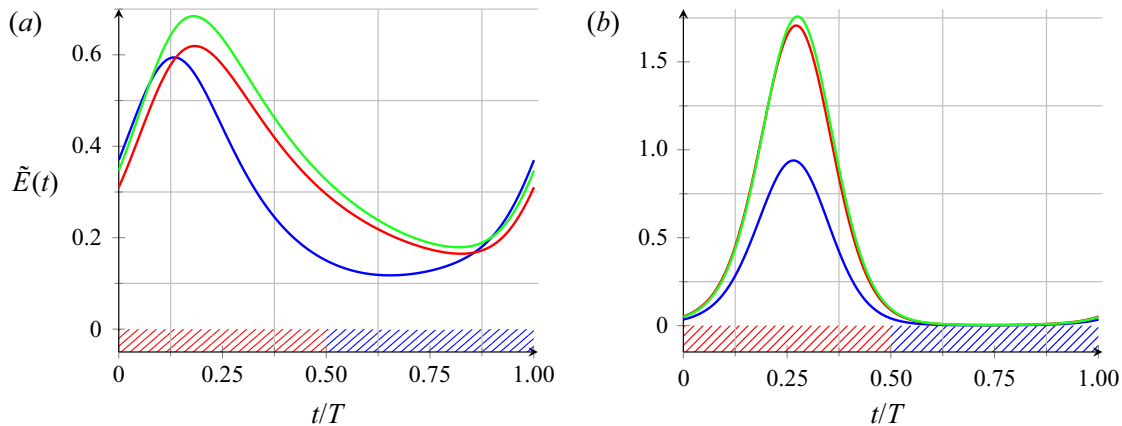


Figure 12. The intracyclic modulations of energy for the TWF perturbations with $\tilde{Q} = 0.2$, $V_R = 1$, $Wo = 10$, $Re = 10\,000$, $\alpha = 1$, $B_* = 4$ and $d_* = 0$. (a) The sTWF mode and (b) the vTWF mode.

6.6. Interaction between TS and sTWF waves

As mentioned earlier, a two-wave mode (i.e. where both sTWF and TS waves interact) may emerge for a given set of parameters.

Here, we will further investigate the occurrence of this Floquet mode. For that purpose, the parameters $Wo = 10$, $B_* = 4$, $d_* = 0$, $V_R = 1$ and $\alpha = 1$ are considered, and the Reynolds number is fixed at $Re = 10\,000$.

In figure 13, the variations with \tilde{Q} of the temporal growth rates ω_i and the circular frequencies ω_r for TS, sTWF and two-wave modes are shown. For the two-wave mode, the variation of ω_r is displayed for the two frequencies associated with the two peaks, as illustrated in figure 7. Figure 13(a) shows that the temporal growth rates of TS and sTWF follow similar paths for $\tilde{Q} = 0.25–0.45$ until their divergence beyond $\tilde{Q} = 0.46$. Within the range $0.28 \leq \tilde{Q} \leq 0.46$, indicated in light blue, the TS Floquet mode exhibits a second peak in its Fourier energy density distribution, which signals a transition to a two-wave mode. In particular, it is observed in figure 13(b) that one peak displays a characteristic frequency in continuity with the sTWF mode, while the second peak follows the value of

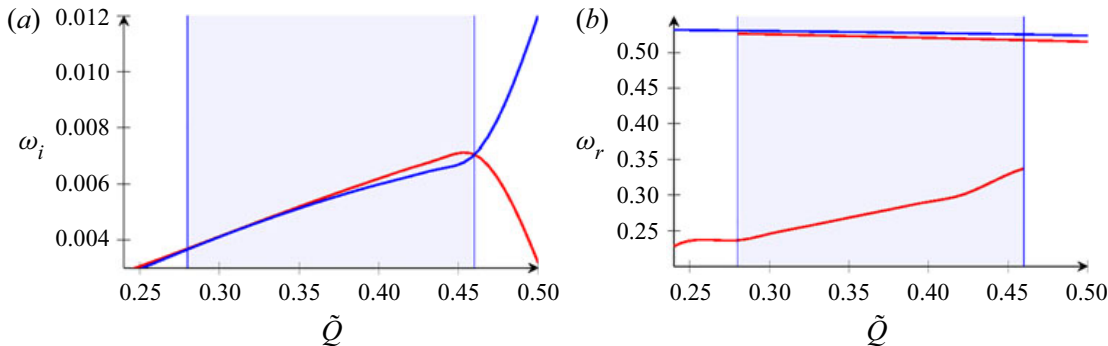


Figure 13. Evolution of (a) temporal growth rates ω_i and (b) circular frequencies ω_r with \tilde{Q} for $V_R = 1$, $Wo = 10$, $Re = 10\,000$, $\alpha = 1$, $B_* = 4$ and $d_* = 0$ (blue for sTWF, red for TS/two-wave mode). The shaded area represents the region where the two-wave mode exists.

ω_r closely corresponding to the TS mode. For $\tilde{Q} \geq 0.46$, the two-wave mode vanishes and only a single peak survives, corresponding to ω_r matching the sTWF mode.

To better illustrate the temporal dynamics associated with the two-wave mode, we show in figure 14 the intracyclic evolution of the total perturbation energy $\tilde{E}(t)$ for different pulsation amplitudes \tilde{Q} and the sinuous symmetry. On the one hand, the TWF mode exhibits almost no effect as \tilde{Q} is increased in the range 0.38–0.48 for both Reynolds numbers. On the other hand, the two-wave mode presents an interesting intracyclic dynamics.

At $\tilde{Q} = 0.38$, growth occurs for both the acceleration and deceleration phases of the base flow. This is consistent with the fact that this Floquet mode shares common features with both TS and TWF waves. When increasing \tilde{Q} , the growth associated with the acceleration phase increases. On the contrary, figure 14 shows that the energy peak in the deceleration phase is damped with \tilde{Q} . It means that the two-wave mode is mainly driven by its TWF contribution as \tilde{Q} is increased from 0.38 to 0.48. In particular, beyond $\tilde{Q} = 0.46$, the TS wave contribution is negligible, consistent with results reported in figure 13. As a consequence, at $\tilde{Q} = 0.46$, the variation of $\tilde{E}(t)$ for TWF and two-wave modes are almost indistinguishable. Beyond $\tilde{Q} = 0.46$, this mode shows the same characteristics as the TWF instabilities, namely, a growth of energy in the acceleration phase of the base flow. The intracyclic behaviour associated with the two-wave mode displays a low-frequency beating during the deceleration phase of the base flow for $0.28 \leq \tilde{Q} \leq 0.46$ (see figure 14). This phenomenon results from an interference between two waves of slightly different frequencies associated with the two peaks in the spectral energy distribution, as shown in figure 15(a) for $\tilde{Q} = 0.38$. The difference between the two peaks indeed corresponds exactly to the frequency beating observed in figure 15(b). To further illustrate this point, $\tilde{E}(t)$ has been computed by filtering the Fourier components in the neighbourhood of either the TS wave or the sTWF wave, using components from the ranges hatched respectively in fuchsia or orange in figure 15(a). The plots of figure 15(b) show that intracyclic dynamics pertaining to either the TS wave or the sTWF wave is recovered and the beating phenomenon is then suppressed.

6.7. Influence of \tilde{Q} and Wo on temporal growth rates

In this section, we investigate the combined effect of wall flexibility and pulsatile base-flow parameters (\tilde{Q} and Wo) on the temporal growth rates of TWF and TS Floquet modes.

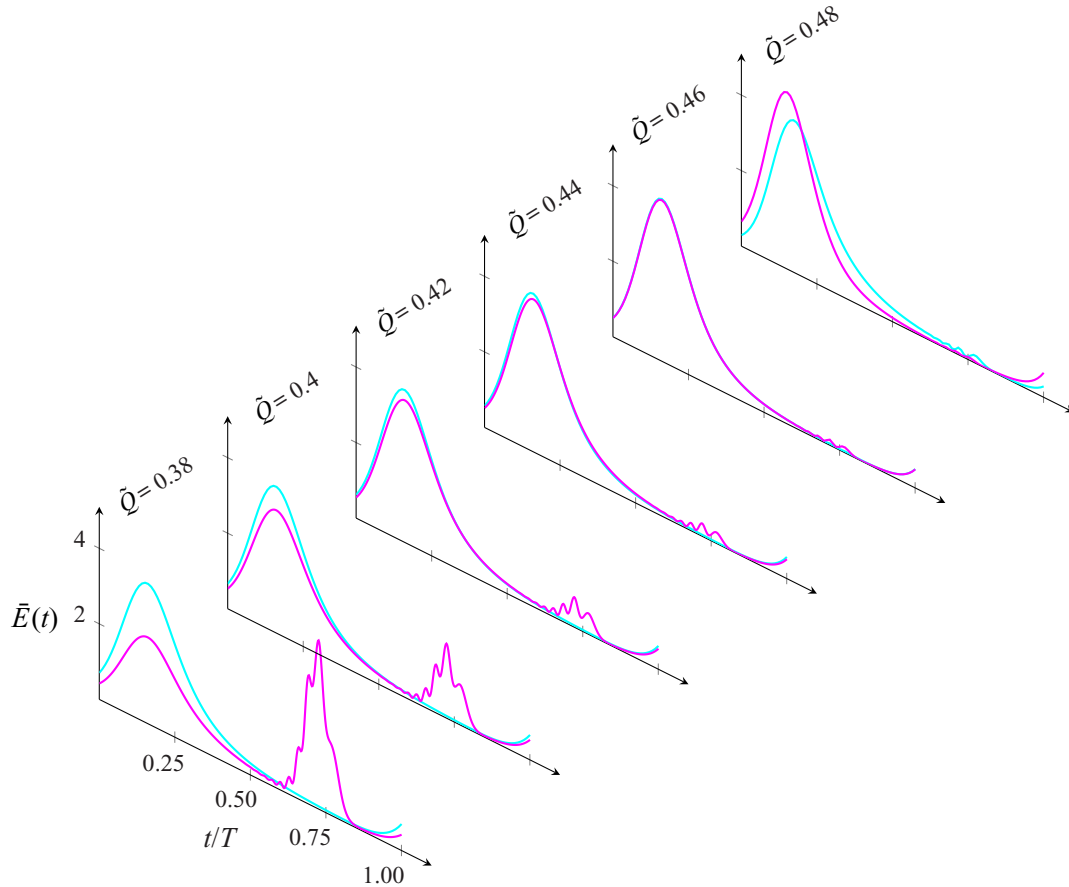


Figure 14. Intracyclic evolution of the total perturbation energy $\tilde{E}(t)$ with $V_R = 1$, $Wo = 10$, $Re = 10\,000$, $\alpha = 1$, $B_* = 4$ and $d_* = 0$ (cyan for sTWf and fuchsia for TS).

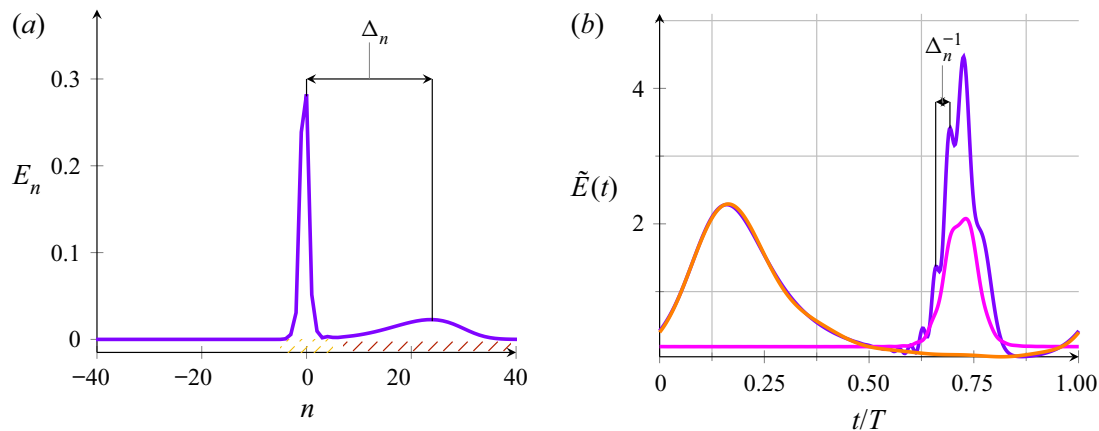


Figure 15. (a) Fourier density distribution and (b) filtered intracyclic total energy for the two-wave mode with $\tilde{Q} = 0.38$, $V_R = 1$, $Wo = 10$, $Re = 10\,000$, $\alpha = 1$, $B_* = 4$ and $d_* = 0$. Blue, full dynamics; fuchsia, TS wave dynamics; and orange, sTWf wave dynamics.

Results are conveniently summarised by monitoring the growth rate ω_i^{\max} associated with the most unstable streamwise instability (i.e. $\omega_i^{\max} = \max_{\alpha} \omega_i$) for a given set of fluid and wall parameters. For illustration purposes, $B_* = 4$ and $d_* = 0$ are fixed.

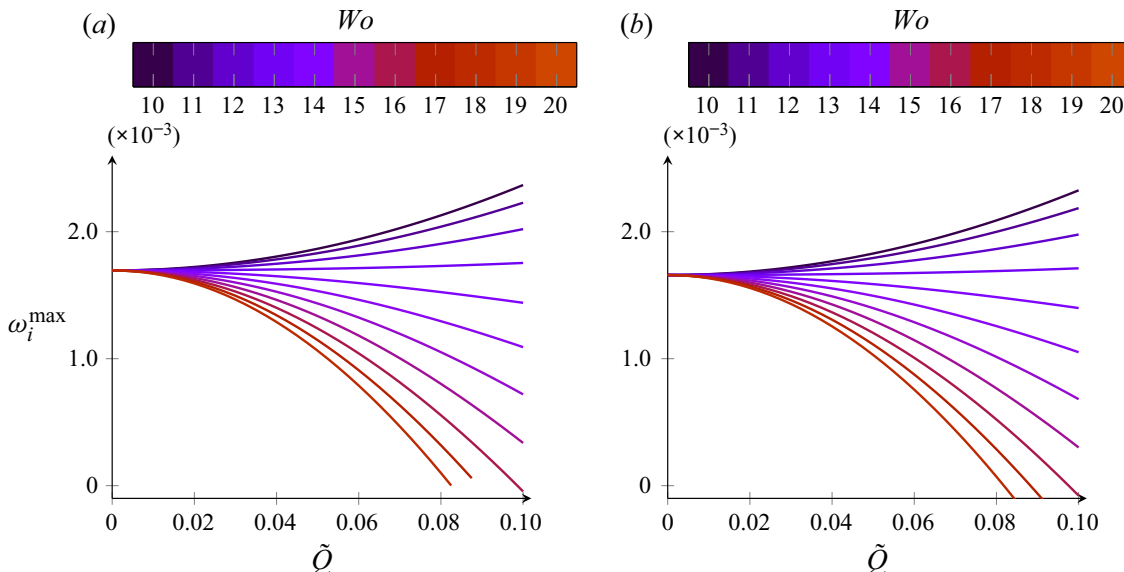


Figure 16. The TS Floquet mode. Maximum temporal growth rates ω_i^{\max} for different amplitudes $\tilde{Q} = 0, \dots, 0.1$ and frequencies $Wo = 10, \dots, 20$, with $Re = 10\,000$, $B_* = 4$ and $d_* = 0$. (a) Rigid wall and (b) $V_R = 0.2$.

Figures 16(a) and 16(b) show the variation of the maximum temporal growth rates with \tilde{Q} and Wo of the TS mode for both the rigid case in (a) and compliant walls ($V_R = 0.2$) in (b).

The TS Floquet modes exhibit a similar dynamics whatever the case considered (either rigid or compliant walls). For $Wo \geq 14$, the temporal growth rate decays with \tilde{Q} for both rigid and flexible cases while it increases for $Wo \leq 13$. One may recall that a similar behaviour is observed for the rigid case (Pier & Schmid 2017).

Figure 17 illustrates the effect of Wo and \tilde{Q} on TWF Floquet modes for $V_R = 1$. The temporal growth rate for the varicose vTWF mode presents two distinguishable phases (figure 17a). For small and moderate values of \tilde{Q} , ω_i^{\max} is damped. Then, one may observe a growth of ω_i^{\max} as \tilde{Q} increases. The turning point depends on the Womersley number. In particular, the corresponding \tilde{Q} is seen to increase with Wo .

The distribution of ω_i^{\max} for the sinuous symmetry exhibits a different behaviour. For weakly pulsatile base flows ($\tilde{Q} < 0.2$), the sTWF mode is destabilised whatever the Wo considered. In particular, this instability is strongly enhanced for the small frequencies of modulation Wo . For moderate values of \tilde{Q} ($0.2 < \tilde{Q} < 0.5$), a more complex behaviour is observed. For this range of amplitudes, the sTWF mode interacts with the TS Floquet mode, and we can no longer distinguish between these two waves. Beyond this point, ω_i^{\max} strongly increases and reaches similar values as its varicose counterpart. An intracyclic modulation amplitude E_{\min}^{\max} , defined as the ratio of the maximum to the minimum of $\tilde{E}(t)$, is computed for the same parameter range as in figure 17, for TWF Floquet modes only. For the varicose symmetry, the plots in figure 18(a) show that E_{\min}^{\max} increases for all Wo under consideration. The evolution of E_{\min}^{\max} for the sinuous symmetry is displayed in figure 18(b). The figure shows that the sTWF Floquet modes exhibit smaller-amplitude variations than their varicose counterparts. In addition, for $\tilde{Q} > 0.5$, a saturation of E_{\min}^{\max} is observed. Such a behaviour occurs beyond the collapse of TWF and TS Floquet modes. One may thus suggest that it is a consequence of the emergence of a transition mode. Comparison with

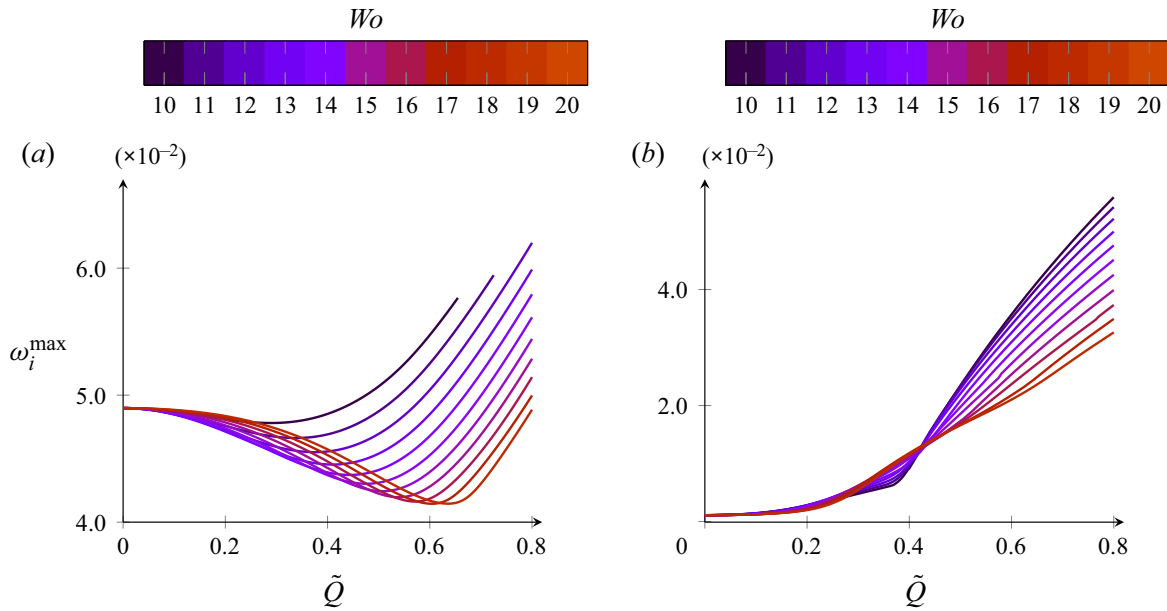


Figure 17. Maximal temporal growth rates ω_i^{\max} for different amplitudes $\tilde{Q} = 0, \dots, 0.7$ and frequencies $Wo = 10, \dots, 20$, with $Re = 10\,000$, $B_* = 4$ and $d_* = 0$; (a) vTWF $V_R = 1$ and (b) sTWF $V_R = 1$.

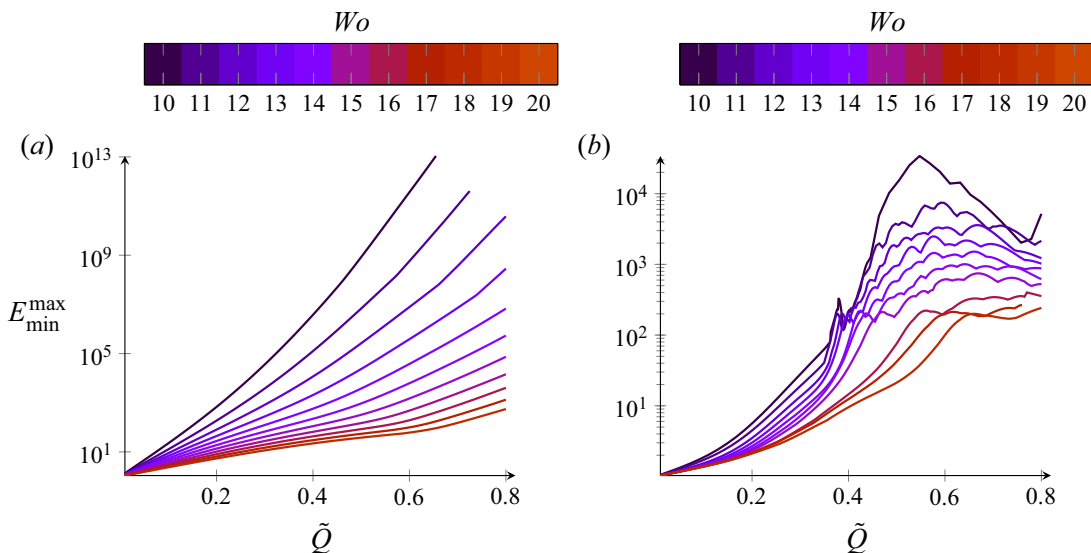


Figure 18. The amplitude of the modulation ratio E_{\min}^{\max} for different amplitudes $\tilde{Q} = 0, \dots, 0.7$ and frequencies $Wo = 10, \dots, 20$, with $Re = 10\,000$, $B_* = 4$, $d_* = 0$ and $V_R = 1$; (a) vTWF modes and (b) sTWF modes.

figure 12 also reveals that the very large values of E_{\min}^{\max} observed for the vTWF modes (figure 18a) are mainly due to the fact that $\tilde{E}(t)$ drops to extremely low levels during the acceleration phase of the pulsating cycle (figure 12b).

6.8. Critical parameters for onset of instability

A complete two-dimensional instability analysis is now performed by exploring a wide range of wall and flow parameters. In a effort to summarise the different results, only critical Reynolds numbers (Re^c) and critical reduced velocities (V_R^c) are monitored (corresponding to the onset of TS or TWF and DIV Floquet modes, respectively).

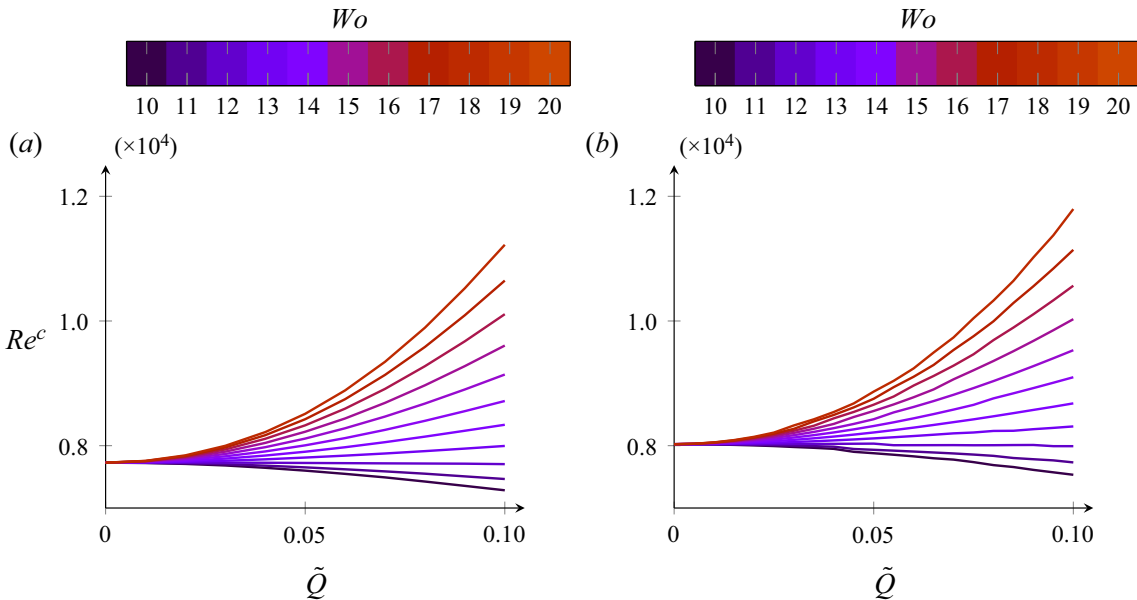


Figure 19. Critical Reynolds number Re^c for TS mode with $B_* = 4$ and $d_* = 0$; (a) $V_R = 0.2$ and (b) $V_R = 0.6$.

The variations of Re^c for the TS mode are computed for $V_R = 0.2$ and $V_R = 0.6$ for different pulsatile flow parameters in figure 19. Beyond $Wo = 13$, the TS Floquet modes are stabilised by the pulsatile flow component. For lower frequencies, the opposite behaviour is observed. For example, at $Wo = 20$, the critical Reynolds number for $\tilde{Q} = 0.10$ is already approximately 50 % larger than the value found for the Poiseuille flow case ($\tilde{Q} = 0$). The dynamics including compliant walls is thus found to be very similar to the rigid walls case (see Pier & Schmid 2017). The critical reduced velocity V_R^c for the TWF modes are shown in figure 20. The varicose TWF displays two phases. For moderate pulsation amplitudes ($\tilde{Q} < 0.4$), the instability is weakly stabilised. For higher pulsation amplitudes, the vTWF mode is destabilised for all the frequencies studied. Unlike the vTWF, the sTWF mode shows a monotonic destabilisation as the pulsation amplitude is increased. The Womersley numbers considered here have almost no effect on the critical curves. Note that even for highly pulsatile flows, onset of TWF instability is always due to the varicose symmetry.

In order to systematically study the linear stability over the entire parameter space, the critical reduced velocity V_R^c is also computed for various wall dissipations d_* (figure 21), flexural rigidities B_* (figure 22) and Reynolds numbers Re (figure 23).

According to the energy classification of Benjamin (1963) and Landahl (1962), the dissipation has a stabilising effect on the TWF instabilities. The plots in figure 21 show the variation of the critical reduced velocity with wall dissipation d_* . For a Poiseuille base flow ($\tilde{Q} = 0$), the critical V_R^c is almost multiplied by a factor 2 when d_* is varied from 0 to 0.02.

An increase in \tilde{Q} leads to stabilisation of the flow for all values of d_* that have been considered (see figure 21). In particular, the overall behaviour is quite similar for d_* varying from 0.005 to 0.04. The critical V_R^c is nearly constant for \tilde{Q} up to 0.05. Beyond this value, V_R^c decreases almost linearly with \tilde{Q} at a similar rate of change. Interestingly, the symmetry of the Floquet mode appears to have a negligible effect on V_R^c for this range of parameters.

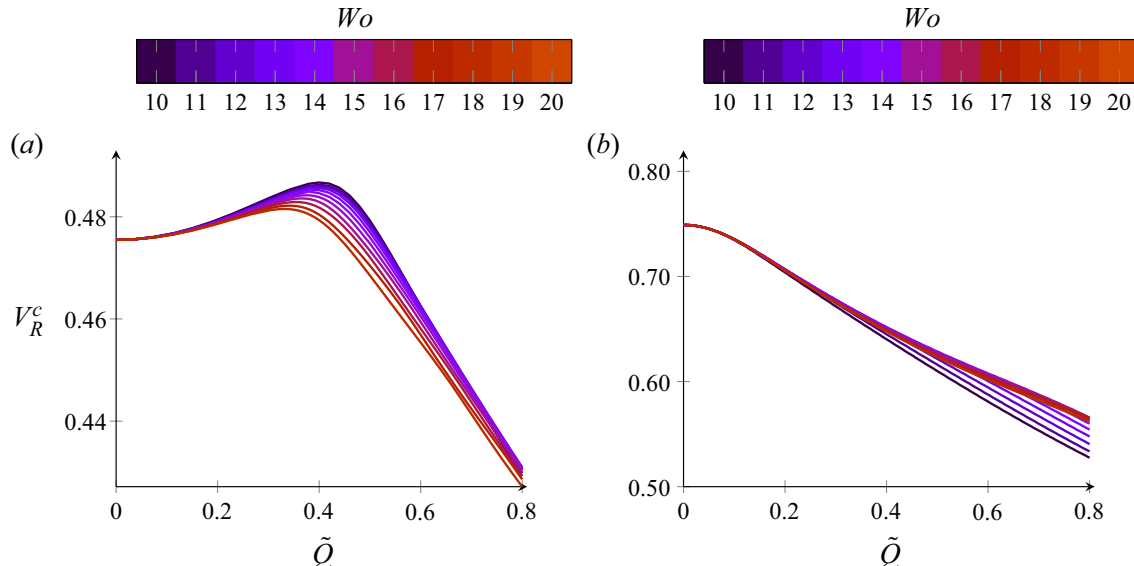


Figure 20. Critical reduced velocities V_R^c for TWF modes and different Wo . The other parameters are: $Re = 10\,000$, $B_* = 4$ and $d_* = 0$; (a) vTWF and (b) sTWF.

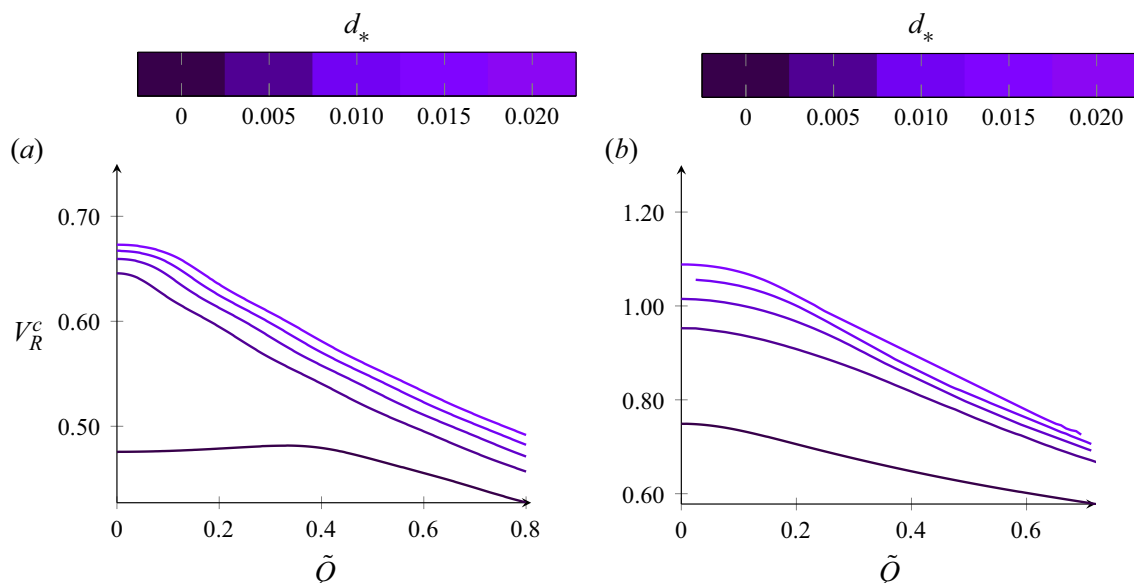


Figure 21. Critical reduced velocities V_R^c for TWF modes for different d_* . The other parameters are: $Wo = 20$, $Re = 10\,000$ and $B_* = 4$; (a) vTWF and (b) sTWF.

The effect of flexural rigidity is illustrated in figure 22. Increasing B_* results in stabilisation of the TWF Floquet modes for all \tilde{Q} that are considered. However, the overall shape of these curves is almost unaffected by B_* for both sinuous and varicose cases. For the varicose case, a nearly constant value of V_R^c is observed up to $\tilde{Q} = 0.3$. Beyond $\tilde{Q} = 0.4$, the critical V_R^c is seen to decrease almost linearly with \tilde{Q} for all flexural rigidities that have been investigated. In particular, the slope seems to be independent of B_* .

The sinuous case appears to be more stable than its varicose counterpart. As for the varicose symmetry, the overall tendency is not affected by B_* . A slight decrease in V_R^c is observed for \tilde{Q} up to 0.1. Beyond $\tilde{Q} = 0.4$, V_R^c exhibits an almost linear behaviour with \tilde{Q} .

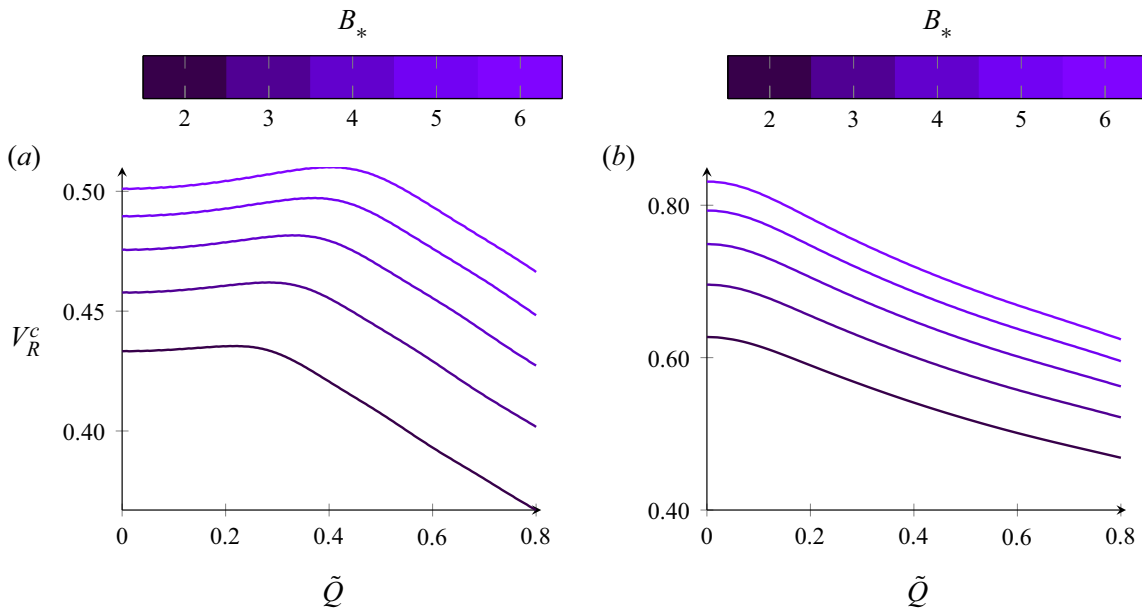


Figure 22. Critical V_R^c for TWF modes for different B_* . The other parameters are: $Wo = 20$, $Re = 10\,000$ and $d_* = 0$; (a) vTWF and (b) sTWF.

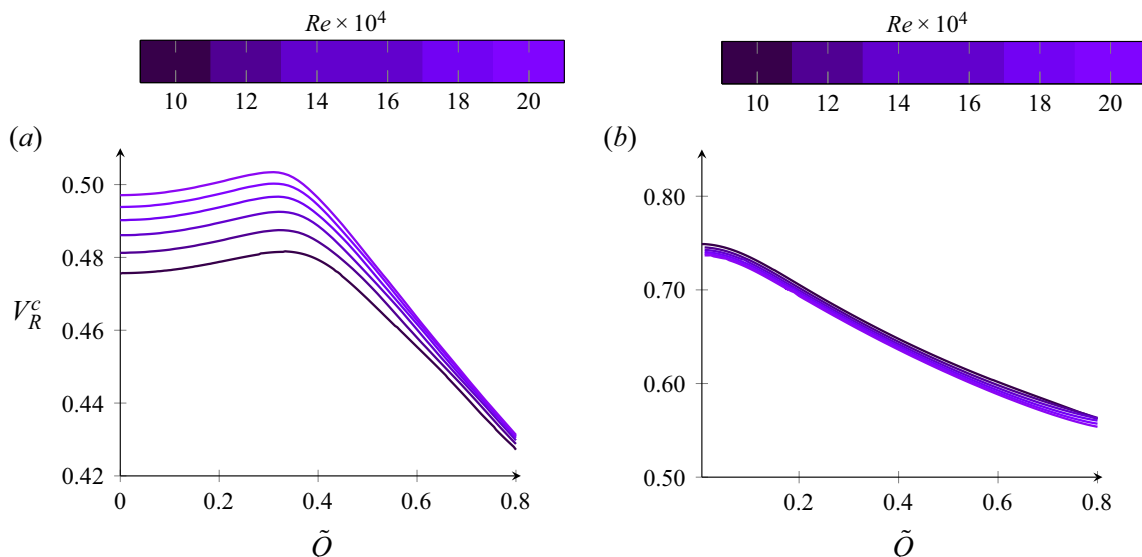


Figure 23. Critical V_R^c for TWF modes for different Re numbers. The other parameters are: $Wo = 20$, $B_* = 4$ and $d_* = 0$; (a) vTWF and (b) sTWF.

The influence of the Reynolds number on V_R^c is shown in figure 23. The onset of Floquet TWF modes is almost unchanged by the Reynolds number for both the varicose and sinuous TWF modes. The insensitivity to Re is more pronounced when \tilde{Q} is increased to large amplitudes. This weak influence has already been reported for the steady case (Lebbal *et al.* 2022).

Finally, in an effort to summarise the influence of the pulsatile base-flow parameters on the DIV mode, we show in figure 24 the critical reduced velocity as a function of Wo for \tilde{Q} varying from 0.0 to 0.6 for $d_* = 15$ and $Re = 10\,000$. The existence of the DIV mode has been documented in figure 6 for this wall dissipation. The figure shows that, for low values of the Womersley number, V_R^c increases with \tilde{Q} . This suggests that the pulsatile base flow

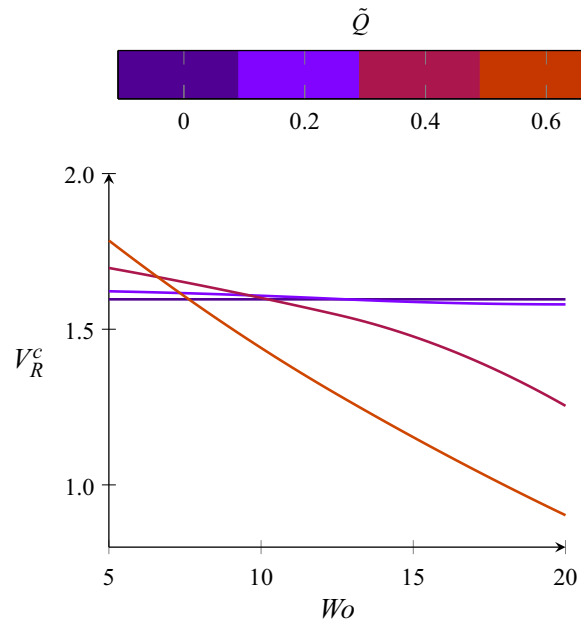


Figure 24. Critical V_R^c for the varicose DIV mode for different Wo and \tilde{Q} . The other parameters are: $Re = 10\,000$, $B_* = 4$ and $d_* = 15$.

has a stabilising effect on the DIV mode for this range of parameters. For Wo beyond 10, the opposite behaviour is observed for all \tilde{Q} that are investigated.

7. Conclusions and discussion

In this paper, we have investigated the dynamics resulting from perturbations developing in harmonically pulsating flows between two compliant walls. The stability analysis is restricted to the time-asymptotic behaviour of the perturbation and to the two-dimensional case within the framework of Floquet theory. A numerical solution strategy has been implemented that is free of spurious modes and greatly reduces the computational effort.

When accounting for wall compliance, we show that the most relevant control parameter is the reduced velocity V_R for TWF Floquet modes. In particular, the Reynolds number appears to have a negligible influence on these modes. As already observed for the steady case (Lebbal *et al.* 2022), the most unstable modes are associated with the varicose symmetry. For the pulsatile flow configurations, we show that the instability onset for these modes is mainly driven by the amplitude of the pulsation rather than its frequency. For \tilde{Q} in the range 0–0.4 and varicose perturbations, the pulsatile base flow is seen to weakly stabilise the TWF Floquet modes (i.e. the critical reduced velocity increases) with respect to the steady flow case. The opposite behaviour is observed for \tilde{Q} larger than 0.4. For the sinuous symmetry, we always observe a flow destabilisation with an increase of \tilde{Q} . When accounting for the wall dissipation, we show that a slight increase of d_* tends to stabilise the TWF Floquet modes for both symmetries whatever the value of \tilde{Q} , in agreement with Benjamin's classification (Benjamin 1963). For the TS Floquet modes, the intracyclic dynamics exhibits strong similarities with the pulsatile flow case in a rigid channel (Pier & Schmid 2017). However, a stronger stabilisation is observed when wall flexibility comes into play. For a significant amount of wall dissipation ($d_* \geq 10$), the onset of the DIV mode is also observed. Although restricted to only the varicose symmetry, we have shown that, for low values of Wo (≈ 5), an increase of \tilde{Q} stabilises the DIV mode, whereas the opposite behaviour is observed for larger values of Wo .

On the one hand, it has been shown that Benjamin's classification still holds for a wide range of parameters. In particular, for fluid–structure interaction modes, similar general trends are observed for steady and pulsatile flow configurations. However, on the other hand, this study has also revealed a more complex flow dynamics that is not found when wall flexibility or pulsating base flows are studied independently. In particular, for some range of Wo and \tilde{Q} a new type of mode has been discovered that shares characteristics of two distinct Floquet modes. This two-wave mode combines properties of both TS and TWF modes. It leads to an interference that generates a beating during the intracyclic dynamics.

To address the practical or experimental relevance of the present findings, we consider the analogy derived by Carpenter & Garrad (1985) for a Kramer-type compliant wall, using the test case detailed by Wiplier & Ehrenstein (2000) for a boundary-layer flow. Using the parameter values used in these papers, corresponding to natural rubber, a non-dimensional reduced velocity of approximately $V_R = 0.4$ is obtained when considering the characteristic flow advection time scale based on the free-stream velocity and the δ_{99} boundary-layer thickness (where the velocity reaches 99 % of the free-stream value). For such a configuration, Wiplier & Ehrenstein (2000) observed the onset of a TWF mode. In order to estimate the value of V_R prevailing in physiological configurations, an approximate value of the equivalent spring stiffness K is required. Considering that a diastole–systole pressure difference of 40 mmHg produces a 2 mm deformation of the main arterial walls (Nichols, O'Rourke & Vlachopoulos 2011), this leads to $K \simeq 3 \cdot 10^6 \text{ kg m}^{-3} \text{ s}^{-2}$. Then, with typical values for blood flow rate and arterial diameters, reduced velocities V_R in the range 0.1–0.2 are obtained. These values are slightly below those required to trigger the different unstable modes that we have investigated here, but they are nonetheless of the same order of magnitude. Also, we recall that the Womersley numbers explored here are in the range of those encountered in blood flow. Thus, we conclude that it is plausible that the instability modes studied here indeed participate in the dynamics of practical configurations.

Extension of the present study to non-modal stability analyses can be considered in a future work, continuing the investigations of Tsigklifis & Lucey (2017) and Pier & Schmid (2021). Finally, it would also be interesting to generalise our analyses to pipe geometries which cover more biologically significant settings. The theoretical developments and numerical tools that have been used in the present investigation can be easily adapted to a formulation in cylindrical coordinates, following the same approach used by Pier & Schmid (2021). A Kramer-type wall could be implemented for cylindrical configurations, using the shell theory developed by Demyanko (2021) for the stability of flows in compliant pipes.

Acknowledgements. Pôle de modélisation et de calcul en sciences de l'ingénieur et de l'information (PMCS2I) of École centrale de Lyon is gratefully acknowledged for providing access to high-performance computing resources.

Declaration of interests. The authors report no conflict of interest. For the purpose of Open Access, the authors have applied a CC-BY public copyright licence to any Author Accepted Manuscript (AAM) version arising from this submission.

Author ORCIDs.

- ⓘ Smail Lebbal <https://orcid.org/0000-0003-4054-6094>;
- ⓘ Frédéric Alizard <https://orcid.org/0000-0002-1741-1602>;
- ⓘ Benoît Pier <https://orcid.org/0000-0001-8663-8694>.

REFERENCES

- BENJAMIN, T.B. 1959 Shearing flow over a wavy boundary. *J. Fluid Mech.* **6**, 161–205.
- BENJAMIN, T.B. 1960 Effects of a flexible boundary on hydrodynamics stability. *J. Fluid Mech.* **9**, 513–532.
- BENJAMIN, T.B. 1963 The threefold classification of unstable disturbances in flexible surfaces bounding inviscid flows. *J. Fluid Mech.* **16**, 436–450.
- BLENNERHASSETT, P.J. & BASSOM, A.P. 2006 The linear stability of high-frequency oscillatory flow in a channel. *J. Fluid Mech.* **556**, 1–25.
- BOYD, J.P. 2001 *Chebyshev and Fourier Spectral Methods*. Dover.
- CARPENTER, P.W. & GARRAD, A.D. 1985 The hydrodynamic stability of flow over Kramer-type compliant surfaces. Part 1. Tollmien–Schlichting instabilities. *J. Fluid Mech.* **155**, 465–510.
- CARPENTER, P.W. & GARRAD, A.D. 1986 The hydrodynamic stability of flow over Kramer-type compliant surfaces. Part 2. Flow-induced surface instabilities. *J. Fluid Mech.* **170**, 199–232.
- CHIU, J.-J. & CHIEN, S. 2011 Effects of disturbed flow on vascular endothelium: pathophysiological basis and clinical perspectives. *Physiol. Rev.* **91**, 327–387.
- DAVIES, C. & CARPENTER, P.W. 1997a Instabilities in a plane channel flow between compliant walls. *J. Fluid Mech.* **352**, 205–243.
- DAVIES, C. & CARPENTER, P.W. 1997b Numerical simulation of the evolution of Tollmien–Schlichting waves over finite compliant panels. *J. Fluid Mech.* **335**, 361–392.
- DAVIS, S.H. 1976 The stability of time-periodic flows. *Annu. Rev. Fluid Mech.* **8**, 57–74.
- DEMYANKO, K.V. 2021 On using the shell theory in stability analysis of fluid flows in compliant pipes. *Comput. Math. Math. Phys.* **61**, 1444–1469.
- DOMARADZKI, J.A. & METCALFE, R.W. 1986 Stabilization of laminar boundary layers by compliant membranes. *Phys. Fluids* **30**, 695–705.
- DRAZIN, P.G. & REID, W.H. 1981 *Hydrodynamic Stability*. Cambridge University Press.
- GAD-EL-HAK, M. 1986 Boundary layer interactions with compliant coatings: an overview. *Appl. Mech. Rev.* **39**, 511–524.
- GAD-EL-HAK, M. 1996 Compliant coatings: a decade of progress. *Appl. Mech. Rev.* **49**, S147–S157.
- GASTER, M. 1988 Is the dolphin a red herring? In *IUTAM Symposium on Turbulence Management and Relaminarisation* (ed. H.W. Liepmann & R. Narasimha), pp. 285–304. Springer.
- GRAY, J. 1936 Studies in animal locomotion: VI. The propulsive powers of the dolphin. *J. Expl Biol.* **13**, 192–199.
- VON KERCZEK, C.H. 1982 The instability of oscillatory plane Poiseuille flow. *J. Fluid Mech.* **116**, 91–114.
- KRAMER, M. 1957 Boundary layer stabilization by distributed damping. *J. Aeronaut. Sci.* **24**, 459–505.
- KU, D.N. 1997 Blood flow in arteries. *Annu. Rev. Fluid Mech.* **29**, 399–434.
- KUMARAN, V. 2021 Stability and the transition to turbulence in the flow through conduits with compliant walls. *J. Fluid Mech.* **924**, P1.
- LANDAHL, M.T. 1962 On the stability of laminar boundary-layer flow over a flat plate with a compliant surface. *J. Fluid Mech.* **13**, 609–632.
- DE LANGRE, E. 2000 Analyse dimensionnelle en interaction fluide–structure. *La Houille Blanche* **3/4**, 14–18.
- LAROSE, P.G. & GROTBORG, J.B. 1997 Flutter and long-wave instabilities in compliant channels conveying developing flows. *J. Fluid Mech.* **331**, 37–58.
- LEBBAL, S., ALIZARD, F. & PIER, B. 2022 Revisiting the linear instabilities of plane channel flow between compliant walls. *Phys. Rev. Fluids* **7**, 023903.
- LUO, X.Y. & PEDLEY, T.J. 1996 A numerical simulation of unsteady flow in a two-dimensional collapsible channel. *J. Fluid Mech.* **314**, 191–225.
- MANNING, M.L., BAMIEH, B. & CARLSON, J.M. 2007 Descriptor approach for eliminating spurious eigenvalues in hydrodynamic equations. [arXiv:0705.1542](https://arxiv.org/abs/0705.1542).
- MILES, J.W. 1957 On the generation of surface waves by shear flows. *J. Fluid Mech.* **3**, 185–199.
- NICHOLS, W.W., O'ROURKE, M.F. & VLACHOPOULOS, C. 2011 *McDonald's Blood Flow in Arteries: Theoretical, Experimental and Clinical Principles*. CRC.
- O'ROURKE, M.F. & HASHIMOTO, J. 2007 Mechanical factors in arterial aging: a clinical perspective. *J. Am. Coll. Cardiol.* **50**, 1–13.
- PEYRET, R. 2002 *Spectral Methods for Incompressible Viscous Flow*. Springer.
- PIER, B. & SCHMID, P.J. 2017 Linear and nonlinear dynamics of pulsatile channel flow. *J. Fluid Mech.* **815**, 435–480.
- PIER, B. & SCHMID, P.J. 2021 Optimal energy growth in pulsatile channel and pipe flows. *J. Fluid Mech.* **926**, A11.
- SCHUMACK, M.R., SCHULTZ, W. & BOYD, J.P. 1991 Spectral method solution of the Stokes equations on nonstaggered grids. *J. Comput. Phys.* **94**, 30–58.

- SEN, P.K. & ARORA, D.S. 1988 On the stability of laminar boundary-layer flow over a flat plate with a compliant surface. *J. Fluid Mech.* **197**, 201–240.
- SHANKAR, V. & KUMARAN, V. 2002 Stability of wall modes in fluid flow past a flexible surface. *Phys. Fluids* **14**, 2324–2338.
- SINGER, B.A., FERZIGER, J.H. & REED, H.L. 1989 Numerical simulations of transition in oscillatory plane channel flow. *J. Fluid Mech.* **208**, 45–66.
- STRAATMAN, A.G., KHAYAT, R.E., HAJ-QASEM, E. & STEINMAN, D.A. 2002 On the hydrodynamic stability of pulsatile flow in a plane channel. *Phys. Fluids* **14**, 1938–1944.
- TSIGKLIFIS, K. & LUCEY, A.D. 2017 Asymptotic stability and transient growth in pulsatile Poiseuille flow through a compliant channel. *J. Fluid Mech.* **820**, 370–399.
- WIPLIER, O. & EHRENSTEIN, U. 2000 Numerical simulation of linear and nonlinear disturbance evolution in a boundary layer with compliant walls. *J. Fluids Struct.* **14**, 157–182.
- WOMERSLEY, J.R. 1955 Method for the calculation of velocity, rate of flow and viscous drag in arteries when pressure gradient is known. *J. Physiol.* **127**, 553–563.
- XU, D., HEIL, M., SEEBÖCK, T. & AVILA, M. 2020a Resonances in pulsatile channel flow with an elastic wall. *Phys. Rev. Lett.* **125**, 254501.
- XU, D., SONG, B. & AVILA, M. 2021 Non-modal transient growth of disturbances in pulsatile and oscillatory pipe flows. *J. Fluid Mech.* **907**, R5.
- XU, D., VARSHNEY, A., MA, X., SONG, B., RIEDL, M., AVILA, M. & HOF, B. 2020b Nonlinear hydrodynamic instability and turbulence in pulsatile flow. *Proc. Natl Acad. Sci. USA* **117**, 11233–11239.

[A31]

Transient energy growth in channel flow with compliant walls

F. Alizard, B. Pier & S. Lebbal

Physical Review Fluids **9**, 043905 (26 pages) (2024)

doi:10.1103/PhysRevFluids.9.043905
<https://hal.archives-ouvertes.fr/hal-04512520>

Transient energy growth in channel flow with compliant walls

Frédéric Alizard , Benoît Pier , and Smail Lebbal

Laboratoire de mécanique des fluides et d'acoustique, CNRS, École centrale de Lyon, Université de Lyon 1, INSA Lyon, 36 avenue Guy-de-Collongue, 69134 Écully, France



(Received 14 September 2023; accepted 19 March 2024; published 9 April 2024)

In this paper, we present a Lagrangian method for searching initial disturbances which maximize their total energy growth after a certain time horizon for linearized fluid-structure interaction problems. We illustrate this approach for the channel flow case with compliant walls. The walls are represented as thin spring-backed plates, the so-called Kramer-type walls. For nearly critical values of the control parameters (reduced velocity V_R and Reynolds number Re), analyses for sinuous or varicose perturbations show that the fluid-structure system can sustain two types of oscillatory motions of large amplitude. The first motion is associated with two-dimensional perturbations that are invariant in the spanwise direction. For that case and a certain range of streamwise wavenumbers, the short-time dynamics of sinuous perturbations is driven by the nonmodal interaction between the Tollmien-Schlichting and the traveling-wave flutter (TWF) modes. The amplitude of the oscillation is found to increase with the reduced velocity, and the optimal gain exhibits larger values than its counterpart computed for a channel flow between rigid walls. For perturbations of varicose symmetry, the transient energy is rapidly governed by the unstable TWF mode without a clear low-frequency oscillation. The second type of motion concerns streamwise-invariant and spanwise-periodic perturbations. In that situation, it is found that perturbations of sinuous symmetry exhibit the largest amplification factors. For moderate values of the reduced velocity, $V_R = \mathcal{O}(1)$, the dynamics is the result of a simple superposition of a standing wave, due to traveling-wave flutter modes propagating downstream and upstream, and the roll-streak dynamics. The variations of these oscillations with the reduced velocity, spanwise wavenumber, and Reynolds number are then investigated in detail for the sinuous case.

DOI: [10.1103/PhysRevFluids.9.043905](https://doi.org/10.1103/PhysRevFluids.9.043905)

I. INTRODUCTION

The interaction between fluid flow and compliant walls has a wide variety of applications in both biological and engineering systems. For instance, after the seminal experiments of Kramer [1], many researchers have illustrated the performance of compliant coatings by altering the flow favorably to extend the laminar region (see Ref. [2] and the recent work of Nagy *et al.* [3]). In the biological context, wall deformability plays an important role in blood flow as well as peristaltic transport, for example, through the intestines and the urogenital tract (see Refs. [4,5] for a review).

In that respect, many efforts have been made to design a representative compliant wall model and to study the asymptotic linear stability due to the coupling between the fluid flow and the solid structure (see the recent review of Kumaran [6]). Among them, the surface-based model consisting of an infinitely thin plate mounted on springs and dampers (the so-called Kramer wall) which interacts with a shear flow received considerable attention over the last few decades. Carpenter and Garrad [7,8] focused on the stability of boundary-layer flows over Kramer-type compliant walls. They provided some confirmation of the transition-delaying potential of compliant coatings. For this model, Carpenter and Garrad [7,8] identified two categories of instability modes: the

fluid-based Tollmien-Schlichting (TS) mode and solid-based fluid-structure instabilities, referenced as FSI modes hereafter. The last category includes both the traveling-wave flutter (TWF) modes and the (almost static) divergence (DIV) modes.

The mechanism responsible for the growth of TWF modes is similar to that governing water surface waves generated by wind [9,10]. The DIV mode is either interpreted as an absolute instability [11] or a modal instability with a nearly vanishing phase velocity for high values of the wall dissipation [12].

While a wide number of investigations has been devoted to study the long-time regime of these instabilities [13–16], only a few have focused on the short-time dynamics. Among them, Hœpffner *et al.* [17] studied the transient energy growth mechanisms for perturbations developing in a channel flow with Kramer-type compliant walls. Their analysis was restricted to streamwise-invariant perturbations (i.e., varying the spanwise wavenumbers β at fixed streamwise wavenumber $\alpha = 0$). The solution is obtained by summing over the eigenmodes that collectively exhibit nonmodal growth. The authors have shown that, for large wall elasticity, the flow can sustain standing waves with large oscillations in time. The most amplified perturbations exhibit sinuous symmetry and are well described by an added-mass effect. The flow behavior is then essentially driven by the standing-wave dynamics rather than by the lift-up effect. However, the authors failed to obtain convergence when increasing the number of modes used in the summation. Thus, a complete overview of the wall flexibility effects onto transient energy growth is still missing. More specifically, the significant case where streaks interact with the standing wave for moderate wall flexibility has not been explored by the previous authors.

For the same flow case, Zengl and Rist [18] computed the optimal gain map in the streamwise-spanwise wavenumber plane with a similar numerical method. These authors showed that the optimal gain does not significantly depend on the wall flexibility. They have also observed that the flow can sustain strong oscillations for oblique waves due to wall compliance. However, the underlying mechanisms are not fully discussed in that study. In addition, this analysis has been carried out for only a single set of compliant wall parameters.

More recently, for pulsatile plane Poiseuille flow bounded by compliant walls, Tsigklifis and Lucey [19] investigated mainly the intracyclic growth features, i.e., the modulation amplitude of a given Floquet mode. Nevertheless, a complete study of nonmodal growth mechanisms associated with the steady case is not given by these authors.

While the analyses discussed above have provided significant insight into some nonmodal mechanisms of a flow interacting with compliant boundaries, they only focus on specific parameter ranges and do not fully capture the complete transient growth scenarios due to the entire set of eigenmodes. Then the above-mentioned studies have some limitations. First, for the streamwise-invariant case ($\alpha = 0$), some essential questions like the influence of the wall flexibility on the amplification of streaks, for instance, has not yet been sufficiently discussed: How does the standing wave interact with the streaks and at what characteristic spanwise scale? Second, how does the amplitude of standing-wave oscillations scale with wall parameters and spanwise wavenumbers β for moderate wall flexibility, and what is the spanwise wavenumber exhibiting oscillatory behavior with highest modulation amplitudes? Third, for the spanwise-invariant case ($\beta = 0$), what are the specific roles of Tollmien-Schlichting waves and traveling-wave flutter modes onto the transient energy growth for short times?

To fill these gaps, we will thus reconsider the transient energy growth problem for fluid flows interacting with a compliant channel, using a Lagrangian approach. It will allow us to overcome the difficulties that arise when summing over the whole spectrum of eigenmodes. The chosen wall model is of Kramer type. We will also adopt the framework described in Ref. [15], where we considered the reduced velocity V_R as the main control parameter for fluid-structure interaction problems [20]. Then, we will discuss the optimal transient energy growth mechanisms for both streamwise-invariant perturbations and disturbances developing in the streamwise-wall-normal plane for a range of reduced velocities and Reynolds numbers.

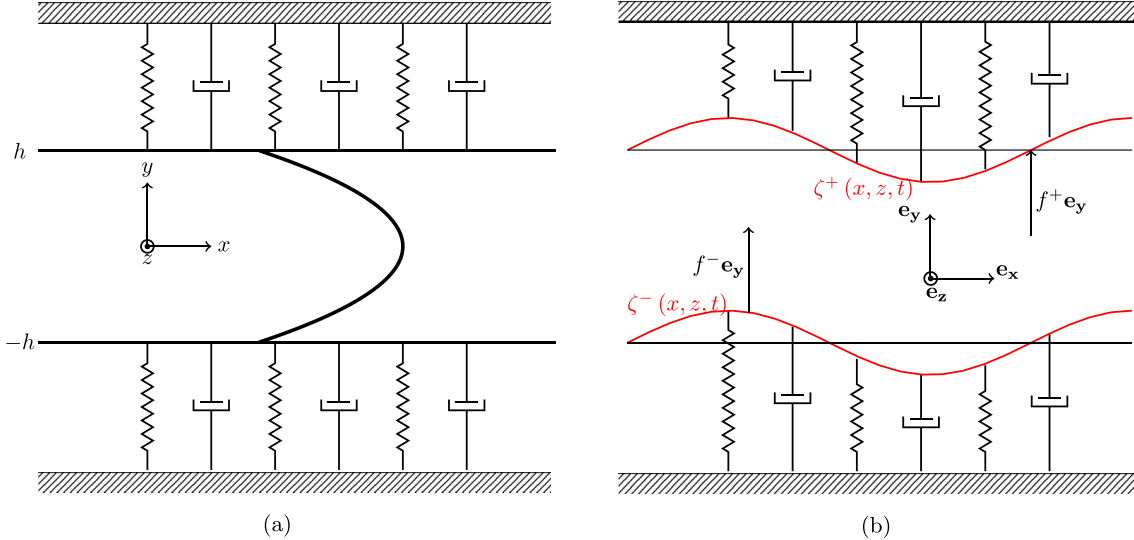


FIG. 1. Channel flow with infinite spring-backed flexible walls. (a) Schematic diagram showing the equilibrium state configuration and (b) wall deformation and coordinate system.

The paper is organized as follows. Section II presents the model and governing equations. In particular, the constrained optimization problem is presented within a Lagrangian framework. The adjoint system of equations, adjoint kinematic conditions, and temporal terminal and initial conditions are given for the linearized fluid-structure interaction system. After having presented the control parameters and the numerical methods in Secs. III and IV, respectively, Sec. V is devoted to give some physical insight into the influence of the reduced velocity and Reynolds number on the short-time dynamics of the perturbation for a range of streamwise and spanwise wavenumbers. Finally, conclusions and prospects are given in the last section.

II. PROBLEM DEFINITION AND SYSTEM OF EQUATIONS

A. Fluid-structure interaction problem

We introduce the Cartesian coordinate system (x, y, z) and unit vectors $(\mathbf{e}_x, \mathbf{e}_y, \mathbf{e}_z)$ associated with streamwise, wall-normal, and spanwise directions, respectively. Hereafter, the study will focus on an incompressible Newtonian fluid, with dynamic viscosity μ and density ρ , between two spring-backed deformable plates, which are allowed to move only in the y direction. As shown in previous theoretical analyses [5,19] for a similar case, the wall motion in x and z directions only plays a minor role in the dynamics and is therefore not considered in the present investigation for simplicity of the model. The instantaneous flow velocity and pressure fields are given by $\mathbf{u}(\mathbf{x}, t) = (u(\mathbf{x}, t), v(\mathbf{x}, t), w(\mathbf{x}, t))$ and $p(\mathbf{x}, t)$, at position $\mathbf{x} = (x, y, z)$ and time t .

Denoting the lower and upper wall positions as $\zeta^\pm(x, z, t)$, the fluid domain corresponds to $\zeta^-(x, z, t) < y < \zeta^+(x, z, t)$ (see Fig. 1), and the flow between the walls follows the incompressible Navier-Stokes equations

$$\frac{\partial \mathbf{u}}{\partial t} + (\mathbf{u} \cdot \nabla) \mathbf{u} = -\frac{1}{\rho} \nabla p + \nu \Delta \mathbf{u}, \quad (1)$$

$$0 = \nabla \cdot \mathbf{u}, \quad (2)$$

where $\nu = \mu/\rho$ denotes the kinematic viscosity. The displacement of the walls is governed by

$$m \frac{\partial^2 \zeta^\pm}{\partial t^2} + d \frac{\partial \zeta^\pm}{\partial t} + (B \Delta^2 - T \Delta + K) \zeta^\pm = f^\pm, \quad (3)$$

where m denotes the mass per unit area of the plates, d their damping coefficient, B the flexural rigidity, T the wall tension, K the spring stiffness, and f^\pm represents the y component of the hydrodynamic forces acting on the plates. Note that in the above equations $\Delta \mathbf{u} = (\partial_{xx} + \partial_{yy} + \partial_{zz})\mathbf{u}$ while $\Delta \zeta = (\partial_{xx} + \partial_{zz})\zeta$ and $\Delta^2 \zeta = (\partial_{x^4} + 2\partial_{x^2 z^2} + \partial_{z^4})\zeta$. The fluid-structure interaction problem is completed with the kinematic conditions

$$u = 0, \quad v = \frac{\partial \zeta^\pm}{\partial t}, \quad w = 0 \quad \text{for } y = \zeta^\pm, \quad (4)$$

associated with no-slip conditions prevailing along the compliant walls.

The unperturbed base configuration corresponds to Poiseuille flow due to a constant pressure gradient within a straight rectangular channel (Fig. 1). It is associated with a steady parabolic streamwise velocity profile $\mathbf{U}(\mathbf{x}) = (U(y), 0, 0)$, with $U(y) = \frac{3}{2}U_m(1 - (y/h)^2)$, between the undeformed walls at $y = \pm h$. Here $U_m = \frac{1}{3}\frac{h^2}{v}\mathcal{G}$ is the mean velocity resulting from a constant streamwise pressure gradient $-\mathcal{G}$. Note that we assume a pressure outside the channel walls always equal to the unperturbed pressure $-\mathcal{G}x$ prevailing inside. The same hypothesis is made by Davies and Carpenter [13,21], Tsigklifis and Lucey [19], and few others since then.

B. Linear governing equations

In the next sections, we will investigate the short-time dynamics of a small perturbation superimposed to the equilibrium state. Therefore, the total flow fields are decomposed as

$$\mathbf{u}(\mathbf{x}, t) = U(y)\mathbf{e}_x + \mathbf{u}'(\mathbf{x}, t), \quad (5)$$

$$p(\mathbf{x}, t) = -\mathcal{G}x + p'(\mathbf{x}, t), \quad (6)$$

where \mathbf{u}' and p' represent the deviations from the base flow fields. Similarly, the positions of both walls are written as

$$\zeta^\pm(x, z, t) = \pm h + \eta^\pm(x, z, t),$$

where η^\pm measures the displacement of the walls from their equilibrium positions at $y = \pm h$.

The assumption of small-amplitude perturbations leads to the linear version of the Navier-Stokes equations:

$$\frac{\partial \mathbf{u}'}{\partial t} + (\mathbf{U} \cdot \nabla) \mathbf{u}' + U_y v' \mathbf{e}_x = -\frac{1}{\rho} \nabla p' + v \Delta \mathbf{u}', \quad (7)$$

$$0 = \nabla \cdot \mathbf{u}'. \quad (8)$$

After linearization of the hydrodynamic forces f^\pm (see Ref. [22] for details), the wall equations are recast as

$$\frac{\partial \eta^\pm}{\partial t} = \gamma^\pm, \quad (9)$$

$$m \frac{\partial \gamma^\pm}{\partial t} = -d\gamma^\pm - (B\Delta^2 - T\Delta + K)\eta^\pm \pm \left(p' - \mu \frac{\partial v'}{\partial y} \right) \Big|_{y=\pm h}, \quad (10)$$

where the wall velocity $\gamma^\pm = \partial_t \eta^\pm$ has been introduced in order to obtain a system of first-order differential equations in time. This system of linear partial differential equations is completed with the associated linearized kinematic conditions:

$$u' = -\eta^\pm \frac{dU}{dy}, \quad v' = \gamma^\pm, \quad w' = 0 \quad \text{at } y = \pm h. \quad (11)$$

See our previous paper [15] for further details about the derivation of the governing equations for small-amplitude perturbations.

C. Optimization framework

For the sake of conciseness, we henceforth omit the prime for the small-amplitude perturbations. We first introduce a measure of the total energy of the perturbation in a computational box of size $L_x \times 2h \times L_z$:

$$E(\mathbf{u}) = \underbrace{\langle\langle \rho \mathbf{u}^2 \rangle\rangle}_{\text{Fluid kinetic energy}} + \underbrace{\sum_{i=\pm} \langle B(\Delta \eta^i)^2 + T \nabla \eta^i \cdot \nabla \eta^i + K(\eta^i)^2 \rangle}_{\text{Wall potential energy}} + \underbrace{\sum_{i=\pm} \langle m(\gamma^i)^2 \rangle}_{\text{Wall kinetic energy}}, \quad (12)$$

where $\langle\langle \cdot \rangle\rangle = \int_0^{L_x} \int_{-h}^h \int_0^{L_z} \cdot \, dx \, dy \, dz$ and $\langle \cdot \rangle = \int_0^{L_x} \int_0^{L_z} \cdot \, dx \, dz$, which represent the integral values either over the whole domain D or along the walls ∂D . Here, E may be written as a function of \mathbf{u} only since η^\pm and γ^\pm can be expressed in terms of the velocity components at the walls using kinematic conditions (11). In Eq. (12), we separate the energy contributions from the walls (i.e., wall potential energy and wall kinetic energy) from the one associated with the fluid (i.e., fluid kinetic energy). This decomposition is also used by Hœpffner *et al.* [17] and Malik *et al.* [12] for transient growth analysis of flows interacting with compliant walls.

The largest total transient energy growth E that a small perturbation can experience over a fixed target time τ is obtained by maximizing the following constrained Lagrangian:

$$\begin{aligned} \mathcal{L} = & E(\mathbf{u}(t = \tau)) - \rho \int_0^\tau \left\langle \left\langle \mathbf{a} \cdot \left(\mathbf{u}_t + \mathbf{U} \cdot \nabla \mathbf{u} + \frac{1}{\rho} \nabla p - v \Delta \mathbf{u} + v U_y \mathbf{e}_x \right) \right\rangle \right\rangle dt - \int_0^\tau \langle\langle \Pi \nabla \cdot \mathbf{u} \rangle\rangle dt \\ & - \int_0^\tau \langle g^+ [m \gamma_t^+ + d \gamma^+ + (B \Delta^2 - T \Delta + K) \eta^+ - p^+ + \mu v_y^+] \rangle dt \\ & - \int_0^\tau \langle g^- [m \gamma_t^- + d \gamma^- + (B \Delta^2 - T \Delta + K) \eta^- + p^- - \mu v_y^-] \rangle dt \\ & - \int_0^\tau \langle e^+ [\eta_t^+ - \gamma^+] \rangle dt - \int_0^\tau \langle e^- [\eta_t^- - \gamma^-] \rangle dt \\ & - \langle\langle \mathbf{a}_0 \cdot [\mathbf{u}(t = 0) - \mathbf{u}_0] \rangle\rangle - \lambda [E(\mathbf{u}_0) - 1], \end{aligned} \quad (13)$$

where the control is $\mathbf{u}_0 = (u_0, v_0, w_0)$ and $u_0^\pm = -\eta_0^\pm U_y|_{\pm=h}$, $v_0^\pm = \gamma_0^\pm$, $w_0^\pm = 0$. In Eq. (13), λ , \mathbf{a}_0 , Π , \mathbf{a} , g^+ , g^- , e^+ , and e^- are the Lagrange multiplier fields imposing the constraints that the initial total perturbation energy equals 1, the perturbation is incompressible, and that the fluid-structure interaction system (10) is satisfied.

Taking variations with respect to all the degrees of freedom, where the boundary conditions are included implicitly when integrating by parts the momentum equations, leads to the adjoint evolution equations for the fields,

$$\begin{aligned} & -\mathbf{a}_t - \mathbf{U} \cdot \nabla \mathbf{u} + \frac{1}{\rho} \nabla \Pi - v \Delta \mathbf{u} + a U_y \mathbf{e}_y = 0, \\ & \nabla \cdot \mathbf{a} = 0, \\ & -mg_t^+ - e^+ + g^+ d - \Pi^+ + \mu b_y^+ = 0, \\ & -mg_t^- - e^- + g^- d + \Pi^- - \mu b_y^- = 0, \\ & -e_t^+ + (B \Delta^2 - T \Delta + K) e^+ - \mu a_y^+ U_y^+ = 0, \\ & -e_t^- + (B \Delta^2 - T \Delta + K) e^- + \mu a_y^- U_y^- = 0, \end{aligned} \quad (14)$$

together with the adjoint kinematic conditions,

$$\begin{aligned} & g^- = b^-, \quad g^+ = b^+, \\ & a^+ = 0, \quad a^- = 0, \end{aligned} \quad (15)$$

the temporal terminal conditions,

for $D \setminus \partial D : \mathbf{a}(t = \tau) = 2\mathbf{u}(t = \tau)$,

$$\text{and for } \partial D : g^\pm(t = \tau) = 2\gamma^\pm(t = \tau), e^\pm(t = \tau) = 2[2\rho h U_y]_{\pm h}^2 + (B\Delta^2 - T\Delta + K)\eta^\pm(t = \tau), \quad (16)$$

and the initial conditions,

for $D \setminus \partial D : \mathbf{a}(t = 0) = 2\lambda\mathbf{u}(t = 0)$,

$$\text{and for } \partial D : g^\pm(t = 0) = 2\lambda\gamma^\pm(t = 0), e^\pm(t = 0) = 2\lambda[2\rho h U_y]_{\pm h}^2 + (B\Delta^2 - T\Delta + K)\eta^\pm(t = 0), \quad (17)$$

where the Lagrange multiplier λ is fixed to verify unit total energy at $t = 0$. Here, the integration along the wall-normal direction is computed with spectral accuracy. A direct and adjoint looping method [23], where the direct system is integrated forward in time and the adjoint problem is advanced backward in time, is hence used to compute the optimal initial perturbation for a given target time τ . A similar technique has already been used for a Couette flow by our team with the same code [24]. In the next sections, the corresponding maximum energy growth is referenced as $G(\tau)$. Since the nonlinear terms are removed from the equations, both direct and adjoint systems can be solved in Fourier space, without any coupling between spatial Fourier modes. In this context, we introduce the following waveform for the different fields:

$$\begin{aligned} \mathbf{u}(x, y, z, t) &= \tilde{\mathbf{u}}(y, t)e^{j(\alpha x + \beta z)} + \text{c.c.}, \quad \mathbf{a}(x, y, z, t) = \tilde{\mathbf{a}}(y, t)e^{j(\alpha x + \beta z)} + \text{c.c.}, \\ \gamma^\pm(x, z, t) &= \tilde{\gamma}^\pm(t)e^{j(\alpha x + \beta z)} + \text{c.c.}, \quad \eta^\pm(x, z, t) = \tilde{\eta}^\pm(t)e^{j(\alpha x + \beta z)} + \text{c.c.}, \\ g^\pm(x, z, t) &= \tilde{g}^\pm(t)e^{j(\alpha x + \beta z)} + \text{c.c.}, \quad e^\pm(x, z, t) = \tilde{e}^\pm(t)e^{j(\alpha x + \beta z)} + \text{c.c.}, \end{aligned}$$

with $\sqrt{j} = -1$ and α and β the streamwise and spanwise wavenumbers, respectively. Again, for simplicity, we omit $\tilde{\cdot}$ in the following.

III. CONTROL PARAMETERS

In the present study, the compliant-channel flow system is characterized by nine dimensional parameters: the volumetric flow rate $[Q] = \text{m}^2 \text{s}^{-1}$, the half height of the channel, $[h] = \text{m}$, the fluid density $[\rho] = \text{kg m}^{-3}$, the kinematic viscosity $[\nu] = \text{m}^2 \text{s}^{-1}$, the mass of the plate per unit area, $[m] = \text{kg m}^{-2}$, the damping coefficient of the wall, $[d] = \text{kg m}^{-2} \text{s}^{-1}$, the bending stiffness of the plate, $[B] = \text{kg m}^2 \text{s}^{-2}$, the wall tension $[T] = \text{kg s}^{-2}$, and the spring stiffness $[K] = \text{kg m}^{-2} \text{s}^{-2}$. Hence, the system may be described by six dimensionless parameters:

$$\begin{aligned} \text{Re} &= \frac{Q}{\nu}, \quad V_R = \frac{Q}{4h^2} \sqrt{\frac{m}{K}}, \quad \Gamma = \frac{m}{\rho h}, \\ d_* &= \frac{d}{\sqrt{mK}}, \quad B_* = \frac{B}{Kh^4}, \quad T_* = \frac{T}{Kh^2}. \end{aligned} \quad (18)$$

Here Re is the Reynolds number based on channel diameter and average flow velocity. The nondimensional wall parameters d_* , B_* , and T_* are relative to the spring stiffness K . Finally, two nondimensional parameters account for the coupling between the fluid and the compliant walls: the mass ratio between the walls and the fluid, Γ ; and the reduced velocity V_R that represents the ratio of the wall characteristic timescale $\sqrt{m/K}$ to the characteristic flow advection timescale $4h^2/Q$ (see Refs. [15,20]). In order to reduce the dimensionality of the control parameter space, and without much loss of generality, we only use $T = 0$ and $\Gamma = 2$ hereafter, and we also set three dimensional parameters at $\rho = 1$, $h = 1$, and $Q = 1$.

IV. NUMERICAL METHODS

The numerical method is here described for the direct system only, since time marching of the adjoint system proceeds in a similar fashion. The approach closely matches the Uzawa algorithm described by Peyret [25]. Spatial directions are approximated with spectral accuracy and a semi-implicit second-order time-marching scheme is used.

As usually done in the incompressible regime, a P_N/P_{N-2} Chebyshev collocation method is used for the spatial discretization. We rewrite the system of equations in vector form with complex components, using $\mathbf{u} = (u_1, u_2, \dots, u_N)$, $\mathbf{v} = (v_1, v_2, \dots, v_N)$, and $\mathbf{w} = (w_1, w_2, \dots, w_N)$ for velocity components and $\mathbf{p} = (p_2, \dots, p_{N-1})$ for the pressure. We also introduce $\tilde{\mathbf{u}} = (u_2, \dots, u_{N-1})$ and $\tilde{\mathbf{v}} = (v_2, \dots, v_{N-1})$, where only the interior points are included. After spatial discretization, with N Chebyshev collocation points, the first and second y -derivative operators acting on velocity fields are recast as \mathbf{D} and \mathbf{D}^2 matrices, respectively. The y -derivative operator on the $N - 2$ grid points for the pressure is represented by matrix \mathbf{D}_p . Finally, we note hereafter the time step Δt and n the number of the time iteration.

The discrete system of the momentum equations for the fluid is then rewritten in matrix form to yield

$$\begin{aligned}\mathbf{M}\tilde{\mathbf{u}}^{n+1} - j\alpha\mathbf{p}^{n+1} &= \tilde{\mathbf{S}}_u^{n+1,n,n-1}, \\ \mathbf{M}\tilde{\mathbf{v}}^{n+1} - \mathbf{D}_p\mathbf{p}^{n+1} &= \tilde{\mathbf{S}}_v^{n+1,n,n-1}, \\ \mathbf{M}\tilde{\mathbf{w}}^{n+1} - j\beta\mathbf{p}^{n+1} &= \mathbf{S}_w^{n,n-1},\end{aligned}\tag{19}$$

and the divergence-free constraint expressed at the interior points reads

$$\tilde{\mathbf{D}}\tilde{\mathbf{v}}^n + j\alpha\tilde{\mathbf{u}}^n + j\beta\tilde{\mathbf{w}}^n = \mathbf{S}_d^n,\tag{20}$$

where $\mathbf{M} = v\tilde{\mathbf{D}}^2 - \sigma\mathbf{I}$ with $\sigma = 3/(2\Delta t) + v(\alpha^2 + \beta^2)$. Here $\tilde{\mathbf{D}}$ and $\tilde{\mathbf{D}}^2$ represent the first and second derivative operators on N grid points, where the first and/or last rows and first and/or last columns are removed. In Eqs. (19) and (20), boundary conditions for u and v are included on the right-hand side of the equations. The boundary conditions are time dependent. As a consequence, in Eq. (20) we have

$$\mathbf{S}_d^n = -(D_{11}v_1^n + D_{1N}v_N^n, D_{21}v_1^n + D_{2N}v_N^n, \dots, D_{N1}v_1^n + D_{NN}v_N^n).$$

For Eqs. (19), we use the following decomposition:

$$\tilde{\mathbf{S}}_u^{n+1,n,n-1} = \mathbf{S}_u^{n,n-1} + \mathbf{C}_u^{n+1}, \quad \tilde{\mathbf{S}}_v^{n+1,n,n-1} = \mathbf{S}_v^{n,n-1} + \mathbf{C}_v^{n+1},$$

with

$$\begin{aligned}\mathbf{S}_u^{n,n-1} &= -(4\tilde{\mathbf{u}}^n - \tilde{\mathbf{u}}^{n-1})/2\Delta t + 2\mathbf{f}_u^n - \mathbf{f}_u^{n-1}, \\ \mathbf{S}_v^{n,n-1} &= -(4\tilde{\mathbf{v}}^n - \tilde{\mathbf{v}}^{n-1})/2\Delta t + 2\mathbf{f}_v^n - \mathbf{f}_v^{n-1}, \\ \mathbf{S}_w^{n,n-1} &= -(4\tilde{\mathbf{w}}^n - \tilde{\mathbf{w}}^{n-1})/2\Delta t + 2\mathbf{f}_w^n - \mathbf{f}_w^{n-1},\end{aligned}$$

where

$$\mathbf{f}_u^n = j\alpha\tilde{\mathbf{U}}\tilde{\mathbf{u}}^n + \tilde{\mathbf{v}}^n\tilde{\mathbf{U}}_y, \quad \mathbf{f}_v^n = j\alpha\tilde{\mathbf{U}}\tilde{\mathbf{v}}^n, \quad \mathbf{f}_w^n = j\beta\tilde{\mathbf{U}}\tilde{\mathbf{w}}^n,$$

and the contribution of the boundary conditions for the second derivatives are included into

$$\begin{aligned}\mathbf{C}_u^n &= -(D_{11}^2u_1^n + D_{1N}^2u_N^n, D_{21}^2u_1^n + D_{2N}^2u_N^n, \dots, D_{N1}^2u_1^n + D_{NN}^2u_N^n), \\ \mathbf{C}_v^n &= -(D_{11}^2v_1^n + D_{1N}^2v_N^n, D_{21}^2v_1^n + D_{2N}^2v_N^n, \dots, D_{N1}^2v_1^n + D_{NN}^2v_N^n).\end{aligned}$$

Applying the divergence operator (20) onto the momentum equations (19), an equation for the pressure is obtained:

$$\mathbf{Q}\mathbf{p}^{n+1} = \mathbf{G}^{n,n-1} + \mathbf{H}^{n+1}, \quad (21)$$

with $\mathbf{Q} = \alpha^2\mathbf{M}^{-1} - \tilde{\mathbf{D}}\mathbf{M}^{-1}\mathbf{D}_p + \beta^2\mathbf{M}^{-1}$ and

$$\begin{aligned} \mathbf{G}^{n,n-1} &= j\alpha\mathbf{M}^{-1}\mathbf{S}_u^{n,n-1} + \tilde{\mathbf{D}}\mathbf{M}^{-1}\mathbf{S}_v^{n,n-1} + j\beta\mathbf{M}^{-1}\mathbf{S}_w^{n,n-1}, \\ \mathbf{H}^{n+1} &= -\mathbf{S}_d^{n+1} + j\alpha\mathbf{M}^{-1}\mathbf{C}_u^{n+1} + \tilde{\mathbf{D}}\mathbf{M}^{-1}\mathbf{C}_v^{n+1}. \end{aligned}$$

Following Davies and Carpenter [21], a three-point implicit time discretization for the wall equations is used to ensure numerical stability:

$$\begin{aligned} m(3\gamma_{\pm}^{n+1} - 4\gamma_{\pm}^n + \gamma_{\pm}^{n-1}) &= 2\Delta t[-d\gamma_{\pm}^{n+1} - (B\Delta^2 + K)\eta_{\pm}^{n+1} \pm p_{1/N}^{n+1} \mp \mu(\mathbf{D}\mathbf{v})_{1/N}^{n+1}], \\ (3\eta_{\pm}^{n+1} - 4\eta_{\pm}^n + \eta_{\pm}^{n-1}) &= 2\Delta t\gamma_{\pm}^{n+1}, \end{aligned} \quad (22)$$

with $\Delta^2 = \alpha^4 + \beta^4 + 2\alpha^2\beta^2$ and where p_1 and p_N are computed using spectral extrapolation. The following system is then solved iteratively at each time step:

$$\begin{aligned} \mathbf{p}^{n+1,k+1} &= \mathbf{Q}^{-1}[\mathbf{G}^{n,n-1} + \mathbf{H}^{n+1,k}], \\ \tilde{\mathbf{u}}^{n+1,k+1} &= \mathbf{M}^{-1}j\alpha\mathbf{p}^{n+1,k+1} + \mathbf{M}^{-1}[\mathbf{S}_u^{n,n-1} + \mathbf{C}_u^{n+1,k}], \\ \tilde{\mathbf{v}}^{n+1,k+1} &= \mathbf{M}^{-1}\mathbf{D}_p\mathbf{p}^{n+1,k+1} + \mathbf{M}^{-1}[\mathbf{S}_v^{n,n-1} + \mathbf{C}_v^{n+1,k}], \\ \mathbf{w}^{n+1,k+1} &= \mathbf{M}^{-1}j\beta\mathbf{p}^{n+1,k+1} + \mathbf{M}^{-1}\mathbf{S}_w^{n,n-1}, \\ \gamma_{\pm}^{n+1,k+1} &= \left[1 + \frac{2\Delta t}{3m}d\right] + \eta_{\pm}^{n+1,k+1}\left[\frac{2\Delta t}{3m}(B\Delta^2 + K)\right] \\ &= \frac{2\Delta t}{3m}[\pm p_{1/N}^{n+1,k+1} \mp \mu(\mathbf{D}\mathbf{v})_{1/N}^{n+1,k+1}] + \frac{4}{3}\gamma_{\pm}^n - \frac{1}{3}\gamma_{\pm}^{n-1}, \\ \eta_{\pm}^{n+1,k+1} &= \frac{2}{3}\Delta t\gamma_{\pm}^{n+1,k+1} = \frac{4}{3}\eta_{\pm}^n - \frac{1}{3}\eta_{\pm}^{n-1}. \end{aligned} \quad (23)$$

In Eqs. (23), the wall part is easily solved by inverting a 2×2 system and the boundary conditions for the velocity components are updated using kinematic conditions. Between 20 and 50 iterations are needed at each time step to converge.

Finally, the numerical method is further improved by considering separately perturbations of sinuous or varicose symmetries and using only half of the channel together with derivative operators appropriate for the symmetry of each component of the different flow fields [26]. The separation between varicose and sinuous cases facilitates the analysis of the driving mechanisms of the dynamics and also allows to run the different symmetries simultaneously on two processors. The present code is an extension of a direct numerical simulation (DNS) code developed by our team which has been well validated for channel and Couette flow simulations with rigid walls [24,27].

V. NUMERICAL VALIDATION

A. Asymptotic case

In this section, we validate the numerical method for time marching the linearized Navier-Stokes equations that include the wall deformation (referenced as LDNS hereafter). Both the direct and adjoint systems are considered. For that purpose, we focus on a case described in a previous paper of our team. The control parameters are fixed to $V_R = 1$, $B_* = 4$, $d_* = 0$, $\alpha = 1$, and $\text{Re} = 10\,000$. For this case, the long-time dynamics is driven by the varicose traveling-wave flutter mode. The linear stability problem has been solved using an algebraic eigenvalue solver. The LDNS is initialized with a random noise. The numerical parameters are fixed to $N = 60$ and $\Delta t = 0.01$. Results are shown in

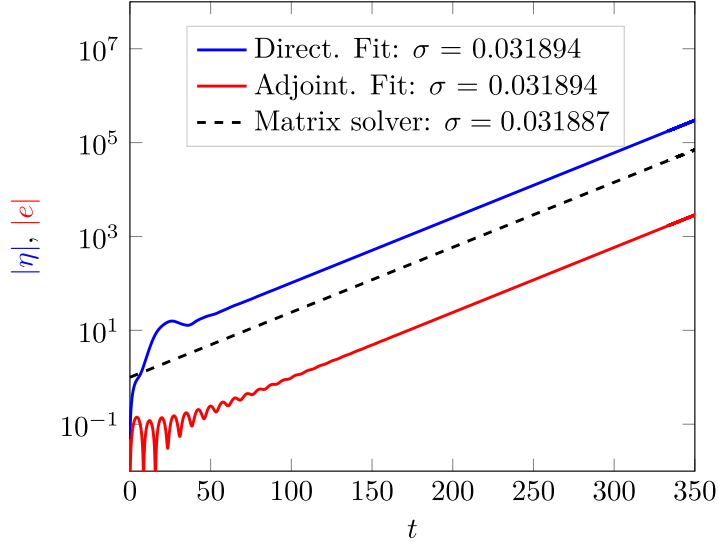


FIG. 2. Validation of the time-marching linear solver for both direct and adjoint formulations for $\text{Re} = 10000$, $\alpha = 1$, $B_* = 4$, $\Gamma = 2$, $d_* = 0$, and $V_R = 1$. Numerical parameters are set to $N = 60$ and $\Delta t = 0.01$. The time evolution of the modulus of the wall vertical displacement for a given random initial perturbation is shown on a logarithmic scale. A linear regression provides a temporal growth rate $\sigma = 0.031894$ for both direct and adjoint solvers. The temporal evolution of the most amplified linear eigenvalues obtained with the eigenvalue matrix solver gives $\sigma = 0.031887$.

Fig. 2, where we have reported the time evolution of the modulus of the wall vertical displacement for both the direct (η) and adjoint systems (e). The figure shows a perfect agreement between the temporal amplification rate obtained with the algebraic eigenvalue solver and the one derived from the linearized Navier-Stokes solver for both the direct and adjoint problems.

In Fig. 3, we also compare the spatial structure of the eigenmodes computed with the eigenvalue solver and the LDNS for the direct system, which again perfectly agree.

B. Transient growth

The coupling between the direct and adjoint solvers and the choice of the energy norm are discussed using results given by Hœpffner *et al.* [17]. For that purpose, we convert the dimensionless values provided by Hœpffner *et al.* [17] to those used in the present paper. Hence, for this case, the reduced velocity is fixed to $V_R = 23.57$, the flexural rigidity is set to $B_* = 4$, the wall dissipation $d_* = 0.0071$, and the Reynolds number $\text{Re} = 6667$. The spanwise and streamwise wavenumbers are fixed to 0.2 and 0, respectively. Two different energy norms are used: the total energy norm (12) and another one based only on the flow kinetic energy inside the domain. The envelopes of the optimal gain G over the target time τ computed using the direct-adjoint looping method for both energy norms are shown in Fig. 4. The number of collocation points used is $N = 60$ and the time step is fixed to $\Delta t = 0.01$. Published results of Hœpffner *et al.* [17] are also reported. The envelope G is either associated with the sinuous or varicose symmetry depending on the chosen time horizon used for the optimization. Figure 4 shows an almost perfect agreement between our time-stepping algorithm and the matrix solver used by Hœpffner *et al.* [17]. Hœpffner *et al.* [17] have used an eigenfunctions basis for the computation of G . The authors have been unable to obtain a true convergence towards the optimal solution when including too many modes in the projection. Especially when considering the whole spectrum, the authors show that the optimal gain tends to blow up. Within the present time-stepping framework, we do not observe any problem for the convergence even when doubling the number of collocation points. It seems therefore more appropriate to use the present method in order to draw definite conclusions about transient growth

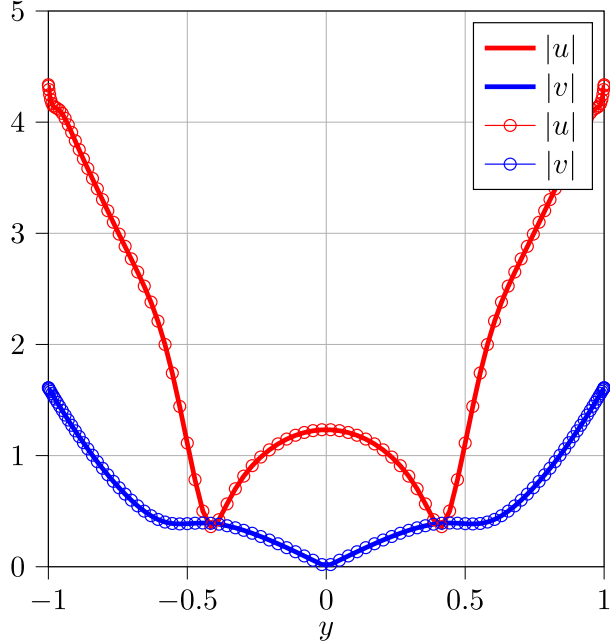


FIG. 3. Same flow case as in Fig. 2. The envelope of the eigenfunctions computed either with the LDNS (in solid lines) or the eigenvalue solver (open circles) are shown.

scenarios investigated hereafter. The figure also shows that while a similar beating phenomenon is recovered for both inner products, the amplitude of the perturbation is clearly decreased by using the fluid kinetic energy norm only. Therefore, it seems inappropriate to restrict the analysis to the fluid kinetic energy only because it fails to take into account a significant level of amplification associated with the wall dynamics. Hereafter, all computations are carried out using the total energy norm. In the next section, the wall dissipation is set to zero and the flexural rigidity is fixed to $B_* = 1$ for illustration purposes.

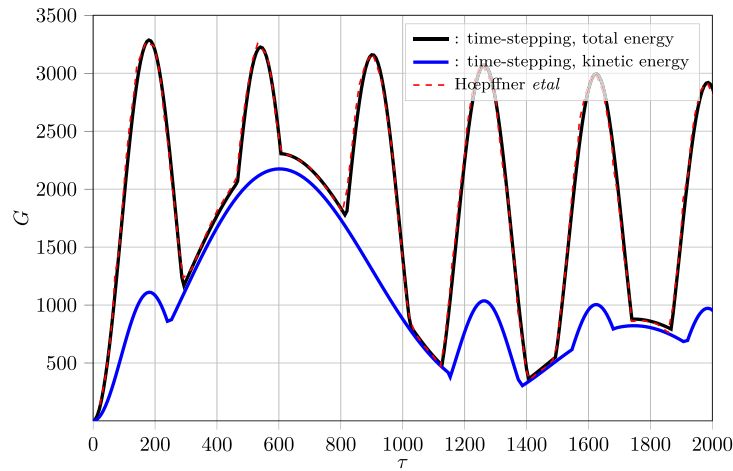


FIG. 4. G as a function of the target time τ for $V_R = 23.57$, $B_* = 4$, $d_* = 0.0071$, $Re = 6667$, $\beta = 0.2$, and $\alpha = 0$. Results extracted from Hoepffner *et al.* [17] are also reported. Computations associated with the total energy norm and the fluid kinetic energy norm inside the domain are shown in black and blue, respectively.

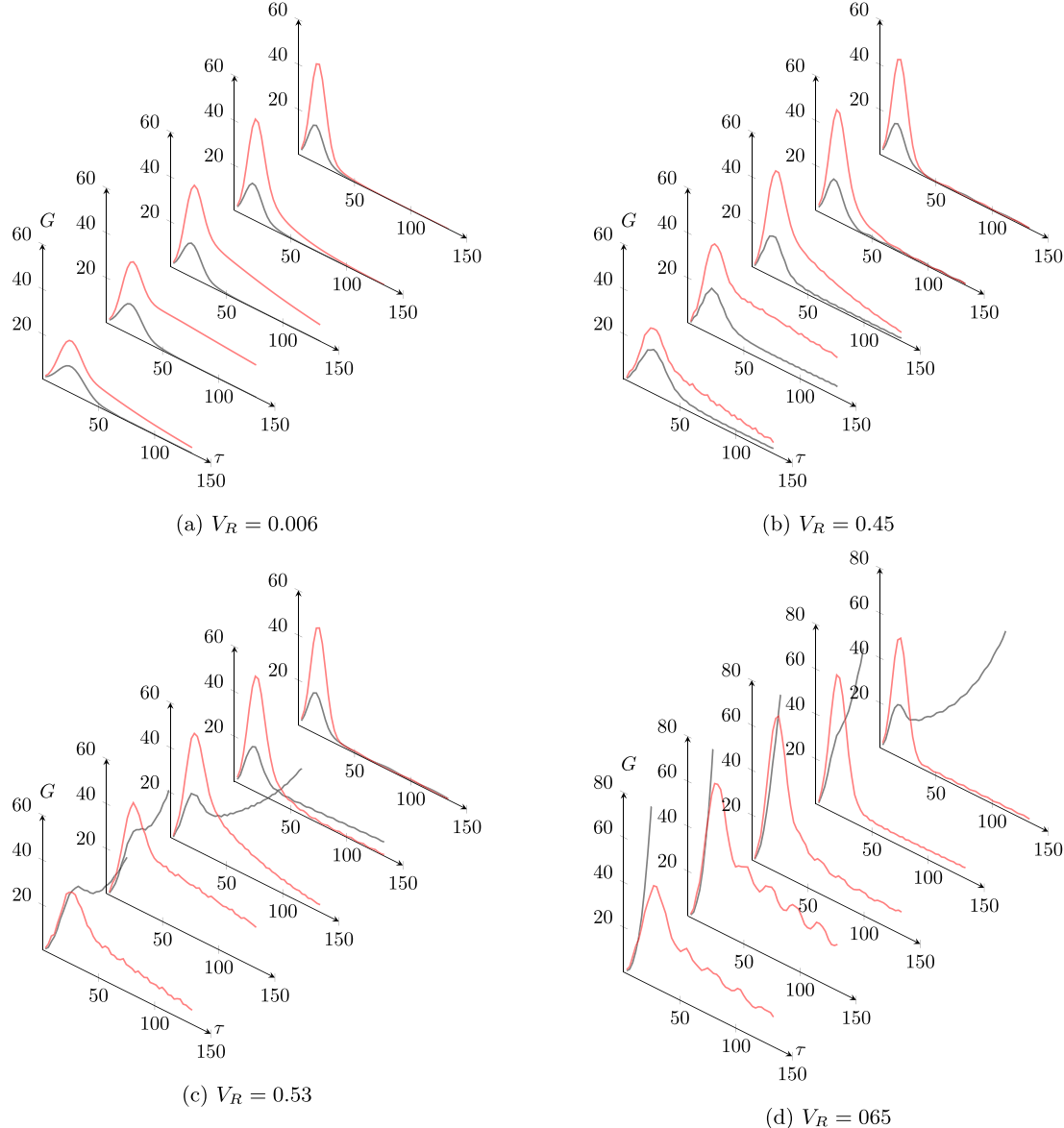


FIG. 5. G as a function of the target time τ for $Re = 6666$ and (a) $V_R = 0.006$, (b) $V_R = 0.45$, (c) $V_R = 0.53$, and (d) $V_R = 0.65$. For all panels, the streamwise wavenumbers are $\alpha = 0.8, 1, 1.2, 1.4$, and 1.6 (from the left to the right). Red, sinuous symmetry; black, varicose symmetry.

VI. RESULTS

A. Optimal growth for $\beta = 0$

In this section, the analysis is restricted to two-dimensional perturbations with vanishing spanwise wavenumber, $\beta = 0$. In Fig. 5, time evolutions of G for various streamwise wavenumbers are shown at different reduced velocity for both the sinuous and varicose symmetries. The figure shows that for V_R varying from $V_R = 0.006$ to $V_R = 0.45$, a weak effect of the wall flexibility is observed for all α that are investigated. When the reduced velocity is increased up to 0.53, the varicose configuration is driven by the asymptotically unstable TWF mode for short times for $\alpha = 0.8$ and 1. One may recall that the varicose case is the most unstable one when considering the asymptotic regime (i.e., the critical reduced velocity is lower than the one associated with the sinuous case [15]).

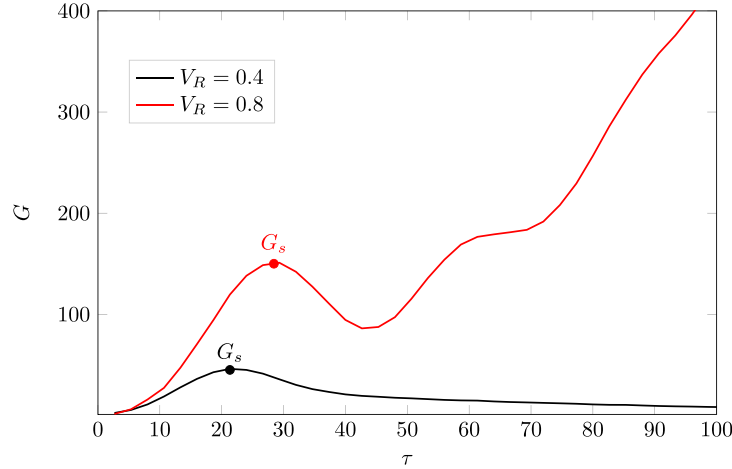


FIG. 6. G as a function of the target time τ for $\text{Re} = 6666$, $\alpha = 1.2$, and $V_R = 0.4, 0.8$.

For $\alpha = 1.2, 1.4$, and 1.6 , a distinct short-time growth is observed with the emergence of a distinct peak in G . For these cases, the sinuous configuration is always the most amplified for short times. For $V_R = 0.65$ and the varicose symmetry, the system is mainly governed by the unstable mode for $\alpha = 0.8, 1.2$, and 1.4 . A distinct peak of G is only observed for $\alpha = 1.6$. Once again, for this streamwise wavenumber, the sinuous symmetry is the most amplified symmetry for short times. In particular, its energy peak in G is seen to increase with the reduced velocity. Hence, focusing our attention on the transient growth mechanism, the sinuous configuration seems to be the most interesting case to investigate. In addition, the sinuous case also exhibits a clear distinct low-frequency beating, not observed for the varicose symmetry [see Fig. 5(d) and $\alpha = 1$]. As a consequence, for the sake of conciseness, we will focus on the sinuous symmetry hereafter.

The influence of the reduced velocity onto the optimal gain G is further illustrated in Fig. 6 for $\alpha = 1.2$, $\text{Re} = 6666$, and target times varying from 0 to 100. We recall that for this Reynolds number, the TS modes are temporally damped for the rigid-wall case. For $V_R = 0.4$, G exhibits a growth for short times and relaxes to zero in the asymptotic regime. For $V_R = 0.8$, G peaks during short times before being damped until $\tau = 25$ and then increases for long times. For this reduced velocity value, the TWF mode is temporally amplified. To further characterize the energy growth for short times, we note G_s , the optimal gain associated with the first peak (see Fig. 6). In Fig. 6, it is clear that G_s depends on V_R . The knowledge of the impact of V_R on G_s is also of strong interest even in the slightly supercritical regime since it provides some information on the receptivity of the system to external disturbances.

Let us now introduce the quantity $G_s^M(\text{Re}, V_R) = \max_\alpha G_s(\text{Re}, V_R, \alpha)$ that measures the maximum gain reached by G_s over α for a given configuration (Re, V_R). The distribution of G_s^M with Re and V_R is shown in Fig. 7(a) and the associated optimal wavenumber α_s^M in Fig. 7(b).

Figure 7 shows that while the TS wave is slightly damped temporally [13] for small values of V_R , the transient growth is enhanced with the wall compliance. In addition, close to the critical value of V_R for the onset of the TWF mode, the transient growth for short times has considerably increased.

Let us now focus on some representative cases. In Fig. 8, the time evolutions of the total energy associated with the optimal initial perturbation for $V_R = 0.6$, $\text{Re} = 8300$, and some target times τ and streamwise wavenumbers α are displayed. For comparison purposes, the envelope G for the rigid case is also reported (in red). The case is represented by a black dot in the maps of Fig. 7. The figure shows that the distribution of the total energy gain for short times is in strong contrast with the rigid-wall counterpart. The compliant walls can either stabilize or enhance the energy growth. One may also notice that energy growth exhibits beating oscillations for some parameters.

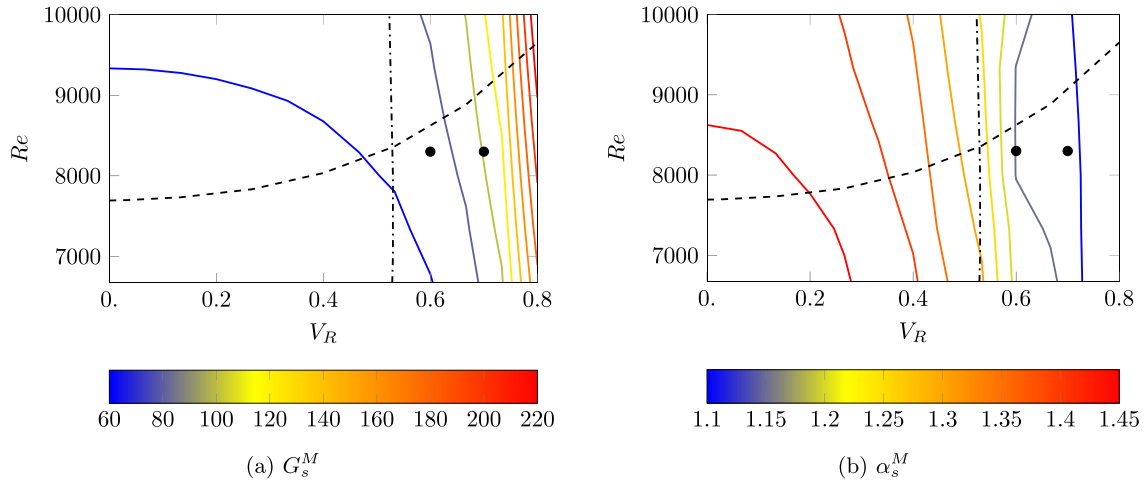


FIG. 7. Isocontours of (a) G_s^M and (b) α_s^M in the (Re, V_R) plane. The dashed line denotes the evolution of the critical Reynolds number with respect to the TS mode. The dash-dotted line represents the evolution of the critical reduced velocity with respect to the TWF mode.

The same analysis is conducted for $V_R = 0.7$ and results are shown in Fig. 9 (the case is also reported in the maps of Fig. 7). The figure shows a similar behavior as the one observed for $V_R = 0.6$ with the exception that the amplitude of the oscillations and the total energy peak G_s^M are enhanced by the wall compliance. Interestingly, the figure also shows that the onset of the exponential instability for the TWF mode occurs at different streamwise wavenumbers from those where the largest oscillations are observed. In an effort to explain the underlying mechanism we show in Fig. 10 a subset of the eigenvalue spectrum for $V_R = 0.7$ and $\alpha = 1$. The complex circular frequency is noted as $\omega = \omega_r + j\omega_i$ with the frequency $\omega_r/2\pi$ and the temporal amplification rate ω_i . In addition to the TS mode, the spectrum exhibits also two distinct modes, the so-called traveling-wave flutter (TWF) modes (see Ref. [15] for further results). One TWF mode is traveling along the downstream direction in x . The other one is traveling in the opposite direction. In Fig. 10, we have also reported the distance between the circular frequency of the TWF mode traveling in the downstream direction and the one associated with the TS mode, labeled $\Delta\omega$. The difference $\Delta\omega$ is seen to be correlated with the time period of the beating process, ΔT , observed in Fig. 9: ΔT is nearly equal to $2\pi/\Delta\omega$. This behavior has also been observed by Davies and Carpenter [21]. It is a consequence of constructive interference between the TS and TWF waves. This interpretation is further illustrated in Fig. 11, where the distributions of ω_r and ω_i with α are shown for both TWF and TS modes. The figure shows that for the range in α where the oscillating behavior is observed in Fig. 9, circular frequencies associated with TS and TWF waves are closely approaching each other. In this region, the two modes have very similar eigenfunctions (i.e., they are nonorthogonal) and their superposition generates an energy growth and a low-frequency beating.

To gain insight into the role of the different modes on the time evolution of $E(t)$, the optimal initial perturbation is expanded onto the basis of eigenvectors. Let us note the initial perturbation $\mathbf{q}_i = \mathbf{V}\hat{\mathbf{a}}$ with $\mathbf{V} = (\hat{\mathbf{q}}_1, \hat{\mathbf{q}}_2, \dots, \hat{\mathbf{q}}_m)$ the m columns containing the discrete eigenvectors (the corresponding eigenvalues are noted $-j\omega_i$, hereafter) and $\hat{\mathbf{a}}$ the vector containing the coefficients of the expansion of \mathbf{q}_i . To find $\hat{\mathbf{a}}$, we use an orthogonal projection based on a Gram-Schmidt orthonormalization process. It is equivalent to require that the projection error is orthogonal to the set of eigenmodes for the chosen subspace of dimension m . The procedure is further detailed in Ref. [28]. The time evolution of \mathbf{q}_i expanded into an eigenmode basis reads $\mathbf{q}_i(t) = \mathbf{V}\mathbf{a}(t)$ with $\mathbf{a}(t) = (\hat{a}_1 e^{-j\omega_1 t}, \hat{a}_2 e^{-j\omega_2 t}, \dots, \hat{a}_m e^{-j\omega_m t})$.

We now consider two representative cases for $Re = 8300$, $\alpha = 1$, and $\tau = 26$. The reduced velocity is fixed either to $V_R = 0.6$ or $V_R = 0.7$. Three subsets of modes are investigated and their

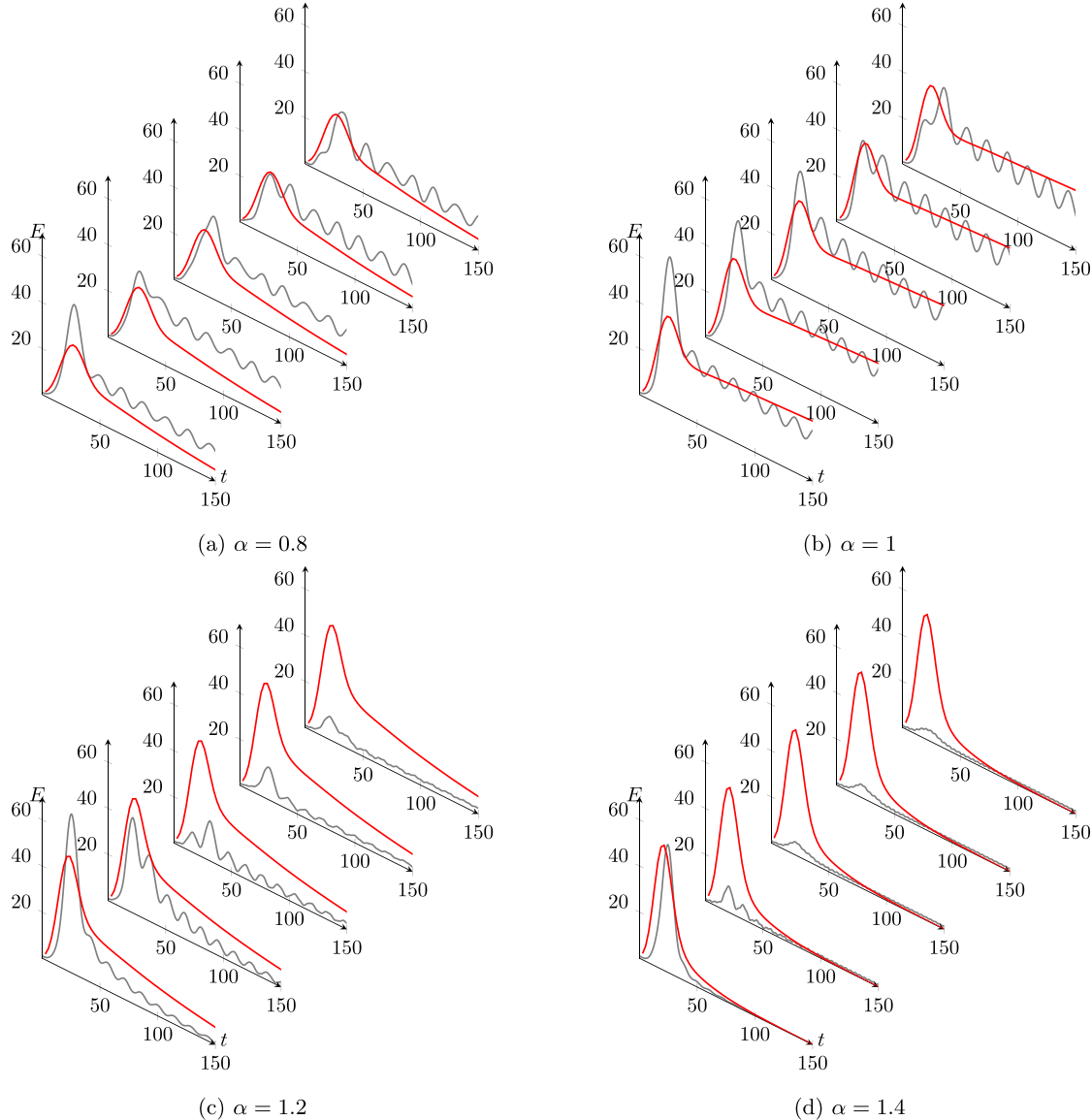


FIG. 8. Time evolution of the total energy for the optimal initial perturbation for $\tau = 26, 66, 133, 200, 266$ (from the left to the right) and $\alpha = 0.8, 1, 1.2, 1.4$. The Reynolds number is fixed to $Re = 8300$ and the reduced velocity is set to $V_R = 0.6$. In red, the envelope G for the rigid case is represented.

dimensions are fixed to $m = 16$. A first subset includes the least damped modes. A second subset includes also the least damped modes but the TWF mode propagating downstream is removed. For the last subset, the TS mode is removed. Time evolutions of the reduced-order models are compared to LDNS results in Fig. 12. The time evolution of the kinetic energy associated with the optimal initial perturbation for the rigid-wall case is also reported in the figure for the same parameters for comparison purposes. For both reduced velocities, the figure shows an almost perfect match between $E(t)$ extracted from the LDNS and $E(t)$ obtained by using the first subspace of modes (i.e., including both TWF and TS modes). It validates the orthogonal projection used in the present study. When the reduced-order model excludes the TWF mode propagating downstream it has as a consequence that the oscillations disappear, as expected. The total energy peak for short time is also reduced. For $V_R = 0.6$, and for large times, the dynamics is mainly driven by the TS mode. For this value of the reduced velocity, the total energy associated with the full system is seen to oscillate

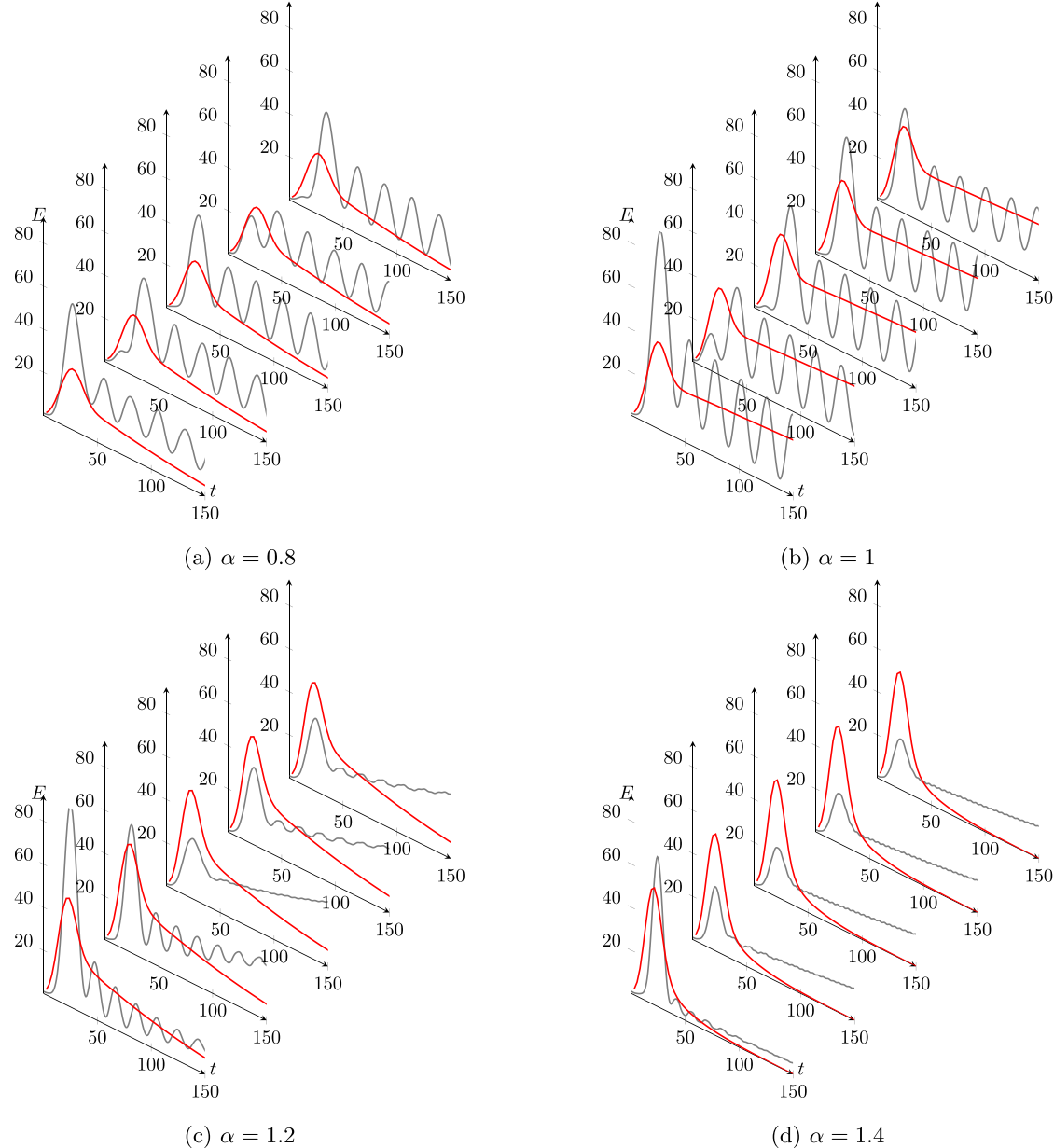
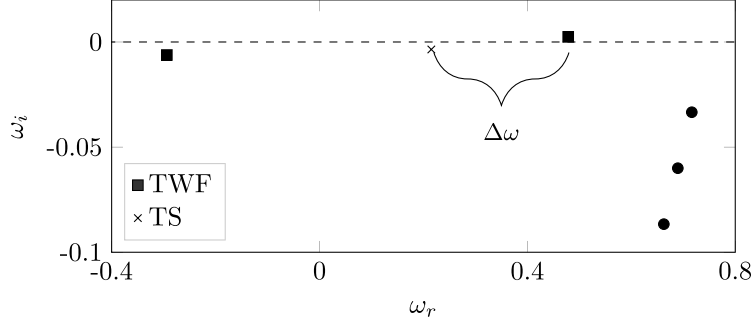
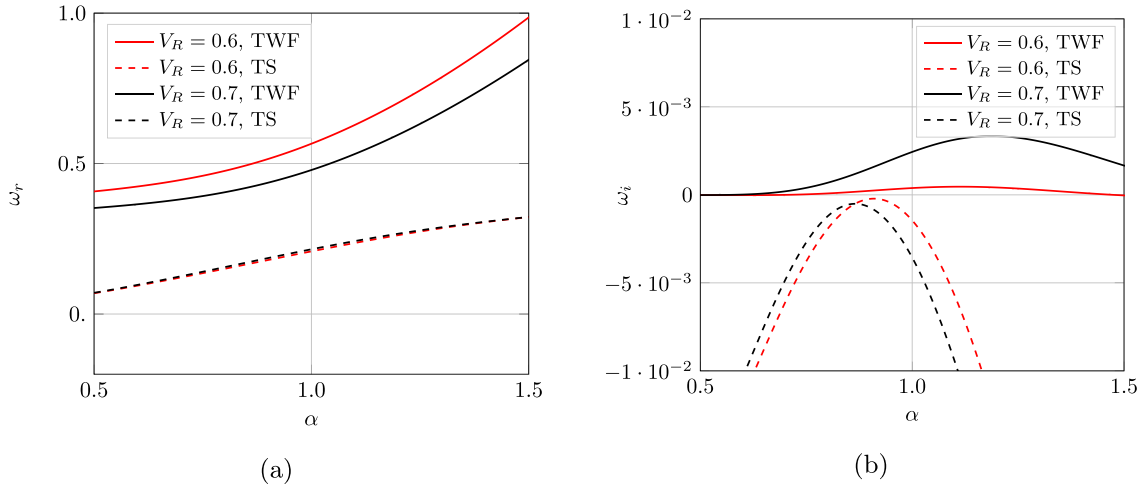
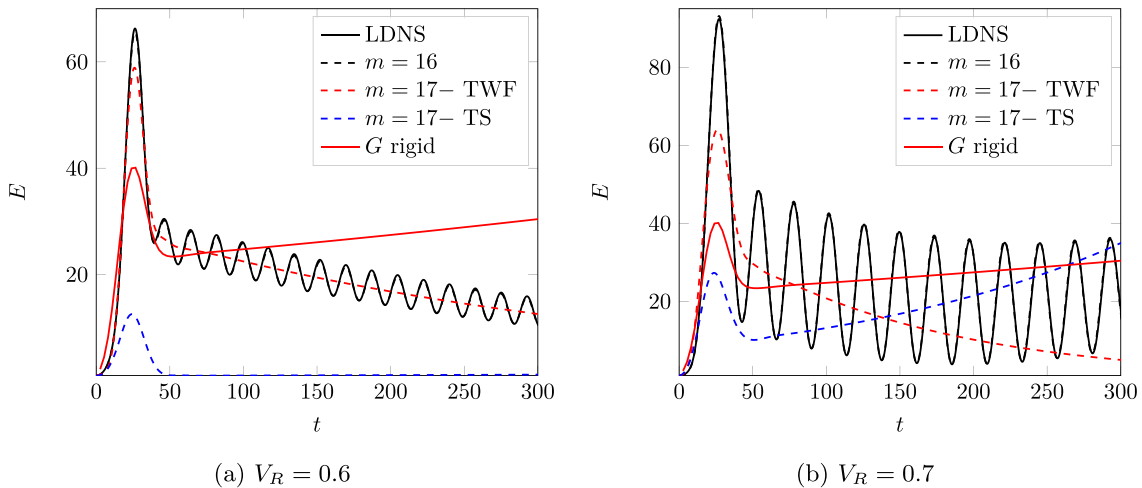


FIG. 9. Time evolution of the total energy for the optimal initial perturbation for $\tau = 26, 66, 133, 200, 266$ (from the left to the right) and $\alpha = 0.8, 1, 1.2, 1.4$. The Reynolds number is fixed to $Re = 8300$ and the reduced velocity is set to $V_R = 0.7$. In red, the envelope G for the rigid case is represented.

with a damping rate close to the TS mode. When considering the subspace where the TS mode is removed, the total energy peak damping is quite important, which indicates the strong influence of the TS mode in the dynamics. For $V_R = 0.7$, the dynamics is modified. For this value of reduced velocity and chosen parameters, the TWF mode is temporally amplified for long times, while the TS mode is damped temporally. It is consistent with the time evolution of $E(t)$ for the subsets of modes excluding either the TS mode or the TWF mode. It has as a consequence that the oscillations observed for the full system are not driven anymore by the temporal amplification rate of the TS wave. One may also note that while the dynamics for the subspace excluding the TS mode exhibits an exponential growth for $t > 50$, the inclusion of the TS mode leads to a delay of the onset of the

FIG. 10. Spectrum for $\text{Re} = 8300$, $V_R = 0.7$, and $\alpha = 1$.FIG. 11. (a) Circular frequency ω_r versus the streamwise wavenumber α and (b) temporal amplification rate ω_i versus α for TS and TWF modes and $\text{Re} = 8300$, $V_R = 0.7$.FIG. 12. Total energy evolution for the optimal initial perturbation projected onto different subsets of eigenmodes for $\text{Re} = 8300$, $\alpha = 1$, $\tau = 26$, and $V_R = 0.6, 0.7$. The envelope G for the rigid case is also reported.

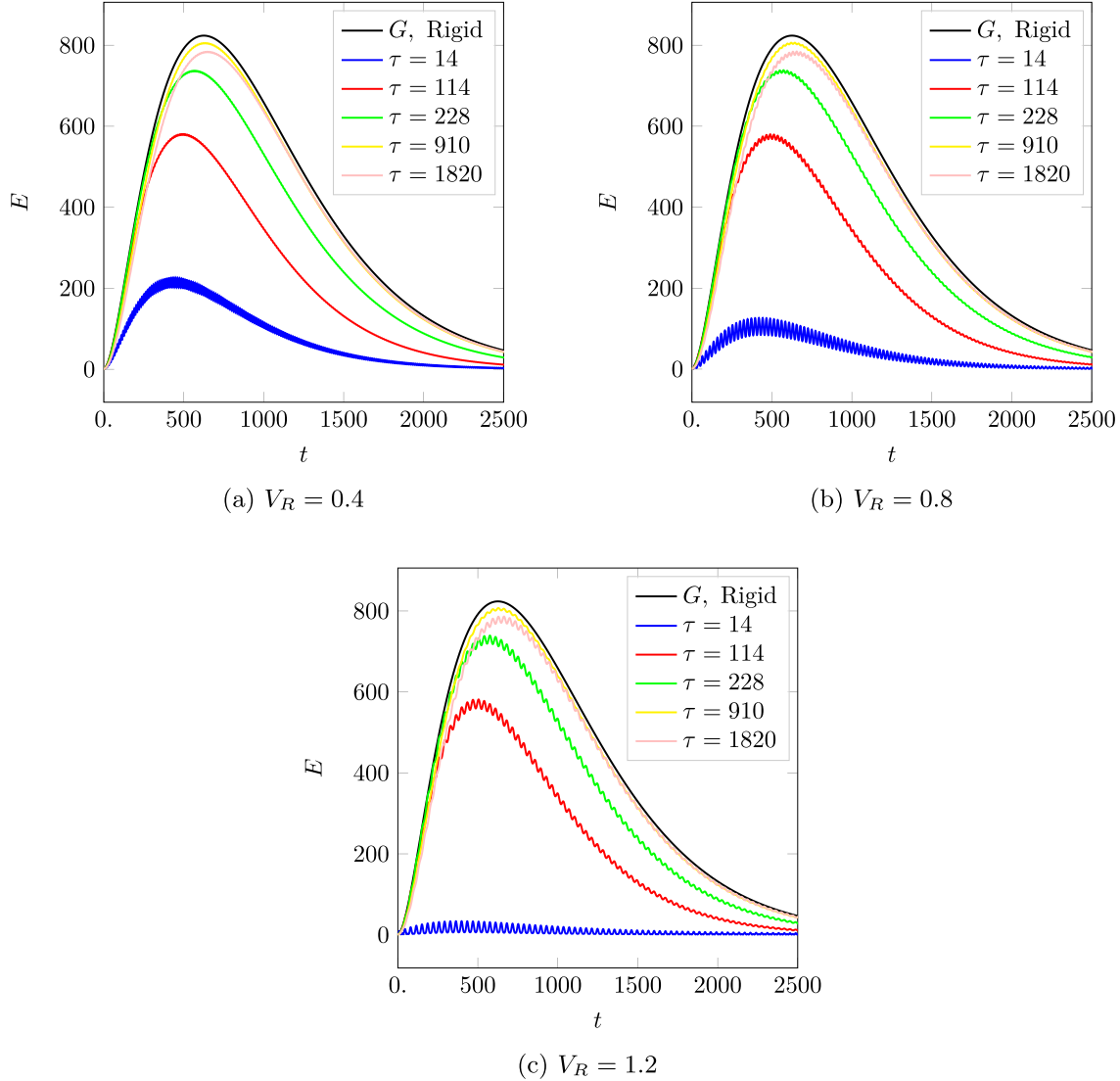


FIG. 13. Time evolution of the total energy for $\text{Re} = 6666$, $\beta = 0.5$, and $V_R = 0.4, 0.8$, and 1.2 and sinuous initial optimal perturbations computed for τ varying from 14 to 1820 . The envelope G for the rigid case is also reported.

total energy growth of the TWF mode. Finally, Fig. 12 shows that an increase of the wall compliance enhances the total energy peak for short times and amplifies the amplitude of the oscillations.

B. Optimal growth for $\alpha = 0$

In this section, we focus on the behavior of perturbations which are infinitely elongated in the streamwise direction x . The transient energy developments are shown in Figs. 13 and 14 for $\beta = 0.5$ and $\text{Re} = 6666$ for the sinuous and varicose symmetries, respectively. The reduced velocity ranges from $V_R = 0.4$ to $V_R = 1.2$ and the target time is varying from $\tau = 14$ to $\tau = 1820$. For comparison purposes, the envelope G is also represented for the rigid-wall case only. For all V_R that are considered, the energy curves exhibit a lower growth than the rigid-wall case and their time evolution features fast oscillations for both symmetries. As discussed in Refs. [17,18], the frequency beating correlates with the frequency of the TWF eigenmodes. As also observed for the two-dimensional (2D) case, the transient energy growth exhibits a larger amplification for the

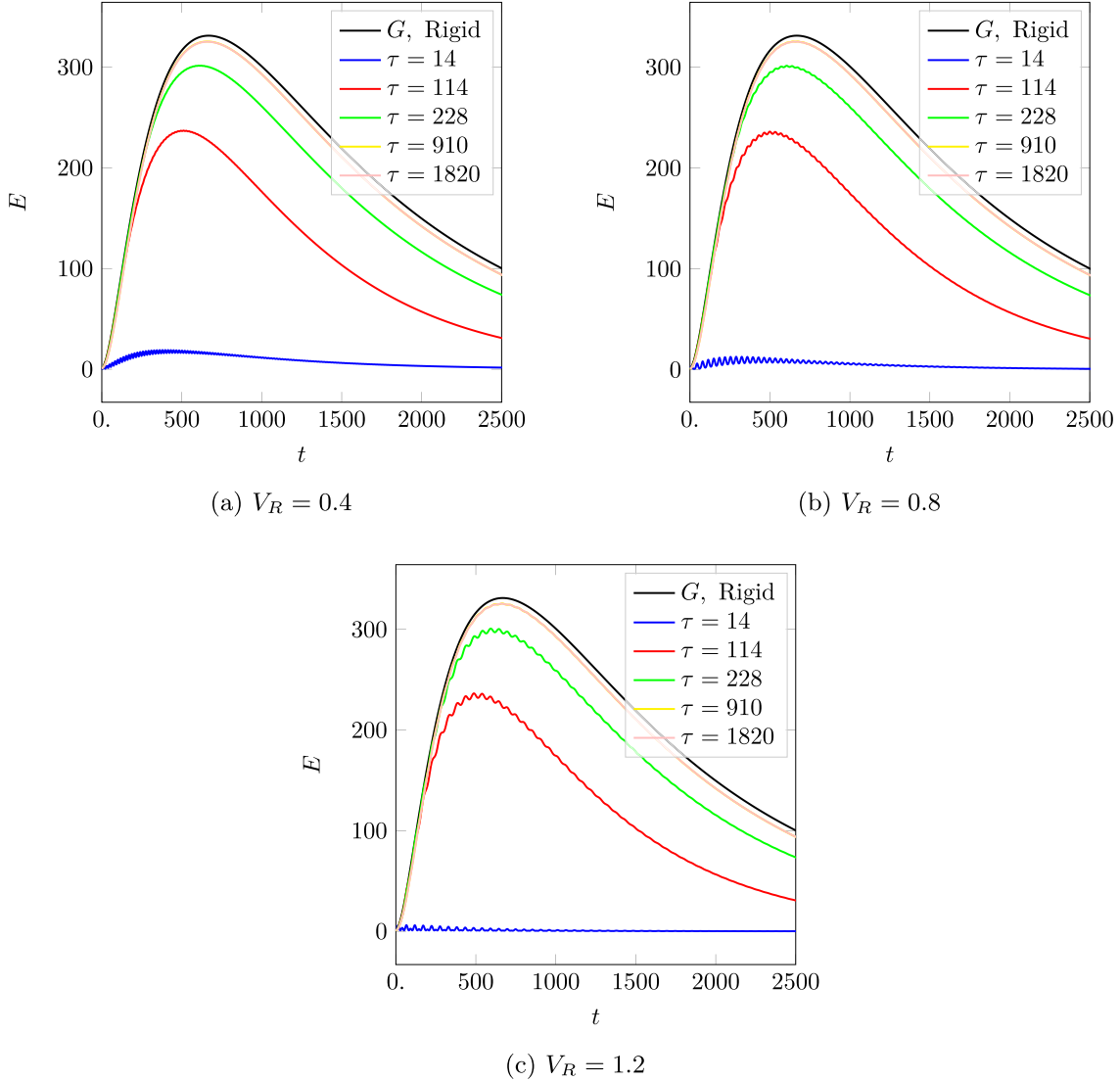


FIG. 14. Time evolution of the total energy for $\text{Re} = 6666$, $\beta = 0.5$, and $V_R = 0.4$, 0.8 , and 1.2 and varicose initial optimal perturbations computed for τ varying from 14 to 1820 . The envelope G for the rigid case is also reported.

sinuous symmetry than the varicose one. For this reason, we restrict our analysis to the sinuous configuration hereafter.

For illustration purposes, we show in Fig. 15(a) the spectrum for the same flow case and $V_R = 1.2$. The figure shows that, in addition to the rigid flow case, there are two eigenmodes that arise from the fluid-structure interaction as observed in the previous section for $\beta = 0$, i.e., two TWF modes propagating in opposite directions. The absolute value of their corresponding circular frequency is noted ω_{TWF} below. For very large V_R , Hœpffner *et al.* [17] (see discussion in section 5.2) have shown that the transient growth is mainly due to the interaction between the two TWF modes where their superposition generates a standing wave that exhibits a low-frequency process. The latter is characterized by a beating period equal to $2\pi/\omega_{\text{TWF}}$.

In Fig. 15(b), the total energy time development associated with the initial optimal perturbation obtained for $\tau = 14$ is reported. For a purely standing wave, the regular pattern is oscillating up and down; as a consequence the beating period associated with its total energy corresponds to π/ω_{TWF} .

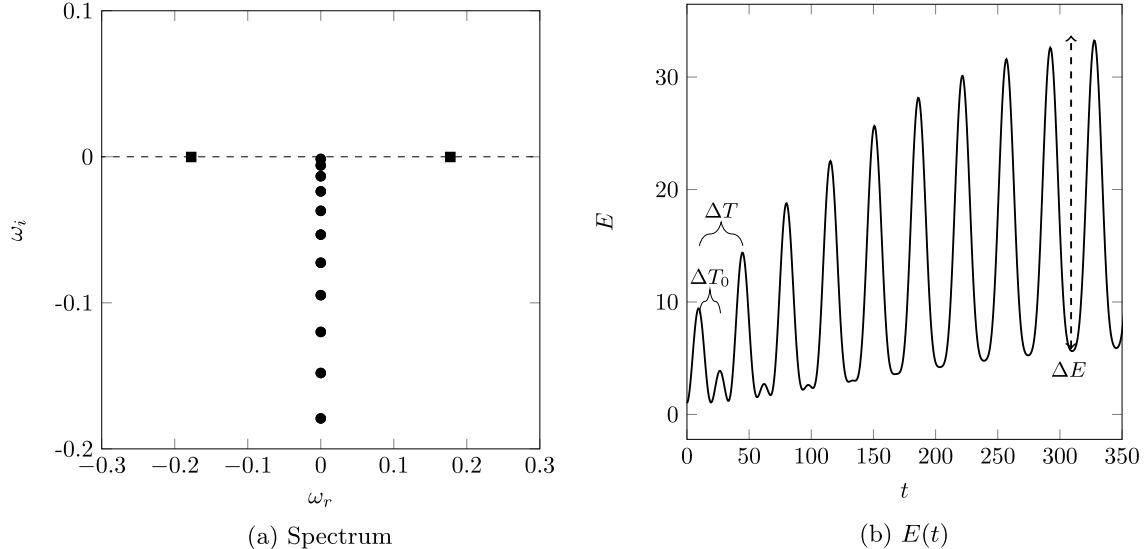


FIG. 15. (a) Spectrum at $\beta = 0.5$, $V_R = 1.2$, and $Re = 6666$. (b) Time evolution of the total energy growth for the initial optimal perturbation computed for $\tau = 14$.

For short times, this is precisely what is observed in Fig. 15(b) (noted ΔT_0). As the perturbation evolves in time, its total energy exhibits a characteristic oscillation of period $\Delta T = 2\pi/\omega_{\text{TWF}}$. It seems to indicate that, for these values of V_R , the mechanism is more complex than a simple superposition of the two TWF modes.

To further investigate the origin of the beating and the impact of the TWF modes on the transient energy growth, we project the initial perturbation on a subspace spanned by a reduced number of eigenmodes, as in the previous section. In Fig. 16(a), $E(t)$ is shown for both the complete LDNS and the reduced-order model (ROM) based on 50 eigenmodes for validation purposes. One may observe a perfect agreement between the two simulations. In the figure, the time evolution of the total energy is also represented for a subset including only the two TWF modes. It generates a standing wave with a characteristic frequency ω_{TWF} . However, its growth in time is far from matching the one given by the LDNS.

In Fig. 16(b), $E(t)$ is plotted for $m = 50$ excluding the TWF modes. The total energy evolution for the rigid-wall case is also reported. This total energy curve does not show any beating process and it displays a transient amplification comparable to the situation prevailing for rigid walls (i.e., associated with a pair of streamwise vortices which generates streaks). In particular, the growth for large times is much higher than the one including TWF modes. It indicates that the inclusion of TWF modes yields to destructive interferences that tend to damp the transient energy growth associated with streak amplification.

Let us now consider an initial perturbation resulting from the superposition of the two previous subsets of modes (i.e., the standing wave and the pair of streamwise vortices). The time evolution of its total energy is shown in Fig. 17. The figure shows that the curve almost matches the one associated with the optimal initial perturbation. It shows that the subsets of modes associated with TWF modes and the discrete branch are nearly orthogonal. Hence, the mechanism seems to be linked to a standing wave oscillating in a streaky developing flow.

The modification of the transient growth mechanism due to the TWF modes is also illustrated through cross sections of velocity components extracted at various times in Figs. 18–20.

In Fig. 18, the time evolution of the optimal perturbation obtained by LDNS is represented for a time interval equal to ΔT . The figure shows that TWF modes lead to damping the intensity of the pair of streamwise vortices during one cycle of the standing wave. It has as a consequence to annihilate the generation of streaks which is consistent with results given in Fig. 16.

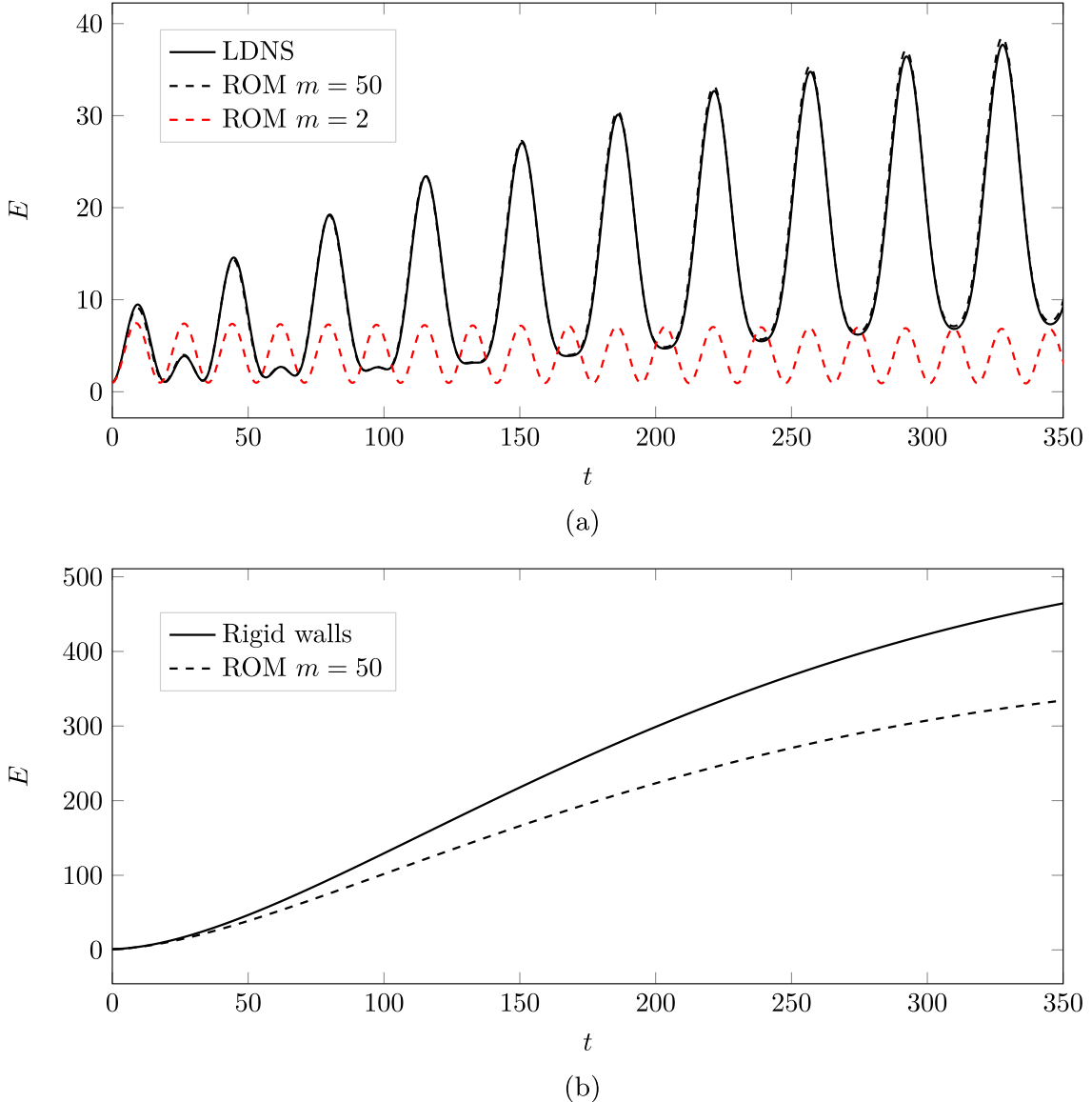


FIG. 16. Time evolutions for the total energy growth for $\beta = 0.5$, $V_R = 1.2$, $Re = 6666$, and $\tau = 14$. (a) LDNS are compared with ROMs for $m = 50$ eigenmodes and the two TWF modes (referenced as $m = 2$). (b) Total energy curves computed with the ROM for $m = 50$ excluding the TWF modes are compared to the rigid-wall case.

A similar simulation is shown in Fig. 19, where the optimal initial perturbation is projected onto the two TWF modes. A purely standing-wave behavior is observed, where the perturbation is mainly concentrated near the walls and oscillates around zero. Finally, the last configuration where the TWF modes are removed from the subset of modes is depicted in Fig. 20. The evolution of the initial perturbation exhibits the fundamental bricks of the lift-up effect, i.e., a pair of streamwise vortices that generate low- and high-speed streaks.

Then, for this value of V_R where the coupling between the fluid and compliant walls is more effective, the importance of the interactions between TWF modes and the discrete branch is crucial to fully describe the phenomenon instead of what is observed for very large values of V_R when the system is governed only by the standing wave (i.e., mainly an effect of the walls [17]).

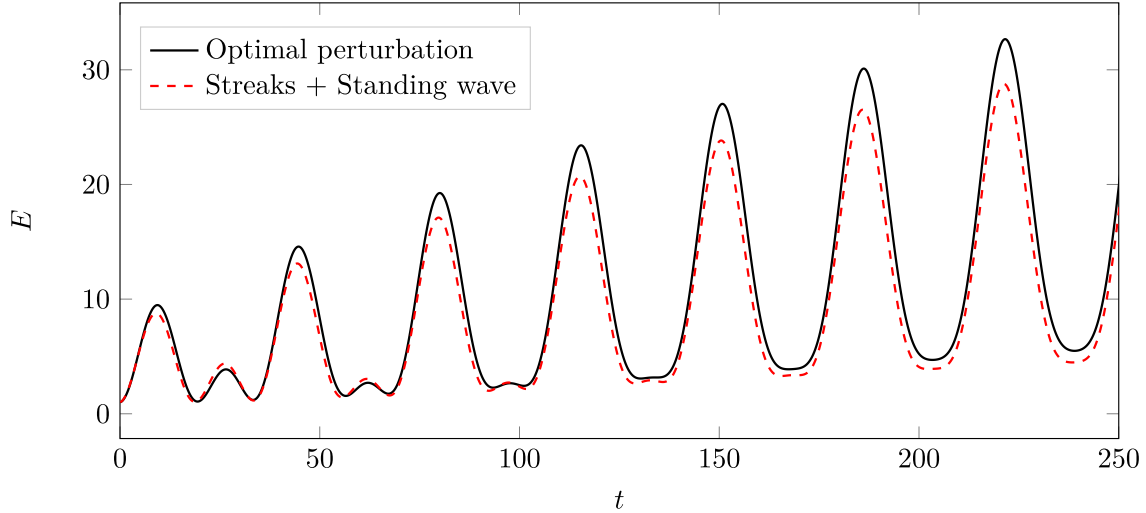


FIG. 17. Time evolutions for the total energy growth for $\beta = 0.5$, $V_R = 1.2$, $Re = 6666$, and $\tau = 14$. The evolution of $E(t)$ for the initial perturbation restricted to the summation of the pair of streamwise vortices and the standing waves is compared to $E(t)$ associated with the optimal perturbation.

Let us now characterize the influence of some parameters on these oscillations. We introduce the quantity $\Delta E(\tau, Re, V_R, \beta)$ which measures the amplitude of the oscillations [see Fig. 15(b)]. In particular, we consider hereafter, $\Delta E^M(Re, V_R, \beta) = \max_{\tau} \Delta E(\tau, Re, V_R, \beta)$. The distribution of

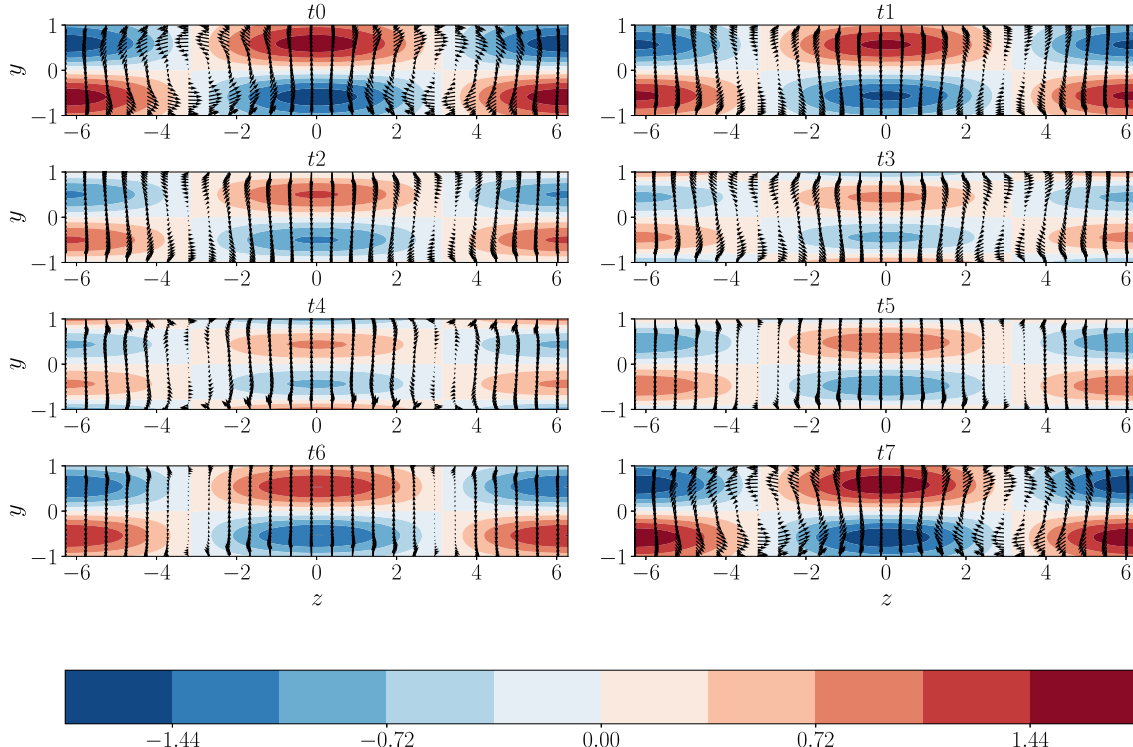


FIG. 18. Cross sections of the optimal perturbation for $\beta = 0.5$, $Re = 6666$, $V_R = 1.2$, and $\tau = 14$ in the (z, y) plane for $t_k = t_i + k/8\Delta T$ with k varying from 0 to 7 and $t_i = 8.7$. Vectors for the cross-stream components and isocontours of the streamwise velocity fields are shown.

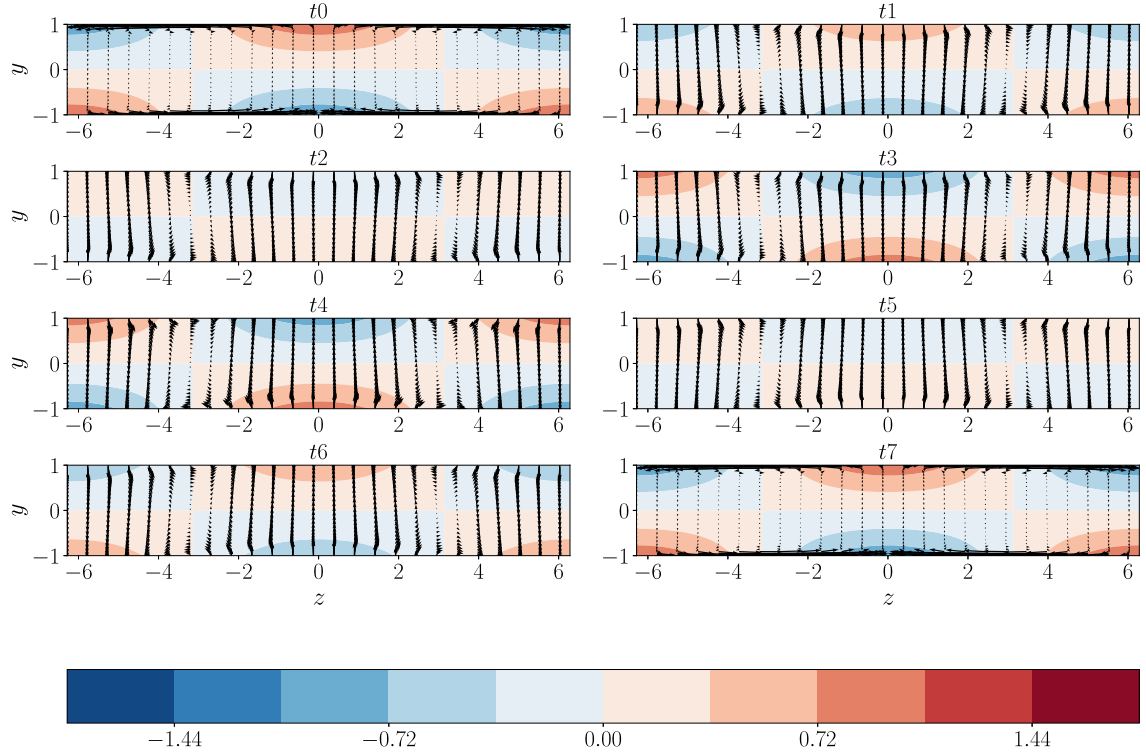


FIG. 19. Cross sections of the optimal perturbation projected onto the two TWF modes for $\beta = 0.5$, $Re = 6666$, $V_r = 1.2$, and $\tau = 14$ in the (z, y) plane for $tk = t_i + k/8\Delta T$ with k varying from 0 to 7 and $t_i = 8.7$. Vectors for the cross-stream components and isocontours of the streamwise velocity fields are shown.

ΔE^M as a function of V_R and β for $Re = 6666$ is shown in Fig. 21. The figure shows that $\Delta E^M(V_R)$ exhibits an almost linear behavior for all spanwise wavenumbers that are investigated. The behavior of the amplitude of the standing-wave oscillation is then further outlined with the parameter A obtained by using the linear approximation $\Delta E^M(Re, V_R, \beta) \approx A(Re, \beta)V_R$. The distribution of A with β for three Reynolds numbers is shown in Fig. 21(b). The figure shows that A peaks for spanwise wavenumbers much smaller than the optimal value of β for streaks and rigid walls (i.e., $\beta = 2$). Besides, the amplitude of the oscillations increases with the Reynolds number and the peak in A is reached for a spanwise wavenumber around $\beta \approx 0.7 - 0.8$ independently of Re . It may confirm the strong interplay between the streaks and the standing wave to dictate the amplitude of the oscillations for this range of V_R , since the TWF modes are mainly independent of the Reynolds number [15].

As discussed above, the frequency of the standing wave is associated with the circular frequency of the TWF mode. In Fig. 22, the distribution of the circular frequency of the TWF mode is shown as a function of V_R and β . Some computations at various Reynolds numbers confirmed that the circular frequency is not dependent on Re (not shown here). The figure shows that the standing-wave frequency is decreasing with an increase of V_R and a decrease in β . In the figure, we also report the added-mass model derived by Höpffner *et al.* [17]. In this model, the authors approximate the wall-normal flow velocity profiles with an exponential curve. Hence, by using an integration along the wall-normal direction of the momentum equation, the action of the pressure force can be associated with an added-mass effect. The equation of the circular frequency is then

$$\omega^2 = \frac{1}{m + m_a} (B\beta^4 + K),$$

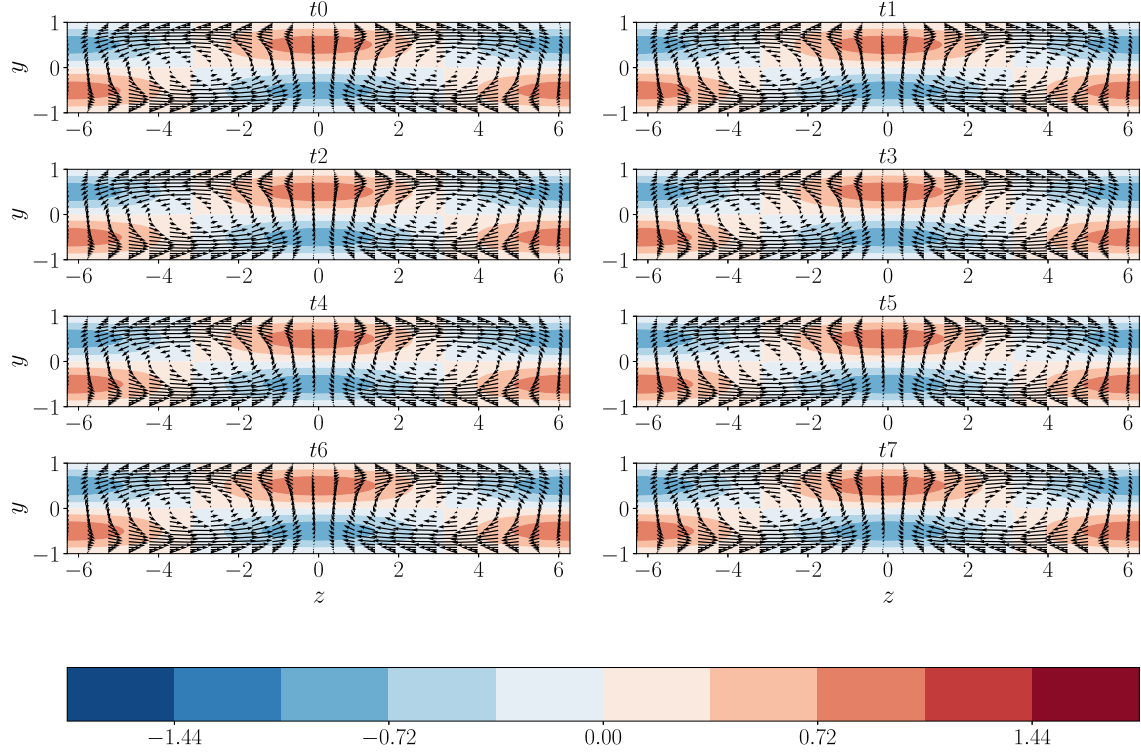


FIG. 20. Cross sections of the optimal perturbation projected onto 50 eigenmodes excluding the two TWF modes for $\beta = 0.5$, $Re = 6666$, $V_r = 1.2$, and $\tau = 14$ in the (z, y) plane for $t_k = t_i + k/8\Delta T$ with k varying from 0 to 7 and $t_i = 256$. Vectors for the cross-stream components and isocontours of the streamwise velocity fields are shown.

with $m_a = \rho h(1 - e^{-\beta})/\beta$. The corresponding values are reported as dashed lines in Fig. 22 where an almost perfect match is observed with the full computation. It validates this model also for moderate values of the reduced velocity.

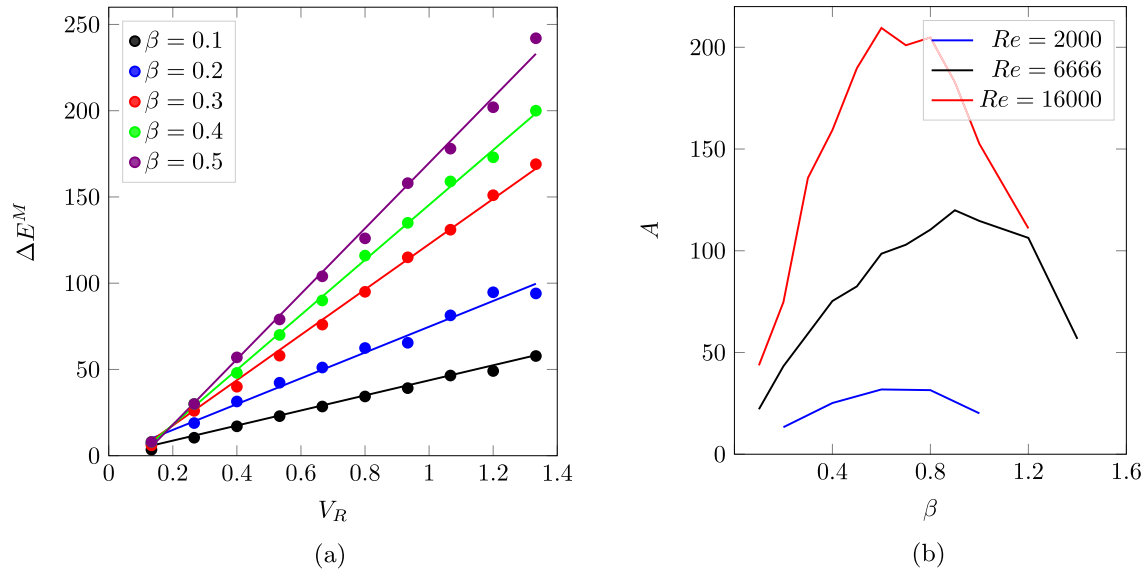


FIG. 21. Amplitude of the oscillations. (a) Distribution of ΔE^M with V_R for various β and $Re = 16000$. (b) Distribution of A as a function of β for $Re = 2000$, 6666 , and 16000 .

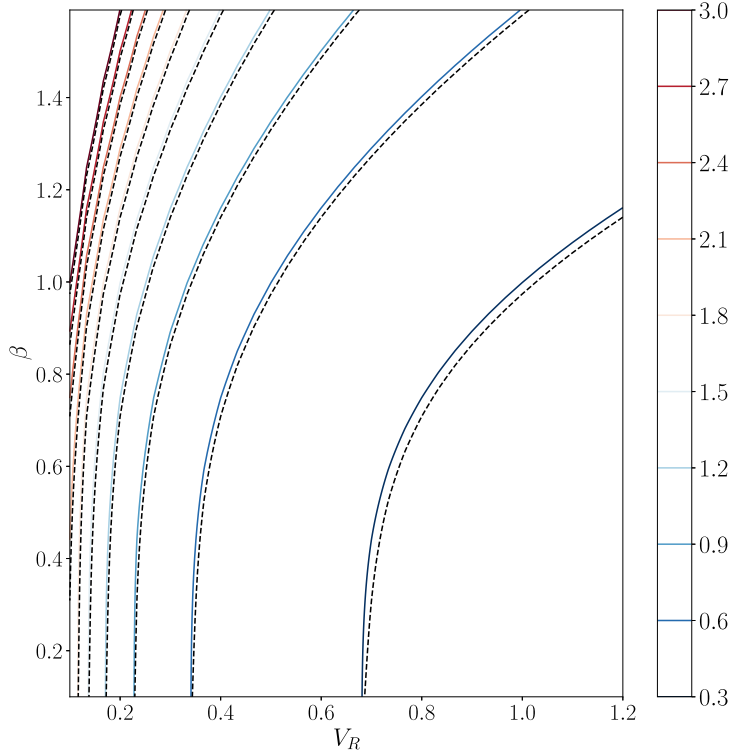


FIG. 22. Frequency of the standing wave as a function of β and V_R . Dashed lines denote the frequency computed with the added-mass model.

VII. DISCUSSION AND CONCLUSIONS

In this paper, the temporal nonmodal growth of two- and three-dimensional perturbations in channel flow over infinite compliant walls has been investigated. From the formalism point of view, we have developed a Lagrangian framework for the constrained optimization problem associated with the linearized fluid-structure interaction system. In comparison with methods used by Hœpffner *et al.* [17] and Zengl and Rist [18] for the same case, which are based on the summation of eigenmodes, the present technique is free of numerical spurious oscillations. The short-time dynamics for either the 2D case or infinitely elongated structures in the streamwise direction is mostly amplified for the sinuous configuration. As a consequence, a large part of the study concerns the sinuous symmetry of the system.

Besides this point, the two key findings from this work are the following. First, for a perturbation developing in the streamwise-wall-normal plane, the short-time dynamics is seen to be strongly modified by the flexibility of the wall. More specifically, a close inspection of the projection of the dynamics onto a subset of modes shows that the coupling between the TS and TWF modes generates strong oscillations. For some range of parameters, when the frequencies of TS and TWF modes are similar, the amplitude of the modulation reaches higher levels than the optimal gain associated with the rigid-wall case. Hence, while the wall compliance contributes to reduce the amplification of TS modes, the total energy growth for short times is enhanced, however. We hope that the present study clearly shows the important roles, in the short-time dynamics, of TS and TWF modes as well as some of the other branches of discrete modes, and could therefore be useful to design a simplified model describing the full dynamics as has been done for the asymptotic regime by Davies and Carpenter [13].

Second, it has been found that the transient dynamics for streamwise-invariant perturbations and $\mathcal{O}(1)$ values of the reduced velocity V_R is driven by the superposition of a standing wave (due to

the interaction between two oppositely propagating TWF modes) and the roll-streak dynamics. In particular, the two corresponding subsets appear nearly orthogonal to each other. The dynamics of the standing wave was clearly highlighted by Hœpffner *et al.* [17]. However, the case studied by these authors was associated with a very high value of the reduced velocity ($V_R \approx 23.5$) and for this specific case, the roll-streak dynamics was totally overwhelmed by the large temporal oscillations of the standing wave. In particular, as underlined in a recent study by Lebbal *et al.* [22], typical values of V_R for blood flow rate and arterial diameters are in the range 0.1–0.2. For aerodynamics applications, the boundary-layer flow interacting with a Kramer-type compliant wall detailed by Wiplier and Ehrenstein [11] gives a reduced velocity of approximately $V_R = 0.4$. Hence, the value used in Ref. [17] is clearly out of range of these applications.

Finally, we provide scaling laws for the amplitude of the oscillations with the Reynolds number, spanwise wave numbers, and critical reduced velocity. The variation of its characteristic frequency is also investigated. For this last point, the added-mass model derived by Hœpffner *et al.* [17] is seen to describe perfectly well the period of the oscillations but not the amplitude of the standing-wave oscillation. As discussed above, the case considered by Hœpffner *et al.* [17] is only associated with large V_R where the dynamics of the full system is mainly driven by the traveling-wave flutter modes. However, as it is shown in the present study, for moderate values of V_R , where there is a stronger interaction between streaks and the standing wave, the model fails to reproduce the full dynamics because it does not include the time evolution of streaks.

Using a range of computations, we show that the amplitude of the oscillation increases linearly with the reduced velocity V_R for a given spanwise wavenumber and Reynolds number. In addition, the optimal spanwise wavenumber leading to the maximum wave oscillation is around $\beta = 0.7$ which can be compared with $\beta = 2$ associated with the spanwise scale that maximizes the streaks amplification. In particular, for β around 0.7, the amplification of streaks is seen to be damped by the standing-wave dynamics. We then hope that these results could be a first step to extend the model derived by Hœpffner *et al.* [17] to moderate values of V_R .

The study could now be adapted without any numerical complications to time-periodic flows which are more representative of artery blood flow, in the same fashion as Pier and Schmid [29] have recently done for the rigid-wall case. The extension of the present analysis to the pipe flow case is also under current intensive scrutiny.

ACKNOWLEDGMENT

Fédération Lyonnaise de Modélisation et Sciences Numériques (FLMSN) is gratefully acknowledged for providing access to high-performance computing resources.

- [1] M. Kramer, Boundary layer stabilization by distributed damping, *J. Aerosp. Sci.* **27**, 69 (1960).
- [2] M. Gad-el-Hak, Boundary layer interactions with compliant coatings: An overview, *Appl. Mech. Rev.* **39**, 511 (1986).
- [3] P. T. Nagy, A. Szabó, and G. Paál, The effect of spanwise and streamwise elastic coating on boundary layer transition, *J. Fluids Struct.* **110**, 103521 (2022).
- [4] J. B. Grotberg and O. E. Jensen, Biofluid mechanics in flexible tubes, *Annu. Rev. Fluid Mech.* **36**, 121 (2004).
- [5] P. G. Larose and J. B. Grotberg, Flutter and long-wave instabilities in compliant channels conveying developing flows, *J. Fluid Mech.* **331**, 37 (1997).
- [6] V. Kumaran, Stability and the transition to turbulence in the flow through conduits with compliant walls, *J. Fluid Mech.* **924**, P1 (2021).
- [7] P. W. Carpenter and A. D. Garrad, The hydrodynamic stability of flow over Kramer-type compliant surfaces. Part 1. Tollmien-Schlichting instabilities, *J. Fluid Mech.* **155**, 465 (1985).

- [8] P. W. Carpenter and A. D. Garrad, The hydrodynamic stability of flow over Kramer-type compliant surfaces. Part 2. Flow-induced surface instabilities, *J. Fluid Mech.* **170**, 199 (1986).
 - [9] J. W. Miles, On the generation of surface waves by shear flows, *J. Fluid Mech.* **3**, 185 (1957).
 - [10] T. B. Benjamin, Shearing flow over a wavy boundary, *J. Fluid Mech.* **6**, 161 (1959).
 - [11] O. Wiplier and U. Ehrenstein, Numerical simulation of linear and nonlinear disturbance evolution in a boundary layer with compliant walls, *J. Fluids Struct.* **14**, 157 (2000).
 - [12] M. Malik, M. Skote, and R. Bouffanais, Growth mechanisms of perturbations in boundary layers over a compliant wall, *Phys. Rev. Fluids* **3**, 013903 (2018).
 - [13] C. Davies and P. W. Carpenter, Instabilities in a plane channel flow between compliant walls, *J. Fluid Mech.* **352**, 205 (1997).
 - [14] V. Shankar and V. Kumaran, Stability of wall modes in fluid flow past a flexible surface, *Phys. Fluids* **14**, 2324 (2002).
 - [15] S. Lebbal, F. Alizard, and B. Pier, Revisiting the linear instabilities of plane channel flow between compliant walls, *Phys. Rev. Fluids* **7**, 023903 (2022).
 - [16] D. Wang, X. Luo, Z. Liu, and P. S. Stewart, Flow-induced surface instabilities in a flexible-walled channel with a heavy wall, *J. Fluid Mech.* **956**, A1 (2023).
 - [17] J. Hoepffner, A. Bottaro, and J. Favier, Mechanisms of non-modal energy amplification in channel flow between compliant walls, *J. Fluid Mech.* **642**, 489 (2010).
 - [18] M. Zengl and U. Rist, Linear-stability investigations for flow-control experiments related to flow over compliant walls, in *Nature-Inspired Fluid Mechanics*, Notes on Numerical Fluid Mechanics and Multi-disciplinary Design Vol. 119 (Springer, Berlin, 2012), pp. 223–237.
 - [19] K. Tsigklifis and A. D. Lucey, Asymptotic stability and transient growth in pulsatile Poiseuille flow through a compliant channel, *J. Fluid Mech.* **820**, 370 (2017).
 - [20] E. de Langre, Analyse dimensionnelle en interaction fluide–structure, *Houille Blanche* **86**, 14 (2000).
 - [21] C. Davies and P. W. Carpenter, Numerical simulation of the evolution of Tollmien-Schlichting waves over finite compliant panels, *J. Fluid Mech.* **335**, 361 (1997).
 - [22] S. Lebbal, F. Alizard, and B. Pier, Linear instabilities of pulsatile plane channel flow between compliant walls, *J. Fluid Mech.* **948**, A15 (2022).
 - [23] P. J. Schmid and D. S. Henningson, *Stability and Transition in Shear Flows*, Applied Mathematical Sciences Vol. 142 (Springer, Berlin, 2001).
 - [24] F. Alizard, L. Le Penven, A. Cadiou, B. Di Pierro, and M. Buffat, Restricted optimal paths to transition in a plane Couette flow, *Eur. J. Mech. B: Fluids* **85**, 261 (2021).
 - [25] R. Peyret, *Spectral Methods for Incompressible Viscous Flow* (Springer, New York, 2002).
 - [26] L. Trefethen, *Spectral Methods in Matlab* (SIAM, Philadelphia, 2000).
 - [27] F. Alizard and D. Biau, Restricted nonlinear model for high- and low-drag events in plane channel flow, *J. Fluid Mech.* **864**, 221 (2019).
 - [28] F. Alizard and J. C. Robinet, Modeling of optimal perturbations in flat plate boundary layer using global modes: Benefits and limits, *Theor. Comput. Fluid Dyn.* **25**, 147 (2011).
 - [29] B. Pier and P. J. Schmid, Optimal energy growth in pulsatile channel and pipe flows, *J. Fluid Mech.* **926**, A11 (2021).